Metal Nanoclusters in Catalysis and Materials Science

The Issue of Size Control

Editors: B. Corain, G. Schmid and N. Toshima

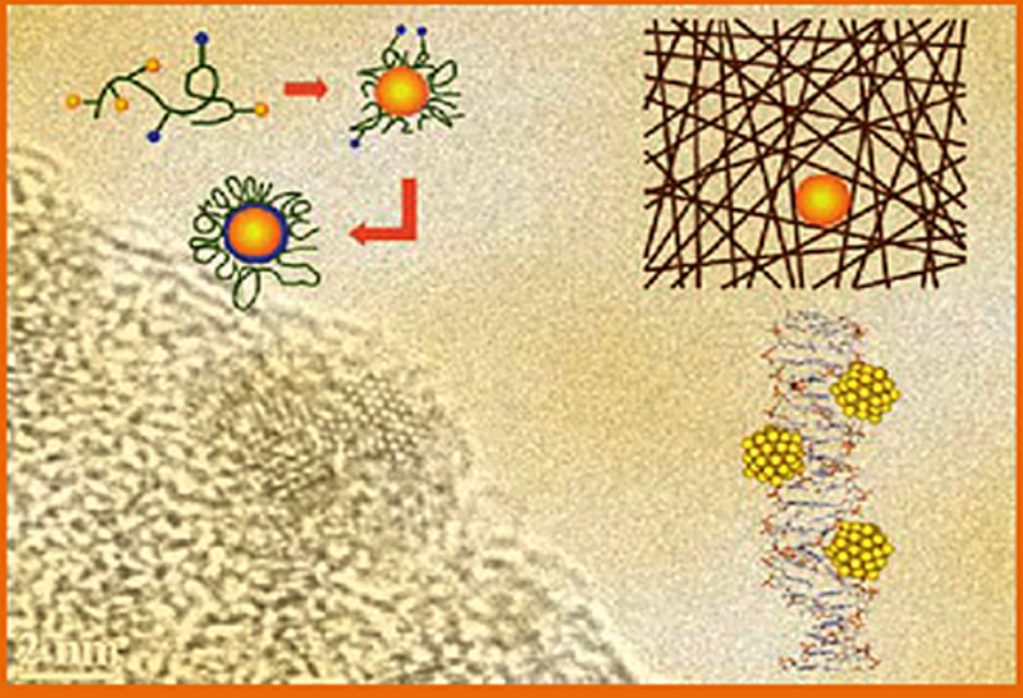

METAL NANOCLUSTERS IN CATALYSIS AND MATERIALS SCIENCE: THE ISSUE OF SIZE CONTROL

This page intentionally left blank

METAL NANOCLUSTERS IN CATALYSIS AND MATERIALS SCIENCE: THE ISSUE OF SIZE CONTROL

EDITED BY

B. CORAIN
Department of Chemical Sciences,
University of Padova, Italy

G. SCHMID
Institut für Anorganische Chemie,
University of Duisburg-Essen,
Essen, Germany

N. TOSHIMA
Department of Materials Science and
Environmental Engineering,
Yamaguchi, Japan

ELSEVIER

AMSTERDAM – BOSTON – HEIDELBERG – LONDON – NEW YORK – OXFORD
PARIS – SAN DIEGO – SAN FRANCISCO – SINGAPORE – SYDNEY – TOKYO

Elsevier
Radarweg 29, PO Box 211, 1000 AE Amsterdam, The Netherlands
Linacre House, Jordan Hill, Oxford OX2 8DP, UK

First edition 2008

Library of Congress Cataloging-in-Publication Data
A catalog record for this book is available from the Library of Congress

British Library Cataloguing in Publication Data
A catalogue record for this book is available from the British Library

ISBN: 978-0-444-53057-8

Printed and bound in The Netherlands

08 09 10 11 12 10 9 8 7 6 5 4 3 2 1

This book is dedicated to Professor Corain's 65th birthday

and

Special thanks are due to Dr. Paolo Centomo for his precious contribution to the desk-editing of the book

Foreword

Physics and chemistry of nanosized species have been the focus of attention of scientists for the last three decades. During this period of time even the name of this field of science has changed. Initially, the science has been dealing with "ultra-dispersed" particles. Later on, the scale of the species under study has been restricted to nanodimension. In fact, the properties of particles within this dimension of sizes differ from the both atoms (molecules) and bulk matter. The worldwide revolutionary developments in the science of nanosized particles became possible because of the efforts of physicists, chemists, biologists, experts in material science, and theoreticians. Later on, this field of science attracted the attention of the representatives of such fields like ethics and economy.

The chapters of the book having been put forward to the reader are related to all practically important fields of interest, discussing a wide frame of points starting from application of nanoparticles in the field of manufacture, the devices for informatics and electronics and ending with self-assembly of metal nanoparticles, their characterization and relevance to biosystems.

All known and used in practice methods of preparation of nanosized particles are discussed in more or less details in the chapters of the book. Two problems are of crucial importance to this field of chemistry. The first issue is to find driving forces, which regulate composition, size, and shape of the species. The task is to find trajectories of self-assembly to get nanosized products in different ways, starting from atoms or metal salts and ending with bulk metals. The second issue is to stabilize the product against the metal core or ligand shell reorganization, decomposition and agglomeration. Both issues are discussed in the book offering many useful approaches.

The main issue of the book is application of nanosized particles in both homogeneous and heterogeneous catalysis. A variety of reactions catalyzed by metal colloids or supported nanosized metals is discussed. The most intriguing reaction seems to be ethane hydrogenolysis catalyzed by Pt clusters on porous carrier and studied by G. A. Somorjai and his group. Another challenging observation by this group is shape isomerization of Pt metal particles affected by the addition of silver ions.

The book is addressed to a wide circle of chemistry, physics, and biology reading public. From the first line itself, this is the book for scientists interested in the syntheses, characterization, and different fields of application of nanosized species.

Ilya I. Moiseev
(Russian Academy of Sciences, Moscow)

Editorial

Metal nanoclusters have been wittily called "strange morsels of matter" by R. Pool in an interesting note that appeared in *Science* in 1990. We agree with him in that metal nanoclusters are to be considered as links between bulky and molecular matter and insofar they represent a unique kind of species. Depending on the temperature and especially on the applied physical method we use to investigate them, they may still behave as a piece of metal or as a molecular-like system that has to be described by means of quantum mechanical rules rather than with those valid for classical physics. In the size regime below ~2 nm quantum properties dominate. Nanoclusters of that size indeed exhibit discrete electronic energy levels like atoms do. This is why they are also called artificial big atoms. It can be foreseen that nanoclusters of that size will play a decisive role in future nanoelectronic devices as single electron switches or transistors. Furthermore, metal nanoclusters begin to significantly influence developments in medicine. Due to their size, they can interact with cell components that are also located on the nanoscale. Novel discoveries in diagnosis as well as in therapy foreshadow chances that never existed before. So, metal nanoclusters are not only fascinating scientific objects, but also applicable in many important practical fields.

In fact, metal nanoclusters are no longer only "strange morsels of matter" but they are designable key components of most important research- and industry-relevant catalysts in chemical processing. In supported metal (0)-based metal catalysts, the metal nanoclusters size is obviously related to the catalyst activity in that this feature relates to specific active surface area. However, for structure-sensitive reactions, metal nanoclusters size (and even shape) relates also to catalytic chemoselectivity. In this specific connection, a paradigmatic example is the remarkable ability of nanostructured Au^0 to catalyse the oxidation of CO to CO_2 with dioxygen in the presence of large excess of dihydrogen only if metal nanoclusters size is close to 3 nm.

Most metal nanoclusters employed in catalytic applications are made up of one metal only. Indeed they may be bi- and polymetallic clusters. In the conventional metal catalysts, bi- and polymetallic nanoclusters or nanoparticles are supported on inorganic supports. The second and third metal can exert a strong effect on activity and selectivity of metal catalysts albeit this effect is not completely clarified. Therefore, the design of polymetallic catalysts is not yet well established, although engineers are eager for it. Now, scientists can control the size and, to some extent, the structure of bimetallic nanoclusters. For example, bimetallic nanoclusters with a core/shell structure are very popular now. If the total size of bimetallic clusters is less than 2 nm, the core could be surrounded by the only one-atom-layered shell. The catalytic property of active site in the shell element can be easily altered by core elements. This will provide a new concept for the catalyst design. Nanotechnology can also provide a tool to design supported catalysts by combination of metal nanoclusters with nanoparticles of inorganic metal oxide. Now, after a long history as metal colloids since Faraday's times, metal nanoclusters have gained a definite position in science and technology.

This book is aimed at being a reference book for all scientists who need to play with the physics, the structure and the chemistry of metal nanoclusters. Its content is organised in two parts in such a way that it may be considered as a textbook (*General Aspects*, Part I) and as a handbook (*Methodologies*, Part II). In the name of the numerous scientists who contributed chapters to the book, we do hope that its presence in the bookshelves of many scientists all over the world for a number of years ahead, will be reassuring for the design, synthesis and characterisation of many useful "strange morsels of matter".

Benedetto Corain Günter Schmid Naoki Toshima

This page intentionally left blank

Contents

This page intentionally left blank

GENERAL ASPECTS

This page intentionally left blank

CHAPTER 1

General Features of Metal Nanoparticles Physics and Chemistry

Günter Schmid

Institute of Inorganic Chemistry, University of Duisburg-Essen, Essen, Germany

1. Introduction

Metal clusters in a classical sense are considered to consist of at least three up to a dozen or more atoms, usually coordinated by ligand molecules like in classical complex chemistry. Typical textbook examples are oligonuclear metal carbonyls like $Co_4(CO)_{12}$ or $Rh_6(CO)_{16}$. Their size usually is <1 nm. Such clusters follow elementary electronic counting rules and exhibit typical molecular behaviour. In contrast, nanoclusters reach a size >1 nm and can, depending on the number of metal atoms they consist of, in many cases be considered as borderline case between molecule and bulk. A discussion of this significant state will follow later in Chapter 2. The expression "nanocluster" is in principle synonymous with the frequently used term "nanoparticle" and the more historical expression "colloid". Nanoclusters or nanoparticles must no longer follow exact stoichiometric compositions. Particles, consisting of dozens or hundreds of atoms may statistically deviate from ideal chemical formula. The deviations rise with increasing numbers of atoms. Also the classical metal colloids, in case of gold known since centuries, typically deviate in size by at least $\pm 10\%$. They also belong to what we now call nanoclusters or nanoparticles as do such small particles as the well-known Au_{55} nanocluster [1] with its well-defined stoichiometry.

What makes metal nanoclusters scientifically so interesting? The answer is that they, in many respects, no longer follow classical physical laws as all bulk materials do, but are correctly to be considered by means of quantum mechanics. This is not only valid for metals. In principle any other solid or in some cases even liquid material exhibit so-called "nano-effects" when reaching a critical size. Nanoscience and nanotechnology are based on those effects. In the course of only 1–2 decades nanosciences and nanotechnology have developed to such an extent that our daily life already is and will be increasingly influenced in a way that cannot be compared with any other technological development in mankind's history [2]. A few examples will help to better understand what is meant.

The melting point of a solid element or a chemical compound in a classical sense is a constant under distinct conditions. Not so, on the nanoscale! For instance, the melting point of bulk gold is known to be 1064 °C. However, gold nanoparticles below ca. 20 nm in diameter begin slowly to melt at lower temperatures. The melting point then dramatically falls down at a size of 3–4 nm [3]. For a 1.5 nm gold nanocluster it is at ca. 500 °C as can also be seen from Figure 1.

The reason for this phenomenon can simply be seen in the fact that the percentage of surface atoms becomes larger the smaller the particles are. In 1.5 nm particles the surface atoms dominate with ca. 80% of the total number of atoms. Surface atoms are less nicely coordinated than inner atoms and therefore are easily mobilized with increasing temperatures and so contribute to a lowered melting point.

"Nano-water", i.e. water in narrow pores and capillaries, can have melting points down to −60 °C! This is an important effect, since it helps to avoid a yearly destruction of stones, rocks and especially of concrete by frost, at least in northern parts of the world. Those materials are usually full of water containing micro- and nanopores.

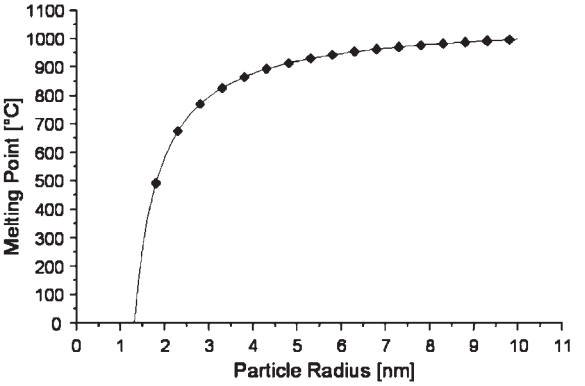

Figure 1. Melting point behaviour of gold nanoparticles.

Metal Nanoclusters in Catalysis and Materials Science: The Issue of Size Control
Edited by B. Corain, G. Schmid and N. Toshima

Relativistic effects result if electrons nearby very heavy atomic nuclei are accelerated to such an extent that Einstein's famous theory of relativity begins to take effect, i.e. the accelerated electrons (usually the s-electrons) gain on weight. This changes the energy difference between s- and d-band: the energy of the s-orbitals is decreasing, whereas as secondary effect that of the d-orbitals is increasing [4]. Altogether, the energy difference becomes smaller and the light absorption shifts to blue with the consequence of the remaining yellow colour. If bulk gold is downsized to ca. 50 nm, the yellow colour spontaneously disappears and turns to blue, further reduction results in purple and finally bright red colours. Although the theory of relativity is of course still valid, another effect dominates: the appearance of plasmon resonances. Plasmon resonances, quantitatively described by the Mie theory, are caused by the interaction of light with the confined electron gas in such small particles, resulting in a collective electron oscillation. The frequency of this oscillation depends on the kind of metal, the size of the corresponding particles, their shape and the surrounding medium. Figure 2 impressively expresses these facts stated before.

2. From Bulk Metals to Quantum Dots

The electronic situation in bulk metals is characterized by the existence of energy bands. They result from the combination of an infinite number of energetically very similar orbitals. The valence band contains the relevant valence electrons, in case of transition metals these are usually s- and d- electrons. The conduction band of metals overlaps to some extent with the valence band and so becomes partially occupied with electrons. These electrons are finally responsible for the electric conductivity of metals. In contrast to the electrons in a filled band, those in the conduction band are fully mobile and make conductivity possible. In semiconductors, valence and conduction bands are separated by a material-specific energy gap, which is too large in insulators to be surmounted under reasonable conditions. If a metal particle is continuously reduced in size, the overlap of valence bond and conduction band is some when disappearing, resulting in a situation to be compared with that in a semiconductor. Further reduction will end up in a situation where the bands turn into more or less discrete energy levels. At this step, the bulk properties of the particles disappear to be substituted to that of a "quantum dot", following quantum mechanical rules. Finally, the development ends up in the formation of a typical molecular situation. Figure 3 elucidates the electronic development of a quantum dot from the bulk situation.

In the following, the electronic changes from the bulk state to a quantum dot shall be discussed in more detail [5].

A three-dimensional (3D) piece of metal can be considered as a crystal of infinite extension in the directions x, y and z with standing waves with the wave numbers k_x, k_y and k_z, each being occupied with two electrons as a maximum. In a piece of bulk metal the energy differences $\Delta k_{x,y,z}$ are so small that $\Delta \rightarrow 0$, identical with quasi-free continuously distributed electrons. Since the energy of free electrons varies with the square of the wave numbers, its dependence on k describes a parabola. Figure 4a shows these relations,

Figure 2. The colour of metallic gold and of gold nanoparticles in ruby glass.

whereas Figure 4b shows the progress of the density of states for free electrons in a 3D bulk system. The energies are quasi-continuous. Their density varies with $\sqrt{E}$.

In an experiment of thoughts the 3D piece of metal shall be reduced in the z-direction to only a few nanometres, comparable with the electronic de Broglie wavelength ($d_z = \lambda$), whereas in x- and y-direction it is kept infinite: a 2D "quantum well" is formed. Compared with the former 3D situation, the electrons in x-and y-direction can still freely move in these directions, but not in the z-direction. Electrons in this direction are confined like in a box. The states are quantized, whereas in x- and y-direction the situation does not differ from that in the 3D case. Figure 5a shows the quantized situation in z-direction with well-defined Δk values $n = 1$, 2, etc., and Figure 5b indicates the Δk values close to 0.

The quasi-continuous curve of the density of states in the 3D case now has a staircase characteristic with discrete energy levels in z-direction.

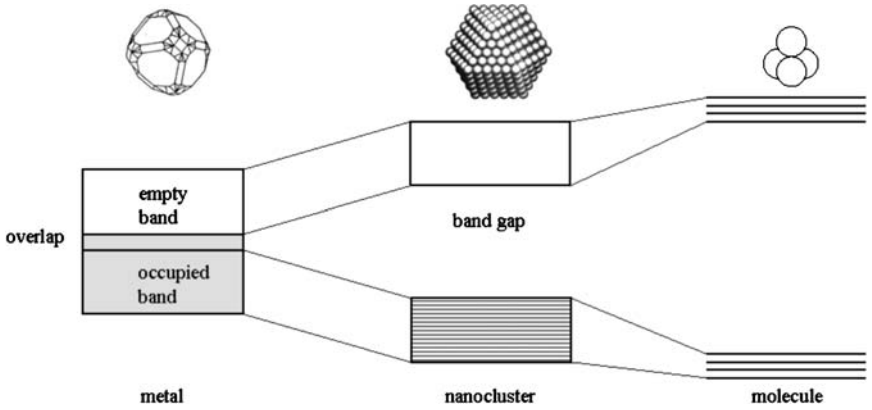

Figure 3. Formation of discrete electronic energy levels on the way from bulk to molecule.

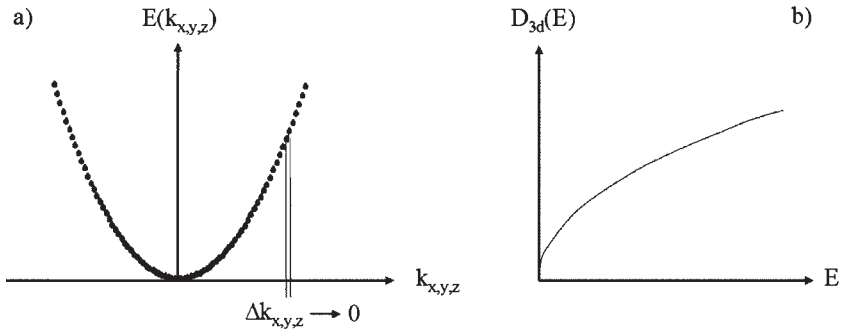

Figure 4. Electrons in a three-dimensional bulk metal. (a) The energy of electrons varies with the square of the wave number. Dependence on k is described by a parabola. (b) Density of states for free electrons is quasi-continuous. (Reprinted from Ref. [5], © 2004, with permission from Wiley-VCH.)

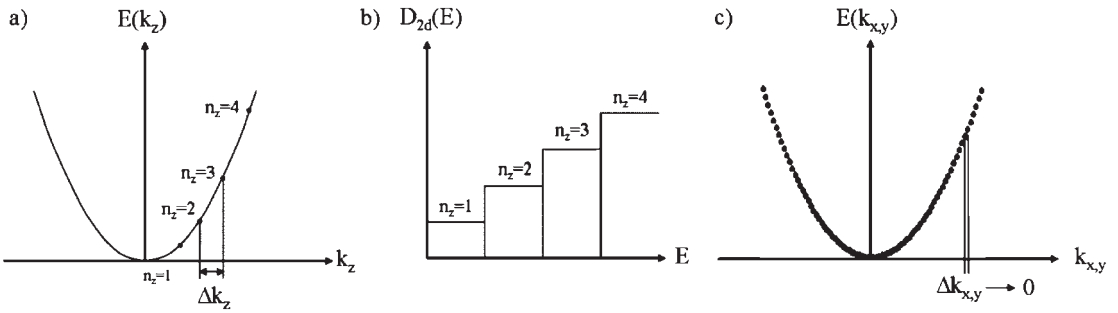

Figure 5. Electrons in a two-dimensional system. (a) The z-direction is reduced to an extension corresponding to the de Broglie wavelength of free electrons resulting in discrete Δk values. (b) Instead of a quasi-continuous situation, a so-called staircase results. (c) In x- and y-direction the situation corresponds to that in Figure 4a. (Reprinted from Ref. [5], © 2004, with permission from Wiley-VCH.)

The intellectual construction of a one-dimensional (1D) system by additional reduction of the y-direction to a few nanometres, results in the curves shown in Figures 6a–c.

The Δk values in y- and z-direction are quantized, but not in x-direction, resulting in a parabola with $\Delta k_x \rightarrow 0$. The density-of-states within the "quantum wire" results in hyperbolas for each individual k_y- and k_z-state.

The final situation and the goal of this consideration is the generation of a zero-dimensional (0D) quantum dot. All three directions are now containing confined electrons. The Δk values in x-, y- and z-direction are properly separated from each other and only discrete energy levels are allowed (Figure 7a). In the density of states diagram (Figure 7b) the situation is mirrored.

3. How to Find Quantum Confined Particles

The above theoretical derivation of a quantum dot does not spare to experimentally find and characterize

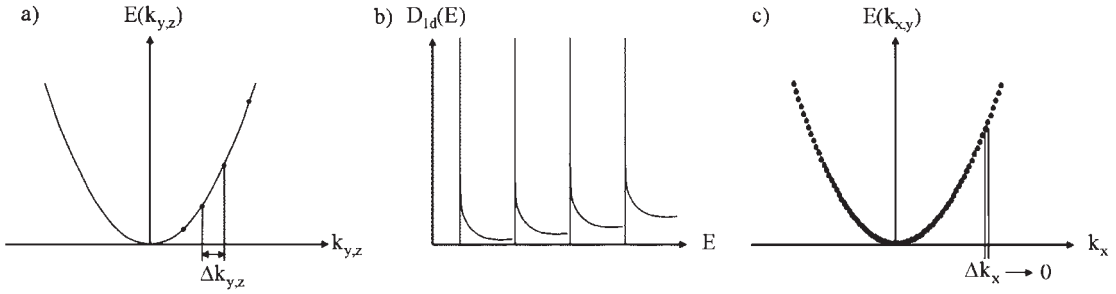

Figure 6. Electrons in a one-dimensional system. (a) Finite Δk values are now existent for y and z. (b) The density of states along the kx-axes corresponds to hyperbolas. (c) The quasi-continuous situation is only given in x-direction. (Reprinted from Ref. [5], © 2004, with permission from Wiley-VCH.)

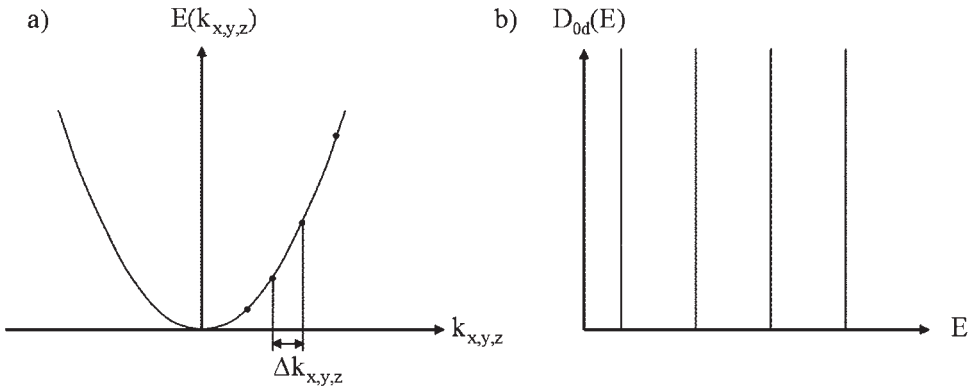

Figure 7. Electronic situation in a zero-dimensional system. (a) Only discrete energy levels are allowed. (b) The density of states is described by discrete energy levels to be occupied by individual electrons. (Reprinted from Ref. [5], © 2004, with permission from Wiley-VCH.)

nanoparticles having size-quantized properties. The generation of nanoparticles will not be treated in this chapter, but will be part of Chapter 2. In the following it shall be demonstrated how the transition from bulk to molecule via the typical quantum-sized situation can be established. The dominant question is: how small or, – coming from the atomic side – how large a metal particle has to be to make quantum size behaviour measurable? Before describing some physical techniques which might give answers, some general features shall be considered.

The chance to observe an electronic confinement in a 0D nanoparticle depends on several conditions:

- the applied physical method,
- the temperature,
- the kind of metal and
- the medium surrounding the nanoparticle.

Different techniques to investigate an existing particle give different answers. Among others, it is a significant point if a quantum dot is investigated individually or as part of an assembly with contacts between each other. Furthermore, it is the characteristic of a physical method to give a method-dependent answer, as will be shown below. One single method will usually not be sufficient to answer all questions. Rather, it is the combination of as many methods as possible to get a satisfying knowledge about the real electronic inner life of a metal nanoparticle.

The temperature of investigation is a most important variable. In some cases it is strictly related with the method applied, in others not. In any case, the temperature has a significant influence on the electronic behaviour of a nanoparticle. Usually, investigations at low temperatures allow significantly more detailed answers than those at elevated temperatures.

The nature of the element under investigation is certainly of some relevance, but not decisive for related elements, say noble metals. On the other hand, it is still not yet known how far the properties of two metal nanoparticles of different elements, but identical size really differ with respect to their quantum size behaviour.

Finally, it is of significant importance what the surrounding medium of a nanocluster consists of with respect to the cluster's electronic properties. A bare cluster in vacuum will behave characteristically different from the same particle that is chemically linked to other atoms, molecules etc. In this context, it must clearly be stated that all results described in the following relate to so-called ligand-protected nanoclusters for several reasons. First of all, it is the chemical synthetic approach to generate defined nanoclusters. Wet-chemical procedures demand for the existence of protecting ligand shells consisting of appropriate molecules (ligands) in order to prevent

coalescence between the particles. Furthermore, such ligand-stabilized nanoclusters can usually be isolated in solid state, but can be re-dissolved in appropriate solvents. However, chemically linked molecules on the surface of nanoparticles influence essentially the corresponding surface atoms, but to some extent also inner atoms, as long as the particles are not too large. So, for practical reasons, the following discussions will mainly relate to ligand-protected particles, not to bare ones. The properties of bare nanoparticles would significantly differ from ligand-protected ones. Furthermore, the nature of the protecting molecules, atoms etc. determine the kind of chemical bond to the surface metal atoms which can be very much different, reaching from weak electrostatic interactions up to covalent bonds.

3.1. Plasmon Resonances of Metal Nanoparticles

As already briefly mentioned in the introduction, some metals exhibit so-called plasmon resonances in the UV–visible spectra, attributed to the interaction of electromagnetic waves (visible light) and the confined electron gas, if a critical size on the nanoscale is reached. The process is sketched in a simplified manner in Figure 8.

Quantitatively the phenomenon is described by the Mie theory [6,7]. For instance, ca. 20 nm particles of gold, silver and copper in water show plasmon signals at 520, 385 and 560 nm, respectively [8]. Measurements are usually performed in dilute solutions or glasses. The colour of the famous ruby glass is due to the presence of such gold nanoparticles (colloids). The wavelength of the absorption maximum depends for a distinct metal on size and shape of the particles as well as of the surrounding medium. Elongated particles may show two maxima if the aspect ratio is $\geqslant 4$. The longitudinal resonance signal at an aspect ratio of 4 in case of gold shifts from 520 to 770 nm. As already discussed generally above, the nature of the protecting medium also significantly influences the wavelength of plasmon resonances. In case of different solvents it is their refraction index which determines the degree of the shift. Increasing refraction indices cause increasing wave numbers [8].

The appearance of a plasmon resonance is strictly related to a distinct size of the corresponding metal, based on the presence of a confined electron gas that interacts with light and so results in typical colours. Is there also a minimum size where plasmon resonance is no longer possible? In any case this must happen if a particle reaches a typical molecular status. There are no longer freely mobile electrons, but only those localized in defined chemical bonds, as is the case for instance in $[Au_{13}(dppm)_6]^{4+}$ (dppm = $Ph_2PCH_2CH_2PPh_2$) [9,10]. However, where is the transition? The existing examples indicate in case of gold that it occurs between ca. 2 and 1.4 nm [11]. The nanocluster $Au_{55}(PPh_3)_{12}Cl_6$ [12,13] with its 1.4 nm gold core no longer shows a plasmon resonance. The reason is to be seen in the strong size-dependence of the 5d–6sp-interband transition and in addition in charge-transfer effects between the nanocluster and its ligands.

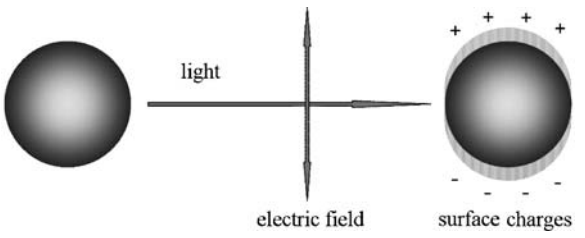

Figure 8. Illustration of the interaction visible light and the confined electron gas of a metal nanoparticle, resulting in a plasmon resonance.

From these examples we may conclude that, as was indicated above, the question of having or not having a quantum confinement in a distinct particle allows different answers. All we may notice in this case is that gold, silver or copper particles of a distinct size must possess confined electron gases, but nanoparticles being too small to show a plasmon resonance cannot be excluded as having no confined electrons. On the contrary, as will be shown later by means of the Au_{55} cluster.

3.2. Size-Dependent Electronic Relaxation

A rather unusual, but nevertheless valuable method to learn more about the transition from bulk to molecule was applied by studying the relaxation behaviour of excited electrons in different gold and platinum particles [14]. The relaxation behaviour of excited electrons in metal particles depends on two fundamental effects: one is the influence of particle size on the electron–phonon coupling, the other one is the size-dependent surface collision rate of electrons. The electron–phonon coupling will be weakened with decreasing particle size due to the reduced overlap between the electron oscillation frequencies and the phonon frequencies. This effect slows down the relaxation. The surface collision rate increases with decreasing particle size, supporting electronic relaxation. So, the two events are of opposite influence on the electronic relaxation behaviour. The smaller the particle, the more dominant the electronic collision becomes. This method is indeed perfectly suited to observe the transition from bulk to molecule. The excitation of the electrons was performed by ≈ 200 fs laser pulses with a second laser pulse for monitoring the population of excited electrons. Three different gold nanoparticles in aqueous solution have been investigated: 15, 1.4 nm (as $Au_{55}(Ph_2PC_6H_4SO_3Na)_{12}Cl_6$) and 0.7 nm (as $Au_{13}(dppmH)_6(NO_3)_4$ [10]). As can be seen from Figure 9, the relaxation behaviour depends characteristically from the particle's size.

The step from 15 to 1.4 nm indicates an increase of the relaxation rate due to a dominant surface effect on the smaller Au_{55} clusters. This finding agrees with a quantum–kinetic model, predicting a remarkable weakening of the electron–phonon coupling going from bulk to small particles [15]. However, the drastic slow-down of relaxation from the 1.4 nm nanocluster to the 0.7 nm Au_{13} species is of great importance. It indicates clearly the molecular character of the Au_{13} cluster without mobile electrons that can be excited like those in bulk or nanoclusters. This result, on the other hand clearly indicates that the transition from bulk to molecule in case of gold happens between Au_{55} and Au_{13}, always considering that the particles are enveloped in a shell of molecules.

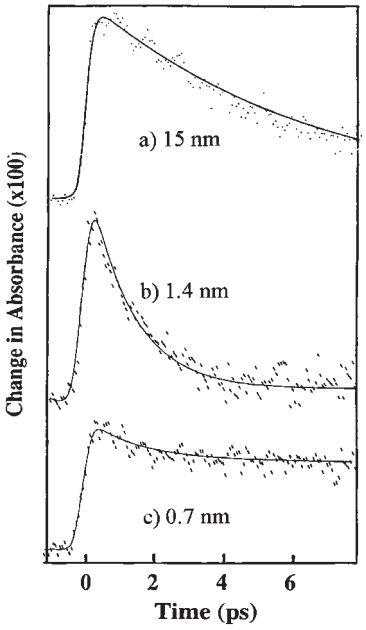

Figure 9. The relaxation behaviour of excited electrons in gold nanoparticles of different size.

Similar results could be gained with platinum particles of 35 and 3 nm in diameter. The difference in the relaxation rates corresponds qualitatively with that of 15 and 1.4 nm gold particles. Due to the lack of smaller Pt clusters the transition to the molecular state could not be studied.

A comparison of the results in Sections 3.1 and 3.2 describing two very different methods implies that the 1.4 nm size obviously plays a significant role. In the plasmon studies it is the first in the row of known particles that does not show a resonance with visible light, in case of the presented relaxation behaviour it represents the species just one step before the molecular state.

3.3. Mößbauer Spectroscopy

The Mößbauer effect bases on the recoilless nuclear resonance of γ-quanta. A γ-quantum emitted at the transition of an excited nuclear state (source) into the ground state can be absorbed by a nucleus in the same ground state (absorber) under the condition that emission and absorption occur recoilless. Otherwise there is no resonance possible. In case of unequal energy difference between excited state and ground state of source and absorber the lacking resonance conditions can be reached by the addition of Doppler energy to the γ-quantum. This can be performed by moving the source; 1 mm s^{-1} results in 5×10^{-8} eV of additional energy. The Mößbauer spectroscopy measures the nuclear resonance in dependence of the speed of the source. Since the energy levels of the nuclear states are remarkably influenced by the chemical environment, Mößbauer spectroscopy is a valuable tool to get information on the interaction between the nucleus of the Mößbauer atom and the surrounding electrons. There are three different types of interactions possible: the electrical monopole interaction, measured as the so-called isomer shift (IS) δ. It gives information on the s-electron density and so allows conclusions on oxidation states, coordination numbers etc. The electrical quadrupole interaction, measured as quadrupole splitting (QS), informs, for instance, on symmetry and ligand field splitting. Finally, the magnetic dipole interaction may lead to a magnetic splitting of the ground state and the excited state. One gets information on the magnetic state of the system.

Table 1. Isomer shifts (IS) and quadrupole splitting (QS) of $Au_{55}(PPh_3)_{12}Cl_6$ and of bulk gold.

Au site	IS (mm s^{-1})	QS (mm s^{-1})
Core	−1.4	0.0
Bare surface	+0.3	1.4
PPh_3-bonded	+0.6	7.1
Cl-bonded	+0.1	4.4
Bulk gold	−1.224	0.0

Mößbauer spectroscopy provides another appropriate tool to study the chemical environment of metal atoms in nanoclusters. IS and QS give information on the different sites of metal atoms. $Au_{55}(PPh_3)_{12}Cl_6$ has been intensively studied in the temperature range of 30–1.25 K and so a remarkable contribution to its geometrical and electronic structure was made [16]. The Au_{55} cluster core is belonging to the so-called full-shell clusters. A full-shell structure is built up by the addition of closely packed 12 atoms around a single central atom resulting in a 13 atomic one-shell cluster. A second shell of 42 atoms yields a two-shell cluster consisting of 55 atoms etc. The nth shell of such a system contains $10n^2 + 2$ atoms. The resulting ideal geometry of a full-shell cluster is cuboctahedral. Due to their complete geometry, full-shell clusters exhibit preferred formation and indicate increased stability compared with non-full-shell particles, as will still be considered later. Table 1 contains the ISs and the QS of the various gold atom sites in the nanocluster and for comparison the data of bulk gold.

Since the 42 surface atoms have different chemical environment, one observes three different signals for bare atoms, PPh_3-coordinated ones and Cl-bonded gold atoms, in agreement with the proposed structure. In connection with the discussion in this chapter, however, it is most remarkable that the IS of the 13 atomic inner part of the Au_{55} cluster is close to that of bulk gold, but nevertheless differs characteristically. The difference between bulk gold and the Au_{13} core is traced back to a slightly lower 6s electron density in the small particle. This is an indication that Au_{13} as the core of the Au_{55} nanocluster differs electronically from bulk.

The next available full-shell cluster that has been investigated by Mößbauer spectroscopy was the four-shell cluster $Pt_{309}phen^*_{36}O_{30\pm10}$ (phen* = 4,7-p-$C_6H_4SO_3Na$ substituted 1,10-phenanthroline) [17]. Its inner core consists of 147 atoms. However, since platinum is not Mößbauer-active, the cluster sample had to be irradiated with thermal neutrons to transfer a fraction of the Pt atoms into ^{197}Au isotopes due to the nuclear reaction $^{196}Pt + n \rightarrow {}^{197}Pt$, followed by $^{197}Pt \rightarrow {}^{197}Au + e^- + \bar{\nu}_e +$ 0.6 MeV ($\bar{\nu}$ = antineutrino) [18]. Table 2 informs on the IS and the QS data.

As can be seen, again the ligated and the unligated surface atoms differ characteristically from each other. The most important observation, however, is that IS and QS of the 147 atomic inner core correspond with that of bulk gold. In contrast to the Au_{13} core in Au_{55}, the "Au_{147}" core of "Pt_{309}" has metallic behaviour, at least at the working temperature of 1.8 K.

3.4. Tunnelling Spectroscopy

The results discussed in Sections 3.1–3.3 turned out as very valuable with respect to the knowledge about the transition from bulk metal to molecule. The most important method, however, to gain direct information from individual metal nanoparticles on their inner electronic life is the tunnelling spectroscopy. The method is based on the single-electron tunnelling (SET) through an intermediate island between two metal electrodes as is indicated in Figure 10.

Table 2. Isomer shifts (IS) and quadrupole splitting (QS) of $Pt_{309}phen^*_{36}O_{30\pm10}$, fractionally transferred into ^{197}Au isotopes.

Au site	IS ($mm\,s^{-1}$)	QS ($mm\,s^{-1}$)
Core	0.0	0.0
Bare surface	+1.7	0.0
Phen*-bonded	+0.9	+5.7
O_2-bonded	+0.5	+5.0
Bulk gold	−1.224	0.0

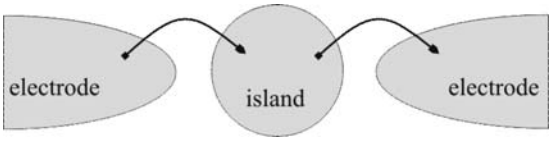

Figure 10. Tunnelling of a single electron from an electrode into an intermediate island causing a Coulomb blockade. If the electrostatic energy is large enough, transport to the counter electrode happens.

Quantum mechanical tunnelling enables electron transport in such devices. Among others, it is dependent on the applied potential. Practically, the insulating tunnel barrier consists of the ligand shell that the nanoclusters under investigation in any case have. To observe tunnelling of single electrons from one electrode into the nanoparticles and from there into the counter electrode, the following condition must be fulfilled: $E_C = e^2/2C \gg k_BT$. E_C is the Coulomb energy which has to be very large compared with the thermal energy k_BT, C the total capacitance of the tunnel contact $2\pi\varepsilon_0\varepsilon_r R$ (R, the radius of the particle, ε, the dielectric constant) and k_B, the Boltzmann constant. The above relation requires either a low temperature or a high Coulomb energy (or both) to observe SET. The chance to observe SET under reasonable temperature conditions increases with decreasing C, i.e. with decreasing size of the particle. The following example illustrates the relevance of temperature and particle size regarding the observation of SET. A ligand-protected 15 nm palladium nanoparticle was trapped between two platinum electrodes [19]. Figure 11a shows the scanning electron microscopic (SEM) image of the device, Figure 11b presents the current (I)–voltage (U) behaviour at two different temperatures.

At 295 K the current increases linearly with the increasing voltage. This means nothing, but that the 15 nm Pd particle follows the Ohm's law at room temperature and so clearly demonstrates bulk behaviour. However, at 4.2 K there is a well-expressed Coulomb blockade to be observed, indicating that in the region from ca. −0.1 to +0.1 V the transfer of electrons is blocked due to the presence of a single electron in the particle. Reaching the appropriate voltage, this electron is transferred to the counter electrode. In other words, the ligand-protected 15 nm Pd particle behaves as a quantum dot, but only at 4.2 K.

The next smaller ligand-protected nanocluster that was investigated by scanning tunneling spectroscopy (STS) was the four-shell cluster $Pt_{309}phen^*_{36}O_{20}$ [20,21]. The diameter of the Pt core is 1.8 nm, about a tenth of the former example. However, even here a Coulomb blockade could only be observed at 4.2 K, i.e. at room temperature the particle still has metallic behaviour. Since

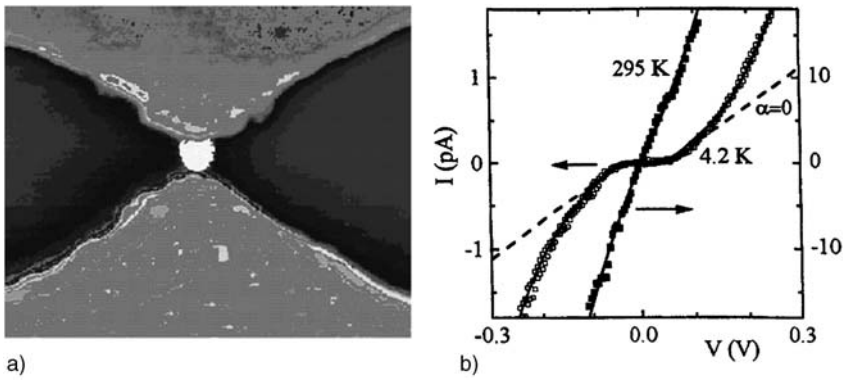

Figure 11. (a) SEM image of a ligand-protected 17 nm Pd particle between two Pt tips. (b) The current voltage behaviour of this system at 295 and 4.2 K with an expressed Coulomb blockade. (Reprinted from Ref. [19], © 1997, with permission from American Institute of Physics.)

the realization of trapping such a small particle between two tips like in case of the 15 nm Pd particle (see Figure 11a) is almost impossible, the experimental setup was modified in such a way that nanoclusters were deposited on a gold substrate from very dilute solutions and then an individual particle was contacted by the STS tip, as is indicated in a simplified manner in Figure 12.

Again, the decisive step on the way from metal to quantum dot and molecule, respectively, is observed when going to the 1.4 nm nanocluster Au_{55}. The small step from 1.8 to 1.4 nm changes the controlled tunnelling conditions in a way that a well-expressed Coulomb blockade can for the first time be registered at room temperature [22]. The experimental setup was performed in a similar way like in the above example. Figure 13 shows the *I–U* curve, registered at room temperature, with a dominating blockade between −500 and +500 mV.

From measurement data gained at 90 K, the capacitance of the cluster was determined as 3.9×10^{-19} F. Temperature-dependent impedance measurements at the same cluster resulted in a very similar value [23].

Coulomb blockades in metallic quantum dots inform on the ability to trap and to store single electrons in a distinct voltage region. Practically this means nothing but to have a single electron switch! If this is the case at room temperature like for $Au_{55}(PPh_3)_{12}Cl_6$, we are provided with the ultimate smallest switch with working temperatures that allow its use in future nanodevices.

The investigation of $Au_{55}(PPh_3)_{12}Cl_6$ at low temperatures allows an interesting view into electronic details. In accordance with the room temperature measurement, a clear evidence for a Coulomb blockade is observed at 7 K under ultra-high vacuum conditions [24]. Figure 14 shows a full-space model of the cluster (14a) and a scanning tunnelling microscopy (STM) image (14b) of an individual cluster, imaged at 7 K.

The STS measurements were performed at two different positions of the cluster surface, as is indicated by (a) and (b). (a) indicates a position above a phenyl ring of a PPh_3 ligand molecule and the position (b) is above a non-covered area. These two measurements were necessary to eliminate a possible influence of the aromatic rings. Instead of the usual *I–U*-characteristic, here dI/dV was used instead of *I*. The Coulomb blockade then appears as a broad minimum exhibiting important details, as can be seen in Figure 15.

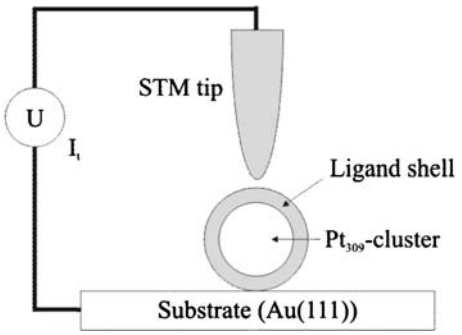

Figure 12. A ligand-protected Pt_{309} nanocluster between an STM tip and an Au (111) surface to determine the current–voltage characteristics.

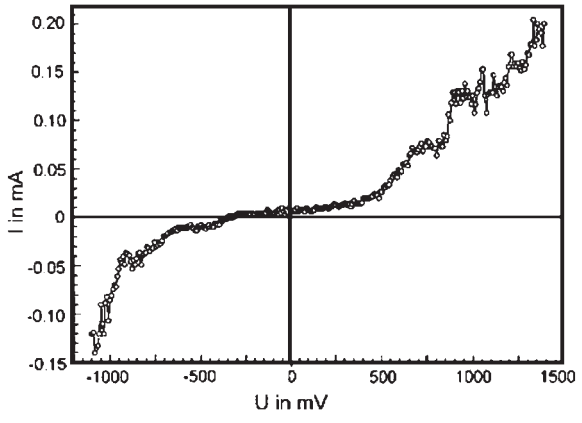

Figure 13. The Coulomb blockade of $Au_{55}(PPh_3)_{12}Cl_6$ at room temperature. (Reprinted from Ref. [22], © 1998, with permission from Springer-Verlag GmbH.)

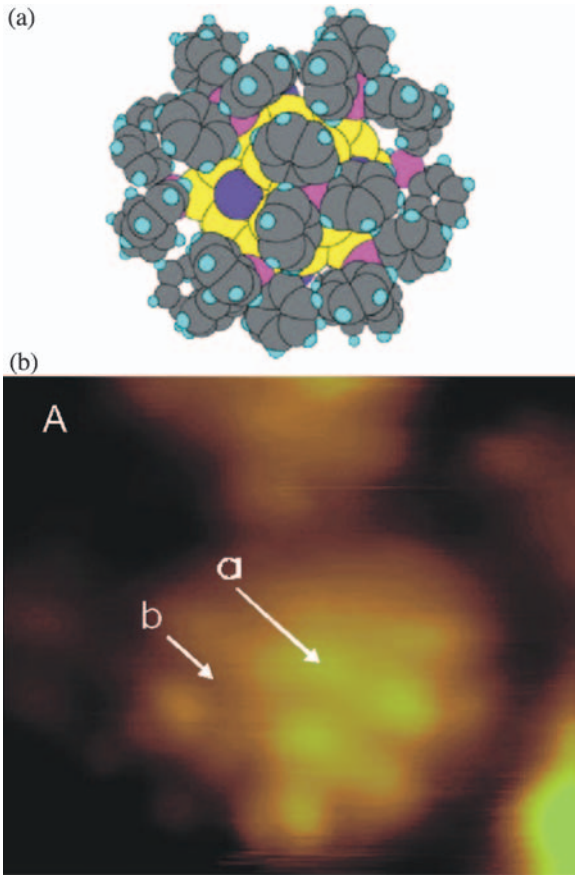

Figure 14. (a) Full-shell model of $Au_{55}(PPh_3)_{12}Cl_6$ and (b) STM image of an individual cluster. The light yellow areas show electron-rich phenyl rings. a and b indicate the different positions of the STM tip where measurements have been performed. (Reprinted from Ref. [24], © 2003, with permission from American Chemical Society.)

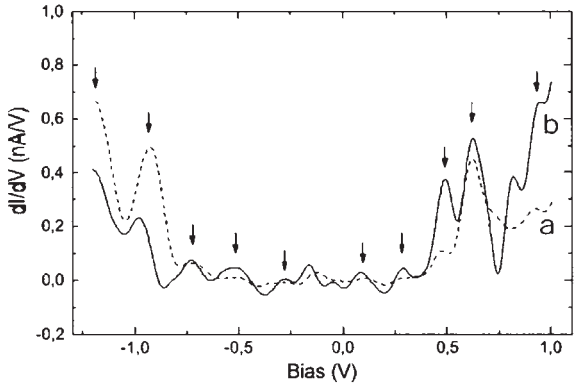

Figure 15. The discrete energy levels in $Au_{55}(PPh_3)_{12}Cl_6$ at 7 K. The level spacing is 135 mV. (Reprinted from Ref. [24], © 2003, with permission from American Chemical Society.)

Discrete energy levels are to be observed for position (a) as well as for position (b) at exactly the same values, in case (b) somewhat better expressed than in (a). The level spacing is 135 mV. This spectrum clearly identifies the Au_{55} cluster as a quantum dot in the classical sense, having discrete electronic energy levels, though broader than in an atom, but nevertheless existent. The description of such quantum dots as "artificial, big atoms" seems indeed to be justified.

4. Self-Assembly of Metal Nanoparticles

Considering three dimensions, self-assembly means nothing but the traditional crystallization, usually of molecules or ions. The forces bringing the crystal's building blocks together are van der Waals or dipole–dipole interactions in case of molecules or electrostatic forces in ionic salts. Considering nanoparticles, the problems may be more delicate. Except few examples, one type of nanoparticles, with or without a protecting ligand shell, do not consist of completely identical particles. They usually differ in the number of atoms as well as in shape, at least to some extent. Crystallization in a classical sense is limited to really identical molecules or oppositely charged ions. The phenomenon that nanoparticles, differing in size and shape, can organize in three and especially in two dimensions is nowadays a well-known fact, but was a surprise when observed for the first time. The term "self-assembly" stems from those observations and is also common for the two-dimensional (2D) arrangement of molecules on surfaces. Some people call this a 2D crystallization. Whatever the historical development might be, in the following the terminus "self-assembly" will be used for 3D, 2D and 1D organization in agreement with the customs in nanoscience.

4.1. Three-Dimensional Self-Assembly

Self-assembly of metal nanoparticles, of course, occurs easier the smaller the difference in size and shape of the nanoparticles is. Most of the known 3D assemblies are built of ligand-protected metal nanoparticles. From mixtures of thiolate-stabilized gold nanoparticles in the size range of 1.5–3.5 nm monodisperse fractions could be gained by fractional crystallization [25]. The fcc-structured building blocks, consisting of 140, 225, 314 and 459 gold atoms, could be detected. Crystals of up to 40 μm were obtained.

Crystalline phases (truncated octahedra) of 5 nm silver particles, thiolate protected as well, have been detected by means of high-resolution transmission electron microscopy (HRTEM) [26–28]. Three-dimensional architectures of 5–6 nm thiolate-stabilized gold particles have also been described [29]. Several other reports on 3D superlattices of metal nanoparticles have become known during the last few years [30–33].

Especially worth mentioning is the 3D self-assembly of FePt alloy-like 4.5 nm particles [34]. Prepared from platinum acetyl acetate and $Fe(CO)_5$ and stabilized by oleic acid and oleyl amine [35], the crystals are formed by slow diffusion of methanol into a FePt solution in toluene over 4 months. The faceted triangular or hexagonal platelets grow up to 30 μm side length. The crystals of the magnetic FePt nanoparticles exhibit a superparamagnetism → ferromagnetism transition at 14 K.

An interesting 3D superlattice of the main group metal tin has recently been generated [36]. When $Sn(NMe_2)_2$ is treated with hexadecylamine and HCl, perfect 3D superstructures of monodisperse 18×15 nm Sn nanoparticles could be characterized.

3D crystals in the micrometre regime are spontaneously formed, if the stoichiometrically exact nanocluster $Au_{55}(PPh_3)_{12}Cl_6$ [12,13] is isolated from dichloromethane solution by evaporation of the solvent [37]. Relative fast degradation of the clusters in solution prevents formation of larger crystals. From small-angle X-ray diffraction investigations the 2θ angle of 4.3° corresponds well with a *d*-value of 2.1 nm in perfect agreement with an fcc arrangement of the clusters in the microcrystals. The hexagonally close-packed arrangement could also be followed from TEM investigations.

A question of general interest is the behaviour of ligand free metal nanoparticles if they do have the opportunity to self-organize. The driving force to arrange is the formation of strong metal–metal bonds. Larger particles (colloids) with rather broad size distribution are known to coalesce when losing the protecting ligand shell to give either polycrystalline metal powders or even mirrors, as is especially known from silver and gold. However, the conditions change if bare clusters of distinct size and defined structure are considered. The frequently mentioned cluster compound $Au_{55}(PPh_3)_{12}Cl_6$ with its ideal cuboctahedral geometry (see Section 3.3) is an ideal candidate, assumed that the ligand shell can be removed under mild conditions. A rather unusual chemical way succeeded in generating bare Au_{55} particles: the phosphine and chlorine ligands of $Au_{55}(PPh_3)_{12}Cl_6$ can be removed by a spherical fourth generation dendrimer molecule having 96 SH functions at the periphery [38]. Thiols easily substitute phosphines due to the formation of stronger Au—S bonds. Using excessive dendrimers the phosphines and obviously the chlorines are quantitatively removed and substituted by thiols. The excessive dendrimer with a quasi-infinite number of equivalent SH groups allows the clusters to move around and occasionally to meet each

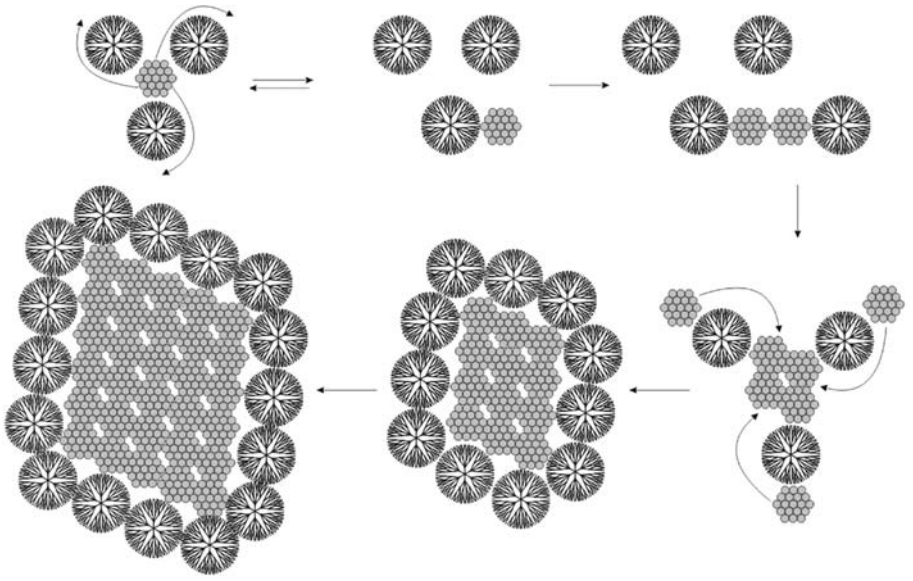

Figure 16. Illustration of the formation of 3D assemblies of bare Au_{55} nanoclusters in an envelope of dendrimer molecules. (Reprinted from Ref. [38], © 2000, with permission from Wiley-VCH.)

Table 3. Small- and wide-angle X-ray data of crystalline $(Au_{55})_n$ species.

2Θangle (°)	d (found) (nm)	d (calculated) (nm)
43.02	$d^1 = 0.21$	$1 \times 0.224^a = 0.224$
31.92	$d^2 = 0.28$	$1 \times 0.274^b = 0.274$
16.10	$d^3 = 0.55$	$2 \times 0.274^b = 0.548$
4.46	$d^4 = 1.98$	$7 \times 0.274^b = 1.918$

Note: The *hkl* values 111 and 110 are reduced by 5% due to the size-determined contraction of the gold–gold distances.
[a]*hkl*: 111 = 0.2355 – 5% = 0.224.
[b]*hkl*: 110 = 0.2884 – 5% = 0.274.

other. In consequence, this leads to the organized growth of Au_{55} building blocks in an envelope of dendrimer molecules. Figure 16 illustrates in a simplified manner the process of cluster growth, ending up in the formation of microcrystals of perfectly organized Au_{55} particles, as can be followed from the TEM image shown in Figure 17a (see Table 3).

Detailed TEM investigations as well as small-angle X-ray diffractometry show the clusters organized via their edges, as is indicated in Figure 17b.

These experiences that have been gained in solution, can be transformed to a quasi-2D level. If a dry dendrimer monolayer, generated on a silicon wafer by spin-coating of a dendrimer solution, is dipped into a dichloromethane solution of $Au_{55}(PPh_3)_{12}Cl_6$ for a very short time and is then dried immediately, a monolayer of the clusters can be detected by means of atomic force microscopy (AFM) measurements [39]. However, if the clusters are allowed to move around for a longer period of time (ca. 1 week) by exposing the monolayer to an atmosphere of dichloromethane, the monolayer first disappears, followed by the slow formation of nanosized crystals on the surface. Figure 18 shows SEM images of increasing magnification.

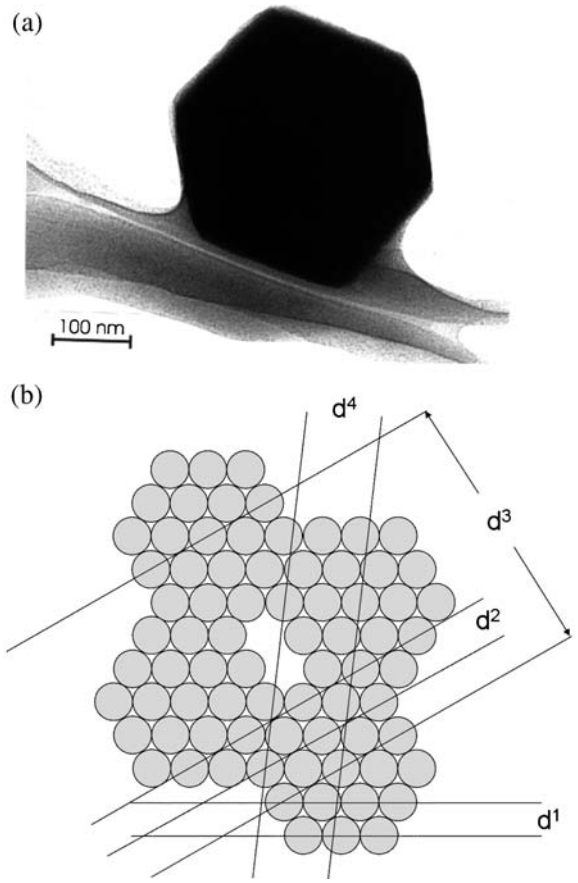

Figure 17. (a) TEM image of a microcrystal of bare Au_{55} nanoclusters. (b) Illustration of the ordering principle indicating periodicities d. Assignments are given in Table 3. (Reprinted from Ref. [38], © 2000, with permission from Wiley-VCH.)

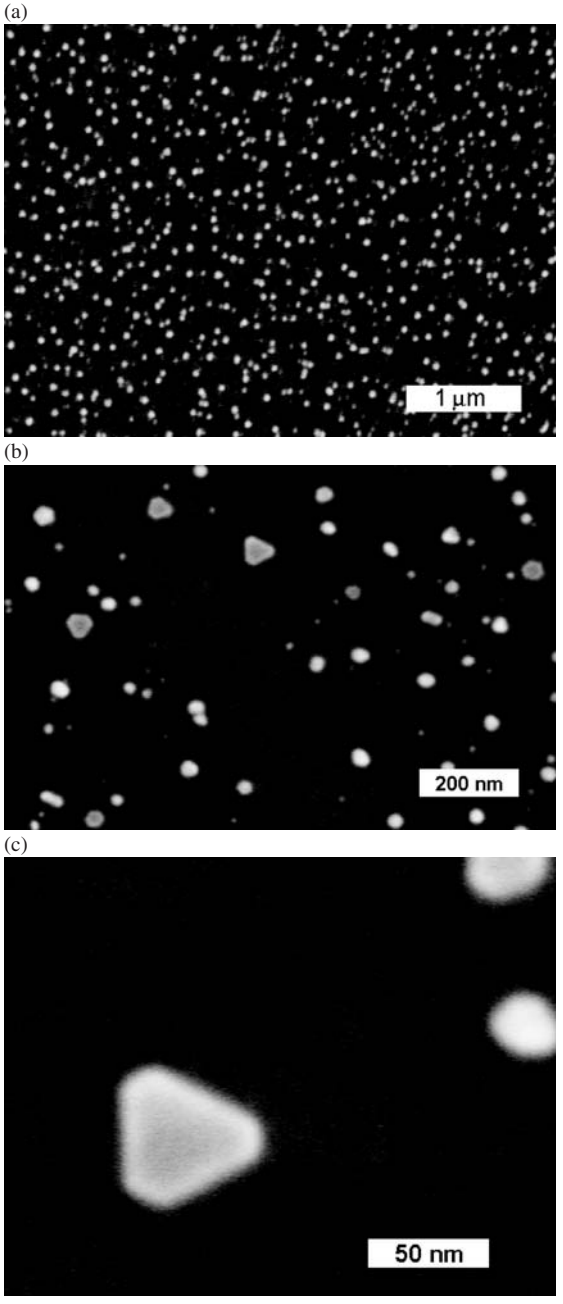

Figure 18. SEM images with increasing magnifications of $(Au_{55})_n$ crystals, generated in a monolayer of dendrimers.

Figure 19 explains what in principle happens: the cluster monolayer on the dendrimer film is mobilized by means of CH_2Cl_2 vapour (a→b). The phosphines are then removed by the SH functions (b→c). The bare Au_{55} nanoclusters move between the dendrimer molecules to form crystals $(Au_{55})_n$ which finally appear on the surface (c→d). The formation of crystalline superlattices of naked Au_{55} particles proves their stability which is founded in their perfect cuboctahedral shape. The $(Au_{55})_n$ species is a novel modification of the element gold.

The stability of the bare cuboctahedral Au_{55} clusters has in addition been demonstrated by their chemical inertness. Any kind of chemical reaction with participation of all atoms would be accompanied by a damage of the structure. This is avoided under reasonable conditions. For instance, Au_{55} clusters on a surface, the ligand shell of which has been removed in an oxygen plasma, do not form oxides under conditions where larger and smaller gold particles of non-full-shell type are oxidized to Au_2O_3. Figure 20 shows the Au-4f photoelectron spectra of various gold species that have been treated in an oxygen plasma as was done with Au_{55}. All of them show oxide bands except Au_{55}; only a very weak shoulder can be found, probably formed from some particles not having the ideal cuboctahedral structure [40].

The same consequences can be drawn from the observation that bare Au_{55} cannot be alloyed with indium vapour, in contrast to different smaller and larger particles and even to bulk gold that forms a phase $AuIn_2$. From Figure 21 it can be seen that again only Au_{55} is resistive towards In vapour since no corresponding signal in the photoelectron spectra can be registered [41].

4.2. Two-Dimensional Arrangements

2D self-assembly of metal nanoparticles requires special conditions since 3D growth of any kind of material is preferred. Two principal strategies to generate 2D organizations of metal nanoparticles have been developed during the last 1–2 decades: true self-assembly, guided self-assembly and aimed structures.

True self-assembly can happen if weak forces between a substrate and the species to be organized help to deposit them from solution and allow them to move around for an optimal organization. Weak interactions between the nanoparticles themselves are additionally demanded because strong forces would rather initiate 3D growth. Dense-packed 2D monolayers are indeed frequently described in the literature. It is not possible to present the very many examples that have become known at this place. A comprehensive overview over the most important results can be found in Ref. [42]. Like in case of 3D organization, the better the uniformity of the particles, the easier and the more perfect and extended the resulting 2D arrangement will be. Again, the precise nanocluster Au_{55} as its water-soluble derivative $Au_{55}(Ph_2PC_6H_4SO_3H)_{12}Cl_6$ shall be selected as an example. Various polymer films bearing aryl groups attract the nanoclusters from solution in an ideal way. It is assumed that weak π–π interactions, for instance between poly(vinylpyrrolidone) (PVP) or poly(*p*-phenyleneethynylene) (PPE) and the phenyl rings of the PPh_3 ligands, support the 2D organization on their surface as is impressively demonstrated by the TEM image shown in Figure 22. Figure 22a shows an area of ca. $0.17\,\mu m^2$ containing about 35,000 nanoclusters, whereas Figure 22b shows a magnified cutout of 5×5 particles of the perfectly square-ordered monolayer.

''Innocent'' surfaces do not allow formation of such extended 2D areas as has been demonstrated by using carbon coated copper grids (for TEM) or liquid surfaces as used for Langmuir–Blodgett techniques. Only islands

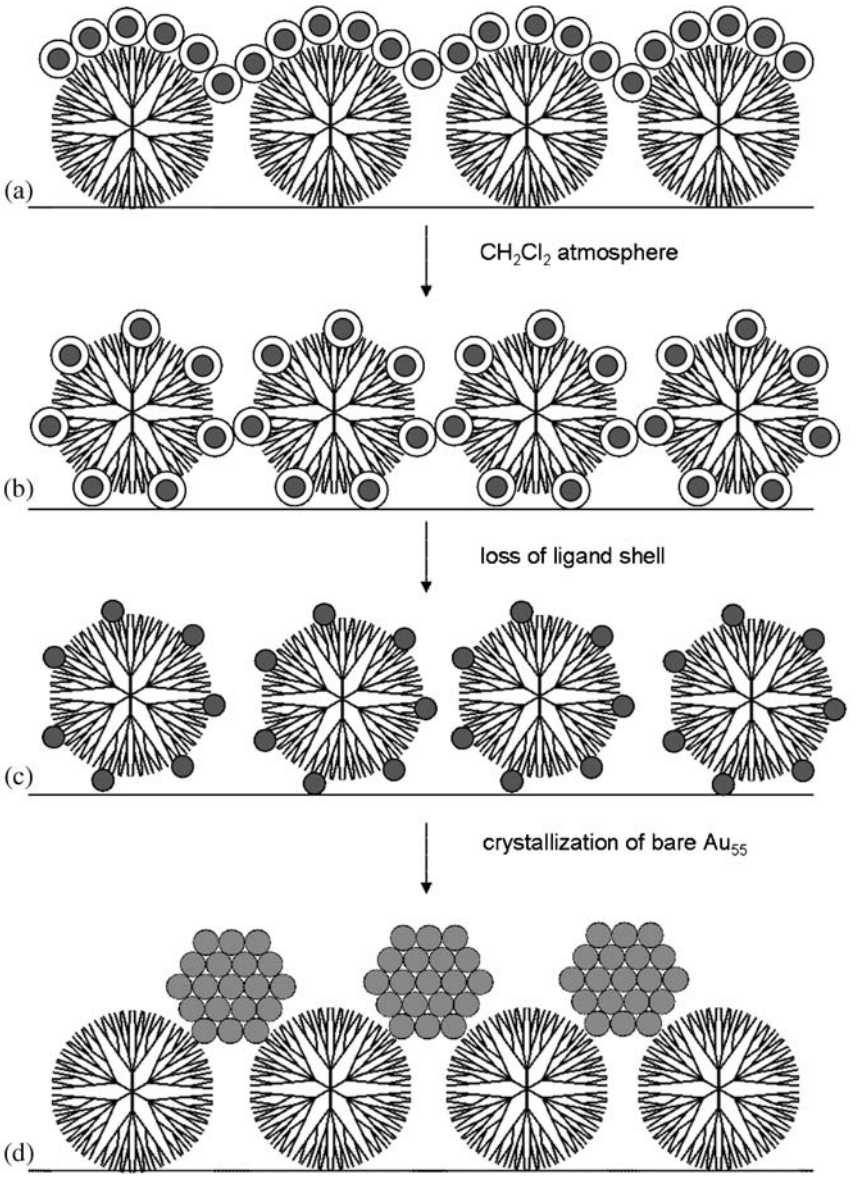

Figure 19. Sketch of the formation of $(Au_{55})_n$ nanocrystals in a dendrimer monolayer. (Reprinted from Ref. [39], © 2005, with permission from Wiley-VCH.)

of limited extensions are formed by self-assembly [42]. Inverse proceedings give similar results, for instance, if polymer surfaces, very successful in combination with aryl-determined cluster surfaces, are combined with alkyl-determined cluster surfaces. Long-range 2D assembly also fails [42].

The indication ''guided self-assembly'' is used, if 2D assembly of nanoparticles is additionally supported by prefabricated surface structures. Excellent results in this connection have been reached by using thin films of A–B-diblock copolymers [43–48]. They contain regularly arranged micelles in which metal nanoparticles of rather monodisperse quality can be grown from corresponding salts by reduction. Figure 23 illustrates the formal process, Figure 24 shows TEM images of gold nanoparticles of different sizes [49]. Except gold, other noble metals like palladium and platinum nanoparticles could be generated two-dimensionally. Less noble elements like titanium or iron can be deposited as oxides.

Polymer-free monolayers of the metal nanoparticles can be gained by a successive treatment of the films in an oxygen plasma [50–52].

Aimed 2D structures are completely artificially generated using appropriate tools. The favourite tool is, without doubt, the AFM tip. Mirkin et al. applied AFM tools to use it as a pen [53,54]. With the help of the water meniscus between tip and surface, which is always present at a room atmosphere, molecules from a reservoir on top of the tip are transported to a surface, which must have strong attraction to at least one end of the molecules.

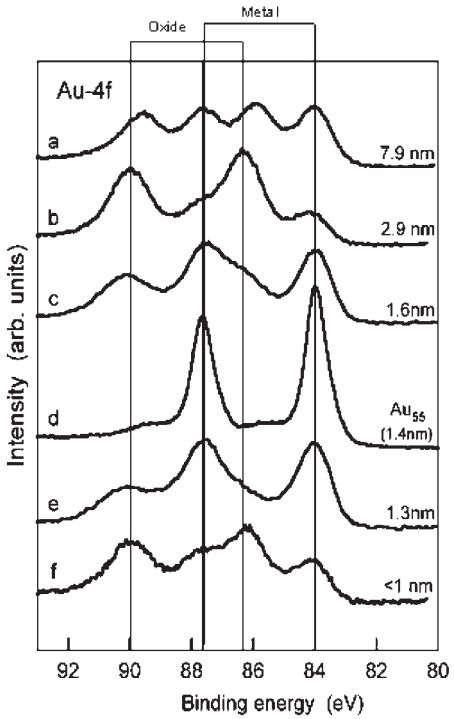

Figure 20. Au-4f photoelectron spectra of different gold nanoparticles, treated in an oxygen plasma. All except Au_{55} (traces) exhibit oxide signals.

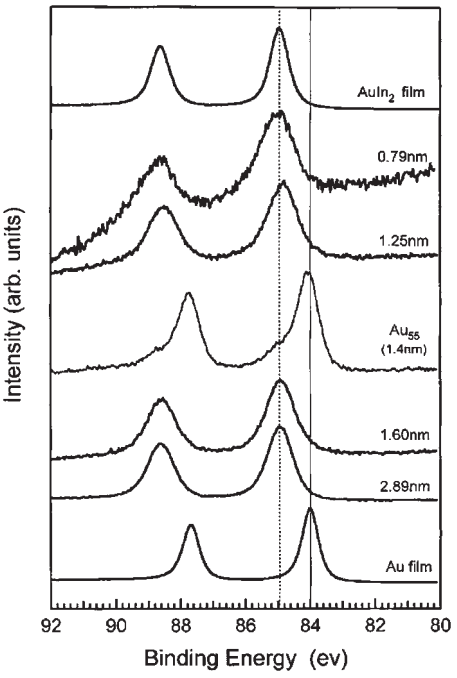

Figure 21. Au-4f photoelectron spectra of different gold nanoparticles treated with indium vapour. All except Au_{55} form alloys. (Reprinted from Ref. [41], © 2005, with permission from American Physical Society.)

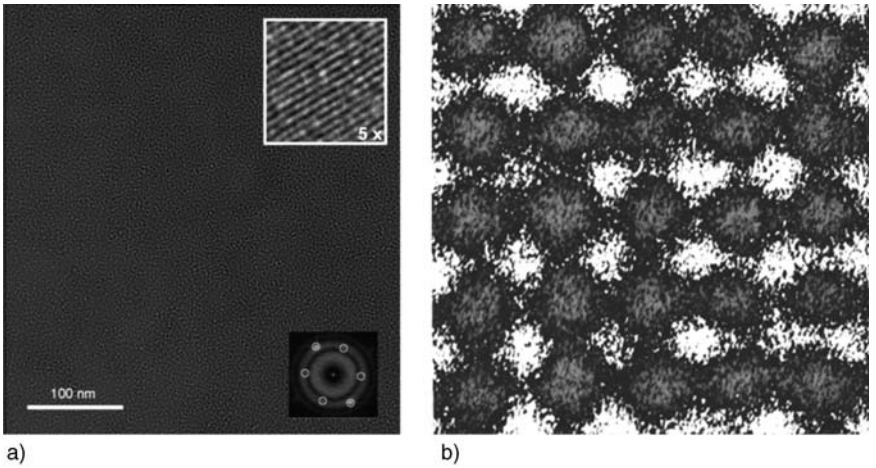

Figure 22. (a) TEM image of an extended square planar $Au_{55}(Ph_2PC_6H_4SO_3H)_{12}Cl_6$ monolayer, (b) magnified cutout. (Reprinted from Ref. [42], © 2004, with permission from Wiley-VCH.)

Thiols and gold surfaces are ideal partners to write any kind of structure in nanometre dimensions. Artificial patterns of appropriately functionalized molecules can be used to bind metal nanoparticles specifically. Figure 25 gives an impression of the individual steps leading to a distinct cluster arrangement.

The AFM tip plays also the dominant role in another technique where CH_3 end groups of a self-assembled monolayer of alkyl chains are oxidized by a conductive tip emitting electric pulses to generate COOH functions [55–57]. The carboxylic functions are then transferred into SH groups by several chemical steps. Gold nanoparticles can then easily be coordinated to the SH groups from solution. Picasso's dove of peace (Figure 26) [58] could so be drawn by 2–6 nm gold nanoparticles as well as different patterns using Au_{55} clusters [59].

In conclusion, the chapters up to here were dealing with the relevance of size with respect to electronic properties

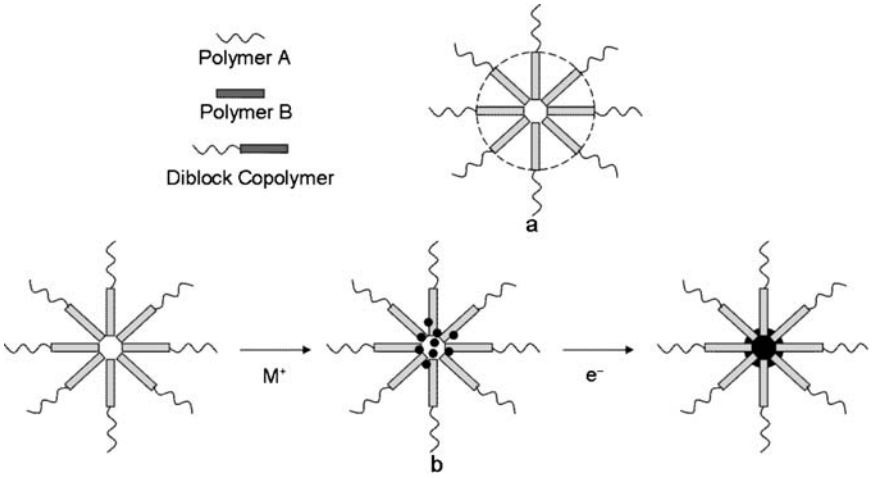

Figure 23. Polymer A and polymer B form the diblock copolymer micelles where metal nanoparticles can be grown.

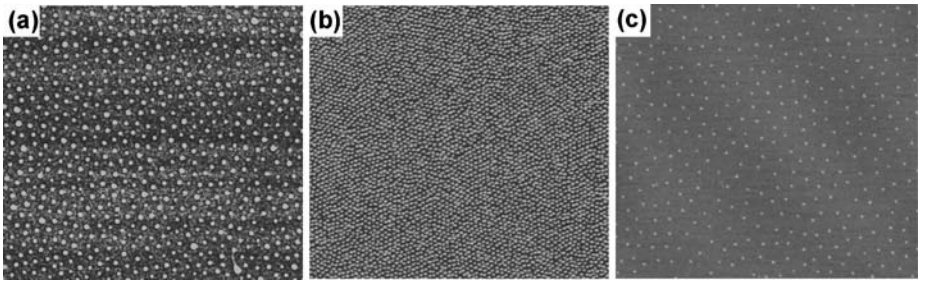

Figure 24. TEM images of different gold nanoparticles grown in the micelles of diblock copolymers. a: 6 nm, b: 4 nm, c: 2.5 nm.

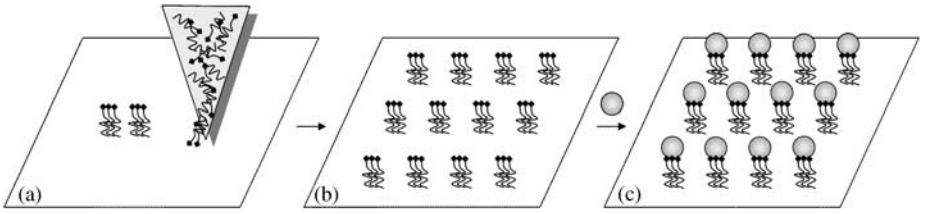

Figure 25. Formation of an artificial structure of metal nanoparticles by dip pen nanolithography using an AFM (a), tip to transport functionalized thiol molecules onto a gold surface (b) and to trap the nanoparticles (c).

of metal nanoparticles and their ability to organize or to be organized in 3D and 2D. The main reason for the enormous interest in these properties is the possible application of metal nanoclusters in future nanodevices, as has already been addressed in Section 3.4. All the self-assembly approaches again are of relevance with respect to applications. Storage systems, based on the electronic storage capacity of nanoparticles, demand a 2D, in the far future possibly a 3D, controlled arrangement of switches or transistors. Though being still far from having working devices, we are now equipped with the necessary information on the electronic behaviour of smallest metal nanoparticles and their principal ability to act as building blocks in future nanodevices. The situation is comparable with that in the past when we learned silicon to be a semiconductor with transistor qualities.

The size of metal nanoparticles plays also a role in a quite different field of nanoscience: the interaction with biosystems with nanoparticles in general, here especially with metal nanoparticles. Chapter 4 will deal with some very recent aspects considering the interaction of noble metal nanoparticles with biomolecules and living cells.

5. The Relevance of Particle Size in Biosystems

There exist numerous reports on the interaction of noble metal nanoparticles, especially those of gold, with DNA. The reason for this intense work in most cases is the use of gold nanoparticles for the analysis of nucleic acids, or proteins. In any case, the interactions between the two

components happen via DNA-gold nanoparticle conjugates with single- or oligofunctional specific oligonucleotide sequences [60–66]. DNA-gold nanoparticle hybrid systems have also been created as switchable systems, due to a reversible aggregation [67]. In any case, functionalization of the gold nanoparticles with specific DNA sequences results in specific interactions with biomolecules. Figure 27 gives an impression of the various steps to such hybrid systems [68]. The particle size in all cases mentioned up to here does not play a significant role.

An important question is how metal nanoparticles without such specific DNA functions interact with DNA or more generally with biosystems up to living cells and if the particles size is of significance. Two nanometre thiol-stabilized Au particles interact with λ-DNA resulting in a kind of 1D particles assemblies [69]. Two to three nanometre Pt particles, protected with a shell of (−)-cinchonidine and acetic acid molecules, add to λ-DNA strands in multilayers making the DNA course easily visible in the TEM [70]. These examples do not indicate a size-detected dependence of the particles–DNA interactions. Rather the nature of the ligand shells may be of significance. This behaviour changes dramatically, if the size of the particles reaches a critical size. $Au_{55}(Ph_2PC_6H_4SO_3H)_{12}Cl_6$ with its gold core of only 1.4 nm interacts with λ-DNA in aqueous solution irreversibly in a manner where the fully or at least partially naked Au_{55} clusters are trapped in the major groves of the DNA [71]. There are three reasons for this unique kind of bonding: (a) the height of the major groves in the B-form (water containing) of DNA is ca. 1.4 nm and so meets perfectly the size of the bare clusters; (b) gold is the most electronegative metal (electronegativity (EN) agrees approximately with that of iodine), so that the attraction of the Au clusters by the negative charges of the DNA phosphates is a driving force and (c) the major groves including the phosphates form an ideal polydentate ligand system, making the binding of the 1.4 nm particles a kinetically extremely stable system. Figure 27 shows the result of molecular modelling calculations [71]. The enclosure of approximately half of the Au_{55} clusters is obvious (Figure 28).

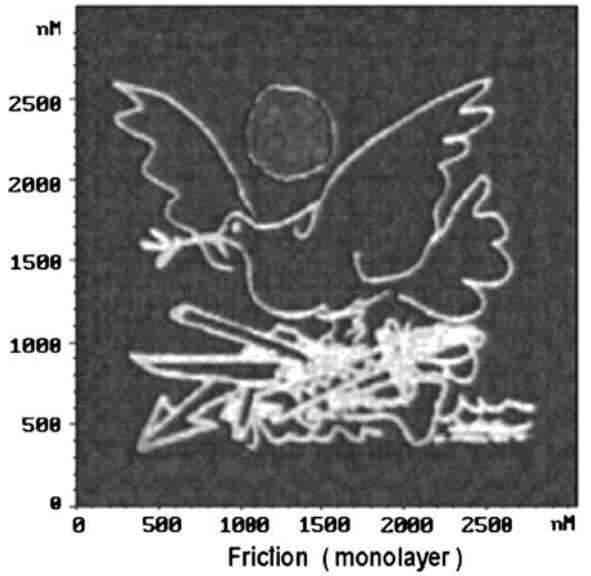

Figure 26. Picasso's dove of peace, drawn with 2–6 nm gold particles. (Reprinted from Ref. [58], © 2004, with permission from American Chemical Society.)

The stability of this DNA/Au_{55} hybrid system was impressively demonstrated by the following observation: if the water backbone of B-DNA is removed by evaporating the water or by any other kind of elimination, the B-DNA shrinks to the so-called A-DNA with a major grove height of only 0.7 nm. One might expect that the shrinking process can either not happen due to the presence of the Au_{55} particles or that the clusters are eliminated. Instead, the shrinking from B- to A-DNA "damages" the particles to such an extent that smaller 0.7 nm particles remain in the reduced major groves. This observation was made in the TEM under ultra-high vacuum conditions.

At this point an interesting question arises: how do metal nanoparticles interact with living cells? The degree of complexity will dramatically increase going from an ex vivo experiment with well-defined components to a living system with a multitude of possible reactants. Gold nanoparticles have been tested regarding their ability to penetrate into cells and a possible cell toxicity [72–75]. Particles of discrete size, namely 4, 12 and 18 nm, are taken up by human K562 leukaemia cells without leaving indications of significant toxicity [76]. However, how do the very small particles, being irreversibly coordinated to DNA, behave? Indeed very different! The study of 11 different human cancer cell lines, which were contacted with aqueous solutions of $Au_{55}(Ph_2PC_6H_4SO_3H)_{12}Cl_6$, clearly resulted in dramatic toxicity [77]. The most significant sensitivity was found for the metastatic melanomas MV3 and BLM. The toxicity of Au_{55} became especially visible by accompanying experiments with the clinically routinely applied cisplatin, which in most cases showed significantly lower toxicity. Using same molar concentrations, in case of the melanoma cells 90% of the cells are viable with cisplatin when 100% of the cells are dead with Au_{55}. Table 4 summarizes the toxicity results and compares the

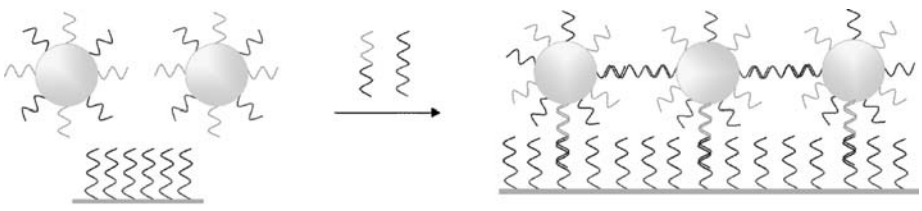

Figure 27. The interaction of DNA modified gold nanoparticles with corresponding DNA sequences to link them between each other and with a substrate.

IC_{50} values of cisplatin and Au_{55} and Figures 29a and b show the course of cell viabilities in dependence of the molar concentrations in case of melanoma cells.

Besides melanoma cells with the extraordinary sensitivity towards Au_{55}, the difference in toxicity is also very obvious for Hek-12 and U-2OS where the effectiveness of Au_{55} is 32 and 18 times higher than that of cisplatin.

Experiments with radioactive cluster compounds (^{198}Au) allowed precise analyses of the particles distribution in the cells. In case of melanoma BLM it was found that 57.5% of the radioactive gold was in the cytoplasma and 42.5% in the cell nucleus. Removal of the cell nuclear proteins, more than 20% of the gold was detected as part of the DNA. These remarkable results agree well with the former observation of the extremely stable complexation of Au_{55} at DNA.

Of course, it has to be assumed that the way of the clusters through the cell membrane and inside the cell is accompanied by numerous interactions with different and complex biomolecules however, the thermodynamically and kinetically most stable situation is reached with the DNA/cluster complex formation.

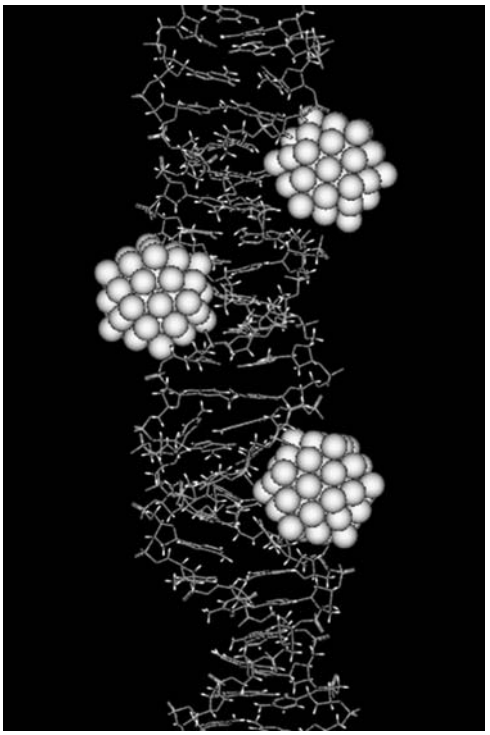

Figure 28. The interaction of Au_{55} clusters with the major groves of B-DNA. (Reprinted from Ref. [71], © 2003, with permission from Wiley-VCH.)

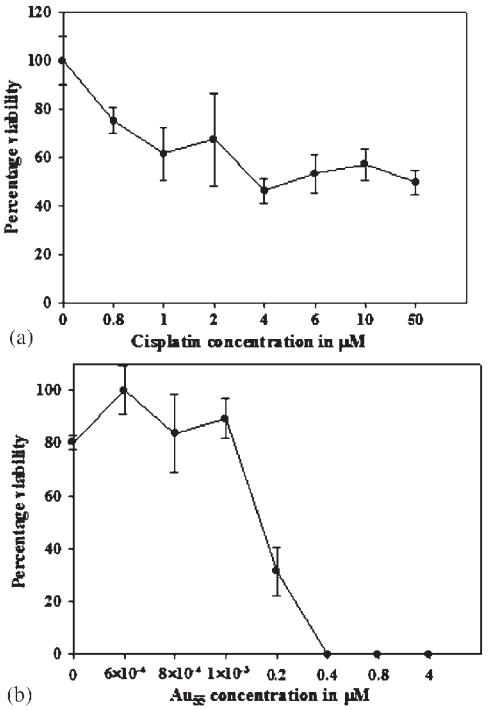

Figure 29. Comparison of the viability of melanoma cells treated with cisplatin (a) and $Au_{55}(Ph_2PC_6H_4SO_3H)_{12}Cl_6$ (b) in dependence of the molar concentrations. (Reprinted from Ref. [77], © 2005, with permission from Wiley-VCH.)

Table 4. Inhibitory concentrations (IC_{50})[a] of cisplatin and Au_{55} incubated with various human cancer and healthy cell lines for 72 and 24 h, respectively.

Cell line		IC_{50} cisplatin 72 h (μM)	IC_{50} Au_{55} 24 h (μM)
MC3T3-E1	Bone cells	26.10±1.27	1.65±0.14
U-20S	Osteosarcoma	11.17±2.02	0.64±0.04
SK-ES-1	Osteosarcoma	0.79±0.17	1.03±0.18
MOR/P	Lung cancer cells	3.30±0.30	2.10±0.10
MOR/CPR	Lung cancer cells	7.10±1.2	2.50±0.10
CCD-919Sk	Fibroblast cells	0.45±0.10	0.62±0.07
BLM	Metastatic melanoma	54.70±7.60	0.30±0.10
M V3	Metastatic melanoma	>50	0.24±0.02
SMel-28	Melanoma	15.60±2.26	1.12±0.16
HeLa	Cervical cancer cells	7.93±0.95	2.29±0.10
Hek-12	Kidney cancer cells[b]	20.13±6.0	0.63±0.02

[a]IC_{50} is defined as the concentration of drug required to inhibit cell growth by 50% compared to a control. The IC_{50} values were calculated from the graphs obtained from the in vitro cytotoxicity assays and are the average of three independent experiments, each performed in triplicate.
[b]Kidney cancer cells transformed with adenovirus.

This example shows impressively that toxicity of a material is by far not only given by the kind of the element or the chemical composition it consists of, but that the size of the interacting species is at least of same importance.

6. Conclusions and Outlook

The miniaturization of matter to a critical specific size often results in dramatic changes of properties. In most cases those events happen on the nanoscale. Nanoscience, and in consequence nanotechnology, describe and use such "nanoeffects" to take profit of novel properties without the need of preparing new chemical compounds.

The reduction of metals to dimensions below 50 nm results in first significant changes of properties which are based on the quantum confinement of electrons, freely mobile in the bulk state. Plasmon resonances are the consequence, changing the typical metallic appearance in numerous cases to very different colours, for instance the famous purple red in case of gold. Things develop even more dramatic if particle sizes around 2 nm are reached. Ligand-protected 1.4 nm Au nanoclusters represent typical quantum dots with discrete electronic energy levels at room temperature, comparable with the situation in atoms. They behave as single electron switches and so represent promising candidates as building blocks in future nanoelectronic devices. Presently, intensive efforts are made to artificially organize such quantum dots on substrates and especially to contact them in a way that they can be addressed individually, a condition for applications as switches or transistors.

The size of metal nanoparticles obviously plays also a significant role considering the interaction with biosystems. The 1.4 nm gold nanoclusters interact irreversibly with DNA due to an extremely stable fixation in the major groves. These findings may lead to the development of novel cancer drugs, as can be concluded from a series of cell experiments.

Numerous other applications of nanosized metal nanoparticles might be mentioned or can be foreseen to become relevant in the near future. This exciting field of science, merging chemistry, physics, biology and medicine is, of course, not restricted to metals. Developments in the world of semiconductors, insulators, supramolecular chemistry and combinations between them open a completely novel world, the nanoworld, which will not only influence science, but humans daily life, beginning with the existence of completely novel computer generations up to great progresses in medicine.

References

1 For summarizing information see (a) G. Schmid (ed.) *Clusters and Colloids*, Wiley-VCH, Weinheim, 1994; (b) G. Schmid (ed.) *Nanoparticles*, Wiley-VCH, Weinheim, 2004.
2 H. Brune, H. Ernst, A. Grunwald, W. Grünwald, H. Hofmann, H. Krug, P. Janich, M. Mayor, W. Rathgeber, G. Schmid, U. Simon, V. Vogel, D. Wyrwa, in C. F. Gethman (ed.) *Wissenschaftethik und Technikfolgenbeurteilung*, *Nanotechnology. Assessment and Perspectives*, Vol. 27, Springer, Berlin-Heidelberg, 2006.
3 T. Castro, R. Reifenberger, E. Choi, R. P. Andres, *Phys. Rev. B* 13 (1990) 8548.
4 M. Kaupp, *Spektrum der Wissenschaften*, December 2005, 90.
5 W. J. Parak, L. Manna, F. C. Simmel, D. Gerion, P. Alivisatos, in G. Schmid (ed.) *Nanoparticles. From Theory to Application*, Wiley-VCH, Weinheim, 2004.
6 G. Mie, *Ann. Phys*. 25 (1908) 377.
7 U. Kreibig, M. Vollmer, *Springer Series in Materials Science 25, Optical Properties of Metal Clusters*, Springer, Berlin-Heidelberg, 1995.
8 H. Brune, H. Ernst, A. Grunwald, W. Grünwald, H. Hofmann, H. Krug, P. Janich, M. Mayor, W. Rathgeber, G. Schmid, U. Simon, V. Vogel, D. Wyrwa, in C. F. Gethman (ed.) *Wissenschaftethik und Technikfolgenbeurteilung*, *Nanotechnology. Assessment and Perspectives*, Vol. 27, Springer, Berlin-Heidelberg 2006, p. 91.
9 C. E. Briant, B. R. C. Theobald, J. W. White, C. K. Bell, D. M. P. Mingos, *J. Chem. Soc. Chem. Commun*. (1981) 201.
10 J. W. A. van der Velden, F. A. Vollenbroek, J. J. Bour, P. I. Beurskens, J. M. M. Smits, W. P. Bosman, *Rec. J. R. Neth. Chem. Soc*. 100 (1981) 148.
11 U. Kreibig, K. Fauth, C. -G. Granqvist, G. Schmid, *Z. Phys. Chem. Neue Folge*, 169 (1990) 11.
12 G. Schmid, R. Boese, R. Pfeil, F. Bandermann, S. Meyer, G. H. M. Calis, J. W. A. van der Velden, *Chem. Ber*. 114 (1981) 3634.
13 G. Schmid, *Inorg. Syntheses* 7 (1990) 214.
14 B. A. Smith, J. Z. Zhang, U. Giebel, G. Schmid, *Chem. Phys. Lett*. 270 (1997) 139.
15 E. D. Belotskii, P. M. Tomchuk, *Surf. Sci*. 239 (1990) 143.
16 H. H. Smit, R. C. Thiel, L. J. de Jongh, *Z. Phys. D* 12 (1989) 193.
17 G. Schmid, B. Morun, J. -O. Malm, Angew. *Chem. Int. Ed. Engl.* 28 (1989) 778.
18 F. M. Mulder, T. A. Stegink, R. C. Thiel, L. J. de Jongh, G. Schmid, *Nature* 367 (1994) 716.
19 A. Bezryadin, C. Dekker, G. Schmid, *Appl. Phys. Lett*. 71 (1997) 1273.
20 H. van Kempen, J. G. A. Dubois, J. W. Gerritsen, G. Schmid, *Physica B* 204 (1995) 51.
21 J. G. A. Dubois, J. W. Gerritsen, S. E. Shafranjuk, E. J. G. Boon, G. Schmid, H. van Kempen, *Europhys. Lett*. 33 (1996) 279.
22 L. F. Chi, M. Hartig, T. Drechsler, Th. Schaak, C. Seidel, H. Fuchs, G. Schmid, *Appl. Phys. Lett. A* 66 (1998) 187.
23 G. Schön, U. Simon, *Colloid Polym. Sci*. 273 (1995) 101.
24 U. Zhang, G. Schmid, U. Hartmann, *Nanoletters* 3 (2003) 305.
25 R. L. Whetten, J. T. Khoury, M. M. Alvarez, S. Murthy, I. Vezmar, Z. L. Wang, P. W. Stephens, C. L. Cleveland, W. D. Luedtke, U. Landmann, *Adv. Mater*. 8 (1996) 428.
26 St. A. Harfenist, Z. L. Wang, M. M. Alvarez, I. Vezmar, R. l. Whetten, *J. Phys. Chem*. 100 (1996) 13904.
27 St. A. Harfenist, Z. L. Wang, R. L. Whetten, I. Vezmar, M. M. Alvarez, *Adv. Mater*. 9 (1997) 817.
28 Z. L. Wang, *Adv. Mater*. 10 (1998) 13.
29 J. E. Martin, J. P. Wilcoxon, J. Odinek, P. Provencio, *J. Phys. Chem.* 104 (2000) 9475.
30 M. P. Pileni, *Appl. Surf. Sci*. 171 (2001) 1.
31 S. Stoeva, K. J. Klabunde, C. M. Sorensen, I. Dragieva, *J. Am. Chem. Soc*. 124 (2002) 2305.
32 J. E. Martin, J. P. Wilcoxon, J. Odinek, P. Provencio, *J. Phys. Chem. B* 106 (2002) 971.
33 L. O. Brown, J. E. Hutchison, *J. Phys. Chem. B* 105 (2001) 8911.
34 E. Shevchenko, D. Talapin, A. Kornowski, F. Wiekhorst, J. Kötzler, M. Haase, A. Rogach, H. Weller, *Adv. Mater*. 14 (2002) 287.

35 S. Sunn, C. B. Murray, D. Weller, L. Folks, A. Moser, *Science* 287 (2000) 1989.
36 K. Soulantica, A. Maisonnat, M. -C. Fromen, M. -J. Casanova, B. Chaudret, *Angew. Chem. Int. Ed.* 42 (2003) 1945.
37 G. Schmid, R. Pugin, T. Sawitowski, U. Simon, B. Marler, *Chem. Commun*. (1999) 1303.
38 G. Schmid, W. Meyer-Zaika, R. Pugin, T. Sawitowski, J. -P. Majoral, A. -M. Caminade, C. -O. Turrin, *Chem. Eur. J.* 6 (2000) 1693.
39 G. Schmid, E. Emmrich, J. -P. Majoral, A. -M. Caminade, *Small* 1 (2005) 73.
40 H.-G. Boyen, G. Kästle, F. Weigl, B. Koslowski, C. Dietrich, P. Ziemann, J. P. Spatz, S. Riethmüller, C. Hartmann, M. Möller, G. Schmid, M. G. Garnier, P. Oelhafen, *Science* 297 (2002) 1533.
41 H.-G. Boyen, A. Ethirajan, G. Kästle, F. Weigl, P. Ziemann, G. Schmid, M. G. Garnier, M. Büttner, P. Oelhafen, *Phys. Rev. Lett.* 94 (2005) 016804-1.
42 G. Schmid, D. V. Talapin, E. V. Shevchenko, in G. Schmid (ed.) *Nanoparticles. From Theory to Application*, Wiley-VCH, Weinheim, 2004, 260.
43 J. P. Spatz, S. Sheiko, M. Möller, *Macromolecules* 29 (1996) 3220.
44 J. P. Spatz, A. Roescher, M. Möller, *Adv. Mater.* 8 (1996) 337.
45 J. P. Spatz, S. Mößner, M. Möller, *Angew. Chem. Int. Ed. Engl.* 35 (1996) 1510.
46 J. P. Spatz, S. Sheiko, M. Möller, *Adv. Mater.* 8 (1996) 513.
47 J. P. Spatz, M. Möller, P. Ziemann, *Physikal. Blätter* 55 (1999) 1.
48 J. P. Spatz, P. Eibeck, S. Mößner, M. Möller, T. Herzog, P. Ziemann, *Adv. Mater.* 10 (1998) 849.
49 M. Möller, J. P. Spatz, A. Roescher, S. Mößner, S. T. Selvan, H.-A. Klok, *Macromol. Symp.* 117 (1997) 207.
50 J. P. Spatz, T. Herzog, S. Mößner, P. Ziemann, M. Möller, in H. Ito, E. Reichmanis, O. Nalamasu, T. Ueno (eds.), *ACS Series, Micro- and Nanopatterning Polymers* 706 (1997) 12.
51 J. P. Spatz, S. Mößner, M. Möller, T. Herzog, A. Plettl, P. Ziemann, *J. Luminescence* 76, 77 (1998) 168.
52 J. P. Spatz, S. Mößner, C. Hartmann, M. Möller, T. Herzog, M. Krieger, H. -G. Boyen, P. Ziemann, B. Kabius, *Langmuir* 16 (2000) 407.
53 R. D. Piner, J. Zhu, F. Xu, S. Hong, C. A. Mirkin, *Science* 283 (1999) 661.
54 S. Hong, J. Zhu, C. A. Mirkin, *Science* 286 (1999) 523.
55 R. Maoz, S. R. Cohen, J. Sagiv, *Adv. Mater*. 11 (1999) 55.
56 R. Maoz, E. Frydman, S. R. Cohen, J. Sagiv, *Adv. Mater*. 12 (2000) 424.
57 R. Maoz, E. Frydman, S. R. Cohen, J. Sagiv, *Adv. Mater*. 12 (2000) 725.
58 S. Liu, R. Maoz, J. Sagiv, *Nanoletters* 4 (2004) 845.
59 S. Liu, R. Maoz, G. Schmid, J. Sagiv, *Nanoletters* 2 (2002) 1055.
60 E. Katz, I. Willner, *Angew. Chem. Int. Ed.* 43 (2004) 6042.
61 C. M. Niemeyer, B. Ceyhan, *Angew. Chem. Int. Ed*. 40 (2001) 3685.
62 J. M. Nam, S. J. Park, C. A. Mirkin, *J. Am. Chem. Soc*. 124 (2002) 3820.
63 J. M. Nam, C. S. Thaxton, C. A. Mirkin, *Science* 301 (2003) 1884.
64 V. Pavlov, Y. Xiao, B. Shlyahovsky, I. Willner, *J. Am. Chem. Soc*. 126 (2004) 11768.
65 C. M. Niemeyer, B. Ceyhan, P. Hazarika, *Angew. Chem. Int. Ed.* 42 (2003) 5766.
66 P. Hazarika, B. Cehan, C. M. Niemeyer, *Small* 1 (2005) 844.
67 P. Hazarika, B. Ceyhan, C. M. Niemeyer, *Angew. Chem. Int. Ed*. 43 (2004) 6469.
68 C. M. Niemeyer, U. Simon, *Eur. J. Inorg. Chem*. (2005) 3641.
69 M. G. Warner, J. E. Hutchison, *Nat. Mater*. 2 (2003) 272.
70 D. Wyrwa, N. Beyer, G. Schmid, *Nanoletters* 2 (2002) 419.
71 Y. Liu, W. Meyer-Zaika, S. Franzka, G. Schmid, M. Tsoli, H. Kuhn, *Angew. Chem. Int. Ed.* 42 (2003) 2853.
72 M. Thomas, A. M. Klibanov, *Proc. Natl. Acad. Sci. U.S.A.* 100 (2003) 9138.
73 A. G. Tkachenko, H. Xie, Y. Liu, D. Coleman, J. Ryan, W. Glomm, M. K. Shipton, S. Franzen, D. L. Feldheim, *Bioconjugate Chem*. 15 (2004) 482.
74 A. G. Tkachenko, H. Xie, Y. Liu, D. Coleman, J. Ryan, W. Glomm, M. K. Shipton, S. Franzen, D. L. Feldheim, *J. Am. Chem. Soc.* 125 (2003) 4700.
75 J. F. Hillyer, R. M. Albrecht, *J. Pharm. Sci*. 90 (2001) 1927.
76 E. E. Connor, J. Mwamuka, A. Gole, C. J. Murphy, M. D. Wyatt, *Small* 1 (2005) 325.
77 M. Tsoli, H. Kuhn, W. Brandau, H. Esche, G. Schmid, *Small* 1 (2005) 841.

CHAPTER 2

Metal Nanoclusters: Synthesis and Strategies for their Size Control

Helmut Bönnemann and Kyatanahalli S. Nagabhushana

Max-Planck-Institut für Kohlenforschung, Mülheim an der Ruhr, Forschungszentrum Karlsruhe, ITC-CPV, Karlsruhe, Germany

1. General Introduction

Nanostructured metal clusters are isolable particles of sizes between 1 and 50 nm. In order to prevent agglomeration, these nanosized entities have to be stabilized by ligand molecules or a whole plethora of "protecting shells." The resulting metal colloids can be redispersed in water ("hydrosols") or organic solvents ("organosols"). Nanostructured metal colloids have been obtained via so-called "top down methods," e.g., by the mechanical grinding of bulk metals and subsequent stabilization of the resulting nanosized metal particles by the addition of colloidal protecting agents [1,2]. The application of "physical means" such as metal vapour techniques for the production of a wide range of nanostructured metal colloids on a preparative laboratory scale has extensively been reviewed in a recent handbook article [3].

The "bottom up methods" of wet chemical nanoparticle preparation rely basically on the following methods:

- chemical reduction of metal salts [4–10] including electrochemical pathways
- thermolysis [11–22], including photolytic [23–38], radiolytic [36], and sonochemical [39–42] pathways
- controlled decomposition of pre-formed metastable organometallics.

The chemical reduction of transition metal salts in the presence of stabilizing agents to generate zerovalent metal colloids in aqueous or organic media was first published in 1857 by Faraday [43]. During his studies on gold sols, Faraday farsightedly concluded "… the gold is reduced in exceedingly fine particles which becoming diffuse, produce a beautiful fluid …." In the early 1950s, Turkevitch established the first reproducible standard recipes for the preparation of metal colloids (e.g., for 20 nm gold by reduction of $[AuCl_4^-]$ with sodium citrate). In addition, he was the first to propose a mechanism for the stepwise formation of nanoclusters based on nucleation and growth [44–46]. Data from modern analytical techniques and more recent thermodynamic and kinetic studies have helped to refine this model considerably, and nowadays "computational chemistry" efficiently assists chemists in the sophisticated design of metal nanoparticles which exhibit special properties needed for specific applications, e.g., in catalysis or in materials science.

2. Mechanistic Considerations on the Formation of Metal Nanoparticles

Before turning to a more detailed description of some preparative methodologies, this section summarizes the different ways in which particles can be stabilized, the mechanisms by which particles form and grow, and examines the considerable contribution of theory to understanding of these processes.

To produce organosol or hydrosols that are stable for extended periods, metal nanoparticles must be encapsulated by addition of suitable protecting agents in order to balance the processes of particle nucleation and growth. It is still to a large extent left to the intuition and the art of the colloidal chemist to find through experience and the careful application of physicochemical rules, the stabilizer that is most appropriate for any given type of particle. Theory, however, has made a significant contribution in the form of quantitative predictions on the stabilities of bi- or trimetallic particles of compositions that are of interest to chemists. It has even provided helpful guidelines for designing particles with specific electronic and geometrical structures to give them the properties sought for a given application such as catalysis.

2.1. Modes of Stabilization

Since the surface areas of metal nanoclusters are enormous relative to their masses, they have an excess surface free energy comparable to the lattice energy, making them

Metal Nanoclusters in Catalysis and Materials Science: The Issue of Size Control
Edited by B. Corain, G. Schmid and N. Toshima

thermodynamically unstable. Protective agents are therefore essential in order to be able to outweigh the attractive van der Waals forces by the repulsive electrostatic and steric forces between adsorbed ions and associated counterions. To achieve sufficient interparticle separation, it can be helpful to use sterically demanding substituents. In addition, the solubility of the metal sol in organic or aqueous phases can be tailored by introducing and varying lipo- or hydrophilic end groups.

Based on the type of protecting shell, the mode of stabilization can be classified as follows:

- electrostatic [44]
- steric (using polymers) (see Section 3.6) [47]
- ligand (P, N, S donors, see Sections 3.1 and 3.2) [48–50]
- electrosteric (see Section 3.3) [51–53]
- solvent (see Section 3.5), e.g., THF [54,55] or propylene carbonate [56]

Electrostatic stabilization results from the electrical double layer formed by the anions and cations interacting with the metallic particle surface. This results in coulombic repulsion between particles. If the electric potential associated with the double layer is sufficiently high, electrostatic repulsion will prevent the particles from agglomerating. A dispersion of metal clusters that are only stabilized electrostatically can, however, coagulate easily if the ionic strength of the dispersing medium is increased sufficiently for the double layer to become compressed. The level of stabilization can be influenced by altering the total charge on the metal cluster surface. The polarity of the solvent affects the degree of particle dispersion.

Steric stabilization is brought about by large organic molecules such as poly(*N*-vinyl-2-pyrrolidone) (PVP) that are firmly adsorbed on the surface of the nanoparticle [47,57]. Polymeric stabilizers establish many weak bonds with the nanoparticle's surface rather than forming less strong bonds at specific sites of the particles. This mode of stabilization has been shown to be very versatile (see Section 3.6).

The introduction of ''organometallic ligands'' as stabilizers by Schmid et al. in 1981 [48] and Vargaftik et al. in 1985 [49] paved the way for the precise molecular definition of metallic ''full shell clusters,'' which are well defined in size and shape [58,59]. P, N, S donors have been exploited extensively over the years (cf. Sections 3.1 and 3.2) [60,61].

Electrosteric (i.e., electrostatic as well as steric) stabilization has proved to be a very reliable means of preventing particle agglomeration. The key feature is to adsorb bulky molecules such as polymers or surfactants at the surface of the particles. These sterically demanding ''surface-active protecting shields'' coordinate strongly to the metal particle's surface and at the same time are very well solvated in the respective medium (organic phase or water). This is the main advantage of using tetra(octyl)ammonium halides as the protective agent. The halide anions of *N*-(octyl)$_4$X have been shown to bind to the metal surface through the negatively charged chloride while the long alkyl chains shield the metallic core like an umbrella (see Figure 1) [51,62].

When the concentration of the stabilizer in solution is high, the particles are forced into restricted conformations: this decreases the entropy and, in turn, increases the free energy. Further, the particles begin to interpenetrate because of the high local concentration of adsorbed bulky protective groups. This causes osmotic repulsion since the solvent immediately re-establishes equilibrium via dilution, thus separating the particles again. In general, electrostatic stabilization is insensitive to impurities and additives that could affect the charge on the stabilizers. This makes this method suitable for multigram syntheses [63]. Solvents such as THF [55], THF/MeOH [64], or propylene carbonate can act as colloidal stabilizers [56]. Long-chain alcohols have also been successfully applied as colloidal stabilizers for metallic nanoparticles [65–81].

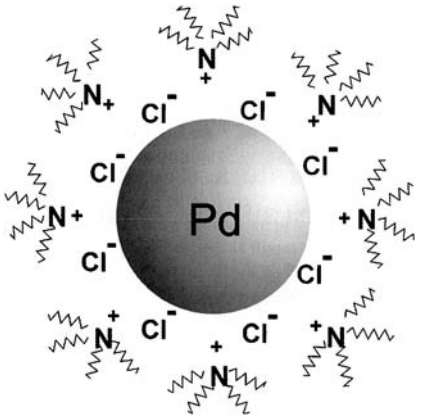

Figure 1. Electrosteric stabilization of a Pd particle by the tetra(octyl)ammonium halide stabilizer. (Reprinted from Ref. [51], © 2004, with permission from Elsevier.)

2.2. Nucleation and Growth Mechanisms

Turkevich who established the first reproducible standard procedure for the preparation of metal colloids [44] also proposed a mechanism for the stepwise formation of nanoclusters based on nucleation, growth, and agglomeration [45,46]. This model, refined by data from modern analytical techniques and results from thermodynamic and kinetic studies, is in essence still valid today (Figure 2) [82].

The metal salt is first reduced to give zerovalent metal atoms. These collide in solution with further metal(0) atoms or with ''sub-clusters'' that have already been formed to give a stable ''seed'' nucleus of 13 metal atoms. This is the first member of the so-called full-shell cluster family (see Section 3.1) and its formation is irreversible. To initiate nucleation, the concentration of metal atoms in solution must be high enough to reach ''supersaturation'' [83,84]. LaMer and coworkers, studying sulphur sols rather than metal nanoclusters [85], were the first to propose that nucleation from supersaturated solutions occurs as a sudden burst; and they also stated that monodispersity is a consequence of carefully separating the nucleation step from the subsequent growth stage (see Figure 2). For metal particles, nucleation is the result of a complicated interplay of factors such as the difference between the redox potentials of the metal salt and the reducing agent, and the reaction conditions including the rate of addition, the reaction temperature, and even the stirring rate. To

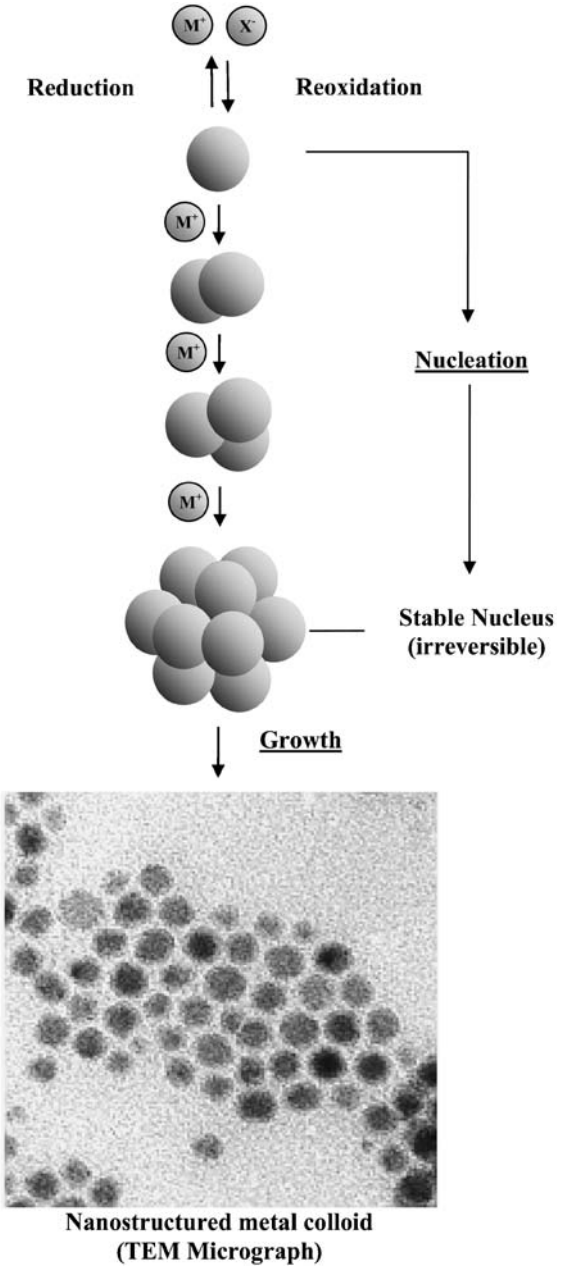

Figure 2. Wet chemical formation of nanostructured metal colloids [82].

achieve a monodisperse sample, the nucleation event must be complete before the growth step begins.

As a rule, short nucleation times are the prerequisite for monodisperse particle formation. A recent mechanistic study showed that when $Pt(acac)_2$ is reduced by alkylaluminium, virtually all the Pt cluster nuclei appear at the same time and have the same size [86]. The nucleation process quickly consumes enough of the metal atoms formed initially to decrease their concentration below the critical threshold. No new metal cluster nuclei are created in the subsequent diffusion-controlled growth stage, during which the remaining metal atoms are taken up by the nuclei already in existence. Since the growth period is almost the same for all the particles, a monodisperse sample is obtained. If nucleation and growth do overlap, then the duration of the growth period will differ between nucleation sites, resulting in an unwanted broad particle size distribution. Subsequent to nucleation, the particle formation depends solely on the specific surface energy of a given metal. If this is significantly higher than the entropy loss, the growing particles tend to undergo "Ostwald ripening" [87] or coalescence – an undesired mechanism that will inevitably broaden the size distribution and cause polydispersity. If the reaction is stopped quickly at this stage the resulting particles are seen to be polydisperse – sometimes with two distinct particle sizes. In practice, the most effective way of ensuring that nucleation is separated from growth is the quick "injection" of strong reduction agents such as hydrides or organometallics to the respective metal salt(s) dissolved in hot liquid media.

A further critical issue for gaining high-quality nanoparticles is the passivation of the metallic surface by adding organic molecules (see Section 3.1). Surface passivation helps to achieve size selectivity (sometimes even yielding well-defined nanocrystals) (see Section 3.1), prevent agglomeration and fusing of particles, and provide for the solubility of the particles in the desired organic or aqueous medium (see the methodology Section 3). In addition, surface passivation can be used to derivatize the metallic surface, providing a means of attaching the nanoparticles to catalyst carriers (see Section 4.1), of linking particles together to form a "network" of particles [88], or of binding them to biomolecules (see Section 4.3).

Recently it was demonstrated experimentally that ligand molecules control particle formation by thermodynamic rather than kinetic means. Thus, Klabunde and coworkers discovered a process which they coined "digestive ripening." Upon heating a highly polydisperse gold colloid with excess ligand it was found that it evolved into a nearly monodispersed system [89–93]. The explanation is that larger particles break down in solution, while at the same time small particles grow until they reach a stable size. This process is the exact reverse of "Ostwald ripening" which, driven by the tendency to lower the surface energy, always favours particle growth. Although this method of generating colloidal nanoparticles is not generally applicable, it has been extended successfully to the production of various nanometals (cf. Chapter 12).

A most significant contribution to the understanding of mechanistic aspects of a metal salt reduction was made recently by Finke et al., with their discovery of the four-step, double autocatalytic mechanism by which transition metal organometallic and metal-salt precursors self-assemble into zerovalent transition metal nanoclusters under reductive conditions (cf. Section 3.8 and references therein). In essence, this concept replaces the generally accepted three-step mechanism of nanoparticle nucleation, autocatalytic growth, and bimolecular agglomeration by the four steps of particle formation depicted in Figure 3. This mechanism was demonstrated by a series of kinetic experiments on the reduction of the low-valent complex $[Pt(COD)PtCl_2]$ with hydrogen in presence of Bu_3N and a

"proton sponge" (1,8-bis(dimethylamino)naphthalene). As shown in Figure 3, the reaction begins with a slow, continuous reduction step (A→B) in which the metal atoms form a nucleus. This is followed by fast autocatalytic surface growth (A + B→2B), and then by bimolecular agglomeration (B + B→C), and finally by an unprecedented step of autocatalytic agglomeration between small (B) and a larger (bulk metal like) clusters (C). This final step is represented in Figure 3 as (B + C→1.5 C).

The mechanism of formation of Pt particles by the organometallic reduction route, however, was found to proceed differently, for example in the "reductive stabilization" of Pt nanoparticles produced by reacting Pt-acetylacetonate with excess trimethylaluminium. Here, derivates of aluminium alkyls act as both reducing agents and colloidal stabilizers. As was shown by a combination of analytical tools, initially a symmetrical organometallic complex is formed that consists of a four-membered ring with alternating aluminium and platinum atoms. This intermediate complex has been trapped and characterized (see Figure 4) [94].

According to anomalous small angle X-ray scattering (ASAXS), this compound slowly decomposes to release redispersible platinum nanoclusters with a mean diameter of 1.2 nm. The protective shell is formed on site by excess aluminium organics.

2.3. Theoretical Considerations

Only in recent years have computers become powerful enough, and theory sophisticated enough to provide

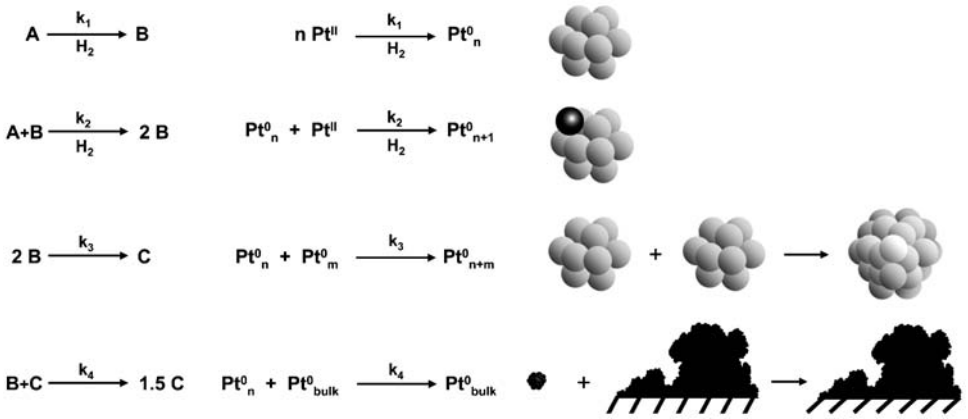

Figure 3. Double autocatalytic pathway for the metal nanocluster formation. (Reprinted from Ref. [299], © 2005, with permission from American Chemical Society.)

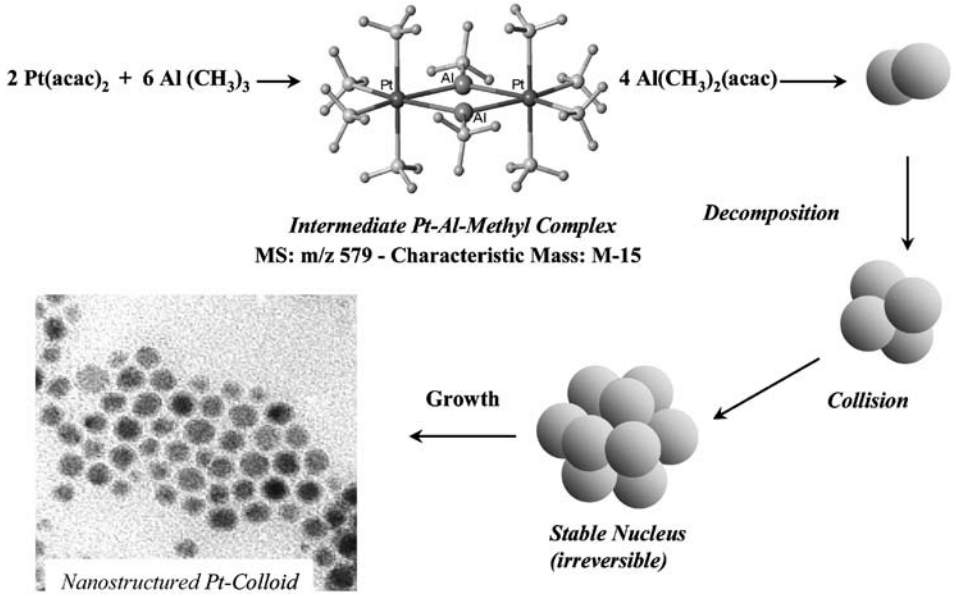

Figure 4. Nanoscopic Pt colloids in the "embryonic state" during "reductive stabilization" [86,94]. (Reprinted from Ref. [53], © 2007, with permission from Wiley-VCH.)

synthetic chemists with theoretical calculations coupled with computational studies which simulate the structure and reactivity of nanoscopic materials. Such studies are proving to be an extremely useful tool for experimentalists. Theoreticians can now calculate in advance with reasonable accuracy (to within 1 kcal/mol) the energetics that govern a process in terms of reaction rates and thermodynamic properties. Synthetic chemists, in turn, are now faced with the challenge of finding viable protocols to prepare nanoparticles that have exactly the structural features favoured by theory. In addition, a truly fundamental mechanistic understanding of chemical mechanisms even including the identification of catalytic sites is now possible and provides a better understanding of the rate-limiting elementary processes. Specifically, a quantitative understanding of the interactions between the adsorbate and the metal surface helps to design or substantially improve nanostructured catalysts, e.g., by introducing defect crystal sites at the particle surface, by tailoring the composition and the inner structure of nanometallic alloys for a specific application, or by selecting the appropriate supports.

The most powerful computational tools currently used are

- ab initio density functional theory and
- ab initio molecular dynamics methods.

Ab initio methods allow the nature of active sites to be elucidated and the influence of supports or solvents on the catalytic kinetics to be predicted. Neurock and coworkers have successfully coupled theory with atomic-scale simulations and have tracked the molecular transformations that occur over different surfaces to assess their catalytic activity and selectivity [95–98]. Relevant examples are the Pt-catalyzed NO decomposition and methanol oxidation. In case of NO decomposition, density functional theory calculations and kinetic Monte Carlo simulations substantially helped to optimize the composition of the nanocatalyst by alloying Pt with Au and creating a specific structure of the Pt_9Au_7 particles. In catalytic methanol decomposition the elementary pathways were identified leading to CO both in the vapour phase and in solution. Van Hove and Baskes have developed the modified embedded atom method (MEAM) [99,100] and applied it together with Monte Carlo simulations for investigating surface segregation phenomena in bimetallic Pt alloy nanoparticles. This method is particularly relevant for the design of Pt alloy particles for the development of CO-tolerant catalysts for the anodes of fuel cells. The authors were able to calculate the electronic and geometrical structures of three Pt alloy particle compositions ($Pt_{75}Ni_{25}$, $Pt_{75}Re_{25}$, and $Pt_{80}Mo_{20}$) [101] and found the following structural features to be advantageous for their use as anode catalysts:

- For $Pt_{75}Ni_{25}$ the optimal structure is an "egg-shell" of Pt covering a Ni-rich core.
- $Pt_{75}Re_{25}$ also adopts a core-shell structure such that a nearly pure Pt shell surrounds a more uniform core formed by Pt–Re
- In $Pt_{80}Mo_{20}$ the faces are occupied only by Pt atoms while the Mo atoms appear at the edges and vertices

Significant (and even spectacular) results were contributed by the group of Norskov to the field of electrocatalysis [102–105]. Theoretical calculations led to the design of novel nanoparticulate anode catalysts for proton exchange membrane fuel cells (PEMFC) which are composed of trimetallic systems where which PtRu is alloyed with a third, non-noble metal such as Co, Ni, or W. Remarkably, the activity trends observed experimentally when using Pt-, PtRu-, PtRuNi-, and PtRuCo electrocatalysts corresponded exactly with the theoretical predictions (cf. Figure 5(a) and (b)) [102].

In case of fuel cell cathodes, theoretical considerations were directed towards optimizing catalysts for O_2 reduction [103]. This has led to the synthesis of Pt_3Co/C nanocatalyst systems and preliminary results again indicate perfect agreement between the calculations and the wet electrochemical results obtained with metal nanoparticles of the composition which theory had recommended [106].

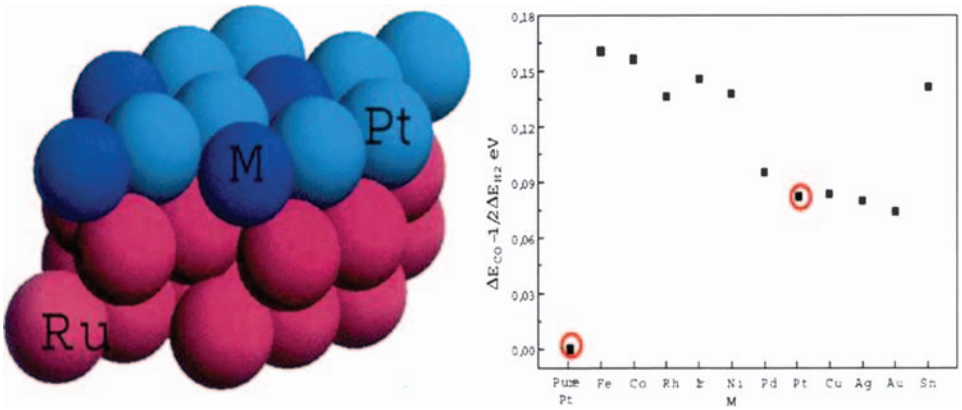

Figure 5. Schematic structure (left) of a ternary alloy on Ru(0 0 1) surface, MPt_2/Ru, with M selected from the set {Fe, Co, Rh, Ir, Ni, Pd, Pt, Cu, Ag, Au, Sn}.The two bottom layers represent Ru atoms while Pt atoms form the top surface atoms. The predicted surface activities of various ternary alloys are shown in the plot (right). (Reprinted from Ref. [102], © 2003, with permission from American Chemical Society.)

3. Synthetic Methodologies and Size Control

After a period of hibernation following the publication of Turkevich's seminal papers in the 1950s [44,46], a whole plethora of preparative protocols has been published since Henglein and coworkers resumed this work in the late 1970s [107,108]. The goal of this chapter is not to present a comprehensive directory of all synthetic papers on nanometal colloids, but to provide the reader with a general survey of a number of modern versions of established preparative methodologies that have been tested and found effective in a number of practical applications.

3.1. Schmid's Full-Shell Clusters

The metal nuclei of the so-called full-shell clusters, also referred to as "magic number clusters," generally exhibit hexagonal or cubic close packing (ccp). Figure 6 shows the stepwise formation of the first "magic-number" clusters built by 13, 55, 147, and 309 atoms.

The first metal atom M can be coordinated by just 12 equivalent atoms to form an M_{13} cluster unit. The general formula for the "magic number" of atoms that must be added to a full-shell nanocluster having n shells to construct the next higher one of $(n+1)$ shells is: $10n^2+2$. If 42 additional metal atoms are coordinated to the outer shell of 12 atoms of the M_{13} cluster (Figure 6 shown in red) the M_{55} cluster is formed (Figure 6 shown in yellow); 92 more atoms lead to the next full-shell cluster M_{147} (Figure 6 shown in dark blue) and a further 162 atoms produce the four-shell M_{309} cluster (Figure 6 shown in light blue). Five shells correspond to 561, seven shells to 1415 atoms, and even eight-shell metal clusters are known consisting of no less than 2057 atoms. It should be mentioned, however, that large full-shell clusters are usually isolated only in the form of more or less "monodisperse" particles exhibiting size deviations of $\pm 10\%$.

Ligand-stabilized Au_{13} clusters were first described by Schmid as early as 1981 [58,59] while the synthesis of the first Pt_{13} cluster (encapsulated by trimethylaluminium) was reported only recently [109]. The Au_{13} clusters exhibit icoshedral structures, whereas Au_{55} was found to take up the ccp structure of bulk gold. Schmid's ligand-protected $Au_{55}(PPh_3)_{12}Cl_6$ cluster really represents the transition from bulk metal to a "metallic molecule" and – since it is presumably the most thoroughly investigated M_{55} unit – it has become the "paradigm" of nanoclusters. The synthesis starts from $(PPh_3)AuCl$, which is reduced by B_2H_6 in a warm aromatic solvent such as toluene [48,110]. Besides functioning as the reducing agent, diborane effectively binds excess PPh_3 in the form of BH_3–PPh_3. Quantitative ligand exchange has made a multitude of derivatives accessible including the water soluble $Ph_2PC_6H_4SO_3$–Au_{55} [111] and the thiol-substituted Au_{55} [112–114]. The multifaceted chemistry of nanoparticulated gold has been recently reviewed [61]. As in case of the ligand-stabilized Au_{55}, the structure of the Pt_{309}-, Pd_{561}- Pd_{1415}-, and Pd_{2057}-cores was found to be ccp according to X-ray diffraction and high-resolution transmission electron microscopy (HRTEM) (for details see Ref. [115]). Au_{55} also represents the prototype of a metallic quantum dot (see Chapters 4 & 5 in Ref. [60]). Aspects of the assembly of gold nanoparticles and their electrical properties in one, two, or three dimensions have been outlined recently in literature [60,61,111–160]. For biomedical applications of Au_{55} see Section 4.3. The outstanding features of the Schmid-type cluster family are their well-defined structures, the exceptional variability of their synthesis, and their broad range of applications from quantum dots to catalysis to biomedicine. The only drawback to the preparation procedure is that it requires B_2H_6, a rather special reducing agent in the hands of the average bench chemist.

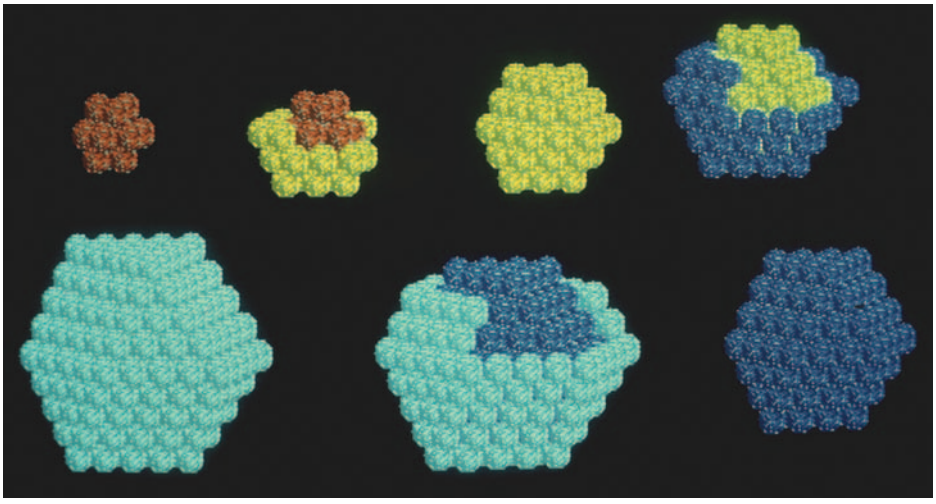

Figure 6. Stepwise formation of full-shell clusters, 13 (1 + 12), 55 (13 + 42), 147 (55 + 92), and 309 (147 + 162). Generally $10n^2+2$ atoms for the nth shell. (Reproduced with kind permission of G. Schmid, University Essen-Duisburg, Germany.)

3.2. Moiseev's "Giant Clusters"

Using hydrogen as the reductant, Moiseev et al. created a series of Pd nanoclusters which exhibit well-defined sizes, shapes, and compositions, similar to those described above in Section 3.1. These nanoclusters can even be regarded as "true inorganic compounds" having a precise formula such as $Pd_{561}L_{\cong 60}$ $(OAc)_{\cong 180}$. (L = phenathroline, bipyridine) [49,161–166]. The "giant Pd cluster" is synthesized in two steps: reduction of palladium(II) acetate in acetic acid by hydrogen gas in the presence of either 1,10-phenanthroline (phen) or 2,2′-bipyridine (bipy) yields an intermediate product $[Pd_4phen(OAC)_2H_4]_{n\approx 100}$ of 2 nm size (Equation (1)).

$$4Pd_3(OCOCH_3)_6 + 3phen + 15H_2 \rightarrow 3Pd_4phen(OCOCH_3)_2H_4 + 18CH_3COOH \quad (1)$$

In acetic acid solution $[Pd_4phen(OAC)_2H_4]_{n\approx 100}$ takes up to 5 Mol of O_2 per gram atom of palladium over ~20 min to give the air stable and water soluble "giant Pd cluster" in 85% yield. The characterization of Moiseev's "giant" cationic palladium clusters and their catalytic properties have recently been reviewed by Finke et al. [167]. Schmid has obtained further members of the "giant cluster family," namely $Pd_{561}phen_{36}$ $O_{\cong 200}$, $Pd_{1415}phen_{60}$ $O_{\cong 1100}$, $Pd_{2057}phen_{84}$ $O_{\cong 1600}$ by reducing Pd salts with hydrogen [168–170].

3.3. Surfactant-Stabilized Nanocolloids and Related Systems

Since the first paper on nanosized metal particles stabilized by surface-active agents appeared in 1979 [171], a considerable body of knowledge has been gained regarding the synthesis, characterization, and potential application of systems of this kind of one or more metals. This is reflected by the number of book chapters and review articles that have been published on this subject since 1991 [3,62,172–182]. A comprehensive review chapter was published recently [53]. Surface-active chemicals are capable of limiting the particle growth at certain stages (size-control) but can be detached easily from the metallic surface, providing active sites to exploit the reactivity of the metallic core for subsequent chemical reactions, e.g., catalysis. However, surfactants acting as colloidal stabilizers not only help to control the particle growth to yield a fairly "monodisperse" size distribution (i.e., size deviations < 5%) but also efficiently encapsulate the nanoclusters, preventing their agglomeration to the metallic bulk. A wide range of lipo- and hydrophilic surfactants of the cationic, anionic, and non-ionic type, including even environmentally benign sugar soaps have been applied successfully as colloidal stabilizers to yield isolable nanometal colloids that can be redispersed to form highly concentrated metal solutions (> 100 mg metal/l) in either organic or aqueous media (see Table 2 in Ref. [177]) [183]. To avoid duplication, only the key features of the most common synthetic methods developed in this field will be summarized below – along with a brief evaluation of their specific advantages and drawbacks.

3.3.1. The Tetraalkylammonium Method

The relatively bulky tetraoctylammonium halides act as powerful protective agents and stabilizers for particles consisting of one or more transition metals of the groups 6–11 of the periodic table [62,172,184]. In this special case, the stabilizing cation $[NR_4]^+$ is combined with the reductant $[Bet_3H]^-$ in the same molecule: the surface-active protective agent $[NR_4]^+[X]^-$ species is formed at the reduction centre itself in high local concentration (see Equation (2)).

$$MX_v + NR_4(Bet_3H) \rightarrow M_{colloid} + vNR_4X + vBet_3 + \frac{v}{2}H_2 \uparrow \quad (2)$$

where M = metals of the groups 6–11; X = Cl, Br; v = 1, 2, 3; and R = alkyl, C_6–C_{20}.

This is the basis of a generally applicable multigram synthesis routes to isolable 1–10 nm organosols of the transition metals that are easily redispersible in high concentration in organic phases (Figure 7) [3,183].

Typically the $[NR_4]^+$-stabilized "raw" organosols contain 6–12 wt% metal but for metals such as rhodium they can be converted to "pure" colloids containing

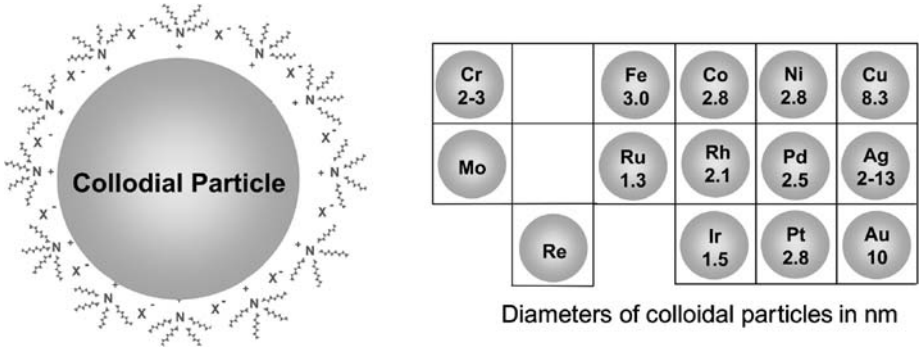

Figure 7. Metal organosols accessible via the $NR_4(Bet_3H)$ route (Equation (2)). (Reprinted from Ref. [53], © 2007, with permission from Wiley-VCH.)

70–85 wt% metal. Structural examinations [51] have revealed that the NR_4X is bound to the metal surface through the negatively charged halogen X while the long alkyl chains shield the metallic core like an umbrella. In this case, an extremely efficient stabilization of the colloidal metal particles is brought about by a well-balanced combination of electrostatic and steric forces in the protective shell. The main drawback of the method is that the size of the particles of the resulting organosols (see Figure 7) cannot be varied by altering the reaction conditions.

The pre-preparation of $NR_4(Bet_3H)$ can, however be avoided by coupling the NR_4X agent to the metal salt prior to the reduction step. Again, high local concentration of the protecting agent is provided right at the reduction centre which allows application of a whole range of conventional reducing agents (Equation (3)) [177].

$$(NR_4)_wMX_vY_w + v\text{Red} \rightarrow M_{\text{colloid}} + v\text{Red}\,X + w\,NR_4Y \quad (3)$$

where M = metals of the groups 4–11; Red = H_2, HCOOH, K, Zn, LiH, $LiBet_3H$, $NaBet_3H$, $KBet_3H$; X,Y = Cl, Br; v, w = 1–3; and R = alkyl, C_6–C_{12}.

Reetz et al. [185] have modified the NR_4^+ stabilization mode using tetraalkylammonium carboxylates of the type N-$(octyl)_4^+RCO_2$ (R = alkyl, aryl, H). As in other cases, this reagent acts both as the reductant and as the colloidal stabilizer (Equation (4)).

$$M^+ + NR_4R'CO_2 - M^0(R_4NR'CO_2)_x + CO_2 + R - R' \quad (4)$$

where M^+ = metal ion; R = octyl; R′ = alkyl, aryl, H.

This variation offers two advantages. First, anaerobic reaction conditions are not required. Second, the particle size can be varied within certain limits depending on the electron withdrawing or donating nature of the substituent R. In case of Pd, the right choice of R in the N-$(octyl)_4^+RCO_2^-$ reagent allows the particle size to be adjusted within the range of 2.2–5.4 nm. In addition, bimetallic colloids such as Pd/Pt (2.2 nm), Pd/Sn (4.4 nm), Pd/Au (3.3 nm), Pd/Rh (1.8 nm), Pt/Ru (1.7 nm), and Pd/Cu (2.2 nm) have been made by this pathway.

In some cases shape-control has also been achieved: tetra(*n*-octyl)ammonium glycolate transforms $Pd(NO_3)_2$ predominantly into *trigonal* Pd particles [186]. Recent work has confirmed that the colloidal protective agents not only prevent particle agglomeration but even provide control of the crystal growth during particle synthesis (see e.g., Ref. [187–191]). The drawbacks of this route are the restriction to noble metal salts and the limited industrial availability of N-$(octyl)_4^+RCO_2^-$.

3.3.2. Reetz's Electrochemical Approach

Using electrons for the electrolytic reduction of metal salts, Reetz and coworkers have introduced a further variation to the tetraalkylammoniumhalide-stabilization mode [192–198]. The overall electrochemical process can be divided into the following steps: (i) oxidative dissolution of the sacrificial Met_{bulk} anode, (ii) migration of Met^{n+} ions to the cathode, (iii) reductive formation of zerovalent metal atoms at the cathode, (iv) formation of metal particles by nucleation and growth, (v) stop of the growth process and stabilization of the particles by tetraoctylammonium ions as colloidal protecting agents, and (vi) precipitation of the nanostructured metal colloids. Advantages of the electrochemical pathway are that it avoids contamination with byproducts resulting from chemical reduction agents, and that the products are easy to isolate from the precipitate. Further, the electrochemical preparation allows size-selective formation of the particles. Experiments using Pd as the sacrificial anode in the electrochemical cell to give $(C_8H_{17})_4N^+Br$-stabilized $Pd^{(0)}$ particles indicate that the particle size depends on the current density applied: high current densities led to small Pd particles (1.4 nm), while low current densities, in contrast, gave larger particles (4.8 nm). As was seen in a careful analysis of tetraalkylammonium-stabilized Pd and Ni with a combination of TEM, elemental analysis and Mössbauer spectroscopy (MS), the size of the particles is not dependent on any single factor but can be altered by adjusting the reaction time, temperature, and the polarity of the solvent. Using this method, metal nanoparticles of Ti, Fe, Co, Ni, Pd, Pt, Ag, and Au have been obtained in good yield. The drawback here is that the technical prerequisites and knowledge for performing electrochemical syntheses are not available everywhere.

3.3.3. Tetraoctylammonium as a Phase Transfer Reagent

The use of tetraoctylammonium salt as phase transfer reagent has been introduced by Brust [199] for the preparation of gold colloids in the size domain of 1–3 nm. This one-step method consists of a two-phase reduction coupled with ion extraction and self-assembly using monolayers of alkane thiols. The two-phase redox reaction controls the growth of the metallic nuclei via the simultaneous attachment of self-assembled thiol monolayers on the growing clusters. The overall reaction is summarized in Equation (5).

$$AuCl_4^-(aq) + N(C_8H_{17})_4 + (C_6H_5Me) \rightarrow N(C_8H_{17})_4 + AuCl_4^-(C_6H_5Me) \quad (5a)$$

$$m\,AuCl_4^-(C_6H_5Me) + n\,C_{12}H_{25}SH(C_6H_5Me) + 3me^- \rightarrow 4mCl^-(aq) + (Au_m)(C_{12}H_{25}SH)_n(C_6H_5Me) \quad (5b)$$

An aqueous solution of auric chloride is mixed with tetraoctylammonium in toluene and the two-phase mixture is stirred until all gold ions have migrated to the organic phase. Dodecanethiol is then added to the organic phase, and to the aqueous layer borohydride is added as the reductant. The reduction of the gold ions is indicated by a colour change in the organic layer. A sequence of precipitation and redispersion steps using toluene and ethanol alternating removes excess tetraoctylammonium selectively. The finally isolated gold colloid contains the metallic nanoparticles covered with a monolayer of dodecanethiol which makes them redispersible in organic solvents. The main advantage of this method lies in the

fact that no anaerobic conditions are needed here. This "beaker glass method" further allows the particle surface to be easily functionalized, and the isolated colloid can be handled like a chemical compound under ambient conditions. In addition, the cluster size can be controlled within certain limits by the reaction conditions. However, this method is restricted to metals which have a strong affinity to thiol groups.

3.3.4. Surfactant-Stabilized Hydrosols

Hydrosols (1–10 nm) composed of one or more metals can be obtained with excellent preparative reproducibility on the multigram scale when the metal salts are treated prior to the reduction step with highly hydrophilic tensides. The metal salts are subsequently reduced using conventional agents such as hydrogen, formic acid, or ethylene glycol (EG), yielding colloidal, nanoscopic hydrosols that can be isolated in the form of highly water soluble powders. In this way, aqueous metal(0) solutions are readily accessible that contain at least 100 mg metal/l and exhibit excellent long-term stability (see Table 2 in Ref. [177]).

Using long-chain alkylsulfobetaines as the stabilizer, a number of highly water soluble nanometal colloids have been isolated in excellent yields (see Figure 8). The core particle size can be tailored between 1 and 10 nm. TEM examinations have shown that the resulting materials are generally monodisperse. Further, a combination of spectroscopic methods confirmed the zerovalent nature of the metal cores [200].

As alternatives to amphiphilic betaines, a wide range of cationic, anionic, and non-ionic surfactants including environmentally benign sugar soaps have been successfully used as colloidal stabilizers [201]. Electrochemical reduction of the metal salts provides a very clean access to water soluble nanometal colloids [192].

Sodium salts of sulfonated triphenylphosphine P(*m*-$C_6H_4SO_3Na)_3$ or alkyltriphenyl-methyltrisulfonates function as stabilizers for hydrosols of colloidal rhodium and $(C_6H_5)_2$P-*p*-$C_6H_5SO_3Na$ has been used by Schmid to prepare water soluble gold clusters which are isolable and redispersible without agglomeration [202].

Since water is the preferred solvent both in industrial technologies and biomedicine, the development of highly hydrophilic metal colloids has been a key step for a number of recently reported practical applications [182,203].

3.4. Solvent-Stabilized Metal Colloids

Solvents such as organic liquids can act as stabilizers [204] for metal colloids, and in case of gold it was even reported that the donor properties of the medium determine the sign and the strength of the induced charge [205]. Also, in case of colloidal metal suspensions even in less polar solvents electrostatic stabilization effects have been assumed to arise from the donor properties of the respective liquid. Most common solvent stabilizations have been achieved with THF or propylenecarbonate. For example, small-sized clusters of zerovalent early transition metals Ti, Zr, V, Nb, and Mn have been stabilized by THF after $[BEt_3H^-]$ reduction of the pre-formed THF adducts (Equation (6)) [54,55,59,206]. Table 1 summarizes the results.

$$x \cdot [TiBr_4 \cdot 2THF] + x \cdot 4K[BEt_3H] \xrightarrow{\text{THF, 6 h, 20 °C}} [Ti \cdot 0.5\,THF]_x + x \cdot 4BEt_3 + x \cdot 4KBr \downarrow + x \cdot 2H_2 \quad (6a)$$

$$x \cdot [TiBr_4 \cdot 2THF] + x \cdot 4K[BEt_3H] \xrightarrow{\text{THF, 6 h, 20 °C}} [Ti \cdot 0.5\,THF]_x + x \cdot 4BEt_3 + x \cdot 4KBr \downarrow + x \cdot 2H_2 \quad (6b)$$

[Mn 0.3 THF] particles (1–2.5 nm) were prepared analogously [207,208] and their physical properties have been analyzed. X-ray absorption spectroscopic (XAS) studies have revealed that the Mn nanoparticles are in the zerovalent metallic state with no stabilizing counter ions from the starting material [207]. THF-stabilized Mn (0) particles exhibit super-paramagnetism below 20 K and were the first example of an antiferromagnetic metal colloid [208]. Along similar lines, nanostructured Ni particles have also been synthesized and found to exhibit superparamagnetic properties [209]. In Equation (6), the THF may be also replaced by tetrahydrothiophene to yield Mn-, Pd-, and Pt-organosols [177].

3.5. Toshima's Alcohol Reduction Method

The "alcohol reduction process" invented by Hirai and Toshima is widely applicable for the preparation of colloidal precious metals stabilized by organic polymers such

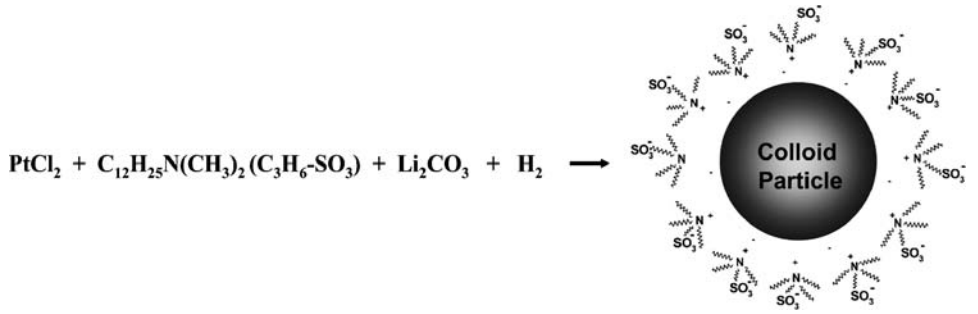

Figure 8. Preparation of sulfobetain-stabilized hydrosols. (Reprinted from Ref. [53], © 2007, with permission from Wiley-VCH.)

Table 1. THF-stabilized organosols of early transition metals. (Reprinted from Ref. [53], © 2007, with permission from Wiley-VCH.)

Solvent Stabilized Early Transition Metal Colloids

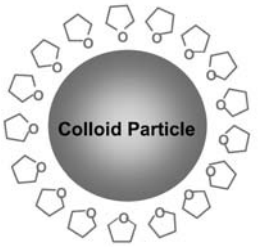

Ti	V	Cr	Mn
Zr	Nb	Mo	
Hf	Ta	W	

Product	Starting material	Reducing agent	T (°C)	t (h)	Metal content (%)	Size (nm)
$[Ti \cdot 0.5\ THF]_x$	$TiBr_4 \cdot 2THF$	$K[BEt_3H]$	Room temperature	6	43.5	–
$[Zr \cdot 0.4\ THF]_x$	$ZrBr_4 \cdot 2THF$	$K[BEt_3H]$	Room temperature	6	42	–
$[V \cdot 0.3\ THF]_x$	$VBr_3 \cdot 3THF$	$K[BEt_3H]$	Room temperature	2	51	–
$[Nb \cdot 0.3\ THF]_x$	$NbCl_4 \cdot 2THF$	$K[BEt_3H]$	Room temperature	4	48	–
$[Mn \cdot 0.3\ THF]_x$	$MnBr_2 \cdot 2THF$	$K[BEt_3H]$	50	3	70	1–2, 5

as PVP, poly(vinyl alcohol) (PVA), and poly(methylvinyl ether). During the salt reduction, alcohols having α-hydrogen atoms are oxidized to the corresponding carbonyl compound (e.g., methanol to formaldehyde, ethanol to acetaldehyde). The method for preparing mono- and bimetallic nanoparticles via the reduction or co-reduction of (eventually mixed) ions has been fully developed by N. Toshima over the years and exploited for numerous applications [47,210–220]. It should be noted that the alcohol has a double function as a reductive agent and the solvent. The reduction of the metal salt(s) is usually performed at reflux temperatures resulting in a fast metal particle formation. The influence of the structure and quantity of the applied alcohol on the particle size has been studied in a whole series of investigations [221–223]. As has been exemplified with Pt-, Pd-, and Rh-nanocolloids, it can be stated as a rule of thumb that small-sized particles are formed using high-boiling alcohols.

3.6. Fiévet's Polyol Method

Liquid polyols are interesting non-aqueous solvents because, like water and mono-alcohols, they are hydrogen bonded liquids and have relatively high permittivity, making them ideal for dissolving ionic and even inorganic solids. Their use in nanoparticle synthesis has therefore opened up a new avenue and has emerged as a significant method for the preparation of a variety of nanopowders, colloids, films, rods, wires and foams. The advantage of polyols is that they can act as both reducing agents and solvents. The reaction, which is performed under aerobic conditions, is applicable to the preparation of nanoparticles of a variety of metals. Polyols, like alcohols, are mild reducing agents and the reaction conditions required can therefore lie between −20 °C and the boiling point of the solvent (up to 250 °C at atmospheric pressure), depending on which metal is to be reduced.

Fiévet et al. [225] have prepared and isolated metallic nanopowders of gold, palladium, iridium, osmium, copper, silver, nickel, cobalt, lead, and cadmium via polyol (EG) reduction (see Equation (7)) The method has recently been reviewed extensively [225,226].

$$HO - CH_2 - CH_2 - OH \rightarrow CH_3 - CHO + H_2O \quad (7a)$$

$$6(CH_3 - CHO) + 2HAuCl_4 \rightarrow 3(CH_3 - CO - CO - CH_3) + 2Au^{(0)} + 8HCl \quad (7b)$$

Without additional stabilizers to control the growth of the nanoparticles, the final products were marred by high degree of agglomeration and the particle size distribution was broad and had irregular shapes [226,227]. In order to generate better dispersions, either the temperature of the reaction can be varied or a precursor can be employed that is partially soluble, which gives rise to an insoluble solid phase that acts as a kind of reservoir. In this way, the supersaturation of the reduced metal atoms in solution can be kept below the critical nucleation level. If the nucleation step is slower, the growth of the nanoparticles can also be controlled, paving the way to better methods of preparing nanoparticles. Similarly, kinetically controlled reactions with substitution of rapid nucleation by heterogeneous nucleation [228] can also be employed to yield better dispersion of metal nanoparticles. Alternately, the use of long-chain polyols (e.g., 1,2-hexanediol) [229] that can also act as protective agents or the use of additional protective agents (e.g., PVP) allows the particle growth to be controlled, which is especially important for those metals that have a higher tendency to coalescence. Monodisperse particles can be generated if a heterogeneous support can act as a controller of particle agglomeration. Alumina-supported Pd, Ag, and Pd–Ag catalysts generated by the polyol method show good dispersion and activity. The size distribution is narrow and the particles are very pure [230].

Nanoparticles of the noble metals have been prepared extensively by the polyol or the modified polyol methods because of the ease of reduction of their salts (Figure 9).

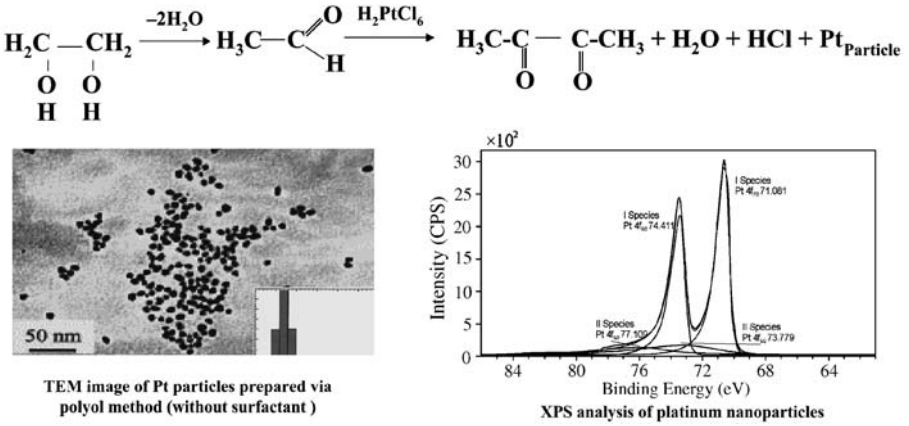

Figure 9. Schematic representation of the polyol process exemplified with Pt. TEM (left) shows a narrow particle size distribution (ca. 3 nm). (Reproduced from [223], © 2000, with permission from Elsevier Science.) Experimental XPS curves (right) fit sufficiently well with the Pt(0) standard. (Reprinted from Ref. [53], © 2007, with permission from Wiley-VCH.)

PVP, a water soluble amine-based polymer, was found to be an optimum protective agent because the reduction of noble metal salts by polyols in the presence of other surfactants often resulted in non-homogenous colloidal dispersions. PVP was the first material to be used for generating silver and silver–palladium stabilized particles by the polyol method [231–233]. By reducing the precursor/PVP ratio, it is even possible to reduce the size of the metal particles to few nanometers. These colloidal particles are isolable but surface contaminations are easily recognized because samples washed with the solvent and dried in the air are subsquently not any more pyrophoric [231,234–236].

PVP has been used as the stabilizing agent in the polyol synthesis to obtain monodisperse particles of Au [236], Pd [237,238], Pt [238], bimetallic Pt/Au [239] alloy, CoNi, FeNi, and FeCoNi [240–243] powders, bimetallic Ni–Cu particles [244], palladium/niobia catalysts [245], Ru [246], Co, and $Co_{80}Ni_{20}$ particles [247], silver nanowires [248]. In addition, Au, Pt, Pd, Ru, and Ir nanoparticles with a narrow particle size distribution have been synthesized and characterized by preparing the corresponding colloids [223,243,249,250]. The noble metals are easiest to reduce by the polyol method while the reaction conditions must be moderately stringent for Cu and severe for the reduction of cobalt, nickel, and their alloys. Interestingly, the reduction of Fe(II) to the metallic state proceeds via disproportion rather than by complete reduction. The Fe(III) produced during the disproportion reaction forms a complex with the polyol and remains in solution. Some key publications on the preparation of nanoparticles by the polyol process are the synthesis and characterization of FePt nanoparticles [229,251], submicron Co/Ni alloys [252], Co, Ni, Pd, and CoNi alloy powders [253], γ-Al_2O_3 supported Ru nanoparticles [254], monodisperse Ni powders [255], Pd-coated Ni nanoparticles [256], and copper metal clusters [257]. Subsequently, the polyol method was extended to the synthesis of metallic powders and films of Ru, Rh, Sn, Re, W, Pt, Fe–Cu, Co–Cu, and Ni–Cu [234]. As an extension to this method, Chow et al. developed electroless (i.e., involving chemical deposition of metal instead of electrodeposition) polyol deposition or metallization of Cu [258,259] and Ni [260], preparation and properties of nanostructured Ni–Co films [261–265], and also Fe–Ni powders and films [266–268].

Surfactants may also be added to the polyol process to control the particle morphology and size [227,232]. In a comparative study [269], we have recently been able to show through X-ray absorption near edge spectroscopy (XANES) and X-ray photoelectron spectroscopy (XPS) studies that the Pt is predominantly in the zerovalent state. However, there are strong indications that a thin layer on the surface of the particles is slightly oxidized. For most applications in catalysis this is only a minor drawback because re-reduction of the oxidized surface occurs readily in the temperature range applied during most catalytic reactions and/or the under reductive conditions the catalyst may be exposed to during, e.g., hydrogenation.

A further variation of the obviously very flexible ''Polyol Method'' has been developed by Younan Xia et al. [270]. The question whether PVP acts solely as a stabilizer or as both a reducing agent and a stabilizer is controversial. The action of PVP as a reducing agent has been reported for the preparation of some gold and silver hydrosols [271–274]. Since no reducing agent was added, it was proposed that partial degradation of the polymer occurs during the formation of nanoparticles from the metal salts under conditions reported, proving the reducing role of PVP. Direct abstraction of hydrogen by the metal ion and/or the reducing action of the macroradicals formed during the degradation of the polymer was proposed as the mechanism of such a reaction. However, studies by Younan Xia et al. [270,275,276] completely contradict these reports and the authors claim that PVP plays no role as a reducing agent at all but acts simply as a protecting agent. Their other significant experimental observation was that the presence of trace amounts of iron species in a polyol process can significantly alter the kinetics of growth of Pt nanostructures, thus ultimately deciding the final morphology of the product. On the reduction of Pt^{IV} to metallic Pt via an intermediate step of Pt^{II} formation, suitable reaction manipulations yield Pt nanostructures in the form of

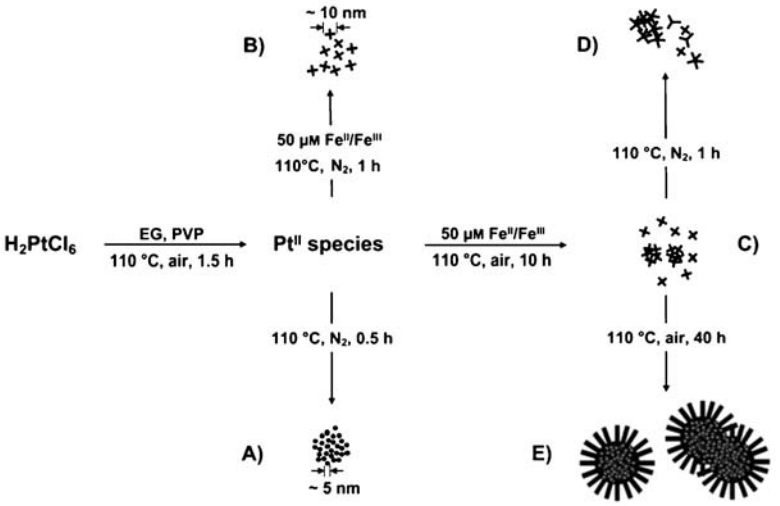

Figure 10. Four different ways of controlling the kinetics of polyol reduction and the corresponding morphologies observed for the Pt nanostructures. As the same amount of PVP was present in all four syntheses illustrated here, the striking differences in morphology were not caused by variation in the PVP concentration. It is assumed that the PVP molecules in these syntheses function only as a stabilizer to prevent the resultant nanoparticles from aggregating into larger structures. (Reprinted from Ref. [270], © 2005, with permission from Wiley-VCH.)

spheres, star-shaped particles, branched multipods, or uniform nanowires. These steps involved coupling the polyol reduction of platinum (IV) precursor with the Fe^{II}/Fe^{III} redox pair and the adsorption of oxygen and/or nitrogen gas. The reaction pathways are summarized in the Figure 10.

After performing the reaction in air at 110 °C for 1.5 h, all of the Pt^{IV} was converted to Pt^{II}. This Pt^{II} solution is stable and can be kept at ambient conditions for months without any change in composition. Formation of Pt nanoparticles from this solution occurs upon further heating in air (1 h, 5 nm spherical nanoparticle) or in nitrogen (0.5 h, 10 nm spherical nanoparticles). This observation reveals that adsorption of oxygen onto the surface of Pt nuclei suppresses the autocatalytic reduction but that the aerated process is still too fast to induce the formation of structures that deviate from the equilibrium shape. The most significant change was seen when Fe^{II} or Fe^{III} (both have the same effect) was introduced during the reduction of the Pt^{II} species. Fe ions readily oxidized both Pt atoms and nuclei back to Pt^{II} species and thus significantly decreased the supersaturation of the Pt atoms. Star-shaped nanoparticles were formed in 1 h in a nitrogen atmosphere (Figure 10B) while branched and morphologically different submicrometer-sized agglomerates were obtained under aerobic conditions, albeit at a much slower rate (Figure 10C). On completion of the reaction, the Pt^{II} species were completely reduced at a very slow rate to form uniform Pt nanowires on the surface of agglomerates. On the other hand, if nitrogen was applied under these conditions, the reduction rate increased slightly and multipods were formed with higher branched structures. These results indicate that oxygen can slow down the growth through both surface adsorption and etching mechanisms when coupled with the Fe ions. Such observations not only illustrate the role of different reagents in controlling the particle size but also demonstrate the variety of structures that can be produced by minor manipulations performed during the reaction.

Recently, it has been demonstrated that Pd nanoparticles with the uniform sizes and shapes can be obtained if oxidative etching is carried out during the polyol synthesis [277]. Colloidal octahedral nanoparticles of Pd with uniform sizes (8 nm) were generated when the metal nanoparticles produced by reduction by polyol (EG) are simultaneously exposed to Cl^-/O_2. Oxidative etching gradually converted the particles from the 4–8 nm twinned cubooctahedra that were formed initially into cubooctahedra particles with an average size of 8 nm that were soluble in the medium. The optimum time for this etching was between 1 and 3 h. A similar study performed on Ag also supports the concept of the role played by halogen and oxygen in the etching mechanism [278].

Magnetic nanoparticles, especially those containing FePt, were originally prepared by vacuum deposition methods. Sun et al. [251] have introduced the first successful wet chemical synthesis of monodispersed FePt nanoparticles by reduction of platinum acetylacetonate and simultaneous decomposition of iron pentacarbonyl in the presence of oleic acid and oleyl amine stabilizers using a long-chain polyol (1,2 hexadecanediol) as reductant in dioctylether medium. Unlike most polyol syntheses, this reaction was performed under inert conditions because of the sensitivity of iron carbonyl. The presence of oleic acid and oleyl amine prevents oxidation but more importantly helps stabilize and generate monodisperse, redispersible colloidal nanoparticles. The size and compositions of the FePt particle were readily tailored by altering the molar concentrations of the precursors: a 3:2 molar ratio of Fe and Pt generates $Fe_{48}Pt_{52}$, a 2:1 molar ratio yields $Fe_{52}Pt_{48}$, and a 4:1 molar ratio produces $Fe_{70}Pt_{30}$. The particle diameters range between 3 and 10 nm with a standard deviation of less than 5%, which signifies exceptional control during the synthesis. Control over the

final size of the nanoparticles can be achieved by generating 3 nm seed particles in situ and then adding more reagents to grow the seeds to the desired size.

Upon deposition onto a support and removal of the solvent, the dispersion of FePt (6 nm) colloidal nanoparticles generates superlattices. The oleic acid–oleyl amine 'capping agents' yield hexagonal close packed multilayers with individual particles separated by ~4 nm, but these capping agents can be easily replaced by their hexyl analogues to give structures with identical particle sizes but where the distance between particles is now reduced to ~1 nm with a concomitant change in structure to a cubic packed multilayer. The robustness of the particles was revealed upon heating the oleyl-capped assemblies to 600 °C in a N_2 atmosphere. Carbonaceous materials arising from decomposition of the capping agents help prevent the particles from agglomerating. Thermal annealing converts the internal particle structure from a chemically disordered face-centered cubic phase to the chemically ordered face-centered tetragonal phase and transforms the nanoparticle superlattices into ferromagnetic nanocrystal assemblies. These assemblies are chemically and mechanically robust and can support high-density magnetization reversal transitions.

Over the years, this method has gained considerable attention and many syntheses are based on variations of it, e.g., employing different Fe precursors [279,280] (cf. also Ref. [281]) or using hexadecanediol as a solvent for the acetylacetonate (acac) derivatives of both metals [282].

3.7. Preparation in Micelles, Reverse Micelles, and Encapsulation

Templates made of surfactants are very effective in order to control the size, shape, and polydispersity of nanosized metal particles. Surfactant micelles may enclose metal ions to form amphiphilic "microreactors" (Figure 11a). Water-in-oil reverse micelles (Figure 11b) or larger vesicles may function in similar ways. On the addition of reducing agents such as hydrazine nanosized metal particles are formed. The size and the shape of the products are "pre-imprinted" by the constrained environment in which they are grown.

Pileni [66,69,70,283] was the first to grow cobalt rods with a length of 300–1500 nm and a diameter between 10 and 30 nm in colloidal micelles (Figure 11a). Cylindrical copper metal particles having identical sizes and shapes can be prepared in a template made of interconnected cylinders [68]. These form monolayers organized in a hexagonal network over very large domains of particles are organized in a hexagonal network. Small or large aggregates can be produced at will depending on the preformed template used. The particles are highly organized and form pseudo-crystals with a face-centered cubic structure. Colloidal metals have also been grown in reverse micelles (i.e., water-in-oil droplets) (Figure 11b) The most recent results obtained in the shape-selective growth of silver and copper nanocrystals using reverse micelles as "microreactors" have been reviewed by Pileni, recently [284]. Amphiphilic block copolymers have been designed for the "pre-imprinted" microreactors by Antonietti et al. [71]. It is an established methodology now to use surfactants as colloidal templates for the controlled formation of noble metal nanospheres having pre-defined structures. Further, the self-assembly of the macromolecules allows the nanoparticles to take up well-defined arrangements on substrates, e.g., in thin films. For example, monodisperse noble metal particles such as gold, silver, palladium, have been applied to prepare thin polymer films. The strategies for the organization of nanoparticles into aggregated structures have been reviewed to summarize the access to two- and three-dimensional arrays of nanoparticles having diameters between 1 and 20 nm [74,75]. The encapsulation of small Pd- and Pd/Au-particles in solid organic [76] or inorganic matrices has also been achieved. For example, gold nanoclusters have been encapsulated in a silica matrix via a sol-gel procedure [79]. Nickel nanoparticles encapsulated in an amorphous carbon matrix have been synthesized by the sonication of $Ni(COD)_2$. The resulting particles were fully characterized by a combination of physical methods. Interestingly, electron energy loss spectroscopy (EELS) and energy filtering transition electron microscopy (EFTEM) analyses have shown that the nickel nanocrystallites are surrounded by amorphous carbon quasi as a "protecting agent" which perfectly protects the nickel surface from oxidation [285]. More

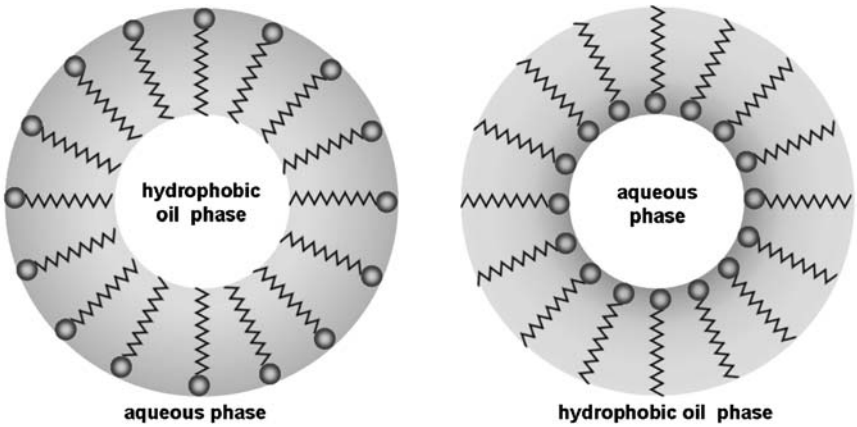

Figure 11. Size- and shape-control of nanoparticles via salt reduction in (a) the hydrophobic core of a surfactant oil in water micelle and (b) the hydrophilic core of a water-in-oil reverse micelle.

recently, highly stable cobalt nanoparticles (8–10 nm) were also obtained via encapsulation with carbon or graphite shells, respectively [286]. Similarly, Au- and Pd/Au-nanoclusters have been encapsulated in a silica matrix via a sol-gel procedure [287].

3.8. Finke's Polyoxoanion- and Tetrabutylammonium-Stabilized Nanoclusters

Finke's system discovered in 1994 represents a special subclass of transition metal nanocluster [167,288,289]. A zerovalent transition metal core consisting of, e.g., 300–900 atoms is doubly stabilized by a cationic surfactant (e.g., NR_4^+) and by an assembly of polyoxoanions (e.g., $P_2W_{15}Nb_3O_{62}^{9-}$). The resulting cluster systems exhibit a rather well-defined stochiometric composition. For example, organometallic complexes such as $[(n\text{-}C_4H_9)_4N]_5Na_3[(1,5\text{-COD})Ir(I)]$ stabilized in solution by bulky polyoxoanions, e.g., $P_2W_{15}Nb_3O_{62}$, function as the molecular precursors. When the precursor is treated in acetone in the presence of excess cyclohexene, the reduction with hydrogen under completely air- and water-free conditions yields nearly monodisperse (i.e., $2 \pm 0.3\,\text{nm} \pm 15\%$) $Ir(0)_{\approx 300}$ nanoclusters where the transition metal core is protected by an assembly of polyoxoanions (see Equation (8)).

$$\begin{aligned} &300[(1,5-\text{COD})\,\text{Ir}\cdot P_2W_{15}Nb_3O_{62}]^{8-} + 750H_2 \\ &\quad \rightarrow 300\text{Cyclooctane} + 1Ir(0)_{\sim 300} \\ &\quad + 300P_2W_{15}Nb_3O_{62}^{9-} + 300H^+ \end{aligned} \tag{8}$$

In the absence of cyclohexene the same procedure yields larger ($Ir(0)_{\approx 900}$) nanoclusters (size: 3 ± 0.4 nm). Besides zerovalent Iridium- [167,288,290], Rh(0)-nanocluster of the Finke-type have been prepared [290–292]. Finke's nanoclusters have been carefully examined using a combination of modern instrumental analysis methods [167]. It was revealed that the Ir(0) core is uncharged and that the iridium particles exhibit an extremely clean, fully exposed, and chemically very reactive metallic surface.

It should be mentioned here that Finke's group has added a whole plethora of significant contributions to the field of metal nanoclusters [295–299] including a recent study on the mechanism for the self-assembly of transition metal nanoparticles [294].

3.9. "Reductive Stabilization" of Metal Colloids by Aluminium Alkyls

"Reductive Stabilization" of nanometallic organosols using an excess of triorganoaluminium as the reductive agent for transition metal salts and simultaneously as the protective shell for the resulting nanometal colloids is a late fruit of the *Ziegler Chemistry* invented at the Max-Planck-Institut für Kohlenforschung, Mülheim, Germany in the early 1950s [300].

As early as 1954, Karl Ziegler [301,302] has assumed that "colloidal nickel" in triethylaluminium is the crucial co-catalyst which effects the "controlled polymerization of ethane." This so-called "nickel effect" was really the basis of the subsequent discovery of the Ziegler catalysts and has later been elucidated in great detail by G. Wilke and coworkers [303]. The early recipes of Ziegler et al. already describe that colloidal nickel is formed in solution when "a trace of nickel-acetylacetonate is added to triisobutylaluminium" [304].

On the basis of this prior knowledge, it was no surprise for us to find a whole plethora of (catalytically very active) metal nanoparticles with tunable size, morphology, and structure when we applied modern analytical tools including structure modelling to revisit Ziegler's classical findings [305–307].

Over the years "Reductive Stabilization" has provided a very effective access to a wide range of organosols composed of one or more transition metals of groups 6–11 at the multigram scale. In a recent review chapter [53], the method has been evaluated. The details of the particle formation process [86,94] are discussed in Section 2.2 (see Figure 4). The "exact structure" of the colloidal protective shell was not precisely determinable. However, quantitative protonolysis experiments showed that unreacted organoaluminium groups such as $Al–CH_3$, $Al–C_2H_5$, or $Al–C_8H_{17}$ are still present in the stabilizer. Nevertheless, this type of organosols stabilized by an organometallic protective shell (which by definition is highly sensitive to air and/or moisture) can easily be isolated under truly anaerobic conditions in the form of dry powders having long-term stability. In addition, they are fully redispersible in dry organic solvents. Table 2 in Ref. [53] gives a number of typical examples for mono- and bimetallic organosols along with the respective particle sizes and elemental analyses. In order to accomplish a broad practical applicability of these materials in a wide range of solvents, including water, we have used the active Al–C bonds in the protective shell for a controlled protonolysis by "modifiers," i.e., long-chain alcohols or organic acids to give Al-alkoxide groups in the stabilizer (see Figure 12).

This "modification" (Figure 12) of the organoaluminium protecting shell allows to tailor the dispersion characteristics of the original organosols in a given solvent up to concentrations of > 100 mg/at. wt. of metal. A vast spectrum of dissolubilities of the colloidal metals in hydrophobic and hydrophilic media (including water) has been achieved this way (cf. Tables 3–5 in Ref. [53]). Inorganic surfaces bearing –OH groups can react with the active Al–C bonds in the colloidal protecting shell, which opens new ways to anchor the nanoparticles firmly on the carrier surface because the modification process does not alter the particle size of the metal core.

Bifunctional spacer molecules of different sizes have been used to construct nanoparticle networks formed via self-assembly of arrays of metal colloid particles prepared via "reductive stabilization" [88,309,310]. A combination of physical methods such as TEM, XAS, ASAXS, metastable impact electron spectroscopy (MIES), and ultraviolet photoelectron spectroscopy (UPS) has revealed that the particles are interlinked through rigid spacer molecules with proton-active functional groups to bind at the active aluminium–carbon sites in the metal-organic protecting shells [88].

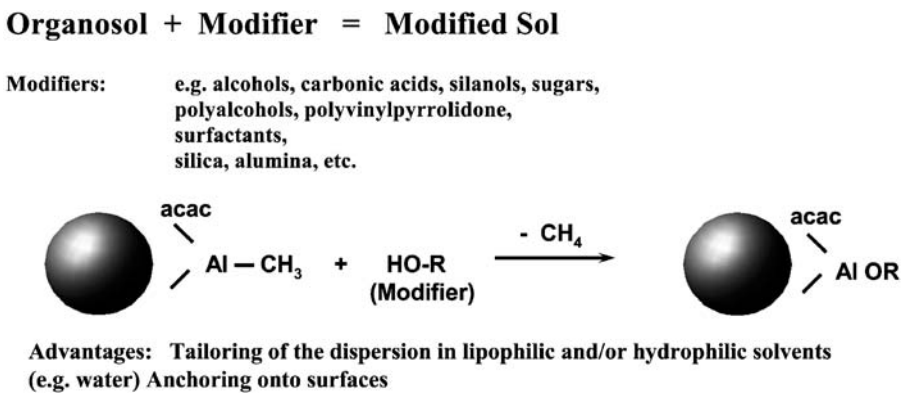

Figure 12. Hydrosols via "modification" of the Al-organic protective shell. (Reprinted from Ref. [53], © 2007, with permission from Wiley-VCH.)

3.10. Controlled Decomposition of Organometallics

The synthesis of metal nanoparticles via the controlled decomposition of pre-prepared organometallic complexes or metal carbonyls where the metals are already in the zerovalent or low-valent state has been known since 1970. The first examples were Pd- and Pt-dibenzylideneacetone complexes where the coordinated ligands detached using either hydrogen of carbon monoxide under mild conditions to give the respective metal nanoparticles [310].

In general, organometallic complexes and several organic salt derivatives of transition metals easily decompose when energy is applied, e.g., in the form of heat, light, or ultrasound. The advantage of this approach is that all types of stabilizers can be applied including surfactants as shown in (Figure 13).

In the meantime, the group of B. Chaudret has developed a versatile methodology for the preparation of monodisperse metal particles of adjustable size which exhibit a very clean metallic surface that displays a remarkable coordination chemistry [311–339]. The most recent results were summarized [340]. Microwave heating provides a more homogeneous particle nucleation and shorter aggregation times and has been used to generate polymer-stabilized Pt colloids (spheres, 2–4 nm, having narrow size distribution) [341–343]. Sonochemical decomposition of metal salts and organometallic complexes has been introduced by Suslick and Gedanken [39–41]. The limitation of photo-, γ-radiolysis, and laser irradiation methods lies in the restriction to low metal concentrations in solution [6,344,345] which makes this variation not suitable to scale up the manufacture of nanostructured metal colloids for practical applications.

A production process for monodisperse, magnetic Co-, Fe/Co-, and Fe-nanocolloids having particle sizes precisely adjustable between 2 and 15 nm and a narrow size distribution has been developed via the controlled thermolysis of metal carbonyls in the presence aluminium alkyls (Figure 14) [346–349].

The particle size depends on the chain length of the aluminium-alkyl group and the concentration of the trialkylaluminium compound applied. If mixtures of, e.g., Fe- and Co-carbonyl compounds are used, Fe/Co alloy particles are formed. When the magnetic particles

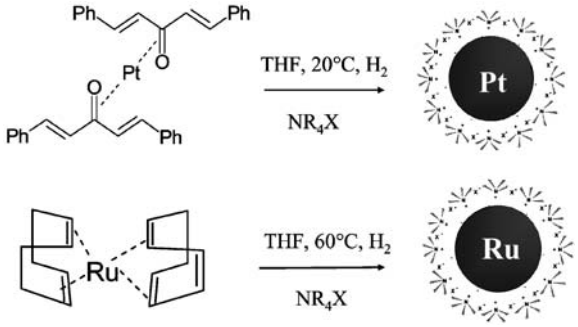

Figure 13. Nanoparticle synthesis through hydrogenolysis of zerovalent metal complexes. (Reprinted from Ref. [53], © 2007, with permission from Wiley-VCH.)

are treated in organic solution with synthetic air containing 3.5 vol% O_2 ("smooth oxidation") the metallic core is "sealed" with a dense layer of Co-oxide-carbonate around the particles which are then stable in air and can be handled safely under ambient conditions [350]. The cobalt nanoparticles can also be protected against oxidation with a highly stable carbon coating [286]. The silver-induced enhancement of the magnetic properties of $CoPt_3$ nanoparticles has been studied recently by Toshima [351]. For a recent overview on the synthesis and characterization of magnetic nanoparticles see Ref. [281].

Controlled decomposition of pre-formed $[(COD)Pt(CH_3)_2]$ in the presence of triorganoaluminium led to the preparation of the first Pt_{13} cluster (size: 0.75 ± 0.1 nm). The one-shell structure and the metallic state were confirmed by XPS and XANES [352].

When exposed to air the organoaluminium shell is transferred to an Al_2O_3 matrix where the Pt_{13} clusters are regularly dispersed (Figure 15). This is a promising pathway for preparing solid catalysts (cf. Section 4.1).

3.11. Heterogeneous Supports as Size-Controlling Agent

Heterogeneous supports, like stabilizers, can prevent metal nanoclusters from agglomerating and they can also

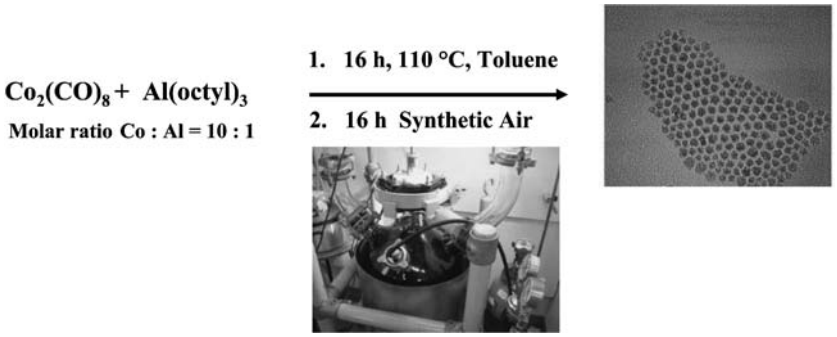

Figure 14. Size-selective formation of air stable Co particles via thermolysis of Co_2CO_8 controlled by aluminium alkyl. (Reprinted from Ref. [53], © 2007, with permission from Wiley-VCH.)

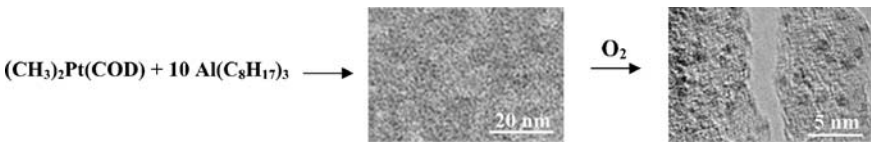

Figure 15. Formation of Pt_{13} clusters stabilized by trialkylaluminium.

regulate particle size, especially when the metal is precipitated directly. Many preparative routes have been described for depositing metal nanoclusters onto various inorganic supports [353–357], not only providing a means of controlling their morphology and behaviour but also widening their range of applications. Composite materials that are devoid of any additional stabilizers have potential applications in areas like surface-enhanced Raman scattering, photonic crystals, catalysis, and in chemical sensors. An advantage of such materials in applications like catalysis is that they can be separated easily from the reaction mixture and products.

The main prerequisites for materials to be used as supports or templates for nanoclusters in a durable form are

- inertness and neutral chemical properties
- a large surface area
- pore sizes optimized for the nanoclusters to be ''hosted'' or encapsulated.

The oxides of Si, Al, Ti, Zr, Ca, Mg, and Zn have often served as convenient supports for metal nanoclusters [358–362]. Conductive glassy carbon or graphite materials have proved to be suitable carriers for electrocatalytic applications [363,364].

The performance of supported metal catalysts depends largely on the structure and composition of the metal particles and the nature of the support. Heterogeneous catalysts which are prepared by the decomposition of organometallic molecular clusters in the presence of a support material generally exhibit a greater uniformity in shape and particle size than those produced by conventional ''salt impregnation systems'' where the nanoparticles are produced on the surface by calcination or a reductive process [365]. For example, carrier-supported metal clusters such as Ir_4/γ-Al_2O_3, Ir_6/γ-Al_2O_3, and Rh_6/zeolite (NaY), which are good catalysts for the hydrogenation of toluene (a reaction that is highly sensitive to the particle size) are best prepared by the decarbonylation of the corresponding metal carbonyl clusters in the presence of the support materials. Nevertheless, the synthesis of non-agglomerated, monodisperse nanoclusters poses a major challenge because colloidal stabilizers are absent. A simple route for generating supported metal nanoclusters is to add suitable support materials to the reaction medium in which the metal salt(s) are dissolved and to use the polyol method (see Section 3.6) for reduction.

A specific example where heterogeneous supports provide nanoparticle size-control is the immobilization of homogeneous silver nanoparticles on polystyrene [366]. This work was extended later to the development of a one-pot method for the size-selective precipitation of silver nanoparticles on PVP-protected thiol-functionalized silica. During the immobilization of very small silver nanoclusters both the size of the silver nanoclusters and the thickness of the silver layer on the support could be controlled directly by the reaction parameters applied (Figure 16) [367].

Similarly, Pd, Ag, and Pd–Ag nanoclusters on alumina have been prepared by the polyol method [230]. Dendrimer encapsulated metal nanoclusters can be obtained by the thermal degradation of the organic dendrimers [368]. If salts of different metals are reduced one after the other in the presence of a support, core-shell type metallic particles are produced. In this case the presence of the support is vital for the success of the preparation. For example, the stepwise reduction of Cu and Pt salts in the presence of a conductive carbon support (Vulcan XC 72) generates copper nanoparticles (6–8 nm) that are coated with smaller particles of Pt (1–2 nm). This system has been found to be a powerful electrocatalyst which exhibits improved CO tolerance combined with high electrocatalytic efficiency. For details see Section 3.7 [53,369].

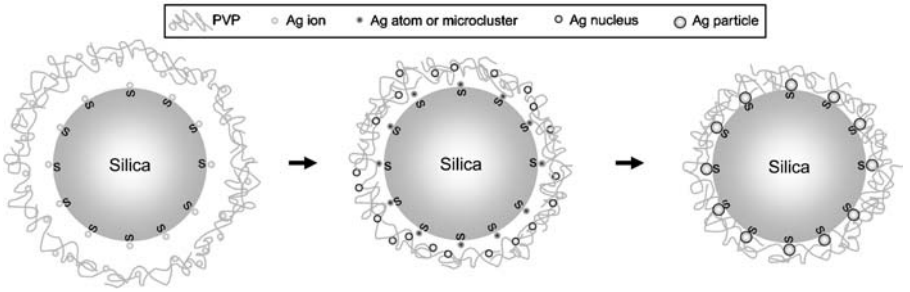

Figure 16. Schematic representation of the mechanism of silver stabilization by silica.

4. Selected Applications

Methods for the design of size- and even shape-controlled [186,190,191,370–372] metallic nanoparticles have reached a rather mature stadium thanks to the contributions of the pioneer groups of the last 25 years. Applications in a number of fields of practical *Nanotechnology* are now moving fast into the focus of R&D [203,373]. For an overview on the potential application of metal nanoparticles in the rapidly growing fields of quantum dots, self-assembly, and electrical properties, the reader is advised to consult recently published specialist review articles, e.g., Refs. [160,281] and book chapters (cf. Chapters 2, 4, and 5 in Ref. [60]). In the following three sub-sections the authors restrict themselves to a brief summary of a few subjects of current practical interest in fields with which they are most familiar.

4.1. Catalysis

Nanostructured metal colloids in the form of organo- or hydrosols can serve as homogeneous – or ''quasi homogeneous''[1] [374] catalysts either in organic, aqueous, or biphasic phases. Alternatively, pre-prepared nanocolloids can be deposited on a diverse range of supports to give high-performance heterogeneous catalysts. To differentiate these from classic heterogeneous catalysts we have coined this approach the ''precursor method'' [375]. In a recent state-of-the-art article, the latest developments at the frontiers of ''nanoparticles as recyclable catalysts'' have been reviewed by Astruc [52] who – in this context, created the term ''semi-heterogeneous'' to describe the specific function of nanoparticulate catalyst systems [52, p. 7853]. The focus of this section is to provide the reader with an overview on the main fields specific of catalysis – such as fine chemicals production, hydrogen storage, and electrocatalysis – where the different preparation methods as discussed in Section 3 have already been successfully applied to prepare novel types of promising ''nanocatalysts.'' Although ''nanocatalysis'' has not found its way into bulk industrial chemical productions yet it can be expected that control of composition, size, and (in some cases) even shape of the active metal centres at the nanoscale associated with a very uniform dispersion will prove successful sooner or later also at the ton-scale. An outlook is given at the end of this section.

The use of ligand-stabilized transition metal nanoparticles in catalysis was demonstrated by Schmid et al. over the years in a series of articles in Refs. [48,50,111,112,119,131,139,141,168,202,374,376,377–380].

Schmid [374] has described phosphine-stabilized Rh_{55} nanoclusters, namely $Rh_{55}[P(t\text{-}Bu)_3]_{12}Cl_{20}$ and $Rh_{55}[PPh_3]_{12}Cl_{20}$, deposited on TiO_2. These systems were reported by to catalyze the heterogeneous hydroformylation of propene with high turnover numbers giving equal amounts of *n*- and *i*-butanal. The observed turnover frequencies are higher than seen with homogeneous complex catalysts but the selectivity was found to be too low for practical applications. In addition, Schmid et al. have applied the classical seed growth method [381] to synthesize layered bimetallic Au/Pd and Pd/Au colloids in the size range of 20–56 nm [379]. The sequential reduction of gold salts and palladium salts with sodium citrate allows the gold core to be coated with Pd. The layered bimetallic colloid is stabilized by trisulfonated triphenylphosphane and sodium sulfanilate. More than 90% metal can be isolated in the solid state. The redispersion in water is possible in high concentration [382]. It was found that even subtle changes in the chain length of the substituents of the alkyl-substituted phenanthrolines used as colloid stabilizers alter the regioselectivity significantly [383]. Seven- and eight-shell palladium clusters on TiO_2, protected by phenanthroline catalyse the semihydrogenation of hex-2-yne to *cis*-hex-2-ene with 93% *cis*-hex-2-ene selectivity. With the 3-*n*-decyl phenanthroline as the stabilizer a similar selectivity resulted. On substitution of the phenanthroline with *n*-butyl or *n*-heptyl groups, however, the activity drops dramatically and the consecutive isomerization or total hydrogenation of the *cis*-hex-2-ene is completely suppressed [377]. Very recently, Schmid and Corain have outlined the scope of nanoparticulated gold in the extremely facile catalytic oxidation of CO to CO_2 [384]. For a more general review on the catalytic applications of Au(0) see Ref. [385]. In addition, the significant contributions F. Schüth et al. currently adds to this rapidly growing field are highly recommended, e.g., Ref. [386].

Solutions of Moiseev's giant Pd colloids [49,161–166] were shown to catalyze a number of reactions in the ''quasi homogeneous'' phase, namely oxidative acetoxylation reactions [162], the oxidative carbonylation of phenol to diphenyl carbonate [166], the hydrogen-transfer reduction of multiple bonds by formic acid [387], the

[1]Also termed soluble heterogeneous catalysts.

reduction of nitriles and nitroarenes, and the acetal formation [49,161] with high turnover frequencies and significant lifetimes.

The catalytic applications of Moiseev's "giant" cationic palladium clusters have extensively been reviewed by Finke et al. [167]. In a recent review chapter we have outlined the potential of surfactant-stabilized nanocolloids in the different fields of catalysis [53]. Our three-step "precursor concept" for the manufacture of heterogeneous "egg-shell" – nanocatalysts catalysts based on surfactant-stabilized organosols or hydrosols was developed in the 1990s [173–177] and has been fully elaborated in recent time as a standard procedure for the manufacture of "egg-shell" – nanometal catalysts, namely for the preparation of high-performance fuel cell catalysts. For details consult the following Refs. [53,181,387].

Reetz et al. have used N-(octyl)$_4$Br-stabilized Pd colloids (typical size, e.g., 3 nm) as precursors to form so-called "cortex-catalysts," where the active metal forms an extremely fine shell of less than 10 nm on the supports (e.g., Al_2O_3). Within the first 1–4 s, the impregnation of Al_2O_3 pellets by dispersed nanostructured metal colloids leads to the time-dependent penetration of the support which is complete after 10 s. "Cortex catalysts" were reported to show a threefold higher activity in olefin hydrogenation than conventionally prepared catalysts of the same metal loading (5% Pd on Al_2O_3) [388].

Solvent-stabilized metal colloids have been shown to exhibit extraordinary catalytic efficiency, namely in the "quasi homogeneous" phase. Unsupported nanoparticles stabilized with surfactants, "capping agents" such as PVP or organoaluminium shells in liquid solvent phases (including water) work as "soluble surfaces" exhibiting very high turnover frequencies associated with reasonable lifetimes – and potentially are recyclable [173–176,389,390]. Reetz has used Pd nanoparticles, formed via salt reduction with tetrabutyl ammonium carboxylates as highly efficient Heck reaction catalysts [185,391] where propylene carbonate-stabilized palladium nanoparticles were also shown to be active [392,393]. McMurry-type coupling reactions to transform aldehydes and ketones into olefins using Bu_4NBr-stabilized Ti colloids (3 nm) were further reported. The THF-protected Ti_{13}- and Zr-nanoclusters were shown to hydrogenate Ti and Zr sponges in the "quasi homogeneous" phase [54,206]. The THF-protected Ti_{13}-nanocluster, in addition, has been tested by several groups to be one of the best available catalysts for reversible hydrogen storage in alanates [394,395]. Even enantioselective hydrogenation reactions were performed using cinchonidine-stabilized Pt colloids in HOAc/MeOH solution [396,397].

Since 1976 until present time Toshima-type nanocolloids always had a major impact on catalysis and electrocatalysis at nanoparticle surfaces [47,210–213,398–407]. The main advantages of these products lie in the efficient control of the inner structure and morphology especially of bimetallic and even multimetallic catalyst systems.

A subtle control of the particle morphology and size can also be brought about using Fiévet's Polyol process for catalyst preparation. The main advantage here is the easy access to nanoparticulate metals at any normally equipped laboratory bench without the restrictions imposed by anaerobic working conditions [224]. It is clear that truly zerovalent metal surfaces cannot be obtained in air. However, using XANES and XPS it has been shown [269] that only small layer at the particle surface is slightly oxidized which – for most applications in catalysis is only a minor drawback.

Micelles in which nanosized metals are incorporated are very stable; they undergo no significant change of the colloidal properties such as size and polydispersity and consequently are effective hydrogenation catalysts. Antonietti and coworkers have found that the morphology of the metal core can be varied between a "cherry" – and a "raspberry" – architecture depending on the strength of the reducing agent. Block copolymer stabilized Pd-"raspberry"-colloids have an extraordinary high metal surface and no additional support is needed for catalytic applications in solution. This type of colloid catalyst combines the advantages of homogeneous and heterogeneous catalysis, i.e., the high selectivity and reactivity of homogeneous hydrogenation catalysts is coupled with the long-term stability of the heterogeneous systems [408,409]. The wide range of 'quasi homogeneous catalysis' using polymers, micelles, or reversed micelles as 'microreactors' has recently been reviewed by Astruc [52]. Meanwhile, this technology has been developed further using hollow sphere encapsulation techniques [410] to produce high temperature stable catalysts.

Finke has reported remarkable catalytic lifetimes for the polyoxoanion- and tetrabutylammonium-stabilized transition metal nanoclusters [288–292]. For example in the catalytic hydrogenation of cyclohexene, a common test for structure insensitive reactions, the Ir(0) nanocluster [296] showed up to 18,000 total turnovers with turnover frequencies of 3200 h^{-1} [293]. As many as 190,000 turnovers were reported in the case of the Rh(0) analogue reported recently. Obviously, the polyoxoanion component prevents the precious metal nanoparticles from aggregating so that the active metals exhibit a high surface area [297].

Reductive stabilization [86,94,305] is probably the most straightforward one-step access to nanoparticulate catalysts – provided that strict anaerobic working conditions either in a glove box or using an argon-protective atmosphere are available. Another advantage of this synthetic procedure lies in the accessibility of very small particle sizes (e.g., Pt(0) particles of 1.2 nm) which gives access to unusually large catalytically active surface areas. Via subsequent protonolysis of the Al–C bonds in the protective shell by "modifier molecules" a wide range of nanometallic hydrosols is produced. Via the "precursor concept" homogeneous and gradient structure alloys, layered bimetallics and decorated particles are all readily accessible on a wide range of supports. The details of this very versatile method to produce a whole plethora of halogen-free structurally controlled small-sized nanometallic catalyst systems have recently been reviewed in extensor [53, Part 5.0].

Controlled decomposition of organometallics leads to nanocatalysts which exhibit a very clean and truly zerovalent metallic surface (cf. [339]). As indicated in Figure 15 in Section 3.10, the organoaluminium shell of the one-shell Pt_{13} cluster (size: 0.75 ± 0.1 nm) obtained via the decomposition of $[(COD)Pt(CH_3)_2]$ in the presence of excess trioctylaluminium [352] is transferred to an Al_2O_3

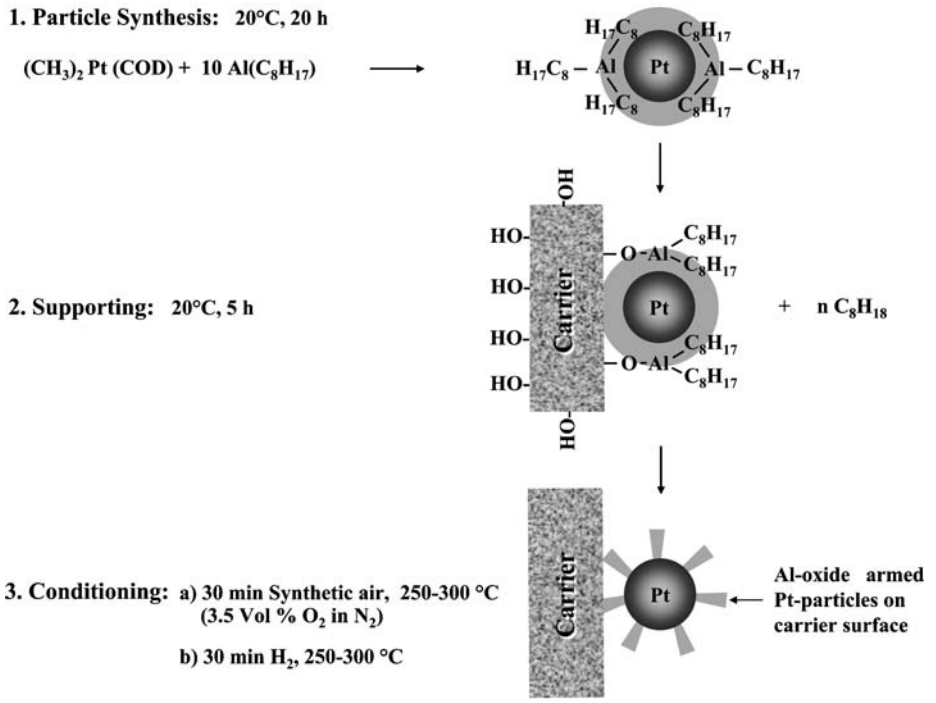

Figure 17. Scheme of the preparation of a heterogeneous Pt catalyst (1.5 ± 0.4 nm) from a colloidal $Pt/Al(C_8H_{17})_3$ precursor.

matrix which gives a heterogeneous catalyst where Pt_{13} clusters are regularly dispersed (though still accessible, e.g., for H_2 or CO as was shown by adsorption measurements. The three-step catalyst preparation pathway which allows the manufacture of – eventually multimetallic – solid catalysts (1–2 nm) having a metal loading of $>20\%$. from metal nanoclusters stabilized only by organoaluminium is summarized in Figure 17.

The Pt_{13} clusters are pre-prepared in organic and subsequently anchored on a high surface area solid oxide surface bearing –OH groups which hydrolyze reactive Al–C bonds in the protective shell. This is completed after 5 h at ambient temperature. In the third step (which we coined ''conditioning'') the dried Pt/Al-oxide catalyst powders are exposed to synthetic air (containing 3.5 vol% O_2 in Ar) and H_2 for 30 min each at 250–300 °C. The particle size of the Pt(0) colloid adsorbed on the support was found to be virtually untouched (1.3 ± 0.4 nm), and after the ''conditioning'' only a moderate growth was determined. The aluminium was found to cover the Pt surface as a thin film of Al-oxide. This keeps the Pt particles apart from each other and accounts for an improved durability which we have reproducibly found in various catalytic test runs [411]. The use of highly magnetic nanomaterials in catalysis has recent been demonstrated by F. Schüth et al., in the ''nanoengineering'' of a magnetically separable hydrogenation catalyst [352].

Finally, two major industrial applications of nanocatalysts should be mentioned that are currently in the transition from basic research to industrial scale-up. Headwaters NanoKinetix and Degussa have developed and patented [412–415] a direct synthesis method for the

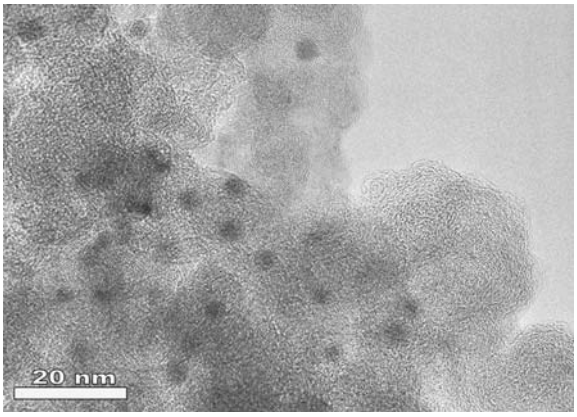

Figure 18. TEM electron micrograph of the supported Pd/Pt nanocatalyst (ca. 4 nm) for the direct production of H_2O_2. (Printed with permission of B. Zhou, Headwaters, Inc.)

production of H_2O_2 from hydrogen and oxygen using a size-defined nanocatalyst (4 nm) where Palladium is the main active component, and a lesser amount of platinum is typically included as well. The support is a porous solid such as carbon, alumina, or silica (Figure 18).

To control the formation of nanoparticles with desired size, composition, structure, dispersion, and stability, a multifunction ''nanoagent'' is used. The active metals (Pd and Pt) react with the functional groups of the ''nanoagent,'' i.e., a polymer template. The polymer template determines the size, monodisperity, composition, and morphology of the particles (which is somewhat reminiscent of the reversed micelles technique mentioned above).

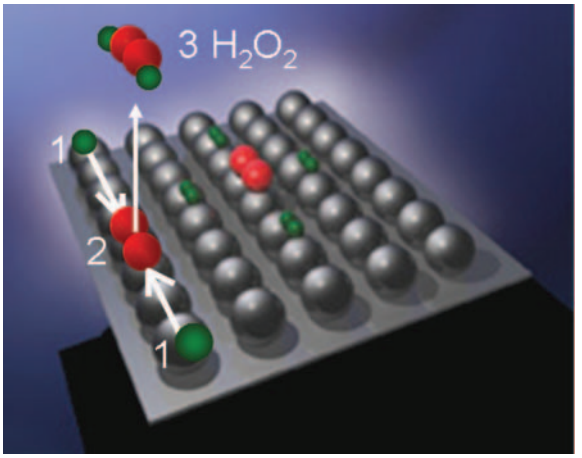

Figure 19. Illustration of the crystal surface control on the hydrogen peroxide reaction pathway. (Reprinted with permission of B. Zhou, Headwaters, Inc.)

Further, encapsulation in the template prevents the nanoparticles from agglomeration, maintaining the nanocatalyst performance for long term which is crucial for commercial application.

Figure 19 illustrates key steps of the H_2O_2 formation at the nanostructured catalyst surface. An important feature is the "imprintment" and maintenance of the (1 1 0) crystal surface through the polymer template because the specific row of metal atoms favours the formation of hydrogen peroxide while minimizing byproducts such as water.

The reaction steps are as follows:

1. hydrogen (H_2) dissociates on the catalyst surface
2. molecularly adsorbed oxygen is attacked by the adsorbed hydrogen
3. hydrogen peroxide dissociates from the catalyst surface.

It is anticipated that the new, environmentally friendly technology designed by Headwaters for H_2O_2 production will soon replace the current anthraquinone process because of the high activity, selectivity, and durability of the novel nanocatalyst.

"Nano for Energy" is the relevant key phrase evaluating the importance of nanocatalysis for the Fischer–Tropsch process which was invented in 1925 at the Kaiser-Wilhelm-Institute for Coal Research[2], Mülheim, Germany, currently regarded as one of the key steps in the huge gas-to-liquid (GTL) [416,417] or biomass-to-liquid (BTL) units [418–423] which are currently debated in industry to substitute ca. 10% of the global supply of diesel fuel by sulfur- and nitrogen-free "Synfuel" within a decade. Kuipers and de Jong [424,425] have recently reported that dispersing metallic cobalt nanoparticles of specific sizes on inert carbon nanofibers yields a new nanotype Fischer–Tropsch catalyst. A combination of physical analytic methods has revealed zerovalent cobalt nanoparticles to be the true "active sites" to convert CO and H_2 into hydrocarbons (and water). Particle size has a strong effect on activity, selectivity, and durability of the catalysts and it was found that cobalt particles with 6 or 8 nm are the optimum size for Fischer–Tropsch catalysis.

[2]In 1949 name changed to Max-Planck Institute für Kohlenforschung.

4.2. Materials

The optical, semiconductor, and electrical properties of metallic nanoparticles including potential applications in a number of fields have been reviewed in Chapter 5 of Schmid's recent book [60].

Recent progress in the manufacture of cost-effective, long-term stable dye sensitized solar cells (DSSC) has been achieved using screen-printing techniques [426]. Screen-printed cells, however, require the accessibility of 1–2 nm Pt nanoparticles where the surface is truly in the zerovalent state. Nanoscale syntheses as discussed in Section 3. of this article will certainly become the key to the ultimate economic viability of photovoltaic electricity production via DSSC [427]. This technology relies on nano-TiO_2, nano-SnO_2, and nano-Pt. Fiévets polyol method (see Section 3.6) and our preparation pathways (Section 3.3) we have been able – in close cooperation with the Fraunhofer Institute ISE (Freiburg, Germany) to produce SnO_2 doped with a nano-Pt layer that could be transformed into a paste to give an effective catalytic layer for the iodide/triiodide reduction [269]. Using nanosized Pt (0) precursors as the catalysts outperforms the conventional platinum catalyst layers. In a comparative study [269], we found catalytic layers fabricated using nanoclusters gained from either the "polyol process" ($0.4\,\Omega\,cm^2$) or via "hydrogen reduction" ($1.1\,\Omega\,cm^2$) to yield the best electrochemical performance for I^-/I_3^- reduction [428,429]. Future work will be focused on the manufacture of low-cost electrode layers based entirely on nanometal oxides, which eliminates the costly Ru-based dye and the use of precious metals.

Potential applications for magnetic nanoparticles include actuators in mechanical engineering, dampers in the automotive industry, high-end loudspeakers and rotating shafts in the drives of hard discs in personal computers. However, due to their relatively low stability towards oxidation under ambient conditions conventionally prepared cobalt and other elemental magnetic nanoparticles (Fe, Ni, etc.) cannot be applied in practice. On the other hand, noble metal alloyed particles such as Co_3Pt or Fe_xPt_{1-x} [281,430] are too costly. Co-, Fe/Co-particles prepared via the size-controlled decomposition of the respective metal carbonyls in the presence of aluminium alkyls can be stabilized against air and moisture via subsequent "smooth oxidation" [350]. These materials are commercially available and have been successfully tested in a number of applications, e.g., high-performance magnetic fluids, magnetic seals, magnetohydrostatic bearings, and global positioning systems (GPS) [431].

4.3. Biomedical Aspects

Nearly all synthetic pathways discussed in Section 3 can principally be applied to synthesize biocompatible metal

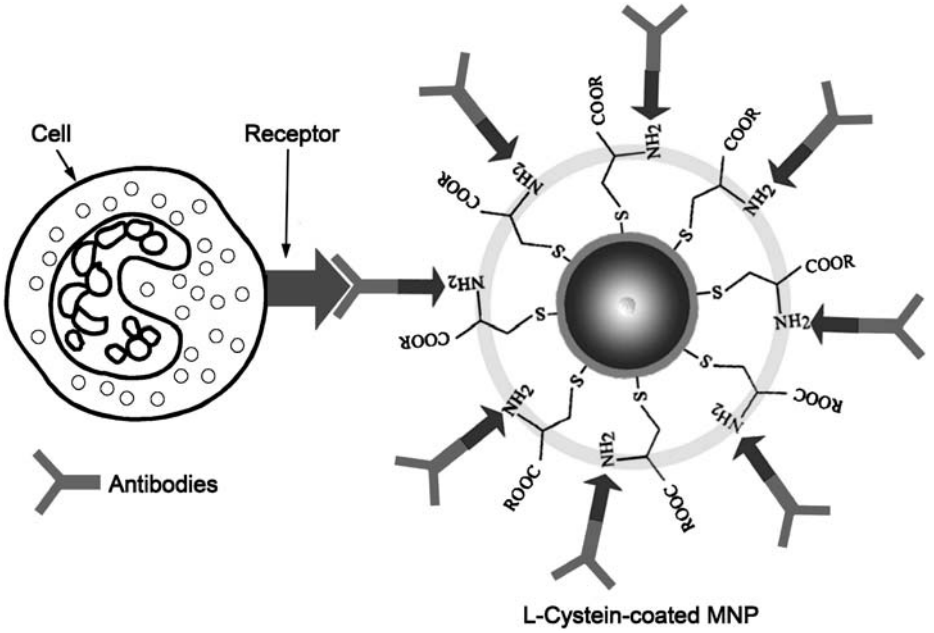

Figure 20. Selective cell targeting via specific monoclonal antibodies and/or antibody fragments directed against cancer cells and linked to the free amino groups of L-cysteine-coated metallic-core magnetic nanoparticles (MNP) (MNP = Co, Fe/Co, size 8–10 nm).

nanoparticles. The main pre-requisite for the application of nanometals in biological systems is that the ligands and/or the capping molecules have bio-friendly functionalities which fit into a given biochemical environment including human blood serum. A recent state-of-the-art review can be found in Chapter 6 of Ref. [60]. For the latest developments by applying, e.g., DNA-conjugates of the Schmid clusters, namely Au_{55}, to biomedical systems the reader should consult Chapter 1 by G. Schmid. It should only mentioned here that recent cellular toxicity tests done with DNA-conjugates of Schmid Au_{55} clusters have conjured up big hopes that Au_{55} clusters or related systems can assist the treatment of certain cancers in the future [432].

In a different way, metallic-core nanoparticles [346–349] (prepared cf. Section 3.10) equipped with biocompatible coats such as L-cysteine or dextrane may be exploited for highly efficient and cell-specific cancer cell targeting, i.e., for improving diagnosis and therapy of human cancer. In a recent "proof-of-principle experiment" an unexpectedly low toxicity of the L-cysteine-covered cobalt nanoparticles was demonstrated [433] For diagnostic purposes, it is expected to use the advantageous magnetic properties of the metallic-core nanoparticles to obtain a contrast medium for MRI with considerably increased sensitivity, capable to detect micro-metastases in the environment of healthy tissues [434–437].

The combination of cancer cell specific targeting, a high magnetic moment and high absolute concentrations in tumour tissues makes this magnetic antibody conjugate highly suitable also for the magnetically induced local heating of tissues aiming for selective hyperthermia. In addition, the antibody fragments can be considered as most appropriate vehicles to convey metal-core biobeads selectively into the cytoplasm of targeted tumour cells [438–440]. Both IR- and XAS-analyses clearly showed cysteine to be bonded exclusively to the particle surface via the –SH group leaving the amino function completely free for subsequent coupling, e.g., with antibody units [350, p. 29]. The principle is shown in Figure 20.

With the help of such nanometallic tools, in some future diseases or predispositions for diseases could potentially be discovered earlier than at present.

5. Conclusions and Outlook

The intention of this chapter is to provide a general survey on the preparative methodologies for the size- and shape-selective synthesis of metallic nanoparticles that have emerged from the benches of chemical basic research during the last few decades and become established as practical standard protocols. Industrial scale-up, however, has only just started to test the economic viability of these procedures and to determine whether they can meet the challenges of a number of very specific applications. The commercial manufacture of such thermodynamically extremely unstable nanoparticles in defined sizes and shapes on the kilo-scale is still confronted by a number of major problems and it remains to be seen how these can be solved.

There is no doubt that metallic nanoparticles that have defined sizes and shapes will become key components of a number of novel, highly sophisticated products, the prototypes of which are currently emerging from the industrial R&D departments. The outlook is promising for the industrial production of defined 1.4 nm metal clusters for use as single electron switches or transistors, for the cost-effective fabrication of ultrapure metallic nanomaterials needed for dye solar cells or sensors, and for the reproducible production of (particularly) efficient and durable

nanocatalysts for applications in the fields of chemistry or energy conversion.

An important field of development is the batched flow production of metal nanoclusters attached to biomolecules such as DNA under GMP laboratory standards. This conjures up hopes of applying metallic nanomaterials coupled with drugs, antibodies, or with oligonucleotides for cell-specific cancer diagnosis and therapy. With the help of such nanometallic tools, it can be expected that diseases or predispositions to diseases will be diagnosed earlier with the help of ''nanodrugs'' than is possible at present.

References

1 E. Gaffet, M. Tachikart, O. El Kedim, R. Rahouadj, *Mater. Charact.* 36 (1996) 185.
2 A. Amulyavichus, A. Daugvila, R. Davidonis, C. Sipavichus, *Fiz. Met. Metalloved.* 85 (1998) 111.
3 U. Kreibig, H. Bönnemann, J. Hormes, in H. S. Nalwa (ed.) *Handbook of Surfaces and Interfaces of Materials*, Vol. 3, Academic Press, San Diego, CA, 2001, 1.
4 X. Fu, Y. Wang, N. Wu, L. Gui, *Langmuir* 18 (2002) 4619.
5 H. Ohde, C. M. Wai, H. Kim, J. Kim, M. Ohde, *J. Am. Chem. Soc.* 124 (2002) 4540.
6 A. Henglein, *J. Phys. Chem. B* 104 (2000) 2201.
7 Y. Li, J. Petroski, M. A. El-Sayed, *J. Phys. Chem. B* 104 (2000) 10956.
8 R. Narayanan, M. A. El-Sayed, *J. Phys. Chem. B* 108 (2004) 5726.
9 R. W. J. Scott, O. M. Wilson, R. M. Crooks, *J. Phys. Chem. B* 109 (2005) 692.
10 R. M. Crooks, M. Zhao, L. Sun, V. Chechik, L. K. Yeung, *Acc. Chem. Res.* 34 (2001) 181.
11 T. W. Smith, US Patent 4252671 (1981)
12 T. W. Smith, US Patent 4252672 (1981)
13 T. W. Smith, US Patent 4252673 (1981)
14 T. W. Smith, US Patent 4252674 (1981)
15 T. W. Smith, US Patent 4252678 (1981)
16 T. Tano, K. Esumi, K. Meguro, *J. Colloid Interface Sci.* 133 (1989) 530.
17 K. Esumi, T. Tano, K. Meguro, *Langmuir* 5 (1989) 268.
18 K. Esumi, T. Tano, K. Torigoe, K. Meguro, *Chem. Mater.* 2 (1990) 564.
19 K. Esumi, M. Suzuki, T. Tano, K. Torigoe, K. Meguro, *Colloids Surf.* 55 (1991) 9.
20 K. Esumi, N. Sato, K. Torigoe, K. Meguro, *J. Colloid Interface Sci.* 149 (1992) 295.
21 K. Esumi, O. Sadakane, K. Torigoe, K. Meguro, *Colloids Surf.* 62 (1992) 255.
22 N. Toshima, Y. Wang, *Chem. Lett.* 22 (1993) 1611.
23 A. Henglein, A. Holzwarth, P. Mulvaney, *J. Phys. Chem.* 96 (1992) 8700.
24 A. Hengelein, J. Lille, *J. Phys. Chem.* 85 (1981) 1246.
25 J. Butler, A. Henglein, *Radiat. Phys. Chem.* 15 (1980) 603.
26 B. G. Ershov, A. Henglein, *J. Phys. Chem.* 97 (1993) 3434.
27 A. Henglein, P. Mulvaney, A. Holzwarth, T. E. Sosebee, A. Fojtik, *Ber. Bunsenges. Phys. Chem.* 96 (1992) 754.
28 A. Henglein, *Ber. Bunsenges. Phys. Chem.* 81 (1977) 556.
29 A. Henglein, R. Tausch-Treml, *J. Colloid Interface Sci.* 80 (1981) 84.
30 A. Mosseri, A. Henglein, E. Janata, *J. Phys. Chem.* 93 (1989) 6791.
31 J. Belloni, M. D. Delcourt, C. Leclerc, *Nouv. J. Chim.* 6 (1982) 507.
32 G. Mills, A. Henglein, *Radiat. Phys. Chem.* 26 (1984) 385.
33 M. O. Delcourt, N. Keghouche, J. Belloni, *Nouv. J. Chim.* 7 (1983) 131.
34 M. O. Delcourt, J. Belloni, J.-L. Marignier, C. Mory, C. Colliex, *Radiat. Phys. Chem.* 23 (1984) 485.
35 J.-L. Marignier, J. Belloni, M. O. Delcourt, J. P. Chavalier, *Nature* 317 (1985) 344.
36 B. G. Ershov, E. Janata, M. Michaelis, A. Henglein, *J. Phys. Chem.* 95 (1991) 8996.
37 B. G. Ershov, E. Janata, A. Henglein, *Radiat. Phys. Chem.* 39 (1992) 123.
38 A. Henglein, M. Guttierez, E. Janata, B. G. Ershov, *J. Phys. Chem.* 96 (1992) 4598.
39 K. S. Suslick, J. Prince, *Annu. Rev. Mater. Sci.* 29 (1999) 295.
40 A. Dhas, A. Gedanken, *J. Mater. Chem.* 8 (1998) 445.
41 Y. Koltypin, A. Fernandez, C. Rojas, J. Campora, P. Palma, R. Prozorov, A. Gedanken, *Chem. Mater.* 11 (1999) 1331.
42 R. A. Sarkar, P. Jeevanandam, S. T. Aruna, Y. Koltypin, A. Gedanken, *J. Mater. Chem.* 9 (1999) 1333.
43 M. Faraday, *Philos. Trans. R. Soc. London* 147 (1857) 145.
44 J. Turkevich, P. C. Stevenson, J. Hillier, *Discuss. Faraday Soc.* 11 (1951) 55.
45 J. Turkevich, G. Kim, *Science* 169 (1970) 873.
46 J. Turkevich, *Gold Bull.* 18 (1985) 86.
47 H. Hirai, Y. Nakao, N. Toshima, K. Adachi, *Chem. Lett.* 5 (1976) 905.
48 G. Schmid, R. Boese, R. Pfeil, F. Bandermann, S. Meyer, G. H. M. Calis, J. A. W. van der Velden, *Chem. Ber.* 114 (1981) 3634.
49 M. N. Vargaftik, V. P. Zargorodnikov, I. P. Stolarov, I. I Moiseev, V. A. Likholobov, D. I. Kouchubey, A. L. Chuvilin, V. I. Zaikovsky, K. I. Zamaraev, G. I. Timofeeva, *Chem. Commun.* 24 (1985) 937.
50 M. Giersig, P. Mulvaney, *Langmuir* 9 (1993) 3408.
51 S. Bucher, J. Hormes, H. Modrow, R. Brinkmann, N. Waldöfner, H. Bönnemann, L. Beuermann, S. Krischok, W. Maus-Friedrichs, V. Kempter, *Surf. Sci.* 497 (2002) 321.
52 D. Astruc, F. Lu, J. R. Aranzaes, *Angew. Chem. Int. Ed.* 44 (2005) 7852.
53 H. Bönnemann, K. S. Nagabhushana, R. M. Richards, in: D. Astruc (ed.) *Nanoparticles and Catalysis*, Chapter 2, Wiley-VCH, Weinheim, 2007, 49.
54 H. Bönnemann, W. Brijoux, *Nanostruct. Mater.* 5 (1995) 135.
55 R. Franke, J. Rothe, J. Pollmann, J. Hormes, H. Bönnemann, W. Brijoux, T. Hindenburg, *J. Am. Chem. Soc.* 118 (1996) 12090.
56 M. T. Reetz, G. Lohmer, *Chem. Commun.* (Cambridge) 16 (1996) 1921.
57 N. Toshima, M. Harada, T. Yonezawa, K. Kushihashi, K. Asakura, *J. Phys. Chem.* 95 (1991) 7448.
58 C. E. Briant, B. R. C. Theobald, J. W. White, C. K. Bell, D. M. P. Mingos, *Chem. Commun.* 20 (1981) 201.
59 J. W. A. van der Velden, F. A. Vollenbroek, J. J. Bour, P. I. Beukskens, J. M. M. Smits, W. P. Bosman, *Rec. J. R. Neth. Chem. Soc.* 100 (1981) 148.
60 G. Schmid (ed.) *Nanoparticles: From Theory to Application*, Wiley-VCH, Weinheim, 2004.
61 G. Schmid, B. Corain, *Eur. J. Inorg. Chem.* 17 (2003) 3081.
62 H. Bönnemann, W. Brijoux, R. Brinkmann, E. Dinjus, T. Joussen, B. Korall, *Angew. Chem. Int. Ed.* 30 (1991) 1312.
63 H. Bönnemann, W. Brijoux, T. Joussen, (to Studiengesellschaft Kohle mbH) US Patent 5580492 (1993).
64 O. Vidoni, K. Philippot, C. Amiens, B. Chaudret, O. Balmes, J.-O. Malm, J.-O. Bovin, F. Senocq, M.-J. Casanove, *Angew. Chem. Int. Ed.* 38 (1999) 3736.
65 D. Mandler, I. Willner, *J. Phys. Chem.* 91 (1987) 3600.
66 J. Tanori, M. P. Pileni, *Langmuir* 13 (1997) 639.
67 M. P. Pileni, *Langmuir* 13 (1997) 3266.

68 M. Antonietti, C. Göltner, *Angew. Chem. Int. Ed. Engl.* 36 (1997) 910.
69 M. P. Pileni, *Supramol. Sci.* 5 (1998) 321.
70 M. P. Pileni, *Adv. Mater.* 10 (1998) 259.
71 M. Antonietti, *Chem. Ing. Tech.* 68 (1996) 518.
72 S. Förster, *Ber. Bunsenges.* 101 (1997) 1671.
73 J. J. Storhoff, R. C. Mucic, C. A. Mirkin, *J. Cluster Sci.* 8 (1997) 179.
74 M. Möller, J. P. Spatz, *Curr. Opin. Colloid Interface Sci.,* 2 (1997) 177.
75 G. B. Sergeev, M. A. Petrukhina, *Prog. Solid State Chem.* 24 (1996) 183.
76 J. P. Wilcoxon, P. Provencio, *J. Phys. Chem. B* 103 (1999) 9809.
77 T. Miyao, N. Toyoizumi, S. Okuda, Y. Imai, K. Tyjima, S. Naito, *Chem. Lett*. 28 (1999) 1125.
78 S. T. Selvan, M. Nogami, A. Nakamura, Y. Hamanaka, *J. Non-Crystalline Solids* 255 28 (1999) 254.
79 M. M. Maye, W. Theng, F. L. Leibowitz, N. K. Ly, C. J. Zhong, *Langmuir* 16 (2000) 490.
80 Y. Niidome, A. Hori, T. Sato, S. Yamada, *Chem. Lett*. 29 (2000) 310.
81 I. Konomi, S. Hyodo, T. Motohiro, *J. Catal*. 192 (2000) 11.
82 M. Maase, Ph.D. Thesis, Verlag Mainz, Aachen, ISBN 3-89653-463-7, 1999.
83 X. Peng, J. Wickham, A. P. Alivisatos, *J. Am. Chem. Soc*. 120 (1998) 5343.
84 C. B. Murray, C. R. Kagan, M. G. Bawendi, *Annu. Rev. Mater. Sci*. 30 (2000) 545.
85 V. K. LaMer, R. H. Dinegar, *J. Am. Chem. Soc*. 72 (1950) 4847.
86 K. Angermund, M. Bühl, U. Endruschat, F. T. Mauschick, R. Mörtel, R. Mynott, B. Tesche, N. Waldöfner, H. Bönnemann, G. Köhl, H. Modrow, J. Hormes, E. Dinjus, F. Gassner, H.-G. Haubold, T. Vad, M. Kaupp, *J. Phys. Chem. B* 107 (2003) 7507.
87 J. H. El Nakat, I. G. Dance, K. J. Fisher, G. D. Willet, *Inorg. Chem*. 30 (1991) 2957.
88 F. Wen, N. Waldöfner, W. Schmidt, K. Angermund, H. Bönnemann, S. Modrow, S. Zinoveva, H. Modrow, J. Hormes, L. Beuermann, S. Rudenkiy, W. M. Friedrichs, V. Kempter, T. Vad, H.-G. Haubold, *Eur. J. Inorg. Chem*. (2005) 3625.
89 X. M. Lin, C. M. Sorensen, K. J. Klabunde, *J. Nanoparticle Res*. 2 (2000) 157.
90 S. I. Soeva, K. J. Klabunde, C. M. Sorensen, I. Dragieva, *J. Am. Chem. Soc*. 124 (2002) 2305.
91 S. I. Soeva, B. L. V. Prasad, S. Uma, P. K. Stoimenov, V. Zaikovski, C. M. Sorensen, K. J. Klabunde, *J. Phys. Chem. B* 107 (2003) 7441.
92 B. L. V. Pradad, S. I. Stoeva, C. M. Sorensen, K. J. Klabunde, *Chem. Mater*. 15 (2003) 935.
93 S. I. Stoeva, V. Zaikovski, B. L. V. Prasad, P. K. Stoimenov, C. M. Sorensen, K. J. Klabunde, *Langmuir* 21 (2005) 10280.
94 K. Angermund, M. Bühl, U. Endruschat, F. T. Mauschick, R. Mörtel, R. Mynott, B. Tesche, N. Waldöfner, H. Bönnemann, G. Köhl, H. Modrow, J. Hormes, E. Dinjus, F. Gassner, H-G. Haubold, T. Vad, *Angew. Chem. Int. Ed*. 41 (2002) 4041.
95 M. Neurock, S. A. Wasileski, D. Mei, *Chem. Eng. Sci*. 59 (2004) 4703.
96 D. Cao, G.-Q. Lu, A. Wieckowski, S. A. Wasileski, M. Neurock, *J. Phys. Chem. B* 109 (2005) 11622.
97 L. Kieken, M. Neurock, D. Mei, *J. Phys. Chem. B* 109 (2005) 2234.
98 M. Neurock, *J. Catal.* 216 (2003) 73.
99 M. I. Baskes, *Phys. Rev. B* 62 (1992) 2727.
100 M. I. Baskes, R. A. Johnson, *Model. Simul. Mater. Sci. Eng.* 2 (1994) 147.
101 G. Wang, M. A. Van Hove, P. N. Ross, M. I. Baskes, *Prog. Surf. Sci.* 79 (2005) 28.
102 P. Strasser, Q. Fan, M. Devenney, W. H. Weinberg, P. Liu, J. K. Nørskov, *J. Phys. Chem. B* 107 (2003) 11013.
103 V. Stamenkovic, B. S. Mun, K. J. J. Mayrhofer, P. N. Ross, N. M. Markovic, J. Rossmeisl, J. Greeley, J. K. Nørskov, *Angew. Chem. Int. Ed*. 45 (2006) 2897.
104 S. Horch, H. T. Lorensen, S. Helveg, E. Lægsgaard, I. Stensgaard, K. W. Jacobsen, J. K. Nørskov, F. Besenbacher, *Nature* 398 (1999) 134.
105 J. K. Nørskov, T. Bligaard, A. Logadottir, S. Bahn, L. B. Hansen, M. Bollinger, H. Bengaard, B. Hammer, Z. Sljivancanin, M. Mavrikakis, Y. Xu, S. Dahl, C. J. H. Jacobsen, *J. Catal.* 209 (2002) 275.
106 L. Colmenares, E. Guerrini, Z. Jusys, K. S. Nagabhushana, E. Dinjus, S. Behrens, W. Habicht, H. Bönnemann, R. J. Behm, *J. Appl. Electrochem.*, in press (2007).
107 R. Tausch-Treml, A. Henglein, J. Lilie, *Ber. Bunsenges. Phys. Chem.* 82 (1978) 1335.
108 A. Henglein, in H. F. Bicke (ed.) *Modern Trends in Colloid Science in Chemistry and Biology*, Birkhauser Verlag, Stuttgart, 1985, 126.
109 F. Wen, H. Bönnemann, R. J. Mynott, B. Spliethoff, C. Weidenthaler, N. Palina, S. Zinoveva, H. Modrow, *Appl. Organomet. Chem.* 19 (2005) 827.
110 G. Schmid, *Inorg. Synth*. 7 (1990) 214.
111 G. Schmid, N. Klein, L. Korste, U. Kreibig, D. Schönauer, *Polyhedron* 7 (1988) 605.
112 G. Schmid, R. Pugin, J.-O. Malm, J.-O. Bovin, *Eur. J. Inorg. Chem*. 6 (1998) 813.
113 G. Schmid, R. Pugin, W. Meyer-Zaika, U. Simon, *Eur. J. Inorg. Chem*. 11 (1999) 2051.
114 L. O. Brown, J. E. Hutchison, *J. Am. Chem. Soc*. 119 (1997) 12384.
115 G. Schmid (ed.) *Clusters and Colloids – From Theory to Applications*, Wiley-VCH, Weinheim, 1994.
116 G. Schmid, *Struct. Bond.* 62 (1985) 51.
117 M. P. J. van Staveren, H. B. Brom, L. J. de Jongh, G. Schmid, *Solid State Commun*. 60 (1986) 319.
118 A. H. A. Smit, R. C. Thiel, L. J. de Jongh, G. Schmid, N. Klein, *Solid State Commun*. 65 (1988) 915.
119 G. Schmid, *Polyhedron* 7 (1988) 2321.
120 R. E. Benfield, J. A. Creighton, D. G. Eadon, G. Schmid, *Z. Phys. D* 12 (1989) 533.
121 M. C. Fairbanks, R. E. Benfield, R. J. Newport, G. Schmid, *Solid State Commun*. 73 (1990) 431.
122 H. Feld, A. Leute, D. Rading, A. Benninghoven, G. Schmid, *Z. Phys. D* 17 (1990) 73.
123 G. Schmid, *Endeavour* 14 (1990) 172.
124 H. Feld, A. Leute, D. Rading, A. Benninghoven, G. Schmid, *J. Am. Chem. Soc*. 112 (1990) 8166.
125 C. Becker, Th. Fries, K. Wandelt, U. Kreibig, G. Schmid, *J. Vac. Sci. Technol*. B9 (1991) 810.
126 U. Kreibig, K. Fauth, C.-G. Granqvist, G. Schmid, *Z. Phys. Chem. Neu Folge* 169 (1990) 11.
127 K. Fauth, U. Kreibig, G. Schmid, *Z. Phys. D* 20 (1991) 297.
128 M. Quinten, I. Sander, P. Steiner, U. Kreibig, K. Fauth, G. Schmid, *Z. Phys. D* 20 (1991) 377.
129 L. E. C. van de Leemput, J. W. Gerritsen, P. H. H. Rongen, R. T. M. Smokers, H. A. Wieringa, H. van Kempen, G. Schmid, *J. Vac. Sci. Technol*. B9 (1991) 814.
130 B. Dusemund, A. Hoffmann, T. Salzmann, U. Kreibig, G. Schmid, *Z. Phys. D* 20 (1991) 305.
131 G. Schmid, *Chem. Rev*. 92 (1992) 1709.
132 G. Schmid, in J. de Jongh (ed.) *Physics and Chemistry of Metal Cluster Compounds*, Kluwer Academic Publishers, Dordrecht, The Netherlands, 1994, 107.
133 U. Simon, G. Schmid, G. Schön, *Angew. Chem. Int. Ed*. 32 (1993) 250.

134 F. M. Mulder, E. A. van der Zeeuw, R. C. Thiel, G. Schmid, *Solid State Commun.* 85 (1993) 93.
135 M. Herrmann, U. Kreibig, G. Schmid, *Z. Phys. D* 26 (1993) 1.
136 J. Baak, H. B. Brom, L. J. de Jongh, G. Schmid, *Z. Phys. D* 26 (1993) 30.
137 H. B. Brom, J. Baak, L. J. de Jongh, F. M. Mulder, R. C. Thiel, G. Schmid, *Z. Phys. D* 26 (1993) 27.
138 P. D. Cluskey, R. J. Newport, R. E. Benfield, S. J. Gurmann, G. Schmid, *Z. Phys. D* 26 (1993) 8.
139 R. Houbertz, T. Feigenspan, F. Mielke, U. Memmert, U. Hartmann, U. Simon, G. Schön, G. Schmid, *Europhys. Lett*. 28 (1994) 641.
140 B. A. Smith, J. Z. Zhang, U. Giebel, G. Schmid, *Chem. Phys. Lett*. 270 (1997) 139.
141 T. Tominaga, S. Tenma, H. Watanabe, U. Giebel, G. Schmid, *Chem. Lett*. 25 (1996) 1033.
142 V. Ruffieux, G. Schmid, P. Braunstein, J. Rosé, *Chem. Eur. J*. 6 (1997) 900.
143 A. Bezryadin, C. Dekker, G. Schmid, *Appl. Phys. Lett*. 71 (1997) 1273.
144 L. F. Chi, M. Hartig, T. Drechsler, Th. Schwaack, C. Seidel, H. Fuchs, G. Schmid, *Appl. Phys. A* 66 (1998) 187.
145 G. Schmid, L. F. Chi, *Adv. Mater*. 10 (1998) 515.
146 G. Schmid, *J. Chem. Soc., Dalton Trans.* 24 (1998) 1077.
147 G. Schmid, R. Pugin, T. Sawitowski, U. Simon, B. Marler, *Chem. Commun*. 24 (1999) 303.
148 G. Schmid, W. Meyer-Zaika, R. Pugin, T. Sawitowshi, J. P. Majoral, A.-M. Caminade, C.-O. Turrin, *Chem. Eur. J*. 6 (2000) 1693.
149 V. Torma, G. Schmid, U. Simon, *Chem. Phys. Chem*. 5 (2001) 321.
150 V. Torma, T. Reuter, O. Vidoni, M. Schumann, C. Radehaus, G. Schmid, *Chem. Phys. Chem*. 8/9 (2001) 546.
151 Y. Liu, M. Schumann, T. Raschke, C. Radehaus, G. Schmid, *Nano Lett*. 8 (2001) 405.
152 T. Sawitowski, Y. Miquel, A. Heilmann, G. Schmid, *Adv. Funct. Mater*. 11 (2001) 435.
153 H.-G. Boyen, G. Kästle, F. Weigl, P. Ziemann, G. Schmid, M. G. Garnier, P. Oelhafen, *Phys. Rev. Lett*. 87 (2001) 276401.
154 H.-G. Boyen, G. Kästle, F. Weigl, B. Koslowski, C. Dietrich, P. Ziemann, J. P. Spatz, S. Riethmüller, C. Hartmann, M. Möller, G. Schmid, M. G. Garnier, P. Oelhafen, *Science* 297 (2002) 1533.
155 V. Torma, O. Vidoni, U. Simon, G. Schmid, *Eur. J. Inorg. Chem*. 6 (2003) 1121.
156 H. Zhang, G. Schmid, U. Hartmann, *Nano Lett*. 3 (2003) 305.
157 G. Schön, U. Simon, *Colloid Polymer Sci*. 273 (1995) 101.
158 G. Schön, U. Simon, *Colloid Polymer Sci*. 273 (1995) 202.
159 U. Simon, *Adv. Mater*. 10 (1998) 1487.
160 G. Schmid, U. Simon, *Chem. Commun.* 47 (2005) 697.
161 M. N. Vargaftik, N. Y. Kozitsyna, N. V. Cherkashina, R. I. Rudyi, D. I. Kochubey, B. N. Novgorodov, I. I. Moiseev, *Kinet. Catal.* 39 (1998) 740.
162 M. N. Vargaftik, V. P. Zargorodnikov, I. P. Stolarov, I. I. Moiseev, D. I. Kochubey, V. A. Likholobov, A. L. Chuvilin, K. I. Zarnaraev, *J. Mol. Catal*. 53 (1989) 315.
163 V. V. Volkov, G. van Tendeloo, G. A. Tsirkov, N. V. Cherkashain, M. N. Vargaftik, I. I. Moiseev, V. M. Novotortsev, A. V. Krit, A. L. Chuvilin, *J. Cryst. Growth* 163 (1996) 377.
164 I. I. Moiseev, M. N. Vargaftik, V. V. Volkov, G. A. Tsirkov, N. V. Cherkashain, V. M. Novotortsev, O. G. Ellett, I. A. Petrunenka, A. L. Chuvilin, A. V. Krit, *Mendeleev Commun*. 3 (1995) 87.
165 V. Oleshko, V. Volkov, W. Jacob, M. Vargaftik, I. I. Moiseev, G. van Tendeloo, *Z. Phys. D* 34 (1995) 283.
166 I. I. Moiseev, M. N. Vargaftik, T. V. Chernysheva, T. A. Stromnova, A. E. Gekhman, G. A. Tsirkov, A. M. Makhlina, *J. Mol. Catal. A: Chem*. 108 (1996) 77.
167 J. D. Aiken III, R. G. Finke, *J. Mol. Catal. A: Chem. 145* (1999) 1.
168 G. Schmid, B. Morun, J.-O. Malm, *Angew. Chem. Int. Ed.* 28 (1989) 778.
169 G. Schmid, *Mater. Chem. Phys*. 29 (1991) 133.
170 G. Schmid, M. Harms, J.-O. Malm, J.-O. Bovin, J. van Ruitenbeck, H. W. Zandbergen, W. T. Fu, *J. Am. Chem. Soc*. 115 (1993) 2046.
171 J. Kiwi, M. Grätzel, *J. Am. Chem. Soc.* 101 (1979) 7214.
172 H. Bönnemann, W. Brijoux, R. Brinkmann, E. Dinjus, R, Fretzen, T. Joussen, B. Korall, *J. Mol. Catal*. 74 (1992) 323.
173 H. Bönnemann, W. Brijoux, R. Brinkmann, R. Fretzen, T. Joussen, R. Köppler, P. Neiteler, J. Richter, *J. Mol. Catal*. 86 (1994) 129.
174 H. Bönnemann, G. Braun, W. Brijoux, R. Brinkmann, A. S. Tilling, K. Seevogel, K. Siepen, *J. Organomet. Chem.* 520 (1996) 143.
175 H. Bönnemann, W. Brijoux, in A. Fürstner (ed.) *Active Metals*, Wiley-VCH, Weinheim, 1996, 339.
176 H. Bönnemann, W. Brijoux, in P. Braunstein, L. A. Oro, P. R. Raithby (eds.) *Metal Clusters in Chemistry*, Vol. 2, Wiley-VCH, Weinheim, 1999, 913.
177 H. Bönnemann, W. Brijoux, in W. Moser (ed.) *Advanced Catalysts and Nanostructured Materials*, Chapter 7, Academic Press, San Diego, CA, 1996, 165.
178 H. Bönnemann, K. S. Nagabhushana, in J. A. Schwarz, C. I. Contescu, K. Putyera (eds.) *Dekker Encyclopedia of Nanoscience and Nanotechnology*, Vol. 1, Marcel Dekker, New York, 2004, 739.
179 H. Bönnemann, K. S. Nagabhushana, in H. S. Nalwa (ed.) *Encyclopedia of Nanoscience and Nanotechnology*, Vol. 1, American Scientific Publishers, Stevenson Ranch, CA, 2004, 777.
180 K. S. Nagabhushana, H. Bönnemann, in B. Zhou, S. Hermans, G. A. Somorjai (eds.) *Nanotechnology in Catalysis*, Vol. 1, Kluwer Academic/Plenum Publishers, New York, 2004, 51.
181 H. Bönnemann, R. Richards, in A. Weikowski, E. R. Savinova, C. G. Vayenas (eds.) *Catalysis and Electrocatalysis at Nanoparticle Surfaces*, Marcel Dekker, New York, 2003, 343.
182 H. S. Nalwa (ed.) *Encyclopedia of Nanoscience and Nanotechnology,* Vol. 1–10, American Scientific Publishers, Stevenson Ranch, CA, 2004.
183 H. Bönnemann, K. S. Nagbhushana, R. M. Richards, in: D. Astruc (ed.): *Nanoparticles and Catalysis*, Chapter 2, Wiley VCH, Weinheim, 2007, 60.
184 H. Bönnemann, R. Brinkmann, R. Köppler, P. Neiteler, J. Richter, *Adv. Mater*. 4 (1992) 804.
185 M. T. Reetz, M. Maase, *Adv. Mater*. 11 (1999) 773.
186 J. S. Bradley, B. Tesche, W. Busse, M. Maase, M. T. Reetz, *J. Am. Chem. Soc*., 122 (2000) 4631.
187 V. F. Puntes, K. M. Krishnan, A. P. Alivisatos, *Science* 291 (2001) 2155.
188 R. Jin, C. A. Mirkin, K. L. Kelly, G. C. Schatz, J. G. Zheng, *Science* 294 (2001) 1901.
189 Y. Sun, Y. Xia, *Science* 298 (2002) 2176.
190 Y.-T. Yu B.-Q. Xu, *Appl. Organomet. Chem*. 20 (2006) 638.
191 S. Kinge, H. Bönnemann, *Appl. Organomet. Chem*. 20 (2006) 784.
192 M. T. Reetz, W. Helbig, *J. Am. Chem. Soc*. 116 (1994) 7401.
193 M. T. Reetz, W. Helbig, S. A. Quaiser, in A. Fürstner (ed.), *Active Metals*, Wiley-VCH, Weinheim, 1996, 279.
194 J. A. Becker, R. Schäfer, W. Festag, W. Ruland, J. H. Wendorf, J. Pebler, S. A. Quaiser, W. Helbig, M. T. Reetz, *J. Chem. Phys*. 103 (1995) 2520.

195 M. T. Reetz, S. A. Quaiser, C. Merk, *Chem. Ber*. 129 (1996) 741.
196 M. T. Reetz, W. Helbig, S. A. Quaiser, *Chem. Mater*. 7 (1995) 2227.
197 M. T. Reetz, S. A. Quaiser, *Angew. Chem. Int. Ed*. 34 (1995) 2240.
198 U. Kolb, S. A. Quaiser, M. Winter, M. T. Reetz, *Chem. Mater*. 8 (1996) 1889.
199 M. Brust, M. Walker, D. Bethell, D. J. Schiffrin, R. Whyman, *J. Chem. Soc. Chem. Commun*. 24 (1994) 801.
200 J. Rothe, J. Pollmann, R. Franke, J. Hormes, H. Bönnemann, W. Brijoux, K. Siepen, J. Richter, *J. Anal. Chem*. 355 (1996) 372.
201 H. Bönnemann, W. Brijoux, R. Brinkmann, J. Richter (to Studiengesellschaft Kohle mbH), US Patent 849482 (1997); US Patent 6090746 (2000).
202 G. Schmid, A. Lehnert, *Angew. Chem. Int. Ed*. 28 (1989) 780.
203 G. Schmid (ed.), *Nanotechnology*, Springer, Berlin, 2006.
204 M. E. Labib, *Colloids Surf*. 29 (1988) 293.
205 M. E. Labib, R. Williams, *J. Colloid Interface Sci*. 97 (1984) 356.
206 H. Bönnemann, B. Korall, *Angew. Chem. Int. Ed*. 31 (1992) 1490.
207 R. Franke, J. Rothe, R. Becker, J. Pollmann, J. Hormes, H. Bönnemann, W. Brijoux, R. Köppler, *Adv. Mater*. 10 (1998) 126.
208 J. Sinzig, L. J. de Jongh, H. Bönnemann, W. Brijoux, R. Köppler, *Appl. Organomet. Chem*. 12 (1998) 387.
209 Y. Volokitin, J. Sinzig, G. Schmid, H. Bönnemann, L. J. de Jongh, *Z. Phys. D*, *At., Mol. Clusters* 40 (1997) 136.
210 H. Hirai, Y. Nakao, N. Toshima, *Chem. Lett*. 7 (1978) 545.
211 H. Hirai, Y. Nakao, N. Toshima, *J. Macromol. Sci. Chem*. A12 (1978) 1117.
212 N. Toshima, T. Yonezawa, *New J. Chem*. 22 (1998) 1179.
213 H. Hirai, Y. Nakao, N. Toshima, *J. Macromol. Sci. Chem*. A13 (1979) 727.
214 C.-R. Bian, S. Suzuki, K, Asakura, L. Ping, N. Toshima, *J. Phys. Chem. B* 106 (2002) 8587.
215 Y. Shiraishi, D. Arakawa, N. Toshima, *Eur. Phys. J. E* 8 (2002) 377.
216 N. Toshima, Y. Shiraishi, T. Matsushita, H. Mukai, K. Hirakawa, *Int. J. Nanosci.* 1 (2002) 397.
217 Y. Shiraishi, D. Ikenada, N. Toshima, *Aust. J. Chem.* 56 (2003) 1025.
218 K. Hirakawa, N. Toshima, *Chem. Lett.* 32 (2003) 78.
219 N. Toshima, M. Kanemaru, Y. Shiraishi, Y. Koga, *J. Phys. Chem. B* 109 (2005) 16326.
220 N. Toshima, in R. Barbucci, F. Ciardelli (eds.) *Recent Advances and Novel Approaches in Macromolecule-Metal Complexes*, Wiley-VCH, Weinheim, 2006, 1.
221 T. Teranishi, M. Miyake, *Chem. Mater*. 10 (1998) 594.
222 G. W. Busser, J. G. van Ommen, and J. A. Lercher, in: *Advanced Catalysis and Nanostructured Materials*, W. R. Moser (ed)., Academic Press, San Diego, (1996) 213.
223 F. Bonet, V. Delmas, S. Grugeon, R. H. Urbina, P.-Y. Silvert, K. T. Elhsissen, *Nanostruct. Mater*. 11 (1999) 1277.
224 F. Fiévet, in T. Sugimoto (ed.) *Fine Particles*, Marcel Dekker, New York, 2000, 460.
225 M. Figlarz, F. Fiévet, J.-P. Lagier, French Patent 8221483 (1985).
226 M. Figlarz, *Mater. Res. Soc. Bull*. 14 (1989) 29.
227 C. D. Sanguesa, R. H. Urbina, M. Figlarz, *J. Solid State Chem*. 100 (1992) 272.
228 F. Fiévet, J.-P. Lager, B. Blin, B. Beaudouin, M. Figlarz, *Solid State Ionics* 32/33 (1989) 198.
229 C. Liu, X. Wu, T. Klemmer, N. Shukla, X. Yang, D. Weller, A. G. Roy, M. Tanase, D. Laughlin, *J. Phys. Chem. B* 108 (2004) 6121.
230 E. A. Sales, B. Benhamida, V. Caizergues, J.-P. Lagier, F. Fiévet, F. B. Verduraz, *Appl. Catal. A: Gen.* 172 (1998) 273.
231 P.-Y. Silvert, V. Vijayakrishnan, P. Vibert, R. H. Urbina, K. T. Elhsissen, *Nanostruct. Mater*. 7 (1996) 611.
232 P.-Y. Silvert, R. H. Urbina, N. Duvauchelle, V. Vijayakrishnan, K. T. Elhsissen, *J. Mater. Chem*. 6 (1996) 573.
233 P.-Y. Silvert, R. H. Urbina, *J. Mater. Chem*. 7 (1997) 293.
234 L. K. Kurihara, G. M. Chow, P. E. Schön, *Nanostruct. Mater*. 5 (1995) 607.
235 S. Komarneni, H. Katsuki, D. Li, A. S. Bhalla, *J. Phys. Condens. Matter* 16 (2004) S1305.
236 P.-Y. Silvert, K. T. Elhsissen, *Solid State Ionics* 82 (1995) 53.
237 C. D. Sanguesa, R. H. Urbina, M. Figlarz, *Solid State Ionics* 63–65 (1993) 25.
238 T. K. Elhsissen, F. Bonet, S. Grugeon, S. Lambert, R. H. Urbina, *J. Mater. Res.* 14 (1999) 3707.
239 T. K. Elhsissen, F. Bonet, P.-Y. Silvert, R. H. Urbina, *J. Alloy. Comp.* 292 (1999) 96.
240 G. Viau, F. F. Vincent, F. Fiévet, *Solid State Ionics* 84 (1996) 259.
241 G. Viau, F. F. Vincent, F. Fiévet, *J. Mater. Chem.* 6 (1996) 1047.
242 P. Toneguzzo, O. Acher, G. Viau, A. Pierrard, F. F. Vincent, F. Fiévet, I. Rosenman, *IEEE Trans. Magn.* 235 (1999) 3469.
243 G. Viau, P. Toneguzzo, A. Pierrard, O. Acher, F. F. Vincent, F. Fiévet, *Scripta Mater.* 44 (2001) 2263.
244 F. Bonet, S. Grugeon, L. Dupont, R. H. Urbina, C. Guery, J. M. Tarascon, *J. Solid State Chem.* 172 (2003) 111.
245 R. Brayner, G. Viau, G. M. da Cruz, F. F. Vincent, F. Fiévet, F. B. Verduraz, *Catal. Today* 57 (2000) 187.
246 G. Viau, R. Brayner, L. Poul, N. Chakroune, E. Lacaze, F. F. Vincent, F. Fiévet, *Chem. Mater.* 15 (2003) 486.
247 N. Chakroune, G. Viau, C. Ricolleau, F. F. Vincent, F. Fiévet, *J. Mater. Chem.* 13 (2003) 312.
248 J. Y. Piquemal, G. Viau, P. Beaunier, F. B. Verduraz, F. Fiévet, *Mater. Res. Bull.* 38 (2003) 389.
249 F. Bonet, K. T. Elhsissen, V. Vijayakrishnan, *Bull. Mater. Sci.* 23 (2000) 165.
250 F. Bonet, S. Grugeon, R. H. Urbina, K. T. Elhsissen, J. M. Tarascon, *Solid State Sci*. 4 (2002) 665.
251 S. Sun, C. B. Murray, D. Weller, L. Folks, A. Moser, *Science* 287 (2000) 1989.
252 P. Elumalai, H. N. Vasan, M. Verelst, P. Lecante, V. Carles, P. Tailhades, *Mater. Res. Bull*. 37 (2002) 353.
253 P. Elumalai, H. N. Vasan, N. Munichandraiah, S. A. Shivashankar, *J. Appl. Electrochem.* 32 (2002) 1005.
254 A. Miyazaki, L. Balint, K. Aika, Y. Nakano, *J. Catal.* 204 (2001) 364.
255 M. S. Hegde, D. Larcher, L. Dupont, B. Beaudouin, K. T. Elhsissen, J. M. Tarascon, *Solid State Ionics* 93 (1996) 33.
256 K. Nagaveni, A. Gayen, G. N. Subbanna, M. S. Hegde, *J. Mater. Chem.* 12 (2002) 3147.
257 P. B. Malla, P. Ravindranathan, S. Komarneni, E. Breval, R. Roy, *J. Mater. Chem.* 2 (1992) 559.
258 G. M. Chow, L. K. Kurihara, D. Ma, C. R. Feng, P. E. Schön, L. J. M. Miranda, *Appl. Phys. Lett.* 70 (1997) 2315.
259 L. J. M. Miranda, Y. Q. Li, G. M. Chow, L. K. Kurihara, *Nanostruct. Mater.* 12 (1999) 653.
260 J. Zhang, G. M. Chow, S. H. Lawrence, C. R. Feng, *Mater. Phys. Mech.* 1 (2000) 11.
261 G. M. Chow, J. Ding, J. Zhang, K. Y. Lee, D. Surani, S. H. Lawrence, *Appl. Phys. Lett.* 74 (1999) 1889.
262 J. Zhang, G. M. Chow, *J. Appl. Phys.* 88 (2000) 2125.
263 G. M. Chow, J. Zhang, Y. Y. Li, J. Ding, W. C. Goh, *Mat. Sci. Eng. A-Struct*. 304 (2001) 194.
264 G. M. Chow, J. Ding, J. Zhang, *J. Appl. Phys. Lett.* 80 (2002) 1028.

265 D. J. Blackwood, Y. Y. Li, G. M. Chow, *J. Electrochem. Soc.* 149 (2002) D27.
266 H. Yin, H. S. O. Chan, G. M. Chow, *Mater. Phys. Mech.* 4 (2001) 56.
267 H. Yin, G. M. Chow, *J. Electrochem. Soc.* 149 (2002) C68.
268 H. Yin, G. M. Chow, *J. Mater. Res.* S 18 (2003) 180.
269 G. Khelashvili, S. Behrens, C. Weidenthaler, C. Vetter, A. Hinsch, R. Kern, K. Skupien, E. Dinjus, H. Bönnemann, *Thin Solid Films*, 511 (2006) 342.
270 J. Chen, T. Herricks, Y. Xia, *Angew. Chem. Int. Ed.* 44 (2005) 2589.
271 T. C. Deivaraj, N. L. Lalla, J. Y. Lee, *J. Colloid Interface Sci.* 289 (2005) 402.
272 A. A. Umar, M. Oyama, *Cryst. Growth Des.* 6 (2006) 818.
273 M. Zhou, S. Chen, S. Zhao, *J. Phys. Chem. B* 110 (2006) 4510.
274 C. E. Hoppe, M. Lazzari, I. P. Blanco, M. A. L. Quintela, *Langmuir* 22 (2006) 7027.
275 J. Chen, T. Herricks, M. Geissler, Y. Xia, *J. Am. Chem. Soc.* 126 (2004) 10854.
276 E. Lee, J. Chen, Y. Yin, C. Campbell, Y. Xia, *Adv. Mater.* 18 (2006) 3271.
277 Y. Xiong, J. Chen, B. Wiley, Y. Xia, *J. Am. Chem. Soc.* 127 (2005) 7332.
278 B. Wiley, T. Herricks, Y. Sun, Y. Xia, *Nano Lett.* 4 (2004) 1733.
279 S. Sun, S. Anders, T. Thomson, J. E. E. Baglin, M. F. Toney, H. F. Hamann, C. B. Murray, B. D. Terris, *J. Phys. Chem. B* 107 (2003) 5419.
280 B. Jeyadevan, A. Hobo, K. Urakawa, C. N. Chinnasamy, K. Shinoda, K. Tohji, *J. Appl. Phys.* 93 (2003) 7575.
281 D. V. Talapin, E. V. Shevchenko, H. Weller, in G. Schmid (ed.), *Nanoparticles: From Theory to Application,* Wiley-VCH, Weinheim, 2004, 199.
282 K. E. Elkins, T. S. Vedantam, J. P. Liu, H. Zeng, S. Sun, Y. Ding, Z. L. Wang, *Nano Lett.* 3 (2003) 1647.
283 M. P. Pileni, *J. Phys. Chem.* 97 (1993) 6961.
284 M. P. Pileni, *J. Experimental Nanosci.* 1 (2006) 13.
285 T. C. Rojas, M. J. Sayagués, A. Caballero, Y. Koltypin, A. Gedanken, L. Posonnet, B. Vacher, J. M. Martin, A. Fernández, *J. Mater. Chem.* 10 (2000) 715.
286 A.-H. Lu, W.-C. Li, N. Matoussevitch, B. Spliethoff, H. Bönnemann, F. Schüth, *Chem. Commun.* (Cambridge) 47 (2005) 98.
287 H. Bönnemann, U. Endruschat, B. Tesche, A. Rufinska, C. W. Lehmann, F. E. Wagner, G. Filoti, V. Parvulescu, V. I. Parvulescu, *Eur. J. Inorg. Chem.* 12 (2000) 819.
288 Y. Liu, R. G. Finke, *J. Am. Chem. Soc.* 116 (1994) 8335.
289 Y. Liu, R. G. Finke, *Inorg. Chem.* 33 (1994) 4891.
290 T. Nagata, M. Pohl, H. Weiner, R. G. Finke, *Inorg. Chem.* 36 (1997) 1366.
291 J. D. Aiken III, R. G. Finke, *J. Am. Chem. Soc.* 120 (1998) 9545.
292 J. D. Aiken III, R. G. Finke, *Chem. Mater.* 11 (1999) 1035.
293 J. D. Aiken III, Y. Lin, R. G. Finke, *J. Mol. Catal. A: Chem.* 114 (1996) 29.
294 L. S. Otto, B. J. Hornstein, R. G. Finke, *Langmuir* 22 (2006) 9357.
295 M. A. Watzky, R. G. Finke, *Chem. Mater.* 9 (1997) 3083.
296 M. A. Watzky, R. G. Finke, *J. Am. Chem. Soc.* 119 (1997) 10382.
297 J. D. Aiken III, R. G. Finke, *J. Am. Chem. Soc.* 121 (1999) 8803.
298 S. Özkar, R. G. Finke, *Coord. Chem. Rev.* 248 (2004) 135.
299 C. Besson, E. E. Finney, R. G. Finke, *J. Am. Chem. Soc.* 127 (2005) 8179.
300 G. Wilke, *Angew. Chem. Int. Ed.* 42 (2003) 5000.
301 K. Ziegler, *Brennstoffchemie*, 35 (1954) 322.
302 H.Weyl, Methoden der organischen Chemie, in E. Müller (Hrsg.) *Band 13/4*, Thieme Verlag, Stuttgart, 1970, 41.
303 K. Fischer, K. Jonas, P. Misbach, R. Stabba, G. Wilke, *Angew. Chem.Int. Ed.* 85 (1973) 1002.
304 K. Ziegler, W.-R. Kroll, W. Larbig, O.-W. Steudel, *Liebigs Ann. Chem.* 629 (1960) 74.
305 C. Melches, Diploma Thesis, Essen, 1996.
306 C. Scholzen, Diploma Thesis, Essen, 1997.
307 H. Bönnemann, W. Brijoux, R. Brinkmann, U. Endruschat, W. Hofstadt, K. Angermund, *Rev. Roum. Chim.* 44 (1999) 1003.
308 H. Bönnemann, N. Waldöfner, H.-G. Haubold, T. Vad, *Chem. Mater.* 14 (2002) 1115.
309 T. Vad, H.-G. Haubold, N. Waldöfner, H. Bönnemann, *J. Appl. Cryst.* 35 (2002) 459.
310 Y. Takahashi, T. Ito, S. Sakai, Y. Ishii, *Chem. Commun.* 11 (1970) 1065.
311 C. Amiens, D. de Caro, B. Chaudret, J. S. Bradley, *J. Am. Chem. Soc.* 115 (1993) 11638.
312 D. deCaro, H. Wally, C. Amiens, B. Chaudret, *J. Chem. Soc. Chem. Commun.* 24 (1994) 1891.
313 A. Rodriguez, C. Amiens, B. Chaudret, M. J. Casanove, P. Lecante, J. S. Bradley, *Chem. Mater.* 8 (1996) 1978.
314 M. Bardaji, O. Vidoni, A. Rodriguez, C. Amiens, B. Chaudret, M. J. Casanove, P. Lecante, *New J. Chem.* 21 (1997) 1243.
315 J. S. Bradley, E. W. Hill, S. Behal, C. Klein, B. Chaudret, A. Duteil, *Chem. Mater.* 4 (1992) 1234.
316 A. Duteil, R. Queau, B. Chaudret, R. Mazel, C. Roucau, J. S. Bradley, *Chem. Mater.* 5 (1993) 341.
317 D. deCaro, V. Agelou, A. Duteil, B. Chaudret, R. Mazel, Ch. Roucau, J. S. Bradley, *New J. Chem.* 19 (1995) 1265.
318 F. Dassenoy, K. Philippot; T. O. Ely, C. Amiens, P. Lecante, E. Snoeck, A. Mosset, M. J. Casanove, B. Chaudret, *New J. Chem.* 19 (1998) 703.
319 J. Osuna, D. deCaro, C. Amiens, B. Chaudret, E. Snoeck, M. Respaud, J. M. Broto, A. Fert, *J. Phys. Chem.* 100 (1996) 14571.
320 T. O. Ely, C. Amiens, B. Chaudret, E. Snoeck, M. Verelst, M. Respaud, J. M. Broto, *Chem. Mater.* 11 (1999) 526.
321 J. S. Bradley, E. W. Hill, B. Chaudret, A. Duteil, *Langmuir* 11 (1995) 693.
322 F. Dassenoy, M. Casanove, P. Lecante, M. Verelst, E. Snoeck, A. Mosset, T. O. Ely, C. Amiens, B. Chaudret, *J. Chem. Phys.* 112 (2000) 8137.
323 M. Verelst, T. Ely, C. Amiens, E. Snoeck, P. Lecante, A. Mosset, M. Respaud, J. Broto, B. Chaudret, *Chem. Mater.* 11 (1999) 2702.
324 K. Soulantica, A. Maisonnat, M. Fromen, M. Casanove, P. Lecante, B. Chaudret, *Angew. Chem. Int. Ed.* 40 (2001) 448.
325 C. Nayral, E. Viala, P. Fau, F. Senocq, J. Jumas, A. Maisonnat, B. Chaudret, *Chem. Eur. J.* 6 (2000) 4082.
326 S. Gomez, K. Plilippot, V. Colliere, B. Chaudret, F. Senocq, P. Lecante, *Chem. Commun.* 19 (2000) 1945.
327 C. Pan, F. Dassenoy, M. J. Casanove, K. Philippot, C. Amiens, P. Lecante, A. Mosset, B. Chaudret, *J. Phys. Chem. B* 103 (1999) 10098.
328 K. Pelzer, O. Vidoni, K. Philippot, B. Chaudret, *Adv. Funct. Mater.* 13 (2003) 118.
329 K. Pelzer, K. Philippot, B. Chaudret, W. M. Zaika, G. Schmid, ZAAC, 629 (2003) 1217.
330 B. Chaudret, *C. R. Phys.* 6 (2005) 117.
331 B. Chaudret, in C. Coperet, B. Chaudret (eds.) *Surface and Interfacial Organometallic Chemistry and Catalysis: Topics in Organometallic Chemistry*, Springer, Verlag 16, 2005, 233.

332 T. O. Ely, C. Pan, C. Amiens, B. Chaudret, F. Dassenoy, P. Lecante, M. J. Casanove, A. Mosset, M. Respaud, J. M. Broto, *J. Phys. Chem. B*. 104 (2000) 695.
333 K. Philippot, B. Chaudret, *C. R. Chim.* 6 (2003) 1019.
334 C. Pan, K. Pelzer, K. Philippot, B. Chaudret, F. Dassenoy, P. Lecante, M.-J. Casanove, *J. Am. Chem. Soc.* 123 (2001) 7584.
335 T. Pery, K. Pelzer, J. Mathes, G. Buntkowski, K. Philippot, H.-H. Limbach, B. Chaudret, *Chem. Phys. Chem.* 6 (2005) 605.
336 V. Mévellec, A. Roucoux, E. Ramirez, K. Philippot, B. Chaudret, *Adv. Synth. Catal.* 346 (2004) 72.
337 S. Jansat, M. Go′mez, K. Philippot, G. Muller, E. Guiu, C. Claver, S. Castillo′n, B. Chaudret, *J. Am. Chem. Soc.* 126 (2004) 1592.
338 M. Gómez, K. Philippot, V. Collière, P. Lecante, G. Muller, B. Chaudret, *New J. Chem.* 27 (2003) 114.
339 K. Pelzer, K. Philippot, B. Chaudret, *Z. Phys. Chem.* 217 (2003) 1539.
340 S. Jansat, D. Picurelli, K. Pelzer, K. Philippot, M. Gomez, G. Muller, P. Lecante, B. Chaudret, *New J. Chem*. 30 (2006) 115.
341 D. Boxall, G. Deluga, E. Kenik, W. King, C. Lukehart, *Chem. Mater*. 13 (2001) 891.
342 S. Komarneni, D. Li, B. Newalkar, H. Katsuki, A. S. Bhalla, *Langmuir* 18 (2002) 5959.
343 K. E. Gonsalves, H. Li, R. Perez, P. Santiago, M. J. Yacaman, *Co-ord. Chem. Rev*. 206–207 (2000) 607.
344 A. Henglein, D. Meisel, *Langmuir* 14 (1998) 7392.
345 J. Belloni, M. Mostafavi, H. Remita, J. L. Marignier, M. O. Delcourt, *New J. Chem*. 22 (1998) 1239.
346 H. Bönnemann, W. Brijoux, R. Brinkmann, N. Matoussevitch, N. Waldöfner, PCT EP 2003/003814 (2003).
347 H. Bönnemann, W. Brijoux, R. Brinkmann, N. Matoussevitch, N. Waldöfner, *Magnetohydrodynamics* 39 (2003) 29.
348 H. Bönnemann, W. Brijoux, R. Brinkmann, N. Matoussevitch, N. Waldöfner, N. Palina, H. Modrow, *Inorg. Chim. Acta* 350 (2003) 617.
349 H. Bönnemann, W. Brijoux, R. Brinkmann, M. Feyer, W. Hofstadt, G. Khelashvili, N. Matoussevitch, K. S. Nagabhushana, *Strem Chemiker* 21 (2004) 1. (Avaliable at: www.strem.com)
350 S. Behrens, H. Bönnemann, N. Matoussevitch, E. Dinjus, H. Modrow, N. Palina, M. Frerichs, V. Kempter, W. Maus-Friedrichs, A. Heinemann, M. Kammel, A. Wiedenmann, *Z. Phys. Chem.* 220 (2005) 3.
351 X. Du, M. Inokuchi, N. Toshima, *Chem. Lett*. 35 (2006) 11.
352 A. Lu, W. Schmidt, N. Matoussevitch, B. Spliethoff, B. Tesche, E. Bill, W. Kiefer, F. Schüth, *Angew. Chem. Int. Ed.* 43 (2004) 4303.
353 D. Lawless, S. Kapoor, P. Kennepohl, D. Meisel, N. Serpone, *J. Phys. Chem. B* 98 (1994) 9619.
354 S. J. Oldenburg, R. D. Averitt, S. L. Westcott, N. J. Halas, *Chem. Phys. Lett*. 288 (1998) 243.
355 Z. J. Jiang, C. Y. Liu, *J. Phys. Chem. B* 107 (2003) 12411.
356 W. Wang, S. A. Asher, *J. Am. Chem. Soc*. 123 (2001) 12528.
357 D. Wang, V. S. Maceira, L. M. L. Marzan, F. Caruso, *Adv. Mater*. 14 (2002) 908.
358 H.-F. Lang, R. A. May, B. L. Iversen, B. D. Chandler, *J. Am. Chem. Soc.* 125 (2003) 14832.
359 V. Johanek, M. Laurin, J. Hoffmann, S. Schauermann, A. W. Grant, B. Kasemo, J. Libuda, H.-J. Freund, *Surf. Sci.* 561 (2004) L218.
360 K.-M. Choi, T. Akita, T. Mizugaki, K. Ebitani, K. Kaneda, *J. Am. Chem. Soc.* 126 (2004) 10657.
361 S. Bertarione, D. Scarano, A. Zecchina, V. Johanek, J. Hoffmann, S. Schauermann, J. Libuda, G. Rupprechter, H.-J. Freund, *J. Catal.* 123 (2004) 64.
362 L. Djakovitch, P. Rollet, *Adv. Synth. Catal.* 346 (2004) 1782.
363 H. Bönnemann, R. Brinkmann, P. Britz, U. Edruschat, R. Mörtel, U. A. Paulus, G. J. Feldmeyer, T. J. Schmidt, H. A. Gasteiger, R. J. Behm, *J. New Mater. Electrochem. Syst*. 3 (2000) 199.
364 U. A. Paulus, U. Endruschat, G. J. Feldmeyer, T. J. Schmidt, H. Bönnemann, R. J. Behm, *J. Catal.* 195 (2000) 383.
365 O. Alexeev, B. C. Gates, *Top. Catal.* 10 (2000) 273.
366 J. M. Lee, D. W. Kim, Y. H. Lee, S. G. Oh, *Chem. Lett*. 34 (2005) 928.
367 J. M. Lee, D. W. Kim, Y. D. Jun, S. G. Oh, *Mater. Res. Bull.* 41 (2006) 1407.
368 Y. M. Chung, H. K. Rhee, *J. Mol. Catal. A Chem.* 206 (2003) 291.
369 K. S. Nagabhushana, C. Weidenthaler, S. Hočevar, D. Strmčnik, M. Gaberšček, A. L. Antozzi, G. N. Martelli, *J. New Mater. Electrochem. Syst.* 9 (2006) 73.
370 T. S. Ahamadi, Z. I. Wang. T. C. Green, A. Henglein, M. A. El-Sayed, *Science* 272 (1996) 1924.
371 T. Herricks, J. Y. Chen, Y. N. Xia, *Nano Lett.* 4 (2004) 2367.
372 I. Lisiecki, *J. Phys. Chem. B* 109 (2005) 12231.
373 J. R. Health, *Acc. Chem. Res.* 32 (1999) 388.
374 H. A. Wicrenga, L. Soethout, I. W. Gerritsen, B. E. C. van do Leemput, H. van Kempen, G. Schmid, *Adv. Mater*. 2 (1990) 482.
375 H. Bönnemann, R. Richards, in W. A. Herrmann, G. Brauer (eds.) *Synthetic Methods of Organometallic and Inorganic Chemistry*, Vol. 10, Chapter 20, Thieme Verlag, Stuttgart, 2002, 209.
376 L. J. de Jongh, J. A. O. de Aguiar, H. B. Brom, G. Longoni, J. M. van Ruitenbeek, G. Schmid, H. H. A. Smit, M. P. J. van Staveren. R. C. Thiel, *Z. Phys. D, At., Mol. Clusters* 12 (1989) 445.
377 G. Schmid, V. Maihack, F. Lantermann, S. Peschel, *J. Chem. Soc., Dalton Trans.* 24 (1996) 589.
378 G. Schmid, H. West, J.-O. Malm, J.-O, Bovin, C. Grenthe, *Chem. Eur. J.* 2 (1996) 1099.
379 U. Simon, R. Flesch, H. Wiggers, G. Schön, G. Schmid, *J. Mater. Chem.* 8 (1998) 517.
380 G. Schmid, S. Emde, V. Maihack, W. Meyer-Zaika, S. Peschel, *J. Mol. Catal. A: Chem.* 107 (1996) 95.
381 J. B. Michel, J. T. Schwartz, in B. Delmon, P. Grange, P. A. Jacobs, G. Poncelet (eds.), *Catalyst Preparation Science IV,* Elsevier, New York, 1987, 669.
382 G. Schmid, H. West, H. Mehles, A. Lehnert, *Inorg. Chem*. 36 (1997) 891.
383 G. Schmid, V. Maihack, F. Lantermann, S. Peschel, *J. Chem. Soc., Dalton Trans*. 24 (1996) 591.
384 G. Schmid, B. Corain, *Eur. J. Inorg. Chem.* 24 (2003) 3093.
385 T. V. Choudary, D.-W. Goodman, *Top. Catal.* 21 (2002) 25.
386 M. Comotti, W.-C. Li, B. Spliethoff, F. Schüth, *J. Am. Chem. Soc*. 128 (2006) 917.
387 H. Bönnemann, R. M. Richards, *Eur. J. Inorg. Chem*. 10 (2001) 2455.
388 M. T. Reetz, S. A. Quaiser, R. Breinbauer, B. Tesche, *Angew. Chem. Int Ed.* 34 (1995) 2728.
389 H. Bönnemann, R. Brinkmann, P. Neiteler, *Appl. Organomet. Chem*. 8 (1994) 361.
390 M. Beller, H. Fischer, K. Kühlein, C.-P. Reisinger, W. A. Herrmann, *J. Organomet. Chem*. 520 (1996) 257.
391 M. T. Reetz, E. Westermann, *Angew. Chem. Int. Ed.* 39 (2000) 165.
392 M. T. Reetz, E. Westermann, R. Lohmer, G. Lohmer, *Tett. Lett.* 39 (1998) 8449.
393 A. H. M. de Vries, J. M. C. A. Mulders, J. H. W. Mommers, H. J. W. Henderckx, J. H. de Vries, *Org. Lett*. 5 (2003) 3285.

394 M. Fichtner, O. Fuhr, O. Kircher, J. Rothe, *Nanotechnology*, 14 (2003) 778.
395 B. Bogdanovic, M. Felderhoff, S. Kaskel, A. Pommerin, K. Schlichte, F. Schüth, *Adv. Mater*. 15 (2003) 1012.
396 H. Bönnemann, G. A. Braun, *Chem. Eur. J*. 3 (1997) 1200.
397 H. Bönnemann, G. A. Braun, *Angew. Chem. Int. Ed. Engl.* 35 (1996) 1992.
398 N. Toshima, T. Yonezawa, *Makromol. Chem. Macromol. Symp*. 59 (1992) 281.
399 T. Yonezawa, N. Toshima, *J. Mol. Catal*. 83 (1993) 167.
400 N. Toshima, T. Yonezawa and K. Kushihashi, *J. Chem. Soc., Faraday Trans.,* 89 (1993) 2537.
401 N. Toshima, Y. Wang, *Langmuir,* 10 (1994) 4574.
402 N. Toshima, in E. Pelizzetti (ed.), *Fine Particles Science and Technology*, Kluwer Academic Publishers, Dordrecht, The Netherlands, 1996, 371.
403 N. Toshima, *Supramol. Sci.* 5 (1998) 395.
404 V. Chechik, R. M. Crooks, *J. Am. Chem. Soc*. 122 (2000) 1243.
405 N. Toshima, in L. M. Liz-Marzán, P. V. Kamat (eds.), *Nanoscale Materials*, Chapter 3, Kluwer Academic Publishers, Dordrecht, The Netherlands, 2003.
406 N. Toshima, in N. Ueyama, A. Harada (eds.), *Macromolecular Nanostructured Materials*, Springer and Kodansha Scientific Ltd., Tokyo, 2004.
407 T. Teranishi, N. Toshima, in A. Woekowski, E. R. Savinova, C. G. Vayenas (eds.), *Catalysis and Electrocatalysis at Nanoparticle Surfaces*, Marcel Dekker, New York, 2003.
408 M. Antonietti, E. Wenz, L. Bronstein, M. Seregina, *Adv. Mater.* 7 (1995) 1000.
409 M. V. Seregina. L. M. Bronstein. O. A. Platonova, D. M. Chernyshov, P. M. Valetsky, J. Hartmann E. Wenz, M. Antonietti, *Chem. Mater*. 9 (1997) 923.
410 P. M. Arnal, M. Comotti, F. Schüth, *Angew. Chem. Int. Ed.* 43 (2006) 8224.
411 H. Bönnemann et. al., in preparation.
412 B. Zhou, L. K. Lee, US Patent 6168775 (2001).
413 B. Zhou, L. K. Lee, US Patent Application No10/401351 (2003).
414 B. Zhou, L. K. Lee, US Patent 6168775 (2005).
415 B. Zhou, R. M. Rueter, S. Parasher, US Patent 7001807 B2 (2006).
416 H. Schulz, *Appl. Catal. A: Gen.* 186 (1999) 3.
417 G. W. Olah, A. Goeppert, G. K. S. Prakash, *Beyond Oil and Gas: The Methanol Economy,* Wiley-VCH. Weinheim, 2006.
418 M. J. A. Tijmensen, *Biomass Bioenergy* 23 (2002) 129.
419 H. Schmieder, J. Abeln, N. Boukis, H. Dinjus, A. Kruse, M. Kluth, G. Petrich, E. Sadri, M. Schacht, *J. Supercrit. Fluids* 17 (2000) 145.
420 E. Dinjus, A. Kruse, *J. Phys. Condens. Matter* 16 (2004) 1161.
421 P. D'Jesus, C. Artiel, N. Boukis, B. K. Czarnetzko, E. Dinjus, *Ind. Eng. Chem. Res*. 44 (2005) 9071.
422 Y. Matsamura, T. Minowa, B. Potic, S. R. A. Kersten, W. Prins, W. P. M. van Swaaij, B. van de Beld, D. C. Elliott, G. G. Neuenschwander, A. Kruse, M. J. Antal Jr., *Biomass Bioenergy* 29 (2005) 269.
423 A. Kruse, E. Dinjus, *Z. Phys. Chem*. 3 (2005) 341.
424 M. Jacoby, *Chem. Eng. News*, June 5, 2006.
425 G. L. Bezemer, J. H. Bitter, H. P. C. E. Kuipers, H. Oosterbeek, J. E. Holewijn, X. Xu, F. Kapteijn, A. J. Van Dillen, K. P. De Jong, *J. Am. Chem. Soc*. 128 (2006) 3956.
426 M. Späth, P. M. Sommeling, J. A. M. van Roosmalen, H. J. P. Smit, N. P. G. van der Burg, D. R. Mahieu, N. J. Bakker, J. M. Kroon, *Prog. Photovolt. Res. Appl.* 11 (2003) 207.
427 M. Grätzel, *Nature*, 414 (2001) 338.
428 H. Bönnemann, G. Khelashvili, S. Behrens, A. Hinsch, K. Skupien, E. Dinjus, *J. Cluster Sci*., 18 (2007) 141.
429 G. Khelashvili, A. Hinsch, S. Behrens, W. Habicht, D. Schild, A. Eichhöfer, R. Sastrawan, K. Skupien, E. Dinjus, H. Bönnemann, *Thin Solid Films,* 515 (2007) 4074.
430 X. Du, M. Inokuchi, N. Toshima, *Chem. Lett*. 35 (2006) 1254.
431 S. Behrens, H. Bönnemann, N. Matoussevitch, A. Gorschinski, E. Dinjus, W. Habicht, J. Bolle, S. Zinoveva, N. Palina, J. Hormes, H. Modrow, S. Bahr, V. Kempter, *J. Phys. Condens. Matter* 18 (2006) 2543.
432 M. Tsoli, H. Kuhn, W. Brandau, H. Esche, G. Schmid, *Small* 1 (2005) 841.
433 O. Mykhalik, Institute of Experimental Oncology, University Hospital (LMU München), private communication, 2006.
434 W. Sauerwein, I. Heselmann, K. Olthoff, H. Sack, C. Fuhrmann, F. Steinberg, U. Becker, F. Zölzer, C. Streffer, *J. Electroanal. Chem.* 342 (1992) 347.
435 P. Bendel, W. Sauerwein, *Med. Phys*. 28 (2001) 1.
436 F. Basilico, W. Sauerwein, F. Pozzi, A. Wittig, R. Moss, L. Mauri, *J. Mass. Spectrom.* 40 (2005) 1546.
437 J.-S. Choi, Y.-W. Jun, S.-I. Yeon, H.-C. Kim, J.-S. Shin, J. Cheon, *J. Am. Chem. Soc.* 128 (2006) 15982.
438 H. Gu, K. Xu, B. Xu, *Chem. Commun.* 84 (2006) 941.
439 J.-H. Lee, Y.-W. Jun. S.-I. Yeon, J.-S. Shin, J. Cheon, *Angew. Chem. Int. Ed.* 118 (2006) 8340.
440 Ch. Zhang, B. Wängler, B. Morgenstern, H. Zentgraf, M. Eisenhut, H. Untenecker, R. Krüger, R. Huss, Ch. Seliger, W. Semmler, F. Kiessling, *Langmuir* 23 (2007) 1427.

CHAPTER 3

Recent Progress in Bimetallic Nanoparticles: Their Preparation, Structures and Functions

Naoki Toshima, Hu Yan,[#] and Yukihide Shiraishi

Department of Materials Science and Environmental Engineering, Tokyo University of Science, Yamaguchi, Japan

1. Introduction

Mono- or bimetallic nanoparticles have attracted a great interest in scientific research and industrial applications such as catalysis, owing to their unique large surface-to-volume ratios and quantum-size effects [1–3]. Since industrial catalysts usually work on the surface of metals, the metal nanoparticles, possessing much larger surface area per unit volume or weight of metal than the bulk metal, have been considered as promising materials for catalysis. From both the scientific and technological point of view, bimetallic nanoparticles composed of two different metal elements are more promising than monometallic nanoparticles, [4,5] because synergestic effect is expected. Bimetallic nanoparticles have shown novel catalytic behaviors based on the effect of second metal element added. This effect of the second metal element can be often explained in terms of an ensemble and/or a ligand effect in catalyses.

Herein we briefly mention historical aspects on preparation of monometallic or bimetallic nanoparticles as science. In 1857, Faraday prepared dispersion solution of Au colloids by chemical reduction of aqueous solution of Au(III) ions with phosphorous [6]. One hundred and thirty-one years later, in 1988, Thomas confirmed that the colloids were composed of Au nanoparticles with 3–30 nm in particle size by means of electron microscope [7]. In 1941, Rampino and Nord prepared colloidal dispersion of Pd by reduction with hydrogen, protected the colloids by addition of synthetic polymer like polyvinylalcohol, applied to the catalysts for the first time [8–10]. In 1951, Turkevich et al. [11] reported an important paper on preparation method of Au nanoparticles. They prepared aqueous dispersions of Au nanoparticles by reducing Au(III) with phosphorous or carbon monoxide (CO), and characterized the nanoparticles by electron microscopy. They also prepared Au nanoparticles with quite narrow size distribution and mean diameters in the range of 10–20 nm by citrate reduction of Au(III) in solution. After 1970 AuPd bimetallic nanoparticles with different microstructures, i.e., alloyed AuPd particles (ca. 25 nm), Pd-coated Au particles (Au/Pd) (ca. 22 nm), and Au-coated Pd particles (Pd/Au) (ca. 30 nm) were prepared by the simultaneous reduction of the corresponding metal salts in the presence of citrate or hydroxylamine as a reducing agent [12,13]. We prepared alcohol dispersions of noble metal nanoparticles by using alcohol as a reducing reagent. This preparation method was developed just in accident. Originally we were investigating on macromolecular metal complexes as models of artificial enzyme. For this purpose we used rhodium(III) chloride as an active center, and poly(L-glutamic acid) as a polymer ligand. In addition, ethanol was added to the aqueous mixtures to solubilize the polymer. The mixtures were treated by heat to complete the complex formation between Rh ions and poly(L-glutamic acid). Then, the color change was observed and the resulting brownish colored solution fortunately showed high catalytic activity for hydrogenization of olefin. This colored solution was later found to be a colloidal dispersion of Rh by TEM observation. Later we used poly(*N*-vinyl-2-pyrrolidone) (PVP) or polyvinylalcohol instead of poly(L-glutamic acid) as a protecting polymer. In fact, PVP was proved to be a useful protecting polymer. It can protect almost all kinds of nanoparticles in various systems. We would like to call PVP "a magic polymer". This alcohol reduction in the presence of PVP can be applied to prepare various kinds of colloidal dispersions in alcohol of noble metal nanoparticles [2,4,5,14]. The smallest Rh particles observed had the size of 0.7 nm in diameter, corresponding to a cluster of 13 atoms. They were used as catalysts for hydrogenation of olefins without precipitation. The alcohol reduction method was also applied to prepare bimetallic nanoparticles by simultaneous reduction of two metal ions [15,16]. The bimetallic structures were first clearly proposed by the technique of extended X-ray absorption fine structure (EXAFS) [16]. Sinfelt and co-workers

[#] Present address: Interdisciplinary Graduate School of Medicine and Engineering, University of Yamanashi, Kofu, Japan

Metal Nanoclusters in Catalysis and Materials Science: The Issue of Size Control
Edited by B. Corain, G. Schmid and N. Toshima

extensively studied on the catalysis of bimetallic nanoparticles [17–21]. The bimetallic nanoparticles have already been used as effective catalysts for the hydrogenation of olefins and carbon-skeleton rearrangement of hydrocarbons, thanks to their efforts. The alloy structure can be carefully examined to understand their catalytic properties. Catalysis of supported metal nanoparticles has been studied for many years and is practically important, but they are not the aims of this review.

The preparations of metal nanoparticles could be classified into two categories: physical and chemical techniques. Evaporation [22–25] or laser ablation [26–29] of metal bulk is utilized to prepare nanoparticles in the physical methods, while reduction of metal ions to neutral atoms, followed by particle growth is the common strategy in chemical methods, which are subdivided into conventional chemical (one- or two-phase systems) [30–36], photochemical [37,38], sonochemical [39,40], electrochemical [41,42], and radiolytic reductions [43,44]. Generally, the chemical methods have the advantage to be able to easily control the primary structures of nanoparticles, such as size, shape, and composition as well as to realize mass production. Such methods for monometallic nanoparticles can be applied to the preparation of bimetallic nanoparticles. The preparations of bimetallic nanoparticles by chemical methods could be usually classified into two categories: simultaneous reduction (or co-reduction) and successive reduction (or decompositions, or first nanoparticle-seeded reduction) approaches for two kinds of metal salts. These approaches often give the different size and structure such as alloy or core/shell to the resulting bimetallic nanoparticles. Various typical structure models of bimetallic nanoparticles are shown in Figure 1.

The precise control of size, its distribution, shape, composition, and crystal structure of bimetallic nanoparticles is crucial in this field. Some strategies to prepare bimetallic nanoparticles were proposed and subsequently the corresponding methods were developed for the purpose of controlled nanoparticles. These methods enable us to find novel chemical and physical properties of bimetallic nanoparticles depending on their structures.

Usually bimetallic nanoparticles as well as monometallic ones are characterized by many probing tools such as UV–visible (UV–Vis) spectroscopy, transmission electron microscopy (TEM), X-ray diffraction (XRD), X-ray photoelectron spectroscopy (XPS), EXAFS, infrared spectroscopy of adsorbed CO (CO-IR), and so on [1,2].

Bimetallic nanoparticles show many interesting functions. The bimetallic nanoparticles are emerging catalysts because of their high surface-to-volume ratios and their novel catalytic behavior caused by the second metal element. Bimetallic nanoparticles were also extensively investigated on ferromagnetic properties since they are expectable memory materials. Such bimetallic nanoparticles usually contain 3d-transition metal, such as Fe, Co, and Ni, as one component element. Recently we demonstrated that the mono- or bimetallic nanoparticles could change or improve electro-optical responsibility of liquid crystal displays (LCDs) [45].

Before 2002 we have previously reviewed on bimetallic nanoparticles and their catalytic properties [5,46,47]. Herein we concentrate on recent researches on the bimetallic nanoparticles from 2003, but also include some important researches previously reviewed by us [5,46,47].

2. Preparation Methods of Bimetallic Nanoparticles

The synthesis of bimetallic nanoparticles is mainly divided into two methods, i.e., chemical and physical method, or ''bottom-up'' and ''top-down'' method. The chemical method involves (1) simultaneous or co-reduction, (2) successive or two-stepped reduction of two kinds of metal ions, and (3) ''self-organization'' of bimetallic nanoparticle by physically mixing two kinds of already-prepared monometallic nanoparticles with or without after-treatments. Bimetallic nanoparticle alloys are prepared usually by the simultaneous reduction while bimetallic nanoparticles with core/shell structures are prepared usually by the successive reduction. In the preparation of bimetallic nanoparticles, one of the most interesting aspects is a core/shell structure. The surface element plays an important role in the functions of metal nanoparticles like catalytic and optical properties, but these properties can be tuned by addition of the second element which may be located on the surface or in the center of the particles adjacent to the surface element. So, we would like to use following marks to inscribe the bimetallic nanoparticles composed of metal 1, M_1 and metal 2, M_2.

M_1M_2 – All kinds of bimetallic nanoparticles including random alloy nanoparticles. In this case M_1 and M_2 should be arranged in an alphabetical order.
M_1/M_2 – Core/shell type structure, more precisely M_1-core/M_2-shell structure.

Main researches on the preparation of the bimetallic nanoparticles were summarized in Table 1a and b.

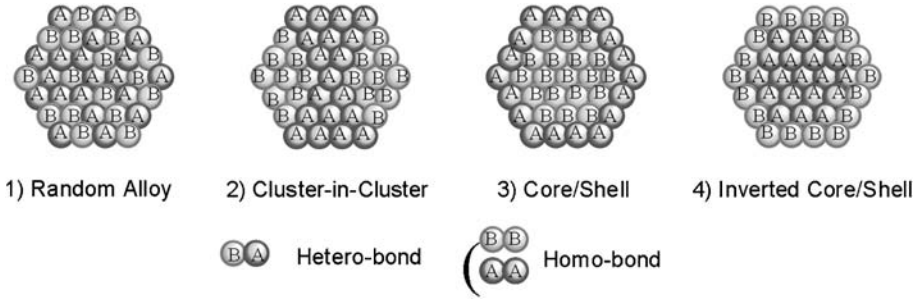

Figure 1. Various structure models of bimetallic nanoparticles.

Table 1. Typical preparations and characterizations of bimetallic nanoparticles reported in literatures.

Metals	Structure	Particle size	Precursors	Protecting agent	Reducing agent	Analysis	Literatures
(a) Simultaneous reduction							
Pt/Pd	–	ca. 1.5 nm	Pd(II), Pt(IV)	PVP	Alcohol	UV–Vis, TEM, EXAFS	[15,16,48]
PtRu	Alloys	ca. 1.1 nm	$Pt(dba)_2$, Ru(COD)(COT)	PVP	H_2	HRTEM	[62]
Ag/Pd	Alloy or core/shell	1–4 nm	Ag(I), Pd(II)	PVP	Acetone/2-porpanol	UV–Vis	[63]
AgHg	Alloy	–	Ag(I), Hg(I)	Poly(ethyleneimine)	$NaBH_4$	UV–Vis	[64]
Pt/Ru	–	–	Pt(IV), Ru(II)	–	$NOct_4(BHEt_3)$	–	[65–67]
Au/Pd	–	–	Au(III), Pd(II)	–	Sonochemical	–	[68,69]
Pt/Pd	–	–	Pt(II), Pd(II)	Dendrimer	$NaBH_4$	–	[70]
Pd/Au	Alloy or core/shell	22–30 nm	Metal salts	–	Citrate or hydroxylamine	–	[12,13]
AuPt	Alloy	–	Metal salts	–	–	UV–Vis, TEM	[50,51]
Pd/Ru	–	–	Metal salts	PVP	$NaBH_4$	–	[61]
AgAu	Alloy	ca. 4 nm	–	Dodecanethiol	–	UV–Vis	[33]
AuPt	Alloy	ca. 2.5 nm	–	Dodecanethiol	–	–	[58]
CuPd	Alloy	<2 nm	Cu(II), Pd(II)	PVP	Glycol	XPS, Raman	[71–73,75]
NiPd	Alloy	ca.1.9 nm	Ni(II), Pd(II)	PVP	Glycol	TEM, XRD, EXAFS	[76–78]
Co/Pt	–	<2 nm	Co(0), Pt(III)	PVP	H_2	XRD	[81]
Au/Pd	Core/shell	ca. 15 nm	Au(III), Pd(II)	–	Ethylene glycol	HRTEM, XRD, XPS	[118]
Au/Pd	Core/shell	ca. 6 nm	Au(III), Pd(II)	*N*,*N*-Dimethyldodecylamine	$NaBH_4$	UV–Vis, TEM, XRD	[119]
Au/Ag	Core/shell	–	Au(III), Ag(I)	Neem leaf broth	–	TEM	[120]
Au/Ag	Core/shell	ca. 10 nm	–	Fractose	–	UV–Vis	[121]
Pt/Au	Core/shell	ca. 3 nm	Pt(IV), Au(III)	PVP	Ethylene glycol	UV–Vis, TEM, EXAFS	[122]
Au/Pt	Core/shell	–	Au(III), Pt(IV)	Trisodium citrate	Tannic acid	UV–Vis, TEM, EXAFS	[123]
Ag/Au	Core/shell	ca. 17 nm	Au(III), Ag(I)	Trisodium citrate	$NaBH_4$	UV–Vis, HRTEM, EXAFS	[124]
Au/Pt	Core/shell	ca. 1.5 nm	Au(III), Pt(IV)	PVP	Alcohol	UV–Vis, TEM	[53]
Au/Pd	Core/shell	ca. 1.9 nm	Au(III), Pd(II)	PVP	Alcohol	UV–Vis, TEM	[52]
Pd/Rh	Core/shell	ca. 2 nm	Pd(II), Rh(III)	PVP	Alcohol	UV–Vis, TEM	[54,55]
Pt/Rh	Core/shell	ca. 2 nm	Pt(IV), Rh(III)	PVP	Alcohol	UV–Vis, TEM, EXAFS	[56]
(b) Successive reduction							
AuPd	Cluster-in-cluster	–	Au-NP, Pd(II)	PVP	Alcohol	TEM, EXAFS	[125]
Pd/Ni	Core/shell	–	–	PVP	Alcohol	–	[126]
Au/M_2[a]	Core/shell	ca. 28 nm	Au-NP, Pt(IV) Pd(II)	*p*-H_2-C_6-H_4SO_3Na	H_3NOHCL	Micro-EDX	[127–130]
Pd/Ag	Core/shell	–	Pd-NP, Ag(I)	–	Formaldehyde	UV–Vis	[131]
Pd/Pt	Core/shell	1.5–5.5 nm	Pd-NP-H_2, PT(IV)	Polymer	H_2	CO-IR	[132]
Pt/Pd	Core/shell	1.5–5.5 nm	Pt-NP-H_2, Pd(II)	Polymer	H_2	CO-IR	[132]
Au/Ag	Core/shell	–	Au-NP, Ag(I)	Octadecylamine	Tyrosine	–	[133]
Ag/Au	Core/shell	ca. 10 nm	Ag-NP, Au(III)	–	γ-Radiation	UV–Vis, HRTEM	[153]
Au/Ag	Core/shell	1–3 nm	Au-NP, Ag(I)	Dendrimer	$NaBH_4$	UV–Vis, TEM	[134]
Au/Ag	Core/shell	–	Au-NP, Ag(I)	PVP	MW/polyol	–	[135]
Ag/Au	Core/shell	–	Ag-NP, Au(III)	–	R-NHOHHC1	TEM, XPS, SERS	[136]
Ag/Au	Core/shell	–	Ag-NP, Au(III)	PVP	Ag-NP	UV–Vis, TEM	[137, 138]
Ag/Au	Core/shell	–	Ag-NP, Au(III)	–	–	TEM, SERS	[139]
Ag/Pt	Core/shell	ca. 15 nm	Ag-NP, Pt(IV)?	Citrate ion	Sodium citrate	UV–Vis, TEM, XPS	[140]
Pt/Ru	Core/shell	ca. 5 nm	Pt(II), Ru(III)	PVP	Sonochemical	TEM	[141]
AgPd	Alloy	–	Ag(I), Pd(II)	Stearate ion	Stearic acid	UV–Vis, TEM, XRD	[142]
Au/Pd	Core/shell	–	Pd-NP, Au(III)	–	Ethylene glycol	UV–Vis	[143]
Pd/Au	Core/shell	–	Pd-NP-H_2, Au(III)	PVP	Ethanol	CO-IR, UV–Vis, TEM	[144]
Co/M_2[b]	Core/shell	4.4–6.6 nm	Co-NP, M_2 ion	–	–	HRTEM, EXAFS	[145]

[a]M_2: Pt, Pd; [b]M_2: Au, Pd, Pt, Cu

Precise control of the primary structures of metallic nanoparticles, such as size, shape, crystal structure, and composition, is crucially important for preparation of the bimetallic nanoparticles because the structures dominate the physical and chemical properties of metal nanoparticles. The particle sizes of the metal nanoparticles strongly depend on protective ability of polymer or low molecular weight ligand used as a protecting agent. The protective ability of polymer in an aqueous solution can be expressed quantatively in terms of "gold number" or "protective value" [4] and R [15,16,48,49]. The "gold number" is defined as the amount of the protective colloid in milligrams which just prevents 10 cm^3 of a red gold sol from changing color to violet on addition of 1 cm^3 of a 10% aqueous solution of NaCl. The smaller the gold number, the stronger is the protective ability of the polymer. In contrast, the "protective value" is defined as the weight of a red gold sol in grams which can just be protected from aggregation by 1 g of the protective colloid on addition of a 1% NaCl solution. In this case, the larger the protective value, the greater is the protective ability. On the other hand, R is defined as the mole ratio of a certain polymer (a repeat unit) or a ligand to a metal. Usually the protective ability is stronger with increasing in the R.

From the viewpoint of size control, bimetallic systems are usually very convenient to produce monodispersed metal nanoparticles [49]. Although the exact reason is not clear yet, this is probably attributed to the redox equilibrium between the two elements.

2.1. Simultaneous or Co-Reduction

Miner et al. [50] prepared monodispersed AuPt and PdPt alloys by simultaneous reduction of the corresponding salt mixtures at various molar ratios. They confirmed that AuPt alloys are formed at any atomic ratio, even if the two metals show a broad miscibility gap between 2 and 85 wt% Au [51]. The homogeneous character of the various AuPt alloys was proven by means of optical spectra, sedimentation measurements, and electron microscopy.

Noble metal ions can be easily reduced to the corresponding zero-valent metal atoms. Therefore, bimetallic nanoparticles consisting of two different noble metals have been extensively investigated for purpose of novel catalysts and optical materials. A simultaneous reduction of two noble metal ions with alcohol is a simple and useful technique to prepare bimetallic nanoparticles. The alcohol reduction of metal ions M_1^{n+} is followed by Equation (1).

$$M_1^{n+} + \frac{n}{2}C_2H_5OH \rightarrow M_1 + \frac{n}{2}CH_3CHO + nH^+ \qquad (1)$$

Pt/Pd bimetallic nanoparticles can be prepared by refluxing the alcohol/water (1:1, v/v) solution of palladium(II) chloride and hexachloroplatinic(IV) acid in the presence of poly(N-vinyl-2-pyrrolidone) (PVP) at ca. 95 °C for 1 h [15,16,48]. The resulting Pd/Pt nanoparticles have a Pt-core/Pd-shell structure with a narrow size distribution and the dispersion is stable against aggregation for several years. The core/shell structure was confirmed by the technique of EAXFS. Composition of Pt/Pd nanoparticles can be controlled by the initially feed amount of two different metal ions, i.e., in this case one can obtain Pt/Pd nanoparticles of Pt/Pd molar ratios from 1/0 to 0/1. Particle sizes of the nanoparticles can also be controlled by the amount of protective polymer, PVP, i.e., PVP/metal molar ratio (R). When Pt/Pd nanoparticles were prepared in the presence of 40-fold PVP to metal ions, i.e., $R = 40$, ca. 1.5 nm nanoparticles were produced [15,16,48], while nanoparticles of ca. 2.5 nm in size were obtained when R is 1 [49]. Similarly Au/Pd [52], Au/Pt [53], Pd/Rh [54,55], and Pt/Rh [56] bimetallic nanoparticles can be prepared. This alcohol reduction method has an advantage that alcohol (usually ethanol) is used both as a solvent and a reducing agent. After the reaction the corresponding aldehyde is produced (usually acetaldehyde), which is easily removed by distillation.

Formation mechanism of the core/shell structure by simultaneous alcohol reduction of two components of noble metal ions M_1^+ and M_2^+ (superscript "$^+$" means cationic species) in the presence of PVP has been proposed as follows (Figure 2): at first both metal ions M_1^+ and M_2^+ can coordinate to PVP (step a). Then one of the metal ions M_1^+ having a higher redox potential can be reduced at first (step b). At this stage another metal ion M_2^+ having a lower redox potential than M_1^+ still remains as an ion. The next step can be divided into two ways. In one path M_2^+ ion can also be reduced to form atom M_2 (step c). At this stage both M_1 and M_2 exist as atoms. Then M_1 atoms aggregate to form a M_1 nanocluster (step d), probably because the coordinate bond between M_1 and PVP is weaker than that between M_2 and PVP. In another path M_1 atoms coagulate to form an M_1 nanocluster while M_2^+ ions exist as ions (step e). Then M_2^+ ions, which coordinate to PVP protecting M_1 nanoclusters, can be reduced to form M_2 atoms (step f). Thus, the M_1 nanoclusters protected by PVP having M_2 atoms can be produced by two paths. At the last step, M_2 atoms can deposit on seed M_1 nanoclusters to form M_1-core/M_2-shell bimetallic nanoparticles (step g). Thus, the core/shell structure can be controlled by the difference of redox potential of M_1^+ and M_2^+, and coordination ability of M_1 and M_2 atoms onto PVP.

An attractive preparation method of alkanethiol-protected Au nanoparticles using a two-phase (toluene/water) reaction with a phase transfer catalyst was reported by Brust and co-workers [31]. The strategy of their method consists of growing the metal nanoparticles with the simultaneous attachment of self-assembled ligand-monolayers on the growing nuclei. In order to make the surface reaction take place during metal nucleation and growth, nanoparticles are grown in a two-phase system. In the method, $AuCl_4^-$ is transferred from aqueous solution to toluene by using tetraoctylammonium bromide as the phase-transfer reagent and reduced with aqueous sodium borohydride in the presence of a long-chain thiol as a protective agent. By the two-phase reaction, Hostetler et al. [57] synthesized Au-based Ag, Pt, Pd, and Cu alloy bimetallic nanoparticles protected by dodecanethiol or didodecyl disulfide, whose thermal, optical, and electronic properties can be systematically altered. Han et al. [33] also prepared dodecanethiol-protected AgAu alloy bimetallic nanoparticles with an average size of ca. 4 nm by a two-phase synthetic route in water/toluene mixture. The position of the surface plasmon band changed linearly between 419 and 522 nm as a function of mole fraction of

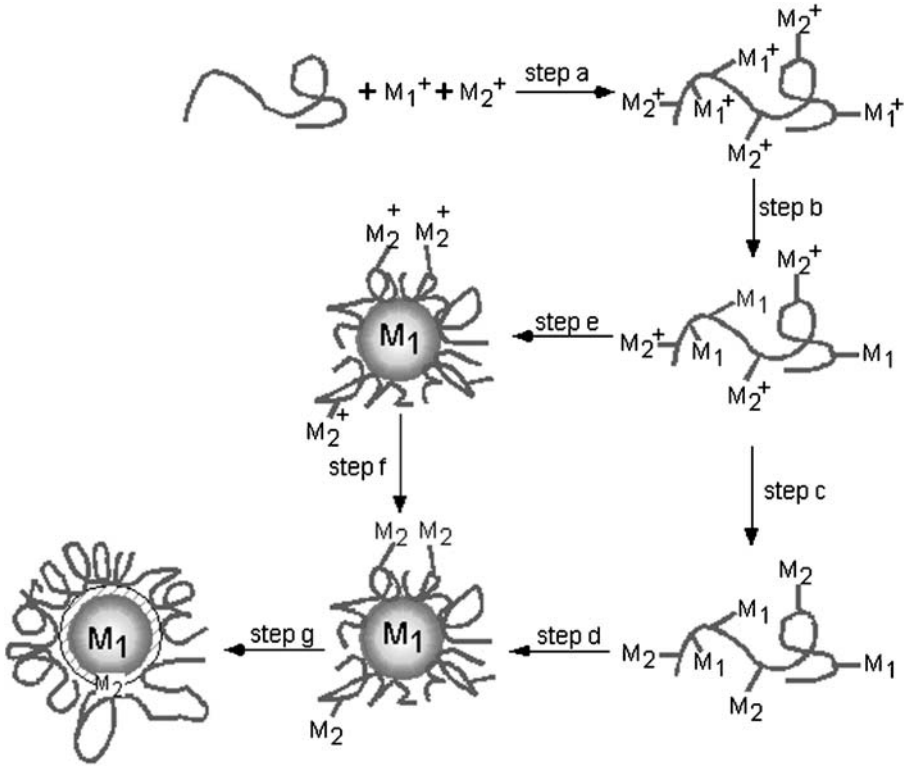

Figure 2. Formation mechanism of M1-core/M2-shell structured bimetallic nanoparticles.

Au (or Ag) content. Decanethiol-protected AuPt alloy bimetallic nanoparticles of ca. 2.5 nm in particle size were similarly prepared [58]. The preparations of PdPt [59] and AuPd [60] bimetallic nanoparticles in water-in-oil (w/o) microemulsions can be realized in two-phase reaction system, in which a surfactant molecule itself works as a protecting agent in these cases.

Liu and co-workers prepared PtRu and PdRu bimetallic nanoparticles by using $NaBH_4$ and PVP as reducing and protective agents, respectively, in solution of the corresponding two kinds of metal salts at room temperature [61]. The bimetallic nanoparticles were more stable than the PVP-protected Ru monometallic nanoparticles. Chaudret and co-workers reported a preparation method which involves reduction of $Pt(dba)_2$ (dba=dibenzylidene acetone) and Ru(COD)(COT) in various molar ratios under H_2 in the presence of PVP that led to the formation of PtRu bimetallic nanoparticles of definite compositions resulting from the relative concentration of the two complexes in the initial solution [62]. The progressive addition of ruthenium into the platinum matrix resulted in structural changes from face-centered cubic (fcc) for high platinum contents to hexagonal close-packed (hcp) for high ruthenium contents. Esumi et al. [63] also prepared AgPd alloy bimetallic nanoparticles by UV photolysis (253.7 nm) of silver perchlorate and palladium acetate in mixture solutions of acetone/2-propanol in the presence of PVP. The AgPd nanoparticles with average size of ca. 1–4 nm shows the sharp optical absorption bands, which shift to longer wavelengths with increasing in molar ratio of silver. Henglein and Brancewicz [64] prepared AgHg bimetallic nanoparticles by the simultaneous reduction of corresponding ions with $NaBH_4$ in the presence of poly(ethyleneimine) as a stabilizer. The nanoparticles have an alloy structure, whose plasmon absorption band is blue-shifted with increasing in Hg/Ag molar ratio. The AgHg nanoparticle alloy is stable up to the Hg/Ag molar ratio of 2:1.

Other one-pot preparations of bimetallic nanoparticles include $NOct_4(BHEt_3)$ reduction of platinum and ruthenium chlorides to provide $Pt_{0.5}Ru_{0.5}$ nanoparticles by Bönnemann et al. [65–67] sonochemical reduction of gold and palladium ions to provide AuPd nanoparticles by Mizukoshi et al. [68,69] and $NaBH_4$ reduction of dendrimer$-PtCl_4^{2-}$ and $-PtCl_4^{2-}$ complexes to provide dendrimer-stabilized PdPt nanoparticles by Crooks et al. [70].

Late transition metal or 3d-transition metal irons, such as cobalt, nickel, and copper, are important for catalysis, magnetism, and optics. Reduction of 3d-transition metal ions to zero-valent metals is quite difficult because of their lower redox potentials than those of noble metal ions. A production of bimetallic nanoparticles between 3d-transition metal and noble metal, however, is not so difficult. In 1993, we successfully established a new preparation method of PVP-protected CuPd bimetallic nanoparticles [71–73]. In this method, bimetallic hydroxide colloid forms in the first step by adjusting the pH value with a sodium hydroxide solution before the reduction process, which is designed to overcome the problems caused by the difference in redox potentials. Then, the bimetallic species

are completely reduced by a polyol process [74], resulting in CuPd bimetallic nanoparticles. One can utilize this method for the formation of Cu monometallic nanoparticles, but the size of Cu nanoparticles become larger than 100 nm, while that of CuPd bimetallic nanoparticles is smaller than 2 nm, indicating the formation of bimetallic nanoparticles. Auger and XPS spectroscopies proved Cu^0 species in CuPd nanoparticles. This polyol method could be applied to the preparation of Cu-rich CuPd nanoparticles [75]. PVP-protected NiPd bimetallic nanoparticles could be also prepared by using nickel sulfate and palladium(II) acetate as precursors [76–78].

Nearly monodispersed CuPd bimetallic nanoparticles were prepared by thermal decomposition of mixtures of the corresponding acetates in high boiling solvents such as bromobenzene, xylenes, and methyl-*iso*-butyl ketone in the absence of stabilizers [79]. The resulting bimetallic nanoparticles often contained CuO in addition to the zero-valent metals. Smaller particle sizes and narrower size distributions without oxide formation in 2-ethoxyethanol in the presence of PVP were reported by Bradley et al. [80]. In this method, only CuPd bimetallic nanoparticles containing less than 50 mol% of copper can be formed. The reduction of $Co(\eta^3\text{-}C_8H_{13})(\eta^4\text{-}C_8H_{12})$ and $Pt_2(dba)_3$ under H_2 in the presence of PVP can provide CoPt bimetallic nanoparticles smaller than 2 nm [81]. In this case, platinum-rich particles adopt an fcc crystalline structure while cobalt-rich particles adopt a non periodic polytetraedral arrangement.

Recently many researches on preparations of AgAu [82–92,120,121,124], AuPt [92–96,122,123], AuPd [92,96–98,118,119], AuCu [84,99], AuSe [100], AgPd [97,101,102], AgPt [103], PtRu [104–106], NiPt [107–110], PdPt [96,111], CuPt [112], PdRh [113], FeRu [114], FePt [114], FeNi [115], CuNi [116], BiNi [117] nanoparticle alloys or cluster-in-cluster structures by simultaneous reduction were reported, as summarized in Table 1a and b.

Au-based bimetallic core/shell nanoparticles can also be prepared by the simultaneous reduction. Harpeness and Gedanken [118] prepared core/shell Au/Pd bimetallic nanoparticles by the simultaneous reduction of the Au(III) and Pd(II) ions. This is a microwave (MW)-assisted polyol reduction method. The thickness of the Pd shell was calculated to be ca. 3 nm, and the Au core diameter is 9 nm. The structure and composition of the bimetallic particles were characterized by high-resolution TEM equipped with a nanoarea energy-dispersive X-ray spectroscopy attachment, TEM, XRD, and XPS. Nath et al. [119] reported a convenient route for preparation of Au-core/Pd-shell bimetallic nanoparticles by co-reduction of Au(III) and Pd(II) precursors in toluene. *N*,*N*-Dimethyldodecylamine was used as a protecting agent for the core/shell particles, which not only imparts stability to the organosol but also controls morphology of the evolved particles. The particles were characterized using UV–Vis, TEM, and XRD measurements. All results substantiate the formation of core/shell structure of the nanoparticles.

Shanker et al. [120] prepared bimetallic Au-core/Ag-shell nanoparticles by the simultaneous reduction of Au(III) and Ag(I) ions in the presence of neem (*Azadirachta indica*) leaf broth as an extracting agent. Competitive reduction of Au(III) and Ag(I) ions occurs simultaneously in solution during exposure to neem leaf extract leads to the preparation of bimetallic Au-core/Ag-shell nanoparticles in solution. TEM revealed that the silver nanoparticles are adsorbed onto the gold nanoparticles, forming a core/shell structure. Panigrahi et al. [121] reported that sugar-assisted stable Au-core/Ag-shell nanoparticles with particles size of ca. 10 nm were prepared by a wet chemical method. Fructose was found to be the best suited sugar for the preparation of smallest particles.

AuPt bimetallic nanoparticles can be prepared by the polyol method and stabilized with poly(*N*-vinyl-2-pyrrolidone) (PVP) [122]. Interesting structure changes were observed in the nanoparticles as the reaction temperature was varied. At lower temperatures no bimetallic nanoparticles were detected, while as the temperature increased bimetallic nanoparticles started to appear, commonly obtaining core/shell nanoparticles. The core/shell structure was preliminarily confirmed by the optical response of the system in the UV–Vis region. An absorption peak centered at 520 nm was observed at low temperatures (100–110 °C); at higher temperatures (130–170 °C) there were non detectable absorption peaks, and finally at the two highest temperatures (180–190 °C) the reappearance of an absorption feature centered at 510 nm was noticed. Based on the results of the UV–Vis spectroscopic, TEM, high-angle annular dark field (HAADF), X-ray absorption near-edge structure (XANES), and EXAFS studies the nanoparticles had Pt-core/Au-shell structure with the elements segregated from each other. Chen et al. [123] examined the amount-dependent change in morphology for a series of AuPt bimetallic nanoparticles prepared using chemical reduction. The Au:Pt molar ratio was varied from 1:1 to 1:4 to prepare Pt shell layers with different thicknesses. The EXAFS results supported the formation of a core/shell structure and inter-diffusion between Au and Pt atoms. The composition of the shell layer, however, was found to be Pt-enriched AuPt alloy.

Ag-core/Au-shell bimetallic nanoparticles were prepared by $NaBH_4$ reduction method [124]. UV–Vis spectra were recorded and compared with various ratios of AuAg alloy nanoparticles. The UV–Vis spectra of bimetallic nanoparticles suggested the formation of core/shell structure. Furthermore, the high-resolution transmission electron microscopy (HRTEM) image of the nanoparticles confirmed the core/shell type configuration directly.

In summary the simultaneous reduction method usually provides alloyed bimetallic nanoparticles or mixtures of two kinds of monometallic nanoparticles. The bimetallic nanoparticles with core/shell structure also form in the simultaneous reduction when the reduction is carried out under mild conditions. In these cases, however, there is difference in redox potentials between the two kinds of metals. Usually the metal with higher redox potential is first reduced to form core part of the bimetallic nanoparticles, and then the metal with lower redox potential is reduced to form shell part on the core, as shown in Figure 2. The coordination ability may play a role in some extent to form a core/shell structure. Therefore, the simultaneous reduction method cannot provide bimetallic nanoparticles with so-called ''inverted'' core/shell structure in which the metal of the core has lower redox potential.

2.2. Successive or Two-Step Reduction

Successive reduction (or two-step reduction) involves the reduction of first metal ions, followed by the reduction of second metal ions. The second metals are usually deposited on the surface of the first metals due to the formation of the strong metallic bond, resulting in core/shell structured bimetallic nanoparticles.

Our first attempt of a successive reduction method was utilized to PVP-protected Au/Pd bimetallic nanoparticles [125]. An alcohol reduction of Pd ions in the presence of Au nanoparticles did not provide the bimetallic nanoparticles but the mixtures of distinct Au and Pd monometallic nanoparticles, while an alcohol reduction of Au ions in the presence of Pd nanoparticles can provide AuPd bimetallic nanoparticles. Unexpectedly, these bimetallic nanoparticles did not have a core/shell structure, which was obtained from a simultaneous reduction of the corresponding two metal ions. This difference in the structure may be derived from the redox potentials of Pd and Au ions. When Au ions are added in the solution of enough small Pd nanoparticles, some Pd atoms on the particles reduce the Au ions to Au atoms. The oxidized Pd ions are then reduced again by an alcohol to deposit on the particles. This process may form with the particles a cluster-in-cluster structure, and does not produce Pd-core/Au-shell bimetallic nanoparticles. On the other hand, the formation of PVP-protected Pd-core/Ni-shell bimetallic nanoparticles proceeded by a successive alcohol reduction [126].

Schmid and co-workers [127–129] successfully prepared ligand-stabilized Au-core/Pt- or Pd-shell bimetallic nanoparticles by a successive reduction. Core of Au nanoparticles with a diameter of 18 nm [11,130] can be covered by Pt or Pd shells, when an aqueous solution of H_2PtCl_6 or H_2PdCl_4 was reduced with H_3NOHCl in the presence of Au nanoparticles. The core/shell nanoparticles were stabilized by water-soluble *p*-$H_2NC_6H_4SO_3Na$. The original red color of the Au nanoparticles then changes to brown-black, which indicates the formation of Pt- or Pd-shell on the surface of Au nanoparticles. In the case of Au/Pt nanoparticles a Au core was surrounded by Pt shell of about 5 nm in thickness, while a Au core was covered by the shell of well-ordered Pd atom in the case of Au/Pd nanoparticles. These core/shell structures were characterized by the energy dispersive X-ray (EDX) microanalysis. By this method, the reverse Pd-core/Au-shell bimetallic nanoparticles were also produced, probably because the nanoparticles are too large to adopt an alloy structure.

Michaelis and Henglein [131] prepared Pd-core/Ag-shell bimetallic nanoparticles by the successive reduction of Ag ions on the surface of Pd nanoparticles (mean radius: 4.6 nm) with formaldehyde. The core/shell nanoparticles, however, became larger and deviated from spherical with an increase in the shell thickness. The Pd/Ag bimetallic nanoparticles had a surface plasmon absorption band close to 380 nm when more than 10-atomic layer of Ag are deposited. When the shell thickness is less than 10-atomic layer, the absorption band is located at shorter wavelengths and the band disappears below about three-atomic layer.

Precise control of the core/shell structures is crucially important in order to improve catalytic and electronic properties of small bimetallic nanoparticles. Some bottlenecks, however, have to be overcome in order to realize the control of core/shell structures. For example, the oxidation of the preformed metal core often takes place by the metal ions for making the shell when the metal ions have a high-redox potential, and large islands of shell metal are produced on the preformed metal core. Therefore, we developed a so-called hydrogen-sacrificial protective strategy, which enables us to prepare the bimetallic nanoparticles in the size range 1.5–5.5 nm with controllable core/shell structures [132]. Noble metals like Pd, Pt, and many others have the ability to adsorb hydrogen and split it to form metal hydrides on the metal surface. Hydrogen atoms adsorbed on noble metals have a very strong reducing ability since they have quite low-redox potential. Consequently, the second metal ions are easily reduced to metal atoms by the hydrogen atoms adsorbed on the first noble metal nanoparticles, and the obtained second metal atoms are deposited on the surface of the first metal nanoparticles to form bimetallic nanoparticles with a core/shell structure. By the strategy, we could prepare Pd-core/Pt-shell and Pt-core/Pd-shell bimetallic nanoparticles with various metal compositions.

Recently many core/shell nanoparticles were successfully prepared by the successive or two-step reduction.

Selvakannan et al. [133] reported that the amino acid tyrosine is an excellent reducing agent to prepare Au-core/Ag-shell nanoparticles under alkaline conditions. The tyrosine molecules already bound to the surface of Au nanoparticles through amine groups in the amino acid may be used to selectively reduce Ag ions at high pH on the surface of the Au nanoparticles, thus leading to a simple strategy for realizing phase-pure Au-core/Ag-shell nanostructures. Wilson et al. [134] reported preparation and characterization of 1–3-nm diameter, structurally well-defined, bimetallic AgAu nanoparticles which were dendrimer-encapsulated. Three different bimetallic structures were prepared: (1) AgAu alloys prepared by co-complexation and subsequent reduction of dendrimer-encapsulated Au(III) and Ag(I); (2) Au-core/Ag-shell; and (3) AuAg-core/Ag-shell structures prepared by a sequential loading method. The AuAg nanoparticles can be extracted from the dendrimer into an organic phase using different surfactants, depending on the shell metal and its oxidation state. This provides a means for characterization of the composition of the shell. UV–Vis, TEM, and single-particle X-ray energy dispersive spectroscopy (EDS) were used to characterize the bimetallic nanoparticles before and after extraction and show that the extraction step does not alter the size or composition of the bimetallic nanoparticles [134]. Tsuji et al. prepared Au core-Ag shell bimetallic nanoparticles by a microwave (MW)-polyol method through the two-step reduction of $AuCl_4^-$ and Ag(I) ions in the presence of PVP as a protecting reagent. When single crystal polygonal Au nanoplates and nanorods were used as seeds, a mixture of various Au-core/Ag-shell nanostructures was prepared after MW heating for only 2 min. Among them, small amounts of novel polygonal and rod types of Au-core/Ag-shell nanostructures, in which morphologies of Au core were kept, were produced [135].

Srnova-Sloutfova et al. [136] prepared layered Ag-core/Au-shell bimetallic nanoparticles by overdeposition of Au

over Ag seeds by the seed-growth method using tetrachloroauric acid, with hydroxylamine hydrochloride as a reducing agent. Nanoparticles prepared by a rapid reduction in the neutral ambient and assembled into 2-D nanoparticulate films by adsorption of 2,2′-bipyridine were characterized by EDX, XPS, surface-enhanced Raman scattering spectroscopy (SERS), and TEM. The results are consistent with Ag core and AgAu alloyed shell composition of the nanoparticles (Ag/AgAu) [136]. Yang et al. [137] reported that difference between the transfer of PVP-protected Au and Ag nanoparticles from an aqueous solution to toluene was used to develop a simple preparation method of bimetallic Ag-core/Au-shell nanoparticles. The core/shell structure of the bimetallic nanoparticles was characterized by UV–Visible spectroscopy, EDX, and TEM measurements. Using this technique, they have found that Ag-core/Au-shell nanoparticles were formed by the seed-mediated growth method using Ag nanoparticles as the seeds. The reversed order of using Au nanoparticles as the seeds, however, could only produce a physical mixture of Ag-core/Au-shell nanoparticles and isolated Ag nanoparticles but not produce Au-core/Ag-shell nanoparticles [137]. Yang et al. also examined replacement reaction between hydrophobilized Ag nanoparticles and hydrophobilized $AuCl_4$ in toluene in detail in order to prepare Ag-core/Au-shell nanoparticles. They concluded that (1) a detectable contraction of the Ag nanoparticle sacrificial templates during the course of the reaction is shown; (2) the deposition of Au on the shrunken Ag templates inhibits further Ag oxidation, resulting in the formation of Ag-core/Au-shell nanoparticles; and (3) the significant red-shift in the surface plasmon resonance (SPR) band is a consequence of shape and chemical composition changes. Effects of solvent and temperature determined the structure and composition of nanoparticles formed in the replacement reaction [138]. Cui et al. prepared layered Ag-core/Au-shell bimetallic nanoparticles by coating Au layers over Ag seeds by a seed-growth method. The composition of Ag_{100-x}/Au_x, particles can vary from $x = 0$ to 30. TEM and SEM images clearly show that the bimetallic nanoparticles are of core/shell structure. They investigated the Ag-core/Au-shell nanoparticles on improvement of detection sensitivity of immunoassay [139].

Yang et al. found that Ag-core/Pt-shell nanoparticles with a core/shell could only be formed by the successive reduction method using Ag nanoparticles as the seeds. Results of measurements of UV–Vis, TEM, EDX, and XPS supported the core/shell structure of the bimetallic nanoparticles. The reverse order of preparation using Pt nanoparticles as the seeds did not provide any core/shell nanoparticles while a physical mixture of Ag nanoparticles and the original Pt seeds was obtained [140].

Vinodgopal et al. prepared Pt/Ru bimetallic nanoparticles by sonochemical reduction of Pt(II) and Ru(III) in aqueous solutions. TEM images indicated that sequential reduction of the Pt(II) followed by the Ru(III) produced Pt-core/Ru-shell bimetallic nanoparticles. In the presence of sodium dodecyl sulfate (SDS), as a stabilizer, the nanoparticles had diameters between 5 and 10 nm. When PVP was used as the stabilizer, the rate of reduction is much faster, giving ultrasmall bimetallic nanoparticles of ca. 5 nm diameter [141].

Damle et al. observed that the reduction of the Pd(II) ions in the stearic acid–Ag nanocomposite film leads to the formation of a mixture of individual Ag and Pd nanoparticles as well as particles in the Ag-core/Pd-shell structure. Thermal treatment of the stearic acid-(Ag/Pd) nanocomposite film at 100 °C, however, resulted in the formation of an AgPd alloy [142].

Kan et al. reported preparation of Au-core/Pd-shell bimetallic nanoparticles by successive or simultaneous sonochemical irradiation of their metal precursors in ethylene glycol, respectively. In the successive method, Pd clusters or nanoparticles are first formed by reduction of $Pd(NO_3)_2$, followed by adding $HAuCl_4$ solution. As a result, Au-core/Pd-shell structured particles are formed, although Pd-core/Au-shell had been expected. In their investigations, the successive method was more effective than the simultaneous one in terms of the formation of the Au-core/Pd-shell nanoparticles [143].

In order to realize the precise control of core/shell structures of small bimetallic nanoparticles, some problems have to be overcome. For example, one problem is that the oxidation of the preformed metal core often takes place by the metal ions for making the shell when the metal ions have a high-redox potential, and large islands of shell metal are produced on the preformed metal core. Therefore, we previously developed a so-called hydrogen-sacrificial protective strategy to prepare the bimetallic nanoparticles in the size range 1.5–5.5 nm with controllable core/shell structures [132]. The strategy can be extended to other systems of bi- or multimetallic nanoparticles.

Reduction of two different precious metal ions by refluxing in ethanol/water in the presence of PVP gave a colloidal dispersion of core/shell structured bimetallic nanoparticles. In the case of Pd and Au ions, e.g., the colloidal dispersions of bimetallic nanoparticles with a Au core/Pd shell structure are produced. In contrast, it is difficult to prepare bimetallic nanoparticles with the inverted core/shell (in this case, Pd-core/Au-shell) structure. The sacrificial hydrogen strategy was used to construct the inverted core/shell structure, where the colloidal dispersions of Pd-cores are treated with hydrogen and then the solution of the second element, Au ions, is slowly added to the dispersions. This novel method, developed by us, gave the inverted core/shell structured bimetallic nanoparticles. The Pd-core/Au-shell structure was confirmed by FT-IR spectra of adsorbed CO [144].

Lee et al. [145] succeeded in preparation of Co-based bimetallic nanoparticles with core/shell structure via transmetalation reaction (Figure 3). The Co-core/Au-shell nanoparticles, e.g., were confirmed to be almost the same in particle size with the seeded Co nanoparticle, as shown in Figure 4.

In summary, we concluded that the successive reduction method easily provides the bimetallic nanoparticles with the core/shell structure according to versatile design. For example, different reducing agents may be used for the first reduction and the second one, respectively, depending on the property of the metal. In some cases of two kinds of metals with much different redox potentials, however, ''inverted'' core/shell nanoparticles are difficult to form even in the successive reduction. The ''inverted'' core/shell structure can be realized by an

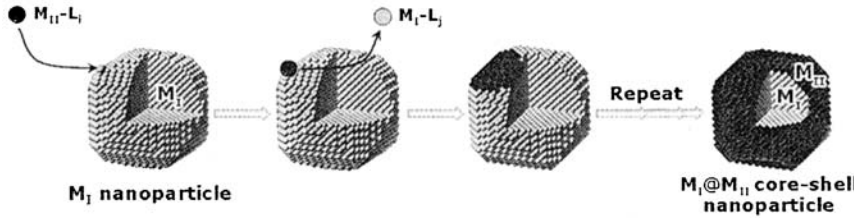

Figure 3. Schematic illustration of core/shell nanoparticle formation via redox transmetalation process. Metal ions (M_{II}) of reactant metal complexes (M_{II}-L_i) are reduced on the surface of M_I nanoparticles while neutral M_I atoms are oxidized to M_I^{y+} by forming a M_I–ligand complex (M_I–L_j) as a resultant reaction byproduct. Repeating this process results in the complete coverage of shell layers on core metals. (Reprinted from Ref. [145], © 2005, with permission from American Chemical Society.)

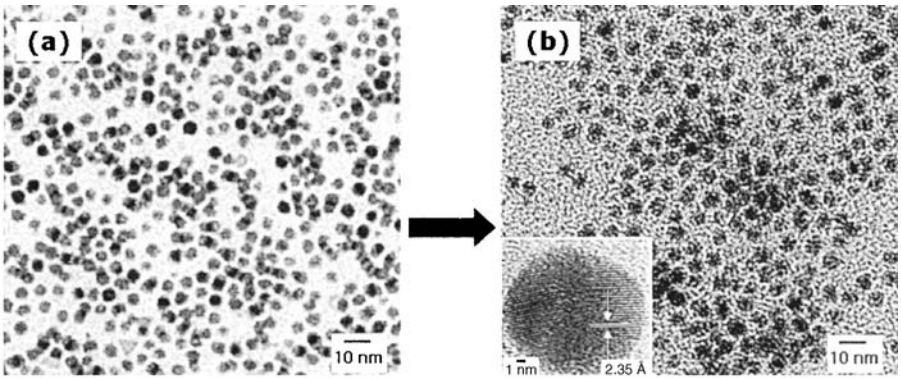

Figure 4. TEM and HRTEM images of (a) 6.5 nm Co nanoparticles and (b) Co-core/Au-shell nanoparticles using Co nanoparticles as the seed material. Lattice distances measured by HRTEM as well-matched to known Au lattice parameters for the (1 1 1) plane (inset). The average size of the Co-core/Au-shell nanoparticles is ca. 6.4 nm, which is similar to the initial size of the Co nanoparticles because the atom exchange process is the only operative reaction. (Reprinted from Ref. [145], © 2005, with permission from American Chemical Society.)

assistance of other technique such as the hydrogen-sacrificial protective strategy [132] or transmetalation reaction [145].

2.3. Physical Mixture of Two Kinds of Monometallic Nanoparticles

Recently we found that low entropy core/shell structured nanoparticles form spontaneously from the physical mixture of a dispersion of Ag nanoparticles and that of another noble metal (Rh Pd, or Pt) at room temperature [146–148]. This discovery initiated from the disappearance of plasmon absorption, attributed to Ag nanoparticles, by mixture of Ag nanoparticles with Rh nanoparticles within an hour [148]. Change of TEM image of the mixtures suggested the formation of pseudo-core/shell structures for the bimetallic products. We used isothermal titration calorimetry (ITC) for investigation on the forming process of the bimetallic nanoparticles. The experimental results showed that the initial step of such a spontaneous process is strongly exothermic. When the alcohol dispersion of PVP-protected Rh nanoparticles with an average diameter of 2.3 nm was titrated into the alcoholic dispersion of PVP-protected Ag nanoparticles, a strong exothermic enthalpy change, ΔH was observed, i.e., $\Delta H = -908$ kJ/mol for Ag(small) nanoparticle with an average diameter 10.8 nm and -963 kJ/mol for Ag(large) nanoparticles with an average diameter 22.5 nm. The strength of interaction increases in the order of Rh/Ag > Pd/Ag > Pt/Ag. The strong exothermic interaction was considered as a driving force to from low entropy bimetallic nanoparticles by the physical mixing of two kinds of monometallic nanoparticles. We also revealed that exothermic interactions occur between a pair of noble metal nanoparticles themselves by using ITC [146]. Based on the results of EF-TEM, preliminary EXAFS, and so on, we speculated the formation mechanism of core/shell structured bimetallic nanoparticles as shown in Figure 5. Although the detailed mechanism to form smaller core/shell particles from pseudo-core/shell aggregated particles is not clear yet, the exothermic interaction may play an important role for this realignment.

Smetana et al. [149] reported a remarkable and simple alloying procedure which involves mixing of separately prepared colloids of pure Au and pure Ag or Cu nanoparticles and then heating in the presence of an alkanethiol under reflux. Results of UV–Vis, EDX, and HRTEM measurements confirmed the formation of alloy structure of the AgAu or AuCu nanoparticles. The nanoparticles of ca. 5.6 nm in diameter for AgAu and ca. 4.8 nm for AuCu underwent facile self-assembly to form 3-D superlattice ordering. During the alloying process, the organic ligands display an extraordinary chemistry in which atom transfer between atomically pure Cu, Ag, and Au metal nanoparticles resulted in the monodisperse alloy nanoparticles.

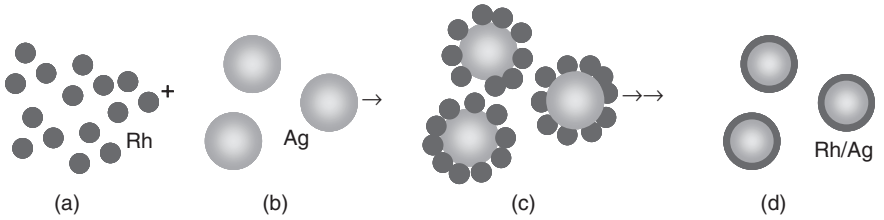

Figure 5. Plausible formation mechanism of core/shell structured bimetallic nanoparticles by a physical mixture. (Reprinted from Ref. [146], © 2005, with permission from American Chemical Society.)

Peng et al. [150] prepared AgAu nanoalloys via three different procedures by using laser-induced heating: (i) mixture of Au nanoparticles and Ag(I) ions irradiated by a 532 nm laser, (ii) mixture of Au and Ag nanoparticles irradiated by a 532 nm laser, and (iii) mixture of Au and Ag nanoparticles irradiated by a 355 nm laser. In procedures (ii), nanoalloys with a sintered structure were obtained. The morphology of the obtained nanoalloys depended not only on the laser wavelength but also on the concentration of nanoparticles in the initial mixture. Large-scale interlinked networks were observed upon laser irradiation when the total concentration of Ag and Au nanoparticles in the mixture increased.

In summary, two kinds of monometallic nanoparticles with smaller particle sizes easily form bimetallic nanoparticles by the physical mixing. The monometallic nanoparticles with stronger interaction also have a trend to form the bimetallic nanoparticles by the mixing. This kind of chemistry between nanoparticles is now becoming open to human beings.

3. Purification and Characterization of Bimetallic Nanoparticles

Principally purification and characterization methods of monometallic nanoparticles are directly applied to those of bimetallic nanoparticles. Purification of metal nanoparticles dispersed in solution is not so easy. So, in classical colloid chemistry, contamination is carefully avoided. For example, people used pure water, distilled three times, and glass vessels, cleaned by steam, for preparation of colloidal dispersions. In addition, the reagents which could not byproduce contaminates were used for the preparation. Recently, however, various kinds of reagents were used for the reaction and protection. Thus, the special purification is often required especially when the nanoparticles are prepared by chemical methods.

The purification methods for metal nanoparticles involve (1) evaporation, (2) centrifugation, (3) extraction, (4) filtration, and (5) other methods.

Evaporation of volatile byproducts and solvents is often used to obtain the solid metal nanoparticles. The residue may contain metal nanoparticles and protective reagents. When the nanoparticles are well protected by ligands or polymers, then the solid residues can be dispersed again without coagulation of the particles. When the nanoparticles are not well protected, however, the evaporation often results in aggregation of the nanoparticles.

The centrifuge is often used to separate metal nanoparticles from contaminates. If the size of nanoparticles is too small, the usual centrifuge is not sufficient. The centrifuge with super high speed is required to get precipitates from nanoparticles. This method is also used to get ultrafine nanoparticles by separation of the rather large nanoparticles.

Extraction by an organic solvent or water can be used to separate metal nanoparticles soluble in an organic solvent or water. This technique can be used only for the nanoparticles protected by organic ligands or polymers. The solubility of protecting reagents with the solvent is crucially important in this technique.

Conventional filtration cannot be applied to the separation in purification of metal nanoparticles. If the metal nanoparticles are protected by polymer, however, the membrane filter, which can cut off the polymer with certain molecular weight, can be used to separate the polymer protected metal nanoparticles. Free metal nanoparticles which are not protected by polymer can pass through the membrane. Ion filter like cellulose can be used to separate ionic species from the reaction mixtures.

Other purification methods include a liquid phase chromatography, electrophoretic separation by mass spectroscopy, separation using magnetic properties, and so on. These separation methods are limited only for the metal nanoparticles having a special property useful for these purification methods.

After purification, the bimetallic nanoparticles are offered to characterization. The characterization techniques were well reviewed previously in literatures [1,2]. In this section, we highlight recent reports on the characterization methods of bimetallic nanoparticles after presenting some previous researches again.

3.1. TEM (HRTEM) Imaging and Electron Diffraction

The most important information about the nanoparticles is the size, shape, and their distributions which crucially influence physical and chemical properties of nanoparticles. TEM is a powerful tool for the characterization of nanoparticles. TEM specimen is easily prepared by placing a drop of the solution of nanoparticles onto a carbon-coated copper microgrid, followed by natural evaporation of the solvent. Even with low magnification TEM one can distinguish the difference in contrast derived from the atomic weight and the lattice direction. Furthermore, selective area electron diffraction can provide information on the crystal structure of nanoparticles.

High resolution TEM (HRTEM) can provide atomic-resolution real-space imaging of the nanoparticles [151,152]. Based on HRTEM image, size of PVP-protected Pt_1Ru_3 bimetallic nanoparticles was calculated to be 1.1 nm in diameter [62]. Although crystal structures can be surely determined by X-ray, electron, and neutron diffraction, the HRTEM is indispensable for characterization of nanoparticles, particularly when the particle shape and composition are concerned. Scanning tunneling microscopy and atomic force microscopy also can provide atomic-resolution images of large crystal surfaces, but they are almost impossible to clearly resolve the atomic lattices of nanoparticles because of the surface coating and the wobbling of nanoparticles under the scanning tip. HRTEM is a powerful and versatile tool that provides not only atomic-resolution lattice images but also chemical information at a spatial resolution of 1 nm or better, allowing direct identification of chemistry of a single nanoparticle [208–211]. EDX analysis as well as electron energy-loss spectroscopy (EELS) analysis of nanoparticles are even more attractive for assessing the compositions and the valence states of constructing metal elements [127]. Recently characterization of bimetallic nanoparticles with TEM (HRTEM) was routinely carried out by scientists in this field [81,112,116,118–120,124,141].

Au-core/Pd-shell bimetallic nanoparticles, prepared by a MW-assisted polyol reduction method, were well characterized by HRTEM. The HRTEM image showed that thickness of the Pd shell was ca. 3 nm, and the Au core diameter is 9 nm [118]. Au-core/Pd-shell bimetallic nanoparticles, prepared by co-reduction of Au(III) and Pd(II) precursors in toluene, were substantiated by the TEM images [119]. Shankar et al. [120] characterized bimetallic Au-core/Ag-shell nanoparticles by TEM. The TEM observations revealed that the Ag nanoparticles were adsorbed onto the Au nanoparticles, forming a core/shell structure. Vinodgopal et al. [141] prepared Pt/Ru bimetallic nanoparticles by sonochemical reduction of Pt(II) and Ru(III) in aqueous solutions. TEM images indicated that sequential reduction of Pt(II) followed by Ru(III) produces particles with a Pt-core/Ru-shell structure with diameters between 5 and 10 nm, as shown in Figure 6. Bimetallic Ag-core/Au-shell nanoparticles, prepared by a $NaBH_4$ reduction method, were directly confirmed by HRTEM [124].

It is noteworthy that the HRTEM cannot distinguish core and shell even by combining X-ray or electron diffraction techniques for some small nanoparticles. If the shell epitaxially grows on the core in the case of two kinds of metals with same crystal type and little difference of lattice constant, the precise structure of the bimetallic nanoparticles cannot be well characterized by the present technique. Hodak et al. [153] investigated Au-core/Ag-shell or Ag-core/Au-shell bimetallic nanoparticles. They confirmed that Au shell forms on Ag core by the epitaxial growth. In the TEM observations, the core/shell structures of Ag/Au nanoparticles are not clear even in the HRTEM images in this case (Figure 7).

Well-mixed CuNi nanoparticles were prepared at the molar ratio Cu(II) to Ni(II) of 1:1 by simultaneous reduction of $CuSO_4$ and $NiCl_2$ with hydrazine in the microemulsion of SDS/*n*-butanol/*n*-heptane/water at 70 °C. TEM photographs showed a narrow distribution of CuNi nanoparticles, essentially monodispersed and having the mean diameter of 12 nm [116]. Chimentao et al. [91] studied the preparation of AgAu alloy nanoparticles based on the phase transfer of metal precursors from aqueous phase to organic phase by fatty amine at room temperature. TEM images revealed the formation of a uniform size distribution of AgAu nanoparticles (ca. 5 nm). PtCu bimetallic alloy nanoparticles can be prepared in w/o microemulsions of water/cetyltrimethyammonium bromide (CTAB)/isooctane/*n*-butanol by the co-reduction of H_2PtCl_6 and $CuCl_2$ with hydrazine at room temperature [112]. HRTEM analyses confirmed the formation of the $PtCu_3$ alloy nanoparticles with a mean diameter of ca. 1.6 nm, where the corresponding lattice spacing of 0.187 nm is consistent with that of the (200) plane of $PtCu_3$ bulk alloy.

3.2. UV–Vis Spectroscopy

An important feature of UV–Vis measurement is to provide us the useful information about formation processes

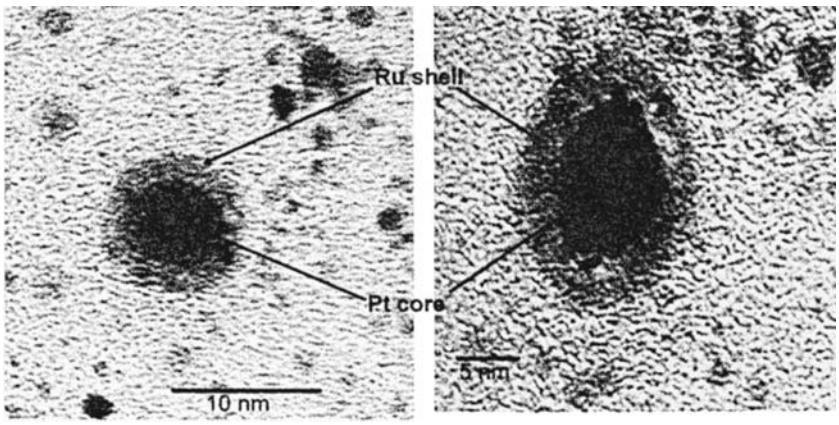

Figure 6. TEM images obtained at an accelerating voltage of 200 kV of Pt-core/Ru-shell nanoparticles prepared by sequential sonication of 1 mM Pt(II) and 1 mM Ru(III) ions at 213 kHz. Two representative particles are shown at different magnification. (Reprinted from Ref. [141], © 2006, with permission from American Chemical Society.)

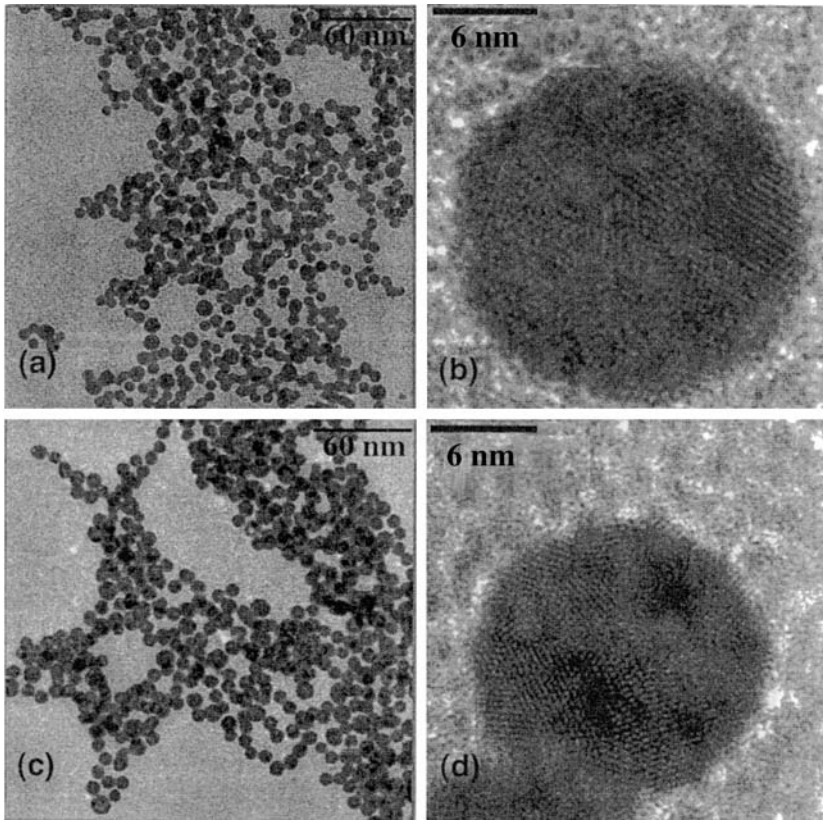

Figure 7. TEM images of Ag-core/Au-shell particles in molar ratio Ag:Au of (a, b): 1:1; (c, d): 1:3. Note the enlargement of the particles as the Au-shell becomes thicker (panels (a) and (c)) as well as the resolution of the lattice planes (panels (b) and (d)). The power spectra indicate that Au grows epitaxially onto the Ag-seeds. (Reprinted from Ref. [153], © 2000, with permission from American Chemical Society.)

and final structures of bimetallic nanoparticles [22,30,33,64,154–168]. Au, Ag, Cu, and Hg nanoparticles have sharp plasmon absorption bands in UV–Vis range. Important information about the structure of bimetallic nanoparticles such as alloy or core/shell structure is obtained by careful analysis of the position of plasmon absorption peak as well as its change.

During reduction of metal ions to prepare the corresponding zero-valent nanoparticles, the color of the solution is drastically changed, i.e., plasmon absorption appears by the formation of zero-valent nanoparticles while the absorption of metal ions disappears by the reduction. Therefore, UV–Vis spectroscopy is useful to confirm both the degree of consumption of precursors by monitoring their ligand-to-metal or metal-to-ligand charge transfer transitions and the formation of band structures of nanoparticles by monitoring the plasmon band or the broad tailing absorption in the range from UV to visible region derived from the inter- and intraband charge transfer transitions.

In 1993, we examined formation processes of PVP-protected AuPt bimetallic nanoparticles by in-situ UV–Vis spectroscopy during the reduction [53]. Figure 8 shows the in-situ UV–Vis spectra during the simultaneous reduction of Au(III) and Pt(IV) ions. In the case of PVP-protected AuPt bimetallic system, Au(III) ions are reduced first accompanying a decrease of peak at ca. 320 nm, followed by the reduction of Pt(IV) ions, decreasing in intensity of the peak at ca. 265 nm, as shown in Figure 8a. The order of the reduction is consistent with the difference of standard redox potentials, i.e., 1.002 V for $[AuCl_3^-]$/Au and 0.68 V for $[PtCl_4^{2-}]$/Pt. After complete reduction of all Au(III) or Pt(IV) ions, the Au atoms aggregate first, followed by deposition of the Pt atoms, indicated by the UV–Vis spectrum (Figure 8b) where the plasmon band at ca. 540 nm due to Au nanoparticles increases first, and then decreases accompanying increase of the plasmon band at ca. 370 nm due to Pt nanoparticles. The formation processes are schematically illustrated in Figure 9 [53].

Michaelis and Henglein [131] investigated formation process of Pd-core/Ag-shell bimetallic nanoparticles by UV–Vis spectroscopy. As shown in Figure 10, the Pd/Ag bimetallic nanoparticles possess a surface plasmon absorption band close to 360 nm when more than 10 monolayers of Ag are deposited. The plasmon absorption band, however, is located at shorter wavelength when the shell thickness is less than 10 monolayers, while the band disappears when the thickness of the shell is below about three-atomic layers.

Chen et al. [82] investigated co-reduction of $HAuCl_4$ and $AgNO_3$ with hydrazine by UV–Vis spectra. The

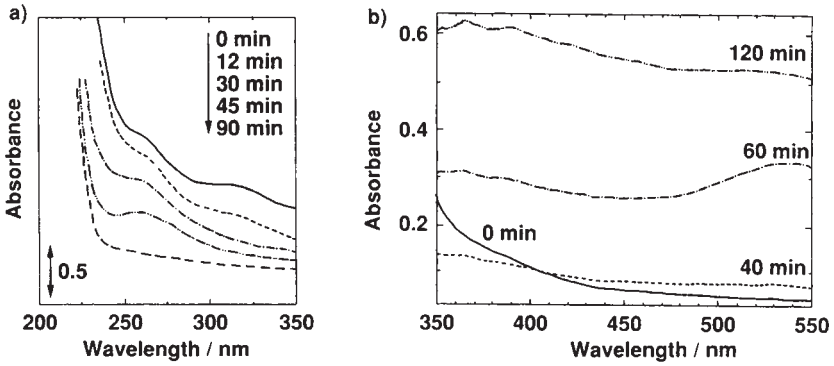

Figure 8. In-situ UV–Vis spectra during the formation of PVP-protected AuPt (1:1) bimetallic system in the region of $\lambda < 350$ nm (a) and $\lambda > 350$ nm (b). (a) Sampling from the solution of the metal ions in ordinary conditions for preparation at 100 °C with refluxing; (b) the solution of the metal ions in a quartz UV cell was heated up to 80 °C without refluxing. (Reprinted from Ref. [53], © 1993, with permission from Elsevier.)

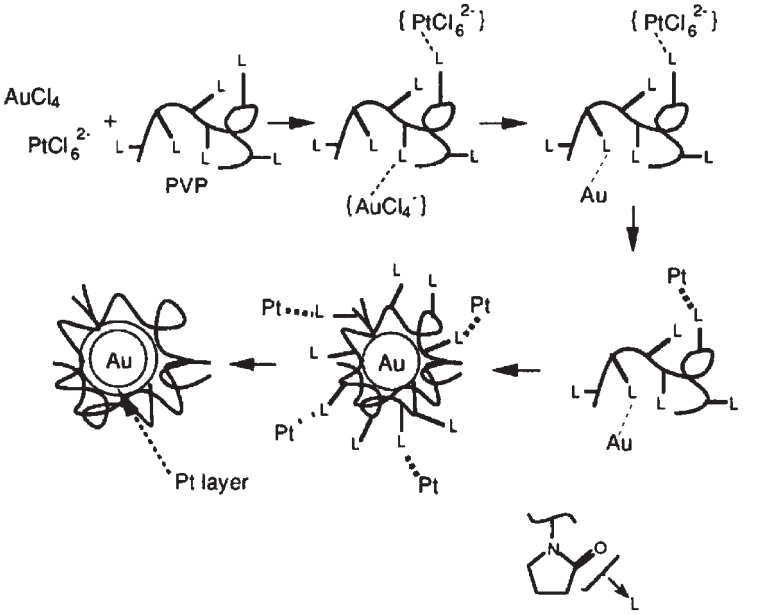

Figure 9. Proposed formation process of PVP-protected AuPt bimetallic system. (Reprinted from Ref. [53], © 1993, with permission from Elsevier.)

UV–Vis absorption spectra of the solutions exhibited only one plasmon absorption and the absorption maximum of the plasmon band red-shifted almost linearly from 400 to 520 nm with increasing Au:Ag molar ratio, revealing the formation of an AgAu alloy. AgAu alloy nanoparticles can also be prepared via reduction of varying mole fractions of $HAuCl_4$ and $AgNO_3$ by sodium borohydride in the presence of sodium citrate as a capping agent [83]. In UV–Vis spectra of the reduction process, the plasmon absorption band of AgAu nanoparticles shifted linearly to the red with increasing Au content. The direct dependence of the metal salt ratio to the shift of the absorbance peak indicated that the nanoparticles were alloy rather than core/shell structure. Rodriguez-Gonzalez et al. [85] performed a time-resolved study of the formation of AgAu alloy nanoparticles during boiling of $AgNO_3$ and $HAuCl_4$ in the presence of sodium citrate by monitoring the UV–Vis spectra of the solutions. The study revealed clear differences with respect to the formation of pure Au particles, and suggested that Au and Ag nanoparticles nucleated separately, but the lattice rearrangement eventually lead to formation of alloy nanoparticles with the expected composition. AgAu bimetallic nanoparticles, whose feed atomic ratios of Au to Ag were 3:1, 1:1, and 1:3, were prepared [88]. UV–Vis spectra indicated that the nanoparticles were not simple physical mixtures of monometallic nanoparticles or core/shell structure but alloy.

AuPt bimetallic nanoparticles, prepared by polyol method and stabilized with PVP, were studied by UV–Vis spectra [122]. In this preparation the reaction temperature

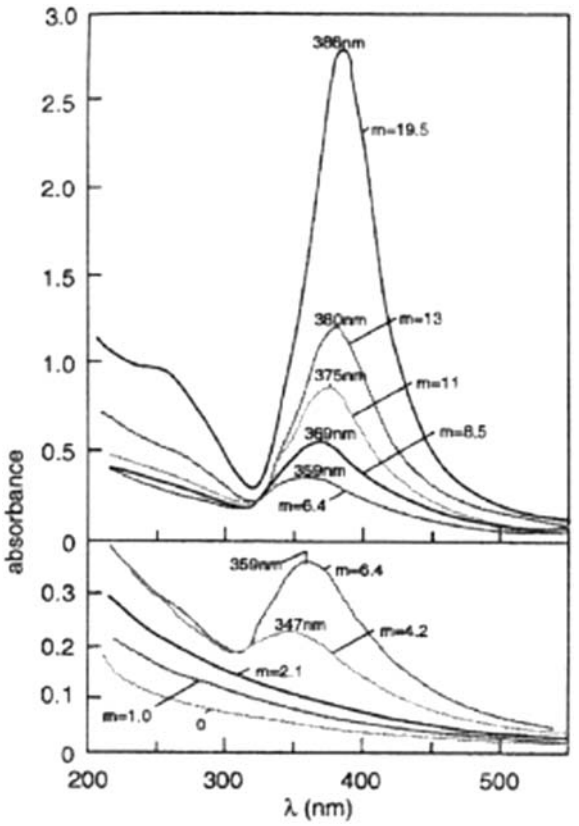

Figure 10. Absorption spectrum of the Pd nanoparticles before (0) and after deposition of various amounts of silver. m: number of monolayers of silver. (Reprinted from Ref. [131], © 1994, with permission from American Chemical Society.)

was crucially important. Interesting structure changes were observed in the nanoparticles as the temperature was varied. At lower temperatures no bimetallic nanoparticles were detected, but as the temperature increased bimetallic nanoparticles started to appear, commonly obtaining core/shell nanoparticles. In the UV–Vis spectra, an absorption peak centered at 520 nm at low temperatures was observed (100–110 °C); at higher temperatures (130–170 °C) there were non detectable absorption peaks, and finally at the two highest temperatures (180–190 °C) the reappearance of an absorption feature centered at 510 nm was noticed. These UV–Vis spectroscopic results indirectly implied the composition of the surface of the particle.

Endo et al. [96] prepared AuPt, AuPd, and PtPd bimetallic nanoparticles with 2–4 nm in particle size in order to investigate catalytic activity for reduction of *p*-nitrophenol in water. The binary features of the nanoparticles were characterized by UV–Vis spectroscopic measurements.

3.3. X-Ray Diffraction

XRD provides useful information on the crystal phase, lattice constant, and average particle size of nanoparticles. In the case of bimetallic nanoparticles, XRD is important

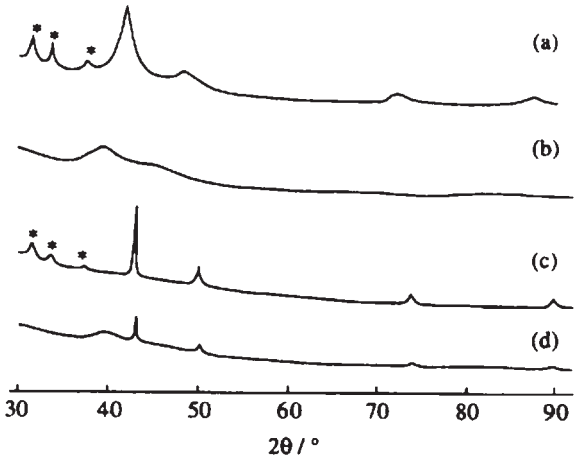

Figure 11. X-ray diffraction patterns of PVP-protected metal nanoparticles: (a) PVP-protected CuPd (Cu:Pd = 2:1) bimetallic nanoparticles; (b) PVP-protected Pd nanoparticles; (c) PVP-protected Cu dispersion; (d) physical mixture of (b) and (c) (Cu:Pd = 2:1). (Reprinted from Ref. [71], © 1993, with permission from The Chemical Society of Japan.)

to confirm whether the bimetallic nanoparticles adopt alloy structure or not. Generally, an alloy consisting of two kinds of metals shows the diffraction peaks between those of two pure metals.

We investigated on structure of CuPd (2:1) bimetallic nanoparticles by XRD [71]. Since the XRD peaks of the PVP-protected CuPd nanoparticles appeared between the corresponding diffraction lines of Cu and Pd nanoparticles, as shown in Figure 11, the bimetallic alloy phase was clearly found to be formed in CuPd (2:1) bimetallic nanoparticles. We also characterized Ag-core/Rh-shell bimetallic nanoparticles, which formed during simple physical mixing of the corresponding monometallic ones, by XRD coupled with TEM [148].

The XRD and TEM showed that the bimetallic nanoparticles with Ag-core/Rh-shell structure spontaneously form by the physical mixture of Ag and Rh nanoparticles. Luo et al. [168] carried out structure characterization of carbon-supported Au/Pt catalysts with different bimetallic compositions by XRD and direct current plasma-atomic emission spectroscopy. The bimetallic nanoparticles were alloy. Au-core/Pd-shell structure of bimetallic nanoparticles, prepared by co-reduction of Au(III) and Pd(II) precursors in toluene, were well supported by XRD data [119]. Pt/Cu bimetallic nanoparticles can be prepared by the co-reduction of H_2PtCl_6 and $CuCl_2$ with hydrazine in w/o microemulsions of water/CTAB/isooctane/*n*-butanol [112]. XRD results showed that there is only one peak in the pattern of bimetallic nanoparticles, corresponding to the (1 1 1) plane of the $PtCu_3$ bulk alloy.

The sharpness of XRD peaks is corresponding with the size of metal nanoparticles. Sherrers's equation is used to estimate the crystalline size of metal nanoparticles. Note that the size estimated from XRD peak width is some times larger than the size measured by TEM, especially when the size is very small. If the size estimated from XRD peak width is smaller than that directly measured by TEM, the particles could be polycrystalline.

3.4. X-Ray Photoelectron Spectroscopy

Generally one can obtain the surface (<10 nm) information such as kind of metals and their valences of bimetallic nanoparticles by means of XPS. As probing area of XPS is in 10 μm–~1 mm size range, the average composition of two different metals near the surface of bimetallic nanoparticles is likely to be evaluated.

On the other hand, the XPS data near the Fermi level provide us the valuable information about the band structures of nanoparticles. XPS spectra near the Fermi level of the PVP-protected Pd nanoparticles, Pd-core/Ni-shell (Ni/Pd = 15/561, 38/561) bimetallic nanoparticles, and bulk Ni powder were investigated by Teranishi et al. [126]. The XPS spectra of the nanoparticles become close to the spectral profile of bulk Ni, as the amount of the deposited Ni increases. The change of the XPS spectrum near the Fermi level, i.e., the density of states, may be related to the variation of the band or molecular orbit structure. Therefore, the band structures of the Pd/Ni nanoparticles at Ni/Pd > 38/561 are close to that of the bulk Ni, which greatly influence the magnetic property of the Pd/Ni nanoparticles.

PtRu nanoparticles can be prepared by w/o reverse micro-emulsions of water/Triton X-100/propanol-2/cyclohexane [105]. The bimetallic nanoparticles were characterized by XPS and other techniques. The XPS analysis revealed the presence of Pt and Ru metal as well as some oxide of ruthenium. Hills et al. [169] studied preparation of Pt/Ru bimetallic nanoparticles via a seeded reductive condensation of one metal precursor onto pre-supported nanoparticles of a second metal. XPS and other analytical data indicated that the preparation method provided fully alloyed bimetallic nanoparticles instead of core/shell structure. AgAu and AuCu bimetallic nanoparticles of various compositions with diameters ca. 3 nm, prepared in chloroform, exhibited characteristic XPS spectra of alloy structures [84].

By XPS spectra, Endo et al. [96] confirmed that formation of binary structure prevented Pd atoms from oxidation in the AuPd and PtPd bimetallic nanoparticles which exhibited higher catalytic activity than monometallic ones. Wang et al. [112]. characterized PtCu bimetallic alloy nanoparticles by XPS. XPS revealed that both elements in the nanoparticles are in zero-valence and possess the characteristic metallic binding energy.

3.5. Extended X-Ray Absorption Fine Structure (EXAFS)

EXAFS analysis is a powerful spectroscopic method for structural analysis which has been extensively applied to the problem of structure determination in nanoparticles, and especially bimetallic nanoparticles [170–172]. The X-ray absorption spectrum of an element contains absorption edges corresponding to the excitation of electrons from various electronic states at energies characteristic of that element, i.e., K edges arise from the excitation of electrons from 1s states, and LI, II, III edges from excitations from 2s, 2p 1/2, and 2p 3/2 states. When the X-ray energy is increased above an edge, oscillations (fine structure) are observed in the absorption coefficient over an energy range of several hundred to over a 1000 eV above the edge. Since these oscillations arise from the interference between waves associated with the emitted photoelectrons and photoelectrons backscattered from the neighboring atoms, they contain useful information on the environment of the absorbing atom. The fine structure can be extracted from the X-ray absorption spectrum which, after data manipulation, is best fit to a computed EXAFS spectrum for a model structural environment for the absorbing atom. The EXAFS is element specific and structure sensitive, and gives information on the number and identity of neighboring atoms and their distances from the absorbing atom. The information most usually sought in an EXAFS measurement comprises the number of scattering atoms of each type and their distances from the absorbing atom, i.e., the composition of the mean coordination sphere about the absorbing atom. When multiple elements are present, they can be analyzed both as the absorbing atom and as the scattering atoms. A fitting technique which takes advantage of the necessary geometric relationships between the various components in a multicomponent system has been developed and is greatly important for the EXAFS analysis of bimetallic nanoparticles [173]. If one uses synchrotron radiation as X-ray source EXAFS data acquisition is enormously shortened, and under favorable circumstances an absorption spectrum can be obtained in less than an hour. Higher concentration of sample is favorable for EXAFS analysis. Concentrations of up to 50% or more can be realized in case of polymer-stabilized bimetallic nanoparticles, and much higher metal concentrations are accessible when ligand-stabilized or surfactant-stabilized nanoparticles are used.

We have previously reported structural determination of bimetallic nanoparticles by the EXAFS measurements. The PVP-protected Pd/Pt(4/1) and Pd/Pt(1/1) bimetallic nanoparticles prepared by means of a simultaneous reduction of $PdCl_2$ and H_2PtCl_6 have a mean diameter of ~1.5 nm with a quite narrow size distribution, indicating that each nanoparticle is composed of 55 metal atoms (magic number) [58]. In the case of Pd/Pt(4/1) bimetallic nanoparticles, the coordination number of Pt atoms around the Pt atom suggests that the Pt atom coordinates predominantly to the other Pt atoms. Moreover, the coordination numbers are quite different from those calculated for the random model, where 42 Pd atoms and 13 Pt atoms are located completely at random. If 42 Pd atoms are located on the surface and the other 13 Pt atoms are at the core of the fcc-structured nanoparticles, then the Pd/Pt ratio is almost 4/1 and the coordination numbers calculated on the basis of the Pt-core model are quite consistent with the values observed from EXAFS. We succeeded in proposing a model structure by EXAFS analysis because our target bimetallic nanoparticles were homogeneous in size and structure. EXAFS analysis of Pd/Pt(1/1) also suggests not the random and separated models, but the Pt-core/Pd-shell structure. Other structural analyses by means of EXAFS were carried out for Pd/Rh [174], Au/Pd [125], NiPd [77] nanoparticles, and so on. The NiPd bimetallic nanoparticles were first proposed to have an alloy structure [77], but later proved to have heterobond-phillic structure [175].

Recently characterization of bimetallic nanoparticles by EXAFS were extensively reported [122–124,176].

Structural transformation of bimetallic Pd/Pt nanoparticles, which were prepared by a sequential loading of H_2PtCl_6 onto the Pd loaded catalyst, was investigated with EXAFS at high temperatures [176]. The results of EXAFS at Pd K and Pt L-III edges showed that Pt was surface-enriched or anchored on the Pd metal core with an increase of the Pt content. The structure of the obtained bimetallic Pd/Pt nanoparticles seemed to be retained upon heating up to 1273 K under ambient condition [176]. Pt/Au bimetallic nanoparticles can be prepared by polyol method and stabilized by PVP [122]. XANES and EXAFS studies were also performed on the samples and their results supported the idea of a Pt-core/Au-shell structure with the elements segregated from each other [122].

Chen et al. [123] examined the amount-dependent change in morphology for a series of Au/Pt bimetallic nanoparticles. The EXAFS results confirmed the formation of a core/shell structure and inter-diffusion between Au and Pt atoms. The composition of the shell layer was found to be Pt-enriched AuPt alloy. They also characterized bimetallic Ag-core/Au-shell nanoparticles by the EXAFS [124].

3.6. CO-IR Spectroscopy

Surface composition and structure of bimetallic nanoparticles are crucially important for their catalytic property as well as their optical property. IR measurement of CO adsorbed on surface metals (CO-IR) is utilized for this purpose. CO is adsorbed on metals not only on-top sites but also in two-fold or three-fold sites, depending on the kinds of metals and their surface structures. The dramatical changes of wavenumber of adsorbed CO occurs depending on the binding structure [177–181].

We performed CO-IR measurement on Pt/Pd bimetallic nanoparticles with core/shell structures and characterized their structures [132]. Figure 12 showed the CO-IR probe spectra of Pd-core/Pt-shell bimetallic nanoparticles with different Pd:Pt ratios.

In Figure 12a (Pd:Pt = 1:2) and 12b (Pd:Pt = 1:1), only the spectral feature of CO adsorbed on the Pt atoms, i.e., a strong band at 2068 cm^{-1} and a very weak broad band at around 1880 cm^{-1}, was observed, while that derived from CO adsorbed on Pd atoms at 1941 cm^{-1} is completely absent, which proved that the Pd-core has been completely covered by a Pt-shell. Recently we also characterized Au-core/Pd-shell bimetallic nanoparticles by the CO-IR [144]. Reduction of two different precious metal ions by refluxing in ethanol/ water in the presence of poly(*N*-vinyl-2-pyrrolidone) (PVP) gave a colloidal dispersion of core/shell structured bimetallic nanoparticles. In the case of Pd and Au ions, the bimetallic nanoparticles with a Au-core/Pd-shell structure are usually produced. In contrast, it is difficult to prepare bimetallic nanoparticles with the inverted core/shell, i.e., Pd-core/Au-shell structure. A sacrificial hydrogen strategy is useful to construct the inverted core/shell structure, where the colloidal dispersions of Pd cores are treated with hydrogen and then the solution of the second element, Au ions, is slowly

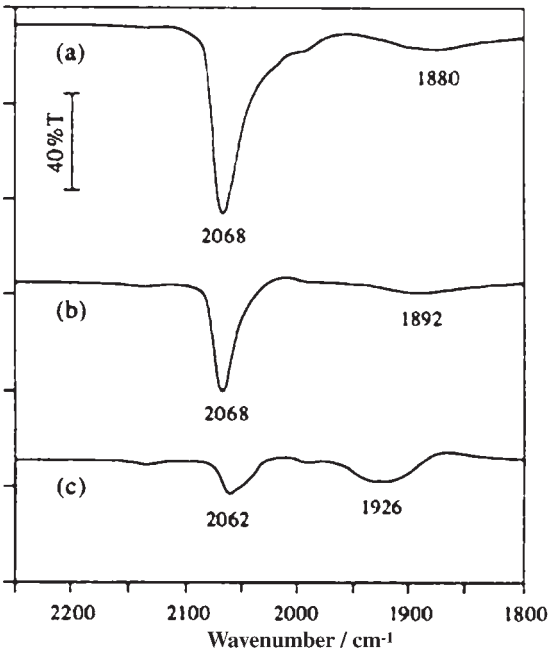

Figure 12. FTIR spectra of CO adsorbed on PVP-protected Pd-core/Pt-shell nanoparticles having a Pt-shell: (a) Pt:Pd = 2:1; (b) Pt:Pd = 1:1; (c) Pt:Pd = 1:4. [Pd]: 0.1 mmol in 10 mL of CH_2Cl_2. (Reprinted from Ref. [132], © 1997, with permission from American Chemical Society.)

added to the dispersions. This novel method, developed by us, gave the inverted core/shell structured bimetallic nanoparticles. The CO-IR spectra indicated the formation of the Pd-core/Au-shell structure. Hydrogenation of methyl acrylate catalyzed by the nanoparticles before and after heat treatment also supported indirectly the inverted core/shell structure of the Pd/Au bimetallic nanoparticles [144].

Solla-Gullon et al. [111] carried out FT-IRs experiments of adsorbed CO for PdPt nanoparticles prepared by reduction of H_2PtCl_6 and K_2PdCl_4 with hydrazine in a w/o microemulsion of water/poly(ethyleneglycol) dodecyl ether (BRIJ(R)30)/*n*-heptane. The experiments gave information on the relative amount of linear- and bridge-bonded CO, which is known to depend on the surface distribution of the two elements.

4. Functions of Bimetallic Nanoparticles

Bimetallic nanoparticles show many interesting functions. Herein we, however, concentrate on catalytic, ferromagnetic, and electro-optical properties of the bimetallic nanoparticles. The bimetallic nanoparticles are emerging catalysts because of their high surface-to-volume ratios and synergestic effect of the second metal element. Bimetallic nanoparticles containing late transition metal or 3d-transition metal, such as Fe, Co, and Ni, as one component element are also extensively investigated on ferromagnetic properties. Recently we demonstrated that the bimetallic nanoparticles could change or improve electro-optical responsibility of LCDs.

4.1. Catalytic Properties of Bimetallic Nanoparticles

Bimetallic nanoparticles (including monometallic ones) have attracted a great interest in scientific research and industrial applications, owing to their unique large surface-to-volume ratios and quantum-size effects [1,2,5,182]. Since industrial catalysts usually work on the surface of metals, the metal nanoparticles, which possess much larger surface area per unit volume or weight of metal than the bulk metal, have been considered as promising materials for catalysis.

Industrial catalysts are usually composed of inorganic supports and metals on the supports. They are often prepared by heat treatment of metal ions on the support at high temperature sometimes under hydrogen. They have very complex structures. For example, they are the mixtures of metal particles with various sizes and shapes. Metal particles often strongly interact with the inorganic supports, thus resulting in the structure of half balls.

The catalytic performance of metal depends on the kinds of metal and supports, size and structure, and addition of other element(s). Thus, many trial and errors have been carried out in order to develop industrial catalysts. Even now, this is true for the research and development of practical catalysts.

Recently, however, the development of nanotechnology may provide the changes on the research and development of practical catalysts. As mentioned in the previous section we can now design and synthesize a metal nanoparticle with not only various sizes and shapes, but also with various combinations of elements and their locations. Thus, we can now design the synergetic effect of two elements. In the case of core/shell structured bimetallic nanoparticles, the shell element can provide a catalytic site and the core element can give an electronic effect (a ligand effect) on the shell element. Since only the atoms on the surface can be attached by substrates, the thickness of the shell should be an important factor to control the catalytic performance.

In 1989, we developed colloidal dispersions of Pt-core/Pd-shell bimetallic nanoparticles by simultaneous reduction of Pd and Pt ions in the presence of poly(*N*-vinyl-2-pyrrolidone) (PVP) [15]. These bimetallic nanoparticles display much higher catalytic activity than the corresponding monometallic nanoparticles, especially at particular molecular ratios of both elements. In the series of the Pt/Pd bimetallic nanoparticles, the particle size was almost constant despite composition and all the bimetallic nanoparticles had a core/shell structure. In other words, all the Pd atoms were located on the surface of the nanoparticles. The high catalytic activity is achieved at the position of 80% Pd and 20% Pt. At this position, the Pd/Pt bimetallic nanoparticles have a complete core/shell structure. Thus, one atomic layer of the bimetallic nanoparticles is composed of only Pd atoms and the core is completely composed of Pt atoms. In this particular particle, all Pd atoms, located on the surface, can provide catalytic sites which are directly affected by Pt core in an electronic way. The catalytic activity can be normalized by the amount of substance, i.e., to the amount of metals (Pd + Pt). If it is normalized by the number of surface Pd atoms, then the catalytic activity is constant around 50–90% of Pd, as shown in Figure 13.

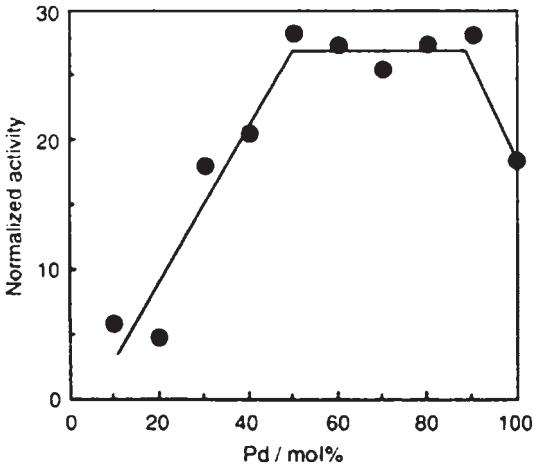

Figure 13. Normalized catalytic activity (in mmol H_2 per mmol surface Pd per s) as a function of metal composition of PVP-stabilized Pd/Pt bimetallic nanoparticles. The normalization was determined by the number of Pd atoms on the surface of the nanoparticle, assuming that Pd atoms exist selectively on the surface. (Reprinted from Ref. [48], © 1993, with permission from Royal Society of Chemistry.)

This means that the improvement of catalytic activity of Pd nanoparticles by involving the Pt core is completely attributed to the electronic effect of the core Pt upon shell Pd. Such clear conclusion can be obtained in this bimetallic system only because the Pt-core/Pd-shell structure can be precisely analyzed by EXAFS and Pd atoms are catalytically active while Pt atoms are inactive.

The CuPd bimetallic nanoparticles were first prepared by thermal decomposition of a bimetallic acetate precursor [79]. Later, well-defined PVP-protected CuPd bimetallic nanoparticles were prepared by reduction of $CuSO_4$ and $Pd(CH_3COO)_2$ in refluxing glycol/dioxane at $pH \approx 10$ in the presence of PVP [72]. These nanoparticles are very important from a viewpoint of catalysis, because they have high catalytic activity for two completely different reactions, i.e., hydration of acrylonitrile to acrylamide and selective partial hydrogenation of 1,3-cyclooctadiene to cycooctene. The former hydration of acrylonitrile is usually catalyzed by Cu and the latter hydrogenation of cyclooctadiene, by Pd. The same CuPd bimetallic nanoparticles can catalyze both reactions, and the catalytic activities of bimetallic nanoparticles are much higher than the corresponding monometallic ones, respectively. This result demonstrates that both Cu and Pd atoms are located in the surface layer of bimetallic nanoparticles. In fact the ensemble effect of Pd is proposed for the hydration of acrylonitrile catalyzed by CuPd bimetallic nanoparticles [132].

After our success in preparation of the colloidal dispersions of Pt-core/Pd-shell bimetallic nanoparticles by simultaneous reduction of $PdCl_2$ and H_2PtCl_6 in refluxing ethanol/water in the presence of poly(*N*-vinyl-2-pyrrolidone) [15,16] several reports have appeared on the formation of the core/shell-structured bimetallic nanoparticles by simultaneous reactions [5,52,68,183].

Now let us consider the core/shell and inverted core/shell structures. The core/shell structure and the inverted

core/shell structure are based on the very same concept [175]. The difference is just which homobond, A–A or B–B, is favored. If A–A bond is preferred to B–B bond, an A-core/B-shell structure is favored, but the inverted core/shell structure can be still constructed. This inverted core/shell structure should be thermodynamically unstable and of great interest. This has been successfully achieved by using the so-called "sacrificial hydrogen strategy" [132]. In the case of PtPd bimetallic nanoparticles, Pd-cores were first prepared. After the Pd-cores were covered by hydride by contact with molecular hydrogen, Pt ions were added to be reduced by hydride adsorbed on the surface of Pd-cores, which resulted in bimetallic nanoparticles with the inverted core/shell structure of Pd-core and Pt-shell. Without the sacrificial hydrogen strategy the successive reduction cannot give rise to the inverted core/shell structure but rather to the cluster-in-cluster structure usually [125]. The thermodynamical instability of the present inverted core/shell structure has been confirmed by the change of the catalytic activity of nanoparticles with inverted core/shell structure with heat treatment [184].

Hydrogenation reactions have been the most extensively studied for measuring the activity of nanoparticles. Noble monometallic (Pd, Pt, Rh) nanoparticles protected by linear polymer like PVP or polyvinylalcohol have high catalytic activities for hydrogenation of olefins [185–187]. We applied PVP-protected Pt/Pd [15,48] and Au/Pd [49] bimetallic nanoparticles with various compositions to the selective hydrogenation of 1,3-cyclooctadiene to cyclooctene. In both cases, the bimetallic nanoparticles with Pd content of 80% showed the highest activity, which is greater than Pd monometallic nanoparticles. Such bimetallic nanoparticles are found to have Pt- or Au-core/Pd-shell structures and all Pd atoms fully cover the particles to form monoatomic layers. This improvement of catalytic activity can be interpreted only by a ligand effect of the core elements.

Since palladium has a high catalytic activity for hydrogenation of diene while platinum has a low one, the effect of particle size should be taken into consideration. The catalytic activity was normalized by the number of Pd atoms on the surface area, calculated from the mean diameters of PdPt nanoparticles measured by TEM and the selective existence of Pd atoms on the surface of bimetallic nanoparticles (suggested by EXAFS results). The dependence of normalized activity on the metal composition is shown in Figure 13 [48]. The activity of surface Pd atoms is almost constant for Pt/Pd bimetallic nanoparticles containing between 50 and 95 mol% of palladium. The normalized activity of surface Pd atoms in the nanoparticles is larger than that of monometallic Pd nanoparticles. As the ionic potential of palladium (8.34 eV) is smaller than that of platinum (9.0 eV), the electronic interaction between the Pt core and the surface shell Pd atoms results in the Pd atoms being deficient in electron density. This is a practical example of the ligand effect, since a substrate with C=C bonds favors the electron-deficient catalytic sites. The similar consideration can be applied to Au/Pd bimetallic nanoparticles with core/shell structure. The selectivity of monoene produced by Pt/Pd and Au/Pd bimetallic nanoparticles was almost 100%. Pd/Rh bimetallic nanoparticles showed the highest catalytic activity for hydrogenation of *cis*-1,3-cyclopentadiene to cyclopentene at a composition of Pd:Rh = 1:2 [55].

Bronstein and co-workers [188] have studied catalytic properties of PdPt, AuPd, and PdZn bimetallic nanoparticles formed in block copolymer micelles derived from polystyrene-*block*-poly-4-vinylpyridine (PS-*b*-P4VP) on dehydrolinalool (3,7-dimethyloctaen-6-yne-1-ol-3, DHL) hydrogenation. It was found from FTIR spectroscopy on CO adsorption and XPS that the second metal (Au, Pt, or Zn) acts as a modifier toward Pd, changing both its electronic structure and its surface geometry. This change provides higher catalytic activity of these bimetallic nanoparticles formed in PS-*b*-P4VP micelles compared to Pd nanoparticles, which can be ascribed mainly to an increase in the number of active centers on the particle surface. High selectivity of DHL-hydrogenation (99.8% at 100% conversion) to linalool (3,7-dimethylocta-1,6-diene-3-ol) was achieved for all bimetallic nanoparticle catalysts, by chemical modification of the nanoparticle surface with pyridine units.

NiPd alloy bimetallic nanoparticles, prepared by the improved polyol reduction method under high temperature, were applied to the catalysis for hydrogenation of nitrobenzene [77] and its derivatives [78]. They were proved to be excellent catalysts with considerable air-resistance property for hydrogenation of nitrobenzene to aniline. Among the bimetallic nanoparticles with various Ni:Pd ratios, Ni:Pd (2:3) nanoparticles were found to be the most active catalyst, whereas Ni:Pd (1:4) nanoparticles showed the highest activity for the hydrogenation of nitrobenzene derivatives. In this case, not only electronic (ligand) effect but also ensemble effect was proposed. Recently, Ag/Au bimetallic nanoparticles of alloy structure with 3–4 nm in size were utilized as a catalyst for reduction of *p*-nitrophenol. The catalytic activities were proportional to the feed ratio of Au in the nanoparticles and showed a maximum at the ratio of Au:Ag = 3:1 [88].

Bimetallic nanoparticles are good catalysts for hydration of acrylonitrile. From a catalytic point of view, bimetallic nanoparticles composed of 3d-transition metal and noble metal with specific structures will provide a great number of new candidates of catalysts for various chemical reactions, since the catalytic properties of bimetallic nanoparticles can be potentially tailored by both the ligand effect and the ensemble effect. Of particular interest are the excellent catalytic properties of Cu/Pd alloy bimetallic nanoparticles for both the selective hydration of acrylonitrile, an important industrial process, and the hydrogenation of carbon–carbon double bonds under mild conditions [71–73]. The rate of the catalytic hydration of acrylonitrile by the PVP-protected Cu:Pd (2:1) bimetallic nanoparticle catalyst is about seven times higher than that of the PVP-protected Cu monometallic nanoparticles. The activity increases with increasing Cu content within the range of Cu:Pd ratio from 1 to 3. The lack of cyanohydrine formation during the catalytic process suggests a nearly 100% selectivity for the amide (Equation (2)).

$$CH_2=CH-CN+H_2O \rightarrow CH_2=CH-CONH_2 \quad (2)$$

A preliminary idea about the acceleration effect of the Pd atoms in the surface on the hydration of acrylonitrile is shown schematically in Figure 14.

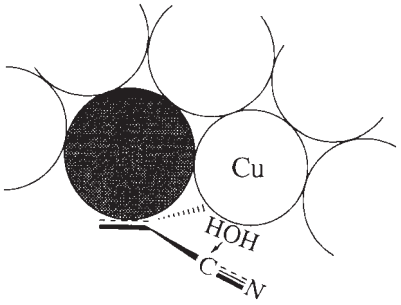

Figure 14. Schematic diagram of the acceleration effect of Pd on the hydration of acrylonitrile. (Reprinted from Ref. [73], © 1994, with permission from Wiley-VCH.)

The coordination of the C–C double bond of the acrylonitrile to the palladium atom in the bimetallic nanoparticles makes the C–N triple bond locate close to the Cu species, thus facilitating the hydration catalyzed by the Cu species. This is a good example of the ensemble effect of bimetallic nanoparticles. The electronic effect of the neighboring atoms in the bimetallic nanoparticles upon the catalytic activity may also be important in this process. He et al. [189] investigated hydrogenation of methyl acrylate using Ag/Pd bimetallic nanoparticles as a catalyst. The catalytic activity of the Pd-on-Ag nanoparticle is 367 times as large as that of commercial Pd black and 1.6 times as large as that of Pd monometallic nanoparticle. The outstanding catalytic activity can be explained by the large fraction of the surface-exposed Pd atoms [192]. Bimetallic nanoparticles of Pt and Sn have been investigated as a catalyst by Cho et al. [190] for hydrogenation of benzene. Their experimental results showed a high selectivity for the hydrogenation of benzene to *n*-hexane with a comparable turnover rate [190]. Thomas et al. [104] found that bimetallic nanoparticles (Ru_6Pd_6, Ru_6Sn, $Ru_{10}Pt_2$, Ru_5Pt, $Ru_{12}Cu_4$, and $Ru_{12}Ag_4$) anchored within silica nanopores exhibited high activities and frequently high selectivities, depending on the composition of the nanocatalyst, in a number of single-step (and often solvent-free) hydrogenations at low temperatures (333–373 K). The selective hydrogenations of polyenes such as 1,5,9-cyclododecatriene and 2,5-norbornadiene were especially efficient. Good performance is found with these nanoparticle catalysts in the hydrogenation of dimethyl terephthalate to 1,4-cyclohexanedimethanol and of benzoic acid to cyclohexanecarboxylic acid or to cyclohexene-1-carboxylic acid, and also in the conversion of benzene to cyclohexene (or cyclohexane), the latter being an increasingly important reaction in the context of the production of nylon. Isolated atoms of noble metals (Pd, Rh, and Pt) in low oxidation states, appropriately complexed and gathered to the inner walls of nanoporous (ca. 3 nm diameter) silica, are very promising enantioselective hydrogenation catalysts [104]. The AuPd bimetallic nanoparticles also exhibited higher catalytic activity for reduction of *p*-nitrophenol than monometallic ones [96]. Ghosh et al. [109] reported catalytic activities of bimetallic NiPt nanoparticles towards the reduction of aromatic nitro compounds. The catalytic activity was superior over monometallic Pt nanoparticles. Moreover, it was found that the rate of reduction of nitroaromatics is sensitive to the composition of the alloy catalysts. It could be attributed to the electronic effect and the segregation behavior of the material in the alloy [109].

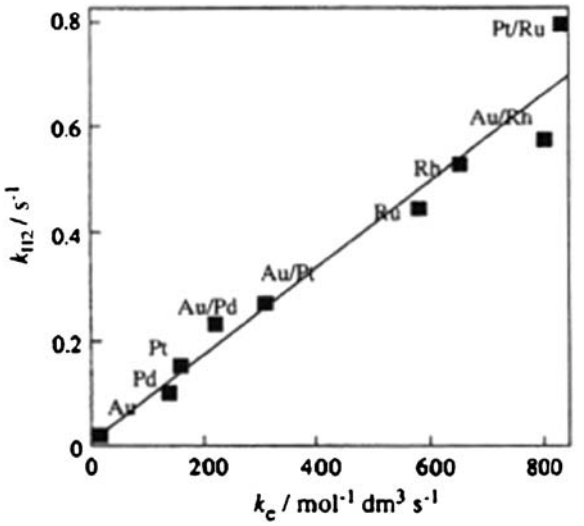

Figure 15. Relationship between electron transfer rate constant k_e and hydrogen generation rate constant K_{H_2}. (Reprinted from Ref. [194], © 2000, with permission from IUPAC.)

Photo-induced hydrogen generation from water can be catalyzed by the bimetallic nanoparticles. Conversion of solar photoenergy is a very important theme for human beings. Construction of an artificial photosynthetic system taking after the natural photosynthesis is a potential method for the solar photoenergy conversion. One of the most important and simplest concepts is visible light-induced decomposition of water to produce oxygen and hydrogen. Noble metal nanoparticles can work as a catalyst for visible light-induced hydrogen generation from water in the system like EDTA/*tris*(bipyridine)ruthenium(II) ($Ru^{II}(bpy)_3$)/methyl viologen (MV)/nanoparticle catalyst [191–193] where metal nanoparticles works as an electron mediator to accept electrons from methyl viologen cation radical ($MV^{+\cdot}$) and donate them to protons producing hydrogen molecules, as shown in Equation (3). Pt nanoparticles (Pt_{NP}) have been considered to be the best catalyst for this purpose.

$$\begin{aligned} Ru^{II}(bpy)_3^* + MV^{2+} &\rightarrow Ru^{III}(bpy)_3 + MV^{+\cdot} \\ MV^{+\cdot} + Pt_{NP} &\rightarrow MV^{2+} + Pt_{NP}^- \\ Pt_{NP}^- + H^+ &\rightarrow Pt_{NP} + H \\ 2H &\rightarrow H_2 \end{aligned} \quad (3)$$

Recently five monometallic (Au, Pd, Pt, Ru, Rh) nanoparticles were investigated as electron mediators together with four core/shell bimetallic (Au/Pd, Au/Pt, Au/Rh, Pt/Ru) nanoparticles [53,194–196]. The linear relationship was observed between the electron transfer rate coefficients and the hydrogen generation rate coefficient as shown in Figure 15.

The bimetallic nanoparticles were generally more active than the corresponding monometallic nanoparticles. The highest catalytic activity was observed for Au/Rh and/or

Pt/Ru bimetallic nanoparticles. In the case of dye-sensitized photochemical water splitters, to which much attention has been received recently, noble metal nanoparticles are often used for the active centers to produce hydrogen gas from water. Bimetallic nanoparticles will be easily replaced by these metal nanoparticles for the sake of saving resources.

Bimetallic nanoparticles were studied for catalysis of electro-oxidation. The study of catalytic oxidation of methanol and CO has broad technological applications, including fuel-cell technology, purification of air in gas products and in long duration space travel, and conversion in automobile exhaust systems [197–199]. The search for highly effective catalysts and detailed mechanistic understanding [200–203] has spanned to the exploration of nanoparticle catalysts [197,198]. Two critical issues facing the exploration of nanoparticle catalysts for methanol oxidation are, however, the propensity of poisoning at traditional platinum group catalysts by adsorbed CO-like species and the tendency of aggregation. Recently, Lou and co-workers applied the thiolate-stabilized AuPt (Pt∼5%) alloy nanoparticles prepared by a standard two-phase synthesis to methanol electro-oxidation [58]. Interestingly, ligand-shell encapsulation and networking added aggregation-resistant and poison-resistant properties to the nanoparticles. As a result of methanol electro-oxidation on a glassy-carbon electrode, the anodic peak current increased with increasing methanol concentration, exhibiting a linear relationship, while the peak current for the cathodic wave decreased with increasing methanol concentration, also exhibiting a linear relationship. These two features are the first set of evidence demonstrating that methanol was oxidized at the nanoparticle catalyst. Recently catalytic activity of supported Au nanoparticles has received much attention [204]. Catalytic activity of the bimetallic AuPd bimetallic nanoparticles, supported on TiO_2, in the CO oxidation revealed a slight synergestic effect compared to the activity of monometallic analogous referred to the estimated surface area of Au and Pd in the bimetallic sample [205]. Recently, Deivaraja et al. [110] utilized carbon-supported NiPt nanoparticles for the electro-oxidation of methanol and compared catalytic activity with a commercial E-TEK Pt/carbon catalyst. The catalytic activity of the bimetallic nanoparticles was higher, and resistance to catalyst deactivation was improved [110]. Ag/Au alloy nanoparticles can also be used as a catalyst for low-temperature CO oxidation [89]. In this case the activity was highly dependent on the hydrogen pretreatment conditions. Reduction at 550–650 °C led to high activity at room temperature, whereas as-prepared or calcinated samples did not show any activity at the same temperature. CO and O^{-2} coadsorption on neighboring sites on the AuAg alloy was stronger than that on either Au or Ag. The strong synergism in the coadsorption of CO and O^{-2} on the AgAu nanoparticle can thus explain the observed synergetic effect in catalysis [89].

The measurement of catalytic activity of PdPt bimetallic nanoparticles over methane combustion showed that the difference in activity with increasing and decreasing reaction temperatures disappeared probably due to the synergestic effect of the formation of the PdPt bimetallic nanoparticles [176].

Another electro-oxidation example catalyzed by bimetallic nanoparticles was reported by D'Souza and Sampath [206]. They prepared Pd-core/Pt-shell bimetallic nanoparticles in a single step in the form of sols, gels, and monoliths, using organically modified silicates, and demonstrated electrocatalysis of ascorbic acid oxidation. Steady-state response of Pd/Pt bimetallic nanoparticles-modified glassy-carbon electrode for ascorbic acid oxidation was rather fast, of the order of a few tens of seconds, and the linearity was observed between the electric current and the concentration of ascorbic acid.

Formation of single-walled carbon nanotubes (SWNTs) was found to be catalyzed by metal nanoparticles [207]. Wang et al. [114] investigated bimetallic catalysts such as FeRu and FePt in the size range of 0.5–3 nm for the efficient growth of SWNTs on flat surfaces. When compared with single-component catalysts such as Fe, Ru, and Pt of similar size, bimetallic catalysts Fe/Ru and Fe/Pt produced at least 200% more SWNTs [114].

These results on catalytic activity of bimetallic nanoparticles are summarized in Table 2.

4.2. Ferromagnetic Properties of Bimetallic Nanoparticles

One of the important physical properties of the bimetallic nanoparticles is a ferromagnetic property. The bimetallic nanoparticles showing the ferromagnetic property usually contain 3d-transition metal, such as Fe, Co, and Ni, as one element. Rare-earth elements like Sm are also important for the ferromagnetism. Considerable progress has been done in ultrahigh-density magnetic recording thanks to the development of metal thin film media with small particles, narrow size distributions, and optimized compositions [214]. In principle, the size-control of noble metal nanoparticles is relatively easy, while it is difficult for the 3d-transition metallic nanoparticles due to easy oxidation. To overcome the problem alloying of 3d-transition metal with noble metal was applied. Two approaches have been considered to prepare small magnetic bimetallic nanoparticles with narrow size distribution. One is successive reduction which involves the formation of small noble metal nanoparticles, followed by the reduction of 3d-transition metal ions. Another one is the simultaneous reduction of noble and 3d-transition metal ions.

Pd/3d-transition metal bimetallic nanoparticles were extensively studied on the ferromagnetism. Pd does not polarize magnetically in bulk metal, but has a giant magnetic moment in the presence of a small amount of a ferromagnetic 3d-transition metal. Crangle and co-workers first found the appearance of the giant magnetic moment by the measurements of paramagnetic susceptibility and ferromagnetic saturation magnetization [215–218]. In their measurements 1 mol% of Fe induces a strong polarization of Pd in a Pd/Fe alloy, resulting in a giant magnetic moment of ∼10 μB per Fe atom [219] and the polarized region of ∼1 nm around the Fe atom [220]. The magnetic enhancement can be investigated in detail by using bimetallic nanoparticles. Then many researches on the Pd/3d-transition bimetallic nanoparticles were reported. The Pd/Fe [221] ,Pd/Ni [76,222], and Pd/Cu

Table 2. Typical applications of bimetallic nanoparticles as catalysts reported in literatures.

Metals	Reaction	Substrate	Main product	Catalytic activity	Selectivity	Literatures
Pt/Pd	Hydrogenation	1,3-Cyclooctadiene	Cyclooctene	Higher than Pd-NP	100%	[15,48]
Au/Pd	Hydrogenation	1,3-Cyclooctadiene	Cyclooctene	Higher than Pd-NP	100%	[49]
Pd/Rh	Hydrogenation	*cis*-1,3-Cyclopentadiene	Cyclopentene	High	–	[55]
PdM_2[a]	Hydrogenation	DHL[b]	3,7-Dimethyloctadiene-1,6-ol-3	Higher than Pd-NP	99.8%	[188]
NiPd	Hydrogenation	Nitrobenzene or derivative	Aniline or derivative	High	–	[77,78]
CuPd	Hydration	Acrylonitrile	Acrylamide	Higher than Cu-NP	100%	[71–73]
M_1/M_2[c]	PIHG[d]	H_2O	H_2	Higher than mono-MP	–	[53,194–196]
AuPt	Electrooxidation	Methanol	–	–	–	[58]
Pd/Pt	Electrooxidation	Ascorbic acid	–	–	–	[206]
RuM_2[e]	Hydrogenation	Benzene	Cyclohexene	High	High	[104]
AgPd	Hydrogenation	Methyl acrylate	–	Higher than Pd black	–	[189]
PtNi	Electrooxidation	Methanol	–	–	–	[108]
PdRh	Hydrogenation	1,3-Cyclooctadiene	Cyclooctene	High	–	[113]
AuPd	Oxidation	CO	CO_2	Higher than mono-NP	–	[205]
FeM_2[f]	Surface growth of SWNT[g]	–	SWNT	Higher than mono-NP	–	[114]
PtNi	Reduction	Aromatic nitro compound	–	Higher than mono-NP	–	[109]
Pt/Sn	Aromatization	*n*-Hexane	Benzene	–	–	[190]
PdPt	Combustion	Methane	–	Higher than mono-NP	–	[176]
PtNi	Electrooxidation	Methanol	–	Higher than Pt/C[h]	–	[110]
M_1/M_2[i]	HCR[j]	–	–	–	–	[212]
PtRu	Electrooxidation	Methanol	–	–	–	[106]
AgAu	Reduction	*p*-Nitrophenol	–	–	–	[88]
Pt/Cu	Reduction	NO_x	–	High	–	[213]
FeNi	Degradation	Trichloroethylene	–	High	–	[115]
AgAu	Oxidation	CO	CO_2	Higher than mono-NP	–	[89]
PdAg	Hydrogenation	*cis,cis*-1,3-Cyclooctadiene	–	–	–	[101]
PdPt	Reduction	*p*-Nitrophenol	–	Higher than Pt-NP	–	[96]

[a]M_2: Pt, Au, Zn.
[b]DHL: 3,7-Dimethyloctaen-6-yne-1-ol-3.
[c]M_1/M_2: Au/Pd, Au/Pt, Au/Rh, Pt/Ru.
[d]PIHG: Photo-induced hydrogen generation.
[e]M_2: Pd, Sn, Pt, Cu, Ag.
[f]M_2: Ru, Pt.
[g]SWNT: Single-wall carbon nanotube.
[h]A commercial E-TEK Pt/C catalyst.
[i]M_1/M_2: Various bimetallic nanoparticles including core/shell structures.
[j]HCR: Homogeneous catalytic reaction including hydrogenation, Heck coupling, and Suzuki reaction.

[71–73,80,180,223–225] nanoparticles were prepared by the conventional gas evaporation method [221], the sol-gel method [222], the simultaneous alcohol reduction of the corresponding metal salts in the presence of the linear polymer [76,80,223,224], and the decomposition of metal salts [225].

Teranishi et al. [126] developed a novel synthetic method of a series of the monodispersed Pd/Ni nanoparticles of the similar size by using a successive reduction. Ni atoms were deposited on 2.5 nm Pd nanoparticles according to the "magic number" of 561 atoms with a five-shell structure [34]. The deposition was carried out in various Ni/Pd molar ratios (1/561, 2/561, 10/561, 15/561, 38/561, 168/561, 281/561, and 561/561) by 1-propanol reduction of nickel acetate in the presence of PVP to produce Pd-core/Ni-shell bimetallic nanoparticles. The size distributions and mean diameters of Pd/Ni nanoparticles are similar to those of Pd nanoparticles, indicating that the size of Pd nanoparticles was maintained by PVP in 1-propanol under reflux, and that the Ni atoms were uniformly deposited on every Pd nanoparticle. In the magnetization measurements of a series of Pd/Ni nanoparticles, the remarkable threshold of the enhancement on the magnetic moment was observed at Ni/Pd = 38/561, and a large enhancement of the magnetic moment corresponding to a giant magnetic moment effect is found above this threshold [126,226–228]. The band structures of the Pd/Ni nanoparticles at Ni/Pd > 38/561 were close to that of the bulk Ni. The appearance of the giant magnetic moment induced on the Pd nanoparticles by the Ni impurity was considered to be closely related to the change in the band structure of the Pd/Ni nanoparticles. Fabrication of 2-D superlattices of the Pd/Ni nanoparticles may make novel magnetic recording devices possible.

Fe/Pt bimetallic nanoparticles are an important class of materials in permanent magnetic applications since they have large uniaxial magnetocrystalline anisotropy [$K_u \approx 7 \times 10^6$ J/m^3] and good chemical stability [229]. As the magnetic stability of individual particles scales with the anisotropy constant, K_u, and the particle volume, V, small Fe/Pt nanoparticles may be promising for future ultrahigh-density magnetic recording media applications [230]. In 2000, Sun and co-workers [231] succeeded in preparation of monodispersed iron–platinum (FePt) nanoparticles by the reduction of platinum acetylacetonate and decomposition of iron pentacarbonyl in the presence of oleic acid and oleyl amine stabilizers. Composition of the FePt nanoparticle was readily controlled, and the size is tunable from 3 to 10 nm diameter with a standard deviation of less than 5%. The bimetallic nanoparticles self-assemble into 3-D superlattices. Thermal annealing can convert the internal particle structure from a chemically disordered fcc phase to the chemically ordered face-centered tetragonal phase and transforms the nanoparticle superlattices into ferromagnetic nanocrystal assemblies.

Recently we investigated ferromagnetic properties of CoPt bimetallic nanoparticles [232,233]. $CoPt_3$ nanoparticles can be prepared by a two-step reduction using $NaBH_4$ as a reductant. The bimetallic nanoparticles were characterized by thermogravimetry (TG) and differential thermal analysis (DTA), FT-IR, TEM) and XRD. Structural and spectroscopic studies showed that the bimetallic nanoparticles adopt an fcc crystalline structure with an average particle size of 2.6 nm. SQUID studies revealed that as-prepared nanoparticles were superparamagnetic at room temperature and ferromagnetic at 1.85 K with coercivity of 980 Oe. Thermal treatment of the samples at 500 °C causes an increase of particle size and a decrease of coercivity [232]. The results indicated that the addition of Ag (5.0 mol%) cannot change the size and crystal structure (i.e., fcc structure) of $CoPt_3$ nanoparticles. SQUID studies, however, revealed that the addition of Ag can notably improve the magnetic properties of $CoPt_3$, which could result from the interaction between Ag and $CoPt_3$ nanoparticles (Figure 16) [233].

Some rare-earth alloys are strong permanent magnets. In $SmCo_5$ bulk alloy with a $CaCu_5$-type crystalline structure is one of such strong permanent magnets practically used in daily life and industries. The $SmCo_5$ magnet shows strong magnet anisotropy, high Curie temperature, high coercivity, and high saturation magnetization. Gu et al. [234] previously reported the preparation of $SmCo_5$ nanoparticles by using $Sm(acac)_3$ and $Co(CO)_8$ as precursors. The resulting nanoparticles were, however, unstable in air, and did not show any coercivity. Recently we have successfully prepared $SmCo_5$ bimetallic nanoparticles by simultaneous reduction of $SmCl_3$ and $Co(acac)_3$ in the presence of PVP at 300 °C. Average particle size of the nanoparticles was determined to be ca. 33 nm based on TEM observation. Result of XRD measurement indicated that the nanoparticles have $CaCu_5$-type

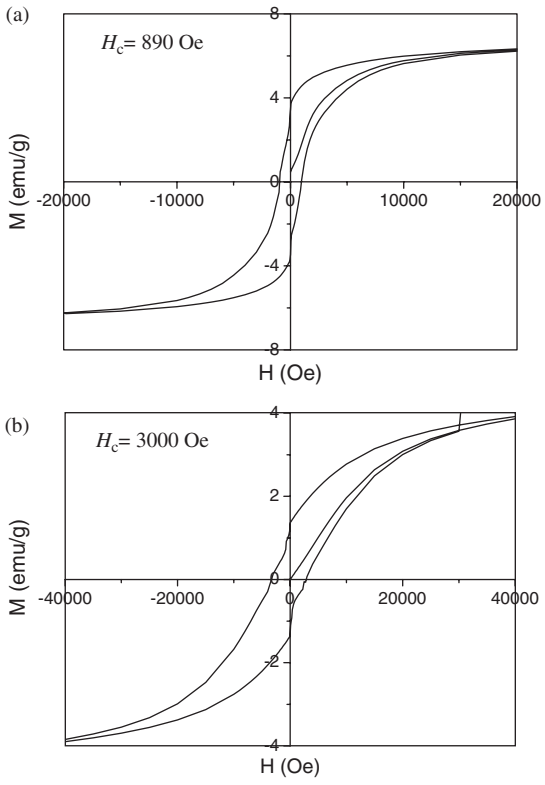

Figure 16. Hysteresis loops at 1.85 K of (a) as-synthesized $CoPt_3$ nanoparticles and (b) $CoPt_3$/Ag nanoparticles. (Reprinted from Ref. [233], © 2006, with permission from The Chemical Society of Japan.)

crystalline structure. Magnetization hysterisis showed high coercivity, 1100 Oe at room temperature, as shown in Figure 17 [235]. To the best of our knowledge, it was the first report on room temperature ferromagnetism of bimetallic nanoparticles containing rare-earth element. Rare-earth nanomagnets could be a candidate for future magnetic memory device, although their stability against oxidation will be a disadvantage of rare-earth nanomagnets.

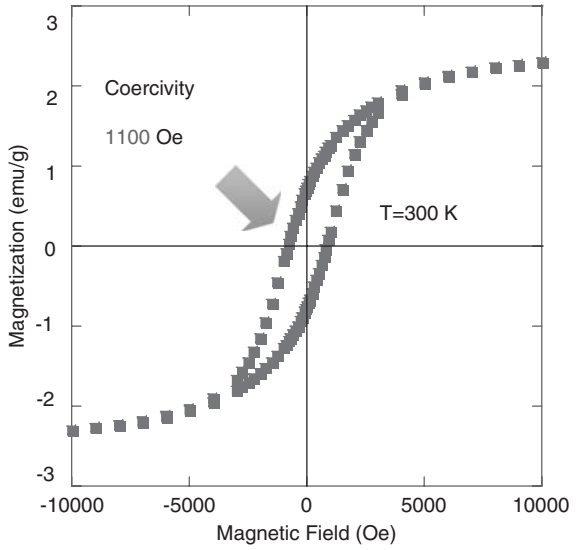

Figure 17. The magnetization hysteresis curve at 300 K of $SmCo_3$ nanoparticles prepared from $SnCl_3$ and $Co(acac)_3$ in the presence of PVP at 573 K. (Reprinted from Ref. [235], © 2006, with permission from Wiley-VCH.)

4.3. Electro-Optical Properties of Bimetallic Nanoparticle-Doped Liquid Crystal Displays

An LCD is a ubiquitous electronic display. Now, it is widely distributed among human daily life, like mobile phones, TV, and personal computers. The LCD has, however, a drawback, i.e., slower response than a plasma display or an electroluminescene display. Recently we have first succeeded in combination of a nanoparticle technology with the LCD technology, which realized fast response of the LCD [45,235,236]. Thus we have found a phenomenon, i.e., a frequency modulation of the LCD doped with metallic nanoparticles. Since the frequency modulation, or electro-optic property depends on the kind of metals, we have prepared AgPd bimetallic nanoparticles protected with a typical liquid crystal molecule, 4-cyano-4′-pentylbiphenyl (5CB) to investigate the electro-optic property [45,235,236].

The 5CB twist nematic liquid crystal doped with 5CB-protected AgPd (atomic ratio, 1:4) bimetallic nanoparticles showed different V-T curves depending on the frequency, as shown in Figure 18 [236]. The frequency range of the frequency modulation effect is wider for the 5CB-AgPd system than that of the 5CB-Pd system [236]. Since 5CB-Ag nanoparticles were unstable to oxidation in the repeated usage, the AgPd bimetallic nanoparticles were the good answer for the present purpose.

Furthermore, the LCD containing the 5CB-protected AgPd nanoparticles showed fast response compared with the LCD containing pure 5CB. The rising response time t_r and the rising delaying time t_{dr} were 1.9 and 0.9 ms, respectively, when the applied voltage and frequency varied from 5.1 V and 100 Hz to 17 V (5 cycles) or 5.1 V and 500 Hz, respectively. The response times were much shorter than those of 5CB, 7.8 and 2.1 ms, respectively [235,236]. Recently practical STN-LCD was doped with AgPd bimetallic nanoparticles, showing fast response

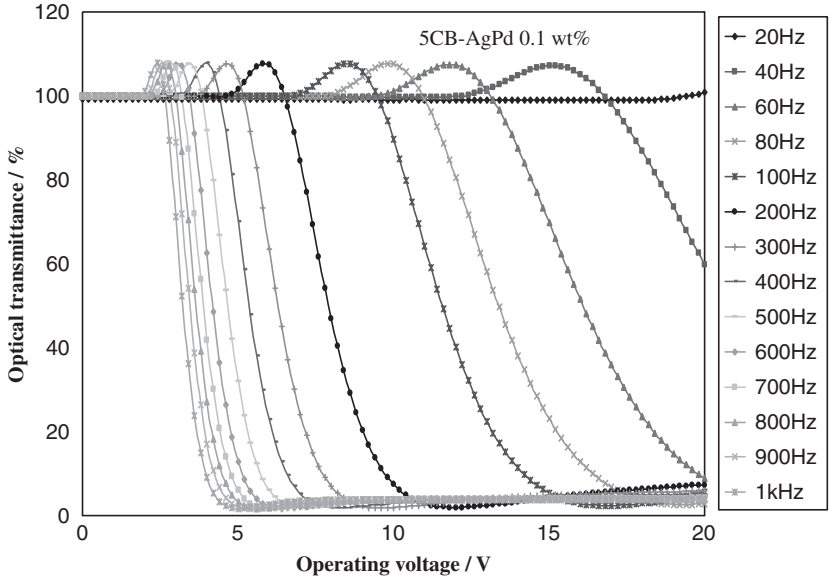

Figure 18. Electro-optic characteristics of an FM/AM-TN LCD with AgPd nanoparticles (5CB-AgPd 0.1%) where the frequency of operating voltages is used as a parameter. (Reprinted from Ref. [236], © 2006, with permission from IEEE.)

even at low temperature, like −10 °C. This could result in practical use of bimetallic nanoparticle-doped STN-LCD as a display for mobile phones, which are often used at low temperature outdoors in winter. Likewise, nanoparticle-doped LCD will provide new generation of LCD.

5. Concluding Remarks

Recent developments in chemistry make it easy to construct the bimetallic nanoparticles with the desired size and structure. Design of not only size and structure of metal parts of the nanoparticles but also properties and alignment of organic phase surrounding the nanoparticles become increasingly important to develop tailor-made catalysts. Recent research targets on metal nanoparticles for catalysis are: (i) control of size and structures of metal parts [237], especially those of bimetallic and multimetallic nanoparticles [238], (ii) control of the structures and properties of the organic surroundings of metal nanoparticles, especially for stabilization of catalysts and improvement of selectivity, and (iii) application of metal nanoparticles to practical catalysts, e.g., by supporting on inorganic supports [239–242]. Monometallic nanoparticle or bimetallic nanoparticle catalysts can now be applied to a lot of reactions. Hydrogenation and hydrosilation of olefins or dienes are one of the most popular reactions. Other kinds of selective reductions and C–C coupling reactions like Heck reaction and Suzuki reaction are the other targets. Oxidation reactions have been less reported because the organic stabilizers are usually less stable for oxidation than for reduction. However, this limitation is now removed by using more stable stabilizers or removing organic stabilizer from inorganic supports. Real tailor-made bimetallic nanoparticle catalysts for industrial purposes will be expected to be developed on the basis of the basic research results on metal nanoparticles in the near future.

From the viewpoint of size control, bimetallic nanoparticles naturally have a strong tendency to provide monodispersed particles, compared with monometallic nanoparticles [49]. This tendency cannot be completely understood yet, but redox properties between two metals might result in this advantageous properties of bimetallic nanoparticles.

Since Sun et al. [231] first reported ferromagnetism of superlattice of FePt bimetallic nanoparticles, the nanoscaled ferromagnetic materials have attracted much attention. We also succeeded in preparation of $SmCo_5$ bimetallic nanoparticles with enough high coercivity (1500 Oe) at room temperature, providing a potential application to super-high-density memory storage. The applications of monometallic or bimetallic nanoparticles to the LCD are an emerging research area. The monometallic or the bimetallic nanoparticles are expected to improve the response time of the LCD, which may further extend the practical application of the LCD.

It is said that the 21st century is the age of nanotechnology since nanoparticles are applicable to an increasing number of areas. Therefore, this research field will occupy the much attention of scientists. Precisely controlling the primary size and structure of metallic nanoparticles, i.e., size, shape, crystal structure, and composition, however, is still most important, because the structures dominate the physical and chemical properties of metallic nanoparticles. The development of methodology to control the primary size, structure, and composition of bimetallic nanoparticles for further improvement of catalytic activity and selectivity and to fabricate novel nanodevices by the bimetallic nanoparticles will be the key of nanotechnology.

References

1 G. Schmid, *Clusters and Colloids: From Theory to Application*, VCH, Weinheim, 1994.
2 N. Toshima, T. Yonezawa, *New J. Chem.* 22 (1998) 1179.
3 N. Toshima, Y. Shiraishi, Catalysis by metallic colloids, in A. T. Hubbard (ed.) *Encyclopedia of Surface and Colloid Science*, Marcel Dekker, New York, 2002, 879–886.
4 H. Hirai, N. Toshima, in Y. Iwasawa, D. Reidel (eds.) *Tailored Metal Catalysts*, Reidel Pub., Dordrecht, 1986.
5 T. Teranishi, N. Toshima, in A. Wieckowski, E. R. Savinova, C. G. Vayenas (eds.) *Catalysis and Electrocatalysis at Nanoparticle Surfaces*, Marcel Dekker Inc., New York, 2003.
6 M. Faraday, *Phil. Trans. R. Soc.* 147 (1857) 145.
7 J. M. Thomas, *Pure Appl. Chem.* 60 (1988) 1517.
8 L. D. Rampio, F. F. Nord, *J. Am. Chem. Soc.* 63 (1941) 2745.
9 L. D. Rampio, F. F. Nord, *J. Am. Chem. Soc.* 63 (1941) 3268.
10 L. D. Rampio, F. F. Nord, *J. Am. Chem. Soc.* 65 (1943) 429.
11 J. Turkevich, P. C. Stevenson, J. Hillier, *Disc. Faraday Soc.* 11 (1951) 55.
12 J. Turkevich, G. Kim, *Science* 169 (1970) 873.
13 J. B. Michel, J. T. Schwartz, in B. Delmon, P. Grange, P. A. Jacobs, G. Poncelet (eds.) *Catalyst Preparation Science*, Vol. IV, Elsevier, New York, 1987, 669.
14 H. Hirai, Y. Nakao, N. Toshima, K. Adachi, *Chem. Lett.* 1976 (1976) 905.
15 N. Toshima, K. Kushihashi, T. Yonezawa, H. Hirai, *Chem. Lett.* 1989 (1989) 1769.
16 N. Toshima, M. Harada, T. Yonezawa, K. Kushihashi, K. Asakura, *J. Phys. Chem.* 95 (1991) 7448.
17 J. H. Sinfelt, *J. Catal.* 29 (1973) 308.
18 J. H. Sinfelt, *Acc. Chem. Res.* 20 (1987) 134.
19 G. Meitzner, G. H. Via, F. W. Lytle, J. H. Sinfelt, *J. Chem. Phys.* 78 (1983) 882.
20 G. Meitzner, G. H. Via, F. W. Lytle, J. H. Sinfelt, *J. Chem. Phys.* 78 (1983) 2533.
21 G. Meitzner, G. H. Via, F. W. Lytle, J. H. Sinfelt, *J. Chem. Phys.* 83 (1985) 4793.
22 G. C. Papavassiliou, *J. Phys. F: Met. Phys.* 6 (1976) L103.
23 K. J. Klabunde, Y. -X. Li, B. -J. Tan, *Chem. Mater.* 3 (1991) 30.
24 N. Sato, H. Hasegawa, K. Tsuji, K. Kimura, *J. Phys. Chem.* 98 (1994) 2143.
25 Y. Takeuchi, T. Ida, K. Kimura, *J. Phys. Chem. B* 101 (1997) 1322.
26 A. Fojtik, A. Henglein, *Ber. Bunsen-Ges. Phys. Chem.* 97 (1993) 252.
27 M. S. Sibbald, G. Chumanov, T. M. Cotton, *J. Phys. Chem.* 100 (1996) 4672.
28 A. M. Morales, C. M. Lieber, *Science* 279 (1998) 208.
29 M. S. Yeh, Y. S. Yang, Y. P. Lee, H. F. Lee, Y. H. Yeh, C. S. Yeh, *J. Phys. Chem. B* 103 (1999) 6851.
30 S. Link, Z. L. Wang, M. A. El-Sayed, *J. Phys. Chem. B* 103 (1999) 3529.
31 M. Brust, M. Walker, D. Bethell, D. J. Schiffrin, R. Whyman, *J. Chem. Soc. Chem. Commun.* 1994 (1994) 801.
32 L. M. Liz-Marzán, A. P. Philipse, *J. Phys. Chem.* 99 (1995) 15120.

33 S. W. Han, Y. Kim, K. Kim, *J. Colloid Interface Sci.* 208 (1998) 272.
34 T. Teranishi, M. Miyake, *Chem. Mater.* 10 (1998) 594.
35 T. Teranishi, I. Kiyokawa, M. Miyake, *Adv. Mater.* 10 (1998) 596.
36 T. Teranishi, M. Hosoe, T. Tanaka, M. Miyake, *J. Phys. Chem. B* 103 (1999) 3818.
37 Y. Yonezawa, T. Sato, S. Kuroda, K. I. Kuge, *J. Chem. Soc. Faraday Trans.* 87 (1991) 1905.
38 H. H. Huang, X. P. Ni, G. L. Loy, C. H. Chew, K. L. Tan, F. C. Loh, J. F. Deng, G. Q. Xu, *Langmuir* 12 (1996) 909.
39 M. M. Mdleleni, T. Hyeon, K. S. Suslick, *J. Am. Chem. Soc.* 120 (1998) 6189.
40 B. Li, Y. Xie, J. Huang, Y. Liu, Y. Qian, *Chem. Mater.* 12 (2000) 2614.
41 M. T. Reetz, W. H. Helbig, *J. Am. Chem. Soc.* 116 (1994) 740.
42 Y. Y. Yu, S. S. Chang, C. L. Lee, C. R. C. Wang, *J. Phys. Chem. B* 101 (1997) 6661.
43 J. L. Marignier, J. Belloni, M. O. Delcourt, J. P. Chevalier, *Nature* 317 (1985) 344.
44 A. Henglein, *J. Phys. Chem. B* 104 (2000) 2201.
45 Y. Shiraishi, N. Toshima, K. Maeda, H. Yoshikawa, J. Xu, S. Kobayashi, *Appl. Phys. Lett.* 81 (2005) 2845.
46 N. Toshima, Polymer-capped bimetallic nanoclusters as active and selective catalysts, in N. Ueyama, A. Harada (eds.) *Macromolecular Nanostructured Materials*, Kodansha/ Springer, Tokyo/Berlin, 2004, 182.
47 N. Toshima, Metal nanoparticles for catalysis, in L. M. Liz-Marzan, P. V. Kamat (eds.) *Nanoscale Materials*, Kluwer Academic Publishers, Dordrecht, 2003, 79.
48 N. Toshima, T. Yonezawa, K. Kushihashi, *J. Chem. Soc. Faraday Trans.* 89 (1993) 2537.
49 N. Toshima, Y. Shiraishi, T. Teranishi, M. Miyake, T. Tominaga, H. Watanabe, W. Brijoux, H. Bönnemann, G. Schmid, *Appl. Organometal. Chem.* 15 (2001) 178.
50 R. S. Miner, S. Namba, J. Turkevich, Proceedings of the 7th International Congress on Catalysis, Kodansha, Tokyo, 1981.
51 M. Hansen, *Constitutions of Binary Alloys*, McGraw Hill, New York, 1958.
52 N. Toshima, M. Harada, Y. Yamazaki, K. Asakura, *J. Phys. Chem.* 96 (1992) 9927.
53 T. Yonezawa, N. Toshima, *J. Mol. Catal.* 83 (1993) 167.
54 M. Harada, K. Asakura, N. Toshima, *Jpn. J. Appl. Phys.* 32 (1993) 451.
55 B. Zhao, N. Toshima, *Chem. Express* 5 (1990) 721.
56 T. Hashimoto, S. Kenji, M. Harada, N. Toshima, *J. Chem. Phys.* 109 (1998) 5627.
57 M. J. Hostetler, C. -J. Zhong, B. K. H. Yen, J. Anderegg, S. M. Gross, N. D. Evans, M. Porter, R. W. Murray, *J. Am. Chem. Soc.* 20 (1998) 9396.
58 Y. Lou, M. M. Maye, L. Han, J. Luo, C. -J. Zhong, *Chem. Commun.* 2001 (2001) 473.
59 R. Touroude, P. Girard, G. Maire, J. Kizling, M. Boutonnet-Kizling, P. Stenius, *Colloids Surf.* 67 (1992) 9.
60 M. -L. Wu, D. -H. Chen, T. -C. Huang, *Chem. Mater.* 13 (2001) 599.
61 M. Liu, W. Yu, H. Liu, J. Zheng, *J. Colloid Interface Sci.* 214 (1999) 231.
62 C. Pan, F. Dassenoy, M. –J. Casanove, K. Philippot, C. Amiens, P. Lecante, A. Mosset, B. Chaudret, *J. Phys. Chem. B* 103 (1999) 10098.
63 K. Esumi, M. Wakabayashi, K. Torigoe, *Colloids Surf. A: Physicochem. Eng. Aspects* 109 (1996) 55.
64 A. Henglein, C. Brancewicz, *Chem. Mater.* 9 (1997) 2164.
65 T. J. Schmidt, M. Noeske, H. A. Gasteiger, R. J. Behm, P. Britz, W. Brijoux, H. Bönnemann, *Langmuir* 13 (1997) 2591.
66 T. J. Schmidt, M. Noeske, H. A. Gasterger, R. J. Behm, P. Britz, H. Bönnemann, *J. Electrochem. Soc.* 145 (1998) 925.
67 W. Vogel, P. Britz, H. Bönnemann, J. Rothe, J. Hormes, *J. Phys. Chem. B* 101 (1997) 11029.
68 Y. Mizukoshi, T. Fujimoto, Y. Nagata, R. Oshima, Y. Maeda, *J. Phys. Chem. B* 104 (2000) 6028.
69 Y. Mizukoshi, K. Okitsu, Y. Maeda, T. A. Yamamoto, R. Oshima, Y. Nagata, *J. Phys. Chem. B* 101 (1997) 7033.
70 R. M. Crooks, M. Zhao, L. Sun, V. Chechik, L. L. Yeung, *Acc. Chem. Res.* 34 (2001) 181.
71 N. Toshima, Y. Wang, *Chem. Lett.* 1993 (1993) 1611.
72 N. Toshima, Y. Wang, *Langmuir* 10 (1994) 4574.
73 N. Toshima, Y. Wang, *Adv. Mater.* 6 (1994) 245.
74 F. Fievet, J. P. Lagier, B. Blin, *Solid State Ionics* 32–33 (1989) 198.
75 P. Lu, J. Dong, N. Toshima, *Langmuir* 15 (1999) 7980.
76 N. Toshima, P. Lu, *Chem. Lett.* 1996 (1996) 729.
77 P. Lu, T. Teranishi, K. Asakura, M. Miyake, N. Toshima, *J. Phys. Chem. B* 103 (1999) 9673.
78 P. Lu, N. Toshima, *Bull. Chem. Soc. Jpn.* 73 (2000) 751.
79 K. Esumi, T. Tano, K. Torigoe, K. Meguro, *Chem. Mater.* 12 (1990) 564.
80 J. S. Bradley, E. W. Hill, C. Klein, B. Chaudret, A. Duteil, *Chem. Mater.* 5 (1993) 254.
81 T. Ould-Ely, C. Pan, C. Amiens, B. Chaudret, F. Dassenoy, P. Lecante, M. -J. Casanove, A. Mosset, M. Respaud, J. -M. Broto, *J. Phys. Chem. B* 104 (2000) 695.
82 D. H. Chen, C. J. Chen, *J. Mater. Chem.* 12 (2002) 1557.
83 M. P. Mallin, C. J. Murphy, *Nano Lett.* 2 (2002) 1235.
84 M. J. Kim, H. J. Na, K. C. Lee, E. A. Yoo, M. Y. Lee, *J. Mater. Chem.* 13 (2003) 1789.
85 B. Rodriguez-Gonzalez, A. Sanchez-Iglesias, M. Giersig, L. M. Liz-Marzan, *Faraday Discuss.* 125 (2004) 133.
86 S. Devarajan, B. Vimalan, S. Sampath, *J. Colloid Interface Sci.* 278 (2004) 126.
87 N. N. Kariuki, J. Luo, M. M. Maye, S. A. Hassan, T. Menard, H. R. Naslund, Y. H. Lin, C. M. Wang, M. H. Engelhard, C. J. Zhong, *Langmuir* 20 (2004) 11240.
88 T. Endo, T. Yoshimura, K. Esumi, *J. Colloid Interface Sci.* 286 (2005) 602.
89 A. Q. Wang, C. M. Chang, C. Y. Mou, *J. Phys. Chem. B* 109 (2005) 18860.
90 A. V. Singh, B. M. Bandgar, M. Kasture, B. L. V. Prasad, M. Sastry, *J. Mater. Chem.* 15 (2005) 5115.
91 R. J. Chimentao, I. Cota, A. Dafinov, F. Medina, J. F. Sueiras, J. L. G. de la Fuente, J. L. G. Fierro, Y. Cesteros, P. Salagre, *J. Mater. Res.* 21 (2006) 105.
92 K. Patel, S. Kapoor, D. P. Dave, T. Mukherjee, *Res. Chem. Chem. Intermed.* 32 (2006) 103.
93 D. Garcia-Gutierrez, C. Gutierrez-Wing, M. Miki-Yoshida, M. Jose-Yacaman, *Appl. Phys. A* 79 (2004) 481.
94 P. N. Njoki, J. Luo, L. Y. Wang, M. M. Maye, H. Quaizar, C. J. Zhong, *Langmuir* 21 (2005) 1623.
95 R. Esparza, J. A. Ascencio, G. Rosas, J. F. S. Ramirez, U. Pal, R. Perez, *J. Nanosci. Nanotechol.* 5 (2005) 641.
96 T. Endo, T. Kuno, T. Yoshimura, K. Esumi, *J. Nanosci. Nanotechol.* 5 (2005) 1875.
97 Y. H. Chen, Y. H. Tseng, C. C. Yeh, *J. Mater. Chem.* 12 (2002) 1419.
98 Y. M. Chung, H. K. Rhee, *J. Colloid Interface Sci.* 271 (2004) 131.
99 U. Pal, J. F. S. Ramirez, H. B. Liu, A. Medina, J. A. Ascencio, *Appl. Phys. A* 79 (2004) 79.
100 S. Nath, A. Pal, S. K. Ghosh, S. Praharaj, S. Panigrahi, S. Kundu, T. Thundat, T. Pal, *J. Nanosci. Nanotechol.* 5 (2005) 1832.
101 S. H. Choi, S. Lee, S. J. Kim, S. H. Sohn, H. D. Kang, Y. P. Zhang, K. P. Lee, J. H. Chun, *Catal. Today* 105 (2005) 59.

102 J. F. Sanchez-Ramirez, J. L. J. Perez, A. C. Orea, R. G. Fuentes, A. Bautista-Hernandez, U. Pal, *J. Nanosci. Nanotechol.* 6 (2006) 685.
103 M. L. Wu, L. B. Lai, *Colloid Surf. A* 244 (2004) 149.
104 J. M. Thomas, B. F. G. Johnson, R. Raja, G. Sankar, P. A. Midgley, *Acc. Chem. Res.* 36 (2003) 20.
105 X. Zhang, K. Y. Chan, *Chem. Mater.* 15 (2003) 451.
106 S. Rojas, F. J. Garcia-Garcia, S. Jaras, M. V. Martinez-Huerta, J. L. G. Fierro, M. Boutonnet, *Appl. Cat. A* 285 (2005) 24.
107 M. Mandal, S. Kundu, S. K. Ghosh, T. K. Sau, S. M. Yusuf, T. Pal, *J. Colloid Interface Sci.* 265 (2003) 23.
108 T. C. Deivaraj, W. X. Chen, J. Y. Lee, *J. Mater. Chem.* 13 (2003) 2555.
109 S. K. Ghosh, M. Mandal, S. Kundu, S. Nath, T. Pal, *Appl. Catal. A* 268 (2004) 61.
110 T. C. Deivaraja, J. Y. Lee, *J. Electrochem. Soc.* 151 (2004) A1832.
111 J. Solla-Gullon, A. Rodes, V. Montiel, A. Aldaz, J. Clavilier, *J. Electroanal. Chem.* 554 (2003) 273.
112 W. H. Wang, X. L. Tian, K. Chen, G. Y. Cao, *Colloid. Surf. A* 273 (2006) 35.
113 Y. M. Chung, H. K. Rhee, *J. Mol. Catal. A* 206 (2003) 291.
114 X. Wang, W. B. Yue, M. S. He, M. H. Liu, J. Zhang, Z. F. Liu, *Chem. Mater.* 16 (2004) 799.
115 Y. H. Tee, E. Grulke, D. Bhattacharyya, *Ind. Eng. Chem. Res.* 44 (2005) 7062.
116 J. Feng, C. P. Zhang, *J. Colloid Interface Sci.* 293 (2006) 414.
117 T. Ould-Ely, J. H. Thurston, A. Kumar, M. Respaud, W. H. Guo, C. Weidenthaler, K. H. Whitmire, *Chem. Mater.* 17 (2005) 4750.
118 R. Harpeness, A. Gedanken, *Langmuir* 20 (2004) 3431.
119 S. Nath, S. Praharaj, S. Panigrahi, S. K. Ghosh, S. Kundu, S. Basu, T. Pal, *Langmuir* 21 (2005) 10405.
120 S. S. Shankar, A. Rai, A. Ahmad, M. Sastry, *J. Colloid Interface Sci.* 275 (2004) 496.
121 S. Panigrahi, S. Kundu, S. K. Ghosh, S. Nath, T. Pal, *Colloid. Surf. A* 264 (2005) 133.
122 D. I. Garcia-Gutierrez, C. E. Gutierrez-Wing, L. Giovanetti, J. M. Ramallo-Lopez, F. G. Requejo, M. Jose-Yacaman, *J. Phys. Chem. B* 109 (2005) 3813.
123 H. M. Chen, H. C. Peng, R. S. Liu, S. F. Hu, L. Y. Jang, *Chem. Phys. Lett.* 420 (2006) 484.
124 H. M. Chen, R. S. Liu, L. Y. Jang, J. F. Lee, S. F. Hu, *Chem. Phys. Lett.* 421 (2006) 118.
125 M. Harada, K. Asakura, N. Toshima, *J. Phys. Chem.* 97 (1993) 5103.
126 T. Teranishi, M. Miyake, *Chem. Mater.* 11 (1999) 3414.
127 G. Schmid, A. Lehnert, J. -O. Malm, J. -O. Bovin, *Angew. Chem. Int. Ed. Engl.* 30 (1991) 874.
128 G. Schmid, H. West, J. -O. Malm, J. -O. Bovin, C. Grenthe, *Chem. Eur. J.* 2 (1996) 1099.
129 A. F. Lee, C. J. Baddeley, C. Hardacre, R. M. Ormerod, R. M. Lambert, G. Schmid, H. West, *J. Phys. Chem.* 99 (1995) 6096.
130 G. Schmid, A. Lehnert, *Angew. Chem. Int. Ed. Engl.* 28 (1989) 780.
131 M. Michaelis, A. Henglein, *J. Phys. Chem.* 98 (1994) 6212.
132 Y. Wang, N. Toshima, *J. Phys. Chem. B* 101 (1997) 5301.
133 P. R. Selvakannan, A. Swami, D. Srisathiyanarayanan, P. S. Shirude, R. Pasricha, A. B. Mandale, M. Sastry, *Langmuir* 20 (2004) 7825.
134 O. M. Wilson, R. W. J. Scott, J. C. Garcia-Martinez, R. M. Crooks, *J. Am. Chem. Soc.* 127 (2005) 1015.
135 M. Tsuji, N. Miyamae, K. Matsumoto, S. Hikino, T. Tsuji, *Chem. Lett.* 34 (2005) 1518.
136 I. Srnova-Sloufova, B. Vlckova, Z. Bastl, T. L. Hasslett, *Langmuir* 20 (2004) 3407.
137 J. Yang, J. Y. Lee, L. X. Chen, H. P. Too, *J. Nanosci. Nanotechol.* 5 (2005) 1095.
138 J. Yang, J. Y. Lee, H. P. Too, *J. Phys. Chem. B* 109 (2005) 19208.
139 Y. Cui, B. Ren, J. L. Yao, R. A. Gu, Z. Q. Tian, *J. Phys. Chem. B* 110 (2006) 4002.
140 J. Yang, J. Y. Lee, L. X. Chen, H. P. Too, *J. Phys. Chem. B* 109 (2005) 5468.
141 K. Vinodgopal, Y. H. He, M. Ashokkumar, F. Grieser, *J. Phys. Chem. B* 110 (2006) 3849.
142 C. Damle, A. Kumar, M. Sastry, *J. Phys. Chem. B* 106 (2002) 297.
143 C. X. Kan, W. P. Cai, C. C. Li, L. D. Zhang, H. Hofmeister, *J. Phys. D* 36 (2003) 1609.
144 Y. Shiraishi, D. Ikenaga, N. Toshima, *Aust. J. Chem.* 56 (2003) 1025.
145 W. R. Lee, M. G. Kim, J. R. Choi, J. I. Park, S. J. Ko, S. J. Oh, J. Cheon, *J. Am. Chem. Soc.* 127 (2005) 16090.
146 N. Toshima, M. Kanemaru, Y. Shiraishi, Y. Koga, *J. Phys. Chem. B* 109 (2005) 16326.
147 M. Kanemaru, Y. Shiraishi, Y. Koga, N. Toshima, *J. Therm. Anal. Calor.* 81 (2005) 523.
148 K. Hirakawa, N. Toshima, *Chem. Lett.* 32 (2003) 78.
149 A. B. Smetana, K. J. Klabunde, C. M. Sorensen, A. A. Ponce, B. Mwale, *J. Phys. Chem. B* 110 (2006) 2155.
150 Z. Q. Peng, B. Spliethoff, B. Tesche, T. Walther, K. Kleinermanns, *J. Phys. Chem. B* 110 (2006) 2549.
151 Z. L. Wang, *J. Phys. Chem. B* 104 (2000) 1153.
152 Z. L. Wang, *Adv. Mater.* 10 (1998) 13.
153 J. H. Hodak, A. Henglein, M. Giersig, G. V. Hartland, *J. Phys. Chem. B* 104 (2000) 11708.
154 J. Belloni, M. Mostafavi, H. Remita, J. L. Marignier, M. O. Delcourt, *New J. Chem.* 22 (1998) 1239.
155 G. Mie, *Ann. Phys.* 25 (1908) 377.
156 U. Kreibig, M. Vollmer, *Optical Properties of Metal Clusters*, Springer, Berlin, 1995.
157 G. C. Papavassiliou, *Prog. Solid State Chem.* 12 (1980) 185.
158 J. A. A. J. Perenboom, P. Wyder, P. Meier, *Phys. Rep.* 78 (1981) 173.
159 A. E. Hughes, S. C. Jain, *Adv. Phys.* 28 (1979) 717.
160 M. Kerker, *The Scattering of Light and other Electromagnetic Radiation*, Academic Press, New York, 1969.
161 C. F. Bohren, D. R. Huffman, *Absorption and Scattering of Light by Small Particles*, Wiley, New York, 1983.
162 J. A. Creighton, D. G. Eadon, *J. Chem. Soc. Faraday Trans.* 87 (1991) 3881.
163 P. Mulvaney, *Langmuir* 12 (1996) 788.
164 J. Sinzig, U. Radtke, M. Quinten, U. Z. Kreibig, *Phys. D* 26 (1993) 242.
165 B. K. Teo, K. Keating, Y. -H. Kao, *J. Am. Chem. Soc.* 109 (1987) 3494.
166 P. Mulvaney, M. Giersig, A. Henglein, *J. Phys. Chem.* 97 (1993) 7061.
167 T. Sato, S. Kuroda, A. Takami, Y. Yonezawa, H. Hada, *Appl. Organomet. Chem.* 5 (1991) 261.
168 J. Luo, M. M. Maye, V. Petkov, N. N. Kariuki, L. Y. Wang, P. Njoki, D. Mott, Y. Lin, C. J. Zhong, *Chem. Mater.* 17 (2005) 3086.
169 C. W. Hills, N. H. Mack, R. G. Nuzzo, *J. Phys. Chem. B* 107 (2003) 2626.
170 J. H. Sinfelt, G. H. Via, F. W. Lytle, *Catal. Rev. Sci. Eng.* 26 (1984) 81.
171 Y. Iwasawa, *X-Ray Absorption Fine Structure for Catalysts and Surfaces, World Scientific Series on Synchrotron Radiation Techniques and Applications*, Vol. 2, World Scientific, Singapore, 1996.
172 D. C. Koningsberger, R. Prins (eds.) *X-Ray Absorption: Techniques of EXAFS, SEXAFS and XANES*, Wiley, New York, 1988.

173 G. H. Via, K. F. Drake Jr., G. Meitzner, F. W. Lytle, J. H. Sinfelt, *Catal. Lett.* 5 (1990) 25.
174 M. Harada, K. Asakura, Y. Ueki, N. Toshima, *J. Phys. Chem.* 97 (1993) 10742.
175 C. -R. Bion, S. Suzuki, K. Asakura, P. Lu, N. Toshima, *J. Phys. Chem. B* 106 (2002) 8587.
176 S. J. Cho, S. K. Kang, *Catal. Today* 93 (2004) 561.
177 J. S. Bradley, J. M. Millar, E. W. Hill, S. Behal, B. Chaudret, A. Duteil, *Faraday Discuss. Chem. Soc.* 30 (1991) 1312.
178 J. S. Bradley, E. W. Hill, S. Behal, C. Klein, B. Chaudret, A. Duteil, *Chem. Mater.* 4 (1992) 1234.
179 D. de Caro, J. S. Bradley, *Langmuir* 13 (1997) 3067.
180 J. S. Bradley, E. W. Hill, B. Chaudret, A. Duteil, *Langmuir* 11 (1995) 693.
181 J. S. Bradley, G. H. Via, L. Bonneviot, E. W. Hill, *Chem. Mater.* 8 (1996) 1895.
182 N. Toshima, Y. Shiraishi, Catalysis by metallic colloids, in A. T. Hubbard (ed.) *Encyclopedia of Surface and Colloid Science*, Marcel Dekker, New York, 2002, 879.
183 M.-L. Wu, D.-H. Chen, T.-C. Huang, *Langmuir* 17 (2001) 3877.
184 N. Toshima, Y. Shiraishi, A. Shiotsuki, D. Ikenaga, Y. Wang, *Eur. Phys. J. D* 16 (2001) 209.
185 H. Hirai, Y. Nakao, N. Toshima, *Chem. Lett.* 1978 (1978) 545.
186 H. Hirai, Y. Nakao, N. Toshima, *J. Macromol. Sci. Chem.* A12 (1979) 1117.
187 H. Hirai, Y. Nakao, N. Toshima, *J. Macromol. Sci. Chem.* A13 (1979) 727.
188 L. M. Brostein, D. M. Chernyshov, I. O. Volkov, M. G. Ezernitskaya, P. M. Valetsky, V. G. Matveeva, E. M. Sulman, *J. Catal.* 196 (2000) 302.
189 J. H. He, I. Ichinose, T. Kunitake, A. Nakao, Y. Shiraishi, N. Toshima, *J. Am. Chem. Soc.* 125 (2003) 11034.
190 S. J. Cho, R. Ryoo, *Catal. Lett.* 97 (2004) 71.
191 N. Toshima, T. Takahashi, H. Hirai, *Chem. Lett.* 1986 (1986) 35.
192 N. Toshima, T. Takahashi, H. Hirai, *Chem. Lett.* 1987 (1987) 1031.
193 N. Toshima, T. Takahashi, H. Hirai, *J. Macromol. Sci. Chem.* A25 (1988) 669.
194 N. Toshima, *Pure Appl. Chem.* 72 (2000) 317.
195 N. Toshima, K. Hirakawa, *Polym. J.* 31 (1999) 1127.
196 N. Toshima, K. Hirakawa, *Appl. Surf. Sci.* 121–122 (1997) 534.
197 S. Wasmus, A. Kuever, *J. Electroanal. Chem.* 461 (1999) 14.
198 J. Lipkowski, P. N. Ross Jr. (eds.) *Electrocatalysis, Frontiers in Electrochemistry*, Vol. 5, VCH, New York, 1997.
199 T. D. Jarvi, S. Sriramulu, E. M. Stuve, *J. Phys. Chem. B* 101 (1998) 3649.
200 M. Valden, X. Lai, D. W. Goodman, *Science* 281 (1998) 1647.
201 M. Haruta, *Catal. Today* 36 (1997) 153.
202 L. D. Burke, P. F. Nugent, *Gold Bull.* 31 (1998) 39.
203 G. C. Bond, *Catal. Rev.* 41 (1999) 319.
204 M. Haruta, *Nature* 437 (2005) 1098.
205 L. Guczi, A. Beck, A. Horvath, Z. Koppany, G. Stefler, K. Frey, I. Sajo, O. Geszti, D. Bazin, J. Lynch, *J. Mol. Catal. A* 204 (2003) 545.
206 L. D'Souza, S. Sampath, *Langmuir* 16 (2000) 8510.
207 S. Iijima, T. Ichihashi, *Nature* 363 (1993) 603.
208 Z. L. Wang, *Characterization of Nanophase Materials*, Wiley-VCH, New York, 2000.
209 D. B. Williams, C. B. Carter, *Transmission Electron Microscopy*, Plenum Press, New York, 1996.
210 Z. L. Wang, Z. C. Kang, *Functional and Smart Materials – Structural Evolution and Structure Analysis*, Chapter 6, Plenum Press, New York, 1988.
211 R. F. Egerton, *Electron Energy-Loss Spectroscopy in the Electron Microscope*. 2nd ed., Plenum Press, New York, 1996.
212 R. W. J. Scott, O. M. Wilson, R. M. Crooks, *J. Phys. Chem. B* 109 (2005) 692.
213 S. H. Zhou, B. Varughese, B. Eichhorn, G. Jackson, K. McIlwrath, *Angew. Chem. Int. Ed.* 44 (2005) 4539.
214 J. S. Li, M. Mirzamaani, X. P. Bian, M. Doerner, S. L. Duan, K. Tang, M. Toney, T. Arnoldussen, M. Madison, *J. Appl. Phys.* 85 (1999) 4286.
215 H. Crangle, *Phil. Mag.* 5 (1960) 335.
216 J. Crangle, W. R. Scott, *J. Appl. Phys.* 36 (1965) 921.
217 R. M. Bozorth, P. A. Wolff, D. D. Davis, V. B. Compton, J. H. Wernick, *Phys. Rev.* 122 (1961) 1157.
218 A. M. Clogston, B. T. Matthias, M. Peter, H. J. Williams, E. Corenzwit, R. C. Sherwood, *Phys. Rev.* 125 (1962) 541.
219 G. J. Nieuwenhusy, *Adv. Phys.* 24 (1975) 515.
220 D. Shaltiel, J. H. Wernick, H. J. Williams, M. Peter, *Phys. Rev.* 135 (1964) A1346.
221 T. Taniyama, E. Ohta, T. Sato, M. Takeda, *Phys. Rev. B* 55 (1997) 977.
222 W. Mörke, R. Lamber, U. Schubert, B. Breitscheidel, *Chem. Mater.* 6 (1994) 1659.
223 Y. Wang, H. F. Liu, N. Toshima, *J. Phys. Chem.* 100 (1996) 19533.
224 L. Zhu, K. S. Liang, B. Zhang, J. S. Bradley, A. E. DePristo, *J. Catal.* 167 (1997) 412.
225 S. Giorgio, C. Chapon, C. R. Henry, *Langmuir* 13 (1997) 2279.
226 N. Nunomura, T. Teranishi, M. Miyake, A. Oki, S. Yamada, N. Toshima, H. Hori, *J. Magn. Magn. Mater.* 177 (1998) 947.
227 N. Nunomura, H. Hori, T. Teranishi, M. Miyake, S. Yamada, *Phys. Lett. A* 249 (1998) 524.
228 H. Hori, T. Teranishi, T. Sasaki, M. Miyake, Y. Yamamoto, S. Yamada, H. Nojiri, M. Motokawa, *Physica B* 294 (2001) 292.
229 K. Inomata, T. Sawa, S. Hashimoto, *J. Appl. Phys.* 64 (1998) 2537.
230 D. Weller, A. Moser, *IEEE Trans. Magn.* 35 (1999) 4423.
231 S. Sun, C. B. Murray, D. Weller, L. Folks, A. Moser, *Science* 287 (2000) 1989.
232 X. Y. Du, M. Inokuchi, N. Toshima, *J. Magn. Magne. Mater.* 299 (2000) 121.
233 X. Y. Du, M. Inokuchi, N. Toshima, *Chem. Lett.* 35 (2006) 1254.
234 H. Gu, B. Xu, J. Rao, R. K. Zhang, X. X. Zhang, K. K. Fung, C. Y. C. Wong, *J. Appl. Phys.* 93 (2003) 7589.
235 N. Toshima, *Macromol. Symp.* 235 (2006) 1.
236 S. Kobayashi, T. Miyam, N. Nishida, Y. Sakai, H. Shiraki, Y. Shiraishi, N. Toshima, *J. Displ. Techol.* 2 (2006) 121.
237 S.-W. Kim, M. Kim, W. Y. Lee, T. Hyeon, *J. Am. Chem. Soc.* 124 (2002) 7642.
238 S. Hermans, R. Raja, J. M. Thomas, B. F. G. Johson, G. Sankar, D. Gleeson, *Angew. Chem. Int. Ed. Engl.* 40 (2001) 1211.
239 H. Bönnemann, W. Brijoux, A. S. Tilling, K. Siepen, *Top. Catal.* 4 (1997) 217.
240 H. Bönnemann, U. Endruschat, B. Tesche, A. Rufínska, C. W. Lehmann, F. E. Wagner, G. Filoti, V. Pârvulescu, V. I. Pârvulescu, *Eur. J. Inorg. Chem.* 2000 (2000) 819.
241 J. P. M. Niederer, A. B. J. Arnold, W. F. Hölderich, B. Spliethof, B. Tesche, M. Reetz, H. Bönnemann, *Top. Catal.* 18 (2002) 265.
242 H. Bönnemann, N. Waldöfner, *Chem. Mater.* 14 (2002) 1115.

This page intentionally left blank

CHAPTER 4

Metal Nanoclusters: Electronic Aspects and Physico-Chemical Characterization

László Guczi[1,2], Zoltán Pászti[2], and Gábor Pető[3]

[1]*Department of Surface Chemistry and Catalysis, Institute of Isotope, HAS, Budapest*
[2]*Laboratory for Nanostructured Metal Catalysts, Institute of Surface Chemistry and Catalysis, Chemical Research Center, Budapest*
[3]*Institute of Technical Physics and Materials Science, HAS, Budapest*

1. Introduction

Over the last few years, research in the area of nanoscience has blossomed into an independent and highly interdisciplinary area [1]. Materials in the nanometer scale (size range 1 nm–1 μm) are typically referred to as nanoparticles, nanocrystals, nanorods, or nanowires. Mono- or multiphase polycrystalline solid materials whose size falls – at least in one dimension – into the nanometer range (typically 1–100 nm) are regarded as representatives of different kinds of nanomaterials. Depending on the number of dimensions in the nanometer domain we can distinguish (i) nanoparticles, (ii) fibrillar structures, e.g. nanotubes, and (iii) layered structures [2,3]. In order to reach the region of nanoparticles the size of the domain should decrease. During size reduction the surface/volume ratio is enlarged and an interface is formed which is transformed into a metastable system through a series of quasi equilibrium states. The key issue in the field of nanoparticles is the easy functionalization of the interface due to its high excess free energy acquired. The surface irregularities, i.e. the presence of steps, kinks, terraces, as well as the ''dangling'' bonds of the atoms located at these sites, make it possible to create highly reactive species. The energy introduced into the system for modification of the surface may originate from various sources. For example, by introducing physical or chemical energies to the system active surface sites, e.g. catalysts, can be prepared [4–6].

Size reduction of metal particles results in several changes of the physico-chemical properties. The primary change is observed in the electronic properties of the metal particles which can be characterized by ultraviolet and X-ray photoelectron spectroscopy (UPS and XPS, respectively) as well as Auger-electron spectroscopy (AES) measurements. Furthermore, morphology of the metal nanoparticles is highly sensitive to the environment, such as ion–metal interaction (e.g. metal–support interaction) influencing also the electronic properties of the metal surface. Since metal nanoparticles have a short-range ordering, these particles are in metastable state, thus they must be stabilized against coalescence to prevent formation of large metal particles.

The unique material properties in this size range come from several sources: (1) quantum size effect [7], where confinement of charge carriers in a small space leads to discrete energy levels; (2) classical charging effects [8], which originate from the discrete nature of the electrical charge; (3) surface/interface effect [9], where properties of surface or interface atoms become much more significant, as the surface to volume ratio increases with decreasing of particle size. Many novel properties of single, isolated nanocrystal have been investigated during the past two decades, such as size-dependent optical absorption and luminescence in semiconductors [10,11], Coulomb blockade phenomena in charge transfer [12], and enhanced surface magnetic moments in magnetic nanocrystals [13].

The exciting aspect of nanocrystal arrays is that they form a truly new class of materials, where the basic building blocks are nanocrystals instead of atoms. The properties of these materials not only depend on which chemical elements used to form the building blocks, but also depend on how many atoms are in each building block and how strongly coupled these building blocks are. Traditional materials can be either crystalline or amorphous, depending on the arrangement of the constituent atoms. Similarly, nanocrystal arrays can also be ordered or disordered. In the former case, they are referred to as nanocrystal superlattices [14–17].

When any materials interact with their environment through solid/gas, solid/liquid, and solid/solid interfaces, the nanometer scale surface created can easily be modified to perform certain functions. The modifications are usually only effective in the few nanometer deep surface layers. This chapter highlights the development of new model nanostructured materials with functionalized interfaces to

Metal Nanoclusters in Catalysis and Materials Science: The Issue of Size Control
Edited by B. Corain, G. Schmid and N. Toshima

promote highly efficient and specific catalysts. The functional characteristics of nanoparticles (morphology, electronic structure) are thoroughly examined at atomic level by means of various techniques, e.g. transmission electron microscopy (TEM), UPS, XPS, AES, atomic force microscopy (AFM), etc. indicating a change in the metal nanoparticles/support interface which has also a consequence for the catalytic activity. In addition to physical methods, correlation is sought between physical characteristics and the material specificity, e.g. catalytic reaction monitored by the turnover frequency (TOF) to elucidate the role of surface ordering, restructuring, etc. Among the factors controlling the catalytic activity is the size of metal/support interface. Moreover, size dependent changes in the electronic structure of the metal nanoparticles are also expected to strongly influence their catalytic properties. Along with size reduction the metal d-valence band structure is investigated and the actual size is determined by UPS and TEM, respectively. The chemisorption and catalytic properties in various systems are also determined.

In Section 2 the general features of the electronic structure of supported metal nanoparticles are reviewed from both experimental and theoretical point of view. Section 3 gives an introduction to sample preparation. In Section 4 the size-dependent electronic properties of silver nanoparticles are presented as an illustrative example, while in Section 5 correlation is sought between the electronic structure and the catalytic properties of gold nanoparticles, with special emphasis on substrate-related issues.

2. General Principles

Small nanoparticles consisting of transition metal atoms possess catalytic properties which vary dramatically with size. An explanation for the factors involved in catalysis is expected from a thorough understanding of the electronic properties of these particles. To elucidate the correlation there has been active investigation of electronic properties and chemisorption of small metal particles. It is also thought that close analogies exist between the properties of small metal particles and regular periodic steps which exist on the surface of bulk metal single crystals [18]. The electronic properties of the stepped surfaces have been probed by several theoretical methods. In a particularly interesting study, surface virtual bound states have been calculated to exist at the Fermi surface of stepped Pt surfaces. While chemisorption may be a localized phenomenon, further understanding is needed how the electronic properties (for small metal particles and stepped surfaces) affect the chemisorptive and catalytic properties.

Application of small metal particles has attracted the attention of the scientists for a long time. As early as in the seventies Turkevich already prepared mono-dispersed gold particles [19], and later, using molecular transition metal carbonyl clusters [20], the importance of small nanoparticles increased considerably. One of the crucial points is whether turnover frequency measured for a given catalytic reaction increases or decreases as the particle size is diminished.

In the literature there are several attempts to measure this function. Che and Bennett found that e.g. for ethylene hydrogenation over palladium catalyst a maximum in TOF was shown as a function of particle size the maximum being at a particle of 0.6 nm diameter [21]. The Japanese school [22–24] observed controversial data on several systems at which TOF increased with reducing the particle size, although opposite results were also measured [25].

Advantages of small metal nanoparticles are: (i) short range ordering, (ii) enhanced interaction with environments due to the high number of dangling bonds, (iii) great variety of the valence band electron structure, and (iv) self-structuring for optimum performance in chemisorption and catalysis.

The valence band structure of very small metal crystallites is expected to differ from that of an infinite crystal for a number of reasons: (a) with a ratio of surface to bulk atoms approaching unity (ca. 2 nm diameter), the potential seen by the nearly free valence electrons will be very different from the periodic potential of an infinite crystal; (b) surface states, if they exist, would be expected to dominate the electronic density of states (DOS); (c) the electronic DOS of very small metal crystallites on a support surface will be affected by the metal–support interactions. It is essential to determine at what crystallite size (or number of atoms per crystallite) the electronic density of sates begins to depart from that of the infinite crystal, as the ''material state'' of the catalyst particle can affect changes in the surface thermodynamics which may control the catalysis and electro-catalysis of heterogeneous reactions as well as the physical properties of the catalyst particle [26].

Photoemission has been proved to be a tool for measurement of the electronic structure of metal nanoparticles. The information is gained for DOS in the valence-band region, ionization threshold, core-level positions, and adsorbate structure. In a very simplified picture photoemission transforms the energy distribution of the bounded electrons into the kinetic energy distribution of free electrons leaving the sample, which can easily be measured:

$$h\nu = \mathrm{KE} + \mathrm{BE} + \phi$$

where KE is the kinetic energy of the electrons after leaving the solid, $h\nu$ is the photon energy, BE is the binding energy in the solid and ϕ is the work function of the spectrometer. Since photoemission involves an electron excitation, a selection rule similar to the familiar ''dipole-selection rule'' in optical spectroscopy determines the probability of transitions observed.

In principle, it should be possible to obtain experimental valence band spectra of highly dispersed metals by photoemission. In practice, such spectra is difficult to obtain because very highly dispersed metals are usually obtained only on nonconductive supports and the resulting charging of the sample causes large chemical shifts and severe broadening of the photoelectron spectra. The purpose of this section is to discuss valence band and core level spectra of highly dispersed metal particles.

2.1. Valence Band and Core Level Characteristics of Metal Nanoparticles

In the eighties Baetzold and his school [27–33] carried out fundamental investigations on small clusters. The

photoemission spectra of Ag and Cu clusters, as a function of their coverage on carbon support, show considerable changes in the spectra as size (or coverage) increases [34]. The spectrum consists of a broad s-band region extending from the Fermi energy (E_F) to -4 eV, whereupon the d-state photoemission commences and extends through -8 eV. The width of the d-state region is sensitive to cluster size. At low coverage, the width of the photoemission spectrum is greater than the intrinsic cluster bandwidth, owing to final-state effects and substrate broadening. As coverage increases, the width of the d-states dominates and the total shape of the spectrum changes. In addition to this effect, there is a shift of -1.0 eV in the d-threshold, which moves toward a lower BE as cluster size increases. These effects are complete at 3.2×10^{15} atoms/cm^2, which corresponds to particles containing on the mean average 200 atoms [35]. A broadening of the d-band and shift in d-threshold toward E_F is observed with increasing cluster size. Below the coverage of 2×10^{15} atoms/cm^2 only one main peak exists in the d-emission region. Molecular orbital calculations for clusters of Ag, Pd, Cu, and Ni revealed that DOS for these clusters agrees closely with the experimental DOS value and displays similar size dependence. The surfaces of these clusters show a negative charge relative to the interior and this effect was analyzed in terms of d-orbital occupancy. As the size of the cluster increases its equilibrium bond length increases in accordance with experiment. The origin of this effect is explained by the electronic interactions involved in band formation. Generally, these efforts have focused on the electronic properties of clusters in the absence of interaction with support. Thus, these studies were primarily aimed at elucidating electronic properties such as BE, ionization potential (IP), valence DOS and electron configuration. Density of states (DOS) profiles determined by extended Hückel theory showed a broadening with increasing number of atoms in this size range. Oscillations in the electron affinity, BE, and IP for open and closed shells of electrons were observed for Ag cluster using the CNDO method [36]. The He(I) photoemission spectra for the bare Ag and Cu clusters show a broadening and shift in d-threshold towards the Fermi energy up to clusters of 150 atoms [32]. The result that transition and noble metal particles of 150 atoms or more are required to attain nearly "bulk-like" photoemission properties is probably one of the most firmly established findings in the area of small particles.

The adsorbate-covered clusters yield a UPS difference spectrum with two peaks on either side of the metal d-states. The dominant changes in the intensity ratio of these peaks occur up to 50-atom Ag clusters which can be rationalized in terms of the cluster d band width and IP, which both depend on cluster size.

Ionization potential of metal clusters is one of the factors affected by cluster size [33]. This study represents the most extensive effort so far to determine the size dependence of IP. The measurements on these clusters showed a decreasing IP with size with apparent oscillatory trend. Even-size particles had a relatively larger IP compared to their odd-size counterparts. The data show oscillatory behavior for small Na clusters with a loss of this oscillation for the larger Na clusters. The IP decreases with cluster size, but even at Na_{14} the value 3.5 eV is far from the bulk work function of 2.3 eV. The trends with size were compared with various quantum mechanical calculations, which show similar oscillations in IP, and classical calculations, which show no oscillations. An attempt to understand the geometries of the Na clusters studied by photoionization was made through the use of a pseudopotential calculation. This procedure requires very accurate computations to make the correct identifications, and the most stable computed structure does not always give an IP in best agreement with experiment.

Further experiments, in which iodine interacts with the cluster, have indicated that a chemisorbed iodine atom interacts significantly with at least 50 Ag atoms. This suggests that a rather long-range type of interaction is involved in determining the UPS He(I) spectrum of this chemisorbed species. It is interesting that the cluster size required for convergence of this property appears to be smaller than the size of 150 atoms required for the cluster UPS He(I) spectrum to become bulk like. The extended Hückel calculations [32] for DOS indicate that the strength of interaction between Cu d-orbitals and I p-orbitals increases as the cluster size increases. The factor responsible for this effect is a shift in the halogen orbitals toward the vacuum level as cluster size increases. This effect is also found with silver clusters and is consistent with the increasing d-bandwidth and decreasing IP as the cluster size increases.

Mason [27] measured photoelectron spectra for several coverage of silver evaporated on amorphous carbon ranging from isolated atoms to bulk. The spectra at lowest coverage show a peak at 6 eV relative to the Fermi level (E_F), which can be assigned to the 4d-levels. As the coverage is increased, the mean cluster size increases and the peak due to the d-levels broaden and eventually splits into two components at higher coverage. The threshold of the d-emission remains $\sim$4 eV below E_F, with a small intensity due to s, p electrons apparent at 0–4 eV. The spectra become bulk-like at coverage of 5×10^{15} atoms/cm^2. XPS was used to study gold deposited on amorphous carbon [37]. The spectra of gold clusters show weak features at 0–2 eV, with more intense structure due to the d-emission at 2–8 eV. The d-emission region of gold consists of two sub-bands. As the cluster size increases, the splitting between these two bands increases from 1.5 eV at single atoms to 2.8 eV at the bulk. The bulk splitting is found at coverage of 5×10^{15} atoms/cm^2, where the cluster consists of several hundred atoms. The d-valence band is broadened on all of the substrates, with a reported bulk width occurring at coverage corresponding to particle diameters of 3 nm supported by TEM measurements.

Palladium clusters deposited on amorphous carbon have been studied by XPS and UPS [28] and both techniques show broadening of the d-band peak as cluster size increases. The d-threshold shifts towards E_F as cluster size increases. In UPS studies the d-emission of the single atom has its peak at 3.0 eV below E_F, whereas the d-threshold is 2 eV below E_F. Palladium clusters evaporated onto SiO_2 have been studied by UPS [38]. At large coverages of the Pd metal evaporated ($> 10^{16}$ atoms/cm^2), a high emission intensity at E_F excited with photons of 21.2 eV (He(I)) or 40.8 eV (He(II)) as excitation source, is observed. This feature is characteristic in the spectra from bulk Pd samples. At the lowest metal coverage (3×10^{14} atoms/cm^2),

corresponding to isolated atoms or very small clusters, the spectra are quite different. The intensity at E_F is negligible with the dominant feature due to Pd appearing at 2.9 eV below E_F, with a full width at half maximum (FWHM) of 2.4 eV, with He(I) excitation. With He(II) radiation this feature appears at 4.0 eV below E_F and this might be due to some surface charging accounting for part of the difference in position found with He(I). The location of this peak due to emission from d-states of single atoms or small clusters being well below E_F has also been reported in UPS studies of Pd on carbon. As the coverage of Pd atoms increased, the emission intensity also enhanced at Fermi level. This is accompanied by a broadening of the d-emission to 5–6 eV, being characteristic of bulk Pd. A critical coverage of 2×10^{15} atoms/cm^2, that corresponds to a mean particle diameter of 2–3 nm, was associated with the onset of metallic behavior.

The FWHM of the valence band of transition metal clusters has been used to determine the transition to bulk-like behavior of the photoemission spectrum. As was mentioned, at the lowest coverage of the evaporated metal onto carbon support, single atoms or very small clusters are obtained. The FWHM in this range is smaller than the value for the corresponding bulk metal, but is broadened considerably over values expected for a free atom. This broadening can be traced to interactions with the carbon support, instrumental broadening, and the final-state multiplet structure. As the coverage increases, the FWHM increases, with a distinct transition to bulk values at coverage slightly higher than 2×10^{15} atoms/cm^2. By electron microscopy, this coverage can be associated with clusters of ~150 atoms.

At low photon energies, momentum-conserving transitions account primarily for the emission features in photoemission. Changes in the final state that accompany changes in photon excitation energy should give changes in the transition matrix element and lead to spectral modulations if the cluster is large enough to have a bulk-like periodic structure. When the cluster is too small to have a periodic structure, the excitation process is primarily molecular and spectral modulations should be absent. The onset of spectral modulations has been reported for both gold and silver clusters evaporated onto carbon [33]. Bulk-gold spectra can be divided into three regions: (1) the sp-band at 0–2 eV, (2) the first d-band at 2–4 eV, and (3) the second d-band at 5–8 eV. Spectral modulations in the intensity of the two d-band regions are apparent at coverage of 2×10^{15} atoms/cm^2 and above. The intensity ratio of the first to the second d-band decreases as photon energy increases. At lower coverage only minor variations occur in the intensity ratio. These data clearly show that clusters at the coverage of 2×10^{15} atoms/cm^2 are needed for bulk-like features. According to electron micrographs, this corresponds to particles with 1.9 nm mean diameter, which have slightly more than 100 atoms.

The extent of splitting of the two d-band regions is dependent upon gold coverage but independent of photon energy. This effect is another convenient measure of the progression to bulk behavior [33]. The splitting increases from 1.4 eV at low coverage to 2.9 eV at high coverage. Although numerous photoemission experiments show close correspondence of many cluster spectral features with the bulk at 100–150 atoms, some bulk features are not completely reproduced. Much larger clusters are required for total convergence. The origin of this slow convergence has been discussed in terms of the properties of surface atoms, uncertainty in momentum, and the distribution of cluster sizes [39]. The surface atoms making up a large percentage of cluster atoms have enhanced vibrational amplitude, and this leads to some breakdown of the strict momentum-conserving selection rule. The finite cluster size thus leads to a broadening of the spectra through uncertainty in momentum. The magnitude of this effect can be estimated with the Heisenberg uncertainty principle. Thus, these factors are responsible for the rather slow convergence to bulk spectra for clusters with more than 100–150 atoms.

The core level BE of clusters is typically greater than the corresponding BE of the bulk metal. The magnitude of the shift from single atom to bulk has been shown to be a function of support material or treatment of the transition metal clusters. These effects may be illustrated for Pd clusters [33]. When the clusters were deposited *in situ* onto carbon, the shift of the $3d_{5/2}$ peak was 0.6 eV between low and high coverage. If the Pd clusters were exposed to air before measurement, a shift of 2.3 eV was reported, even though no contamination was observed with XPS. This core level measured for Pd evaporated onto SiO_2 *in situ* showed a shift of 1.6 eV between the highest and lowest coverage. The core shifts between small noble-metal clusters and the bulk has been reported to be quite small for a variety of cases. For Ag evaporated onto carbon the shift is ~0.2 eV, and the shift is reported to be 0.6 eV for Cu deposited on the same support. The $4f_{7/2}$ core level of gold shifts 0.45 eV between small Au particles and bulk on Al_2O_3. The position of the $2p_{3/2}$ core level of Cu deposited on polystyrene by evaporation has shown an anomalous dependence upon cluster size. At the lowest coverage the $2p_{3/2}$ core level has a BE 1.5 eV less than bulk copper. This behavior is contrary to the data discussed above, where the core level has a greater BE in the atomic state. As copper coverage increases, the core level splits into a doublet with a new peak at higher BE than the bulk. This new peak becomes dominant with increased coverage and shifts towards the bulk value. The peak observed at lowest coverage is attributed to copper atoms positioned at an unusual substrate site where the electron density is high, in order to account for extremely large relaxation energy. A broadening of core levels has been reported for small metal clusters such as Pd on SiO_2 or Au implanted on SiO_2 [33]. The $3d_{5/2}$ half-width at lowest coverage of deposited on Pd on SiO_2 is ~1 eV greater than in the bulk. The origin of this effect is not completely known, although several explanations have been provisionally advanced. These include a reduced-screening model leading to changes in potential for the hole and the possibility of matrix inhomogeneity creating a variety of substrate interatomic potentials.

Extended X-ray absorption fine structure (EXAFS) and photoemission measurements have been carried out on clusters ranging from isolated atoms to aggregates large enough to acquire bulk metal properties. EXAFS studies of copper show a substantial contraction of the nearest-neighbor Cu–Cu distance for small clusters. In addition, the onset of the K edge shifts toward higher energy as the cluster size decreases [40].

The experiments showed that the BE shift observed in small metal nanoparticles on a support are due to the initial state effects. The spectra are quantitatively similar to those of bulk alloys. The shift can be towards higher or lower BE depending on the nature of the supporting substrate. When the substrate has localized p- or d-orbitals with BE overlapping those of the cluster d-orbital, the shift generally lowers the BE. On less interactive substrates such as carbon the metal support intercation is weak and the shifts are towards higher BE for the cluster relative to the bulk metal. For weakly interacting substrates the variation in core level BE and the valence d-band splitting are linear functions of average coordination number. The BE shift with increasing size in such cases may be correlated to the variation in the d-electron count which is thought to result from (s, p)-d rehybridization or intra-atomic charge transfer [41].

Although the general result is that with decreasing particle size the BE shifts for higher values, Bellamy et al. [42] arrived at different phenomenon. Investigating the UPS and Auger spectra of Ni and Pd aggregates on a SiO_2 substrate it shows surprising results. Whereas the width of the UPS spectra increases for both metals when the crystallite size increases, the width of their Auger spectra increases for Pd and decreases for Ni. These results can be interpreted theoretically by a continuous change of the electronic configuration from the free atom to the bulk. However, the variation of the valence bandwidth with size should also be taken into account. Therefore, it was necessary to perform calculations that include this variation of bandwidth and correlation effects simultaneously.

One of the interesting examples is the metal molecular cluster, like $Os_3(CO)_{12}$ in which during decomposition a dramatic change in the metal core-level BE occurs [43]. The condensation of $Os_3(CO)_{12}$ was reproduced on various substrates for various coverages up to 8.0 nm. In every case the core level BE shift s was the same within an uncertainty of 0.1 eV. It is concluded that an interaction would take place through the CO ligands which could no longer be considered similar to each other. In no case, even for very small coverage thicknesses (1.0 nm), did the C 1s and O 1s peaks associated with the CO ligand exhibit any broadening or splitting. It is therefore concluded that the observed changes in BE values are characteristic of alterations in the size and density of the deposit itself.

The metal size clearly increases when the decomposition takes place on the substrate. Nevertheless, the overall shift after complete decomposition is the same both on crystalline and amorphous substrates. This can be explained by the assumption that the increase of the number of the metal atoms in the cluster takes place also on an amorphous substrate, on a scale high enough to shift the core levels but low enough to maintain a constant emitted intensity ratio between the substrate and the metal core levels. The authors concluded therefore that the core-level position is highly ''size-sensitive'' in the range of very small particles, e.g. <100 atoms where the associated electronic properties are primarily atomic. However, on approaching the metallic state for >100 atoms, the core-level shift is a much poorer criterion of the cluster size.

Photoemission is particularly sensitive for monitoring the growth of very small particles with reference to the BE values of the core levels. On the other hand, for large particles the emitted intensities are the key features.

For normal case the nanoparticles are grafted to a support of various structures and the photoelectron spectroscopy is used to determine the particle size simply comparing the signal resulting from the particles and the support. Davis [44,45] as well as Kuijpers [46] developed a simple method for obtaining particle size information from photoemission results which is formulated by considering the intensity ratio for two dispersed phase core levels with different kinetic energy. This analysis predicts a high sensitivity for detecting particle size differences for sizes in the range of about 1–5 nm. A major advantage of this approach over earlier methods involving the dispersed phase to support phase intensity ratio is a reduced dependence on surface roughness and physical properties of the catalyst. A straightforward methodology for obtaining particle size information from photoemission results has been developed and exemplified by considering the intensity ratio for two dispersed phase core levels with different kinetic energy.

The valence band for the Pt foil, Pt/SiO_2, and SiO_2 clearly show that the very intense peak at Fermi level is due to the d-state of Pt, while on a highly dispersed system (Pt/SiO_2) there is a shift of the d-states to the higher energies [26]. The major problem with this valence band measurement is two sided, first there can be a charging effect as mentioned above, the second one is that sometimes interaction between metals and support occurs, e.g. silicide formation. To make this problem clearer, sometimes small metal particles are evaporated on a metal single crystal, which will be discussed in detail in the next sections.

2.2. Theoretical Modeling

As was mentioned previously, photoemission has proved to be a valuable tool for measurement of the electronic structure of metal cluster particles. The information measured includes mapping the cluster DOS, ionization threshold, core-level positions, and adsorbate structure. These studies have been directed mainly toward elucidation of the convergence of these electronic properties towards their bulk analogues. Although we will explore several studies in detail, we can say that studies from different laboratories support the view that particles of 150 atoms or more are required to attain nearly ''bulk-like'' photoemission properties of transition and noble metal clusters. This result is probably one of the most firmly established findings in the area of small particles.

The complexity of the particle size related changes in the cluster geometry and electronic structure renders the results of the theoretical calculations extremely useful when analyzing the experimentally observed trends.

In his pioneering work Baetzold used the Hartree–Fock (HF) method for quantum mechanical calculations for the cluster structure (the details are summarized in Reference 33). The value of the HF procedure is that it yields the best possible single-determinant wave function, which in turn should give correct values for expectation values of single-particle operators such as electric moments and

charge distributions [47]. Closed-shell systems were studied where all the electrons are paired. During the calculation an approximate form was applied for treating cluster problems. The simplest approximate [48] method is the Extended Hückel (EH) theory. Parameters are chosen from experimental data and designed to take into account the electron–electron terms not explicitly considered. Only the valence orbitals of the atom are considered, because core–orbital interactions would be small within this computational framework.

The next version of increased sophistication in computational methods includes CNDO [49]. The CNDO begins with the zero-differential overlap approximation. Here the Slater valence atomic orbitals are used, as in EH theory. The zero-differential overlap approximation eliminates many two-center and all higher-center electron–electron terms. The remaining two-center electron–electron terms are computed with s-orbital to give a term characteristic of the two atomic centers, taking into account the appropriate orbital exponents. One-center terms are computed likewise. An empirical parameter is introduced to replace some of the more complex integrals. This parameter is often evaluated by fit to some known data. Finally, atomic IP and electron-affinity data are introduced into the theory by identification of some of the integrals with atomic terms. The energy is computed within this framework. The explicit formulas have been used in computation for transition metal atoms were presented [50]. This method is self-consistent in that a starting wave function is introduced and several iterative cycles are carried out to achieve the converged result.

In the HF procedure a source of some error is introduced by computing the interaction of an electron with the average field due to the remaining electrons. This approximation neglects the instantaneous repulsions between pairs of electrons, leading to an error in the total energy called the correlation energy. This correlation energy contribution can be computed by taking linear combinations of different excited-state determinants.

In this approximation the potential is spherically averaged about each atom and taken as small metal particles constant in regions outside the sphere. In the actual calculation there are three potential regions: an inner-sphere region around each nucleus, an outer-sphere region surrounding the cluster, and an intersphere region containing the volume within the outer sphere but not within the inner sphere. The potential is assumed constant in the intersphere region.

The extended Hückel procedure gives some information about the clusters with various sizes.

(i) *Cluster geometry* of small clusters of the IB metals, examined by EH method, shows a distinct preference for chain over more compact structures. For instance, 6-atom Cu cluster was more stable as a chain than as other structures. Baetzold [50] also found similar structure for silver clusters, that is the straight chains were most stable and their computed equilibrium bond length was less than that for the other structures. The reason for the stability of small linear clusters may be understood from the molecular orbital concepts. For 3-atom Ag cluster the 5s-orbitals play the dominant role in bonding. The highest occupied molecular orbital of the neutral cluster is antibonding and thus destabilized versus the atomic level 7.56 eV. The destabilization is much greater for the triangular than for the linear structure, leading to the stability of the latter. EH calculations have suggested preferential stability for icosahedral structures for Pd but not for Ag. Both metals have bulk fcc lattices with computed electronic structures of approximately: Ag $d^{10}s^{1}$ and Pd $d^{9.2}s^{0.8}$. These results may be understood by a qualitative argument. The icosahedral structure leads to broader bandwidths than the fcc structure, owing to the more closely packed surfaces. Since the filled band is slightly destabilizing, the icosahedral structure is destabilized relative to the fcc structure for the d^{10} Ag, whereas this effect is not present for the $d^{9.2}$ Pd. The computations showed this effect to persist for several different parameter sets up to 55-atom clusters. The qualitative argument for determining stability advanced above suggests stability for clusters with d^5 up to nearly d^{10} configurations, but fcc stability for d occupations less than d^5. These arguments hold for small clusters when the difference in bandwidth between icosahedral and fcc is significant. Methods of solid-state physics closely related to EH theory, have been used to compare stability of icosahedral and fcc clusters. The icosahedral structures are preferred up to 150-atom clusters, with greater stability of fcc at larger sizes. These results and the EH results discussed above seem to be consistent.

In principle, the CNDO method represents an improvement over the EH method in calculation of geometries, bond lengths, and energetic properties of the metal cluster. Calculations of cluster geometries for Cu and Ag by the CNDO method have suggested the greater stability of linear chains over three-dimensional structures in many small clusters. Later work with improved parameter sets that allow greater s-p-d hybridization has shown an energetic balance between the various geometries. There is a trend towards greater stability of the three-dimensional geometry compared to linear geometry as size of the IB metal cluster increases. Linear is more stable for Cu_3 and Cu_4, but the most stable structures of the larger sizes were Cu_5-bipyramid, Cu_6-square bipyramid, Cu_7-Cu_9-face-centered-cubic structure. The trend is a greater stability for even-sized clusters, where closed electron shells are present, in comparison to odd-sized clusters.

(ii) *Bond lengths*. There seems to be general agreement that the equilibrium bond length computed within EH procedures increases as cluster size increases. In computations within the standard version of EH with no repulsive terms added, the bond length expanded from 0.21 nm for Ag_2 to 0.265 nm for Ag_{l4} linear chain. This lengthening is valid for Pd, Cu, and Ni [51]. This is attributed to fewer nearest neighbors in the cluster versus the bulk.

(iii) *Binding energies.* The binding energy in a metal cluster increases with size. In EH calculations for silver, BE increases for computations up to 55 atoms and remains at roughly 1/3 of the bulk experimental value[50]. Similar results were found for several other transition metal clusters. The calculations [52] for Cu_{13} gave a BE per atom of 18 kcal, which is far from the bulk experimental value of 82 kcal/mol. It has also been computed that the cohesive energy increases with particle size for various degrees of d band filling for fcc clusters [53]. The values computed showed a rapid convergence to the bulk.

(iv) *Energy of electronic transition*. The energy of the first electronic transition is computed to decrease with increasing size of the IB metal clusters. This was shown for linear Ag clusters by computing the gap between the highest occupied molecular orbital and the lowest unoccupied molecular orbital [50]. This spacing decreased from ~3 eV for Ag_2 to ~0.5 eV for Ag_{20}. This consideration does not take into account matrix elements between initial and final states.

By CNDO calculation BE is an increasing function of cluster size for Ag clusters and for Ni clusters [54]. The calculations for Ni clusters showed that the contribution an atom makes to the total BE is proportional to its coordination number [54]. The orbital energies of Ni follow a smooth function of cluster size. As size increases, LUMO decreases and HOMO increases. This represents a convergence of IP and electron affinity values with increase in size.

(v) *Ionization potential.* The ionization potential decreases as cluster size increases, as expected from known trends in these values. The trend with cluster size has been investigated [55] for very large clusters containing up to 135 atoms of Cu, Au, and Ag. For example, in the calculation for Cu clusters, IP decreased from the atom value of 7.72 eV to 4.70 eV for the 135-atom fcc cluster. The IP of Cu cluster was calculated by CNDO as a difference in total energy. The closed shells have relatively greater stability than the open shells

(vi) *Density of states (DOS)*. The density of states of metal clusters can be measured with photoemission. The EH calculations using single-zeta d-orbital with exponents given by HF atomic calculations gave cluster d-bandwidths of only a few tenths of eV, which were much smaller than bulk experimental bandwidths of several electron volts [56]. The EH calculations using double-zeta d-orbitals, gave much larger d-bandwidths for the same cluster sizes, while other computed properties were not significantly changed. It is now recognized that double-zeta d-orbitals are required in EH calculations of the DOS. The convergence of cluster properties towards the bulk was also examined in EH calculations. Thus, it is possible to compute properties of clusters and the bulk by using identical approximations and parameters within the same computational framework. An example of this procedure is shown in Figure 1, where the DOS is examined for various silver clusters up to 166 atoms in comparison to the bulk [32]. Here the development of a band structure is clearly seen as a broadening of the DOS with size (see Figure 1). In addition, the HOMO value shifts 2.5 eV towards the vacuum level as size increases from two atoms to the bulk. The broadening of the d-band of metal clusters is plotted versus size in Figure 1 [32,57]. A reduced bandwidth, obtained by dividing the cluster value by the bulk computed value, is shown. The 4d-, 5s-, and sp-orbitals are employed in the calculation, which leads to the DOS curves shown in Figure 1. The d-state region of high intensity 4 eV below the Fermi energy or HOMO level is observed. As size increases, the d- and s-band portions of the spectra broaden. Several different parameter sets were examined and clearly show that clusters with more than 100 atoms are needed to give a width approaching that of the bulk.

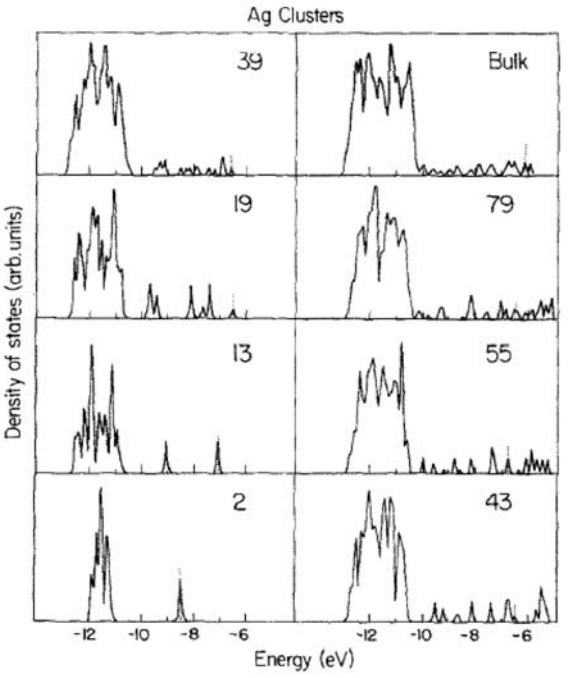

Figure 1. Density of states for various Ag clusters computed for 4d-, 5 s-, and 5p-orbitals within the extended Hückel method. (Reprinted from Ref. [32], © 1981, with permission from Elsevier.)

The valence DOS has been computed for Ni and Ag clusters within the CNDO formalism. Blyholder [54] examined the Ni_6 and Ni_{13} clusters. In both cases of s- and p-orbitals are occupied and lie well below the d-orbitals. Most of the intensity is near the middle of the d-orbitals with a fall-off in intensity as the HOMO is approached. Density of states for Ag_7, Ag_{10}, Ag_{13}, and Ag_{19} clusters shows a strong d-component cc. 3.5 eV wide. The

d-levels appear ~4 eV below the HOMO, as expected from their position observed in the bulk. For Pd_{19}, however, we note a considerable decrease in density near the HOMO with a maximum deeper in the band.

(vii) *Charge distribution*. The EH procedure predicts an accumulation of charge on atoms with low coordination if the valence s-, p-, or d-molecular orbitals of a given type are more than half-filled. Thus for cluster atoms like Pd, where the average electronic occupation is $\sim d^{9.5}s^{0.5}$, there would be an excess of d electrons and a deficiency of s electrons on surface atoms relative to the inside atoms in a cluster.

The charge distribution determined within clusters by CNDO has been reported for only a few cases. Let us consider only one cluster, the 13-atom fcc cluster with only two geometrically different types of atom. There is a center atom with 12 nearest neighbors, and there are 12 surface atoms each with 4 nearest neighbors. At the equilibrium bond length (0.34 nm) the center atom has a net positive charge, but this situation is reversed at the bulk experimental distance (0.288 nm).

To sum up, theory plays an important role in the understanding of cluster properties. Certainly, theory provides the conceptual basis from which experiments can be planned and analyzed. The calculations discussed here all involve some sort of approximations, which lead to different predictions in some cases. Similarly, the experimental search for systems that obey one or another different theory is welcome.

2.3. Metal–Cluster Interaction on Single Crystal Interface

It is a rare case when metallic clusters are generated in the gas phase, e.g. by using a nozzle through which metal vapors going through and are forming small metallic clusters [58,59]. The stability of these metallic clusters is very low and they easily agglomerate to form larger particles. It means that metallic clusters should be stabilized either by an oxide support or on a single crystal surface. In both cases, in particular in the latter, electron transfer occurs between the nanoparticles and the single crystal which significantly affects the electronic properties of the nanoparticles.

One of the earliest works has investigated the geometric and electronic properties of submonolayer and monolayer (ML) copper films grown by vapor deposition on a clean Ru(0 0 0 1) substrate using AES combined with thermal desorption mass spectroscopy (TDS), work function ($\Delta\phi$) measurements, and energy-dependent angular resolved UV photoemission using synchrotron radiation. A pronounced influence of the deposition temperature on the morphology of the Cu films was established in that lower temperatures favor an island growth mechanism (Stranski–Krastanov or Volmer–Weber type). At this stage the charge displacement per Cu atom is lower and the lateral binding between the Cu atoms makes the removal rather difficult [60]. Higher deposition temperature leads to a more uniform spreading and a layer-by-layer growth (Frank van der Merwe type). At low coverage (below 0.1 ML) Cu is predominantly atomically dispersed and bonded to the Ru surface resulting in electron charge displacement towards Cu. For thicker Cu films grown under the latter conditions angular resolved photoemission reveals the existence of two-dimensional Cu bands even before the monolayer has reached completion; the experimentally determined band dispersions agree quite well with recent theoretical calculations [60].

Similar results were obtained during the valence band and core level studies of ultrathin Fe layers deposited on a Cr(1 0 0) surface at room temperature using ARPES, UPS, and XPS. The UPS spectra show an important structure in the bulk Fe spectrum, whose band centroid lies at 0.9 eV. A weaker and broader band lying around 3 eV is also observed in all the series. When reducing the coverage, this strong feature progressively moves toward higher binding energies and is finally replaced by a Cr feature lying at 1.7 eV. It worth mentioning that for the 1 ML the strongest peak is shifted by 0.25 eV toward higher binding energies with respect to the Fe bulk situation. Transitions from Fe minority and majority spin bands are still observed for coverage of about 1 monolayer, showing that Fe retains its magnetic ground state; the persistence of the magnetic satellite in the Fe 3s core levels also supports this conclusion. These studies agree with theoretical calculations which predict an enhanced magnetic moment for ultra thin Fe layers on Cr(1 0 0) [61].

Room temperature deposition of silver on Pd(1 0 0) produces a rather sharp Ag/Pd interface [62]. The interaction with a palladium surface induces a shift of Ag 3d core levels to lower binding energies (up to 0.7 eV) while the Pd 3d level BE, is virtually unchanged. In the same time silver deposition alters the palladium valence band already at small silver coverage. Annealing of the Ag/Pd system at 520 K induces inter-diffusion of Ag and Pd atoms at all silver coverage. In the case when silver multilayer was deposited on the palladium surface, the layered silver transforms into a clustered structure slightly enriched with Pd atoms. A hybridization of the localized Pd 4d level and the silver sp-band produces virtual bound state at 2 eV below the Fermi level.

Further annealing induces additional Ag overlayer enrichment with Pd atoms, causing a substantial intensity increase of the Pd resonant state, while the intensity at the Fermi level remained very small. This is a clear indication of the localized character of the Pd 4d state. The annealing of the Ag multilayer produces a surface alloy with a composition very close to $Ag_{0.5}Pd_{0.5}$ which has a DOS at the Fermi level substantially smaller than the pure palladium. The annealing at higher temperature produces a Pd(1 1 0) surface with very small but very persistent amount of silver, which is in the form of three-dimensional clusters, located most probably below the first Pd(1 1 0) layer.

Goodman and coworkers have investigated the electronic interactions in Cu/Rh(1 0 0), Cu/Ru(0 0 0 1), Ni/Ru(0 0 0 1), Ni/W(1 1 0), and Pd/W(1 1 0) by means of XPS [63–70]. The shifts in the core-level binding energies indicate that the adatoms in a monolayer of Ni, Cu, or Pd

are electronically perturbed with respect to the surface atoms of Ni(1 0 0), Cu(1 0 0), or Pd(1 0 0). The magnitude of the electronic perturbations is larger for Pd/W(1 1 0) and Cu/Rh(1 1 0). Particularly interesting are the cases of strained pseudomorphic overlayer, in which the electronic perturbations are a result of (1) variations that occur in the admetal–admetal interactions when the admetal adopts the lattice parameters of the substrate and (2) electronic interactions between the admetal and substrate (i.e. formation of chemical bonds, transfer of charge, polarization effects, etc.) observed for many bimetallic systems. The present results show a correlation between the shifts in the XPS surface core-level binding energies and the variations in the desorption temperature of CO from metal adlayers [63]. An ''initial-state'' argument suggests that this correlation arises due to changes in DOS of the overlayer metal near the Fermi level upon adsorption onto a dissimilar metal. This, in turn, affects the magnitude of the back bonding from the overlayer metal to adsorbed CO and thus the metal–CO bond strength. These data then show that shifts in core-level binding energies can provide useful information about the electronic interactions that occur in bimetallic systems and successfully predict changes in certain chemical properties of metal overlayer systems, as well.

Further investigation was pursued on ultrathin films of Cu on Rh(1 0 0) and Ru(0 0 0 1) by using XPS. The effects of surface annealing temperature, adsorbate coverage (film thickness), and CO chemisorption were investigated. The XPS data show that the atoms in a monolayer of Cu supported on Rh(1 0 0) or Ru(0 0 0 1) are electronically also perturbed with respect to the surface atoms of Cu(1 0 0). The magnitude of the electronic perturbations is larger for Cu/Rh(1 0 0). Measurements of the Cu $2p_{3/2}$ XPS peak position of Cu/Rh(1 0 0) and Cu/Ru(0 0 0 1) as a function of film thickness show that the Cu–Rh and Cu–Ru interactions affect the electronic properties of two or three layers of Cu atoms. The shifts in XPS binding energies and CO desorption temperatures can be explained in terms of (1) variations that occur in the Cu–Cu interaction when Cu adopts the lattice parameters of Rh(1 0 0) or Ru(0 0 0 1) in a pseudomorphic adlayer and (2) modifications in the electronic properties of the Cu adatoms, caused by the Cu–Rh and Cu–Ru interactions [64]. A correlation exists between the shifts in the Cu XPS binding energies and the variations in the desorption temperature of CO from the Cu adlayers. The XPS results show a net transfer of charge from the Cu overlayers upon CO chemisorption.

Further studies were carried out on the Pd/Mo(1 1 0), Pd/Ru(0 0 0 1), and Cu/Mo(1 1 0) systems. The shifts in core-level binding energies indicate that adatoms in a monolayer of Cu or Pd are electronically perturbed with respect to surface atoms of Cu(1 0 0) or Pd(1 0 0). By comparing these results with those previously presented in the literature for adlayers of Pd or Cu, a simple theory is developed that explains the nature of electron donor–electron acceptor interactions in metal overlayer; formation of surface metal–metal bonds leads to a gain in electrons by the element initially having the larger fraction of empty states in its valence band. This behavior indicates that the electro-negativities of the surface atoms are substantially different from those of the bulk [65].

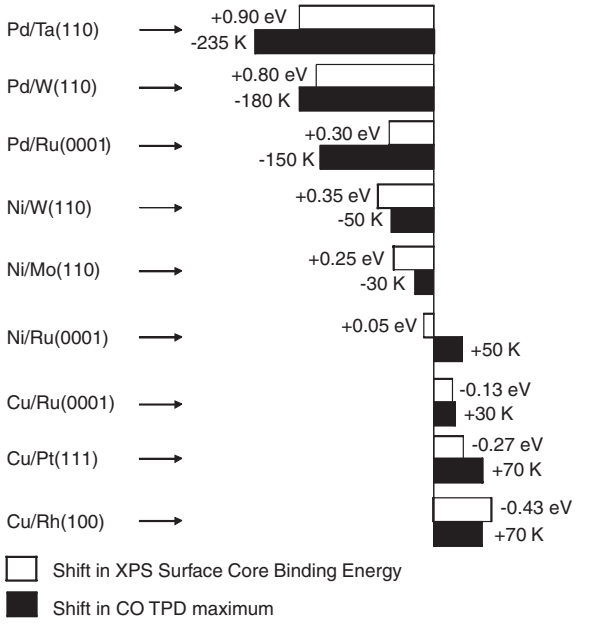

Figure 2. Correlation between the shift in surface core level BE and the shift in CO TPD. The properties of the Pd, Ni, and Cu monolyers are compared with the corresponding values for the (1 0 0) face of pure metals. (Reprinted from Ref. [67], © 1991, with permission from American Chemical Society.)

Figure 2 displays a qualitative correlation between the increase or decrease in CO desorption temperature and relative shifts in surface core-level binding energies (Pd(3d5/2), Ni(2p3/2), or Cu(2p3/2); all measured before adsorbing CO) [66]. In general, a reduction in BE of a core level is accompanied by an enhancement in the strength of the bond between CO and the supported metal monolayer. Likewise, an opposite relationship is observed for an increase in core-level BE. The correlation observed in Figure 2 can be explained in terms of a model based on ''initial-state effects''. The chemisorption bond on metal is dominated by the electron density of the occupied metal orbital to the lowest unoccupied $2\pi^*$-orbital of CO. A shift towards lower BE decreases the separation of $E_{2\pi}$–E_{vb} thus the back donation increases and vice versa.

The effects of adsorbate coverage (film thickness) on the Pd $3d_{5/2}$ XPS peak positions of the Pd/W(1 1 0), Pd/Re(0 0 0 1), and Pd/Mo(1 1 0) systems were systematically investigated [63]. The peak positions reported for Pd coverage in excess of 1 ML represent a product of electrons emitted from surface and subsurface atoms. For the case of Pd(1 0 0), theoretical calculation suggest that the Pd $3d_{5/2}$ XPS BE of the surface atoms is 0.4 eV lower than that of bulk Pd. A similar difference has been observed experimentally for Ni and Pt surfaces. These shifts in BE are a consequence of variations in the coordination number of the surface atoms compared to bulk atom. If we reference the combined peak of bulk and surface atoms in 40 ML of Pd on W(1 1 0) to that of Pd(1 0 0) a difference of -0.8 eV is obtained between the Pd $3d_{5/2}$ BE of a pseudomorphic monolayer of Pd on W(1 1 0) and that of the surface atoms of Pd(1 0 0). The corresponding shifts

for $Pd_{1.0}/Re(0\,0\,0\,1)$ and $Pd_{1.0}/Mo(1\,1\,0)$ are 0.65 and 0.90 eV, respectively. The influence of adsorbate coverage found for the Pd $3d_{5/2}$ peak is similar to that for the Pd 4d band as the core and valence levels of supported Pd monolayer appear at higher BE than those of bulk Pd.

The adsorption and growth of Cu films on the Ru(0 0 0 1) surface were studied by work function measurements, low-energy electron diffraction (LEED), AES and temperature programmed desorption (TPD). The results indicate that for submonolayer depositions at 100 K, Cu grows in a dispersed mode forming 2D islands pseudomorphic to the Ru(0 0 0 1) substrate upon annealing to 300 K. This behavior is seen to continue to the 1 ML level. Additional Cu deposition to 2 ML shows a similar 2D island growth but with an epitaxial Cu(1 1 1) structure. Subsequent annealing in both these cases to 900 K enhances the 2D character of the films but does not affect the overall structure AES and LEED results show that a 900 K anneal of Cu films in excess of 2 ML leads to three-dimensional Cu(1 1 1) island formation exposing areas of the surface covered by the original Cu bilayer – one pseudomorphic and one epitaxial. The effects of Cu on the chemisorptive properties of Ru(0 0 0 1) toward CO were also studied by TPD. It was found that Cu attenuates the CO adsorption relative to the open Ru(0 0 0 1) sites on approximately a one-to-one basis. In addition, at the 1 ML level the TPD spectrum shows features which are intermediate between those for the tightly bound CO/Ru system and the weakly bound CO/Cu case. A feature of the TPD spectra of CO on submonolayer Cu deposits is identified with mixed Cu/Ru sites, i.e. at the 2D Cu island edges, and allows an estimate of the 2D Cu island sizes to be made. The results and conclusions of this study differ markedly from previous single-crystal studies but are consistent with recent observations of Cu adsorbed onto an epitaxial Ru(0 0 0 1) film grown on a Mo(1 1 0) surface [67].

The interaction of ultrathin films of Ni and Pd with W(1 1 0) has been examined using XPS and the effects of annealing temperature and adsorbate coverage (film thickness) are investigated. The XPS data show that the atoms in a monolayer of Pd or Ni supported on W(1 1 0) are electronically perturbed with respect to the surface atoms of Pd(1 0 0) and Ni(1 0 0). The magnitude of the electronic perturbations is larger for Pd than for Ni adatoms. The results indicate that the difference in Pd $3d_{5/2}$ XPS binding energies between a pseudomorphic monolayer of Pd on W(1 1 0) and the surface atoms of Pd(1 0 0) correlates with the variations observed for the desorption temperature of CO (i.e. the strength of the Pd–CO bond) on these surfaces. A similar correlation is seen for the Ni $2p_{3/2}$ XPS binding energies of Ni/W(1 1 0) and Ni(1 0 0) and the CO desorption temperatures from these surfaces. The shifts in XPS binding energies and CO desorption temperatures can be explained in terms of: (1) variations that occur in the Ni–Ni and Pd–Pd interactions when Ni and Pd adopt the lattice parameters of W(1 1 0) in a pseudomorphic adlayer; and (2) transfer of electron density from the metal overlayer to the W(1 1 0) substrate upon adsorption. Measurements of the Pd $3d_{5/2}$ XPS BE of Pd/W(1 1 0) as a function of film thickness indicate that the Pd–W interaction affects the electronic properties of several layers of Pd atoms [68].

The interaction of a Pd atom with Ti(0 0 1), Ru(0 0 1), and Pd(1 1 1) surfaces has been studied using semiempirical MO-SCF calculations (INDO/l) and cluster models. In addition, the electronic properties of the diatomic PdTi, PdRu, and Pd_2 molecules have been examined using *ab initio* SCF calculations. The results of the calculations indicate that the charge transfer in the Pd–Ti and Pd–Ru bonds is small. For supported Pd monolayers, the Pd–substrate bonds can be described as mainly metallic, with a small degree of ionic character. Adsorption of Pd on an early transition metal induces a reduction in the electron population of the Pd 4d-orbitals by: (1) charge transfer from Pd to the metal substrate, and (2) rehybridization of the Pd (4d, 5s, 5p) levels. The magnitude of both phenomena increases when the fraction of empty orbitals in the valence band of the metal substrate rises. The Pd(4d) + Pd(5s, 5p) electron transfer plays an important role in the strength of the bimetallic bonds: the larger this rehybridization, the stronger the Pd–substrate bond. Electronic perturbations induced by Ti or Ru on Pd reduce the CO-chemisorption ability of Pd by weakening simultaneously the Pd(4d)–CO($2\pi^*$) and Pd(5s, 5p)–CO(5a) bonding interactions. For adsorption of CO on supported Pd, the π back-donation and strength of the Pd–CO bond decrease when the fraction of empty states in the valence band of the support increases [69].

The electronic properties of ultrathin films of Ni on Ru(0 0 0 1) and Mo(1 1 0) have been studied using XPS. The effects of Ni coverage (film thickness) are investigated for both substrates as is the effect of surface annealing temperature for the Ru(0 0 0 1) substrate. In addition the effects of CO and H_2 chemisorption on Ni-covered Mo(1 1 0) and CO chemisorption on Ni-covered Ru(0 0 0 1) are examined. The results indicate that the atoms in 1 ML of Ni on Mo(1 1 0) are electronically perturbed with respect to Ni(1 0 0) surface atoms, while there is no electronic perturbation for a monolayer of Ni on Ru(0 0 0 1). There is qualitative agreement between the shifts measured in the core-level binding energies and the corresponding CO desorption temperatures. The shifts can be explained by: (1) variations in the Ni–Ni interactions caused by a change in geometry of Ni surface atoms on Ru(0 0 0 1) or Mo(1 1 0) as compared to Ni(1 0 0), and (2) the effects of Ni–Ru and Ni–Mo interactions. The adsorption of CO and H_2 induces a decrease in the electron density of the Ni adlayers [70].

The interaction of Pd and Au with Al(1 1 1) has been studied using *ab initio* SCF calculations and cluster models. The bonding mechanism of Pd and Au on Al(1 1 1) involves electron transfer from the valence d-orbitals of the admetals toward the substrate, and a compensating charge transfer from the substrate into the valence (sp)-orbitals of the admetals. Pd behaves as a net electron donor ($Pd^{\delta+}$, $\delta = 0.25$e), while Au acts as a net electron acceptor ($Au^{\delta-}$, $\delta = 0.01$e). In spite of this difference in the net direction of charge transfer, both admetals show shifts toward higher BE in their d-bands, as a consequence of losses in the d-electron population. The electronic perturbations observed after bonding Pd to Al are as large as those found for Pd bonded to early-transition metals, and much bigger than those found when Pd is bonded to late-transition metals. Similar trends are seen for Au adatoms. In general, the reduction in the Pd(4d) or Au(5d)

population increases when the fraction of empty states in the valence band of the substrate rises. Changes in the electronic and chemical properties of Pd overlayers (positive binding-energy shifts in the core and valence levels of the admetal, decrease in the work function of the substrate, reduction in the CO-desorption temperature from Pd) can be explained in terms of a simple model that involves Pd(4d) + substrate charge transfer and Pd(4d) + Pd(5s, 5p) rehybridization [71].

The electronic structure of small nanoparticles can be studied by model experiments when a submonolayer of increasing thickness is built up on a single crystal surface. For instance Pd atoms in the interfacial layers on Cu(1 0 0) experience positive core level BE shifts. A negative core level shift is observed for Cu, consistent with charge transfer from Pd to Cu. Valence band spectra show a Pd-derived feature 1.6 eV below the Fermi level, characteristic of Pd in a Cu matrix. As the Pd coverage increases above 0.5 ML, the Pd core level shift decreases and the valence band spectra become increasingly Pd-like. The CO-derived features in the valence band spectra of CO adsorbed on the Pd sites show a positive BE shift relative to CO–Pd(1 0 0) but no shake-up. The shifts in the core level and valence band spectra are predictive of the altered CO chemisorption properties of Pd in the interfacial alloy structures [72]. Similar results have been obtained for Pt/Cu(1 1 1) employing AES, PES, XPD, and LEED to investigate the growth of the first few monolayers of Pt/Cu(1 1 1). Each layer is built up by adsorption of single atoms or very small clusters, which around the half monolayer coverage condense into a more homogeneous layer. The interface is relatively sharp, for there is no evidence for much interdiffusion and the first layer of Pt is quasi-epitaxial on the Cu substrate. The Pt is in compression, and this strain relaxes, probably by the introduction of defects as growth proceeds. At coverages above 5 ML the Pt film resembles the Pt(1 1 1) surface [73].

The binding energies of two-dimensional Cu-adatom clusters on the Cu(1 0 0) and Cu(1 1 1) faces have been calculated as a function of cluster size and shape by means of molecular statics calculations. A simple model is presented to calculate BE of a large adatom cluster by adding the contributions to BE of the individual atoms in the cluster. The contribution of an individual atom depends on the occupation of nearest neighbor as well as next-nearest neighbor sites on the Cu(1 0 0) surface. At low temperatures, square and rectangular islands with an aspect ratio close to unity are the most stable configurations on the Cu(1 0 0) surface, while on the Cu(1 1 1) surface hexagonal islands, in which all atoms have at least three nearest neighbors in the island, are found to be the most stable. At higher temperatures, the corners of large adatom islands on Cu(1 0 0) are rounded due to entropic effects, as is shown by two-dimensional model calculations with interactions according to the atom-embedding calculations [74].

It is well established that the Auger parameter is a very useful concept, which is not affected by the reference level used in the analysis of the data (the Fermi or the vacuum level) [75]. Moreover, the Auger parameter, being a difference between two peaks recorded on the same energy scale, does not depend on surface charging. It appears that Auger parameter measurements are very useful complementary data to core level shift to separate the real size effect of nanoparticles from other processes (e.g. charging) disturbing observations. At the simplest level it can be demonstrated that the Auger parameter shift is related to differences in the final state extra-atomic relaxation energy ΔR^{ea}:

$$\Delta\alpha' = 2\Delta R^{ea} \tag{1}$$

Recent work on the Auger parameter concept has shown that the relative value of ΔR^{ea} depends on the screening mechanism. In the case of the nonlocal screening mechanism ΔR^{ea} can be estimated to a good approximation considering the electrostatic interaction between the core hole and nearest-neighbor ligands characterized by their electronic polarizability, number, and local geometry, according to the following expression:

$$R^{ea}(\text{eV}) = \frac{(14.4/2)n\alpha}{R4(1 + D\alpha/R3)} \tag{2}$$

where α is the ligand electronic polarizability in Å^3, R is the distance of the ligands from the core-ionized atom in Å, D is a parameter related to the local geometry and n is the number of the nearest-neighbor ligands. D values for several local geometries have been calculated and reported. From Equations (1) and (2) it follows that if n, D, and R are similar in two compounds, higher values of α' (and therefore of R^{ea}) are related to higher values of the electronic polarizability α. It is important to note that if the electronic polarizability becomes very large ($\alpha \to \infty$), as occurs in the metallic state, we have

$$R^{ea}(\text{eV}) = \frac{(14.4/2)n}{RD} \tag{3}$$

This simple electrostatic model permits the estimation of Auger parameter shifts of core-ionized atoms in compounds with respect to the free atom in the gas phase. It is shown that the Auger parameter shift is a function of the number, distance, electronic polarizability, and local geometry of the nearest-neighbor ligands around the core-ionized atom. The relationship between the Cu Auger parameter shifts and the nuclearity of Cu clusters entrapped in zeolites showed that the model is useful to estimate this dependence. The model has also been applied to rationalize Auger parameter data on small copper clusters supported on α-Al_2O_3 (0 0 0 1) surfaces and polycrystalline ZnO and graphite [75].

Photoemission experiments have been performed to investigate the electronic structure of Cu adlayers on a Pt(1 1 1) surface. The evolution of the 3d states as a function of Cu coverage is observed at the Cooper minimum of the Pt 5d emission ($h\nu = 150$ eV), where the Cu 3d emission is enhanced. For Cu coverage up to ~0.6 ML, the 3d states give a symmetrical and resonance-like peak with a maximum at −2.6 to −2.1 eV with respect to the Fermi level (E_F), and a full width at half maximum of 1.4 to 0.5 eV. Between 0.6 and 1 ML the Cu 3d emission increased around −3.5 eV suggesting two-dimensional delocalization which increases with increasing Cu coverage. Beyond ~1 ML, Cu–Cu bonding states appear below −4 eV as well. This shows an interesting absence of Cu-derived emission near E_F, in contrast with the flat

emission at the corresponding energies shown by pure Cu. For small (~0.6 ML) submonolayer coverage, the Cu $2p_{1/2}$ core level BE shifted (upward) by 0.60 to 0.65 eV relative to the bulk Cu $2p_{1/2}$ core level. The adsorption of Cu "removes" the Pt $4f_{7/2}$ surface core level, which then becomes bulk like. The adsorption of Cu also results in a work-function decrease which cannot be interpreted by charge transfer [76].

Co/Si interface formation was monitored by a high-depth-resolution medium-energy ion scattering (MEIS) spectroscopy. High purity Co films were deposited either at room temperature (RT) or at 400 °C onto clean Si(1 1 1) substrate using 150 eV ion beam deposition (IBD). After Co deposition a postfurnace anneal under N_2 induced silicide formation. The structure and the effect of annealing on the electrical properties of these epitaxial films were investigated by MEIS and four-point probe measurements, respectively. Finally barrier heights were measured in this range of annealing temperature using the CV technique [77]. Evidence of epitaxial growth of Co silicide on p-type Si(1 1 1) by low-energy IBD even at RT was found. The results will provide information on the use of such silicide either for metallization on ultra-shallow junctions or other applications for future submicrometer devices.

Co was also studied deposited onto a native SiO_2 covered Si(1 0 0) substrate [78,79]. In Figure 3 we show the valence band UPS spectrum of the $Co/SiO_2/Si(1\,0\,0)$ system. The spectrum of the initially deposited film is characteristic of bulk cobalt with significant Fermi level (top curve). When the Co film is sputtered by Ar^+ ion bombardment the valence band of Co 3d shifts by 0.5 eV towards higher binding energies (middle curve) [78]. Detailed studies unambiguously pointed out that this shift is not the result of either charging effect, or cobalt silicide formation which is one of the most undesirable surface processes, but due to the reduction of particle size. This is further proven by the shift of the Co 2p core level band by 0.5 eV towards higher binding energies measured by XPS and also evidenced by the Auger parameter, which alters with the XPS core level binding energies.

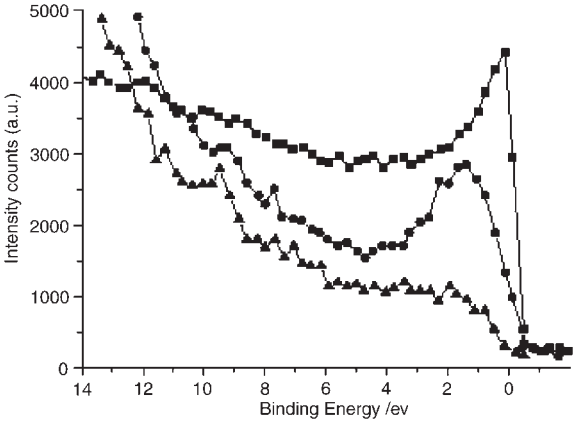

Figure 3. Valence band spectra of Co/Si(1 0 0). Upper curve: UPS spectra for 100 nm thick Co/Si(1 1 1) film; middle curve: thinned 4–5 nm Co/Si(1 1 1) film after ion etching (Co nanoparticles); lower curve: clean silicon substrate after removing the Co layer by *in situ* sputtering. The photoemission data were obtained by He(I) excitation. (Reprinted from Ref. [78], © 1994, with permission from Springer.)

2.4. *Interpretation of the Electronic Structure of Transition and Noble Metal Nanoparticles*

In the previous Sections (2.1–2.3) we summarized the experimental and computational results concerning on the size-dependent electronic structure of nanoparticles supported by more or less inert (carbon or oxide) and strongly interacting (metallic) substrates. In the following sections the (usually qualitative) models will be discussed in detail, which were developed to interpret the observed data. The emphasis will be placed on systems prepared on inert supports, since – as it was described in Section 2.3 – the behavior of metal adatoms or adlayers on metallic substrates can be understood in terms of charge transfer processes.

The numerous studies in the previous decades established several general trends for the size dependent changes in the electronic structure of supported metal nanoparticles. The binding energy of different spectral components like the metal core levels, the midpoint of the valence band or the Fermi-edge is relatively easily measurable. The common observation is that these components shift towards larger binding energies with decreasing nanoparticle size, although the extent of the shift seems to be substrate dependent [80–88]. At the same time, the width of the core levels increases as the particle sizes are decreased. Although the shift and broadening of the core levels with decreasing cluster size is an almost universal phenomenon (with the very few exceptions mentioned in Section 2.1), the interpretation of the observations turns out to be very complicated and often contradictory. The main problem is that the measured BE is affected not only by the initial state of the excited electron, but also by the relaxation of the hole created during the photoemission and its interaction with the outgoing photoelectron.

In one of the earliest qualitative explanations [41] the role of the initial state processes was emphasized. It was suggested that since the localized valence d-electrons are much more coupled to the core levels by the Coulomb interaction than the delocalized s-, p-electrons, a decrease in the d-character of the valence band should lead to increasing core level binding energies and vice versa. Therefore, in order to explain the core level shift towards higher binding energies, the model assumes increasing s-d hybridization with decreasing particle size. Indeed, the characteristic changes of the d-bands of transition and noble metal nanoparticles (see Section 2.1) may indicate the increase in s–d hybridization. The driving force for the increasing s–d hybridization may be a decrease in the bond length, which was observed in very small clusters [89–92] and predicted in the early computational works of Baetzold [31]. Unfortunately, theoretical calculations, which could verify the size dependent change in the s-d hybridization, are still missing for nanoparticles with several hundreds or several thousands of atoms, although certain optical measurements seem to confirm the occurrence of enhanced s–d hybridization in clusters with sizes in the few nm range [93,94].

At the same time, the observed BE shifts can also be interpreted solely in terms of final state effects [95]. If one

assumes that the electronic structure of the metals changes smoothly from the highly hybridized band structure of the bulk towards the discrete levels of the isolated atoms, it is plausible to expect that the electrons become more and more localized as the particle size is decreased, which means that the extent of s–d hybridization should decrease with decreasing particle size. Since the more localized d-electrons are less effective in screening the hole created during the photoemission, the relaxation energy of the final state decreases, which leads to an apparent BE increase. Experiments carried out using metal nanoparticles supported by different oxide substrates revealed a correlation between the polarizability of the substrate and the core level shift of the nanoparticles, which supports the importance of the relaxation effects in interpreting the core level shifts [96].

In addition, if the hole created during the photoemission is not neutralized immediately, the unit positive charge appears as a surface charge on the nanoparticle. The Coulomb interaction between the charged particle and the photoelectron tends to decrease the kinetic energy of the latter, which again results in a BE shift towards higher values [80,97].

The combination of the above-described final state processes gives a plausible explanation for the size-dependent shift of the spectral elements towards higher binding energies [80,81]. In this model the role of the hole left in the particle after the photoemission is twofold. On one hand, its relaxation energy decreases with increasing localization of the valence electrons, resulting in increasing BE with decreasing particle size. On the other hand, interaction of the photoelectron with the size-dependent potential of the charged particle again shifts the measured binding energies toward higher values as the particle size is decreased. It is important to note that the final state effects increase BE of the different spectral elements with more or less the same value, as far as the particle remains metallic. If, however, the particles are too small to be metallic, the mechanism of the screening changes and the shift of the different spectral components is no longer the same.

In the preceding considerations it was implicitly assumed that the particles are monodisperse, i.e. the particle size distribution is narrow. In fact the most widely used method for preparation of supported nanoparticles is evaporation of submonolayer amounts of metals onto the previously cleaned substrate. Therefore, particle formation involves several steps such as adsorption and desorption of metal atoms, diffusion on the substrate, nucleation and island growth. The resulting size distribution is usually slightly asymmetric towards the larger particle sizes and often can be very well described by the so-called lognormal distribution [98]. Although the width of the size distribution can be to some extent influenced by special measures [98,99], preparation of monodisperse distributions is practically impossible. In addition, neutralization of the photoionised nanoparticles supported on weakly conducting substrates is also a process of statistical nature, which has a characteristic time in the same order of magnitude than the other characteristic times of the photoemission [88,98]. The effect of the unneutralized hole on the measured photoelectron energies taking into account the statistical nature of the neutralization can be regarded as a dynamic final state effect [98]. Considering also the particle size distribution, a recent quantitative evaluation [88] of the dynamic final state effect shows that the process leads to shift and asymmetric broadening of the spectral features towards higher binding energies. In particular, model calculations indicate that at room temperature and at moderate instrumental resolutions the UPS spectrum of a Fermi-edge at 0 eV BE distorted by the dynamic final state effect and the spectrum of a Fermi-edge shifted towards higher binding energies is indistinguishable [88,98].

Although the dynamic final state effect can also explain the broadening of the core levels, the expected shift for the Fermi-edge and the core levels should still be quite similar. In fact, in numerous experiments [83,84,86,96,100,101] significantly different shifts were observed for the different spectral elements, which indicates that beyond the final state effects – which probably still give important contributions to shifts – initial state effects also have to be considered.

As far as the valence band DOS is concerned, decrease of the valence bandwidth with decreasing particle size is a very general observation, which was confirmed for all of the studied noble and transition metals (see e.g. [27,32,37,38,80–87,98,101]). A very tentative explanation is based on the fact that the effective number of the neighbors of a given atom decreases as the particle size decreases. Consequently, the interaction of the d-electrons localized on neighboring atoms (which causes the splitting and overlap of the d-levels which leads to the band formation) is also expected to decrease [81], resulting in the reduction of the d-bandwidth. The effect is analogous to the bandwidth decrease observed for metal surfaces [95] or obtained during dilution of metal alloys. Quantitatively, it is possible to evaluate by electronic structure calculations the dependence of the d-bandwidth on the coordination number:

$$\frac{D_{\mathrm{VB}}}{D_{\mathrm{VB}}^{\mathrm{B}}} \approx \sqrt{\frac{z}{z^{\mathrm{B}}}} \tag{4}$$

where z and z^{B} are the coordination numbers for the given sample and the bulk material, while D_{VB} and $D_{\mathrm{VB}}^{\mathrm{B}}$ are the corresponding valence band widths, respectively [95,102]. It is worth to note that while this simple description grabs the most important interaction behind the size dependent changes in the valence band electronic structure, the details of the evolution of the bulk band structure cannot be predicted in this way. The shape and the width of the valence band, for example, converges towards the bulk electronic structure only at much higher particle sizes than one could expect from the above formula [103,104]. In the following sections we will discuss this issue in more detail (see Section 4).

Accepting that the electronic structure of the metal clusters is in between the discreet electronic levels of the isolated atoms and the band structure of the metals, it is expectable that under a certain size the particle becomes nonmetallic. Indeed, theoretical estimations [102,105] suggest that the gap between the filled and empty electron states becomes comparable with the energy of the thermal excitations in clusters smaller than 50–100 atoms or 1 nm in size, where the particles start to behave as insulators. A

photoemission and inverse photoemission study of Ag and Pd nanoparticles deposited onto amorphous carbon revealed the appearance of a gap between the filled and unfilled states [100]. Later, scanning tunneling spectroscopy measurements also confirmed the loss of metallic behavior in very small particles [106,107] or at least indicated the appearance of discreet electronic levels in clusters with less than 2–300 atoms [98].

At the other limit of the size range of the nanoparticles, still interesting size dependent electronic properties can occur. It is well established that the electronic structure of the noble metals along the Γ-L line in the first Brillouin-zone contains a gap between the d-states and the conduction states well above the Fermi level. It results in the formation of a nearly free two-dimensional electron gas at the (1 1 1) crystal face (which is perpendicular to the Γ-L direction), known as the Shockley surface state. Nanoparticles containing several times 10^4 atoms (in the 5–10 nm size range) are generally believed to exhibit bulk-like electronic structure. Experiments indicate that such large particles prepared under UHV environment are usually truncated octahedrons [92], often with large (1 1 1) facets on the top of them, which, accordingly, can support the Shockley surface state. Since the edges of the (1 1 1) top face form potential barriers for the electrons, the surface state of these nanoparticles can be regarded as a laterally confined two-dimensional electron gas. The electronic levels of the confined surface state can be measured both by UPS and scanning tunneling spectroscopy[98] where the experimental data were compared also to the results of simple theoretical calculations.

It may be clear from the presented results that in spite of the significant efforts, the understanding of the size dependence of the electronic structure of the supported nanoparticles is still far from being complete. The changes observed with respect to the bulk electronic structure can usually be attributed to more than one processes, the relative importance being practically unknown. Alternative sample preparation techniques may give new data which can help in elucidating further details of the effects governing the evolution of the electronic structure of the materials from the atoms to the bulk state.

2.5. Controlling Particle Size

Having considered the major electronic properties, now we have to call the reader's attention to two fundamental problems with nanoparticles from which all conflicting data originated. First, in a catalytic reaction the metal particle size, in particular in nano size range, plays a crucial role. The catalytic activity is related to turnover frequency, that is calculated by the number of converted molecules/(time × number of surface sites). However, the intrinsic activity of the site on, e.g., terraces, corners, or kinks is not identical. Therefore, if the size of small metal particles is not uniform, TOF is calculated from an average particle size. Consequently the rate from which the TOF is calculated refers to an average rate, the composition of which is unknown. Second, the spacing between the particles is also nonuniform. This is why the compiled data collected by Ribeiro et al. [108] are randomly altered. Accordingly, in the ideal case both the size and the spacing of metal particles on a support should be uniform and regular.

Now the question arises how the size of metal particles can be reduced to the size-range of nanoparticles. There are several methods available from the literatures; however, these are not the ones, which – in most cases – result in uniform size and spacing on the surface. Nevertheless, it is still worth mentioning some of them: (i) using zeolite encaged metal clusters [109–113], (ii) organometallic molecular clusters deposited on inorganic oxide supports [114–116], (iii) inverse micelle technique [117,118]. Recent application of thin film technology based techniques offers a new approach to fabricate uniform size of metal nanoparticles as detailed and discussed [119–123].

When the metal nanoparticles are inserted into zeolite supercages, the size of the metal particles is confined according to the size of the supercage. However, after reduction of the precursor metal ions in a stream of hydrogen, the protons replacing the metal ions in the cation exchange position also interfere with the metal particles, influencing thereby their chemisorption and catalytic properties.

As an alternative approach towards the above requirement, Somorjai introduced the method of electron lithography [119] which represents an advanced "HIGHTECH" sample preparation technique. The method ensures uniform particle size and spacing: e.g. Pt particles of 25 nm size could be placed with 50 nm separation. This array showed a uniform activity similar to those measured on single crystal in ethylene hydrogenation. The only difficulty with the method is that the particle size is so far not small enough. Comprehensive reviews have been lined up for the effect of dispersion and its role in heterogeneous catalysis [23,124,125].

Another thin film technology based nanoparticle preparation route is gas condensation, in which metal vapor is cooled to high levels of supersaturation in an inert gas ambient [126–128]. In these experiments particles necessarily nucleate in the gas phase. In a promising extension of this technique a pulsed laser beam replaces the conventionally used thermal metal vapor source [120,121,129–134].

At the same time, thin film technology offers a very interesting way for reaching the nanometric size regime by removing atoms from already existing, not necessarily nanosized particles. The main difficulty lies in how to choose the source of energy, which initiates material removal from the original particles. Recent studies indicating that irradiation of nanoparticles with intense laser beams can induce significant reduction in the particle size [135–137] proving the feasibility of this approach.

Ion bombardment could be another potential technique to sputter off some materials from the surface of a thin layer, thereby preparing nanoparticles. Especially because of the inevitable ballistic and chemically guided mixing processes, it was conventionally regarded as a predominantly destructive process. However, successful ion beam induced nanoparticle preparation experiments carried out by using high energy bombarding beams [138–144] suggest that sputtering with low energy ion beams may similarly offer a valuable method for post-deposition modification of the properties of already existing surface nanosystems. Unfortunately, in spite of its conceptual

simplicity, there are only very few indications of the feasibility of this nanoparticle preparation approach [78,79,122,123,145–147].

3. Nanoparticle Formation by Ion Etching of Island Thin Films

In practice, one can imagine two fundamentally different preparation strategies for synthesis of nanostrucures. The more traditional methods involve addition of atoms to growing nuclei by maintaining high levels of supersaturation around them. Nanoparticle preparation by condensing vapors on solid surfaces – which is the almost exclusively applied technique in electronic structure studies due to its UHV compatible nature, gas condensation methods, or even controlled reduction of metal ions by or in the vicinity of the support surface [148,149] are examples for sample preparation utilizing this idea. The opposite approach, based on *removal* of atoms from already existing – not necessarily nanosized – particles could, however, be equally feasible. For example experiments indicate that both intense laser fields and ion beams [123] can successfully be applied to tailor the sizes of metal islands. Nanocluster preparation by size reduction can give interesting new insight into the size dependence of the physical properties of the materials. If one can adjust the particle sizes from the bulk-like size region towards isolated atoms, the identification of the size range where a property (e.g. the electronic structure) starts to be size dependent becomes possible.

The scheme of the process can be seen in Figure 4 [123]. The morphological changes of a silver island thin film deposited onto native oxide covered Si during etching with low energy Ar^+ ions are summarized in Figure 5 [123]. In the initial stage of the sputtering process the size distribution is relatively broad, peaking around 10–15 nm (Figure 5(a)). After a short period of sputtering the size distribution becomes bimodal (Figure 5(b)), the smallest particles start to disappear while the concentration of the larger structures continuously decreases (Figure 5(c)). Finally, the size distribution becomes unimodal and quite homogeneous, with a maximum below 5 nm (Figure 5(d)). Electron diffraction reveals that the silver particles remain crystalline until the end of the sputtering process. The diffraction patterns indicate the lack of any preferred orientation of the silver nanoparticles, while the appearance of the broad rings is due to gradual amorphization of the Si substrate. We obtained very similar results with amorphous carbon as support.

The experimental data presented confirm that – at least after the disappearance of the smallest elements at the beginning of the sputtering – the particle sizes can indeed be adjusted by the applied ion dose, which allows us to follow the size dependent changes of the physical properties of the particles from the bulk limit.

Nevertheless, one has to keep in mind that during the complicated processes of the ion–solid interaction mixing or even ion bombardment induced chemical reactions may occur between the components of the islands and the substrate. In general, events following the impact of

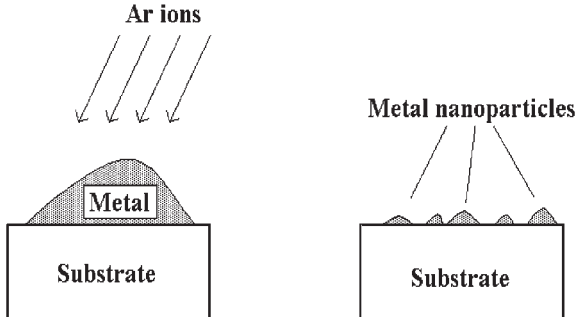

Figure 4. Scheme of nanoparticle formation during ion etching. (Reprinted from Ref. [123], © 2003, with permission from Springer.)

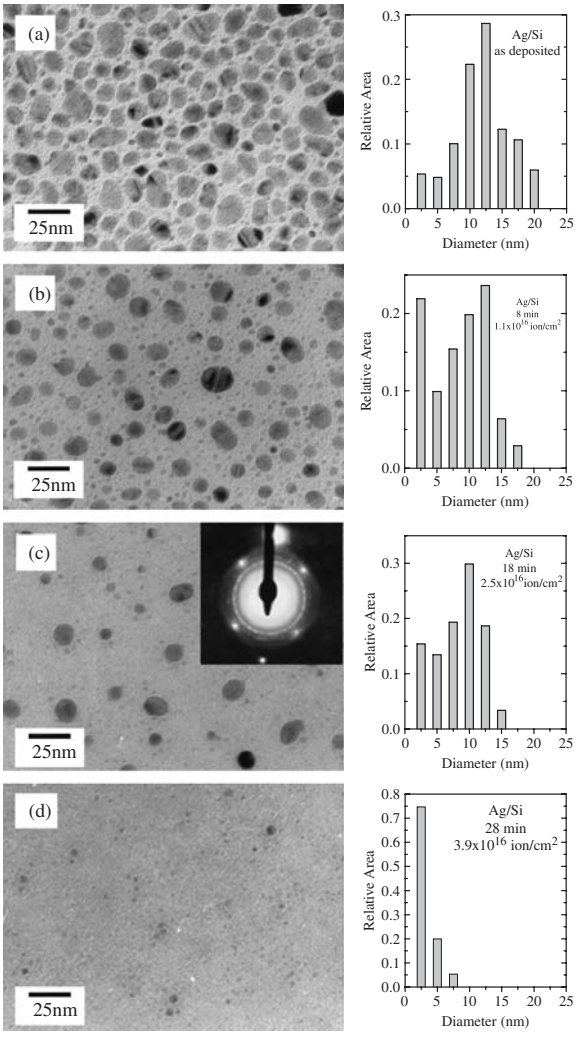

Figure 5. Morphology and particle size distribution of an island silver thin film deposited on native oxide covered silicon (a) before ion bombardment and after (b) 0.5 keV Ar^+ sputtering with 1.1×10^{16}, (c): 2.5×10^{16}, and (d): 3.9×10^{16} ion/cm^2 dose. Sputtering speed for silver was around 3–4 ML/min. Total elapsed sputtering time is indicated on each size distribution graphs. (Reprinted from Ref. [123], © 2003, with permission from Springer.)

energetic ions belong to one of two categories [150–152]. The first of them, the so-called ballistic processes are connected to the random motion of the atoms in the collision cascade which always lead to random mixing. The ballistic processes create a highly nonequilibrium state with a huge number of lattice defects, which then relaxes towards a lower free energy state by diffusion processes (radiation enhanced diffusion) in the second category of the radiation aftereffects. The direction of these relaxation processes depends on the thermochemical properties of the components of the island/substrate couple [151–154]. If, for example, the island/substrate couple is characterized by a strongly negative heat of mixing (i.e. formation of compounds or solid solution is preferred), the diffusion dominated processes further increase the extent of the mixing. On the contrary, if the heat of mixing of the materials in the island/substrate couple is highly positive, chemically guided diffusion processes may even overcompensate the ballistic mixing, leading to phase separation with formation of new islands. According to the literature, nanoparticle formation in heavily ion-implanted ceramics [155], glasses [156,157] oxides, or even semiconductors [158–161] can be understood by the dominance of these chemically guided demixing processes over ballistic mixing. A detailed discussion of the interplay between the ballistic and chemically guided processes and their impact on the morphology development during ion etching of island thin films is described in Reference [123].

Although the above-presented results suggest that in case of a substrate/island couple with high positive heat of mixing the adverse effects of ballistic mixing during size reduction by ion bombardment can be avoided, we always performed careful control experiments to make sure that the nanoparticles are not contaminated by the substrate material. One of the most promising systems from this sense is the Ag/Si couple, where we were able to prove the complete lack of mixing [123]. In the following sections we will present our results concerning on the size dependence of the Ag nanoparticles, which serve as an illustrative example for the general trends described in Section 2.

4. Electronic Structure of Silver Nanoparticles

In noble metals the filled d-band lies 2–4 eV below the Fermi-level, while DOS at the Fermi-energy is dominated by the free electron-like s-states. This offers the possibility of examining separately their responses to reduction of the particle size.

The sample preparation process corresponded to that described above. A discontinuous silver thin film with partially coalesced 30–40 nm islands was deposited onto a native oxide covered Si(1 0 0) substrate, the native oxide serving as a diffusion barrier against intermixing. The sample was loaded into the electron spectrometer, where the island sizes were diminished by 1 keV Ar^+ ion bombardment. The UPS and XPS spectra of the valence band and the characteristic core levels were recorded at certain stages of the sputtering process. TEM images taken at the end of the sputtering revealed that the morphology is practically the same as presented in Figure 5: the substrate is covered by particles of 3–4 nm diameter. The particle height is estimated to be around 2 nm, assuming that the original aspect ratio of the particles was preserved during sputtering.

Figure 6 [162] summarizes the most prominent electronic structure changes in the silver valence band and core levels during the size reduction process. All data in the figure are presented as a function of the Ag/Si atomic ratio "visible" by XPS (i.e. the ratio of the Ag $3d_{5/2}$ and Si 2s core level intensities, weighted by the corresponding atomic sensitivity factors [163]). Binding energies are referred to the $2p_{3/2}$ core level and the Fermi edge of the grounded Cu sample holder. A rough estimation of the corresponding particle size is also given.

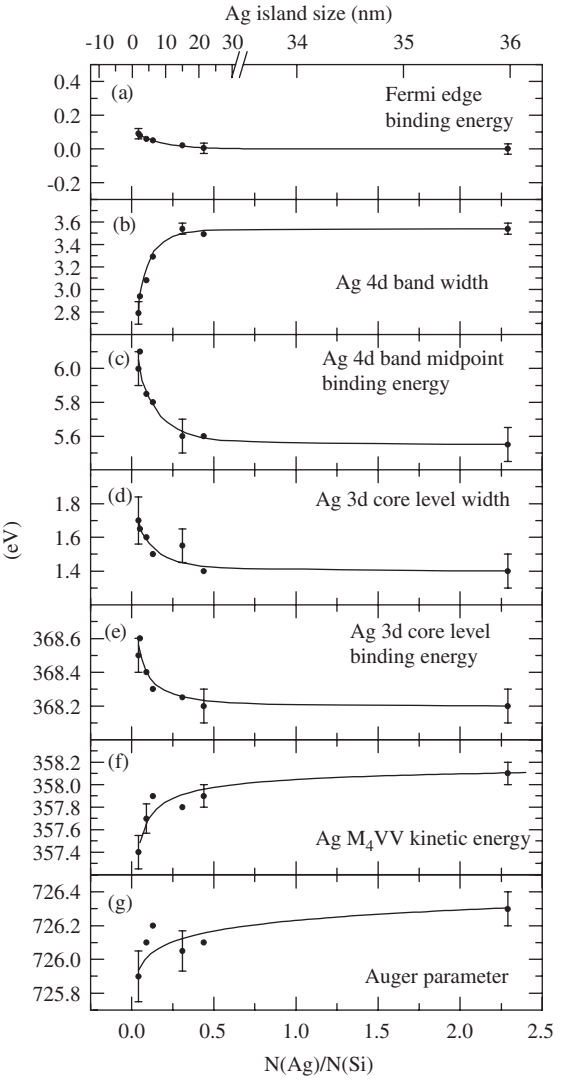

Figure 6. Spectral characteristics of Ag nanoparticles prepared on native oxide covered Si substrate. (a) Binding energy of the Fermi edge; (b) Full width at half maximum of the Ag 4d valence band; (c) Binding energy of the midpoint of the Ag 4d band; (d) full width at half maximum of the Ag $3d_{5/2}$ core level; (e) Binding energy of the Ag $3d_{5/2}$ core level; (f) Kinetic energy of the Ag M_4VV Auger-transition; (g) The Auger-parameter. (Reprinted from Ref. [162], © 2003, with permission from Springer.)

Before sputtering, all spectral characteristics are identical to those measured in bulk silver. During reduction of the particle sizes we observed a 0.5 eV BE shift and a 0.3–0.4 eV broadening for the silver $3d_{5/2}$ core level. The Ag M_4VV Auger lines shifted by 0.7 eV towards lower kinetic energy. Accordingly, the Auger parameter defined as $\alpha' = E_B^{Ag3d} + E_{kin}^{AgMVV}$ decreases by 0.3–0.4 eV with respect to the bulk value. The width of the 4d valence band decreases by 0.7 eV. The Ag Fermi edge measured by UPS, however, showed only a very small shift. Binding energies of the peaks belonging to the substrate did not show any appreciable shift.

When discussing the data presented in Figure 6, it is worth to note that all observed spectral changes are in accordance with the usual trends characteristic for nanoparticles with decreasing size. Although both the Ag MVV kinetic energy and the Ag $3d_{5/2}$ BE change during the size reduction process, their values remain far from the data characteristic for Ag alloys or Ag compounds with atmospheric contaminants (Figure 7), confirming the cleanliness of the nanoparticles.

On the other hand, the significantly different shift of the Ag core levels and the Fermi edge suggests that the observed changes cannot be explained by a simple final state effect. In addition, taking into account that the ΔE_B^{Ag3d} BE shift of the Ag 3d levels can be separated into a ΔV initial state contribution and a ΔR final state contribution [96,164]

$$\Delta E_B^{Ag3d} = \Delta V - \Delta R \tag{5}$$

where the final state contribution can be estimated with the change of the Auger parameter $\Delta\alpha$ as (see also Equation (1)) [96,164]

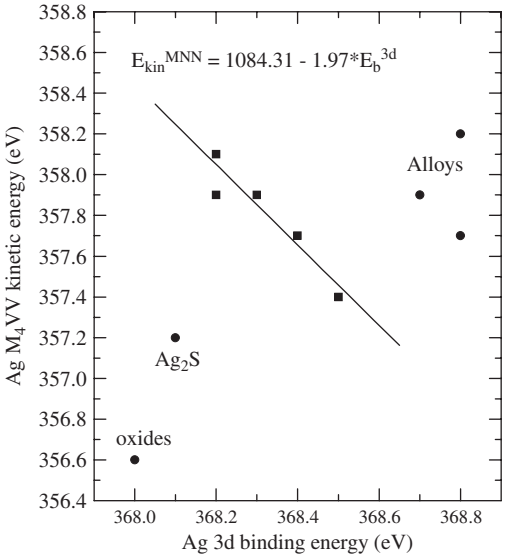

Figure 7. Dependence of the kinetic energy of the Ag M_4VV Auger-transition on BE of the Ag $3d_{5/2}$ core level during ion bombardment of the Ag islands. The characteristic energies of certain silver compounds and alloys are also shown for comparison. (Data compiled from Ref. [163].)

$$\Delta\alpha' = 2\Delta R \tag{6}$$

one can get a relationship using the definition of the Auger parameter between the change of the kinetic energy of the Ag MVV Auger line and BE of the Ag 3d lines [165]:

$$\Delta E_{Kin}^{AgMVV} = 2\Delta V - 3\Delta E_B^{Ag3d} \tag{7}$$

This equation means that if the initial state contribution is constant, the plot of the kinetic energy of the Ag MVV Auger peak with respect of BE of the Ag 3d core levels should give a straight line with the slope of -3. Using the data of Figure 6, the change of the kinetic energy of the Ag MVV transition turns out indeed to be linearly dependent on BE of the Ag $3d_{5/2}$ peak, although the slope of the line is around -2, rather than -3 (see Figure 7), which, under the assumptions of this simple model, is possible only if the initial state contribution ΔV is also a linear function of the shift of the 3d levels: $(\Delta V/\Delta E_B^{Ag3d}) = const. > 0$. Nevertheless, further analysis of the change of the Auger parameter [96,164] indicates that the observed shifts can be consistently explained only by assuming changes not solely in the photoemission initial state but also in the final state relaxation.

The change of the initial state energy of the silver core levels during size reduction clearly suggests that there should be size dependent changes in the valence band DOS of the Ag nanoparticles, which can be visualized by valence band XPS and UPS measurements.

In Figure 8 [146] we present the valence band XPS and UPS spectra of the silver nanoparticles at different stages of the size reduction process. The contribution of the substrate was subtracted. The parameter at each spectrum is the measured Ag/Si ratio.

The main contribution to the XPS valence band spectra (Figure 8(a)) comes from the Ag 4d band located between 3 and 8 eV. At the beginning of the sputtering, the shape of the 4d band is practically identical with those measured for bulk Ag. This indicates again that in the "as prepared" sample the island sizes are large enough – 30–40 nm according to the TEM data – to show bulk-like electronic structure. As sputtering proceeds, the 4d band first rounds off, losing its peak at 4.8 eV, then its maximum at 5.4 eV BE shifts towards higher binding energies (to 6.0 eV in the end), which is accompanied by a narrowing of the band, which was already seen in Figure 6. This is exactly what was observed for the Ag 4d band on carbon or silicon substrate by other authors using XPS [27,32,81,83,101]. However, due to the limited resolution of XPS the details in the change of the electronic structure induced by the size reduction cannot be monitored.

More detailed information can be obtained from the better resolved UPS spectra shown in Figure 8(b). While in the initial stage of the sputtering the spectrum is again identical to that of bulk polycrystalline Ag, it becomes obvious that the shift and narrowing in the 4d band observed by XPS is a consequence of the gradual reduction of the lowest BE peak (at 4.8 eV) in the valence band. It can be mentioned that qualitatively similar changes were observed in Ag nanoparticles prepared by traditional methods on graphite: the decrease of the ratio of the two main 4d peaks was detected with decreasing cluster size [101]. It is interesting to note that the Ag/Si ratio at which

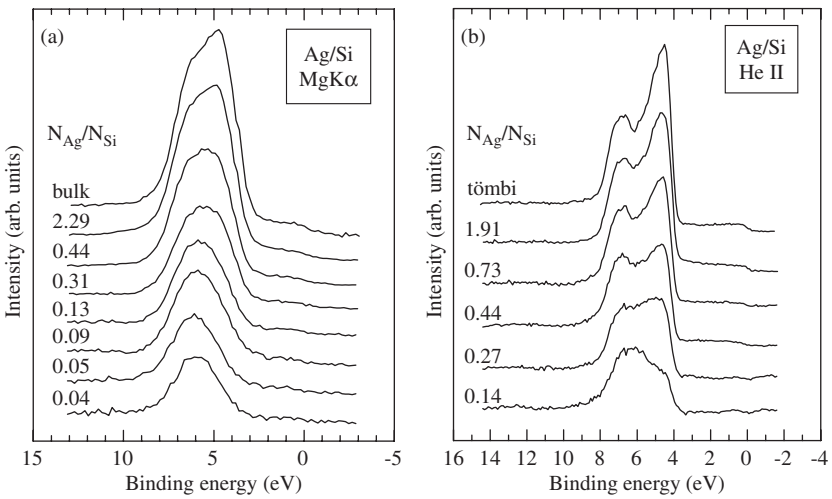

Figure 8. Valence band XPS (a) and UPS (b) spectra of silver islands on native oxide covered Si(1 0 0) during bombardment with 1 keV Ar^+ ions. Substrate related contributions are removed. Numbers at each spectra stand for the Ag/Si ratio determined from the appropriate XPS core level spectra. The uppermost curve is the spectrum of polycrystalline bulk Ag. (Reprinted from Ref. [146], © 1998, with permission from Elsevier.)

the core level shift becomes observable is significantly lower than that at the beginning of the valence band changes. This tendency seems to be in agreement with other published data [83,86,101,164], suggesting that the core level shift is – at least partly – a consequence of changes in the valence band DOS.

According to the presented results, one can conclude that the most size sensitive part of the valence band of the silver nanoparticles is the region of the low BE d-states. The size dependent changes of this spectral region are so prominent that they cannot be understood by any explanation based solely on final state effects. In addition, a model based on the idea of band narrowing with decreasing coordination number cannot explain the change of the intensity ratio of the main 4d components, especially in a size range where the change of the coordination number is still relatively small. In Reference 99 the photoelectron spectrum of relatively large (1 1 1) oriented Au nanoparticles is understood in terms of the bulk electronic structure of Au(1 1 1) single crystals, although the change of the intensity ratio of the two prominent 5d features is noted. Such a comparison is, however, not justified in our case since electron diffraction revealed no preferential nanoparticle orientation.

Instead, we believe the electronic structure changes are a collective effect of several distinct processes. For example, at surfaces the loss of the bulk symmetry will induce electronic states with different DOS compared to bulk. As the particle sizes are decreased, the contribution of these surface related states becomes more prominent. On the other hand, the decrease of the coordination number is expected to diminish the d-d and s-d hybridization and the crystal field splitting, therefore leading to narrowing of the valence d-band. At the same time, bond length contraction (i.e. a kind of ''reconstruction''), which was observed in small particles [89–92], should increase the overlap of the d-orbitals of the neighboring atoms, partially restoring the width of the d-band.

Since, however, the size dependence of these effects may be strongly different, their relative impact on the electronic structure of the nanoparticles will probably also change with the particle size. For example, the reduction of the coordination number becomes significant only if the particles are smaller than a few hundreds of atoms [102] thus, this effect will probably negligibly influence the electronic structure of the particles in the few nm size range. Since, according to the presented data, valence band changes often begin below 10 nm particle size, it is possible that the change of the most size-dependent states is governed by surface-related processes, including the potential increase of the s-d hybridization, as already suggested in the literature [93,164]. Nevertheless, theoretical evidence for the existence of such an effect is still missing.

5. Gold Nanoparticles

The research on gold has widened up in the last decade and even today it is considered as one of the metals for future catalysis. Haruta et al. discovered exceptionally high activity of gold nanoparticles supported on Co_3O_4, Fe_2O_3, and TiO_2 oxides in CO and H_2 oxidation [23,166], NO reduction [167], water–gas shift reaction [168], CO_2 hydrogenation [169], and catalytic combustion of methanol [170], when dispersion of the gold particles approached 100%.

We are focusing our discussions on gold nanoparticles because here the effect of size decrease is the most spectacular as bulk gold is one of the most inactive noble metal being resistant against any ambient effects, whereas gold nanoparticles are extremely active, e.g. in CO oxidation at sub ambient temperature. We have to address the electronic properties of the gold nanoparticles due to size reduction, the effect of interaction of gold nanoparticles with the support, the effect of valence state and

finally the nature of chemical bonding between nanoparticles and substrate.

5.1. Valence Band of Gold Nanoparticles [171–173]

The noble metal nanoparticles are good candidates for the investigation of nanoparticles because they have strongly different localized (fully occupied d-band) and delocalized (s-states) valence states exhibiting different size dependencies. Copper, silver, and gold all belong to this category, having different valence bands from the transition metals with unfilled d-valence states. This difference is very clearly seen in the case of Co vs. Cu and Ag. On the other hand copper and silver have very similar size-dependent tendencies. However the electronic structure of gold nanoparticles can be different from silver, copper, and cobalt as well.

The environment (e.g. the substrate) of the nanoparticles is a critical experimental parameter, which should be inert with respect to the nanoparticles. In the case of gold the native SiO_2 covered Si(1 0 0) seems to be an environment without any influence on the valence band of Au nanoparticles. The chemical and catalytic properties which are probably strongly correlated with the electronic structures of different systems, give another possibility to use and check the size dependent properties of nanoparticles.

Important information can be obtained from model system using well defined gold thin films deposited by thermal evaporation onto a Si(1 0 0) wafer covered by native oxide of nanometer thickness. The gold layer is discontinuous consisting of separate islands with an average thickness around 10 nm. The electronic structure of the Au nanoparticles was determined by measuring the energy distribution of photoelectrons excited by He(I) (UPS) or AlKα (XPS) radiation. The energy resolution was 0.15 eV in UPS and 0.8 eV in the XPS region. The samples were cleaned by Ar^+ ion bombardment for a few minutes.

The size of the gold islands was altered with further Ar^+ ion bombardment at 0.5–2 keV ion energy as is described in Section 3 and shown schematically in Figure 4. By this process the height as well as the lateral size of the islands decreased. The size reduction process for Au nanoparticles was characterized by the sputtering time during the *in situ* Ar^+ ion bombardment and by the Au/Si ratio. The native oxide layer on the Si substrate served as a barrier against the Si–Au interaction, but it was thin enough to avoid electrical charging.

The size of the nanoparticles was determined with TEM after the final ion bombardment on the same sample. The samples for TEM investigation were prepared by extraction replica method. The particles were stripped off the substrate surface by means of collodion which was covered by carbon film. The collodion was dissolved after carbon deposition.

Figure 9 [171] shows the Au 4f emission of the nanoparticles at different steps of the sputtering. The as-cleaned spectrum (curve (a)) is equivalent to the published data of bulk gold. The Au/Si ratio was around 3.3, showing that the gold film was discontinuous. With further ion bombardment, the position of the 4f emission shifted to higher BE, while the Au/Si ratio decreased to 2 and 1.3 (curves (b) and (c), respectively), showing that the coverage of the Au film decreased together with the size of the Au islands. The shift of the Au 4f level is another indication of the size decrease of Au nanoparticles, similarly as it was observed for Cu [145] and Ag [146] (see Section 4).

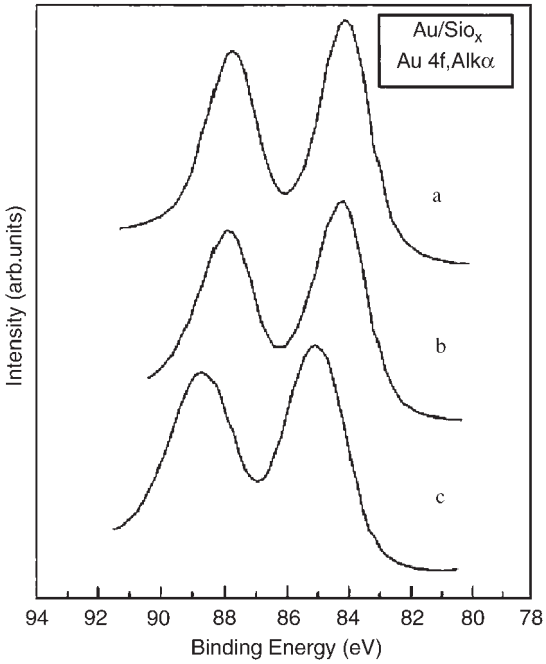

Figure 9. Photoemission from 4f atomic level of Au after surface cleaning (a) and 15-min (b) and 30-min (c) Ar^+ ion bombardment. (Reprinted from Ref. [171], © 2002, with permission from Elsevier.)

The size dependence of the valence band is shown in Figure 10 [171]. The spectra were obtained with AlKα excitation. In Figure 10 the curves (a), (b), and (c) represent the same samples as those in Figure 9. In spite the relatively low resolution, it is obvious that the Au 5d peak at 4 eV BE strongly decreases or even disappears with decreasing particle size (curves (b) and (c)) compared to the well-known bulk spectrum given by curve (a). The size dependence of the valence band DOS can be investigated with much better resolution by ultraviolet photoemission using He(I) excitation. The result is shown in Figure 11 [171]. The valence band spectra of the sample at the beginning of the sputtering is identical with that measured for bulk gold (curve (a)) but with longer sputtering, i.e. with decreasing the size of nanoparticles the valence band 5d states are redistributed. Firstly the peak at around 2–3 eV BE starts to decrease, and when it has more or less disappeared, the other peak at 6–7 eV BE decreases. Finally, the whole d-valence band is redistributed below a certain size of Au nanoparticles. The modification of the d-states at lower BE is similar to that observed for copper and silver, but change at higher BE is characteristic of Au only.

A clear size dependence is visible at Fermi level, although this change is observable only at smaller particles.

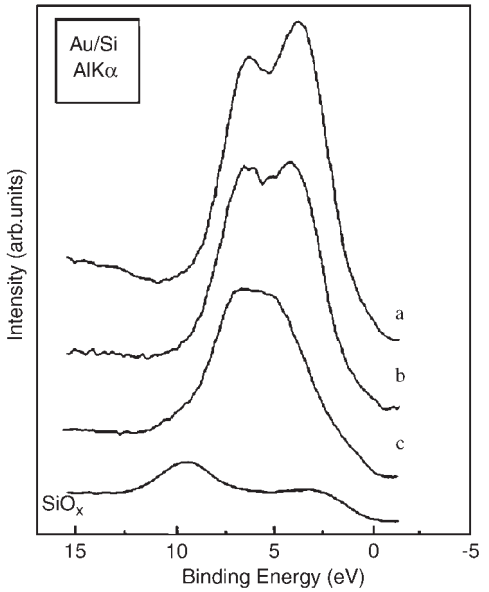

Figure 10. Energy distribution curves of photoelectrons (EDCs) excited by AlKα radiation. The curves (a), (b), and (c) were obtained after the same sputtering as in Figure 9. (Reprinted from Ref. [171], © 2002, with permission from Elsevier.)

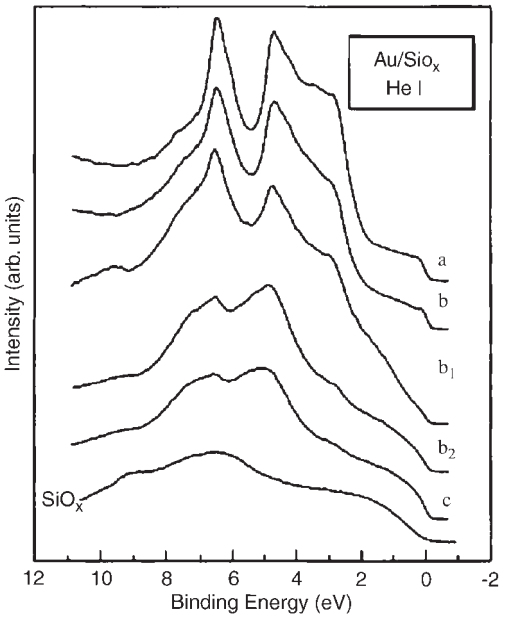

Figure 11. Size dependence of the UPS valence band spectra from gold nanoparticles. The sputtering time on curves (a), (b), and (c) are the same as in Figure 9. Curves (b_1) and (b_2) were recorded after 20 and 25 min. (Reprinted from Ref. [171], © 2002, with permission from Elsevier.)

The detailed size dependence at the Fermi level is shown in Figure 12 [171]. Although the Fermi cutoff is already detectable even at the smallest particle size (curve (c)), there is change near the Fermi level in the 0–0.6 eV BE

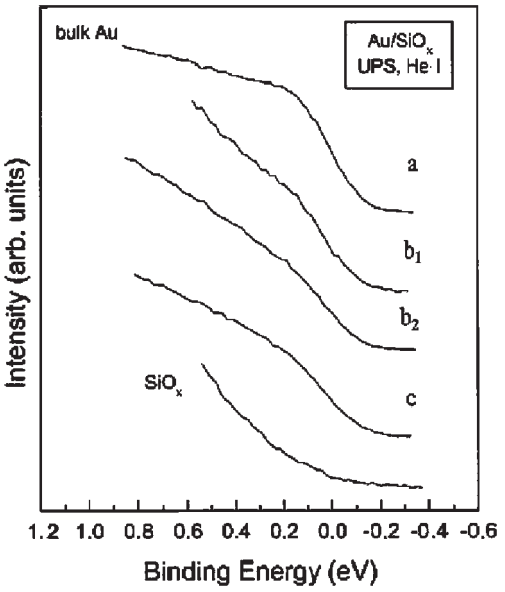

Figure 12. Size dependence of the photoemission data for gold nanoparticles at Fermi level (a), (b_1), (b_2), and (c), respectively. Curve SiO_2 represents the emission from the support only. (Reprinted from Ref. [171], © 2002, with permission from Elsevier.)

region. The separate emission from the SiO_2/Si substrate shows that the observed effect can only be correlated with Au emission. However, emission from the substrate should also be taken into consideration. The size of the gold nanoparticles was measured by TEM on the same sample that was used for the photoemission measurement. Two types of gold features are visible on the TEM micrograph. The smaller particles with around 5 nm diameter are isolated particles. Their sizes are in agreement with the expected measures. The other features – at least 200 nm in diameter – seem to be too large to exhibit size effects. These, however, consist of particles nearly as small as the isolated ones. These aggregates of small particles could be in agreement with the photoemission data if they were separated from each other.

As a conclusion the size dependence of the valence band of Au nanoparticles is similar to that observed for Cu and Ag in the lowest BE region of valence d-states. The highest BE part of the valence d-states is size dependent which is not the case for Cu or Ag. The existing models cannot explain the size dependence, i.e. the assumption of the narrowing or broadening of the valence band d-states. A new model including some structural changes induced modification in atomic potential or in s-p-d hybridization would be needed to explain the observed experimental data. Although there is size dependent modification in the DOS near the Fermi level, metal/nonmetal transition is not detectable at this size range of nanoparticles.

Extended X-ray absorption fine structure (EXAFS) and photoemission measurements carried out on the clusters ranging from isolated atoms to aggregates large enough to acquire bulk metal properties, is also could be a measure for the electronic properties [40]. Copper shows a

substantial contraction of the nearest-neighbor Cu–Cu distance for small clusters. In addition, the onset of the K absorption edge shifts toward higher energy as the cluster size decreases. Variable energy photoemission spectra of gold clusters show the evolution of band structure with increasing cluster size [40].

5.2. Catalytic Properties of Gold Nanoparticles

Electronic structure can be monitored if small gold particles are deposited over metal single crystals. As an example, ultra thin layers of gold grown on a substrate, clearly indicates such a change in electron properties. For instance, dissociative adsorption of H_2 (D_2) on Au thin films grown on an Ir(1 1 1) surface has been studied with temperature-programmed desorption (TPD) using a quadrupole mass spectrometer (QMS) and nuclear reaction analysis [174]. Thin Au(1 1 1) film is epitaxially grown on Ir(1 1 1), as confirmed by LEED and scanning tunneling microscopy (STM). H_2 (D_2) was dissociatively adsorbed on this Au(1 1 1) film, although it is well known that Au surfaces are noble enough not to dissociate hydrogen molecules. The effect of the resulting electron localization (narrowing of the s-bands) becomes more remarkable with increased filling by the impurity/overlayer d-electrons. This model explains the unexpected high reactivity of the thin Au(1 1 1) surface, where narrowing of the s-band is responsible. Moreover, it was found that H (D) atoms can be confined into the interface between the Ir surface and the Au thin film.

Norskov and his school [175–177] and others [178,179] have made theoretical calculations to study the high reactivity of gold nanoparticles. First, they assumed that the 10-atom cluster (Au_{10}) is neutral. A charged cluster is, therefore, not necessary for a large reactivity, but of course charging may help. There are two possible explanations of the high catalytic activity of the Au_{10} cluster. One is that the electronic structure of the Au atoms in the cluster is significantly different from Au atoms at the surface of a large crystal. That is, very low coordinated Au atoms are able to interact stronger with adsorbate, and Au_{10} has sites with a geometry which is particularly well matching for reactions involving bond breaking (and formation) in small molecules where two atoms or molecules are close to each other and both need to be stabilized. This picture offers an immediate explanation of the special reactivity of nanosized Au clusters. Only clusters in the nanoscale regime have the very low coordinated Au atoms and a sufficiently large fraction of corner sites. The present calculations also suggest that the small size of particles is not enough criteria, they must have a high fraction of special geometries. This implies that size and shape of the particles are both important parameters.

Density Functional Theory (DFT) has shown that low-coordinated sites on the gold nanoparticles can adsorb small inorganic molecules such as O_2 and CO, and the presence of these sites is the key factor for the catalytic properties of supported gold nanoclusters. Other contributions, induced by the presence of the support, can provide parallel channels for the reaction and modulate the final efficiency of Au-based catalysts. Also these calculations extended for the adsorption of O and CO on flat and stepped Au(1 1 1) surfaces are used to investigate effects which may increase the reactivity of Au. The adsorption energy does not depend on the number of Au layers if there are more than two layers. Steps are found to bind considerably stronger than the Au(1 1 1) terraces and an expansive strain has the same effect. On this basis it is suggested that the unusually large catalytic activity of highly-dispersed Au particles may in part be due to high step densities on the small particles and/or strain effects due to the mismatch at the Au/support interface. In conclusion, three effects might make gold surfaces chemically more reactive towards O_2 and CO adsorption: (i) quantum–size effects in one dimension, (ii) the effect of steps, and (iii) the effect of strain. For thin, flat Au slabs, there is no dependence of the adsorption properties of O_2 and CO on the number of Au layers. Since the step density increases as the particle size decreases this provides one explanation of the unusual catalytic activity of nanosized gold particles. Such a strain must be induced by the interaction with the support, and again this strain effect must increase rapidly with decreasing particle size.

Molina and Hammer [178] also presented review of recent DFT studies of the reactivity towards CO oxidation of supported Au nanoparticles. The possible structure of the periphery of the interface between a Au particle and an oxide support is discussed. A certain structure, in which low coordinated Au atoms are overhanging the support without binding directly to the oxide atoms, is argued to be prototypical of medium-sized Au particles. This structure is shown to be particularly active both at the edges and at the corners of Au particles. Examples from the literature of Au systems supported on MgO(1 0 0) and rutile-TiO_2(1 1 0) are reviewed and new data are given for the reactivity of facet, edge, and corner sites of a Au_{34} cluster supported on MgO(1 0 0). On the nonreducible oxide support, MgO(1 0 0), the CO oxidation is found to occur via CO adsorption to the Au particles and subsequent CO-promoted O_2 capture and formation of a CO–O_2 reaction intermediate complex. On the reducible oxide support, TiO_2(1 1 0), the O_2 is found to adsorb independently of the CO. However, on this support, the reaction still proceeds via CO–O_2 formation rather than via O_2 dissociation.

Hybrid density functional calculations have been carried out for Au–O_2, Au–CO, Au_{13}, Au_{13}–O_2, Au_{13}–CO, Au_{13}–H_2, and Au_{55} clusters to discuss the catalytic behavior of Au clusters with different sizes and structures for CO oxidation [179]. From these calculations, it was found that O_2 and CO could adsorb onto several Au model systems. Especially, icosahedral Au_{13} cluster has a relatively weak interaction with O_2 while both icosahedral and cubooctahedral Au_{13} clusters have interactions with CO. These findings suggest that the surfaces of the Au clusters are the active sites for the catalytic reactions on the supported and unsupported Au catalysts.

The interaction of adsorbed thiol molecules with gold nanoparticles as a function of the mean particle size has also been studied [180]. Monochromated X-ray Photoelectron Spectroscopy (MXPS) measurements showed the attachment of the thiol sulfur headgroup onto the cluster surface leading to a positive BE shift in the Au 4f core-level. No line width broadening could be observed indicating that the thiol–gold interaction affects the whole

particle and not only the surface, where the actual Au–S bond is located. In fact, one can observe rather a narrowing of the line width for smaller particles. The positive BE shifts depend on the cluster size and increase with decreasing diameter. A maximum shift of 0.41 eV could be measured for the smallest particles (~1 nm). The valence band spectra exhibited positive BE shifts similar to the Au 4f core-levels, but smaller in absolute values. Changes in the valence band shape were interpreted as re-hybridization of Au 5d electrons due to the creation of Au–S bonds. Furthermore, a disappearance of the Fermi edge was observed upon thiol adsorption, which could be due to a sulfur-induced metal insulator transition of the gold cluster. Thiol adsorption on gold clusters induces similar changes in the electronic properties as is known from finite-size effects in naked, i.e. uncovered, gold particles. For experiments with metal-core/organic-shell particles this has the consequence that it may be difficult to determine if a measured feature is an intrinsic property of the metal-core or due to core–shell interactions. On the other hand, the findings also show the feasibility to tune certain properties of deposited gold particles by thiol adsorption.

One of the most interesting areas in the field of gold nanoparticles is when they are deposited over TiO_2. As turns out from the following part, the results obtained by different research groups are still a subject of debate.

Electronic properties of Au nanoparticles grown on stoichiometric and reduced TiO_2(1 1 0) substrates were studied by MEIS and UPS using synchrotron-radiation light [181]. Initially, two-dimensional (2D) islands with a height of one and two atomic layers were grown and exposure to higher coverage increased the islands height to form three-dimensional (3D) islands on the stoichiometric TiO_2(1 1 0) substrate. In contrast, on reduced TiO_2 3D islands start to grow from the initial stage with a small Au coverage (0.1 ML, $1\,\mathrm{ML} = 1.39 \times 10^{15}\,\mathrm{atoms/cm^2}$). The appearance of Au(1 1 1) is probably due to oxygen vacancies acting as a nucleation site. Above 0.7 ML, all the islands become 3D ones taking a shape of a partial sphere and the Au clusters become metallic for both substrates. As a result, the Au 4f and Ti 3p core level shifts together with the valence band spectra are observed. The Ti 3p peak for the oxygen-deficient surface shifts to higher BE by 0.25 ± 0.05 eV compared to that for the stoichiometric surface, indicating downward band bending by an electron charge transfer from an oxygen-vacancy induced surface state band to n-type TiO_2 substrate. Higher BE shifts of Au 4f peaks observed for both substrates reveal an electron charge transfer from Au to TiO_2 substrates. The work function change of Au nanoparticles supported on the stoichiometric and reduced TiO_2 substrates were also a function of Au coverage and explained clearly by the above surface and interface dipoles.

The electronic interaction between TiO_2(1 1 0) surfaces and Au clusters has been investigated by UPS and STM to elucidate the high catalytic activity of Au/TiO_2 [182]. With increasing Au amount, the shift of O 2p nonbonding peak towards the Fermi level and the decrease in the Ti 3d peak area were precisely observed in the valence band photoelectron spectra of Au/TiO_2(1 1 0). With increasing the Au coverage, the steep energy shifts of the O 2p nonbonding state and the disappearance of the Ti 3d states were observed in the low coverage range. Simultaneously, the authors observed the preferential fixing and the growth of the Au clusters at the surface defects, such as step edges, on TiO_2(1 1 0). These results indicate that the Au clusters supported on TiO_2(1 1 0) are negatively charged due to the electron transfer from the surface defects to the Au clusters. The feature of the electron transfer was dominant at the Au cluster size of less than 3 nm, in which Au/TiO_2 catalysts show the high catalytic activity.

The interaction between gold clusters and TiO_2 (1 1 0) surface is also investigated via cluster nucleation and growth using STM [183]. The nucleation of gold preferentially occurs along the step edges and below 0.1 ML coverage it determines the initial deposition. The Au cluster growth seems to be 3D starting from the lowest coverage. The cluster density is independent of the surface preparation mode and the surface defect density due to the cluster interaction with the oxygen-depleted TiO_2.

Goodman and coworkers fabricated model Au/TiO_2(1 1 0) sample by epitaxially grown Ti film on Mo(1 1 0) surface. They have demonstrated how the CO oxidation rate over model Au/TiO_2(1 1 0) catalysts correlates with the thickness of gold particles and their band gap as probed by STM (this is defined as the length of the plateau in I–V plot in STS) [184,185]. The maximum activity occurs on particles that are two atomic layers thick and at band gap of 0.2–0.6 eV and this corresponds to ~5 nm gold particles. More information can be obtained from the Au $4f_{7/2}$ BE shift as a function of particle size [186] using TiO_2 and SiO_2 supports. As was mentioned the shift is originated mainly from the final state effect. For bulk the positive hole after photoelectron ejection is fully screened by the delocalized electrons in the valence band. On the other hand, in small nanoparticles the screening is less than in bulk, thus the kinetic energy measured of the photoelectrons is lower than in that measured for the bulk due to the Coulomb interaction between the positive hole and the photoelectrons. Consequently BE of the electrons is higher. The BE shift is about 0.8 eV and 1.6 eV for Au/TiO_2 and Au/SiO_2, respectively. Since the Au coverage to reach the BE characteristic of that of bulk value is higher on SiO_2 than on TiO_2, the difference can be interpreted by the result of the relative abilities of the metal oxide support to shield the final-state hole via extra-atomic relaxation. Thus the SiO_2 would signify a greater screening ability. That is, TiO_2 has a larger interaction with gold.

Density Functional Theory (DFT) calculation, however, does not fully support the strong interaction of gold with TiO_2 support [187]. In contrast to the Cu and Ag, in which case they found a strong interaction with the bridging oxygen with a transfer of the outer s-electrons to Ti 3d states, Au forms weaker bonds at these sites with formation of a covalent polar bond. On Ti sites weak interaction occurs with no charge transfer. The bonding at these sites is due to metal polarization.

Campbell studied the vapor deposition of Au onto TiO_2(1 1 0) with XPS, LEED, and ISS techniques [188]. The average coverage, at which the surface switches from 2D to 3D Au particle growths, increases between 0.08 ± 0.01 and 0.16 ± 0.01 ML as the oxide temperature decreases from 300 to 155 K. It increased by over twofold with oxide surface defect density, induced either by mild sputtering or by annealing in vacuum. This suggests that

islands nucleate at defects and that the migration of Au adatoms has unusual energetics. Oxygen adatoms were produced on 2D and 3D gold islands on $TiO_2(1\,1\,0)$ using a hot filament to excite (or dissociate) O_2 gas [189,190]. The dissociative adsorption of O_2 is thought to be impossible on pure, bulk Au surfaces. However, the unusual catalytic activity demonstrated by small Au particles on TiO_2 (in e.g. CO oxidation) may be related to this stronger bonding oxygen. The titration reaction of adsorbed oxygen on Au particles with CO gas ($CO_g + O_a \rightarrow CO_2$) is very rapid at room temperature, and its rate increases as island thickness increases (i.e. as the oxygen adsorption energy decreases) [189]. Thin islands of Au on TiO_2 have a very weak bond to CO, so that Au sites are still free (nonpoisoned by CO) at room temperature. It is possible that these bind oxygen so strongly that they can dissociatively adsorb O_2, allowing room-temperature catalytic oxidation to proceed at steady state. The thermal thickening kinetics of these Au islands has been measured using temperature-programmed ion scattering spectroscopy (TPISS) [188]. Typical results show that Au island thickening begins at 300 K, but requires temperatures in excess of 900 K for completion. This very broad temperature range turns out to be very difficult to model kinetically. It suggests some unusual island energetics, whereby the activation energy for the rate-limiting step varies dramatically with the extent of sintering.

Molecular-dynamics simulations also showed that spherical gold clusters is stable in the form of FCC crystal structure in a size range of $n = 13$–555 [191]. This is more likely a key factor in developing extremely high catalytic activity on reducible TiO_2 as a support material. Thus, it controls the electronic structure of Au nanoparticles (e.g. band gap and BE shift of Au $4f_{7/2}$ band) and thereby the catalytic activity.

Now, we have to address the one of the most crucial features of the gold nanoparticle catalysis: whether the gold is in metallic or ionic state. Evidence is presented and discussed by Scurrell group for the involvement of ionic gold, probably Au^+ in catalysis by supported gold [192]. Various catalytic systems and various experimental techniques have been used for reactions involving carbon monoxide. Mössbauer effect spectroscopy on gold–titania and gold–titania–zirconia reveals the co-existence of Au(0), Au(I), and Au(III), but only the Au(I) content correlates directly with the activity of these solids for CO oxidation. XPS data suggest that a small (ca. 6%) fraction of the gold present in gold–titania–zirconia catalysts is present in an electron deficient state relative to Au(0). For gold–iron oxide catalysts, high water–gas shift activity is obtained for samples in which a partial reduction of the gold, initially present as Au(III), has occurred. For gold–HY zeolites, in which the gold is initially introduced as Au(III) by ion-exchange from $[Au(en2)]^{3+}$, samples become catalytically active only after a considerable induction period has been exceeded. The induction period is shortened and the activity of the catalysts increased by pre-treatment with sodium borohydride, and some degree of reduction of the gold is assessed to have occurred. Further evidence that nonequivalent states of gold exist (i.e. metallic and ionic gold) in active CO oxidation catalysts based on gold–titania is provided by the fact that partial removal of gold occurs when the solids are treated with solutions containing cyanide ions under oxidative conditions. The specific activity refereeing to unit surface of gold increases with decreasing gold content, when the gold content is lowered by such treatment. The results are consistent with the requirement for Au(I) involvement in the catalytic reaction, though a role for Au(0) is not ruled out.

Recent studies [193] of the CO oxidation activity exhibited by highly dispersed nano-gold (Au) catalysts have reached the following conclusions: (a) bilayer structures of Au are critical; (b) a strong interaction between Au and the support leads to wetting and electron rich Au; (c) oxidative environments deactivate Au catalyst by re-oxidizing the support, which causes the Au to de-wet and sinter. Recent results have shown that the direct intervention of the support is not necessary to facilitate the CO oxidation reaction; therefore, an Au-only mechanism is sufficient to explain the reaction kinetics.

Recent results [194] in catalysis by supported gold showed contradictory proposals concerning the nature of the active sites in supported gold catalysts. The present evidence from a set of complementary experimental methods characterizing $Au/\alpha\text{-}Fe_2O_3$ catalysts, demonstrate that cationic gold plays a crucial role in catalyzing CO oxidation at 298 K, as well as in the hydrogenation of croton aldehyde. The catalysts were structurally and chemically analyzed by HREM and STEM-XEDS. A combination of EXAFS, *in situ* XANES, XPS, and Mössbauer effect spectroscopy demonstrates the important role of cationic gold in the activity of these iron oxide-supported gold catalysts.

A number of oxide-supported gold catalysts [195] have been prepared by deposition – precipitation, with variation of the pH over a wide range, the optimum pH for high activity being 8 for TiO_2, 7.5 for Fe_2O_3, and 7 for SnO_2 and CeO_2. Whereas the activity shown by Au/TiO_2 and Au/Fe_2O_3 decreased linearly with time, Au/CeO_2 and Au/SnO_2 underwent an initial major deactivation. Addition of iron in the preparation lowered the rate of deactivation when TiO_2, SnO_2, and CeO_2 were used as supports, and imparted activity when as with Bi_2O_3 it was previously lacking. XPS revealed the existence of a broad multi-state iron-containing region, and TEM and STEM/EDX indicated that small gold particles (1.5–4 nm) were partly in contact with it. Improved stability is therefore due to gold particles being in contact with an iron phase such as FeO(OH); calcination removed the stabilisation.

Infrared spectra of CO adsorbed on gold nanoparticles [196] supported on oxidized and reduced TiO_2 also support the participation of zero valent gold. Depending on which pre-treatment is used, different stretching bands related to gold carbonyls have been found. On calcined samples the predominant absorption band is at $2110-2120\,cm^{-1}$, assigned to CO adsorbed linearly on nanometric gold metallic particles; on highly dehydrated, oxidized samples, a band at $2154\,cm^{-1}$ is detected, ascribed to CO adsorbed on oxidized gold sites; on reduced samples some new bands in the frequency range 2050–$1900\,cm^{-1}$ are produced, assigned to CO adsorbed linearly and bridge-bonded on gold small clusters, perturbed by the negative charge produced in support reduction.

In recent studies the structure of gold clusters of different sizes supported on various metal oxides (Al_2O_3, TiO_2, SiO_2) exposed to different CO oxidation conditions was investigated *in situ* using X-ray absorption spectroscopy at the Au L_{III} edge [197]. In all catalysts, the only phase detected during catalysis was Au(0). In the most active sample with small gold particles (Au/Al_2O_3), variation in the electronic structure of the gold clusters with changing reaction conditions was observed by XANES spectroscopy and ascribed to the adsorption of CO on the metallic gold clusters. FEFF8 calculations proved that the changes in the XANES signal of Au/Al_2O_3 can be explained by backdonation of d-electrons into the 2π*-orbitals of CO. For Au/Al_2O_3, the presence of Au–O backscattering in the EXAFS suggested weak cluster–support interactions.

XPS revealed that on samples [198] consisting of the gold phase and the iron oxide on aerogel support, an increase occurs in the surface coverage of hydroxyl groups and the Fe^{2+}/Fe^{3+} ratio due to the addition of gold as well as a transition of gold from oxidized to metallic states due to calcination. In the presence of gold species, the Fe^{3+} satellite structure in XPS was not produced. The crystallinity of c-maghemite was found quite stable with respect to gold addition and thermal treatment. The methanol oxidation carried out in an ambient flow reactor, was found to be enhanced with decreasing catalyst pretreatment temperatures and with increasing gold loadings up to 5 wt.%. A wide selectivity pattern formed between dimethyl ether and carbon dioxide products. The ionic gold was more active than the metallic gold towards the total combustion to carbon dioxide. The surface nature has been proven to transform from strong Lewis acidic to high basic characters due to the formation of reactive hydroxyl groups near by the gold sites.

In summary, the major message of the investigations carried out so far is that:

(i) The electronic structure in the valence band changes as the size of gold nanoparticles decreases. There are also core level shift towards higher binding energies, but it is decisive only the when Auger parameter is shifted parallel.
(ii) Electron interaction must exist between gold nanoparticles and the supports for high catalytic activity.
(iii) The valence state of gold (metallic or cationic) is still questionable.
(iv) In order to explain the catalytic behavior in relation with the structure of catalyst we have to refer to other single crystal works. Single crystal studies, when metallic gold was evaporated on single crystal of TiO_2 (and not starting from Au ions) [185], indicated that the maximum catalytic activity started when the electronic structure of gold was just at border of the transition between ionic (large band gap) and metallic character. That is, for the catalytic activity metallic gold is required, but beyond this a strong interaction between the metal and support along the perimeter interface is required.

To further refine this phenomenon a model experiment was performed to find a direct correlation between the size and electronic structure as well as activity of supported gold in the CO oxidation [171,172,199] 10 nm gold thin films were deposited onto $SiO_2/Si(1\,0\,0)$ wafer [171]. The electronic structure of the Au nanoparticles was determined by UPS measuring the energy distribution of the photoelectrons excited by He (I). The samples were cleaned by Ar^+ ion bombardment for a few minutes. The gold film was ion implanted with Ar^+ ions at 4 keV and 10^{15} atom/cm^2 dose [171,199]. The native SiO_2 oxide layer on the Si(1 0 0) substrate served as a barrier against the Si–Au interaction, but it was thin enough to avoid electric charging. The Au 4f and Si 2p core levels were also measured to detect BE and the average coverage of Au on the Si substrate. As indicated in Figure 11 shape of the Au 5d valence band structure changed that was indicated by a decrease in the valence bands both at 2–3 eV BE and at 6–7 eV BE. Finally, the whole d-valence states are redistributed below a certain size of Au nanoparticles. The separate emission from the Si/SiO_2 substrate shows that the observed effect can only be correlated with Au emission.

The UPS indicated structure change is associated with size reduction as the discontinuous gold film is transformed into rod-shape and spherical particles with size of 5–10 nm. Accordingly, with size reduction the activity displayed in CO oxidation is also altered: the rate increased from 6.7×10^{-3} to 2×10^{-2} mol min^{-1} cm^{-2}. Consequently, not only the gold–reducible oxide interaction is responsible for the increased activity, but also size reduction. Indeed, small clusters themselves are able to activate the reaction components shown by theoretical calculations performed for 10–15-atom clusters, which can activate easily oxygen [177,200], but in real catalyst, even at the smallest active ensemble, it consists of a few hundreds atoms.

Although the gold particle size has importance in systems, which do not contain reducible oxide, such as MgO [201], still the majority of data indicate that high activity is related to the gold/oxide interface. The importance of this experiment is further underlined by the fact that within a 4–10 nm range of Au particle size the system is active [183], but around the gold particle within a short distance the support must be defected in order to activate the reaction components.

5.3. The Role of Gold/Oxide Interface

Metal oxides of variable oxidation state as supports or support modifiers [202] are well known in gold catalysis. In the previous section we have already indicated some metal–support interactions influencing the electronic state of gold nanoparticles as well as the metallic or ionic state of gold. Of the numerous literatures we have to mention Haruta and Date [169], Bond [195], as well as Goodman works [186,203]. Further results can be found on the iron oxide system in recent literatures [162,204].

The electron interaction between nanosized gold particles and iron oxide support is only one factor which determines the properties of the gold/oxide system. For instance, in the $Au/FeO_x/SiO_2/Si(1\,0\,0)$ model sample the depth profile (after successive Ar^+ ion bombardment at a

flux of $1-2\times10^{13}$ ion/cm^2 s^{-1}) the valence band spectra compared with those recorded on $Au/SiO_2/Si(1\,0\,0)$ shows that in the latter sample a shift in the Au 5d valence band towards higher binding energies vs. decreasing the Au/Si ratio is observed, while this shift is absent when the Au/Fe ratio decreases. It means the metallic gold state is stabilized by iron oxide whereas without iron oxide a gold–silicon interaction becomes predominant [147].

In the same samples – according to recent studies – the high activity in the oxidized state was associated with amorphous iron oxide with Fe 2p BE. = 711.3 eV because there was no significant change in the gold particle size (for as prepared, oxidized and reduced samples, 3.8, 4.1, and 5 nm, respectively). It was established that in developing the catalytic activity the gold should be metallic and the support should be amorphous with high BE and the reaction occurs along the perimeter of gold particles. XPS results revealed that after oxidation and reduction the Au 4f peaks did not show any appreciable shift, the $4f_{7/2}$ peak being at 84.5 eV. The unchanged position of the Au peaks in the XPS spectra after oxidation and reduction pretreatments is likely ascribed to the presence of FeO_x stabilizing the gold electronic levels. Annealing in vacuum and hydrogen somewhat reduces the iron oxides. TEM micrographs show that in the ''as-prepared'' sample the FeO_x support is amorphous. On the oxidative treatments the size of Au particles slightly increases (4.1 nm) while FeO_x still remains amorphous. On the reduced sample the diameter of gold further increases (5 nm) and two new FeO_x lines in the electron diffraction picture are developed. The new crystalline FeO_x phases are identified and assigned as c-maghemite, which is the cubic form of the Fe_2O_3 compared to the rhombohedral form of the Fe_2O_3 hematite. The gold size distribution becomes more symmetric.

The initial rates of CO oxidation were determined on the samples treated in different ways. The reactivity of the samples investigated in the preliminary experiments decreases in the sequence of $Au/FeO_x/SiO_x/Si(1\,0\,0) > FeO_x/SiO_x/Si(1\,0\,0) > Au/SiO_2/Si(1\,0\,0) > Si(1\,0\,0)$. The $Au/FeO_x/SiO_2/Si(1\,0\,0)$ catalyst has the highest initial activity. The results along with XPS and TEM data demonstrate that the interaction of gold nanoparticles and iron oxide tends to stabilize the metal character of gold and due to this stabilization, the Au/FeO_x catalyst has enhanced activity in the CO oxidation.

To sum up, it can be established that for developing significant catalytic activity we need (i) the presence of metallic gold particles (3–4 nm in diameter), (ii) amorphous iron oxide support in oxidized state with significant interfacing with gold particles along the perimeter, and (iii) slightly reduced iron oxide as support with oxygen defect sites. The presence of these three factors may create the sites along the gold/support perimeter which are a prerequisite for high catalytic activity in CO oxidation.

The catalytic activity in the CO oxidation should significantly increase due to the gold/oxide interface around the perimeter of nanoparticles [147], therefore, we assumed that this is true regardless of the sequence of gold or FeO_x deposition provided that iron oxide is amorphous. When iron oxide is deposited onto $Au/SiO_2/Si(1\,0\,0)$ we call it ''inverse interface''.

Table 1. Effect of FeO_x deposition onto Au particles on reaction rate of CO oxidation.

Sample	Initial rate (r_0), μmol/s/cm^2
$FeO_x/SiO_2/Si(100)$	2.3×10^{-2}
Implanted $Au/SiO_2/Si(100)$ used in catalytic reactions	1.5×10^{-3}
Implanted $Au/SiO_2/Si(100)$ after FeO_x ablation	9.5×10^{-2}

In Table 1 the rate shows about a four-fold increase in the initial rate of CO oxidation measured on $FeO_x/Au/SiO_2/Si(1\,0\,0)$ as compared with $FeO_x/SiO_2/Si(1\,0\,0)$ and about 60 times higher initial rate comparing to the base implanted $Au/SiO_2/Si(1\,0\,0)$ after catalytic reactions [199]. These results indeed indicate that in addition to the sole size effect, the presence of the Au/FeO_x interface significantly influence the CO oxidation. Similar effect was observed when gold was deposited on activated carbon fiber and sequentially promoted by FeO_x [205].

To further clarify this effect, model experiments were performed in which the gold layer or gold nanoparticles were covered with a well-defined oxide layer [206]. Iron oxide layers of 5–10 nm thickness were deposited by pulsed laser techniques (PLD) onto either Au films or nanosized Au particles supported by $SiO_2/Si(1\,0\,0)$. Samples were characterized by AFM, XPS, and time-of-flight secondary ion mass spectrometry (TOF SIMS) before and after measurements of the CO oxidation activity. Comparison was made with reference samples either free of iron oxide and/or free of Au particles/films. The initial activity of iron oxide/Au nanoparticles/$SiO_2/Si(1\,0\,0)$ turned out to be the highest followed by the sample containing a sandwiched Au film. While some reaction-induced changes in the chemical composition of the iron oxide overlayer (''FeO_x'', which can be regarded as a mixture of Fe_2O_3, FeO, and FeOOH according to an XPS analysis of the Fe 2p and O 1s core levels) were seen, no Au segregation at the surface was detected by TOF SIMS. The XPS Au 4f spectra indicated, however, that Au atoms might be injected and trapped in this layer. The catalytic activity of the $FeO_x/Au/SiO_2/Si(1\,0\,0)$ samples must be attributed to active sites located on the 5–10 nm iron oxide overlayer promoted by gold underneath. Since Au nanoparticles and Au films caused promotion we infer that an electronic effect is in operation due to the occurrence of an FeO_x/Au interface in both cases. Since the promotion is stronger for Au nanoparticles the hypothesis of a particle size dependent electronic effect may be advanced. For thicker FeO_x of about 40–60 nm no promotion by Au was found. Sample morphologies are such that the FeO_x/Au interface cannot directly interact with CO and O_2. This means that not only the well-known FeO_x/Au perimeter (triple interface) can display promotion of the CO oxidation.

In our case the chemical composition and, consequently, the structure of the iron oxide is changed with time during reaction. Gold diffusion from film and nanoparticles underneath may occur but seem not to be the decisive factor in promoting the CO oxidation activity.

We infer the importance of the FeO_x/Au interface which occurs for films as well as nanoparticles. However, since we observe FeO_x/Au nanoparticles/SiO_2/Si(1 0 0) to be the most active of all samples we advance the hypothesis of the occurrence of a strong electronic effect at the FeO_x/nanoparticle interface "coupling through" the FeO_x layer thus producing the high catalytic activity. Au promotion was also experienced in the catalytic activity of TiO_2 overlayers [207].

The effect of oxide/metal inverse interface is indeed a very exciting problem. The oxidation of Ce films on Pt(1 1 1) by O_2 and N_2O and the thermal properties of the resulting oxide layers have been studied by a combination of LEED [208]. Thick films of Ce (>1 ML) undergo incomplete oxidation due to passivation by the overlying oxide. Subsequent thermal treatment leads to in-diffusion of oxygen with (in the case of CeO_2) conversion of Ce^{4+} to Ce^{3+}. In the case of N_2O, adsorption only leads to the formation of Ce_2O_3. It was found that when a dispersed catalyst is annealed to 800 K in vacuum, only partial reduction of Ce^{4+} to Ce^{3+} occurs. This suggests that intimate contact between the metal and oxide phases is indeed crucial to facilitate oxygen release from the oxide lattice, thereby maximizing catalyst efficiency. The effect should be even more marked if this Pt-induced destabilization of ceria induces actual catalytic activity on the oxide surface. The labile high BE oxygen state was observed. This capping species undergoes reduction in H_2 at low temperatures and therefore probably plays an important catalytic role. Similar effects were observed in CO oxidation on Pt(1 1 1)/CeO_2 [209]. If the CeO_2 coverage is around 1.3–10 ML (no exposed Pt), the activity is much higher than on Pt(1 1 1) or CeO_2 alone. The authors concluded that the reaction occurred at the surface of the thin oxide film whose properties were radically altered by the presence of the underlying fully encapsulated Pt. As possible explanation, the electron transfer from metal to oxide was considered to reduce the enthalpy for oxygen vacancy formation in the oxide. Liu and Vannice have carried out similar experiments on Au/TiO_2 and TiO_2/Au model systems deposited on a Pt foil [210]. AES and CO adsorption measurements suggest that in both TiO_2/Au and Au/TiO_2 samples the authors were not able to achieve a continuous oxide film.

In a recent work van Steen [211] has shown that the "electronic factor" is only important for very small gold clusters, whereas on larger particles the interface effect becomes a decisive factor. Lewis et al. have studied the structure of vanadia films on an Au(1 1 1) single crystal [212] and an Au foil [213]. The structure of the supporting gold influences the ordering of the vanadia. Under vacuum conditions oxygen was found to desorb from V_2O_5 and after hydrogen treatment some oxygen was removed as H_2O resulting in surface segregation of bulk oxygen. Similarly, when iron oxide is deposited on Pt(1 1 1) and Pt(1 0 0) the chemical reactivity is strongly influenced by the substrate orientation [214]. These examples explain how the subsurface metallic structure may influence the reactivity of the outermost oxide layer.

The structure of the overlayer also affects the reactivity [215]. Methanol was studied on TiO_2 nanoparticles supported on Au(1 1 1). The nanoparticles formed by oxidation of sputtered Ti metal on Au(1 1 1) have TiO_2 stoichiometry and the reactivity of these particles towards methanol was compared to the reactivity of TiO_2(1 1 0), the most thermodynamically stable single crystal surface. The reactivity of the nanoparticles differed from that of the TiO_2(1 1 0) stoichiometric surface. Specifically, the nanoparticles produced methane from methanol while the TiO_2(1 1 0) did not. This difference is attributed to under-coordinated titanium cations present on facets of the nanoparticles, which lead to methane formation. The differences in reactivity towards methanol between the nanoparticles and the extended TiO_2(1 1 0) suggest that the three-dimensional, local structure plays a very significant role in the reactivity of these nanoparticles towards methanol.

We have to note that ultrathin oxide layers can exhibit special behavior by enabling the coupling of structural distortions and charge transfer beyond that allowed in the bulk [216]. The first-principles calculations showed that ultrathin layers of titania, a prototypical oxide, are active in stabilizing adsorption of O_2 on Au overlayers. The adsorbed O_2 molecules induce charge redistribution in Au that penetrates to the Au/titania interface, which responds through structural distortions that lower the total energy of the system. If metastable nanostructures of reducible oxides have been grown on metal surfaces, the reducing character of the metal substrate helps to create active vacancy sites across the supported ultrathin oxide, which can allow wetting by transition metal catalysts. The oxidation state of supported oxide nanostructures can also be tailored. Such oxide nanostructures and ultrathin films are likely to have much more flexibility to distort in response to adsorbates, compared to bulk oxide supports. The control of the features of nanostructures on substrates that can exhibit interface-fluxionality suggests that improved catalysts and sensors can be designed by replacing traditional reducible oxide supports by ultrathin oxide films.

6. Conclusions

Physical properties of metal nanoparticles show characteristic size-dependent changes as their size increases from the limit of isolated atoms towards macroscopic dimensions.

The size-dependent features of the electronic structure have been explored, with special emphasis on the evolution of the valence band DOS of transition and noble metals as the particle size increases.

The available experimental data and computational results for nanoparticles supported on inert as well as interacting substrates as carbon, oxides, and metals have been reviewed in detail.

The effects of the interaction between the nanoparticles and the substrate on the electronic structure of the nanoparticles have been discussed.

Correlation has been suggested between the morphology, electronic structure and catalytic properties of supported gold nanoparticles with special attention to the role of the substrate/interface behaviour.

References

1 G. Timp (ed.) *Nanotechnology*, 1st ed., Springer-Verlag, New York, 1999.
2 G. A. Somorjai, *Chemistry of Two Dimensions: Surfaces*, Cornell University Press, Ithaca, New York, 1981.
3 G. A. Somorjai, *Introduction to Surface Chemistry and Catalysis*, John Wiley, New York, 1991.
4 B. C. Gates, L. Guczi, H. Knözinger (eds.) *Metal Cluster in Catalysis*, *Stud. Surf. Sci. Catal.*, Vol. 29, Elsevier Science Publishing Company, Amsterdam, 1986.
5 K. C. Waugh, F. Solymosi, L. L. Hegedus (eds.) *New Development in the Surface Chemistry of Metals, Topics in Catalysis*, Vol. 14, Kluwer Academic/Plenum Publishers, Dordrecht, The Netherlands, 2001.
6 M. Rosoff (ed.) *Nano-Surface Chemistry*, Marcel Decker Inc., New York, 2002.
7 W. P. Halperin, *Rev. Mod. Phys.* 58 (1986) 533.
8 M. A Kastner, *Rev. Mod. Phys.* 64 (1992) 849.
9 R. Pool, *Science* 248 (1990) 1186.
10 S. Empedocles, M. Bawendi, *Acc. Chem. Res.* 32 (1999) 389.
11 S. Chen, R. S. Ingram, M. J. Hostetler, J. J Pietron, R. W. Murray, T. G. Schaaff, J. T. Khoury, M. M. Alvarez, R. L. Whetten, *Science* 280 (1998) 2098.
12 M. Nirmal, L. Brus, *Acc. Chem. Res.* 32 (1999) 407.
13 J. Bucher, D. C. Douglass, L. A. Bloomfield, *Phys. Rev. Lett.* 66 (1991) 3052.
14 C. B. Murray, C. R. Kagan, M. G. Bawendi, *Annu. Rev. Mater. Sci.* 30 (2000) 545.
15 C. P. Collier, T. Vossmeyer, J. R. Heath, *Annu. Rev. Phys. Chem.* 49 (1998) 371.
16 M. P. Pileni, *J. Phys. Chem. B* 105 (2001) 3358.
17 H. Weller, *Angew. Chem. Int. Ed. Engl.* 35 (1996) 1079.
18 L. L. Kesmodel, G. A. Somorjai, *Acc. Chem. Res.* 9 (1976) 392.
19 J. Turkevich, G. Kim, *Science* 169 (1970) 873.
20 L. Guczi, in M. J. Phillips, M. Ternan (eds.) *Proceedings of 9th International Congress on Catalysis*, Chemical Institute of Canada, Ottawa, 1989, 114.
21 M. Che, C. O. Bennett, *Adv. Catal.* 36 (1989) 55.
22 H. Sakurai, M. Haruta, *Catal. Today* 29 (1996) 361.
23 M. Haruta, *Catal Today* 36 (1997) 153.
24 Y. Yuan, K. Asakura, H. Wan, K. Tsai, Y. Iwasawa, *Chem. Lett.* 9 (1996) 755.
25 M. Haruta, S. Tsubota, T. Kobayashi, H. Kageyama, M. J. Jenet, B. Delmon, *J. Catal.* 144 (1993) 175.
26 P. N. Ross, K. Kinoshita, P. Stonehart, *J. Catal.* 32 (1974) 163.
27 M. G. Mason, R. C. Baetzold, *J. Chem. Phys.* 64 (1976) 271.
28 M. G. Mason, L. J. Gerenser, S.-T. Lee, *Phys. Rev. Lett.* 39 (1977) 288.
29 R. C. Baetzold, *J. Phys. Chem.* 82 (1978) 738.
30 R. C. Baetzold, M. G. Mason, J. F. Hamilton, *J. Chem. Phys.* 72 (1980) 366.
31 R. C. Baetzold in B. Pullman (ed.) *Catalysis in Chemistry and Biochemistry, Theory and Experiment*, D. Reidel, Boston, 1979, 191.
32 R. C. Baetzold, *Surf. Sci.* 106 (1981) 243.
33 R. C. Baetzold, J. F. Hamilton, *Progr. Solid State Chem.*, Vol. 15, Pergamon Press Ltd, 1983, 1.
34 R.C. Baetzold, L.J. Gerenser, *Chem. Phys. Lett.* 73 (1980) 67.
35 J. F. Hamilton, P. C. Logel, *Thin Solid Films* 23 (1974) 89.
36 R. C. Baetzold, *J. Chem. Phys.* 68 (1978) 555.
37 M. G. Mason, S.-T. Lee, G. Apai, *Chem. Phys. Lett.* 76 (1980) 51.
38 Y. Takasu, R. Unwin, B. Tesche, A. M. Bradshaw, *Surf. Sci.* 77 (1978) 219.
39 G. Apai, S.-T. Lee, M. G. Mason, *Solid State Commun.* 37 (1981) 213.
40 J. F. Hamilton, G. Apai, S. T. Lee, M. G. Mason, *Growth and Properties of Metal Clusters*, Elsevier Sci. Publ. Co., Amsterdam, 1980, 387.
41 M. G. Mason, *Phys. Rev. B* 27 (1983) 748.
42 B. Bellamy, A. Masson, V. Degouveia, M. C. Desjonqukres, D. Spanjaard G. Treglia, *J. Phys. Condens. Matter* 1 (1989) 5875.
43 P. Legare, Y. Sakisaka, C. F. Brucker, T. N. Rhodin, *Surf. Sci.* 139 (1984) 316.
44 S. M. Davis, *J. Catal.* 117 (1989) 432.
45 S. M. Davis, *J. Catal.* 122 (1990) 240.
46 H. P. C. E. Kuipers, *Solid State Ionics* 16 (1985) 15.
47 A. O. Turner, *Methods in Molecular Orbital Theory*, Chapter 5, Prentice-Hall, Englewood Cliffs, NJ, 1974.
48 R. Hoffmann, *J. Chem. Phys.* 39 (1963) 137.
49 J. A. Pope, G. A. Segal, *J. Chem. Phys.* 44 (1966) 3289.
50 R. C. Baetzold, *J. Chem. Phys.* 55 (1971) 4363.
51 B. Pullman (ed.) *Catalysis in Chemistry and Biochemistry, Theory and Experiment*, D. Reidel, Boston, 1979, 191.
52 A. B. Anderson, *J. Chem. Phys.* 68 (1978) 1744.
53 F. Cyrot-Lackmann, M. C. Desjonqueres, M. B. Gordon, *J. Phys. (Paris)* 38 (1977) C2–C55.
54 G. Blyholder, *Surf. Sci.* 42 (1974) 249.
55 E. R. Davidson, S. C. Fain, Jr., *J. Vac. Sci. Technol.* 13 (1976) 209.
56 R. C. Baetzold, R. E. Mack, *J. Chem. Phys.* 62 (1975) 1513.
57 R. C. Baetzold, *Inorg. Chem.* 20 (1981) 118.
58 D. J. Trevor, D. M. Cox, A. Kaldor, *J. Am. Chem. Soc.* 112 (1990) 3742.
59 W. Eberhardt, P. Fayet, D. M. Cox, Z. Fu, A. Kaldor, R. Sherwood, D. Sondericker, *Phys. Rev. Lett.* 64 (1990) 780.
60 J. C. Vickerman, K. Christmann G. Ertl, P. Heimann, F. J. Himpsel, D. E. Eastman, *Surf. Sci.* 134 (1983) 367.
61 E. Beaurepaire, F. Scheurer, V. Schorsch, B. Carriere, J. P. Deville, O. Heckmann, *Surf. Sci.* 251–252 (1991) 36.
62 P. Pervan, M. Milun, *Surf. Sci.* 264 (1992) 135.
63 J. A. Rodriguez, R. A. Campbell, D. Wayne Goodman, *J. Phys. Chem.* 94 (1990) 6936.
64 J. A. Rodriguez, R. A. Campbell, D. Wayne Goodman, *J. Phys. Chem.* 95 (1991) 2477.
65 J. A. Rodriguez, R. A. Campbell, D. Wayne Goodman, *J. Phys. Chem.* 95 (1991) 5716.
66 J. A. Rodriguez, D. Wayne Goodman, *J. Phys. Chem.* 95 (1991) 4196.
67 J. E. Houston, C. H. F. Peden, D. S. Blair and D. W. Goodman, *Surf. Sci.* 167 (1986) 427.
68 R. A. Campbell, J. A. Rodriguez and D. W. Goodman, *Surf. Sci.* 240 (1990) 71.
69 J. A. Rodriguez, *Surf. Sci.* 303 (1994) 366.
70 R. A. Campbell, J. A. Rodriguez, D. W. Goodman, *Surf. Sci.* 256 (1991) 272.
71 J. A. Rodriguez, *Surf. Sci.* 318 (1994) 253.
72 T. D. Pope, K. Griffiths, P. R. Norton, *Surf. Sci.* 306 (1994) 294.
73 R. Belkhou, N. T. Barrett, C. Guillot, A. Barbier, J. Eugkne, B. Carriére, D. Naumovic, J. Osterwalder, *Appl. Surf. Sci.* 65–66 (1993) 63.
74 M. Breeman, G. T. Barkema, D. O. Boerma, *Surf. Sci.* 323 (1995) 71.
75 G. Moretti, P. Porta, *Surf. Sci.* 287–288 (1993) 1076.
76 M. L. Shek, P. M. Stefan, I. Lindau, W. E. Spicer, *Phys. Rev. B* 27 (1983) 7277.
77 A. Bousetta, A. H. AI Bayati, L. A. van den Berg, D. G. Armour, *Appl. Surf. Sci.* 56-58 (1992) 480.
78 G. Pető, G. Molnár, G. Bogdányi, L. Guczi, *Catal. Lett.* 26 (1994) 383.

79 G. Bogdányi, Z. Zsoldos, G. Pető, L. Guczi, *Surf. Sci.* 306 (1994) L563.
80 G. K. Wertheim, S. B. DiCenzo, S. E. Youngquist, *Phys. Rev. Lett.* 51 (1983) 2310.
81 G. K. Wertheim, S. B. DiCenzo, D. N. E. Buchanan, *Phys. Rev. B* 33 (1986) 5384.
82 S. B. DiCenzo, S. D. Berry, E. H. Hartford Jr., *Phys. Rev. B* 38 (1988) 8465.
83 A. R. Pennisi, E. Costanzo, G. Faraci, Y. Hwu, G. Margaritondo, *Phys. Lett. A* 169 (1992) 87.
84 E. Costanzo, G. Faraci, A. R. Pennisi, S. Ravesi, A. Terrasi, G. Margaritondo, *Solid State Commun.* 81 (1992) 155.
85 M. W. Ruckman, B. Xia, D. Shih, *Phys. Rev. B* 50 (1994) 17682.
86 S. DiNardo, L. Lozzi, M. Passacantando, P. Picozzi, S. Santucci, M. DeCrescenzi, *Surf. Sci.* 307–309 (1994) 922.
87 D. J. Huang, G. Reisfeld, M. Strongin, *Phys. Rev. B* 55 (1997) R1977.
88 H. Hövel, B. Grimm, M. Pollmann, B. Reihl, *Phys. Rev. Lett.* 81 (1998) 4608.
89 G. Apai, J. F. Hamilton, J. Stoohr, A. Thompson, *Phys. Rev. Lett.* 43 (1979) 165.
90 M. DeCrescenzi, M. Diociaiuti, L. Lozzi, P. Picoozzi, S. Santucci, *Phys. Rev. B* 35 (1987) 5997.
91 M. Gautier, L. Pham Van, J. P. Duraud, *Europhys. Lett.* 18 (1992) 175.
92 L. D. Marks, *Rep. Progr. Phys.* 57 (1994) 603.
93 E. Anno, *Surf. Sci.* 268 (1992) 135.
94 E. Anno, *J. Appl. Phys.* 85 (1999) 887.
95 P. H. Citrin, G. K. Wertheim, *Phys. Rev. B* 27 (1983) 3176.
96 S. Kohiki, *Appl. Surf. Sci.* 25 (1986) 81.
97 S. L. Qiu, X. Pan, M. Strongin, P. H. Citrin, *Phys. Rev. B* 36 (1987) 1292.
98 H. Hövel, I. Barke, *Progr. Surf. Sci.* 81 (2006) 53.
99 A. Berkó, G. Klivényi, F. Solymosi, *J. Catal.* 182 (1999) 511.
100 V. Vijayakrishnan, A. Chainani, D. D. Sarma, C. N. R. Rao, *J. Phys. Chem.* 96 (1992) 8679.
101 G. Faraci, E. Costanzo, A. R. Pennisi, Y. Hwu, G. Margaritondo, *Z. Phys. D* 23 (1992) 263.
102 F. Aguilera-Granja, S. Bouarab, A. Vega, J. A. Alonso, J. M. Montejano-Carrizales, *Solid State Commun.* 104 (1997) 635.
103 W. F. Egelhoff Jr., *Appl. Surf. Sci.* 11-12 (1982) 761.
104 B. Frick, K. Jacobi, *Surf. Sci.* 178 (1986) 907.
105 J. Zhao, X. Chen, G. Wang, *Phys. Rev. B* 50 (1994) 15424.
106 C. N. R. Rao, V. Vijayakrishnan, Hemantkumar N. Aiyer, G. U. Kulkarni, G. N. Subbanna, *J. Phys. Chem.* 97 (1993) 11157.
107 N. Hemantkumar, Aiyer, V. Vijayakrishnan, G. N. Subbanna, C. N. R. Rao, *Surf. Sci.* 313 (1994) 392.
108 F. H. Ribeiro, A. E. Schach von Wittenau, C. H. Bartholomew, G. A. Somorjai, *Catal. Rev. Sci. Eng.*, 39 (1997) 49.
109 P. W. Jacobs, F. H. Ribeiro, G. A. Somorjai, S. J. Wind, *Catal. Lett.* 37 (1996) 131.
110 T. Beutel, Z. Zhang, W. M. H. Sachtler, H. Knözinger, *J. Phys. Chem.* 97 (1993) 3579.
111 M. Ichikawa, L. Rao, T. Ito, A. Fukuoka, *Faraday Discuss. Chem. Soc.* 87 (1989) 232.
112 B. M. Choudary, K. Matusek, K. Lázár, L. Guczi, *J. Chem. Soc. Chem. Commun.* (1988) 592.
113 L. Guczi, I. Kiricsi, *Appl. Catal. A* 186 (1999) 375.
114 I. Böszörményi, S. Dobos, K. Lázár, Z. Schay, L. Guczi, *Surf. Sci.* 156 (1985) 995.
115 K. Lázár, K. Matusek, J. Mink, S. Dobos, L. Guczi, A. Vizi-Orosz, L. Markó, *J. Catal.* 87 (1984) 163.
116 L. Guczi, A. Beck, A. Horváth, D. Horváth, *Topics Catal.* 19 (2002) 157.
117 M. Boutonnet, J. Kizling, R. Touroude, G. Maire, P. Stenius, *Catal. Lett.* 9 (1991) 347.
118 R. Touroude, P. Girard, G. Maire, J. Kizling, P. Stenius, M. Boutonnet Kizling, *Colloids Surf.* 67 (1992) 9.
119 A. S. Eppler, G. Rupprechter, L. Guczi, G. A. Somorjai, *J. Phys. Chem. B* 101 (1997) 9973.
120 Z. Pászti, Z.E. Horváth, G. Petõ, A. Karacs, L. Guczi, *Appl. Surf. Sci.* 109–110 (1997) 67.
121 Z. Pászti, G. Petõ, Z.E. Horváth, A. Karacs, *Appl. Surf. Sci.* 168 (2000) 114.
122 Z. Pászti, G. Pető, Z. E. Horváth, O. Geszti, A. Karacs, L. Guczi, *Nucl. Instr. Methods B* 178 (2001) 131.
123 Z. Pászti, G. Pető, Z. E. Horváth, O. Geszti, A. Karacs, L. Guczi, *Appl. Phys. A* 76 (2003) 577.
124 F. H. Ribeiro, G. A. Somorjai, *Rec. Trav. Chim. Pays-Bas* 113 (1994) 419.
125 P. L. J. Gunter, J. W. Niemantsverdriet, F. H. Ribeiro, G. A. Somorjai, *Catal. Rev. Sci. Eng.* 39 (1997) 77.
126 C. G. Granqvist, R. A. Buhrman, *J. Appl. Phys.* 47 (1976) 2200.
127 H. Gleiter, *Progr. Mater. Sci.* 33 (1989) 223.
128 R. Uyeda, *Progr. Mater. Sci.* 35 (1991) 1.
129 Q. Li, T. Sasaki, N. Koshizaki, *Appl. Phys. A* 69 (1990) 115.
130 T. Koyama, S. Ohtsuka, H. Nagata, S. Tanaka, *J. Cryst. Growth* 117 (1992) 156.
131 T. Yoshida, S. Takeyama, Y. Yamada, K. Mutoh, *Appl. Phys. Lett.* 68 (1996) 1772.
132 A. G. Gnedovets, E. B. Kul'batskii, I. Smurov, G. Flamant, *Appl. Surf. Sci.* 96–98 (1996) 272.
133 T. Makimura, T. Mizuta, K. Murakami, *Appl. Phys. Lett.* 76 (2000) 1401.
134 D. B. Geohegan, A. A. Puretzky, G. Duscher, S. Pennycook, *Appl. Phys. Lett.* 72 (1998) 2987.
135 M. Kaempfe, H. Hofmeister, S. Hopfe, G. Seifert, H. Graener, *J. Phys. Chem. B* 104 (2000) 11847.
136 A. L. Stepanov, D. E. Hole, P. D. Townsend, *Nucl. Instrum. Methods B* 166–167 (2000) 882.
137 F. Stietz, *Appl. Phys. A* 72 (2001) 381.
138 F. Gonella, *Nucl. Instrum. Methods B* 166–167 (2000) 831.
139 Z. Liu, H. Li, X. Feng, S. Ren, H. Wang, Z. Liu, B. Lu, *J. Appl. Phys.* 84 (1998) 1913.
140 T. Kobayashi, A. Nakanishi, K. Fukumura, G. Langouche, *J. Appl. Phys.* 83 (1998) 4631.
141 L. Thomé, J. Jagielski, G. Rizza, F. Garrido, J. C. Pivin, *Appl. Phys. A* 66 (1998) 327.
142 L. Thomé, G. Rizza, F. Garrido, M. Gusso, L. Tapfer, A. Quaranta, *Appl. Phys. A* 67 (1998) 241.
143 G. C. Rizza, M. Strobel, K. H. Heinig, H. Bernas, *Nucl. Instrum. Methods B* 178 (2001) 78.
144 C. J. McHargue, S. X. Ren, P. S. Sklad, L. F. Allard, J. Hunn, *Nucl. Instrum. Methods B* 116 (1996) 173.
145 Z. Pászti, G. Pető, Z. E. Horváth, A. Karacs, L. Guczi, *J. Phys. Chem. B* 101 (1997) 2109.
146 Z. Pászti, G. Pető, Z. E. Horváth, A. Karacs, L. Guczi, *Solid State Commun.* 107 (1998) 329.
147 L. Guczi, D. Horváth, Z. Pászti, L. Tóth, Z. E. Horváth, A. Karacs, G. Pető, *J. Phys. Chem. B* 104 (2000) 3183.
148 A. Beck, A. Horváth, A. Sárkány, L. Guczi, *Curr. Appl. Phys.* 6 (2006) 200.
149 A. Horváth, A. Beck, A. Sárkány, G. Stefler, Z. Varga, O. Geszti, L. Tóth, L. Guczi, *J. Phys. Chem. B* 110 (2006) 15417.
150 R. S. Averback, *Nucl. Instrum. Methods B* 15 (1986) 675.
151 Y.-T. Cheng, *Mater. Sci. Rep.* 5 (1990) 45.
152 R. Kelly, A. Miotello, *Nucl. Instrum. Methods B* 122 (1997) 374.
153 A. Miotello, R. Kelly, *Surf. Sci.* 314 (1994) 275.
154 A. Miotello, R. Kelly, *Surf. Sci.* 329 (1995) 289.

155 C. J. McHargue, D. L. Joslin, C. W. White, *Nucl. Instrum. Methods B* 91 (1994) 549.
156 P. Mazzoldi, G. W. Arnold, G. Battaglin, R. Bertoncello, F. Gonella, *Nucl. Instrum. Methods B* 91 (1994) 478.
157 N. Kishimoto, N. Umeda, Y. Takeda, C. G. Lee, V. T. Gritsyna, *Nucl. Instrum. Methods B* 148 (1999) 1017.
158 R. S. Daley, R. G. Musket, *Nucl. Instrum. Methods B* 80–81 (1993) 802.
159 J. Fauré, Ch. Angelov M. Kalitzova, S. Simov, *Nucl. Instrum. Methods B* 132 (1997) 418.
160 E. Johnson, A. Johansen, L. Sarholt, U. Dahmen, *Nucl. Instrum. Methods B* 148 (1999) 1034.
161 K. Milants, P. Hendrickx, H. Pattyn, *Nucl. Instrum. Methods B* 80–81 (1993) 1014.
162 L. Guczi, Z. Pászti, G. Pető, in G. A. Somorjai, S. Hermans, B. Zhang (eds.) *Nanotechnology in Catalysis*, Chapter 22, Kluwer Publ. Co., Amsterdam, 2003.
163 J. F. Moulder, W. F. Stickle, P. E. Sobol, K. D. Bomben, J. Chastain (eds.) *PHI Handbook of Photoelectron Spectroscopy*, Perkin-Elmer Corp. Physical Electronics Division, Eden Prairie, MN, 1992.
164 I. Jirka, *Surf. Sci.* 232 (1990) 307.
165 Y. Wu, E. Garfunkel, T. E. Madey, *J. Vac. Sci. Technol. A* 14 (1996) 1662.
166 M, Haruta, N. Yamada, T. Kobayashi, S. J. Iijima, *J. Catal.* 115 (1989) 301.
167 A. Ueda, T. Oshima, M. Haruta, *Appl. Catal. B* 12 (1997) 81.
168 D. Andreeva, T. Tabakova; V. Idakiev, P. Christov, R. Giovanoli, *Appl. Catal. A* 169 (1998) 9.
169 M. Haruta, M. Daté, *Appl. Catal. A* 222 (2001) 427.
170 M. Haruta, A. Ueda, S. Tsubota, R. M. Torres Sanches, *Catal. Today* 29 (1996) 443.
171 G. Pető, G. L. Molnár, Z. Pászti, O. Geszti, A. Beck, L. Guczi, *Mater. Sci. Eng. C* 19 (2002) 95.
172 G. Pető, O. Geszti, G. Molnár, Cs. S. Daróczi, A. Karacs, L. Guczi, A. Beck, K. Frey, *Mater. Sci. Eng. C* 23 (2003) 733.
173 L. Guczi, G. Pető, A. Beck, Z. Pászti, *Topics Catal.* 29 (2004) 129.
174 M. Okada, S. Ogura, W. A. Dino, M. Wilde, K. Fukutani, T. Kasai, *Appl. Catal. A* 291 (2005) 55.
175 I. N. Remediakis, N. Lopez, J. K. Nørskov, *Appl. Catal. A* 291 (2005) 13.
176 M. Mavrikakis, P. Stoltze, J. K. Nørskov, *Catal. Lett.* 64 (2000) 101.
177 N. Lopez, J. K. Norskov, *J. Am. Chem. Soc.* 124 (2002) 11262.
178 L. M. Molina, B. Hammer, *Appl. Catal. A* 291 (2005) 21.
179 M. Okumura, Y. Kitagawa, M. Haruta, K. Yamaguchi, *Appl. Catal. A* 291 (2005) 37.
180 M. Büttner, H. Kröger, I. Gerhards, D. Mathys, P. Oelhafen, *Thin Solid Films* 495 (2006) 180.
181 T. Okazawa, M. Kohyama, Y. Kido, *Surf. Sci.* 600 (2006) 4430.
182 T. Minato, T. Susaki, S. Shiraki, H. S. Kato, M. Kawai, K Aika, *Surf. Sci.* 566–568 (2004) 1012.
183 N. Spiridis, J. Haber, J. Korecki, *Vacuum* 63 (2001) 99.
184 M. Valden, S. Pak, X. Lai, D.W. Goodman, *Catal. Lett.* 56 (1998) 7.
185 M. Valden, X. Lai, D. W. Goodman, *Science* 281 (1998) 1647.
186 C. C. Chusuei, X. Lai, K. Luo, D. W. Goodman, *Topics Catal.* 14 (2001) 71.
187 L. Giordano, G. Pacchioni, T. Bredow, J. F. Sanz, *Surf. Sci.* 471 (2001) 21.
188 S. C. Parker, A. W. Grant, V. Bondzie, C. T. Campbell, *Surf. Sci.* 441 (1999) 10.
189 V. Bondzie, S. C. Parker, C. T. Campbell, *Catal. Lett.* 63 (1999) 143.
190 V. Bondzie, S. C. Parker, C. T. Campbell, *J. Vac. Sci. Technol. A* 17 (1999) 1717.
191 S. Erkoc, *Physica E* 8 (2001) 210.
192 D. Boyd, S. Golunski, G. R. Hearne, T. Magadzu, K. Mallick, M. C. Raphulu, A. Venugopal, M. S. Scurrell, *Appl. Catal. A* 292 (2005) 76.
193 T. V. Choudhary, D. W. Goodman, *Appl. Catal. A* 291 (2005) 32.
194 G. J. Hutchings, M. S. Hall, A. F. Carley, Ph. Landon, B. E. Solsona, Ch. J. Kiely, A. Herzing, M. Makkee, J. A. Moulijn, A. Overweg, J. Carlos F.-G. J. Guzman, B. C. Gates, *J. Catal.* 242 (2006) 71.
195 F. Moreau, G. C. Bond, *Catal. Today*, 114 (2006) 362.
196 F. Boccuzzi, A. Chiorino, M. Manzoli, *Surf. Sci.* 454–456 (2000) 942.
197 N. Weiher, E. Bus, L. Delannoy, C. Louis, D. E. Ramaker, J. T. Miller, J. A. van Bokhoven, *J. Catal.* 240 (2006) 100.
198 C-T. Wang, S.-H. Ro, *J. Non-Cryst. Solids* 352 (2006) 35.
199 L. Guczi, G. Pető, A. Beck, K. Frey, O. Geszti, G. Molnár, Cs. S. Daróczi, *J. Am. Chem. Soc.* 125 (2003) 4332.
200 J. Guzman, B. C. Gates, *Nano Lett.*, 1 (2001) 689.
201 D. A. Cunningham, W. Vogel, H. Kageyama, S. Tsubota, M. Haruta, *J. Catal.* 177 (1998) 1.
202 J. L. Margitfalvi, M. Hegedűs, A. Szegedi and I. Sajó, *Appl. Catal. A* 272 (2004) 87.
203 W. T. Wallace, B. K. Min, D. W. Goodman, *Topics Catal.* 34 (2005) 17.
204 L. Guczi, Z. Pászti, K. Frey, A. Beck, G. Pető, Cs. S. Daróczy, *Topics Catal.* 39 (2006) 137.
205 D. A. Dulushev, L. Kiwi-Minsker, I. Yuranov, E. I. Surunova, P.A. Buffat, A. Renken, *J. Catal.* 210 (2002) 149.
206 L. Guczi, K. Frey, A. Beck, G. Pető, Cs. S. Daróczi, N. Kruse, S. Chenakin, *Appl. Catal. A* 291 (2005) 116.
207 K. Frey, A. Beck, G. Pető, Gy. Molnár, L. Guczi, *Catal. Commun.* 7 (2006) 64.
208 C. Hardacre, G. M. Roe, R. M. Lambert, *Surf. Sci.* 326 (1995) 1.
209 C. Hardacre, R. M. Ormerod, R. M. Lambert, *J. Phys. Chem.* 98 (1994) 10901.
210 Z. M. Liu, M. A. Vannice, *Catal. Lett.* 43 (1997) 51.
211 N. S. Phala, G. Klatt, E. van Steen, S. A. French, A. A. Sokol, C. R. A- Catlow, *Phys. Chem. Chem. Phys.* 7 (2005) 2440.
212 K. B. Lewis, S. T. Oyama, G. A. Somorjai, *Surf. Sci.* 233 (1990) 75.
213 K. B. Lewis, S. T. Oyama, G. A. Somorjai, *Appl. Surf. Sci.* 52 (1991) 241.
214 G. H. Vurens, V. Maurice, M. Salmeron, G. A. Somorjai, *Surf. Sci.* 268 (1992) 170.
215 E. Farfan-Arribas, J. Biener, C. M. Friend, R. J. Madix, *Surf. Sci.* 591 (2005) 1.
216 S. Y. Quek, C. M. Friend, E. Kaxiras, *Surf. Sci.* 600 (2006) 3388.

This page intentionally left blank

CHAPTER 5

Application of Metal Nanoclusters in Nanoelectronics

Eva Koplin and Ulrich Simon

Institute of Inorganic Chemistry, RWTH Aachen University, D-52056 Aachen, Germany

1. Introduction

Modern microelectronics as the basis for electronic information storage and processing tends to continuous miniaturization. This turns out to be the only evident concept for improving the performance of integrated circuits. Since the late 1970s, CMOS (complementary metal-oxide semiconductor) technology is the key technology for device fabrication in computer industries. This dominance will maintain for the next two decades, at least for the set-up of logic elements. In the early stage of this technology, at the end of 1970s the complexity of the chip design appeared as a limiting factor, which had been overcome by computer-aided design. More than 10 years later the increased integration rates created unexpected obstacles in power- and heat-management, which are still remaining. Nevertheless, optical lithographic fabrication techniques allow mass fabrication down to 50 nm and less and advanced techniques, like extreme ultraviolet lithography, X-ray proximity lithography, imprinting lithography and focused electron- and ion-beam techniques will guarantee the exponential downscaling according to the famous Moore's law. This has repeatedly been demonstrated by the fabrication of transistor elements with feature size of less than 10 nm [1,2].

However, fundamental physical limits together with the enormous technical and financial efforts require the development of new technologies, which may substitute CMOS technology in course of further miniaturization and mass fabrication. At least at that point new concepts for scalable technologies need to be developed, and therefore the search for the most promising materials, processes and structures have inspired a lot of academic and industrial working groups to synthesize and to exploit the electrical transport properties of nanomaterials and molecular assemblies for the design of functional systems on the nanometer level.

Among these one of the most promising concepts is the development of single electron (SE) devices, which retain their scalability down to the molecular level. At present, due to exploitation of charging (Coulomb) effects in metallic SE devices comprising tunnel junctions with submicrometer size, individual charge carriers can be handled [3]. Although charging effects have earlier been observed in granular thin metal films [4,5], the field of single electronics as direction in its own was born more in the late eighties, when ultra-small metal–insulator–metal (MIM) sandwich structures (tunnel junctions) and simple systems of those have started to be intensively studied both theoretically and experimentally [6]. The discreteness of the electric charge becomes essential and the tunneling of electrons in a system of such junctions can be affected by Coulomb interaction of electrons, which can be varied by an externally applied voltage or by injected charges. The simplest arrangement for a two-terminal device is a metal island between two metallic electrodes separated from each other by a dielectric environment. By transferring a single electron from the electrodes to the island by applying a certain voltage, the island is charged negatively and the electrodes keep the positive image charge, whereas the overall charge is kept to zero. In this situation, the electrostatic energy, i.e. the SE charging energy $E_c = e^2/2C$, where e is the elementary charge and C is the self-capacitance of the metallic island, is stored in the arrangement. In this stage the device is in the Coulomb-blockaded state and the threshold voltage has to overcome the Coulomb blockade to add an electron via the source electrode or to let it leave via the drain electrode. The Coulomb blockade results from the increase of the potential energy when one electron is added to an initially uncharged particle and it scales roughly with $1/r$ (r = radius of the nanoparticle). Since it can be estimated from the charging energy of a macroscopic metallic sphere scaled down to the nanometer range, the Coulomb blockade is sometimes regarded as a "classical size effect". In order to suppress thermal fluctuations of the charge, E_c must by far exceed $k_B T$. Consequently, by decreasing the island size down to one or two nanometers, handling of single electrons becomes realistic even in the range of room temperature.

Different approaches have been discussed up to now how to reach this size scale and consequently how to bridge the size gap between the conventionally fabricated circuit elements of some ten nanometers in size and at least the true atomic or molecular scale. In that concern noble metal nanoclusters have attracted much attention.

Metal Nanoclusters in Catalysis and Materials Science: The Issue of Size Control
Edited by B. Corain, G. Schmid and N. Toshima

They can be synthesized with a distinct particle size of two nanometers or less, and the large charging energy which is determined by the particle size and their embedding into the respective "environment", i.e. a ligand shell or linking molecules, they fulfill the prerequisites to be used as functional elements in SE devices at room temperature and above. This has been shown repeatedly in many works using different experimental techniques. It will be described in the following that most of these results have been obtained from scanning tunneling spectroscopy (STS). However, in recent years the fabrication of nanoelectrode devices has made a great impact to this field of research. Nevertheless, the use of these chemically tailored nanomaterials for device fabrication requires parallelized and scalable methods for the self-assembly (SA) into functional units in one, two or three dimensions. Furthermore, one needs to find out and to understand the many control parameters for a directed assembly and for the adjustment of the electrical transport properties to the desired application.

The aim of this chapter is to acquaint the reader the physical principles of SE tunneling devices to be used in nanoelectronics. Based on this the charge transport properties of nanocluster assemblies in one, two and three dimensions will be discussed. By means of selected examples it will be demonstrated that ligand-stabilized nanoclusters of noble metals may be suitable building blocks for nanoelectronic devices.

2. The Working Principle of Single Electron Devices

In the following, the working principle of SE-based elements is briefly described [3]: Electric current in a macroscopic metallic conductor is associated with motion of a huge amount of free electrons over the entire conductor. In spite of the discrete nature of the charge carriers the current flow in a metal is quasi-continuous. In contrast, in an isolated nanoscaled piece of metal (islands), the number of electrons in there is always an integer and, at least, countable. An electrical circuit of such islands should present a number of reservoirs for free electrons, which should be small and well conducting, and which are separated by poorly permeable tunneling barriers. As long as the size of these islands is larger than the atomic scale, they certainly comprise a huge amount of free charge carriers. But, however, handling of individual charges is still possible if the characteristic electric capacitance of the island C is small enough, i.e. the charging energy is large enough to overcome thermal fluctuations. Such a circuit deals with a small and defined amount of excess electrons on islands changing their distribution over the islands in time in a desirable way. This is the concept of single charge storage (SCS) and the respective electronic transport process is called SE tunneling (SET).

In order to realize this practically the following two principal conditions must be fulfilled:

- the insulating barriers separating the conducting islands from each other should be much higher than the characteristic resistance expressed via fundamental constants, the so-called resistance quantum, $R_q = h/e^2 = 25.8\,k\Omega$. Then the electrons in the island can be considered as to be localized and their number already behaves classically, although they undergo thermodynamic fluctuations as every statistical variable.
- in order to have these thermal fluctuations small enough and consequently to make the exchange of electrons controllable, the energy associated with charging by one extra electron should be essential with respect to the characteristic thermal energy $k_B T$. This is the charging energy E_C and it depends on the charge Q, on the size and on the charge of capacitances of junctions, gates, conductors, etc. in the vicinity of the island. The smaller the island the smaller the capacitance and the larger E_C as well as the temperature, at which SE charging can be observed experimentally.

2.1. The Single Electron Box

The simplest storage device is the SE box for injected/ejected electrons, i.e. a device, which can control the number of electrons in a quantum dot (island) [7] (Figure 1).

Such an element can be implemented into a charge-state logic, which bases on a) a bistable or, if more than one charge is deposited on the island, b) a multi-stable configuration. Since one electron represents one bit, which can be transferred from one island to the next, power consumption of such a device is extremely small. This will be of great advantage for minimizing the power loss and the heat development. However, the unavoidable drawbacks of SET logic devices are actually the large output impedance, which makes the elements intrinsically slow. Furthermore, such elements are extremely sensitive toward background charges. Thus, the application of SET elements will apparently be restricted on charge sensing and on memory elements.

2.2. The Single Electron Transistor

As a switching device capable for ultra-large-scale integrated circuits (ULSIs) comprises only one Coulomb island with two leads (electrodes) and a capacitively coupled gate electrode attached to it. This system works as a simple on/off switch and it is often called the SE transistor. Applying a voltage to the outer electrodes of this circuit may either cause sequential transfer of electrons onto and out of the central island or to have no charge transport, i.e. the transistor remains in non-conductive state. The result

Figure 1. The tunneling of a single electron (SE) between two metal electrodes through an intermediate island (quantum dot) can be blocked of the electrostatic energy of a single excess electron trapped on the central island. In case of non-symmetric tunneling barriers (e.g. tunneling junction on the left, and ideal (infinite-resistance) capacitor on the right), this device model describes a "SE box".

depends on the voltage U, applied to the electrodes as well as on the voltage U_g applied to the gate.

Such elements can be utilized for the set up of devices with non-volatile memory function as well as in SET/CMOS hybrid circuits, working even at room temperature [8]. Such transistor elements can be fabricated with different techniques, ranging from silicon-based technology up to chemical SA. While SE transistors with multiple nanoparticle charge storage have a great potential to replace flash memories as non-volatile memories, the highest integration rate might be expected from chemically based concepts, where metal or semiconductor nanoclusters assembled at nanocontacts form simple or complex elements with single or multiple SET function.

3. Single Electron Tunneling in Nanoclusters

The theoretical background of SET has found its experimental manifestation in lithographically fabricated capacitors, as they are found in conventional computer circuits. These typically have capacitances in the pF range. Due to the extremely low-charging energies, they consequently would need to be cooled down in the sub-mK range for SE operation. Furthermore, such a capacitor is typically driven at an operation voltage of 10–100 mV, which would lead to storage of a few ten thousand electrons per charging. Going to advanced electron beam or extreme UV lithography, which allows the fabrication tunnel junctions with a typical size of 30 nm × 30 nm or less, devices still may have to be cooled down to, at least, liquid Helium. The utilization of the SET events for applications up to the range of room temperature leads to the necessity to decrease the junction capacitance essentially, down to 1–2 nm. This can be realized by use of chemically synthesized metal nanoclusters in a size range of a few nanometers. These nanoclusters are stabilized by organic molecules, the ligands, which surround the metal cores and play the role of an insulating layer in contact with neighboring clusters as well as with electrodes. To use these particles as building blocks for a new nanoscale architecture, generally new techniques for a defined organization of such nanoclusters are needed to be developed to build up SE circuits of different complexity. So far, it has become evident that utilizing the principles of SA by controlling inter-molecular interaction, which is one of the main interests of supermolecular chemistry, will be a key feature in this development.

However, size effects in metal nanoclusters of these sizes require a slight modification of the above-mentioned principal conditions for ''classical'' SET.

At low temperature, junctions with nanoclusters with sizes below 1–2 nm possesses, besides the Coulomb staircase, the fine structure due to energy quantization inside the clusters. Nevertheless, the interpretation of the electrical response of such a device is complicated by the fact that the RC-time becomes as short as characteristic time of the energy relaxation inside the cluster. Consequently, the distribution of electrons is no longer the pure Fermi one. Thus, the tunneling characteristics of single nanoclusters provide information of its electron energy spectrum, particularly of the density of levels, their degeneracy etc. However, this may be utilized in the future in a multiple-value logic.

3.1. Thin Film Structures and STM Single Electron Systems

Almost two decades ago fabrication techniques for the realization of the previously mentioned ''traditional'' SE circuits, like transistors, have been developed [9,10]. One of these techniques is the so-called shadow-evaporation technique, which bases on the evaporation of metal (usually Al) films through fine-patterned masks, which is typically made of polymer resist by means of an electron-beam lithographic process. The mask provides a number of thin splits, determining the sizes and shapes of resulting wires and islands, respectively as well as the bridges interrupting them. The latter determine the position of the wanted tunnel junctions and gates. Due to the composite polymer resist layer, which may chemically be underetched, the resulting mask is rigidly fixed above the substrate and its bridges become suspended above it. Such arrangements of splits and bridges permit to evaporate metals onto the substrate from various angles, which allows different positions of the resulting evaporated layers.

In order to form a set of islands connected by tunnel junctions, the evaporation is usually made from two or three different angles in two or three steps, respectively, with an intermediate oxidation process, when aluminum is used. Due to adjusting the angles, the linear sizes of the resulting overlapping area of the first and the second metallic layers can be even smaller than the width of the strips, i.e. some ten nm. At the same time a gate electrode coupled to the islands only capacitively should not overlap them, which is taken into account in the mask pattern design. After double evaporation the mask and the supporting layer are lifted off. Figure 2 shows such SE transistor fabricated as an $Al–Al_2O_3–Al$ stack [11].

The resulting barrier of Al_2O_3 with a desirable thickness of a few nanometers is mechanically and chemically

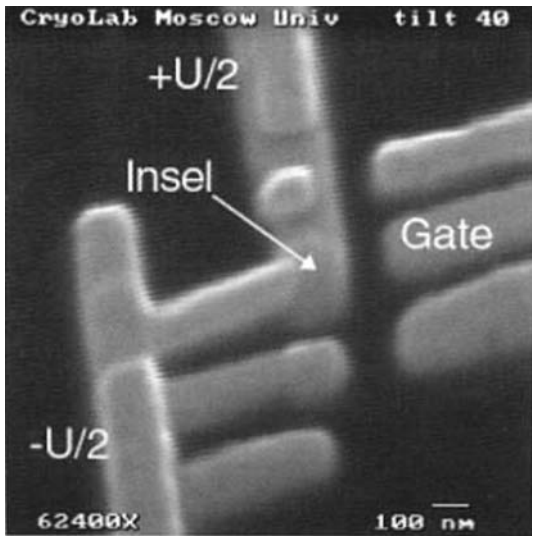

Figure 2. Scanning electron micrograph of a SE transistor with source and drain (+U/2 and −U/2, respectively) feeding the central island (Insel), which is capacitively coupled to a gate electrode. The size of the central island is about 60 nm × 60 nm.

stable. The height of the corresponding energy barrier is about 1 eV and it readily provides a tunnel resistance in the range of 100 kΩ for the junctions of the above-mentioned size. The resulting capacitance of such tunnel junctions is about 10^{-16} F. This means that these circuits operate reliably only at temperatures below 1 K, which is just attainable with immense technical effort.

Meanwhile more advanced fabrication techniques have been developed for the fabrication of much smaller SE transistors. Among these the miniaturization together with novel design concepts, like multiple-gate structures, has lead to a reliable technology platform, which allows the fabrication of SE elements working at room temperature. However, this is accompanied with huge experimental and financial efforts. An alternative route is the use of ligand-stabilized metal nanoclusters as building blocks. The drastic reduction of the sizes and therefore of the capacitances of tunnel junctions, respectively, are basically realized, e.g. in a double junction system consisting of a small metallic cluster (droplet) lying on an thin insulating film on a conduction support and the tip of the scanning tunneling microscope (STM, Figure 3).

One of the junctions, which is between the ground plane and the metal particle is mechanically fixed, while another one which is between the particle and the STM tip is adjustable.

The structures described above were successfully and repeatedly realized in practice. As an early example, a one-dimensional (1D) arrangement forming a double-barrier SET junction working at room temperature has been realized by a STM tip above Au particles of approximately 4 nm in diameter obtained by metal evaporation on a 1 nm thick layer of ZrO_2 (tunnel barrier) on a flat Au substrate [12]. The experimentally determined capacitance of the nanoparticle–substrate junction is about 10^{-18} F. The value is in good agreement with the theoretically estimated value-based on the model of a parallel-plate capacitor with ZrO_2 as a defined dielectric. One year later, Dorogi et al. prepared layers of isolated nanoclusters from a multiple expansion cluster source on self-assembled monolayers of xylene-a,a′-dithiol (XYL), and studied the electrical transport through the tunnel junction in a ultrahigh vacuum system with an STM. The tunneling current as a function of applied voltage yields evidence for SET at room temperature and by fitting the $I(U)$ curves to a Coulomb blockade model, the electrical resistance of the XYL molecules could be estimated as about 9 MΩ [13]. This result is found to be in good agreement with theoretical expectations [14]. Wang et al. have calculated a resistance of 12.5 MΩ for these molecules. Based on the elastic scattering Green's function theory, they have developed an approach to characterize the electron transport process in molecular devices. This approach allows the description of the coupling between the molecule, forming the tunnel barrier, and metals, forming the electrodes, at the hybrid density functional theory level. For XYL $I(U)$ curves have been calculated, which are found to be in good agreement with experimentally obtained ones at room temperature.

These examples show that by means of metal nanoclusters SET is accessible at room temperature. However for highly redundant SET devices, particle-size distribution has to be avoided, which is not possible when metal evaporation is used for cluster fabrication in the examples given above.

4. Zero-Dimensional Structures: SET on Single Chemically Tailored Nanoclusters

One of the first results obtained on single chemically tailored nanoclusters has been reported by van Kempen et al. in 1995 [15,16]. They performed STS at 4.2 K on a $Pt_{309}phen_{36}O_{20}$-cluster, synthesized by Schmid and coworkers (Figure 4).

The $I(U)$ characteristics reveal clear charging effects, which indicate sufficiently insulating tunnel barriers between the cluster and the substrate. The experimentally observed charging energies vary from 50–500 meV, while a value of 140 meV would be expected, assuming a continuous density of state in the clusters and a dielectric constant $\varepsilon_r = 10$ for the ligand molecules and applying the classical formula $E_C = e^2/4\pi\varepsilon_0\varepsilon_r R$ (with R = radius of the cluster).

The variation in E_C can be caused by diverse reasons, which have to be taken into account: E_C will depend on the exact way in which the cluster lies on the substrate since the clusters have different facets (squares and triangles). Additionally the ligands, which for simplification have been assumed to be a spherical dress for the cluster, may have different orientations varying from cluster to cluster with respect to the underlying substrate, thus causing a different tunnel barrier between the cluster and

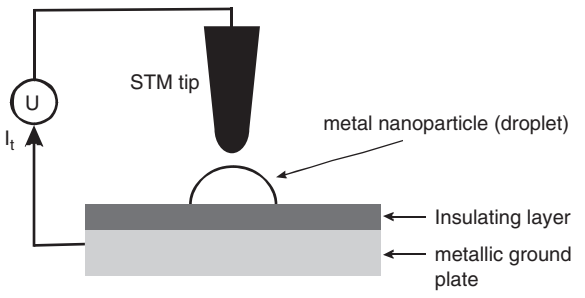

Figure 3. SE two-junction system consisting of a scanning tunneling microscope (STM) tip and a metallic nanoclusters as a central electrode on a ground plane.

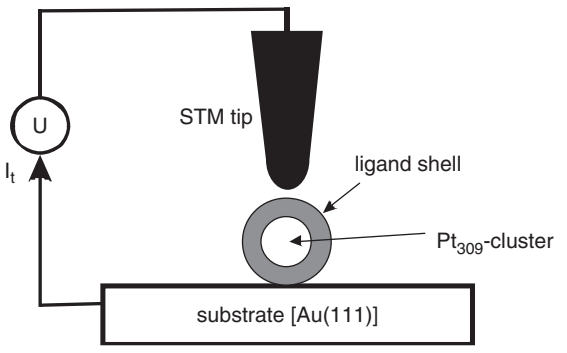

Figure 4. A single ligand stabilized Pt_{309}-cluster between STM tip and an Au(1 1 1) facet. The junction between the cluster and the substrate is built up by the ligand shell.

the ground, and therefore a different capacitance. Finally the tunnel junction between cluster and substrate may differ for different clusters as the effect of residual water molecules from the solvent, which may be physically or chemically bound to the cluster surface or to the ligand shell.

In some cases additional structures on the charging characteristic were observed, which might be expected from a discrete electron-level spectrum in the cluster caused by the quantum-size effect. Averin and Korotkov reported on theoretical investigations on the effect of discrete levels on the charging characteristics [17]. They extended the existing "orthodox" theory of correlated SET in a double normal-metal tunnel junction to the case of a nanoscaled central electrode. Therefore the $I(U)$ characteristics should show small-scale singularities reflecting the structure of the energy spectrum of the central electrode, i.e. the nanoparticle. Resulting from the small junction capacitance according to $\tau = R_T \cdot C$, where R_T is the resistance of the respective tunnel barrier and C is the capacitance of the junction, the energy-relaxation rate becomes evident due to the small recharging time τ. The fit of the spectra lies between 20 and 50 meV, as the theoretical prediction for the level splitting Δ according to $\Delta = 4E_F/3N$ or a refined approach by Halperin [18] leads to an assumed splitting of approximately 8 meV (E_F is the Fermi energy of the metal and N is the number of free electrons). The measurements reflect the discreetness of the level spectrum in the clusters as big as the 2.2 nm Pt_{309} cluster, although different reasons are discussed in the cited paper.

STS could be observed up to the range of room temperature on smaller ligand stabilized metal clusters of 1.4 nm, i.e. $Au_{55}(PPh_3)_{12}Cl_6$ (Au_{55}). 3D compacts of the clusters, as from cluster pellets, gave hints on SE transfer in the $I(U)$ curves taken at room temperature [19]. Though in these investigations neither the vertical nor the lateral arrangement of the clusters is well defined, as it would be in a 1-, 2- or 3D superlattice, the charging energy has a wider spread as it would be expected from the estimation of the charging energy of a single cluster according to the formula mentioned above.

Tunneling spectroscopy on Au_{55} cluster monolayers prepared on various technically relevant substrates was studied by Chi et al. [20]. The samples were obtained by utilizing a two-step SA process and a combined Langmuir–Blodgett/SA-process. Coulomb blockade originating from the double barrier at the ligand stabilized cluster as the central electrode up to the range of room temperature could be followed by spectroscopy (Figure 5).

The capacitance of the cluster was calculated from a fit of the experimental data at 90 K to be 3.9×10^{-19} F. This value, which is very sensitive toward residual charges and nearby background charges, is close to the value of the microscopic capacitance, which was determined earlier by temperature-dependent impedance measurements [21]. Furthermore these results are found to be in good agreement with the capacitance data obtained on the above-mentioned gold nanoclusters on a XYL-modified Au(1 1 1) surface [13,22].

On low-temperature tunneling spectroscopy on individual Au_{55} clusters under ultra-high vacuum conditions has been reported recently by Zhang et al. [23]. According to the before mentioned results, they gave a clear evidence of the Coulomb blockade. The conductivity appears to be largely suppressed in this regime, however, is not zero, which is attributed to a certain probability of co-tunneling within the Coulomb gap at the finite temperature of 7 K. Thermal motion is sufficiently reduced at that temperature and the molecular structure of the ligand shell is partly visible. The STM image fits fairly well to the space-filling model of the cluster. Both are shown in Figure 6.

The two locations at which the tunneling spectra have been recorded can be seen in Figure 7. One location is

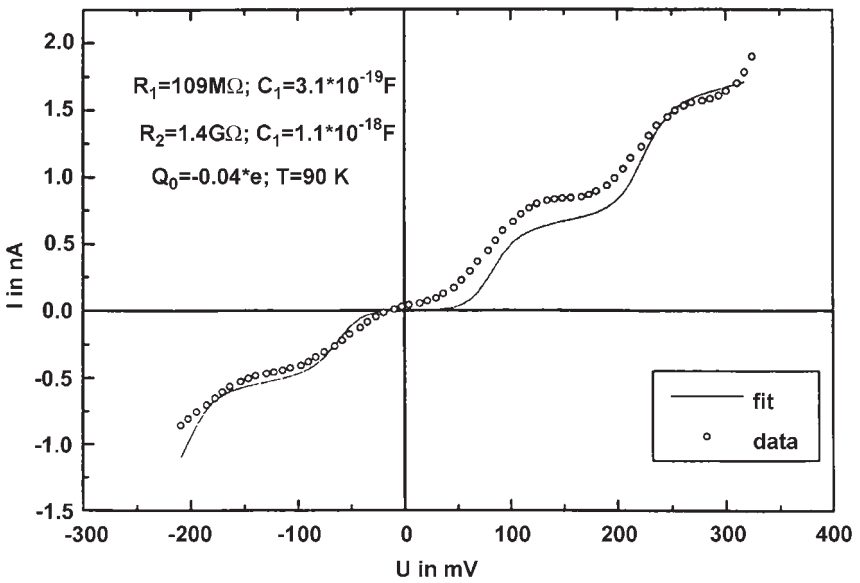

Figure 5. SET on a single ligand-stabilized Au_{55} cluster at 90 K. The junction capacitance was calculated to be 3×10^{-19} F by fitting. (Reprinted with permission from Ref. [20], © 2004, Springer.)

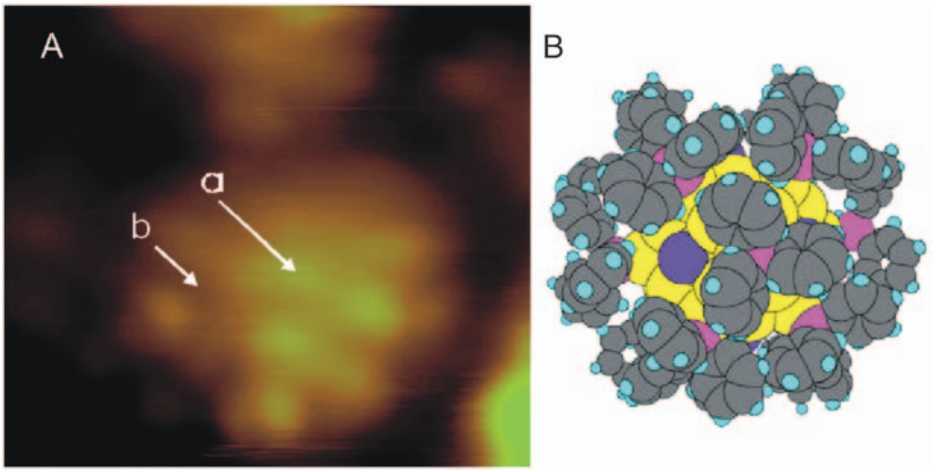

Figure 6. (A) STM image of a single $Au_{55}[P(C_6H_5)_3]_{12}Cl_6$ cluster on an Au(1 1 1) surface at 7 K, obtained at a bias of 2 V and a current of 100 pA using a Pt–Ir tip. Image size: 3.3 nm × 2.9 nm. (B) Space-filling model of the cluster compound: Cuboctahedral core with 55 Au atoms (yellow), 12 $P(C_6H_5)_3$ molecules (with P: pink, C: gray and H: blue) bound to the 12 edges of the cuboctahedron and six Cl atoms (violet) located in the center of the six square faces of the Au core. Comparison between (A) and (B) shows that the STM resolves the C_6H_5 rings. Spectroscopic data were acquired at the two distinct locations (a) and (b) marked in (A). (Reprinted with permission from Ref. [23], © 2003, American Chemical Society.)

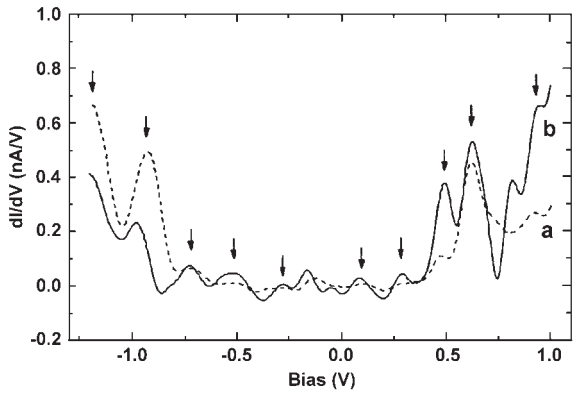

Figure 7. Tunneling spectra acquired at the two distinct locations marked in Figure 6A. The dashed curve was taken right above C_6H_5 ring and the solid ones next to the ring. The bias refers to the substrate potential. The arrows indicate conductivity peaks, which precisely coincide for both spectra. (Reprinted with permission from Ref. [23], © 2003, American Chemical Society.)

right above a C_6H_5 ring of the PPh_3 ligand and the second one is next to the ring. Figure 7 shows the conductivity peaks, which precisely coincide for both spectra.

This indicates that the discrete energy levels of the cluster become visible in terms of conductivity oscillations with an average-level spacing of 135 meV. Comparing this value to the one expected of a simple free-electron model the "electronically apparent" cluster diameter is about 1.0 nm. This is significantly smaller than the geometrically determined diameter of 1.4 nm for Au_{55} and slightly larger than the expected value of 0.84 nm of Au_{13}. In the author's opinion, this difference is most likely caused by the six Cl atoms located at the six square facets of the cuboctahedral Au_{55} surface. Due to its high electronegativity, Cl can remove one electron from the Au_{55} core. Nonetheless, the cluster exhibits metallic behavior within the discrete energy levels.

4.1. Metal Nanoclusters in Single Electron Devices

In order to utilize the opportunities, which arise from the room temperature SET pecularities, for beyond singular laboratory experimentation applications, principally two different routes have been followed with respect to the experimental design. On the one hand techniques have been developed to fabricate metallic electrodes, which enable the addressing of a few or even single nanoclusters by electron-beam lithography. On the other hand, STS techniques have been developed further for chemical control of gating of the central island in a SET transistor or far the chemical switching of the tunneling barrier, i.e. the insulating organic molecules, separating the nanoclusters from the underlying support.

4.2. Mesoscopic Arrays with Nanoelectrodes

Alivisatos and coworkers reported on the realization of an electrode structure scaled down to the level of a single Au nanocluster [24]. They combined optical lithography and angle evaporation techniques (see previous discussion of SET-device fabrication) to define a narrow gap of a few nanometers between two Au leads on a Si substrate. The Au leads were functionalized with hexane-1,6-dithiol, which binds linearly to the Au surface. 5.8 nm Au nanoclusters were immobilized from solution between the leads via the free dithiol end, which faces the solution. Slight current steps in the $I(U)$ characteristic at 77 K were reflected by the resulting device (see Figure 8). By curve fitting to classical Coulomb blockade models, the resistances are 32 MΩ and 2 GΩ, respectively, and the junction

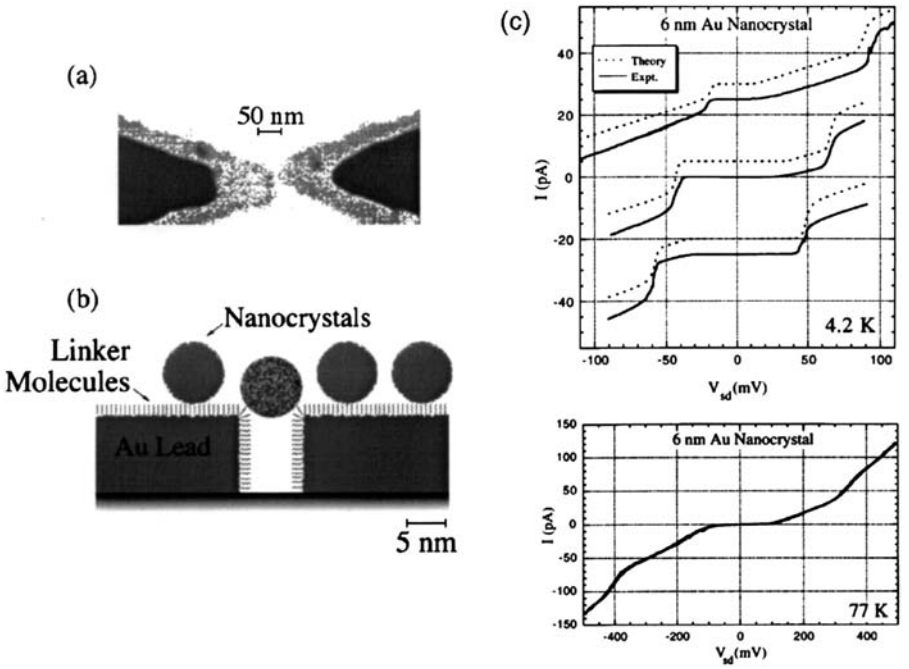

Figure 8. (a) Field emission scanning electron micrograph of a lead structure before the nanocrystals are introduced. The light gray region is formed by the angle of evaporation, and is ~10 nm thick. The darker region is from a normal angle of evaporation and is ~70 nm thick. (b) Schematic cross-section of nanocrystals bound via a bifunctional linker molecule to the leads. Transport between the leads occurs through the mottled nanocrystal bridging the gap. (c) I–V_{sd} (sd = source-drain) characteristic of a 5.8 nm diameter Au nanocrystal measured at 4.2 K. The solid lines show three I–V curves measured over the course of several days. Each is offset for clarity. These different curves result from changes in the local charge distribution about the dot. The dashed lines are fits to the data using the orthodox Coulomb blockade model as discussed. I–V_{sd} characteristic of a 5.8 nm diameter Au nanocrystal measured at 77 K. Several Coulomb steps of period ΔV_{sd} ~200 mV can be seen. (Reprinted with permission from Ref. [25], © 1996, American Institute of Physics.)

capacitances are 2.1×10^{-18} F, respectively. In a further development of this device, a gate electrode for external control of the current flow through the central island, a CdSe nanocluster, could be applied to realize a SET transistor [25].

On detailed electrical characteristics of a SET transistor utilizing charging effects on metal nanoclusters were reported by Sato et al. [26]. A self-assembled chain of colloidal gold nanoparticles was connected to metal electrodes, which were formed by electron-beam lithography. The cross-linking of the particles as well as their connection to the electrodes results from a linkage by bifunctional organic molecules, which present the tunnel barriers.

By using alkylsiloxane molecules as an adhesion agent, gold nanoclusters with an average diameter of 10 nm were deposited on a thermally grown SiO_2 surface on a Si substrate. After formation of Si–O–Si bond by thermal treatment, terminal amino groups of the silane were attached to gold nanoclusters to form a sub-monolayer. After this coating led to the formation of a sub-monolayer, 1,6-hexanedithiol was added to inter-connect the particles with a more defined spacing. The coverage was completed by means of a second immersion into a gold particle solution and the dithiol molecules maintained the distance between the particles, while the second layer filled the gaps between the particles of the first one, however, forming chains of 2–4 particles. As this procedure was performed on a SiO_2 substrate, equipped with source, drain and gate metal electrodes defined by electron-beam lithography, the particles form a chain of at least three particles bridging the gap between the outer driving electrodes (Figure 9).

The number of nanoclusters in the bridge chain differed from device to device since not all steps of this procedure could be controlled in detail, but in any case a Coulomb gap could be observed up to 77 K indicating electron conduction dominated by SE charging, whereas the nonlinearity is smeared out at room temperature. Using a model circuit for a three-dot (four junction) SET transistor, simulation and fitting of the data indicated the capacitance of all junctions in the chain to be $1.8–2\cdot10^{-18}$ F and the calculated Coulomb gap to be in reasonably good agreement with the value of 150 mV obtained from the measured $I(U)$ characteristic, which was systematically squeezed by applying a gate voltage of -0.4–0.4 V. The plot of the current through the device was clearly dependent on the gate voltage and showed typical current oscillations, proving that the desired function of the SE transistor had been achieved. Samanta et al. [27] proposed a Green's function-based method to estimate the transmission function of electrons across the dithiol ligands from which the resistance R per molecule was calculated by the Landauer formula, i.e. $R = (h/2e^2)/T(E_g)$, where $T(E_g)$ is the transmission function, i.e. $T\sim\exp\,[2(mE_g)^{1/2}/\hbar]$. The resulting resistance was estimated to be $R\approx30\,G\Omega$, assuming a barrier height $E_g\approx2.8$ eV in the dithiol molecules.

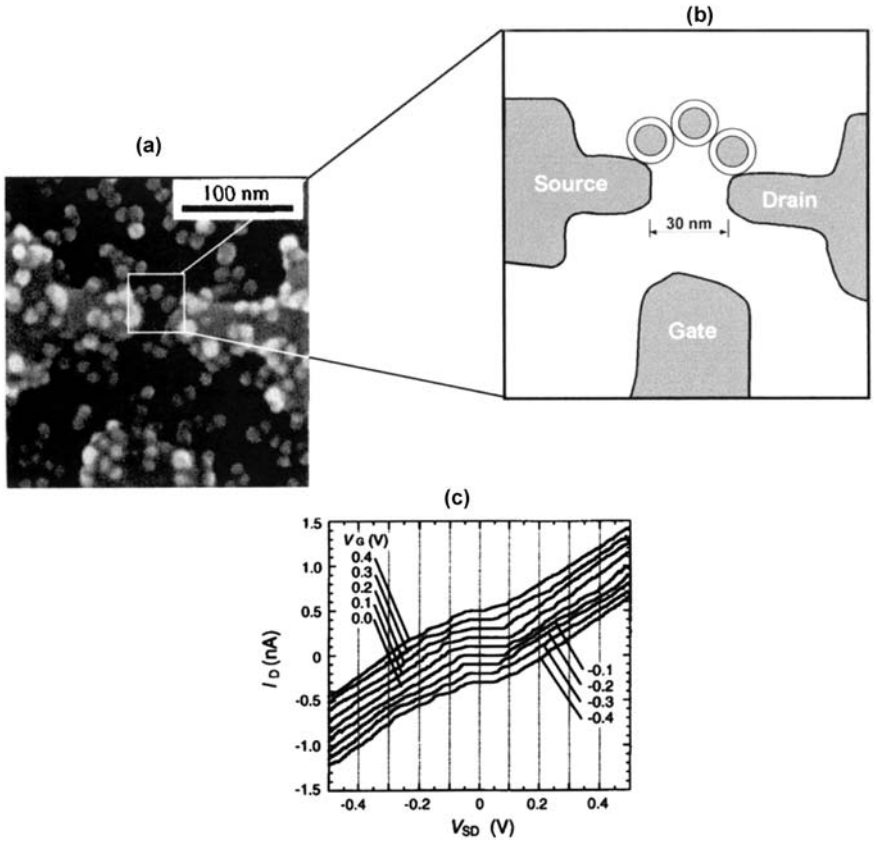

Figure 9. SET transistor, based on self-assembling of gold nanoclusters on electrodes fabricated by electron-beam epitaxy. (Reprinted with permission from Ref. [26], © 1997, American Institute of Physics.)

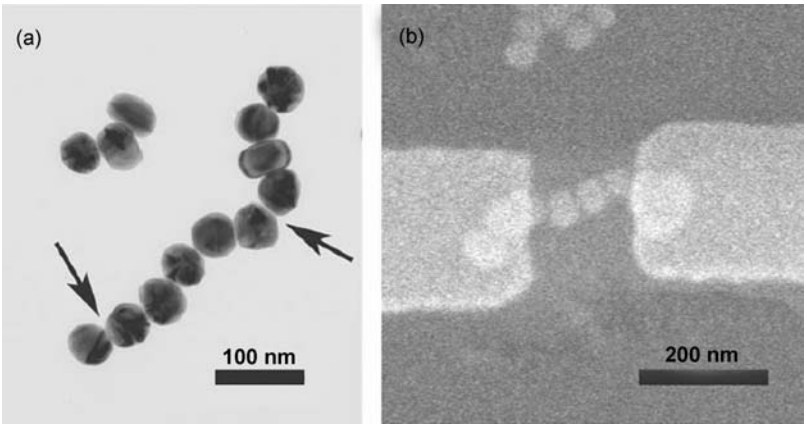

Figure 10. (a) Transmission-electron microscope micrograph of a self-assembled chain of 50 nm Au particles functionalized with octanethiol molecules; arrows indicate parallel crystal facets. (b) Two-island device fabricated by contacting a self-assembled chain of the nanoparticles. The two-particles framing the two-island particles form part of the electrodes, such that all three-tunnel junctions are formed by self-assembly and not by lithography. (Reprinted with permission from Ref. [28], © 2006, American Institute of Physics.)

A similar route has been followed most recently by Weiss et al. who have fabricated a multi-island SE device from self-assembled 1D gold nanocrystal chains [28]. They assembled thiol-stabilized 50 nm Au particles in a chain-like structure and used subsequently electron-beam lithography for electrode fabrication. Here it has to be pointed out that the 1D structure appeared to be stable enough to retain its structure and composition over the entire lithographic fabrication process (Figure 10).

Figure 11a shows the differential conductance dI/dV_{DS}, as a function of drain source V_{DS} and gate V_G voltages, of the double-island structure, whose micrograph is shown in

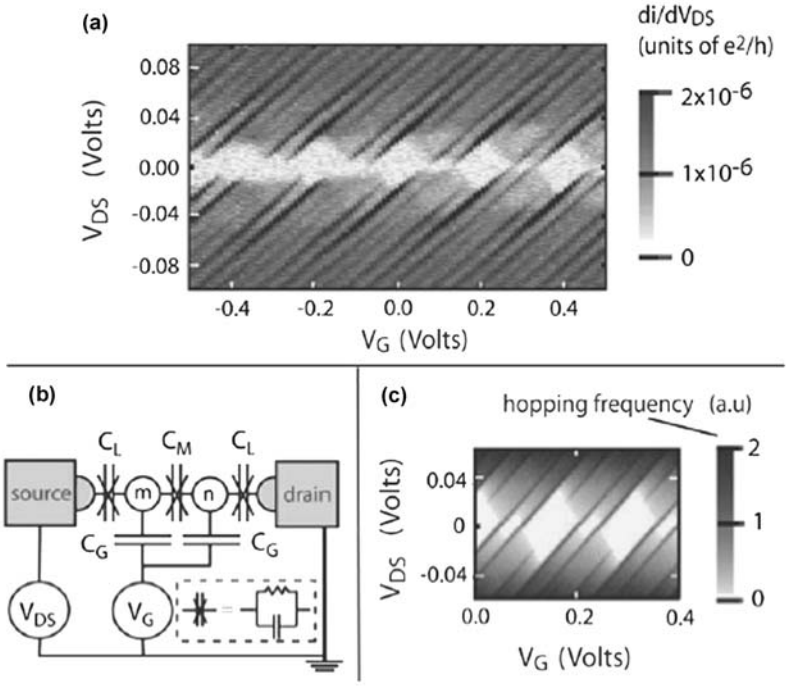

Figure 11. Experimental and predicted differential conductance plots of the double-island device of Figure 10(b). (a) Differential conductance measured at 4.2 K; four peaks are found per gate period. Above the threshold for the Coulomb blockade, the current can be described as linear with small oscillations superposed, which give the peaks in dI/dV_{DS}. The linear component corresponds to a resistance of ~20 GΩ. (b) Electrical modeling of the device. The silicon substrate acts as a common gate electrode for both islands. (c) Monte Carlo simulation of a stability plot for the double-island device at 4.2 K with capacitance values obtained from finite-element modeling: $C_G = 0.84$ aF (island-gate capacitance), $C_M = 3.7$ aF (inter-island capacitance), $C_L = 4.9$ aF (lead-island capacitance); the left, middle and right tunnel junction resistances were, respectively, set to 0.1, 10 and 10 GΩ to reproduce the experimental data. (Reprinted with permission from Ref. [28], © 2006, American Institute of Physics.)

Figure 11b. Close to $V_{DS} = 0$, the conductance is suppressed due to Coulomb blockade. Two Coulomb-blockade regions (appearing as large and small white diamonds near drain-source voltage $V_{DS} = 0$) have been observed. Furthermore four peaks in dI/dV_{DS} (appearing as diagonal dark lines) per gate period were recorded. The Coulomb charging energy was deduced from the size of the diamonds and gave a value of ~20 meV. Therefore, these well-resolved structures can only be observed at liquid He temperature. The authors pointed out that a remarkable property of this device is the high ratio of gate capacitance to total capacitance. This is an order of magnitude larger than what has been observed by Klein et al. [25]. The authors claim that this is the result of incorporating the nanoparticles into the edge of each electrode, reducing the capacitance between the outermost island and the electrode. This allows accessing multiple charge states with moderate gate voltages, which is an important requirement for nanoelectronic devices. Furthermore the device shows an enormous high stability of the electronic properties, as compared to formerly built devices of this kind.

Another technique, which allows the controlled deposition of a single nanoparticle between two metal nanoelectrodes, i.e. the technique of electrostatic trapping (ET) was reported by Schmid and Dekker [29]. A polarized metal nanoparticle is attracted to the strongest point of an electric field, which was applied to two Pt electrodes (Figure 12).

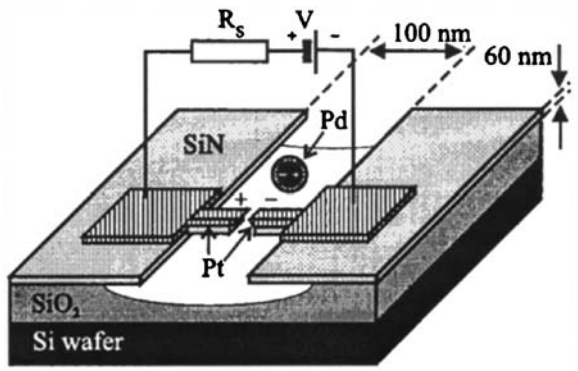

Figure 12. Schematic representation of the setup for single particle measurements by electrostatic trapping (ET). Pt denotes two freestanding Pt electrodes (dashed region). A ligand-stabilized Pd cluster is polarized by the applied voltage and attracted to the gap between the Pt electrodes. (Reprinted with permission from Ref. [29], © 1997, American Institute of Physics.)

The particles can be immobilized from solution in the gap between the Pt electrodes. The electrodes were fabricated by thermal growth on Si and their size could be reduced down to 4 nm. On top of the structure a 60 nm SiN film was deposited, whereas a 100 nm slit in the SiN film with a local constriction with 20 nm spacing was opened by

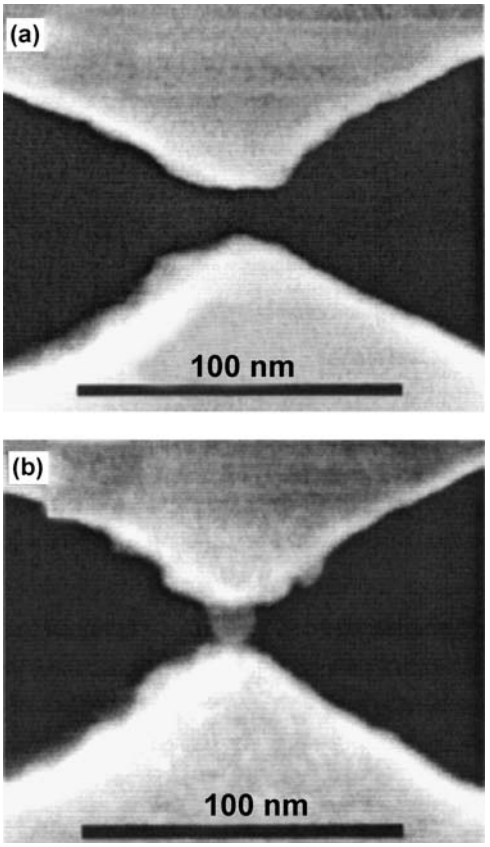

Figure 13. (a) Pt electrodes (white) separated by a $\approx$14 nm gap. (b) After ET, the same electrodes are bridged by a single $\approx$17 nm Pd particle. (Reprinted with permission from Ref. [29], © 1997, American Institute of Physics.)

electron-beam lithography with PMMA and reactive-ion etching. Under-etching with HF enabled the formation of free-standing SiN "fingers", which were sputtered with Pt to reduce the gap width down to 4 nm (Figure 13).

To study the electrical transport properties of this double-barrier system Pd nanoclusters have been trapped in this gap. Figure 14 shows a typical $I(U)$ curve. The most pronounced feature at 4.2 K is the Coulomb gap at a voltage of about 55 mV, which disappears at 295 K. Above the gap voltage, the $I(U)$ curve is not linear, but increases exponentially, which was explained by a suppression of the effective tunnel barrier by the applied voltage.

Smaller Au_{55} clusters have be deposited by ET in a three-electrode arrangement [30] to increase the temperature, where SE charging in nanoelectrode arrays may occur. Using an electron-beam lithography process, three tungsten electrodes were fabricated from a 25 nm tungsten layer on a Si wafer with a 80 nm thick SiO_2 layer. The minimum feature size turned out to be 50 nm with 20–50 nm gaps between the contacts. Quasi-1D chains of the 1.4 nm Au particles are formed upon ET. At room temperature these chains exhibit Coulomb blockade effects between -0.5 and $+0.5$ V, however, without any singularities in the characteristic, which could refer to the electronic structure of the particles (Figure 15).

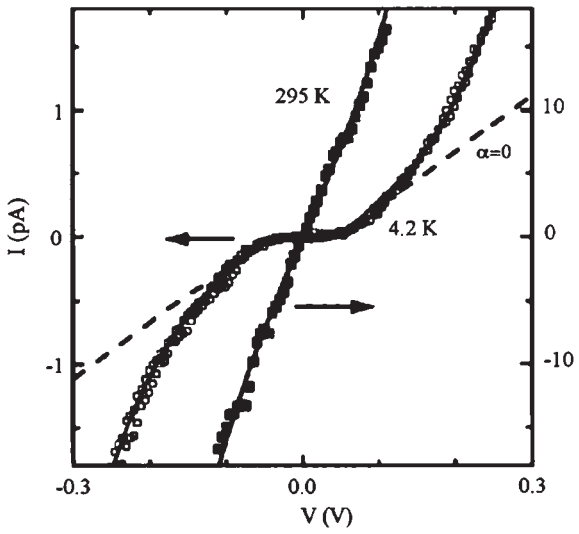

Figure 14. I–V curves measured at 4.2 K (open squares) and at 295 K (solid squares). The solid curves denote fits of the KN model. Fitting parameters for these curves are $V_c = 55$ mV, $R_0 = 1.1 \times 10^{11}\,\Omega$, $q_0 = 0.15e$ (offset charge) and $a = E\ (c/h) = 0.5$. The dashed curve ($a = 0$) represents the conventional model, which assumes a voltage-independent tunnel barrier. (Reprinted with permission from Ref. [29], © 1997, American Institute of Physics.)

Bates et al. reported the construction and characterization of a gold nanoparticle wire assembled using Mg^{2+}-dependent RNA–RNA interactions for the future assembly of practical nanocircuits [31]. They used magnesium ion-mediated RNA–RNA loop-receptor interactions, in conjunction with 15 nm or 30 nm gold nanoclusters derivatized with DNA to prepare self-assembled nanowires. A wire was deposited between lithographically fabricated nanoelectrodes and exhibited non-linear activated conduction by electron hopping at 150–300 K (Figure 16).

In the high temperature regime, the conductivity was found to be simply thermally activated and the data was modeled as $\sigma = \sigma_0 \exp(-W/kT)$, where σ_0 is the maximum conductivity, W is the activation energy and k is the Boltzman constant giving $W = 0.29$ eV and $\sigma_0 = 10$ mS. Below 160 K the rate of change of conductivity with temperature was reduced significantly, indicating deviating conductivity processes.

Another biomolecularely-based approach for the assembly of nanoscale electrical circuits was reported on by Chung et al. [32]. They used direct-write dip-pen nanolithography (DPN) to add specific local chemical functionality in the form of specific DNA sequences to lithographically defined electrodes with 20–100 nm gap distance. 20 nm or 30 nm oligonucleotide-functionalized gold nanocluster were immobilized between the electrodes using linker-oligonucleotide strands to induce circuit assembly (Figure 17).

$I(U)$ characteristics were measured for different temperatures and a Coulomb gap could be observed at 4.2 K, depending on nanoparticle size: The smaller particles have smaller capacitances and higher charging energies, and

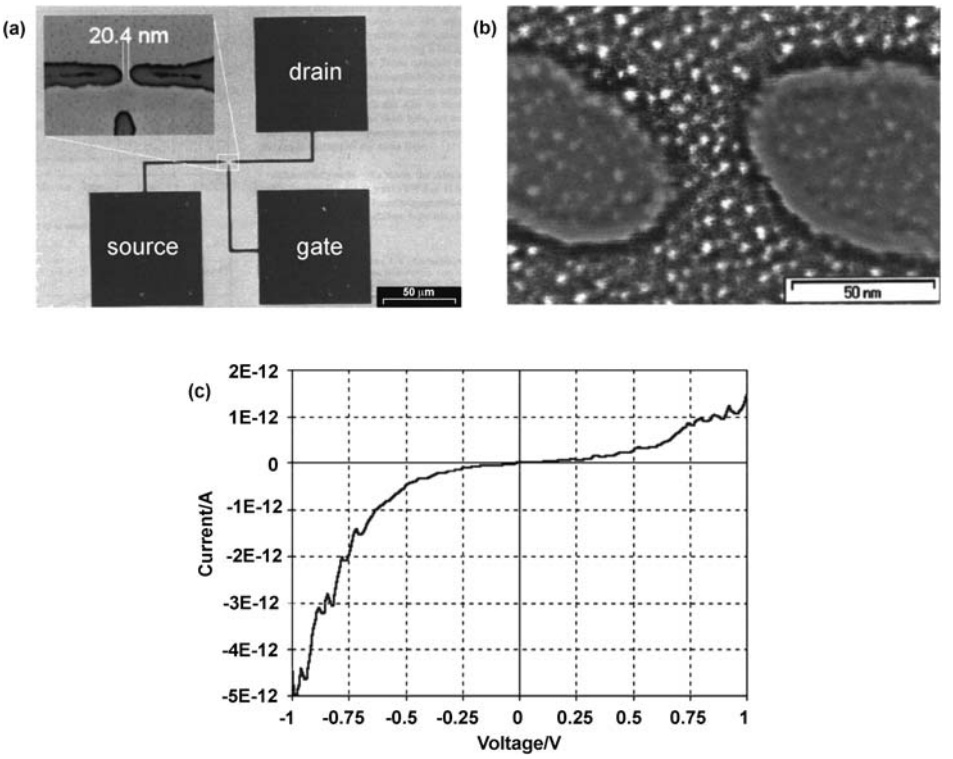

Figure 15. (a) SEM image of a three-terminal device with source, drain and gate electrodes. The inset shows in magnification the gap in the tungsten electrodes. (b) High resolution SEM of Au55 clusters forming a quasi-1D chain. (c) $I(U)$ characteristic of the device. (Reprinted with permission from Ref. [30], © 2001, American Chemical Society.)

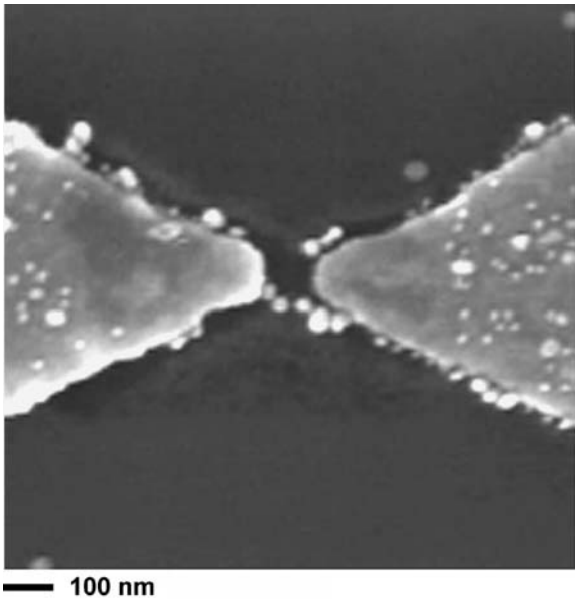

Figure 16. Scanning electron micrograph of a pair of nanoelectrodes with gold nanoparticles immobilized into the gap using a mixture of large particles small particles derivatized with RNA phosphate buffer containing NaCl in the presence of Mg^{2+}. (Reprinted with permission from Ref. [31], © 2006, American Chemical Society.)

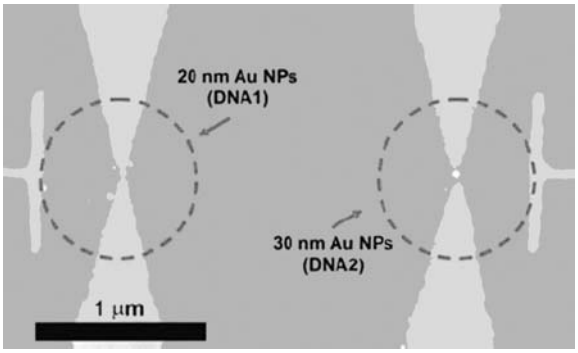

Figure 17. SEM image of single 20 nm and 30 nm-diameter Au nanoparticles asembled from solution and bridging the two adjacent nanoelectrode junctions. (Reprinted with permission from Ref. [32], © 2005, Wiley-VCH.)

thus exhibit wider Coulomb gaps ($\approx$73 mV for the 20 nm particles and $\approx$25 mV for the 30 nm particles, respectively), which provides further evidence for the immobilization of a single electrically active cluster into the electrode junctions.

On the way to more reliability in device fabrication, Kronholz et al. reported on the reproducible fabrication of protected metal nanoelectrodes on silicon chips with $<$30 nm gap width and their electrochemical characterization [33]. For the fabrication of the chips, an optical lithography step and two electron-beam steps are combined (Figure 18).

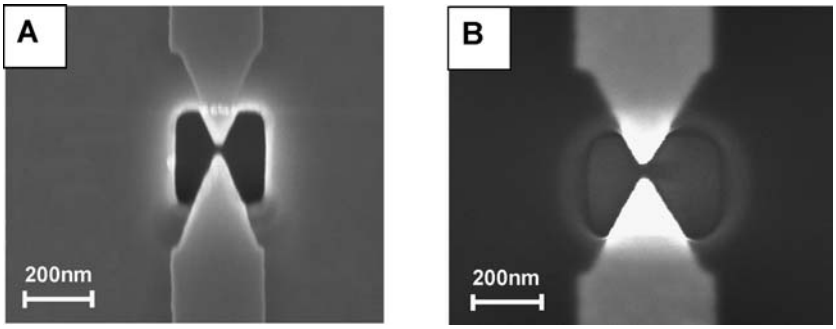

Figure 18. Nanoelectrodes with a 30 nm gap, access window 200 × 200 nm, having a $SiO_2/Si_3N_4/SiO_2$ (A) or a PMMA based (B) protection layer.

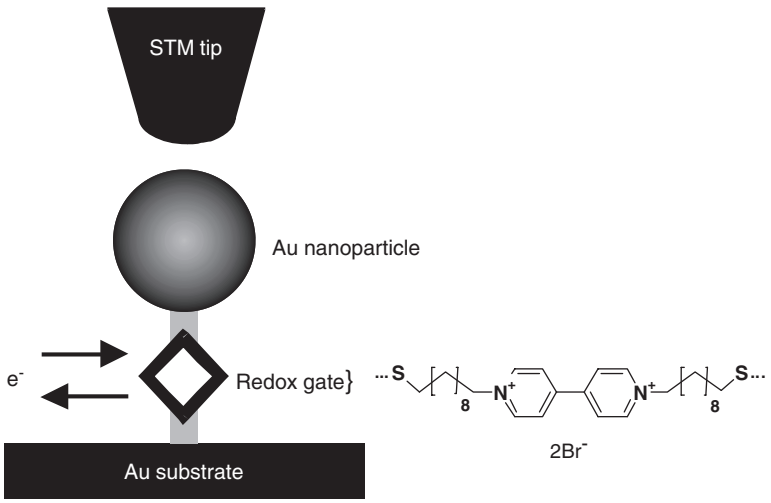

Figure 19. Scheme describing the redox switch, which is based on a viologen redox center incorporated within the nanoclusters ligand shell. For simplification the counterelectrode is not shown. (Adapted with permission from Ref. [34], © 2000, Nature Publishing Group.)

The following electrode position of copper on one or both of the gold electrodes appeared to be a promising strategy to narrow the gap between the lithographically fabricated electrodes down to a few Ångtrom units to realize a platform for the addressing of nanometer-sized functional components like small clusters or biomolecules, and was investigated by cyclovoltammetric measurements.

4.3. Chemical Switching and Gating of Current Through Nanoclusters

The opportunity to chemically control the size of the cluster as well as the thickness, composition and state of charge of the ligand shell is a significant advantage of incorporating nanocluster in SE devices. The current flow through such a device will therefore be very sensitive to any charges and impurities residing on the nanocluster or in the ligand shell. This sensitivity can be used for switching the ''transparency'' of the ligand shell or for applying the ligands as ''chemical gates'' to manipulate the SET current.

Schiffrin and coworkers have reported about how control of the transparency of the insulation barriers between a substrate and a nanoparticle in a STS experiment can be gained [34] (Figure 19).

They used a bipyridyl moiety (viologen group, V^{2+}) incorporated in the ligand shell of the particle as a redox group. Into this group, electrons were incorporated under electrochemical control, while the transparency of the insulating barrier was measured by STS. The reduction of V^{2+} to the radical $V^{\bullet+}$ leads to a significant decrease of the barrier height and further reduction to V° results in a huge increase of the barrier height. The supporting effect of a half-filled molecular orbital in $V^{\bullet+}$ is reflected by this result, which might lead to an extension of the electronic wave function from the nanocluster to the substrate via the orbitals of the radical $V^{\bullet+}$. Electron pairing in the LUMO (lowest unoccupied molecular orbital) suppresses the direct electronic interaction as soon as V° is formed.

It was shown that switching of the SET current through a ligand-stabilized nanocluster can be induced by electron injection into a specific redox group within the barriers of the tunnel junction. A great challenge will be the integration of those switching elements into a self-assembled SET circuitry, as the configuration, which was studied in this work, requires the reduction by at least 30 electrons to change the transparency of the barrier in the nanoparticle layer.

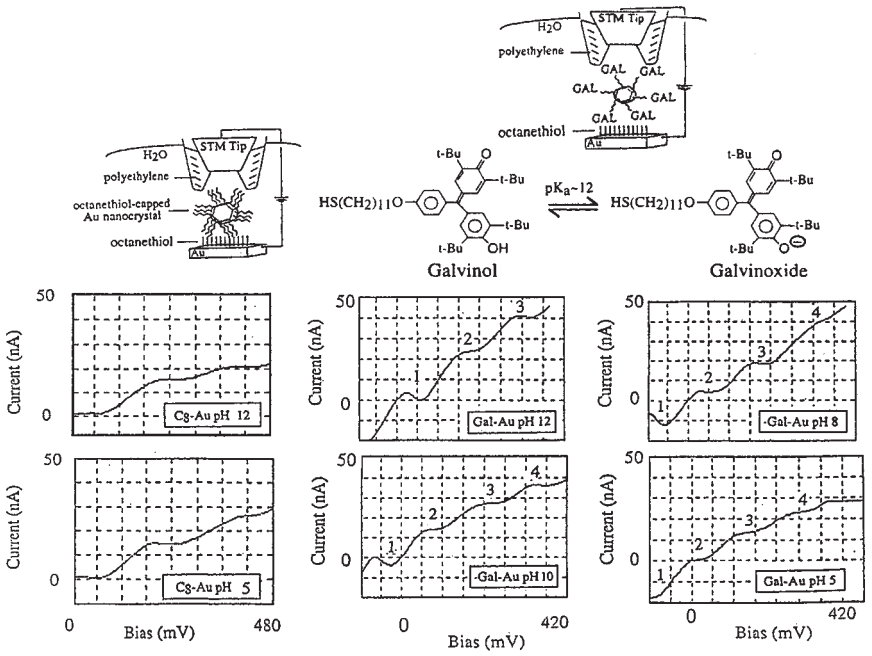

Figure 20. $I(U)$ curves for C_8–Au (left) and Gal–Au (right) in H_2O as a function of pH (adjusted with phosphate buffer). The numbers 1–4 in the Gal–Au data identify voltage plateaus. Cartoons of the experimental arrangements for measuring curves of individual nanoclusters in solution are shown at the top of each data column. The insulated STM tip, ligand-capped Au nanocluster and an octanethiol-coated planar Au substrate are shown. Length and shapes are not to scale. (Reprinted with permission from Ref. [35], © 1998, American Chemical Society.)

The possibility of employing particle capping ligands as "chemical gates" to control the SET current flow in a STS configuration has been considered by Feldheim et al. [35]. They reported on $I(U)$ characteristics of ligand-stabilized Au nanocluster in aqueous solutions, whereas octanethiol-stabilized 5 nm clusters and galvinol-stabilized 3 nm clusters were used as the central island. About 15 galvinol ligands were introduced into the ligand shell, as galvinol represents a pH-active probe with $pK_a \sim 12$. Galvinol, however, is converted to the galvinoxide anion upon increasing the pH, charging the ligand shell negatively. The authors present a collection of $I(U)$ characteristics with several clear current steps and voltage plateaus, reflecting SET in the individual particles for galvine and octanethiol nanoclusters in H_2O. Galvine reacts sensitively on pH changes from 5, via 8 and to 12, while only small differences in the positions and magnitudes of the staircase voltage plateaus appear for octanethiol-stabilized Au cluster upon changing the pH. The authors state that, firstly, from pH 5 to pH 8 a subtle shift (ca. 30 mV) in the entire staircase to positive bias potentials is noticable. In $I(U)$ curves obtained at pH between 10 and 12 (from ca. 60–120 mV), this shift is even more prevalent. Secondly, with increasing pH $\Delta(U) = e/c$ decreases in magnitude. Thirdly, at pH $\geq$ 8 slight peaks are evident in the $I(U)$ curves. These chemically induced changes lead to an increase of negative charge on the cluster and have two consequences, i.e. (i) from $\sim 2.2 \times 10^{-18}$ F at pH 5, the total self-capacitance of the nanoclusters decreases to $\sim 0.31 \times 10^{-18}$ F at pH 12 and (ii), causing a shift of the Coulomb blockade to positive bias potentials, the induced negative charge from forming galvanoxide acts like a negatively charged gate in solid-state SET devices. The authors conclude, that the notion of pH-gated SET is supported by the fact that potential shifts and capacitance changes are only observed for galvine-stabilized Au and not in octanethiol-stabilized Au (Figure 20).

For the first time it was shown that SET is dependent on the nature of the stabilizing ligands as well as on the composition of the solution, surrounding the functional array.

This has some interesting consequences. Where SET currents should be sensitive to single redox or analysts events, this will be useful for studying chemical signal transduction. Barsotti et al. reported on the formation of metal nanoparticle-based SE transistors as DNA sensors [36]. Via electron-beam lithography and using a focused ion beam, an insulating gap was cut in a conductive gold wire. The ends of this wire were functionalized using DPN and assembly of nanoclusters occurred selectively on the patterned regions. Preliminary results showed a 100-fold decrease in resistance after nanoparticle assembly. The authors state that improved resolution in gap formation and DPN will allow for the assembly of single nanoclusters in the gap, which than can serve as a SET for DNA sensing in the future.

5. From Single Particle Properties to Collective Charge Transport

The single particle properties, which have been discussed in the previous section showed the meaning of the large charging energy of metal nanoclusters as a prerequisite for

SET events at elevated temperature. Together with the limited number of free electrons, this may lead us to regard them as artificial atoms. This raises fundamental questions about the design of "artificial molecules" or "artificial solids" built up from these nanoscale sub-units [37–39]. Remacle and Levine reviewed the ideas associated with the use of chemically fabricated quantum dots as building blocks for a new state of matter [40].

Students in the first chemistry courses learn that the simplest molecule H_2 is formed due to the overlap of the electron wave function centered on the individual hydrogen atoms. Correspondingly, also the wave functions of the artificial atoms can overlap and electrons can coherently and reversibly tunnel between them, which is the basis for a covalent bond. In continuation the ordered assembly of identical nanoclusters is one, two or three dimensions represents the formation of an artificial solid or superlattice. The fabrication of 2D and of 3D ordered superlattices has been demonstrated already some time ago in several works [41–49]. Furthermore it is possible to mix nanoclusters of different chemical composition, of bimodal size or of different shape to obtain tailored nanoalloys [48,49]. Such artificial solids exhibit delocalized electron states depending on the strength of the electronic coupling between the adjacent nanoclusters. The latter will depend on the size of the nanoclusters, the nature and the covering density of the organic ligands, the particle spacing and on the symmetry of packing.

In order to discuss the signatures of localization and delocalization and its significance for the application of nanoclusters in microelectronic devices, the following chapters will give examples about the electrical properties of nanoclusters arrays, distinguished according to their dimensionality.

5.1. One-Dimensional Arrangements

In the previous chapters, examples of 1D arrays of nanoclusters have been given, where self-assembly or ET were used to address the arrays for electrical transport measurements. So far it is evident that these methods did not lead to strictly 1D defect-free arrangements. Furthermore, inherent disorder cannot be avoided. This means that the electrical transport properties through a "perfect" array could only be studies theoretically up to now.

As an example for such a theoretical approach might serve a work by Schoeller and coworkers [50]. They calculated the quantum transport through 1D arrays of metallic nanoclusters assembled to DNA (an overview about the methods to fabricate such assemblies is given in reference [51]). They calculated the current and shot noise through such a system theoretically as functions of various parameters, e.g. the applied gate and bias voltage, the temperature and the strength of dissipative effects. They especially focused on the role of the geometry of the array since it was intended to design the electron transport properties by controlling the shape of the device. As a model system (Figure 21), they assumed that gate, leads and nanoparticles are ideal conductors while the other parts of the system (substrate, DNA, ligand shell) are modeled as dielectrics. They calculated the transport properties from an incoherent tunneling picture using a semiclassical master equation approach. In contrast to the standard orthodox theory, they took into account the discreteness of the electronic structure of the nanoclusters together with dissipative effects. Tunneling was treated as a perturbation while the Coulomb interaction between charged nanoclusters was taken into account non-perturbatively within a capacitance model.

With these calculations they identified single particle levels in the $I(U)$ characteristics as fine steps for a two-nanoparticle array. These fine structures can be distinguished from usual Coulomb steps since they are smeared out by increasing temperature. For an array of nanoclusters with uniformly growing diameters they found a striking asymmetry of the $I(U)$ characteristics in the low bias-voltage regime, whereas for larger bias voltages the $I(U)$ curves are symmetric and approximately independent of gate voltage applied (Figure 22). They identified the mechanism of asymmetry as a combined effect of Coulomb interaction, asymmetric capacitance matrices and/or asymmetric sizes of nanoclusters. Furthermore they found that the offset voltage increases with array length whereas the asymptotic conductance can increase or decrease with array length depending on the specific design of the sizes of the nanoparticles.

For particles with finite width of the electronic spectrum, a pronounced negative differential conductance (NDC) effect occurs which can be tuned by varying the tunneling to the leads (Figure 23). The effect occurs because strong tunneling to the reservoirs induces, for high bias voltage, an asymmetry of the charge distribution in the array resulting in a large offset of the electronic spectra between the nanoclusters. Therefore tunneling is suppressed due to the finite bandwidth. In this way a tuneable NDC effect is proposed with possible technological applications.

5.2. Two-Dimensional Arrangements

An electronic conduction across a network of 4 nm gold nanoclusters inter-connected by di-isonitrile ligands (1,4-di(4-isocyanophenylethynyl)-2-ethylbenzene) forming a conjugated, rigid molecule with an approximate inter-cluster spacing of 2.2 nm was reported by Janes et al. in 1995 [52]. The 2D assembly was obtained from the deposition of nanoclusters from a colloidal solution and following reactive addition of linking molecules. As the layers were deposited on a SiO_2-supported GaAs wafer with gold contacts with separations of 500 and 450 nm, electrical characterization of the system was realizable.

The $I(U)$ characteristic of the arrays showed a linear behavior over a broad voltage range. If each cluster is assumed to have six nearest neighbors and a cluster-to-cluster capacitance of 2×10^{-19} F is implied, the total dot capacitance will be 1.2×10^{-18} F. A corresponding charging energy can thus be approximated to 11 meV, which is only about half of the characteristic thermal energy at room temperature. This excludes a development of a Coulomb gap at room temperature.

From comparable samples with 2D cluster linkage Andres et al. reported on the charging energy of the

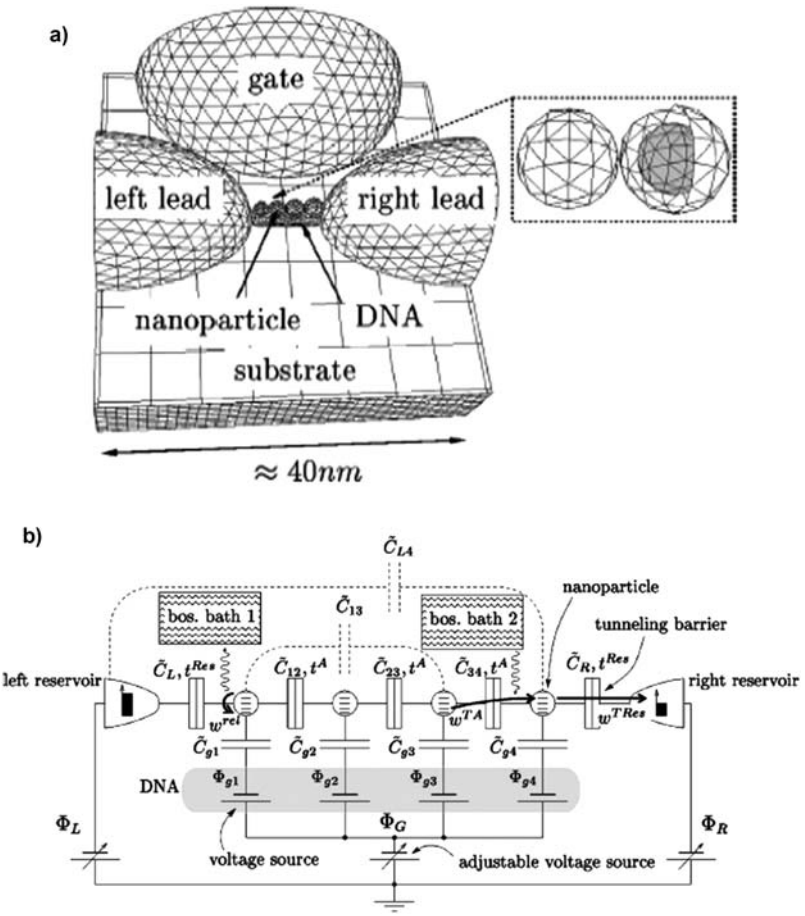

Figure 21. Device geometry (a) and model system (b) used for the calculation of the $I(U)$ characteristics. (Reprinted with permission from Ref. [50], © 2005, American Physical Society.)

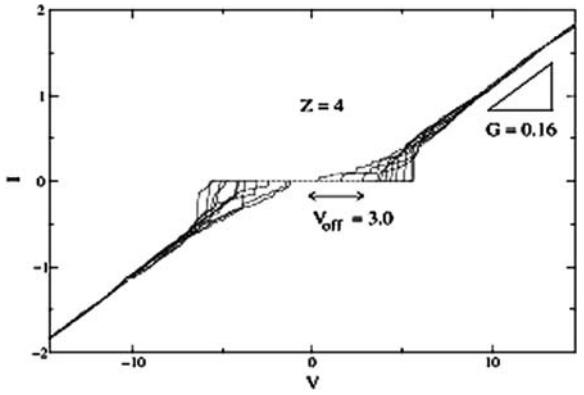

Figure 22. $I(U)$ curve for a nanocluster array with four nanoparticles. (Reprinted with permission from Ref. 50, © 2005, American Physical Society.)

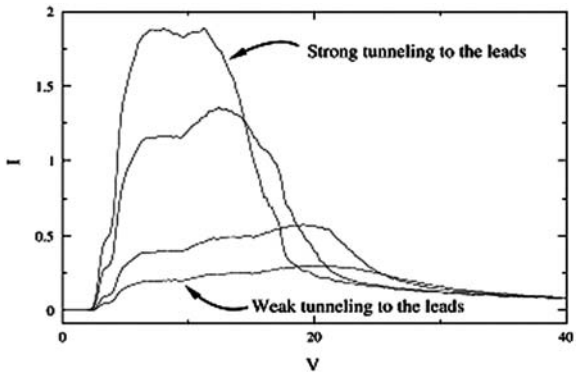

Figure 23. $I(U)$ curve illustrating the pronounced NDC effect. (Reprinted with permission from Ref. [50], © 2005, American Physical Society.)

nanoclusters obtained from temperature dependent DC measurements. According to the Arrhenius relation $Y_0 = Y_\infty \exp(-E_A/k_B T)$, where Y_∞ is the conduction as $T \to \infty$, E_A is the activation energy and k_B, Boltzmann's constant, Coulomb charging with a charging energy of $E_A = 97\,\text{meV}$ was stated [53]. The inter-particle resistance was given to be $0.9\,\text{M}\Omega$, from which a single-molecule resistance of $29\,\text{M}\Omega$ was calculated. This result has found to be in good agreement with the prediction of $43\,\text{M}\Omega$ obtained from Hückel–MO calculations [54].

On the formation of electrically conducting DNA-assembled 15 nm gold nanoparticle monolayers was reported by Koplin et al. [55]. A monolayer of gold nanoclusters was obtained from DNA-directed immobilization on flat silicon substrates, exhibiting particle densities, which are high enough to enable electronic exchange between the particles. The electrical features of the layers were determined by room temperature DC measurements and temperature-dependent impedance spectroscopy, which showed pronounced field dependence as well as thermal activation of the conductivity, reflecting classical hopping transport. This bears a strong resemblance to 3D nanoparticle structures. According to the hopping theory, the activation energy increased with increasing inter-particle spacing. According to the Arrhenius relation, an activation energy of 301 meV could be calculated from the impedance data for the DNA-immobilized gold nanoparticle monolayer with a mean particle distance of 9.3 ± 1.3 nm.

Temperature-dependent DC transport measurements on self-assembled, dodecanethiol-passivated, ≈ 7 nm silver nanoclusters Langmuir monolayers as a function of particle-size distribution induced disorder have been reported by Beverly et al. [56]. The superlattices disorder was adjusted by a stepwise variation of the particle-size distribution. They reported on electrical transport properties, from 300 to 10 K, of six different monolayers of ≈ 7 nm silver nanoclusters in which the particle-size distribution was varied from 6.6 to 13.8%. All films exhibited metallic conductivity above ≈ 200 K and then activated transport below 200 K. At lower temperatures, between 30 and 100 K, a second transition (T_{cross}) was observed as the system crossed over from simple activated transport to a third regime of variable range hopping (VRH). T_{cross} correlated linearly with the particle-size distribution width, implying that the superlattice disorder is the major variable upon which T_{cross} depends (Figure 24).

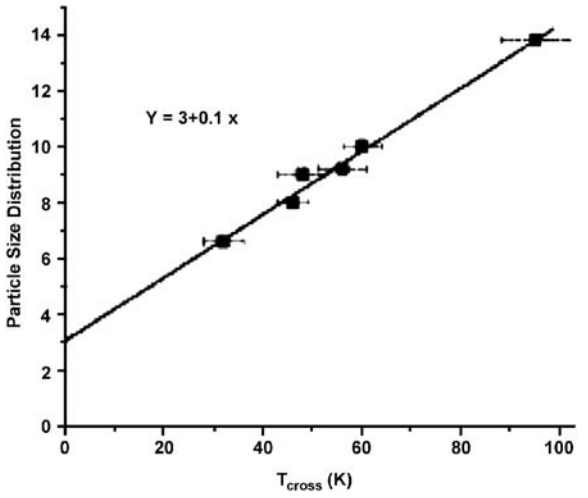

Figure 24. Plot of the particle-size distribution versus the transition temperature T_{cross}, which describes the crossover point between an activated transport mechanism ($\ln(R) \propto E_a/T$ and variable range hopping (VRH) ($\ln(R) \propto T^{-1/2}$). Note that T_{cross} has a 0 K value at a finite (3%) particle-size distribution. (Reprinted with permission from Ref. [56], © 2002, American Chemical Society.)

The measurements extrapolate to generate a 0 K value of T_{cross} at a size-distribution width of approximately 3%. The authors argue that these results imply that it may be possible to observe a true metallic conductivity to near 0 K in a 2D nanocluster array, giving a sufficiently narrow size distribution.

From comparable systems with a particle-size distribution width of 7%, experimental and computational results for temperature-dependent conductivity measurements were reported on by Remacle et al. [57]. At low temperatures, the $I(U)$ characteristics have a sigmoid shape and are non-linear (Figure 25).

As the temperature is increased, the behavior of the array becomes ohmic. This is the experimental signature of the switching from a VRH at low temperature to an activated behavior at high temperature. In the computations, the temperature range over which the transition takes place is larger than in the experiments. This results predominantly from the smaller size of the array, which was chosen for the computations. The size of the ordered domains in the experiments is about 25–100 times higher, which reflects 25–100 times more dots and accordingly higher density of states.

5.3. *Three-Dimensional Arrangements*

Pileni and coworkers reported on signatures of a transition from single particle properties to 3D charge transports properties, visible in a room temperature tunneling spectroscopy study on 4.3 nm Ag nanoclusters, stabilized in reverse micelles [58]. In electrical transport measurements on single-particles deposited on Au (1 1 1) substrates, it could be shown that on increasing the applied voltage, charging of small capacitances of the double-junction occurs and due to the Coulomb-blockade effect, the detected current is close to zero. The Coulomb blocking state, i.e. a zero bias and the onset of conductivity through the nanoclusters above the threshold voltage was clearly indicated by the $I(U)$ curve as well as the dI/dU versus U-plots (insert in Figure 26). The particles arrange in a hexagonally ordered monolayer when depositing them from solution with higher concentrations. Compared to the isolated particles, the tunneling current through this layer shows a less pronounced non-linearity in the $I(U)$ curve as well as a smaller Coulomb gap. This indicates the onset of ohmic contributions to the overall conductance of the system. The Coulomb gap almost vanishes and the $I(U)$ characteristic is a purely ohmic one at low voltages regarding 3D arrangements of the particles, which form a self-organized closed packed fcc structure. This reflects additional transport paths for electrons that appear between the adjacent nanoclusters in the 3D systems, smearing out the Coulomb gap between the individual particles due to the coupling of the electron states in the close-packed system.

The electrical DC and AC response of compacts of ligand-stabilized nanoclusters also reflects the electrical behavior of the 3D system [21]. At high temperature, i.e. several tens of Kelvin below room temperature, the temperature dependent DC and AC conductivity follows a simply activated behavior according to the

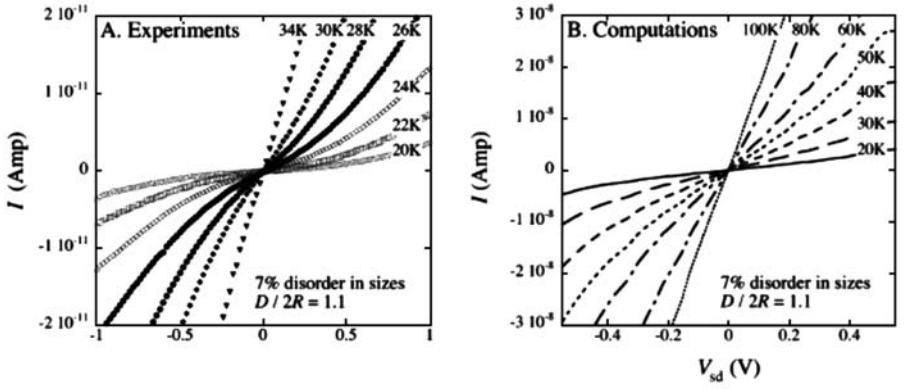

Figure 25. Experimental and computed $I(U)$ curves. (A) The experimentally measured $I(U)$ curves from an array of 7 nm Ag nanoparticles with a 7% size distribution and $D/2R = 1.1$. (B) The calculated $I(U)$ curves computed for an array of 8911 dots with 7% fluctuation in size and 7% packing disorder. $2R = 7$ nm and the compression level, $D/2R = 1.1$. (Reprinted with permission from Ref. [57], © 2003, American Chemical Society.)

Arrhenius relation

$$\sigma(T) = \sigma_0 + \exp\frac{-E_A}{k_B T},$$

where E_A is the activation energy. With decreasing measuring temperature E_A becomes temperature dependent. Accordingly down to very low temperature, the conductivity follows the VRH expression, proposed by Mott [59]:

$$\sigma(T) = \sigma_0 + \exp\left(\frac{-T_0}{T}\right)^{\gamma}$$

with $\gamma = 1/(d + 1)$ in d dimensions. $\gamma = 0.5$ is predominantly observed in the case of the compacted metal cluster compounds, although $\gamma = 0.25$ $(d = 3)$ might be expected from this general expression. The electric field-dependent conductivity, which reflects pronounced non-ohmic behavior at strong electric fields as well as, the temperature dependence disclose a pronounced similarity to different heterogeneous materials, like cermets, doped and amorphous semiconductors or metal- and carbon-insulator composites. Van Staveren and Adriaanse applied different physical models of hopping conductivity to analyze this behavior with the conclusion that the experimental data can be best fitted with a thermally activated stochastic multiple site hopping process, whereas at high temperature around room temperature nearest neighbor hops dominate [60–62].

At low temperature, the number of charge carriers participating in the hopping process does not change with temperature. At high temperatures, where $k_B T$ becomes comparable to the charging energy E_c of the metal particle (note that E_c is determined by the total capacitance of the particle, and is therefore dependent on the particle size as well as on the inter-particle spacing, i.e. the dot-to-dot distance), thermally excited extra-charge carriers are participating in the hopping process instead. Thus, the activation energy reflects the energy needed to transfer one electron from an electrically neutral particle to another, even at high temperature. It is the charge disproportionation energy and it has its atomic analog in the disproportionation energy of atoms or molecules in chemical redox reactions. At low temperatures, if all particles become electrically neutral, the hopping transport is expected to become zero. All reports on the electrical conductivity reflect a residual conductivity at very low temperature, therefore it becomes obvious again that packing, shape and size distribution prevent the localization sites from being identical, as it was already pointed out in the beginning of this chapter.

Orientational disorder and packing irregularities in terms of a modified Anderson–Hubbard Hamiltonian [63,64] will lead to a distribution of the on-site Coulomb interaction as well as of the interaction of electrons on different (at least neighboring) sites as it was explicitly pointed out by Cuevas et al. [65]. Compared to the Coulomb-gap model of Efros and Sklovskii [66], they took into account three different states of charge of the mesoscopic particles, i.e. neutral, positively and negatively charged. The VRH behavior, which dominates the electrical properties at low temperatures, can conclusively be explained with this model.

Coming back to the high-temperature regime, nearest-neighbor hopping is predominant, at least at temperatures around 300 K. This led to the question, whether by means of bifunctional spacer molecules, which define the interparticles spacing by the molecule length, the charging energy of such cluster materials can be chemically tailored. With the family of ligand-stabilized metal clusters $Au_{55}(PPh_3)_{12}C_{16}$ and $Pd_{561}(phen)_{36}O_{200}$, by using bifunctional spacers with NH_2- on SH-groups on each terminus, this concept has been realized [67–70]. When the cluster spacing is increased by the spacer molecules while the cluster size is kept constant, an almost linear increase of the activation energy was observed. As long as the other geometric and dielectric parameters are kept constant this can be explained by a decrease of the junction capacitance C, which scales with $1/d$ (d = particle spacing).

As long as the spacer molecules are not covalently bound to the cluster surface and the spacer molecules have no delocalized π-electron system along their backbone between their termini, this relation is valid. The respective activation energy drops as soon as covalently linking species, equipped with delocalized π electrons

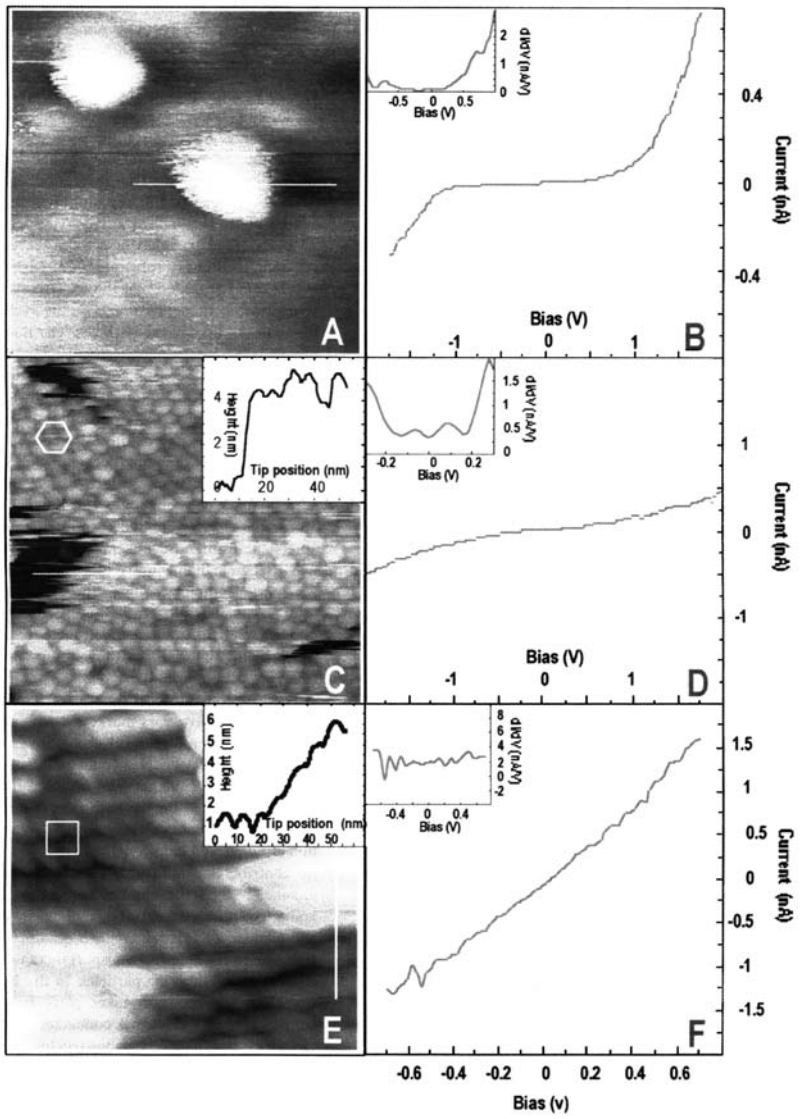

Figure 26. Constant current mode STM image of isolated (A), self-organized in close-packed hexagonal network (C) and in fcc structure (E) of silver nanoclusters deposited on Au(1 1 1) substrate (scan size: (A) $17.1 \times 17.1\,\mathrm{nm}^2$, $U_t = -1\,\mathrm{V}$, $I_t = 1\,\mathrm{nA}$, (C) $136 \times 136\,\mathrm{nm}^2$, $U_t = -2.5\,\mathrm{V}$, $I_t = 0.8\,\mathrm{nA}$, (E) $143 \times 143\,\mathrm{nm}^2$, $U_t = -2.2\,\mathrm{V}$, $I_t = 0.72\,\mathrm{nA}$). $I(U)$ curves and their derivatives in the inserts of isolated (B), self-organized in close-packed hexagonal network (D) and in fcc structure (F) of silver nanoclusters deposited on Au(1 1 1) substrate. (Reprinted with permission from Ref. [58], © 2000, Wiley-VCH.)

enable inter-cluster electron transfer, depending on the electronic structure of the molecules and their respective length. At least by integral conductance measurements, the electron transport through individual organic molecules can be displayed. This is supporting information about the nature of electron transport on the molecular level. These results are illustrated in Figure 27, representing the activation energies versus cluster–cluster distance of the covalently and non-covalently linked cluster materials as summarized in Table 1.

For highly ordered 3D systems, Terril et al. showed that the electron-hopping conductivity depends on the activation energy of the electron transfer and the electronic coupling term β [71]. They took the latter as a measure for the participation of the ligands in the conduction process. It controls the dynamics of electron core-to-core tunneling through the intervening ligand shell and through the non-bonding contacts between ligand shells on adjacent nanoclusters. The authors described the electron hopping as a thermally activated process in which the electron-tunneling barrier properties appear in the conductivity pre-exponential term of the Arrhenius relation: $\sigma_{EL}(\delta, T) = \{\sigma_0 \exp[-\beta\delta]\} \exp[-E_A/RT]$. In this equation β is the electron-tunneling coefficient, δ is the average nanoparticle core edge–edge distance, E_A is the activation energy and T is the temperature. The pre-exponential term ($\sigma_0 \exp[-\beta\delta]$) is the equivalent of an infinite-temperature electronic conductivity.

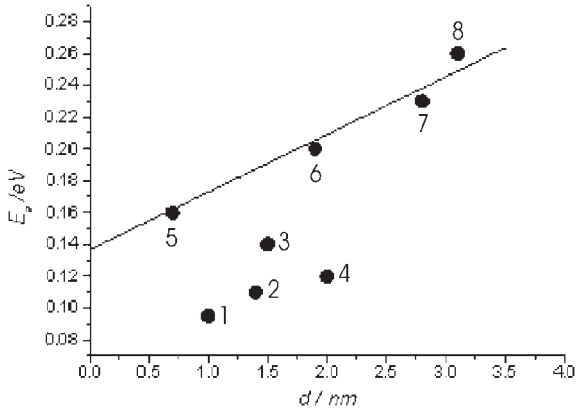

Figure 27. Activation energies versus cluster–cluster distances of the covalently (1–4) and the non-covalently (5–8) organized systems (Table 1).

Wuelfing et al. reported the temperature dependence of β for alkanethiolate chains connecting 2.2 nm gold nanoclusters [72]. The temperature dependence observed was attributed to the larger activation-barrier energies at the longer chain lengths. The variation in E_A can be avoided by plotting the Arrhenius intercepts against δ. Depending on the electronic structure of the ligand molecules, different β values can be observed, ranging from 0.8 to 1.0 $Å^{-1}$ for alkane ligands and from 0.4 to 0.6 $Å^{-1}$ for fully conjugated ligands [73].

Quinn et al. observed that for arrays of 1.6 nm gold nanoclusters. The nanoclusters behave as weakly coupled molecular solids comprising discrete nanoscale metallic island separated by insulating ligand barriers [74]. The SE nanocluster charging energy, governed by the particle diameter, the dielectric properties of the passivating ligands and classical electrostatic coupling between neighboring cores, as well as the inter-particle tunnel-barrier resistance, arising from the insulating nature of the ligand shell separating the cores and the dimensionality of the network of conducting paths are found to be parameters dominating charge transport.

Temperature-dependent DC measurements on thin films of these nanoclusters yielded a narrow range of array-charging energies $106\,\text{meV} < E_A < 112\,\text{meV}$, assuming Arrhenius-like simple thermally activated behavior. From the orthodox theory $E_A = e^2/2C_\Sigma$, they calculated a total capacitance of $C_\Sigma = 0.75\,\text{aF}$ for a mean activation energy of $E_A = 108\,\text{meV}$. The total capacitance is given by the self-capacitance of an isolated nanocluster (C_0) and the inter-particle capacitance arising from nearest neighbor interactions (C_{nn}): $C_\Sigma = C_0 + C_{nn}$. Estimating the self-capacitance by simple electrostatics by treating the nanocluster as a conducting sphere of diameter d, embedded in a dielectric of relative permittivity ε, thus the self-capacitance $C_0 = 2\pi\varepsilon_0\varepsilon d$ can be calculated to $C_0 \approx 0.25\,\text{aF}$ for $d = 1.65\,\text{nm}$ and $\varepsilon = 2.7$. Since the value for the total capacitance exceeds the estimated nanocluster self-capacitance, this suggests a substantial contribution from classical electrostatic inter-particle coupling from neighboring particles in the array.

6. Conclusion and Future Directions

In this chapter it has been demonstrated that the electrical properties of metal nanoclusters are mainly determined by the Coulomb charging energy and that the respective phenomena can, in principle, be understood in terms of SE tunneling within the framework of the ''orthodox theory'' of SET and could be utilized for the fabrication of simple or complex nanoelectronic devices. Furthermore, for the smallest particles discussed here, like Au_{55}, additional effects due to the discreteness of the energy states occur. This may be a great opportunity for a generally new type of electronic devices, which base on multi-stable switching. These effects have not been studied experimentally or theoretically in much detail. Thus, most of the presently applied models are at least incomplete with respect to the huge variety of the different control parameters in the chemical design of molecularly organized nanoclusters. In other words, the complex interplay of size and size distribution, of constitution, symmetry and conformation of the ligand molecules, of the state of charge of the particles, of the embedding media and dielectric environment is not far enough understood. Therefore, the electrical properties need to be studied further to prove the reliability of the design strategies as described here for technological applications.

It is evident that chemically tailored metal nanoclusters carry a huge potential to achieve a central position in the evolution of novel device concepts for a post-CMOS time. Along with this process remains an open question: whether these nanoclusters or other molecular objects, like nanotubes or organic/organometallic molecules are stable under the operating conditions of a high-performance electrical circuit? With respect to circuit design, precise control over size and topology is needed. Some of the approaches for self-assembly are described briefly in this chapter and the use of complex bimolecular systems, like DNA strands or scaffolds hold the promise to excess hierarchically organized structures of high complexity. This covers, e.g. the deposition of nanoclusters along such biomolecules [75–78], the selective metalization [79–82], as well as the full self-assembly of circuit elements, like transistors [83] (for an overview, see e.g. [51] or [84]). However, even the best approaches will not solve the problems of inherent defects due to orientational disorder, isotope effects, etc.

Nevertheless, SET devices, as they can build up with chemically tailored building blocks, control the motion of just a few electrons instead of several hundred or thousand ones. Since power consumption is roughly proportional to the number of electrons transferred from a voltage source to the ground in logic operations, SET devices may reduce the power consumption drastically [85].

As a consequence one might expect that the future needs to rely on hybrid elements which arise from advanced UV- and electron-beam lithography, from imprint techniques or automated and parallelized nanomanipulation techniques, like dip-pen lithography or focused ion-beam techniques in combination with supramolecular approaches for the assembly of molecular inorganic/organic hybrid system. Nevertheless, it is evident for any kind of chemical approach that falling back onto the present-day

Table 1. Data representing activation energies and cluster–cluster distance of the covalently- and non-covalently-linked cluster materials.

Linking system	Distance (nm)	E_A (eV)
Covalently linked		
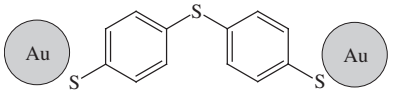 **1**	1.1	0.095
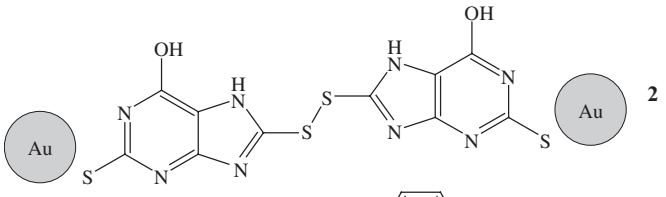 **2**	1.6	0.11
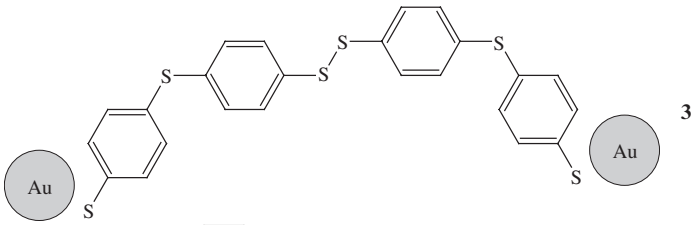 **3**	2.3	0.12
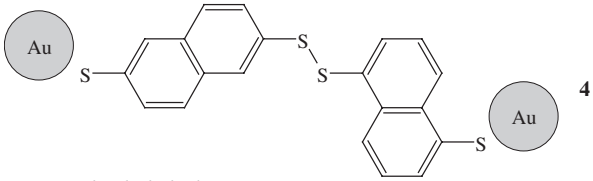 **4**	1.5	0.14
Non-covalently linked		
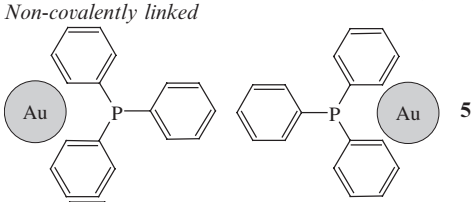 **5**	0.7	0.16
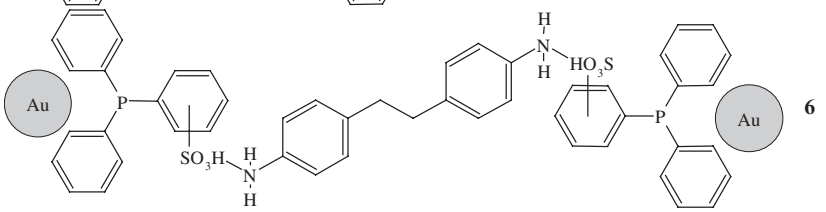 **6**	1.9	0.2
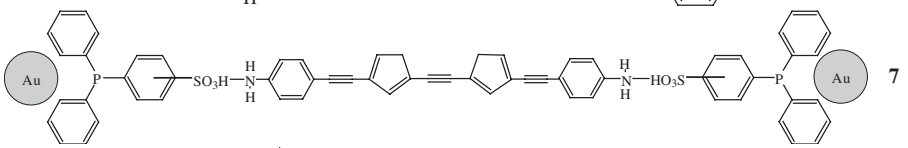 **7**	2.8	0.23
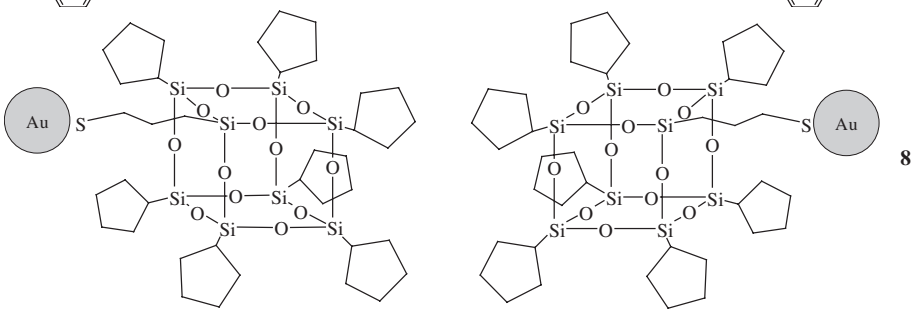 **8**	3.1	0.26

paradigm of information exchange in logic elements or memory devices will require defect-tolerant computer architectures with suitable, intelligent software, as it was first described by Williams et al. [86]. On the other hand, alternative routes beyond classical solid-state electronics might be developed, which require more complex architectures and different principles of information exchange, where the burden with respect to redundancy, current density, performance speed and especially contact resistance and charge redistribution at the lead-molecule interface are less relevant. Solving of these problems will undoubtedly be one of the great challenges in modern materials chemistry.

References

1 C. R. Kagan, A. Afzali, R. Martel, L. M. Gignac, P. P. Solomon, A. G. Schrott, B. Ek, *Nanolett.* 3 (2003) 119.
2 C. R. Barret, *MRS Bull.* 31 (2006) 906.
3 U. Simon, in G. Schmid (ed.) *Nanoclusters. From Theory to Application*, Wiley-VCH, Weinheim, 2004, 328 (For a comprehensive discussion of single electronics and for further references).
4 I. Giaver, H. R. Zeller, *Phys. Rev. Lett.* 20 (1968) 1504.
5 I. Giaver, *Phys. Rev.* 181 (1969) 789.
6 M. H. Devoret, H. Grabert, in H. Grabert and M. H. Devoret (eds.) *Single charge tunneling Coulomb blockade phenomena in nanostructures*, Nato ASI Series, Vol. 294, Plenum Press, New York, 1992, 1.
7 K. Uchida, in R. Waser (ed.) *Nanoelectronics and Information Technology*, Wiley-VCH, Weinheim, (2003) 425.
8 K. Uchida, J. Koga, R. Ohba, A. Toriumi, *ISSCC Dig. Tech. Paper* 1 (2002) 206, 460.
9 H. Grabert, *Z. Phys.* B 85 (1991) 319.
10 M. H. Devoret, *Bull. Bur. Nat. Métrol.* 22 (1991) 7.
11 BMBF Report, Info. Phys. Tech. No. 22 (1998), VDI-Technologiezentrum, Düsseldorf.
12 D. Anselmetti, D. Richmont, A. Baratoff, G. Borer, M. Dreier, M. Bernasconi, H.J. Güntherodt, *Europhys. Lett.* 25 (4) (1994) 297.
13 M. Dorogi, J. Gomez, R. Osifchin, R. P. Andres, R. Reifenberger, *Phys. Rev. B* 52 (12) (1995) 9071.
14 Ch. K. Wang, Y. Fu, Y. Luo, *Phys. Chem. Chem. Phys.* 3 (2001) 5017.
15 H. van Kempen, J. G. A. Dubois, J. W. Gerritsen, G. Schmid, *Physica B* 204 (1995) 51.
16 J. G. A. Dubois, J. W. Gerritsen, S. E. Shafranjuk, E. J. G. Boon, G. Schmid, H. van Kempen, *Europhys. Lett.* 33 (4) (1996) 279.
17 D. V. Averin, and A. N. Korotkov, *J. Low Temp. Phys.* 80 (3–4) (1990) 173.
18 W. P. Halperin, *Rev. Mod. Phys.* 58 (3) (1986) 533.
19 R. Houbertz, T. Feigenspan, F. Mielke, U. Memmert, U. Hartmann, U. Simon, G. Schön, G. Schmid, *Europhys. Lett.* 28 (9) (1994) 641.
20 L. F. Chi, M. Hartig, T. Drechsler, Th. Schaak, C. Seidel, H. Fuchs, G. Schmid, *Appl. Phys. A* 66 (1998) 187.
21 G. Schön, U. Simon, *Colloid. Polym. Sci.* 273 (1995) 101.
22 R. P. Andres, Th. Bein, M. Dorogi, S. Feng, J. I. Henderson, C. P. Kubiak, W. Mahoney, R. G. Osifchin, R. Reifenberger, *Science* 272 (1996) 1323.
23 U. Zhang, G. Schmid, U. Hartmann, *Nanolett.* 3 (2003) 305.
24 D. L. Klein, O. L. McEuen, J. E. Bowenkatari, R. Roth, A. P. Alivisator, *Appl. Phys. Lett.* 68 (1996) 2574.
25 D. L. Klein, R. Roth, A. Lim, A. P. Alivisatos, P. L. McEuen, *Nature* 389 (1997) 699.
26 T. Sato, H. Ahmed, D. Brown, B. F. H. Johnson, *J. Appl. Phys.* 82 (2) (1997) 696.
27 M. P. Samanta, W. Tian, S. Datta, *Phys. Rev. B* 53 (1996) R7626.
28 D. N. Weiss, X. Brokmann, L. E. Calvet, M. A. Kastner, M. G. Bawendi, *Appl. Phys. Lett.* 88 (2006) 143507.
29 A. Bezryadin, C. Dekker, G. Schmid, *Appl. Phys. Lett.* 71 (1997) 1273.
30 G. Schmid, Y.P. Liu, M. Schumann, Th. Raschke, Ch. Radehaus, *Nano Lett.* 1 (8) (2001) 405.
31 A. D. Bates, B. P. Callen, J. M. Cooper, R. Cosstick, C. Geary, A. Glidle, L. Jaeger, J. L. Pearson, M. Proupin-Pérez, C. Xu, D. R. S. Cumming, *Nano Lett.* 6 (2006) 445.
32 S. W. Chung, D. S. Ginger, M. W. Morales, Z. Zhang, V. Chandrasekhar, M. A. Ratner, C. A. Mirkin, *Small* 1 (2005) 64.
33 S. Kronholz, S. Karthäuser, G. Mészaros, T. Wandlowski, A. van der Hart, R. Waser, *Microelectron. Eng.* 83 (2006) 1702.
34 D. Gittnis, D. Bethell, D. J. Schiffrin, R. J. Nichols, *Nature* 408 (2000) 67.
35 L. C. Brousseau, ILL, Qi Zhao, D. A. Schultz, D. L. Feldheim, *J. Am. Chem. Soc.* 120 (1998) 7645.
36 R. Barsotti, F. Stellacci (2006) http://mit.edu/dmse/sunmag/res_dnasensing.shtml, 2006/12/14.
37 D. L. Feldheim, C. D. Keating, *Chem. Soc. Rev.* 27 (1998) 1.
38 (a) U. Simon, *Adv. Mater.* 10 (1998) 1487; (b) U. Simon, in *Metal Clusters in Chemistry*, Vol. 3, Wiley-VCH, Weinheim, 1999, 1342.
39 U. Simon, G. Schön, in H. S. Nalwa (ed.) *Handbook of Nanostructured Materials and Nanotechnology*, Vol. 3, Academic Press, San Diego, 2000, 131.
40 F. Remacle, R. D. Levine, *Chem. Phys. Chem.* 2 (2001) 20.
41 C. B. Murray, C. R. Kayan, M. G. Bawendi, *Science* 270 (1995) 1335.
42 H. S. Sun, C. B. Murray, D. Weller, C. Folks, A. Moser, *Science* 287 (2000) 1989.
43 C. P. Collier, R. J. Sayhally, J. J. Shiang, S. E. Henricks, J. R. Heath, *Science* 277 (1) (1997) 1978.
44 A. P. Alivisatos, *Science* 271 (1996) 933.
45 C. B. Murray, D. J. Norris, M. G. Bawendi, *J. Amer. Chem. Soc.* 115 (1993) 8706.
46 R. L. Whetten, J. T. Khonry, M. M. Alvarez, S. Murthym I. Vezmar, Z. L. Wang, P. W. Stephens, C. L. Cleveland, W. D. Luetke, U. Landman, *Adv. Mater.* 8 (1996) 428.
47 A. Talets, V. Russier, A. Courty, M. P. Pileni, *Phys. Rev. B.* 59 (1999) 13350.
48 C. J. Kieley, J. Fink, M. Brust, D. Bethell, D. J. Shiffrin, *Nature* 396 (1998) 444.
49 C. J. Kieley, J. Fink, J. G. Zheng, M. Brust, D. Bethell, D. J. Shiffrin, *Adv. Mater.* 12 (2000) 640.
50 S. Semrau, H. Schoeller, W. Wenzel, *Phys. Rev. B* 72 (2005) 205443.
51 C. M. Niemeyer, U. Simon, *Eur. J. Inorg. Chem.* (2005) 3641.
52 D. B. Janes, V. R. Kolagunta, R. G. Osifchin, J. D. Bielefeld, R. P. Andres, J. I. Henderson, C. P. Kubiak, *Superlattices Microstruct.* 18(4) (1995) 275.
53 R. P. Andres, J. D. Bielefeld, J. I. Henderson, D. B. Janes, V. R. Kolagunta, C. P. Kubiak, W. J. Mahoney, R. G. Osifchin, *Science* 273 (1996) 1690.
54 M. P. Samanta, W. Tian, S. Datta, J. I. Henderson, C. P. Kubiak, *Phys. Rev. B* 53 (1996) R7625.
55 E. Koplin, C. M. Niemeyer, U. Simon, *J. Mater. Chem.* 16 (2006) 1338.
56 K. C. Beverly, J. F. Sampaio, J. R. Heath, *J. Phys. Chem.* B 106 (2002) 2131.
57 F. Remacle, K. C. Beverly, J. R. Heath, R. D. Levine, *J. Phys. Chem. B* 107 (2003) 13892.

58 A. Taleb, F. Silly, A. O, Gusev, F. Charra, M. P. Pileni, *Adv. Mater.* 12(9) (2000) 633.
59 N. F. Mott, *Phil. Mag.* 19 (1969) 835.
60 M. P. J. van Staveren, H. B. Brom, L. J. de Jongh, *Phys. Rep.* 208 (1991) 1.
61 L. J. Adriaanse, PhD. Thesis, University of Leiden, Netherlands (1997)
62 L. J. de Jongh, in L. J. de Jongh (ed.) *Physics and Chemistry of Metal Cluster Compounds*, Kluwer Academic Publishers, Dordrecht (1994) 1.
63 P. W. Anderson, *Phys. Rev.* 109 (1958) 1492.
64 J. Hubbard, *Proc. Roy. Soc. A* 277 (1964) 237.
65 E. Cuevas, M. Ortuño, J. Ruiz, *Phys. Rev. Lett.* 12 (1993) 1871.
66 A. L. Efros, B. I. Skklovskii, *Phys. Status Solidi B* 76 (1976) 475.
67 U. Simon, R. Flesch, H. Wiggers, G. Schön, G. Schmid, *J. Mater. Chem.* 8 (1998) 517.
68 U. Simon, *Mater. Res. Soc. Symp. Proc.* (2000) 581 77.
69 V. Torma, O. Vidoni, U. Simon, G. Schmid, *Eur. J. Inorg. Chem.* 2003 (6) (2003) 1121.
70 G. Schmid, U. Simon, *Chem. Commun.* (2005) 697.
71 R. H. Terrill, T. A. Postlethwaite, C. H. Chen, C. D. Poon, A. Terzis, A. Chen, J. E. Hutchison, M. R. Clark, G. Wignall, J. D. Londono, R. Superfine, M. Falvo, C. S. Johnson Jr., E. T. Samulski, R. W. Murray, *J. Am. Chem. Soc.* 117 (1995) 12537.
72 W. P. Wuelfing, S. J. Green, D. E. Cliffel, J. J. Pietron, R. W. Murray, *J. Am. Chem. Soc.* 122 (2000) 11465.
73 W. P. Wuelfing, R. W. Murray, *J. Phys. Chem. B* 106 (2002) 3139 and references therein.
74 A. J. Quinn, M. Biancardo, L. Floyd, M. Belloni, P. R. Ashton, J. A. Preece, C. A. Bignozzi, G. Redmond, *J. Mater. Chem.* 15 (2005) 4403.
75 J. D. Le, Y. Pinto, N. C. Seeman, K. Musier-Forsyth, T. A. Taton, R. A. Kiehl, *Nano Lett.* 4(12) (2004) 2343.
76 J. Sharma, R. Chhabra, Y. Liu, Y. Ke, H. Yan, *Angew. Chem.* 118 (2006) 744.
77 M. G. Warner, J. E. Hutchison, *Nat. Mater.* 2 (4) (2003) 272.
78 M. Noyong, K. Gloddek, J. Mayer, Th. Weirich, U. Simon, *J. Cluster Sci.* 18 (2006) 193.
79 E. Braun, Y. Eichen, U. Sivan, G. Ben-Yoseph, *Nature* (1998) 775.
80 K. Keren, M. Krueger, R. Gilad, G. Ben-Yoseph, U. Sivan, E. Braun, *Science* 297 (2002) 72.
81 G. A. Burley, J. Gierlich, M. R. Mofid, H. Nir, S. Tal, Y. Eichen, T. Carell, *J. Am. Chem. Soc.* 128(5) (2006) 1398.
82 M. Fischler, U. Simon, H. Nir, Y. Eichen, G. A. Burley, J. Gierlich, P. M. E. Gramlich, Th. Carell, *Small* 3 (2007) 1049.
83 K. Keren, R. S. Berman, E. Buchstab, U. Sivan, E. Braun, *Science* 302 (2003) 1380.
84 M. Fischler, U. Simon, in *Nano Science and Technology*, Springer-Verlag, Heidelberg, 2006, in press.
85 K. Uchida in R. Waser (ed.) Nanoelectronics and Information Technology, Wiley-VCH, 2003, 427.
86 J. R. Heath, P. Kuckes, G. Snider, S. Williams, *Science* 280 (1998) 1716.

CHAPTER 6

Nanoscale Characterization of Metal Nanoclusters by Means of X-Ray Diffraction (XRD) and Transmission Electron Microscopy (TEM) Techniques

Patrizia Canton[1], Pier Francesco Fazzini[2], Carlo Meneghini[3,4], Alvise Benedetti[1], and Giulio Pozzi[5]

[1]*Department of Physical Chemistry, University of Venice, Venezia-Mestre, Italy*
[2]*CEMES, Toulouse Cedex 4, France*
[3]*Department of Physics, University of Roma Tre, Rome, Italy*
[4]*OGG-GILDA c/o ESRF Grenoble, France*
[5]*Department of Physics, University of Bologna, and IMM-CNR, Bologna, Italy*

1. General Introduction

The study of the small dimensional systems is a very active field of research because of their peculiar properties, which are intriguing from a fundamental point of view and interesting for many applications. Such properties derive from the high surface to volume ratio, which implies the presence of a high number of surface atoms that have a coordination which is very different from those of the bulk ones. They derive also from the small dimensions which, becoming smaller than the coherence length of the electrons, modify their electronic properties and their response to external fields. Among such systems, small aggregates of atoms (nanoclusters), already widely utilized in many applications like catalysis, optics and electronic devices [1–5], are widely studied to understand deeply their peculiar physical and chemical properties [6–8] and to clarify how these properties evolve with the particle dimensions: from the atomic to the bulk properties.

Many different topics are involved in the study of metallic nanoparticles and many fundamental issues can be present: for example, which is the influence of the nanoparticle size, shape and composition on the chemical activity of heterogeneous catalysts? Or, considering another problem, at what size does a small particle behave like the bulk material, for example, changing from an insulator to a semiconductor [9–12]? An enormous amount of literature is published on metallic nanoclusters; this review is focusing on the relevant problem concerning the characterization of metallic nanosized materials from the morphological and crystallographic point of view. Such a characterization is not a straightforward task since many aspects have to be considered as the nanocluster structures depend, in general, on several parameters such as: composition, synthesis methods, thermal history and treatments, environmental variables (pressure, chemical atmosphere), supports and so on. Clusters' production often involves thermodynamic and/or kinetic aspects; metastable phases may be found (see, for example, granular alloys [13, and references therein]) and mixtures of phases representing the statistical thermodynamics of the energies of different structures may be present. As these are the correlations, in order to fully understand the physico-chemical behavior of nanosized materials and their properties, the use of complementary techniques is necessary to comprehend the many parameters involved.

In this review we focus mainly on X-ray powder diffraction (XRPD) methods, because they probe the average crystallographic structure in samples and allow, through an accurate analysis of diffraction line shape, the extraction of relevant information concerning crystallite size, structural imperfections arising from stress/strain, crystallographic defects (dislocations and staking faults) as well as compositional and chemical inhomogeneities.

The power of X-ray methods can be extended to investigate the local structure on a scale of a few angstroms by means of the analysis of the fine structure and the radial distribution function.

However, it is also important to complement this averaged information with the direct observations of the nanoparticles under study, and from this point of view

Metal Nanoclusters in Catalysis and Materials Science: The Issue of Size Control
Edited by B. Corain, G. Schmid and N. Toshima

TEM techniques represent a very good choice, in spite of the fact that only single particles or a very limited number of them inside the sample can be investigated.

Here we first present high resolution electron microscopy (HREM), which is a very established method [14–16] able to give, by simple inspection of the high magnification images, relevant information about the shape of the nanoparticle, its degree of crystallinity and the presence of defects. We will focus on a new method, electron holography (EH), which, regarded initially as a highly interesting but seemingly useless academic game, has now evolved to a stage where it can play a relevant role at the very forefront of nanoscale characterization. In fact, not only textbooks [17–19] but also many review articles have and are being published; among them, one of the most recent and complete is that in Ref. [20].

2. XRD Techniques

2.1. Introduction

The total scattering signal obtained from a sample contains parasitic contributions coming from amorphous phases, background, substrate and so on. The XRD signal of nanosized and, in general, poorly crystallized materials is weak, with broad and poorly defined diffraction peaks, so that it can become hardly distinguishable from the background made of the parasitic contributions [21,22]. The difficulty to extract quantitative information from the diffraction patterns of nanosized and poorly crystallized compounds is the reason why XRPD techniques were mostly used to support the structural and microstructural features obtained by other techniques such as chemisorption, temperature programmed reduction or electron microscopy micrographs. Important new developments of theoretical approach (Rietveld method, full profile fitting and structural simulations) and instrumental apparatus, in particular synchrotron radiation (SR) sources, renewed the interest for these techniques. In fact, the high beam quality available on last generation SR sources coupled with improved detection systems, like linear and area detectors (imaging plates (IP) and charge coupled device (CCD) cameras), opened new horizons for studying diluted compounds and doing time-resolved measurements [23]. The high resolution XRD patterns available on SR facilities permit to exploit fully the Rietveld structural refinement capabilities and advanced profile fitting methods, enhancing the possibility to extract accurate structural information from XRD patterns of nanostructured materials. Furthermore, the high counting statistics in XRD patterns, in particular when using multidetectors and large area detectors, make it possible to distinguish and analyze quantitatively also weak XRD signals of nanosized/poorly crystallized particles, even in presence of intense parasitic contributions. Finally, the availability of high energy X-ray beams on last generation SR facilities (up to and even higher than 100 keV) makes it possible to probe local structure from the analysis of full Debye scattering [75].

We will give here a survey of the main techniques of XRPD data widely employed in characterizing metal nanoclusters.

2.2. Powder Diffraction

The theory of X-ray diffraction (XRD) on single crystals was developed by Laue and Bragg in the early 1900s. Due to the finite size, a real crystal is intrinsically never perfect. As we will se below such a finite size may affect the breadth of the diffraction peaks. Dealing with real materials, and with nanoclusters in particular, single crystals are rare. From a crystallographic point of view, ''powder'' means a large amount of small crystallites randomly oriented in space. Each crystallite represents a coherently diffracting domain. In a powder sample the random crystallite distribution distributes the Bragg peak intensities along the cones (Debye cones) around the direction of the incoming X-ray beam k_0, this giving rise to the so-called Debye rings on a plane perpendicular to k_0.

The analysis of XRPD patterns is an important tool studying the crystallographic structure and composition of ''powder'' compounds including the possibility to study deviation from ideal crystallinity, i.e. defects. Looking at an X-ray powder diffractogram the peak position reflects the crystallographic symmetry (unit cell size and shape) while the peak intensity is related to the unit cell composition (atomic positions). The shape of diffraction lines is related to ''defects'', i.e. deviation from the ideal crystallinity: finite crystallite size and strain lead to broadening of the XRPD lines so that the analysis of diffraction line shape may supply information about sample microstructure and defects distribution at the atomic level.

Besides the instrumental effects (mainly experimental resolution) the main sources of line broadening are:

(i) finite size of the coherently diffracting domains (crystallites);
(ii) extended defects, such as staking faults, antiphase boundaries and dislocations, which involves faulting in the $(h\,k\,l)$ plane sequences;
(iii) not-uniform strains within the crystallites due to point defects, plastic deformations, poor crystallinity and so on.

Other defects should be considered, such as uniform strain, which causes isotropic contraction/expansion of the cell giving rise to diffraction line shifts (but not broadening), chemical and/or phase segregation and so on.

2.2.1. Peak Profile Analysis

We will give here a short overview of the most common XRPD techniques used to study the microstructure of materials, starting from the most used and simple Scherrer method to the quite complex Warren–Averbach method, which is able to extract all the information available on sample microstructure and defects.

The position of diffraction line, as well as the location of its maximum $I(2\theta_0)$, is the most commonly used parameter to quantify the lattice parameters and interplane distances. The full width of intensity distribution at half maximum Γ (FWHM) is the simplest measure of the peak breadth. An alternative method estimates the peak width

by its integral breadth β:

$$\beta = \frac{\int I(2\theta')d(2\theta')}{I(2\theta_0)} \tag{1}$$

where $\theta' = \theta - \theta_0$ and $I(2\theta - 2\theta_0)$ is the intensity of the diffracted peak centered at the $2\theta_0$, while $I(2\theta_0)$ is the maximum peak intensity. The integral breadth represents the width of a rectangle having the same height and area of the considered diffraction peak. For some purposes it is used a "shape" factor ϕ defined as:

$$\phi = \frac{\Gamma}{\beta} \tag{2}$$

The observed profile $P(2\theta)$ of a Bragg peak at $\theta_0 = \theta_{hkl}$ is a convolution product between the instrumental profile $r(2\theta)$ and the physical profile $p(2\theta)$:

$$P(2\theta) = \int p(2\theta')r(2\theta' - 2\theta_0)d2\theta' + B(2\theta) \tag{3}$$

in which $B(2\theta)$ is the background contribution. The physical profile $p(2\theta)$ is given in turn by the convolution of size and strain broadening effects [24].

It is often convenient modeling the peak shape assuming some analytical functions [25]. The most commonly used functions are, at present, the Voigt and pseudo-Voigt functions, a combination of a Gaussian (G) and a Lorentzian (L) function centered at $2\theta_0$. An expression for Gaussian and Lorentzian contributions is:

$$\begin{aligned} G &= \frac{\sqrt{\ln 2}}{H\sqrt{\pi}}\exp\left[\frac{-\ln(2)(s-s_0)^2}{H^2}\right], \\ L &= \frac{4}{\pi H}\left[\frac{1+4(s-s_0)^2}{H^2}\right]^{-1} \\ \text{pseudo} - \text{Voigt} &= \eta L + (1-\eta)G \\ \text{Voigt} &= L \otimes G \end{aligned} \tag{4}$$

where $s = 2\sin(\theta)/\lambda$

The Voigt function is a convolution product ($\otimes$) between L and G. As the convolution is expensive from a computational point of view, the pseudo-Voigt form is more often used. The pseudo-Voigt is characterized by a "mixing" parameter η, representing the fraction of Lorentzian contribution, i.e. $\eta = 1(0)$ means pure Lorentzian (Gaussian) profile shape. Gaussian and Lorentzian breadths can be treated as independent parameters in some expressions.

The representation of the diffraction line shape by Fourier series allows, in principle, deconvoluting the contributions giving rise to a given line shape. This approach relies on the possibility to clearly recognize the entire peak shape, so this approach can be very accurate in dealing with high symmetry systems and well-defined diffraction lines but it becomes progressively weaker for less defined peak profiles in which the peak tails become confused with the background.

The "peak profile analysis" techniques allow separating the intrinsic and extrinsic causes producing peak broadening and shift. Accurate peak profile analysis requires the instrumental broadening well characterized and, in general, significantly smaller than the one due to sample defects (size and strain). New high quality X-ray sources and

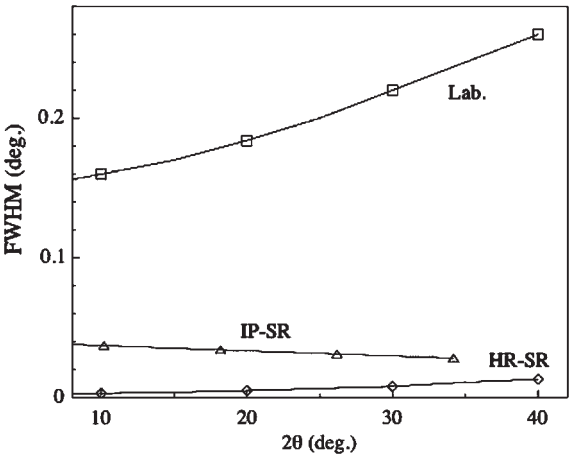

Figure 1. Experimental broadening (FWHM) as a function of angle for three different experimental set-ups measured on profile reference standard (LaB_6 NIST). Lab.: laboratory diffractometer (Phylips X'pert). HR-SR: ID31 beamline at the European Synchrotron Radiation Facility (ESRF), one of the highest resolution beamline actually operative. IP-SR: BM08-GILDA beamline at the ESRF, using an area detector (imaging plate). Decreasing of the experimental broadening with increasing diffraction angle is characteristics of flat plate area detector geometry. (Thanks to Dr. M. Merlini for providing experimental data.)

instrumentation are giving a great impulse to this kind of analysis. As the larger crystallite size that can be probed is primarily limited by instrumental resolution (see Figure 1) we have that on conventional diffractometers (laboratory XRD generators) the largest cluster size is limited ~45–50 nm. On high resolution SR diffractometers crystallite sizes up to several hundred nanometers (200–500 nm) can be probed. The possibility to probe small crystallites, more interesting for our purposes, is limited principally by statistics (Figure 2): small crystallites give rise to broad weak peaks, which require high statistics to be distinguished from the background (see Figure 3). High flux SR beamlines allow studying nanometer-sized particles; area detectors, allowing the highest counting statistics, permit to study 1–2 nm-sized materials. Dealing with sub-nanometer-sized materials total diffuse scattering (Debye scattering) and local probes, like X-ray absorption fine structure (XAFS), are more suitable.

Accurate theories were developed for peak shape analysis and are widely described in the literature [26–29].

In the next section we will give a summary of the most important results and formulae for peak shape analysis.

2.2.1.1. The Crystallite Size and the Scherrer Formula. The Scherrer formula is based on a restricted assumption assuming that the peak shape is dominated by size effects. The problem of Bragg line broadening, originating from particle size, was first investigated by Scherrer [30] who derived the well-known and widely used law:

$$\langle L \rangle = \frac{k\lambda}{\Gamma \cos\theta_0} \tag{5}$$

which relates the diffraction width Γ and the average size of the crystallites (i.e. coherently diffracting domains) $\langle L \rangle$.

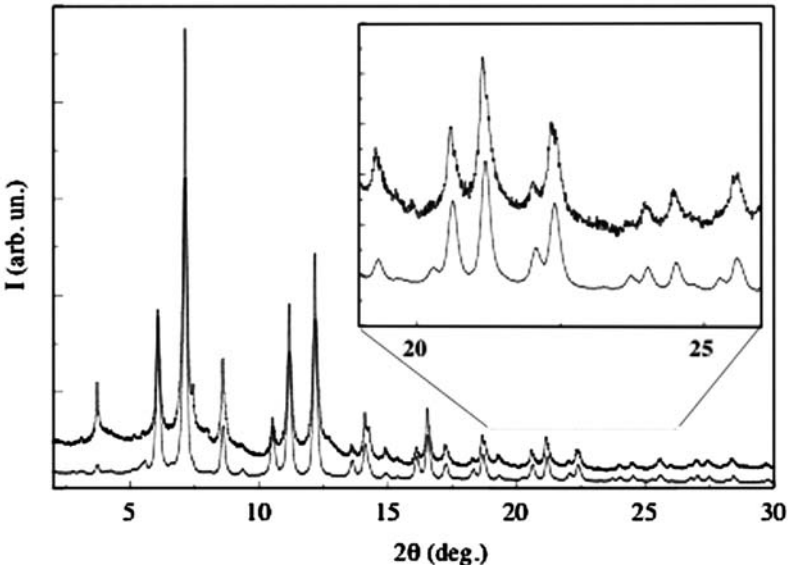

Figure 2. Dealing with nanosized materials' instrumental resolution can be less relevant than flux. The highest statistics is generally obtained, even on SR facilities, using area detectors: the diffractogram collected on nanosized Co–Al_2O_3 particles on BM08-GILDA (ESRF) using an area detector in 10 min (lower curves) is compared with the one collected in several hours on ID31 beamline (ESRF) using the high resolution set-up (upper curves). Experimental peak profile is almost insensitive on the different instrumental resolution, but the statistics reachable using area detector is definitively better. (Thanks to Dr. M. Merlini for providing experimental data.)

θ_0 is Bragg angle, λ the X-ray wavelength and k a constant close to unity which depends on the shape of the crystallites: for example, $k = 0.94$ for cubic shape crystallites [36]. The Scherrer formula is generally used for qualitative and semi-quantitative purposes or to describe relative changes in crystallite sizes as a function of sample, treatment and other effects, so the approximate value $k = 0.94$ is generally assumed as Scherrer constant.

In the simplest approach Γ is the full width of the peak (measured in radians) subtended by the half maximum intensity (FWHM) corrected for the instrumental broadening. The correction for instrumental broadening is very important and can be omitted only if the instrumental broadening is much less than the FWHM of the studied diffraction profile, which is always the case in presence of small nanoclusters. The integral breadth can be used in order to evaluate the crystallite size. In the case of Gaussian peak shape, it is:

$$\Gamma = \beta\sqrt{\frac{4\ \ln 2}{\pi}} \approx 0.94\beta \tag{6}$$

As a consequence, the Scherrer formula can be written as:

$$\langle L\rangle = \frac{\lambda}{\beta\ \cos\theta_0} = \frac{1}{\Delta s} \tag{7}$$

with λ the wavelength and $s = 2\sin(\theta)/\lambda$ so that Δs is the integral breadth in s abscissa.

In the case of Lorentzial shape $\Gamma = (2/\pi)\beta \sim 0.64\beta$ while the relation in the case of Voigt and pseudo-Voigt functions can be found in Ref. [45].

It is important to note that this formula gives only an average value of the crystallite size; if, for example, we have a polydispersed ensemble of spherical particles with density probability of the diameter sizes $N(D)$, the average size $\langle L\rangle$ obtained by the Scherrer formula is related to the diameter by:

$$\langle L\rangle = \frac{3\int_0^\infty D^4 N(D)dD}{4\int_0^\infty D^3 N(D)dD} \equiv \frac{3\langle D^4\rangle}{4\langle D^3\rangle} \tag{8}$$

This peculiar kind of average is known as "volume weighted" average.

In order to properly take into account the instrumental broadening, the function describing the peak shape must be considered. In the case of Lorentzian shape it is $\beta_{\text{size}} = \beta_{\text{exp}} - \beta_{\text{instr}}$ while for Gaussian shape $\beta^2_{\text{size}} = \beta^2_{\text{exp}} - \beta^2_{\text{instr}}$. In the case of pseudo-Voigt function, Gaussian and Lorentzian contributions must be treated separately [39].

In nanosized materials instrumental effects are generally negligible, especially when working on SR instruments; however, the background may be high and partially masking the true line shape; for this reason it must be treated with care.

2.2.1.2. The Strain Broadening. A further step with respect to the Scherrer approximation is to consider not only the broadening of the diffraction peaks due to crystallite size, but also the broadening coming from not-uniform strains. In this case the application of the simple Scherrer formula can underestimate the crystallite size. The strain contributions to the diffraction line broadening were first observed by Stokes and Wilson [31]; they observed that the average not-uniform strain is related to the peak broadening by:

$$\varepsilon_{\text{str}} = \frac{\beta_{\text{str}}}{4\ \tan\theta} \tag{9}$$

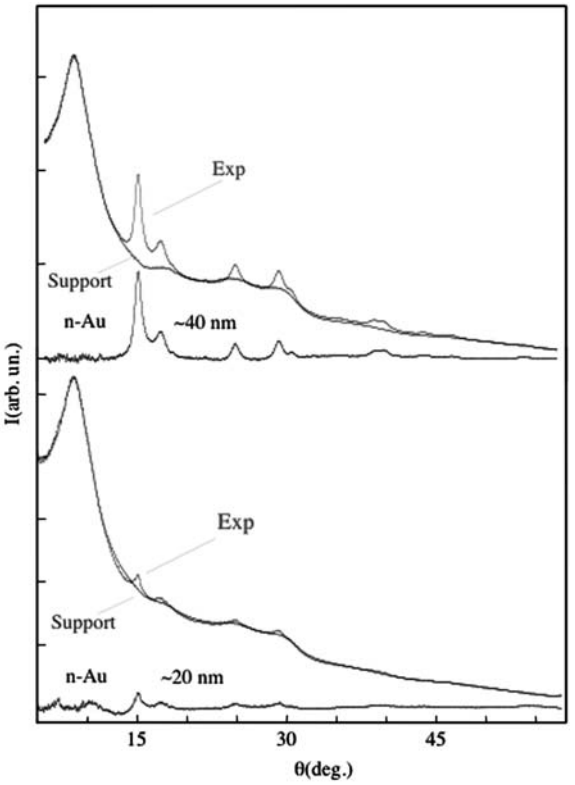

Figure 3. Example of XRPD on small Au clusters supported on silica. Total diffraction intensity has been measured with area detector (IP) on BM08-GILDA beamline at the ESRF with $\lambda = 0.6211$ Å and ~2 min exposure time. Diffraction patterns were collected on Au-supported sample (Exp) and on silica support (Support). Difference patterns, corrected for fluorescence, IP efficiency, etc., are shown (n-Au).

where β_{str} is the integral peak breadth due to the strain and $\varepsilon_{str} = \Delta L/L$ (with L the undistorted distance and ΔL the component of the strain in the direction perpendicular to the reflecting planes) the weighted averaged strain. It is important to note that the size and the strain affect the peak breadth with different θ dependences. Such a difference allows, at least in principle, to distinguish between the two effects. The Williamson–Hall [32] plot represents a simplified method to extract size and strain contributions to the line shape. In case of combined size and strain broadenings it can be written:

$$\beta_{sam}(\theta)\cos(\theta) = \lambda L_{size} + 4\varepsilon_{str}\sin(\theta) \tag{10}$$

where $\beta_{sam}(\theta)$ is the integral breadth for different diffraction peaks and L_{size} the average crystallite size. The effect of the instrumental broadening can be treated as described above.

From Equation (10) it is possible, at least in principle, to distinguish between size and strain effects plotting $\beta_{exp}\cos(\theta)$ vs. $4\sin(\theta)$. The linear regression fit allows to extract the average size from intercept at $\sin\theta = 0$ and the average strain from regression line slope [33,34,42].

This method is based on the possibility to clearly distinguish several diffraction peaks. Then its applicability is limited when dealing with low symmetry systems (several partially superimposed diffraction lines) and nanosized materials (broad weak diffraction peaks).

2.2.1.3. The Fourier Analysis of the Peak Shape (Warren–Averbach Method). The most accurate way of extracting and distinguishing between size and strain effects is to analyze the complete shape of several peaks in the diffraction pattern. The method known as the "Warren–Averbach analysis" allows a precise study of the relation between the peak shape and the sample microstructure [35,36]. This method is based on the Fourier analysis of the whole diffraction line shape of several reflections in the pattern instead of using FWHM (Γ) or integral breadth (β). The Fourier analysis approach is a systematic way to obtain information concerning the distribution of the column height and strain perpendicular to the analyzed direction. This kind of analysis not only uses the whole information contained in the diffraction peak but it also allows a rigorous correction of the instrumental broadening. The power of this method is that it does not need to assume any particular analytical form for the peak shape or for the instrumental breadth.

The method is based on the following steps:

- Several peaks of interest (ideally higher order reflections of the same type: $h\,k\,l$, $2h$, $2k$, $2l$, $3h$, $3k$, $3l$, …, nh, nk, nl) are fitted by Fourier series; the same procedure is applied to the diffraction lines of a reference sample, in which size and strain effects are negligible, in order to determine the instrumental line broadening. Such information is used in order to deconvolute instrumental broadening from sample effects (Stokes–Fourier deconvolution [36]).
- Information concerning size distribution and strain profile can be obtained from the cosine Fourier coefficients, which describe the symmetric peak broadening.

This analysis is based on the fact that any periodic function can be approximated, at any order, by a Fourier series:

$$I(s) = \sum_{-\infty}^{+\infty} A_n \cos[2\pi n d_{hkl}(s - s_0)] + \sum_{-\infty}^{+\infty} B_n \sin[2\pi n d_{hkl}(s - s_0)] \tag{11}$$

where $s = 2\sin(\theta)/\lambda$, while d_{hkl} is the interplanar spacing of the considered reflection and nd_{hkl} the distance normal to the reflecting planes. If l is the distance in the crystal normal to the reflecting planes ($h\,k\,l$), $l = nd_{hkl}$ [26], so the discrete sum in Equation (11) can be rewritten as an integral:

$$I(s) = \int [A(l)\cos[2\pi l(s - s_0)] + B(l)\sin[2\pi l(s - s_0)]]dl \tag{11a}$$

where, as it is possible to show [36], the coefficients of the cosines, $A(l)$, account for the symmetric contributions to

the diffraction peak shape (width), while sine coefficients $B(l)$ describe the asymmetric contributions.

It is a known property of Fourier transforms that given a convolution product in the reciprocal space, it becomes a simple product of the Fourier transforms of each term in the real space. Then, as the peak broadening is due to the convolution of size and strains (and instrumental) effects, the Fourier transform $A(l)$ of the peak profile $I(s)$ is [36]:

$$\begin{aligned} A(l) &= \mathrm{FT}[I(s)] \\ A(l) &= A_{\mathrm{size}}(l)A_{\mathrm{strain}}(l,n) \end{aligned} \tag{12}$$

with $A_{\mathrm{size}}(l)$ and $A_{\mathrm{strain}}(l, n)$ the Fourier transforms of size and strain contributions. In the case of not negligible instrumental broadening an additional product must be considered taking the FT of the instrumental broadening from measurements on reference compounds.

It is possible to show that $A_{\mathrm{strain}}(l,n) = \langle \exp(\mathrm{i}2\pi s l \varepsilon_{\mathrm{str}}) \rangle \sim \exp(-2\pi^2 s^2 l^2 \langle \varepsilon_{\mathrm{str}}^2 \rangle)$ (this is exact in case of Gaussian distribution of strain [36]), then:

$$\ln A(l) = \ln A_{\mathrm{size}}(l) - 2\pi^2 \langle \varepsilon^2(l) \rangle \frac{l^2}{d_{hkl}^2} \tag{13}$$

Measuring higher order (n) reflections it will be: $1/d_{hkl}^2 = n^2/d_{nh,nk,nl}^2$, then:

$$\ln A(l) = \ln A_{\mathrm{size}}(l) - 2\pi^2 l^2 \langle \varepsilon^2(l) \rangle \frac{n^2}{d_{nh,nk,nl}^2} \tag{14}$$

In order to separate the two contributions, without introducing any other hypotheses on the shape of the function $A_{\mathrm{size}}(l)$ and $A_{\mathrm{strain}}(l, n)$, we only have to measure several peaks belonging to the same family (i.e. 0 0 1, 0 0 2, 0 0 4, …), and then it will be possible to separate the broadening due to the size from the broadening due to the distortion (strain), since the former is the same for all the peaks belonging to the same family, while the latter depends on the order n of the peak. The particle size coefficients are retrieved by plotting $\ln(A(l))$ vs. $(1/d_{hkl})^2$ and extrapolating to $1/d_{hkl} = 0$. This approach is known as the "Warren–Averbach analysis". Mathematical aspects of the approximations introduced to obtain formula (14) can be found in the paper of Delhez and Mittemeijer [37].

It is clear that the Warren–Averbach method of separation of size and strain broadenings (and possibly the instrumental contribution) is the less constrained method for the analysis of diffraction line shape. The main advantage between the Fourier transform method and the simpler approaches based on the integral peak breadth is that Fourier method may give the distribution of crystallite sizes instead of the average value. The main disadvantage is that the Fourier method is more prone to errors if peak tails are not accurately modeled; this is the reason why the Fourier methods are difficult to apply in presence of peak overlapping and/or in case of small peak to background ratio.

When $A_{\mathrm{size}}(l)$ is known, we can obtain $\langle L \rangle_{\mathrm{F}}$, the average size of the column of cell perpendicular to the selected family of planes, since for the small value of l it holds that:

$$A_{\mathrm{size}}(l) \approx 1 - \frac{|l|}{\langle L \rangle_{\mathrm{F}}} \tag{15}$$

As already noted in the case of the Scherrer equation, if we have a polydispersed ensemble of spheres the dimensions obtained by Fourier analysis correspond to:

$$\langle L \rangle_{\mathrm{F}} = \frac{2\int_0^\infty D^3 N(D) dD}{3\int_0^\infty D^2 N(D) dD} \equiv \frac{2\langle D^3 \rangle}{3\langle D^2 \rangle} \tag{16}$$

that is a "surface weighted" mean value.

It is worth to note that this dimension is directly comparable with the specific surface area obtained from chemisorption measurements [38].

Theoretically, it is also possible to obtain the volume weighted distribution function $g(l)$ of the column length l:

$$g(l) \propto \frac{d^2(A_{\mathrm{size}}(l))}{dl^2} \tag{17}$$

From the slopes of the straight lines, the strain distribution $\langle \varepsilon^2(l) \rangle$ is obtained. Furthermore, knowing the shape of the particles, it is possible to have the distribution of the particle sizes [39,40].

If, for example, we know that the particle shape is spherical, the size distribution of the particle diameters $G(l)$ is:

$$G(l) \propto \frac{d}{dl}\frac{g(l)}{l} \propto \frac{d}{dl}\left[\frac{1}{l}\frac{d^2(A_{\mathrm{size}}(l))}{dl^2}\right] \tag{18}$$

The last two formulae, especially the second one, are rarely used because the obtained distributions $g(l)$ and $G(l)$ are very often meaningless [41].

There is another difficulty related to the application of these analytical techniques, especially dealing with very small particles: it is often impossible to find a couple of peaks belonging to the same family, so it is impossible to separate the size and strain broadenings. In these cases, the broadening is usually assumed to be only due to the size effect, but it is important to remember that we are probably underestimating the crystallite dimensions.

In this short summary of peak profile analysis, we only considered the broadening due to the dimension and the strain, and we have considered only the Fourier-cosines transform (i.e. the symmetric part of the peak) that is the most frequent case.

Other kinds of defects could give rise to peak broadening, for example: the staking faults. In this case, the equation taking into account this phenomenon depends on the peculiar structure of the crystals and the analysis can be more complex: some defects, in fact, introduce profile asymmetry and a shift in the position of some selected peaks [26].

So far no hypotheses are required concerning the true shape of the peak profile. However, in order to avoid or reduce the difficulties related to the overlapping of the peaks, the experimental noise, the resolution of the data and the separation peak-background, the approach most frequently used fits by means of a least squared method the diffraction peaks using some suitable functions that allow the analytical Fourier transform, as, for example, Voigt or pseudo-Voigt functions (4) which are the more often used.

This approach also allows an easy correction of the diffraction peaks from the instrumental broadening that can be obtained by fitting the peak profile of a standard

material (with well-formed and large crystallites). The corrected Fourier transform can be obtained simply by dividing the observed peak by the Fourier transform of the instrumental function.

Another typical problem met in this kind of analysis is known as the "hook effect". It is due to an overestimation of the background line to the detriment of the peak tails. As a consequence, the low order Fourier coefficients of the profile are underestimated. In the fitting procedure by pseudo-Voigt functions, this problem occurs if the Gauss content is so high that the second derivative of the Fourier coefficients is negative; this is obviously physically impossible because it represents a probability density.

An alternative approach, giving better results if the peak width is very close to the instrumental one, is to take into account the instrumental contribution (by a convolution of the refined peak due to the sample and the instrumental profile) during the profile fitting procedure [42].

This analysis gives satisfactory results concerning the average crystallite sizes even in unfavorable experimental conditions such as overlapped or very weak and noisy peaks, and it allows an easy treatment of non-perfect monochromaticity of the radiation. But, it is important to emphasize that it is almost impossible to obtain the "promised" detailed description of the crystallite size and strain distributions. This is a fundamental problem related to the adopted procedure that is based on the "a priori" choice of the peak shape that inevitably imposes the general shape of such distributions [40]. For these reasons, the average dimension and strains remain the only reliable information.

As a consequence of this short discussion, we can conclude that the shapes of the distribution obtained by the Warren–Averbach analysis may be less reliable as the results can be strongly influenced by the method chosen for data reduction and treatment. On the contrary, the average crystallite dimension is very stable and it is almost independent of the adopted analytical method.

An interesting discussion about reliability of size/strain analysis methods can be found in Ref. [29] where the results on peak shape analysis of a round-robin sample are reported and commented.

2.2.2. The Rietveld Method

2.2.2.1. Introduction. The Rietveld profile fitting approach belongs to the total profile fitting (TPF) methods for the analysis of XRD patterns. Instead of analyzing single or few selected diffraction lines, TPF methods refine (generally with standard least squared fitting procedures) the whole diffraction patterns using some analytical profile function and an appropriate background. Peak overlapping, as in the case of low symmetry and/or poor crystallinity and/or complex unit cells, limits the reliability of these methods. The Rietveld method [43–45], originally designed to analyze neutron diffraction data, overcomes this problem adding structural information and physical constraints (unit cell symmetries, atomic positions and so on). This approach had a huge success in quantitative analysis of diffraction patterns (neutron and X-ray), single-phase as well as multiphase samples, despite their high or low symmetry. In the last 10 years, the use of the "Rietveld" method provided an important improvement to the analysis of powder diffraction data and is widely employed in many different research fields. For example, it is successfully employed in studies of complex systems such as zeolites, usually having large and low symmetry unit cells, as well as in Earth science to study natural materials characterized by complex mixture of many different phases. This approach allows to obtain a great deal of information from the study of the whole powder diffraction pattern; the use of physical constraints allows dealing with low symmetry systems in which not-overlapping diffraction peaks are hardly present.

The Rietveld analysis is mainly used for refining the structures of crystalline phases and to perform quantitative analysis of multiphase samples. The quantitative analysis is possible since the Rietveld method can easily deal with diffraction patterns with strongly overlapped peaks, while preferred orientation can be quantitatively treated.

In this section, we will describe the principal features of the main methods and the information that the Rietveld analysis generally delivers, especially related to the investigations on poor crystallites and multiphase compounds. This introduction is not exhaustive: there are hundreds of articles that explore practically all of the aspects of this kind of analysis and now, 40 years after the first article [43], new improvements and results are still being published.

2.2.2.2. The Rietveld Fit of the Global Diffraction Pattern. The philosophy of the Rietveld method is to obtain the information relative to the crystalline phases by fitting the whole diffraction powder pattern with constraints imposed by crystallographic symmetry and cell composition. Differently from the non-structural least squared fitting methods, the Rietveld analysis uses the structural information and constraints to evaluate the diffraction pattern of the different phases constituting the diffraction experimental data.

The Bragg peaks belonging to the crystalline phases and a background (modeled via empirical functions) give rise to the experimental pattern. The background is mainly composed by parasitic scattering (e.g. air scattering), fluorescence, Compton scattering, thermal diffuse scattering (TDS) and, if present, the scattering from amorphous materials and/or nanoparticles having subnanometric dimensions. For this reason the quantitative analysis of the background is generally very hard, and then it is generally described by some empirical functions (usually high-order polynomials or series).

The diffraction lines due to the crystalline phases in the samples are modeled using the unit cell symmetry and size, in order to determine the Bragg peak positions θ_0^i. Peak intensities (peak areas) are calculated according to the structure factors $|F_0|^2$ (which depend on the unit cell composition, the atomic positions and the thermal factors). Peak shapes are described by some profile functions $\Phi(2\theta - 2\theta_0)$ (usually pseudo-Voigt and Pearson VII). Effects due to instrumental aberrations, uniform strain and preferred orientations and anisotropic broadening can be taken into account.

The preferred orientation is due to the lack of randomness in the orientation of the crystallites constituting

the sample; this effect causes the enhancing of some reflections with respect to the others because these are more favorably oriented with respect to the analyzing beam. The ability of the Rietveld method to manage this last effect has been an important improvement in quantitative phase analysis based on diffraction data.

Taking into account all these effects, the intensity due to a crystalline phase is given by:

$$Y_{\mathrm{cr}}(2\theta) = KAP\left\{\sum_{k=1}^{n_{\mathrm{B}}} J_k L_k O_k |F_k|^2 \Phi(2\theta - 2\theta_k)\right\} \quad (19)$$

The used symbols are: K, scale factor; n_{B}, number of Bragg peaks; A, correction factor for absorption; P, polarization factor; J_k, multiplicity factor; L_k, Lorentz factor; O_k, preferred orientation correction; $|F_k|^2$ squared structure factor for the kth reflection, including the Debye–Waller factor; Φ, normalized profile function describing the profile of the kth reflection.

The formulae reported here refer to measurements done at constant wavelength (angle dispersive) that are the most frequently used, but a similar formula exists if energy dispersive methods are used, even if the analysis of energy dispersive data is generally less accurate and reliable for quantitative purposes due to the energy dependence of several intrinsic (i.e. atomic scattering factors and absorption corrections) and experimental parameters (i.e. energy resolution and detector efficiency).

The calculated global pattern will be obtained by summing the intensities due to the different crystalline phases and background:

$$I_{\mathrm{cal}}(s) = I_{\mathrm{BKG}}(s) + \sum I^k_{\mathrm{cr}}(s) \quad (20)$$

where $s = 2\sin(\theta)/\lambda$

This function depends on many parameters that will be refined using the least squared method.

The main parameters can be divided into four groups:

1. Structural parameters:
   - the lattice parameters of the phases that influence the peak positions;
   - the atomic coordinates and their thermal parameters (taking into account the thermal motion).
2. Peak shape parameters:
   - the normalized peak function $\Phi(2\theta-2\theta_0)$ usually depends on two or more parameters. The most important is the FWHM (the peak width). There are some additional parameters that control the "shape" of the peak. As discussed in Section 2.2.1.3, the shape of the diffraction peak is related to the microstructure: mainly crystallite dimension and strain. Some versions of the Rietveld code allow the simultaneous refinement of the microstructure (i.e. crystallites' dimension and strain) as obtained by the peak shape study [46,47].
3. Scale parameters K (related to the relative amount of the phase).
4. Instrumental and sample parameters: error in the wavelength, sample transparency, etc.

Even if the main intent of the Rietveld analysis is the structure refinement in material science, sometimes the information relative to the structure is not the heart of the matter.

The study of the peak shape gives important information relative to the microstructure of the sample even when it is included in the Rietveld code. Actually, in order to perform the Warren–Averbach analysis or other microstructural studies, it is not necessary to use the Rietveld analysis, but it is often sufficient to operate with less complex, non-structural peak fitting procedures.

There is, in any case, an important advantage in using the Rietveld analysis, which is the possibility of quantifying the phase to which we are ascribing the microstructure properties.

2.2.2.3. Quantitative Phase Analysis by Rietveld Refinement. The quantitative analysis can be performed through the Rietveld method because the number of the elemental cells of each phase is: $N \propto KV_{\mathrm{c}}$, where K and V_{c} are the refined scale factor and the cell volumes, respectively. So, the weight fraction of the lth phase is given by:

$$W_l = \frac{N_l \sum_{i=1}^{n_l} w_l^i}{\sum_{j=1}^{N} N_j \sum_{i=1}^{n_l} w_j^i} = \frac{K_l V_{\mathrm{cl}} M_l Z_l}{\sum_{j=1}^{N} K_l V_{\mathrm{cl}} M_j Z_j} \quad (21)$$

where n_l is the number of atoms, w_l^i the atomic weight of the ith atom of the lth phase, M_l the mass of the unit formula and Z_l the number of the unit formula in the cell [48].

This formula works only if all the phases in the sample are crystalline and are refined in the Rietveld procedure so that the relative scale, cell volume and cell composition are known.

If an amorphous phase is present in the sample, it is still possible to perform the quantitative analysis by introducing a small amount of crystalline powder with the known weight fraction W_{N+1} that will be the $N+1$ phase in the sample, so the equation becomes:

$$W_{N+1} = \frac{N_{N+1} \sum_{i=1}^{n_l} w_l^i}{W_1 + \sum_{l=2}^{N-1} N_l \sum_{i=1}^{n_l} w_l^i} \quad (22)$$

where W_1 is the weight of the unknown phase that can now be obtained by inverting the above equation.

This approach, called "internal standard method", works even if the composition of the amorphous phase is unknown.

For the quantitative analysis based on the XRD, the most serious problems are related to the microabsorption phenomenon [49,50]. The origin of this effect is due to the different X-ray absorptions from particles belonging to different phases. It depends on the average particle dimensions (not on crystallite sizes) constituting each phase, and on their linear absorption coefficients. It is particularly important when the sample is constituted by phases with very different linear absorption coefficients and coarse powders. This effect becomes progressively weak using higher energy X-ray beam, as on SR beamlines.

The use of Equation (22) is very general, but it is also possible, with accurate measurements and data treatment, to perform the quantitative phase analysis in semi-crystalline materials without using any internal standard. This procedure is possible only if the chemical compositions of all the phases, including the amorphous one, are known. If the composition of the amorphous phase is unknown, the quantitative analysis without using any internal standard can still be used provided that the chemical composition of the whole sample is available [51]. This approach, until now, has been developed only for the XRD with Bragg–Brentano geometry that is one of the most diffused techniques in powder diffraction laboratories.

The theoretical basis on which this kind of analysis is based is a Fourier transform property of the global integrated intensity on the reciprocal space.

Such integral depends only on the kind and on the amount of atoms present in every phase, and it is independent of their atomic spatial order, allowing it to be applied to both crystalline and amorphous materials [52].

The main hypothesis on which this result is based is the "atomicity", meaning the electronic densities of the different atoms are not overlapped.

So for a phase containing $\boldsymbol{N} = Nn$ atoms:

$$\begin{aligned}\int_0^\infty I^{\text{corr}}(s)4\pi s^2\,ds &\propto \sum_{i=1}^{\boldsymbol{N}} \int_0^\infty [|f_i^0|^2 + I_i^{\text{inc}}]4\pi s^2\,ds \\ &= N\sum_{i=1}^{n} \int_0^\infty [|f_i^0|^2 + I_i^{\text{inc}}]4\pi s^2\,ds\end{aligned} \tag{23}$$

where we have supposed that the $\boldsymbol{N}$ atoms can be organized in N composition units, for instance, the molecular unit; each of these units is composed of n atoms.

The symbols used here are: I^{corr}, diffracted intensity corrected for absorption, polarization and air scattering; f_i^0, tabulated atomic scattering factor of the ith atom; I_i^{inc}, incoherent scattering of the ith atom corrected by the Breit–Dirac factor, by air and sample absorption, and for the band pass function of the monochromator if present on the diffracted beam [53,54].

It is important to note that expression (23) can be applied to the crystalline phase intensities only if we include, in the first integral, its own smooth diffuse background and not just the intensity belonging to the crystalline peaks. In fact, a pure crystalline sample also has a smooth background due to the incoherent inelastic scattering (i.e. Compton scattering), the TDS, disorder scattering and, very often, unresolved tails of overlapped peaks.

An expression including the diffuse background of a crystalline phase was calculated for a Bragg–Brentano geometry [55]:

$$I_{\text{cr}}(2\theta) = KAP\left\{\sum_{k=1}^{n_{\text{B}}} J_k L_k |F_k|^2 \Phi(2\theta - 2\theta_k) + Y^{bk}\right\} \tag{24}$$

where

$$Y_{bk} = \frac{16\pi^2 V_{\text{c}}}{180\lambda^3}\sum_j^{\text{cell}}\left[I_j^{\text{inc}} + \left[1 - \exp\left(\frac{2B_j \sin^2(\theta)}{\lambda^2}\right)\right]\left|f_j^0\right|^2\right] \tag{25}$$

The symbols used are: V_{c}, unit cell volume; B_j, isotropic thermal factor of the jth atom.

Expression (25) describes the smooth background belonging to a crystalline phase due to the incoherent (or Compton) scattering and the TDS or disorder scattering. The last contribution in (25) is very approximate because it is known that the TDS has a very complicated shape with very large peaks centered in the same position as the Bragg ones [56].

The global intensity, corrected for the air scattering, can be divided into its components:

$$I_{\text{exp}}(s) - I_{\text{air}}(s) = I_{\text{am}}(s) + \sum I_{\text{cr}}^k(s) \tag{25a}$$

where $s = 2\sin(\theta)/\lambda$, I_{am} is the amorphous contribution (if present) and I_{cr}^k the kth crystalline phase. The scattering of the amorphous phase can be obtained experimentally from a fully amorphous sample or, if this is not available, it can be described by some analytical functions that can be refined by the fitting procedure (the latter choice can result in a difficult refinement because of the correlation among the background parameters) [51].

It is important to note that this second choice is possible because expression (25) includes the smooth background belonging to the crystalline phases, so it can be separated from the background due to the amorphous phase. A typical example, where the amorphous phase is not available, is the study of crystallization process. In this case, the composition and the diffraction pattern of the amorphous phase can change a lot.

So, when in a multiphase sample, it is possible to separate the contribution to the diffraction pattern of each phase ($Y_l(s)$). Relation (26) permits the evaluation of the relative weight fractions W_l if the chemical compositions of the phases and of the global sample are known:

$$\begin{aligned}CN_l &= \frac{\int_0^\infty (Y_l/AP)(s)s^2\,ds}{\sum_{i=1}^{n_l}\int_0^\infty [|f_i^0|^2 + I_i^{\text{inc}}]s^2\,ds}, \\ CN_{\text{global}} &= \frac{\int_0^\infty ((Y_{\text{exp}} - Y_{\text{air}})/AP)(s)s^2\,ds}{\sum_{i=1}^{n_{\text{global}}}\int_0^\infty [|f_i^0|^2 + I_i^{\text{inc}}]s^2\,ds}\end{aligned} \tag{26}$$

$$W_l = \frac{N_l \sum_{i=1}^{n_l} w_l^i}{N_{\text{global}} \sum_{i=1}^{n_{\text{global}}} w_{\text{global}}^i} \tag{27}$$

Here n_l and n_{global} are the number of atoms of the composition unit and w_l^i and w_{global}^i the atomic weights of the ith atom of the lth phase or of the overall sample. A and P are the absorption and polarization factors for which the measured intensities must be corrected.

These formulae are useful if the composition of the overall sample is known, but they also work if the composition of every single phase is known. In this last case, Equation (27) becomes:

$$W_l = \frac{N_l \sum_{i=1}^{n_l} w_l^i}{\sum_{j=1}^{M_{\text{phases}}} N_j \sum_{i=1}^{n_j} w_j^i} \tag{28}$$

Formulae (21) and (26) use different definitions of the composition unit N, but, actually, these two approaches are the same. In fact, when a phase is crystalline, Equation (26) combined with Equation (24) gives [52]:

$$CN_l = \frac{\int_0^\infty (Y_l/AP)(s)s^2\,ds}{\sum_{i=1}^{n_l}\int_0^\infty [|f_i^0|^2 + I_i^{\text{inc}}]s^2\,ds} = \frac{16\pi^2 K_l V_l}{180\lambda^3} \tag{29}$$

This property avoids the evaluation of the integrals in Equations (26) and (29) for the crystalline phases, but, more important, it proves the equivalence of the approaches based on Equations (29) and (21), if all of the phases are crystalline.

From the operative point of view, the value of ratio (26) can be estimated by calculating the mean value of the ratio $N_l(s_p)$ in the range of $s_p > 1.0\,\text{Å}^{-1}$, i.e. $CN_l = \lim_{s_p\to\infty} N_l(s_p)$, with:

$$N_l(s_p) = \frac{\int_{s_{\min}}^{s_p}(Y_l/AP)(s)s^2\,ds}{\sum_i^n \int_{s_{\min}}^{s_p}[|f_i^0|^2 + I_i^{\text{inc}}]s^2\,ds}, \qquad s_{\min} = \frac{2\,\sin(\theta_{\min})}{\lambda} \tag{30}$$

and $\theta_{\min}$ is the initial measured angle that must be as low as possible.

This procedure allows quantitative phase analysis without using any internal standard, but it requires the knowledge of the composition of the sample and a careful treatment of the experimental data, which have to be corrected for the air scattering.

We must note that the profile functions usually applied in Rietveld analysis often correspond to very special cases of size and strain broadenings. A better approach could be using line profiles directly derived taking size and strain distributions from physical models and appropriate structural simulations (see, for example, Refs. [57–59]). It is worth citing that recently, some attempts to full profile fitting have been reported, in which full physical meaning parameters were used [60–63]. However, accounting for all the physical reasons causing the peak broadening can be a hard task requiring a perfect a priori knowledge and a perfect control on the experimental apparatus, sample morphology, background, parasitic contributions and so on. As several physical mechanisms may cause similar effects on the diffractograms, heavy correlation effects among the parameters may occur affecting the reliability of the results. This restricts the applicability of these approaches to very special cases. On the contrary, the use of general profile functions (Voigt, pseudo-Voigt, Pearson VII and so on) available in standard Rietveld programs allows to obtain reliable parameters, reproducible and comparable; these parameters can be a posteriori correlated to physical models.

2.2.3. Radial Distribution Functions

All real crystals have deviation from the ideal crystallographic structure due to atomic displacements from their ideal positions in the unit cell. These displacements may be dynamic (thermal) or static (disorder). If these displacements are uncorrelated a weakening in the Bragg peaks at high angles is present. Some materials may present correlated disorder so that the short-range order can be very different from the "average" long-range order; in this case the correlation effect can be seen by standard diffraction only if the correlation length is long enough (see, for example, Ref. [64]).

The diffraction patterns of nanosized materials are characterized by pronounced diffuse background while Bragg peaks are, in general, few, weak and broad. In these materials, the diffuse background is not a simple parasitic contribution but may contain relevant structural information about the phases under investigation if, for example, sub-nanometric particles and/or amorphous phases are involved. Even in amorphous structures, the lacking of long-range order does not prevent some (even high) degrees of short-range order, even if restricted on scales of few angstroms; this is the case of liquids, glass ionic solutions and so on. Even in long-range disordered materials the interatomic potentials impose constraints on bond distances and angles that limit the degree of randomness giving rise to some regularity on atomic distributions. However, dealing with amorphous materials, the traditional crystallographic methods fail, so their structure was usually described using statistical methods based on the formalism of atomic pair distribution functions (PDF) [36,65,66].

The PDF analysis methods have been used for a long time to study the structure of glasses and liquids [66]; the developing of XAFS spectroscopy [67,68], which is a powerful accurate probe for studying local structure on a scale of few angstroms [69], restricted the practical application of X-ray PDF methods, while XAFS, due to its simple application and its chemical selectivity, has became the favorite investigation technique addressed to local structure. XAFS and crystallography have been widely employed as complementary techniques studying the atomic structure of the materials: the former one probing short-range order on a scale of few angstroms and the second one describing symmetries and long-range order features.

Nanosized materials are characterized by different degrees of atomic order at different scales so that, as highlighted earlier [70], the PDF formalism can be a useful tool directly probing atomic order at long, short and intermediate ranges. The neutron scattering was historically preferred for the PDF analysis due to the wider reciprocal space exploitable and the better statistics at high angles due to the atomic neutron cross-sections that do not decrease at high angles as the atomic scattering factors do. The recent development of modern experimental XRD instrumentations suitable for high quality PDF analysis [71–74] is pushing up the interest on this technique, especially in the field of nanosized compounds [75–79].

The atomic PDF is related to the probability to find a spherical shell around a generic atom (scattering center) in the material – it is defined as: $G(r) = 4\pi\rho[\rho(r)–\rho_0]$, where $\rho(r)$ and ρ_0 are, respectively, the local and average atomic number densities and r the radial distance. $G(r)$ is the Fourier transform of the total structure factor $S(q)$:

$$G(r) = \frac{2}{\pi}\int_0^{q_{\max}} q[S(q) - 1]q\,\sin(qr)\,dq \tag{31}$$

where $q = 4\pi \sin(\theta)\lambda^{-1}$ [Å^{-1}] is the exchanged momentum vector. $S(q)$, in turn, is related to the coherent part of the total diffracted intensity of the sample:

$$S(q) = 1 + \frac{I^{\mathrm{coh}}(q) + \sum x_i |f_i(q)|^2}{\sum x_i f_i(q)^2} \tag{32}$$

where I^{coh} is the coherent scattering intensity per atom (in electron units), x_i the atomic concentration and $f_i(q)$ the atomic scattering factor for the ith atomic species in the sample.

It is clear that Equation (32) includes the total diffracted intensity, not only the Bragg diffracted one. Then both long range (Bragg peaks) and local structure (Debye diffuse scattering) contribute to $S(q)$ pushing the analysis of PDF beyond the Bragg scattering analysis.

Very important prerequisites for accurate PDF analysis are diffractograms with high momentum transfer (q) so that a short X-ray incident wavelength is required. However, at high q values the atomic scattering factors become weak while the inelastic contribution (Compton scattering) increases till it becomes the largest fraction of the total scattering intensity. Then, long collection times are required for accurate PDF determination. Wide q-range and high counting statistics are both difficult to obtain on laboratory X-ray diffractometers, so, for a long time, PDF methods were applied on neutron diffraction facilities [70]. Recently, instruments for high energy diffraction (up and over 100 keV) became available on several last generation SR facilities as, for example, the European Synchrotron Radiation Facility (ESRF) (Grenoble, France), the Advanced Photon Source (APS) of Argonne National Laboratory (USA) and the Spring-8 (Japan), thus allowing data collection using X-ray sources. Furthermore, relevant improvements for PDF analysis are obtained using large area detectors such as IP [72] since 2D data collection allows keeping the collection time in the second/minute range while reaching the highest counting statistics. Moreover, the area detectors provide the higher counting statistics at higher angles, allowing the partial balance of the decreasing of the atomic scattering factors. IP have suitable characteristics for high quality PDF, in particular high efficiency at high energy, wide dynamical range and low background (electronic noise). Modern read-out devices make available large area (up to 400 mm × 400 mm) and small pixel size (down to 50 μm × 50 μm) allowing angular resolution below 0.1° and exceptional high counting statistics.

In standard crystallographic analysis (for example, Rietveld refinement) relevant signal is often restricted to Bragg peak intensity and shape, while "background" is generally modeled by empirical functions and subtracted. Dealing with PDF the whole scattering signal is concerned; for this reason data treatment is an important step to be performed with care and often via a trial and error procedure. The experimental intensity $I^{\mathrm{exp}}(q)$ must be properly cleaned from all the parasitic contributions contaminating the sample diffraction signal, such as the sample holder, amorphous matrixes, air scattering, Compton scattering and so on. All the pattern deformations, such as absorption, detector efficiency and SR flux decay (on step scanning diffractometers), must be properly considered for the most reliable $G(r)$'s. A particular care must be given in removing all the low frequency pattern deformations, which may produce unphysical features and deformation of real $G(r)$ peaks at low r-values.

The peaks in $G(r)$ represent the average "real" PDF in the sample, convoluted with the Fourier window (extension of the data in the q space). On amorphous materials PDF information is restricted to few near neighbor shells and the analysis may be done fitting each $G(r)$ peak with appropriate atomic distribution models [80,81]. The average structure of nanocrystalline materials may result from a variety of competing size and (local) compositional dependent structures, which may coexist. The physical structures in $G(r)$ may extend up to several tenth of angstroms; then the PDF analysis of nanocrystalline materials may result complex. Differently from crystallography, in which many methods have been developed in order to individuate the symmetries and distinguish the involved phases, in PDF analysis several models may fit the data, so additional information (chemistry, microscopy, etc.) must be considered, and several models must be compared with the experimental PDF in a trial and error procedure. The models that account best for the experimental features are then used to refine the structural parameters. Example of PDF analysis on nanocrystalline materials may be found in recent literature (see, for example, Refs. [77,79,82,83]).

The total scattering analysis can be used also for the morphological characterization: a method for reliably estimating the particle size by PDF analysis which goes beyond the Scherrer peak shape analysis applied to gold nanoparticles is presented in Ref. [83]. Modeling the total scattering intensity via a distribution of particle sizes and crystallographic phases in complex nanocluster materials is also a way to understand the peculiar structures of nanosized materials (see, for example, Refs. [57,84]).

3. TEM

3.1. HREM and Image Formation

The strong impact in the science of transmission electron microscopy (TEM) (as well as of any imaging technique) is due to the fact that the information content of an image is immediately and effectively processed by the eye and the brain.

Figure 4 shows a high resolution image of nanoparticles dispersed over an amorphous holey carbon film: the overall projected shape of the particles and the particle degree of crystallinity can immediately be recognized by the presence of regular lattice fringes (see, for example, particle A), as well as by the presence of structure defects where the fringes are distorted, e.g. in particle B.

However, going from the former qualitative analysis to a more quantitative one is much more troublesome, as the correct and quantitative interpretation of the results should carefully take into account all the steps into which the process of image formation in the electron microscope is divided.

They are, going from the specimen to the image: (i) interaction of electrons with the specimen; (ii) propagation of electrons from the specimen to the final recording

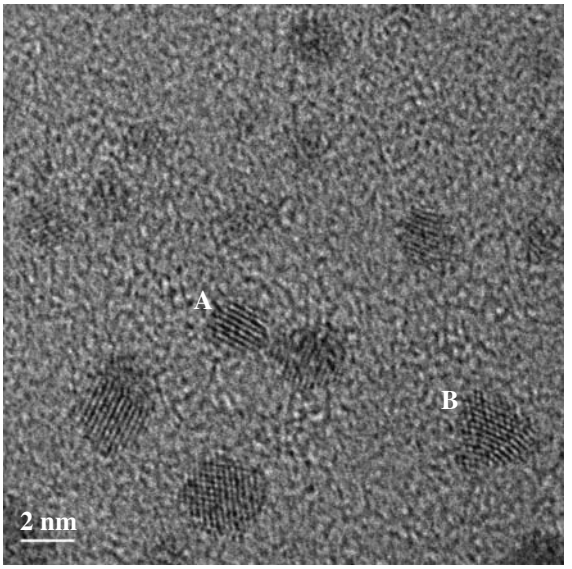

Figure 4. HREM of gold nanoparticles. A is a particle showing no defects, while B shows structural defects (twinnings). TEM micrograph taken with Jeol JEM3010, Department of Physical Chemistry University of Venice (Italy).

plane through the microscope lenses; (iii) detection of electrons by means of a photographic plate or an in-line electronic image read-out device.

It is usually assumed that the result of the propagation of electrons from the electron gun to the specimen is a plane wave. Partial coherence and/or convergent spherical illumination can then be accounted for by a partially coherent superposition of a set of plane waves.

Moreover, instead of describing the electrons by the Dirac equation, that is fully taking into account relativistic effects due to the high acceleration voltage, a modified form of the Schröedinger equation is used, in which electron energy and wavelength are replaced by the equivalent relativistically corrected expressions [85].

By considering only elastic scattering events, the interaction of the specimen with the electron beam can be described through a complex transmission function (object wave-function) $O(\vec{r})$ which represents the ratio between the outgoing and the incoming electron wave-functions; $\vec{r} = (x, y)$ is a two-dimensional vector lying on a plane perpendicular to the optic axis z which is parallel, and in the same direction, to the electron beam. In the standard phase object approximation:

$$O(\vec{r}) = \mathrm{e}^{\mathrm{i}\phi(\vec{r})} \tag{33}$$

where the phase term $\phi(\vec{r})$ is given by:

$$\phi(\vec{r}) = \frac{\pi}{\lambda E}\int_l V(\vec{r}, z)dz - \frac{2\pi e}{h}\int_l A_z(\vec{r}, z)dz \tag{34}$$

The integral is taken along a trajectory l parallel to the optical axis, passing inside and outside the specimen, and which must include stray fields; $V(\vec{r}, z)$ and $A_z(\vec{r}, z)$ are the electrostatic potential and the z component of the magnetic vector potential $\vec{A}(\vec{r}, z)$, respectively; E a factor that becomes the accelerating voltage in the non-relativistic approximation. e, λ and h are the absolute values of the electron charge, the electron wavelength and the Planck constant, respectively.

As the information is mainly encoded through the phase (the observable quantity being the phase difference), it is important to recall that, contrary to the optical case where three-dimensional effects are strikingly impressive, only essentially two-dimensional information is available in TEM. In fact, in the electric case $\phi(\vec{r})$ is proportional to the potential averaged along the electron path, whereas, in the magnetic case, the maximum of information encoded in the beam corresponds to the magnetic flux enclosed between two trajectories. Therefore, once the three-dimensional electromagnetic field is known, it is possible to determine the two-dimensional phase difference, but not the reverse.

The electrostatic potential includes the contributions both of applied external fields on a mesoscopic scale, as is the case of p–n junctions, and of the atoms building up the specimen at a microscopic scale, so that also the structural information is encoded in the object phase. However, it turns out that the phase object approximation at the atomic level holds only for very thin specimen, but can be implemented to cover also the case of thicker specimens by means of the multislice method [86,87]. By this approach the specimen is divided into thin slices, for each of which the phase object approximation holds, and the propagation between slices is treated by means of the standard Kirchhoff–Fresnel theory. In this way the exit wave-function is calculated by a series of interaction–propagation steps over the slices, and the specimen is no longer a pure phase object amplitude but structural information is transferred also into an amplitude term. Today most of the computer programs used for the interpretation of high resolution images are based on this algorithm [88–90], which has been shown to be able to treat, in addition to the interaction problem, also the propagation of electrons through the microscope lenses [91,92].

Therefore, if $O(\vec{r})$ is the exit wave-function, the image wave-function $\psi(\vec{r})$ taking into account the microscope aberrations is given by:

$$\psi(\vec{r}) = O(\vec{r}) \otimes \mathrm{FT}^{-1}[B(\vec{u})\mathrm{e}^{\mathrm{i}\chi(\vec{u})}] = C(\vec{r})\mathrm{e}^{\mathrm{i}\varphi(\vec{r})} \tag{35}$$

where $\otimes$ is the convolution, FT the Fourier transform, $\chi(\vec{u})$ the isoplanatic wave aberration function of the objective lens, including the effects of the defocus Δz and of the spherical aberration C_s; $\vec{u} = (u_x, u_y)$ the spatial frequency vector and $B(\vec{u})$ takes into account the effect of the objective aperture. $C(\vec{r})$ and $\varphi(\vec{r})$ are the amplitude and the phase, respectively, of the image wave-function.

The distortions in the aberrated image can be better understood if a weak sinusoidal phase grating is considered [93], described by the object wave:

$$O(\vec{r}) = 1 + \mathrm{i}\varphi_0 \cos(2\pi u_0 x) \tag{36}$$

Then the image wave-function is given by:

$$\begin{aligned}\psi(\vec{r}) = 1 &- \varphi_0 \cos(2\pi u_0 x)\sin(\chi(u_0)) \\ &+ \mathrm{i}\varphi_0 \cos(2\pi u_0 x)\cos(\chi(u_0))\end{aligned} \tag{37}$$

and is modulated in both amplitude and phase by the transfer functions $\sin(\chi)$ and $\cos(\chi)$.

Further degradation of the information encoded in the electron beam takes place in the recording step since the signal is proportional to the square modulus of the image wave-function, i.e. neglecting small second order terms:

$$I(\bar{r}) = |\psi(\bar{r})|^2 = 1 + 2\varphi_0 \cos(2\pi u_0 x)\sin(\chi(u_0)) \qquad (38)$$

This equation shows that only limited information is preserved. In particular, depending on the spatial frequency u_0, no information is transferred at all at the zeroes of the phase-contrast function $\sin(\chi)$. The loss of information is even more serious when the phase object approximation holds and for ideal imaging: in that case the phase information is completely lost in the Gaussian image of the object and special methods; the so-called phase-contrast [94,95] methods should be employed in order to partly recover this information.

For the high resolution case, the phase-contrast effects are automatically introduced owing to the combined effect of defocus and spherical aberration, which gives rise to an image of a structure complicated by the fact that also the amplitude term, resulting from the propagation process, interacts in a non-linear way with the phase term [16,89,90,96].

Quantitative image interpretation is therefore a challenging task. Nevertheless, a set of useful information on the particle crystalline structures (including defects) and on their size can be obtained, and this explains why HREM technique is one of the most used and well established in the framework of nanoparticle studies [14–16,97]; as an example, Figure 4 shows which kind of information can be obtained.

3.2. Electron Holography

Gabor devised in-line EH [98,99] in 1948 as a new technique able to circumvent the resolving power of the electron microscope, which was at that time ~1.2 nm. However, EH has attained its concrete development only in the last two decades, thanks to the introduction in electron microscopy of high brightness sources, such as field emission guns (FEG) [100]. This latter source, combined with a versatile electron interferometer, such as the Möllenstedt–Düker electron biprism [101], allows the recording of high quality off-axis holograms, which can be reconstructed and processed by optical and/or digital means. The whole process can be carried out also in line by using the newly developed slow-scan CCD cameras [102]. With respect to the standard phase-contrast methods in electron microscopy [94,95] holography allows the extraction of quantitative information with increased sensitivity limits owing to the use of phase amplification methods, which have no counterpart in electron microscopy [17–19].

3.2.1. Basic Principles for Recording and Processing Electron Holograms

In brief, holography is a two step imaging process, by means of which it is possible to record and subsequently recover both the amplitude and the phase of the object wave-function. This is accomplished in the off-axis image scheme by superimposing in the first step, within the electron microscope, a tilted coherent plane reference wave $R = e^{2\pi i u_C x}$ with carrier spatial frequency u_C, on an image $\psi(\bar{r})$ of the object wave-function. Both wave-front and amplitude beam splitting devices can be used for realizing this task [103]. However, the most diffused and versatile type of electron interferometer is the Möllenstedt–Düker electron biprism [101], which belongs to the class of wave-front division interferometers.

The biprism is realized by placing a thin charged wire W between two earthed plates P, along the y direction (see Figure 5), and is located under the back focal plane of the objective lens Ob. The wire splits the wave front of the incoming electron beam and its electrostatic field produces a deflection and a subsequent overlapping in the observation plane OP below the wire. As the width of the overlapping region and the interference fringe spacing can be controlled by varying the charge on the wire, by means of an external voltage supply, it is possible to obtain electron interferograms and holograms. In particular, if the interference region contains a large number of fringes superimposed on a focused image of the specimen, then the interferogram is called image off-axis electron hologram. The preferred arrangement is to use only one-half of the object plane for the specimen S, illuminated by the coherent beam EB, and the other for the reference beam, as shown in Figure 5. If the specimen occupies the whole

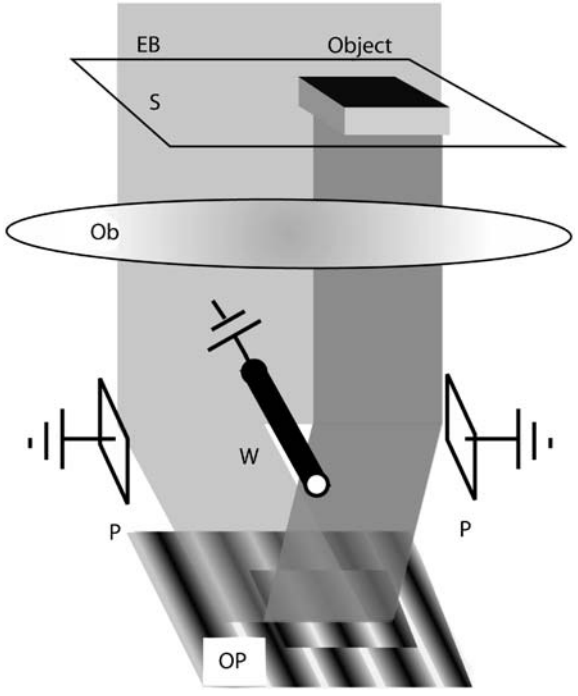

Figure 5. Schematic arrangement for hologram formation with an electron biprism. A plane wave illuminates the specimen placed off-axis. After the object lens a wire is placed between two earthed plates. The wire is the electron optical analog of a Fresnel biprism and causes the unperturbed and perturbed waves forming the electron hologram to interfere. The object phase-shift causes a displacement in the hologram fringes, and is thus observable.

plane, the interpretation of the pattern is more difficult because the information available concerns the phase difference between points in the specimen. Finally, it should be noted that the whole set-up comprises additional lenses in the condenser stage for reduction of the source to an angular size smaller than that of the interference fringes as seen from the biprism wire, in order to ensure that they are of high contrast. Moreover, the fringe system which forms in the observation plane is magnified by the remaining lenses of the microscope, so that the fringe spacing matches with the resolution of the recording medium.

The intensity recorded in the interferogram, henceforth called hologram, is given by

$$H(\vec{r}) = |R+\psi|^2 = |R|^2 + |\psi|^2 + \psi^* R + \psi R^* = 1 + C(\vec{r})^2 + 2C(\vec{r})\cos(2\pi x u_C + \varphi(\vec{r})) \quad (39)$$

showing that both amplitude C and phase $\varphi(\vec{r})$ of the image wave-function are encoded in the hologram, contrary to the conventional intensity $I(\vec{r}) = |C(\vec{r})^2|$.

The original idea of Gabor was to recover the information contained in the hologram by optical means. This is the second step, reconstruction and processing, of the holographic method. Today, however, image reconstruction by numerical methods presents considerable advantages with respect to the light optical technique. In this case the Fourier transform of the hologram H is taken and the side-band given by $\mathrm{FT}[O(r)](\vec{u}+u_C\vec{i})e^{i\chi(\vec{u}+u_C\vec{i})}$, where $\mathrm{FT}[O(r)]$ is the Fourier transform of the object wave, is selected by means of a digital aperture.

Therefore, in order to obtain the complete separation of the reconstructed wave from the other terms, the carrier fringe spacing $s = 1/u_C$ should be at least two or three times finer than the finest detail to be resolved in the image. This is the main reason why these experiments are difficult to realize, unless the electron microscope is equipped with a FEG.

Shifting the origin in the Fourier space by $u_C\vec{i}$, we obtain the wave-function $\mathrm{FT}[O(r)]e^{i\chi(\vec{u})}$, from which the lens aberration term can be eliminated in principle by multiplication with the inverse of the aberration phase factor $e^{-i\chi(\vec{u})}$. The inverse Fourier transform gives finally the amplitude and phase of the true object wave $O(\vec{r})$.

This whole process will be again illustrated step by step in the following section with reference to the case study of nanocatalysts.

3.3. Electron Holography applied to Size-Controlled Nanocatalysts

As remarked in the previous section EH is able to retrieve phase and amplitude information separately and with a resolution comparable with that of conventional HREM observations.

To obtain the images shown in the following, a specimen made of a porous resin in which gold nanoparticles were embedded was used [104]. The particles had already been observed by HREM to have an average radius in the range of 5–10 nm. Let us follow all the necessary steps to measure the phase-shift associated with one of the embedded particle. How this information can be interpreted will be discussed in the following.

First of all it must be noted that, as already remarked in the previous section, commercially available FEG microscopes are perfectly suited for holographic experiments. The only non-standard accessory that is needed in order to be able to record holograms is an electron biprism, which is also commercially available for the vast majority of microscopes. If there is no need for atomic resolution (as it is not the case in the examples which will be shown) a standard 1k × 1k CCD camera can be used for the acquisition. Phase information can then be reconstructed through digital procedures. There is also no need for particular alignment procedures, the ones normally used for conventional TEM remaining valid for holography. Nevertheless, it is of vital importance to operate the microscope in gun and illumination conditions providing coherence good enough for interference fringes to be formed.

This can be achieved by means of astigmatic illumination where the condenser stigmators are used to form an elliptic illumination area strongly elongated in the direction perpendicular to the biprism wire (i.e. to the interference fringes). An explication of why this setting works and how to obtain it can be found in Ref. [96] which is also suggested as a general reference for the practical issues concerning holographic observations. When the beam conditions have been optimized an interference image of the object can be obtained. Regions near a hole must be used so that the reference part of the incoming wave is in fact unperturbed. Standard focusing steps and objective astigmatism correction are normally made at this point and an image as the one shown in Figure 6 is obtained. The image looks like a normal TEM image to which an interference field has been superimposed.

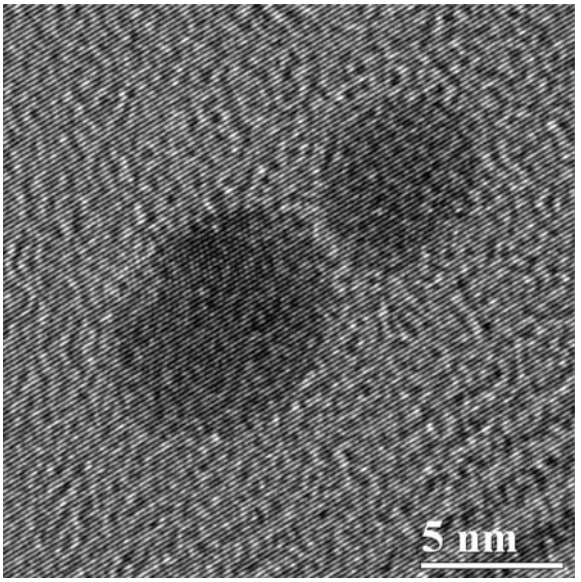

Figure 6. A hologram of two gold particles embedded in a polymeric matrix. The image does not include the full hologram; only the part of the original TEM image including the particles has been selected for an easier visualization of the interference fringes. (Thanks to Prof. B. Corain and Dr. P. Centomo (University of Padova, Italy) for providing the specimen and to Dr. P. G. Merli and to Dr. L. Ortolani (IMM-CNR Bologna, Italy) for the use of the FEI FEG-TEM.)

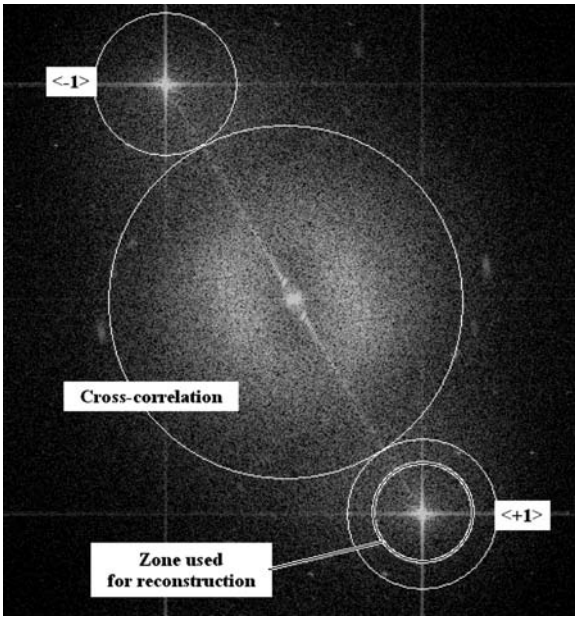

Figure 7. Fourier transform of image reported in Figure 6. The $\langle +1 \rangle$ and $\langle -1 \rangle$ and cross-correlation zones are shown together with the zone used to obtain Figure 8. The selected zone corresponds to a spatial resolution in phase of 0.4 nm.

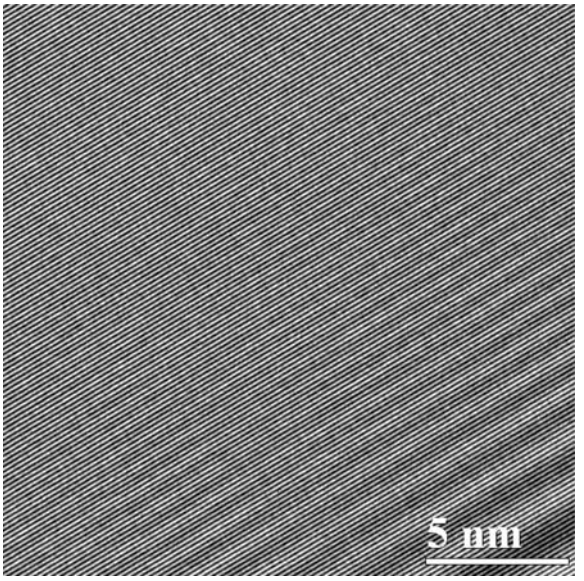

Figure 8. Reference hologram associated with image reported in Figure 6. The same sub-area of the hologram of the image has been cut out from the full reference hologram to better display the associated interference fringes. Thanks to Dr. P. G. Merli and to Dr. L. Ortolani (IMM - CNR Bologna, Italy) for the use of the FEI FEG - TEM.

The fringe displacements, not easily detectable in the hologram, encode the phase-shift information.

To decode this information the image is Fourier transformed through a fast Fourier transform (FFT) (see Figure 7). In Figure 7 three regions surrounding three bright spots have been enclosed with three white circles.

As seen in the previous section, the regions surrounding the $\langle 1 \rangle$ and $\langle -1 \rangle$ spots correspond to the Fourier transform of the electron wave-function and to its complex-conjugate, respectively. Note that which spot is the $\langle 1 \rangle$ and which is the $\langle -1 \rangle$ depends on the position of the unperturbed wave (i.e. of the hole in the specimen) and on the definition of Fourier transform used in the FFT. At this point, a circle inside the $\langle +1 \rangle$ zone must be selected for the reconstruction (the one used in this example is the inner circle shown in the $\langle +1 \rangle$ zone of Figure 7). The side disk radius is proportional to the spatial resolution of the reconstructed phase (the final resolution being the inverse of the higher enclosed frequency) and must be chosen so that no part of the cross-correlation surrounding the central spot is included. Since the distance between a side spot and the central one is inversely proportional to the biprism voltage, the final spatial resolution depends on the wire bias. A good condition to obtain the three disks' separation corresponds to a choice of the fringe spacing that is two or three times the required resolution, the exact value depending on the strength of the observed object. A stronger object will have a larger cross-correlation, thus requiring the use of a smaller fringe spacing s. It is also important to correctly choose the magnification value. When a good condition is found, the side-band can be separated out with a sharp (or Hanning [105,106]) circular mask and inversely Fourier transformed to obtain the complex image of the wave front Ψ. At this point the phase $\varphi = \arctan(\mathrm{Im}\{\Psi\}/\mathrm{Re}\{\Psi\})$ can be obtained. But there are still two problems to solve to be able to use the measured phase information.

First of all, when the phase is reconstructed in this way it brings information not only on the object but also on lens distortions and CCD camera imperfections. All these spurious effects also cause fringe deflections in the final image, thus contributing to the digitally reconstructed phase information. To overcome this problem, a hologram is normally taken in a region where no object is present (see Figure 8).

This reference image must be taken in the very same condition of the object hologram so that for each reconstruction two subsequent images are normally used. The reference hologram is reconstructed in the same way as the object hologram and the corrected phase $\varphi = \varphi_{\mathrm{Obj}} - \varphi_{\mathrm{Ref}}$ is used for data interpretation.

Another problem is arising from the fact that the range of variation of the original phase function is unrestricted, while the range of the numerically reconstructed wave is limited to a range of $[-\pi/2, \pi/2]$ by the use of the arctan function in the reconstruction process. As a consequence, a so-called phase-unwrap routine must be used to restore the continuous variation of the measured phase. Many procedures can be found in literature to accomplish this task. An algorithm that proved particularly effective in the case of gold catalysts is explained in Ref. [107] and has been successfully implemented and used in our observations. After applying the unwrapping procedure to the reference-corrected reconstructed phase the obtained information can be interpreted. The phase obtained from Figures 6 and 8 is shown in Figure 9.

To interpret the obtained information we can note that since the particles are not magnetic the only contribution in Equation (34) is due to the electrostatic field. An

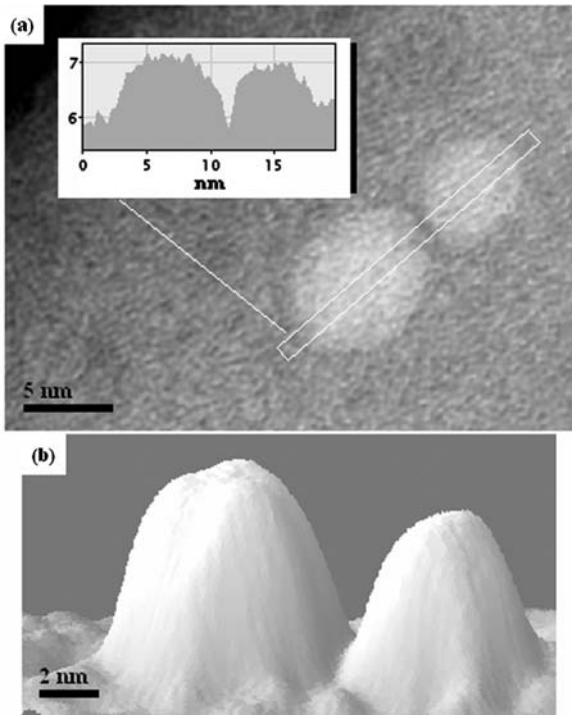

Figure 9. Phase reconstruction of image reported in Figure 6 using the reference of image reported in Figure 8. The phase map is shown in (a), which includes a laterally averaged line-scan of 15 pixels. (b) A surface map of the two particles' shape is displayed. The surface plot has been heavily noise filtered through Gaussian smoothing to better display the particles' shape.

approximation conventionally used to describe the electric properties of a material in electron microscopy is to consider the contribution of the mean-inner-potential (MIP) of the material to the electron motion [1,108].

In this approximation Equation (34) reduces to:

$$\varphi(x,y) = \frac{1}{\lambda E}[V_0 - V_0^{\mathrm{Sub}}]t(x,y) \tag{40}$$

where V_0 is the particle MIP, V_0^{Sub} the substrate MIP (which appears in the expression since the particle is embedded) and $t(x, y)$ the particle thickness in the point (x, y). At this point it could be tempting to look for a tabulated value for the gold and polymer MIP to extract, through $t(x, y)$, the tri-dimensional particle shape. These values have been measured or simulated for many materials [17,109] but it has been also recently observed [110–112] that the MIP of objects having a nanometer scale varies with particle dimension. This variation is quite marked and even if the existence of this effect represents, in this particular example, a limitation, it could be of great interest for a single-nanoparticle electron characterization. For example, discussion is still open about the possibility of connecting the MIP increase with the arising of the catalytic behavior in particles with a diameter smaller than 5 nm. EH opens, in this sense, an entirely new field of study, being able to access new kinds of information. Returning to the example, the interpretation of the particle phase-shift is still troublesome, since no precise data exist on the MIP of small particles.

For this reason another example whose interpretation is more direct will be given in the following.

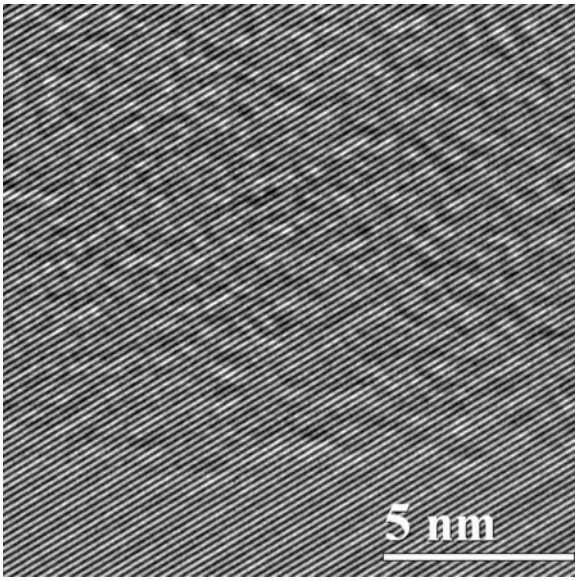

Figure 10. A hologram of a size-controlled catalyst support. The image does not include the full hologram; only a part of the original TEM image has been selected for an easier visualization of the interference fringes. (Thanks to Prof. B. Corain and Dr. P. Centomo (University of Padova, Italy) for providing the specimen.) Thanks to Dr. P. G. Merli and to Dr. L. Ortolani (IMM-CNR Bologna, Italy) for the use of the FEI FEG-TEM.

3.4. *Observation of a Size-Controlled Catalyst Support*

In the field of supported metal catalysis very little is known about the possible role of the supporting material for controlling the nucleation and growth of the metal nanoclusters. One of the still unresolved issues is represented by the determination of the pore sizes and morphology, until now defined by indirect techniques (for example, ISEC, SAXS [41,104]). For this reason, in the previously observed material, not only the gold nanoparticles, but also the supporting polymer can be of interest. The possible presence of the pores would in fact be evidenced by a drop of the phase-shift in proximity of the hole itself. With reference to Figure 10, for example, it is clear how the pore presence, which is not visible in the image itself, is encoded in the fringe shift and can be digitally reconstructed. The pore presence is in fact shown in Figure 11 in which the reconstructed phase of Figure 10 is shown.

A series of observations in different areas of the specimen have unambiguously evidenced the presence of a porous structure. Moreover, it has been observed that the density of pores is higher where the particle density is reduced, suggesting that the particles nucleate on the pores of the substrate and that the pores, which are not filled, are not completely reduced in the final thermal process.

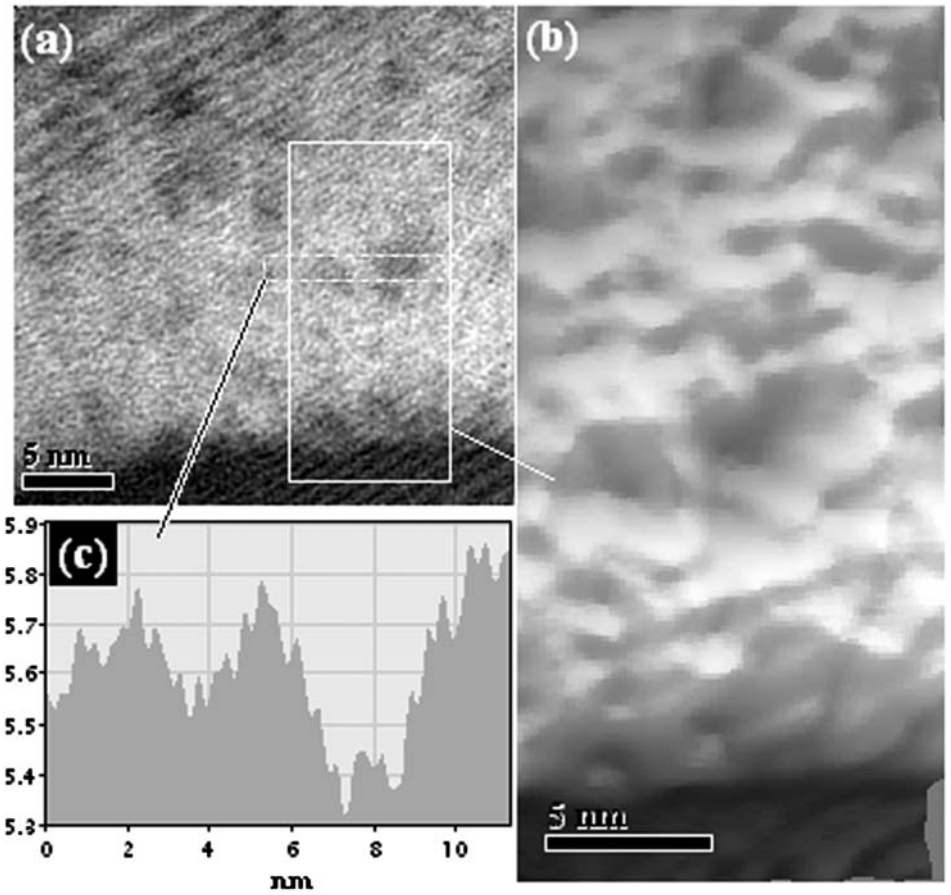

Figure 11. Phase reconstruction of the whole hologram of image shown in Figure 10 showing that some pores still exist in the thermically annealed specimen. Phase map is displayed in (a) together with a line-scan averaged over a width of 30 pixels (c) and a surface plot (b) taken from a smaller region of (a). The surface plot has been heavily noise filtered through Gaussian smoothing to better display the holes' shape.

EH can be used in this case to obtain direct information on the substrate structure, and to characterize the growth process of metal catalysts.

4. Conclusions

In this paper we have endeavored to present a review of some characterization methods of metal nanoclusters, focusing, among the extremely vast array of methods and techniques, on two of them, XRD and TEM, on which we have direct experience, and emphasizing also some recent developments, like the radial distribution function in XRD and EH in TEM.

We recognize that also within this restriction, other interesting topics are still missing.

For instance, with the introduction of SR sources, particles with a radius of a few nanometers can be studied with conventional methods. This has also stimulated a new kind of microscopy, named diffraction microscopy, where the Fraunhofer diffraction intensity patterns are measured at fine intervals in reciprocal space. By means of this oversampling a computer assisted solution of the phase problem can be found [113–115] (see Spence for a review [116]).

We have also not mentioned the last breakthrough in electron microscopy, where the spherical aberration problem has been finally solved by means of multipole lenses [117,118], and new aberration corrected electron microscopes are entering the market.

It can be readily anticipated that the new instrumentation, having extended the point resolution of the microscope up to its information limit [117], will provide even better high resolution images of nanoclusters, and also that it will not supersede, but emphasize, the role of EH, as the relevant structural information encoded in the phase (which is still completely lost in the recording process) can be retrieved corrected by all coherent aberrations.

References

1 M. Haruta, *Catal. Today* 36 (1997) 153.
2 R. P. Andres, T. Bein, M. Dorogi, S. Feng, J. I. Henderson, C. P. Kubiak, W. Mahoney, R. G. Osifchin, R. Reifenberger, *Science* 272 (1996) 1323.

3 D. Zanchet, C. M. Micheel, W. J. Parak, D. Gerion, A. P. Alivisatos, *Nanoletters* 1 (2001) 32.
4 Q. Sun, Q. Wang, B. K. Rao, P. Jena, *Phys. Rev. Lett.* 93 (2004) 186803.
5 J. H. Hainfeld, D. N Slatkin, H. M. Smilowitz, *Phys. Med. Biol.* 49 (2004) N309.
6 P. Cheyssac, R. Kofman, G. Mattei, P. G. Merli, A. Migliori, A. Stella, *Superlattices Microstruct.* 17(1) (1995) 47.
7 P. Cheyssac, R. Kofman, P. G. Merli, A. Migliori, A. Stella, *Mater. Res. Soc. Symp. Proc.* 332 (1994) 109.
8 P. Cheyssac, M. Geddo, R. Kofman, P. G. Merli, A. Migliori, A. Stella, P. Tognini, *Mater. Sci. Forum* 195 (1995) 161.
9 V. Vijayakrishnan, A. Chainani, D. D. Sarma, C. N. R. Rao, *J. Phys. Chem.* 96 (1992) 8679.
10 C. N. Ramachandra Rao, G. U. Kulkarni, P. John Thomas, P. P. Edwards, *Chem. Soc. Rev.* 29 (2000) 27.
11 U. Simon, *Adv. Mater.* 10 (1998) 1487.
12 D. M. Wood, N. W. Ashcroft, *Phys. Rev. B* 25 (1982) 6255.
13 A. Garcia Prieto, M. L. Fdez Gubieda, C. Meneghini, A. Garcia-Arribas, S. Mobilio, *Phys. Rev. B* 67 (2003) 224415.
14 P. Buseck, J. M. Cowley, L. Eyring, *High Resolution Transmission Electron Microscopy and Related Techniques*, Oxford University Press, Oxford, 1989.
15 S. Horiuchi, *Fundamentals of High-Resolution Transmission Electron Microscopy*, North-Holland, Amsterdam, 1994.
16 J. C. H. Spence, *High-Resolution Electron Microscopy*. 3rd ed., Oxford University Press, Oxford, 2003.
17 E. Völkl, L. F. Allard, D. C. Joy (eds.), *Introduction to Electron Holography*, Kluver Academic/Plenum Publishers, New york, 1999.
18 A. Tonomura, *Electron Holography, Springer Series in Optical Sciences*, Springer, Berlin, 1999.
19 A. Tonomura, L. F. Allard, G. Pozzi, D. C. Joy, Y. A. Ono (eds.) *Electron Holography: Proceedings of the International Workshop on Electron Holography, North-Holland Delta Series*, Elsevier, Amsterdam, 1995.
20 R. E. Dunin-Borkowski, M. R. McCartney, D. J. Smith, in H. S. Nalwa (ed.) *Encyclopedia of Nanoscience and Nanotechnology*, Vol. 3, American Scientific Publishers, CA, USA, 2004, 41.
21 P. Canton, R. Olindo, F. Pinna, G. Strukul, P. Riello, M. Meneghetti, G. Cerrato, C. Morterra, A. Benedetti, *Chem. Mater.* 13(5) (2001) 1634.
22 P. Riello, P. Canton, A. Benedetti, *Langmuir* 14(23) (1998) 6617.
23 P. Canton, C. Meneghini, P. Riello, A. Benedetti, in B. M. Weckhuysen (ed.) *In-Situ Spectroscopy of Catalysts*, American Scientific Publishers, CA, USA, 2004.
24 D. Balzar, in R. Snyder, J. Fiala, H. J. Bunge (eds.) *Defects and Microstructural Analysis by Diffraction*, IUCr/Oxford University Press, Oxford, 1999, 94.
25 R. A. Young, D. Wiles, *J. Appl. Cryst.* 15 (1982) 430.
26 C. N. J. Wagner, in J. B. Cohen, J. E. Hilliard (eds.) *Local Atomic Arrangements Studied by X-Ray Diffraction, Vol. 35, Metallurgical Society Conferences*, Gordon and Breach Science Publishers, Chicago, 1965, 219.
27 R. Delhez, T. H. Keijser, J. I. Langford, D. Louer, E. J. Mittemeijer, E. J. Sonneveld, in R. A. Young (ed.) *The Rietveld Method, IUCR Monograph 5*, Oxford University Press, Oxford, 1993.
28 S. A. Howard, K. D. Preston, in D. L. Bish, J. E. Post (eds.) *Reviews in Mineralogy*, Vol. 20, Mineralogical Society of America, WA, USA, 1989.
29 D. Balzar, N. Audebrand, M. R. Daymond, A. Fitch, A. Hewat, J. I. Langford, A. Le Bail, D. Louër, O. Masson, C. N. McCowan, N. C. Popa, P. W. Stephens, B. H. Toby, *J. Appl. Cryst.* 37 (2004) 911.
30 P. Scherrer, *Göttinger Nachrichten* 2 (1918) 98.
31 A. R. Stokes, A. J. C. Wilson, *Proc. Phys. Soc. Lond.* 56 (1944) 174.
32 G. K. Williamson, W. H. Hall, *Acta Metall.* 1 (1953) 22.
33 X. D. Zhou, W. Huebner, *Appl. Phys. Lett.* 79 (2001) 3512.
34 J. I. Langford, D. Louer, P. Scardi, *J. Appl. Cryst.* 33 (2000) 964.
35 B. E. Warren, B. L. Averbach, *J. Appl. Phys.* 21 (1950) 595.
36 B. E. Warren, *X-Ray Diffraction*, Addison-Wesley, Reading, MA, 1969.
37 R. Delhez, E. J. Mittemeijer, *J. Appl. Cryst.* 9 (1976) 223.
38 R. J. Matyi, L. H. Schwartz, J. B. Butt, *Catal. Rev. Sci. Eng.* 29 (1987) 41.
39 W. L. Smith, *J. Appl. Cryst.* 9 (1976) 187.
40 S. Ciccariello, G. Fagherazzi, A. Benedetti, *Acta Cryst.* A46 (1990) 187.
41 A. Guinier, *X-Ray Diffraction: In Crystals, Imperfect Crystals, and Amorphous Bodies*, Dover Publications, NY, USA, 1994.
42 S. Enzo, G. Fagherazzi, A. Benedetti, S. Polizzi, *J. Appl. Cryst.* 21 (1988) 536.
43 H. M. Rietveld, *Acta Crystallogr.* 22 (1967) 151.
44 H. M. Rietveld, *J. Appl. Crystallogr.* 2 (1969) 65.
45 R. A. Young, *The Rietveld Method*, Oxford University Press, Oxford, 1993.
46 L. Lutterotti, P. Scardi, *J. Appl. Cryst.* 23 (1990) 246.
47 L. Lutterotti, P. Scardi, *J. Appl. Cryst.* 25 (1992) 459.
48 R. J. Hill, C. J. Howard, *J. Appl. Cryst.* 20 (1987) 467.
49 G. W. Brindley, *Philos. Mag.* 36 (1945) 347.
50 J. C. Taylor, C. E. Matulis, *J. Appl. Cryst.* 24 (1991) 14.
51 P. Riello, P. Canton, G. Fagherazzi, *J. Appl. Cryst.* 31 (1998) 78.
52 P. Riello, G. Fagherazzi, P. Canton, *Acta Cryst.* A54 (1998) 219.
53 W. Ruland, *Acta Cryst.* 14 (1961) 1180.
54 W. Ruland, *Br. J. Appl. Phys.* 15 (1964) 1301.
55 P. Riello, G. Fagherazzi, D. Clemente, P. Canton, *J. Appl. Cryst.* 28 (1995) 115.
56 B. Borie, *Acta Cryst.* 14 (1961) 566.
57 A. Cervellino, C. Giannini, A. Guagliardi, *J. Appl. Cryst.* 36 (2003) 1148.
58 Z. Kaszkur, *J. Appl. Cryst.* 33 (2000) 87.
59 P. Scardi, M. Leoni, D. G. Lamas, E. D. Cabanillas, *Powder Diffraction* 20 (2005) 352.
60 P. Scardi, M. Leoni, *Acta Cryst.* A57 (2001) 604.
61 T. Ungar, J. Gubicza, G. Ribárik, A. Borbely, *J. Appl. Cryst.* 34 (2001) 298.
62 P. Scardi, M. Leoni, *Acta Cryst.* A58 (2002) 190.
63 M. Leoni, T. Confente, P. Scardi, *Z. Kristallogr.*, Suppl. 23 (2006) 249.
64 V. Petkov, I.-K. Jeong, J. S. Chung, M. F. Thorpe, S. Kycia, S. J. L. Billinge, *Phys. Rev. Lett.* 83 (1999) 4089.
65 H. P. Klug, L. E. Alexander, *X-Ray Diffraction Procedures for Polycrystalline and Amorphous Materials*, Wiley, New York, NY, 1974.
66 M. Magini, G. Licheri, G. Piccaluga, G. Pascina, G. Pinna, *X-Ray Diffraction of Ions in Aqueous Solutions*, CRC Press, Boca Raton, FL, 1988.
67 A. Filipponi, A. Di Cicco, C. R. Natoli, *Phys. Rev. B* 52 (1995) 15122.
68 A. Filipponi, A. Di Cicco, C. R. Natoli, *Phys. Rev. B* 52 (1995) 15135.
69 A. Filipponi, *J. Phys. Condens. Matter* 13 (2001) 23.
70 B. H. Toby, T. Egami, *Acta Cryst.* A48 (1992) 336.
71 C. Meneghini, A. Balerna, F. Boscherini, S. Pascarelli, S. Mobilio, *J. Synchrotron Radiat.* 5 (1998) 1258.
72 P. J. Chupas, X. Qiu, G. C. Hanson, P. L. Lee, C. P. Grey, S. J. L. Billinge, *J. Appl. Cryst.* 36 (2003) 1342.
73 V. Petkov, D. Qadir, S. D. Shastri, *Solid State Commun.* 129 (2004) 239.

74 S. Kohara, K. Suzuya, K. Takeuchi, *J. Jpn. Soc. Microgravity Appl.* 22 (2005) 100.
75 T. Egami, S. Billinge (eds.) *Underneath the Bragg Peaks: Structural Analysis of Complex Materials*, Elsevier Science, Amsterdam, 2003.
76 T. Proffen, S. J. L. Billinge, T. Egami, D. Louca, *Z. Kristallogr.* 218 (2003) 132.
77 V. Petkov, S. J. L. Billinge, P. Larson, S. D. Mahanti, T. Vogt, K. K. Rangan, M. G. Kanatzidis, *Phys. Rev. B* 65 (2002) 092105.
78 M. Gateshki, V. Petkov, S. K. Pradhan, T. Vogt, *J. Appl. Cryst.* 38 (2005) 772.
79 J. B. Parise, S. M. Antao, F. M. Michel, C. D. Martin, P. J. Chupas, S. D. Shastri, P. L. Lee, *J. Synchrotron Radiat.* 12 (2005) 554.
80 R. L. Mozzi, B. E. Warren, *J. Appl. Cryst.* 2 (1969) 164.
81 C. Meneghini, F. Boscherini, F. Evangelisti, S. Mobilio, *Phys. Rev. B* 50 (1994) 11535.
82 V. Petkov, M. Gateshki, J. Choi, E. G. Gillan, Y. Ren, *J. Mater. Chem.* 15 (2005) 4654.
83 B. D. Hall, D. Zanchet, D. Ugarte, *J. Appl. Cryst.* 33 (2000) 1335.
84 D. Zanchet, B. D. Hall, D. Ugarte, *J. Phys. Chem. B* 104 (2000) 11013.
85 P. W. Hawkes, E. Kasper, *Principles of Electron Optics*, Vol. 3, Academic, London, 1996.
86 P. Goodman, A. F. Moodie, *Acta Cryst. A* 30 (1974) 280.
87 D. Van Dick, *Adv. Electron. Electron Phys.* 65 (1985) 295.
88 (a) P. A. Stadelmann, *Ultramicroscopy* 21 (1987) 131; (b) http://cimewww.epfl.ch/people/stadelmann/jemsWebSite/jems.html.
89 E. J. Kirkland, *Advanced Computing in Electron Microscopy*, Plenum Press, New York, NY, 1998.
90 MacTempas: Image Analysis Program by R. Kilaas, http://www.totalresolution.com.
91 G. Pozzi, *Adv. Imaging Electron. Phys.* 93 (1995) 173.
92 A. Di Sebastiano, G. Pozzi, *J. Mod. Opt.* 43 (1996) 2367.
93 H. Lichte, *Ultramicroscopy* 20 (1986) 293.
94 R. H. Wade, *Adv. Opt. Electron Microsc.* 5 (1973) 239.
95 J. N. Chapman, *J. Phys. D* 17 (1984) 623.
96 M. Lehmann, H. Lichte, *Microsc. Microanal.* 8 (2002) 447.
97 D. B. Williams, C. B. Carter, *Transmission Electron Microscopy*, Plenum Press, New York, NY, 1996.
98 D. Gabor, *Nature* 61 (1948) 777.
99 D. Gabor, *Proc. R. Soc. Lond. Ser. A* 197 (1949) 454.
100 J. F. Hainfield, in O. Johari (ed.) *Scanning Electron Microscopy*, Vol. 1, ITTRI, Chicago, 1977, 591.
101 G. Möllenstedt, H. Düker, *Z. Phys.* 145 (1956) 377.
102 W. J. De Ruiter, J. K. Weiss, *Rev. Sci. Instrum.* 63 (1992) 4314.
103 G. F. Missiroli, G. Pozzi, U. Valdrè, *J. Phys. E* 14 (1981) 649.
104 B. Corain, K. Jerabek, P. Centomo, P. Canton, *Angew. Chem. Int. Ed.* 43(8) (2004) 959.
105 G. Ade, R. Lauer, *Optik* 88 (1991) 103.
106 G. Ade, R. Lauer, *Optik* 91 (1992) 5.
107 M. A. Schofield, Y. Zhu, *Opt. Lett.* 28(14) (2003) 1194.
108 D. K. Saldin, J. C. H. Spence, *Ultramicroscopy* 55(4) (1994) 397.
109 P. Kruse, M. Schowalter, D. Lamoen, A. Rosenauer, D. Gerthsen, *Ultramicroscopy* 106(2) (2006) 105.
110 S. Ichikawa, T. Akita, M. Okumura, M. Haruta, K. Tanaka, M. Kohyama, *J. Electron Microsc.* 52 (2003) 21.
111 S. Ichikawa, T. Akita, M. Okumura, M. Kohyama, K. Tanaka, *JEOL News* 38 (2003) 6.
112 M. Wanner, D. Bach, D. Gerthsen, R. Werner, B. Tesche, *Ultramicroscopy* 106(4–5) (2006) 341.
113 J. Miao, P. Charalamborous, J. Kirz, D. Sayre, *Nature* 400 (1999) 342.
114 Y. Nishino, J. Miao, T. Ishikawa, *Phys. Rev. B* 68 (2003) 220101(R).
115 J. M. Zuo, I. Vartanyants, M. Gao, R. Zhang, L. A. Nagahara, *Science* 300 (2003) 1419.
116 J. C. H. Spence, in P. Hawkes, J. C. H. Spence (eds.) *Science of Microscopy*, Chapter 19, Springer, New York, 2006.
117 M. Haider, S. Uhlemann, E. Schwan, H. Rose, B. Kabius, K. Urban, *Nature* 392 (1998) 768.
118 M. Haider, H. Rose, S, Uhlemann, E. Schwan, B. Kabius, K. Urban, *Ultramicroscopy* 75 (1998) 53.

This page intentionally left blank

CHAPTER 7

Platinum Nanoclusters' Size and Surface Structure Sensitivity of Catalytic Reactions

Robert M. Rioux[1,2], Hyunjoon Song[1,2], Peidong Yang[1,2], and Gabor A. Somorjai[1,2]

[1]*Department of Chemistry, University of California, Berkeley, USA*
[2]*Materials Sciences Division, Lawrence Berkeley National Laboratory, Berkeley, USA*

1. Introduction

The focus of heterogeneous catalysis during much of the 20th century was to improve the "activity" of important catalytic processes, that is, the turnover rate to produce more product molecules per site per unit time [1]. To this end, catalyst synthetic methods aimed to produce highly dispersed and stable catalysts in order to maximize the active surface-area. Studies of the macroscopic kinetics of reactions were utilized to optimize the reaction conditions [2]. Model surfaces in the form of metal single crystals were employed to study, with the help of surface science techniques, the elementary surface processes of adsorption, surface diffusion, reactivity, and desorption; and how surface structure and composition influence these processes. Surface science studies coupled with reactivity measurements at high pressure using high pressure reaction cells led to correlations between reaction turnover and the molecular mechanisms of surface reactions [3,4]. Major advances in catalysis science for relatively simple reactions (i.e., single product) were achieved including ammonia synthesis [5], CO oxidation [6] and hydrogenation (to methane) [7], and the hydrogenation of olefins to alkanes [8].

In the 21st century, the major challenge for catalysis science is to understand the molecular features of catalytic structure that control and dictate reaction selectivity [9]. We strive to produce only the desired molecule while minimizing the formation of thermodynamically stable unwanted by-products. The molecular ingredients and/or the structural features of the catalyst surface that control selectivity are not well-understood compared with the features that control activity in a single product surface reaction. The reason for this is shown schematically in Figure 1 [10]. Small differences in the activation energy ($\Delta G^{\ddagger}$) for a simple parallel reaction sequence can lead to large changes in selectivity. The potential energy barriers that dictate the final product distribution change with surface structure and composition.

In this chapter, we demonstrate the design of high surface area catalysts with controlled, tunable properties and systematically demonstrate the influence of particle size on reaction selectivity for multipath catalytic reactions. Solution-phase methods for the synthesis of metal colloids are utilized to produce monodisperse platinum nanoparticles in the 1–10 nm range [11–13]. This size range is catalytically relevant, and represents a range where changes in the properties of small transition nanoparticles are most dramatic [14]. The synthesis of Pt nanoparticles with controlled surface structure (cubic, cuboctahedral, and octahedral) by the addition of small quantities of sacrificial metal ions has been demonstrated [15]. The monodisperse shape-controlled nanoparticles are substitutes for metal single crystals. The nanoparticles are deposited in the form of a two–dimensional (2D) film using a Langmuir–Blodgett (LB) technique [15] or encapsulated in a 3D mesoporous silica support [16,17]. Catalysts, both 2D and 3D variants, are characterized by a variety of physical and chemical methods, such as X-ray diffraction (XRD), electron microscopy, physical and chemical adsorption, infrared spectroscopy, and chemical reactivity (ethylene hydrogenation or CO oxidation). We use ethane hydrogenolysis [13,16] and cyclohexene hydrogenation–dehydrogenation [18] as two examples of the influence of particle size on reaction activity and selectivity.

This approach of using 2D and 3D monodisperse nanoparticles in catalytic reaction studies ushers in a new era that will permit the identification of the molecular and structural features of selectivity [4,9]. Metal particle size, nanoparticle surface-structure, oxide–metal interface sites, selective site blocking, and hydrogen pressure have been implicated as important factors influencing reaction selectivity. We believe additional molecular ingredients of selectivity will be uncovered by coupling the synthesis of monodisperse nanoparticles with simultaneous studies of catalytic reaction selectivity as a function of the structural properties of these model nanoparticle catalyst systems.

Metal Nanoclusters in Catalysis and Materials Science: The Issue of Size Control
Edited by B. Corain, G. Schmid and N. Toshima

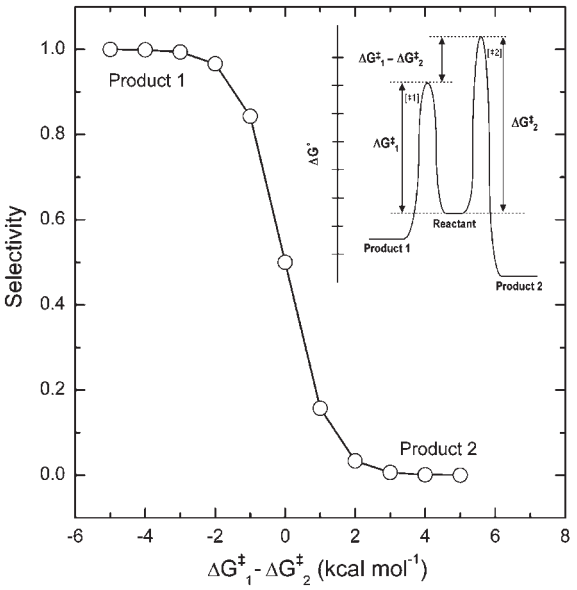

Figure 1. Selectivity is determined by the relative difference in activation energy between two possible products, while the rates of reaction to product 1 or 2 are determined by the absolute activation barriers, $\Delta G_1^{\ddagger}$ and $\Delta G_2^{\ddagger}$. Curve calculated assuming $\Delta G_2^{\ddagger} = 18$ kcal mol^{-1} and a temperature of 300 K. Inset is a simplified potential energy diagram for the conversion of a reactant into two parallel products [10]. (Reprinted from Ref. [10], © 2002, with permission from American Chemical Society.)

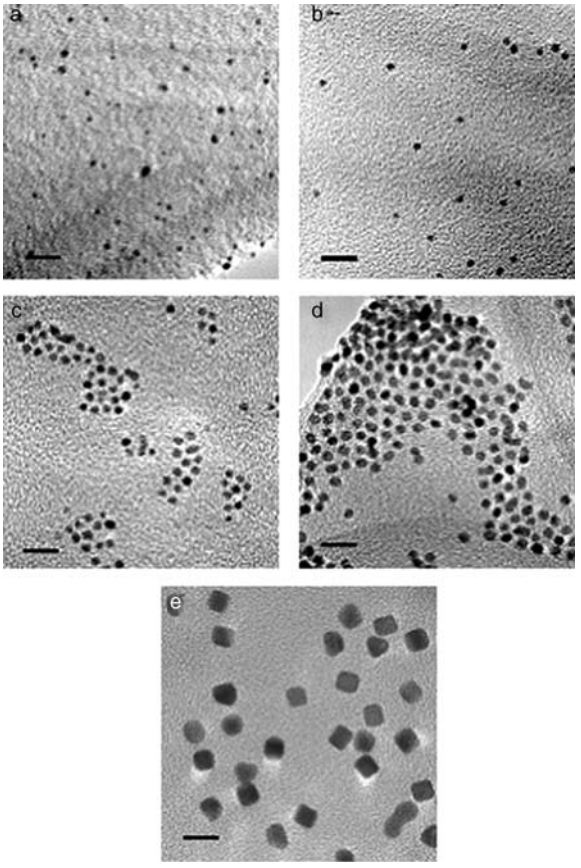

Figure 2. TEM images of the Pt nanoparticles of (a) 1.7 nm, (b) 2.6 nm, (c) 2.9 nm, (d) 3.6 nm, and (e) 7.1 nm. The scale bars represent 10 nm [13]. (Reprinted from Ref. [13], © 2005, with permission from American Chemical Society.)

2. Platinum Nanoparticle Synthesis and Structural Characterization

2.1. General Synthesis of Pt Nanoparticles

Colloidal platinum nanoparticles with different size and shape were synthesized by alcohol reduction methods. Alcohol serves as both a solvent for dissolving metal precursors and surfactants and a reducing agent to produce Pt(0) colloids. Dihydrogen hexachloroplatinate, H_2PtCl_6, is an ideal metal precursor due to its good solubility in polar solvents. Poly(vinylpyrrolidone) (PVP), a well-known polymer to stabilize metallic colloids [19], was introduced into the Pt colloid synthesis to stabilize Pt nanoparticles in solution by preventing particle aggregation. In the presence of PVP, the reaction between alcohol (RCH_2OH) and metal precursor occurred according to the following stoichiometry

$$H_2PtCl_6 + 2RCH_2OH \rightarrow \text{Pt(0) nanoparticles} + 2RCHO + 6HCl$$

where R = H, CH_3, or CH_2OH.

All Pt(0) nanoparticles were washed with water and ethanol to completely remove physisorbed polymers from the nanoparticle surface. The final particles were stable and stored in water at the same concentration (3×10^{-3} M based on the original Pt salt concentration). The long-term stability is attributed to PVP monolayer(s) coating the nanoparticle surface. The addition of excess PVP to the aqueous solution was not necessary.

2.2. Pt Nanoparticle Synthesis at Different Reaction Temperatures: Control of Nucleation-Growth Kinetics

Pt nanoparticles in the range of 1.7–7.1 nm were successfully synthesized by an alcohol reduction method [13]. Particle sizes depended on the reaction temperature; the smallest 1.7-nm particles were obtained in ethylene glycol (EG) at 433 K, while 2.9-nm particles were produced in boiling methanol (338 K), indicating that higher reaction temperatures generate more Pt nuclei in a short period affording smaller Pt nanoparticles. The 3.6-nm particles were synthesized by a seed-mediated growth of the 2.9-nm particles. The largest 7.1-nm Pt particles were synthesized by slow and continuous alternating addition of Pt precursor and PVP solutions to refluxing EG. The slow addition kept the Pt nuclei concentration at a low level and continuous supply of the Pt precursor led exclusively to nuclei growth.

All Pt nanoparticles were monodisperse and the size distribution was less than 10%. The average particle sizes

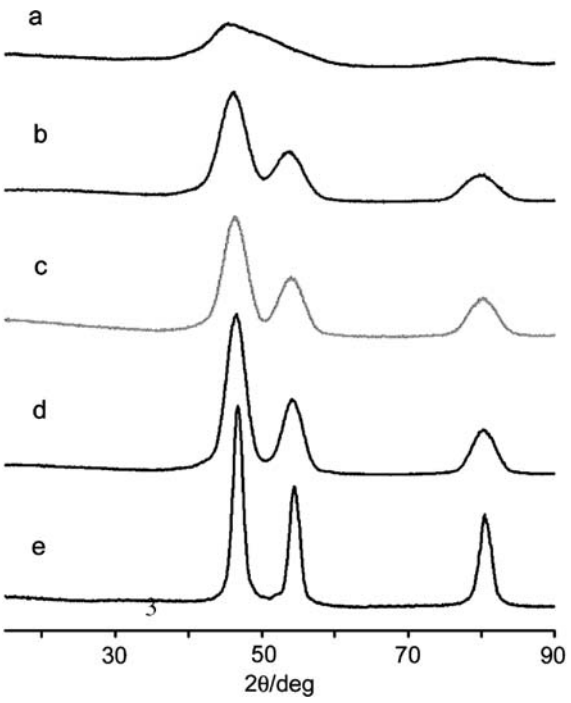

Figure 3. XRD data for free-standing Pt particles of (a) 1.7 nm, (b) 2.6 nm, (c) 2.9 nm, (d) 3.6 nm, and (e) 7.1 nm [13]. (Reprinted from Ref. [13], © 2005, with permission from American Chemical Society.)

were measured by transmission electron microscopy (TEM) (Figure 2) and XRD (Figure 3). The peaks at $2\theta = 45.9^\circ$, 54.0°, and 80.1° are Bragg reflections of Pt(1 1 1), (2 0 0), and (2 2 0), respectively.

Average sizes were estimated as 1.73 ± 0.26 (1.7), 2.48 ± 0.22 (2.6), 2.80 ± 0.21 (2.9), 3.39 ± 0.26 (3.6), and 7.16 ± 0.37 (7.1) nm, respectively, in which the values in the parentheses were calculated by the Debye–Scherrer equation from XRD line-broadening of the Pt(1 1 1) Bragg reflection.

2.3. Shape Control of Monodisperse Pt Nanocrystals by Ag^+ Addition

Shape control during colloidal synthesis of metal nanoparticles is accomplished by influencing the growth process such that one growth direction is kinetically favored over another. Shape control has been accomplished is by the addition of small concentrations of foreign metal ions to the colloid synthesis [20,21]. Shape control is particularly interesting in fundamental catalytic applications because they are particle mimics of extended single crystal surfaces used in surface science [9]. Pt nanocrystals in the shapes of cubic, cuboctahedral, and octahedral were successfully synthesized by the addition of silver ions to a modified polyol process [15,17]. Different concentrations of $AgNO_3$–EG solution were introduced to boiling EG prior to Pt precursor addition. Separately, EG solutions of dihydrogen hexachloroplatinate and PVP solutions were

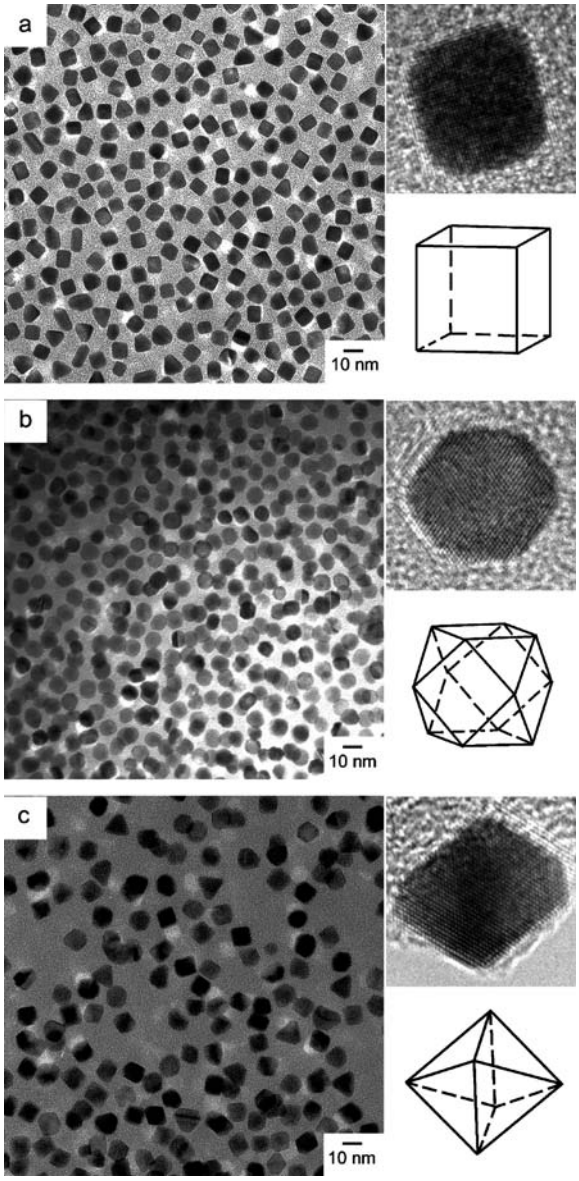

Figure 4. TEM images of the (a) Pt cubes, (b) Pt cuboctahedra, and (c) Pt octahedra. Inset images are corresponding HRTEM images and ideal structural models [15]. (Reprinted from Ref. [15], © 2005, with permission from American Chemical Society.)

slowly and alternately added to the reaction mixture over 16 min. The resulting mixture was refluxed for an additional 5 min, then purified by repetitive precipitation/dispersion procedure. A mixture of Pt nanoparticle shapes such as cubes, tetrahedra, spheres, and faceted particles were produced without silver ion addition. However, upon the addition of 1.1 mol% (with respect to the Pt concentration) silver nitrate, cubes with a longest vertex to vertex distance of 9.4 nm were produced with 80% yield (Figure 4a). The minor shape (10%) was tetrahedral. The addition of an 11 mol% $AgNO_3$ solution led to the exclusive formation of Pt cuboctahedra (Figure 4b), and further increase of the silver nitrate concentration to 32 mol%

Table 1. Yield and average size of shape-controlled Pt nanoparticles [15].

Amount of Ag added[a] (mol.%)	Major shape yield[b] and average size[c]	Minor shape yield[b] and average size[c]	XRD particle size (nm)[d]
0	Cubes with rounded edges ~40%	Spheres, ~30% Irregular rods, ~20% Tetrahedra, ~10%	7.1
1.1	Cubes ~80%, 9.4±0.6 nm	Tetrahedra ~10%, 9.8±0.7 nm	7.5
11	Cuboctahedra ~100%, 9.1±0.6 nm	–	8.4
32	Octahedra~80%, 9.8±0.6 nm	Tetrahedra ~10%, 9.9±0.7 nm	8.9

[a]With respect to the Pt salt concentration.
[b]Statistically determined values based on counting 250 particles.
[c]Largest vertex to vertex distance.
[d]Based on the Debye–Scherrer equation.

yielded octahedra with ~80% selectivity and tetrahedra (Figure 4c) constituting the minor product (~10%). The shapes, sizes, and minor shapes observed with the addition of increasing concentrations of $AgNO_3$ solutions to the Pt polyol process are summarized in Table 1 [15].

All particles with different shapes have a similar size of 9–10 nm (longest vertex to vertex distance) with narrow size distributions less than 7%. High-resolution TEM (HRTEM) images show their projections with the corresponding lattice fringes (Figure 4 insets). Cubes are aligned along the [0 0 1] axis normal to the substrate with the [1 0 0] lattice fringe. The cuboctahedra represent elongated hexagonal projections with the [1 1 1] lattice fringe, identical to those of an ideal cuboctahedral structure standing along the [1 1 0] zone axis. Octahedra are oriented along [1 1 0] and [1 0 0] directions, resulting in diamond and square projections, respectively. Cube surfaces are terminated by [1 0 0] facets, and octahedra and tetrahedra display [1 1 1] facets on their surface exclusively. Cuboctahedra expose both [1 0 0] and [1 1 1] facets with an area ratio of 1:0.58. Consequently, tuning of $AgNO_3$ concentration adjusts Pt particle shape and the ratio of [1 0 0]/[1 1 1] surfaces, which may lead to different catalytic properties.

The addition of Ag^+ enhances the [1 0 0] surface growth, and/or suppresses the [1 1 1] growth. Ag^+ is readily reduced by EG at high temperature resulting in reduced silver species such as Ag_4^{2+} clusters. These clusters are deposited onto certain crystallographic surface of the Pt seeds, which promotes anisotropic growth of polyhedral structures. Strüber et al. [22] reported that the desorption energy of Ag atoms on the Pt(1 0 0) surface is larger than that of Ag on Pt(1 1 1), indicating the silver atoms adsorbed on the [1 0 0] facets are more stable. However, the real experimental conditions are potentially more complex than expected. For instance, the reduced silver species are readily exchanged by the reduction of platinum ions via galvanic replacement due to a favorable electrochemical potential ($4Ag + H_2PtCl_6 \rightarrow 4AgCl + Pt(0) + 2HCl$), and the silver chloride is rapidly generated and precipitated in the presence of chloride ions. Silver by-products such as Ag(0) and AgCl were not sufficiently removed from the Pt nanoparticles by precipitation/redispersion cycles. Elemental analyses demonstrate that cubes and cuboctahedra retain ~100% of the original Ag quantity, while the octahedra retain ~40% of the original Ag quantity [15].

3. Two-Dimensional Deposition on Oxide Surfaces

3.1. Two-Dimensional Deposition and Characterization of Pt Nanoparticles on Oxide Surfaces

A 2D model catalyst system is a valuable tool for understanding nanosize effect of the metal crystallites and the role of the metal-oxide support interface. Metal nanoparticles have been fabricated on single crystalline silicon surfaces using various lithographic techniques [9]. These systems generate crystalline metal nanoparticles on silicon substrates which have been used to study reaction kinetics of small molecule hydrogenation and its poisoning by carbon monoxide [23]. While these techniques have the capability to produce structures with 10^9–10^{11} nanoparticles (mm^2–cm^2 of metal surface area), they are serial processing techniques requiring expensive and specialized equipment [9]. An alternate approach has been developed in which Pt nanoparticles produced by solution-based synthesis are deposited on the silicon substrate to provide alternative 2D model catalysts. This method has several advantages over the lithography-based techniques – (i) high-density particle arrays are available, (ii) size and shape of each particle is precisely controlled, and (iii) the process can be readily modified for a high-throughput fabrication. Generation of 2D nanoparticle arrays was accomplished using Langmuir-Blodgett (LB) methods [15]. Pt cubes were dispersed in chloroform, and the Pt cube solution was slowly dropped on the water surface in an LB trough. The Pt layers on the water surface were collected on TEM grids using the horizontal Langmuir–Schäffer lift-off method. As the surface pressure is increased, the surface coverage of the Pt particles increases. The Pt cubes do not aggregate and are evenly distributed over the entire grid surface. The surface coverage rapidly increased from 7.6 to 40% when the surface pressure increased from 3.6 to 6.0 $mN\,m^{-1}$. Further compression of the Pt layer generated a nearly closed-packed distribution of Pt nanoparticles, and eventually formed multilayer structures at a pressure of 10.6 $mN\,m^{-1}$. Figure 5 represents the relation between surface coverage (or particle density) and surface pressure of the Pt layer.

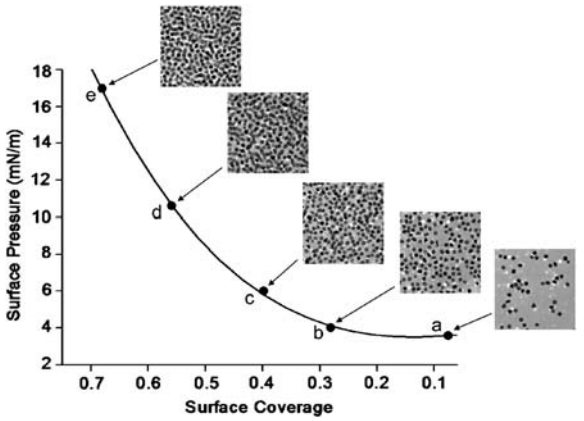

Figure 5. Pt cube coverage (estimated from TEM data) as a function of the surface pressure during the Langmuir–Blodgett process. The TEM images are at the surface pressures of (a) 3.6, (b) 4.0, (c) 6.0, (d) 10.6, and (e) 16.9 mN/m [15]. (Reprinted from Ref. [15], © 2005, with permission from American Chemical Society.)

Pt cuboctahedra and octahedra were also deposited on the silica substrate in an identical manner. These 2D model catalysts have the attributes of tunable particle density and the deposition of the different particles changes the relative ratio of exposed [1 0 0] and [1 1 1] surfaces.

After deposition onto planar substrates by LB methods, the surface regulating polymer, PVP must be removed from the surface. Figure 6 is the thermogravimetric profile of PVP decomposition during temperature-programmed oxidation (TPO) for both free PVP and Pt–PVP cubes. Comparison of the curves demonstrates that Pt catalyzes the oxidation of PVP resulting in a lower temperature (~473 K) required for PVP removal. Free PVP begins decomposing at ~600 K in oxygen. Complete combustion products, CO_2 and H_2O were the only gas phase products detected during TPO experiments [24]. There were no observable nitrogen containing compounds in the gas phase; the fate of nitrogen during combustion is unknown, although it is possible the amount of volatile reduced nitrogen (NH_3) and oxidized nitrogen (NO_x) formed were below the detection limit of the mass spectrometer. An NO_x peak evolves over a very large temperature range with a maximum concentration at ~753 K during TPO of pure PVP. The total amount evolved only amounts to 10% of the total nitrogen content [24]. It is also possible that nitrogen leaves the reactor as a product that was not analyzed for by mass spectrometry.

Dendrimer-protected colloids are capable of adsorbing carbon monoxide while suspended in solution, but upon removal from solution and support on a high surface area metal oxide, CO adsorption was nil presumably due to the collapse of the dendrimer [25]. It is proposed that a similar phenomena occurs on PVP-protected Pt colloids because removal of solvent molecules from the void space in between polymer chains most likely causes them to collapse on each other. Titration of the exposed surface area of colloid solution PVP-protected platinum nanoparticles demonstrated 50% of the total metal surface area was available for reaction, and this exposed area was present as

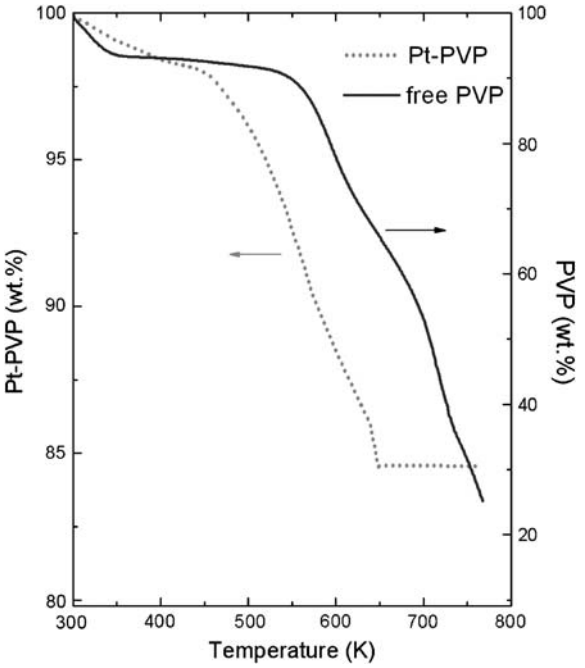

Figure 6. Thermogravimetric analysis (TGA) of free 55 K PVP and 7.1 nm Pt–PVP nanoparticles in oxygen. Oxidative decomposition of free PVP begins at ~573 K, while significant weight loss due to the catalyzed oxidation of PVP on PVP-protected Pt nanoparticles occurs at ~473 K. It appears that PVP layer is not a complete monolayer or the entanglement of PVP chains causes a porous polymer layer enabling oxygen diffusion to the nanoparticle surface [17]. (Reprinted from Ref. [17], © 2006, with permission from Springer.)

ensembles of neighboring atoms [26]. CO adsorption of LB monolayer films of PVP-protected Pt cubes was used as a probe of the PVP–Pt interaction and the state of the surface (Figure 7) [27]. Carbon monoxide adsorption is a common probe of catalyst structure and surface cleanliness because it is very sensitive to surface coordination and the presence of coadsorbates. Monolayer amounts of PVP have a significant influence on CO adsorption behavior. The amount of CO adsorbed is substantially decreased and the peak position significantly red-shifted compared to adsorption on monolayers subjected to a low-temperature oxidation–reduction treatment [27] and a Pt(1 0 0) single crystal [28]. After cyclic oxidation–reduction cycles, the sum frequency generation (SFG) peak intensity for the atop bound CO increases and blueshifts to 2085 cm^{-1}, in good agreement with the peak position for atop CO on Pt(1 0 0) at saturation coverage [28].

Pt cube monolayers were catalytically active for the oxidation of carbon monoxide after the removal of PVP. Figure 8 are first-order decay plots of the atop CO SFG signal as a function of time at different temperatures. As the temperature is increased, the SFG signal decreases at a much faster rate due to the increased rate of oxidation. Determination of the first-order decay rate constant as a function of temperature enables calculation of the apparent activation energy (E_{app}), which is shown in the inset of Figure 8. The activation energy measured by a standard technique, gas chromatography is in good agreement with

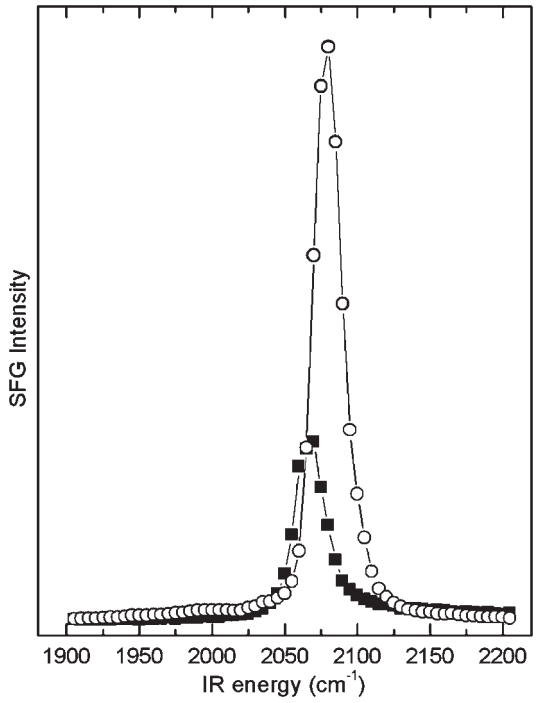

Figure 7. Total internal reflection sum frequency generation (TIR-SFG) vibrational spectroscopy of high-pressure room temperature adsorption of carbon monoxide on PVP-protected Pt cube monolayers and calcined (373 K, 3 h) monolayers [27]. The infrared spectra demonstrate CO is adsorbed at atop sites, but is considerably red-shifted on the PVP-protected Pt cubes. After calcination, the atop frequency blueshifts to 2085 cm^{-1} in good agreement with CO adsorption on Pt(1 0 0) at high coverages [28]. (Reprinted from Ref. [27], © 2006, with permission from American Chemical Society.)

the SFG results. The activation energy reported on a Pt(1 0 0) single crystal [29] is lower (14 kcal mol^{-1}) than those reported here, but it is well-known that the ratio of reactant pressure can have a large impact on the measured apparent activation energy [29].

Further studies on cyclic oxidation–reduction treated Pt cube monolayers demonstrate that upon adsorption of high-pressure ethylene, surface species found on Pt(1 1 1) single crystals are identified [30]. C–H resonances for ethylidyne and di-σ bonded ethylene suggest that the ethylidyne formed upon adsorption under high-pressure ethylene stabilizes the pseudohexagonal (5×20) reconstructed surface of Pt(1 0 0). Ethylidyne forms over threefold hollow sites of surfaces with hexagonal symmetry [31]. These results are in agreement with low-pressure ethylene adsorption on Pt(1 0 0). No ethylidyne is formed on Pt(1 0 0) after adsorption of 4L ethylene at 200 K (and pumping out to remove ethylene from the gas phase) and heating to room temperature. The only identified species was di-σ bonded ethylene, which desorbed or decomposed upon heating. Increasing the pressure (statically) to 5×10^{-7} Torr, the conversion of di-σ bonded ethylene to ethylidyne with increasing temperature was observed, in agreement with an independent ultrahigh vacuum (UHV) study by Masel and coworkers who identified ethylidyne on the pseudohexagonal (5×20) Pt(1 0 0) surface with temperature-programmed desorption and high-resolution electron energy loss spectroscopy [32].

3.2. Three-Dimensional Deposition of Pt Nanocrystals by Capillary Inclusion

Industrially relevant catalysts are composed of active metal nanoparticles in the 1–10 nm size range supported on high surface-area metal oxides or carbon. Metal nanoparticles are classically synthesized by the adsorption or ion exchange of metal precursors on metal oxides and their subsequent decomposition. Ion-exchange methods lead to high-dispersion samples because of an electrostatic interaction between metal precursor and oxide surface. The technique is limited by the appropriate choice of metal precursor (opposite charge of oxide surface) and operating conditions (pH of solution to induce surface charge) [33]. Precursor adsorption methods, such as impregnation or incipient wetness rely on physical forces (i.e., capillarity), which are simple and easily implemented on a large scale but the experimental conditions must be ideal to achieve a catalyst with satisfactory properties. However, both methods suffer from a similar problem; particle size is actually determined by a combination of the metal loading and activation (decomposition of the precursor) processes, which are often difficult to control [34]. During activation, it is common for nanoparticles to sinter leading to poorly dispersed systems with broad particle size distributions. These shortcomings preclude either method from being considered as part of a design strategy for supported model catalysts. For highly controlled catalyst synthesis, the idea is to effectively hybridize the controlled synthesis of the two primary components of a supported catalyst – metal nanoparticles and support. Our approach toward catalyst preparation is distinct from traditional methods because the metal nanoparticle synthesis is done prior to its inclusion in a support structure. The first approach is the mechanical inclusion of well-defined Pt nanoparticles onto mesoporous supports, termed capillary inclusion (CI) (Scheme 1) [13].

Santa Barbara Amorphous (SBA-15) silica with an average pore diameter of 9.0 nm is large enough to embed Pt nanoparticles smaller than ~7 nm. SBA-15 is synthesized according to the original procedure reported in the literature [35]. Pt particles with different sizes (1.7–7.1 nm) were mixed with SBA-15 in a 1:1 vol./vol. mixture of water and ethanol. Low-power sonication for 3 h at room temperature led to the dispersion of nanoparticles throughout the entire channel structure of SBA-15. XRD, and TEM analysis provide proof that nanoparticles do not aggregate and the SBA-15 mesopores are not disrupted by the inclusion process (Figure 9).

Without sonication, Pt particles adsorb primarily on the external surface of SBA-15 and at the mesopore openings. Sonication promotes homogeneous inclusion and deposition of Pt nanoparticles on the inner surface of the support mesopores, because ca. 90% of the total surface area is from the inner pore walls. Heat treatment

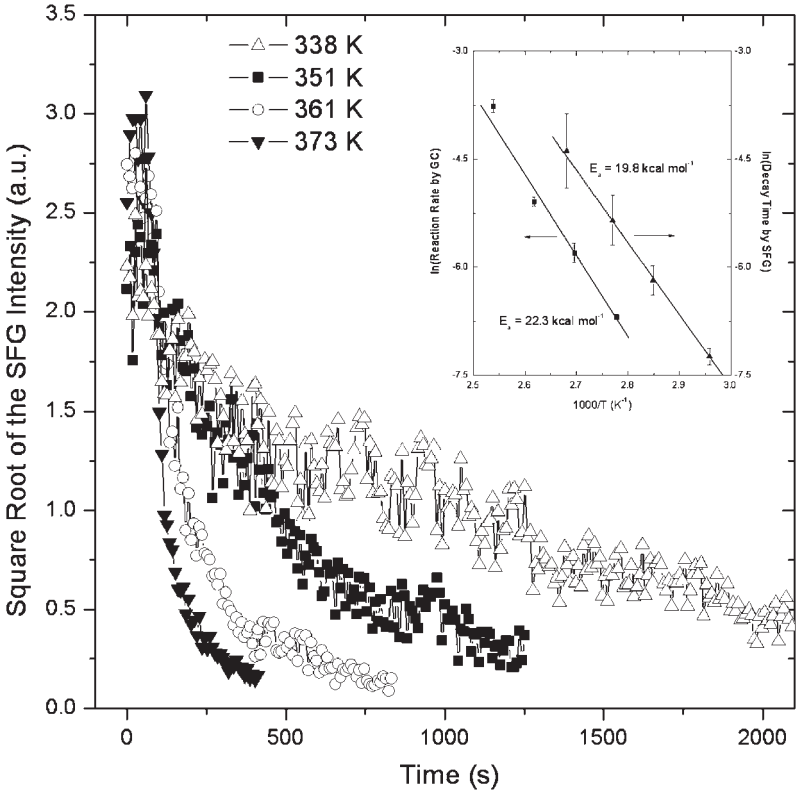

Figure 8. Rate of carbon monoxide oxidation on calcined Pt cube monolayer as a function of temperature [27]. The square root of the SFG intensity as a function of time was fit with a first-order decay function to determine the rate of CO oxidation. Inset is an Arrhenius plot for the determination of the apparent activation energy by both SFG and gas chromatography. Reaction conditions were pre-adsorbed and 76 Torr O_2 (flowing). (Reprinted from Ref. [27], © 2006, with permission from American Chemical Society.)

under reducing conditions for a high metal content (~14 wt.%) Pt/SBA-15 led to the formation of Pt rod-type structure in the silica matrix, which confirmed that the Pt particles were located inside the channels [13]. The silica channels served as a template for rod formation. Different sizes of metal nanoparticles were successfully incorporated into the mesoporous SBA-15 yielding Pt(X)/SBA-15-CI catalysts ($X = 1.7$, 2.6, 2.9, 3.6, and 7.1 nm). Metal contents of the catalysts were nominally 1 wt.%, but actual loadings with respect to the total weight were 0.73–0.95 wt.% platinum.

Prior to inclusion of PVP-protected Pt nanoparticles; the SBA-15 silica is calcined at 823 K for 12 h to remove residual templating polymer. Removal of PVP is required for catalyst activation. Due to the decomposition profile of PVP (Figure 6), temperatures > 623 K were chosen for ex situ calcination of Pt/SBA-15 catalysts. Ex-situ refers to calcination of ~300–500 mg of catalyst in a tube furnace in pure oxygen for 12–24 h at temperatures ranging from 623 to 723 K (particle size dependent) [13]. Catalysts were activated in He for 1 h and reduced at 673 K in H_2 for 1 h. After removal, the particle size was determined by chemisorption. Table 2 is a summary of chemisorption data for CI catalysts as well as nanoparticle encapsulation (NE) catalysts (see description of these samples in proceeding section).

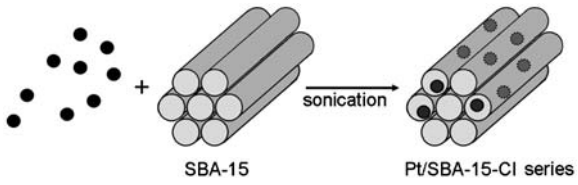

Scheme 1. Inclusion of size-controlled PVP-protected Pt nanoparticles in calcined mesoporous SBA-15 silica matrices. Mechanical agitation by low-power sonication affords a high dispersion of nanoparticles ranging in size from ~1 to 7 nm in the mesopore channels. The method is referred to as capillary inclusion (CI). The technique is limited by the size of nanoparticles that can fit into the 6–9 nm diameter mesopores [13]. (Reprinted from Ref. [13], © 2005, with permission from American Chemical Society.)

Monolayer uptakes were obtained by extrapolating isotherms to zero pressure. Dispersions for all catalysts were determined using four separate methods: H_2 chemisorption, CO chemisorption, O_2 chemisorption, and H_2–O_2 titration (Pt_s–$O + 3/2H_2 \rightarrow Pt_s$–$H + H_2O$) [36]. Fractional dispersions for the Pt/SBA-15 series range from 0.13 to 0.31 based on total H_2–O_2 titration uptakes. A 3.2% Pt/SiO_2 catalyst prepared by ion exchange (Pt/SiO_2-IE) [37] serving as a standard had an irreversible

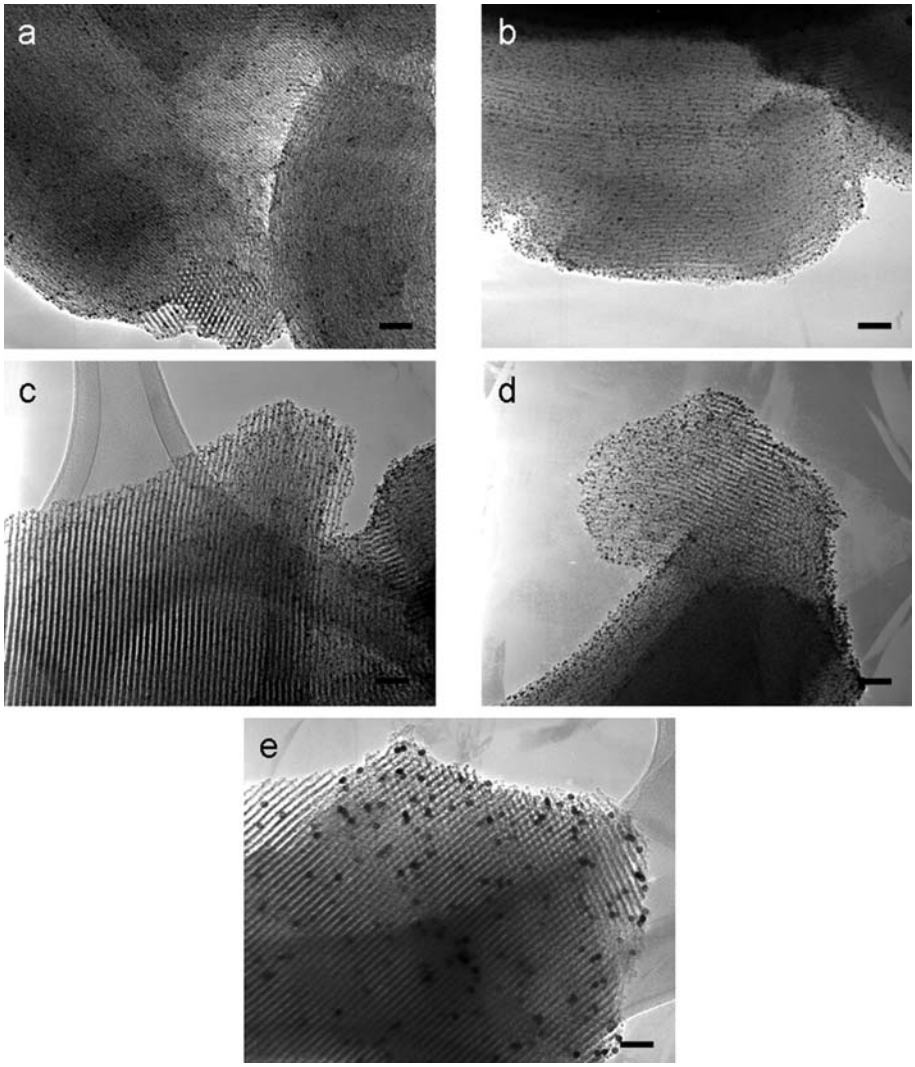

Figure 9. TEM images of the Pt(X)/SBA-15-CI catalysts. X = (a) 1.7 nm, (b) 2.6 nm, (c) 2.9 nm, (d) 3.6 nm, and (e) 7.1 nm. The scale bars represent 20 nm [13]. (Reprinted from Ref. [13], © 2005, with permission from American Chemical Society.)

measured uptake corresponding to a dispersion greater than unity. The Pt particle size based on chemisorption was calculated according to the equation $d(\text{nm}) = 1.13/D$, where D is the metallic dispersion. The above equation assumes spherical particles and a Pt atom density of 1.25×10^{19} atoms m^{-2} [38]. Particle sizes determined by chemisorption trend with the TEM and XRD particle size. XRD measurements on the supported Pt/SBA-15 particles indicated that the Pt particles were not agglomerated by sonication or the pretreatment procedure; however, as shown in Table 2, there is a significant difference in the measured particle size between the two techniques (chemisorption and XRD). Two possible explanations exist to explain this large discrepancy in particle size. Synthesis of the Pt nanoparticles requires the use of a template polymer (PVP, in our case) that prevents particles from agglomerating while in solution. PVP bonds strongly to the Pt surface and is difficult to remove after the particles have been dispersed within the SBA-15 matrix. The discrepancy between chemisorption and XRD particle size is most likely due to a reduced exposed surface area because of remaining polymer on the Pt surface. XRD is insensitive to this residual polymer, while chemisorption directly probes this loss of surface area.

The kinetics of ethylene hydrogenation on small Pt crystallites has been studied by a number of researchers. The reaction rate is invariant with the size of the metal nanoparticle, and a structure-sensitive reaction according to the classification proposed by Boudart [39]. Hydrogenation of ethylene is directly proportional to the exposed surface area and is utilized as an additional characterization of CI and NE catalysts. Ethylene hydrogenation reaction rates and kinetic parameters for the CI catalyst series are summarized in Table 3. The turnover rate is $\sim 0.7\,\text{s}^{-1}$ for all particle sizes; these rates are lower in some cases than those measured on other types of supported Pt catalysts [40]. The lower activity per surface

Table 2. Selective gas adsorption uptakes and average particle size for both series of Pt/SBA-15 catalysts [13,16].

Catalyst[a]	Selective gas uptake ($\mu mol\,g^{-1}$)[b]			Particle size (nm)		
	$H_{2,total}$	CO_{irr}	H_2–$O_{2,total}$	Dispersion, D[c]	Chemisorption[d]	XRD
3.2% Pt/SiO_2-IE	133	152	262	1[e]	1	–
6.3% Pt/SiO_2 (EUROPT-1)	151	175	334	0.69	1.6	1.8
Pt powder	16.7	13.7	30.3	0.004	287	>100
Capillary inclusion series						
0.73% Pt(1.7 nm)/SBA-15	7.4	12.2	17.4	0.31	3.6	–
0.95% Pt(2.9 nm)/SBA-1	6.8	7.8	18.1	0.25	4.6	3.0
1.0% Pt(3.6 nm)/SBA-15	4	9.3	15.6	0.20	5.6	3.8
1.01% Pt(7.1 nm)/SBA-15	2.1	4.6	10.1	0.13	8.7	7.8
Nanoparticle encapsulation series						
0.6% Pt(1.7 nm)/SBA-15	4.5	12	19.1	0.41	2.7	–
0.77% Pt(2.9 nm)/SBA-15	6	10	21.8	0.36	3.1	–
0.6% Pt(3.6 nm)/SBA-15	4	7.4	12.5	0.27	4.2	–
0.62% Pt(7.1 nm)/SBA-15	2	3.2	5.6	0.11	9.5	7.9

[a]Pt content determined by inductively coupled plasma–atomic emission spectrometry (ICP–AES).
[b]Monolayer uptakes ($P = 0$) determined at 295 K.
[c]Based on total H_2–O_2 titration uptake at $P = 0$.
[d]Based on $d(nm) = 1.13/D$.
[e]Dispersion greater than unity calculated; assumed 100% dispersion for calculation of turnover frequency.

atom (i.e., turnover frequency (TOF)) is most likely due to the influence of residual PVP on the surface of the Pt particle. The measured apparent activation energy is $\sim$7.5 kcal mol^{-1} for all catalysts, while reaction orders in ethylene and hydrogen are $\sim$0 and 0.7, respectively.

3.3. Three-Dimensional Deposition of Pt Nanoparticles by Nanoparticle Encapsulation

The mechanical incorporation of active nanoparticles into the silica pore structure is very promising for the general synthesis of supported catalysts, although particles larger than the support's pore diameter cannot be incorporated into the mesopore structure. To overcome this limitation, pre-defined Pt particles were mixed with silica precursors, and the mesoporous silica structures were grown by a hydrothermal method. This process is referred to as nanoparticle encapsulation (NE) (Scheme 2) [16] because the resulting silica encapsulates metal nanoparticles inside the pore structure.

The acidic conditions of standard SBA-15 synthesis [35] cause the precipitation of metal nanoparticles without silica encapsulation, or the formation of amorphous silica due to the presence of the polymer used for nanoparticle synthesis. Therefore, the SBA-15 framework was synthesized under neutral condition using sodium fluoride as a hydrolysis catalyst and tetramethylorthosilicate (TMOS) as the silica precursor. Pt particles with different sizes were dispersed in the aqueous template polymer solution; sodium fluoride and TMOS were added to the reaction mixture. The slurry aged at 313 K for a day, followed by an additional day at 373 K. Pt(X)/SBA-15-NE (X = 1.7, 2.9, 3.6, and 7.1nm) catalysts were obtained by ex-situ calcination (see Section 3.2). TEM images of the ordered Pt/silica catalysts are shown in Figure 10. Severe nanoparticle aggregation or phase separation is eliminated under neutral pH conditions.

Pt particles remain highly dispersed in the reaction mixture during mesostructure formation. All measurements including XRD, SAXS, and TEM indicate a well-ordered silica structure. N_2 physisorption measurement indicated high surface areas (523–661 $m^2\,g^{-1}$) and mesosized pores (112–113 Å) for the silica supports produced in the presence of different Pt particles.

Characterization of the catalyst surface by Chemisorption was conducted to determine the extent of PVP removal. Particle sizes calculated based on H_2–O_2 titration measurements are in better agreement with TEM (Figure 2) and XRD (Figure 3) calculated sizes of the free-standing particles than the CI catalyst series. The better agreement is most likely due to a more complete removal of PVP. The NE catalysts are washed with copious amounts of water and ethanol to remove the triblock copolymer template from the silica mesostructure. PVP is soluble in both solvents and may be removed from the particle surface during washing. Infrared spectroscopic investigation of CO adsorption on the NE catalyst series confirmed that combined washing and ex situ calcination were sufficient for PVP removal (although very weak C–H and C=O bands due to PVP were observed). Figure 11 is the infrared spectra of atop bound CO on the NE series of reduced catalysts [16]. The peak position blueshifts by more than 15 cm^{-1} as the particle size increases from 1.7 to 7.1 nm, while the peak full width at half maximum (FWHM) decreases as the particle size increases suggesting the number of energetically distinct sites capable of adsorbing CO decrease with increasing particle size. These observations are in agreement with statistical calculations of the fraction of different surface atoms for idealized shapes [41]. As the particle size increases, a majority of the surface atoms are

Table 3. Ethylene hydrogenation reaction rates and kinetic parameters for both series of Pt/SBA-15 catalysts [13,16].

Catalyst[a]	Activity[b] ($\mu mol\, g^{-1}\, s^{-1}$)	TOF[c] (s^{-1})	E_a[d] ($kcal\, mol^{-1}$)	Reaction orders	
				C_2H_4[d]	H_2[d]
3.2% Pt/SiO_2-IE	623	3.8	8	−0.1	0.62
Pt powder	69	3.4	8.9	−0.1	0.4
Capillary inclusion series					
0.73% Pt(1.7 nm)/SBA-15	8.3	0.71	6.9	0.1	0.75
0.95% Pt(2.9 nm)/SBA-15	8.5	0.7	7.9	0.05	0.77
1.0% Pt(3.6 nm)/SBA-15	6.7	0.64	6.9	0.11	0.69
1.01% Pt(7.1 nm)/SBA-15	4.2	0.62	8.2	0.05	0.7
Nanoparticle encapsulation series					
0.6% Pt(1.7 nm)/SBA-15	45	3.5	10.5	~0	0.57
0.77% Pt(2.9 nm)/SBA-15	50	3.5	9.8	~0	0.48
0.6% Pt(3.6 nm)/SBA-15	28	3.4	10.1	0.1	0.47
0.62% Pt(7.1 nm)/SBA-15	11	3.2	12.1	0.1	0.51

[a]Pt content determined by ICP–AES.
[b]Initial activity. Reaction conditions were 10 Torr C_2H_4, 100 Torr H_2, and 298 K.
[c]Normalized to the number of surface atoms determined by total H_2–O_2 titration.
[d]For reaction conditions for capillary inclusion series, see Ref. [13]. For reaction conditions for nanoparticle encapsulation series, see Ref. [16].

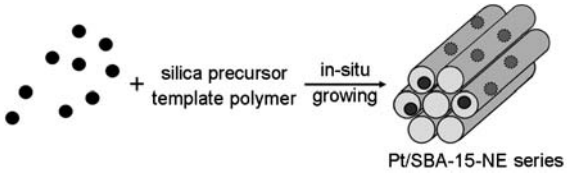

Scheme 2. Encapsulation of size- and shape-controlled Pt nanoparticles under neutral hydrothermal synthesis conditions of SBA-15. Silica templating block copolymers and silica precursors were added to PVP-protected Pt nanoparticle solutions and subjected to the standard SBA-15 silica synthesis conditions. Neutral, rather than acidic pH conditions were employed to prevent particle aggregation and amorphous silica formation [16]. (Reprinted from Ref. [16], © 2006, with permission from American Chemical Society.)

found in large terraces, in which all atoms have essentially the same reactivity, but in the case of smaller particles, the fraction of surface atoms at edge or corners become significant.

Similar to the CI catalyst series, NE catalysts were additionally characterized by ethylene hydrogenation. The intrinsic activity measured on a per gram Pt basis were higher than the corresponding particle size in the CI catalyst family, and TOFs were a factor of five higher on the NE series (~3.5 s^{-1}) [16]. The rates (activity and TOF) for the NE catalysts, as well as the apparent activation energy and partial pressure dependencies are summarized in Table 3. Apparent activation energies are slightly higher on the NE series, the ethylene reaction order is unchanged, and the hydrogen order is 0.5 compared with 0.75 for the CI catalyst series.

The shape-controlled nanoparticles were incorporated into the silica framework by NE by the procedure outlined in Scheme 2. These catalysts are denoted as Pt(X′)/SBA-15-NE where X′ = cubes, cuboctahedra, and octahedra. An example of a Pt nanoparticle cube catalyst is shown Figure 12 [17].

Previous results demonstrated Ag was incorporated into shape-controlled nanoparticles at Pt/Ag molar ratios ranging from 0.014 to 0.14, or ~0.04 wt.% Ag in ~0.5 wt.% Pt catalysts [17]. Rates of ethylene hydrogenation were sensitive to the amount of Ag retained in the Pt nanoparticles (Table 4). Rates decreased by two orders of magnitude when the Pt/Ag molar ratio increased by two orders of magnitude from the cubic to octahedral particles. The apparent activation energy also increased with increasing Ag incorporation. The addition of Ag to a Pt catalyst had a negative impact on catalyst activity for propylene hydrogenation [42,43]. It is well-known that Ag dissolves in nitric acid solutions (~5 M) to form $AgNO_3$ precipitates according to the following reaction; $2HNO_3 + Ag^0 \rightarrow AgNO_3 + NO_2 + H_2O$ [44]. Platinum is only partially soluble in nitric acid, therefore its dissolution is orders of magnitude slower than silver resulting in selective etching. Silver was removed from Pt(octahedra)/SBA-15 catalysts by selective etching using ~5 M nitric acid at 333 k. The Pt/Ag molar ratio decreased from 0.14 to 0.013 with no loss of Pt from the sample as determined by elemental analysis. Correspondingly, the rate of ethylene hydrogenation on Pt(octahedra)/SBA-15 catalysts increased by two orders of magnitude and the apparent activation energy decreased after washing (Table 4). It appears that only a small amount of residual Ag is required to alter the activity of Pt for olefin hydrogenation. The cubes (without etching) contain a comparable amount of Ag as etched octahedra samples, and hydrogenation rates are similar. Preliminary electron microscopy results demonstrate etching had no apparent effect on the size or shape of the octahedral particle. It is proposed that the Ag is most likely present as small clusters on the Pt nanoparticle surface because it was not detected by synchrotron-based XRD [45], and is easily etched at room temperature in 5 M nitric acid solutions.

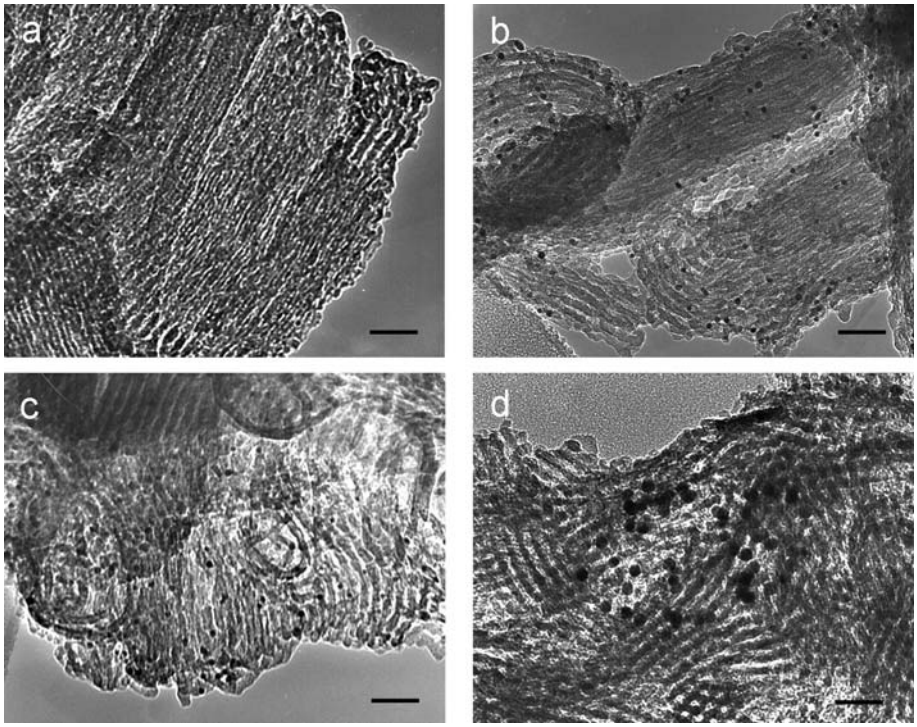

Figure 10. TEM images of the Pt(X)/SBA-15-NE catalysts. X = (a) 1.7 nm, (b) 2.9 nm, (c) 3.6 nm, and (d) 7.1 nm. The scale bars represent 40 nm [16]. (Reprinted from Ref. [16], © 2006, with permission from American Chemical Society.)

4. Influence of Particle Size on Reaction Activity and Selectivity

There are a number of examples demonstrating the influence of particle size on reaction selectivity. The selectivity of Co-based Fischer–Tropsch catalyst has been studied as a function of particle size [46]. Larger particles favor a higher production of larger hydrocarbons (Cn, $n \geq 6$). Isomerization of n-pentane is favored over Pt/SiO_2 catalysts with larger particles, while smaller particles favor hydrogenolysis [48]. Particle size was also shown to influence selectivity during the hydrogenation of α,β-unsaturated aldehydes (i.e., crotonaldehyde), with larger particles more selective for the formation of the unsaturated alcohol, requiring preferential hydrogenation of the C═O group over the C═C group [48,49]. Conversely, Mohr et al. [50] have shown that the edges of single crystalline gold particles are the active sites for the preferred C═O hydrogenation of acrolein, suggesting that smaller particles with a greater number of edge sites are more selective for the unsaturated alcohol. Reaction studies on Pt single crystals have shown that close-packed planes such as Pt(1 1 1) are selective for C═O bond hydrogenation, while corrugated surfaces such as Pt(1 1 0) are more selective for hydrogenation of the conjugated C═C bond of 3-methylcrotonaldehyde [51]. The number of examples of particle size selectivity correlations is few in number compared to particle size activity correlations but it is apparent that such correlations exist and will become better defined as catalyst structures are synthesized with more uniform properties. We demonstrate the influence of particle size on selectivity for two hydrocarbon conversion reactions. It is well-known that the rate of alkane hydrogenolysis is sensitive to particle size, with smaller particle being more active than larger particles. For this reaction, smaller particles are also less selective for alkane formation than the larger particles because of the substantial selectivity to carbonaceous deposits. In the second example, we demonstrate how selectivity is a complex function of both catalyst properties and reaction conditions. During the hydrogenation–dehydrogenation of cyclohexene, we show that the selectivity to benzene is a function of both particle size and H_2 pressure at a constant temperature. The ability to alter selectivity with H_2 pressure is demonstrated and discussed.

4.1. Ethane Hydrogenolysis is Sensitive to Pt Particle Size

The hydrogenolysis of alkanes has been studied extensively because of the well-known sensitivity of hydrogenolysis rates on surface structure [52,53]. As a test of particle surface structure, the hydrogenolysis of ethane was examined over Pt/SBA-15 catalysts (Figure 13). Table 5 is a summary of the kinetic results. Ethane hydrogenolysis is sensitive to particle size with TOFs varying by at least two orders of magnitude for catalysts containing Pt particles from 1 to 7 nm. Apparent reaction orders in ethane and hydrogen were 1 and ~ -3, respectively, for the Pt/SBA-15-NE series (Table 5). The observed reaction

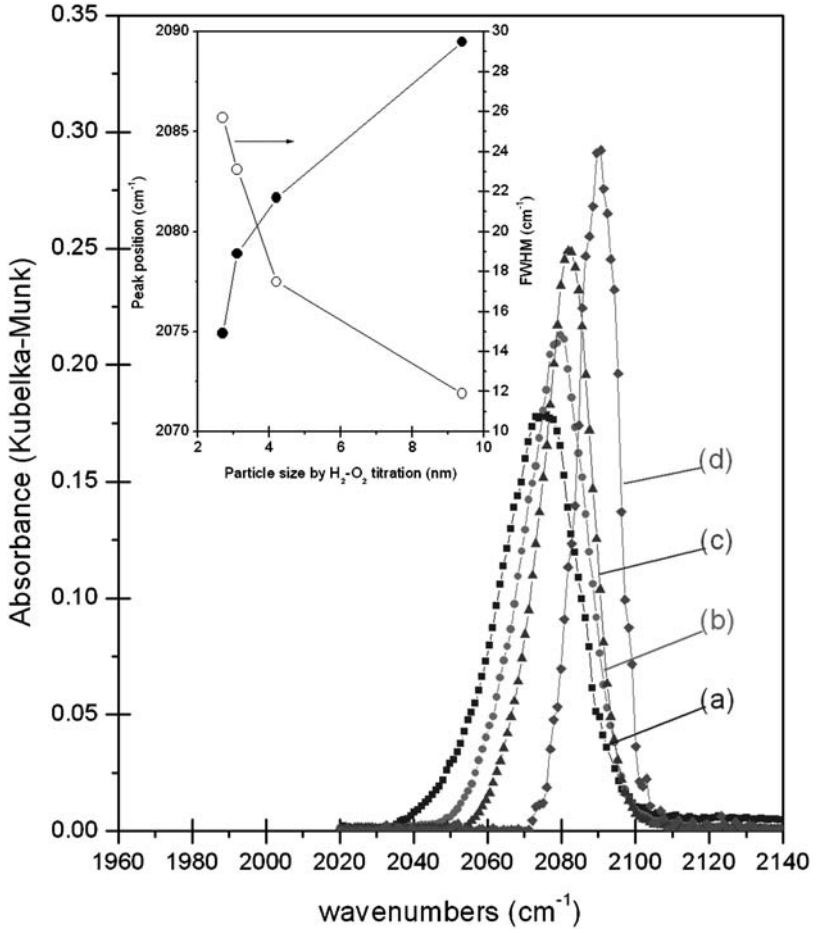

Figure 11. Infrared spectrum of CO adsorption at 295 K for the Pt/SBA-15 catalyst series: (a) 2.33% Pt(1.7 nm)/SBA-15, (b) 2.69% Pt(2.9 nm)/SBA-15, (c) 2.62% Pt(3.6 nm)/SBA-15, and (d) 2.86% Pt(7.1 nm)/SBA-15. Inset is the peak position and FWHM of the atop CO stretching vibration as a function of particle size at room temperature. Peak heights have been modified for clarity [16]. (Reprinted from Ref. [16], © 2006, with permission from American Chemical Society.)

orders are in agreement with measurements on other supported Pt catalysts [55]. The apparent activation energies increase with decreasing metal dispersion.

An ion-exchanged 3.2% Pt/SiO_2-IE catalyst with particles of ~1 nm was the most active ($6.4 \times 10^{-2}\,s^{-1}$ at 658 K) and had an apparent activation energy of 54 kcal mol^{-1}. Apparent activation energies increased to ~75 kcal mol^{-1} on the 0.62% Pt(7.1 nm)/SBA-15-NE catalyst. The apparent pre-exponential factors assuming a power rate law, $r_{CH_4} = k_{app} P_{C_2H_6} P_{H_2}^{-3}$ with $k_{app} = Ae^{-E_{app}/RT}$ varied by four orders of magnitude (10^{25}–10^{29} Torr^2 s^{-1}) over the particle size range studied. The influence of particle size on catalytic activity and the measured apparent activation energy are shown in Figure 13. The TOF for methane formation decreases as the particle size increases; similar trends have been observed on supported Pt catalysts [55,56]. A linear increase in the apparent activation energy is found with increasing particle size up to 3.6 nm, after which the activation energy is unchanged with larger particle size. A maximum in ethane hydrogenolysis TOF was observed for Pt/Al_2O_3 catalysts with Pt particles ranging from 1.7 to 5 nm [57]; they also observed a minimum in the apparent activation energy with particle size, after ~4 nm there is no change in the apparent activation energy. Rates of ethane hydrogenolysis follow a trend of decreasing rate with increasing metal particle size on the Pt/SBA-15 series, although significant discrepancies do exist and have been highlighted in a recent review [58]. Two independent studies of ethane hydrogenolysis on Pt(1 1 1) have determined similar TOFs of ~0.3 s^{-1} at standard conditions, which is an order of magnitude higher than Pt(1.7 nm)/SBA-15 and three orders of magnitude higher than Pt(7.1 nm)/SBA-15.

Large ensembles of Pt atoms are necessary for ethane hydrogenolysis because the C_2 intermediate is most likely bonded to multiple Pt atoms and adjacent sites are needed for H_2 adsorption. The need for a large Pt ensemble is most likely not the only requirement for an appropriate active site for ethane hydrogenolysis. Goodwin and coworkers suggest that these ensembles must also be properly oriented [59]. Comparison of ethane hydrogenolysis rates on Ni(1 1 1) and (1 0 0) led Goodman to postulate that the spatial coordination of surface metal atoms is a decisive factor in determining reactivity; differences in spacing between surface atoms on the two surfaces could

account for the differences in activity [60]. The number of atoms in the ensemble varies with metal, most likely due to the stoichiometry of the C_2H_x species in which the C–C bond is broken. In the case of Ni, methane forms through a surface carbide followed by hydrogen reduction, suggesting that a 12-atom ensemble is required [61]. On Pt, the proposed C_2 intermediate that undergoes C–C bond cleavage on Pt is the ethyl radical, C_2H_5 [62,63]. In this case, the ensemble size may be significantly reduced but the orientation of the atoms comprising that ensemble is still critical; most likely requiring a fraction of the ensemble to be composed of atomic steps, kinks, or other sources of surface roughness. Theoretical calculations of C_2H_x fragment stability on Pt slabs and clusters have shown that barriers to bond activation are lower on a stepped Pt(2 1 1) surface relative to a flat Pt(1 1 1) surface [64,65]. Correspondingly, the activated complexes along the hydrogenolysis reaction coordinate are stabilized on the stepped surface relative to the flat surface. Small metal crystallites have a higher proportion of coordinatively unsaturated surface atoms, analogous to a stepped single crystal, while the surfaces of large Pt particle are terminated primarily by low-index, high-coordination surfaces. It appears that reactions involving C_2H_x and their activated complexes occur on these defect sites because they provide more stable bonding. Recent work has shown that methane activation rates increased with Pt dispersion suggesting that CH_x species are stabilized on coordinatively unsaturated atoms [66]. The identity of the active site for C–H and C–C bond activation is unknown, but particle size dependent catalytic behavior of ethane hydrogenolysis suggests that surface roughness is a primary component of the active site.

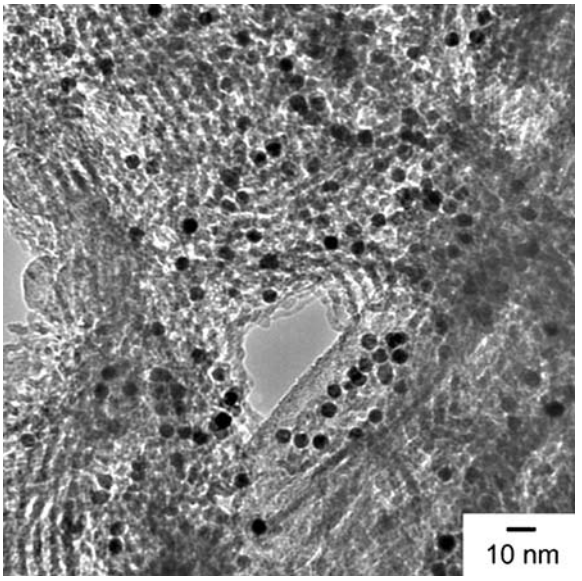

Figure 12. TEM image of the Pt(cubes)/SBA-15-NE catalyst after calcination [17]. (Reprinted from Ref. [17], © 2006, with permission from Springer.)

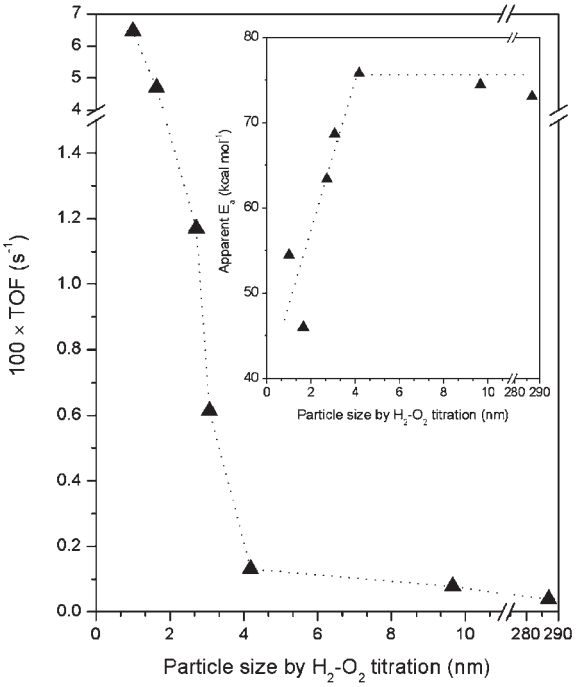

Figure 13. Dependence of ethane hydrogenolysis TOF and apparent activation energy on Pt particle size. TOFs decrease by two orders of magnitude over the size range, while the apparent activation energy increases. Coordinatively unsaturated surface atoms in small particles have a higher reactivity and subsequently a smaller barrier for hydrogenolysis than highly coordinated surface atoms of larger particles. TOFs were measured at 20 Torr C_2H_6, 200 Torr H_2, and 658 K [16]. (Reprinted from Ref. [16], © 2006, with permission from American Chemical Society.)

Table 4. Ag/Pt molar ratio and its influence on ethylene hydrogenation rates and apparent activation energy for nanoparticle encapsulated shape-controlled Pt nanoparticles [17].

Catalyst[a]	Ag content[a] (ppm)	Ag/Pt molar ratio[a]	TOF[b] (s^{-1})	E_a[c] (kcal mol^{-1})
0.55% Pt(cube)/SBA-15	43	0.014	8.6	9.9
0.67% Pt(cuboctahedral)/SBA-15	378	0.102	0.4	10.8
0.48% Pt(octahedral)/SBA-15	326	0.123	0.02	13.4
0.43% Pt(octahedral-*no etch*)/SBA-15	617	0.25	0.015	10.6
0.43%Pt(octahedral-*etched*)/SBA-15	60	0.025	6.8	9.4

[a]Pt and Ag content determined by ICP–AES.
[b]Reaction conditions were 10 Torr C_2H_4, 100 Torr H_2, and 298 K.
[c]Reaction conditions were 10 Torr C_2H_4, 100 Torr H_2 and 273–373 K (catalyst dependent).

Table 5. Ethane hydrogenolysis reaction rates and kinetic parameters for both series of Pt/SBA-15 catalysts [13,16].

Catalyst[a]	Activity[b] ($\mu mol\,g^{-1}\,s^{-1}$)	TOF[c] ($(10^2) \times s^{-1}$)	E_a[d] ($kcal\,mol^{-1}$)	Reaction orders	
				C_2H_6[d]	H_2[d]
3.2% Pt/SiO_2-IE	10.6	6.5	54.5	0.99	−2.8
6.3% Pt/SiO_2 (EUROPT-1)	11.3	4.7	46	0.9	−1.8
Pt powder	0.007	0.04	70.5	0.99	−2.6
Capillary inclusion series					
0.73% Pt(1.7 nm)/SBA-15	0.38	3.4	49	0.7	−1.9
0.95% Pt(2.9 nm)/SBA-15	0.29	2.4	54	0.65	−1.9
1.0% Pt(3.6 nm)/SBA-15	0.25	2.5	57	0.75	−1.9
1.01% Pt(7.1 nm)/SBA-15	0.1	1.2	49	0.75	−1.9
Nanoparticle encapsulation series					
0.6% Pt(1.7 nm)/SBA-15	0.16	1.2	63.4	1	−3.1
0.77% Pt(2.9 nm)/SBA-15	0.08	0.6	68.7	1.1	−3
0.6% Pt(3.6 nm)/SBA-15	0.01	0.1	75.8	0.97	−2.9
0.62% Pt(7.1 nm)/SBA-15	0.007	0.08	74.5	1	−2.6

[a]Pt content determined by ICP–AES.
[b]Initial activity. Reaction conditions were 20 Torr C_2H_6, 200 Torr H_2, and 658 K.
[c]Normalized to the number of surface atoms determined by total H_2–O_2 titration.
[d]For reaction conditions for capillary inclusion series, see Ref. [13]. For reaction conditions for nanoparticle encapsulation series, see Ref. [16].

4.2. Structure Sensitivity of Ethane Decomposition to Surface Carbon During Hydrogenolysis

Methane is the only product observed in the gas phase, but consideration of the decomposition of ethane to surface carbon as a reaction pathway is an important parameter for the design of hydrogenolysis catalysts. For example, Vang et al. [67] demonstrated that step sites on a Ni single crystal are significantly more reactive for C–C bond breaking than terrace atoms. In another study, two competing reaction pathways were found for methanol decomposition – C–H bond activation leading to the formation of CO_2 at terrace sites and C–O bond scission leading to carbon covered step sites [68]. In these examples, the morphology and surface roughness of the surface not only influence activity, but also play an important role in determining reaction selectivity.

The extent to which carbon is deposited on Pt/SBA-15 after hydrogenolysis is determined by H_2–O_2 titration. The adsorption of probe molecules can be used to determine the fraction of the surface covered with carbon [69,70]. Table 6 demonstrates that the fraction of the Pt surface covered with carbon used in this study varied from 10 to 30% and was dependent on particle size. The significantly higher fractional carbon coverage after ethane hydrogenolysis on the Pt(2.9 nm)/SBA-15 catalysts is due to the presence of a higher fraction of coordinatively unsaturated surface atoms, which promote formation of irreversibly chemisorbed unreactive carbon. While this carbon was removed by oxidative treatment restoring the original surface area, it appears that under reducing conditions this carbon is unreactive and most likely deposited during the first few turnovers on surface atoms with the highest coordinative unsaturation. On Pt(1 1 1), Rodriguez and Goodman have shown that the amount of surface carbon after ethane hydrogenolysis in a 100-fold excess of hydrogen is temperature dependent, with the coverage increasing approximately linearly with temperature. Approximately 35% of the surface was covered with carbon as determined by Auger electron spectroscopy at 620 K [71]. At lower H_2/C_2H_6 ratios ($H_2/C_2H_6 = 10$), the coverage of the Pt(1 1 1) surface after ethane hydrogenolysis at 620 K is 60% [72]. The difference between the fraction of carbon coverage reported for single crystals and the Pt/SBA-15 catalysts is most likely due to the support serving as a sink for coke precursors as proposed by Parera et al. [73]. Reaction selectivity is structure sensitive due to competing reaction pathways occurring at different rates on distinct surface sites.

4.3. Intrinsic Selectivity to Benzene During Cyclohexene Hydrogenation–Dehydrogenation is Sensitive to Pt Particle Size

The influence of particle size on selectivity is in general difficult to study because the influence is often subtle, therefore requiring materials with very controlled and defined properties. For simplicity, a two-product reaction, either parallel or series, in which only one reaction is structure sensitive should demonstrate changes in reaction selectivity with particle size. As the particle size decreases, the fraction of surface atoms with reduced coordination decreases [41]. The monodisperse 1.7–7.1 nm Pt particles we have synthesized are excellent candidates for selectivity studies. Reactions involving molecules with multiple functional groups (such as unsaturated aldehydes (i.e., crotonaldehyde) or epoxides (e.g., 3,4 epoxy-1-butene) are popular candidates to study the influence of particle size on selectivity. In these examples, the reaction sequence is rather complicated with parallel and serial reaction pathways leading to a complex dependence of selectivity on particle size. We have chosen to examine a relatively simpler reaction, the hydrogenation–dehydrogenation of cyclohexene (Ch). This reaction has been studied extensively on Pt single crystals by McCrea and Somorjai [74] and supported Pt catalysts by O'Rear and Boudart [75].

Table 6. Cyclohexene hydrogenation-dehydrogenation rates on Pt/SBA-15 nanoparticle encapsulation catalyst series [18].

Catalyst[a]	Hydrogenation			Dehydrogenation			Selectivity to C_6H_6[e] (%)
	Activity[b] ($\mu mol\, g^{-1}\, s^{-1}$)	TOF[b,c] (s^{-1})	E_a[d] ($kcal\, mol^{-1}$)	Activity[b] ($\mu mol\, g^{-1}\, s^{-1}$)	TOF[b,c] (s^{-1})	E_a[d] ($kcal\, mol^{-1}$)	
0.6% Pt(1.7 nm)/SBA-15	78.2	6.2	8.7	205.5	16.3	17	72.4
0.77% Pt(2.9 nm)/SBA-15	139.2	9.8	9.1	149.2	10.5	19.1	51.7
0.6% Pt(3.6 nm)/SBA-15	147.8	17.8	9.4	67.3	8.1	20.9	31.2
0.62% Pt(7.1 nm)/SBA-15	70.6	20.2	9.8	24.5	7.0	24.1	25.7

[a]Pt content determined by ICP–AES.
[b]Reaction conditions were 10 Torr C_6H_{10}, 200 Torr H_2, and 448 K.
[c]Normalized to the number of surface atoms determined by total H_2–O_2 titration.
[d]Reaction conditions were 10 Torr C_6H_{10}, 200 Torr H_2, and 273–323 K for hydrogenation (400–443 K for dehydrogenation).
[e]Selectivity at 448 K based on experimentally measured turnover frequencies (10 Torr C_6H_{10}, 200 Torr H_2).

Apparent activation energies are approximately double for the dehydrogenation reaction on most types of Pt catalysts [18,74]. Therefore temperature is the most straightforward variable to control selectivity. The temperature influences selectivity because of not only thermodynamic considerations, but also the influence of temperature on coverage drastically influences selectivity.

The kinetics of cyclohexene hydrogenation and dehydrogenation on the NE catalyst were examined. The temperature dependence of cyclohexene hydrogenation and dehydrogenation follow normal Arrhenius behavior at low temperatures but deviate at higher temperatures (i.e., inverse Arrhenius behavior). The inverse behavior is more subtle for the dehydrogenation pathway and because it occurs at temperatures where benzene is formed exclusively, it will not be presented in this discussion. The inverse Arrhenius behavior is attributed to a decrease in the hydrogen [76] or organic coverage [77]. It has also been proposed that a decrease in organic coverage led to inverse Arrhenius behavior during benzene hydrogenation over supported Fe [77] and cyclohexene hydrogenation over Pt(1 1 1) [78]. The temperature behavior of both reactions over a series of five Pt/SiO_2 catalysts including a highly dispersed Pt/SiO_2 catalyst [37] is shown in Figure 14. Apparent activation energies are a function of particle size for each reaction; low-temperature E_{app} for hydrogenation ranges from ~8.5 to 9.5 $kcal\, mol^{-1}$ and 17–24 $kcal\, mol^{-1}$ for dehydrogenation. The apparent activation energies and rates at 448 K are summarized in Table 6.

There is an apparent structure sensitivity (factor of ~3 difference for both reactions) with one increasing and the other decreasing with particle size. The temperature (448 K) is in the regime where the influence of particle size begins to become apparent. Figure 15 is an example of the *intrinsic* structure sensitivity for both reactions. At 310 K, we believe the surface is at high coverage (Ch and hydrogen), the hydrogenation rate is invariant with particle size, while the dehydrogenation rate (at 448 K, temperature at which the surface coverage is low) depends on particle size, by a factor of five over the size regime examined. The differences between rates (and therefore selectivity) shown in Figure 15 and Table 6 are due to thermodynamic consequence of adsorption that significantly influences the kinetic outcome. The hydrogenation rate becomes structure-sensitive at higher temperatures due to a particle size dependent H_2 coverage effect (see Figure 14).

4.4. Apparent Changes in Reaction Selectivity at Low Hydrogen Coverage

The selectivity during Ch hydrogenation at a slightly lower temperature (than mentioned in Table 6) is shown in Figure 16. The reported selectivities to benzene are significantly lower at 418 than 448 K.

For example, benzene selectivity on Pt(7.1 nm)/SBA-15 at 418 K is 4%, while at 448 K, it is 25%. While the differences in apparent activation energy account for some of this change, it cannot account for all of it. Both these temperatures fall within the region of inverse Arrhenius behavior; the bend-over behavior for hydrogenation at higher temperatures is attributed to a decrease in H_2 coverage. Thermodynamically, adsorption is an exothermic process and hydrogen adsorption is much more temperature sensitive than cyclohexene adsorption. Paál et al. suggested that the inverse Arrhenius behavior for *n*-hexane reforming catalysts is due to decreased a decrease in hydrogen coverage and the most appropriate way to determine activation energies is to measure the maximum rate at each temperature which we determined is a function of particle size [76]. For the series of Pt(X)/SBA-15 catalysts, Ch hydrogenation rates at lower temperature (i.e., 418 K) recover to a greater extent with H_2 pressure than 448 K (data not shown, see Ref. [18]). This suggests that the greater observable difference between selectivity at the two temperatures is a consequence of both the reaction kinetics (i.e., differences in *true* activation energy) and a hydrogen coverage effect, which is particle size dependent. The Arrhenius plots demonstrate the particle size dependence; the 7.1 nm has higher hydrogen coverage than the 1 nm particles at temperatures above 400 K.

This work demonstrates that selectivity is related to catalyst structure in a very complex way. In the case of Ch hydrogenation/dehydrogenation, it is the interaction of hydrogen rather than Ch that dictates the observed

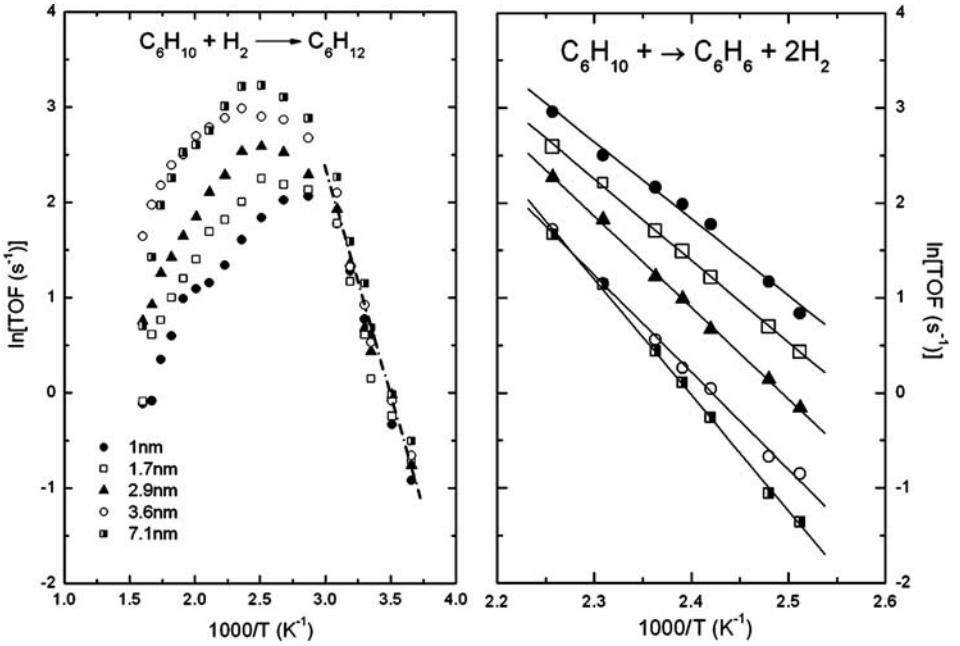

Figure 14. Arrhenius plots for cyclohexene (Ch) hydrogenation and dehydrogenation on Pt/SiO_2 catalysts. Inverse Arrhenius behavior is observed during both the hydrogenation and dehydrogenation. The inverse data for Ch dehydrogenation is not shown because it occurs at high temperatures where no cyclohexane is formed. For Ch hydrogenation, the inverse Arrhenius behavior leads to large changes in selectivity due to significant differences in hydrogen coverage with particle size under reaction conditions [18].

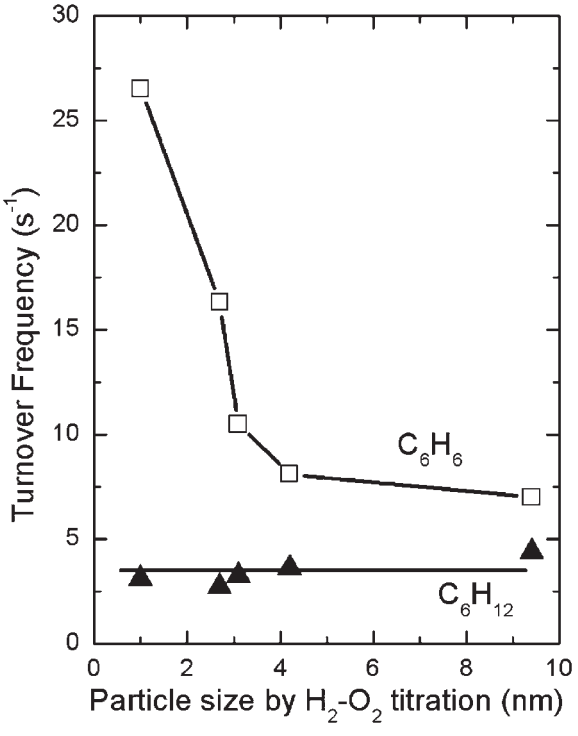

Figure 15. Turnover rate for cyclohexene hydrogenation and dehydrogenation as a function of particle size. Reaction conditions are 10 Torr C_6H_{10}, 200 Torr H_2, and 310 K for hydrogenation and 448 K for dehydrogenation, respectively [18].

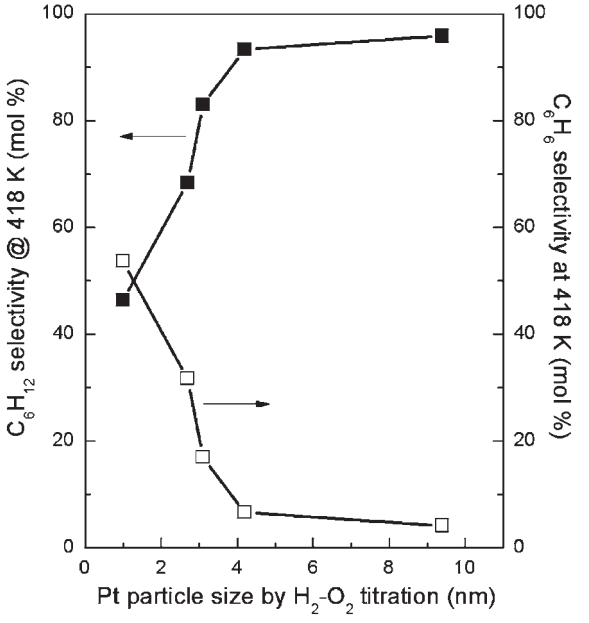

Figure 16. Selectivity to benzene and cyclohexane at 10 Torr C_6H_{10}, 200 Torr H_2, and 418 K [18].

selectivity on catalysts with different particle sizes. Studies continue in our laboratory to develop novel methods of catalyst design in order to understand the influence of particle size on reaction selectivity.

5. Summary

Two new methods of catalyst synthesis were developed with the intention of creating high surface-area catalysts with tunable properties. Pt nanoparticles with monodisperse particle size and/or controlled surface structure were chosen as the tunable variables for these novel catalysts. Colloidal Pt nanoparticles were synthesized by alcohol reduction methods in the presence of a surface protecting polymer, PVP, while shape-controlled Pt nanoparticles were reduced in solution in the presence of sacrificial metal ions and PVP. The addition of varying amounts of Ag to a polyol solution with a Pt precursor led to the selective formation of cubic, cuboctahedral, or octahedral Pt particles. The Pt particles are supported by three different methods. The first method based on LB film formation followed by lift-off of Pt nanoparticle monolayers onto a single crystalline silicon substrate served as high-density 2D nanoparticle array catalysts. Their catalytic properties were assessed with CO oxidation followed by SFG vibrational spectroscopy. The second and third method of catalyst preparation involved incorporating PVP-protected Pt nanoparticles into high surface area mesoporous silica by either inclusion in the mesopore channels with sonication or the hydrothermal growth and subsequent encapsulation of the silica matrix around the nanoparticles. Catalysts prepared by both methods were active for ethylene hydrogenation, although the NE series was more active due to a more effective pretreatment for PVP removal from the catalyst surface. Both catalyst series demonstrate structure sensitivity for ethane hydrogenolysis, although the effect was much greater on the encapsulated catalysts. Catalysts with smaller Pt particles were active for methane formation, but also more inclined to produce carbonaceous residues on the catalyst surface. A size influence on selectivity was observed during the hydrogenation–dehydrogenation of cyclohexene. In the case of dehydrogenation, this reaction is structure sensitive, while hydrogenation rates are invariant with particle size. Smaller particle sizes were much more active for dehydrogenation activity, exemplified by the lower apparent activation energies. The selectivity to benzene was a function of hydrogen pressure at a constant temperature and decreased for all particle sizes when the hydrogen pressure was increased. The synthesis of these catalysts is a general procedure that enables the construction of numerous metal/support systems for the study of structure-selectivity correlations in heterogeneous catalysis.

References

1 G. A. Somorjai, *Introduction to Surface Chemistry and Catalysis*, Wiley, New York, 1994.
2 G. A. Somorjai, Y. G. Borodko, *Catal. Lett*. 76 (2001) 1.
3 G. Ertl, *Angew. Chem. Int. Ed.* 15 (1976) 391.
4 G. A. Somorjai, A. M. Contreras, M. Montano, R. M. Rioux, *PNAS* 103 (2006) 10577.
5 D. R. Strongin, J. Carrazza, S. R. Bare, G. A. Somorjai, *J. Catal.* 103 (1987) 213.
6 K. R. McCrea, J. S. Parker, G. A. Somorjai, *J. Phys. Chem. B* 106 (2002) 10854.
7 Y. Borodko, G. A. Somorjai, *Appl. Catal., A* 186 (1999) 355.
8 P. S. Cremer, G. A. Somorjai, *J. Chem. Soc., Faraday Trans.* 91 (1995) 3671.
9 G. A. Somorjai, R. M. Rioux, *Catal. Today* 100 (2005) 201.
10 F. Zaera, *J. Phys. Chem. B* 106 (2002) 4043.
11 T. Teranish, M. Hosoe, T. Tanaka, M. Miyake, *J. Phys. Chem. B* 103 (1999) 3818.
12 Y. Wang, J. Ren, K. Deng, L. Gui, Y. Tang, *Chem. Mater.* 12 (2000) 1622.
13 R. M. Rioux, H. Song, J. D. Hoefelmeyer, P. Yang, G. A. Somorjai, *J. Phys. Chem. B* 109 (2005) 2192.
14 C. N. R. Rao, G. U. Kulkarni, P. J. Thomas, P. P. Edwards, *Chem. Eur. J*. 8 (2002) 29.
15 H. Song, F. Kim, S. Connor, G. A. Somorjai, P. Yang, *J. Phys. Chem. B* 109 (2005) 188.
16 H. Song, R. M. Rioux, J. D. Hoefelmeyer, R. Komor, K. Niesz, M. Grass, P. Yang, G. A. Somorjai, *J. Am. Chem. Soc.* 128 (2006) 3027.
17 R. M. Rioux, H. Song, M. Grass, S. Habas, K. Niesz, J. D. Hoefelmeyer, P. Yang, G. A. Somorjai, *Top. Catal.* 39 (2006) 167.
18 R. M. Rioux, B. Hsu, M. Grass, H. Song, P. Yang, G. A. Somorjai, to be published, 2007.
19 L. S. Ott, B. J. Hornstein, R. G. Finke, *Langmuir* 22 (2006) 9357.
20 B. Wiley, Y. G. Sun, Y. N. Xia, *Langmuir* 21 (2005) 8077.
21 F. Kim, S. Connor, H. Song, T. Kuykendall, P. Yang, *Angew. Chem. Int. Ed.* 43 (2004) 3673.
22 (a) U. Strüber, J. Küppers, *Thin Solid Films* 250 (1994) 101; (b) Th. Härtel, U. Strüber, J. Küppers, *Thin Solid Films* 229 (1993) 163.
23 S. Kwon, X. Yan, A. M. Contreras, J. A. Liddle, G. A. Somorjai, J. Bokor, *Nano Lett.* 5 (2005) 2557.
24 R. M. Rioux, T. J. Toops, M. Grass, K. Niesz, H. Song, J. D. Hoefelmeyer, P. Yang, G. A. Somorjai, to be submitted, 2007.
25 L. W. Beakley, S. E. Yost, R. Cheng, B. D. Chandler, *Appl. Catal., A* 292 (2005) 124.
26 J. S. Bradley, W. Busser, *Catal. Lett.* 63 (1999) 127.
27 S. J. Kweskin, R. M. Rioux, S. E. Habas, K. Komvopolous, P. Yang, G. A. Somorjai, *J. Phys. Chem. B* 110 (2006) 15920.
28 K. McCrea, J. S. Parker, P. Chen, G. Somorjai. *Surf. Sci.* 494 (2001) 238.
29 P. J. Berlowitz, C. H. F. Peden, D. W. Goodman, *J. Phys. Chem.* 92 (1988) 5213.
30 S. J. Kweskin, R. M. Rioux, S. E. Habas, K. Komvopolous, P. Yang, G. A. Somorjai, to be submitted, 2007.
31 U. Starke, A. Barbieri, N. Materer, M. A. Van Hove, G. A. Somorjai, *Surf. Sci.* 286 (1993) 1.
32 G. H. Hatzikos, R. I. Masel, *J. Vac. Sci. Technol., A* 5 (1987) 831.
33 J. P. Brunelle, *Pure Appl. Chem.* 50 (1978) 1211.
34 R. Schlogl, S. B. Abd Hamid, *Angew. Chem. Int. Ed.* 43 (2004) 1628.
35 D. Zhao, Q. Huo, J. Feng, B. F. Chmelka, G. D. Stucky, *J. Am. Chem. Soc.* 120 (1998) 6024.
36 J. E. Benson, M. Boudart, *J. Catal.* 4 (1965) 704.
37 U. K. Singh, M. A. Vannice, *J. Catal.* 191 (2000) 165.
38 J. R. Anderson, *Structure of Metallic Catalysts*, Academic Press, New York, 1975.

39 M. Boudart, *Adv. Catal*. 20 (1969) 153.
40 (a) R. D. Cortright, S. A. Goddard, J. E. Rekoske, J. A. Dumesic, *J. Catal.* 127 (1991) 342; (b) J. C. Schlatter, M. Boudart, *J. Catal.* 24 (1972) 482; (c) T. A. Dorling, M. J. Eastlake, R. L. Moss, *J. Catal*. 14 (1969) 23.
41 R. van Hardeveld, F. Hartog, *Surf. Sci*. 15 (1969) 189.
42 R. Campostrini, G. Carturan, R. M. Baraka, *J. Mol. Catal.* 78 (1993) 169.
43 R. Campostrini, G. Carturan, S. Dirè, P. Scardi, *J. Mol. Catal.* 53 (1989) L13.
44 C. Özmetin, M. Çopur, A. Yartasi, M. M. Kocakerim, *Ind. Eng. Chem. Res.* 37 (1998) 4641.
45 S. E. Habas, P. Yang, unpublished results, 2006.
46 R. C. Reuel, C. H. Bartholomew, *J. Catal*. 85 (1984) 78.
47 J. P. Brunelle, A. Sugier, J. F. Le Page, *J. Catal*. 43 (1976) 273.
48 P. Gallezot, D. Richard, *Catal. Rev. -Sci. Eng*. 40 (1998) 81.
49 B. Coq, F. Figueras, *Coord. Chem. Rev.* 178–180 (1991) 1753.
50 C. Mohr, H. Hofmeister, J. Radnik, P. Claus, *J. Am. Chem. Soc*. 125 (2003) 1905.
51 C. M. Pradier, T. Birchem, Y. Berthier, G. Cordier, *Catal. Lett*. 29 (1994) 371.
52 G. A. Martin, *J. Catal.* 60 (1979) 452.
53 J. L. Carter, J. A. Cusumano, J. H. Sinfelt, *J. Phys. Chem.* 70 (1966) 2257.
54 J. H. Sinfelt, W. F. Taylor, D. J. C. Yates, *J. Phys. Chem.* 68 (1965) 95.
55 L. Guczi, B. S. Gudkov, *React. Kinet. Catal. Lett.* 1–2 (1978) 95.
56 J. Barbier, A. Morales, R. Maurel, *Bull. Soc. Chim. Fr.* (1978) I31.
57 D. Nazimek, J. Ryczkowski, *React. Kinet. Catal. Lett.* 40 (1989) 145.
58 P. L. J. Gunter, J. W. H. Niemandsverdriet, F. H. Ribeiro, G. A. Somorjai, *Catal. Rev. -Sci. Eng.* 39 (1997) 77.
59 J. G. Goodwin, S. Kim, W. D. Rhodes, in J. J. Spivey (ed.) *Catalysis*, Vol. 17, Chapter 8, The Royal Society of Chemistry, Cambridge, U.K., 2004.
60 D. W. Goodman, *Surf. Sci.* 123 (1980) L679.
61 G. A. Martin, *Catal. Rev. -Sci. Eng.* 30 (1988) 519.
62 R. D. Cortright, R. M. Watwe, B. E. Spiewak, J. A. Dumesic. *Catal. Today* 53 (1999) 395.
63 B. S. Gudkov, L. Guczi, P. Tétényi, *J. Catal.* 74 (1982) 207.
64 R. M. Watwe, B. E. Spiewak, R. D. Cortright, J. A. Dumesic, *J. Catal.* 180 (1998) 184.
65 R. M. Watwe, R. D. Cortright, J. K. Nørskov, J. A. Dumesic, *J. Phys. Chem. B* 104 (2000) 2299.
66 J. Wei, E. Iglesia, *J. Phys. Chem. B* 108 (2004) 4094.
67 R. T. Vang, K. Honkala, S. Dahl, E. K. Vestergaard, J. Schnadt, E. Lægsgaard, B. S. Clausen, J. K. Nørskov, F. Besenbacher, *Nat. Mater.* 4 (2005) 160.
68 J. Hoffman, I. Meusal, J. Hartmann, J. Libuda, H. J. Freund, *J. Catal.* 204 (2001) 378.
69 F. J. Rivera-Latas, R. A. Dalla Betta, M. Boudart, *AIChE J.* 38 (1992) 771.
70 F. Zaera, G. A. Somorjai, *Langmuir* 2 (1986) 686.
71 J. A. Rodriguez, D. W. Goodman, *J. Phys. Chem.* 94 (1990) 5342.
72 F. Zaera, G. A. Somorjai, *J. Am. Chem. Soc.* 89 (1985) 3211.
73 J. M. Parera, N. S. Figoli, E. M. Traffano, J. N. Beltramini, E. E. Martinelli, *Appl. Catal.* 5 (1983) 33.
74 K.R. McCrea, G.A. Somorjai, *J. Mol. Catal. A: Chem.* 163 (2000) 43.
75 D. J. L. O'Rear, M. Boudart, *J. Catal.* 94 (1985) 225.
76 (a) Z. Paál, *J. Catal.* 91 (1985) 181; (b) Z. Paál, P.G. Menon, *Catal. Rev.-Sci. Eng.* 25 (1983) 223.
77 K. J. Yoon, M. A. Vannice, *J. Catal.* 82 (1983) 457.
78 M. Yang, R. M. Rioux, G. A. Somorjai, *J. Catal.* 237 (2006) 255.

CHAPTER 8

Metal Nanoclusters in Catalysis: Effects of Nanoparticle Size, Shape, and Structure

F. Klasovsky and P. Claus

Ernst-Berl-Institute/Chemical Technology II, Darmstadt University of Technology

1. General Considerations

1.1. Heterogeneous Catalysis and the Concept of Structure Sensitivity

In the majority of reactions in chemical industry, high product yields stem from the involvement of catalytic processes, either in a homogeneous or heterogeneous fashion. Whereas the homogeneous operation mode suffers from, for example, higher catalyst losses, heterogeneous catalysis offers a much more convenient separation of products and catalyst. Mostly in terms of bulk oxides or supported metal catalysts, they are therefore applied in the fabrication of a wide range of products like, for example, fine chemicals, plastics, and fertilizers or reduction of environmental pollution by cleaning up automotive exhaust gases in three-way catalytic converters.

Despite its widespread implementation for decades, heterogeneous catalysis increasingly attracts flourishing research activities. Mainspring of new developments in this field is the simple fact that most industrial catalytic reactions still do not proceed efficiently. Present and future challenges lie in the sectors of ecology (waste avoidance and reduced consumption of feedstocks), efficiency (energy-saving and highly selective processes with high atomic economy), as well as profitability (creation of processes of high space velocity).

Examples for necessary process improvements through catalyst research are the development of one-step processes for a number of bulk products like acetaldehyde and acetic acid (from ethane), phenol (from benzene), acrolein (from propane), or allyl alcohol (from acrolein). For example, allyl alcohol, a chemical which is used in the production of plasticizers, flame resistors and fungicides, can be manufactured via gas-phase acetoxylation of propene in the Hoechst [1] or Bayer process [2], isomerization of propene oxide (BASF-Wyandotte), or by technologies involving the alkaline hydrolysis of allyl chloride (Dow and Shell) thereby producing stoichiometric amounts of unavoidable by-products. However, if there is a catalyst capable of selectively hydrogenate the carbonyl group of acrolein (leaving the olefinic double bond intact), allyl alcohol can be manufactured in a one-pot synthesis. Unlike in the preceding decades (industrial research), the development of highly selective heterogeneous catalysts nowadays (in academia) is often accompanied by the search for the reactions' underlying processes and mechanisms. Numerous investigations have increased the understanding of catalyzed reactions on a molecular base and resulted in a spectrum of general, theoretical concepts [3].

Typically, supported metal catalysts are used in order to hydrogenate or oxidize the educt to the desired compound. Such catalysts often contain a metal (for example, 0.5–5 wt.%), which was deposited on the surface of a support (e.g., SiO_2, Al_2O_3, TiO_2, zeolites, activated carbon) by means of an appropriate catalyst synthesis procedure (Figure 1).

Since heterogeneous catalysis is a phenomenon which is exclusively based on the reactivity of surface atoms, a high fraction of the latter, exposed towards reactants, is desired. This demand can be equated with a high degree of dispersion of the metal or a very small particle size, that is, in the lower nanometer range of approximately 1–5 nm.

Attempts to determine how the activity of the catalyst (or the selectivity which is, in a rough approximation, the ratio of reaction rates) depends upon the metal particle size have been undertaken for many decades. In 1962, one of the most important figures in catalysis research, M. Boudart, proposed a definition for structure sensitivity [4,5]. A heterogeneously catalyzed reaction is considered to be structure sensitive if its rate, referred to the number of active sites and, thus, expressed as turnover-frequency (TOF), depends on the particle size of the active component or a specific crystallographic orientation of the exposed catalyst surface. Boudart later expanded this model proposing that structure sensitivity is related to the number of (metal surface) atoms to which a crucial reaction intermediate is bound [6].

According to Bond [7] and Burch [8], structure-sensitive reactions can be divided into four categories, thereby broadening the original classifications built by

Metal Nanoclusters in Catalysis and Materials Science: The Issue of Size Control
Edited by B. Corain, G. Schmid and N. Toshima

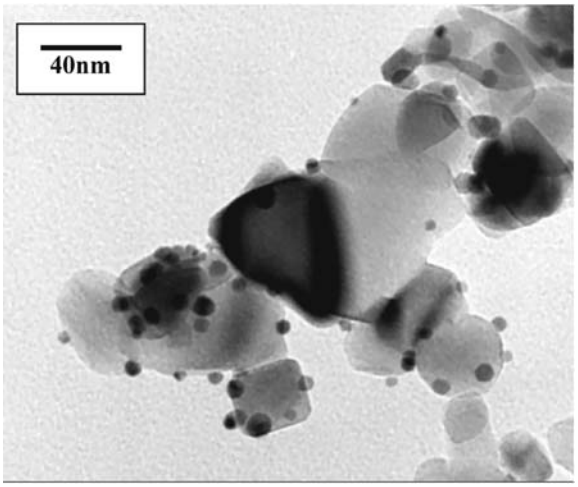

Figure 1. TEM image of a titania supported gold catalyst (1.7 wt.% Au) prepared by deposition-precipitation (gold particle size = 5.3 ± 0.3 nm, dispersion = 36%). (Reprinted from Reference [84], © 2000, with permission from American Chemical Society).

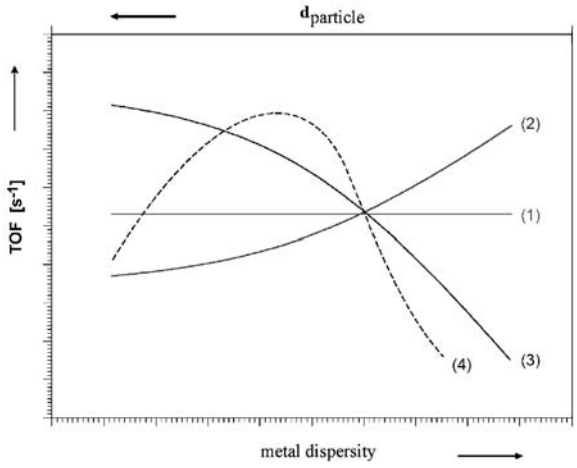

Figure 2. Structure-insensitive reaction (1), sympathetic (2)/antipathetic structure sensitivity (3), and TOF reaching a maximum with varying particle size (4) [9].

Boudart [4]: TOFs can either be independent of particle size (structure-insensitive reactions), increase (antipathetic structure sensitivity) or decrease (sympathetic structure sensitivity) with growing particle size, or cross a maximum (Figure 2).

Structure sensitivity is not a single phenomenon but can often be regarded as a set of independent, but interlinked mechanisms. At the very beginning it is important to realize that the term particle size effect (PSE) not only refers to the size of active component particles but moreover comprises effects deriving from peculiarities in their morphology, that is, their shape and structure.

Before investigating the effect of size, shape, and structure on catalytic behavior, that is, TOFs, a set of five requirements concerning the metal particles has to be met. Besides a monodisperse size distribution, the nanoparticles should be fully reduced, unpoisoned, unperturbed by the carrier gas, and unpromoted (Che and Bennett [9]). Note, that the labels "structure-sensitive" and "structure-insensitive" are an oversimplification which can be overcome, according to Bond [10], by the more useful "degree of structure sensitivity". However, discussing the issue of particle-size effects on the catalyst performance it must be kept in mind that size reduction of metal particles results in the formation of nanoparticles having short-range order and metastable state.

This review covers the personal view of the authors deduced from the literature starting in the middle of the Nineties with special emphasis on the very last years; former examples of structure-sensitive reactions up to this date comprise, for example, the Pd-catalyzed hydrogenation of butyne, butadiene, isoprene [11], aromatic nitro compounds [12], and of acetylene to ethylene [13]. In contrast, benzene hydrogenation over Pt catalysts is considered to be structure insensitive [14]; the same holds true for acetonitrile hydrogenation over Fe/MgO [15], CO hydrogenation over Pd [16], and benzene hydrogenation over Ni [17]. For earlier reviews on this field we refer to Coq [18], Che and Bennett [9], Bond [7], as well as Ponec and Bond [20].

1.2. Phenomenological Descriptions of Structure Sensitivity

Structure sensitivity can be easily detected by relating observed TOF with the dispersion D of metal nanoparticles (of size R) present in a catalyst. According to early approaches from Farin and Avnir [21,22], these factors can be connected using the reaction dimension DR and a new constant k:

$$\log\ \mathrm{TOF} = \log\ k + (\mathrm{DR} - 2)\log\ R$$

In 1997, Arai [23] simplified this equation introducing more plausible parameters. Structure sensitivity exists, if the dependence of observed TOF on the particles' dispersion D can be described by a linear relation with the (non-zero) slope n and the ordinate log TOF*, the latter standing for TOF at an extreme of $D = 1$ (two-dimensional metal islands):

$$\log\ \mathrm{TOF} = \log\ \mathrm{TOF}^* + n \log\ D$$

Applying this equation to the results obtained by Bond [7] for n-butane hydrogenolysis over 0.5 wt.% Ru/SiO_2, Arai elucidated that the activity of two-dimensional Ru islands on a distinct support is independent of the preparation method. Depending on the support, either positive (SiO_2) or negative (Al_2O_3) structure sensitivities (i.e., positive or negative slopes) can be observed which can, for the case of alumina, be traced back to an electronic manipulation of Ru by residual Ru^{x+} species and the formation of an Al–Ru alloy.

1.3. Preparation of Catalysts with controlled Size, Shape and Structure

As mentioned before, heterogeneous catalysts (except unsupported ones) consist of mono-/bi-/multimetallic

metal nanoparticles or a mixture of them, supported on (in-) organic solid materials. Typical metals comprise the light (i.e., Ru, Rh, Pd) and heavy (i.e., Os, Ir, Pt) platinum metals as well as the iron metals (i.e., Fe, Co, Ni). To a lesser extent, the coinage metals (i.e., Cu, Ag, Au) and other less frequently used elements like Re (→Rheniforming) or Y (in bimetallic catalysts) are applied in industrial or academic catalysis. Whereas in industry only a small number of support materials are in fact used (SiO_2, Al_2O_3, TiO_2, active carbon), "academic catalysts" offer a wide spectrum of oxidic (e.g., ZnO [24], MgO [25], ZrO_2 [26], CeO_2 [27], Fe_2O_3 [28]), other inorganic (e.g., TiO_xN_y [29]) and organic materials (e.g., polymers [30], carbon nanotubes [31], or polyaniline [32]).

The identification of structure sensitivity would be both impossible and useless if there did not exist reproducible recipes able to generate metal nanoparticles on a small scale and under controlled conditions, that is, with narrow size and/or shape distribution onto supports. Metal nanoparticles of controlled size, shape, and structure are attractive not only for catalytic applications, but are important, for example in optics, data storage, or electronics (c.f. Chapter 5). In order not to anticipate other chapters of this book (esp. Chapter 2), remarks will therefore be confined to few examples.

The most frequently used preparation techniques for heterogeneous precious metal catalysts include impregnation (wet or incipient wetness), deposition and (co-) precipitation techniques as well as the deposition of preformed colloids. Whereas with the first technique investigations on attainable particle shapes and structures are scarce, the latter offers the opportunity to investigate shape-selective particle formation without interference of the (rather complex) support materials. Accordingly, Pd nanoparticles are affordable either as cuboctahedra (3.2–3.6 nm) [33] or as platelets with [1 1 1]-Faces [34], and detailed investigations on the shape-determining factors have been performed by Liew [35]. Comparable efforts have been undertaken with platinum [36], silver [37], and gold [38].

The following sections will give a showcase overview of structure-sensitive reaction classes highlighting some of the most recently investigated catalytic systems. They are grouped on the basis of the following reaction classes: hydrogenation, oxidation, C–C coupling, and cleavage reactions.

2. Hydrogenation Reactions

2.1. Hydrogenation of CO to Methanol over ZnO

Besides supported (transition) metal catalysts, structure sensitivity can also be observed with bare (oxidic) support materials, too. In 2003, Hinrichsen et al. [39] investigated methanol synthesis at 30 bar and 300 °C over differently prepared zinc oxides, namely by precipitation, coprecipitation with alumina, and thermolysis of zinc siloxide precursor. Particle sizes, as determined by N_2 physisorption and XRD, varied from 261 nm for a commercial material to 7.0 nm for the thermolytically obtained material. Plotting the areal rates against BET surface areas (Figure 3) reveals enhanced activity for the low surface area zinc

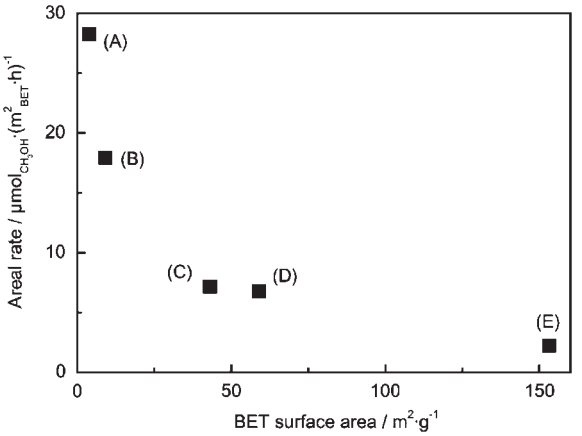

Figure 3. Activity of powdered ZnO samples employed in MeOH synthesis ($p = 30$ bar, $T = 573$ K, $Q = 10$ mL/min [64% H_2, 8% CO_2, 6% CO, 22% He]). Particle diameters of the different batches of ZnO decrease from batch A to E. (Reprinted from Reference [39], © 2003, with permission from Royal Society of Chemistry).

oxides (i.e., those exhibiting larger particles). Based on both EXAFS and TEM investigations, preponderance of highly crystalline, polar surfaces on the larger particles was made responsible for the observed phenomenon.

2.2. Hydrogenation of Monoalkenes

Heterogeneously catalyzed hydrogenation of alkenes is generally considered to be a structure-insensitive reaction, as was deduced from numerous studies on more or less complex model catalyst systems [40–54]. However, the following sections will give examples of the opposite case.

2.2.1. Propene Hydrogenation over Pt–Au/TiO_2

A study concerning the lowermost particle size necessary for admitting a reaction to occur is provided by Amiridis et al. [55] in their investigations of propene hydrogenation. For metal particle sizes greater than 2 nm, hydrogenation of simple olefins is considered to be structure insensitive [56]. Comparing bimetallic Au–Pt catalysts prepared by either co-impregnation (H_2PtCl_6 and $HAuCl_4$) or from a heterobimetallic precursor ($Pt_2Au_4(CC'Bu)_8$), initial TOFs in Amiridis' study differed by almost three orders of magnitude. A combination of TEM and CO adsorption studies revealed real bimetallic nanoparticles with a uniform size distribution for the latter, cluster-derived catalyst, exhibiting a surface containing only about 15 at.% platinum. Referring to investigations on the minimum Pt ensemble size necessary for olefin hydrogenation (provided by Bond [57]), Amiridis followed that also in propene hydrogenation over Pt–Au/TiO_2 a minimum ensemble of Pt atoms is necessary for a successful concomitant adsorption of olefin and hydrogen. However, beside this dilution effect of gold on the bimetallic particles, an electronic impact can not be excluded. An application of Amiridis'

cluster-derived catalysts in oxidation reactions will be discussed in Section 3.1.

2.2.2. *trans*-2-Pentene Hydrogenation over Pd/Al_2O_3

Whereas alkene hydrogenation is generally considered to be a structure-insensitive reaction, Shaikhutdinov et al. [58] recently reported on structure sensitivity during the hydrogenation of *trans*-2-pentene over an alumina-supported Pd model catalyst. With the help of TPD measurements, interaction between substrate and metal was shown to occur via a di-σ bound mode which is enhanced on particle terraces. Consequently, desorption temperatures of the deuterated products increase with decreasing particle size, as this type of surface site dominates on larger particles. In contrast, π-bound ethene is assumed to be the active species for ethene hydrogenation. Such coordination is provided by both terraces and low-coordinated surface sites thereby corroborating the experimentally observed structure insensitivity.

2.3. Hydrogenation of Dienes: 1,3-Butadiene

Structure sensitivity of 1,3-butadiene hydrogenation was recently investigated by Rupprechter et al. [59] on well-defined $Pd/Al_2O_3/NiAl(1\,1\,0)$ single crystals.

Applying evaporation methods under UHV conditions, Pd particle sizes in the range between 2 and 8 nm could be obtained, corresponding to dispersions of 61 to 16%, respectively. For all the investigated catalysts and until full conversion, the observed exclusive formation of butenes could be explained assuming stronger adsorption of 1,3-butadiene compared with the butenes. Initial conversion rates were linear in time due to an adsorption/desorption-limited regime, whereas the obvious preference of 1,2-hydrogenation compared to 1,4-hydrogenation typical for smaller particles still requires interpretation. As electronic reasons should be ruled out for Pd particles > 3 nm [59], the observed linear dependence of TOF on particle size over the whole size range was traced back to two different effects. The reaction was proved to be particle size independent for $d_{Pd} \geq 4$ nm; in this regime, TOFs, normalized by number of Pd surface atoms within incomplete (1 1 1) facets, turned out to be constant. For $d_{Pd} < 4$ nm, the effect of an increasing normalized TOF is outweighed by decreasing portion of this kind of surface sites.

2.4. Selective Hydrogenation of Alkynes to Alkenes

As described above, Shaikhutdinov [58] proved pentenes reacted faster on larger particles. In the case of alkynes, some cases of structure sensitivity over Pd catalysts were reported earlier [11,60–62]. An interesting aspect in this regard was the observation, that selective hydrogenation to the respective alkene was in the case of propyne [11] and butyne [61,63,64] accompanied by distinct carbon deposition. Interesting investigations on the hydrogenation of the homologue 1-pentyne over Pd catalysts were performed recently by Teschner et al. [65], bringing hereby the aforementioned aspects in causality. Investigating pulse hydrogenation and catalyst mass change after continuous hydrogenation, a significant uptake of carbon by the Pd metal could be denoted which confirms earlier results obtained with XRD [66] and DFT [67] methods. Using *in-situ* XPS measurements, Teschner could detect adsorbed carbonaceous species during the hydrogenation on Pd foil and 5 wt.% Pd/CNT (Figure 4(b) and (c)).

According to a depth-profiling XPS experiment, the carbonaceous species were confined to a 3-Å-thick layer on a 14-Å-thick Pd–C surface which could be formed only at low $p(H_2)$ or low H_2/pentyne ratio. A model was derived which describes the palladium surface to consist of three Pd–C double layers on Pd bulk with subsurface and dissolved carbon and hydrogen, respectively (Figure 5). It could be shown in the hydrogenation experiments that this Pd–C surface phase effectively suppresses the emergence of bulk-dissolved hydrogen by either complete elimination or at least mitigation. As such hydrogen is highly reactive and unselective, the presence of a Pd–C-''sealing'' strongly enhances selectivity to pentene.

According to further XPS experiments (Figure 4(a)), such a ''sealing'' cannot be formed on Pd(1 1 1), which is in total accordance with the facts that the necessary carbon–carbon bond breaking has been shown to be structure-sensitive [68,69], and carbon diffusion into the bulk of Pd(1 1 1) is energetically unfavorable [67]. In conclusion it is clear that Pd catalysts exhibiting particles confined only or mainly by (1 1 1) surfaces can not selectively hydrogenate 1-pentyne to 1-pentene.

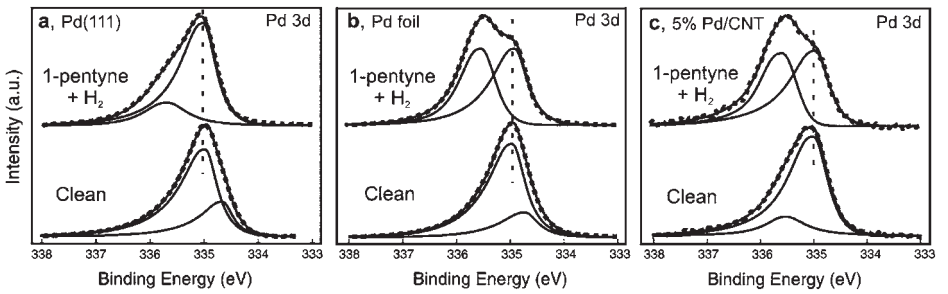

Figure 4. Pd $3d_{5/2}$ binding energies of (a) Pd(1 1 1), (b) Pd foil, and (c) 5% Pd/CNT in the reaction mixture of 0.85 mbar H_2 + 0.05 mbar 1-pentyne at 358 K. (Reprinted from Reference [65], © 2006, with permission from Elsevier).

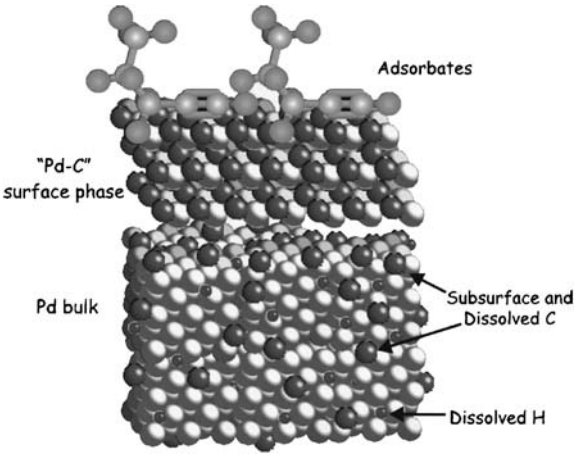

Figure 5. Model of the palladium surface during 1-pentyne hydrogenation. (Reprinted from Reference [65], © 2006, with permission from Elsevier).

2.5. Hydrogenation of Simple Carbonyl Compounds: Acetone over Cu/SiO_2

An intriguing example for TOF reaching a maximum with variation of particle size is reported by Vannice et al. [70], who investigated acetone hydrogenation over silica-supported copper catalysts (prepared via incipient wetness and impregnation techniques, respectively), copper chromite, and pure copper powder. While significant deactivation was observed for the reaction at 423 K, a clear increase in initial TOFs with growing Cu particle sizes could be detected up to a size of 110 nm. A 20 wt.% catalyst exhibiting 176 nm Cu particles again showed a reduced TOF. Structure sensitivity in this elevated range of particle size was already observed earlier by Che and Bennett [9] for CO hydrogenation and ethylene partial oxidation over Ag catalysts. As Burch [8] demonstrated, classic explanations for this behavior fail, given that both geometrical (ratio of sites with different coordination environment) and electronic properties (e.g., DOS, ionization potential, binding energies) only change negligibly with respect to bulk metal from a particle size of 5 nm onwards. In the case of Vannices' catalysts, investigation by a microwave frequency cavity absorption technique, however, provides hints for the influence of the Cu nanoparticles' electric conductivity on their catalytic behavior. Unfortunately, no data validating or disapproving this assumption on a physico-chemical basis can be provided.

2.6. Hydrogenation of α,β-Unsaturated Organic Compounds

2.6.1. Selective Hydrogenation of α,β-Unsaturated Aldehydes

The selective hydrogenation of α,β-unsaturated aldehydes to allylic alcohols (desired products) and/or saturated aldehydes is of commercial relevance, as mentioned in the introduction, and has been attracting much interest for fundamental research in catalysis. This reaction offers an exemplar of catalyst influence on regioselective reactions (Figure 6). Among the competing attack on either the C=C double bond or the carbonyl group, the first one is favored with most metals (Pt, Rh, Pd, or Cu) due to kinetic and thermodynamic reasons [71–73] (free reaction enthalpy lower by 35 kJ/mol). Moreover, formation of the saturated aldehyde from the unsaturated alcohol is possible via an isomerization reaction.

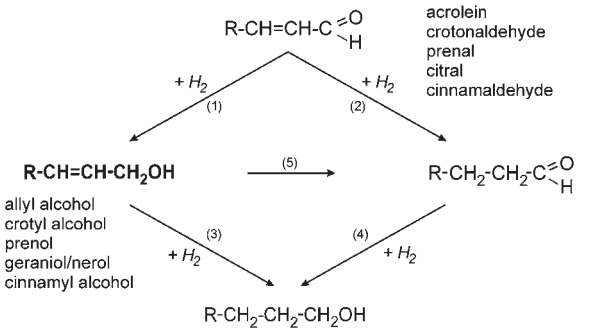

Figure 6. Reaction network of the hydrogenation of α,β-unsaturated aldehydes.

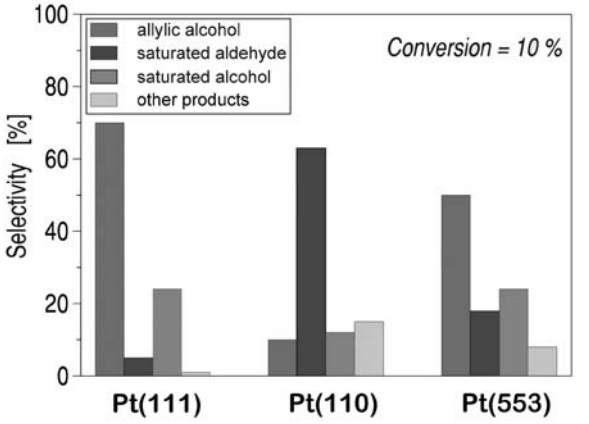

Figure 7. Structure-sensitivity of prenal (3-methyl-crotonaldehyde) hydrogenation over Pt single crystals ($p_{H2} = 200$ Torr, $p_{prenal} = 0.007$ Torr, $T = 353$ K) [74].

Hydrogenation of prenal (3-methyl-crotonaldehyde) in the gas phase over platinum single crystals is an expressive example for a structure-sensitive reaction of a complex molecule (Figure 7). On Pt (1 1 1) at 353 K the main product is the unsaturated alcohol, whereas on the Pt (1 1 0) crystal face just the saturated aldehyde and the saturated alcohol are formed. The (1 1 1) crystal face builds up a closed packed structure, so that the accommodation of the two methyl groups is hindered. In contrast, the corrugated (1 1 0) crystal face enables the activation of the whole conjugated system of the molecule followed by 1,4-addition of hydrogen. Prenal hydrogenation on the Pt(5 5 3) surface with (1 1 1) terraces and steps lowered the yield of unsaturated alcohol compared to Pt (1 1 1), since steric constraints are less stringent on stepped surfaces [74–77].

However, in the literature controversial discussions about the issue of structure sensitivity can be found which are further complicated by an (apparent) dependency on the structure of the organic substrate and the support material. For example, Citral [78,79] and crotonaldehyde [80,81] hydrogenation over Pt catalysts and acrolein hydrogenation over Ag [82,83] and Au [84,85] catalysts was stated to be structure sensitive whereas platinum-catalyzed crotonaldehyde hydrogenation was not [86]. More precisely, citral hydrogenation is a structure-sensitive reaction, since TOF first increases with increasing Pt particle diameter in the range of 1–5 nm and then just changes to a minor degree in the particle diameter range of 5–30 nm [78]. Besides TOF, the particle diameter can also influence the selectivity of a reaction giving rise to a structure-sensitive selectivity behavior. As an example, the selectivity in crotonaldehyde hydrogenation to the unsaturated alcohol increases with increasing metal particle size over Pt catalysts [80], whereas smaller metal particles favor the hydrogenation of the olefinic double bond. The effect can be explained in terms of decreased electron density of the d-orbitals with decreasing metal particle size, so that the repulsive four electron interaction between the metal surface and the C=C double bond decreases. Furthermore, as particle size decreases, the amount of edges and corners of the particle increases and it was concluded that this allows unconstrained adsorption of both double bonds in crotonaldehyde. In contrast, with increasing Pt particle sizes, the fraction of Pt(1 1 1) crystal faces increases favoring the selective hydrogenation of the C=O double bond. The impact of metal particle size on the selectivity was also shown in liquid-phase hydrogenation of cinnamaldehyde over carbon and graphite supported Pt catalysts [87–89]. Again an increase in selectivity to the unsaturated alcohol could be observed with increasing metal particle size which can be rationalized by different adsorption geometries of cinnamaldehyde over Pt depending on the metal particle size. With increasing metal particle size the steric repulsion of the phenyl group and the metal surface increases, hindering the adsorption of the olefinic double bond on the metal surface. As a matter of fact similar structure sensitivity was not observed for citral hydrogenation [90], and hydrogenation of this substrate over Ru/Al_2O_3 at 333 K provides an example of a structure-insensitive reaction [91].

In the hydrogenation of acrolein over Ag/TiO_2 catalysts, the effect of both, decreasing particle size (1.5 nm after reduction at 773 K (HTR) vs. 3 nm after reduction at 473 K (LTR)) and increasing particle coverage by several atomic layers thick TiO_x, as obtained by HTR resulted in a decrease of the catalyst activity and selectivity to allyl alcohol (from ~42% to ~27%) [83]. This behavior and the absence of Ti^{3+} at the very catalyst surface point to the fact that, different from the case of catalysts like Pt/TiO_2 [86], TiO_x/Ti^{3+} species do not act as special sites for the carbonyl group activation with Ag/TiO_2 catalysts. Furthermore, the catalytic activity and selectivity to crotyl alcohol increased with increasing Ag particle size showing that also crotonaldehyde hydrogenation is structure-sensitive [82]. These studies led to the conclusion that the active sites issue of Ag/TiO_2 catalysts exhibiting a truncated Ag particle morphology deviating from the spherical shape must be addressed to other structural features like faceting, multiple twinning, or even selective coverage by TiO_x.

Over Au/TiO_2 catalysts, although they were prepared by three different preparation methods, a similar antipathetic structure sensitivity was also observed for acrolein hydrogenation which was explained in terms of quantum size effects below 2 nm altering the electronic properties of the metal [84]. However, by applying the same preparation method of deposition–precipitation, using various pHs in order to obtain Au/ZrO_2 catalysts with various gold particle sizes (4.0, 6.9, and 7.7 nm), structure-sensitivity was found in a way that the TOF decreased by nearly one order of magnitude, and the selectivity to allyl alcohol was increased from 15 to 35% with increasing particle size [85].

Structure sensitivity may have its core in the ability of nanostructured matter to occur in metastable non-equilibrium structures, for example as coordinatively unsaturated sites (e.g., edges, kinks) induced by rough surfaces, as matter with lattice strain or multiple twinned particles (MTPs) [92]. The question arises how the hydrogenation properties of gold catalysts are influenced by these nanoscale properties of gold. The influence of the pretreatment of a 2.2 wt.% Au/ZrO_2-DP catalyst in H_2 on nanostructure and catalytic properties during acrolein hydrogenation in the gas phase was established by correlating HRTEM and catalytic results [85]. It was shown that a higher amount of MTPs resulted in a lowering of selectivity to the desired product allyl alcohol (Table 1), and also the TOF was decreased.

Therefore, the main demand for catalyst synthesis was that supported gold catalysts with single crystalline gold particles must be prepared to obtain higher selectivities to the unsaturated alcohol. Moreover, the higher activity of Au/TiO_2 compared to that of Au/ZrO_2 was attributed to the fact that the gold particles (average particle size of ca. 5 nm on both supports) were round shaped on TiO_2 and facetted on ZrO_2 [85]. This is in agreement with the finding that the proportion of low-coordinated sites is much lower after pretreatment at 773 K than at 473 K, and the decrease in catalytic activity and TOF, observed in crotonaldehyde hydrogenation [93] when the reduction temperature increases from 473 K to 773 K, is attributed to the smoothing of the outer surface of the gold particles, that is, to the decrease in the number of low-coordinated sites. The selectivity to crotyl alcohol, in the 5–50%

Table 1. Changes of nanostructure and catalytic properties during acrolein hydrogenation in the gas phase[1] after pretreatment of a ZrO_2 supported gold catalyst[2] with H_2 (taken from [85]).

	T_{red} [K][3]	573	573	723
	t_{red} [h][4]	3	18	3
d_{Au} [nm]		7.7	9.2	8.3
Rel. amount MTPs [%]		25	54	30
Selectivity to allyl alcohol [%]		35	20	37
TOF [/s]		0.045	0.022	0.045

[1] $T = 513$ K, $p_{total} = 2$ MPa, molar ratio $H_2/Ac = 20$, $W/F^0_{CA} = 15.3$ g h/mol.
[2] 2.2 wt.% Au/ZrO_2-DP.
[3] Reduction temperature.
[4] Reduction time.

conversion range, was 60–70% and independent of the reduction temperature, and almost constant as a function of the particle size.

The problem of relating particle-size effects with the observed catalytic properties can be seen from a recently published study of Abid et al. [94], who investigated the hydrogenation of crotonaldehyde over ceria-supported platinum (prepared by an incipient wetness technique using $Pt(NH_3)_4(NO_3)_2$). Currently, several reasons for observed preference of either butanal or crotyl alcohol reaction products in this system are up to discussion, namely formation of Pt–Ce- alloys, particle decoration with unreduced ceria or electronic effects of partially reduced ceria [95–97]. Abid investigated in detail the influence of both loading and reduction temperature on activity and selectivities. Using in-depth characterization by HRTEM and XPS, epitaxial growth of Pt(1 1 1) on CeO_2(1 1 1) (separated by a thin layer of $CePt_5$ (1 1 1)) was detected, resulting in an expansion of Pt(1 1 1) lattice parameter by 3.3%. Yet without theoretical proofs, it was deduced that this expansion, observed on cuboctahedral moirée particles, is responsible for an enhanced adsorption of the carbonly group affording the hydrogenation to crotyl alcohol. According to Abid, species comparable to the Pt–TiO_x interfacial sites described by Sen and Vannice [98] are of minor influence, as they lead to blocking of active sites for both crotyl alcohol and butanal formation. This hypothesis is supported by the low activity of low loaded 1 wt.% Pt/CeO_2 where the interface between Pt and reduced support species should be maximal due to the small metal particle size. As a result, the observed dependence of selectivities on the Pt nanoparticle size stems from a size-dependent strong-metal-support interaction (SMSI) between platinum and the CeO_2 support.

While changes of the morphology of the metal particles (rounded, facetted, single crystalline, multiply twinned particles) and, thus, the catalytic properties can be induced by appropriate pretreatment conditions of the catalyst (see above), the relative amount of various surface sites (edges, corners, and faces) can be influenced by depositing a second metal exclusively on the parent metal giving rise to a principle change of the nanoparticle structure. This approach was successful when indium was added to zinc oxide supported gold nanoparticles ($d_{Au} = 9$ nm) [99] where a statistically proven selective decoration of gold particle faces has been observed by detailed HRTEM analysis, leaving edges free (Figure 8).

EDX analysis revealed a homogeneous distribution of indium on the gold particles, and no monometallic indium deposits were found. With a bimetallic Au–In/ZnO catalyst used for acrolein hydrogenation, the desired allyl alcohol was the main product formed with a high selectivity of 63% (at $T = 593$ K and $p_{total} = 2$ MPa). From the experimentally proven correlation between surface structure and catalytic data of Au/ZnO and Au–In/ZnO, including site-time-yields for the formation of the individual products, the edges of single crystalline gold particles have been identified as active sites for the preferred C=O hydrogenation [98]. The Au–In system is the first example showing the important impact of a second metal for tuning the selectivity of a gold catalyst in selective hydrogenation of functional groups.

However, it should be noted that the structure of those bimetallic particles (Ag–In) can be changed under the conditions of the catalytic reaction, that is, in presence of the reactants, as recently shown by *in situ* X-ray absorption spectroscopy of acrolein hydrogenation [100].

2.6.2. Hydrogenation of Allyl Alcohol

An example of structure sensitivity for unsupported palladium nanoparticles is provided by Crooks et al. [101] in their investigations concerning the hydrogenation of allyl alcohol in a liquid phase process. Applying Pd colloids stabilized by sixth-generation hydroxyl-terminated polyamidoamine dendrimers (G6-OH), a clear dependence of hydrogen conversion on the particle size could be detected while keeping the total amount of Pd constant. Based on calculations of the number of surface, face and defect (vertex and edge) atoms, normalized TOFs were computed for each of these surface site types. Above particle diameters of 1.5 nm, zero slope of the TOFs for faces revealed these sites to be the preferred ones for allyl alcohol hydrogenation. Accordingly, in this range structure sensitivity is based on geometric reasons. An increase in face-site TOFs with decreasing particle size below this limit should, according to Crooks, be founded on electronic effects.

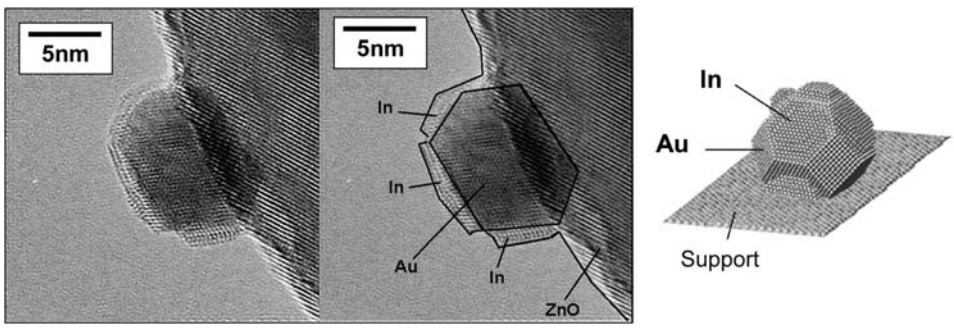

Figure 8. HRTEM image of Au–In/ZnO (left), and surface model (right). Indium preferentially decorates the outer faces of the gold particles while the edges remain uncovered. (Reprinted from P. Claus, *Appl. Catal. A: General* 291 (2005) 222, © 2005, with permission from Elsevier).

2.7. Hydrogenation of Glucose

An example for a non-structure-sensitive reaction is provided by Davis et al. [102], who investigated the liquid-phase hydrogenation of glucose over carbon and silica based ruthenium catalysts with particle sizes between 1.1 and 2.4 nm. Depending on catalyst loading which was between 0.56 wt.% and 5 wt.%, dispersion decreased from 91% to 43%. At the same time, TOFs varied only insignificantly in a range between 0.21 1/s and 0.32 1/s.

3. Oxidation Reactions

3.1. Oxidation of Propene over $AuPt/SiO_2$ and Pt/SiO_2

As discussed in Chapter 2.2.1, cluster-derived 0.5 wt.% Pt_2Au_4/SiO_2 catalysts showed a decrease in propene hydrogenation activity when the size of Pt ensembles fell below a value necessary for adsorption of all reactants. Earlier, Amiridis et al. [103] investigated the same catalyst for the gas-phase oxidation of propene by either oxygen or NO. In comparison with a monometallic 1 wt.% Pt catalyst and a 1 wt.% Pt + 2 wt.% Au catalyst (both prepared via impregnation), the cluster-derived catalyst showed minor activities, thereby exhibiting only slightly smaller particle sizes (3.4 nm vs. 4.6 nm and 4.7 nm, respectively). In accordance with FTIR spectroscopy of adsorbed CO and investigations on the $^{16}O/^{18}O$ homoexchange reaction, the real bimetallic character of the as-prepared catalyst was proved. Investigations of other groups concerning propene oxidation over Pt/Al_2O_3 [104], oxidation of cyclopentane, methane, and benzene [105,106], or reduction of NO by either propylene [107,108] or octane [109] indicated a distinct antipathetic structure-sensitivity for hydrocarbon oxidation over Pt. As a result, Amiridis inferred that Au in the bimetallic particles influenced Pt more than could be expected from the aforementioned particle size reduction. While a geometric effect in terms of breaking up surface-confined Pt ensembles could be expected, differences of singleton frequencies of adsorbed CO between Pt/SiO_2 and $AuPt/SiO_2$ provided clear evidence for an electronic modification of Pt by Au.

3.2. CO Oxidation over Supported Au and Pt Catalysts

Since Haruta's works in the 1980s [110] CO oxidation is one of the major applications of supported gold catalysts. Interestingly, this metal/substrate combination exhibits much more pronounced structure sensitivity than the Pd, Pt, and Ir catalyzed analogues [9].

Schüth and coworkers [24] investigated the influence of support materials on catalysts' activities in gold-catalyzed CO oxidation using a colloid deposition method for catalyst preparation. While temperatures of half conversion ($T_{1/2}$) of about −10 °C could be reached with titania and alumina supported catalysts, much higher $T_{1/2}$ values were obtained for the zinc oxide and zirconia supported analogues (Figure 9). According to TEM investigations, the gold nanoparticles, stabilized with polyvinyl alcohol, could be immobilized without changing particle size distributions. As a conclusion, support influences on the particle shape, especially defect formation, were supposed to be the origin of different CO-oxidation activities.

As mentioned above, the identification of structure sensitivity becomes difficult if other factors besides particle size influence the catalyst's activity. In order to avoid influences stemming from differences in, for example, metal content, chloride content, or support morphology, CO oxidation was investigated by Overbury et al. [111] over Au/TiO_2 catalysts prepared from two single batches. Within each of the batches, particle size variation (1.8 to 11.8 nm for the 4.5 wt.% batch and 2.0 to 10.2 nm for the 7.2 wt.% batch) was generated via thermal sintering of the catalysts. As very thin Au platelets or rafts can not be identified by electron microscopy, particle size determination here was performed using *in-situ* EXAFS. With varying particle size, the resulting rates (normalized by total gold content) varied by over two orders of magnitude, and the TOF-particle size dependence fits a power law ($d^{-1,8}$ for the 7.2 wt.% and $d^{-1,0}$ for the 4.5 wt.% catalyst). It was interesting to note that with equal particle size the lower loaded catalyst always exhibited higher TOFs which could potentially be related to a lower particle number density. Only the TOF-particle size dependence for the lower loaded catalyst can be explained on the basis of active peripheral sites between gold and the support. From a comparison with the step-site density dependence from the particle size it is concluded that

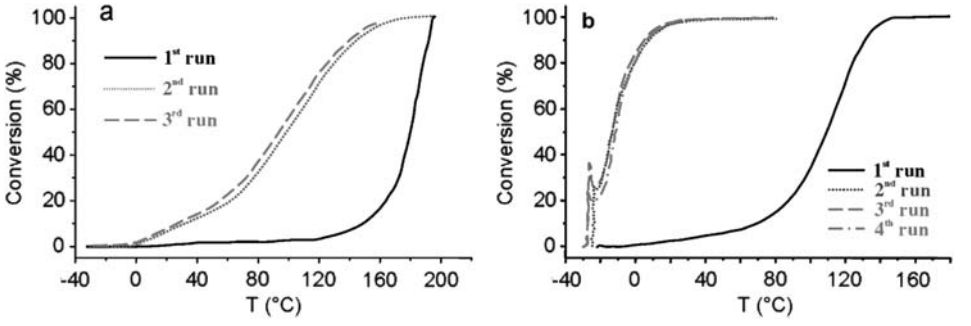

Figure 9. CO conversion as a function of temperature for supported gold catalysts (a) Au/ZrO_2, (b) Au/TiO_2 (both PVA protected) (Reprinted from Reference [24], © 2006, with permission from American Chemical Society).

the most active sites are lower coordinated than step sites; with the higher loaded catalyst, corners seem to be the reaction sites. As electronic effects can be ruled out for particles larger than 2 nm, the observed structure sensitivity was assumed to stem mainly from very low-coordinated sites (kinks).

Quite the opposite behavior (sympathetic structure sensitivity) can be observed when CO oxidation is performed over Pt catalysts. In Uner's [112] investigations different particle sizes were again realized starting from a single batch and subsequent heat treatments. In accordance with the well-known enhanced reactivity of CO adsorbed on planar surfaces [113–115] CO TOFs increased by a factor of ~3 when dispersion was reduced from 63 to 4%. Investigating furthermore CO oxidation in hydrogen atmosphere (PROX), temperatures of half CO conversion dropped with increasing dispersion, whereas CO selectivity at $T < 235\,^{\circ}C$ raised in the same direction.

3.3. NO Oxidation over Supported Pt Catalysts

Not at least for the development of environment-friendly transportation systems various efforts are currently undertaken to reduce the NO_x emission of combustion processes. Prerequisite for all potential technologies (e.g., ammonia SCR or continuously regenerating particulate filters) is a catalyst able to fully oxidize NO to NO_2. Utilizing a 5-factor 2-level high throughput experimentation (HTE) approach, Schmitz et al. [116] investigated a set of 32 catalysts, prepared as either 0.75 or 1.5 wt.% from $Pt(NO_3)_2$ or $Pt(NH_3)_4(NO_3)_2$ on SiO_2 or Al_2O_3, calcined in dry air or N_2 at either 300 or 500 °C with optional subsequent reduction in H_2. In accordance with earlier works on alumina [106,107,117,118] or silica [119] supported Pt catalysts, the samples investigated here exhibited a sympathetic structure sensitivity effect with the TOF increasing by a factor of 39 for 23 nm particles on Al_2O_3 and a factor of 29 for 39 nm particles on SiO_2 when compared to the 2.5 nm particles on both supports (Figure 10).

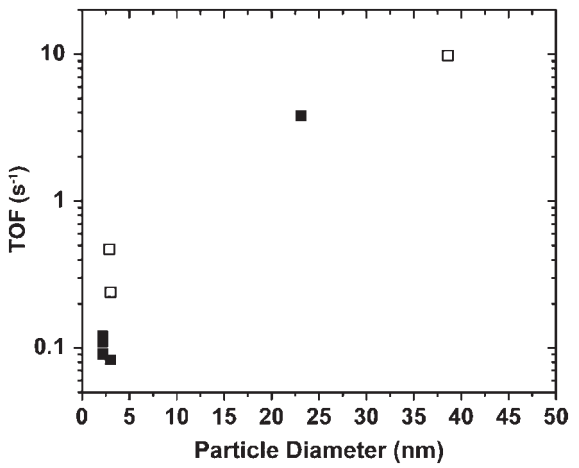

Figure 10. Change in intrinsic NO oxidation rate with Pt particle size for the Pt/Al_2O_3 (■) and Pt/SiO_2 (□) systems. (Reprinted from Reference [116], © 2006, with permission from Elsevier).

Although no explanation for the underlying mechanistic details can be given, the support and pretreatment conditions clearly have a strong effect on catalyst performance. Highest mean rates are obtained with reduced catalysts based on silica whereas the precursor seems to have only a negligible effect.

3.4. Selective Oxidation of Highly Functionalized Molecules

The liquid-phase oxidation of glycerol was carried out by using carbon-supported gold particles of different sizes (2.7–42 nm) which were prepared by a colloidal route [120]. Indeed, a particle-size effect was observed because the selectivity to glyceric acid was increased to 75% with smaller particle sizes ($d_{optimum} = 3.7$ nm).

Another reaction which is of interest within the concept of catalytic conversion of renewable resources [121] is the oxidation of glucose to gluconic acid. A series of Au/C catalysts was prepared by the gold-sol method with different reducing agents and different kinds of carbon supports providing Au mean particle diameters in the range of 3–6 nm [122]. The most active gold catalyst exhibited a specific gold surface area of 94.2 m^2/g. It could be shown that D-Glucose oxidation is a structure-sensitive reaction since a significant increase in reaction rate could be observed with increasing Au specific surface area at the same reaction conditions.

4. C–C Coupling Reactions: Fischer–Tropsch Synthesis

CO hydrogenation, according to a number of publications [123–125] is considered to be a structure-sensitive reaction. This is mainly due to size-dependant CO adsorption, which can occur either in a linear (preferred on smaller particles), a geminal, or a bridged mode (preferred over larger particles). Concerning particle-size effects for silica-supported Rh catalysts, Bao et al. [126] investigated pore-confined synthesis of metal nanoparticles obtained from $RhCl_3$ precursors. The observed linear increase in CO TOF (max. 85/h) was correlated with growing Rh particle sizes in the range of 2.5–5 nm. According to Bao, this phenomenon can be traced back to the enhanced activity of bridge-bound CO (favored with the larger particles), but also to easier accessibility to the larger particles via the larger pores. Additionally, growing particle sizes promoted the formation of methane and C_2 oxygenates which should as well be due to the preponderance of bridge-bound (i.e., non-dissociated) CO.

As was demonstrated in the preceding sections, structure-sensitivity phenomena are mostly confined to particle size regimes smaller than 3–4 nm. A process of industrial relevance was investigated by de Jong et al. [127] in their study on cobalt particle size effects in the Fischer–Tropsch reaction. Earlier works noted distinct drop in activity for Co particles smaller than 10 nm and ascribed this phenomenon to either a partial oxide or carbide formation which should be enhanced for particles in this size regime [128–139]. In order to avoid similar effects, de Jong used

Co particles supported on graphitized carbon nano fibers which by XPS were shown to prevail in the metallic state. While conversion and selectivities for catalysts exhibiting particle sizes >6 nm were insensitive with respect to particle size, TOF markedly decreased below this size limit (Figure 11 left). Accordingly, increased methane selectivity was explained by an enhanced availability of dissociated hydrogen on the Co surface (Figure 11 right). Based on XANES derived Co coordination numbers, significant restructurization of metal particle surfaces leading to faceted particles is believed to take place. This effect, in conjunction with ''nonclassical structure sensitivity'', according to de Jong, is responsible for the observed behavior.

5. Cleavage Reactions

5.1. Ethane Hydrogenolysis over Pt/SBA-15

Investigating the most simple hydrogenolysis reaction, that of ethane, is very instructive as it comprises two of the most important processes in heterogeneous catalysis in one reaction: C–H and C–C bond activation. Whereas a H/D exchange takes place already at ~430 K [140], the rate of C_2H_5 hydrogenolysis on Pt(1 1 1) was three orders of magnitude lower [141]. Already in 1969 Boudart [4] reported on structure sensitivity for this reaction which was discussed closer in later years; Guczi and Gudkov [142], for example, reported on antipathetic behavior for Pt particle sizes in the 3–20 nm size range.

Recently, Somorjai, Yang et al. [143] examined this reaction over ~1 wt.% Pt/SBA-15 utilizing an elaborate preparation protocol. Preformed Pt nanoparticle sols of five different mean sizes, obtained by alcohol reduction in the presence of a protecting polymer (PVP) were combined with SBA-15 silica exhibiting 9 nm pores. After 3 h low-power ultrasonic treatment, the Pt particles were evenly distributed throughout the pores of the support (Figure 12 (a)–(e)).

Interaction of ethane with Pt surfaces can theoretically occur via ethyl (C_2H_5), ethylidene ($CHCH_3$), vinyl ($CHCH_2$), and vinylidene (CCH_2) species [144,145] and the cleavage of the C–C bond is believed to occur in highly dehydrogenated species at low hydrogen-to-ethane ratios and vice versa [146]. With decreasing particle sizes, TOFs of Somorjai's and Yang's catalysts increased by a factor of 3, confirming the system's antipathetic behavior (Figure 12(e)). It is proposed that the hydrogenolysis

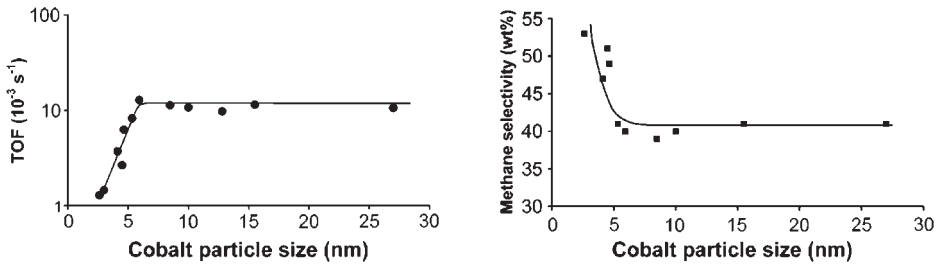

Figure 11. The influence of cobalt particle size on the TOF (left) and on methane selectivity (right; 220 °C, $H_2/CO = 2$, 1 bar). (Reprinted from Reference [127], © 2006, with permission from American Chemical Society).

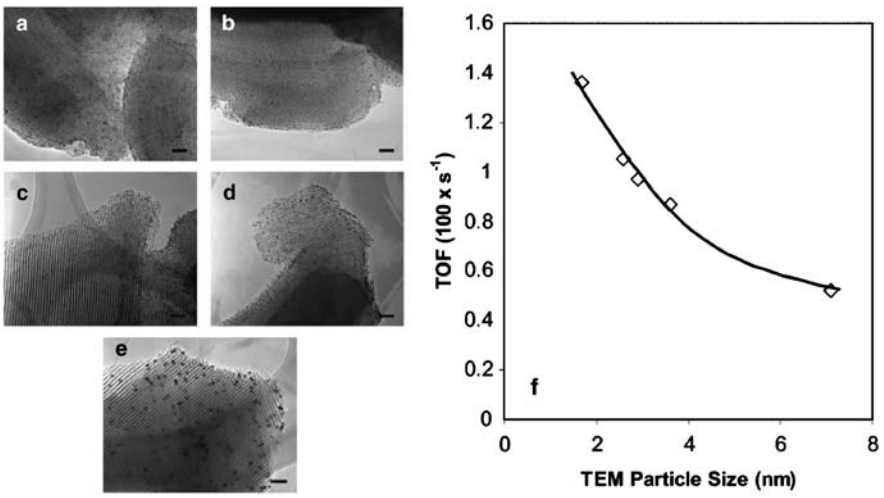

Figure 12. TEM images of the Pt(X)/SBA-15 catalysts: X = (a) 1.7 nm, (b) 2.6 nm, (c) 2.9 nm, (d) 3.6 nm, and (e) 7.1 nm (the scale bars represent 20 nm); (f): structure sensitivity of ethane hydrogenolysis on ~1% Pt(X)/SBA-15 with Pt particle sizes ranging from $X = 1.7$ to 7.1 nm. Rates corrected to 20 Torr C_2H_6, 200 Torr H_2, and 643 K. (Reprinted from Reference [143], © 2005, with permission from American Chemical Society).

involves C_2H_x species and their activated complexes; they are more stably bound on Pt defect sites which are more abundant on smaller particles.

5.2. Hydrodechlorination of Chlorophenols over Ni/SiO$_2$

An apparent particle size effect for the hydrodechlorination of 2-chlorophenol and 2,4-dichlorophenol was observed by Keane et al. [147]. Investigating silica supported Ni catalysts (derived from either nickel nitrate or nickel ethanediamine) with particles in the size range between 1.4 and 16.8 nm, enhanced rates for both reactions were observed with increased size over the full range (Figure 13). As electronic factors can be ruled out in this dimension, the observed behavior is traced back to some sort of ensemble effect, known from CFC transformations over Pd/Al_2O_3 [148]. Due to electronic deactivation of the substrate, hydrodechlorination of the dichlorophenol is discriminated in comparison to the monosubstituted substrate.

Disregarding structure sensitivity effects, further works [149] denote the promoting influence of an electropositive metal in bimetallic Pd–Yb catalysts for enhanced hydrodechlorination of chlorobenzene, 1,2- and 1,3-dichlorobenzene.

6. Reasons for Size, Shape, and Structure Effects

6.1. Electronic Aspects

Changing the size of metal particles leads to a change in the atom's mean coordination number, as in smaller particles the number ratio of surface atoms to bulk atoms increases. As a result, the metal's valence band becomes more narrow, the density of states in the vicinity of the Fermi niveau decreases and the band center shifts towards higher energies [150]. It can thus be easily understood that metal nanoparticles' chemistry differs from that of the bulk materials as proved by Gan [151] who confirmed in 2001 that below 2 nm size, PtNP exhibit non-metallic behavior. For further discussions on this topic the reader is referred to Chapter 1.

One of the first examples encountering this so-called *quantum size effect* was a communication by Carter et al. [152] in 1966 who reported on decreasing ethane hydrogenolysis activities on silica–alumina supported nickel with increasing temperature during annealing in H_2 (370–700 °C). The resulting change in particle size from 4 to 8.8 nm was shown to change magnetic properties of the Ni particles dramatically; consequently, the observed sharp increase in hydrogenolysis activity was assumed to be due to changes in the particles' electronic structure.

Main obstacle in identifying quantum-size effects as a reason for structure sensitivity stems from the difficult discrimination from geometric influences; the latter will be discussed in the next paragraph.

6.2. Geometric Aspects

Besides electronic effects, structure sensitivity phenomena can be understood on the basis of geometric effects. The shape of (metal) nanoparticles is determined by the minimization of the particles' free surface energy. According to Wulff's law, this requirement is met if (on condition of thermodynamic equilibrium) for all surfaces that delimit the (crystalline) particle, the ratio between their corresponding energies σ_i and their distance to the particle center h_i is constant [153]. In (non-model) catalysts, the particles' real structure however is furthermore determined by the interaction with the support [154] and by the formation of defects for which Figure 14 shows an example.

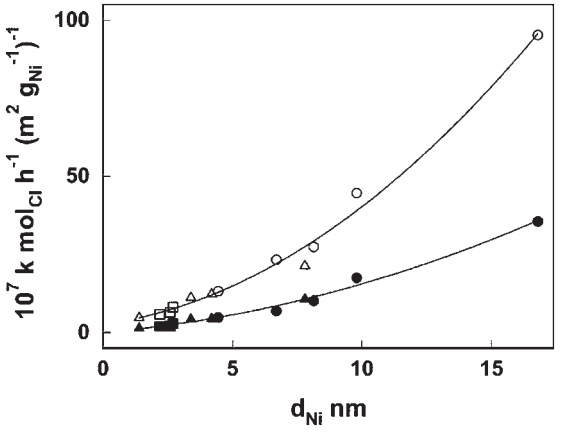

Figure 13. Specific 2-CP (open symbols) and 2,4-DCP (solid symbols) hydrodechlorination rate constant (k) as a function of the average Ni particle diameter (d_{Ni}) for reaction over Ni catalysts prepared via impregnation with nitrate (○,●), deposition-precipitation (△,▲) and impregnation with nickel ethanediamine (□,■): $T = 423$ K; reaction data refer to aqueous solutions. (Reprinted from Reference [147], © 2003, with permission from Royal Society of Chemistry).

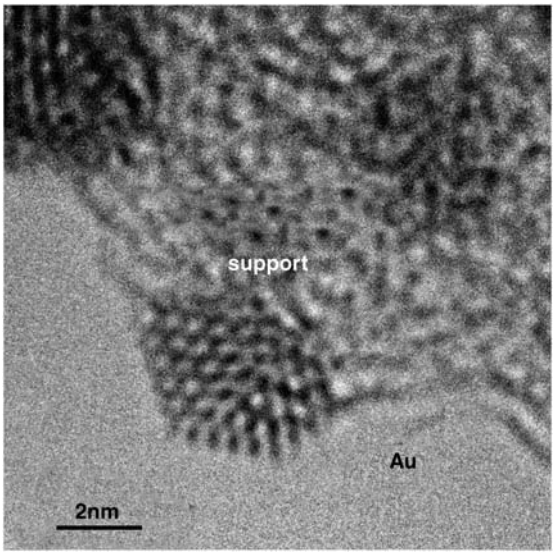

Figure 14. Au nanoparticle on polyaniline support with twin boundary (F. Klasovsky, P. Claus, unpublished results, 2006).

According to the model of van Hardefeld and Hartog [155], varying the size of metal particles changes the preponderance of atoms placed at the corners (denoted C_6^6), edges (C_7^5), or faces (C_9^3) as it is demonstrated in Figure 15 for the case of silver particles. According to Balandin's multiplet theory [156] the ability of a substrate to interfere with a surface depends on the accordance of the substrate geometry with the local coordination environment; analogous effects are known with the behavior of oxide catalysts (Hedvall-Effekt [157,158]). Hence it becomes clear that a given reaction's TOF or selectivities can depend on the particle shape and size.

As was for example seen with Pd and Pt (Section 2.6.1, crotonaldehyde), dense (1 1 1) metal faces are not favorable to C=C coordination. Accordingly, greater participation of this face in the catalyst surface, with large faceted particles or by support epitaxy, can favor the unsaturated alcohol [159].

Another example for geometry influence in hydrogenation reactions was recently presented by Jackson et al. [160] who investigated hydrogenation of *para*-toluidine; a reaction that is only rarely documented in the literature [161,162] (Figure 16). During low-temperature liquid-phase hydrogenation over Rh/SiO_2 catalysts, a weak but pronounced antipathetic effect was observed. Variation in Rh particle size between 1.2 and 2.5 nm increased TOF by a factor of 1.5 and could be traced back to the dominance of plane face surface Rh atoms. Consequently, this finding is in accordance with similar antipathetic behavior observed earlier for benzene hydrogenation over Rh/Al_2O_3 [163], Pt/Al_2O_3 [164], and iridium [165] catalysts.

Recently, Libuda et al. [166] discovered an aspect of particle-size-dependent phenomena which could hitherto be helpful in interpreting possibly structure-sensitive reactions. Scrutinizing Pd particles deposited in different sizes between 2 and 100 nm on Fe_3O_4, they discovered a size-dependent oxidation to Pd oxides. As could be shown in an earlier work, this oxidation starts at the metal–support interface, and its products are stabilized by the support; a bulk oxidation can be excluded [167]. A combination of scanning tunneling microscopy and molecular beam experiments using CO and O_2 beams unveiled a thorough oxidizability of Pd to PdO when in a size range <3 nm. Pd particles of 3 nm to approx. 10 nm size could be oxidized only slowly and partly, mainly at the particle–support interface, whereas the oxidation of larger particles (10–100 nm) suffers from severe kinetic hindrance. As a result, the maximum oxygen content in an oxide supported Pd catalyst passes through a maximum for a Pd particle size of about 7 nm (Figure 17). Below this point, Pd can be significantly oxidized, however, only minor amounts of Pd can be deposited on a support before coalescence occurs, and so the amount of oxidizable support interface remains low. Above this point, the net particle–support interface increases, but formation of oxides is kinetically hindered.

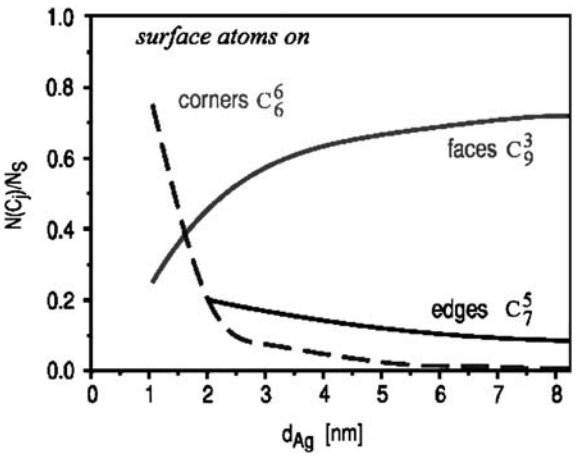

Figure 15. Relative fraction of different kinds of surface sites in silver particles. (Reprinted from Reference [82], © 1999, with permission from American Chemical Society).

6.3. Strain or Compression Aspects

Besides geometric and electronic influences, another interesting aspect was recently highlighted by Kibler et al. [168] who investigated current–potential curves of pseudomorphic Pd monolayers on different single crystal substrates. As it is known from earlier works of Nørskov [169], straining a metal whose d band is more than half filled leads to an increase in the d-band center energy. As a result, its catalytic activity increases, indicated by a decrease in its electrochemical potential vs. SCE. In contrast, a further lowering of d-band center energy leads to an attenuation of adsorbate binding strength that, in conjunction with enhanced reactivity, results in a

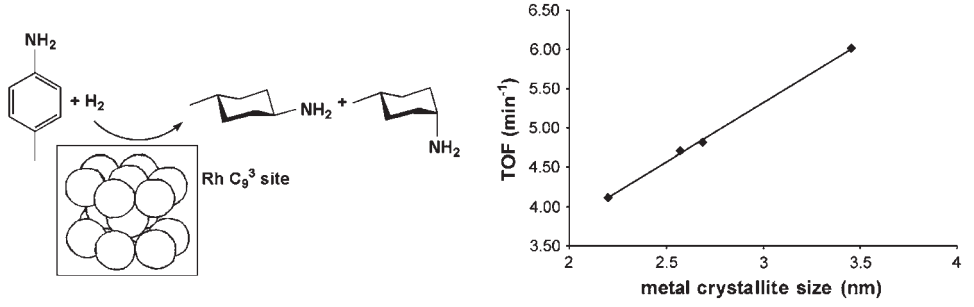

Figure 16. Hydrogenation of *p*-toluidine on plane face surface Rh atoms (left); effect of metal crystallite size on TOF (right). (Reprinted from Reference [160], © 2006, with permission from Elsevier).

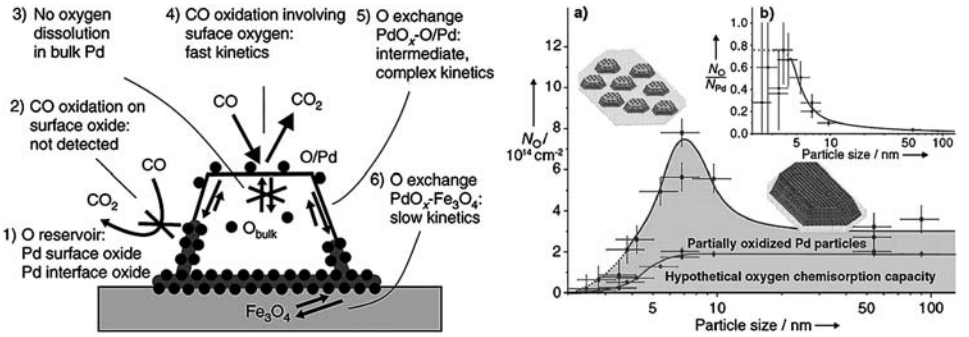

Figure 17. Oxygen storage mechanism and CO oxidation on a Pd/Fe_2O_3 model catalyst (left); oxygen storage after 100 s exposure at 500 K as a function of particle size (right): (a) Hypothetical oxygen release assuming regular chemisorption on metallic Pd particles only and no oxidation (lower, dark-grey curve) and experimentally determined oxygen release on partially oxidized Pd particle (upper, light-grey curve); (b) mean stoichiometry of the Pd particles after oxygen treatment. (Reprinted from Reference [166], © 2006, with permission from Wiley-VCH).

volcano-like behavior of reaction rates. Accordingly, electrooxidation of formic acid yields maximum currents when the active palladium thin layer is deposited on a PtRu (1 1 1) surface.

6.4. Conclusions

The catalyst/reaction systems presented in this review show that the mechanism of catalysis are more complicated than assuming a simple geometric model (metal particle size) or, for example, a perimeter-interface model which is suggested to be the active site in CO oxidation [170]. It is obvious, that a single "size" parameter cannot describe the function of a heterogeneous catalyst as suggested in the headline of this review. Metastable non-equilibrium states under the reaction conditions of the individual catalytic process, for example objects with lattice strain or multiple twinned particles where the small size prevents recrystallization into the form found at equilibrium, must be considered as the origin of the particle-size dependency of the catalytic properties [92]. This was shown, for example, in the case of gold catalysts used for the selective hydrogenation of acrolein (see Chapter 2.6.1). The distribution of coordinatively unsaturated sites (cus), that is, edge, kink, corner, and terrace sites, which can be compressed as "roughness" of the surface, is controlled by morphology of the nanoparticle. Among several effects which can contribute to the catalytic properties, for example in the CO oxidation by supported gold nanoparticles, the most important effect seems to be related to the availability of many low-coordinated gold atoms on the small particles as shown by Nørskov and co-workers [171]. Other effects, for example those related to the interaction with the support, charge transfer or layer thickness may also contribute but to a considerably smaller extent. DFT calculations point to a hierarchy of the effects, where the largest is a change in reactivity due to changes in the metal coordination number, that is, the largest activity is associated with the presence of a high concentration of low-coordinated sites on the surface of very small particles.

References

1 G. Roscher, H. Schmitz, Hoechst, DE-OS 1949537, 1969.
2 B. Engelhard, J. Grolig, M. Martin, K.-H. Reissinger, G. Scharfe, et al., Bayer, DE-OS 1933538, 1969.
3 G. Ertl, H. Knözinger, F. Schüth, J. Weitkamp (eds.) *Handbook of Heterogeneous Catalysis*. 1st ed., Wiley-VCH, 1997, 911.
4 M. Boudart, *Adv. Catal. Relat. Subj*. 20 (1969) 153.
5 M. Boudart, G. Bond, P. Weller, F. Tompkins (eds.) Proc. 6th Int. Congr. Catal., Vol. 1, The Chem. Soc., London, 1977, 1.
6 M. Boudart, *J. Mol. Catal*. 30 (1985) 27.
7 G. C. Bond, *Chem. Soc. Rev*. 20 (1991) 441.
8 R. Burch, G. Bond, G. Webb (eds.) *A specialist Periodical Report, Catalysis*, Vol. 7, The Royal Society of Chemistry, London, 1985.
9 M. Che, C. O. Bennett, *Adv. Catal*. 36 (1989) 55.
10 G. C. Bond, *Metal-Catalysed Reactions of Hydrocarbons*, Springer, New York, 2005, 231.
11 J. P. Boiteaux, J. Cosyns, S. Vasudevan, *Appl. Catal*. 6 (1983) 41.
12 G. Carturan, G. Facchin, G. Cocco, G. Navazio, G. Gubitosa, *J. Catal.* 82 (1983) 56.
13 C. E. Gigola, H. R. Aduriz, P. Bodnariuk, *Appl. Catal.* 27 (1986) 133.
14 M. A. Vannice, S. D. Lin, *J. Catal.* 143 (1993) 539.
15 G. Bond, F. S. Stone, *Stud. Surf. Sci. Catal*. 101 (1996) 257.
16 G. Somorjai, *Chemistry in Two Dimensions: Surfaces*, Cornell University Press, Ithaka, USA, 1981, 401.
17 M. Boudart, G. Djéga-Mariandassou, *Kinetics of Heterogeneous Catalytic Reactions*, Princeton University Press, Princeton (USA), 1984, 157.
18 B. Coq, F. Figueras, *Coord. Chem. Rev*. 178–180 (1998) 1753.
19 G. C. Bond, *Acc. Chem. Res*. 26 (1993) 490.
20 V. Ponec, G. C. Bond, *Stud. Surf. Sci. Catal*. Vol. 95, Catalysis by Metals and Alloys, Elsevier, 1995, 280.
21 D. Farin, D. Avnir, *J. Am. Chem. Soc.* 110 (1988) 2039.
22 D. Farin, D. Avnir, *J. Catal.* 120 (1989) 55.
23 M. Arai, *J. Chem. Eng. Jpn*. 30(6) (1997) 1123.
24 F. Schüth, M. Comotti, W. C. Li, B. Spliethoff, *J. Am. Chem. Soc.* 128(3) (2006) 917.
25 V. R. Choudhary, N. S. Patil, B. S. Uphade, P. Jana, S. K. Bhargava, *J. Catal.* 223(1) (2004) 236.
26 A. Baiker, J. D. Grunwaldt, C. Kiener, C. Wögerbauer, *J. Catal*. 181(2) (1999) 223.
27 M. Stephanopoulos, H. Saltsburg, Q. Fu, *Science* 301 (2003) 935.

28 C. Milone, R. Ingoglia, S. Galvagno, *Gold Bull.* 39(2) (2006) 54.
29 M. A. Centeno, I. Carrizosa, J. A. Odriozola, *Appl. Catal. A: General* 246(2) (2003) 365.
30 K. G. Neoh, L. Cen, Q. Cai, E. T. Kang, *J. Colloid Interface Sci.* 300(1) (2006) 190.
31 S. Ramaprabhu, M. Shaijumon, N. Rajalakshmi, *Appl. Phys. Lett.* 88(25) (2006) 253105.
32 F. Klasovsky, M. Steffan, J. Arras, P. Claus, *The Open Physical Chemistry Journal* 1 (2007) 1.
33 G. Schmid, M. Harms, J. Malm, J. Bovin, J. Ruitenbeck, H. Zandbergen, W. Fu, *J. Am. Chem. Soc.* 115 (1993) 2046.
34 S. Mecking, U. Schlotterbeck, C. Aymonier, R. Thomann, H. Hofmeister, M. Tromp, W. Richtering, *Adv. Funct. Mater.* 14(10) (2004) 999.
35 K. Y. Liew, H. Choo, B. He, H. Liu, J. Li, *J. Mol. Catal. A: Chem.* 244(1–2) (2006) 217.
36 A. Miyazaki, S. Yoshida, Y. Nakano, I. Balint, *Chem. Lett.* 34(1) (2005) 74.
37 Y. Xia, B. Wiley, Y. Sun, B. Mayers, *Chem. Eur. J.* 11(2) (2005) 454.
38 L. Liz-Marzán, A. Sánchez-Iglesias, I. Pastoriza-Santos, J. Pérez-Juste, B. Rodríguez-Gonzáles, F. García de Abajo, *Adv. Mater.* 18(19) (2006) 2529.
39 H. Wilmer, M. Kurtz, K. V. Klementiev, O. P. Tkachenko, W. Grünert, O. Hinrichsen, A. Birkner, S. Rabe, K. Merz, M. Driess, C. Wöll, M. Muhler, *Phys. Chem. Chem. Phys.* 5 (2003) 4736.
40 G. A. Somorjai, *Introduction to Surface Chemistry and Catalysis*, Wiley, New York, 1994.
41 D. R. Rainer, D. W. Goodman, *J. Mol. Catal. A: Chem.* 131 (1998) 259.
42 M. Frank, M. Bumer, *Phys. Chem. Chem. Phys.* 2 (2000) 3723.
43 F. Zaera, *Prog. Surf. Sci.* 69 (2001) 1.
44 S. T. Ceyer, *Acc. Chem. Res.* 34 (2001) 737.
45 (a) N. Sheppard, C. De La Cruz, *Adv. Catal.* 41 (1996) 1; (b) N. Sheppard, C. De La Cruz, *Adv. Catal.* 42 (1998) 181.
46 J. A. Gates, L. L. Kesmodel, *Surf. Sci.* 124 (1983) 68.
47 M. Neurock, R. A. van Santen, *J. Phys. Chem. B* 104 (2000) 11127.
48 S. K. Shaikhutdinov, M. Heemeier, M. Bumer, T. Lear, D. Lennon, R. J. Oldman, S. D. Jackson, H.-J. Freund, *J. Catal.* 200 (2001) 350.
49 S. K. Shaikhutdinov, M. Frank, M. Bumer, S. D. Jackson, R. J. Oldman, J. C. Hemminger, H.-J. Freund, *Catal. Lett.* 80 (2002) 115.
50 D. Stacchiola, S. Azad, L. Burkholder, W. T. Tysoe, *J. Phys. Chem. B* 105 (2001) 11233.
51 D. Stacchiola, W. T. Tysoe, *Surf. Sci.* 540 (2003) L600.
52 D. Stacchiola, L. Burkholder, W. T. Tysoe, *Surf. Sci.* 542 (2003) 129.
53 P. S. Cremer, G. A. Somorjai, *J. Chem. Soc. Faraday Trans.* 91 (1995) 3671.
54 M. Sock, A. Eicher, S. Surnev, J. N. Andersen, B. Kltzer, K. Hayek, M. G. Ramsey, F. P. Netzer, *Surf. Sci.* 545 (2003) 122.
55 L. B. Ortiz-Soto, J. R. Monnier, M. D. Amiridis, *Catal. Lett.* 107(1–2) (2006) 13.
56 M. Boudart, M. McDonald, *J. Phys. Chem.* 88 (1984) 2185.
57 G. Bond, *Catalysis by Metals*, Acedemic Press, New York, 1962.
58 A. M. Doyle, S. K. Shaikhutdinov, H.-J. Freund, *Angew. Chem.* 117 (2005) 635.
59 J. Silvestre-Albero, G. Rupprechter, H.-J. Freund, *J. Catal.* 240 (2006) 58.
60 D. R. Kennedy, G. Webb, S. D. Jackson, D. Lennon, *Appl. Catal. A.* 259 (2004) 109.
61 R. Marshall, G. Webb, S. D. Jackson, D. Lennon, *J. Mol. Catal. A Chem.* 226 (2005) 227.
62 D. Lennon, D. R. Kennedy, G. Webb, S. D. Jackson, *Stud. Surf. Sci. Catal.* 126 (1999) 341.
63 P. Maetz, R. Touroude, *Appl. Catal. A* 149 (1997) 189.
64 S. D. Jackson, G. D. McLellan, G. Webb, L. Conyers, M. B. T. Keegan, S. Mather, S. Simpson, P. B. Wells, D. A. Whan, R. Whyman, *J. Catal.* 162 (1996) 10.
65 D. Teschner, E. Vass, M. Hävekcer, S. Zafeiratos, P. Schnörch, H. Sauer, A. Knop-Gericke, R. Schlögl, M. Chamam, A. Wootsch, A. S. Canning, J. J. Gamman, S. D. Jackson, J. McGregor, L. F. Gladden, *J. Catal.* 242 (2006) 26.
66 S. B. Ziemecki, G. A. Jones, D. G. Swartzfager, R. L. Harlow, J. Faber Jr., *J. Am. Chem. Soc.* 107 (1985) 4547.
67 L. Gracia, M. Calatayud, J. Andrés, C. Minot, M. Salmeron, *Phys. Rev. B* 71 (2005) 033407.
68 J. A. Rodriguez, D. W. Goodman, *Surf. Sci. Rep.* 14 (1991) 1.
69 Z. Paál, P. Tétényi, *Nature* 267 (1977) 234.
70 R. S. Rao, A. B. Walters, M. A. Vannice, *J. Phys. Chem. B* 109 (2005) 2086.
71 V. Ponec, *Appl. Catal. A: General* 149 (1997) 27.
72 P. Claus, *Top. Catal.* 5 (1998) 51.
73 P. Gallezot, D. Richard, *Catal. Rev. Sci. Eng.* 40 (1998) 81.
74 Y. Berthier, C.-M. Pradier, *Bull. Soc. Chim. Fr.* 134 (1997) 773.
75 T. Birchem, C. M. Pradier, Y. Berthier, G. Cordier, *J. Catal.* 146 (1994) 503.
76 C. M. Pradier, T. Birchem, Y. Berthier, G. Cordier, *Catal. Lett.* 29 (1994) 371.
77 T. Birchem, C. M. Pradier, Y. Berthier, G. Cordier, *J. Catal.* 161 (1996) 68.
78 U. K. Singh, M. A. Vannice, *Appl. Catal. A: General* 231 (2001) 1.
79 U. K. Singh, Ph.D. Thesis, Pennsylvania State University, 2000.
80 M. Englisch, A. Jentys, J. A. Lercher, *J. Catal.* 166 (1997) 25.
81 M. Englisch, V. S. Ranade, J. A. Lercher, *Appl. Catal.* 163 (1997) 111.
82 P. Claus, H. Hofmeister, *J. Phys. Chem. B.* 103 (1999) 2766.
83 W. Grünert, A. Brückner, H. Hofmeister, P. Claus, *J. Phys. Chem. B* 108 (2004) 5709.
84 P. Claus, A. Brückner, C. Mohr, H. Hofmeister, *J. Am. Chem. Soc.* 122 (2000) 11430.
85 C. Mohr, H. Hofmeister, P. Claus, *J. Catal.* 213 (2003) 86.
86 M. A. Vannice, B. Sen, *J. Catal.* 115 (1989) 65.
87 A. Giroir-Fendler, D. Richard, P. Gallezot, in M. Guisnet, J. Barrault, C. Bouchoule, D. Duprez, C. Montassier, G. Perot (eds.) *Stud. Surf. Sci. Catal.*, Vol. 41, Elsevier, Amsterdam, 1988, 171.
88 A. Giroir-Fendler, D. Richard, P. Gallezot, *Catal. Lett.* 5 (1990) 175.
89 P. Gallezot, A. Giroir-Fendler, D. Richard, in W. E. Pascoe (ed.) *Catalysis of Organic Reactions*, Dekker, New York, 1992, 1.
90 S. Galvagno, C. Milone, A. Donato, G. Neri, R. Pietropaolo, *Catal. Lett.* 18 (1993) 349.
91 L. Mercadante, G. Neri, A. Donato, S. Galvagno, *J. Mol. Catal. A: Chem.* 105 (1996) 93.
92 R. Schlögl, S. Bee Abd Hamid, *Angew. Chem. Int. Ed.* 43 (2004) 1628.
93 R. Zanella, C. Louis, S. Giorgio, R. Touroude, *J. Catal.* 223 (2004) 328.
94 M. Abid, V. Paul-Boncour, R. Touroude, *Appl. Catal. A: General* 297 (2006) 48.
95 M. Abid, G. Ehret, R. Touroude, *Appl. Catal. A* 217 (2001) 219.
96 P. Conception, A. Corma, J. Silvestre-Albero, V. Franco, Y. Chane-Ching, *J. Am. Chem. Soc.* 126 (2004) 5523.

97 S. Bernal, J. Calvino, M. Cauqui, J. Gattica, C. Lopez Cartes, J. Perez Omil, J. Pintado, *Catal. Today* 77 (2003) 385.
98 B. Sen, M. Vannice, *J. Catal.* 113 (1988) 52.
99 C. Mohr, H. Hofmeister, J. Radnik, P. Claus, *J. Am. Chem. Soc*. 125 (2003) 1905.
100 F. Haass, M. Bron, H. Fuess, P. Claus, *Appl. Catal*. 318 (2007) 9.
101 O. M. Wilson, M. R. Knecht, J. C. Garcia-Martinez, R. M. Crooks, *J. Am. Chem. Soc*. 128 (2006) 4510.
102 E. P. Maris, W. C. Ketchie, V. Oleshko, R. J. Davis, *J. Phys. Chem. B* 110 (2006) 7869.
103 C. Mihut, C. Descorme, D. Duprez, M. D. Amiridis, *J. Catal*. 212 (2002) 125.
104 L. M. Carballo, E. E. Wolf, *J. Catal.* 53 (1987) 366.
105 T. F. Garetto, C. R. Apesteguia, *Catal. Today* 62 (2000) 189.
106 T. F. Garetto, C. R. Apesteguia, *Appl. Catal. B* 32 (2000) 83.
107 J.-H. Lee, H. H. Kung, *Catal. Lett*. 51 (1998) 1.
108 P. Denton, A. Giroir-Fendler, H. Praliaud, M. Primet, *J. Catal*. 189 (2000) 410.
109 R. Burch, P. Fornasiero, B. W. L. Southward, *Chem. Commun*. (1998) 625.
110 M. Haruta, N. Yamada, T. Kobayahsi, S. Iijima, *J. Catal.* 115 (1989) 301.
111 S. H. Overbury, V. Schwatz, D. R. Mullins, W. Yan, S. Dai, *J. Catal*. 241 (2006) 56.
112 B. Atalik, D. Uner, *J. Catal.* 241 (2006) 268.
113 J. L. Gland, M. R. McClellan, R. F. McFeely, *J. Chem. Phys*. 79 (1983) 6349.
114 A. Szabo, M. A. Henderson, J. T. Yates, *J. Chem. Phys*. 96 (1992) 6191.
115 J. Z. Xu, J. T. Yates, *J. Chem. Phys*. 99 (1993) 725.
116 P. J. Schmitz, R. J. Kudla, A. R. Drews, A. E. Chen, C. K. Lowe-Ma, R. W. McCabe, W. F. Schneider, C. T. Goralski Jr., *Appl. Catal. B: Environmental* 67 (2006) 246.
117 L. Olsson, E. Fridell, *J. Catal*. 210 (2002) 340.
118 S. S. Mulla, N. Chen. W. N. Delgass, W. S. Epling, F. H. Ribeiro, *Catal. Lett*. 100 (2005) 267.
119 E. Xue, K. Seshan, J. R. H. Ross, *Appl. Catal. B: Environmental* 11 (1996) 65.
120 S. Demirel-Gülen, M. Lucas, P. Claus, Catal. Today (Special issue "CarboCat," L. Kiwi-Minsker, A. Renken, Guest-editors) 102–103 (2005) 166.
121 P. Claus, H. Vogel, *Chem. Ing. Techn*. 78 (2006) 991.
122 Y. Önal, S. Schimpf, P. Claus, *J. Catal*. 223 (2004) 122.
123 I. Balint, A. Miyazaki, K. Aika, *J. Catal*. 207 (2002) 66.
124 M. Ojeda, S. Rojas, M. Boutonnet, F. J. Perez-Alonso, F. Javier Garia-Garcia, J. L. G. Fierro, *Appl. Catal. A* 274 (2004) 33.
125 H Arakawa, K. Takeuchi, T. Matsuzaki, Y. Sugi, *Chem. Lett*. 9 (1984) 1607.
126 S. Zhou, H. Zhao, D. Ma, S. Miao, M. Cheng, X. Bao, *Z. Phys. Chem*. 219 (2005) 949.
127 G. L. Bezemer, J. H. Bitter, H. P. C. E. Kuipers, H. Oosterbeek, J. E. Holewijn, X. Xu, K. F. Kapteijn, A. Jos van Dillen, K. P. de Jong, *J. Am. Chem. Soc*. 128 (2006) 3956.
128 R. C. Reuel, C. H. Bartholomew, *J. Catal.* 85 (1984) 78.
129 A. S. Lisitsyn, A. V. Golovin, V. L. Kuznetsov, Y. I. Yermakov, *Cl. Mol. Chem*. 1 (1984) 115.
130 A. S. Lisitsyn, A. V. Golovin, V. L. Kuznetsov, Y. I. Yermakov, *J. Catal.* 95 (1985) 527.
131 G. I. Bezemer, A. van Laak, A. J. van Dillen, K. P. de Jong, *Stud. Surf. Sci. Catal*. 147 (2004) 259.
132 A. Martinez, C. Lopez, F. Marquez, I. Diaz, *J. Catal*. 220 (2003) 486.
133 A. Barbier, A. Tuel, I. Arcon, A. Kodre, G. A. Martin, *J. Catal*. 200 (2001) 106.
134 L. Fu, C. H. Bartholomew, *J. Catal*. 92 (1985) 376.
135 J. H. Lee, D. K. Lee, S. K. Ihm, *J. Catal*. 113 (1988) 544.
136 S. W. Ho, M. Houalla, D. M. Hercules, *J. Phys. Chem.* 94 (1990) 6396.
137 A. M. Saib, M. Claeys, E. van Stehen, *Catal. Today* 71 (2002) 395.
138 S. L. Soled, E. Iglesia, R. A. Fiato, J. E. Baumgartner, H. Vroman, S. Miseo, *Top. Catal*. 26 (2003) 101.
139 G. Jacobs, T. K. Das, Y. Q. Zhang, J. L. Li, G. Racoillet, B. H. Davis, *Appl. Catal. A* 233 (2002) 263.
140 J. R. Anderson, B. G. Baker, *Proc. R. Soc. (London) A* 271 (1963) 402.
141 F. Zaera, G. A. Somorjai, *J. Phys. Chem.* 89 (1985) 3211.
142 L. Guczi, B. S. Gudkov, *React. Kinet. Catal. Lett*. 9 (1978) 343.
143 R. M. Rioux, H. Song, J. D. Hoefelmeyer, P. Yang, G. A. Somorjai, *J. Phys. Chem. B* 109 (2005) 2192.
144 R. M. Watwe, B. E. Spiewak, R. D. Cortright, J. A. Dumesic, *J. Catal*. 180 (1998) 184.
145 R. M. Watwe, R. D. Cortright, J. K. Nørskov, J. A. Dumesic, *J. Phys. Chem. B* 104 (2000) 2299.
146 B. S. Gudkov, G. Guczi, P. Tétényi, *J. Catal*. 74 (1982) 207.
147 G. Pina, C. Louis, M. A. Keane, *Phys. Chem. Chem. Phys*. 5 (2003) 1924.
148 W. Juszczyk, A. Mallinowski, Z. Karpinski, *Appl. Catal. A* 166 (1998) 311.
149 S. Jujjuri, E. Ding, E. L. Hommel, S. G. Shore, M. A. Keane, *J. Catal*. 239 (2006) 486.
150 C. R. Henry, *Surf. Sci. Rep*. 31 (1998) 235.
151 S. Gan, L. Liang, D. Baer, M. Sievers, G. Herman, C. Peden, *J. Phys. Chem. B* 105 (2001) 2412.
152 J. L. Carter, J. A. Cusumano, J. H. Sinfelt, *J. Phys. Chem.* 70(7) (1966) 2257.
153 Honigmann, R. Gleichgewichts- und Wachstumsformen von Kristallen, Steinkopf-Verlag, Darmstadt, 1958.
154 M. Baumer, H.-J. Freund, *Prog. Surf. Sci*. 61(7–8) (1999) 127.
155 R. van Hardefeld, F. Hartog, *Surf. Sci*. 15 (1969) 189.
156 B. Trapnell, *Adv. Catal.* 2 (1951) 1.
157 G. Bliznakov, S. Angelov, S. Manev, *J. Catal.* 33(1) (1974) 138.
158 P. Selwood, *J. Catal.* 56(2) (1979) 297.
159 F. Delbecq, P. Sautet, *J. Catal.* 152(1995) 217.
160 K. T. Hindle, S. D. Jackson, D. Stirling, G. Webb, *J. Catal.* 241 (2006) 417.
161 M. Freifelder, G. R. Stone, *J. Org. Chem*. 27 (1962) 3568.
162 V. S. Ranade, R. Prins, *J. Catal.* 185 (1999) 479.
163 G. A. Del Angel, B. Coq, G. Ferrat, F. Figueras, S. Fuentes, *Surf. Sci.* 156 (1985) 943.
164 F. Flores, R. L. Burwell Jr., J. B. Butt, *J. Chem. Soc. Faraday Trans*. 88(8) (1992) 1191.
165 Z. Hu, F. S. Xia, S. K. Purnell, O. Alexeev, S. Kawi, S. E. Deutsch, B. C. Gates, *Nature* 372 (1994) 346.
166 T. Schalow, B. Brandt, D. E. Starr, M. Laurin, S. K. Shaikhutdinov, S. Schauermann, J. Libuda, H.-J. Freund, *Angew. Chem*. 118 (2006) 3775.
167 T. Schalow, M. Laurin, B. Brandt, S. Schauermann, S. Guimond, H. Kuhlenbeck, D. E. Starr, S. K. Shaikhutdinov, J. Libuda, H.-J. Freund, *Angew. Chem*. 117 (2005) 7773.
168 L. A. Kibler, A. M. El-Aziz, R. Hoyer, D. M. Kolb, *Angew. Chem*. 117 (2005) 2116.
169 A. Ruban, B. Hammer, P. Stoltze, H. L. Skriver, J. K. Nørskov, *J. Mol. Catal. A Chem.* 115 (1997) 421.
170 M. Haruta, *Catal. Today* 36 (1997) 153.
171 N. Lopez, T. V. W. Janssens, B. S. Clausen, Y. Xu, M. Mavrikakis, T. Bligaard, J. K. Nørskov, *J. Catal.* 223 (2004) 232.

This page intentionally left blank

CHAPTER 9

Relevance of Metal Nanoclusters Size Control in Gold(0) Catalytic Chemistry

Masatake Haruta

Department of Applied Chemistry, Graduate School of Urban Environmental Sciences, Tokyo Metropolitan University, Japan

1. Introduction

Alchemy was developed in Europe in the medieval age and it founded the origin of modern chemistry [1]. The brilliantly shining color and the almost perfect chemical inertness of gold has attracted men and women as a symbol of eternal power and beauty. It is therefore reasonable that so many people dreamed to produce gold artificially. Even Newton was deeply involved in the chemical synthesis of gold [2].

Due to this history, gold has long been neglected as an element of valuable functions. For example, gold was regarded to be almost inactive as a catalyst and was indeed much less active than palladium and platinum [3]. During the course of synthesizing mixed oxides of gold with base transition metals, I found in 1982 that when gold was coprecipitated with 3d transition metals and calcined at temperatures above 570 K, the mixed oxides exhibit high catalytic activities for CO oxidation even at a temperature as low as 200 K [4]. Later, the mixed oxides were proved by Iijima with a transmission electron microscopy to be composed of hemispherical ultrafine particles of gold attached strongly to the base metal oxide supports [5]. The surprisingly high catalytic activities generated by nanoparticulate gold were introduced as one of the typical examples which could demonstrate the benefit of nanoscience and technology [6].

This chapter focuses on recent attempts which demonstrate how size control can turn inert gold into excellent catalyst. There have already been published many general reviews on gold catalysts in a wider scope [7–12]. The global market sales of catalysts amount to 8.9 billion US dollars in 2003 [13]. The market is almost equally shared by four sectors: petroleum refinery, chemical production, polymer production, and environmental maintenance. In the whole market of chemical catalysts, oxidation comes after polymerization (49%) and occupies 18%, exceeding the shares of organic synthesis (15%) and synthesis gas production (10%). Gold is expected to make significant contributions to oxidation processes, because it can often exhibit better catalytic performances than palladium and platinum in selective oxidation of hydrocarbons and organic oxygenates [14,15].

Gold has recently been launched as a break in R&D activities. In both the 13th International Congress on Catalysis, Paris, July 2004 and the 5th World Conference on Oxidation Catalysis, Sapporo, September 2005, papers dealing with Au occupied about 9%, which exceeded that of Pt catalysts, 4% in the case of 5WCOC. The number of scientific papers dealing with Au catalysts has recently grown exponentially as shown in Figure 1, and exceeded 700 in 2005.

2. Size Control of Metal Nanoclusters in Supported Gold Catalysts

In the past, gold catalysts were usually prepared by impregnating the support materials with tetrachloroauric acid ($HAuCl_4$) followed by calcination in air and often by reduction with H_2 [3,16,17]. A typical structure for such conventional gold catalysts is schematically drawn at the left side in Figure 2. Spherical gold particles with diameters larger than 30 nm are simply mixed with the particles of the support metal oxides. With this structure gold is poorly active as a catalyst. In contrast, when gold is attached as hemispherical particles with diameters below 10 nm to each particle of metal oxide supports, as shown in the right side of Figure 2, it exhibits surprisingly high catalytic activities for many reactions.

In order to deposit gold on the supports with high dispersion as nanoparticles (NPs) and clusters, there are at least nine techniques which can be classified into five categories: well mixed precursors, specific surface interaction, mixing gold colloids [18], physical deposition [19,20], and direct reduction [21]. The former two categories are schematically presented in Figure 3.

Metal Nanoclusters in Catalysis and Materials Science: The Issue of Size Control
Edited by B. Corain, G. Schmid and N. Toshima

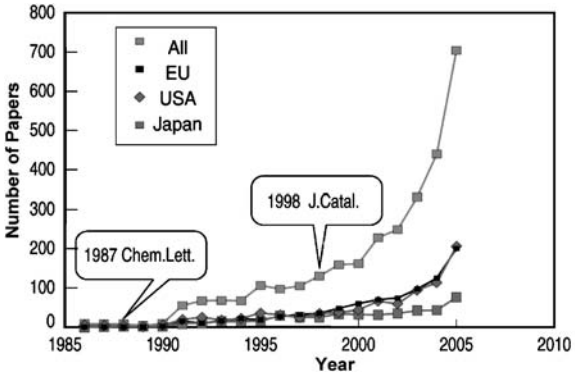

Figure 1. Annual increase in the number of papers dealing with gold catalysts.

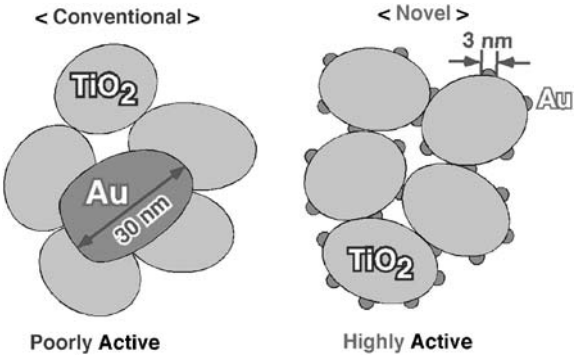

Figure 2. Schematic representation for the structural differences between the conventional and novel gold catalysts.

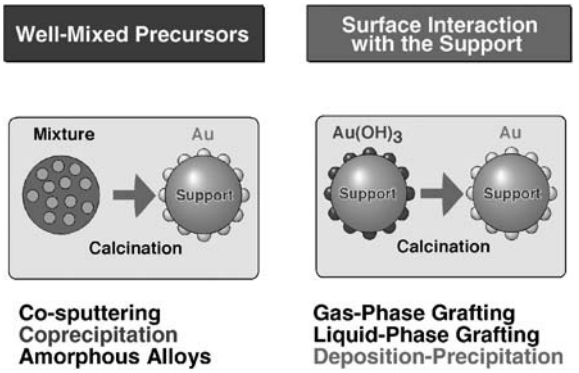

Figure 3. Two major categories for preparing highly dispersed gold catalysts.

2.1. *Preparation of Well-Mixed Precursors of Gold with the Metal Components of the Supports*

The possible strategies are: coprecipitation to prepare mixed hydroxides or carbonates [5], cosputtering of gold and the metal components of the supports by Ar containing O_2 to prepare mixed oxides [23], and amorphous alloying to prepare metallic mixed precursors [24]. These

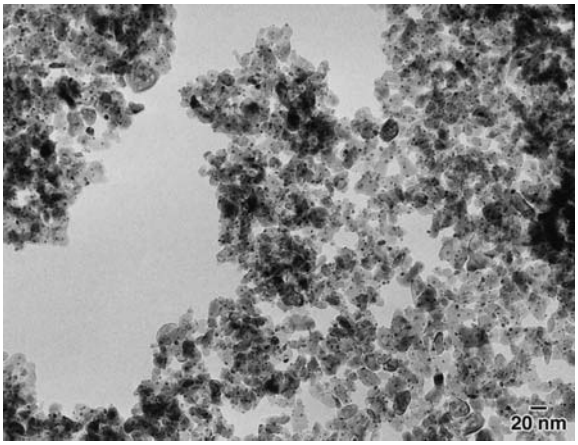

Figure 4. TEM for Au/Fe_2O_3 coprecipitate calcined at 673 K in air. Atomic ratio of Au/Fe is 1/19.

precursors are calcined in air, usually at temperatures above 570 K to transform gold species into metallic particles and the counter metal species into metal oxides. Figure 4 shows that in the coprecipitated Au/Fe catalyst gold particles with diameters around 3 nm are homogeneously dispersed on α-Fe_2O_3 particles of about 50 nm in diameter [5]. It should be noted that an aqueous solution of $HAuCl_4$ and ferric nitrate mixture is poured into aqueous sodium carbonate solution in a short period (within 3 min) to obtain such homogeneously distributed gold NPs. In a recent paper [25] which claimed that oxidic gold species were more active than metallic gold, Au/Fe coprecipitates were produced in completely opposite procedures, by the drop-wise addition of sodium carbonate solution into metal salts solution. In this case, the Au/Fe precipitates were produced at different pH and therefore with different compositions, resulting in inferior catalytic activity to that of the normal coprecipitates.

2.2. *Utilization of Specific Surface Interaction of Gold Compounds with the Metal Oxide Supports*

The approach comprises: deposition–precipitation (DP) of $Au(OH)_3$ onto the hydroxide surfaces of metal oxide supports from an alkaline solution of $HAuCl_4$ [26] and grafting of organo gold complexes such as dimethyl gold (III)acetylacetonate (hereafter denoted as Au acac complex) [27] and $Au(PPh_3)(NO_3)$ [28] either in gas and liquid phase are advantageous in that a variety of metal oxides commercially available in the forms of powder, sphere, honeycomb can be used as supports.

Typical experimental procedures are as follows for DP method, which is used for the industrial production of gold catalysts. To an aqueous solution of $HAuCl_4$, the pH of which is 2–3, an aqueous solution of NaOH is added to adjust the pH at a fix point in the range of 6–10. In neutral or weakly basic solution $AuCl_4^-$ ion is transformed into $AuCl_n(OH)_{4-n}^-$ ($n = 4 \sim 0$). To this solution support materials are immersed or dispersed. When the pH, concentration, and temperature are carefully adjusted, solid $Au(OH)_3$ precipitate is deposited exclusively on the

surfaces of the support without precipitation in the solution. The precursors are washed to remove chloride and sodium ions and then dried and calcined. Figure 5 shows a TEM for a typical catalyst Au/TiO_2, where gold particles are nearly hemispherical and are attached to TiO_2 at their flat planes.

An advanced technique for DP method developed by Louis is to use urea as a precipitating reagent and to continue aging for one night or day to form $Au-NH_4^+$ complexes [29]. This technique can lead to higher metal loadings above 10 wt%, higher metal capture efficiency, and smaller gold particles.

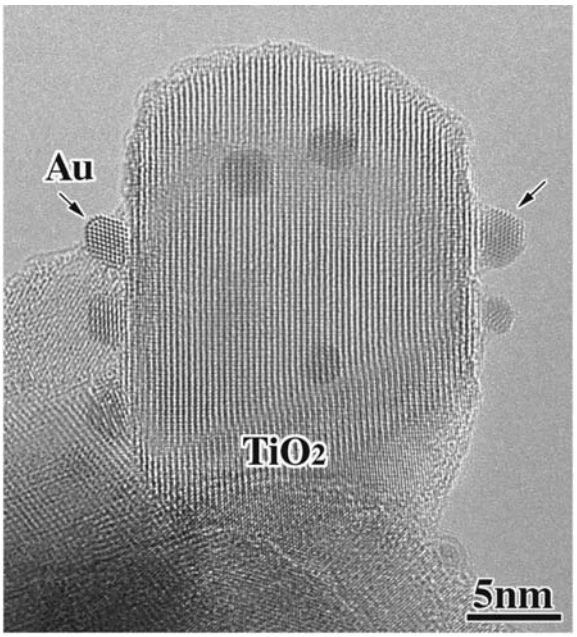

Figure 5. Au/TiO_2 prepared by DP followed by calcination at 573 K [by the courtesy of Dr. Akita, AIST].

Another modification is to add magnesium citrate to deposit smaller gold particles during coprecipitation or DP for preparing Au/TiO_2 and $Au/Mg(OH)_2$ [30,31]. As shown in Figure 6, under a controlled pH above 7, magnesium citrate is only partly dissociated and the concentration of free citrate anion in starting solution is limited by dissociation equilibrium thus causing no reduction of gold complex ions in liquid phase. Citrate ions are strongly adsorbed on $Mg(OH)_2$ surfaces and remain even after decomposition of $Au(OH)_3$ during calcination, preventing gold metallic particles from coagulation.

Gas-phase grafting (GG) is characteristic in that gold can be deposited even on the acidic surfaces, such as activated carbon and on SiO_2 [27]. The vapor of gold acac complex is adsorbed on the support powder probably through the interaction of electron-rich oxygen atoms in acetylacetonate and then calcined in air to decompose it into metallic gold particles.

2.3. Mixing of Gold Colloids with the Support Materials [32]

This method is especially valid for the preparation of gold NPs mixed with activated carbon, which are active and stable for the selective oxidation of hydrocarbons and alcohols in water. Over activated carbon gold could not be directly deposited as NPs by using the techniques described above, such as DP and even by GG. Gold colloids with mean diameters from 2.5 to 10 nm stabilized by poly vinyl alcohol or poly vinyl pyrrolidone are used.

2.4. Vacuum Evaporation of Gold Metal Atoms and/or Clusters

Over single crystal surfaces with defect sites, vacuum deposition of gold vapor or size-selected gold anion clusters at low temperatures can lead to relatively homogeneous

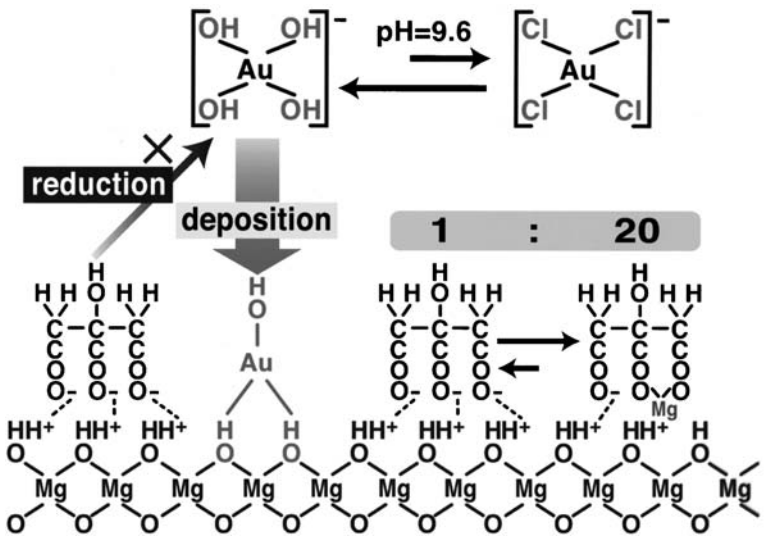

Figure 6. Postulated role of magnesium citrate in the deposition precipitation of gold hydroxide on $Mg(OH)_2$.

dispersion of gold after annealing [33]. To powder supports, magnetron radio frequency sputtering techniques are also applicable producing stable gold catalysts such as Au/Al_2O_3, Au/Co_3O_4 without alkaline and chloride ion impurities [34,35].

2.5. Direct Reduction on the Support Surfaces

When organic polymers are used as supports, it is not allowed to calcine them at temperatures above 473 K. We have recently developed a technique to deposit gold NPs on polymer beads by reducing gold complex ions exclusively on the support surfaces without reduction in liquid phase by controlling concentration, reducing agents, temperature, and pH [36]. As in the case of metal oxide supports [21], gold NPs can be deposited on the microbeads of polymers such as PVC, PMMA, and PS, as shown in Figure 7 [37]. This technique is also applicable to activated carbons.

There are a few important points to note concerning the preparation of highly dispersed gold NPs. Chloride anion markedly enhances the coagulation of gold NPs so that the removal of chloride anion from the catalyst precursors before calcination is important. This is why coprecipitation and DP methods are advantageous over the impregnation method. The second point is that GG of Au acac complex leads to non-selective deposition of gold NPs while DP from aqueous solutions leads to selective deposition of gold NPs. For example, over $Ti–SiO_2$ supports, GG can deposit gold NPs over SiO_2 surfaces in addition to Ti cation sites, whereas DP can deposit gold NPs only on the Ti cation sites but not on SiO_2 surfaces. This difference in the site of gold deposition can tune the catalytic behavior, for example, in the reaction of propylene with O_2 and H_2 in gas phase [22].

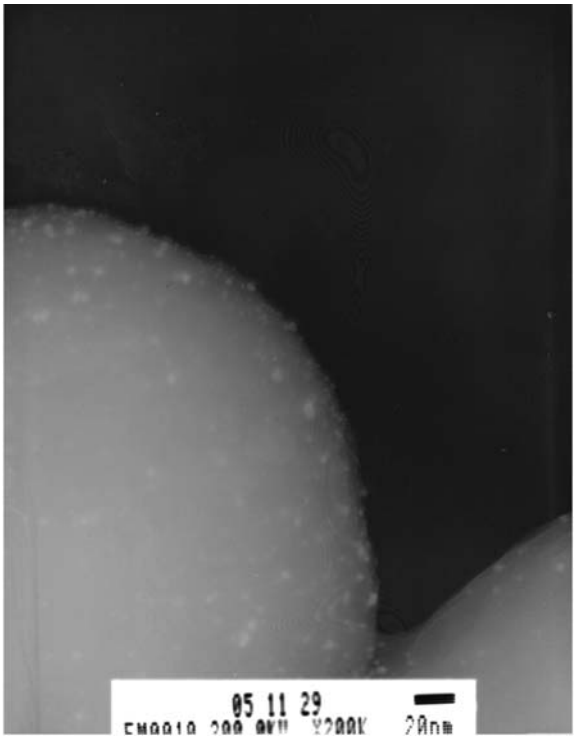

Figure 7. Gold NPs directly deposited on PVC microbeads by deposition–reduction method.

3. Support and Size Effect in Gold Catalytic Chemistry

Many reactions have so far been studied by using gold NPs supported on a variety of materials or stabilized as colloids by polymer ligands [7–10]. Among oxidation, hydrogenation, steam reforming, water gas shift reaction, reduction of nitrogen oxides, and so forth, gold NPs are especially superior to other noble metal catalysts in oxidations at low temperatures below 473 K. In this chapter, three oxidation reactions, CO oxidation, propylene epoxidation, and aerobic liquid phase oxidation of alcohols, are chosen to clarify the unique and practical catalytic properties of gold NPs. The oxidation of CO at low temperature is receiving growing attention in applications to indoor air quality control and CO removal from hydrogen for fuel cells. Direct gas-phase propylene ($CH_3CH=CH_2$) epoxidation to produce propylene oxide (PO) is regarded as a sort of ''Holy Grail'' in catalysis research, because hydrogen abstraction in $–CH_3$ group preferentially takes place to produce acrolein ($OHCCH=CH_2$). Aerobic alcohol oxidation in water is becoming important in relation to the development of new environmentally benign and biomass-based chemical processes.

Concerning the mechanisms how gold, inert as a metal, can exhibit surprisingly high catalytic activities and selectivities, several hypotheses have been proposed. They can be classified in terms of active sites or reaction sites [38], which may change in some cases depending on support materials even for the same reactions.

3.1. CO Oxidation

The active sites or reaction sites proposed until now for CO oxidation over gold catalysts with different support metal oxides are as follows:

(a) Perimeter interfaces around gold NPs as reaction sites for CO and O_2 [12,39]: Al_2O_3, SiO_2, TiO_2, MnO_2, Fe_2O_3, Co_3O_4, NiO, ZnO, ZrO_2, CeO_2.
(b) Edge and corner sites of gold NPs [40].
(c) Surfaces of gold clusters or thin layers having electronically different nature [31,41,42]: $Be(OH)_2$, $Mg(OH)_2$, MgO, TiO_2.
(d) Cationic gold (Au^+ or Au^{3+}) embedded in the support [25,43–46]: Fe_2O_3, La_2O_3, CeO_2, $La(OH)_3$.

Among the above four hypotheses, the first one, gold NPs supported on base metal oxides lead to the highest catalytic activity and stability. Their characteristic features can be summarized in the following points [11,12].

(1) The high catalytic activity for CO oxidation at temperature below 273 K emerges when correctly

coprecipitated precursors are calcined at 573 K and above, whereas the catalytic activity for H_2 oxidation emerges even after calcination at lower temperatures [5] (Figure 8). On the other hand, inversely coprecipitated precursors prefer calcination at lower temperatures [24]. It is assumed based on characterization with TEM, EXAFS/XANES, Moessbauer, and so forth that cationic gold species are responsible for CO oxidation at room temperature. The latter catalyst is, however, less active, probably because the dispersion of gold might be heterogeneous (note in this case that interpretation of characterization data is complicated) and that the interaction with ferric hydroxides or oxides might be weak.

(2) The catalytic activity markedly depends on the contact structure of gold with the supports. Remarkably high activity emerges when hemispherical gold NPs are attached to the support at their flat planes. This contact structure is often epitaxial as shown in Figure 9 and provides longer perimeter distance around gold NPs.

(3) The selection of support is also important because it always changes catalytic activity and stability of gold NPs. When gold NPs are deposited on activated carbons and polymers [36], they are completely inactive for gas-phase CO oxidation although as small as 5 nm. Acidic metal oxides such as Al_2O_3–SiO_2 are also negative as supports for gold NPs [27]. Reducible or semiconductive metal oxides are most suitable as supports in terms of activity and stability of gold NPs.

(4) The catalytic activity depends on the size of gold NPs. The precursors are washed, dried, and calcined in air at temperatures above 570 K, where gold species are transformed into metallic particles. The critical size for the genesis of catalytic activity is 10 nm, below which edges and corners occupy a certain fraction and provide sites for reactant adsorption. At 2.0 nm the catalytic properties change dramatically in some cases owing to quantum size effect.

(5) Active gold catalysts are advantageous in that water usually enhances the catalytic activity [39]. Reducible or semiconductive metal oxide supports do not need moisture for room temperature catalytic activity, while non-reducible metal oxides such as Al_2O_3 and SiO_2 do [39] (Figure 10).

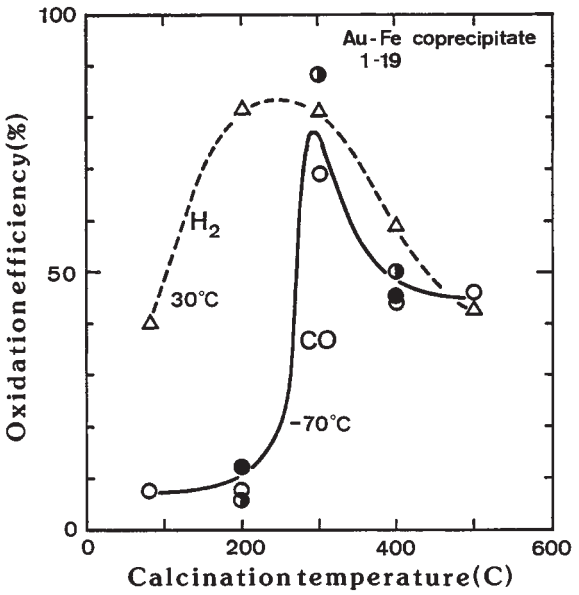

Figure 8. Oxidation efficiencies of H_2 and CO over the Au/Fe(1/19) coprecipitate calcined at different temperatures.

A hypothesis that edge and corner sites work as active sites can explain why turn over frequency (TOF), which is defined as the reaction rate per one active site, in the case of metal catalysts, per surface exposed metal atom, increases with a decrease in the diameter of gold particles. However, it fails to explain the significant contribution of support materials and the contact structure of gold NPs. It seems to be reasonable that those edges and corners act as the sites for adsorption of one of the reactants, for example, CO in its oxidation.

Another hypothesis that a change in electronic properties of gold at thickness of two atoms [42] presents the highest catalytic activity makes arguments too much simplified. A dramatic change in catalytic properties may happen in this region of size by quantum size effect on some metal oxides, but this is not the essential condition for gold to be catalytically active. This physical model neglects the direct participation of support in the reaction,

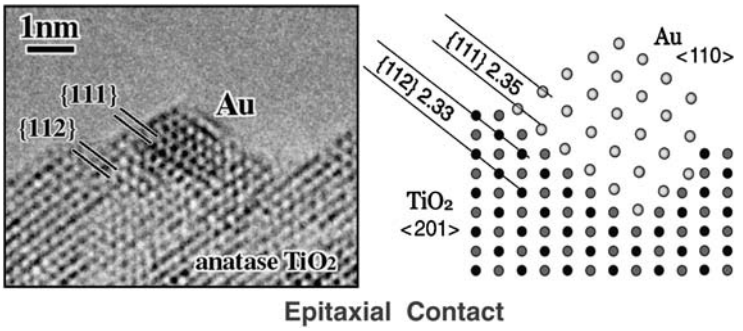

Figure 9. TEM and schematic representation of Au/TiO_2 interfaces [12].

which is proved to be significant by the influence of support materials and moisture effect.

The experimental results (Figure 11) presented by Goodman and his coworkers [42] may be valid to discuss the catalytic behavior of gold clusters smaller than 2.0 nm in diameter. It should be noted that in their model catalysts the effect of Mo support on the nature of gold layers through a very thin layer of TiO_2 is not negligible and the catalytic activity reported might be initial rates, not steady-state ones on which catalytic activity is discussed for real powder catalysts. On the other hand, it has been reported that gold clusters on a single crystal of MgO become active for CO oxidation when they are composed of at least eight atoms [41]. The enhancing role of H_2O for CO oxidation is investigated by the DFT calculation and is ascribed to the enhanced dissociation of O_2 molecules, as shown in Figure 12 [47].

Another example that small clusters exhibit high catalytic activity is seen in $Au/Mg(OH)_2$ prepared by DP [31]. Only when gold clusters are composed of 13 atoms they exhibit high catalytic activity for CO oxidation even at 200 K. Furthermore, it is suggested by computer simulation of X-ray scattering that what is active is icosahedron but not cubo-octahedron (Figure 13).

The hypothesis that cationic gold (Au^+ and/or Au^{3+}) is catalytically active still needs further experimental evidences because during reaction those oxidic gold species might be transformed into metallic particles. If this is a really working mechanism for most of metal oxide supports, why is calcination at temperature above 570 K necessary for the genesis of high activity at 200 K? Although it may happen that gold oxides are more active than bulk gold metals, it is doubtful that such gold oxides are stable, especially under the presence of reducing molecules, and are more active than metallic Au NPs. In the case of water gas shift reaction, our Au/CeO_2 catalysts containing many Au NPs of about 2 nm in addition to large gold particles of about 15 nm are more active than a commercial $Cu/ZnO/Al_2O_3$ catalyst [48], whereas the catalysts investigated by Flytzani-Stephanopoulos's group are less active

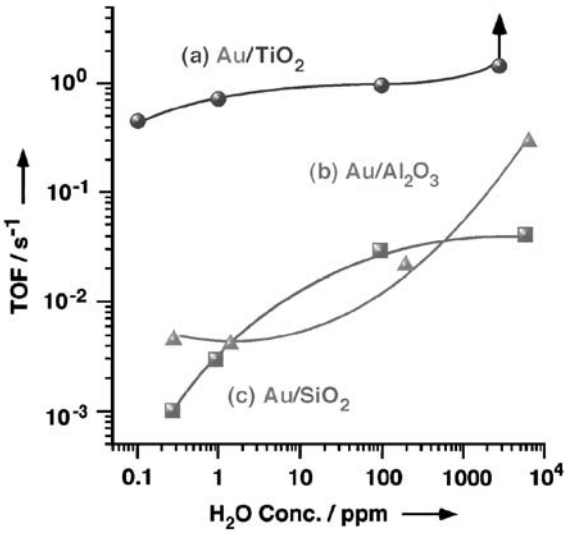

Figure 10. Effect of moisture concentration on TOF for CO oxidation [39].

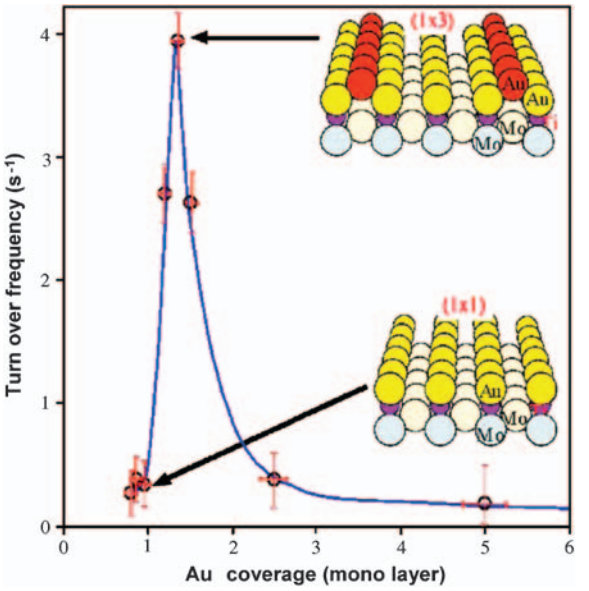

Figure 11. Turn over frequency for CO oxidation over $Au/TiO_2/Mo$ model catalysts [42].

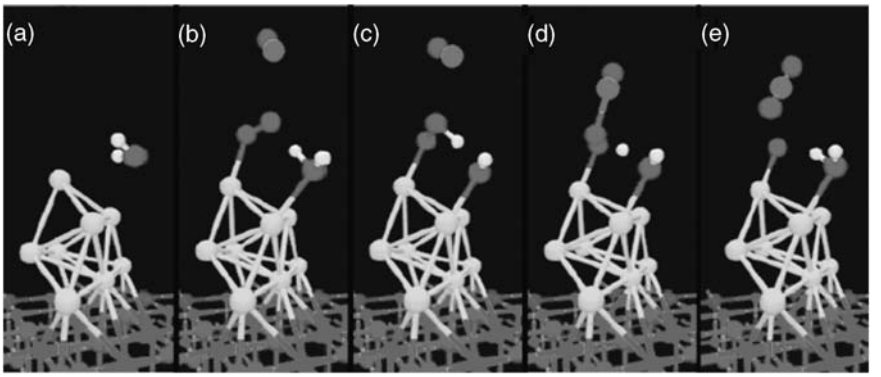

Figure 12. Promoting effect of moisture on CO oxidation over an eight atoms gold cluster on MgO single crystal [47].

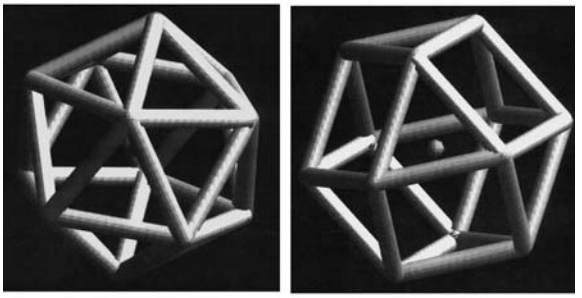

Figure 13. CO oxidation over 13 atoms gold clusters having different three-dimensional structures supported on $Mg(OH)_2$ [30].

[44,45]. It should be noted that only an annular dark field scanning transmission electron microscope allows us to detect such small Au NPs dispersed on heavy CeO_2 support. Even though large metallic gold particles are removed by NaCN solution, it might happen that during water gas shift reaction, oxidic gold species are reduced to form small Au NPs.

However, in some cases oxidic gold species may be the active sites for CO oxidation. Gates reported that oxidic gold dispersed on La_2O_3 by using GG of Au acac complex is active at room temperature [43]. On the other hand, we have recently found that over Au/La coprecipitates calcined at temperatures below 500 K are active even at 193 K [46]. The EXAFS and XANES analyses of the active samples showed that oxidic gold stabilized by $La(OH)_3$ is responsible for low-temperature activity.

Most probable reaction pathways are shown in Figure 14 [39]. The perimeter interfaces around gold NPs work as reaction sites between CO adsorbed on the gold surfaces, most probably on edges and corner sites, and oxygen species activated at the support-side perimeters [12,39]. This mechanism can explain all the above features from (1) to (5). The perimeter mechanism is compatible with the fact that the high catalytic activity appears when Au-containing precursors are calcined at temperatures above 570 K, where gold particles grow to 3–5 nm in diameter.

Reaction takes place at the perimeter between CO adsorbed on gold surfaces and oxygen activated on the support surfaces. Water enhances the dissociation of O_2 and the desorption of carbonate species [39]. The perimeter distance becomes the longest when hemispherical gold particles are attached to the supports at their flat planes, as schematically shown in Figure 15 [40]. As seen from this figure, perimeter length as reaction sites (red) together with edge and corner as adsorption sites (blue) increases in number with a decrease in the diameter of gold particles. This is why TOF is remarkably dependent on the contact structure (Figure 16) and the size of gold particles. In contrast, TOF is almost independent of the shape and

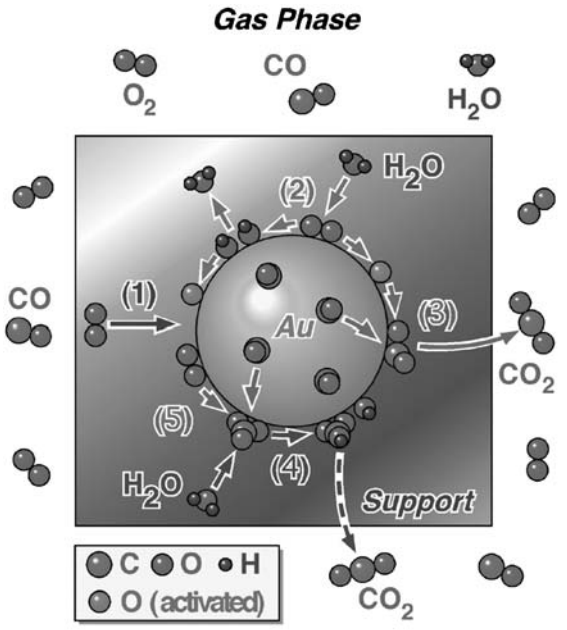

Figure 14. Reaction pathways for CO oxidation over supported gold catalysts [39].

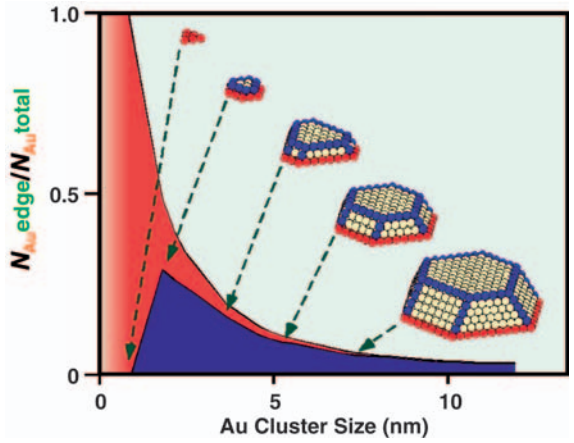

Figure 15. Ratio of edge and perimeter atoms as a function of particle diameter [40].

contact structure of platinum particles because the reaction of CO with oxygen takes place only over the metal surfaces without direct participation of the support materials in the reaction.

The enhancing effect of moisture shown in Figure 10 can be readily explained by the involvement of surface OH groups over Al_2O_3 and SiO_2, where the dissociative adsorption of oxygen molecule hardly takes place. The hypothesis (c), physical model, has difficulty in interpreting different catalytic behavior of gold NPs in the presence of moisture depending on the type of metal oxide supports.

Figure 17 shows that TOF for CO oxidation increases with a decrease in the diameter of gold from 5 nm. This

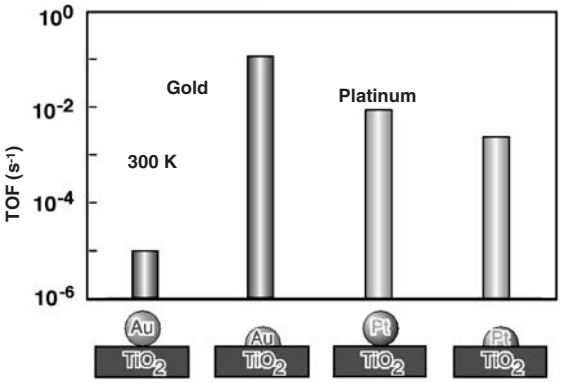

Figure 16. Effect of contact structure on the catalytic activity in CO oxidation over supported Pt and Au NPs.

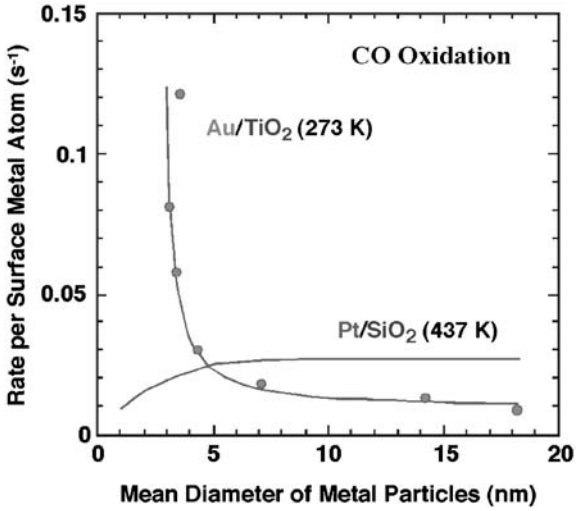

Figure 17. TOFs for CO oxidation over Pt/SiO_2 and Au/TiO_2 as a function of metal particle diameter.

tendency coincides well with the curves for the fractions of edge and perimeter sites in Figure 15. In addition, as shown in Figure 18 [49], the adsorption of CO becomes appreciable only when the size of gold is smaller than 10 nm, indicating that the sites for CO to adsorb may be edges and corners but not on the flat terrace sites of gold.

At the perimeter interfaces gold may exist as cationic species bound to oxygen anions and OH groups as proposed by Bond and Thompson [50]. Gates reported EXAFS analyses during CO oxidation over Au/TiO_2 showing that the catalytic activity reaches a maximum at a specific ratio of cationic gold divided by metallic zero-valent gold [51]. This fact supports that metallic particles of gold are needed for CO adsorption and oxidic gold is necessary for O_2 activation, probably at the perimeter sites.

3.2. *Propylene Epoxidation*

The latest industrial strides in PO synthesis are liquid phase epoxidation of propylene with H_2O_2 over TS

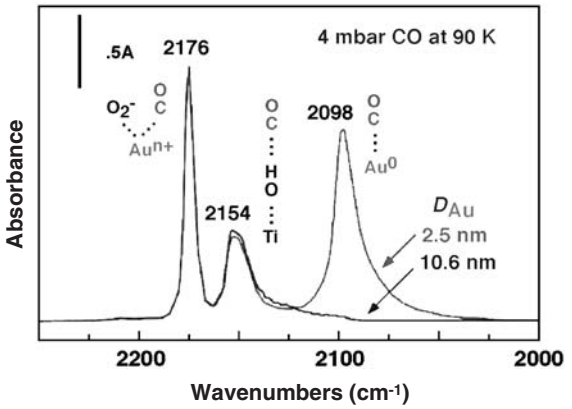

Figure 18. FT-IR for CO adsorbed on Au/TiO_2 having different sizes of gold particles [49].

(titanosilicalite)-1 catalyst and the epoxidation with cumyl hydroperoxide followed by the reduction of produced cumyl alcohol with H_2 to recycle cumene. A common feature of these recent processes is that, in addition to O_2, H_2 is also consumed in another process separated from the epoxidation process of propylene. Therefore, a reasonable extension in the near future is to use both O_2 and H_2 simultaneously in one single step, namely, reductive activation of oxygen molecule. While the energy required to activate O_2 for reaction by directly splitting it into its constituent atoms is 119 Kcal/mol, which is larger than C–H bonding energies, the copresence of H_2 can activate oxygen under less extreme conditions with energy input of less than 2.4 Kcal/mol, leading to a feasible alternative method of controlling the reactivity of oxygen species so as to produce valuable organic oxygenates [14].

In the liquid phase of MeOH or BuOH as a solvent palladium-based catalysts are used being supported on TS-1. In batch reactors, the selectivity to PO is lower than 50% and hydrogenation to produce propane prevails [52,53], whereas PO selectivity is improved to 88%–99% when semibatch reactors [53–55] or flow reactors are used [56]. The space time yield (STY) of PO exceeds 100 g PO/h/k-cat., which is comparable to the STY for the current industrial production of ethylene oxide by using molecular oxygen alone and Ag/Al_2O_3 catalysts. It should be noted that STY of PO has recently been reaching a level of 100 g PO/h/k-cat. in the gas phase containing C_3H_6, O_2, and H_2, as well. In the gas phase epoxidation, only coinage metals Ag and Au are selective to PO, when they are deposited on anatase TiO_2 or titanium silicates by DP. In contrast, palladium and platinum are selective not to oxidation but to hydrogenation to form propane in the gas phase.

Hayashi and Haruta found that gold deposited on TiO_2 could produce PO with selectivities above 90% in an inert gas stream containing C_3H_6, O_2, and H_2 at temperatures below 373 K [57]. Among a variety of metal oxide supports, only TiO_2, not with rutile and amorphous structure but with anatase structure, is effective. The requirement to the size of gold particles is also very strict. Figure 19 shows that a diameter of 2–5 nm is optimum to produce PO whereas small gold clusters below 2 nm produce

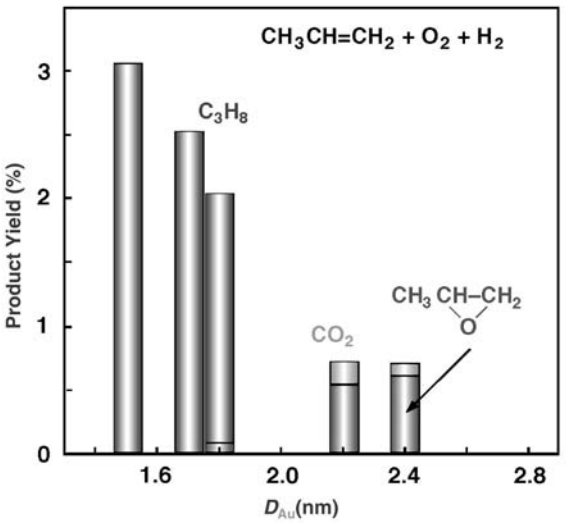

Figure 19. Product yields by the reaction of propylene with O_2 and H_2 over Au/TiO_2 catalysts as a function of mean diameter of gold particles.

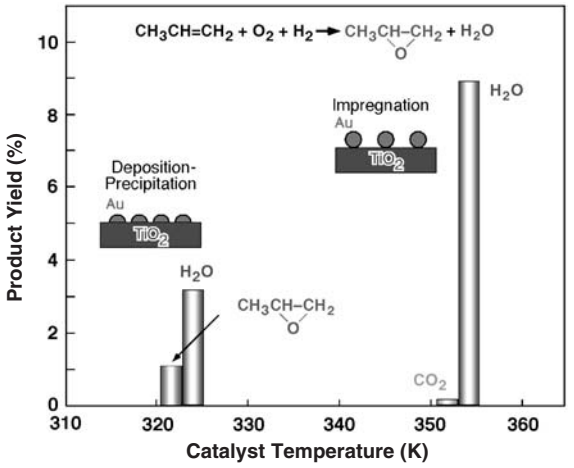

Figure 20. Product yields over Au/TiO_2 catalysts prepared by different methods.

propane almost exclusively [57,58]. This phenomenon suggests that small gold clusters behave like palladium and platinum in the copresence of O_2, in other words, can dissociate H_2 molecule at low temperatures.

Preparation method and conditions are crucial to the catalytic performance of Au/TiO_2 [57–61]. As seen from Figure 20, when hemispherical gold particles are attached to the TiO_2 surfaces at their flat planes by DP method, PO is selectively produced. Impregnation method, which brings about large spherical gold particles simply loaded on TiO_2, resulted in the combustion of C_3H_6 and H_2 yielding a large amount of H_2O and a small amount of CO_2 at a relatively high temperature. Ion exchange by using $[Au(ethylenediamine)_2]Cl_3$ results in the production of propane probably due to smaller sizes of gold particles at a limited metal loading [60]. Mixing of size-controlled gold colloids with TiO_2 powder does not produce PO but produces propane when [tetrakis(hydroxymethyl)-phosphonium chloride] (THPC) is used as a stabilizer for gold colloids [59,60]. In contrast, gold colloids obtained in the presence of poly-vinylpyrrolidone (PVP) or do-decylthiol lead to Au/TiO_2 catalysts selective to PO [61,62], although their catalytic performances are inferior to those of DP catalysts.

Over Au/anatase TiO_2 the reaction should be carried out at a temperature below 373 K because otherwise PO is further oxidized to acetone and CO_2 and H_2O. Accordingly, STY of PO is below 10 g PO/h/k-cat., which is one order of magnitude lower than that of ethylene oxide in industrial processes. Much larger STY of PO can be obtained by replacing TiO_2 with TiO_2 highly dispersed on SiO_2 surfaces, titanium silicalites, and titanium silicates and by operating the reaction at a temperature from 423 to 473 K.

Currently there are four major lines of approach towards gas-phase epoxidation of propylene: (1) mechanistic studies of Au/TiO_2 catalysts through kinetics, spectroscopic identification of adsorbed species and surface science, (2) experimental and theoretical investigation of Au/TS-1 catalysts, (3) improvement of catalyst life of Au/3-D mesoporous $Ti–SiO_2$ catalysts, and (4) replacement of Au with Ag on TS-1 support.

3.2.1. Mechanistic Study of Au/TiO_2 Catalysts

Relatively detailed study has been done for the reaction pathways over Au/TiO_2 catalysts mainly because of simplicity in catalytic material components. The rate of PO formation at temperatures around 323 K does not depend on the partial pressure of C_3H_6 up to 20 vol% and then decreases with an increase, while it increases monotonously with the partial pressure of O_2 and H_2 [57]. A kinetic isotope effect of H_2 and D_2 was also observed [63]. These rate dependencies indicate that active oxygen species are formed by the reaction of O_2 and H_2 and that this reaction is rate-determining [57,63,64].

Propylene is adsorbed on the surfaces of both gold NPs and the TiO_2 support, which was indicated by temperature programmed desorption (TPD) experiments for Au/TiO_2 catalyst and the TiO_2 support treated similarly as in catalyst preparation [57]. The adsorption of propylene occurs nearly to saturation and tends to inhibit the epoxidation at higher partial pressure. Propylene adsorbs on Au (1 1 1) and Au (1 0 0) surfaces with its molecular plane tilted slightly with respect to the surface plane [65]. Desorption activation energy is 9.4 kcal/mol on Au (1 1 1) and Au (1 0 0) and is slightly lower than 10.8–12.6 kcal/mol on Ag (1 1 0) and appreciably lower than 19 kcal/mol on Pd (1 1 1). On oxygen covered surfaces of gold propylene adsorbs more tightly than the bare metal surfaces. DFT calculation suggests that propylene binds to a corner atom on gold clusters [66]. The binding involves an electron density transfer from the HOMO of propylene to one of the LUMOs of gold, thus leading stronger bond to Au_n^+ than to Au_n. It is surprising that binding energy of propylene to positively charged mono-atomic silver and gold clusters is calculated to be 38.2 and 65.7 kcal/mol, respectively, showing stronger bonding for $Au(C_3H_6)^+$ [67].

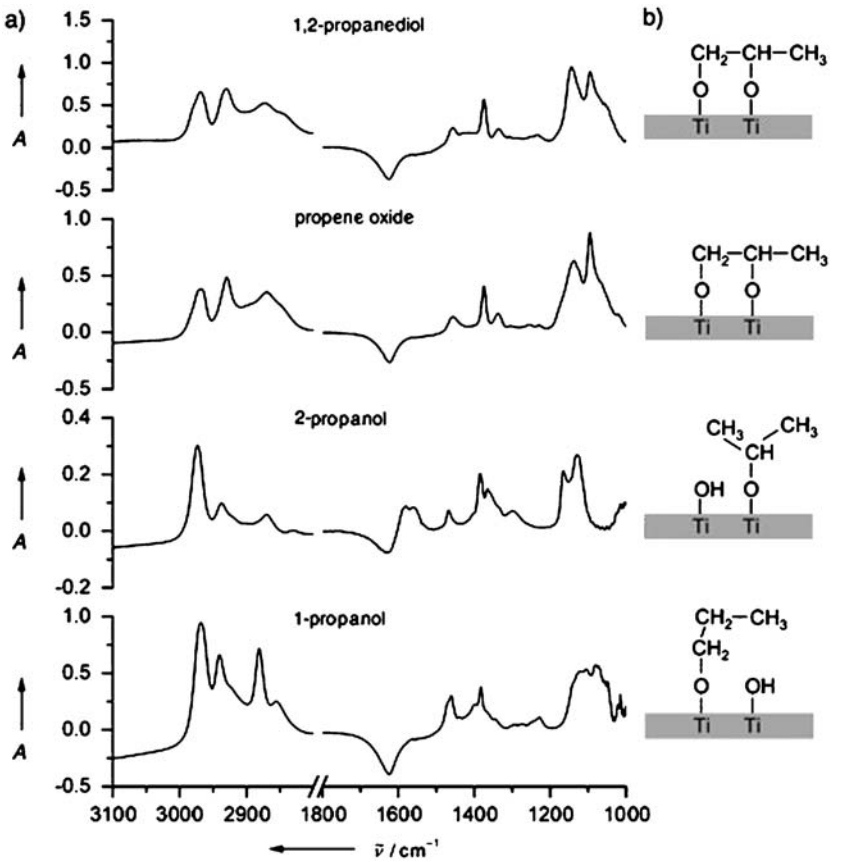

Figure 21. FT-IR spectra for PO-related compounds introduced to Au/TiO_2 catalyst [70].

Campbell reported that propylene adsorbs weakly on gold surfaces and adsorbs moderately on TiO_2 (1 1 0) with a desorption activation energy of 11.3 kcal/mol and that propylene adsorbs most strongly at the perimeter of gold islands on TiO_2 (1 1 0) [68].

Nujhuis and coworkers [69] assume, based on FT-IR investigation, that propylene is adsorbed on the surfaces of Au particles but not on TiO_2 surfaces. On the other hand, they interpreted that bidentate propoxy species which were identified by FT-IR (Figure 21) are adsorbed on the TiO_2 surfaces. They finally propose that propylene is most likely adsorbed at the perimeter interfaces between gold NPs and the TiO_2 support to explain the formation of bidentate propoxy species on TiO_2 surfaces by the aid of gold NPs [70]. Water in the reactant gas stream enhances the desorption of PO from the catalyst surfaces but it in turn suppresses the adsorption of C_3H_6 resulting in minor change in steady-state catalytic activity after 5 h [71].

The identification of surface adsorbed species has been carried out with FT-IR [69] and Raman spectroscopy [70] during reaction and with GC-MS after epoxidation reaction [72]. The aggregation of gold NPs is not appreciable during reaction at temperatures below 473 K [69,72]. Catalyst deactivation, which happens within a few hours causing a decrease in C_3H_6 conversion by about 50%, can be accounted for by the accumulation of successively oxidized compounds after isomerization and cracking of

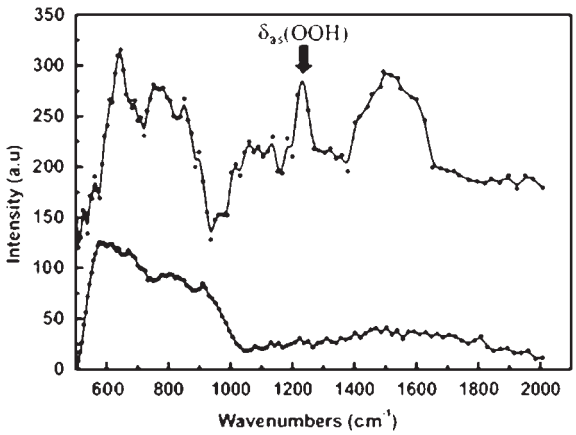

Figure 22. Inelastic neutron scattering for Au/TiO_2 [73].

propylene oxygenates and their oligomerized compounds [72]. Nijhuis et al. [69,70] have also identified intermediate species during reaction: the major adsorbates are bidentate carbonate/carboxylate/formate species.

As for oxygen species, significantly important knowledge has been accumulated both by experimental and theoretical investigation. Goodman and his coworkers reported inelastic neutron scattering evidence (Figure 22)

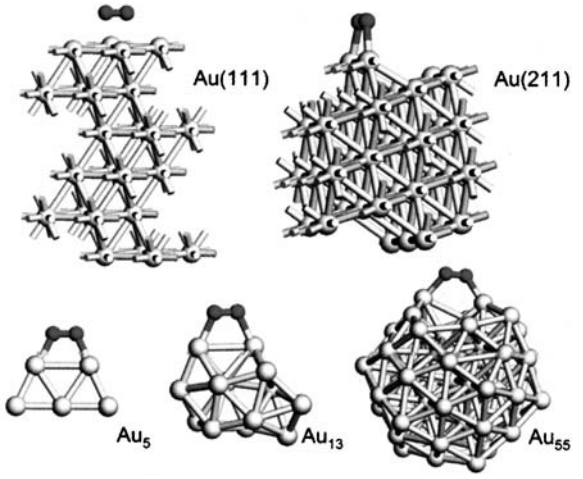

Figure 23. Adsorption of oxygen molecule over gold clusters with different sizes [74].

for the formation of OOH and H_2O_2 species from O_2 and H_2 on the Au/TiO_2 catalyst [73]. Barton and Podkolzin based on experimental and theoretical investigation proposed that water formation from O_2 and H_2 over gold deposited on SiO_2, MFI zeolite, and TS-1 proceeds through the formation of OOH and H_2O_2 intermediates [74]. The catalytic activity of gold on MFI or TS-1 is higher than that of Au/SiO_2 by 60–70 times, which can be ascribed to the higher concentration of 13 atoms clusters of gold on MFI and TS-1 supports than on SiO_2 supports. As shown in Figure 22 [74], 13 atoms gold clusters can be incorporated into the pore intersection in MFI zeolite structure. Gold clusters smaller than that are less reactive due to the instability of OOH intermediate whereas larger gold particles are less reactive due to the instability of adsorbed oxygen. In the epoxidation as well as H_2O_2 formation, the rate-determining step is assumed to be the addition of H_2 in gas phase to the surface adsorbed OOH to form H_2O_2 [64,74], whereas Nijhuis and coworkers [64,70,75] emphasize the importance of two other reaction steps, a reactive adsorption of propylene on TiO_2 to produce bidentate propoxy species, and a reactive desorption of this adsorbed species to form PO.

An intensive work on density function theory (DFT) calculations has been done to seek for probable pathways for the formation of H_2O_2 [76,77] and PO [78,79] through collaboration of theoreticians and experimentalists. The gold clusters composed of 3–55 atoms having positive or negative electric charges were studied for H_2O_2 synthesis as the key step in propylene epoxidation [74,76,77]. Thomson and Delgass made calculation for Au_3, A_4^+, Au_5, and Au_5^- clusters in the gas phase and noted that both neutral and charged Au clusters are active for the formation of H_2O_2 [77]. They suggested that in the gas phase A_4^+ is the most active, while Barton and Podkolzin [74] reported for MFI-supported gold clusters that intermediate-size Au_{13} clusters is the most active for water synthesis.

The DFT calculation indicated that the rate-determining step is the attack of Au-OOH to the C=C double bond to form PO with activation barrier of 19.6 kcal/mol [79]. Since Ti-based support is indispensable to obtain high selectivity to PO, it is reasonably assumed that isolated tertrahedrally coordinated Ti participate in the epoxidation. Ti sites located adjacent to Si vacancies in the TS-1 lattice are more reactive than fully coordinated Ti sites and may be the site for epoxidation. Another pathway is also probable, namely, epoxidation on the surfaces of Au [79] (Figure 23).

3.2.2. Improvements of Catalytic Performance of Au/TS-1

Although Au/TS-1 is advantageous in catalyst stability owing to the well-crystallized structure and hydrophobicity, the catalytic performance was inferior to gold supported on 3-D mesoporous titanosilicates in terms of propylene conversion, PO selectivity, H_2 utilization efficiency [80]. However, recently Delgass has obtained high PO space time yield of 134 g PO/h/kg-cat. (propylene conversion 10%, PO selectivity 76%), which is comparable to that of ethylene oxide in commercial plants, by using 0.081 wt% Au/TS-1 as a catalyst [81]. The key to success is to pretreat the TS-1 support in 1 M aqueous solution of NH_4NO_3 at 353 K for 15 h. The remarkable enhancement seems to be due to the selective deposition of gold near the Ti sites as well as to an increase in actual gold loadings, presumably because of the preferential formation of Au–amine complex.

Although Au particles with mean diameters around 5–6 nm were observed by TEM, Delgass assumes based on DFT calculations that such large particles are neither active nor selective but small Au clusters such as Au_3 are responsible for the epoxidation of propylene [76–78]. According to this hypothesis, TS-1 is useful as a support to confine small Au clusters into the spaces of microcages. Figure 24 shows a sharp contrast in research strategy between Delgass's group and Haruta's group in terms of the size of Au particles and pores of the $Ti–SiO_2$ supports. It also shows the position of Ag/TS-1 catalysts studied by Guo's group.

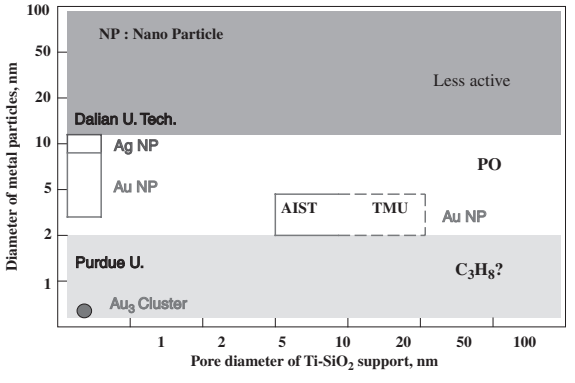

Figure 24. Size of metal particles and support pores in silver and gold catalysts for gas-phase propylene epoxidation.

3.2.3. Improvement of Catalyst Life of Au/3-D Mesoporous Ti–SiO_2

Figure 25 shows that the yield of PO increases with an increase in the diameter of pores of titanium silicate supports including TS-1, Ti-MCM-41, and -48 [82]. This suggests that larger pores are advantageous, especially for the smooth diffusion of reactants and rapid escape of the product, PO [72,83,84]. Although non-porous support was expected to facilitate the desorption of PO, Ti deposited on superfine non-porous SiO_2 (diameter 10–140 nm, specific surface area 77 m^2/g) did not result in higher yield of PO [85]. TEM observations showed that the population density of gold particles over the surfaces of non-porous supports was small in comparison with those for micro and mesoporous supports probably because of the lack of defect sites.

Over Au deposited on 3-D mesoporous Ti–SiO_2 with pore diameter of 9 nm, one of the best results was obtained. At an SV of 4000 h/mL/g-cat., propylene conversion above 8%, PO selectivity of 91% giving a steady STY of 80 g PO/h/kg-cat. [84]. The surfaces of 3-D mesoporous Ti–SiO_2 were trimethylsilylated for rendering hydrophobicity, which enables higher temperature operation of reaction [86]. As a solid phase promoter, alkaline or alkaline earth metal chlorides are efficient, however, chloride anions markedly enhance the coagulation of Au particles in a short period [87]. Finally, $Ba(NO_3)_2$ was selected as the best promoter which might kill the steady acid sites as BaO (after calcination) on the catalyst surfaces [84,88].

Figure 26 shows that trimethylamine (TMA), a strong Lewis base with a pK_a value of 9.9, introduced to the reactant gas stream at a concentration of 10–20 ppm, appreciably improves the catalytic performances in every aspect of catalytic performance, propylene conversion, PO selectivity, H_2 utilization efficiency, and catalyst life [88]. It is worth noting that TMA makes used catalysts better than fresh catalysts in catalytic performances. TMA might kill the mobile acid sites which appear and disappear intermittently, suppressing byproduct formation from PO.

A schematic representation for the reaction pathways is given in Figure 27 [88]. At the surfaces or perimeter interfaces of gold NPs O_2 and H_2 react with each other to form H_2O_2. Gold is catalytically as active as palladium for the direct synthesis of H_2O_2 [89–91]. Figure 28 draws a

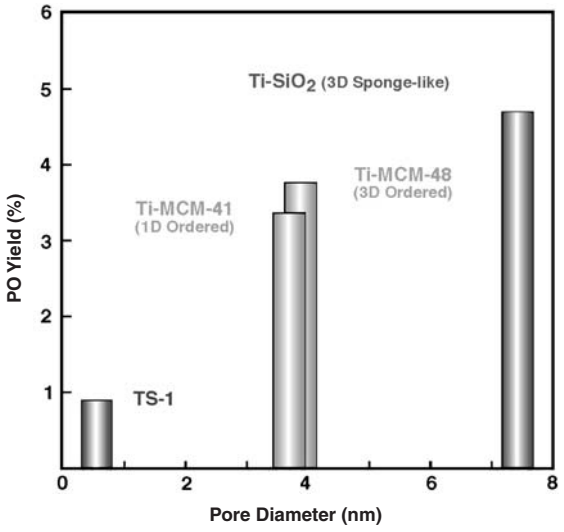

Figure 25. PO yields over gold catalysts as a function of pore diameter of Ti–SiO_2 support.

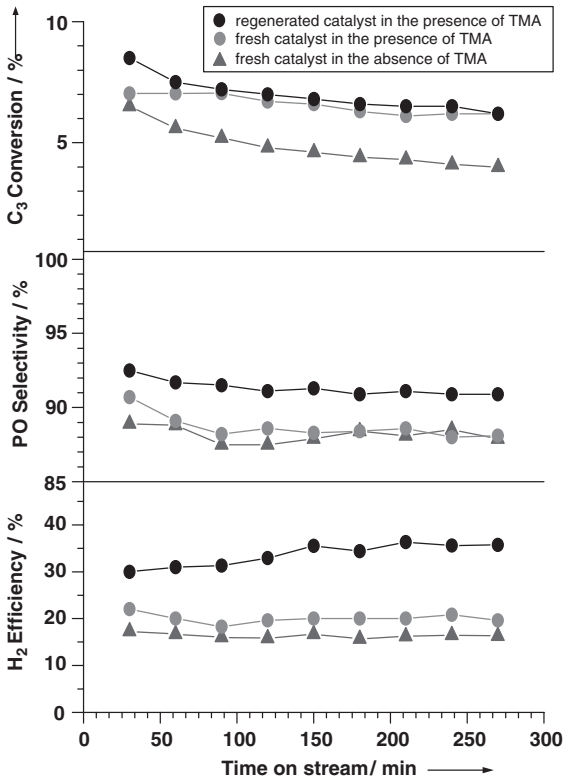

Figure 26. Effect of trimethylamine (TMA) addition to the reactant gases on propylene epoxidation [88].

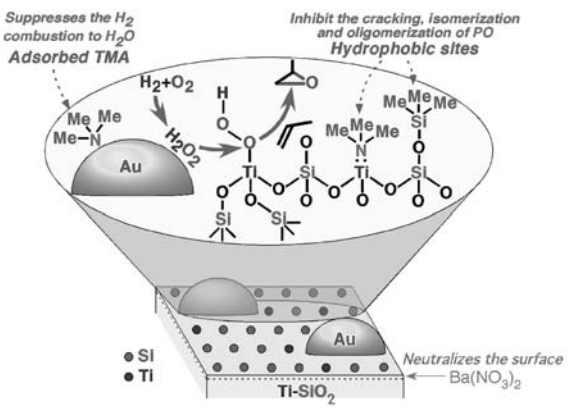

Figure 27. Probable pathways for propylene epoxidation over surface modified Ti–SiO_2 catalysts [88].

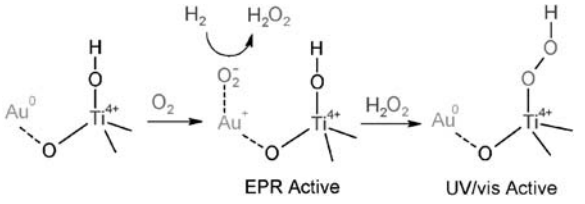

Figure 28. Possible mechanistic model for the activation of molecular oxygen over Au/Ti–SiO_2 catalysts [92].

probable mechanism at an atomic level for the activation of oxygen molecule [92]. Electron paramagnetic resonance spectroscopy detected O_2^- species after epoxidation of propylene. Hydrogen peroxide formed at the gold surfaces then moves to isolated sites of Ti cations to form Ti-OOH species. This oxidic species, which were detected by UV–Vis spectroscopy as shown in Figure 29, reacts with propylene adsorbed on the support surfaces to form PO. TMA can also adsorb on the gold surfaces and depresses the combustion of H_2 to form H_2O, thus leading to improved H_2 utilization efficiency.

3.2.4. Replacement of Gold with Silver

It is interesting to note that silver can also do similar job as that of gold under the same reaction conditions. In 2001 Shueth showed that silver deposited on TiO_2 (Degussa-Huels AG, P25) could also produce PO in the gas phase composed of propylene, O_2, H_2, and N_2 with selectivity above 90% at propylene conversion of 0.36% [93]. Soon after Guo reported that Ag deposited on TS-1 exhibited better performances (propylene conversion 1.4%, PO selectivity 93.5%), while he claimed that silver supported on TiO_2 was not active for PO synthesis [94–96].

A common feature for both Ag/TiO_2 and Ag/TS-1 catalysts is that catalyst preparation is crucial. Among impregnation, ion exchange, microemulsion, sol-gel, and DP techniques, only DP technique led to activity at a temperature of 323 K or above and PO selectivity higher than 60%. Since DP technique forms hemispherical metal particles strongly attached to the metal oxide supports, the significantly large influence of preparation methods implies that the contact structure of silver particles with the TiO_2 support might be important for PO synthesis, as in the case of supported gold catalysts. The requirements to silver are that silver should not be fully reduced to metallic species and that silver particles should be in the range of 2–4 nm in diameter (on TiO_2 support) or at around 8 nm (on TS-1 support). Accordingly, there is an optimum Ag loading of 2 wt%, above which the major product switches to propanal. The above requirements to silver catalysts are almost identical to those to gold catalysts except for the necessity of oxidic species, indicating that catalytic mechanism may be similar between silver and gold. It has not yet been reported that propane is produced over Ag catalysts instead of PO.

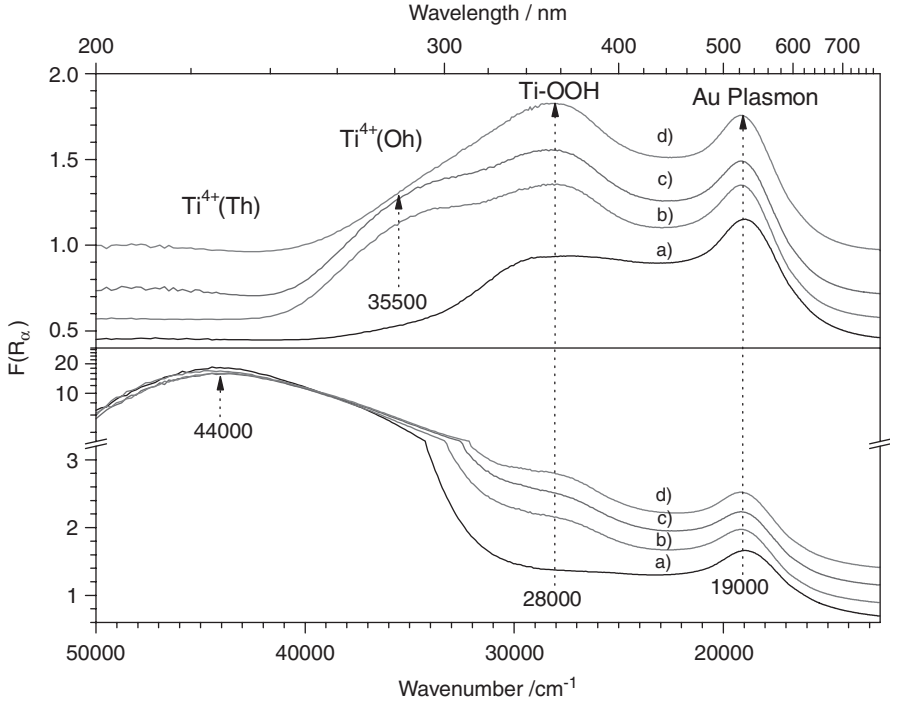

Figure 29. *In situ* UV/Vis spectra for propylene epoxidation on Au/Ti–SiO_2 [88] (bottom: $BaSO_4$ referenced, and top: Ti–SiO_2 referenced): (a) under Ar at 298 K before propylene epoxidation, (b) under $C_3H_6/H_2/O_2$/Ar at 423 K for 120 min, (c) under $C_3H_6/H_2/O_2$/Ar at 423 K for 270 min, (d) under Ar at 298 K after propylene epoxidation. Offsets are used for clarity.

3.3. Selective Oxidation in Liquid Phase

In the selective oxidation of glucose to gluconic acid over gold NPs supported on activated carbon in aqueous alkaline solution (Figure 30), the conversion is jumped up at a particle diameter of 6.5 nm and then increases proportionally with the reciprocal diameter, namely with surface area [97]. In this reaction, unsupported gold particles stabilized by polymer ligands also exhibit similar catalytic activity, indicating that only metallic gold NPs smaller than 6.5 nm are specifically active and below this size TOF is independent of the particle diameter.

We have recently deposited directly onto activated carbons and polymer microbeads by deposition–reduction method and have found that gold NPs on polymers exhibit remarkably high catalytic activity, which may exceed those of Au/activated carbons and Au/ fine CeO_2. The type of polymers and their functional groups are critical to the catalytic activity.

Figure 31 shows that among metal oxide supports, TOF markedly changes depending on not only the kind of metal oxides but also on their size [98]. Especially, fine particles of CeO_2 with mean diameter of 5 nm present the highest catalytic activity. On the other hand, Prati and her coworkers [31] reported that gold NPs supported on activated carbons are very active and selective in the liquid phase oxidation of various alcohols.

Bio-ethanol is attracting growing interests in relation to the shift of raw materials from petroleum to biomass. A pioneering work by Christensen is that over $MgAl_2O_3$ support gold is much more selective to acetic acid than palladium and platinum in the aerobic oxidation of ethanol in water in a batch reactor. Figure 32 shows that selectivity to acetic acid exceeds 80% [99]. In contrast, Au/SiO_2 catalysts prepared by deposition reduction method in an aprotic solvent produce selectively acetoaldehyde (>90%) at 573 K and ethyl acetate (86%) at 373 K in a flow reactor [100]. Hutchings at al. recently reported that gold supported on activated carbons can also catalyze selective oxidation of hydrocarbons as well as alcohols [15,101].

A detailed study on the size effect of gold has been carried out by the group of Tsukuda [102]. Figure 33

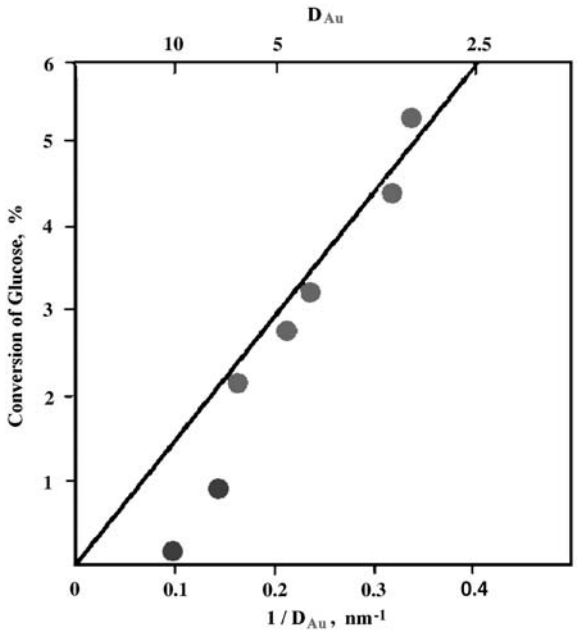

Figure 30. Conversion of glucose as a function of reciprocal diameter of gold particles supported on activated carbon.

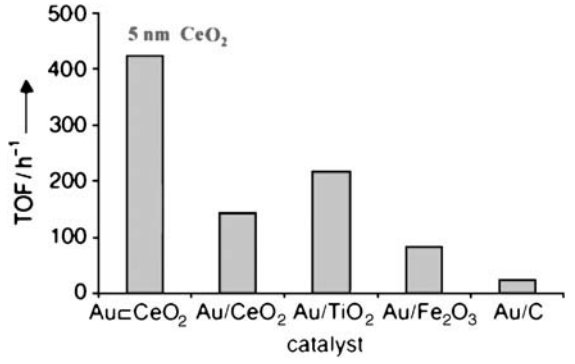

Figure 31. Effect of metal oxide supports in glucose oxidation over gold catalysts [98].

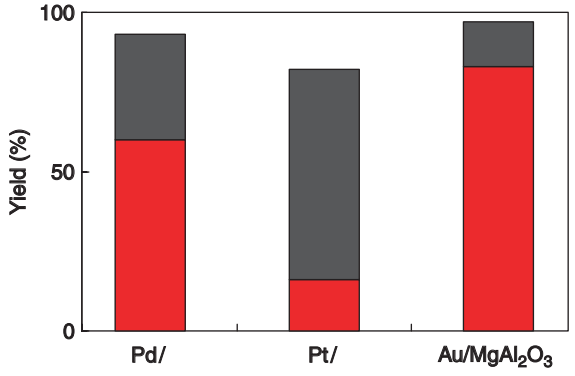

Figure 32. Aerobic oxidation of EtOH in water in a batch reactor [99].

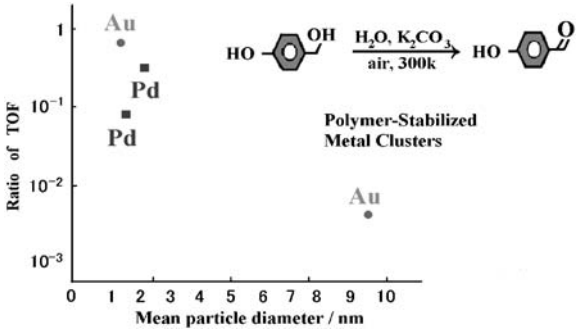

Figure 33. Catalytic activity for the oxidation of hydroxybenzyl alcohol with O_2 as a function of mean particle diameter of Pd and Au [102].

shows that TOF sharply increase with a decrease in the diameter of gold NPs stabilized by polymer ligands in the aerobic oxidation of hydroxybenzyl alcohol, whereas TOF of palladium decreases with a decrease in diameter. It can be assumed that smaller palladium clusters tend to be readily oxidized to loose catalytic activity.

4. Future Prospects: Potentials of Gold Clusters

A big dream can be drawn in the future in the field of metal clusters. The critical size for noble metals is 2.0 nm in diameter, 300 atoms in number, below which the electronic state differs from that of bulk and gold is no more metallic. How can we distinguish clusters from NPs by experiments? A simple technique is to measure visible light absorbance because no surface plasmon absorption takes place over gold clusters, whereas gold NPs exhibit beautiful pink or purple color owing to dipolar plasmon excitation. It is likely that some magic numbers and even magic structures will present dramatic changes in physicochemical properties. An advantageous feature of gold in practical applications is that even such small clusters can be stable in ambient atmosphere. Gibbs free energy for oxide formation is positive only for gold ($+53.3$ kJ/molO_2) and negative for the other metals (Ag: -22.4, Pt: -168 kJ/molO_2). A few typical examples that gold clusters are promising are described below.

In the epoxidation of propylene with O_2 and H_2, the product suddenly shifts from PO to propane when the mean particle diameter of gold NPs goes down to 2.0 nm (Figure 19) [57]. This shift from partial oxidation to hydrogenation means that gold clusters behave like Pt and Pd to dissociate hydrogen molecule when they are small enough and when oxygen is present. As a model catalyst, gold clusters were deposited on a single crystal TiO_2 (rutile) by vacuum evaporation and each of them was measured for the diameter and height, work function, and energy gap. Figure 34 shows a typical picture obtained by a scanning tunnel spectroscopy (STM). Figure 35 clearly shows that both work function and energy gap tend to shift from those of bulk gold at a height of 0.4 nm, which corresponds to two atoms layer of gold [103].

The second example is 55 atoms cluster reported by Boyen's group of University of Ulm [104]. They measured XPS spectra for gold clusters with different diameters which were deposited on silicon substrate and were exposed to radio frequency oxygen plasma, namely, dissociated atomic oxygen. Except for 55 atoms cluster, two peaks assigned to Au^{3+} were observed in Au 4f orbital, showing that 55 atoms cluster is more inert than bulk gold. It is interesting to note that similar-sized gold clusters with diameters of 1.2 nm exhibit higher catalytic activity than palladium in selective oxidation of hydroxybenzyl alcohol in an aqueous solution while larger gold particles are much less active (Figure 33) [102].

The third example is 20 atoms cluster reported by Wang of Washington State University [105]. Negatively charged 20 atoms cluster of gold shows larger HOMO–LUMO gap than negatively charged bucky fullerene, indicating that gold 20 atoms cluster is more stable. The most probable structure is estimated by computer calculation to be tetrahedron, where all 20 atoms are located on the surface and no atom is present inside.

Lastly, gold supported on $Mg(OH)_2$ is very active for CO oxidation even at 200 K [30]. However, it suddenly died after 4 months. Transmission electron microscopy could not clarify the reason because no appreciable change in particle diameter was observed. X-ray scattering due to gold clusters was measured experimentally. The

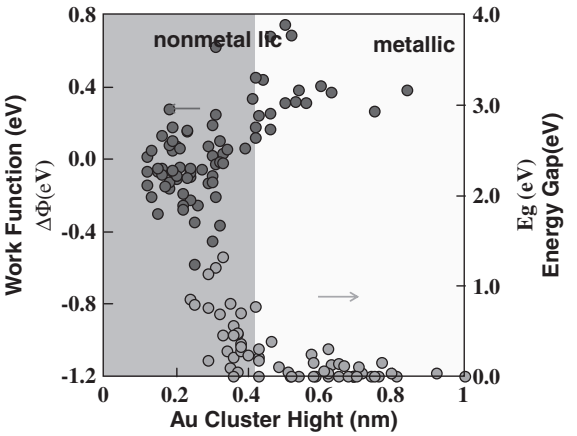

Figure 35. Work function and energy gap as a function of the height of gold clusters deposited on single crystal of anatase TiO_2 [103].

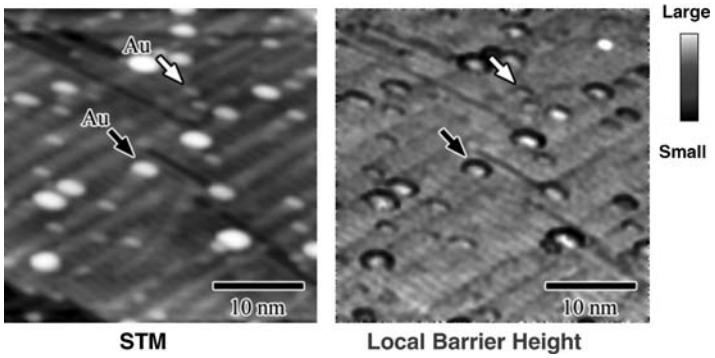

Figure 34. Scanning tunnel microscopy and local barrier height for gold clusters deposited on a single rutile TiO_2 substrate [103].

subsequent computer simulation for the X-ray scattering based on Debye Function Analysis is carried out to estimate the number of atoms and the structure, suggesting that only 13 atoms clusters exhibit high activity in CO oxidation and, furthermore, icosahedron is active but not cubo-octahedron (Figure 13).

5. Conclusions

(1) Preparation methods and conditions are crucial to obtain active and/or selective gold catalysts because the active state of gold, namely, NPs, small clusters, or cations, changes depending on the type of reactions in gas phase or in liquid phase, and support materials. However, majority of reactions tested so far with gold catalysts are enhanced in the presence of metallic Au NPs. In gas phase, the perimeter interfaces may facilitate the reaction between one reactant adsorbed on the gold surfaces and another adsorbed on the support surfaces. In liquid phase, especially in water, the surfaces of metallic gold NPs alone can activate all the reactants by the aid of water molecule.

(2) Minimization of the size down to 2 nm is very rewarding for gold to become catalytically active and selective; for example, CO oxidation at a temperature as low as 200 K, epoxidation of propylene to PO, partial oxidation of alcohols with molecular oxygen in liquid phase. This is because of the increased length of perimeter around gold particles and of increased number of sites for adsorption on the gold surfaces such as edges and corners.

(3) Further dramatic changes can happen in chemical reactivities of gold clusters with diameters smaller than 2 nm. The contribution of support materials including metal oxides, carbons, and polymers to the genesis of unique catalytic properties may be much greater than in the case of NPs and therefore may provide an expanding new field of research.

References

1 A. G. Debus, *The Chemical Philosophy*, Neale Watson Academic Pub., 1977.
2 B. J. T. Dobbs, *The Janus Faces of Genius – The Role of Alchemy in Newton's Thought*, Cambridge Univ. Press, Cambridge, 1991.
3 J. Schwank, *Gold Bull.* 16 (1983) 103.
4 M. Haruta, T. Kobayashi, H. Sano, N. Yamada, *Chem. Lett.* (1987) 405.
5 M. Haruta, N. Yamada, T. Kobayashi, S. Iijima, *J. Catal.* 115 (1989) 301.
6 P. H. Abelson, *Science* 288 (2000) 269.
7 G. C. Bond, D. T. Thompson, *Catal. Rev. Sci. Eng.* 41 (1999) 319.
8 M. Haruta, M. Date, *Appl. Catal. A: Gen.* 222 (2001) 427.
9 G. C. Bond, D. T. Thompson, *Catalysis by Gold*, Imperial College Press, London, 2006.
10 A. S. Hashmi, G. J. Hutchings, *Angew. Chem. Int. Ed.* 45 (2006) 7896.
11 M. Haruta, *CATTECH* 6 (2002) 102.
12 M. Haruta, *Chem. Rec.* 3 (2003) 75.
13 *Chem. Eng. News*, Sept. 20, 1999, p. 7; March 9, 1992, p. 27.
14 M. Haruta, *Nature* 437 (2005) 1098.
15 M. D. Hughes, Y.-J. Xu, P. Jenkins, P. MacMorn, P. Landon, D. I. Enache, A. F. Carley, G. A. Attard, G. J. Hutchings, F. King, E. H. Stitt, P. Johnston, K. Griffin, C. J. Kiely, *Nature* 437 (2005) 1132.
16 G. C. Bond, P. A. Sermon, G. Webb, D. A. Buchanan, P. B. Wells, *J. Chem. Soc. Chem. Commun.* (1973) 444.
17 G. Cocco, S. Enzo, G. Fagherazzi, L. Schiffini, I. W. Bassi, G. Vlaic, S. Galvagno, G. Parravano, *J. Phys. Chem.* 83 (1979) 2527.
18 J.-D. Grunwaldt, C. Kiener, C. Woegerbauer, A. Baiker, *J. Catal.* 181 (1999) 223.
19 Q. Guo, K. Luo, K. A. Davis, D. W. Goodman, *Surf. Interface Anal.* 32 (2001) 161.
20 V. A. Bondzie, S. C. Parker, C. T. Campbell, *Catal. Lett.* 63 (1999) 143.
21 T. Sugimoto, *Monodispersed Particles*, Elsevier, Amsterdam, 2001, 322.
22 M. Haruta, B. S. Uphade, S. Tsubota, A. Miyamoto, *Res. Chem. Intermed.* 24 (1998) 329.
23 T. Kobayashi, M. Haruta, S. Tsubota, H. Sano, *Sens. Actuators* B1 (1990) 222.
24 M. Shibata, N. Kuwata, T. Matsumoto, H. Kimura, *Chem. Lett.* (1985) 1605.
25 G. J. Hutchings, M. S. Hall, A. F. Carley, P. Landon, B. E. Solsona, C. J. Kiely, A. Herzing, M. Makkee, J. A. Moulijn, A. Overweg, J. C. Fierro-Gonzalez, J. Guzman, B. C. Gates, *J. Catal.* 242 (2006) 71.
26 S. Tsubota, M. Haruta, T. Kobayashi, A. Ueda, Y. Nakahara, *Studies Surf. Sci. Catal.* 63 (1997) 695.
27 M. Okumura, S. Tsubota, M. Haruta, *J. Mol. Catal. A: Chem.* 199 (2003)73.
28 Y. Yuan, A. P. Kozlova, K. Asakura, H. Wan, K. Tsai, Y. Iwasawa, *J. Catal.* 170 (1997)191.
29 R. Zanella, L. Delannoy, C. Luis, *Appl. Catal. A: Gen.* 291 (2005) 62.
30 D. A. H. Cunningham, W. Vogel, R. M. Torres Sanchez, K. Tanaka, M. Haruta, *J. Catal.* 183 (1999) 24.
31 D. A. H. Cunningham, W. Vogel, H. Kageyama, S. Tsubota, M. Haruta, *J. Catal.* 177 (1998) 1.
32 L. Prati, F. Porta, *Appl. Catal. A: Gen.* 291 (2005) 199.
33 W. T. Wallace, R. L. Whetten, *J. Phys. Chem. B* 104 (2000) 10964.
34 L. A. Brey, T. E. Wood, G. M. Buccellato, M. E. Jones, C. S. Chamberlain, A. R. Siedle, 3M Innovative Properties Co., US Patent 2005/0095189 A1.
35 G. M. Veith, A. R. Lupini, S. J. Pennycook, G. W. Ownby, N. J. Dudney, *J. Catal.* 231 (2005) 151.
36 M. Haruta, N. Ueda, N. Kinoshita, W. Minagawa, Jpn. Patent (Tokugan) 2006–18721.
37 M. Haruta, W. Minagawa, N. Kinoshita, K. Kuroda, Abstracts Gold 2006, Limerick, Sept. 2006, 155.
38 A. Cho, *Science* 299 (2003) 1684.
39 M. Date, M. Okumura, S. Tsubota, M. Haruta, *Angew. Chem. Int. Ed.* 43 (2004) 2129.
40 M. Mavrikakis, P. Stolze, J. K. Norskov, *Catal. Lett.* 64 (2000) 101.
41 U. Heiz, W.-D. Schneider, *J. Phys. D: Appl. Phys.* 33 (2000) R85.
42 M. S. Chen, D. W. Goodman, *Science* 306 (2004) 252.
43 J. C. Fierro-Gonzalez, V. A. Bhirud, B. Gates, *Chem. Commun.* (2005) 5275.
44 Q. Fu, H. Saltsburg, M. Flytzani-Stephanopoulos, *Science* 301 (2003) 935.
45 W. Deng, J. De Jesus, H. Saltsburg, M. Flytzani-Stephanopoulos, *Appl. Catal. A: Gen.* 291 (2005) 126.
46 I. Okuda, T. Takei, M. Haruta, unpublished data.
47 A. Bongiorno, U. Landman, *Phys. Rev. Lett.* 95 (2005) 106102.

48 H. Sakurai, T. Akita, S. Tsubota, M. Kiuchi, M. Haruta, *Appl. Catal. A: Gen.* 291 (2005) 179.
49 F. Boccuzzi, A. Chiorino, M. Manzoli, P. Lu, T. Akita, S. Ichikawa, M. Haruta, *J. Catal.* 202 (2001) 256.
50 G. C. Bond, D. T. Thompson, *Gold Bull.* 33 (2000) 41.
51 J. Guzman, B. Gates, *J. Am. Chem. Soc.* 126 (2004) 2672.
52 W. F. Hoelderich, *Appl. Catal. A: Gen.* 487 (2000) 194.
53 W. Laufer, W. F. Hoelderich, *Appl. Catal. A: Gen.* 213 (2001) 163.
54 (a) A. Sato, T. Miyake, Jpn. Pat. Tokkaihei 4-352771; (b) A. Sato, T. Miyake, T. Saito, *Shokubai (Catalysts and Catalysis)* 34 (1992) 132.
55 R. Meiers, U. Dingerdissen, W. F. Hoelderich, *J. Catal.* 176 (1998) 376.
56 M. G. Clerici, G. Belussi, U. Romano, *J. Catal.* 129 (1991) 159.
57 T. Hayashi, K. Tanaka, M. Haruta, *J. Catal.* 178 (1998) 566.
58 K. Tanaka, T. Hayashi, M. Haruta, *J. Japan Inst. Metals* 60 (1996) 693.
59 A. Zwijnenburg, M. Saleh, M. Makkee, J. A. Moulijn, *Catal. Today* 72 (2002) 59.
60 E. E. Stangland, B. Taylor, R. P. Andres, W. N. Delgass, *J. Phys. Chem. B* 109 (2005) 2321.
61 A. Zwijnenburg, A. Goossens, W. G. Sloof, M. W. J. Craje, A. M. van der Kraan, L. Jos de Jongh, M. Makkee, J. A. Moulijn, *J. Phys. Chem. B* 106 (2002) 9853.
62 J. Chou, E. W. McFarland, *Chem. Commun.* (2004) 1648.
63 E. E. Stangland, K. B. Stavens, R. P. Andres, W. N. Delgass, *J. Catal.* 191 (2000) 332.
64 T. A. Nijhuis, M. Makkee, J. A. Moulijn, B. M. Weckhuysen, *Ind. Eng. Chem. Res.* 45 (2006) 3447.
65 K. A. Davis, D. W. Goodman, *J. Phys. Chem. B* 104 (2000) 8557.
66 S. Chretien, H. Metiu, *J. Chem. Phys.* 121 (2004) 3756.
67 R. Olson, S. Varganov, M. S. Gordon, H. Metiu, *Chem. Phys. Lett.* 412 (2005) 416.
68 H. M. Ajo, V. A. Bondzie, C. T. Campbell, *Catal. Lett.* 78 (2002) 359.
69 T. A. Nijhuis, T. Visser, B. M. Weckhuysen, *Angew. Chem. Int. Ed.* 44 (2005) 1115.
70 T. A. Nijhuis, B. M. Weckhuysen, *Chem. Commun.* (2005) 6002.
71 T. A. Nijhuis, T. Visser, B. M. Weckhuysen, *J. Phys. Chem. B* 109 (2005) 19309.
72 B. S. Uphade, T. Akita, T. Nakamura, M. Haruta, *J. Catal.* 209 (2002) 331.
73 C. Sivadinarayana, T. V. Choudhary, L. L. Daemen, J. Eckert, D. W. Goodman, *J. Am. Chem. Soc.* 126 (2004) 38.
74 D. G. Barton, S. G. Podkolzin, *J. Phys. Chem. B* 109 (2005) 2262.
75 T. A. Nijhuis, T. Q. Gardner, B. M. Weckhuysen, *J. Catal.* 236 (2005) 153.
76 D. H. Wells, Jr., W. N. Delgass, K. T. Thomson, *J. Catal.* 225 (2004) 69.
77 A. M. Joshi, W. N. Delgass, K. T. Thomson, *J. Phys. Chem. B* 109 (2005) 22392.
78 D. H. Wells Jr., W. N. Delgass, K. T. Thomson, *J. Am. Chem. Soc.* 126 (2004) 2956.
79 A. M. Joshi, W. N. Delgass, K. T. Thomson, *J. Phys. Chem. B* 110 (2006) 2572.
80 N. Yap, T. P. Andress, W. N. Delgass, *J. Catal.* 226 (2004) 156.
81 L. Gumaranatunge, W. N. Delgass, *J. Catal.* 232 (2005) 38.
82 A. K. Sinha, S. Seelan, S. Tsubota, M. Haruta, *Catal. Today* 29 (2004) 95.
83 Y. A. Kalvechev, T. Hayashi, S. Tsubota, M. Haruta, *J. Catal.* 183 (1999) 228.
84 A. K. Sinha, S. Seelan, S. Tsubota, M. Haruta, *Angew. Chem. Int. Ed.* 43 (2004) 1546.
85 C. Qi, T. Akita, M. Okumura, M. Haruta, *Appl. Catal. A: Gen.* 218 (2001) 81.
86 C. Qi, T. Akita, M. Okumura, M. Haruta, *Appl. Catal. A: Gen.* 253 (2003) 75.
87 B. S. Uphade, M. Okumura, S. Tsubota, M. Haruta, *Appl. Catal. A: Gen.* 190 (2000) 43.
88 B. Chowdhury, J. J. Bravo-Suarez, M. Date, S. Tsubota, M. Haruta, *Angew. Chem. Int. Ed.* 45 (2005) 412.
89 M. Okumura, Y. Kitagawa, K. Yamaguchi, T. Akita, S. Tsubota, M. Haruta, *Chem. Lett.* 32 (2003) 822.
90 T. Ishihara, Y. Ohura, S. Yoshida, Y. Hata, H. Nishiguchi, Y. Takita, *Appl. Catal. A: Gen.* 291 (2005) 215.
91 B. E. Solsona, J. K. Edwards, P. Landon, A. F. Carley, A. Herzing, C. J. Kiely, G. J. Hutchings, *Chem. Mater.* 18 (2006) 2689.
92 B. Chowdhury, J. J. Bravo-Suarez, N. Mimura, J. Lu, K. Bando, S. Tsubota, M. Haruta, *J. Phys. Chem. B* 110 (2006) 22995.
93 A. Lange de Oliveira, A. Wolf, F. Schueth, *Catal. Lett.* 73 (2001) 157.
94 R. Wang, X. Guo, X. Wang, J. Hao, G. Li, J. Xiu, *Appl. Catal. A: Gen.* 261 (2004) 7.
95 X. Guo, R. Wang, X. Wang, J. Hao, *Catal. Today* 93–95 (2004) 211.
96 C. Wang, X. Guo, X. Wang, R. Wang, J. Hao, *Catal. Lett.* 96 (2004) 79.
97 M. Comotti, C. D. Pina, R. Matarrese, M. Rossi, A. Siani, *Angew. Chem. Int. Ed.* 43 (2004) 5812.
98 A. Abad, P. Concepcion, A. Corma, H. Garcia, *Angew. Chem. Int. Ed.* 44 (2005) 4066.
99 C. H. Christensen, B. Jorgensen, J. Rass-Hansen, K. Egeblad, R. Madsen, S. K. Klitgaard, S. M. Hansen, M. R. Hansen, H. C. Andersen, A. Riisager, *Angew. Chem. Int. Ed.* 45 (2006) 4648.
100 N. Zheng, G. D. Stucky, *J. Am. Chem. Soc.* 128 (2006) 14278.
101 D. I. Enache, J. K. Edwards, P. Landon, B. Solsona-Espriu, A. F. Carley, A. A. Herzing, M. Watanabe, C. Kiely, D. W. Knight, G. J. Hutchings, *Science* 311 (2006) 362.
102 T. Tsukuda, *J. Am. Chem. Soc.* 127 (2005) 9374.
103 W. Maeda, M. Okumura, S. Tsubota, M. Kohyama, M. Haruta, *Appl. Surf. Sci.* 222 (2004) 409.
104 H.-G. Boyen, G. Kastle, F. Weigl, B. Koslowski, C. Dietrich, P. Ziemann, J. P. Spatz, S. Riethmuller, C. Hartmann, M. Moller, G. Schmid, M. G. Garnier, P. Oelhafen, *Science* 297 (2002) 1533.
105 J. Li, X. Li, H-J. Zhai, L-S. Wang, *Science* 299 (2003) 864.

This page intentionally left blank

CHAPTER 10

Metal Nanoclusters Supported on Cross-Linked Functional Polymers: A Class of Emerging Metal Catalysts

Marco Zecca, Paolo Centomo, and Benedetto Corain

Department of Chemical Sciences, University of Padova, Italy

1. Introduction

Supported metal catalysts, M^0/S, are typically two-components materials built up with a nanostructured metal component, in which the metal centre is in the zero oxidation state (M^0), and with an inorganic support (S), quite various in its chemical and structural features [1]. M^0 is the component typically deputed to the electronic activation of the reagents involved in the catalyzed reactions. S is typically a microstructured component mainly deputed to the physical support and to the dispersion of M^0 nanoclusters.

The catalytic chemistry of M^0 depends on the elementary properties of M and on the structure and size of the M^0 nanoclusters (''quantum dots'') [2]. S may play a role as a reactivity enhancer of M^0/S as a whole (co-catalytic role) and/or as a promoter of its catalytic chemoselectivity (promotional role) [3,4].

The proposal of cross-linked functional polymers (CFPs) as supports of metal nanoclusters to be employed in catalytic applications dates back to 1969 [5]. The inventors of the relevant Bergbau Chemie patent, which describes the one-pot synthesis of the industrially important solvent methylisobutylketone (MIBK) from acetone and dihydrogen, recognised in CFPs the ability of carrying metal nanoclusters and of providing the catalyst with another specific function at the same time. They produced in this way a smart bifunctional catalyst for the acid-catalysed condensation of acetone to 4-hydroxy-4-methyl-2-pentanone, its dehydration to mesytylene oxide and the hydrogenation of the latter to MIBK [6]. Catalysts based on CFPs of this type are currently employed in at least three other industrial processes, i.e. the synthesis of MTBE with feedstocks rich in unsaturated substrates different from isobutene (Erdölchemie process) [7], the removal of ppm amounts of O_2 from industrial waters [8] and the production of alkanes and of branched ethers for the manufacturing of green petrol (BP etherol process) [7].

The concept of bifunctionality can be suitably expanded (Scheme 1) to produce multifunctional catalysts bearing both diverse nanostructured metals and diverse chemical functionalities for performing complementary catalytic tasks.

The fine concept embodied in the proposal of CFPs as supports of nanostructured metal phases, experienced in fact an almost total inattention in the academic Catalysis community until the mid-nineties, when a few research groups started a systematic exploration of the field [9–12].

1.1. General Aspects

CFPs are isotropic materials built up with cross-linked polymer chains that are normally originated by the homo- or co-polymerization of vinyl monomers, the most important of which is styrene [13]. Similar observations are also valid for the cross-linking agent. In fact, the commonest one is divinylbenzene, but diolefins such as methylenebisacrylamide (MBAA) and ehylenedimethacrylate (EDMA) are also popular (Figure 1) [14].

CFPs are normally manufactured as submillimetric beads or powders (Figure 2) [15]. A convenient simplified comparison between the micrometer and nanometer scale morphology of gel-type and macroreticular resins is illustrated in Figure 3.

It is essential to stress the crucial feature of CFPs, i.e. their ability to accomplish a chemical task only when they are in the swollen state. Swelling occurs when the molecules of a liquid put in touch with a cross-linked polymer penetrate inside the polymer framework (Figure 4). For gel-type CFPs, this process implies an appreciable increase of the total volume of the materials. For

Metal Nanoclusters in Catalysis and Materials Science: The Issue of Size Control
Edited by B. Corain, G. Schmid and N. Toshima

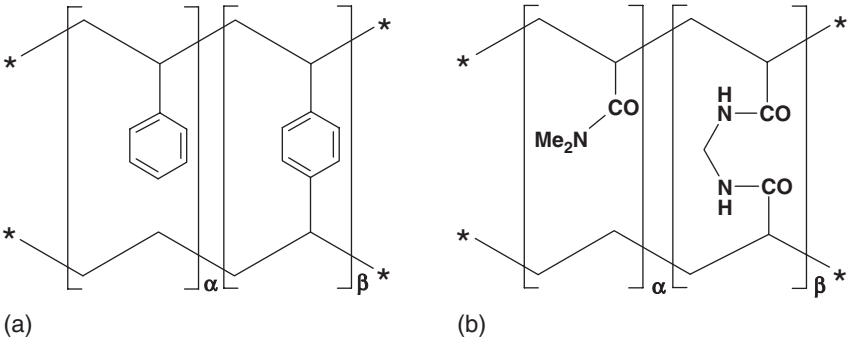

Figure 1. Sketch of the primary structure (vide infra) of cross-linked polystyrene (a) and of a typical cross-linked poly-vinyil co-monomer-functional co-monomer-cross-linker (b) [14].

$$M^0/\textcircled{P}\text{-}F_i$$

M = metal centre **Ⓟ = CFP** **($F_i = F_1, F_2, \ldots, F_n$)**

Scheme 1. The concept of polyfunctionality of a nanocomposite obtained from a nanostructured metal (0) and a cross-linked functional polymer.

macroreticular CFPs, swelling involves only small fractions of the polymer mass and quite often the apparent change in the polymer volume is hardly appreciable. The ability of a liquid to swell a CFP depends on its ability to solvate the polymer chains and a fully swollen polymer framework can be considered to some extent as a viscous pseudosolution or suspension.

When a bead of a gel-type CFP material is in the dry state, for practical purposes it can be considered as a solid material (thus possessing a mass, a volume and a shape). When in the swollen state, a CFP material can be still considered as a solid from the practical point of view, but this circumstance is now an authentic approximation. In fact, physico-chemical analysis reveals that under some circumstances this alleged solid material is rather a very viscous liquid. More precisely, it is a suspension of interconnected polymer chains in the swelling agent. Each swollen CFP bead can be considered as a drop, which can retain a definite shape owing to the existence of the polymer framework.

A decisive clarification of these concepts stems from at least four fine physico-chemical analytical means, i.e. ISEC [16–18], ESR spectroscopy of paramagnetic probe(s) either dissolved in the swelling medium [19] or directly bound to the macromolecular chains [20], $\{^{13}C\}$ CP-MAS NMR of pendants of the polymer backbone carried out both on dry and swollen samples [21] and PGSE-NMR of the swelling medium employed to swell a given polymer framework in a given application [22]. The combined employment of these analytical tools offers a convergent, sound support of the statements in the previous paragraph [10,11,21] (Figure 5).

ISEC is a size-exclusion chromatography technique, in which the stationary phase is the CFP to be to characterized [16–18] and the eluates are geometrically well-defined steric probes. From the determined retention volumes in a given solvent and on the basis of suitable morphological models, ISEC analysis provides the nanometer-level morphology of the analyzed gel-type or macroreticular [23] resin. The information may be given as volumetric distribution ($ml\,g^{-1}$) of the polymer chains concentration ($nm\,nm^{-3}$) or as volumetric distribution of ''cylindrical pores'' (nm). As a matter of fact, the results in terms of cylindrical pores[1] is by far to be preferred when CFPs are used as template for the production of size-controlled metal nanoclusters [24].

ESR provides useful indirect information on the nanoscale porosity of CFPs, after their swelling in a medium in which a suitable spin probe is dissolved. According to the investigation by Corain and associates, the rotational mobility of the spin probe can be nicely correlated to the nanoporosity of the examined CFP, in a quantitative fashion [14,25].

PGSE-NMR provides direct information on the translational mobility of a liquid medium capable of swelling a given CFP. The self-diffusion coefficient of the swelling agent is found to be related to the nanoporosity of the matrix as determined from ISEC and to the rotational correlation time of a suitable paramagnetic probe (ESR) [22].

$\{^{13}C\}$-CP-MAS NMR provides subtle information about the degree of solvation of the polymer chains of a CFP in a given solvent and consequently it may be qualitatively correlated with the nanometer scale morphology of the polymer matrix. In fact, the prerequisite that enables a polymer framework to develop a nanoporosity is the ability of the polymer chains and its pendants to be suitably solvated by the liquid medium [26–28]. Therefore, $\{^{13}C\}$-CP-MAS NMR spectra provide the basis for a first level screening of the possibility of a CFP in a given solvent to be employed as an hexo-template, able to accommodate metal nanoclusters chemically produced in its interior (see below and Ref. [29]).

[1]According to their diameter, pores are conventionally classified as macropores ($d > 50$ nm), mesopores ($2 < d < 50$ nm) and micropores ($d < 2$ nm). For nanometer-sized pores the term ''nanopores'' has been also used for some time (Handbook of Porous Solids, F. Schüth, K. Sing, J. Weitkamp (eds.), Wiley-VCH, Berlin, 2002) but the definition of nanopores is not fully established. In this chapter the term ''nanopore'' will be used for pores with $1 < d < 10$ nm.

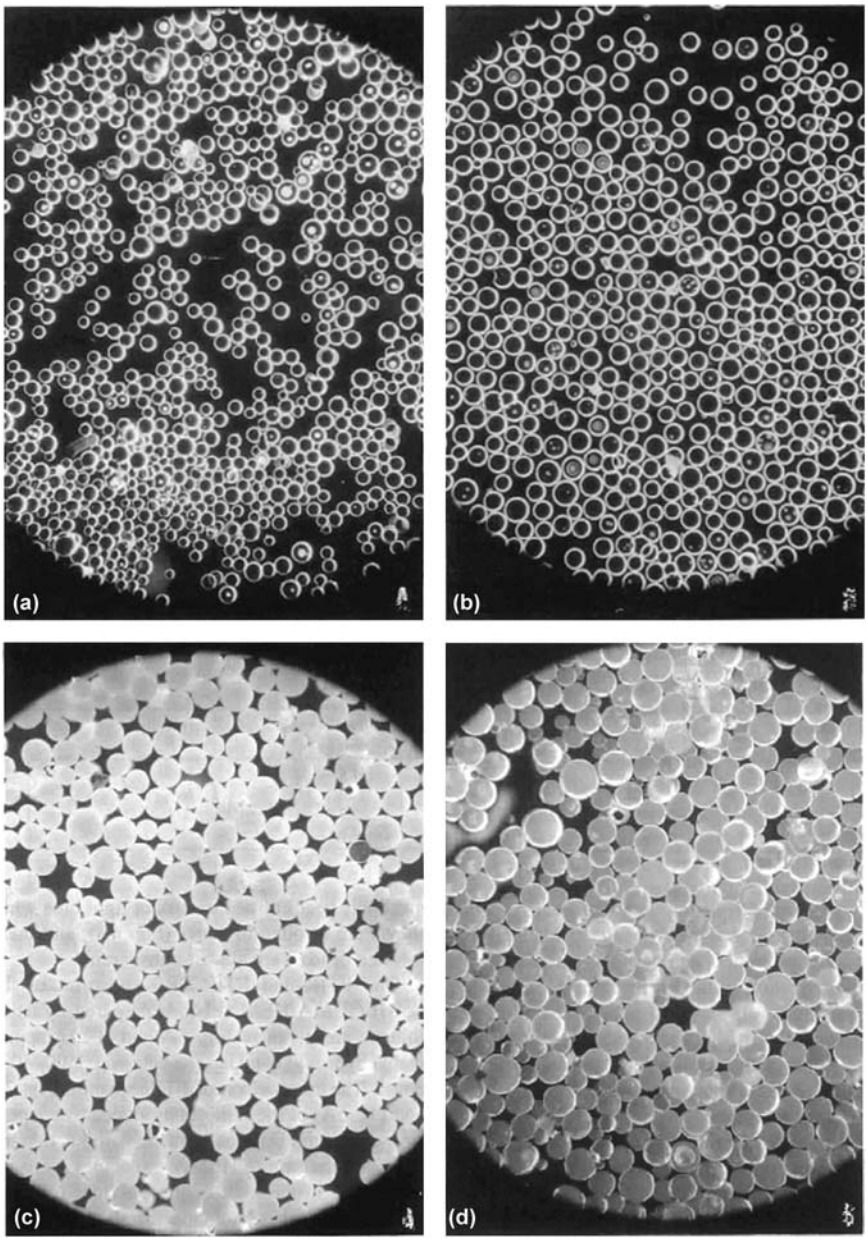

Figure 2. Representative optical micrographs of poly-HEMA cross-linked with EDMA. (a) and (b) represent the gel-type polymer produced by suspension co-polymerization in the dry and swollen state, respectively. (c) and (d) represent the macroreticular polymer produced by suspension co-polymerization in the presence of a porogen (toluene), in the dry and swollen (vide infra) state, respectively [13]. (Reprinted from Ref. [15], © 1996, with permission from Elsevier.)

1.2. Why Cross-Linked Functional Polymers as Supports for Producing Innovative M^0/S Catalysts?

CFPs are (disappointingly underscored) ideal supports for the preparation of supported M^0 nanostructured catalysts to be employed under liquid phase conditions.

A few arguments and relevant features supporting this statement are listed and illustrated below.

1.2.1. Attitude to Metalation and to the Facile Transformation into M^0/CFPs Nanocomposites

CFPs are ideal supports to be metalated on chemical bases. One of the simplest ways is the treatment of the CFP with solutions of metal compounds. Under these conditions, metalation requires the previous swelling of the resin, the introduction of a metal precursor and the

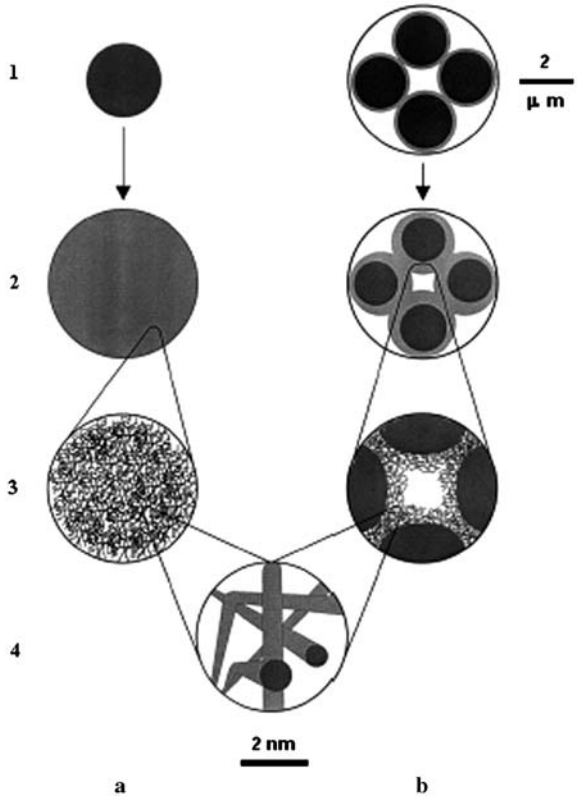

Figure 3. Schematic representation of the micro- and nanoscale morphology of gel-type (a) and macroreticular (b) resins [13]. Level **1** is the representation of the dry materials. Level **2** is the representation of the microporous swollen materials at the same linear scale: swelling involves the whole polymeric mass in the gel-type resin (**2**a) and the macropore walls in the macroreticular resin (**2**b). The morphology of the swollen polymer mass is similar in both gel-type and macroreticular resins (**3**a,b). Nanopores are actually formed by the void space surrounding the polymeric chains, as shown in level **4**, and are a few nanometer wide. (Reprinted from Ref. [12], © 2003, with permission from Elsevier.)

reduction thereof to produce the polymer-supported metal nanoclusters (Reduction of Immobilized Metal Precursor, RIMP). This process is depicted in Figure 6 for both gel-type and macroreticular CFPs.

The introduction of the metal precursor into the CFP can occur upon metal co-ordination or ion exchange (Scheme 2).

In the first place the ease of these reactions depends on the swelling behavior of the polymeric support. If the liquid employed for dissolving the metal precursor swells the support to a relatively high extent, the interior of the swollen polymer will be readily accessible (Figure 7) [30].

If the support is devoid of functional groups apt to interact with the metal precursor, there are not chemical forces facilitating the metal uptake. Under these conditions, metal uptake is driven by absorption forces and can still occur, but it is controlled by simple diffusion. This situation can favor an eggshell radial distribution of the metal precursor over a homogeneous one [31].

1.2.2. Multifunctionality

CFPs may be employed to obtain M^0/CFP nanocomposites, in which the catalytic action of the active metal nanoclusters may be flanked by that of functional groups randomly present inside the polymer framework or by that exerted by the nanoclusters of a second metal present in the same polymer framework. In this connection a classic example is the catalyzed synthesis of MIBK from acetone and dihydrogen over a Pd^0/Ⓟ–SO_3H catalyst, in which the sulfonic group catalyzes very effectively the condensation of two acetone molecules to give mesytylene oxide that is subsequently hydrogenated to give MIBK, thanks to the catalytic action of Pd^0 nanoclusters [8].

1.2.3. Polymer Matrix–Substrate and Matrix–Products Compatibility

In M^0/CFP nanocomposites, reagents are requested to enter the interior of the catalyst particles. To achieve this goal, the partition coefficient between the liquid phase and the swollen-gel phase (see Figure 6) must be favorable to all reagents involved in the catalytic action. In fact, in the case of reagents of different lipo- or hydrophilicity (e.g. A, lipophilic and B, hydrophilic), their ability to penetrate the interior of the support particle depends dramatically on the lipo- or hydrophilic nature of the polymer framework. If the support is definitely lipophilic, only reagent A will be able to penetrate the swollen body of the polymer matrix and it will be activated by the M^0 nanoclusters. If the reaction product is much less lipophilic than the reagent, its egress from the catalyst particle will be favored, with beneficial consequences on catalyst selectivity when the M^0 nanoclusters could also catalyze further transformation of the product [32–34].

1.2.4. Reagents Size Exclusion

If a mixture of organic substrates are to be catalytically transformed into suitable products upon the action of M^0 nanoclusters present inside a nanostructurally well defined CFP, a reagent size exclusion will take place with uniquely beneficial effects in terms of chemoselectivity [35,36].

1.2.5. Relevance of the Microstructure of CFP to the Chemoselectivity of M^0/CFP Catalysts

This argument will be illustrated on the basis of a recent case history investigated by Corain and associates [37]. In the very important selective hydrogenation of dioxygen with dihydrogen to hydrogen peroxide, a dramatic microstructural effect is observed in the action of two Pd^0/resin catalyst. Nanostructured Pd^0 (1%) supported on PS-DVB resins either macroreticular (K2621) or gel-type in nature (K1221) (see Figure 6) exhibits a quite contrasting behavior as far as the issue of chemoselectivity is concerned. In fact, whereas controlled reduction of dioxygen

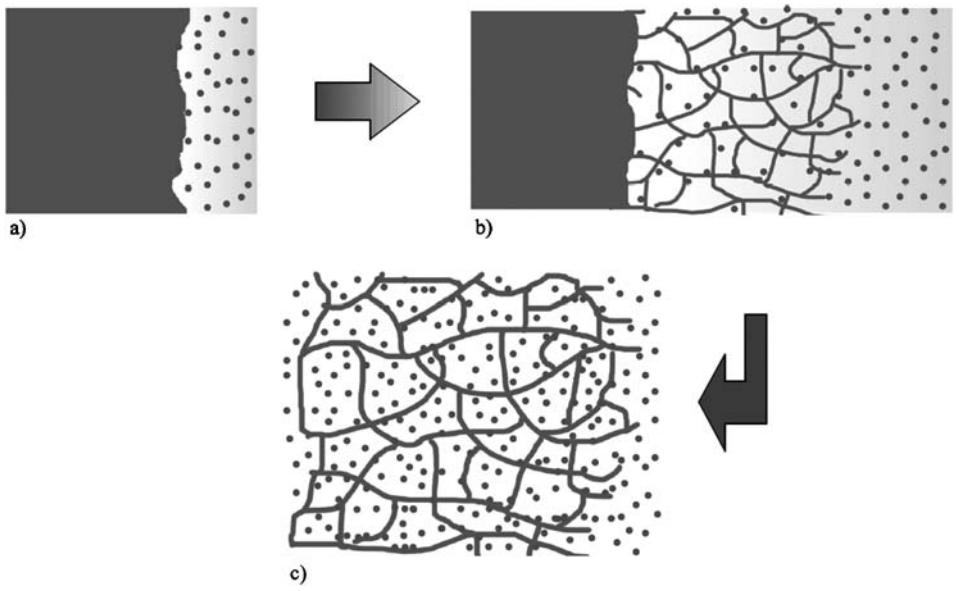

Figure 4. Schematic description of the swelling process. The molecules of the swelling liquid start to penetrate inside the polymer framework from its surface (a) and to solvate the polymer chains. The polymer chain start to stretch out and to move away from one another: the apparent volume of the polymer increases and the first nanopores are formed (b). Swelling stops when increasing elastic forces set up by the unfolding of the polymer chains counterbalance the forces which drive the molecules of the swelling agent into the polymer framework (c).

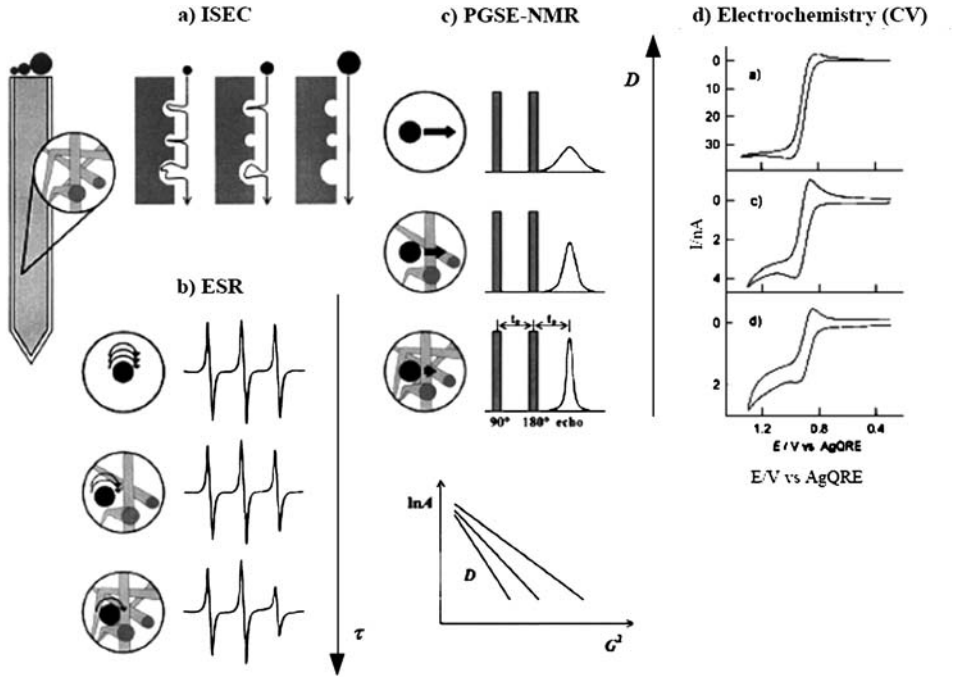

Figure 5. Schematic description of a multi-technique approach to the assessment of molecular mobility inside swollen polymeric frameworks as a phenomenon dependent on their morphology at the nanometric scale [14, 21, 22, 108].

to H_2O_2 is quantitatively promoted by Pd^0/K2621, the undesired dioxygen reduction to H_2O quantitatively occurs in the presence of Pd^0/K1221. TEM analysis of the two catalysts reveals that Pd^0 nanoclusters are rather similar in size. At the moment it is not known whether the reaction is structure sensitive or not, but in any case the small difference in size does not seem the most likely cause of the dramatic effect on chemoselectivity.

1.2.6. The Issue of Thermostability

CFP are normally quite resistant to thermal degradation, under dinitrogen, and depolymerisation starts in the 280–320 °C range, in the dry state [21]. This makes M^0/CFPs quite suitable for operations in the liquid phase occurring at mild to moderate temperatures. CFPs featured by polymer chains possessing significant molecular pendants might experience partial degradation (i.e. pendants degradation) tens of centigrades before the start of de-polymerisation.

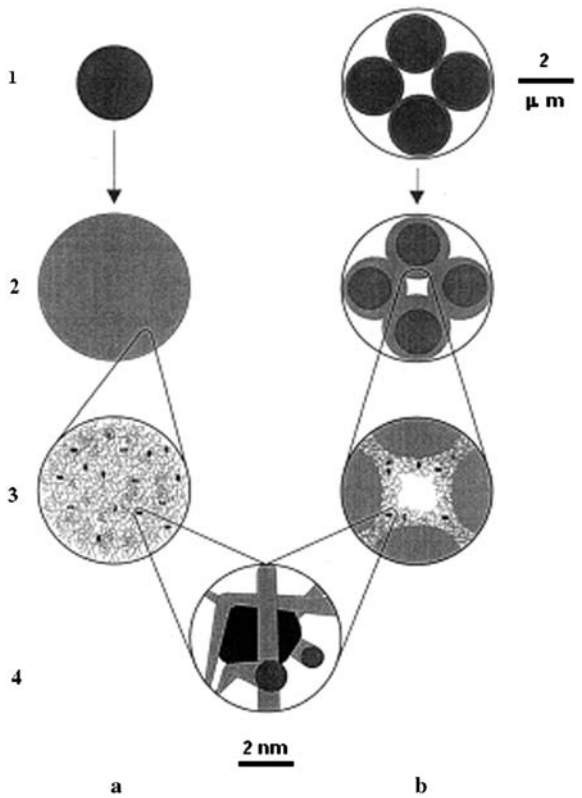

Figure 6. Schematic representation of the micro- and nanoscale morphology of nanoclustered metal catalysts supported on gel-type (a) and macroreticular (b) resins [13]. The nanoclusters are represented as black spots. Level **1** is the representation of the dry materials. Level **2** is the representation of the microporous swollen materials at the same linear scale: swelling involves the whole mass of the catalyst supported on the gel-type resin (**2**a) and the macropore walls in the catalyst supported on macroreticular resin (**2**b). The metal nanoclusters can be dispersed only in the swollen fractions of the supports, hence their distribution throughout the polymeric mass can be homogeneous in the gel-type supports, but not in the macroreticular ones (**3**a,b). In both cases, the metal nanoclusters are entangled into the polymeric framework and their nano-environment is similar in both cases, as shown in level **4**.

1.2.7. The Issue of Mechanical Stability

CFPs, especially the macroreticular ones, suffer of an appreciable fragility and require considerable attention to mechanical stress when employed in slurry reactors. A case history has been evaluated in this connection [29] and a considerable stability to friction in the case of some Pd^0/gel-type resin catalysts has been recorded (Figure 8). In any case, it has been observed that a shaken reactor is by far preferable to any rotationally stirred ones [29].

1.2.8. The Issue of Filterability, Re-Usability and Non-Pirophoric Character of M^0/CFPs

These issues are really major ones in research laboratories dealing with specialty chemicals and first level scale-up. Filterability can be a problem with M^0 catalysts supported on classic materials such as carbon, owing to their tendency to pulverisation to give nanometer-sized catalyst particles that turn out to be very difficult to be recovered and successfully reused.

A recently commercialized Pd^0/polyurea catalyst (Pd^0/EnCat™, Reaxa Ltd., Manchester) [38] is claimed to match these requirements. Pd^0/gel-type CFP prepared in Corain's laboratories also match these requirements [39] and might become soon technologically relevant commercial catalysts.

2. Historical Background

CFPs have been of outstanding technological importance for decades and ion exchange is by far the most widespread industrial and commercial application of this kind of materials [40]. A great number of polymeric ion-exchangers are commercially available nowadays. They come in variable bead size, morphology (gel-type, macroreticular) and nature of the functional groups (e.g. sulfonic, carboxylic, amino, ammonium) [40]. Broadly speaking, purification and separation processes likely still represent the most important industrial application of CFPs and certainly allow for most of their overall consumption worldwide [40].

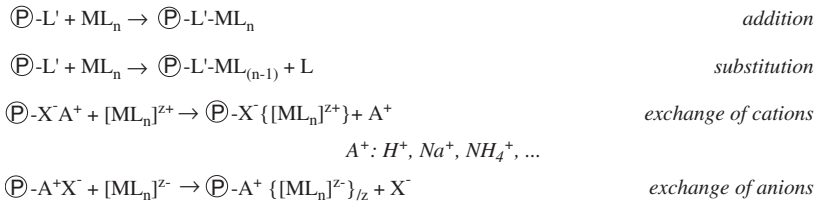

Scheme 2. Possible reaction for metal uptake by CFPs.

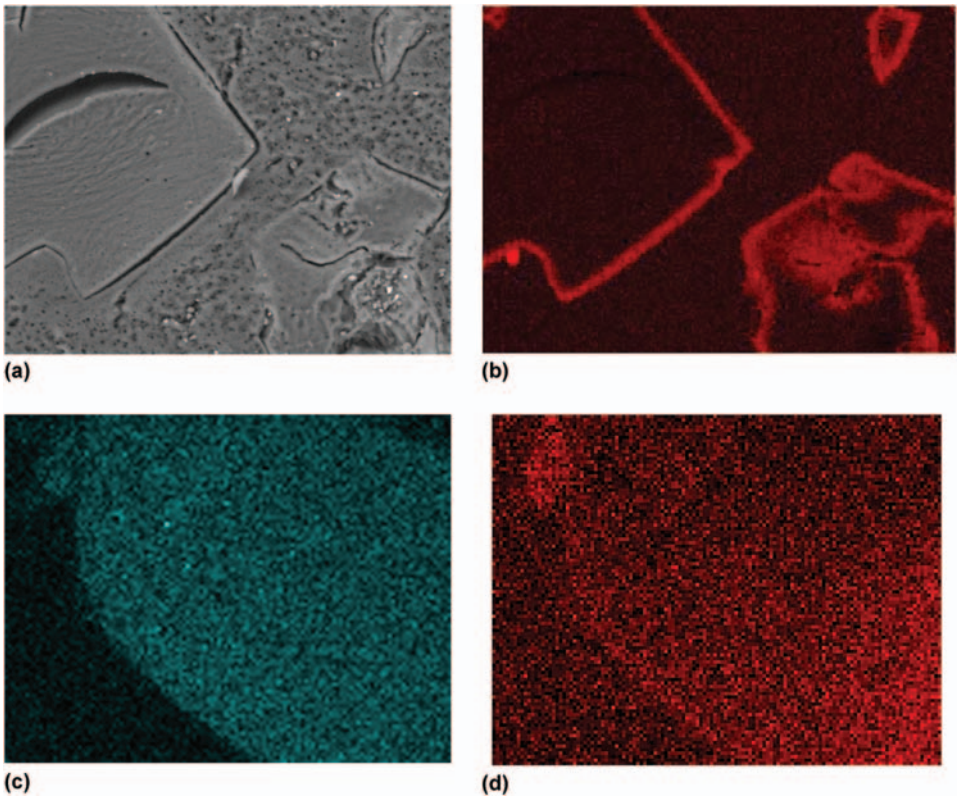

Figure 7. SEM and XRMA microphotographs of palladium catalysts supported on the amphiphilic resin made by DMAA, MTEA, MBAA (cross-linker) [30]. Microphotographs (a) and (b) show an image and the radial palladium distribution after uptake of $[Pd(OAc)_2]$ from water/acetone: the precursor diffuses only into the outer layer of the relatively little swollen CFP; after reduction the nanoclusters remain close to the edge of the catalyst beads. Microphotographs (c) and (d) show the radial distribution of sulfur and palladium, respectively, after uptake of $[PdCl_4]^{2-}$ from water: after reduction palladium is homogenously distributed throughout the catalyst particles. This indicates that under these conditions the CFP was swollen enough to allow the metal precursor to readily penetrate the whole of polymeric mass. (Reprinted from Ref. [30], © 2005, with permission from Elsevier.)

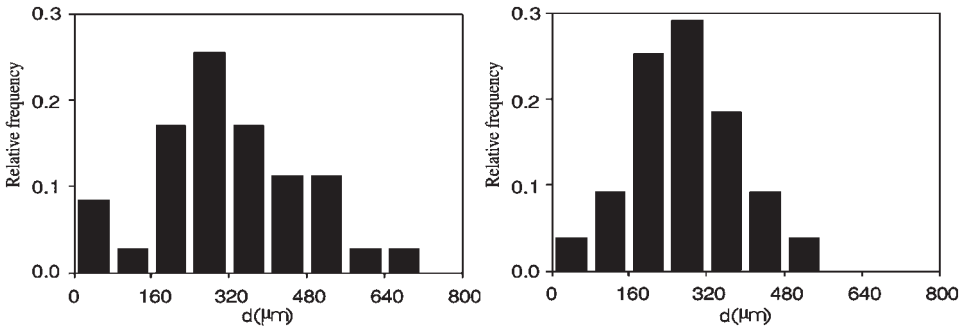

Figure 8. Relative size distribution for the $MPIF^{-}Na^{+}/Pd^{0}$ catalyst particles before (left, 35 particles) and after catalytic tests (right, 75 particles, magnetic stirring). Arithmetic average diameters 319 and 276 mm were determined for particles before and after catalytic tests, respectively. Image Pro Plus program. (Reprinted from Ref. [29], © 2003, with permission from Elsevier.)

The basic chemical structure of ion exchangers is the same for most of them. They are quite often formed by PS-DVB cross-linked frameworks, with different kind and degree of functionalization, cross-linking degree, specific surface area and porosity. The large-scale industrial production of PS-DVB resins started more than 50 years ago [40]. The ready availability of these materials attracted the attention of chemists interested into chemical synthesis and processing, from both the academia and the industry. By the mid of the seventies in past century, the potential of CFPs based on the PS-DVB skeleton was demonstrated in both solid-state synthesis [41–44] and heterogeneous acid catalysis [45–47]. For the discovery and development of the solid-state synthesis of polypeptides Bruce Merrifield was awarded the Nobel Prize in Chemistry in 1984. The SNAM PROGETTI process for the synthesis of

methyl-*tert*-butyl ether, catalyzed by sulfonated PS-DVB, is still one of the current technologies for the production of this important and other related anti-knock fuel additives on a huge scale (the total installed plant capacity is about 20×10^6 tons per year [6]).

In the sixties of past century, a few patents issued to Bergbau Chemie [5,48,49] and to Mobil Oil [50–52], respectively described the use of CFPs as supports for catalytically active metal nanoclusters and as carriers for heterogenized metal complexes of catalytic relevance. For the latter catalysts the term ''hybrid phase catalysts'' later came into use [53,54]. At that time coordination chemistry and organo-transition metal chemistry were in full development. Homogeneous transition metal catalysis was expected to grow in industrial relevance [54], but catalyst separation was generally a major problem for continuous processing. That is why the concept of hybrid catalysis became very popular in a short time [55].

The Bergbau Chemie patents on polymer-supported metal catalysts described the synthesis of MIBK from acetone over either a mixture of Pd/C and a strongly acidic sulfonic ion-exchange resin or a *bifunctional* palladium catalyst *directly supported* on the acidic resin. Resin-supported palladium catalysts of this kind are still employed for the industrial production of MIBK [6]. A bifunctional silver catalyst based on the same concept had been also reported in the same period [56]. The feasibility of bifunctional catalysis with organic solid acids (sulfonic resins) was also illustrated in 1975 by Gates and co-workers, who emphasized the ''straightforwardness of rational design of a resin catalyst'' based on the circumstance that resins ''have catalytic properties much more easily predicted than those of inorganic solids'' [57]. An earlier example of the use of organic matrices as catalytic supports for metal catalysts had been reported by Dunsworth and Nord [58]. They prepared a palladium catalyst by drying a swollen PVA gel containing the metal in colloidal form. However, the concept of CFPs-supported heterogeneous metal catalysts was not as successful as the concept of hybrid catalysis. To date not more than 70 papers have been published on this subject, if we do not consider the cases were (would-be) hybrid catalysts were unintentionally transformed into M^0/CFP ones under reaction conditions. In spite of this, the industrial scope of CFPs-supported heterogeneous metal catalysts is unquestionably larger than that of hybrid catalysis and a number of processes based on this technology (Table 1) have been practiced since relatively long time, as mentioned in the introduction.

However the scenario is changing quickly. The interest into M^0/CFPs catalysts has been steadily growing since 1990. Only about 10 relevant papers, including the seminal patents to Bergbau Chemie, appeared before that year. About 20 additional papers were published in the next decade and 40 more, or so, have appeared since 2000 to date. A review by Biffis and Kralik, covering the field up to about 2000, is available [59]. It also describes the application of linear polymers as catalytic supports for metal catalysts, which are outside the scope of this chapter. In the last five years research in this field has clearly accelerated with main contributions from Corain and associates and from Ley's group in Cambridge. Development of Ley's work led to the commercialization of the micro-encapsulated Pd^{II} and Pd^0-EnCat catalysts [38]. Even the classical synthesis of MIBK from acetone over Amberlyst CH28 bifunctional catalyst has been recently rediscovered and its kinetics investigated [60].

The early nineties of past century were apparently the turning point of this story. Till then heterogeneous metal catalysis used to be almost exclusively a tool for large scale, heavy chemical processing (petrochemistry, production of commodities, etc.) [1]. Typical reaction conditions are usually too severe for the employment of organic supports, which are neither chemically nor mechanically and thermally stable enough to withstand them. Moreover, industrial heterogeneous catalysis generally occurs under solid–gas conditions, where polymer-supported metals are likely inactive or very poorly active, as elegantly demonstrated by Biffis et al. in a study of CO pulse chemisorption over a palladium catalyst supported on a macroreticular commercial resin (Bayer UCP 118). In the dry, unswollen catalyst the metal was unable to adsorb CO molecule in spite of the permanent macroporosity of the support [62]. This depends on the unique morphology of cross-linked polymers in comparison with inorganic, rigid solids, as shown in the previous section and described in greater detail below. Finally, CFPs can be more expensive than conventional inorganic supports. This is clearly a disadvantage where the catalyst's price is a major processing cost, due to low added value of the product and/ or to the huge catalyst's loads typical of large-scale production.

However, urged by increasing environmental concern, academic and industrial researchers are in restless search of more efficient, cleaner ways to synthesize and produce chemicals. One obvious approach to environmentally friendly chemistry is the replacement of stoichiometric

Table 1. Industrial applications of M^0/CFP catalysts.

	Synthesis of MIBK	Synthesis of MTBE	Removal of O_2 from water[a]
Feedstock	Acetone	Methanol, Raffinate II[b]	Dioxygen dissolved in water
Reactions	Condensation–hydrogenation (bifunctional catalysis)	Condensation, hydrogenation[c]	Hydrogenation
Catalyst	Pd on sulfonated PS-DVB	Pd on sulfonated PS-DVB	Pd on sulfonated PS-DVB
References	[6]	[61]	[8]

[a]Down to ppb level.

[b]The hydrocarbon feedstock (Raffinate II) is a mixture of isobutene and other hydrocarbons, including dienes and alkynes, which must be hydrogenated as their presence would be troublesome for downstream operations.

[c]The condensation of methanol with isobutene and the highly chemoselective hydrogenation of dienes and alkynes are independently promoted by the active acidic sites (–SO_3H) and by the active metal.

reactions with catalytic ones. In this perspective, about 20 years ago heterogeneous catalysis started to be considered suitable for the synthesis of fine chemicals too [63]. Fine chemicals are usually organic substances of relatively low thermal stability and are synthesized under mild to moderate conditions, which are compatible with the employment of cross-linked polymers as supports for metal catalysts. In this perspective the use of CFPs as catalytic supports is economically feasible. The (industrial) synthesis of fine chemicals is typically carried out on a relatively small scale, quite often under batch conditions, and the products have generally a high added value. These circumstances can make the catalyst cost acceptable even for relatively expensive ones.

In conclusion, the scope of polymeric supports in heterogeneous metal catalysis has been steadily expanding in recent years and we expect that it will be even more so in the close future, with predictable scientific and technological breakthroughs.

3. Polymeric Supports, Metals and Preparation of the Catalysts

3.1. Polymeric Supports

Polymers form a very wide class of materials, which can be classified according to different criteria. Some of them, pertaining to the present discussion, are listed below:

(i) the nature of the polymerization process (polycondensation, polyaddition);
(ii) the presence of a cross-linker (polyaddition polymers, CFPs)
(iii) the morphology (for cross-linked materials);
(iv) the chemical structure (the nature of the monomers and the kind of functionalization).

A list of the polymers reported as catalytic supports in the literature reviewed here is given in Table 2.

Polycondensation polymers, like polyesters or polyamides, are obtained by condensation reactions of monomers, which entail elimination of small molecules (e.g. water or a hydrogen halide), usually under acid/ base catalysis conditions. Polyolefins and polyacrylates are typical polyaddition products, which can be obtained by radical, ionic and transition metal catalyzed polymerization. The process usually requires an initiator (a radical precursor, a salt, electromagnetic radiation) or a catalyst (a transition metal). Cross-linked polyaddition polymers have been almost exclusively used so far as catalytic supports, in academic research, with few exceptions (for examples of metal catalysts on polyamides see Ref. [95–98]).

Polyureas were among the first polycondensation polymers to be employed as catalytic supports for heterogeneous metal catalysts. The first report about palladium on polyurea, by Zhang and Neckers [99] dates back to 1979. They obtained their catalyst in a two step preparation, where the co-monomers (2,4- toluendiisocyanate, TDI, and the complex between palladium acetate and 4,4′-diamino-2,2′-bipyriridine) were condensed together and palladium(II) subsequently reduced with $LiAlH_4$[2]. This is a case of polymerization of a metal containing monomer starting from a metal-containing monomer, which is pretty uncommon [100–102].

Polyureas are currently employed for the commercial production of EnCat catalysts by Reaxa [38]. In this case the matrix is generated in the presence of a palladium(II) precursor, typically the diacetate, in a microencapsulation process. The starting material is a mixture of oligomers of TDI which are partially hydrolyzed to generate the amino groups required for the condensation reaction (Scheme 3). Due to the degree of functionalization of the oligomers employed, the obtained polymer matrix is cross-linked and not linear as in the case of Zhang and Neckers's polyureas [99]. During microencapsulation, palladium(II) is not reduced and the ensuing material is a palladium(II) form of the EnCat catalyst.

Polybenzimidazole (PBI) and polypyrrol (PPY) were investigated as supports by Hong-Li and Frechet [84,103] and by Gautron et al. [104], respectively. Whereas PBI can be considered as a ''conventional'' polyaddition polymer, PPY is obtained through the oxidative coupling of pyrrole in the presence of $PdCl_2$. The process entails the elimination of one HCl molecule, mediated by palladium, per monomeric unit and PPY can be broadly considered a polycondensation polymer. Also, in these cases the polymers are linear (not cross-linked), but they are soluble only in a limited number of solvents, a disadvantage for their processing, but a bonus for their employment as supports for heterogeneous metal catalysts.

As to polyaddition polymers, almost all the supports described in the literature are cross-linked. As shown for the polycondensation polymers, this is not strictly required, provided the catalysts are used with liquids where they are insoluble. However, not only cross-linking ensures that the support is insoluble, but a suitable cross-linking degree provides acceptable mechanical stability of the material. This could be a bonus, because changes in the fluido-dynamics of the system, troublesome separation and catalyst loss could be the adverse consequences of mechanical degradation. Moreover, the cross-linking degree affects the morphology of CFPs. Highly cross-linked CFPs (cross-linking degree $\geq 15\%$ ca.) are generally macroreticular. They possess *permanent* pores (meso- and macropores, from a few tens up to several hundreds of nanometer in diameter) and can exhibit specific surface areas *in the dry state* comparable to those of porous inorganic solids. However, this specific feature is not necessarily a real advantage when a M^0/CFP catalyst is used under solid–liquid conditions, as will be illustrated below.

As anticipated in the introduction, cross-linked polymers *swell*, to variable extent, when put in contact with liquids. Therefore, the working state of any cross-linked organic polymer under solid–liquid conditions, no matter if it is a catalyst, a support or a carrier for solid state synthesis, is the swollen state. In macroreticular CFPs swelling does not involve the whole polymeric mass: it is

[2]Allegedly, the product of the reduction is a bipyridyl palladium(0) complex. This is not likely and our personal opinion is that the obtained material is a supported metal palladium catalyst. This is the reason why the paper was included in this review.

Table 2. Scope of CFPs employed as supports for heterogeneous M^0 catalysts as apparent from the open literature to date.

References	Chemical structure[a]	Cross-linker	Functional group[b]	Notes
Gel-type				
[64]	Poly-DMA	MBAA	$-CH_2CH_2S(CH_3)$	
[64]	Polyacrylate	DVB	$-CH_2CH_2SO_3H$	
[65]	Polyacrylate	DVB	$-CH_2CH_2N(CH_3)_2$	
[65]	PCEA	DVB	–CN	
[65]	Polyacrylate	DVB	–COOH	
[65]	PVPY	DVB	pyri	
[30,66]	Poly-DMA	MBAA	$-CH_2CH_2S(CH_3)$	
[67]	PS	DVB	$-NR_3Cl$; $-SO_3Na$	Amberlite IRA 400; IR 120[c]
[32,68]	Poly-DOMA	EDMA	pyri	
[69]	Copoly{styrene-acrylate}	DVB	$-SO_3H$	
[70]	PS	DVB	dipyridylamine	PS modified with PEG lateral chains
[71]	Poly-MMA	EDMA	Pyri; $-CH_2CH_2N(CH_3)_2$	Microgels[d]
[72,73]	Poly-DMA	MBAA	–COOH, $-SO_3H$	
[29]	Poly-DMA	MBAA	–COONa, $-SO_3Na$	
[31,74–77]	PS	DVB	$-CH_2N(CH_2COONa)_2$	Chelate resins exchanged with metal ions
[78,79]	PS	DVB	$-SO_3H$	DOWEX resin[c]
[80]	Copoly{styrene-acrylate}	DVB/ MBAA	$-SO_3H$	
[62]	PVPY	DVB	pyri	
[81–83]	Copoly{styrene-acrylate}	MBAA	$-SO_3H$	
[33,34]	Acrylamide gel	MBAA	$-CH_2CH_2NH_2$	
[84]	PS	DVB	2-benzimidazolyl	
Macroreticular				
[60]	PS	DVB	$-SO_3H$	Amberlyst CH28[c]
[64]	PS	DVB	$-SO_3H$	Lewatit K2621[c]
[85,86]	PS	DVB	None	Hyper cross-linked
[62,87,88]	PS	DVB	$-SO_3H$	UCP 118[c]
[88]	PS	DVB	$-SO_3H$	SPC 118[c]
[89]	PS	DVB	–	
[90,91]	PVPYR	DAP	$-NC(O)CH_2CH_2CH_2$	cld = 25%–52%
[23]	PS	DVB	$-SO_3H$	Lewatit OC 1038[c]
[92]	PS	DVB	$-SO_3Na$	Amberlyst 15[c]
[92]	PS	DVB	$-C_6H_4PPh_2$	From reaction of XAD-2 with sodium phosphinate
[93,94]	PS	DVB	$-NR_3OH$	Amberlyst A 27 OH[c]
[5,48,49]	PS	DVB	$-SO_3H$	DOWEX 50 WX 8[c]

[a]Nature of the most abundant comonomer.
[b]Nature of the groups devoted to metal uptake.
[c]Commercial ion-exchanger.
[d]Intramolecularly cross-linked polymers.

limited to the walls of the permanent pores, hence does not imply large changes in the apparent volume of the polymeric material. The importance of the morphology of the swollen polymer layer at the pore walls was smartly demonstrated by Jerabek in 1989 [23]. He showed that two palladium catalysts supported on macroreticular sulfonated PS-DVB resins, featured by different cross-linking degrees, exhibited practically the same catalytic activity in the hydrogenation of cyclopentene. One of the catalysts (Lewatit OC 1038) was a Bayer commercial catalyst. The other catalyst was prepared by the author starting from a partially sulfonated PS-DVB resin. This resin was macroreticular in nature, but much less cross-linked than Lewatit OC 1038. The catalysts were almost equally active in the hydrogenation of neat cyclopentene at 30 °C under 1 MPa H_2, in spite of the higher BET surface area (dry state) of Lewatit OC 1038 ($26\,m^2\,g^{-1}$ vs. $8.5\,m^2\,g^{-1}$). In this pioneering study, Jerabek assessed the swollen-state morphology of the catalysts with a specific technique, ISEC [105,106,16–18]. ISEC characterization of the catalysts showed in fact that in the least cross-linked catalyst (the home-made one) the layer of swollen polymer beneath the macropore surface contained domains with polymer chain concentration much lower than that observed in the commercial, more cross-linked catalyst.

In general, cross-links are not uniformly distributed throughout the polymer framework. Due to the higher reactivity of cross-linkers (they have at least two C=C double bonds per molecule) the first nuclei of polymer mass are much more cross-linked than polymer mass formed in the final stages of the polymerization process [13]. Therefore, in macroreticular resins the polymer mass just beneath the surface of the permanent pores is relatively little cross-linked and is able to swell when a liquid fills the permanent pores[3]. The thickness of the layer of swollen polymer mass (gel-like) depends on the swelling ability of the liquid and on the overall cross-linking degree: the higher the cross-linking degree, the thinner the gel-like layer. This concept has been recognized since long

[3]On the other hand, the "core" of the polymeric mass, much more cross-linked, is in general hardly accessible.

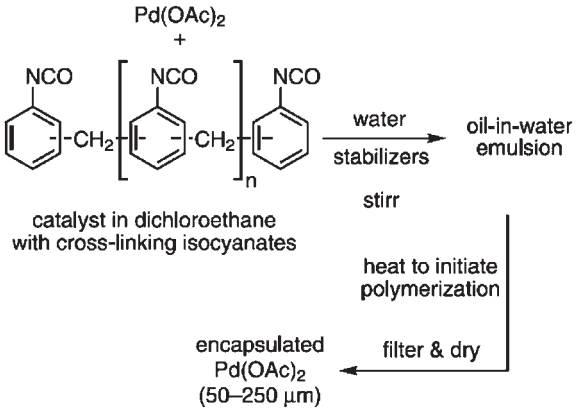

Scheme 3. Preparation of EnCat catalyst by microencapsulation. (Reprinted with permission Ref. [38], © 2005, with permission from Sigma-Aldrich Co.)

in the field of ion exchange [107]. Jerabek's results confirmed on a quantitative basis the intuitive conclusion that in the more cross-linked Lewatit OC 1038 material Pd^0 nanoclusters were not fully accessible and therefore mostly excluded from the catalytic action. This is the consequence of much smaller swelling of the pore walls during the catalytic process in comparison with swelling during the incorporation of the metal precursor (see below). For this very reason, polymer-supported metal catalysts are not suited to gas–solid application, where there is no liquid to provide adequate swelling of the polymer mass.

This argument is confirmed by the study of CO pulse chemisorption by Biffis at al., mentioned above. In this piece of investigation, the authors prepared a 2% (w/w) palladium catalyst supported by Lewatit UCP 118, a macroreticular resin (nominal cld = 18%) from Bayer. Its TEM characterization showed a remarkably heterogeneous distribution of the metal nanoclusters, which are apparently located close to the surface of the polymer nodules [62] (Figure 9).

The observed distribution can be readily explained upon assuming that the only part of polymer framework accessible to the metal precursor was the layer of swollen polymer beneath the pore surface. UCP 118 was metalated with a solution of $[Pd(AcO)_2]$ in THF/water (2/1) and palladium(II) was subsequently reduced with a solution of $NaBH_4$ in ethanol. In the chemisorption experiment, saturation of the metal surface was achieved at a CO/Pd molar ratio as low as 0.02. For sake of comparison, a Pd/SiO_2 material (1.2% w/w) was exposed to CO under the same conditions and saturation was achieved at a CO/Pd molar ratio around 0.5. These observations clearly demonstrate that whereas palladium(II) is accessible to the reactant under solid–liquid conditions, when a swollen polymer layer forms beneath the pore surface, this is not true for palladium metal under gas–solid conditions, when swelling of the pore walls does not occur. In spite of this, it was reported that the treatment of dry resins containing immobilized metal precursors [92,85] with dihydrogen gas is an effective way to produce polymer-supported metal nanoclusters. This could be the consequence of the small size of H_2 molecules, which

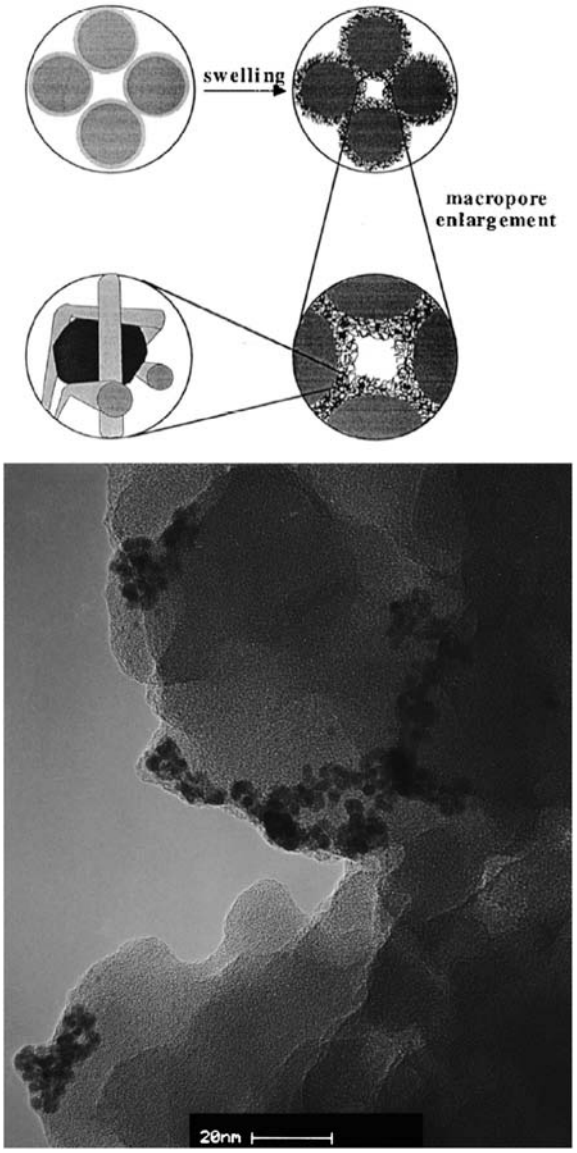

Figure 9. Distribution of palladium nanoclusters in a M^0/CFP catalyst based on the macroreticular resin Lewatit UCP 118. (Reprinted from Ref. [62], © 2000, with permission from Elsevier.)

makes them able to penetrate into very dense polymer frameworks.

All these findings and related observations emphasize the role of the gel-type layer decorating the surface of macropores as the "working arena" [107] in Pd^0 catalysts supported on macroreticular CFPs (Figure 6). Therefore the knowledge of phenomena which occur inside a swollen, gel-type polymer framework during the catalytic process are of the utmost importance for better understanding of the behavior of CFPs as catalytic supports, even when they are macroreticular. In this perspective, fundamental research work on fully gel-type supports can be highly informative and for this reason the work by

Corain and associates on M^0/CFP catalysts has been so far focused on this kind of materials. In particular, great attention was paid to the correlation between the morphology of the support and features of CFPs supported metal catalysts, such as their molecular accessibility [14,21,22,25,108] or the size of metal nanoclusters generated inside swollen polymer frameworks (for a specific study see Ref. [68]).

Both commercial polymeric materials and polymeric supports, synthesized *ad hoc*, were employed. The scope of monomers and polymerization procedures which can be employed is very large. New functional groups can be introduced into pre-formed polymeric materials (e.g. sulfonation of polystyrene), for the purpose of tailoring their properties. In this sense, polymeric support are very versatile materials, which can be designed according to the needs of the preparation of the catalyst and of the catalytic reaction. For instance, swelling behavior, which is so important for solid–liquid applications, can be controlled by changing the cross-linking degree, the nature of the cross-linker and of the monomers. Some monomers make the CFP hydrophobic (e.g. polyestyrene, *n*-dodecylmethacrylate), some make it hydrophilic (e.g. sulfonated monomers, MAA) and some other allow it to obtain amphiphilic CFPs, with a pretty broad solvent compatibility spectrum (e.g. DMA, [109]). Hydrophobic polymers swell better in apolar or little polar solvents and hydrophilic ones swell better in water or polar solvents. Hydrophobicity and hydrophilicity not only affect the swelling behavior (the solvent compatibility) of CFPs, but also the sorption of solutes (substrate compatibility). A hydrophilic reagent is attracted into a polymer-supported catalyst from bulk solution and a hydrophilic product will be retained inside the solid catalyst to a relatively high extent if the polymeric support is hydrophilic. By contrast, a hydrophilic reagent will have a little tendency, if any, to enter a hydrophobic polymeric support and a hydrophilic product will tend to be readily expelled from a hydrophobic catalyst. Hydrophobic species, of course, behave the other way round. Substrate compatibility, therefore, must be taken into account and can be exploited to gain some control over the concentration of reagents and products inside the catalyst [33,34].

For the purpose of metal uptake, both ionic groups ($-SO_3^-$, $-COO^-$, in both H^+ or Na^+ form; $-NR_3^+$, in both OH^- or Cl^- form) and Lewis base groups (amino, pyridyl, benzimidazoyl, thiol, methylsulfide, nitrile) were employed (see Table 2). They can be introduced during the polymerization reaction, upon using a properly functionalized monomer (2- or 4-vinylpyridine, methacrylic acid, acrylonitrile, ethylacrylates (or methacrylates) with proper substitution of the ethyl group in the 2 position; these are all commercially available) or post-functionalization of the CFP. As the metal amount in the catalyst required for the catalytic application is generally low (a few percent in weight), the amount of functional groups for metal "docking" can be low as well. In this perspective, co-polymers of a prevailing monomer ("structural monomer"), which imparts the proper solvent–substrate compatibility, of a second monomer ("functional" or "auxiliary" monomer), which attends to metal uptake, and of the cross-linker can be particularly useful.

3.2. Metals

The choice of the metals is strictly related to the catalytic application. As we shall show later, the catalytic reaction most commonly investigated with polymer supported M^0/CFP catalysts is hydrogenation (Table 3). The overwhelming majority of catalytic studies concerns the hydrogenation of alkenes and by far the most commonly employed metal is palladium, followed by platinum. Examples of rhodium and ruthenium hydrogenation catalysts supported on polymeric supports are very rare.

A few articles deal with oxidation reactions, in particular with alcohol oxidation. They are generally very recent and in some cases gold is the active metal. This highlights the upsurging interest for both catalytic oxidation reactions and gold catalysis. Finally, a number of publications deal with the synthesis of MIBK from acetone over bifunctional palladium catalysts supported by acidic sulfonated resins (one of the most important industrial achievements of polymer supported metal catalysis), the direct synthesis of hydrogen peroxide from the elements, oxidative carbonylation and carboxylation reactions, C–C coupling reaction and catalytic abatement of nitrates in water (selective hydrogenation to N_2). Again, the metals employed are palladium and gold and, in some cases, bimetallic Pd/Au and Pd/Cu systems. There are occasional reports on the preparation of CFPs-supported metals not followed by catalytic tests, such as silver and nickel on Amberlite 15 [92] or cobalt on HPS [86]. In general, noble or late transition metals are most commonly employed: they can be easily reduced and kept in the zero valent state, although oxidation on aging can be significant when the metal is in the form of small nanoclusters. As many of them are active in hydrogenation reactions the latter are quite often chosen to test the M^0/CFP catalysts. Hydrogenation of organic unsaturated substrate has been a well established, important method in organic synthesis since long. Many palladium catalysts are known and applied (Pd on carbon in particular) and it is easy to compare the performance of new catalysts with that of well established ones. In addition, hydrogenation usually proceeds quite smoothly, under mild conditions (room temperature, atmospheric pressure) and therefore it can also be carried out with very simple equipment. If one looks at the scope of metals and catalytic reactions investigated so far, it is quite clear that model systems have been mainly taken into account, with very few exceptions. This reflects the mostly academic nature of the work, which has been carried out in this field so far.

3.3. Methods of Catalyst Preparation

Inspection of the literature reveals that the active metals can be mainly introduced into the supports in three ways:

(a) introduction of a suitable metal precursor into the support and generation of the metal nanoclusters therein through reduction or decomposition of the precursor (RIMP);
(b) synthesis of the polymeric support in the presence of a suitable metal precursor and generation of the

Table 3. Scope of heterogeneous catalysis with M^0/CFP catalysts as apparent from the open literature to date.

Reference	Metal	Substrate
Hydrogenation		
[65]	Pt	Citral
[32,69]	Pd	EAQ
[110]	Pd[a]	Alkenes (including α,β-unsaturated carbonyls, styrenes, allyl derivatives), nitrotoluene, diphenylacetylene
[111]	Pd, Pt	Citral
[112,113]	Pd	Ketones, epoxides (hydrogen transfer from formic acid)
[98]	Pt	Crotonaldehyde
[31,74,75]	Pd	Alkenes
[79]	Pd, Co	Nitrotoluene
[80]	Pd	Cyclohexene, cyclohex-2-enone
[81,82,114,115]	Pd	Cyclohexene
[116]	Pt	Allylic alcohol
[89]	Pt	Cinnamaldehyde
[117]	Pt	Acrylic acid
[89]	Pt	Nitrotoluene
[118]	Ru	Benzene
[101,115]	Pd	Nitrotoluene
[90,91]	Pd	Alkenes
[33]	Rh	Alkenes
[34,77]	Pt	Alkenes, dienes
[23]	Pd	Cyclopentene
[84,103]	Pd	Nitroaromatics, alkenes
[99]	Pd	Alkenes
[93,94]	Pd	Cyclohexene, allyl alcohol
Oxidation		
[30,66]	Au, Pd	Alcohols
[70]	Pd	Alcohols
[85]	Pt	L-Sorbose
[92]	Pd, Pt	Ethanol
Miscellanea		
[5,60]	Pd	Acetone (bifunctional catalyst; synthesis of MIBK)
[32,64]	Pd, Au	Synthesis of H_2O_2 (from the elements or through H_2EAQ)
[67]	Au	Amines, epoxides (carbonylation and carboxylation with CO_2)
[119]	Au	Amines (oxidative carbonylation with CO/O_2 to carbamates and symmetric ureas)
[104]	Pd-Cu	Hydrogenation of nitrates in water
[120–122]	Pd-Cu	Hydrogenation of nitrates in water
[123]	Pd	*p*-nitrobromobenzene (couplings with *n*-butylacrylate[b], phenylboronic acid[c], phenyltrimethyltin[d])
[124]	Pd	Iodobenzene (coupling with *n*-butylacrylate[b])

[a]Palladium was reduced *in situ* with H_2 (5 MPa) before the addition of the substrate.
[b]Heck reaction.
[c]Suzuki reaction.
[d]Stille reaction.

metal nanoclusters therein through reduction or decomposition of the precursor (Incorporation of Metal during the Polymerization and Reduction, IMPR);

(c) introduction of preformed metal nanoclusters into the support (Immobilization of Metal Nanoclusters, IMN).

3.3.1. Reduction of Immobilized Metal Precursors (RIMP)

The first general method, RIMP, is by far the most widely employed. As shown in Table 2 CFPs employed as catalytic supports usually possess functional groups suited for ion exchange (–SO_3H or –SO_3Na, –COOH or –COONa, –NR_3X) or metal coordination (amino, cyano, pyridyl, thiol, sulfide, benzimidazolyl, pyrrolidyl,…). The treatment of a CFP with a solution of a proper metal precursor allows the introduction of the latter in an easy way, with ion exchange or ligand addition/replacement processes providing the driving force for the metal uptake (Scheme 2). Under these conditions excess amount of solvent (with respect to the amount strictly required for full polymer swelling) and relatively low metal precursor amounts can be employed. In spite of the dilution, metal uptake is often quantitative and the desired final metal weight percentage in the catalyst (0.1–10%, w/w, for catalytic application) can be attained with no or little metal waste.

If the employed CFP is a gel-type resin, the solvent must be a good swelling agent for the support. Under full swelling conditions, the whole or a large proportion of the polymer framework is accessible to the metal centers. Higher metal loadings and homogeneous metal distribution throughout the support beads can be attained in this

way. Whether this is an advantage or not depends on the conditions of the catalytic reaction: if the swelling degree of a M^0/CFP catalyst, as a whole, will be smaller under duty than during its preparation, a fraction of the metal nanoclusters will not be accessible and will be unused. The same also holds for macroreticular resins: if swelling beneath the pore walls during the use of the catalyst is smaller than during its preparation, the thickness of the gel-type layer laying beneath the pore surface will be smaller as well and the metal component will not be fully exploitable. Therefore much attention must be paid to the compatibility of the support with all the solvents to be employed in both catalysts preparation (metal precursor introduction, metal reduction-metal nanocluster generation) and use (catalytic reaction). In principle, the best solution is to prepare the catalyst in the same solvent of the catalytic reaction, but this is not always possible. Optimal conditions are the balance between different experimental parameters, such as the chemical structure of the polymer, the nature of metal precursor and the reducing agent (if any), the nature of reagents and products. For instance, sulfonated or carboxylated resins generally swell to a considerable extent in water and this solvent is particularly apt for ion exchange. If we consider that cationic or anionic complexes of the noble metals listed in Table 3 are readily available and water soluble, metal incorporation could be safely carried out with aqueous solutions thereof. If metal nanoclusters are generated by reduction with excess aqueous or alcoholic $NaBH_4$, a commonly employed procedure, the support is transformed into its sodium form. However, sulfonated or carboxylated resins in Na-form generally swell in methanol and ethanol, which are very common solvents for hydrogenation reactions, to a smaller extent than in water. Hence a catalyst prepared in this way could not be suitable for hydrogenation reactions with no modification (e.g. reverting to the H-form). When a single solvent cannot be used for both catalyst preparation and the catalytic reaction it is possible to design the polymeric support and impart a broad solvent compatibility to it. In this sense, co-polymers derived from DMA have proven to be useful in a number of cases [29,30,66,73].

A very interesting feature of cross-linked polymeric supports is their ability in giving metal nanoclusters of small, controlled size. The ability of ion-exchange resin Amberlyst 15 to give very small nanoclusters was observed by Hanson et al. as early as 1974 [92] in a really pioneering study on the preparation and characterization of palladium, platinum, silver and nickel metal catalysts over Amberlyst 15. Hanson et al. prepared their catalysts by means of the RIMP method and employed different reduction protocols. The metalated resin was either treated with flowing H_2 in the dry state or with a basic aqueous solution of hydrazine or ethylformate. The way of reduction affected the size of the metal nanoclusters. In the catalyst prepared by H_2 reduction, no signals were observed at XRD analysis. TEM measurements (as early as 1974!) confirmed that the metal nanoclusters were typically 2 nm in diameter and the size was pretty uniform (reported standard deviations were ca. 25% or smaller), with no appreciable differences between platinum and palladium. In the catalysts prepared with aqueous solutions of the reducing agent a small number of large metal nanoparticles was observed, in addition to the 2 nm-sized nanocluster, with both XRD analysis and TEM. The size of the large nanoparticles ranged from ca. 10 to 30 nm. These data supported the conclusion that the *small nanoclusters* were formed *within the polymer framework* and the *large nanoparticles* were formed *in the permanent pores* (whose diameter was 20–60 nm on average). The formation of metal nanoparticles in the pores was possible only with the reducing agent in solution. In this case, swelling of the polymer network made possible the extraction of the metal into the macropores during the reduction. This cannot occur during the H_2 treatment of the dry materials. This underpins an important feature in the RIMP preparation of polymer supported metal catalysts: the metal precursor can move throughout the swollen polymer framework during the reduction. This can affect the radial distribution of the metal in the final catalyst (see later). The results of Hanson et al. also highlights the ability of cross-linked polymeric material to act as size templates in the production of metal nanoclusters, *provided they are generated inside the polymer framework*.

The same ability was observed later in HPS by Sidorov et al. [85,86]. HPS is a PS or PS-DVB resin, which does not possess functional group apt to ion exchange or ligand addition/substitution reactions. It has a nominal cld higher than 100%, due to inter-phenyl methylene bridges formed by reacting linear polystyrene or lightly cross-linked swollen PS-DVB resins with ethylene dichloride [86]. This yields a very rigid, permanently nanoporous framework, with extremely high BET surface areas (around $1000\,m^2\,g^{-1}$) and small nano-pore diameter (a few nanometers). Owing to the absence of specific functional groups, sorption of the metal precursor onto HPS was carried out with an incipient wetness impregnation procedure. When a HPS batch with a surface area of $833\,m^2\,g^{-1}$ and nanopores of about 2.0 nm was impregnated with a THF or methanol solution of H_2PtCl_6, dried and treated with H_2 for 3 h at room temperature, 1.3 nm (THF) and 1.4 nm (MeOH) platinum nanoclusters were obtained, with an overall metal loading of 7.5–8.3% (w/w) [85]. With cobalt 2.0 nm nanoparticles were obtained in the same support, after impregnation with isopropanol or DMF solutions of $[Co_2(CO)_8]$ and subsequent drying and thermal decomposition of the precursor [86]. The size of cobalt nanoparticles was assessed by means of TEM and ferromagnetic resonance spectroscopy, which yielded comparable results. In addition, the Co nanoparticle size was independent of both the weight metal percentage up to 8% and of the time of thermal decomposition of the precursor. A very interesting feature of these metal nanoparticles is the closeness of their size to that of the nanopores. From these data it is apparent that the metal nanocluster size cannot exceed the diameter of the cavities where they were generated: the polymeric support acted as a ''mold'', able to restrict the growth of the metal nanoparticles. In view of the absence in HPS of functional groups able of strongly interacting with the metal centers or nanoparticles a simple steric effect was proposed. This template effect had already been exploited by Ziolo to prepare magnetic nanoparticles of ferric oxide [125]. For this peculiar way of size control in nanostructured matter Ziolo introduced the term ''Template Controlled

Table 4. Relationship between the nanoporosity of some gel-type CFPs and the size of M^0 nanoclusters supported thereon.

No.	Support	cld (% mol)	Metal	Pore diameter[a] (nm)	Diameter of nanoclusters (nm)	References
1	Copoly-{DMA-MTEA-MBAA}	8	Au	2.5	2.2	[66]
			Pd		2.3	
2	Copoly-{DOMA-VPY-EDMA}	4	Pd	3.4	3.5 (TEM), 3.3 (XRD, Rietveld), 2.6 (Number distribution function)	[68]
3	Copoly-{DMA-MAA-MBAA}	4	Pd	3.2	2.0	[72]
4	Copoly-{MMA-MAEA-EDMA}	5	Pd	[b]	8.9	[71]
		10	Pd		4.2	
		10	Pt		4.4	
		20	Pd		3.1	
5	Copoly-{MMA-VPY-EDMA}	10	Pd	[b]	4.2	[71]
			Pt		4.0	

[a]Average value or the value of the most abundant volume fraction.
[b]The supports are soluble microgels and pore diameter cannot be measured.

Synthesis'' (TCS). The very same term was independently proporsed by Corain and associates for the size controlled synthesis of palladium nanoparticles in 2004 [68]. In a number of cases they observed that palladium nanoclusters, supported on gel-type resins of different nature and obtained with the RIMP method, exhibited a remarkable agreement between the size of the cavities of swollen supports (as assessed by means of ISEC, see Section 4) and the diameter of the metal nanoclusters (Table 4, Entries 1–3) [10,11,66,71,72,87].

In the case of a highly chemoselective palladium catalyst for the hydrogenation of EAQ [32] the correlation between the support morphology in the swollen state and the nanocluster size was studied in great detail [68]. In particular, the introduction of metal precursor into the copoly-{DOMA-VPY-EDMA} matrix, its reduction to generate the nanoclusters and the ISEC characterization of the morphology of the swollen gel-type resin were carried out in the same solvent (THF), so that the morphological data can be unambiguously compared (Figure 10).

The agreement between the values of the two quantities is remarkable and it was further confirmed by a fine XRD investigation. When the contribution of the polymer matrix to the total scattering was eliminated (Rietveld method), the observed average size of the palladium nanoclusters was strictly close to the TEM datum (Table 4, entry 2). An excellent degree of size control was also achieved when functionalized microgels were employed instead of resins to generate the metal nanoclusters. Microgels are a special class of *intramolecularly* covalently cross-linked polymers (in this respect they are akin to polypeptides, where intrachain cross-links are provided by internal hydrogen bonds) and, differently from resins, are soluble. They can be obtained by co-polymerization of dilute solutions of co-monomers cross-linker [71,126] references therein]. In a detailed study Biffis et al. showed that the higher the cross-linking degree the smaller the metal nanoclusters. The metal nanoclusters size apparently did not depend on the nature of either the functional groups of the microgel (amino or pyridyl) or of the metal (Pd or Pt). These and the other data collated in Table 4 (Entries 4,5) support the hypothesis that the size template effect observed is mainly steric (physical) in nature, as proposed by Sidorov et al. for the HPS-supported metals, and that the metal nanocluster size is controlled mainly by the morphology of the polymeric material, which is a consequence of its swelling behavior.

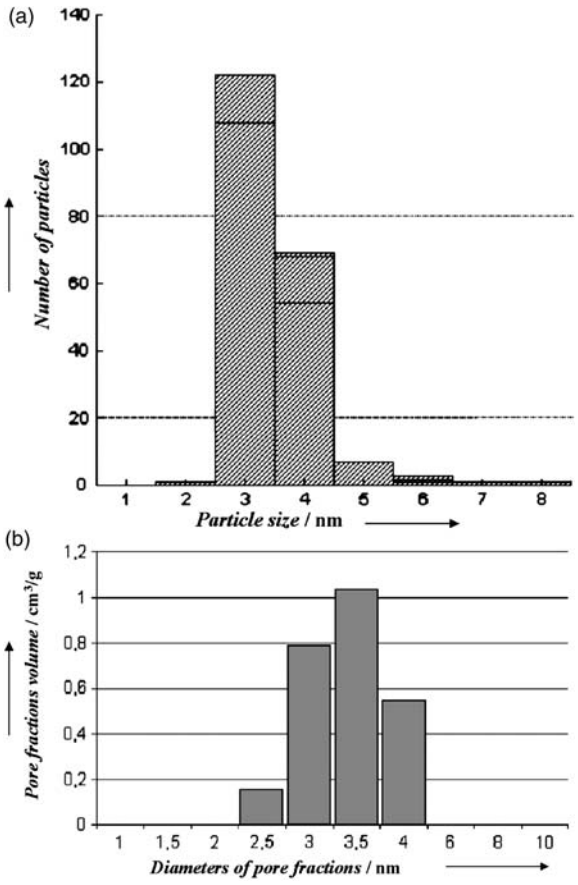

Figure 10. Pore volume distribution of the support as assessed with ISEC (a) and the metal nanoclusters size distribution as assessed with TEM (b) for a Pd^0/CFP catalyst. (Reprinted from Ref. [68], © 2004 with permission from Wiley.)

As anticipated in Section 1.2.1, also the radial distribution of the metal precursor across the support beads is strongly dependent on the swelling behavior of the employed CFP (Figure 7). However, RIMP method requires the reduction of the immobilized metal precursor and migration of the metal during this step can also occur. Therefore it must be born in mind that the radial distribution of the active metal in the final catalyst can be different from that of its precursor. For instance Henson et al. observed a peripheral radial distribution in their platinum catalysts on Amberlyst 15 in contrast with the homogeneous distribution of the immobilized precursor, when the latter was reduced with hydrogen flowing on the *dried* material. As redistribution of the metal in the dry resin is not feasible, it was concluded that migration took place during the drying procedure, favored by the remarkable stability of the platinum(II) precursor, $[Pt(NH_3)_4]^{2+}$ [92]. By contrast, when the precursor was reduced with an aqueous solution of hydrazine, the final catalysts maintained the same homogeneous radial distribution of the parent materials. Similar results were also obtained by Kralik et al. [127] in the preparation of palladium catalysts supported on a co-polymer of DMA, the potassium salt of MAESA and MBAA as the cross-linker. After introducing palladium(II) into the supports with a homogeneous radial distribution, the metal centers were reduced with either $NaBH_4$ in large excess (alcoholic solution) or hydrogen. In both cases the material to be reduced was swollen in ethanol. Whereas the homogeneous distribution of palladium was preserved with $NaBH_4$, an eggshell distribution was observed after reduction with hydrogen. In this case, the different results obtained with the two reducing agents were interpreted as due to their different diffusion rate within the catalyst as compared to that of the palladium(II) metal centers. $NaBH_4$ is much more soluble than H_2 in ethanol and was present in large excess. The polymeric support was pretty well swollen by the solvent and therefore the inward diffusion of the reducing agent was faster than the outward diffusion of the metal centers. As the results the latter were reduced at their original positions in the material. Due to the low solubility at the moderate pressure applied, H_2 concentration in ethanol was pretty low and its inward diffusion was slower than the outward diffusion of the metal centers, which could be reduced only close to the edges of the polymer beads. The same happened when a relatively little concentrated solution of $NaBH_4$ in ethanol was employed.

3.3.2. Incorporation of Metal precursors during Polymerization and Reduction (IMPR)

The second general method, IMPR, for the preparation of polymer supported metal catalysts is much less popular. In spite of this, microencapsulation of palladium in a polyurea matrix, generated by interfacial polymerization of isocyanate oligomers in the presence of palladium acetate [128], proved to be very effective in the production of the EnCat catalysts (Scheme 3). In this case, the formation of the polymer matrix implies only hydrolysis-condensation processes, and is therefore much more compatible with the presence of a transition metal compound. That is why palladium(II) survives the microencapsulation reaction and the catalysts are obtained with the metal in this oxidation state. Microencapsulated palladium nanoparticles can be obtained by reduction with either dihydrogen of formic acid. The latter reducing agent gave much smaller nanoparticle size (ca. 2 nm) than the former (larger than 5 nm) [112].

A similar approach was applied by Zhang and Neckers, who prepared a polymeric matrix by polycondensation of a comonomer which was also a dipyridyl complex of palladium(II) [99]. In the case of Pd/Cu catalysts supported by polypyrrole investigated by Gautron et al. [104], the polymer must be generated in the presence of a stoichiometric amount of a palladium(II) compound, which takes part to the oxidative coupling of pyrrole rings and is directly transformed into palladium(0). This is a particular case where the precursor of the active metal is a stoichiometric aid in the polymerization reaction. The obvious disadvantage, in this case, is that the amount of palladium in the final material cannot be changed at will.

The production of polymeric supports in the presence of a metal compound by means of a polyaddition process, and in particular by radical polymerization, is even less common. This is due to the intrinsic difficulty to generate radicals and keep the radical propagation chain alive in the presence of transition metal centers. Transition metals generally possess several available oxidation states and can react easily with radicals, with the doubly adverse effect of terminating the polymerization reaction and decomposing the metal compound [55]. In spite of this, this approach was employed by Huang and He [90] to prepare palladium catalysts supported on poly-VPYR cross-linked with DAP[4]. A much greater amount of radical initiator (AIBN, ca. 4% mol) than usual (1%) was required to obtain materials with acceptable mechanical properties, the polymerization mixture turned from the initial yellow color (due to $PdCl_2$) to dark-gray and more than 40% of palladium was lost during the preparation. All these observations highlight how troublesome radical polymerizations in the presence of transition metal compounds can be. However, the catalysts were obtained in a one-pot fashion, in that palladium(II) was reduced to palladium(0) during the polymerization, as proved by XPS measurements.

The use of γ-ray induced radical polymerization proved to be a successful alternative for the radical co-polymerization of metal complexes with ligands containing acrylic C=C double bonds [100–102,129,130]. In particular, the palladium(II) complex *cis*-$[PdCl_2(ICPA)_2]$ (**1**, Scheme 4) was co-polymerized in DMF solution with DMA and MBAA (cross-linker, 4% mol), with no degradation of the metal center [100,101].

The reduction of palladium(II) with an alcoholic solution of $NaBH_4$ [101] or by treatment *in situ* of the methanol-swollen material under hydrogen [129] yielded a supported palladium catalyst, referred to as self supported by the authors [101,129]. The same co-polymerization reaction was carried out *inside the nanopores* of a DMF-swollen gel-type resin made by DMA and MBAA (cross-linker, 4% mol) [101,129], thus obtaining a sequential IPN [131]. Also this material was transformed into a

[4]The choice of diallylphtalate as the cross-linker is somewhat surprising, because allylic compounds are not very reactive in radical polymerizations due to the stability of the allyl radicals.

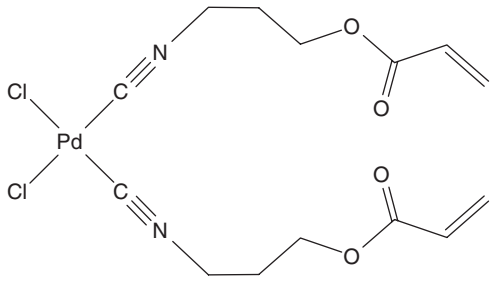

Scheme 4. Sketch of the structure of compound **1**.

supported palladium catalyst (IOPN catalyst) upon reduction of palladium(II) with an alcoholic solution of $NaBH_4$ or by treatment *in situ* of the methanol-swollen material under hydrogen [129].

3.3.3. Immobilization of Pre-Formed Metal Nanoclusters (IMN)

The third general method for the preparation of polymer supported metal catalysts, i.e. the introduction of preformed metal nanoclusters into the support, IMN, has also been applied in limited number of cases [33,34,89,123]. In principle this approach has the advantage that size control can be achieved during the pre-formation of the metal nanoclusters, provided they do not undergo sintering during their introduction into the support. The field of the synthesis of size-controlled metal nanoclusters has been greatly expanding for the last two decades. Several methods are available for the synthesis of stabilized, size-controlled soluble metal nanoclusters [132]. For the preparation of polymer supported metal catalysts, rhodium, palladium and platinum pre-formed nanoclusters were employed. Almost invariably they were stabilized by linear polymer, with the only exception of a citrate-stabilized palladium colloid [123]. In some cases, the preformed metal nanoclusters, Pt/PVPYR [89] or Pd/PVPYR, Pd/PVA, Pd/citrate [123] were simply adsorbed onto the support from the respective solutions. For the platinum catalysts [89], PS-DVB[5] or metal oxides were employed. PVPY, cross-linked with ca. 4% mol DVB, was employed for the palladium catalysts [123]. Yu et al. treated for a fixed time (24 h) the supports with the Pt/PVPYR solution at room conditions. After filtration the solid was Soxhlet extracted (ethanol/ water, 1/1, v/v) for 24 h and finally dried *in vacuo* for 5 h at room temperature. Allegedly, this procedure allowed the complete removal of the protecting polymer from the metal surface with no variation of the nanoparticle size (1.1 nm; no TEM micrographs were presented in the paper and no details on TEM data were given), and the final catalysts generally contained 0.5% (w/w) palladium. Pathak et al., on the contrary, repeatedly treated the PVPY support with aliquots of the colloidal solutions up to saturation of the available surface of the support, corresponding to a final palladium load of ca. 4% (w/w). The diameter of the palladium nanoparticles in the final catalysts ranged between 1 and 4 nm. Also in this case the authors argued that the protecting polymer was completely displaced from the palladium surface, owing to a much stronger interaction of pyridyl nitrogen atoms with the nanoparticles in comparison with the functional groups of PVPYR and PVA. In agreement with this hypothesis, the observed catalytic activity in C–C coupling reactions was independent of the original protecting agent and when the nanoparticles were deposited onto an amino-functionalized resin no activity at all was observed.

A more sophisticated approach was adopted by Toshima and co-workers, which is highlighted in Scheme 5 [33,34].

In this case, the pre-formed metal nanoparticles (Pt or Rh) were stabilized by a co-polymer of MMA (ca. 35%, mol) and VPYR. Whereas Rh nanoparticles were formed by the well-known alcohol process starting from $RhCl_3$ [133–137], Pt nanoparticles were prepared by photochemical reduction of K_2PtCl_4 in solution in the presence of the protecting polymer. The ester residues were employed to covalently attach the polymer protected metal nanoparticles to a commercial aminoethyl functionalizzed polyacrylamide gel through an amide bond. In this case the goal is different from that of Yu et al. and Pathak et al., who aimed at preparing classical heterogeneous metal catalysts. By contrast, Toshima and co-workers aimed at a heterogenized version of the soluble metal nanoparticles: in this sense their approach resembles more closely hybrid catalysis rather than classical heterogeneous catalysis. The experimental procedure for the immobilization of the nanoparticles is again straightforwardly simple: a solution of the polymer-stabilized nanoparticles is added to the water-swollen gel and kept under stirring for three days. No particular prescriptions were given in the experimental parts of the relevant papers. After repeatedly washing with water, the recovered solid was washed with methanol and simply dried *in vacuo* at 50 °C. Surprisingly, no information on the nanoparticle size after their immobilization were given. The immobilization was successful also in the presence of 0.1 M NaCl as an ionic strength buffer and no release of metal nanoparticles was observed in the pH range 2–13 for both metals. This highlights the remarkable strength of the support-nanoparticles interaction, which cannot be simply physical in nature. Moreover, no immobilization was achieved with acrylamide gels devoid of

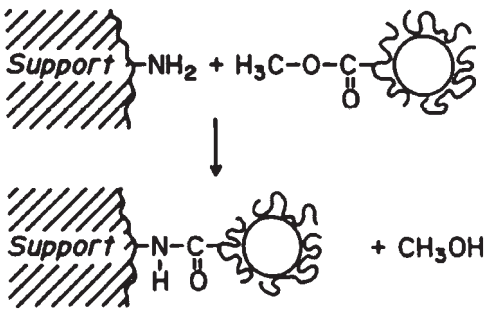

Scheme 5. Covalent attachment to an amino-functionalized gel of pre-formed, polymer-stabilized metal (Rh, Pt) nanoparticles. (Reprinted from Ref. [33], © 1991, with permission from the American chemical Society.)

[5]No details were given on the kind of PS resin employed.

amino functional groups. The kinetics of the immobilization process was elegantly investigated for platinum: methyl ester residues were replaced with *p*-nitrophenylester residue. The ensuing *p*-nitrophenol can be easily monitored by UV-Vis spectroscopy. In this way pseudo-first order rate constants for the aminolysis of the *p*-nitrophenylester residues in the protecting polymer were measured.

It is well known that metal nanoclusters can be stabilized by solvent molecules (see for example Ref. [132]). Very small metal aggregates (solvated metal atoms) can be prepared by co-condensation of metal and solvent vapors at low temperature and subsequent, controlled melting of the dispersion of the metal in the solid matrix of the frozen solvent (Metal Vapor Synthesis) ([138] and references therein). Solutions of solvated metal atoms can be employed for the deposition of metal nanoclusters onto solid supports (see [139] for an example). This procedure was employed for the preparation of platinum and palladium catalysts over gel-type resins for the hydrogenation of citral and the Heck coupling of iodobenzene and *n*-butylacrylate, respectively [65,124]. In this case, the kind of functionalization of the polymeric support was not as important as in Toshima's immobilization procedure and the metal could be deposited onto materials of different nature. For platinum it was quite easy to prepare catalysts supported by ion-exchange resins containing metal ions such as Co^{2+}, Fe^{3+}, Zn^{2+}, which proved very effective in enhancing the selectivity of platinum in the hydrogenation of citral to geraniol/nerol [65].

3.4. Organic–Inorganic Composites

Kunz and associates and Corain and associates have reported on the preparation of Pd^0 catalysts supported on polymeric matrices belonging to inorganic–organic composites. Corain et al. described the preparation of palladium catalysts supported on the same polymeric matrices employed in Ref. [21,30] (DMA, MAA, MBAA; DMAA, MEASA, MBAA), with silica (22–30% w/w), nanometrically dispersed inside the relevant polymeric frameworks. Silica was generated by hydrolysis of TEOS inside either (a) the polymeric support or (b) the Pd^0/CFP catalyst after swelling the organic materials with a hydroalcoholic solution of TEOS. The catalysts obtained along route (b) proved to be active in the hydrogenation of 1 M cyclohenexe at 27 °C and 500 kPa, though 3–4 time less than the parent polymer-supported materials [29]. On the other hand, the composite catalysts exhibited a much better mechanical stability and, being much more dense, their recovery from the reaction mixture turned out to be straightforward. Again Corain and associates prepared a silica–organic composite by the co-polymerization of the organometallic monomer **1** with DMAA and MBAA within the pores of Daltosil 150. This material was completely inactive in the hydrogenation of 1 M NT in methanol at room temperature and 100 kPa: under hydrogen it even did not change its color from the original yellow. Apparently, the simple procedure employed to generate the polymeric part of the composite completely plugged the silica pores and made palladium unavailable to interaction with hydrogen and other reacting species [101].

A similar approach was later employed by Kunz and co-workers to obtain polymer/carrier composites [140,141]. In this case conventional porous catalyst carriers (with pore diameters ranging from micro- to millimeters) were impregnated with a solution of the monomer, the cross-linker and the radical initiator in an apolar solvent. After starting the polymerization the polymer precipitated inside the pores of the carrier (precipitation polymerization) as micrometer-sized spheres. The monomer concentration was such as to avoid plugging of the carrier pores and to allow the formation of pores within the polymeric phase too. This ensured a good accessibility of the support. Kunz and co-workers were able to prepare composites of polymers with sulfonic acid, benzylchloride, quarternary ammonium, amino, pyridyl and imidazolyl groups, i.e. many of the most commonly employed in polymeric supports (see Table 2). Metals were introduced in the composite with the common RIMP approach described in Section 3.3.1 (both static and dynamic conditions could be applied to both the immobilization and the reduction of the metal precursor).

Moreover, these new composites were prepared in different physical shapes, such as rings and monoliths. They are of course apt to continuous operation in fixed bed reactors and this can help in circumventing some engineering problems in the use of polymer supported metal catalysts[6]. The fluido-dynamics of the reported arrangements were shown to be favorable for the ion-exchange process, as compared to fixed beds of pure ion-exchange resins, with a considerable decrease of diffusion restrictions to mass-transport and an appreciable increase in the contribution of convective forces [140]. Of course, continuous operation in supported metal catalysis is feasible only when the polymer supported catalyst is truly heterogeneous and metal leaching under solid–liquid reaction conditions, which are typical for polymer supported metal catalysts and reagents, is absent or negligible. Unfortunately this is not always the case, so that this problem is not a trivial one. For instance, Kunz and co-workers reported on the activity of a palladium catalyst in the Heck and Suzuki reaction [140]. C–C couplings of aryl halides over Pd supported catalyst is just one of the most popular and clearly demonstrated cases where palladium species in solution, leached from the solid (*would-be-heterogeneous*) catalyst, are the actual active species [142–144]. In spite of this, the work of Kunz's group has the merit to show that polymeric supports in catalysis are not only more useful, versatile and elegant than conventional inorganic supports from the chemical point of view, but can also be very interesting from the technical standpoint.

4. Molecular Mobility Inside Swollen CFPs

From the discussion in the previous sections, it is apparent that whatever the morphology of the CFP, macroreticular or gel-type, the metal nanoclusters in polymer-supported heterogeneous metal catalysts are

[6]These materials are useful not only for catalytic application, but also for continuous reactions of polymer fixed reagents (solid-phase synthesis).

mainly embedded within a swollen polymer framework. In the absence of a swelling agent, the polymer framework is collapsed over the metal nanoparticles. Under these conditions molecules from another phase in touch with the catalyst cannot diffuse inside it and cannot interact with the metal nanoclusters. This does not mean that catalytic action is impossible at all: it simply implies that polymer-supported catalyst must operate in the presence of a swelling agent, i.e. generally under solid–liquid conditions. In the swollen catalyst, the accessibility of the active component is ensured by the presence of the temporary nanopores and mesopores, even in macroreticular materials (see Figure 6). These pores have actually diameters in the order of the nanometers or a few tens of nanometers (< 50 nm), i.e. 1–2 orders of magnitude larger than in zeolites. From this simple comparison, it is clear that swollen polymer-supported metal catalysts can be active enough for technical application and, as a matter of fact, this is the case for the industrial processes listed in Table 1.

In any case, with nanopores of 1–10 nm in diameter important restrictions to mass transport within the catalyst (internal diffusion) could be envisaged. Before discussing briefly how diffusion phenomena inside swollen polymer-supported catalysts can be investigated, it is worth recalling that they are relevant only when the overall chemical catalytic transformation occurs under *diffusion regime*, i.e. when the diffusion is slow enough to be the rate-determining step. If the overall process is under *kinetic regime*, i.e. if the chemical reaction taking place over the metal surface is the rate-determining step, diffusion phenomena are not determining and *no effects of the morphology* of the supports should be observed on the apparent reaction rate. Other support effects could however play a role and, in particular, the compatibility with the substrate, which will tend to concentrate into the catalyst in as much as its affinity to the support is great. Kinetic regime can be generally attained by decreasing the size of the beads of solid particles. In this way the dimension of the particles in the direction of diffusion approaches the average free path of diffusing molecules, thus eliminating mass transport restrictions [145]. This has proven true also for CFP-supported palladium catalysts in the hydrogenation of cyclohexene [81]. However, from the practical point of view this can imply so little size of the catalyst beads, that the solid cannot be comfortably managed. For instance, the very efficient packing of tiny solid particles makes their recovery by filtration quite difficult and implies very high pressure drops through the catalyst in fixed beds arrangements. In conclusion, diffusion phenomena in CFP-supported catalysts cannot be generally ignored. However, many authors did not seem, unfortunately, fully aware of the far-reaching implications of this circumstance. In some cases the dry state specific surface area of macroreticular polymeric supports has been taken into account as an accessibility parameter, but this did not prove always useful. As far as polymer supported heterogeneous catalysis is concerned the most specific and extensive investigation on this subject has been carried out jointly by Corain and Jerabek and their associates [14,21,22]. In particular, they thoroughly investigated on the relationship between the morphology at the nanometric scale of swollen gel materials and the mobility of solutes (rotational and translational) and of solvents (self-diffusion).

The problem of transport of molecules through swollen gels is of general interest. It not only pertains to catalysis, but also to the field of chromatographic separations over polymeric stationary phases, where the partition of a solute between the mobile phase (liquid phase) and a swollen polymeric stationary phase (gel phase) is a process of the utmost importance. As with all the chemical and physicochemical processes, the thermodynamic and the kinetic aspect must be distinguished also in partition between phases.

Ogston's model [146] provides a way to predict partition constants of a solute between a solution and swollen gels. It rests on the description of swollen gels (no matter if cross-linked or not cross-linked) as random suspensions of rigid rods (the polymeric chains) of very high expectation ratio (length to diameter) in a liquid. This picture is much closer to the actual physical state of the system than the cylindrical or conic pore model. The nanoporous system of the swollen gel is represented by the void space among the rods, which is occupied by the swelling agent. The sum of the lengths of each rod or rod section crossing a portion of the gel over the total volume of that portion (void + rods) gives the characteristic property of "polymer chain concentration", usually expressed in $\mathrm{nm\,nm^{-3}}$. Typical values range from $0.1\,\mathrm{nm\,nm^{-3}}$ (approximately corresponding to a very accessible gel phase, similar to a solution of a linear polymer) to $2.0\,\mathrm{nm\,nm^{-3}}$ (corresponding to a very dense gel phase, scarcely accessible even to small molecules). The other characteristic parameter is the diameter of the rods. With these two parameters and the hydrodynamic radii of solutes partitioning between the swollen gel and a liquid phase in touch with it, Ogston's model provides theoretical values of the relevant partition constants, which are calculated as:

$$K = e^{[-\pi c(r_c + r_s)^2]} \tag{1}$$

where c is the polymer chain concentration, r_c the radius of the polymer chain, r_s the radius of the diffusing solute.

The model, therefore, predicts the elution behavior of solutes during a chromatographic process over a swollen gel as the stationary phase as a function of solute size and of the gel nanomorphology. On the reverse, from the elution behavior of solutes of known molecular size it is possible to extract the polymer chain concentration from chromatographic experiments, where an unknown swollen gel is the stationary phase. This is the basis of the ISEC, which is so often mentioned through this chapter [16,17,105,106].

The application of Ogston's model to real systems is not always straightforward. In fact, real swollen gels are hardly homogeneous, i.e. they are not usually featured by a single value of the polymer chain concentration, while the rod radius can be considered constant throughout the whole of the gel volume. This is easy to understand for cross-linked polyaddition polymers, where the intrinsic features of the polymerization kinetics generally imply a non-homogeneous distribution of cross-links in the material. This problem is coped with by studying the elution behavior of a number of solutes of known molecular size, different from one another. The investigated gel is then considered as a set

of discrete gel-phase fractions (or domains), each one featured by its characteristic value of the polymer chain density. Mathematical fitting of a number of experimental elution volumes obtained for different solutes allows to extract the volume proportion of single domains, along with their local polymer chain density [16]. ISEC thus provides a detailed, quantitative description of the morphology of the swollen gel at the nanometric level. This description has qualitatively the same physical meaning of the pore volume distribution as a function of pore size, which is provided by the classical cylindrical pore model for porous solids. In fact, the experimental elution volumes from ISEC experiments can be fitted with the cylindrical pore model, too. This provides a more friendly description of the porosity of the swollen gel, though not fully adherent to its real physical nature[7]. This proved particularly useful for comparing the diameter of metal nanoclusters generated within swollen gel-type resins, according to TCS procedures (see Section 3.3.1), with the size of the "cavities" available for their growth. Another complication in the application of Ogston's model to real systems is that Equation (1) rests on the assumption that the partition process is entirely driven by steric factors and that no enthalpic interactions occur between the polymer and the solute. This is of course not always the case in real systems and restricts the scope of the model and of the ISEC technique. For instance, for this reason ISEC characterization is generally not feasible with alcohols as the mobile phase (swelling agents).

The polymer chain concentration and the polymer chain radius were employed to assess the rotational mobility of a molecule within a swollen gel [14]. To this purpose the gel is considered a thick, viscous polymer suspension. Its viscosity can be evaluated with the following equation, proposed by Nicodemo and Nicolais for concentrated suspensions of polymeric fibers [147]:

$$\eta = \eta_0 e^{v\phi} \tag{2}$$

where η is the viscosity inside the swollen gel, η_0 is the viscosity in pure swelling agent, v an adjustable parameter, ϕ is a volume fraction of the polymer in the swollen gel.

Viscosity is a useful quantity, in that both rotational and translation mobility of molecules in solution are viscosity dependent and can be related to viscosity through the Stokes–Einstein equation:

$$\tau = \frac{4\pi r_s^3}{k_B T}\eta \quad \text{(Stokes}-\text{Einstein equation for rotational diffusion)} \tag{3}$$

$$D = \frac{k_B T}{6\pi r_s \eta} \quad \text{(Stokes}-\text{Einstein equation for translational diffusion)} \tag{4}$$

It should be appreciated that according to Equations (2), (3) and (4) τ and D respond in similar ways to changes of polymer chain concentration. For instance, combination of Equations (2) and (3) predicts, for a homogeneous gel (i.e. with a single polymer chain density value) a linear relationship between the polymer chain density and $\ln(\tau)$[8], with an intercept corresponding to the value of τ of freely rotating molecules in solution. Hence, measurement of τ of suitable probes inside a swollen gel can convey information relevant also to diffusion phenomena within the same gel, provided the molecular mobility is controlled by viscosity. Values of τ can be directly extracted from ESR spectra of paramagnetic probes (without spectra simulation) provided the molecules are in the fast rotational regime ($\tau < 10^{-9}$ s). In typical experiments, a gel-type polymer is swollen with a diluted solution (usually 10^{-4} M) of TEMPONE (a stable nitroxide organic radical), in the desired solvent. The polymer is swollen to incipient wetness to eliminate any contribution to the spectra from the paramagnetic probe in bulk solution liquid phase. For gel-type swollen resins with cross-linking degree up to 6–8%, the confined paramagnetic probe is still generally in the fast rotational regime.

As mentioned above, real swollen gels are usually heterogeneous, rather than homogeneous, in nature and therefore molecules located in different parts of the swollen material will also rotate at different rates. In order to take this into account, Biffis et al. treated each fraction of the real heterogeneous gel, with its characteristic value of polymer chain concentrartion, as a single, independent homogeneous gel. Under the assumption of slow (on the ESR timescale) exchange of the paramagnetic probe molecules among the virtually independent homogeneous gels, an average τ value was expressed as a function of the parameters of the Ogston's model obtained from ISEC characterization (Equation (5)) [14].

$$\tau = \sum \left(\frac{K_i V_i}{\sum K_i V_i} \right) \tau_i \tag{5}$$

On the basis of this equation, experimental τ values for a number of different gels with increasing cross-linking degrees were fitted using K_i and V_i values from discrete ISEC experiments and this allowed the correct prediction of the hydrodynamic radius of TEMPONE [14]. In fact the rotational molecular mobility turned out to be quantitatively related to the nanomorphology of the swollen gel. The relationship between τ and the polymer chain density is logarithmic, according to the hypothesis that molecular mobility inside the swollen gel is viscosity dependent. This is confirmed by the values of activation energies for the molecular rotation of paramagnetic probes inside swollen gel, obtained from ESR spectra collected at different temperatures [21,22,25,108], which were always typical for viscosity controlled processes. The effect of electrolytes addition also points to both rotational and translational molecular mobility inside swollen gel-type CFPs as viscosity controlled phenomena [108]. It was also found that the value of $\ln(\tau)$ is often correlated to

[7]The model yields reliable values of pore radii, but the volume of large pores tend to be overestimated, hence it is not fully reliable on a quantitative basis.

[8]The combination of Equations (2) and (3) actually predicts a linear relationship between $\ln(\tau)$ and φ. However, according to the Ogston's model, for a homogeneous gel $\varphi = \pi r_c c$, where r_c is the radius of the polymer chain and c is the polymer chain concentration and a linear relationship is expected between $\ln(\tau)$ and c, too. Similarly, the combination of Equations (2) and (4) predicts a linear relationship also between ln(D) and both φ and c.

the average polymer chain density of a heterogeneous gel with an intercept corresponding to the value of τ in bulk solution [14,148]. Average polymer chain concentration is not the most appropriate descriptor of a swollen gel, but it is much easier to handle and its relationship with τ has been satisfactorily employed for interpreting and modeling the behavior of real CFP-supported metal catalysts [81,82]. However, keeping with Ogston's model, if we consider that the overall polymer chain length of a given CFP does not change upon swelling or shrinking and that these processes simply entail the widening or narrowing of the polymer chain distances, the average polymer chain concentration can be considered inversely proportional to the overall volume of the swollen gel. This is a direct indicator of the swelling ability (swellability) of a gel-type cross-linked polymer in a given solvent and can be determined (not by fitting, but experimentally) from ISEC characterization of a swollen gel. From this point of view it should be more reliable of the average polymer chain concentration as an accessibility parameter. A related quantity is the so-called "Bulk Expanded Volume" (BEV) of a gel-type cross-linked polymer. BEV measurements do not require chromatographic experiments and are therefore much easier. They imply the determination of the amount of swelling agent required to swell a sample of the investigated polymer, previously packed in a proper container (usually a glass column) [149]. The results of these experiments, however, are biased by the amount of swelling agent filling the *interparticle* voids, which generally cannot be completely eliminated. Therefore BEV measurements are dependent on the packing of the polymer and are not as accurate as swellability values from ISEC.

As a matter of facts, both the average polymer chain concentration and the swollen gel volume (swellability) have been successfully employed to mathematically model the behavior of palladium catalysts in the hydrogenation of cyclohexene [81,82,114,150] and of NT under diffusional regime [78]. For instance, the application of the following equation:

$$D = D_0 e^{-a_D/S} \tag{6}$$

where S is the total specific volume of the swollen polymer, was proposed to calculate diffusion coefficients of the reagents inside a palladium catalyst supported by a copolymer of DMA and SSNa, cross-linked with MBAA (4 or 8%, mol) in the hydrogenation of cyclohexene in methanol (1 M, Pd/alkene $= 4 \times 10^{-4}$, room temperature, 0.5 MPa). The model based on Equation (6) provided an excellent fitting of the experimental data and allowed the prediction of the effectiveness factor of the catalyst as a function of the palladium loading and of the size of the catalyst beads [114,150]. In another study, Kralik et al. investigated on the same reaction with a different palladium catalysts (0.22% and 2.2%, w/w) supported on copolymers of styrene and MAESA, cross-linked with MBAA (1 or 3%, mol) under otherwise similar conditions (only the Pd/alkene ratio was changed to 2.5×10^{-4}) [81,82]. When the reactions were carried out under diffusional regime, the apparent initial rates over the least (most accessible) and the most (least accessible) cross-linked catalysts were in the 1.21 and 1.66 ratios for the 0.22% and the 2.2% Pd catalysts, respectively (entries 7, 8 of Table 2 and entries 7, 8 of Table 3 in Ref. [81]). Relevant data on the average polymer chain concentrations, polymer swellabilities, rotational correlation times of TEMPONE in methanol swollen materials and self-diffusion coefficient of methanol in the methanol swollen materials (see below) are given in Table 5.

It can be appreciated that the ratios between apc and S values, respectively, are strictly comparable. The ratios between τ and D′ values are also in good agreement to each other and compare fairly well with the ratios of the initial rates observed for the 2.2% Pd catalysts. Kralik et al. also used Equation (6) to calculate the diffusion coefficients of reagents in the hydrogenation of NT to AT with a palladium catalysts supported on Dowex 50 W × 4, a gel-type commercial PS-DVB resin. The mathematical model provided again an excellent fitting of the kinetic data and allowed to predict the concentration profiles for hydrogen and NT across the catalyst beads and how the palladium radial distribution across the catalyst beads changed after the reaction, owing to metal leaching [78].

Molecular translational mobility (diffusion) inside swollen gel-type CFP was also investigated by Corain and associates. In particular, the diffusion of the molecules of the swelling agent (self diffusion) was investigated by means of $\{^1H\}$-PGSE-NMR [152] experiments [21,22,108]. In every investigated system parallel trends of τ, as measured for proper paramagnetic probes from their ESR spectra, and of the self diffusion coefficient of the swelling agent were detected when the cross-linking degree or the polymer chain density of the swollen polymer framework were changed. When these two quantities were increased the molecular mobility, as expected, decreased. Also for self diffusion of the swelling agent inside swollen gel-type CFPs the energy of activation was typical for viscosity controlled phenomena [21,22,108]. Quite recently, it was possible to gather information also on the diffusion of solutes inside swollen gel-type CFPs, by means of CV with ultramicrodisk electrodes [108]. Nitroxide radicals are not only paramagnetic probes, but also electrochemically active. They give raise to a one-electron reversible redox system so that it was possible to compare the CV behavior of TEMPONE diffusing in a number of swollen PVPYR polymers, cross-linked with MBAA (1, 2, 3, 4, 5% mol), with its τ values inside the same swollen CFPs. In both cases the swelling agent (and solvent for CV experiments) was DMF, the self-diffusion coefficients of which were determined by means of $\{^1H\}$-PGSE-NMR. Under proper conditions and with a proper

Table 5. Average polymer chain concentration (apc), polymer swellability (S), rotational correlation times of TEMPONE (τ) and self-diffusion coefficient of methanol (D') in the swollen 2.2% Pd catalysts.

cld	apc ($nmnm^{-3}$)[a]	S (cm^3g^{-1})[a]	τ (ps)	D' (cm^2s^{-1})
1	0.16	2.72	60	1.8
3	0.24	1.89	115	1.1
Ratios	1.5^{-1}	1.45	1.91	1.63

[a]Measured in water (ISEC characterization based on the Ogston's model assumption is not generally reliable in alcohols owing to the occurrence of enthalpic interactions [151]).

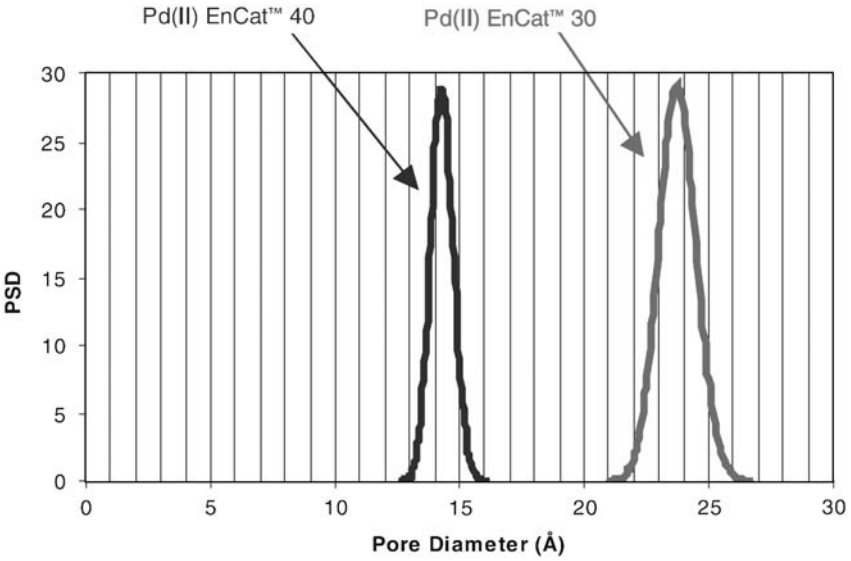

Figure 11. Pore size distribution of palladium(II) EnCat^{TM} 30 and palladium(II) EnCat 40 swollen in THF; the materials differ in the isocyanate/solvent ratio in the microencapsulation mixture (see text), which was 30/70 and 40/60 (w/w), respectively. (Reprinted from Ref. [38], © 2005, with permission from Reaxa Ltd.)

experimental setup [108], redox processes taking place at the working electrode in CV experiments are diffusion controlled and the diffusion coefficient of the redox probe (TEMPONE in this case) can be measured. The model by Johansson and Löfroth [153], which is also based on the Ogston description of gels, was used to take into account correctly the hydrodynamic radius of TEMPONE in treating the CV data. All the data were found to converge, in that the natural logarithms of the rotational correlation time of TEMPONE, of its diffusion coefficients inside the swollen CFPs and of the self diffusion of the swelling agent (DMF) were controlled by viscosity and responded linearly to changes in the volume fractions of the polymers (i.e. to the polymer chain concentration).

To summarize, there is a sizable and self-consistent body of data indicating that rotational and translational mobility of molecules inside swollen gel-type CFPs are interrelated and controlled mainly by viscosity. Accordingly, τ, self-diffusion and diffusion coefficients bear the same information (at least for comparative purposes) concerning diffusion rates within swollen gel phases. However, the measurement of τ is by far the most simple (it requires only the collection of a single spectrum). For this reason, only τ values have been used so far in the interpretation of diffusion phenomena in swollen heterogeneous metal catalysts supported on CFPs [81,82].

The discussion above shows that the morphological characterization of swollen CFPs employed as catalytic supports *in the working state* is very important for the evaluation of internal diffusion phenomena. It is a misfortune that generally these features have not apparently been paid proper attention so far in the relevant literature. To our knowledge, only in the case of EnCat catalysts the importance of the assessment of the micro-porosity of the materials in the working state was recognized [38]. To this purpose a "chromatographic porosimetry" technique coupled to the mathematical treatment of the chromatographic data with a commercial software was employed [38]. This analysis is similar to ISEC: it showed that increasing the proportion of isocyanate in the mixture for microencapsulation yielded smaller pores in the THF swollen final material and that the pores are essentially monodispersed (Figure 11).

5. Catalysis

The scope of catalytic application of polymer-supported metal catalysts has been illustrated in Table 3. We have already mentioned that most of the papers published in the open literature describe model reactions. One of the consequences is that no industrial breakthroughs have appeared in the last 30 years and that the scenario of industrial application of heterogeneous metal catalysts supported on CFPs is essentially the same as of the mid-1970s. On the other hand, it should be born in mind that it can be difficult to gather news on the development of new catalysts in industrial R&D laboratories or about small-scale applications, typical of fine chemistry and specialty chemicals, the predictably most promising field of expansion for this kind of catalysts. Moreover, it is apparent that only a little number of research groups have taken up systematic investigation in the field of polymer-supported metal catalysis. The most important contribution came, respectively, from Corain's, Toshima's and Ley's groups. As mentioned above, Ley's work opened the way to the production of the commercial EnCat catalysts. The palladium(II) EnCat catalysts, which are not strictly pertinent to the scope of this chapter, were employed mainly in C–C coupling reactions (Heck, Suzuki, Stille, carbonylation) of aryl halides. The catalysts were tested under both batch and continuous-flow conditions and also in supercritical CO_2. They proved promising for combinatorial chemistry applications, such as the parallel synthesis of chemical libraries by means of

Suzuki couplings. Palladium(0) EnCat catalysts were mainly tested in hydrogenation (simple alkenes and aryl nitrogroups) and hydrogen transfer reduction reactions (ketones, epoxides, nitro enamines). Synthesis, characterization and performances of the EnCat catalysts have been extensively reviewed in 2005 by Pears and Smith [38]. The interested reader is therefore referred to Ref. [38] for full details. The lack of breakthroughs in catalytic application of heterogeneous metal catalysts supported on CFPs probably stems from the general unawareness of the unique properties of polymeric supports. Polymeric supports are generally and correctly appreciated for the ease of functionalization. From this point of view, they are undoubtedly much more flexible and designable than classical inorganic supports for heterogeneous catalysis. However, the limited knowledge of their features in the working state prevents the full exploitation of their potential. Although no industrial application of the EnCat catalysts has been reported so far [38], we believe that their appearance was an important step in extending the scope of heterogeneous metal catalysts supported on CFPs.

5.1. Hydrogenation Reactions

As mentioned in Section 3.2, hydrogenation is by far the most investigated catalytic reaction and palladium the most commonly employed metal, followed by platinum. The most common substrates for catalytic hydrogenation tests are simple alkenes, cyclic alkenes and unsaturated carbonylic compounds. In the latter case, conjugated substrates (α,β-unsaturated aldehydes, acrylic acid) have received particular attention.

The performances of metal catalysts supported on CFPs and on traditional supports were compared in a number of papers [33,34,89,101,111–113, 118,129]. The most common benchmark catalysts were nanostructured noble metals on carbon, which are commercially available and routinely employed for the hydrogenation of organic substrates. In some cases, it was actually found that a M^0/CFP catalyst was less active than a M^0/C one [101,111,129]. In the hydrogenation of citral (a mixture of E and Z isomers, 0.1 M in isopropanol, molar citral/Pt = 25, 70 °C, 0.5 MPa) a platinum catalyst supported on vinylpyridine polyethylene fibers was found ten times less active than Pt^0/C or Pt^0/Al_2O_3 [111]. Palladium catalysts were much more active, but no comparative data of activity with respect to Pd^0/C were given. The causes of the low activity of the platinum catalyst were not investigated. Self-supported and IOPN catalysts [101,129] obtained by the co-polymerization of the organometallic monomer **1** (see Section 3.3.2) were compared to commercial Pd^0/C in the hydrogenation of NT (1 M in methanol, NT/Pd = 200, 20 °C; 105 kPa [101], 0.5 MPa [129]) to AT [129,101]. The apparent reaction rates decreased in the order Pd^0/C > self-supported catalyst[9] > IOPN catalyst. Kinetic plots suggested that mass transport was rate limiting (diffusion regime). At 105 kPa the initial apparent rates of the self-supported and of the IOPN catalysts were about three and four times smaller, respectively, than the apparent rate over commercial Pd^0/C. At 0.5 MPa all the reactions were faster, but the rates over the self-supported and the IOPN catalysts were 4 and 14 times smaller, respectively, than the apparent rate over commercial Pd^0/C. The different radial distribution of palladium, as assessed by XRM analysis of the element across the catalyst beads, accounted for the difference in the apparent rates. Whereas the palladium distribution in the commercial Pd^0/C catalyst was eggshell [101], the metal nanoclusters were homogeneously distributed throughout the particles of the polymer-supported catalysts. This also explains why the rate over Pd^0/C was much more sensitive to changes in the pressure of hydrogen. The higher apparent rate over the self-supported catalysts highlights the better molecular mobility inside its polymeric framework in comparison with the IOPN catalyst. This was confirmed by the values of τ of TEMPONE measured in the methanol-swollen materials.

In other cases the apparent reaction rate over polymer-supported metals was *higher* than over the same metal on carbon or other inorganic supports. The hydrogen transfer hydrogenation of arylketones and of benzylepoxides with Palladium(0) EnCat catalysts was faster than with Pd^0/C. Moreover, better chemoselectivity of the Palladium(0) EnCat catalysts was claimed, in that the newly formed alcohols did not undergo further hydrogenolysis of the C–O bond [112,113]. Although it was not reported whether the reaction proceeded under kinetic or diffusion regime, these results highlight the good accessibility of the Palladium(0) EnCat catalysts. Better performance of CFPs supported Pt^0 and Pd^0 nanoclusters, as compared to the same nanostructured metals on inorganic oxides, was observed by Liu and co-workers in the hydrogenation of cinnamaldehyde (0.05 M in EtOH/H_2O 1/1, v/v; Pt^0 on MgO, Al_2O_3, TiO_2; Pt/aldehyde = 1.7×10^{-3}; Pt/NaOH = 1; 60 °C; 4 MPa) [89] and by Huang and He in the hydrogenation of cyclooctene (1 M in MeOH; Pd^0 on SiO_2; 30 °C; 105 kPa) [90]. The platinum catalyst over porous PS-DVB resin obtained by Liu, was equally active as Pt^0/MgO, but remarkably more selective toward cynnamic alcohol. The reactions were carried out in the presence of NaOH, which is a selectivity promoter [154]. Therefore, the good to very good values of selectivity toward the unsaturated alcohol observed cannot be attributed exclusively to intrinsic properties of the catalysts. However, the polymer-supported catalyst is apparently more sensitive to the effect of the promoter. Huang and He observed that the apparent reaction rate was dependent on the polarity of the solvent and that the CFP supported catalyst was more sensitive to this parameter than the silica-supported one. The best solvent was methanol and the worst was benzene: the rate over Pd^0/SiO_2 in methanol was higher than over Pd^0/CFP in benzene [90]. This is by no means surprising, because the working state morphology of the support in CFPs-supported catalysts is dependent on its swelling behavior, as illustrated above. Higher rates with Pd^0 supported on Amberlyst 27, as compared to Pd^0/C and $Pd^0/BaSO_4$, were observed by Sabadier et al. and Lazcano et al. in the hydrogenation of cyclohexenes and allyl alcohol, respectively, in ethanol, at 25 °C and 10 MPa (cyclohexenes) or 0.1–2.5 MPa (allyl alcohol) [93,94]. The catalysts were introduced into the

[9] See Section 3.3.2 for the description of the self-supported and IOPN catalysts.

Table 6. Initial hydrogenation rates[a] in EtOH/H_2O (1/1, v/v) of simple and functionalized alkenes (0.05 M) over platinum or rhodium catalysts (30 °C, 105 kPa, M/alkene = 2×10^{-3}, mol/mol).

	Pt			Rh		
	R_{gel}[b]	R_{gel}/R_{nano}[c]	R_{gel}/R_{carbon}[d]	R_{gel}[b]	R_{gel}/R_{nano}[c]	R_{gel}/R_{carbon}[d]
Ethylvinylether	160	0.47	100	610	0.52	79
1-hexene	110	0.33	34	190	0.15	5
cyclohexene	36	0.15	17	150	0.21	21
1-pentene	–	–	–	150	0.10	
cyclopentene	–	–	–	230	0.21	5.2
2-methyl-2-pentene	–	–	–	13	0.19	–
Mesityl oxide	22	0.10	2	30	0.13	2.5
Methylvinylketone	–	–	–	330	0.43	–
Methylacrylate	–	–	–	290	0.27	–
Allylamine	–	–	–	200	0.44	–
Allyl alcohol	–	–	–	79	0.61	–
3-butenol	–	–	–	140	0.45	–
Acrylic acid	–	–	–	120	3.6	7.5
3-butenoic acid	–	–	–	130	4.2	–
Acrylonitrile	22	0.49	[e]	–	–	–
Acrylamide	100	0.56	77	–	–	–

[a] $M mol_{H2} \cdot mol_{Rh}^{-1} s^{-1}$.
[b] R_{gel} = rate over the immobilized nanoparticles.
[c] R_{nano} = rate with parent stabilized nanoparticles dispersed in the liquid phase.
[d] R_{carbon} = rate over Pt^0/C or Rh^0/C catalyst (5%).
[e] Pt^0/C was inactive.

reaction vessel as $[PdCl_4]^{2-}$-exchanged resins without reduction of the metal. Although the authors claim that the behavior of their catalysts is markedly different from that of other pre-reduced catalysts such as Pd^0/C, the reduction of palladium(II) probably occurred *in situ* to yield a Pd^0 supported catalyst and the reduced form is the active one. Sabadier and Germain observed also a decrease in the apparent reaction rate in the order cyclohexene > 2,3-dimethylcyclohexene > 1,2-dimethylcyclohexene, which they attributed to increasing mass transport restrictions with increasing steric hindrance around the C=C double bond. Akashi and co-workers prepared a platinum catalyst (Pt^0/PS-IPA), supported on PS microspheres with grafted poly-IPA branches, which served to protect the platinum nanoparticles formed by solvent reduction of H_2PtCl_6 in an ethanol suspension of the support [116]. This catalyst was much more active than Pt^0/C in the hydrogenation of allylic alcohol at 25 °C and 105 kPa. Akashi and co-workers prepared also a Pt^0 catalyst supported on commercial PS beads (Pt^0/PS). It was more active than Pt^0/C, too, but was much less stable than Pt^0/PS-IPA. Whereas the latter could be recycled seven times with only slight changes in the initial rate, Pt^0/PS was almost completely inactive at the sixth recycle.

The most spectacular results, in terms of comparison between CFPs- and carbon-supported metal catalysts, were likely provided by Toshima and co-workers [33,34]. As illustrated in Section 3.3.3, they were able to produce platinum and rhodium catalysts by the covalent immobilization of pre-formed, stabilized metal nanoclusters into an amine functionalized acrylamide gel (Scheme 5). To this purpose, the metal nanoparticles were stabilized by a linear co-polymer of MMA and VPYR. The reaction between its ester functions and the amine groups of the gel produced the covalent link between the support and the stabilized nanoclusters. The catalysts were tested in a number of hydrogenation reactions (Table 6) and compared with both the parent nanostructured metal precursors and Pt^0/C or Rh^0/C. The immobilized catalysts always turned out to be more active than the carbon supported counterparts and in some cases the observed apparent rate was two orders of magnitude larger. The causes of this remarkably higher activity were not investigated, but the authors emphasized the good swelling behavior of the polymeric support in the employed solvent (EtOH/H_2O, 1/1 v/v). Not unexpectedly, the parent polymer-stabilized metal nanoparticles dispersed in the liquid phase were generally more active than the gel-supported counterparts [33,34]. The lowering of the initial reaction rate upon immobilization was convincingly correlated with the substrate–support compatibility. The employed acrylamide gel is highly hydrophilic. For the platinum series, it was found that the apparent reaction rate was roughly correlated with the solubility in water of the substrates, taken as a hydrophilicity parameter.

For the rhodium series the substrate–support compatibility was measured as $(\delta_{gel}-\delta_{substrate})^2$, where δ is the solubility parameter of the gel or the substrate. The solubility parameter is a thermodynamic quantity related to the enthalpy of mixing of substances and can be estimated also for polymeric materials [155,156]. According to its physical meaning, the smaller $(\delta_{gel}-\delta_{substrate})^2$, the higher the substrate-support affinity. The $\log(R_{gel}/R_{nano})$ was clearly dependent on $(\delta_{gel}-\delta_{substrate})^2$ (Figure 12).

This result suggests that the reaction rate observed with the gel-immobilized catalysts is lower owing to the smaller concentration of the substrate inside the catalyst with respect to the liquid phase. This implies that the partition of substrates between the catalyst and the bulk liquid phase is fast. This could not be the case always and deviations

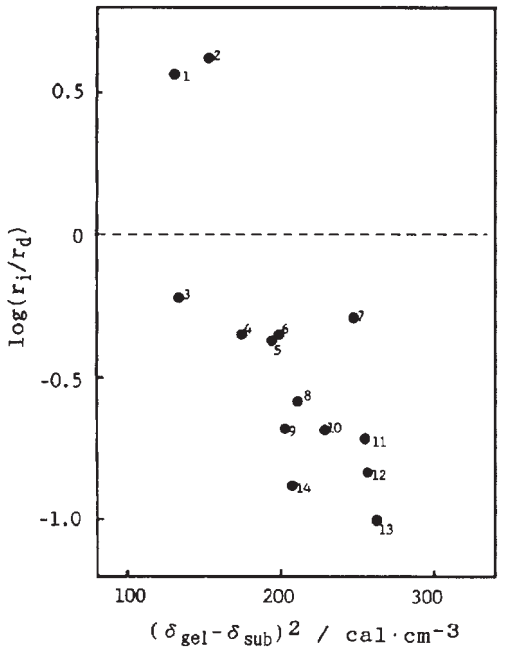

Figure 12. The relationship between the logarithm of the relative hydrogenation rate over CFP-supported rhodium nanoclusters, with respect to the polymer-stabilized nanostructured catalyst, for a number of a number of alkenes, as a function of their affinity to the support (expressed as the square difference of the solubility parameter of the support and of the substrate). (Reprinted from Ref. [33], © 1991, with permission from the American Chemical Society.)

were observed with some substrates. Probably mass transport restrictions also play a role in some cases. The only substrates which were hydrogenated faster with the immobilized Rh catalyst than with the stabilized nanoparticles were carboxylic acids (acrylic, 3-butenoic; points 1 and 2 in Figure 12). In this case the specific interaction between the carboxylic (acid) groups and the amino (basic) residues of the gel lead to very high substrate concentration inside the catalyst, much higher than predicted by the value of $(\delta_{gel}-\delta_{substrate})^2$. The importance of the substrate–solvent–support compatibility in connection with apparent catalytic activity also emerged from the results of Zhang and Neckers [99]. They studied the hydrogenation of a number of alkenes, with or without hydroxyl groups, in solvents of different polarity (methanol or THF) and in mixed solvents over a polyurea-supported palladium catalyst [99]. The apparent reaction rates were found to be dependent on the substrate–solvent combination. On the other hand, Zecca et al. showed that when the solvent–support compatibility is much higher than the substrate–support compatibility, differences in the reaction rates of different substrates can be leveled off [80]. Thus, despite their different lipophilicity, cyclohexene and cyclo-2-hexenone were hydrogenated (1 M, 25 °C; 0.5 MPa, 1.0 MPa, Pd/alkene $= 2.5 \times 10^{-4}$; 1.5 MPa, Pd/alkene $= 1.25 \times 10^{-4}$) at comparable initial rates over Pd^0 catalysts (0.27–0.46%, w/w) supported on CFPs obtained from DMA, MAESA and MBAA [80]. In the same investigation the ability of the functional groups of the polymeric supports to promote the metal catalysts was also observed (see below).

The substrate–support compatibility can be employed to regulate not only the activity, as shown above, but also the selectivity of metal catalysts supported on CFPs. This was illustrated by Biffis et al. and Bombi et al. in the palladium catalyzed hydrogenation of EAQ to H_2EAQ [69,32]. This is the key reaction in the industrial production of hydrogen peroxide and the hydrogenation of the aromatic rings of H_2EAQ (over-reduction) is detrimental to the economy of the process [6]. H_2EAQ is a dihydroxy compound and should be therefore more hydrophilic (less lypophilic) than EAQ. The use of a palladium catalyst supported by a very lypophilic CFP should favor the expulsion of the newly formed H_2EAQ from the catalysts particles, thus protecting the product from over-reduction. With a co-polymer of DOMA (92%) and MAA (4%), cross-linked with EDMA (4%) as the support, a 1% Pd catalyst gave a selectivity to H_2EAQ equal to 96%. The best selectivity with a genuine sample of the industrial Pd^0/Al_2O_3 catalyst under the same conditions was 95%. The activity of the CFP-supported catalyst was one order of magnitude lower than that of the industrial one. The latter was made lypophilic too, by treatment with triethoxyethylsilane. The catalytic activity of the modified catalyst dropped to the same level of the polymer-supported catalyst, probably owing to low hydrogen concentration within the catalyst particles. At the same time, the selectivity of the modified Pd^0/Al_2O_3 catalyst also dropped to 88%. Even worse results were obtained when triethoxyoctyl- or triethoxyhexadecylsilane were used, i.e. with increasing hydrophobicity of the modified catalyst. The concept of substrate–support compatibility worked well with the polymeric support, but not with the inorganic one: this underpins the uniqueness of CFPs as catalytic supports as compared with inorganic solids. The control of the hydrophilic/hydrophobic properties of the support was also exploited to obtain Ru^0 catalysts for the partial hydrogenation of benzene to cyclohexene more selective than Ru^0/C [118]. In aqueous environment and in the presence of zinc salts, good selectivity could be achieved [157,158]. The use of a relatively hydrophilic CFP as the support for ruthenium allowed to bring the selectivity up to 9% at ca. 43% conversion (110 °C; 1.5 MPa; benzene/ water = 4/3, v/v; Zn/Ru $= 6 \times 10^{-3}$, w/w) from less than 0.5% at the same conversion for Ru^0/C (100 °C; Zn/Ru > 1, w/w). The CFP-supported catalysts required smaller amounts of promoter (zinc salt) and, in fact, they were almost equally selective also when it was absent. Dini et al. tested a number of Ru^0 catalysts on different supports, including CFPs (Amberlite IR 120 and Amberlite CG 400), in the gas–solid phase hydrogenation of benzene. At 140–190 °C and 0.1 MPa CFP-supported Ru^0 was very little active, if any [95].

The combination of hydrophilicity and hydrophobicity into a single polymeric support can lead to interesting results. Amphiphilic materials, containing both hydrophilic and hydrophobic domains, appreciably swell in a range of solvents of quite different polarity (see for example the characterization of amphiphilic CFPs given in Ref. [82]). This concept has been elegantly applied by Uozumi and Nakao in both reduction [159] and oxidation reactions (see Section 5.2) [70] catalyzed by

CFP-supported palladium nanoparticles in aqueous environment. They employed a gel-type (1% cross-linked) PS-DVB resin modified by PEG branches ending with 2,2′-dipyridylamino functional groups ($0.4\,mmol\,g^{-1}$). Uozumi and co-workers had already been using for some years similar supports for the preparation of hybrid phase Pd^{II} catalysts (immobilized Pd^{II} phosphino-complexes) apt to operation in water [160]. The supported palladium catalyst was prepared by the RIMP method, starting from a toluene solution of $[Pd(OAc)_2]$, and reduction of the obtained immobilized dipyridyl Pd^{II} complex in refluxing benzyl alcohol. The average diameter of the nanoclusters was 9.1 nm (TEM), with 50% of the observed diameters in the 8–10 nm range. The final metal load was 3.9% (w/w, $0.37\,mmol_{Pd}\,g^{-1}$) [70]. This catalyst was effective in the hydrogenation *in water suspension* of ring- and α-substituted styrenes, including cynnamic derivatives. Under the employed condition (25 °C, 105 kPa, 24 h, 5% mol Pd) neither the aromatic ring nor carbonyl groups, but only the vinyl C=C double bond were hydrogenated. The same catalyst was active also in the hydrodechlorination of a number of mono-, di- and trichlorobenzenes in aqueous environment under hydrogen transfer conditions (2-propanol/water, 9/1, v/v; 25 °C; $(NH_4)HCO_2$/substrate = 3, mol; 5% mol Pd; 2 h). Yields in the corresponding dehalogenated benzene derivatives were very high (> 90%) and independent of the nature of substituents. Pentachloroaniline was transformed into aniline with 85% yield under the same conditions.

Another interesting feature of CFPs as catalytic supports for metal catalysts is the ease of embedding the active metal and a promoter in a single material. Strictly speaking, such a material is not bifunctional, but it certainly is "multitasking", in that it exerts distinct catalytic actions (catalysis, promotion). Metal ions can be promoters, as either activity or selectivity enhancers (and sometimes of both), in hydrogenation reactions. For instance, this is well established in the case of the hydrogenation of α,β-unsaturated aldehydes, where Lewis acids are able to increase the selectivity of Pt^0 catalysts toward the corresponding unsaturated alcohol [154]. In a recent study, Centomo et al. showed that the hydrogenation of citral can be carried out over CFP-supported platinum catalysts with much better selectivity than with Pt^0/SiO_2 and Pt^0/Al_2O_3 ones [65]. In monometallic catalysts the selectivity was highly dependent on the method of preparation: whereas a RIMP method gave poorly selective (and generally poorly active) catalyst, the deposition of the metal from mesitylene solutions of solvated metal atoms, obtained by Metal Vapor Synthesis (see Section 3.3.3), gave active and selective materials. Selectivity toward geraniol/nerol as high as ca. 45% at 80–90% conversion was obtained over CFP-supported platinum, to be compared with less than 20% at similar conversion over Pt^0/SiO_2 or Pt^0/Al_2O_3 catalysts prepared with the same method. The activity of the best polymer supported catalysts was comparable with that of the catalysts supported by the inorganic oxides. One of the employed CFP, PMAA cross-linked with DVB, was also an ion-exchanger. Prior to platinum deposition, as described above, M^{2+} ions were readily immobilized in the resins, upon treatment with aqueous or alcoholic solutions of the metal diacetates (M = Fe, Co, Zn). The selectivity was raised to 80–90% at 80–90% conversion. Whereas the selectivity enhancement was associated to an appreciable decrease of catalytic activity for Fe^{2+} and Zn^{2+} modified catalysts, for the Co^{2+} modified catalyst lowering of activity was less than 50%. In one case, the employed CFP was PVPY, cross-linked with DVB. The monometallic Pt catalyst was 54% selective toward geraniol/nerol at 20–30% conversion, but it was poorly active and it was not possible to achieve a high citral conversion. The catalyst supported on Co^{2+}-modified PVPY was not only much more selective (ca. 90%), but also more stable. Full conversion of the substrate was achieved with the same high selectivity observed at low conversion.

Catalyst promotion by modification with metal ions of platinum and palladium catalysts supported on CFPs was observed also by Toshima and co-workers [31,74,75,76] and by Wang and He [161] in the hydrogenation of several alkenes [74,161], dienes [74,75,76] and acrylic acid [31,74]. Toshima and co-workers investigated on the activity of platinum and palladium supported on PS-DVB resins functionalized with iminodiacetic acid groups, which served as ion-exchange sites for the immobilization of auxiliary metal ions (Na^+, Mg^{2+}, Al^{3+}, Ln^{3+}; Ln = lanthanoid). Several experimental parameters were taken into account, such as the order of metal loading (Pt or Pd first and then the metal ion or the other way round), the drying procedures and the radial distribution of the metal. The nature of the auxiliary metal ion affected the BET specific surface area of the materials, but no straightforward correlation with the observed reaction rates was found. Lanthanoid ions, particularly Nd^{3+}, gave palladium catalysts more active in the hydrogenation of acrylic acid [31] in ethanol (0.025 M, 30 °C, 105 kPa, Pd/acrylic acid = 2.3×10^{-3}, mol) than other ions. The origin of the effectiveness of Ln^{3+} ions as promoters was unclear: a palladium–Ln^{3+} interaction through the space or an acceleration of substrates diffusion inside the catalyst, favored by its coordination to Ln^{3+} were both proposed. It should be appreciated that in the second case the introduction of Ln^{3+} ions would affect the substrate–support compatibility rather than truly promoting the catalyst.

The promotion of the active metal can be provided also by the functional groups present in the polymeric support, as shown by Zecca et al. in a rare example of investigation on the catalytic activity of palladium over CFPs in the hydrogenation of cycloalkenes under firmly established *kinetic regime* [80]. Under kinetic regime the apparent rate corresponds to the intrinsic rate of the chemical reaction taking place over the surface of the active metal and therefore reflects its real catalytic activity. In this study different supports, containing variable amounts of amide groups from both DMA (one of the comonomers) and MBAA (the cross-linker), were employed as supports for palladium catalysts (0.27–0.46%, w/w). The initial rates of hydrogenation of cyclohexene and cyclohex-2-en-1-one in methanol (1 M, 25 °C; 0.5 MPa, 1.0 MPa, Pd/alkene = 2.5×10^{-4}; 1.5 MPa, Pd/alkene = 1.25×10^{-4}) were linearly dependent on the Pd/N molar ratio in the catalysts for both substrates at all the investigated pressures. This suggested an interaction, of the amide groups with the metal leading to increasing catalytic activity.

The hydrogenation of organic nitrocompounds has received relatively little attention. The only reports on this

reaction were published by Li and Frechet [84,103], by Corain and associates [129,101] and by Kralik and associates [78,79,115]. This is likely due to the fact that palladium on carbon is firmly established as the standard catalyst for the hydrogenation of nitrocompounds, also in the industrial practice, and that palladium catalysts may be readily deactivated by metal leaching. As mentioned in Section 4, the deactivation process was mathematically modeled by Kralik and associates. The palladium(0) catalysts supported on CFP show similar reactivity to palladium on carbon, i.e. the nitroderivatives are hydrogenated to the corresponding amines. The papers by Li and Frechet on the hydrogenation of nitrocompounds are the only examples of the use of PBI as the support for heterogeneous metal catalysts. Interestingly, they found a dependence of the initial rate of nitrobenzene hydrogenation on the Pd/substrate ratio, which suggests that the reaction could have proceeded under kinetic regime (Parr reactor, 25 °C, 105 kPa initial pressure). This seems in line with the high accessibility exhibited by PBI particles in several solvents, as observed by D'Archivio et al. [162].

5.2. Oxidation and Miscellaneous Reactions

Partial, selective oxidation of organic compounds is important from the point of view of both industrial chemical processing and laboratory scale synthesis [163]. Many oxidations use to be carried out with stoichiometric oxidants and in environmentally unfriendly solvents. For these reasons catalytic methods have been pursued since long. As a matter of fact, the palladium and platinum catalysts supported on Amberlyst 15, prepared by Hanson et al. as early as 1974, were among the first catalysts ever reported in the open literature and were tested in the oxidation of liquid ethanol at 45 °C with flowing oxygen, sparged into the alcohol [92]. The reaction rate was low (3–10 h for 2% conversion) and limited by gas–liquid diffusion of oxygen. Partial oxidation products (acetaldehyde, acetic acid, ethyl acetate) were observed at low conversion over pre-reduced catalysts only. By admission of the authors, the catalytic study was incomplete and was not pursued any further. Twentyfive years separate this first report from the next paper on oxidation catalyzed by polymer supported metals. In 1999 Lin et al. [164] investigated on the oxidation of ethanol in water over 1% (w/w) palladium catalysts in a fixed bed reactor. Pd^0 was either supported on macroreticular PS-DVB or γ-alumina. Under the employed conditions (95 °C, 362 kPa, air/EtOH = 2.37, WHSV = 2.4 $g_{EtOH}\,h^{-1}\,g_{Pd}^{-1}$) the Pd^0/CFP was more active than Pd^0/γ-Al_2O_3. The much more hydrophobic polymeric support favored the removal of water from the surroundings of the metal surface, which was more readily available for ethanol. On the other hand, Pd^0/CFP was much less selective toward acetaldehyde (the desired product) and much less stable against metal leaching and metal sintering. In 2001 Sidorov et al. reported on the catalytic activity of platinum catalysts supported on HPS in the oxidation of L-sorbose to 2-keto-gulonic acid with O_2 in water [85]. As usual in the selective oxidation of alcohols with dioxygen in water, a base ($NaHCO_3$) was required to control the pH of the solution, a critical parameter to control selectivity [165]. Under optimized conditions a 98% selectivity was achieved at full conversion. The best catalyst could be used 15 times with preservation of its activity and selectivity. Uozumi and Nakao employed their Pd^0 catalyst supported on the amphiphilic PS-DVB-PEG gel-type resin described above also in the oxidation of alcohols with dioxygen in water (0.77 mmol alcohol/cm^3 water; reflux; 105 kPa O_2). Benzyl alcohol was smoothly oxidized to benzaldehyde (97% yield in 1.5 h), with 1% mol palladium with respect to the substrate. α-Substituted benzyl (secondary) alcohols required 5% mol palladium and prolonged reaction time (20 h). For the conversion of aliphatic cyclo-alkyl alcohols even more drastic conditions were applied (20% mol palladium and 20 h). This reflects a general trend in the reactivity of alcohols [165]. In all cases the products were the corresponding ketones, which are not readily further oxidized. The catalyst was tested also in the oxidation of *n*-butanol, *n*-hexanol and *n*-octanol: in this case the presence of 0.2 M K_2CO_3 was necessary. High yields (>90%) were obtained with 20% mol palladium after 40 h and the only product was always the corresponding carboxylic acid. The catalyst was not selective at all for the partial oxidation product, the aldehyde. Quite recently the same group reported on the oxidation of alcohols with Pt(0) catalysts supported on the same amphiphilic polymeric matrix [166].

Much more selective catalysts for the oxidation of butanol with dioxygen in water were reported by Burato et al. [30,66]. A number of monometallic gold and palladium catalysts and a bimetallic Au–Pd catalyst were applied and compared to Au^0/C, Pd^0/C and Au^0–Pd^0/C catalysts in the oxidation of butanal to butanoic acid and to the oxidation of *n*-butanol to butanal in water (substrate 0.23 M; 70 °C; 315 kPa O_2; metal/substrate = 0.1% mol; 2 h). The employed CFP were gel-type CFPs of DMAA and MTEA, cross-linked with MBAA and a gel-type CFP of MAA and VPY, cross-linked with MBAA. These materials were the first Au^0 catalysts supported on CFPs to be applied to oxidation. In spite of the presence of alkyl sulfide groups (sulfur compounds quite often are poisons to supported metal catalysts) the catalysts were active in both reactions. The Au and Pd monometallic catalysts showed similar apparent activity in the oxydation of butanal to butanoic acid and were both roughly twice as active as the metals supported on carbon. TEM characterization showed that the metal nanoclusters on carbon were much larger than those supported on CFPs. According to the authors this was the cause of the higher activity of CFP-supported metals. As to the bimetallic catalysts, whereas the carbon-supported one was more active than Au^0/C and Pd^0/C, Au^0-Pd^0/CFP was less active than both Au^0/CFP and Pd^0/CFP. In the oxidation of *n*-butanol, which required the presence of a base (either NaOH or K_2CO_3; alcohol/base = 1 mol/mol), the monometallic and bimetallic catalysts supported on both carbon and CFPs generally exhibited comparable performances. The apparent activity was correlated neither to the nanocluster size nor to the cross-linking degree and different catalysts responded differently when the base was changed from NaOH to K_2CO_3. Full conversion was achieved only with the bimetallic catalyst, but it was

completely selective toward butanoic acid. The best selectivity was observed with Au supported on co-poly-{MAA-VPY-MBAA}: at 40% conversion of butanol, butanal amounted to 70% of total products, corresponding to 28% yield. The best yield obtained with carbon-supported catalysts was roughly half of this value. This demonstrates the potential of CFPs as catalytic supports also in oxidation reactions.

The first Au^0 catalysts ever supported on a CFP were reported by Shi and Deng [119] as applied to the oxidative carbonylation of aniline and its *p*-substituted derivatives to methylacarbamates or symmetric diarylureas. The catalysts were supported on a commercial ion exchange resin (Merck Ion exchanger IV) and prepared by the RIMP method. Both aqueous and acetone solution of $HAuCl_4 \cdot 4H_2O$ were employed for metal immobilization. It was found that treatment with NaOH (but not with KOH) prior to metal immobilization was necessary to achieve active catalysts. No relationship with the BET surface areas of dried materials, ranging from 1.4 to $1.9\,m^2\,g^{-1}$, was observed. The immobilization of gold from acetone gave much better catalysts. For the latter an eggshell radial distribution of gold seems likely in view of the hydrophilic nature of the support. No specific data were given by the authors on this feature, but the TEM microphotograph reported in Ref. [119] is compatible with this hypothesis. In addition, a slight increase in the catalytic activity was observed with decreasing gold loading. This could be the consequence of increasingly small nanoclusters as the metal content decreases, as would be expected for highly accessible active metal. In a subsequent paper [67], Shi et al. showed that in another set of gold catalysts for carboxylation of aniline and epoxides, supported on Amberlite IRA 400 and prepared by the same procedure, nanoparticle size increased with gold loadings (ca. 3, 6, 10 and 12 nm for 0.01, 0.05, 0.1, 0.5% w/w Au in the catalyst, respectively). Allegedly the metal nanoclusters were located "on the surface of the polymer". No gold(III) was found in the catalysts of oxidative carbonylation (XPS), indicating that the metal was reduced upon immobilization. However, none of these catalysts showed complete reduction to Au^0. In the most active ones the binding energy for the Au $4f_{7/2}$ level was 84.2–84.4 eV, consistent with the presence of positively charged gold [119]. The very same value was later found by Shi et al. in the catalysts supported on Amberlite IRA 400, which were active for the carboxylation of epoxides and anilines with CO_2 to give cyclic alkyl carbonates and symmetric diarylureas [67]. These catalysts were reported to be much more active than classic acid-base catalysts and much more active than Pd^0 or Rh^0 on the same support.

It is worth mentioning that both the carboxylation of epoxides and anilines are acid–base reactions, which do not entail redox processes. Therefore a catalyst active in these reactions must provide acid–base functionality. In this perspective, positively charged gold could be the real player, although a co-catalytic or promotion effect of zerovalent gold could also be important. Therefore the catalysts for the oxidative carbonylation of aniline, supported on Merck Ion-exchanger IV, could be actually bifunctional. On one side, Au^0 could catalyze the oxidation of CO with O_2 to CO_2, a reaction for which it is extremely active, provided the nanoparticles have proper shape and size [3,4]. On the other side, positively charged gold could catalyze the subsequent carboxylation of aniline, as it was observed with gold catalysts supported by Amberlite IRA 400. At the moment it is not clear whether the polymeric supports has a specific role or not.

A few papers have been devoted to the preparation of CFP-supported Pd^0 catalysts applied to coupling reactions involving aryl halides (Heck, Suzuki, Stille reactions [167]). In the oldest, dating back to 2000, Pathak et al. described the deposition of preformed palladium nanoparticles, stabilized by PVPYR, on microspheres of PVPY/DVB (4% cross-linked), according to an IMN procedure. As a part of the characterization, the material was tested in the couplings of 4-nitrobromobenzene with *n*-butylacrylate (Heck), phenylboronic acid (Suzuki) and trimethyphenyltin (Stille). These are standard reactions and the aryl halide is a very reactive one. Consequently, the catalytic results do not convey any particularly interesting information. The authors claimed that the metal did not undergo leaching on the basis of the TEM microphotographs of the fresh and recovered catalyst. According to them, TEM did not show any significant change of the coverage of polymeric microsphere. This is a loose evidence and does not by any means prove the heterogeneity of the catalyst. As mentioned above (Section 3.4), there is a huge and consistent body of literature showing that supported palladium catalysts reported so far for C–C couplings of aryl halides were actually sources of soluble molecular palladium species and that catalysis was at least in part homogeneous [142–144]. As a matter of fact aryl halides react with nanostructured palladium. Reetz and Westermann [168] showed that stabilized palladium nanoparticles react with stoichiometric amounts of iodobenzene, under conditions relevant to C–C coupling, to give palladium(II) complexes, containing [Pd(Ar)X] units, in solution. As to palladium supported on CFPs, Biffis et al. observed extensive dissolution of palladium nanoparticles, supported on either a commercial PS-DVB sulfonated ion-exchanger, owing to the action of halobenzenes in solution of *N,N*-dimethylacetamide (one of the most common solvents for the Heck reaction) [169]. The same excess amount of the aryl halide employed in real catalytic runs was applied. It was also found that the presence of good ligands to palladium(II), such as acetate ions (commonly used as the base in Heck reactions), enhances the extent of palladium leaching and that the leached species are highly active as coupling catalysts. Similar results were obtained with alumina as the support. A later publication by Caporusso et al. [124] showed that a number of palladium catalysts supported on CFPs functionalized with *N,N*-dimethylamino, cyano, carboxyl and pyridyl groups also behaved as sources of active species in solution and that reaction rate was correlated with the leaching degree *during* the reaction, in analogy to the results of Köhler and co-workers, who employed inorganic supports [170]. Only with PVPY/DVB as the support there was some evidence that supported species, of unclear nature, could have contributed to the overall catalytic activity. In fact, the addition of a considerable amount of the bare support (PVPY/DVB with no palladium) did not fully quench the reaction, in

spite of the known ability of PVPY resins to scavenge palladium [171,172]. However, the participation of supported species to the catalytic activity of this system should be more firmly proved. In general, the performance of CFP-supported palladium catalysts in the C–C coupling reactions of aryl halides is similar to that of both homogeneous systems and of palladium supported on inorganic solids.

Gautron et al. and Gašparovičová et al. have investigated on polymer supported palladium–copper catalysts for the selective hydrogenation of nitrates to dinitrogen, in water [104,120–122]. This could be a method for the abatement of nitrate concentration in soft water from different sources below the legal limits for drinking water. To avoid the over-reduction to NH_4^+, which is also a regulated pollution hazard, the reaction must be carried out under acidic conditions and control of pH is important for the purpose of high selectivity. Gautron et al. employed PPY as the catalytic support, but the catalysts were not active in the hydrogenation of nitrate and promoted only the hydrogenation of nitrite. Gašparovičová et al. employed commercial ion-exchangers, for both cations (Dowex 50 W × 4) [120] and anions (Dowex 1 × 4) [121,122]. In the first case, the level of NH_4^+ in the final solution (batch-wise reaction) was low owing to immobilization of ammonium ions into the resin, but selectivity toward N_2 was only 60%. In addition, metal leaching (especially of copper) was observed upon restoration of the ion-exchange capacity by washing the spent catalysts with aqueous HCl. Better results were obtained with Dowex 1 × 4 as the support. Enhanced activity was observed owing to easier mass transfer of NO_3^- ions in the anion exchanger. Moreover lower copper leaching levels were observed. In this connection, it was found that mechanic degradation of the catalyst under magnetic stirring conditions favored the leaching process.

6. Conclusions

Cross-linked functional polymers appear to be suitable supports for catalytically active metal(0) nanoclusters.

The resulting M^0/CFP nanocomposites with M = Pd, Pt, Ag and Au exhibit in general satisfactory handiness in the laboratory atmosphere and chemical stability under operational conditions, re-usability, mechanical robustness (under proper conditions), plain filterability. Their reactivity is quite comparable to that of conventional M^0/S (S = carbon, inorganic support) catalysts. M^0/CFP are to be employed in the liquid phase.

Synthesis conditions can to be tuned to enable a homogeneous or a peripheral distribution of M^0 nanoclusters through the body of the support particles.

For macroreticular CFPs, the accessibility of reagents and removal of the products is guaranteed by the intrinsic micrometer- and nanometer-scale morphology of the support. For gel-type CFPs, the same positive features are enabled by the proper choice of cross-linking degree and swelling medium.

A major reason of attention to M^0/CFP catalysts appears to be their multifunctionality prospects (vide infra) made feasible by the clear possibility of producing multimetal M_1^0, M_2^0, ... M_n^0/CFP catalysts and by the employment of smart supports bearing designed chemical functions able to perform either a co-catalytic role in multisteps syntheses (see the case of MIBK synthesis) or reactivity enhancement effects. A second important reason of attention (yet to be properly evaluated) is the ability of the swollen support particles to condition the concentration of reagents and products in their interior.

A wise combination of all these features will be the key reason for proposing M^0/CFP materials as technologically relevant innovative tools in heterogeneous metal catalysis.

Abbreviations and Symbols

Polymers

HPS	Hyper cross-linked polystyrene
PA	Polyamide (nylon)
PBI	Polybenzimidazol
PCEA	Polycyanoethylacrylate
PE	Polyethylene
PMAA	Poly-{methacrylic acid}
PMMA	Polymethylmethacrylate
PPY	Polypyrrole
PS	Polystyrene
PU	Polyurea
PVA	Polyvinylalcohol
PVPY	Polyvinylpyridine
PVPYR	Polyvinylpyrrolidinone

Monomers

DMA	*N,N*-dimethylacrylamide
DOMA	*n*-dodecylamethacrylate
IPA	(*N,N*-diisopropyl)-acrylamide
MAA	Methacrylic acid
MAEA	2-(*N,N*-dimethylamino)ethylmethacrylate
MAESA	2-methacryloxy-ethylsulfonic acid
MMA	Methylmethacrylate
MTEA	2-(methylthio)ethylmethacrylate
SSH	p-styrylsulfonic acid
SSNa	Sodium *p*-styrylsulfonate
TDI	2,4-toluene diisocyanate
VPY	4-vinylpyridine
VPYR	*N*-vinylpyrrolidinone

Cross-linkers

DAP	Diallylphtalate
DVB	Divinylbenzene
EDMA	Ethylene glycol dimethacrylate
MBAA	N,N′-methylene bis acrylamide

Miscellanea

AIBN	Azo-bis-isobutyronitrile
Apc	average polymer chain concentration
AT	4-aminotoluene (p-toluidine)
BET	Brunauer-Emmet-Teller
Cld	cross-linking degree
CP-MAS NMR	Cross Polarization-Magic Angle Spinning Nuclear Magnetic Spectroscopy
CV	Cyclic voltammetry
DMF	*N,N*-dimethylformamide
EAQ	2-ethylanthraquinone
ESR	Electron Spin Resonance
H_2EAQ	2-ethylanthrahydroquinone
ICPA	3-isocyano-propylacrylate
IOPN	Interpenetrating Oraganometallic Polymer Network
IPN	Interpenetrating Polymer Network
ISEC	Inverse steric exclusion chromatography
MIBK	Methyl-tert-butylketone
NT	4-nitrotoluene
PGSE-NMR	Pulse Field Gradient Spin Echo-Nuclear Magnetic Spectroscopy
Pyri	Pyridyl
S	Swellability (= weight specific swollen gel volume)
SEM	Scanning electron microscopy
TEM	Transmission electron microscopy
TEMPONE	2,2,6,6-tetramethyl-4-oxo-1-oxy-piperidine
TEOS	tetraethoxysilane
WHSV	Weight hourly space velocity
XRD(A)	X-ray Diffraction (Analysis)
XRM	X-ray microprobe
D	Diffusion coefficient
D′	Self-diffusion coefficient of a liquid
τ	Rotational correlation time

References

1 G. Ertl, H. Knötzinger, J. Weitkamp (eds.) *Handbook of Heterogeneous Catalysis*, Wiley-VCH, Weinheim, 1997.
2 P. Claus, *Appl. Catal. A: Gen.* 29 (2005) 222.
3 M. Haruta, *CATTECH* 6(3) (2002) 102.
4 M. Haruta, *Gold Bull.* 37 (2004) 27.
5 J. Wöllner, W. Neier, Bergbau und chemie (Homberg), German patent 1260454 (1966).
6 K. Weissermel, H. Arpe, *Industrial Organic Chemistry*, 4th ed., Wiley-VCH, Weinheim, 2003.
7 D. C. Sherrington, *Chem. Commun.* (1998) 2275.
8 R. Wagner, P. M. Lange, *Erdöl, Erdgas, Köhle* 105 (1989) 414.
9 B. Corain, M. Kralik, *J. Mol. Catal. A: Chem.* 159 (2000) 153.
10 B. Corain, M. Kralik, *J. Mol. Catal. A: Chem.* 173 (2001) 99.
11 B. Corain, M. Kralik, *J. Mol. Catal. A: Chem.* 200 (2003) 333.
12 B. Corain, P. Centomo, S. Lora, M. Kralik, *J. Mol. Catal. A: Chem.* 204–205 (2003) 755.
13 A. Guyot in D. C. Sherrington, P. Hodge (eds.) *Synthesis and Separations Using Functional Polymers*, Wiley, New York, 1988, 1.
14 A. Biffis, B. Corain, M. Zecca, C. Corvaja, K. Jeràbek, *J. Am. Chem. Soc.* 117 (1995) 1603.
15 K. Kesenci, A. Tuncel, E. Piskin, *React. Funct. Polym.* 31 (1996) 137.
16 K. Jeràbek, *Anal. Chem.* 57 (1985) 1595.
17 K. Jeràbek, *Anal. Chem.* 57 (1985) 1598.
18 K. Jeràbek in M. Potschka, P. L. Dubin (eds.) *Cross Evaluation of Strategies in Size-exclusion Chromatography, ACS Symposium Series 635, American Chemical Society*, Washington, DC, 1996, 211.
19 P. L. Nordio in L. J. Berliner (ed.) *Spin Labeling, Theory and Applications*, Vol. I, Academic Press, New York, 1976, 5.
20 S. L. Regen, *Macromolecules* 8 (1975) 689.
21 F. Pozzar, A. Sassi, G. Pace, S. Lora, A. A. D'Archivio, K. Jeràbek, A. Grassi, B. Corain, *Chem. Eur. J.* 11 (2005) 7395.
22 A. A. D'Archivio, L. Galantini, A. Panatta, E. Tettamanti, B. Corain, *J. Phys. Chem. B* 102 (1998) 6774.
23 K. Jeràbek, *J. Mol. Catal.* 55 (1989) 247.
24 B. Corain, P. Centomo, C. Burato, P. Canton (This Book, Chapter 29).
25 M. Zecca, A. Biffis, G. Palma, C. Corvaja, S. Lora, K. Jeràbek, B. Corain, *Macromolecules* 29 (1996) 4655.
26 C. A. Frye, *Solid State NMR for Chemists*, C. F. Press, Guelph, Canada, 1983.
27 J. S. Frye, G. E. Maciel, *J. Mag. Res.* 48 (1982) 125.
28 G. Metz, M. Ziliox, S. O. Smith, *Solid State Nucl. Magn. Reson.* 7 (1996) 155.
29 M. Kralik, V. Kratky, P. Centomo, P. Guerriero, S. Lora, B. Corain, *J. Mol. Catal. A: Chem.* 195 (2003) 219.
30 C. Burato, P. Centomo, G. Pace, M. Favaro, L. Prati, B. Corain, *J. Mol. Catal. A: Chem.* 238 (2005) 26.
31 T. Teranishi, N. Toshima, *Dalton Trans.* (1994) 2967.
32 A. Biffis, R. Ricoveri, S. Campestrini, M. Kralik, K. Jeràbek, B. Corain, *Chem. Eur. J.* 8 (2002) 2962.
33 M. Ohtaki, M. Komiyama, H. Hirai, N. Toshima, *Macromolecules* 24 (1991) 5567.
34 M. Ohtaki, N. Toshima, M. Komiyama, H. Hirai, *Bull. Chem. Soc. Jpn.* 63 (1990) 1433.
35 R. H. Grubbs, L. C. Kroll, *J. Am. Chem. Soc.* 93 (1971) 3062.
36 P. Hodge, *Chem. Soc. Rev.* 26 (1997) 417.
37 C. Burato, S. Campestrini, P. Centomo, K. Jeràbek, P. Canton, P. Canu, B. Corain, unpublished results.
38 D. Pears, S. C. Smith, *Aldrichimica Acta* 38 (2005) 23.
39 P. Centomo, D. Gasparovicova, D. Pears, M. Kralik, M. Zecca, K. Jeràbek, B. Corain, unpublished results.
40 K. Dorfner, *Ion-exchangers*, W. De Gruyter, Berlin/New York 1991.
41 R. B. Merrifield, *J. Am. Chem. Soc.* 85 (1963) 2149.
42 R. B. Merrifield, J. M. Stewart, N. Jernberg, *Anal. Chem.* 38 (1966) 1905.
43 B. Gutte, R. B. Merrifield, *J. Biol. Chem.* 246 (1971) 1922.
44 R. L. Letsinger, M. J. Kornet, *J. Am. Chem. Soc.* 85 (1963) 3045.
45 F. Ancillotti, E. Pescarollo, M. Massi Mauri, US patent 4039590 (1977).
46 F. Ancillotti, M. Massi Mauri, E. Pescarollo, *J. Catal.* 46 (1977) 49.
47 G. J. Huthchings, C. P. Nicolaides, M. S. Scurrell, *Catal. Today* 15 (1992) 23.
48 H. Giehring, Bergbau und chemie (Homberg), German patent 1238453 (1965).
49 J. Wöllner, Bergbau und chemie (Homberg), German patent 1193931 (1963).
50 W. O. Haag, D. D. Whitehurst, German patent 1800371 (1969).
51 W. O. Haag, D. D. Whitehurst, German patent 1800379 (1969).

52 W. O. Haag, D. D. Whitehurst, German patent 1800380 (1969).
53 R. H. Grubbs, *CHEMTECH* 7 (1977) 512.
54 G. Parshall, *Homogeneous Catalysis*, Wiley, New York, 1980.
55 R. F. Hartley, *Supported Metal Complexes*, D. Reidel, Dordrecth, 1985.
56 R. A. Khaibullina, L. G. Fatkulina, K. R. Rustamov, *Int. Chem. Eng.* 7 (1967) 536.
57 J. M. Tibbitt, B. C. Gates, J. R. Katzer, *J. Catal.* 38 (1975) 505.
58 W. P. Dunsworth, F. F. Nord in W. Frankerburg, G. V. I. Komarewsky, V. I. Rideal (eds.) *Advances in Catalysis and Related Subjects*, Academic Press, New York, 1954.
59 M. Kralik, A. Biffis, *J. Mol. Catal. A: Chem.* 177 (2001) 113.
60 S. Talwalkar, S. Mahajani, *Appl. Catal. A: General* 302 (2006) 140.
61 P. M. Lange, F. Martinola, S. Höckle, *Hydrocarbon Process.* 64 (1985) 51.
62 A. Biffis, H. Landes, K. Jeràbek, B. Corain, *J. Mol. Catal. A: Chem.* 151 (2000) 283.
63 M. Guisnet, J. Barrault, C. Bouchoule, D. Duprez, C. Montassier, G. Pérot (eds.) *Heterogeneous Catalysis and Fine Chemicals*, Elsevier, Amsterdam, 1988.
64 C. Burato, P. Centomo, M. Rizzoli, A. Biffis, S. Campestrini, B. Corain, *Adv. Synth. Catal.* 348 (2006) 255.
65 P. Centomo, M. Zecca, S. Lora, G. Vitulli, A. M. Caporusso, M. L. Tropeano, C. Milone, S. Galvagno, B. Corain, *J. Catal.* 229 (2005) 283.
66 B. Corain, C. Burato, P. Centomo, S. Lora, W. Meyer-Zaika, G. Schmid, *J. Mol. Catal. A: Chem.* 225 (2005) 189.
67 F. Shi, Q. Zhang, Y. Ma, Y. He, Y. Deng, *J. Am. Chem. Soc.* 127 (2005) 4182.
68 B. Corain, K. Jeràbek, P. Centomo, P. Canton, *Angew. Chem. Int. Ed.* 43 (2004) 959.
69 G. Bombi, S. Lora, M. Zancato, A. A. D'Archivio, K. Jeràbek, B. Corain, *J. Mol. Catal. A: Chem.* 194 (2003) 273.
70 Y. Uozumi, R. Nakao, *Angew. Chem. Int. Ed.* 115 (2003) 204.
71 A. Biffis, N. Orlandi, B. Corain, *Adv. Mater.* 15 (2003) 1551.
72 F. Artuso, A. A. D'Archivio, S. Lora, K. Jeràbek, M. Králik, B. Corain, *Chem. Eur. J.* 9 (2003) 5292.
73 M. Králik, V. Kratky, M. De Rosso, M. Tonelli, S. Lora, B. Corain, *Chem. Eur. J.* 9 (2003) 209.
74 N. Toshima, Y. Shiraishia, T. Teranishi, *J. Mol. Catal. A: Chem.* 177 (2001) 139.
75 N. Toshima, T. Teranishi, H. Asanuma, Y. Saito, *J. Phys. Chem.* 96(9) (1992) 3796.
76 N. Toshima, T. Teranishi, Y. Saito, *Makromol. Chem. Macromol. Symp.* 59 (1992) 327.
77 N. Toshima, T. Teranishi, H. Asanuma, Y. Saito, *Chem. Lett.* 19 (1990) 819.
78 M. Kralik, R. Fisera, M. Zecca, A. A. D'Archivio, L. Galantini, K. Jeràbek, B. Corain, *Collect. Czech. Chem. Commun.* 63 (1998) 1074.
79 M. Kralik, V. Kratky, M. Hronec, M. Zecca, B. Corain, *Stud. Surf. Sci. Catal.* 130 (2000) 2321.
80 M. Zecca, R. Fisera, G. Palma, S. Lora, M. Hronec, M. Králik, *Chem. Eur. J.* 6 (2000) 1980.
81 M. Králik, M. Zecca, P. Bianchin, A. A. D'Archivio, L. Galantini, B. Corain, *J. Mol. Catal. A: Chem.* 130 (1998) 85.
82 M. Zecca, M. Králik, M. Boaro, G. Palma, S. Lora, M. Zancato, B. Corain, *J. Mol. Catal. A: Chem.* 129 (1998) 27.
83 B. Corain, A. A. D'Archivio, L. Galantini, K. Jeràbek, M. Kràlik, S. Lora, G. Palma, M. Zecca, in *Supported reagents and catalysts in chemistry*, B. K. Hodnett, A. P. Kybett, J. H. Clark, K, Smith (eds.), Cambridge (UK) RSC, 1998, 182.
84 N. Li, J. M. J. Fréchet, *React. Polym.* 6 (1987) 311.
85 S. N. Sidorov, I. V. Volkov, V. A. Davankov, M. P. Tsyurupa, P. M. Valetsky, L. M. Bronstein, R. Karlinsey, J. W. Zwanziger, V. G. Matveeva, E. M. Sulman, N. V. Lakina, E. A. Wilder, R. J. Spontak, *J. Am. Chem. Soc.* 123 (2001) 10502.
86 S. N. Sidorov, L. M. Bronstein, V. A. Davankov, M. P. Tsyurupa, S. P. Solodovnikov, P. M. Valetsky, *Chem. Mater.* 11 (1999) 3210.
87 A. Biffis, A. A. D'Archivio, K. Jeràbek, G. Schmid, B. Corain, *Adv. Mater.* 12 (2000) 1909.
88 A. Biffis, K. Jeràbek, A. A. D'Archivio, L. Galantini, B. Corain, *Stud. Surf. Sci. Catal.* 130 (2000) 2327.
89 W. Yu, H. Liu, X. An, *J. Mol. Catal. A: Chem.* 129 (1998) L9.
90 S. Huang, B. He, *React. Polym.* 23 (1994) 11.
91 S. Huang, B. He, *React. Polym.* 23 (1994) 1.
92 D. L. Hanson, J. R. Katzer, B. C. Gates, G. C. A. Schuit, H. F. Harnsberger, *J. Catal.* 32 (1974) 204.
93 R. L. Lazcano, M. P. Pedrosa, J. Sabadie, J. Germain, *Bull. Soc. Chim. Fr.* (1974) 1129.
94 J. Sabadie, J. Germain, *Bull. Soc. Chim. Fr.* (1974) 1133.
95 P. Dini, D. Dones, S. Montelatici, N. Giordano, *J. Catal.* 30 (1973) 1.
96 S. Galvagno, A. Donato, G. Neri, D. Pietropaolo, P. Staiti, *React. Kinet. Catal. Lett.* 37 (1988) 443.
97 Z. M. Michalska, B. Ostaszewski, J. Zientarska, J. W. Sobczak, *J. Mol. Catal. A: Chem.* 129 (1998) 207.
98 Z. M. Michalska, B. Ostaszewskia, J. Zientarska, J. M. Rynkowski, *J. Mol. Catal. A: Chem.* 185 (2002) 279.
99 K. Zhang, D. C. Neckers, *J. Polym. Sci. Polym. Chem. Ed.* 21 (1983) 3115.
100 B. Corain, F. O. Sam, M. Zecca, S. Lora, Palma G, *Angew. Chem. Int. Ed. Eng.* 29 (1990) 384.
101 B. Corain, M. Zecca, A. Biffis, S. Lora, G. Palma, *J. Organomet. Chem.* 475 (1994) 283.
102 M. Bertolin, M. Zecca, G. Favero, G. Palma, S. Lora, D. Ajò, B. Corain, *J. Appl. Pol. Sci.* 65 (1997) 2201.
103 N. Li, J. M. J. Fréchet, *J. Chem. Soc., Chem. Commun.* (1985) 1100.
104 E. Gautron, A. Garron, E. Bost, F. Epron, *Catal. Commun.* 4 (2003) 435.
105 I. Halász, K. Martin, *Angew. Chem. Int. Ed. Eng.* 17 (1978) 901.
106 D. H. Freeman, I. C. Poinescu, *Anal. Chem.* 49 (1977) 1183.
107 L. R. Albright, *React. Polym.* 4 (1986) 155.
108 B. Corain, A. A. D'Archivio, L. Galantini, S. Lora, A. A. Isse, F. Maran, *Chem. Eur. J.* 13 (2007) 2392.
109 R. Arshady, *Adv. Mater.* 3 (1991) 182.
110 N. Bremeyer, S. V. Ley, C. Ramarao, I. M. Shirley, S. C. Smith, *Synlett* 11 (2002) 1843.
111 J. Aumo, J. Lilja, P. Mäki-Arvela, T. Salmi, M. Sundell, H. Vainio, D. Y. Murzin, *Catal. Lett.* 84 (2002) 219.
112 S. V. Ley, C. Mitchell, D. Pears, C. Ramarao, J. Yu, W. Zhou, *Org. Lett.* 5 (2003) 4665.
113 J. Yu, H. Wu, C. Ramarao, J. B. Spencer, S. V. Ley, *Chem. Commun.* (2003) 678.
114 A. Biffis, B. Corain, Z. Cvengrosova, M. Hronec, K. Jeràbek, M. Králik, *Appl. Catal. A: General* 124 (1995) 355.
115 M. Kralik, M. Hronec, V. Jorik, S. Lora, G. Palma, M. Zecca, A. Biffis, B. Corain, *J. Mol. Catal. A: Chem.* 101 (1995) 143.

116 C. Chen, M. Chen, T. Serizawa, M. Akashi, *Chem. Commun.* (1998) 831.
117 T. Teranishi, K. Nakata, M. Miyake, N. Toshima, *Chem. Lett.* 25 (1996) 277.
118 M. Hronec, Z. Cvengrosová, M. Králik, G. Palma, B. Corain, *J. Mol. Catal. A: Chem.* 105 (1996) 25.
119 F. Shi, Y. Deng, *J. Catal.* 211 (2002) 548.
120 D. Gašparovičová, M. Kralik, M. Hronec, *Collect. Czech. Chem. Commun.* 64 (1999) 502.
121 D. Gašparovičová, M. Kralik, M. Hronec, A. Biffis, M. Zecca, B. Corain, *J. Mol. Catal. A: Chem.* 244 (2006) 258.
122 D. Gašparovičová, M. Králik, M. Hronec, Z. Vallušová, Vinek H, B. Corain, *J. Mol. Catal. A: Chem.* 264 (2006) 93.
123 S. Pathak, M. T. Greci, R. C. Kwong, K. Mercado, G. K. S. Prakash, G. A. Olah, M. E. Thompson, *Chem. Mater.* 12 (2000) 1985.
124 A. M. Caporusso, P. Innocenti, L. A. Aronica, G. Vitulli, R. Gallina, A. Biifis, M. Zecca, B. Corain, *J. Catal.* 234 (2005) 1.
125 R. F. Ziolo, E. P. Giannelis, B. A. Weinstein, M. P. O'Horo, B. N. Ganguly, V. Mehrotra, M. W. Russell, D. R. Huffman, *Science* 257 (1992) 219.
126 A. Biffis (This Book, Chapter 20).
127 M. Kralik, M. Hronec, S. Lora, G. Palma, M. Zecca, A. Biffis, B. Corain, *J. Mol. Catal. A: Chem.* 97 (1995) 145.
128 C. Ramarao, S. V. Ley, S. C. Smith, I. M. Shirley, N. DeAlmeida, *Chem. Commun.* (2002) 1132.
129 A. Primavera, M. Zecca, B. Corain, *J. Mol. Catal. A: Chem.* 108 (1996) 131.
130 B. Corain, M. Zecca, P. Mastrorilli, S. Lora, G. Palma, *Makromol. Chem. Rapid. Commun.* 14 (1993) 799.
131 L. H. Sperling, *CHEMTECH* 18 (1988) 104.
132 H. Bönnemann K. S. Nagabhushana (This Book, Chapter 2).
133 H. Hirai, Y. Nakao, N. Toshima, *Chem. Lett.* 7 (1978) 545.
134 H. Hirai, *J. Macromol. Sci. Chem.* A13 (1979) 633.
135 H. Hirai, H. Chawanya, N. Toshima, *React. Polym.* 3 (1985) 127.
136 H. Hirai, H. Wakabayashi, M. Komiyama, *Bull. Chem. Soc. Jpn.* 59 (1986) 545.
137 Y. Nakao, K. Kaeriyama, *J. Colloid. Interface Sci.* 131 (1989) 186.
138 G. Vitulli, M. Bernini, S. Bertozzi, E. Pitzalis, P. Salvadori, S. Coluccia, G. Martra, *Chem. Mater.* 14 (2002) 1183.
139 G. Marconi, P. Pertici, C. Evangelisti, A. M. Caporusso, G. Vitulli, G. Capannelli, H. Hoang, T. W. Turney, *J. Organomet. Chem.* 689 (2004) 639.
140 U. Kunz, A. Kirschning, H. Wen, W. Solodenko, R. Cecilia, C. O. Kappe, T. Turek, *Catal. Today* 105 (2005) 318.
141 A. Kirschning, C. Altwicker, G. Dräger, J. Harders, N. Hoffmann, U. Hoffmann, H. Schönfeld, W. Solodenko, U. Kunz, *Angew. Chem. Int. Ed.* 40 (2001) 3995.
142 A. Biffis, M. Zecca, M. Basato, *J. Mol. Catal. A: Chem.* 173 (2001) 249.
143 N. T. S. Phan, M. Van Der Sluys, C. W. Jones, *Adv. Synth. Catal.* 348 (2006) 609.
144 J. G. de Vries, *Dalton Trans.* (2006) 421.
145 C. H. Satterfield, *Heterogeneous Catalysis in Industrial Pratice*. 2nd ed., McGraw-Hill, New York, 1991.
146 A. G. Ogston, *Trans. Faraday Soc.* 54 (1958) 1754.
147 L. Nicodemo, L. Nicolais, *Polymer* 15 (1974) 589.
148 B. Corain, M. Zecca, C. Corvaja, G. Palma, S. Lora, K. Jeràbek in R. H. Baney, L. R. Gilliom, S. Hirano, H. K. Schmidt (eds.) *Submicron Multiphase Materials: Symposium Held April 28–30, 1992*, San Francisco, CA, USA, Materials Research Society, 1992, 103.
149 K. W. Pepper, D. Reichenberg, D. K. Hale, *J. Chem. Soc.* (1952) 3129.
150 A. Biffis, B. Corain, Z. Cvengrosova, M. Hronec, K. Jeràbek, M. Králik, *Appl. Catal. A: General* 142 (1996) 327.
151 K. Jeràbek, *Polymer* 27 (1986) 971.
152 P. T. Callaghan, *Principles of Nucelar Magnetic Resonance Microscopy*, Oxford University Press, New York, 1991.
153 L. Johansson, C. Elvingson, J. J.-E. Löfroth, *Macromolecules* 24 (1991) 6024.
154 P. Gallezot, D. Richard, *Catal. Rev. Sci. Eng.* 40 (1998) 81.
155 A. M. Barton, *Chem. Rev.* 75 (1975) 731.
156 E. A. Grulke in J. Brandrup, E. H. Immergut (eds.) *Polymer Handbook*, 3rd ed., Wiley, New York, 1989.
157 H. Nagahara, M. Kohishi, European patent 220525 (1986 to Asahi Chem. Ind.).
158 H. Nagahara, M. Kohishi, Japan patent 6281332 (1986 to Asahi Chem. Ind.).
159 R. Nakao, H. Rhee, Y. Uozumi, *Org. Lett.* 7 (2005) 163.
160 Y. Uozumi, Y. Nakai, *Org. Lett.* 4 (2002) 2997.
161 L. Wang, B. He, *React. Polym.* 12 (1990) 45.
162 A. A. D'Archivio, L. Galantini, A. Biffis, K. Jerábek, B. Corain, *Chem. Eur. J.* 6 (2000) 794.
163 R. A. Sheldon, H. van Bekkum (eds.) *Fine Chemicals Through Heterogeneous Catalysis*, Wiley-VCH, Weinheim, 2001.
164 T. Lin, D. Chung, J. Chang, *Ind. Eng. Chem. Res.* 38 (1999) 1271.
165 T. Mallat, A. Baiker, *Chem. Rev.* 104 (2004) 3037.
166 Y. M. A. Yamada, T. Arakawa, H. Hocke, Y. Uozumi, *Angew. Chem. Int. Ed.* 46 (2007) 704.
167 J. Tsuji, *Palladium Reagents and Catalysts: New Perspectives for the 21st Century*, Wiley-VCH, Weinheim, 2004.
168 M. T. Reetz, E. Westermann, *Angew. Chem. Int. Ed.* 39 (2000) 165.
169 A. Biffis, M. Zecca, M. Basato, *Eur. J. Inorg. Chem.* (2001) 1131.
170 S. S. Pröckl, W. Kleist, M. A. Gruber, K. Köhler, *Angew. Chem. Int. Ed.* 43 (2004) 1881.
171 K. Yu, W. Sommer, J. M. Richardson, M. Weck, C. W. Jones, *Adv. Synth. Catal.* 347 (2005) 161.
172 S. Klingelhöfer, W. Heitz, A. Greiner, S. Oestreich, S. Förster, M. Antonietti, *J. Am. Chem. Soc.* 119 (1997) 10116.

CHAPTER 11

Digestive Ripening, or "Nanomachining," to Achieve Nanocrystal Size Control

Kenneth J. Klabunde[1], Christopher M. Sorensen[2], Savka I. Stoeva[3], Bagavatula L.V. Prasad[4], Alexander B. Smetana[5], and Xiao-Min Lin[6]

[1]*Department of Chemistry, Kansas State University, 111 Willard Hall, Manhattan, KS 66506-3701, USA*
[2]*Department of Physics, Kansas State University, 116 Cardwell Hall, 1700 Anderson Avenue Manhattan, KS 66506-2601, USA*
[3]*Department of Chemistry, Northwestern University, 2145 Sheridan Road, Evanston, IL 60208-3113, USA*
[4]*National Chemical Laboratory, Dr. Homi Bhabha Road, Pune 411 008, India*
[5]*University of Idaho, Moscow, ID 83844, USA and the Wright-Patterson Air Force Base, Dayton, OH 45433-5543, USA*
[6]*Chemistry Division and Center for Nanoscale Materials, Argonne National Laboratory, 9700 South Cass Avenue, Argonne, IL 60439-4831, USA*

1. Introduction

The art of creating monodispersed colloids has been in existence for more than a century since the pioneering work by Faraday on gold sol [1]. During the middle part of the last century, La Mer and their colleagues utilized the "growth by diffusion" method to prepare highly monodispersed sulfur sol which showed high-order Tyndall spectra in the visible scattered light from these solutions [2,3]. It was, however, not until two decades ago that the issue of controlling particle size in colloidal suspension became the central focus of colloidal chemistry. This was largely due to the discovery of size-dependent physical properties in small nanoparticles. It is now well established that when the size of the materials becomes smaller than some relevant physical length scale, the properties of the materials deviate dramatically from their bulk properties. For instance, the absorption and photoluminescence of semiconductor quantum dots have a strong size dependence [4,5]; also, charge injection onto a single nanoparticle needs to overcome Coulomb charging energy, which scales with the particle size [6,7]; and the switching of magnetic moment in magnetic nanoparticles is related to both the anisotropy of the materials and the particle volume [8]. Using nanoparticles as catalysis in many chemical reactions can greatly enhance the global reaction kinetics [9]. Except for a few cases that utilize a single nanoparticle as a functional device, most applications of nanoparticles require a large ensemble of nanoparticles, thus the monodispersity of the sample becomes an important factor that controls whether the size-dependent properties from single nanoparticles is maintained at the macroscopic level.

The basic principle of chemical synthesis of nanoparticles is to initiate chemical reactions and control the nucleation and growth of the reaction products. In order to achieve monodispersity, LaMer has shown that the separation of the nucleation stage from the growth stage is an important factor to be considered (Figure 1).

When the monomer concentration of the reaction product increases beyond the nucleation threshold, nuclei begin to form in the solution. This process quickly consumes the monomer concentration, and decreases its value below the nucleation threshold. In the following growth stage, no new nucleation sites are created, and the particle growth is controlled by diffusion of monomers to the existing nuclei. When the concentration of the monomer reaches the particle solubility threshold, the particle can no longer grow through the diffusion of monomers. The evolution of the colloids beyond this point is determined by the surface energy of the particles. If the gain through the surface energy is much larger than the entropy loss, then the particles can further grow through Ostwald ripening or the coalescence process, both of which lead to spreading of particle-size distribution.

Following La Mer's concept, one obvious experimental strategy to create monodispersed colloids is to induce a short burst of nucleation events, followed by the process to maintain the monomer concentration in the growth by diffusion region or quench the reaction completely. For instance, high-temperature thermal decomposition of organometallic compounds has been widely adopted to synthesize particles with high crystallinity and monodispersity. Using trioctylphosphine oxide (TOPO) as a surface ligand, Dinega et al. showed that the decomposition of $Co_2(CO)_8$ yielded nanoparticles with the ε-phase,

Metal Nanoclusters in Catalysis and Materials Science: The Issue of Size Control
Edited by B. Corain, G. Schmid and N. Toshima

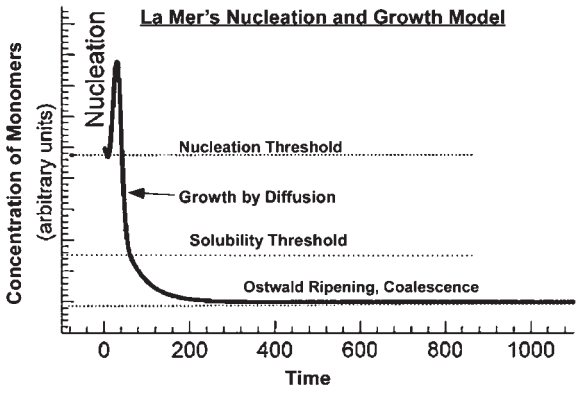

Figure 1. Nucleation and growth pathway of nanoparticles in a typical chemical reaction.

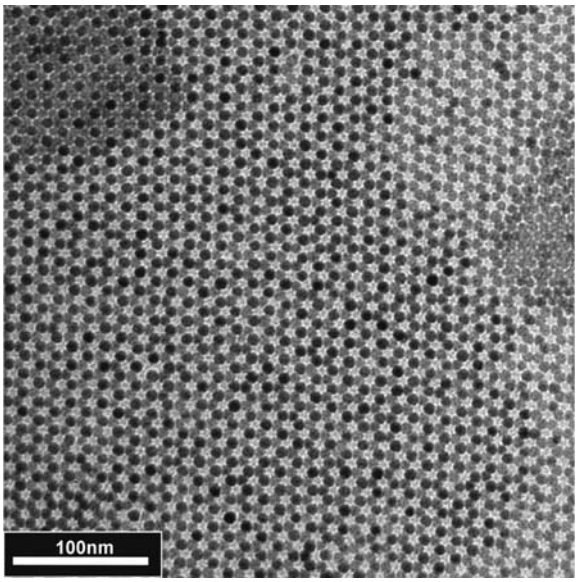

Figure 2. Co-nanocrystals synthesized using high-temperature thermal decomposition technique using thermal OA and TOPO as ligands.

a distorted face-centered cubic (fcc) structure that is absent in bulk cobalt [10]. Monodispersed cobalt nanoparticles were obtained by using both oleic acid (OA) and TOPO as ligands in 1,2-dichlorobenzene (Figure 2) [11].

Similarly, the thermal decomposition of iron pentacarbonyl, $Fe(CO)_5$, produced iron nanoparticles using TOPO as a solvent. Subsequent oxidation by a chemical reagent led to the formation of monodispersed maghemite nanoparticles [12]. The extraordinary control of particle-size distribution within 1 nm was recently demonstrated using an iron–oleate complex as precursor [13,14]. Simultaneous decomposition of metal carbonyl with the reduction of metal salt at high temperature leads to bimetallic alloy particles, such as FePt and CoPt nanoparticles. Because of the high coercivity of their corresponding L10 phase, these bimetallic nanoparticles are being actively investigated for potential magnetic storage applications. Growth of monodispersed II–VI semiconductor nanocrystals was achieved by rapid injection of metal–organic precursors into a vigorously stirred flask containing a hot coordinating solvent, such as long-chain alkylphosphines R_3P, alkylphosphine oxides R_3PO or alkylamines [15]. The high reaction temperature (>150–350 °C) of these reactions facilitates the removal of crystalline defects and results in high-quality magnetic nanoparticles. However, the toxicity of the solvents, ligands, and precursors used in these types of syntheses might limit their applications to a certain extent [16].

Another way to limit Ostwald ripening and coalescence process, which are the primary reasons for inducing polydispersity, is to carry out the chemical reactions within a confined environment. Microemulsion-based syntheses belong to this category. A microemulsion is a thermodynamically stable dispersion of two relatively immiscible liquids stabilized by surfactant molecules [17]. Depending on relative concentrations, surfactant molecules self-assemble into a variety of structures in the solvent mixture, such as micelles, bilayers, and vesicles. Most commonly used structures in nanoparticle synthesis are micelles, either as reverse (water-in-oil) or normal (oil-in-water) form. In both cases, the dispersed phase consists of monodispersed droplets in the size range of 2–100 nm. This dispersed phase provides a confined environment for synthesizing nanoscale particles [18,19]. Early pioneering work by Boutonnet et al. showed that microemulsions of water/cetyltrimethylammonium bromide (CTAB)/octanol and water/pentaethyleneglycol dodecyl ether/hexane can be used to dissolve metal ions, and subsequently be reduced by hydrogen or hydrazine, resulting in the formation of monodispersed Pt, Pd, Rh, and Ir nanoparticles [20]. Borohydride reduction of cobalt chloride in water/didodecyldimethyl ammonium bromide (DDAB)/toluene results in the formation of Co nanoparticles [21–23]. Another micelle system that has been widely used in nanoparticle synthesis consists of water/sodium *bis* (2-ethylhexyl) sulfosuccinate(AOT)/alkane. The water droplets formed by AOT in alkane have a small degree of polydispersity, and the micelle size can be controlled by the composition ratio w(= [water]/[AOT]) [24]. Pileni et al. have used AOT micelles to synthesize a variety of transition metal particles, including, Cu, Co [25,26]. O'Connor et al. also used AOT micelles to synthesize a series of ferrite particles, MFe_2O_4; (M = Co; Mn; Fe) [27]. These microemulsion-based syntheses are easy to perform at relatively low temperatures, but they suffer from the disadvantage that the particles are typically less crystalline and more polydispersed because of the slow nucleation rate.

Despite the successful developments of many syntheses mentioned above, the control of particle size remains empirical in many cases. A key issue that remains to be understood more deeply is what role the surfactant and ligand molecules play in these syntheses. It is commonly believed that micelle size controls the particle size to some extent [18]. However, many surfactants are only weakly bound to the surface of the nanoparticles and particle can grow much larger than the size of the micelle. In organometallic-based synthesis, a typical strategy is to utilize a pair of ligands that have different binding affinities [11]. A tightly binding ligand will favor slow growth, while a

weakly coordinating ligand will promote rapid growth. By adjusting the ratio of these two types of ligands, the nanoparticle size can be regulated. Nevertheless, the detailed mechanism of the ligand effects in these syntheses remains unclear. An interesting question to ask is whether strongly binding ligands can affect particle size through a thermodynamic pathway, rather than through a kinetic process. Experimentally, the evidence that ligand molecules play a much more active role in controlling particle formation, possibly through a thermodynamic pathway, came from experiments on gold–dodecanethiol nanoparticles colloid. In these systems, we discovered a digestive ripening process in which a highly polydispersed colloids evolved into a much more monodispersed system upon heating with excess ligand molecules [28–32]. This process occurs through the breakdown of large particles and the growth of small particles, until a stable-size region is reached. This is in sharp contrast with Ostwald ripening in which the growth of particle is always favored due to lowering of surface energy. We have since observed the narrowing of particle-size dispersion with several different types of ligands and other transition metals. In this chapter, we will review some of our experimental data, along with the discussion regarding the possible mechanism behind this new ripening process.

2. Synthesis Strategy

2.1. The Concept of Digestive Ripening

As we begin the discussion of digestive ripening, it is important to point out that nanoparticles are unusually reactive. Nanoparticles are often polycrystalline with several crystal interfaces/particle [32]. They also can have unusual surface morphologies during and after growth, with high surface concentrations of defect sites, edges, and corners [33]. In addition, of course, a collection of nanoparticles possesses high surface area. All of these features lead to a special "nanochemistry," meaning that certain ligands can bind strongly to their surfaces.

This brings us to the concept of digestive ripening or what could be termed "nanomachining," which, briefly, is the heating or refluxing of a solution of nanoparticles in the presence of an excess of surface-active ligand. Now, it is thermodynamically possible that some ligands could remove an atom from the nanoparticle, or a collection of ligands could remove a cluster of atoms from the nanoparticle surface. These ligand–atom or ligand–cluster adducts could then move to another nanoparticle and deposit them, thereby setting up a dynamic situation where atoms/clusters are being shuttled around from one particle to the next. This concept is similar to what solvents do as molecular crystals slowly grow and transform into perfect single crystals, for example, growth of perfect sugar crystals or quartz crystals. In such processes, the key to success is always choice of solvent, concentration, temperature, time, etc. It is the same with digestive ripening. The choice of ligand, solvent, concentration, temperature, and time are all crucial to success.

Let us now consider the theoretical aspects of such a process.

2.2. A Possible Explanation of Why Digestive Ripening Occurs

Digestive ripening is enigmatic because a broad distribution of particle sizes becomes narrow by both small particles becoming bigger and large particles becoming smaller to achieve an equilibrium size. Well-known Ostwald ripening involves only the latter, viz. small particles become bigger, and unlike digestive ripening, no equilibrium size is achieved. The particles grow forever in Ostwald ripening.

Ostwald ripening is driven by the positive surface energy, the specific, per gram amount of which can be lessened with particle growth. The change in Gibbs free energy when a particle forms is composed of two terms, a bulk term and a surface term as

$$\Delta G = \frac{4\pi}{3} r^3 n(\mu_p - \mu_s) + 4\pi r^2 \sigma \tag{1}$$

In Equation (1) we assume particles are spherical with radius r. The chemical potentials are μ_p and μ_s for the particle and the solvated atoms or molecules, respectively, n is the number of moles per unit volume and σ is the surface energy (or tension). Since the particle has formed, we can take the bulk term as negative with $\Delta\mu = \mu_p - \mu_s < 0$ hence favorable, but formation of the surface costs energy so is positive and unfavorable. These two functionalities yield a maximum in ΔG. Differentiation of Equation (1) finds this maximum to be at a critical size r_c given by

$$r_c = \frac{2\sigma}{n|\Delta\mu|} \tag{2}$$

Beyond this critical size, the particles grow at the expense of particles less than the critical size. This can be seen graphically in Figure 3 where ΔG is plotted versus size r (surface + bulk, dot dash curve).

Particles less than r_c slide down the potential hill to zero and particles greater than r_c slide down the other side of the potential hill and grow. It is important to realize

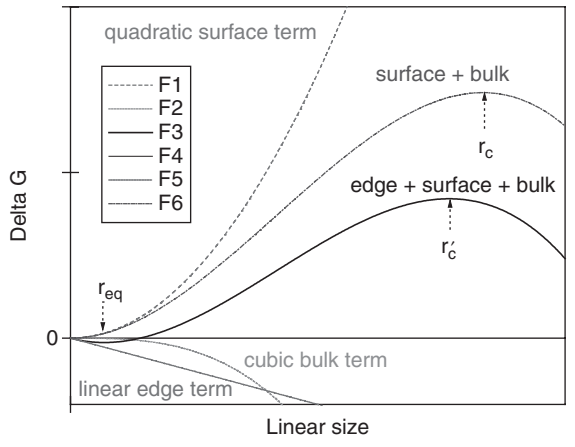

Figure 3. Change in Gibbs free energy upon formation of a nanoparticle from solvated atoms.

that Equation (1) can yield no intermediate equilibrium size.

How then does digestive ripening yield an equilibrium size with big particles getting smaller and small particles getting bigger? A proposal generically similar to the well-known Equation (1) is to include another size-dependent term but with yet a different functionality. A realistic description of the particle is not as a sphere but as some solid polygonal structure with atoms in four different sites: bulk, surface, edge, and corner. These sites have dimensionalities of 3, 2, 1, and 0, respectively. Hence we generalize Equation (1) as

$$\Delta G = a_3 r^3 + a_2 r^2 + a_1 r + a_0 \tag{3}$$

Having no functionality with size, the constant corner site term is not important and can be set to zero (recall potential energies are relative), i.e., $a_0 = 0$. The edge term $a_1 r$, however, can play a significant role. In Figure 1 we have included a negative linear-edge term and represent Equation (3) as a solid black line. Since the linear term has the lowest power functionality, it will dominate the free energy at small size. The next power is the positive surface term with quadratic functionality. As the size grows this term takes over and leaves a minimum in the free-energy curve. This minimum implies an equilibrium size given by

$$r_{\mathrm{eq}} = \frac{(a_2 - \sqrt{a_2^2 - 3a_1 a_3})}{3a_3}. \tag{4}$$

At large size the cubic bulk term finally dominates and suggests that the system would still grow without bound if particles could pass the modified critical size r_c'; this is Ostwald ripening.

The advantage of the explanations of Equation (3) is its simplicity. It seems certain that the bulk (r^3) and surface (r^2) terms exist. The simplest way to get a minimum in ΔG is to include the linear term. The problem with this explanation is that it leaves us with the question why would edge sites have negative hence favorable energies when face sites have positive, disfavorable energies? We do not know. We do know, however, that the system with surface-adsorbed ligands is complex. Perhaps that complexity can lead to such an unexpected consequence.

3. Results

As discussed above, the digestive ripening technique is a simple, yet efficient route to convert polydispersed nanoparticles into highly monodispersed ones by refluxing the colloidal solution in the presence of an excess stabilizing ligand. In this section, we describe the applicability of the digestive ripening method for the synthesis of colloids composed of particles with a narrow-size distribution. We provide examples for the preparation of colloids composed of metals (Au, Ag, and Cu).

3.1. Gold

Gold nanoparticles with a narrow-size distribution can be prepared by two, completely different, synthetic routes,

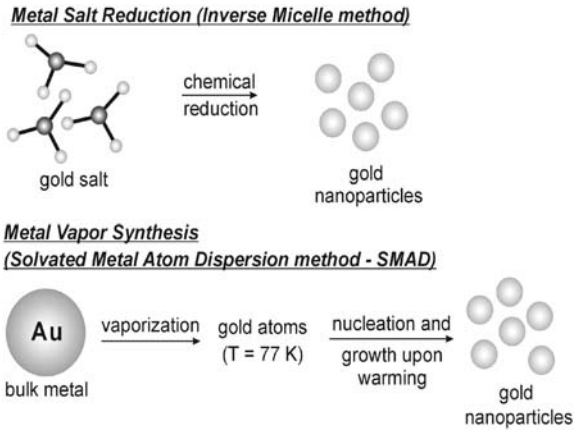

Figure 4. Different synthetic routes used for preparation of gold nanoparticles. (Reprinted with permission from Ref. [30], © 2003, American Chemical Society.)

both using the digestive ripening process to achieve nanoparticles highly uniform in size and shape (Figure 4).

In both cases, the Au nanoparticles behave as molecular crystals in respect that they can be dissolved, precipitated, and redispersed in solvents without change in properties. The first method is based on a reduction process carried out in an inverse micelle system. The second synthetic route involves vaporization of a metal under vacuum and co-deposition of the atoms with the vapors of a solvent on the walls of a reactor cooled to liquid nitrogen temperature (77 K). Nucleation and growth of the nanoparticles take place during the warm-up stage. This procedure is known as the solvated metal atom dispersion (SMAD) method.

3.1.1. Inverse Micelle Method

A major characteristic of inverse micelle systems is their ability to solubilize water and other polar or ionic compounds (e.g., metal salts), which are not soluble or slightly soluble in non-polar solvents [34]. The solubilization ability of inverse micelles makes them excellent systems for many applications. Inverse micelles and microemulsions are used respectively as ''nanoreactors'' and ''microreactors'' for drug encapsulation, biomolecule solubilization, and as model systems of a variety of bioprocesses such as cell membrane functions and enzyme catalysis [34–36]. These constrained structures are also widely applied as templates for preparation of nanoparticles [37,38]. Inverse micelles, however, are not rigid but dynamic systems that exchange surfactant molecules at a microsecond rate with one another and with individual monomer surfactant molecules in solution [34,38]. The compounds dissolved in the micellar core also undergo rapid exchange upon collisions of micelles. This inherent property of inverse micelles has an important effect on the size distribution of nanoparticles prepared in such systems. The particles are generally with broad-size distribution and extensive size-selective procedures are applied to obtain particles with relatively narrow size distribution ($\sigma \sim 10$–15%) [38,39]. In some embodiments, the initial

particles are further stabilized by surface passivation with a suitable capping agent [39–41].

Another strategy for synthesis of ligand-stabilized nanoparticles uses a two-phase system, initially proposed for the preparation of dodecanethiol-stabilized gold particles [42–46]. The important point is that the capping ligand is present in the system (dissolved into the organic phase) before the reduction starts. The role of the surfactant (usually alkylammonium salt) is to transfer the metal ions (dissolved into the aqueous medium) through the phase boundary where the reduction process takes place. The particles synthesized in this manner are often called monolayer-protected clusters (MPC) and can be repeatedly isolated from the solvent and redispersed without considerable aggregation. However, the initial particle-size distribution is broad and further manipulation procedures are needed to obtain particles with σ less than 10%.

Our group at Kansas State University has discovered a unique protocol for manipulating the size and morphology of gold nanoparticles after they are already prepared [28–32,47–49]. The phenomena are induced by specific types of molecules interacting with the gold nanoparticles: (1) molecules (ligands) that have functional groups with a strong affinity for adsorption on gold surfaces with the formation of relatively strong bonds, such as alkanethiols (RSH), and (2) positively charged quaternary alkylammonium surfactants such as DDAB. Significantly, it was demonstrated that the morphology and dimensions of the gold nanoparticles could be reversibly controlled in solvent at room temperature or reflux depending upon the relative ratio of alkanethiol to DDAB [32].

The major synthetic steps for the preparation of Au colloids by the chemical reduction method are presented in Figure 5.

First, polyhedral-shaped Au nanoparticles (Figure 6A) are synthesized by sodium borohydride reduction of $AuCl_3$ dissolved in toluene in the presence of DDAB (step 1).

In a typical reaction, 0.034 g of $AuCl_3$ (99.99%) is dissolved by sonication (20 min) in 10 mL 0.02 M solution of DDAB (Fluka) in toluene (freshly degassed) under an argon atmosphere, resulting in a dark-orange solution. Reduction of the gold salt is carried out by the dropwise addition of 40 μL of freshly prepared 9.3 M $NaBH_4$ (Aldrich) aqueous solution. Dark-purple Au colloid composed of particles with various shapes and sizes forms at the end of the process (Figure 6A). The ''as-prepared'' Au particles are highly defective and thus amenable to break up upon the addition of RSH at room temperature (typically $n(RSH)/n(Au) = 30{:}1$ molar ratio). The reason for the polydispersity of the particles is the inherent dynamic nature of the inverse micelles as discussed above. The addition of alkanethiol at ambient conditions to the as-prepared Au colloid (step 2) induces drastic changes in the size and morphology of the nanoparticles. The large polyhedral gold particles, initially present into the system, are no longer found in the colloids. Instead, the polyhedral particles are broken apart by the alkanethiols (Section 4 describes the same effect with ligands with

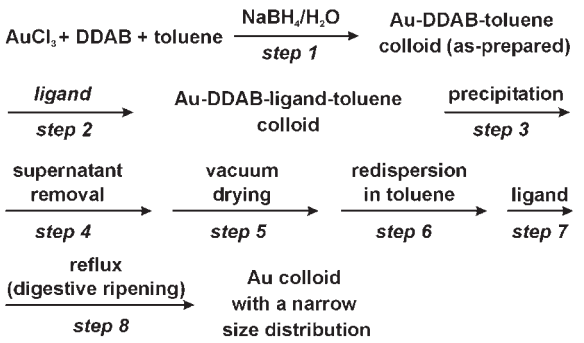

Figure 5. Synthetic steps for preparation of monodispersed Au nanoparticles by the inverse micelle method and digestive ripening.

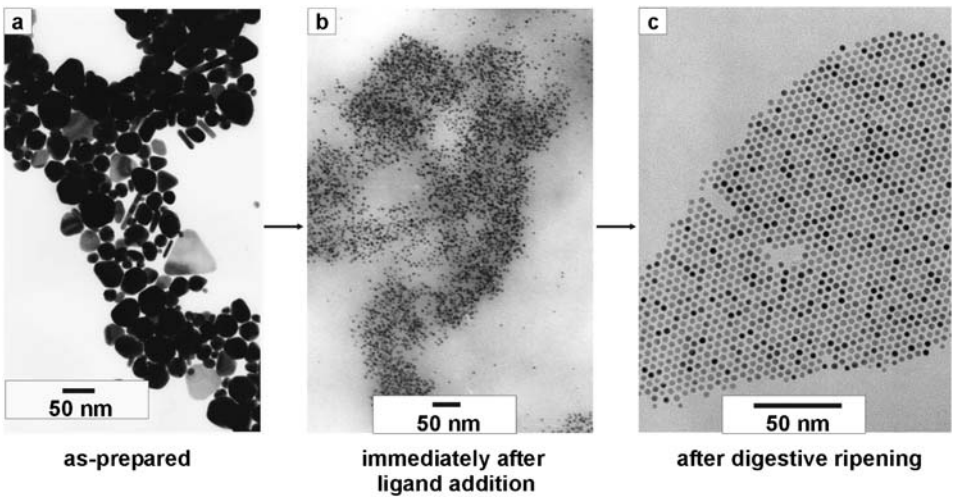

Figure 6. TEM micrographs representing the transformations of (a) polydispersed nanoparticles upon (b) alkanethiol addition at room temperature and (c) after digestive ripening (inverse micelle system). (Reprinted with permission from Ref. [49], © 2002, American Chemical Society.)

other functional groups) to small spherical particles with sizes varying from 2 to 6 nm. Figure 6B is a representative TEM micrograph of the small particles formed after alkanethiol injection to the as-prepared colloid. This phenomenon is particularly interesting and deserves attention since the entire process takes place at ambient conditions and practically immediately after the ligand is introduced into the system. Initially, these small, spherical particles are not monodispersed, but upon purification (steps 3–7), followed by reflux (digestive ripening) for 90 min under an argon atmosphere (step 8), monodispersed nanoparticles with an average diameter of 5 nm form, which are the stable products under the given conditions (Figure 6C) [50].

3.1.2. SMAD Method

The digestive ripening method is particularly advantageous in large-scale syntheses where the traditional size-selective procedures are difficult to be implemented. The SMAD technique allows synthesis of large amounts of colloidal solutions and obviates the need for some purification procedures. The SMAD method was initially used as a very efficient method to produce highly dispersed metal nanoparticles in an active form [51]. Such materials turned out to be extremely active in many catalytic schemes due to the high degree of dispersion and the lack of stabilizing ligands on their surface [52]. In this respect, the SMAD method provides the unique possibility to synthesize materials in a nanoparticulate form without ligand protection (so-called ''naked'' particles) dispersed in various solvents. Such materials are not monodispersed but they could be very beneficial not only for catalytic applications, as well as for studying chemical reactivities of metal surfaces [53]. We have developed a greatly modified SMAD process which utilizes a novel combination of solvents and stabilizing ligands, at controlled times and temperatures. The modified SMAD method in combination with the digestive ripening procedure allow the preparation of gram quantities of ligand-stabilized gold nanoparticles with a narrow-size distribution in nonaqueous [29] and aqueous solvents [54].

The major synthetic steps for the preparation of nonaqueous Au colloids by the SMAD method are presented in Figure 7.

The SMAD process is carried out under dynamic vacuum (4×10^{-3} Torr) in a stationary reactor submerged in liquid nitrogen [29,51,54]. First, dodecanethiol (8 mL) and toluene (40 mL) are frozen at the bottom of the reactor. Next, elemental Au (0.2–0.4 g) is evaporated and co-deposited with acetone vapors (100 mL) on the walls of the vessel. After the process is complete, the liquid nitrogen Dewar is removed and the deep-red colored Au–acetone matrix is allowed to warm. Upon melting, the Au–acetone matrix mixes with toluene and dodecanethiol and the color of the colloidal solution becomes deep brown. Agitation is typically commenced for ~45 min. The Au–acetone–toluene–thiol solution is siphoned into a Schlenk tube. The as-prepared Au–acetone–toluene–thiol colloid is composed of particles with sizes ranging from 5 to 40 nm with no definite geometrical shapes (Figure 8A).

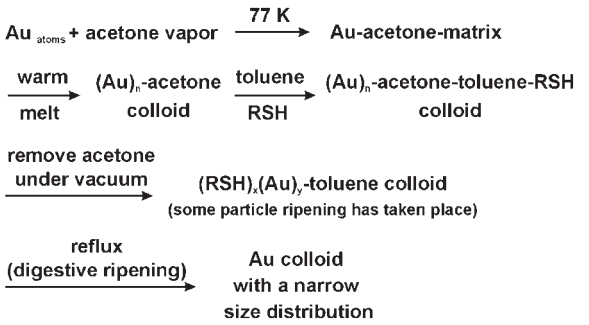

Figure 7. Synthetic steps for preparation of monodispersed gold nanoparticles by the SMAD method and digestive ripening. (Reprinted with permission from Ref. [29], © 2002, American Chemical Society.)

Next, the acetone is evaporated under vacuum and the resulting Au–toluene–thiol colloid is characterized by a drastic change of the size and shape of the particles. Nearly spherical particles with sizes in the range of 1 to 6 nm are dominant suggesting that some ripening has already taken place, presumably due to the strong adsorption of dodecanethiol molecules on their surface (Figure 8B). There are also a small number of remnant larger particles (10–40 nm). The colloid is then refluxed (digestively ripened) for 90 min under argon atmosphere. The digestive ripening process is the key step for obtaining monodispersed thiol-protected Au nanoparticles. The final colloidal solution contains high-quality Au nanoparticles stabilized by dodecanethiol with an average diameter of 4.5 nm (Figure 8C).

3.1.3. Nanocrystal Superlattice Formation

The Au nanoparticles obtained by the inverse micelle and SMAD methods can be used as ''building blocks'' for the formation of ordered nanoparticle arrays with properties of both fundamental and practical interest [15,55,56]. Digestively ripened Au nanoparticles have a strong tendency toward superlattice formation due to the uniformity in size and shape of the nanoparticles present in both systems. Nanocrystal superlattices are formed by a deposition of Au colloidal solution on a support at ambient conditions. Depending on the density of the colloidal droplet and evaporation kinetics, both two-dimensional (2D) and 3D superlattices can be formed. Superlattices composed of Au nanoparticles prepared by the two methods were extensively characterized by transmission electron microscopy (TEM), high resolution transmission electron microscopy (HRTEM), atomic force microscopy (AFM), X-ray diffraction (XRD), and electron diffraction [30,57]. In some cases, the superlattices took on fcc structures (Figure 9), while in other instances, hexagonal close packed (hcp) structures formed (Figure 10).

3.2. Silver

With the groundwork of digestive ripening laid out by the investigations of gold nanoparticles, the need arose to

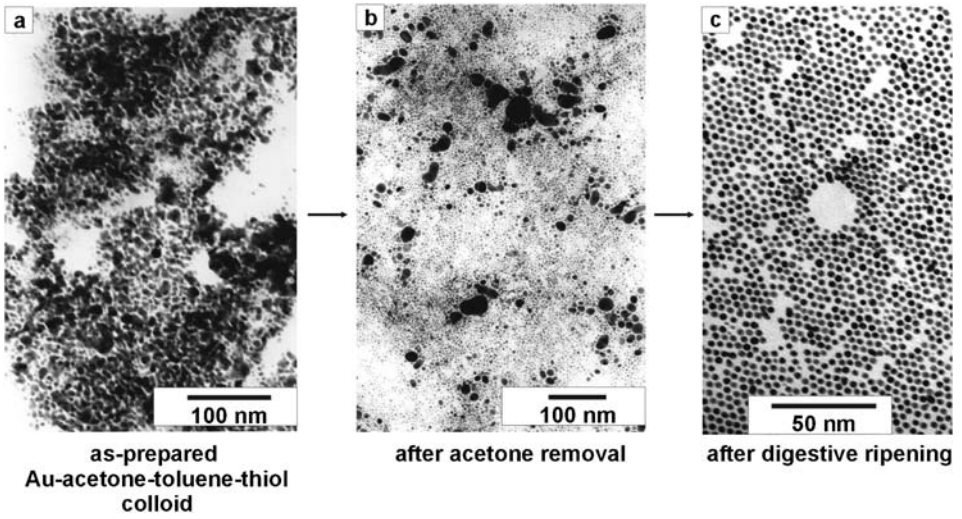

Figure 8. TEM micrographs representing the Au nanoparticles at different stages of the synthetic process (SMAD system). (Reprinted with permission from Ref. [29], © 2002, American Chemical Society.)

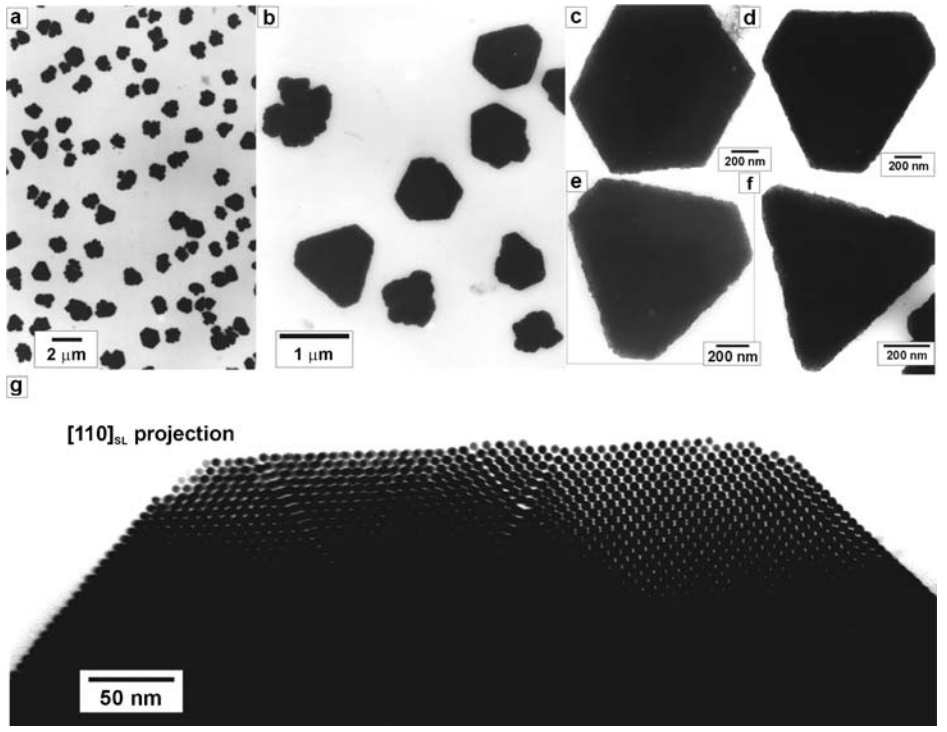

Figure 9. TEM micrographs of nanocrystal superlattices of Au nanoparticles prepared by the inverse micelle method and digestive ripening. (a) and (b) low-magnification images; (c)–(f) regularly-shaped nanocrystal superlattices; (g) magnified image of a superlattice edge. Note the perfect arrangement of the Au nanoparticles. (Reprinted with permission from Ref. [30], © 2003, American Chemical Society.)

determine if digestive ripening could be extended to create nanoparticles of different elements. To accomplish this, silver was chosen as the most logical candidate as it is chemically similar to gold, and few experimental changes should be needed to achieve success. The reagent polydispersed silver particles were created via the SMAD method described above. This synthetic route creates a colloid of nanoparticles of typically 0.2 g of silver metal dispersed in an environment of toluene and do-decanethiol. The concentration of the metal in the

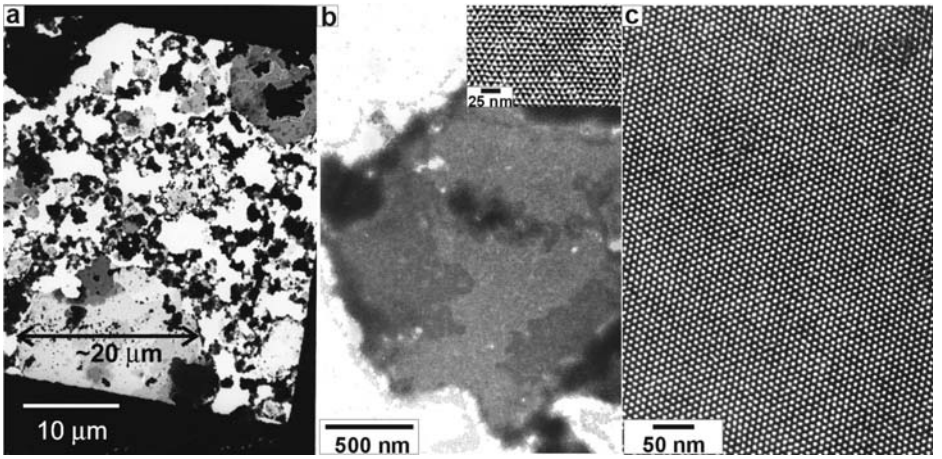

Figure 10. TEM micrographs of hcp nanocrystal superlattices of Au nanoparticles prepared by the SMAD method. (a) low-magnification image; (b) and (c) magnified images. The inset in (b) demonstrates the triangular shape contrast typical for hcp ordering. Note the perfect particle arrangement in (c). (Reprinted with permission from Ref. [30], © 2003, American Chemical Society.)

solvent was approximately 0.027 mol/L. The amount of dodecanethiol to metal atoms is a 20:1 ratio providing a large excess of ligand in solution in addition to those bonded to the surface of the particles [58].

This initial colloid is never exposed to air and all procedures are conducted under argon to protect the particles from reaction with air, which prevents complete digestion. Digestive ripening is carried out in a glass Schlenk tube fitted with a rubber septum. Through the septum, argon is passed over the reaction and out through an oil bubbler. The Schlenk tube is chosen such that it is large enough for reflux to occur inside without significant loss of solvent. The polydispersed nanoparticle mixture is then heated to the boiling point of the solvent until equilibrium is reached and the particle size is uniform. This can be determined partially through taking aliquots of colloid, dilute, and observe the UV–Vis spectrum. If the surface plasmon resonance peak stabilizes in respect to peak position and width, the digestive ripening process is most likely complete. Final characterization should be done with an electron microscope. The particle transformation to a monodispersed silver colloid is shown in Figures 11 and 12.

In an attempt to create particles with different sizes and properties, ligands other than dodecanethiol were used to create polydispersed colloids from the SMAD method. Thus, dodecylamine, trioctyl phosphine, and dodecyl alcohol were used in addition to dodecanethiol. The results of these studies led to nearly monodispersed stable colloids for the phosphine protected particles at 6.3 nm in diameter (Figure 13).

A minority of the dodecylamine particles was found to be monodispersed at the enlarged size of 14 nm in diameter (Figure 14).

Further experimentation may lead to a homogeneous sample; however, it does appear that the amine head group does not have as strong an affinity for the silver atoms as the mercapto group. The dodecyl alcohol ligand was a poor ligand for creation of silver particles and only large particles were produced that were either too unreactive to undergo digestive ripening or the ligand was not effective enough to facilitate the atom transfer between particles.

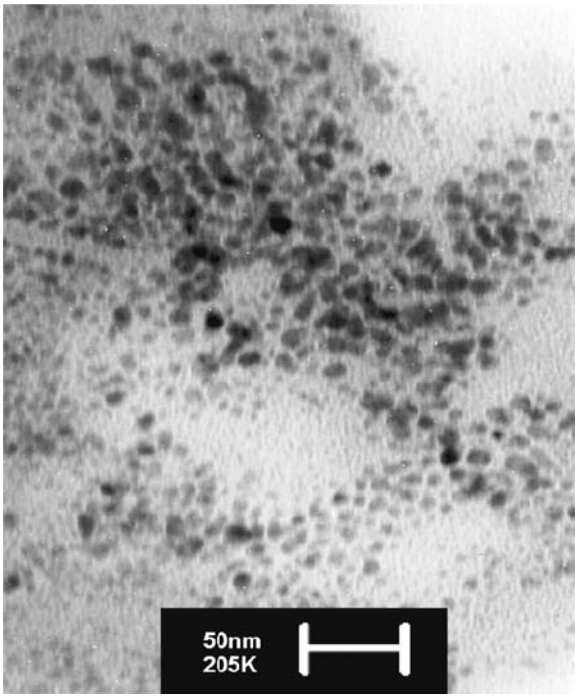

Figure 11. TEM of SMAD prepared Ag nanoparticles before digestive ripening.

A testament to the lower reactivity of silver compared to gold in digestive ripening is the longer reaction times. For the same concentration of material, it takes several hours to completely ripen the colloid. This may have a lot to do with the greater size of the initial particles provided by the SMAD, compared with gold. In order to

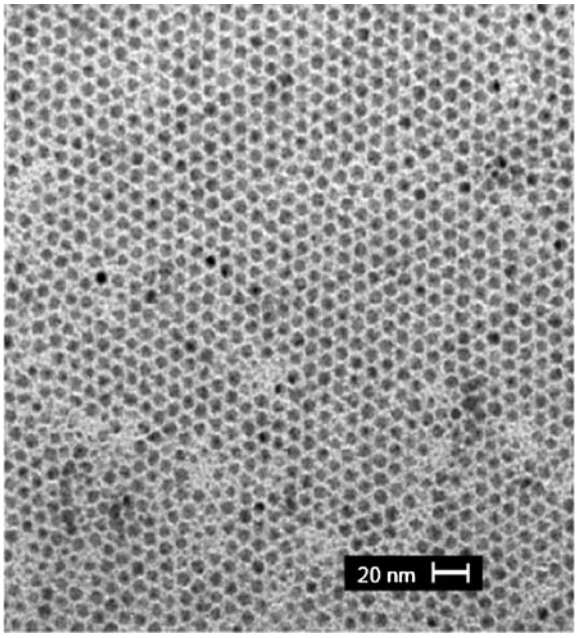

Figure 12. TEM micrograph of the Ag colloid in Figure 11 after digestive ripening.

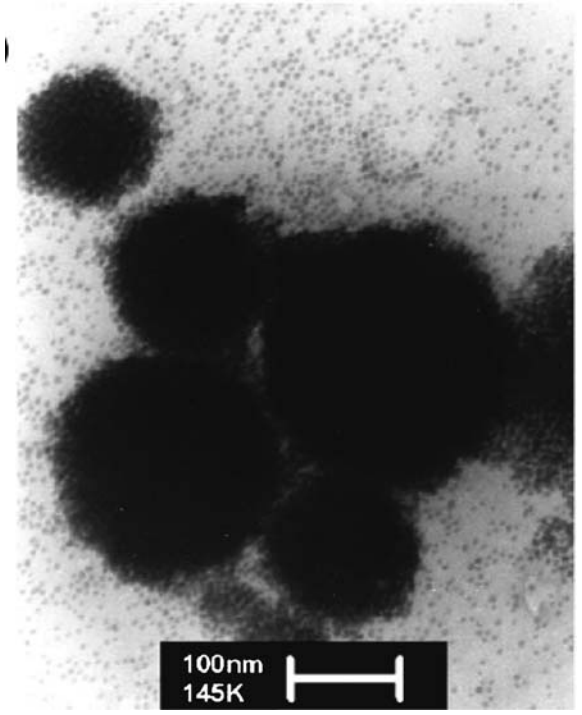

Figure 13. TEM micrograph of trioctyl phosphine (TOP)-stabilized Ag nanoparticles.

decrease the time necessary for digestive ripening of silver, 4-*tert*-butyl-toluene was often used as a solvent instead of toluene. Though chemically similar, the boiling point for 4-*tert*-butyl-toluene is at 198 °C compared to 120 °C for toluene [58].

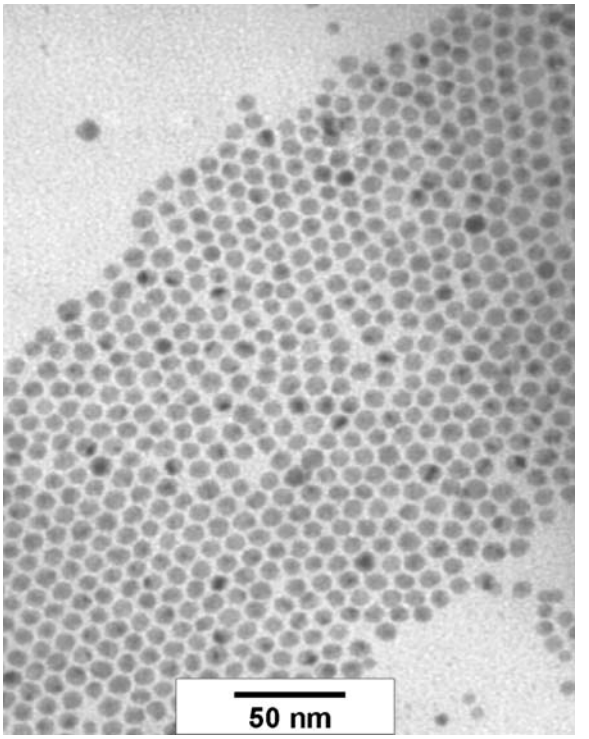

Figure 14. TEM micrograph of dodecylamine-stabilized Ag nanoparticles.

3.3. Digestive Ripening as a Route to Create Alloy Nanoparticles: Silver–Gold and Copper–Gold [59]

Having shown that digestive ripening is amenable to other elements on the periodic table the question was raised as to what would happen if two elementally *different* colloids were mixed and both subjected to digestive ripening simultaneously. If atoms were interchanging between particles of two different but chemically similar metals, alloy formation could take place. The experimental conditions to this procedure are identical to that discussed above. Equimolar amounts of gold and silver colloids were introduced into a single Schlenk tube under an argon atmosphere. Each separate metal colloid was composed of particles previously digestively ripened such that the particle-size distribution was narrow, and the ratio of metal to dodecanethiol was in a ratio of 1:20 in each case. The solvent of choice was initially 4-*tert*-butyl-toluene to ensure a reasonable time scale for the reaction. The progress of the digestive ripening was once again followed in situ via UV–Vis spectroscopy but this time with dramatic results (Figure 15).

The separate particles of silver and gold display their own distinct plasmon peaks at 420 and 520 nm, respectively at the beginning of the reaction. As digestive ripening proceeds, the two peaks slowly converge with the end result being the complete disappearance of the initial plasmon peaks from separate metal particles and the formation of a new plasmon peak of a value intermediate of the two. This peak is consistent with alloy particles from other research groups and theoretical modeling. The

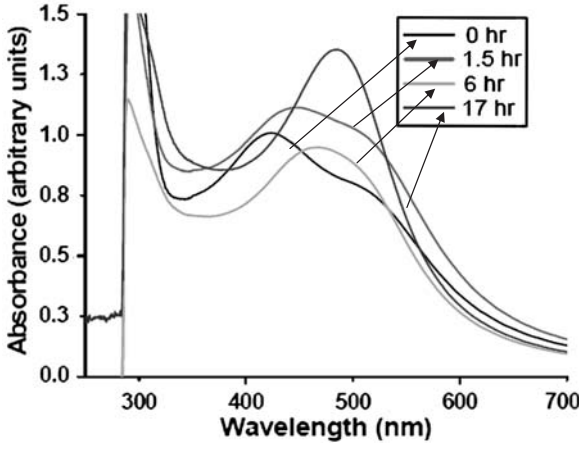

Figure 15. Ag/Au alloy formation by digestive ripening of Au and Ag monodispersed particles followed by UV–Vis. (Reprinted with permission from Ref. [59], © 2006, American Chemical Society.)

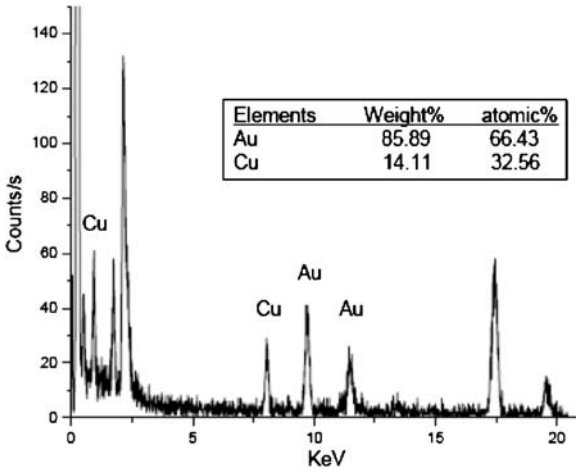

Figure 16. EDX spectrum of a single Cu/Au alloy particle. (Reprinted with permission from Ref. [59], © 2006, American Chemical Society.)

spectral mapping of the progress of the reaction is displayed below.

Remarkably the position of the final plasmon peak of the alloy particles is dependent on the molar ratio of gold to silver nanoparticles. When the ratio is shifted favoring either metal, an alloy of any desired composition can be formed. This alloying phenomenon indicates that it is possible for true tuneability of the properties of a set of nanoparticles.

The alloying process through digestive ripening was tested for its versatility by attempting to alloy copper and gold particles. UV–Vis spectra do not show as stark a distinction between reagents and products since the copper nanoparticles do not have a strong plasmon absorbance. The final product does show a significant red shift of the original gold plasmon peak denoting metallic mixing within the particles. To confirm the presence of intermetallic particles an EDX spectrum was obtained of a single particle isolated on a grid in an HRTEM microscope. Peaks from each element are clearly represented in the particle as shown in Figure 16.

Now given an experimental tool to track the progress of digestive ripening, studies were conducted to determine the effects of temperature and concentration on the reaction time. With respect to temperature, using dioctyl ether as a solvent, the digestive ripening temperature was increased to 300 °C. This reduced the reaction time to 30 min from 17 h at 200 °C. The alloying reaction was attempted at 100 °C, but despite some conversion of the gold and silver plasmon peaks, a final narrow peak could not be obtained. This information suggests that some atomic diffusion must take place in each individual particle and is most likely the limiting step in the alloying process. If the temperature of reaction is too low, the atoms do not have sufficient energy to migrate to the center of the particles. In similar conditions alloying has been observed at 300 °C between gold and copper in a solid state from nanoparticles in close proximity where interparticle diffusion was shown to be the primary mechanism of transfer. In a similar manner, concentrations of 10%, 100%, and 300% were tested at 200 °C to observe the effects of concentration on digestive ripening. The reaction time was 35, 17, and 3 h, respectively.

We postulate that if a naturally stable alloy exists for a particle, it could be achieved from its precursors under the right conditions from digestive ripening [59].

3.4. Copper

Copper, being more chemically reactive than gold or silver, does undergo digestive ripening [60], but with the formation of a layer of oxidized metal, probably Cu^{+}. Thus, thiol-stabilized copper nanoparticles, after digestive ripening, do not exhibit the expected plasmon absorption, apparently due to this oxidized layer. However, the particles are quite monodispersed and form large, beautiful superlattices.

3.5. Digestive Ripening of Binuclear Systems, Such As CdSe

There are promising results for certain binuclear systems, such as CdSe [61]. The choice of ligand, temperature, and time will be crucial in achieving complete success, and not simply Ostwald ripening. It is certainly possible that many nanoparticle–ligand systems could be amenable to achieving large amounts of monodispersed ligated particles by digestive ripening.

4. A Case History: Gold With Varying Ligands

After demonstrating the utility of the ''digestive ripening'' process using dodecanethiol for obtaining monodispersed gold nanoparticles prepared by different procedures [29,47], the suitability of different ligands (thiols with varying chain lengths and ligands with different head groups than thiol) for this procedure was contemplated. This assumed significance for many reasons: (i) There

were not many procedures available for obtaining monodispersed gold nanoparticles using ligands other than thiols, (ii) the diversity in the ligand molecules available with other functional groups such as amines and phosphines could make the monodispersed nanoparticles capped by them as attractive candidates for varying applications, and (iii) the digestive ripening procedure offers a simple route where the desired ligand can be added at a later stage of the colloid preparation and avoids size-selective precipitation, thus allowing a procedure for producing monodispersed systems on a large synthetic scale. With this premise, various ligands were considered that could be used as digestive ripening agents for gold colloids prepared by the reverse micelle route described previously. Based on the knowledge available with dodecanethiol, we started looking at thiols with varying chain lengths and functional groups that can be derived from elements close to the sulfur group in the periodic table. Thus the final ligands chosen were thiols (with alkane chain lengths $C_8H_{17}SH$ abbreviated as C_8-, $C_{10}H_{21}SH$:C_{10}-, $C_{12}H_{25}SH$:C_{12}-, and $C_{16}H_{33}SH$:C_{16}-), amines ($C_{12}H_{25}SH$:C_{12}-), phosphines ($(C_8H_{17})_3P$), alcohols ($C_{12}H_{25}OH$: $C_{12}OH$), halides ($C_{12}H_{25}Br$ and $C_{12}H_{25}I$:$C_{12}X$), silanes ($C_{18}H_{37}SiH_3$), and simple alkanes ($C_{10}H_{22}$). The experimental procedure for the digestive ripening process with different ligands is detailed below.

4.1. Experimental Procedure

To facilitate a smooth discussion we split the experimental part to three steps (Figure 17):

4.1.1. First Step

The first step involves the addition of the chosen ligand to the as-prepared colloid. The as-prepared colloid itself is obtained by reducing the metal salt solution (34 mg $AuCl_3$ and 105 mg of DDAB in 10 mL toluene) under vigorous stirring by dropwise addition of 36 μL of 9.4 M aqueous $NaBH_4$ [31]. It was observed that the original orange-red DDAB–$AuCl_3$–toluene solution turned very dark bluish-red within a few minutes, indicating the formation of gold nanoparticles. Then the ligands to be tested for digestive ripening were added to this colloidal dispersion by keeping the molar ratio of Au:ligand as 1:30. The as-prepared nanoparticles obtained with DDAB were largely prismatic in shape with a varied size range of 5–200 nm (Figure 6A). It was observed that mere addition of ligand itself (at room temperature) brings about dramatic changes in the size and shape of gold nanoparticles. Except for simple alkanes, all the other ligands listed above seem to result in breaking of the particles leading to largely spherical particles of narrower size distribution than those we started with (Figures 18 and 19) [31].

Careful TEM analyses (with alkane thiols) clearly showed that the big prismatic particles are indeed broken into small particles (Figure 20) upon ligand addition [32].

Since only simple alkanes are not able to bring about this size change, it can be concluded that all of those ligands, which possess a functional head group are capable of breaking the bigger particles to smaller ones. The fact that excess ligand is being used (Au:ligand ratio as 1:30) and that tetra-alkyl ammonium bromides are not very good capping/stabilizing agents, could be the possible reasons for the changes observed here.

There are two questions that needed to be answered here. (1) How can the ligand access the interiors of big prismatic particles to lead to the smaller particles? and (2) Why do the ligands lead to smaller particles at all? While it is difficult to conclusively find answers to both the questions, the first step in the digestive ripening procedure offers some leads. (1) The big prismatic particles obtained by the reverse micelle-based synthesis are loaded with defects such as twinning boundaries and stacking faults.

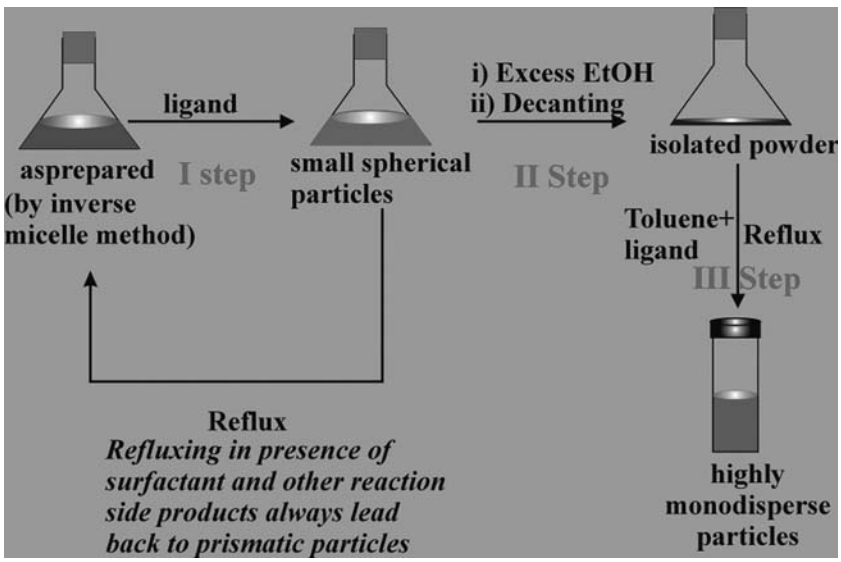

Figure 17. Different steps involved in the digestive ripening procedure of colloids prepared by the inverse micelle method.

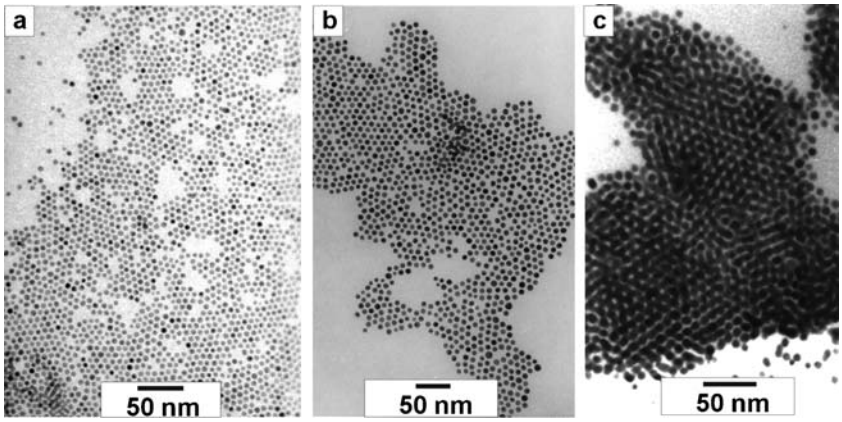

Figure 18. TEM micrographs of Au nanoparticles prepared by the inverse micelle method stabilized by (a) TOP, (b) dodecylamine, and (c) octadecylsilane after digestive ripening.

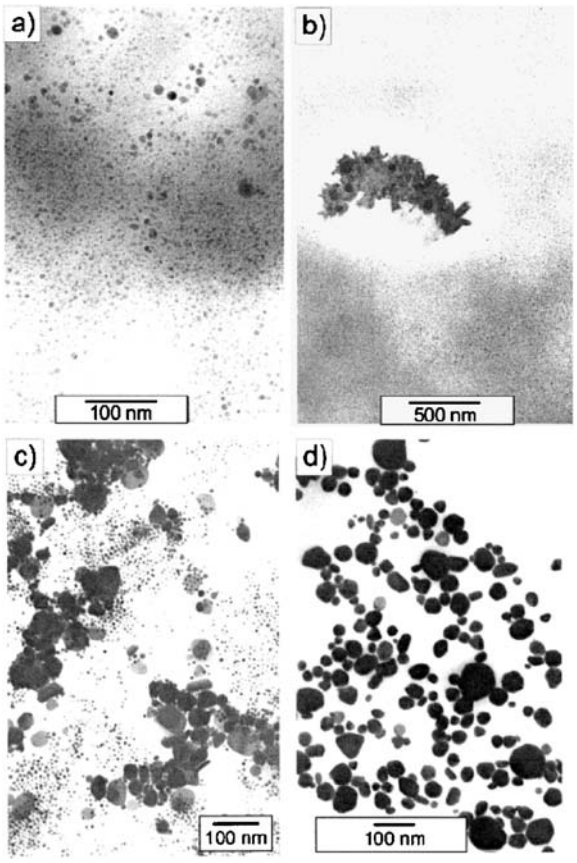

Figure 19. TEM images of different colloids after additions of unsuccessful digestive ripening ligands. (a) dodecyliodide (b) dodecylbromide (c) dodecylalchohol, and (d) decane. (Reprinted with permission from Ref. [31], © 2003, American Chemical Society.)

These cause great strain at the crystal interfaces providing ample scope for the ligand to attack these sites. The reasons for the stabilization of the smaller particles by these ligands as compared to DDAB could be as follows. Ligand binding to the surface of the nanoparticle is expected to lead to a gain in the chemical binding energy [62]. On the other hand, the nanoparticle surface possesses high surface energy, which they try to minimize by growing to larger sizes. Therefore, there is always a competition between these two and the different ligands used tend to break the big prismatic particles to different extents based on equilibrium between these two competing forces. However, it should be remembered that this still is done at room temperature and hence a true equilibrium may still not have been achieved explaining the polydispersity still observed.

4.1.2. Second Step

The second step involves the removal of the excess initial reagents (like the surfactant and the side products of the reducing agents, etc.) by precipitating the ligand capped Au nanoparticles by adding excess ethanol to it. These points are elaborated in a little more detail further. Here the ligands employed can be classified into two simple categories, unsuccessful digestive ripening agents (alkyl halides, alcohols, and alkanes) and successful digestive ripening agents and (thiols, phosphines, amines, and silanes).

Alkyl halides, alcohols, and alkanes: As mentioned previously, except simple alkanes, all the other ligands used in the study were found to be effective in the first step, i.e., breaking of the largely polydispersed and different-shaped particles into smaller spherical-shaped particles. However, among the ligands that can break up the particles, alkyl halides and alcohols fail in the second step where we try to isolate the ligand-capped nanoparticles by ethanol addition [31]. Probably these ligands are not strongly attached to the Au surface and hence ethanol addition removes them from the surface of nanoparticles making the nanoparticles irreversibly aggregate and therefore not amenable to digestive ripening any further.

4.1.2.1. Thiols, Phosphines, Amines, and Silanes.

With these ligands, ethanol addition clearly gives a precipitate that can be isolated and readily redispersed in toluene or any other non-polar solvent again.

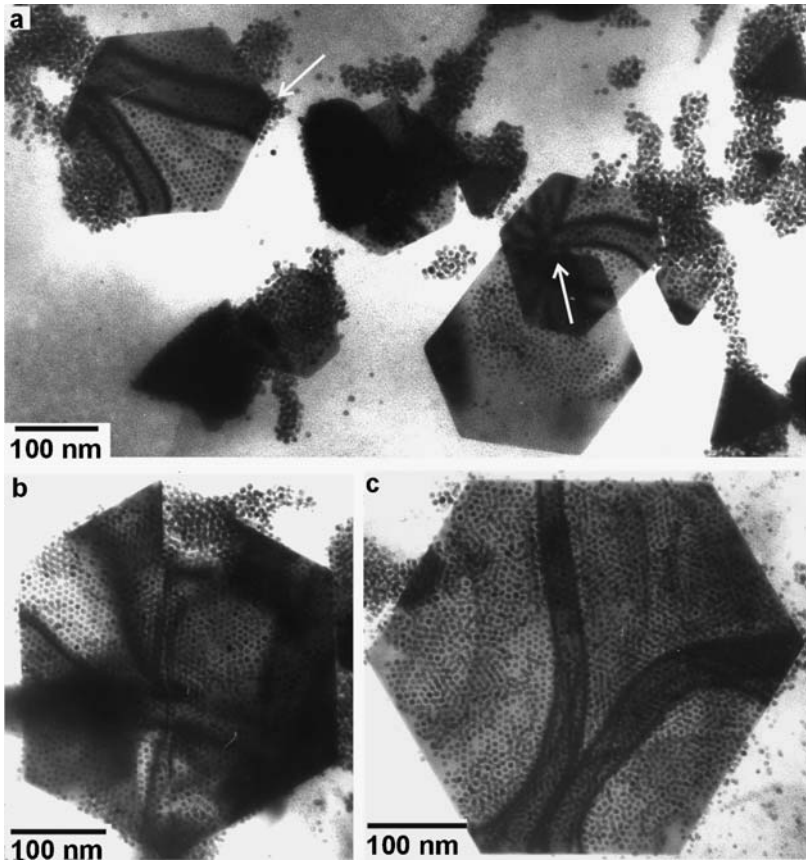

Figure 20. A TEM snapshot of large polyhedral particles prepared by the inverse micelle system being broken by the ligand addition. The ligand featured here is decanethiol. (Reprinted with permission from Ref. [32], © 2005, American Chemical Society.)

4.1.3. Third Step

For the digestive ripening process the isolated precipitate is dried under vacuum and redispersed in toluene with an additional dose of ligand added (in the same Au:ligand = 1:30 ratio). This is subjected to refluxing under argon atmosphere for 1 h to result in a highly monodispersed system. As mentioned previously, mere addition of the ligands tends to break the big prismatic particles to different extents at room temperature. However, the particles are still polydispersed due to the lack of true equilibrium. The refluxing and the availability of excess ligand probably facilitates a true equilibrium state resulting in highly monodispersed nanoparticles.

4.2. Results and Discussion

4.2.1. Thiols with Varying Chain Lengths

When thiols with varying chain lengths, such as C_8-, C_{10}-, C_{12}- and C_{16}- are used, we observe very interesting trends [47]. First, all the colloids under reflux conditions display a strong reddish color. Nanoparticles, especially those of coinage metals like gold and silver, display striking colors in the visible region of the electromagnetic spectrum. These colors arise due to the collective oscillation of the conduction electrons in response to the alternating electric field of the incident electromagnetic radiation and the wavelength at which resonance occurs is termed as the surface plasmon resonance [63]. It is now well established that the position of this surface plasmon resonance depends on size, shape, and the proximity of the nanoparticles to each other [64]. After digestive ripening with different thiols, when the dispersion is cooled to room temperature, interesting changes in the optical properties are observed (Figure 21).

In the case of C_8- thiol all the nanoparticles precipitate to the bottom of the vial with the supernatant not showing any color. C_{10}- and C_{12}- thiol cases also indicate the formation of a precipitate while the supernatant still displays the characteristic color of gold nanoparticles. No precipitation is observed in C_{16}- case and the colloid retains the initial strong reddish color. The UV–Vis spectra as obtained for different colloids capped with varying alkyl chain lengths are shown in Figure 21. It should be noted here that there is not great variation in the average particle size and increases from 4.5 to 5.5 nm as the digestive ripening agent is changed from C_8- to C_{16}- though the optical properties display great variation. As can be seen, both the nanoparticle dispersions digestively ripened

with C_8- and C_{10}- thiols display a peak around 530 nm characteristic of the gold nanoparticles along with a strong absorbance in the near infra red region above 700 nm. The strong absorbance in this region is attributed to the aggregation of colloid, which is corroborated by the observation that these two systems show precipitation when the colloid is cooled to room temperature from reflux conditions. The C_{12}- digestively ripened colloid shows a small shoulder at 640 nm along with the 530 nm peak. This feature is also attributed to the aggregation of nanoparticles and is supported by the precipitation we observed. In the C_{16}- case, no extra peak other than the surface plasmon resonance is seen and indeed no precipitation in this case is obtained indicating that the nanoparticles are quite independent from each other in solution. While the optical properties and the precipitation observed could even come from random aggregates of nanoparticles, TEM images (Figure 22) unequivocally show that in case of digestive ripening fairly well-ordered aggregates of nanoparticles are obtained [49].

As expected from the visual observations and as suggested by optical properties, the C_8- digestively ripened colloid shows only ordered 3D superlattices (Figure 22A) of nanoparticles all over the TEM grid. As indicated, the supernatant here is colorless pointing to the fact that all the nanoparticles are indeed participating in the superstructures.

In the case of C_{10}- and C_{12}- thiols, many superlattices are observed along (Figure 22B and C) with few individual particles arranged in hexagonal order probably during the drying process on the grid. On the other hand, the C_{16}- thiol displays (Figure 22D) only 2D-ordered structures on the grid. In this case, the nanoparticles are independent from each other in solution. The nanoparticles come together again while the solution is dried on the grid leading to the 2D structures observed. Actually, these features may qualitatively be explained by determining the dispersive (van der Waals) potential between two nanoparticles of radii R_A and R_B at the distance of closest approach D by invoking the direct pairwise summation over atomic dispersional attractions proportional to $-1/R$ [65].

Thus, we see that the digestive ripening process leads to highly monodispersed nanoparticles that can come together to form ordered superstructures similar to atoms or molecules that form crystals from a supersaturated solution. Then if the superstructure formation can indeed be related to atomic/molecular crystallization, it should also be possible to make these supercrystals more soluble in the solvent with a change of temperature. Indeed, the optical spectra of the three colloids prepared by the different thiols discussed above exhibit only the gold plasmon band at 80 °C suggesting the solubilization of these "superlattices" at the elevated temperatures [49].

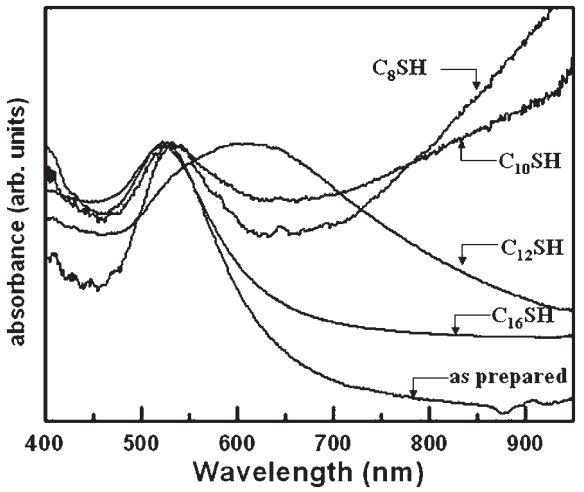

Figure 21. Room-temperature optical-absorption spectra of various digestively ripened Au colloids prepared by the inverse-micelle method. For comparison, the spectrum of the as-prepared colloid is also displayed. (Reprinted with permission from Ref. [49], © 2002, American Chemical Society.)

4.2.2. Phosphines and Amines

As observed with thiols, digestive ripening of the gold nanoparticles with amines and phosphines also leads to highly monodispersed colloids [31]. However, the average particle sizes obtained here are 7.2 nm (phosphines) and 8.6 nm (amines), larger than the thiol cases. The trend in the particle sizes obtained (average size varying as $RNH_2 > R_3P > RSH$) cannot be explained conclusively at this moment. However, by invoking semiqualitative theories such as hard-acid soft-base theory, gold or any metal in the zero oxidation state is usually considered a soft acid and interacts well with soft bases. Among the ligands we selected, RSH and R_3P, are listed as soft bases and RNH_2 as a hard base. Thus, RSH and R_3P will have

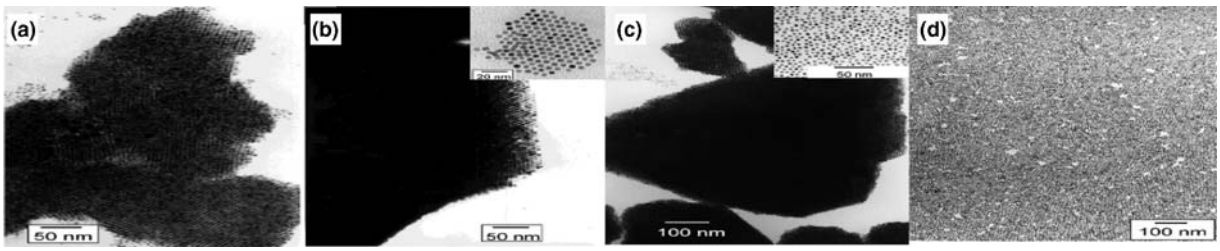

Figure 22. TEM micrographs of digestively ripened Au colloids prepared by the inverse micelle method with (a) octanethiol, (b) decanethiol, (c) dodecanethiol, and (d) hexadecanethiol. (Reprinted with permission from Ref. [49], © 2002, American Chemical Society.)

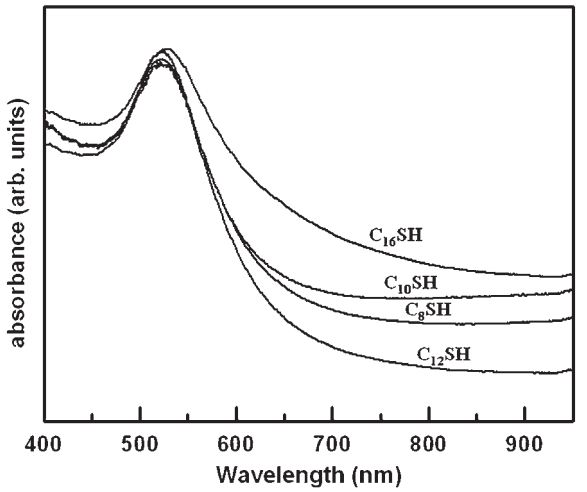

Figure 23. Optical absorption spectra at 80 °C of various digestively ripened Au colloids prepared by the inverse micelle method. (Reprinted with permission from Ref. [49], © 2002, American Chemical Society.)

stronger affinity toward gold while RNH_2 will have a weaker affinity. As explained previously, the stabilization of a particular size of nanoparticles might be controlled by thermodynamics with the free-energy minimum resulting from a combination of a size-dependent surface and edge-site energy. Then the weaker ligand–gold binding energy would stabilize the larger particles and vice versa.

4.2.3. Silanes

Silanes are probably the most surprising digestive ripening agents of all the ligands described so far in the sense that they attach to the gold surfaces in a slightly different manner than the other ligands. It has been reported that silanes of the formula RSiH3 form self-assembled monolayers on the Au(1 1 1) surface by forming weak covalent bonds and, consequently, the Si–H bond becomes very weak [66]. (Indeed, when ethanol was added to the silane-capped gold particles, rapid evolution of hydrogen gas was observed.) These silane-capped gold nanoparticles can then be subjected to digestive ripening under inert atmosphere that lead to monodispersed nanoparticles and even form ordered superstructures (Figure 23).

This reaction needs to be carried out under inert conditions and, in fact, when the reaction was carried out in presence of a little moisture a dramatic formation of nanowires, filaments, and tubes is observed (Figure 24) [67].

The elemental analysis and EDX analysis reveal the chemical composition of the structures to be $C_{18}H_{37}SiO_{1.5}$. It is observed that at the tip of each of these 1D structures, one gold nanoparticle is present. This suggests that gold nanoparticle acts as a catalyst and template for the formation of these nanowires. The following steps discerned below may be involved in the formation of nanowires. First, alkylsilane gets attached to the gold nanoparticle surface losing the three hydrogens and forming three weak Au–Si bonds in the process. The

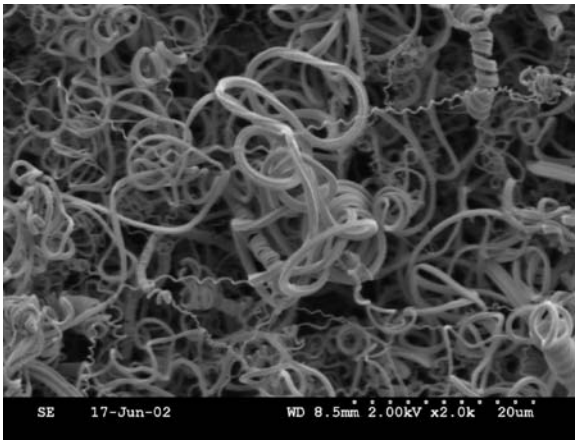

Figure 24. SEM micrograph of siloxane nanowires obtained by the reflux of octadecylsilane with Au nanoparticles in presence of water.

weak Au–Si bonds in presence of moisture lead to the formation of $RSi(OH)_3$ on the surface of the nanoparticle. These $RSi(OH)_3$ subsequently undergo inter-molecular condensation leading to the observed nanostructures.

5. Conclusions

5.1. Advantages

The digestive ripening approach, when it is applicable, allows high-yield syntheses of monodispersed ligand-capped nanocrystals. This is important because so many future applications are going to be dependent on the availability of such materials. In fact, a series of interesting examples regarding self-assembly [68–72], long-range order [73] and binary (such as AB_{13}) superlattices [74,75] have appeared, and these papers show the considerable novelty and promise of such 2D and 3D structures [74–77]. In fact, the digestive ripening process was employed in many of these examples.

5.2. Future Developments

Digestive ripening, or "nanomachining," is dependent on strong ligand–metal (or metal ion) interactions, concentrations, temperatures, time, solvent, and ligand/mixed ligand choices. These variables are a good thing, in the sense that chemists and material scientists have the opportunity to manipulate numerous nanomaterials under a wide variety of conditions. Both aqueous and non-aqueous solvents can be employed, with appropriate ligands. So, the future opportunities are great [78,79].

References

1 M. Faraday, *Philos. Trans. R. Soc. London, Ser. A.* 147 (1857) 145.
2 I. Johnson, V. K. La Mer, *J. Am. Chem. Soc.* 69 (1947) 1184.
3 H. Reiss, *J. Am. Chem. Soc.* 19 (1951) 482.

4 A. P. Alivisatos, *Science* 271 (1996) 933.
5 C. B. Murray, D. J. Norris, M. G. Bawendi, *J. Am. Chem. Soc.* 115 (1993) 8706.
6 W. P. Halperin, *Rev. Mod. Phys.* 58 (1986) 533.
7 M. A. Kastner, *Rev. Mod. Phys.* 64 (1992) 849.
8 B. D. Cullity, *Introduction to Magnetic Materials*, Addison-Wesley, London, 1972.
9 V. Johanek, M. Laurin, A. W. Grant, B. Kasemo, C. R. Henry, J. Libuda, *Science* 304 (2004) 1639.
10 D. P. Dinega, M. G. Bawendi, *Angew. Chem. Int. Ed. Engl.* 38 (1999) 1788.
11 V. F. Puntes, K. M. Krishan, A. P. Alivisatos, *Appl. Phys. Lett.* 78 (2001) 2187.
12 T. Hyeon, S. S. Lee, J. Park, Y. Chung, H. B. Na, *J. Am. Chem. Soc.* 123 (2001) 12798.
13 J. Park, E. Lee, N. M. Hwang, M. Kang, S. C. Kim, Y. Hwang, J. G. Park, H. J. Noh, J. Y. Kim, J. H. Park, T. Hyeon, *Angew.Chem. Int. Ed.* 44 (2005) 2872.
14 J. Park, K. An, Y. Hwang, J. G. Park, H. J. Noh, J. Y. Kim, J. H. Park, N. M. Hwang, T. Hyeon, *Nat. Mater.* 3 (2004) 891.
15 C. B. Murray, C. R. Kagan, M. G. Bawendi, *Annu. Rev. Mater. Sci.* 30 (2000) 545.
16 Z. A. Peng, X. Peng, *J. Am. Chem. Soc.* (2001) 123, 168.
17 J. N. Israelachvili, *Intermolecular and Surface Forces*, Academic Press Ltd., San Diego, 2003.
18 M. P. Pileni, *J. Phys. Chem. B* 105 (2001) 3358.
19 K. Osseo-Asare, F. J. Arriagada, in G. L. Messing, S. Hirano, H. Hausner (eds.) *Ceramic Powder Science*, Vol. 3, American Ceramic Society, Columbus, OH 1990, 3.
20 M. Boutonnet, J. Kizling, P. Stenius, G. Maire, *Colloids Surf.* 5 (1982) 209.
21 G. N. Glavee, K. J. Klabunde, C. M. Sorensen, G. C. Hadjipanayis, *Inorg. Chem.* 32 (1993) 474.
22 X. M. Lin, C. M. Sorensen, K. J. Klabunde, G. C. Hajipanayis, *J. Mater. Res.* 14 (1999) 1542.
23 J. P. Wilcoxon, J. E. Martin, P. Provencio, *Langmuir* 16 (2000) 9912.
24 J. Eastoe, B. H. Robinson, D. C. Steytler, D. Thorn-Lesson, *Adv. Colloid. Interface Sci.* 36 (1991) 1.
25 M. P. Pileni, *Adv. Funct. Mater.* 11 (2001) 323.
26 C. Petit, A. Taleb, M. P. Pileni, *J. Phys. Chem. B* 103 (1999) 1805.
27 C. T. Seip, E. E. Carpenter, C. J. O'Connor, V. T. John, S. Li, *IEEE Trans. Mag.* 34 (1998) 1111.
28 X. M. Lin, C. M. Sorensen, K. J. Klabunde, *J. Nanopart. Res.* 2 (2000) 157.
29 S. I. Stoeva, K. J. Klabunde, C. M. Sorensen, I. Dragieva, *J. Am. Chem. Soc.* 124 (2002) 2305.
30 S. I. Stoeva, B. L. V. Prasad, S. Uma, P. K. Stoimenov, V. Zaikovski, C. M. Sorensen, K. J. Klabunde, *J. Phys. Chem. B* 107 (2003) 7441.
31 B. L. V. Prasad, S. I., Stoeva, C. M. Sorensen, K. J. Klabunde, *Chem. Mater.* 15 (2003) 935.
32 S. I. Stoeva, V. Zaikovski, B. L. V. Prasad, P. K. Stoimenov, C. M. Sorensen, K. J. Klabunde, *Langmuir* 21 (2005) 10280.
33 K. J. Klabunde (ed.) *Nanoscale Materials in Chemistry*, Wiley Interscience, New York, 2001, 1.
34 O. A. El Seoud, Reversed micelles and water-in-oil microemulsions, in W. L. Hinze (ed.) *Organized Assemblies in Chemical Analysis*, Vol. 1, Wiley, New York, NY 1994, 1.
35 J. H. Fendler, in T. F. Yen, R. D. Gilbert, J. H. Fendler (eds.) *Membrane-Mimetic Approach to Nanotechnology in Advances in the Applications of Membrane-Mimetic Chemistry*, Plenum Press, New York, NY 1994, 1.
36 M. P. Pileni, *Cryst. Res. Technol.* 33 (1998) 1155.
37 M. P. Pileni, in J. S. Bradley (ed.) *Colloidal Assemblies Used as Microreactors in Handbook of Surface and Colloid Chemistry*, CRC, Boca Raton, FL 1997, 495.
38 J. S. Bradley, in G. Schmid (ed.) *The Chemistry of Transition Metal Colloids*, Wiley-VCH, Weinheim, 1994, 459.
39 M. P. Pileni, A. Taleb, C. Petit, *J. Dispersion Sci. Technol.* 19 (1998) 185.
40 J. Lin, W. Zhou, C. J. O'Connor, *Mater. Lett.* 49 (2001) 282.
41 J. E. Martin, J. P. Wilcoxon, J. Odinek, P. Provencio, *J. Phys. Chem.* 104 (2000) 9475.
42 M. Brust, M. Walker, D. Bethel, D. J. Schiffrin, R. Whyman, *J. Chem. Soc. Chem. Commun.* (1994) 801.
43 A. C. Templeton, W. P. Wuelfing, R. W. Murray, Acc. Chem. Res. 33 (2000) 27.
44 R. Whetten, J. T. Khoury, M. Alvarez, S Murthy, I. Vezmar, Z. L. Wang, P. W. Stephens, C. L. Cleveland, W. D. Luedtke, U. Landman, *Adv. Mater.* 8 (1996) 428.
45 D. Aherne, S. N. Rao, D. Fitzmaurice, *J. Phys. Chem. B* 103 (1999) 1821.
46 J. R. Heath, C. M. Knobler, D. V. Leff, *J. Phys. Chem. B* 101 (1997) 189.
47 (a) X. M. Lin, G. M. Wang, C. M. Sorensen, K. J. Klabunde, *J. Phys. Chem. B* 103 (1999) 5488; (b) X. M. Lin, H. M. Jaeger, C. M. Sorensen, K. J. Klabunde, *J. Phys. Chem. B* 105 (2001) 3353.
48 X. M. Lin, C. M. Sorensen, K. J. Klabunde, *Chem. Mater.* 11 (1999) 198.
49 B. L. V. Prasad, S. I. Stoeva, C. M. Sorensen, K. J. Klabunde, *Langmuir* 18 (2002) 7515.
50 The effect of the alkanethiol chain length upon the size of the nanoparticles after the digestive ripening procedure is discussed in reference 49.
51 M. Franklin, K. J. Klabunde, in K. S. Suslick (ed.) High-Energy Processes in Organometallic Chemistry, *ACS Symposium Series*, 1987, 246.
52 K. J. Klabunde, Y. Li, B. Tan, *Chem. Mater.* 3 (1991) 30.
53 Y. Imizu, K. J. Klabunde, *Inorg. Chem.* 23 (1984) 3602.
54 S. I. Stoeva, A. B. Smetana, C. M. Sorensen, K. J. Klabunde, to be published.
55 C. P. Collier, T. Vossmeyer, J. R. Heath, *Annu. Rev. Phys. Chem.* 49 (1998) 371 and references therein.
56 A. L. Rogach, D. V. Talapin, E. V. Shevchenko, A. Kornowski, H Weller, *Adv. Funct. Mater.* 12 (2002) 653.
57 P. K. Stoimenov, S. I. Stoeva, B. L. V. Prasad, C. M. Sorensen, K. J. Klabunde, *SPIE Proceedings* 5513 (2004) 174.
58 A. B. Smetana, K. J. Klabunde, C. M. Sorensen, *J. Colloid Int. Sci.* 284 (2005) 521.
59 A. B. Smetana, K. J. Klabunde, C. M. Sorensen, A. A. Ponce, B. Mwale, *J. Phys. Chem. B.* 110 (2006) 2155.
60 A. A. Ponce, A. B. Smetana, S. I. Stoeva, K. J. Klabunde, C. M. Sorensen *Nanostructured and Advanced Materials*, Springer, Netherlands, 2005, 309.
61 S. Cingarapu, D. Heroux, unpublished results.
62 (a) V. Chikan, D. F. Kelley, *J. Phys. Chem. B* 106 (2002) 3794; (b) T. Sugimoto, *Adv. Colloid Interface Sci.* 28 (1987) 65; (c) D. V. Leff, P. C. Ohara, J. R. Heath, W. M. Gelbart, *J. Phys. Chem.* 99 (1995) 7036.
63 (a) S. Link, M. A. El-Sayed, *Annu. Rev. Phys. Chem.* 54 (2003) 331; (b) P. Mulvaney, *Langmuir* 12 (1996) 788; (c) A. Henglein, *J. Phy. Chem.* 97 (1993) 5457.
64 K. L. Kelly, E. Coronado, L. I. Zhao, G. C. Schatz, *J. Phys. Chem. B.* 107 (2003) 668.
65 (a) H. C. Hamaker, *Physica* 4 (1937) 1058; (b) P. C. Ohara, D. V. Leff, J. R. Heath, W. M. Gelbart, *Phys. Rev. Lett.* 75 (1995) 3466.
66 (a) K. T. Nicholson, K. Z. Zhang, M. M. Banaszak Holl, *J. Am. Chem. Soc.* 121 (1999) 3232; (b) T. M. Owens, K. T. Nicholson, M. M. Banaszak Holl, S. Suzer, *J. Am. Chem. Soc.* 124 (2002) 6800; (c) A. Marchenko, N. Katsonis, D. Fichou, C Aubert, M. Malacria, *J. Am. Chem. Soc.* 124 (2002) 9998.

67 B. L. V. Prasad, S. I. Stoeva, C. M. Sorensen, V. Zaikovski, K. J. Klabunde, *J. Am. Chem. Soc.* 125 (2003) 10488.
68 A. Levchenko, C. K. Lee, A. N. Parikh, A. Navrotsky, *Chem. Mater.* 17 (2005) 5428.
69 R. Jin, S. Egusa, N. F. Sherer, *J. Am. Chem. Soc.* 126 (2004) 9900.
70 S W. Kim, J. Park, Y. Jang, Y. Chung, S. Hwang, T. Hyeon, *Nano Lett.* 3 (2003) 1289.
71 B. A. Korgel, S. Fullam, S. Connelly, D. Fitzmaurice, *J. Phys. Chem. B* 102 (1998) 8379.
72 L. O. Brown, J. E. Hutchison, *J. Am. Chem. Soc.* 121 (1999) 882.
73 X. M. Lin, H. M. Jaeger, C. M. Sorensen, K. J. Klabunde, *J. Phys. Chem. B.* 105 (2001) 3353.
74 E. V. Shevchenko, D. V. Talapin, S. O'Brien, C. B. Murray, *J. Am. Chem. Soc.* 127 (2005) 8741.
75 E. V. Shevchenko, D. V. Talapin, N. A. Kotov, S. O'Brien, C. M. Murray, *Nature* 439 (5) (2006) 55.
76 E. V. Shevchenko, D. V. Talapin, C. B. Murray, S. O'Brien, *J. Am. Chem. Soc.* 128 (2006) 3620.
77 B. Rodriguez-Gonzalez, A. Sanchez-Iglesias, M. Giersig, L. M. Liz-Marzan, *Faraday Discuss.* 125 (2004) 133.
78 S. I. Stoeva, J. S. Lee, J. E. Smith, S. T. Rosen, C. A. Mirkin, *J. Am. Chem. Soc.* 128 (2006) 8378.
79 K. J. Klabunde, S. Stoeva, C. M. Sorensen, U.S. Patent 6,502,403 B2, (May 13, 2003).

This page intentionally left blank

METHODOLOGIES

This page intentionally left blank

CHAPTER 12

Gold Nanoparticles: From Preparation to Catalytic Evaluation

Michele Rossi, Cristina Della Pina, Ermelinda Falletta, and Roberto Matarrese

Department CIMA, University of Milano, Milan, Italy

1. Introduction

In the last decade the discovery of the surprising activity of gold, in form of nanometric particles, has opened new horizons for its application in the selective oxidation and high temperature combustion of organic compounds [1–20]. Particular interest has been devoted by researchers of Milan University to the selective oxidation of the alcoholic and aldehydic groups with molecular oxygen, discovering for the first time the use of gold catalysis for liquid-phase oxidation in organic synthesis [1]. According to many different studies, the catalytic activity and selectivity of supported gold depend on the nature of the support and the preparation method [2,3]. Among the various techniques for obtaining supported gold catalysts, co-precipitation [21], deposition–precipitation [22], vapour-phase deposition [23], co-sputtering [24] and impregnation of phosphine complexes or clusters [25,26] have been proposed as methods for preparing active catalysts mainly for CO abatement but also for organic synthesis. In liquid-phase applications, the deposition of colloidal gold (sol) on oxides and activated carbons has been proposed as a suitable method for preparing gold catalysts, the great advantage being the possibility of tuning the particle size in a monomodal-like manner [27,28]. A deep investigation on gold sol preparation was made by Turkevich et al. [29], who proposed a still valid two-step mechanism, consisting of nucleation and growth, for the formation of nanoparticles in the range of 20 nm.

Recently, the pushing demand of gold particles below 10 nm for catalytic purposes has stimulated more oriented studies [5]. For producing stable colloidal dispersions, a metal salt is generally reduced to the zero-oxidation state in the presence of a protecting agent. In fact, during the growth process, we need to stabilize the metal particles at the desired dimension for avoiding agglomeration phenomena, by means of an organic shell which can act both as an electrostatic or steric stabilizer. However, important problems arise when we use common protecting agents. The presence of shielding compounds interferes with subsequent processes, as the formation of metal–support interactions is able to stabilize supported particles. Moreover, the shielding effect of the colloid protectors prevents the contact of metal particles with the reacting molecules, thus avoiding the use of unsupported colloidal particles as a catalytic system [11].

Considering different techniques for producing gold sols, the mentioned Turkevich's reduction by citrate ion provides gold sols with a large mean diameter (ca. 20 nm) and with a wide size distribution. On the contrary, the reduction of a chloroauric solution with tetrakis(hydroxymethyl)phosphonium chloride (THPC)–NaOH system [30], or with sodium borohydride in the presence of various polymeric molecules, like polyvinylalcohol (PVA) and polyvinylpyrrolidone (PVP) [5], represents a more suitable procedure for producing small particles with a narrow distribution. Therefore, the careful choice of the protecting agent is of basic importance for tailoring the morphology and activity of the resulting catalysts [28,31,32] and in this chapter its role in liquid-phase oxidation will be highlighted. The discussion will be focused on the use of a protector, PVA, and a short mention will be given on a new class of protecting agents formed by polyhydroxylated compounds, in particular D-glucose.

As a case history, this chapter will discuss the larger scale preparation of the 1% Au/C catalyst done on request of the World Gold Council (WGC) [33] to be used as a reference catalyst for the scientific community. In order to evaluate the catalysts, tests have been done in the oxidation of ethane-1,2-diol to glycolate, which was historically the first application of gold in liquid-phase oxidation [1], and in the oxidation of D-glucose to sodium D-gluconate, the latter being an industrial intermediate for water-soluble cleansing agents and food additive. Although the current method for glucose oxidation is based on a biochemical transformation, recent developments showed that the gold catalytic route could be a valid alternative to the enzymatic way [11,12,17–20].

Metal Nanoclusters in Catalysis and Materials Science: The Issue of Size Control
Edited by B. Corain, G. Schmid and N. Toshima

2. Synthesis Strategy

The strategy for preparing gold catalysts for liquid-phase oxidation is based on environment friendly and cheap methodologies with the aim to produce 3–5 nm particles, well dispersed on carbon supports, to be applied also to large-scale preparations.

Therefore, water as a solvent, metal gold dissolved in aqua regia ($HAuCl_4$) as the starting material, sodium tetrahydrogenborate as a powerful water-compatible reducing agent and PVA or carbohydrates as biocompatible protecting agents are the basic ingredients for the preparation performed at room temperature and pressure.

Carbon was chosen as a supporting material on the basis of the high performance of the resulting catalyst and also for the easy recovery of gold from the spent material. Correlations among various experimental conditions and the resultant morphology were derived by XRD and TEM analyses, whereas catalytic tests were performed using cheap substrates, as glucose and ethane-1,2-diol (ethylene glycol). Molecular oxygen was used as the oxidant under mild conditions in water solution.

2.1. Experimental

Gold of 99.9999% purity in sponge from Fluka was used. Two types of carbon support, namely Vulcan XC72R from CABOT and X40S from CAMEL (Table 1), were investigated. $NaBH_4$, of purity >96%, and PVA ($M = 10{,}000$ Da) were supplied from Aldrich. Ethylene glycol (99.5% pure), D-glucose monohydrate (99% pure), glycolic acid (99% pure) and δ-gluconolactone (99% pure) from Fluka were used as reagents and reference compounds, without further purification. NaOH (Merck) was 99.9% pure and stored under nitrogen. Volumetric solutions of HCl and HNO_3 (Riedel-de Haen) were used. Gaseous oxygen (SIAD) was 99.99% pure. MilliQ® water obtained by an Academic A-10 Millipore apparatus was used as solvent for all experiments and preparations.

2.2. Gold Sol Preparation

As reported elsewhere [5,28], protected gold sols have been generated by reducing $HAuCl_4$ to Au(0) in the presence of a large synthetic macromolecule, PVA, having a mean molecular weight of 10,000 Da, and D-glucose, a polyhydroxylated natural product.

2.2.1. Hydrogen Tetrachloroaurate Solution

A mother solution of $HAuCl_4$ (10 g/L of Au) was prepared dissolving gold powder (5 g) in aqua regia (100 mL) by gently heating at 40–50 °C under magnetic stirring. After gold dissolution, the liquid phase was evaporated, the solid material dissolved in 10 M HCl (10 mL) and the liquid distilled off. This operation was repeated four times in order to remove HNO_3. Finally, the solid residue was dissolved in H_2O (20 mL) and the liquid evaporated, repeating this operation four times. The resultant solid was then dissolved in water at a total volume of 500 mL (gold solution 1).

2.2.2. PVA Solution

Two grams of PVA (10,000 Da) was dissolved in hot water and diluted to a total volume of 100 mL.

2.2.3. $NaBH_4$ Solution

Fresh solutions were prepared by dissolving 100–200 mg of $NaBH_4$ in 10–20 mL H_2O.

2.2.4. Pre-Treatment of Supporting Materials

Carbon supports, Vulcan XC72R and X40S, were employed just after heating in the air at 350 °C for 2 h and cooling at room temperature.

2.2.5. Gold Sol Preparation: General Procedure

In a 1 L round bottom flask, 5 mL of the mother gold solution 1 (50 mg Au), a variable amount of PVA solution (Tables 2, 4 and 5) or solid D-glucose (Table 3) were dissolved in water to produce the below reported concentrations. Two molar HCl and 2 M NaOH were used for adjusting the pH (Table 4). Under vigorous stirring (40 mm × 7 mm Teflon spinning bar, 1700 rpm) the below indicated amount of $NaBH_4$ solution (Table 5 and Figure 2) was rapidly added at room temperature. Stirring was interrupted a few seconds after $NaBH_4$ addition. The yellow-tea to red dispersions were handled in the air within 30 min.

2.3. Catalyst Preparation

One percent Au/C catalysts were prepared according to the following general procedure: the fresh sol, prepared as

Table 2. Influence of PVA amount on the gold particle dimension.

PVA:Au (wt.%)	0.67	0.20	0.05	0.03	0.02
Particle diameter (nm)	2.4	2.7	2.8	3.2	3.3

[Au] = 100 mg/L; $NaBH_4$/Au = 1. Mean diameter from XRPD.

Table 1. Carbon data-sheet.

Name	Supplier	Origin	Surface area (BET) (m^2/g)	Pore volume (mL/g)	Pore diameter (nm)	S (%)
X40S	Camel	Coconut shell	1300	0.370	0.7–0.9	<0.1
XC72R	Cabot	Naphtha pyrolysis	254	0.192	–	0.5

Table 3. Influence of glucose amounts on the gold nanoparticle dimension.

Glucose:Au (wt.%)	3000	300	70	30	4
Particle diameter (nm)	2.5	2.7	2.6	2.7	8

[Au] = 100 mg/L; $NaBH_4$/Au = 1. Mean diameter from XRPD.

Table 4. Influence of pH on particle dimension and sol stability using PVA as a protecting agent.

Parameters		Particle dimension (nm) on standing		
PH	PVA/Au	t_0	0.5 h	3 h
7.5	0.67	2.4	2.4	2.4
2.8	0.67	3.4	3.6	4.0
2.0	0.67	4.4	4.5	4.8
7.5	0.05	2.8	3.3	4.8
2.8	0.05	5.3	7.2	8.2
2.0	0.05	6.6	8.2	8.4

[Au] = 100 mg/L; $NaBH_4$/Au = 1. Mean diameter from XRPD.

Table 5. Influence of pH on particle dimension and sol stability using glucose as a protecting agent.

Parameters		Particle dimension (nm) on standing		
PH	Glucose/Au (wt.%)	t_0	0.5 h	3 h
6.9	3000	2.5	2.8	3.2
2.8	3000	2.6	2.9	3.0
6.9	300	2.9	3.2	3.4
2.8	300	3.3	3.4	3.6
6.9	30	2.5	3.3	3.8
2.8	30	6.1	6.2	6.3

[Au] = 100 mg/L; $NaBH_4$/Au = 1. Mean diameter from XRPD.

in Section 2.2.5, containing 20 mg of total gold, was transferred into a 300 mL beaker and treated with 2 g of the carbon powder under stirring for 0.5 h. For higher gold loading (Table 8), the procedure was repeated in a larger beaker (2 L) where the gold sols containing 50 mg of Au were treated with the required quantity of XC72R carbon (0.45–4.95 g). The slurry was filtered, the catalyst washed thoroughly with warm water (500 mL, 60 °C) and the catalyst was stored in the wet form (ca. 50%). The adsorption of gold was checked by determining the residual metal in the filtrate. Water content in the catalyst was determined by drying at 150 °C in air for 5 h.

2.4. Analytical Procedures

Gold analysis was performed using a Jobyn Yvon JY24 instrument. Particle size determinations were carried out by the direct images obtained with a HRTEM (JEOL 2000 EX Microscope equipped with polar piece and top entry stage), and by X-ray diffraction analysis on powdered samples, XRPD, using a Rigaku D III-MAX horizontal-scan powder diffractometer with Cu Kα radiation.

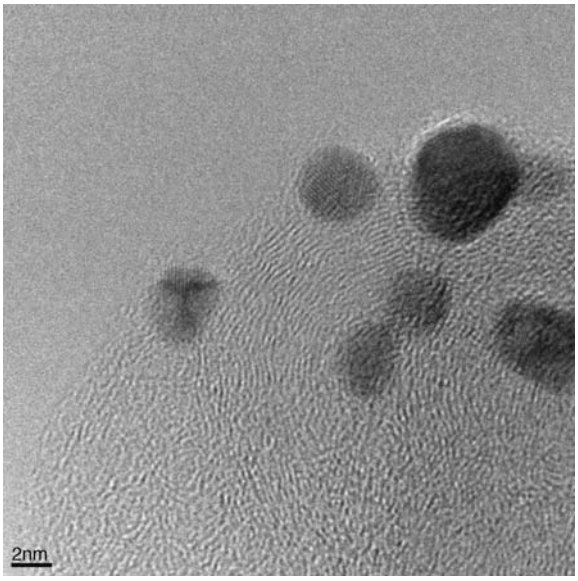

Figure 1. TEM image of 1% Au supported on XC/72R carbon. Bar: 2 nm.

Calculation of the mean diameter was done by means of the Scherrer equation [34] and the atomic percentage of gold at the carbon surface was determined by XPS, M-Probe Instrument (SSI) equipped with a monochromatic Al Kα source (1486.6 eV).

3. Results

3.1. Morphological Aspects

The Vulcan XC72R carbon powder has been chosen as a trap of gold particles owing to the possibility of a high gold loading and the short adsorption time (Section 3.1.6) allowing the particle size determination by TEM or XRD analysis. In order to investigate the effect of carbon adsorption on gold particle dimension, TEM analysis has been performed on a drop of sol evaporated on a copper grid and on the same sol after supporting on carbon: by comparison, almost no difference is detectable in the two cases. Therefore, for the following discussion, we can assume that adsorption on carbon does not alter the dimension of the original nanoparticles at least at low gold loading (1%). Figure 1 shows the spherical images of gold particles supported on carbon.

3.1.1. Influence of the PVA Protecting Agent on Particle Size

The importance of minimizing the quantity of the protecting compounds in the colloid preparation is particularly true when using PVA in large-scale preparations owing to foam formation on stirring, as well as catalytic inhibition of this compound, thus requiring an efficient removal of its residue. Starting from a 100 mg/L Au

concentration and using a fixed $NaBH_4$/Au ratio of 1 (w/w), the ratio PVA/Au has been varied from 0.67 to 0.02 in order to investigate the influence on the dimension of the resultant gold particles (Table 2).

Considering that during the sol preparation, foaming is evident over 10 mg/L of PVA, a good compromise can be reached employing 5 mg/L of PVA, corresponding to PVA/Au = 0.05. In fact, despite the small amount of the protecting agent, the resultant mean particle diameter was still quite low, 2.8 nm.

Under these conditions, PVA-protected dispersions are stable in the air at room temperature at least for 1 h. Particle aggregation has been observed by standing several hours as shown in the next sections.

3.1.2. Influence of the Protecting Agent D-Glucose

Despite the great efficiency of PVA as a stabilizer of gold nanoparticles, the necessity of a thorough washing of the catalyst for its deep elimination has prompted the investigation of possible convenient substitutes. It has been found that polyhydroxylated compounds as sugars, in particular glucose, fructose and sucrose, are suitable compounds for protecting colloidal particles [12]. Moreover, the use of these molecules does not require a careful washing of the catalyst, being sugars compatible with catalytic applications. For the following catalytic evaluation, D-glucose showed a further advantage of being the substrate to be oxidized in one of the model reactions. Therefore, a study on the influence of different amounts of glucose employed in the synthesis of colloidal gold is here discussed.

From the data of Table 3 it is evident how glucose acts as a protector of gold particles on a different scale with respect to PVA. In fact, a large quantity of this sugar, in the order of grams per litre, is needed for stabilizing the 2–3 nm gold particles. However, considering the low cost and the compatibility in catalytic application, glucose could represent an acceptable choice for preparing gold catalysts.

At room temperature and in the presence of oxygen the colloidal dispersion stabilized by glucose is less stable than the PVA stabilized ones owing to the slow glucose aerobic oxidation: growth of particles from 2.7 to 3.5 nm has been observed in a few hours.

3.1.3. Influence of pH in the Sol Preparation

Monitoring the pH value during the preparation of gold sol, which leads to the below reported results, it has been observed that pH moves from ca. 3.2, before $NaBH_4$ addition, to ca. 6.9, after $NaBH_4$ addition. In this section a discussion of the influence of the initial pH value on the properties of the colloidal dispersion stabilized by a large amount (PVA/Au = 0.67) or a low amount (PVA/Au = 0.05) of stabilizer is presented. Proper amounts of HCl or NaOH were used to produce the reported pH values.

The negative effect of strong acidic conditions (pH 2 and 2.8) in the reduction step appears evident in Table 4, producing large particles, in the range of 3.4–6.6 nm, while on increasing the pH smaller gold particles can be obtained. In particular, close to the uncorrected pH value of 7.5, the smallest mean diameters (2.4–2.8 nm) were observed. Following the evolution of the particle size in the time, sol dispersion, produced in almost neutral solutions and containing a high amount of PVA, ensured more than 3 h stability, whereas in a shorter time important phenomena of aggregation occurred under acidic conditions and mainly using the lower PVA content.

In the case of glucose-protected particles, a less important influence of the pH has been observed using more than 7 g/L of glucose. As shown in Table 5, the resultant gold dispersion showed a slow but constant increment of the particle size on standing (ca. 10–20% in 3 h).

3.1.4. Influence of the Amount of $NaBH_4$

Important changes in particle size have been observed by varying the amount of the reducing agent (Table 6 and Figure 2). ICP analysis of the filtered water did not detect any important gold residue after immobilization on

Table 6. Influence of different amounts of $NaBH_4$ on particle dimension.

$NaBH_4$/Au (wt.%)	PVA/Au (wt.%)	Particle diameter (nm)
0.2	0.67	3.2
0.5	0.67	2.4
1	0.67	2.4
2	0.67	3.8
0.2	0.05	11.8
0.5	0.05	10.2
1	0.05	2.8
2	0.05	7.0

[Au] = 100 mg/L. Mean diameter from XRPD.

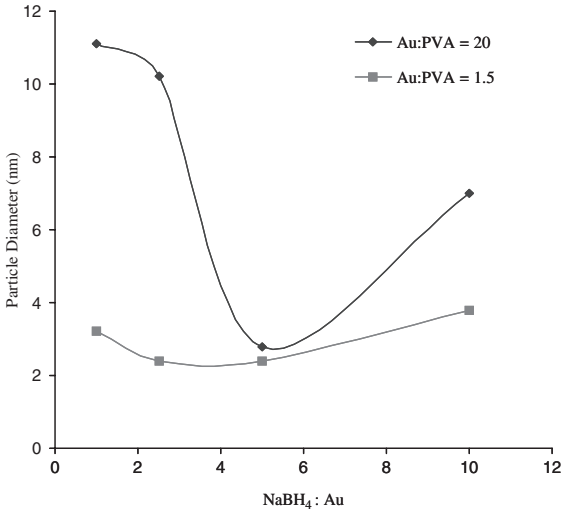

Figure 2. Particle diameter trend with different $NaBH_4$ amounts (mol/mol). [Au] = 100 mg/L. Mean diameter from XRPD.

carbon, thus demonstrating the complete reduction of gold in all the experiments.

The data show that the best result can be obtained using the $NaBH_4$/Au ratio of 1, corresponding to a ca. 5:1 molar ratio in favour of $NaBH_4$, which allows the formation of the smallest particles. Larger particles were formed in correspondence of the lower and higher amounts of $NaBH_4$. Above this value, a destabilizing effect of the excess of electrolytes is probably responsible of agglomeration. This is supported by the positive compensation of a higher amount of PVA giving rise to the lower flat curve in Figure 2. Also a lower amount of the reducing agent is not suitable for obtaining small particles, and this effect could be due to a slow reduction which favours the growth of a low number of gold nuclei.

It is worth noting that, under the optimized conditions, similar dimensions, namely 2.4 and 2.8 nm, can be reached independently from the examined quantity of PVA.

3.1.5. Influence of Gold Sol Concentration

Scipio reported that by varying $HAuCl_4$ concentration from 6 to 110 mg/L it is possible to obtain gold particles with a mean diameter of 1.8–5.5 nm on $NaBH_4$ reduction [35]. With the aim of extending the sol deposition technique to a large-scale application, we have restricted our experimental procedure to concentrations above 100 mg/L of Au, using two different PVA/Au ratios (0.67 and 0.05). The results are reported in Table 7.

It is evident that the $HAuCl_4$ and PVA concentrations play a complex and non-separable role in determining the resulting metal particle size: doubling the Au concentration, from 100 to 200 mg/L, only a marginal increment (from 2.4 to 2.7 nm) was observed at the higher PVA/Au ratio, whereas a more important effect (from 2.8 to 3.7 nm) occurred at the lower PVA/Au value. In any case, a remarkable result is given by using PVA/Au = 0.05 and gold concentration of 200 mg/L, allowing a mean particle diameter of 3.7 nm. Considering the whole results of this preliminary test, a limit to the application of the sol deposition method for catalyst production seems to be represented by the highest Au concentration of 400 mg/L associated with a PVA/Au ratio to be finely balanced just below foam formation. In view of scaling-up the preparation, this is an important point which could limit the plant dimension.

Table 7. Influence of gold sol concentration on particle diameter.

Gold sol concentration (mg/L)	PVA/Au (wt.%)	Particle diameter (nm)
100	0.67	2.4
200	0.67	2.7
400	0.67	4.1
100	0.05	2.8
200	0.05	3.7
400	0.05	5.6

$NaBH_4$/Au = 1 wt.%.

3.1.6. Influence of Gold Loading (Au/C)

In this section a study on the gold loading capacity of the XC72R carbon is reported.

According to the procedure of sol deposition described in Section 2.3, more than 10% Au can be deposited on XC72R, thus allowing the use of the catalysts in fuel cells and other electrochemical applications [36]. In all the experiments the common mother gold solution 1 (Section 2.3) was used containing a low PVA amount (PVA:Au = 0.05) in order to facilitate the adsorption step. Table 8 shows the results. According to ICP analysis, an almost total gold adsorption was obtained.

Despite a wide range of gold deposited on carbon, from 0.5 to 10%, no variation of the particle size resulted in the final catalysts. This represents an important result at least for two reasons: the first is the previously mentioned electrochemical application, where we outline the possibility to produce a highly charged carbon containing small particles; the second reason is related to the use of XC72R carbon as a trap for evaluating the particle dimension of the colloidal dispersions, because the absence of aggregation phenomena also in gold rich systems validates the procedure applied in the previous determinations.

3.1.7. Reproducibility

Five different preparations, from the sol production to the adsorption step, were carried out to verify the reproducibility of the dimension of the gold particles supported on XC72R carbon. In Table 9 the results are collected, indicating a fairly good confidence with the experiments reported in the above sections.

3.1.8. Influence of Different Carbons as a Gold Supporting Material

As mentioned in Section 3.1, the pyrolytic carbon XC72R resulted useful for immobilizing gold sol particles owing

Table 8. Influence of Au:C ratio on particle size and adsorption time.

Au loading on (%)	Particle diameter (nm)	Adsorption time (min)
0.5	2.8	5
1	2.8	5
2	2.8	5
5	2.8	10
10	2.8	15

XC72R carbon. [Au] = 100 mg/L. pH 6.9. Mean diameter from XRPD.

Table 9. Reproducibility tests.

Preparation	1	2	3	4	5
Mean diameter (nm)	3.1	3.1	3.2	2.9	2.8

[Au] = 100 mg/L; $NaBH_4$/Au = 1. PVA/Au = 0.05. pH 6.9. Mean diameter from XRPD.

Table 10. Influence of pH on the particle diameter.

PVA/Au (wt.%)	pH	Au (%)	*d* (nm)
0.67	7.5	0.55	2.8
0.67	2.8	0.85	5.8
0.05	7.5	0.62	3.1
0.05	2.8	0.90	8.0

X40S carbon. [Au] = 100 mg/L. Mean diameter from XRPD.

Table 11. Chemical parameters used for preparing large-scale standard catalysts.

Parameters	XC72R	X40S
Number of preparations	2	12
Amount (g)	500	80
V_{sol} (L)	25	4
$[Au]_{sol}$ (mg/L)	200	200
PVA/Au (wt.%)	0.05	0.05
$NaBH_4$/Au (wt.%)	1	1
pH adsorption	7.0	2.7
Stirring (rpm)	Mechanic, 800	Magnetic, 1750

to the excellent adsorption properties. In order to investigate the catalytic properties, a second carbon, Camel X40S, of vegetal origin, has been also taken in consideration. Before studying the catalytic applications, the adsorption properties of the X40S carbon were investigated on a 2 g scale preparation. Under neutral conditions, X40S showed a low adsorption capacity, 0.5–0.6 wt.% Au, representing the limit of gold loading from a 100 mg/L Au sol; it increased up to 1% when gold was adsorbed under acidic conditions (pH 2.7, Table 10). However, as a consequence of lowering pH, the particle size increased from 2.8 nm at pH 7.5 to 5.8 nm at pH 2.8.

Compared with XC72R carbon, this surprisingly low adsorbing capacity of X40S is apparently in contrast with the five times higher surface area of the latter (Table 1) which would suggest a higher loading ability. It is possible to justify the results as due to the presence of a lower amount of functional groups in X40S, but mainly located at the carbon surface, where carboxylates and phenols predominate [37]. This hypothesis agrees with the XPS data showing a much higher Au/C ratio in X40S with respect to XC72R carbon (Table 12). However, the nature and the quantity of the surface groups in the naphtha derived Vulcan XC72R are presently unknown and this avoids a conclusive interpretation.

4. A Case History

The WGC [33] is an organization which was founded, formed and funded in 1987 by the world's leading gold mining companies with the aim of stimulating and maximizing the demand for, and holding of, gold by consumers, investors, industry and the official sector. As well as undertaking marketing initiatives to drive demand, the WGC is also instrumental in working to lower regulatory barriers to the widespread ownership of gold products, helping to develop distribution systems and promoting the role of gold as a reserve asset in the official sector. The WGC has recently taken the initiative in commissioning the preparation of a number of gold reference catalysts, with the main objective of enabling researchers to benchmark their own catalyst formulations against a common reference catalyst, thereby permitting more accurate comparison with other research results. Three of the reference catalysts are represented by gold on oxide supports made by Süd Chemie-Japan, under the supervision of Dr. Masatake Haruta, with characterization at AIST, Japan, supervised by Dr. Susumu Tsubota. The fourth catalyst is gold on carbon produced at University of Milano. In the following sections the large-scale preparation of a nominal 1% Au/C catalyst is presented, outlining the scaling-up effects. The following general procedures have been adopted: (a) generation of a colloidal dispersion of gold particles having a mean diameter of ca. 4 nm, as a compromise between final activity and feasibility on a medium size scale; (b) deposition of gold particles on two different activated carbons; (c) evaluation of the morphological properties; (d) evaluation of the catalytic properties.

Table 12. Characterization of the large-scale catalyst preparation.

Batch	Carbon	Amount (g)	Gold particle dimension (nm)	Surface Au/C (XPS)	Total gold, Au% (ICP)
1a	XC72R	500	4.2	0.12	1.0
2a	XC72R	500	3.0	0.15	1.0
1b	X40S	80	8.6	1.36	0.71
2b	X40S	80	6.9	1.51	0.90
3b	X40S	80	5.9	2.01	0.70
4b	X40S	80	6.3	1.58	0.89
5b	X40S	80	5.9	1.89	0.81
6b	X40S	80	9.6	1.74	0.82
7b	X40S	80	6.3	1.29	0.82
8b	X40S	80	9.5	1.56	0.78
9b	X40S	80	5.6	1.88	0.79
10b	X40S	80	5.7	1.59	0.69
11b	X40S	80	6.3	1.78	0.80
12b	X40S	80	5.4	1.74	0.73

4.1. *Au/C WGC Reference Catalyst Preparation and Characterization*

Following the general procedures reported in Section 2, a larger scale preparation was investigated in order to supply 1 kg catalyst. Despite the promising results obtained with the glucose-protected sols, the application of PVA was decided as a colloid stabilizer owing to a longer familiarity with its use. Two carbons were considered as a candidate for producing a catalyst having a nominal content of 1 wt.% metal, namely the XC72R used throughout the previous sections for evaluating the dimension of the gold particles, and the coconut shell derived X40S. In the first case, two 500 g preparations were carried out starting from 25 L of $HAuCl_4$ solutions (200 mg/L Au) under the conditions reported in Table 10. In the case of XC40S, 12 preparations of 4 L sols were performed [12] (Table 11).

After filtration, a deep washing of the resultant catalyst with hot water, until negative chloride test, was made for each preparation. For avoiding foam formation, PVA was used in a low quantity (PVA/Au = 0.05) as suggested by the preliminary tests.

Table 12 reports the characterization of the resulting materials. In order to comment the subsequent kinetic data, XPS data were collected in order to confirm the presence of the 4f peak of metal gold at 84.0 eV and also for deriving the amount of exposed gold at the carbon surface. In Table 13 the comparison between 2 and 500 g scale preparations is reported.

As a general comment on the morphological properties, the XC72R carbon allows a fairly good scaling-up possibility. In fact, the two 500 g preparations produced the desired 1% gold loading with negligible loss of gold. Mean gold particle dimensions of 3 and 4.2 nm were obtained in the two lots, and this fact highlights problems of reproducibility. However, this result is close to the planned ones of 3–5 nm particles, but is far from the 2.8 nm size determined in the 2 g preparation under acceptable conditions of reproducibility (Section 3.1.7).

A less satisfactory result has been obtained in the case of X40S carbon. First of all, it was not possible to meet the effective 1% loading despite the fact that the adsorption step was done at the favourable pH value of 2.7, which had the drawback to promote large gold particles (Table 10): starting from the nominal 1% solution, after 30 min of contact time, gold was adsorbed in the range of 0.70–0.90%, with a mean value of 0.79%, and no benefit was observed on prolonging the adsorption time to 12 h. The mean size of gold particles in the 12 different preparations was 6.8 nm, a value similar to the 2 g preparation under similar conditions (6.4 nm, Table 13).

Comparing the histogram derived by a TEM image of the Au/X40S preparation (Figure 3(A)) with the XRD analysis (Table 13), it has been observed that the larger TEM particles derive mainly by agglomeration. In fact, the mean dimension of coherent scattering crystallites, determined by XRD technique, resulted inferior to the mean diameter derived by TEM photographs in supported gold, where agglomerates larger than 10 nm shift the diameter to higher value with respect to the original sol. According to the lower XRD values, these aggregates retain their XRD identity.

Considering the gold particles immobilized on XC72R carbon, a much more uniform size distribution can be observed with respect to X40S carbon (Figure 3(B)).

Therefore, from a morphological point of view, the adsorption step has to be considered as the most critical

Table 13. Physico-chemical properties: comparison of the large-scale and small-scale Au/X40S and Au/XC72R catalysts.

Catalyst	Physico-chemical properties	2 g scale	Large scale
Au/XC72R	Crystallite dimension by XRD (nm)	2.8	3.4
	Mean particle size by HRTEM (nm)	–	3.8
	Superficiality by XPS (Au/C (%))	0.14	0.13
	Adsorbed gold by ICP (%)	1.0	1.0
Au/X40S	Crystallite dimension by XRD (nm)	6.4	6.7
	Mean particle size by HRTEM (nm)	–	10.5
	Superficiality by XPS (Au/C (%))	1.85	1.60
	Adsorbed gold by ICP (%)	0.85	0.8

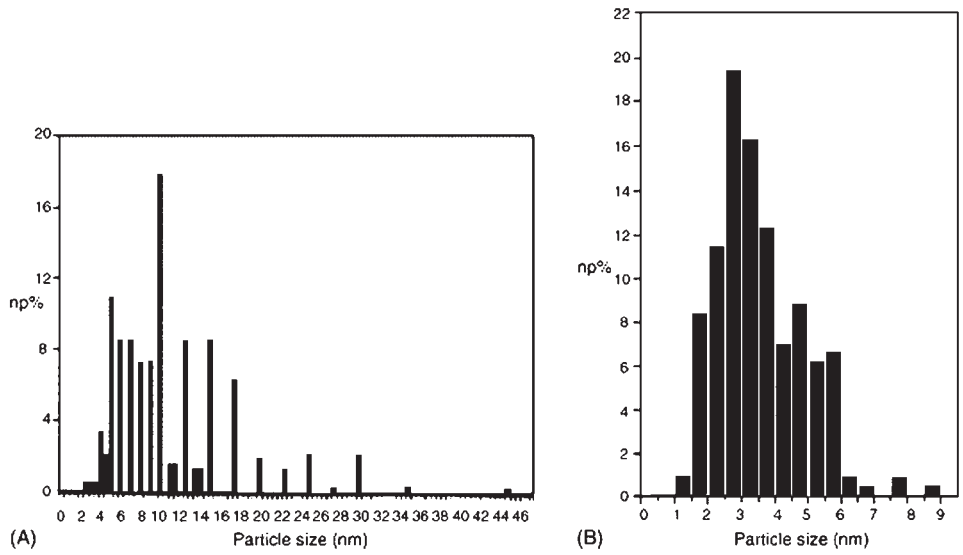

Figure 3. Particle size distribution of the gold particles after deposition in the large-scale preparation on (A) X40S and (B) XC72R.

one for addressing the particle size distribution and the choice of carbon plays a fundamental role.

5. Oxidation Tests

5.1. Glucose Oxidation

The catalyst evaluation was carried out at atmospheric pressure by bubbling oxygen through the slurry (1000 N cm^3/min) and controlling the pH at 9.5. The experiments were performed by using a 751 GPD Titrino (Metrohm) equipped with a 5 M NaOH reserve. Glucose and the catalyst (S/M = 20,000 mol/mol) were mixed in MilliQ water to obtain a 50 wt.% solution. The temperature of the stirred mixture was kept at 323 K and NaOH was added automatically to maintain pH of the solution at the desired value. Gluconic acid formation versus time was derived from the added amount of NaOH. HPLC and NMR analyses showed a selectivity superior to 96%.

5.2. Ethane-1,2-diol Oxidation

The catalyst evaluation was carried out in a temperature controlled glass reactor (50 mL) with an electronic magnetic stirrer connected to a reserve containing molecular oxygen at 303 kPa. A flow–time diagram of the oxygen uptake was plotted by using a mass flow connected to a PC through an A/D board. In all the experiments, ethylene glycol and catalyst (S/M = 1000 mol/mol) were mixed with water ([S] = 0.4 M) in basic condition (S/NaOH = 1 mol/mol). The reactor was pressurized at 303 kPa of oxygen and the temperature was kept at 343.2 K. After a period of equilibration (10 min), the mixture was stirred and the zero time was taken. The time conversion plots were obtained by titrating the total organic acidity.

5.3. Analysis of Products

The products were identified and quantified by comparison with reference samples. Both the quantitative and qualitative analyses were performed by HPLC; ^{13}C NMR was also used for qualitative analysis.

5.3.1. HPLC Analysis

Analyses were performed on a Varian 9010 instrument equipped with a Varian 9050 UV (210 nm) and a Waters 2410 R.I. detector. An Alltech OA-1000 column (300 mm × 6.5 mm) was used with aqueous H_2SO_4 0.01 M (pH 2.1) (0.4 mL/min) as the eluent. No problem arose in the case of ethylene glycol–glycolic acid separation. Due to peaks overlapping, glucose and gluconic acid were quantified using two in series detectors, considering the absence of adsorption bands of glucose in the UV detector at 210 nm, and evaluating their sum by the IR detector.

5.3.2. NMR Analysis

^{13}C NMR spectra were recorded in water on a Bruker 300 MHz without adjusting the pH. The assignment of peaks in the oxidation of glucose was made by comparison with original samples.

5.3.3. Titration Procedure

The evaluation of the total organic acidity was performed by neutralizing (to pH 10–11) a sample of product with NaOH and then retro-titrating with HCl.

5.4. Results and Discussion

Concerning the application of gold catalysis to glucose oxidation, stressing conditions (glucose/Au = 20,000) were chosen in order to simulate an industrial test. Under such conditions, high TOF values were observed, ranging from 12,500 to 25,000 h^{-1}, as calculated at 50% conversion (Figure 4).

Considering the correlation between morphological and kinetic properties, the results here observed only partly agree with the expected higher activity of the smaller particles, almost independently of the support. In fact, according to kinetic studies on unsupported and supported gold particles, the key factor governing the initial activity should be the number of exposed gold atoms, which is related to the particle dimension [11]. In particular, a linear correlation has been found between catalytic activity and the inverse of diameter. Therefore, the smallest 2.8 nm particles obtained in the 2 g scale preparations of Au on XC72R produced the most active catalyst. However, the 2 g preparation of Au/X40S ($d = 6.4$ nm) is more active than the 500 g preparation of Au/XC72R ($d = 3.4$ nm), indicating an important effect of sulphur impurities which are present in XC72R and almost absent in X40S carbon (Table 1).

Moreover, the reported tests provide further support to the great availability of gold centres in the catalysts for

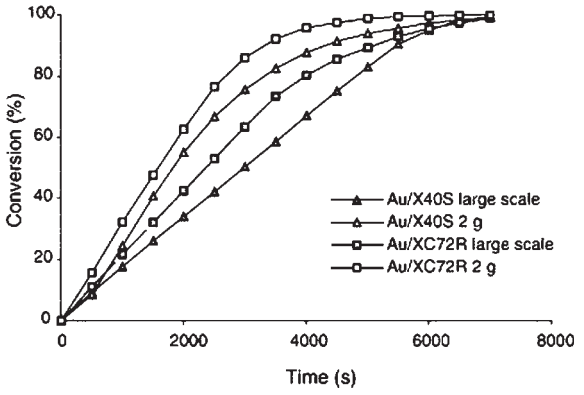

Figure 4. Catalytic activity of the Au/C large-scale preparations and the 2 g preparation in glucose oxidation. Reaction conditions: glucose 50 wt.%; S/M ratio 20,000; O_2 flow 1 N L/min; stirring rate 1700 rpm. pH 9.5.

Table 14. Catalytic activity and selectivity of the 12 g × 80 g Au/X40S preparations and 2 g × 500 g Au/XC72R (a) and 2 g preparations (b) in the ethylene glycol oxidation.

Carbon/ scale	Batch	Conversion (%)	TOF (h^{-1})	Selectivity to glycolic acid (%)
Au/X40S 80 g	1	52	1040	94
	2	69	1380	99
	3	50	1000	98
	4	55	1100	92
	5	64	1280	95
	6	62	1240	95
	7	40	800	93
	8	43	860	96
	9	63	1260	94
	10	54	1080	91
	11	54	1080	96
	12	54	1080	95
X40S 2 g	1	60	1200	96
Au/XC72R 500 g	1	22	440	94
	2	23	260	92
Au/XC72R 2 g	1	37	740	91

Conversion determined at 30 min reaction time. Experimental conditions: $P_{O_2} = 303.9$ kPa; substrate/catalyst ratio = 1000; [substrate] = 0.3 mol/L; substrate/NaOH ratio = 1; $T = 343.2$ K.

glucose oxidation, owing to the absence of important diffusion constrains. In particular, we outline that the gold rich surface of X40S (Au/C = 1.29–2.01, from XPS data of Table 12) behaves similarly to the poorer surface of XC72R (Au/C = 0.12–0.15).

Much more difficult is the interpretation of the behaviour of supported catalysts in the ethane-1,2-diol oxidation. In fact, despite the smaller gold particles, Au/XC72R displayed the worst performance either considering the 2 g preparation or the larger preparations (Table 14).

One should remember the parameters that, in principle, could favour gold supported on the X40S carbon, namely the higher superficiality of gold and the lower sulphur content (Table 1). Information on the rate limiting step in alcohols oxidation by gold is presently lacking: it would be of great interest to compare the kinetic and molecular models proposed for glucose oxidation [11,18] with analogous ones related to ethane-1,2-diol oxidation for interpreting the observed results.

A promising contribution to the preparation of gold catalyst for liquid-phase oxidation is represented by the use of glucose as a protecting agent. However, at the present time, we have not yet applied glucose as a protecting agent in large-scale preparation and, therefore, no scaling-up effects can be discussed in this case.

6. Conclusions

This study has shown that the immobilization of preformed gold sol on carbon could represent a valid technique for 80–500 g catalyst preparations. Peculiar properties, mainly connected to the nature of carbon support, can be outlined as the different adsorption capacities and the sulphur contents. Particularly in the case of ethane-1,2-diol, the higher Au/C ratio derived by XPS technique seems to be responsible of the higher activity for gold supported on X40S carbon. In the case of glucose oxidation, a quite high activity, comparable with enzymatic systems, can be obtained with different carbons. In this latter case gold particle size and sulphur poisoning play concomitant effects influencing the reaction rate. Scaling-up effects have been observed which are mainly due to the growth of gold particles in larger scale preparations.

References

1 L. Prati, M. Rossi, *J. Catal.* 176 (1998) 552.
2 G. C. Bond, D. Thompson, *Catal. Rev.-Sci. Eng.* 41 (1999) 319.
3 G. C. Bond, D. Thompson, *Gold Bull.* 33 (2000) 41.
4 C. Bianchi, F. Porta, L. Prati, M. Rossi, *Top. Catal.* 13 (2000) 231.
5 S. Coluccia, G. Martra, F. Porta, L. Prati, M. Rossi, *Catal. Today* 61 (2000) 165.
6 D. Andreeva, V. Idakiev, T. Tabakova, L. Ilieva, P. Falaras, A. Bourlinos, A. Travlos, *Catal. Today* 72 (2002) 51.
7 S. Biella, L. Prati, M. Rossi, *Inorg. Chim. Acta* 349 (2003) 253.
8 S. Biella, L. Prati, M. Rossi, *J. Mol. Catal. A: Chem.* 197 (2003) 207.
9 S. Biella, M. Rossi, *Chem. Commun.* (2003) 378.
10 D. Andreeva, R. Nedyalkova, L. Ilieva, M. V. Abrashev, *Appl. Catal. A* 246 (2003) 29.
11 M. Comotti, C. Della Pina, R. Matarrese, M. Rossi, *Angew. Chem. Int. Ed.* 43 (2004) 5812.
12 M. Comotti, C. Della Pina, R. Matarrese, M. Rossi, A. Siani, *Appl. Catal. A* 291 (2005) 204.
13 C. Della Pina, E. Falletta, M. Rossi, *La Chim. l'Ind.* 87 (2005) 44.
14 D. Hughes, Y. J. Xu, P. Jenkins, P. McMorn, P. Landon, D. I. Enache, A. F. Carley, G. A. Attard, G. J. Hutchings, F. King, E. H. Stitt, P. Johnston, K. Griffin K, C. J. Kiely, *Nature* 437 (2005) 1132.
15 J. Guzman, S. Carrettin, A. Corma, *Angew. Chem. Int. Ed.* 44 (2005) 4778.
16 D. I. Enache, J. F. Edwards, P. Landon, B. Solsona-Espriu, A. F. Carley, A. A. Herzing, M. Watanabe, C. J. Kiely, D. W. Knight, G. J. Hutchings, *Science* 362 (2006) 5759.
17 P. Beltrame, M. Comotti, C. Della Pina, M. Rossi, *Appl. Catal. A* 297 (2006) 1.
18 M. Comotti, C. Della Pina, E. Falletta, M. Rossi, *Adv. Synth. Catal.* 348 (2006) 313.
19 M. Comotti, C. Della Pina, M. Rossi, *J. Mol. Catal. A: Chem.* 251 (2006) 89.
20 M. Comotti, W. C. Li, B. Spliethoff, F. Schueth, *J. Am. Chem. Soc.* 128 (2006) 917.
21 M. Haruta, N. Yamada, T. Tobayashi, S. Iijima, *J. Catal.* 151 (1989) 301.
22 S. Tsubota, D. A. Cunningham, Y. Bando, M. Haruta, in G. Poncelet, J. Martens, B. Delmon, P. A. Jacobs, P. Grange (eds.) *Preparation of Catalysts VI*, Vol. 91, Elsevier, Amsterdam, 1995, 227.
23 M. Okumura, S. Nakamura, S. Tsubota, T. Nakamura, M. Azuma, M. Haruta, *Catal. Lett.* 51 (1998) 53.
24 M. Haruta, *Catal. Today* 36 (1997) 153.
25 L. Prati, M. Rossi, *Stud. Surf. Sci. Catal.* 110 (1997) 509.
26 A. I. Kozlov, A. P. Kozlova, H. Liu, Y. Iwasawa, *Appl. Catal. A* 82 (1999) 9.

27 J. D. Grundwaldt, C. Kiener, C. Wogerbauer, A. Baiker, *J. Catal.* 181 (1999) 223.
28 G. Martra, L. Prati, *Gold Bull.* 32 (1999) 96.
29 J. Turkevich, P. C. Stevenson, J. Hillier, *Discuss. Faraday Soc.* 11 (1957) 55.
30 D. G. Duff, A. Baiker, P. Edwards, *Chem. Commun.* (1993) 96.
31 A. B. R. Mayer, J. E. Mark, *Polym. Bull.* 37 (1996) 683.
32 F. Porta, M. Rossi, *J. Mol. Catal. A: Chem.* 553 (2003) 553.
33 World Gold Council reference catalysts web site: www.gold.org/discover/sci_indu/gold_catalysts/refcat.html.
34 A. L. Patterson, *Phys. Rev.* 56 (1939) 972.
35 R. G. Scipio, *Anal. Biochem.* 236 (1996) 168.
36 D. T. Thomson, *Platinum Met. Rev.* 48 (2004) 169.
37 C. L. Bianchi, S. Biella, A. Gervasini, L. Prati, M. Rossi, *Catal. Lett.* 85 (2003) 91.

CHAPTER 13

Photocatalytic Deposition and Plasmon-Induced Dissolution of Metal Nanoparticles on TiO_2

Tetsu Tatsuma and Kazuki Matsubara

Institute of Industrial Science, University of Tokyo

1. Introduction

Plasmon resonance, which is collective oscillation of conduction electrons induced by an electromagnetic wave, is one of the intriguing properties of metals. In particular, metal nanoparticles absorb light of a specific wavelength due to the plasmon resonance, and thereby exhibit a corresponding color. Gold, silver, and copper nanoparticles have therefore been used for stained glasses and cut glasses. The resonance wavelength depends on the size and shape of nanoparticles, the interparticle distance, and the dielectric property of the surrounding medium. This means that, if the size of the nanoparticles can be controlled reversibly, the color can be controlled in turn.

In this chapter, photoelectrochemical control of size and color of silver nanoparticles, i.e., multicolor photochromism [1], is described. Silver nanoparticles are deposited on UV-irradiated TiO_2 by photocatalytic means [2]. Size of the nanoparticles can be roughly controlled in the photocatalytic deposition process. However, it is rather important that this method provides nanoparticles with broadly distributed sizes. The deposited silver nanoparticles are able to be dissolved partially and reduced in size by plasmon-induced photoelectrochemical oxidation in the presence of an appropriate electron acceptor such as oxygen. If a monochromatic visible light is used, only the particles that are resonant with the light are dissolved. That is, size-selective dissolution is possible [3]. This is the principle of the multicolor photochromism.

The present technique enables light-induced redox reaction: UV light-induced oxidative dissolution and visible light-induced reductive deposition of silver nanoparticles. Reversible control of the particle size is therefore possible in principle. The reversible redox process can be applied to surface patterning and a photoelectrochemical actuator, besides the multicolor photochromism.

2. Synthetic Strategy: Photoelectrochemical Approaches

2.1. UV Light-Induced Deposition of Metal Nanoparticles

A TiO_2 film (normally nanoporous) or a TiO_2 single crystal (advantageous for observation of deposited metal nanoparticles) is soaked in a solution containing Ag^+ (e.g., aqueous or ethanol solution of $AgNO_3$), and irradiated with UV light. Alternatively, a TiO_2 film on which Ag^+ is adsorbed may be irradiated. As a result, electrons in the TiO_2 valence band are excited to the conduction band (Equation (1)), and the excited electrons (e^-_{CB}) are transferred to Ag^+ resulting in deposition of silver nanoparticles (Equation (2)) (Figure 1a).

$$TiO_2\ \text{particle} \xrightarrow{\text{UV light}} TiO_2\ \text{particle}^*(e^-_{CB} + h^+_{VB}) \quad (1)$$

$$Ag^+ + e^-_{CB} \rightarrow Ag \quad (2)$$

Simultaneously, an electron donor, i.e., water or ethanol, is oxidized by the holes generated in the valence band (h^+_{VB}) (Equation (3)).

$$\text{Donor} + h^+_{VB} \rightarrow \text{Donor(ox)} \quad (3)$$

Thus, silver nanoparticles grow gradually during UV light irradiation (processes a1–a3 in Figure 2). Nanoparticles of other noble metals such as gold, copper, platinum, and palladium can also be deposited by this method.

2.2. Visible Light-Induced Dissolution of Silver Nanoparticles

The silver-loaded TiO_2 film is irradiated with visible light (normally monochromatic light from a lamp with a

Metal Nanoclusters in Catalysis and Materials Science: The Issue of Size Control
Edited by B. Corain, G. Schmid and N. Toshima

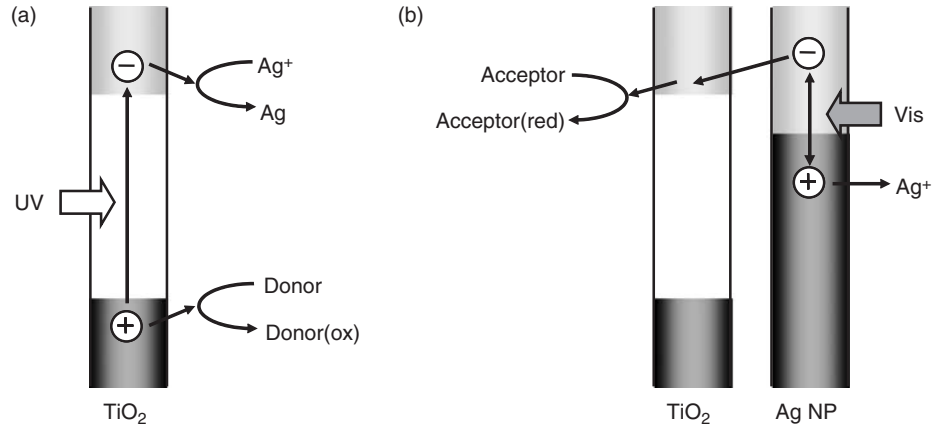

Figure 1. Mechanisms of photoelectrochemical deposition and dissolution of silver nanoparticles (Ag NPs): (a) UV light-induced deposition and (b) visible light-induced dissolution.

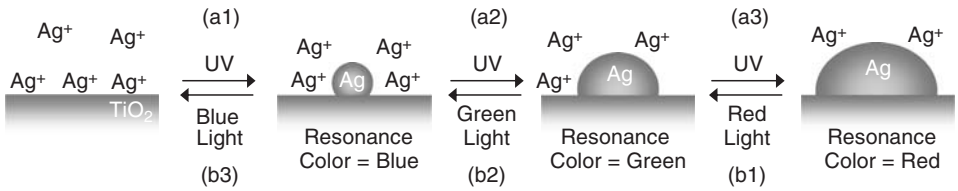

Figure 2. UV light-induced deposition of silver nanoparticles (a1–a3) and wavelength-selective visible light-induced dissolution of silver nanoparticles (b1–b3).

band-pass filter or a laser) in air or in water. As a result, electrons at the metal surface are excited due to plasmon resonance (Equation. (4)) and the excited electrons (e_{ex}^-) are transferred to an electron acceptor (Equation (5)), e.g., ambient oxygen or dissolved oxygen, likely via TiO_2 (and non-excited silver nanoparticles) (Figure 1b) [4–6]. Dissolution of Ag^+ accompanies the electron transfer to the acceptor.

$$\text{Ag particle} \xrightarrow{\text{Visible light}} \text{Ag particle}^*(e_{ex}^- + Ag^+) \quad (4)$$

$$\text{Acceptor} + e_{ex}^- \rightarrow \text{Acceptor(red)} \quad (5)$$

This process occurs only at the silver nanoparticles of which resonance wavelength is in accordance with the incident light wavelength. Therefore, size-specific dissolution is possible (processes b1–b3 in Figure 2).

Instead of TiO_2, ZnO can also be used [6]. Commercially available silver nanoparticles cast on TiO_2 can be used instead of the photocatalytically deposited silver nanoparticles [6].

3. Results

3.1. UV Light-Induced Deposition of Metal Nanoparticles

As a rutile TiO_2 single crystal is irradiated with UV light in a $AgNO_3$ solution, silver nanoparticles are deposited and grown gradually (Figure 3).

Figure 4 shows a typical time-course of lateral diameter of the nanoparticles. The error bar stretching gradually is indicative of increasing size distribution.

Figure 5 shows the correlation between the particle height and the lateral diameter.

It is obvious that larger nanoparticles are more anisotropic in comparison with smaller particles. Large and flattened particles should be, in turn, in better contact with the TiO_2 substrate, which has substantially high dielectric constant (~2.52). In addition, the distance between the deposited particles should decrease as the particles grow. All these facts suggest that the resonance wavelength of the silver nanoparticles should redshift as the particles grow, because increasing particle diameter, increasing particle anisotropy, enhancing matrix dielectricity, and decreasing interparticle distance are all causative of the redshift owing to enhanced quadrupole or higher multipole resonance [7,8]. Therefore, it is reasonable that the polydisperse silver particles exhibit broad extinction (extinction = absorption + scattering) over the whole visible wavelength region (data not shown).

When a nanoporous TiO_2 film consisting of TiO_2 nanoparticles is used instead of the single crystal, the extinction band of silver nanoparticles deposited by UV-irradiation is much broader. This is probably because the nanopores in the TiO_2 film mold the silver nanoparticles into various anisotropic shapes [9], although direct observation of the particles in the nanopores is difficult.

3.2. Visible Light-Induced Dissolution of Silver Nanoparticles

Upon irradiation with a monochromatic visible light, extinction of the silver nanoparticles deposited on a

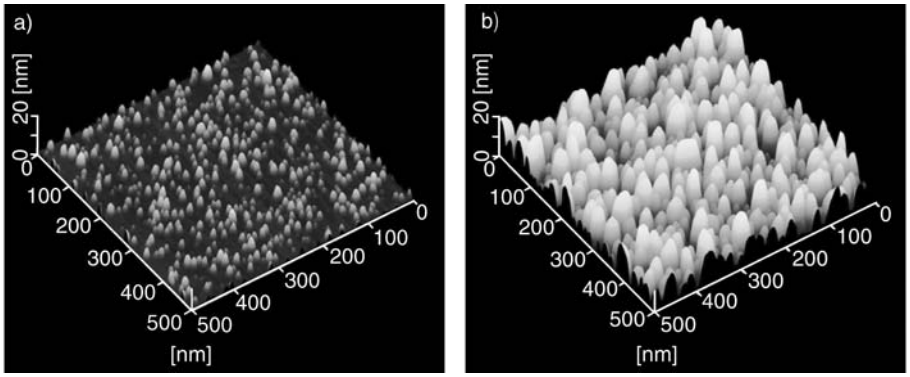

Figure 3. AFM images of the silver nanoparticles on the TiO_2(1 0 0) single crystal at the deposition times of (a) 15 s and (b) 180 s. The images were recorded in a tapping mode with driving frequency of 110–150 kHz at a scan rate of ~1 Hz by using a silicon cantilever with a normal spring constant of 15 Nm^{-1} (SI-DF20, Seiko instruments).

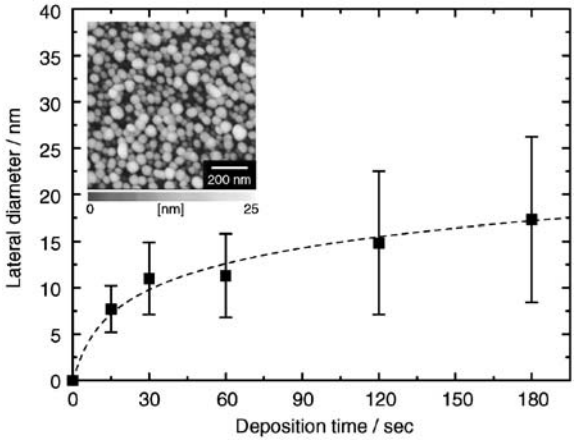

Figure 4. Time-course of the lateral diameter of the silver nanoparticles deposited on the rutile TiO_2(1 0 0) single crystal ($9 \times 9 \times 0.5$ mm) under UV light (wavelength = 310 nm, FWHM = 10 nm, light intensity ~1.0 mW cm^{-2}). The dashed line is guide for the eyes. The error bars indicate the standard deviations. Inset shows the corresponding AFM image of the sample after the irradiation with UV light for 180 s.

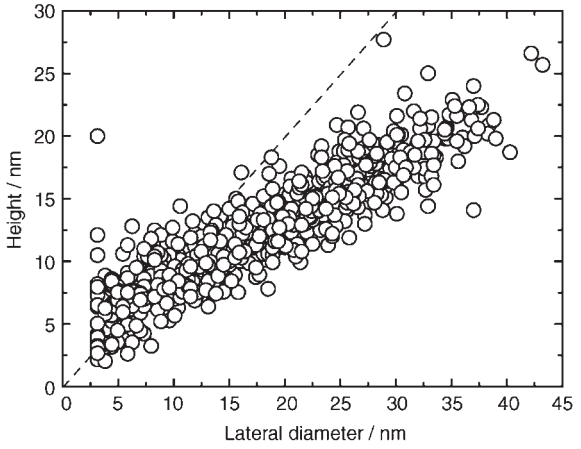

Figure 5. Height of the silver nanoparticles plotted as a function of their lateral diameter, determined by extended particle analysis for the AFM image (silver deposition time was 180 s). The broken line is for perfect spheres (height/diameter = 1).

single-crystalline TiO_2 or deposited in a nanoporous TiO_2 film decreases at around the excitation wavelength and typically increases in the other wavelength regions (Figure 6).

Those spectral changes, especially the decrease in the extinction, change the color of the film (initially brown or brownish gray) to a color similar to that of the incident light [1,9]. The spectral change is a consequence of changes in the particle size. When the excitation wavelength is large, the number of large particles decrease and that of small particles increase (Figure 7), and vice versa.

The spectral and morphological changes can be explained as follows (Figure 8).

When the polydisperse silver nanoparticles are irradiated with a monochromatic light, only the nanoparticles that are resonant with the incident light are excited and the excited electrons are transferred to TiO_2, giving rise to liberation of Ag^+. The resonant particles are thus reduced in size until they become non-resonant. Some of the electrons transferred to TiO_2 are accepted by ambient oxygen, and the other electrons are recombined with the liberated Ag^+ in the vicinity of the mother particle, on a bare TiO_2 to produce a new silver nanoparticle or on a non-resonant particle to grow it. In either event, the recombination processes result in an increase in the number of non-resonant particles. Thus, the extinction decreases at the excitation wavelength and increases at the other wavelength regions.

In the meantime, to protect the silver nanoparticles from the photoelectrochemical dissolution, the particles may be coated with a polymer matrix or a hydrophobic thiol [10].

3.3. Applications

The present photoelectrochemical deposition/dissolution method is applicable to reversible control of the particle size. A typical application taking advantage of the method is the multicolor photochromism. Additional applications include surface patterning and photoelectrochemical actuator. The patterning is possible by using a thiol-modified silver

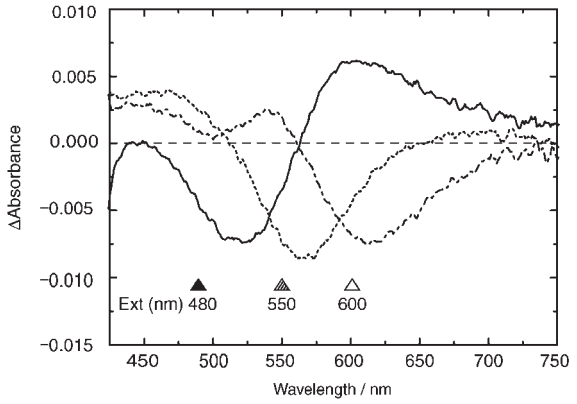

Figure 6. Difference extinction spectra of the silver nanoparticles on the rutile TiO_2(100) single crystal after irradiation with monochromatic visible light (wavelength = 480 nm, light intensity ~5.0 mW cm^{-2}, irradiation time = 30 min; 550 nm, ~5.0 mW cm^{-2}, 30 min; 600 nm, ~3.0 mW cm^{-2}, 60 min (FWHM = 10 nm)).

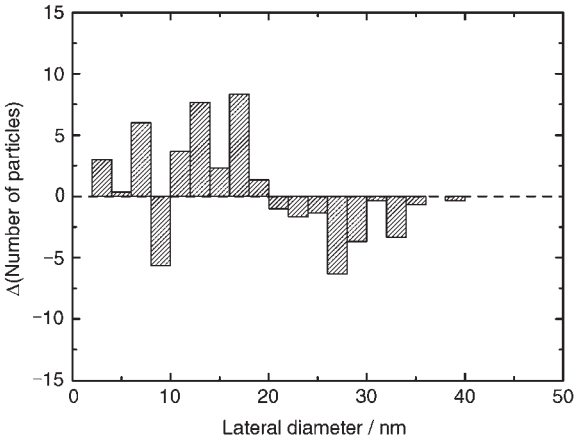

Figure 7. Difference lateral diameter histogram of the silver nanoparticles deposited on the TiO_2(100) surface after irradiation with monochromatic light at 600 nm (30 min, ~5.0 mW cm^{-2}).

nanoparticles on a TiO_2 film [11]. If the film is irradiated with visible light through a photomask, the thiol molecules can be removed only in the irradiated regions. Photoelectrochemical actuators [12] consist of a polyacrylate gel containing TiO_2 particles and a metal ion. The interaction between polymer chains can be controlled reversibly by the photoelectrochemical deposition/dissolution processes, resulting in actuation based on swelling/shrinking of the gel.

4. A Case History

4.1. Deposition

A single-crystalline rutile TiO_2 (100)-oriented) plate (9 × 9 × 0.5 mm, Shinkosha) was pretreated successively overnight with 3% aqueous NH_4OH and 1 M aqueous NaOH. The TiO_2 plate immersed in pure water was irradiated overnight with UV light using a black-light lamp.

Aqueous 1 M $AgNO_3$ was mixed with equivolume of ethanol. A 30-μL aliquot of the solution was cast on the TiO_2(100) surface. The surface was irradiated with UV light using a Hg–Xe lamp (Luminar Ace LA-300UV, Hayashi Watch Works) equipped with a band-pass filter (wavelength = 310 nm, full width at half maximum (FWHM) = 10 nm, light intensity ~1.0 mW cm^{-2}) for 180 s.

The deposited silver nanoparticles are shown in Figure 3. Changes in the average lateral diameter of the particles are depicted in Figure 4. Anisotropy of the deposited polydisperse nanoparticles is shown in Figure 5.

4.2. Dissolution

After the photoelectrochemical deposition of the silver nanoparticles, the TiO_2(100) plate was thoroughly rinsed with water and dried. Then it was irradiated with a monochromatic visible light (wavelength = 480 nm, light intensity ~5.0 mW cm^{-2}, irradiation time = 30 min; 550 nm, ~5.0 mW cm^{-2}, 30 min; 600 nm, ~3.0 mW cm^{-2}, 60 min (FWHM = 10 nm)).

Spectral changes of the nanoparticles on TiO_2 upon the irradiation are shown in Figure 6. The accompanying changes in the size distribution of the particles are depicted in Figure 7.

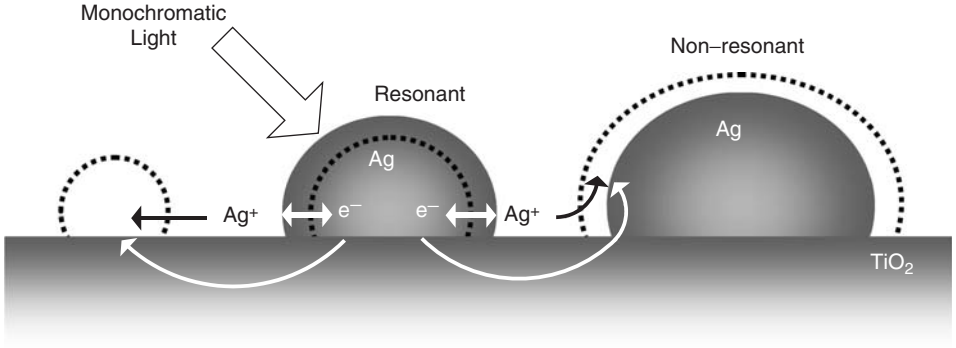

Figure 8. Mechanisms of the photoelectrochemically induced morphological changes of the silver nanoparticles deposited on TiO_2.

5. Conclusions

Silver nanoparticles can be deposited on TiO_2 by UV-irradiation. Deposition of polydisperse silver particles is a key to multicolor photochromism. The nanoparticles with different size have different resonant wavelength. Upon irradiation with a monochromatic visible light, only the resonant particle is excited and photoelectrochemically dissolved, giving rise to a decrease in the extinction at around the excitation wavelength. This spectral change is the essence of the multicolor photochromism. The present photoelectrochemical deposition/dissolution processes can be applied to reversible control of the particle size.

References

1 Y. Ohko, T. Tatsuma, T. Fujii, K. Naoi, C. Niwa, Y. Kubota, A. Fujishima, *Nat. Mater.* 2 (2003) 29.
2 A. Fujishima, K. Honda, *Nature* 238 (1972) 37.
3 K. Matsubara, T. Tatsuma, *Adv. Mater*., in press (doi: 10.1002/adma.200602823).
4 Y. Tian, T. Tatsuma, *Chem. Commun.* (2004) 1810.
5 Y. Tian, T. Tatsuma, *J. Am. Chem. Soc.* 127 (2005) 7632.
6 K. Kawahara, K. Suzuki, Y. Ohko, T. Tatsuma, *Phys. Chem. Chem. Phys.* 7 (2005) 3851.
7 T. Jensen, L. Kelly, A. Lazarides, G. C. Schatz, *J. Cluster Sci.* 10 (1999) 295.
8 S. Link, M. A. El-Sayed, *J. Phys. Chem. B* 103 (1999) 8410.
9 K. Naoi, Y. Ohko, T. Tatsuma, *J. Am. Chem. Soc.* 126 (2004) 3664.
10 K. Naoi, Y. Ohko, T. Tatsuma, *Chem. Commun.* (2005) 1288.
11 Y. Tian, H. Notsu, T. Tatsuma, *Photochem. Photobiol. Sci.* 4 (2005) 598.
12 K. Takada, T. Miyazaki, N. Tanaka, T. Tatsuma, *Chem. Commun.* (2006) 2024.

This page intentionally left blank

CHAPTER 14

Synthesis of Metal Nanoclusters upon Using Ion Implantation

P. Mazzoldi and G. Mattei

Department of Physics, University of Padova, Padova, Italy

1. Introduction

Composite materials formed by metal nanoclusters embedded in glass matrices (metal nanocluster composite glass, MNCG) are the object of several studies owing to their peculiar properties suitable for application in several fields, such as non-linear optics, photoluminescence, or catalysis [1–6]. Recently, sensitizing effects for rare-earth ions luminescence have also been reported as due to energy transfer between metallic nanoclusters and Er ions in silica glass [7]. Nanoclusters dispersed in dielectric matrices also exhibit interesting magnetic properties, such as superparamagnetic behavior, enhanced coercivity, shift of the hysteresis loop, and large magnetotransport features [8].

Glass-based composites are in general expected to play an important role as materials for various nanotechnological applications, due to the low cost, ease of processing, high durability, resistance, and high transparency, with the possibility of tailoring the behavior of the glass-based structures. Many studies have been dedicated to the properties of MNCG. In general, the physical properties of these systems change dramatically in the transition from atom to molecule to cluster to solid, where the cluster regime is characterized by the confinement effects that make MNCGs peculiarly interesting. For example, experiments which showed the transition from atomic over molecular to bulk plasmon absorption features have been performed with Ag clusters in photosensitive glasses during the last four decades. Updated review articles dealing with MNCGs are currently published, each one covering one or more particular aspects, ranging from preparation techniques to properties and characterization.

A general treatment of quantum dot materials including MNCGs is presented in Ref. [5], while glasses for optoelectronic devices, particularly MNCGs, are treated in Refs. [1,2,4,9,10]. The theoretical aspects of MNCG properties are approached in the literature under a great variety of view points, for example, by treating the electronic properties of metal clusters [11], or focusing on the quantum size effect [12]. Non-linear optical properties of small metal particles are treated in details in Refs. [13,14], while Refs. [15,16] present extended reviews on theoretical and experimental aspects of the optical response of metal clusters. Recent aspects concerning the interface properties of MNCGs are in Ref. [17], and Ref. [18] presents a review of all-optical switching via non-linear optical materials.

M. Faraday made the first attempt to explain the nature of the color induced in glasses by small metal precipitates [19]. Further attempts to describe the optical behavior of clusters embedded in a matrix as a homogeneous medium with an effective dielectric function were made by Maxwell–Garnett [20,21]. A complete analytical solution to the scattering of an electromagnetic wave by a spherical isolated cluster embedded in a non-absorbing medium was given in the same years by G. Mie [22]. Applications of Maxwell–Garnett and G. Mie theories will be presented in Section 2.2.4.

The synthesis of MNCGs can be obtained by sol–gel, sputtering, chemical vapor-deposition techniques. Ion implantation of metal or semiconductor ions into glass has been explored since the last decade as a useful technique to produce nanocomposite materials in which nanometer sized metal or semiconductor particles are embedded in dielectric matrices [1,2,4,23–29]. Furthermore, ion implantation has been used as the first step of combined methodologies that involve other treatments such as thermal annealing in controlled atmosphere, laser, or ion irradiation [30–32].

In Appendix A, for the sake of clarity, we reported some of the acronyms used throughout the text, whereas in Appendix B a brief description of the experimental characterization techniques used for the present work is added.

2. Synthesis Strategy

2.1. Ion-Implantation Technique

Ion implantation consists of the injection of energetic ions beneath the surface of a material. Due to the high energy

Metal Nanoclusters in Catalysis and Materials Science: The Issue of Size Control
Edited by B. Corain, G. Schmid and N. Toshima

involved in the interaction process between the incident ions and the matrix atoms any elemental species can be introduced into the near surface region of any substrate.

This technology, supported from basic particle–solid interaction physics studies, rapidly evolved, gaining a strategic position in the semiconductor industry starting in the 1970s [33–34]. The extensive R&D activity developed in silicon technology determined the investigation of several Laboratories into other material systems that might benefit from ion-implantation alloying. The application of ion implantation on non-semiconductor materials required considerably higher ion fluences than on semiconductors. Ion implantation is nowadays a well-established technique to modify the near-surface region of a material by the introduction of energetic ions accelerated through a potential difference in the keV–MeV region. Its use is today widespread in different areas, spanning from the microelectronic industrial production to the synthesis of new materials to end up with academic and fundamental investigations on ion–solid interaction.

The ion-beam applications involve either modifications/engineering of the material surface or its analysis and are correlated to the interactions of the energetic ions with the electrons (electronic energy loss) or nuclei (nuclear energy loss) of the target material. The bombardment of a matrix with energetic ions produces regions of lattice disorder, which results from the physical processes responsible for slowing the ion down and allowing it to come to rest in the matrix. There are two energy-loss mechanisms that contribute to the slowing down processes: (i) nuclear collisions, in which energy is transmitted as translatory motion to the target atom as a whole, and (ii) electronic collisions, in which the moving particle excites or ejects atomic electrons.

The total energy-loss rate $\mathrm{d}E/\mathrm{d}x$ can be expressed as:

$$\frac{\mathrm{d}E}{\mathrm{d}x} = \left.\frac{\mathrm{d}E}{\mathrm{d}x}\right|_{\mathrm{n}} + \left.\frac{\mathrm{d}E}{\mathrm{d}x}\right|_{\mathrm{e}} \tag{1}$$

where the subscripts n and e denote nuclear and electronic collisions, respectively. By normalizing the energy loss for the atomic target density N (atoms/cm^3), one obtains the stopping power S (eV cm^2/atom) as the sum of the nuclear S_{n} and electronic S_{e} contributions: $S = S_{\mathrm{e}} + S_{\mathrm{n}}$. The interaction processes occur on a time scale of picoseconds and length scales as low as nanometers. Nuclear collisions can involve large discrete energy losses and significant angular deflections of the ion trajectory. This process is responsible for lattice disorder by the displacement of atoms from their positions in the lattice. The elastic collisions produce either highly damaged lattices following implantation or a net of damaged structures whose density depends on lattice reordering (i.e., annealing) during the implantation process. Typically, electronic collisions involve smaller energy losses per collision, negligible deflection of the ion trajectory, and negligible lattice disorder. However in insulating materials, radiation damage is also induced in the electronic stopping power regime, due to the break of interatomic bonds. Various models like thermal spike model and Coulomb explosion model have been introduced in order to describe the phenomenon in different materials. For a general review on this topic particularly focused on implantation in insulators see Ref. [35].

The relative importance of the two energy-loss mechanisms changes with the energy E and atomic number of the incident ion Z_1: nuclear stopping predominates for low E and high Z_1, whereas electronic stopping takes over for high E and low Z_1. In Figure 1(a and b) the nuclear and electronic part of the energy-loss function is plotted for Au^+ and He^+ implantation in SiO_2: it is clear that for typical implantation energies of few hundreds of keV in the case of Au the nuclear component dominates over the electronic one, whereas in the He implantation the energy loss is practically completely due to electronic excitation. The relative contribution of the nuclear or electronic stopping power normalized to the total $S_{\mathrm{n}}/(S_{\mathrm{e}} + S_{\mathrm{n}})$ and $S_{\mathrm{e}}/(S_{\mathrm{e}} + S_{\mathrm{n}})$ is shown in Figure 1(c and d) for Au and He, respectively.

As the ion enters the target, it starts to lose energy via multiple collisions with the target atoms, describing a path which is quite complicated. The statistical distribution of the ions implanted can be described by a peak function, which can be roughly approximated by a Gaussian function centered at the average projected range R_{P}, on the perpendicular to the sample surface, with a half width ΔR_{P} called the straggling (Figure 2(a)). The R_{P} and ΔR_{P} values are functions of energy and mass of implanted ion.

Figure 2(b) shows a plot of the in-depth Au concentration profile for three different energies at constant fluence (also called dose, i.e., the integral of the concentration profile). In Figure 2(c and d) the range and straggling for Au and He implantation in SiO_2 are compared: it is clear that the range increases by decreasing the implanted ion mass or increasing the implantation energy. In general, the shape of the implanted profile depends strongly on the energy and on the couple ion/target, and significant deviation from Gaussian-like profile can be obtained.

Implants at different energies can be used in order to obtain a flat doping ion distribution.

It is possible to simulate the kinetics of ion implantation by means of several computer codes: one of the most popular is SRIM (i.e., stopping and range of ions in matter). It is a Monte Carlo calculation which follows the ion into the target, making detailed calculations of the energy transferred to every target atom collision. All the quantities like projected range, ion damage, target ionization, and so on are simulated by averaging over a suitable number of ion trajectories: the higher the ion number the better the precision of the calculation. SRIM code traces back to the original works on range algorithms [36] and on stopping theory [37]. SRIM is able to simulate complex targets made of compound materials with layered structures of different materials. It calculates both the final 3D distribution of the ions and also all kinetic phenomena associated with the ion's energy loss: target damage, sputtering, ionization, and phonon production. All target atom cascades in the target are followed in detail. One main limitation of SRIM calculation is that it does not take into account the accumulated damage, i.e., each simulated ion travels inside an undamaged target. This implies that phenomena like radiation enhanced diffusion (RED) which can play a role during high-fluence ion implantation (like those for synthesizing nanoclusters considered in the present review) cannot be simulated. Other Monte Carlo codes which are able to follow at a good level of approximation the accumulated damage

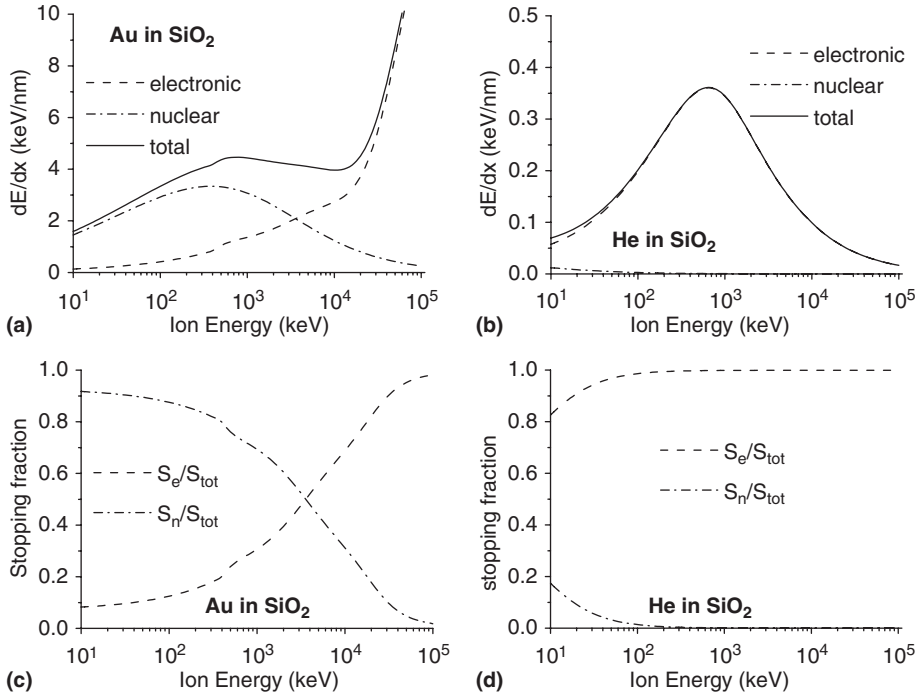

Figure 1. Electronic and nuclear energy loss function of (a) Au implanted in SiO_2 and (b) He implanted in SiO_2. The fraction of the electronic S_e or nuclear S_n stopping power with respect to the total ($S_{tot} = S_e + S_n$) for Au (c) and He (d). (Reprinted from Ref. [1], © 2005, with permission from Italian Physical Society.)

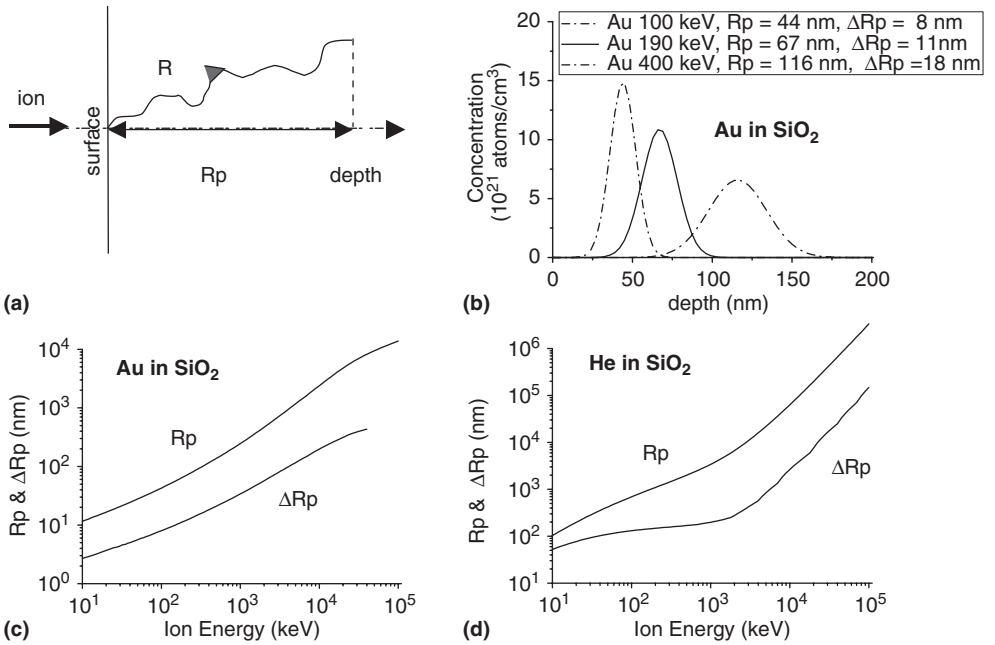

Figure 2. (a) Range R and projected range R_P along the implantation direction perpendicular to the sample surface. (b) In-depth Au concentration profile in silica for three different implantation energies (100, 190, 400 keV) at constant fluence. (c) Projected range R_P and straggling ΔR_P for Au implantation in SiO_2; (d) projected range R_P and straggling ΔR_P for He implantation in SiO_2. (Reprinted from Ref. [1], © 2005, with permission from Italian Physical Society.)

(i.e., to make a so-called dynamical calculation) have been developed, like for instance the TRIDYN [38] or DYNA codes [39,40].

When setting up an actual ion implantation in a target, after choosing the ion and the target, the most important parameters which have to be optimized are:

- Implantation energy: it controls the penetration depth inside the target. Typical values are in the keV–MeV energy range.
- Implantation dose or fluence: it controls the amount of dopant (i.e., its local concentration) introduced in the target per unit surface area. It is measured in ions/cm^2 and it is the integral over the depth of the concentration profile. Typical values in the nanocluster synthesis are 10^{15}–10^{17} ions/cm^2. For a comparison, the typical fluence values for semiconductor doping processes are 10^{13}–10^{14} ions/cm^2.
- Current density or flux: is the number of ions introduced per unit time and unit surface area of the target. It is generally measured in μA/cm^2 and it affects the power density released to the target. Therefore, when dealing with insulating targets like glasses, the flux is of paramount importance to avoid (or to control) the sample heating during implantation. Typical fluxes used in high-fluence implantations are 0.1–10 μA/cm^2, taking into account that above 2–5 μA/cm^2 thermal heating in insulators should be considered and reduced by cooling the target holder.
- Target temperature: it can affect the dynamics of damage self-recovery or of the damage formation. Implantation at cryogenic temperatures can be used to freeze the damage by reducing the diffusion of the atoms. On the other hand, by increasing the temperature, the amorphized regions of the target can be recrystallized or in the case of insulators, by implanting at high temperature (400–900 °C) the recovery of the network can be favored together with the diffusivity of the implanted species.

By ion implantation, very large doping concentration values can be obtained in the ion irradiated region, with a modification of chemical and physical material properties. A proper choice of implantation energies and fluences allows to predetermine the composition, the depth, and the spatial shape of the modified layer. A fundamental feature of ion implantation is that the implantation process is not a thermodynamic equilibrium process. Consequently the usual solubility limits of the implanted ions in the host can be largely overcome, achieving local impurity concentrations inaccessible by conventional synthesis routes. The ion distribution is controlled not only by the experimental parameters of the implantation process (i.e., energy, current, fluence), but also by the diffusion coefficients of the different species (implanted ions and displaced matrix atoms). The change of diffusion rates into the solid, enhanced by the production of defects due to irradiation, can favor either the aggregation of the dopant or their diffusion inside the target. Depending on the choice of the implanted atom and the dielectric target, implantation of "metal" ions in dielectric substrate gives rise to the formation of new compounds and/or metallic nanoparticles. The processes governing the chemical and physical interaction between the implanted ions and the host matrix atoms, very crucial for the final system configuration, are not completely understood in particular in terms of the relative roles of electronic and nuclear energy release [41]. Some models have been so far developed using a simple statistical model and describing the role of a crystalline host matrix structure in the determination of the final compounds upon ion irradiation [42–44]. In Ref. [45] some criterions to predict the formation of small clusters by ion implantation in SiO_2 glass have been proposed, based on physical and chemical considerations, taking into account the defects produced during ion implantation in silica and the free energy for the oxide formation as the quantity giving the measure of the chemical interaction and, in particular [46,47], the electronegativity of the implanted element. Research Groups from Padova and Venice Universities proposed a model [23], originating from the investigation of Ref. [48] on the compositional modification induced by ion implantation on alloys, oxides, and other substances. The proposed model distinguishes two different steps in the ion-implantation process: (1) a high-energy ballistic regime giving rise to the substrate damage (defects, knock-on events, etc.) (2) a low-energy, chemically guided processes inducing the formation of compounds that can be determined on the basis of thermodynamical considerations, taking into account the Gibbs energy variation for a chemical reaction between the implanted element (assumed in the gaseous form) and the silica molecule at the matrix temperature. The two-step model predicts correctly the formation of various compounds and the formation of metallic clusters at room temperature [1].

To this respect, ion implantation is a very efficient technique as it can introduce any desired amount of the foreign phase in the host, without thermodynamic limitations typical of other synthesis techniques: we stress that this is due to the fact the ion implantation is a non-equilibrium technique. The control of cluster size with dimensions in the nanometer range either during the synthesis process or after subsequent thermal annealing is one of the challenging issues of nanocluster technology. Due to the Gaussian-like concentration profile, for single ion implantation at fixed energy a typical value of the size dispersion, $\Delta R/R$, is about 30–50%, which is higher than the best-performing colloidal chemistry synthesis procedure. Nevertheless, this value can be reduced by performing multiple-energy implantation which produces a flat dopant concentration profile. Moreover, this technique does not require multistep processing for the nanocomposite synthesis in different matrices.

The post-implantation thermal treatments have a twofold meaning: (i) annealing of the implantation-induced defects; (ii) growth of the nucleated embryos by means of suitable combination of annealing atmosphere, temperature, and time. In silica, for instance, annealing of the implantation damage requires temperature near or above 600 °C: at these temperatures the thermal diffusion of the implanted species can be quite effective in modifying the post-implantation dopant distribution, promoting either redistribution of implanted species, or clustering around nucleated embryos. Therefore a precise understanding of the microscopic mechanisms influencing the evolution of cluster size during thermal annealing is of paramount

importance [42–44]. Sequential double implantation of noble or transition metals in glass has been explored as a suitable method for creating nanocrystalline clusters within a thin layer of a glass matrix [1,2] below the percolation limit. The non-equilibrium nature of the process may result in the formation of binary metal clusters with composition and crystalline structure different from those predicted by thermodynamics considerations. The implants of two species, considered for binary metal cluster composition, are sequentially performed, choosing the implantation energies and fluencies, in order to obtain the same projected ranges and the required concentration ratio. Figure 3 shows the X-ray photoelectron spectroscopy (XPS) profiles of Au, at an energy of 190 keV, and Cu, at 90 keV, implanted in SiO_2, at the same fluence of 3×10^{16} ions/cm^2 [31,32]. After the implantation, the sample was annealed in reducing atmosphere in order to determine the formation of AuCu alloy nanoclusters. The projected range was of about 70 nm for both ions.

In conclusion, we want underline that three categories can all be defined as ion-beam processing or ion-beam-induced modification of materials:

a) Ion-beam direct synthesis: the direct synthesis of mono- or bi-elemental nanoclusters by single or sequential implantation of the ions constituting the clusters inside the host matrix. This is the most intuitive approach and generally it can be coupled to suitable post-implantation thermal annealing of the samples in controlled atmosphere. In this approach ion beam is used to create a supersaturated solid solution of the implanted ions inside the matrix. The solution, either during implantation itself or after thermal treatments, starts to nucleate and well-defined nanoclusters can be obtained.
b) Ion-beam modification: the energy released by the implanted ions is used to modify already formed clusters by changing their size, shape, composition, and topology. In particular we will see that this mode can be conveniently applied to modify the electromagnetic environment around a nanocluster by the formation of peculiar cluster-satellite topology or to promote a selective de-alloying in bimetallic nanoclusters.
c) Ion-beam indirect synthesis: the ion beam in this case is used to tailor the energy deposited in the target (nuclear vs. electronic, in-depth distribution, etc.) so as to promote nucleation of clusters made of atoms already present in the host matrix, by using auxiliary techniques like for instance ion-exchange.

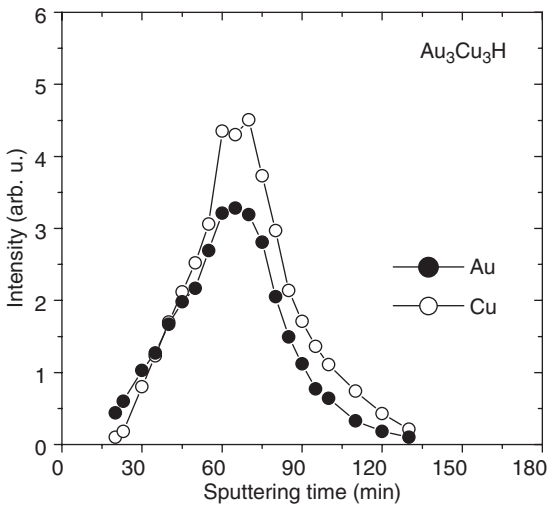

Figure 3. XPS concentration profiles of Au and Cu in the sample Au_3Cu_3 after 1 h thermal annealing at 900 °C in reducing atmosphere.

2.2. Ion-Beam Direct Synthesis: Nanocluster Growth Mechanisms

In the following, we will focus the discussion on how to use ion implantation to produce monoatomic nanoclusters inside a silica glass host. We investigated this crucial problem with a systematic study of the kinetics of gold atom clustering during annealing of gold-implanted silica [49–50]. The use of gold is due to its reduced chemical interaction with the elements constituting the matrix, therefore allowing to focus just on the clustering and growth phenomena, without possible interferences due to formation of bonds with Si or O atoms of the matrix. Moreover, gold has a low diffusivity [51] in comparison to other noble metals like silver for example: this minimizes the role of diffusion controlled processes, which occur during thermal annealings and, consequently, one has the possibility to vary the size and density distribution of nanoparticles by means of the atmosphere in which annealings take place. The precipitation processes that occur during either implantation or annealing of ion-implanted materials may be schematically divided in three steps not necessarily strictly separated: (i) nucleation, (ii) non-competitive or diffusion-limited growth, (iii) competitive growth (i.e., coarsening or Ostwald ripening) regime. Impurity implantation at local concentrations exceeding the solubility threshold in the matrix [49,52] (i.e., for fluences $\geq 10^{16}$ Au$^+$/cm^2 in the case of gold in silica, in our experimental conditions) results, in the first stage of the precipitation process, in a system of new phase precipitates, i.e., gold particles with radius exceeding the critical one, R_c. It is natural to assume that the radiation-induced defects, both point and extended defects, may act as nucleating centers in implanted materials and that heterogeneous nucleation takes place [49].

2.2.1. Nucleation

Assuming the embryos as spherical particles of radius R the variation of the Gibbs $\Delta G(R)$ free energy can be written as $\Delta G(R) = -4\pi/3\ R^3 \Delta g_V + 4\pi R^2 \sigma$, with Δg_V and σ the bulk free energy per unit volume and the surface energy, respectively. The maximum of $\Delta G(R)$ with respect to the radius defines the critical radius $R_c = 2\sigma/\Delta g_V$.

During the initial stage of annealing, the particles (already formed after implantation) with radius exceeding the critical one grow directly by solute depletion of the surrounding matrix, without competing with the growth of any others.

2.2.2. Diffusion-Limited Growth and Ostwald Ripening

The nucleation stage is followed by two different kinetic regimes of cluster growth: (i) a diffusional one (occurring at the earlier stage of growth) which is characterized by a time dependence of cluster radius scaling as $(Dt)^{1/2}$, where D is the diffusion coefficient and t the diffusion time; (ii) a coarsening regime (occurring at longer annealing times) with a radius scaling as $(Dt)^{1/3}$. The two equations that govern the diffusion-limited growth and the coarsening regimes [53–55] are:

$$R^2(t) = R_0^2 + 2\frac{C_s - C_e}{C_p - C_e}Dt \tag{2}$$

$$R^3(t) = R_0^3 + \frac{8}{9}\frac{\sigma V_a^2 C_\infty}{k_B T}Dt \tag{3}$$

where R_0 is the value of R at $t = 0$ (which accounts for the radius of the already formed precipitates by implantation), C_p the concentration of the solute in the precipitates and C_s and C_e the concentration in the matrix, just before the growth, and the equilibrium concentration in the matrix, respectively, C_∞ is the equilibrium solute concentration at planar interface, σ the surface tension, and V_a the atomic volume [56]. The difference C_s–C_e defines the degree of supersaturation that decreases during the precipitation stage.

2.2.3. Experimental Results

To study the nucleation and growth of Au nanoclusters in silica within the above theoretical frame, we implanted fused silica slides with 190 keV-energy Au^+ ions, at room temperature and current densities lower than 2 μA/cm^2, to reduce sample heating [49,50]. The implantation conditions were chosen to have, after annealing, a subsurface buried layer of Au nanoparticle precipitation of about 100 nm thickness. The peak concentration of dopant is about 10–15 at.%, which is above the threshold for spontaneous colloid precipitation (about 1 at.%). Two sets of thermal treatments were performed: (i) isochronal, at constant time (1 h) and at different temperatures in air, in a H_2–Ar gas mixture, or in pure Ar; (ii) isothermal, at constant temperature (900 °C), for different annealing times in oxidizing (air) atmosphere. The evolution of cluster size with the temperature during air annealing can be seen in the transmission electron microscopy (TEM) cross-sectional views of Figure 4(a–d), where for comparison the TEM micrograph of the Ar-annealed sample at 900 °C is also shown. Almost spherical Au clusters of different size are present in all the samples up to a depth of ~130 nm from the sample surface.

Due to low gold diffusivity, the centroid of gold concentration does not move appreciably during the annealing and remains approximately near the implantation projected range (~70 nm), where, as the temperature increases, the largest clusters are formed. The cluster size distributions for the TEM analyzed samples are also reported in Figure 4(e). The progressive shift of the average cluster size towards higher values and the corresponding broadening of the distribution is evident. The results of TEM analysis give for the average cluster diameter (average value ± standard deviation of the experimental distribution) $\langle D \rangle_{400\,^\circ C} = 1.6 \pm 0.8$ nm (similar mean diameter value is obtained in as implanted sample), $\langle D \rangle_{700\,^\circ C} = 2.1 \pm 0.9$ nm, $\langle D \rangle_{900\,^\circ C} = 5.3 \pm 3.9$ nm for the samples annealed in air at 400 °C, 700 °C, and 900 °C, respectively. Samples annealed in Ar and H_2–Ar atmospheres at 900 °C present diameter values ($\langle D \rangle_{900\,^\circ C} = 2.1 \pm 0.9$ nm and $\langle D \rangle_{900\,^\circ C} = 2.5 \pm 1.2$ nm, respectively) comparable to that in as-implanted. To better understand these results, we have analyzed them as a function of the temperature. Figure 4(f) reports the Arrhenius plot of the squared average cluster radius after annealing in air or Ar, at fixed time, 1 h. The corresponding data for the H_2–Ar atmosphere are not reported, being very similar to the Ar case.

From Figure 4(f), we observe that below 700–800 °C the cluster radius increases very slowly with the annealing

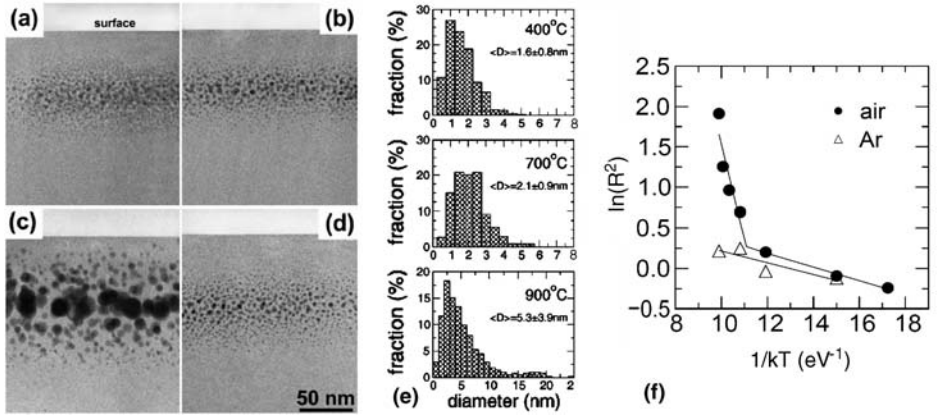

Figure 4. Cross-sectional bright-field TEM views of Au-implanted silica samples at 3×10^{16} Au^+/cm^2, 190 keV, annealed for 1 h at: (a) 400 °C in air, (b) 700 °C in air, (c) 900 °C in air, and (d) 900 °C in Ar, respectively; (e) the histograms of the size distribution of the samples annealed 1 h in air at different temperatures; (f) Arrhenius plot of the squared average cluster radius R^2 after 1 h annealing in air (filled circles) or argon (empty triangles). Solid lines are linear fit to the experimental data.

temperature, at constant time, independently from the atmosphere composition, due to low gold diffusivity. This very modest temperature dependence suggests a diffusion mechanism controlled by radiation damage [57–58]. The measured activation energy of 1.17 eV/atom for gold diffusion in silica during annealing in air, in the temperature range from 750 to 900 °C, is very different from the literature value of 2.14 eV/atom [51]. Note however that the activation energy for the molecular oxygen diffusion in silica through an interstitial mechanism is in the range 1.1–1.3 eV/atom [59,60]. Considering that the clustering process is associated with gold diffusion, in order to explain the role of oxygen in promoting gold diffusivity we interpreted [49] the results by assuming a thermodynamic interaction between oxygen and gold in the framework of the thermodynamics of irreversible processes.

The continuity equations for the excess O_2 and Au atomic concentration n_i and n_j are:

$$\frac{\partial n_i}{\partial t} = D_{ii}\frac{\partial^2 n_i}{\partial x^2} + D_{ij}\frac{\partial^2 n_j}{\partial x^2} \tag{4}$$

$$\frac{\partial n_j}{\partial t} = D_{jj}\frac{\partial^2 n_j}{\partial x^2} + D_{ji}\frac{\partial^2 n_i}{\partial x^2} \tag{5}$$

where subscripts i and j stand for O_2 and Au, respectively, D's are the "diffusion coefficients" which are considered independent of concentration (dilute impurity limit), related to the Kelvin–Onsager phenomenological coefficients [49].

Considering now the continuity equation governing the Au^0 transport we see that, even if the D_{jj} coefficient is small in low-medium temperature regime (700–900 °C), the D_{ji} coefficient may have significant values in the same interval temperature: this implies that just the motion of the permeating oxygen drives the Au^0 diffusion. In other words, the precipitation of the metallic element is induced by the oxygen flux through the crossed correlation coefficient D_{ji}. It is not possible to compare the activation energy of the thermodynamic correlation coefficient D_{ji} with literature data because of the general lack of information in the field of correlation coefficients. However, since the diffusion of the permeating oxygen drives the gold movement, it is not surprising to obtain a D_{ji} coefficient governed by an activation energy quite similar to the one of the interstitially diffusing O_2 molecule.

In conclusion, the main results of the investigation of the temperature dependence of the cluster radius under isochronal annealing (1 h) may be summarized as follows: (i) annealing in air is more effective in promoting cluster aggregation with respect to reducing or neutral atmosphere; (ii) the squared average cluster radius in an Arrhenius plot shows two different regimes upon air annealing, which can be explained by a general model for gold atom diffusion interacting with excess oxygen coming from the external ambient. The clustering regime characterized by an activation energy of 1.17 eV/atom, very different from that appropriate to gold diffusion in silica (2.14 eV/atom), is then attributed to the thermodynamic correlation coefficient, D_{ji}. We have thus extended the analysis of the gold clustering problem for annealing in air considering annealing time intervals exceeding 1 h, when coarsening becomes most probably the relevant cluster growth mechanism. The evolution of the cluster size as a function of the air annealing time can be followed in the cluster size distributions, as measured in the TEM analyzed samples (Figure 5(a–d)), including the as-implanted sample. As the annealing time interval increases, largest spherical Au clusters are formed and a corresponding broadening of the distribution is evident. The results of TEM analysis give the following average cluster diameters: $\langle D\rangle_{\text{as-impl.}} = 2.0 \pm 1.0$ nm, $\langle D\rangle_{1h} = 3.6 \pm 1.9$ nm, $\langle D\rangle_{3h} = 5.6 \pm 3.5$ nm, and $\langle D\rangle_{12h} = 12.6 \pm 7.2$ nm.

In Figure 5(e) we report R^2 (the square of the average radius of the growing particles) as a function of t (these values have been obtained either by TEM analysis or by fitting the optical absorption spectra). We observe a linear relation between the two quantities with a change of the slope in the range between 4 and 5 h. This linearity is expected when the cluster growth is only due to the precipitation process of a supersaturated solution. The change of the slope in the plot suggests that the kinetics of cluster growth is modified. Without considering a possible change of the D parameter, not easily understandable in long-time annealing experiments, the discontinuity may be explained by considering that the coarsening regime occurs. In fact, the experimental radius values, corresponding to annealing time intervals of 6, 7, 8, 12 h, well agree with a $t^{1/3}$ law of growth, as expected in the Ostwald ripening regime, as in Figure 5(f). In our experimental conditions we observe the occurrence of the transition from a diffusion-limited regime to Ostwald ripening for annealing time intervals in the range between 4 and 5 h. From the slopes of the linear fit in Figure 5(e and f) together with Equations (2) and (3), we estimated the gold cluster surface tension σ. The obtained value of 1.5×10^{-4} J/cm^2 is consistent with the measured gold surface tension value of a "free surface" [61].

2.2.4. *Linear Absorption of Embedded Metal Clusters: The Mie Theory*

In this Section we want to present one of the fingerprints of noble-metal cluster formation, that is the development of a well-defined absorption band in the visible or near UV spectrum which is called the surface plasma resonance (SPR) absorption. SPR is typical of s-type metals like noble and alkali metals and it is due to a collective excitation of the delocalized conduction electrons confined within the cluster volume [15]. The theory developed by G. Mie in 1908 [22], for spherical non-interacting nanoparticles of radius R embedded in a non-absorbing medium with dielectric constant ε_m (i.e. with a refractive index $n = \varepsilon_m^{1/2}$) gives the extinction cross-section $\sigma(\omega,R)$ in the dipolar approximation as:

$$\sigma(\omega,R) = 9\frac{\omega}{c}\varepsilon_m^{3/2}V_0 \times \frac{\varepsilon_2(\omega,R)}{(\varepsilon_1(\omega,R)+2\varepsilon_m)^2+\varepsilon_2^2(\omega,R))} \tag{6}$$

where V_0 is the cluster volume, c the speed of light in vacuum, and $\varepsilon(\omega,R) \equiv \varepsilon_1(\omega,R) + i\varepsilon_2(\omega,R)$ the size-dependent

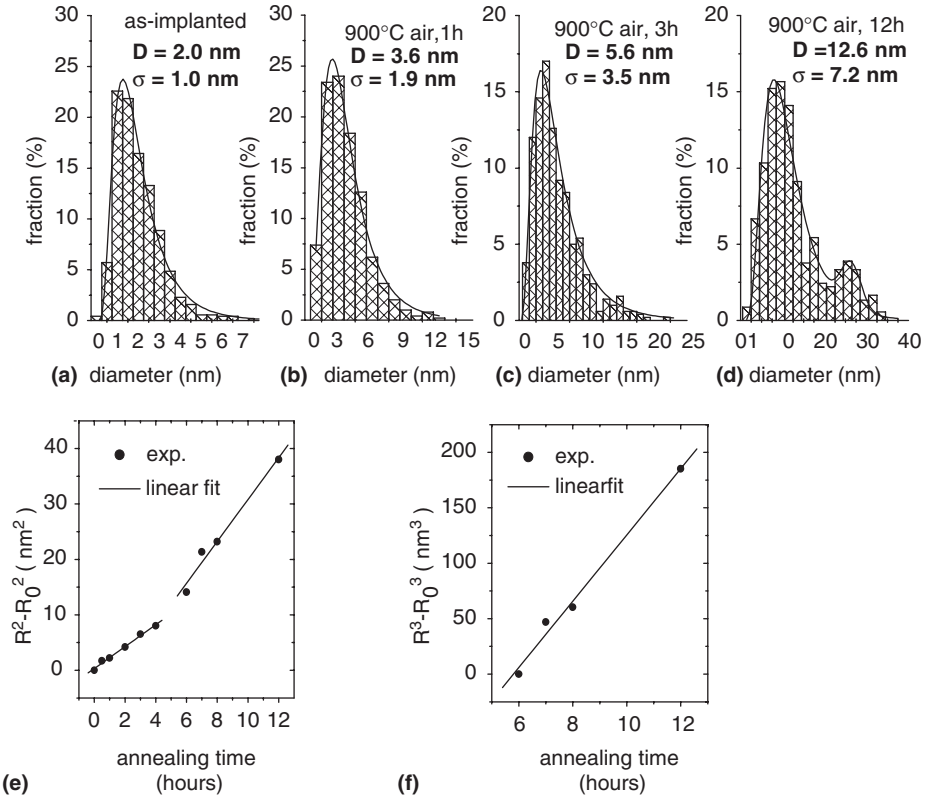

Figure 5. (a–d) Histogram of size distribution for the as-implanted and annealed for 1 h, 3 h, 12 h samples, at 900 °C in air; (e) $R^2(t)$–R_0^2 and (f) $R^3(t)$–R_0^3 evolution for annealing in air at 900 °C for different time intervals. Solid lines are the linear fits to the experimental data (filled circles).

complex dielectric function of the cluster. The SPR resonance holds when the denominator is vanishingly small. This approximation is valid for isolated clusters when the radius is much less than the wavelength $\lambda = c(2\pi/\omega)$: when this is not the case, retardation effects inside the cluster make the electrons oscillate not all with the same phase of the local field and high-order multipolar expansion should be taken into account in the general Mie formula [15]. One relevant point concerns the size dependence of the cluster dielectric function. Following Ref. [15], the size correction is obtained by modifying the Drude-like part due to delocalized free s-electrons introducing a size-dependent damping frequency which accounts for the increased scattering at the cluster surface.

To better illustrate the main factors influencing the position and the shape of the SPR absorption band, in Figure 6(a) the effect of the cluster radius is shown for Ag nanoclusters in silica: when the size is no longer negligible with respect to the wavelength there is a red-shift of the SPR position with the appearance of multipolar peaks in the UV–blue region. The effect of the matrix for a fixed cluster size is described for $R = 2.5$ nm Au clusters in Figure 6(b): the higher the matrix dielectric constant the more red-shifted is the SPR. Finally, the effect of the composition is shown in Figure 6(c) for $R = 5$ nm clusters of Ag, Au, and Cu in silica.

The optical absorption spectra of Au-implanted silica samples annealed in air or Ar for 1 h at different temperatures are shown in Figure 7(a and b) respectively. The above formalism has been applied (Figure 7) to extract the size distribution of Au clusters upon thermal annealing from the optical density (OD) absorption measurements to complement the TEM analysis, as reported in Figures 4 and 5. The good level of agreement is shown in Figure 7(c). The kinetics of cluster growth can be followed as a function of the time in Figure 7(d) for annealing in air at 900 °C.

2.2.5. Ion Implantation in Polymer Matrix

With the aim of giving a further contribution to the understanding of this field we have investigated the gold precipitation process induced by ion implantation in a polyimide matrix [62]. We focused on gold for two main reasons: (i) its chemical inertness, which allows to decouple cluster nucleation from the chemical interaction of the implanted species with the matrix components; (ii) the large optical absorption cross-section of gold nanoclusters (SPR) in the VIS region at wavelengths larger than the optical absorption edge of the chosen polyimide. We have investigated the nanostructural, compositional, and optical properties of Au-pyromellitic dianhydride-4,4′ oxydianiline (PMDA-ODA) polyimide thin films prepared by implanting different fluences of Au^+ ions at the same

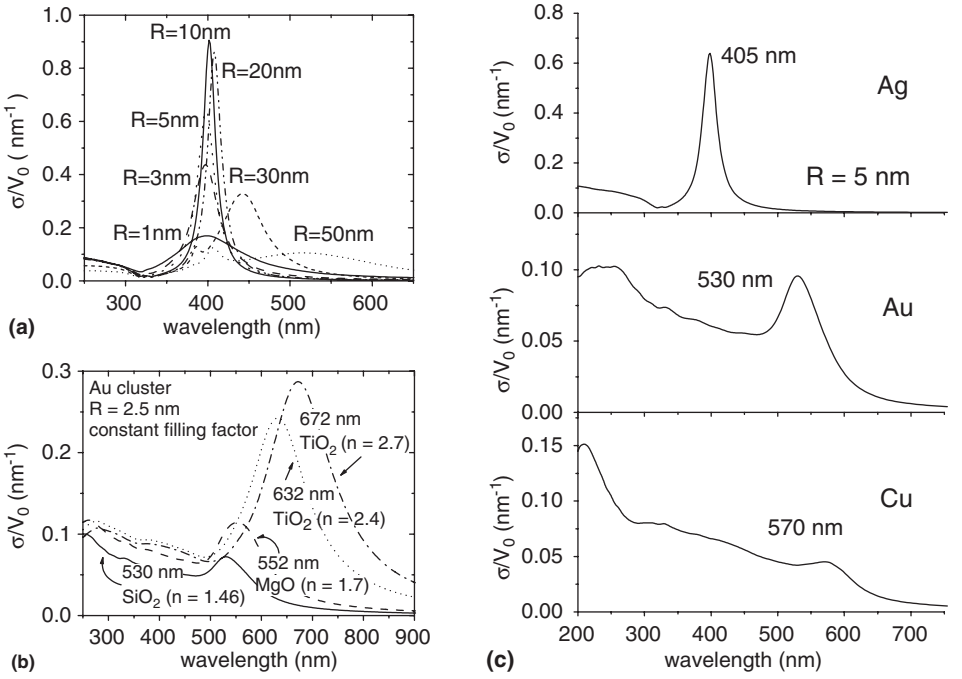

Figure 6. Absorption spectra of spherical non-interacting nanoclusters embedded in no absorbing matrices: (a) effect of the size for Ag nanoclusters in silica; (b) effect of the matrix for $R = 2.5$ nm Au clusters (the refractive index $n = \varepsilon_m^{1/2}$ and the position of the plasma resonance are reported for each considered matrix); (c) effect of the cluster composition for $R = 5$ nm noble-metal clusters (Ag, Au, Cu) in silica. (Reprinted from Ref. [1], © 2005, with permission from Italian Physical Society.)

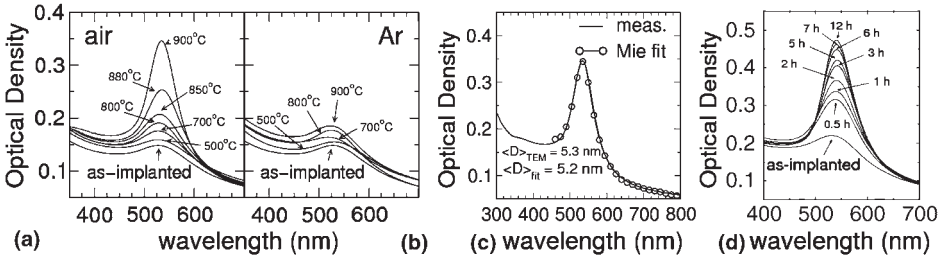

Figure 7. Optical absorption spectra of Au-implanted silica samples annealed in air (a) or Ar (b) for 1 h at different temperatures. (c) Nonlinear fit (empty circles) to the optical absorption spectrum of the sample annealed at 900 °C in air, from which the average cluster diameter $\langle D \rangle_{\text{fit}}$ is obtained and compared to the TEM measured one, $\langle D \rangle_{\text{TEM}}$. (d) Evolution of the optical spectra of Au-implanted silica annealed in air at 900 °C for different time intervals.

energy. Thin films of PMDA–ODA polyimide with a thickness of 100 ± 2 nm were deposited by glow discharge vapor deposition polymerization (GDVDP) on pure silica matrix. This is a very recently developed method [63] for the deposition of very thin polyimide coatings, alternative to the other better-known deposition methods such as spinning, vapor deposition polymerization, and ionized cluster beam deposition. These films were then implanted at different fluences at a beam energy of 100 keV, which corresponds to a projected range of about 60 nm and a straggling of 9 nm, with an ion current density of about $0.3\,\mu A/cm^2$. In order to avoid heating of the polymer films during the implantation, the sample holder was water-cooled. The bright-field TEM micrograph of the sample, in Figure 8(a), shows spherical Au nanoparticles dispersed in a 40 nm thick layer, embedded between two nanoparticle-free layers: a 10 nm thick surface layer and a bottom layer of about 30 nm. The particle size distribution (Figure 8(b)) has an average value of 2.3 nm and a standard deviation of 1.3 nm. A depth profile composition by energy dispersive X-ray microanalysis (EDS) evidenced that the C content of the surface layer is higher with respect to the rest of the film, according to literature data [64,65]. Figure 8(d) reports the X-ray diffraction patterns indicating the crystalline structure of nanoclusters and their formation for an implantation fluence higher than $10^{16}\,Au^+/cm^2$.

The TEM data have been used to simulate, in the frame of the Mie theory and Maxwell–Garnett effective medium approximation [15], the optical absorption spectra of the sample implanted with $5 \times 10^{16}\,Au^+/cm^2$. The results are reported in Figure 8(c). In the first model used to describe

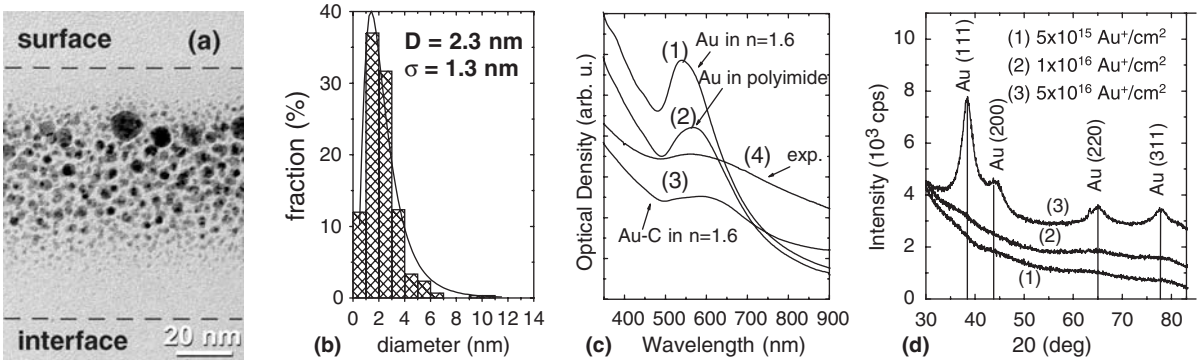

Figure 8. TEM and optical absorption of the sample implanted with $5 \times 10^{16}\,Au^+/cm^2$: (a) TEM cross-sectional micrograph (dashed lines represent the free surface and film–substrate interface); (b) nanoparticles size distribution; (c) simulated optical spectra: (1) Au cluster in a non-absorbing medium with $n = 1.6$; (2) Au cluster in polyimide (absorbing); (3) Au(core)–C(shell) cluster in a non-absorbing medium with $n = 1.6$; (4) the experimental spectrum of Au-implanted polyimide sample. (d) X-ray diffraction patterns as a function of the implantation fluence.

the nanocomposite absorption properties, spherical Au clusters with size 2.3 nm are surrounded by a matrix with refractive index of about 1.6, typical of the aromatic polyimides (this assumption can be justified by the above analysis on the local polymer composition near the Au clusters). The simulation, in which the experimental bulk dielectric function of gold has been size-corrected according to Ref. [15], gives a narrow resonance centered at 550 nm instead of a large band centered at 560 nm. Even considering that the matrix could have a larger refraction index due to implantation damage [66], the simulation does not reproduce the measured spectrum because the SPR simply shifts to larger wavelengths without any FWHM broadening.

We consider a second model in which the Au cluster is surrounded by a very thin carbon layer, forming a core–shell particle dispersed in a polyimide matrix. Including this shell, the resonance band red-shifts but now the SPR is strongly damped by the Au–C interaction. The best agreement between experimental and simulations is obtained for a C shell thickness of about 0.8 nm, indicating that locally the composition of the matrix can be carbon-enriched. In order to account for possible effects of the matrix absorption (previously neglected by using a purely real refractive index), a calculation has been also made in the frame of effective medium theory by using for the polyimide a complex dielectric function obtained from transmittance–reflectance measurements performed on the as-deposited film [67]. The calculated absorption shows a better agreement with the experimental spectrum with respect to the non-absorptive case, but the local correction with a C-rich shell around the gold core seems to be qualitatively more effective in reproducing the experimental data and it is more consistent with the graphitization process usually observed in polymers after ion-irradiation. Actually, this carbon shell should be hardly perceptible in the TEM image due to the very low contrast with the polymer matrix. The combination of GDVDP technique (that allows depositing nanometric thin films) with ion implantation (suitable for doping materials with a large number of elements) could be a promising method to obtain new polymer-based nanostructured films with magnetic, optical, rheological, sensing, and electronic properties. The optical gas sensing features of virgin polyimide thin film deposited by glow discharge vapor deposition polymerization and of gold-implanted films have been recently studied by using optical absorption and surface plasmon resonance transduction techniques [68] and will be presented in Section 4.2.

3. Ion-Beam Direct Synthesis: Bimetallic Clusters

Sequential ion implantation of two different metal species at suitable energies and fluences to maximize the overlap between the implanted species and control their local relative concentration may give rise to different nanocluster structures, with the possible presence of separated families of pure metal clusters, crystalline alloy clusters, or core–shell structures. The formation of clusters of a certain nature depends critically on the implantation parameters, implant sequence, and the temperature at which the process is realized. Moreover, post-implantation treatments such as annealing in controlled atmosphere and/or ion or laser irradiation have been demonstrated to be effective in driving the system towards different stable cluster structures. As a general rule, the criterion valid for bulk systems of miscibility of the two elements as a constraint for alloy formation is not so stringent in the case of nanoclusters. This is due to the incomplete onset of the bulk properties triggered by the large number of atoms at the surface that makes a cluster more similar to a molecular than to a massive system [69]. This leads to new possible alloy phases, which may be thermodynamically unfavored in the bulk. In the case of noble-metal-based systems (Au–Cu, Au–Ag, Pd–Ag, and Pd–Cu) perfect miscibility is expected from the bulk phase diagrams and in fact sequentially as-implanted samples exhibit direct alloying [1,2,4]. On the contrary, systems like Co–Cu or Au–Fe which are not miscible in the bulk showed nanoalloy formation after sequential implantation in silica. Binary nanoparticles can be present as alloys but also as core–shell structure that can have new properties due to

the interaction or combination of the properties of the two parts of the nanoparticle. The nanostructure of the binary nanoparticles depends both on the chemical reactivity of the implanted species [23,70] and on the alloy formation heat. For a more detailed description of the nanostructure obtained by sequential ion implantation in silica see Ref. [1].

As shown in the previous Sections, in the case of noble-metal clusters the SPR in the visible range is a clear fingerprint of nanoparticles formation [15]. Similarly, for noble-metal alloys the SPR resonance is located in between those of the pure elements, and is triggered by the complex interplay between the modified free electrons and interband absorptions. This can be seen in Figure 9, which shows a comparison between optical absorption OD spectra either simulated with the Mie theory [15,22] for 3 nm clusters of pure Au, Ag, and $Au_{0.4}Ag_{0.6}$ alloy in silica (Figure 9(a)), or measured for analogous systems [31] in ion-implanted silica (Figure 9(b)).

Linear absorption measurements can therefore give the first indication of possible alloy formation. Nevertheless, in systems containing transition metals (Pd–Ag, Co–Ni, …) such a simple technique is no longer effective as interband transitions completely mask the SPR peak, resulting in a structurless absorption, which hinders any unambiguous identification of the alloy. In such cases, one has to rely on structural techniques like TEM (selected-area electron diffraction, SAED and energy-dispersive X-ray spectroscopy, EDS) or EXAFS (extended X-ray absorption fine structure) to establish alloy formation.

We summarize in Table 1 some of the most relevant results, obtained by our group, on binary alloy nanoclusters in silica by using ion implantation.

3.1. Magnetic Binary Clusters

As an example of binary clusters for magnetic applications, we present the study performed on Ni–Co alloy [78]. The Co–Ni phase diagram was investigated by performing sequential ion implantation in silica of Co and Ni at the same energy of 180 keV ($R_p \sim 150$ nm) but with different fluences in order to have a constant total Co+Ni fluence (15×10^{16} ions/cm^2 or 30×10^{16} ions/cm^2). For the 1:1 Co:Ni ratio, we also performed sequential implants at two energies (180 keV and 70 keV) for each element to have a flatter concentration profile for a total fluence of 40×10^{16} ions/cm^2. All the samples investigated exhibit Co_xNi_{1-x} alloy nanoclusters. In this case, OD spectra are not useful for alloying detection due to the above-mentioned damping of the SPR due to interband transitions [15]. SAED analysis was able to monitor a phase transition from f.c.c. to h.c.p. as the Co content in the system is greater than 70%, in agreement with bulk Co–Ni alloy. It is interesting to note that similar Co–Ni alloy system obtained by our group with the sol–gel route, exhibited at all the Co/Ni ratios the f.c.c. structure [81]. As the lattice parameters of the f.c.c. phases of Co and Ni differ by a quantity that is at the limit of SAED quantification for nanoclustered systems (mostly due to the size-dependent broadening of the diffraction peaks), we performed also EDS compositional analysis with a sub-nanometer electron probe on single clusters which demonstrated the presence of both Co and Ni.

Figure 10(a) shows a TEM image of a sample containing Co and Ni in the ratio 4–1 (Co4Ni1) whereas Figure 10(b) is a TEM image of the Co1Ni1 sample (implanted at a total fluence 40×10^{16} ions/cm^2): the SAED pattern for Co1Ni1 sample exhibits a single alloy f.c.c. phase with lattice parameter $a = 0.3533(12)$ nm, whereas, when the

Table 1. Nanostructure of some investigated systems obtained by sequential ion implantation without subsequent annealing.

System	Nanostructure	Ref.
Au–Cu	Alloy	[32]
Au–Ag	Alloy	[71]
Au–Fe	Alloy	[72]
Fe–Al	Alloy	[73]
Pd–Ag	Alloy	[74]
Pd–Fe	Alloy	[75]
Pd–Cu	Alloy	[76]
Cu–Ni	Alloy	[77]
Ni–Co	Alloy	[78]
Co–Cu	Alloy*	[78]
Ag–S	Core–shell	[79]
Ga–N	Separated	[80]
In–N	Separated	

The labeling A–B indicates the implantation order: first ion A and then ion B.
*h.c.p. and f.c.c. phase coexistence.

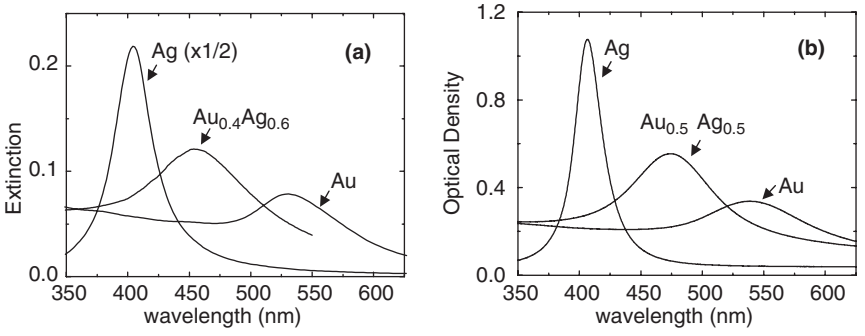

Figure 9. Comparison between a simulation based on the Mie theory of OD in the UV–Vis range for 3 nm clusters of pure Au, Ag, and $Au_{0.4}Ag_{0.6}$ alloy in silica (a), with the experimental OD of the same systems in ion-implanted silica (b). (Reprinted from Ref. [1], © 2005, with permission from Italian Physical Society).

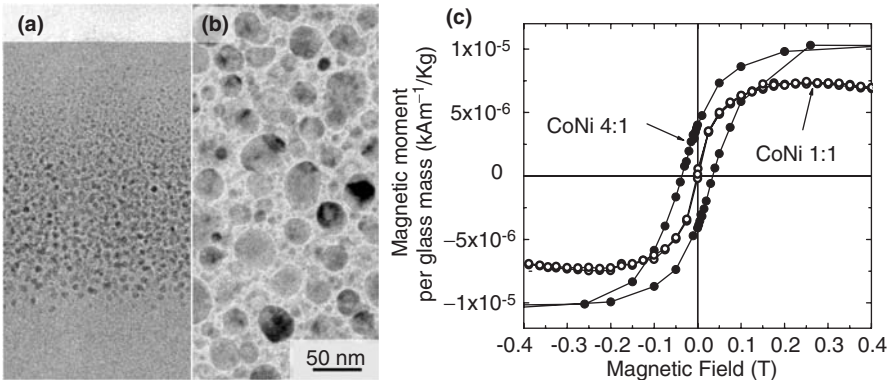

Figure 10. (a) Cross-sectional bright-field TEM image of sequentially ion-implanted silica with Co and Ni with a concentration ratio of 4:1 for a total fluence 30×10^{16} ions/cm^2; (b) planar bright-field TEM image of sequentially ion-implanted silica with Co and Ni with a concentration ratio of 1:1 for a total fluence 40×10^{16} ions/cm^2; (c) comparison between the room temperature hysteresis loop of f.c.c. Co1Ni1 and h.c.p. Co4Ni1 samples. (Reprinted from Ref. [1], © 2005, with permission from Italian Physical Society.)

Co concentration in the alloy is increased above 70% (Co4Ni1), an h.c.p. diffraction pattern is obtained. The difference in structure as a function of the Co contents in the alloy is of paramount importance for controlling the magnetic properties. In Figure 10(c) the hysteresis loop of f.c.c. Co1Ni1 and h.c.p. Co4Ni1 samples (at the same total fluence) are compared: the average cluster size in both samples is similar (about 5 nm) but the h.c.p. phase (Co4Ni1) exhibits a coercive field which is absent in the f.c.c. phase (Co1Ni1). This is due to the reduction in symmetry of the hexagonal unit cell with respect to the cubic one.

3.2. *Metastable Alloys*

We want now to discuss in detail the formation of metastable alloys, as Au–Fe [72]. The interest of investigating this type of systems is in the combination of two metals with different application areas: while Fe or Fe-based nanocomposites are among the most investigated magnetic material, AuFe nanoparticles could combine two kinds of properties, magnetic and optical. Bulk Au–Fe alloys can be obtained by different out-of-equilibrium methods [82] showing interesting magnetic, magneto-transport, and magneto-optical properties [83–88]. In particular the $L1_0$ ordered structure has been observed in thin films [84]. Nanoparticles with this structure, typically characterized by a large magnetocrystalline anisotropy, could be very interesting ferromagnetic recording applications. However most works related to Au–Fe nanoparticles have considered core–shell or onion-like nanostructures [89–91]. Only recently the formation by electronic beam evaporation technique of Fe–Au nanoparticles with complex structure has been reported [92]. In our work [72] we showed the possibility of obtaining Au–Fe alloy nanoparticles by sequential implantation technique. The implantation energies were 190 keV for Au and 90 keV for Fe to obtain the same projected range (about 70 nm), in order to maximize the overlap between the concentration depth profiles of both species. For comparison, also single implants of gold and iron were performed with the same implantation conditions. The bimetallic Au–Fe sample was heat treated in a conventional furnace at different temperatures between 400 °C and 900 °C in a flowing gas mixture of Ar(90%)–H_2(10%) for 1 h. Despite the two species not being miscible in the bulk, structural characterizations show that the nanoparticles produced are an Au–Fe alloy. The bright-field cross-sectional TEM micrograph of the Au–Fe as implanted sample shows that the largest clusters are found at a depth of about 50–60 nm (to be compared with the nominal range of 70 nm). The nanoparticles were spherical with an average size of 4–6 nm with a broad size distribution (few very large clusters up to 20 nm in size are indeed present in the middle of the implanted region). SAED and GIXRD patterns (see Figure 11(a)) indicate a single f.c.c. structure with a lattice parameter of 0.395(1) nm, which is different from the pure gold f.c.c. value ($a = 0.4082$ nm). Fe has typically a b.c.c. arrangement with a lattice parameter of 0.2870 nm. On the other hand, the Fe f.c.c. phase can have a lattice parameter ranging from 0.340 nm to 0.388 nm [93]. All these values are not consistent with the measured one for the Au–Fe sample. At 600 °C we observe a splitting of the original single f.c.c. phase in two f.c.c. phases with lattice parameters equal to 0.404(1) nm and 0.396(1) nm, respectively. This indicates that a strong structural rearrangement took place. The first value is more similar to that of gold, although smaller than it, and the last one is similar to that of the as-implanted sample. Therefore diffraction results can be consistently interpreted with the formation of an Au–Fe f.c.c. solid solution in as-implanted sample, and a de-alloying process starting at about 600 °C.

To be more confident on alloy formation, we performed EDS compositional analysis with an electron probe size of 1 nm FWHM focused on isolated clusters: as expected for bimetallic clusters, Au and Fe signals are together present in the spectrum. The measured Au/Fe atomic ratio on the largest clusters is about 1.6 ± 0.2, indicating an Au-enriched alloy. Moreover also preliminary EXAFS spectroscopy on the sample evidenced a clear Au–Fe correlation, unambiguously confirming alloy

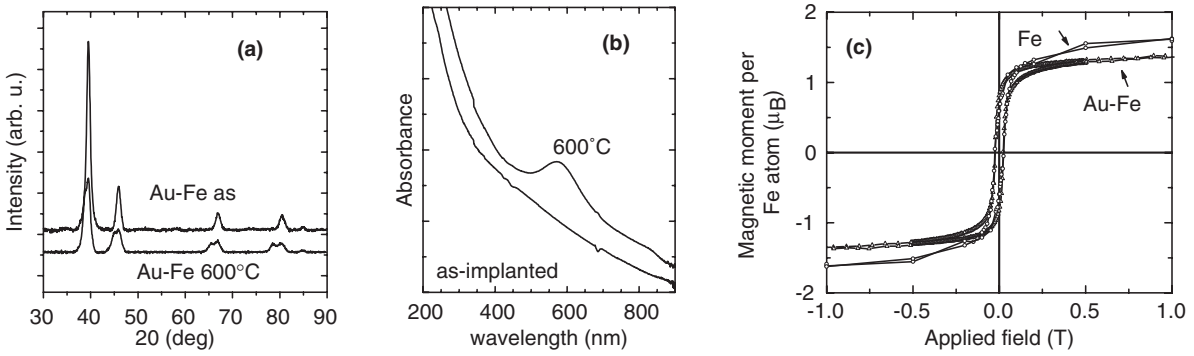

Figure 11. Grazing incidence X-ray diffraction patterns (a) and OD spectra (b) of the as-implanted Au–Fe sample and of the sample after annealing at 600 °C for 1 h in reducing atmosphere. (c) Hysteresis loops of the as implanted Au–Fe and of the only-Fe samples measured at 3 K.

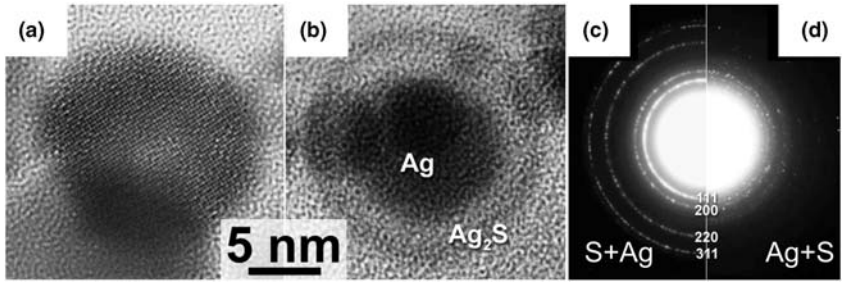

Figure 12. Cross-sectional TEM images of a silica sample implanted with Ag and S: (a) high-resolution image showing the lattice planes of the Ag_2S shell; (b) bright-field showing the contrast between the Ag core and the Ag_2S shell; (c) and (d) are the diffraction pattern of the sample sequentially implanted with S followed by Ag and with Ag followed by S, respectively. (Reprinted from Ref. [1], © 2005, with permission from Italian Physical Society.)

formation. Considering the Au/Fe ratio measured by EDS, the Fe atoms that do not participate to the alloy should be dispersed in the matrix probably in an oxidized form [94]. Au–Fe alloy formation reflects on the optical absorption spectrum of the sample shown in Figure 11(b). It is well known that pure Au nanoparticles in silica exhibit a SPR absorption at about 530 nm [1]. This band is absent in the Au–Fe sample, indicating a strong electronic interaction between Au and Fe atoms which is able to damp the SPR resonance by means of strong interband transitions. After annealing at 600 °C the Au-related SPR absorption is evident, confirming the occurrence of the de-alloying process. These interband transitions should also affect the magnetic behavior of the nanocomposite. In Figure 11(c) the hysteresis loops measured at 3 K of the Au–Fe and only-Fe samples are shown. The spectra were corrected for the diamagnetic contribution of the silica and normalized to the measured Fe fluence. The magnetic moment per Fe atom at 6 T of the Au–Fe sample is slightly smaller (1.4 ± 0.1 μ_B) than that of the only Fe sample (1.8 ± 0.1 μ_B). The coercive field of both samples are similar, 24 ± 1 mT. The magnetic order in Fe–Au alloys can depend on the composition, structure and on the chemical order. The dependence of the Fe magnetic moment per atom has been measured as function of the Au_xFe_{100-x} composition in melt spinning alloys [82]. The Fe magnetic moment for $10 < x < 75$ is constant, 2.2 μ_B, and this value decreases for larger Au contents, confirming that the composition of the Au–Fe alloy obtained in the present work should be enriched in Au.

3.3. Core–Shell Structure

Sequential ion implantation gives rise to ''mixed'' clusters, in the sense that both elements are present on the same cluster but each one maintaining its structure in a core–shell arrangement. Fused silica slides were sequentially implanted at room temperature with Ag (65 keV energy) and S (30 keV) ions at a fluence of 5×10^{16} ions/cm^2 and 2×10^{16} ions/cm^2, respectively, to obtain the same projected range of about 40 nm [79]. In Figure 12(a) a high-resolution TEM image shows the lattice fringes arising from the shell made of Ag_2S in the acanthite form superimposed on the core composed of Ag. In Figure 12(b) a bright-field view of the sample sequentially implanted first with Ag and then with S ions shows a spherical core–shell cluster with a clear contrast between the Ag core and the Ag_2S shell. It is interesting to note that no mixed clusters are obtained upon reversing the implantation order: performing first S and then Ag implantation (S–Ag sample), only Ag clusters are detected while S takes part to the formation of thiosilicate species [79]. This can be seen in Figure 12(c and d) which compare the SAED electronic diffraction of the two samples: Figure 12(c)

shows an f.c.c. pattern of silver nanoclusters in the S–Ag sample, whereas Figure 12(d) shows both the f.c.c. reflections of Ag nanoclusters and the monoclinic one of the Ag_2S shell.

4. Some Case Histories

4.1. Non-Linear Optical Properties of Au-Based Alloys

Metal quantum-dot composites, in particular MNCGs, exhibit an enhanced optical Kerr susceptibility, $\chi^{(3)}$, whose real part is related to the n_2 coefficient of the intensity dependent refractive index, usually defined as $n(I) = n_0 + n_2 I$, where n_0 and I are the linear refractive index and the intensity of the light, respectively. Correspondingly, also a non-linear absorption takes place which can be described macroscopically by the intensity-dependent absorption coefficient $\alpha(I) = \alpha_0 + \beta I$, where α_0 and β are the linear and non-linear absorption coefficients, respectively. The intraband and interband electronic transitions that contribute to the effective $\chi^{(3)}$ turn out to depend on the type of metal and the form and size of the clusters, as well as on the metal–dielectric bonds [10] Suitable methodologies are therefore needed for tailoring the formation of small metal clusters within the glass, with the aim being to fabricate non-linear glasses with prescribed optical performances. This non-linearity can be described for centro-symmetric systems (like randomly dispersed nanoclusters in an amorphous matrix, which do not exhibit even order contributions) as a third-order correction in the external field **E** to the linear polarization **P**, whose component i reads:

$$P_i = \left(\varepsilon_0 \sum_j \chi^{(1)}_{ij} E_j + \sum_j \chi^{(3)}_{ijkl} E_j E^*_k E_l \right) \tag{7}$$

The third-order optical Kerr susceptibility of nanocomposites, χ_{eff}, formed by a non-absorbing matrix, with dielectric constant ε_m, containing metal nanoclusters with low volume fraction p (i.e., filling factor) is given [95] by:

$$\chi^{(3)}_{\text{eff}} = p \chi^{(3)}_{\text{clu}} |f_c|^2 f_c^2 \tag{8}$$

$$f_c = \frac{3\varepsilon_m}{\varepsilon + 2\varepsilon_m} \tag{9}$$

where $\chi^{(3)}_{\text{clu}}$ is the non-linear contribution of the clusters, ε the metal dielectric constant, and f_c the local field enhancement factor. Mutual electromagnetic interactions among nanoparticles determine an increase of the modulus of f_c.

MNCGs exhibit high non-linearity in the picosecond regime [27,96,97]. They could offer the possibility to realize all-optical switching devices, that is, operating in a time range faster than the electronic ones and without converting optical signals to electronic form. Among the techniques for the measurement of the non-linear refractive index of a material, Z-scan technique, originally proposed by Sheik-Bahae et al. [98], allows to determine both sign and magnitude of n_2 [99,100]. Z-scan technique is very sensitive to detect small non-linear refractions, however it is difficult to discriminate between electronic and thermal effects. In particular, the use of high repetition-rate lasers [3,96,101] may trigger important heating of the composite glasses, giving rise to thermo-optical non-linearities (due to cumulative heating of the sample) that can obscure all fast relaxation processes. In Ref. [95] we evidenced and evaluated the importance of the heating effects among the physical origins of the non-linear optical properties exhibited by MNCGs. To avoid sample heating, Z-scan measurements were performed using a ring-cavity, mode-locked Nd:glass laser as a source. This laser supplies single shots at a very low repetition rate (about 1 Hz), each one being a train of about 100 pulses of nearly equal intensity. The single pulse duration is about 6 ps, and the time separation between two pulses is about 5 ns, avoiding cumulative heating effects. The laser peak power was about 140 MW. We used both the fundamental ($\lambda = 1064$ nm) and the second harmonic ($\lambda = 532$ nm) of the laser. Very interesting fast non-linear optical properties are shown by the MNCGs containing AuAg and AuCu nanoclusters, produced by ion implantation, with non-linear refractive index n_2 of $(-1.6 \pm 0.3) \times 10^{-10}$ cm^2/W and $(+6.3 \pm 1.2) \times 10^{-11}$ cm^2/W, at 527 nm of wavelength [95,102], respectively. Just to have an idea of the increase in the non-linear optical properties due to the nanoclusters, the pure silica matrix has a $n_2(SiO_2) = 5 \times 10^{-16}$ cm^2/W. The peculiarities of this experimental finding are the very large modulus value of n_2 and the sign change according to the cluster composition. Such high value of the fast n_2 coefficient has never been detected in MNCGs up to now [103]. An explanation of this evidence can be given by considering that for metal volume fractions (i.e., filling factors) p around 0.1 and near the SPR wavelength, the mutual electromagnetic interactions among nanoparticles begin to induce deviations from the low-p approximation of the third-order optical Kerr susceptibility, $\chi^{(3)}_{\text{eff}}$ [95]. Mutual interaction among nanoparticles [104] could then explain the large values of the n_2 coefficients. As far as the sign reversal of the non-linear refractive index as a function of the cluster composition is concerned, this evidence in a MNCG is related to the relative position in wavelength of the nanoparticle surface plasmon band with respect to the used laser (527 nm). The local-field enhancement factor for alloy nanoclusters embedded in silica glass has been computed in the frame of Mie theory, starting from experimental bulk dielectric functions of a metallic Au–Ag alloy and correcting them for the finite size of the particles [95]. Indeed, the negative sign of n_2 is well explained by considering the wavelength dependence of the nanoparticles local-field factor.

Interesting nanostructures, that may present an interaction among nanoclusters, with consequent increase of local field enhancement factor are obtained by irradiating AuCu alloy clusters with Ne ions at 190 keV [30].

The irradiation conditions were chosen to avoid overlap of the implanted Ne atoms with the already formed clusters: the R_P of the Ne ions is indeed about 410 nm with a straggling of about 100 nm. Therefore irradiating ions release part of their energy crossing the region in which the bimetallic nanoclusters are present (centered around a depth of 70 nm).

The effect is shown in Figure 13(b and c) in comparison with the unirradiated reference, Figure 13(a). The most evident result is the new topology of the clusters: around each original cluster a set of satellite clusters of about 1–2 nm are present with an average distance of about 3 nm from the cluster surface, similarly to what reported in a ion-beam mixing experiment of Au islands irradiated by Au MeV-ions [105,106]. In those works, the NCs halo observed around the larger Au precipitates was explained in terms of the ballistic process, which dissolves NCs into the SiO_2 host by ion mixing, and of the large increase in the solute concentration in the matrix with a subsequent precipitation. In those experiments the nuclear components of the energy loss (S_n) was comparable to the electronic one (S_e), whereas in Ref. [30] for 190 keV Ne ion irradiation the ratio S_e/S_n is about 3. Two points are worth noting in the present experiment: (i) the asymmetry in the density of the satellites around the clusters: a closer inspection at Figure 13(c) shows that they are more dense and slightly larger in the region opposite to the surface (i.e., to the irradiating beam direction) with respect to the cluster; (ii) the composition of the satellites: EDS compositional analysis with a focused electron beam of 2 nm FWHM of the FEG-TEM in the central part of the cluster (region 1 of Figure 13(c)) gives an Au/Cu atomic ratio (measured at AuL and CuK) of 1.3 ± 0.1, whereas the same ratio measured in region 2 (i.e., on the satellite clusters) results to be 3.2 ± 0.3, indicating a preferential extraction of Au from the original clusters. The asymmetry in the satellite cluster density supports the hypothesis of a relevant contribution of the S_n component of the energy loss in the creation of an elemental-selective vacancy formation in the NCs, which could be also responsible for the preferential Au out-coming from the original alloy.

Similar results are obtained for AuAg nanoclusters after irradiation with He, Ne, or Kr ions [25]. Fused silica slides were sequentially implanted with Au^+ and Ag^+ ions at room temperature at ion energies of 190 keV for Au and 130 keV for Ag and fluences of 3×10^{16} ions/cm^2 for both ions. Implanted slides were then heat treated in a conventional furnace in air at 800 °C for 1 h. The annealing conditions were chosen to produce large and well-separated clusters. This is the reference sample, in the following labeled as AuAg. The reference sample was irradiated with He, Ne, Ar, or Kr at different fluence and energy so as to deposit the same energy and power density on the sample.

In Figure 14(a) the bright-field TEM cross-sectional image of the reference AuAg sample is shown. The size distribution of the clusters has an average diameter $\langle D \rangle = 11.7$ nm and a standard deviation of the experimental bimodal distribution $\sigma = 6.4$ nm. The effect of

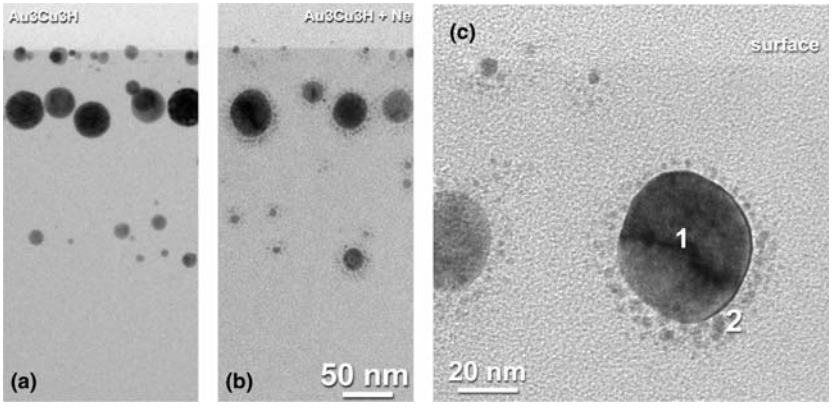

Figure 13. Bright-field TEM cross-sectional micrograph of the sample Au_3Cu_3H (annealing in H_2 (4%)–N_2 atmosphere at 900 °C for 1 h) before (a) and after irradiation at room temperature with 190 keV Ne ions, at a fluence of 1×10^{17} ions/cm^2 (b). In (c) the satellite-like topology of the clusters is shown at higher magnification (Reprinted from Ref. [1], with permission from SIF.)

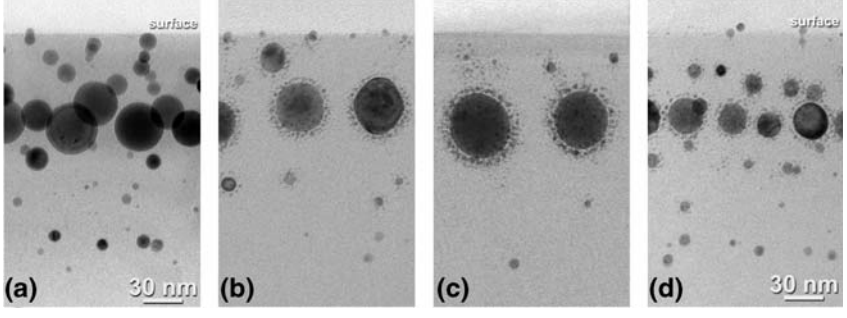

Figure 14. Bright-field TEM cross-sectional micrograph of the sample AuAg before (a) and after irradiation at room temperature with 100 keV Ne ions at a fluence of 5×10^{16} ions/cm^2 (b); with 190 keV Ar at a fluence of 2.5×10^{16} ions/cm^2 (c) and with 190 keV Ar at a fluence of 1×10^{16} ions/cm^2 (d). (Reprinted from Ref. [1], © 2005, with permission from Italian Physical Society.)

irradiating the AuAg sample with Ne ions at 100 keV and with Ar at 190 keV is shown in Figure 14(b and c), respectively. Ion irradiation promotes the formation of satellite clusters around each original cluster (similar images are obtained after irradiation with 25 keV He ions and with 380 keV Kr ions). Moreover, comparing Figure 14(b and c) we note that the Ar-irradiated AuAg sample has a larger volumetric density of satellite clusters than the Ne-irradiated AuAg sample. Increasing the nuclear fraction of the energy loss increases the formation of vacancies in the original cluster during the collisional cascade (as obtained by Monte Carlo simulations). To investigate the effect of the fluence during the irradiation process, in Figure 14(d) we report the bright field TEM cross-sectional image of the AuAg sample irradiated with Ar at 190 keV at a fluence ($1 \cdot 10^{16}$ ions/cm^2) lower than that of Figure 14(c). We note that higher the fluence, the larger is the volumetric density of satellite clusters around each original cluster.

EDS compositional analysis with a focused 2 nm electron beam of the FEG–TEM in the central part of mother cluster on the Ar-irradiated AuAg sample, gives an Au/Ag ratio (measured at AuL and AgL) of 1.4 ± 0.1, whereas the same ratio measured on the satellite clusters is 2.3 ± 0.8. Similar ratios have been found from EDS analysis on AuAg sample irradiated with He, Ne, or Kr ions. EDS analysis reveals therefore a preferential extraction of Au atoms from the original cluster and this selective dealloying process is independent of the particular system investigated (we obtained similar results for Ne-irradiated AuCu cluster, as previously reported).

The peculiar topology of the core-satellite nanoclusters in the ion-irradiated samples results in a red-shift of the SPR absorption band of the system, due to a strong coupling between the core and the satellite nanoclusters, which strongly affects the local field near the core surface. In Figure 15 we report preliminary results [107] in the frame of the Generalized Multiparticle Mie (GMM) approximation which improves the simple Mie approach which is valid for non-interacting clusters. The experimental core-satellite nanostructure obtained upon He irradiation on AuAg nanocluster (see Figure 15(a)) is modeled as in Figure 15(b), producing the modulus of the local field on a section in the equatorial plane of the system shown in Figure 15(c) and calculated at the SPR position of the system (460 nm). A field enhancement of about 15 is obtained, which could be exploited for controlling the non-linear optical properties of these systems.

4.2. Gas-Sensors

We have investigated [68] the optical gas-sensing properties of PMDA–ODA polyimide thin films prepared by implanting different fluences of Au^+ ions, as presented in the Section 2.2.5, in the presence of mixtures containing vapors of methanol, ethanol, and gases, like NO_2 and NH_3, in dry air. Also, we studied the SPR in the virgin polyimide to discuss the gas-sensing mechanism taking place in the Au-polyimide nanocomposite samples. A specific experimental set-up was realized to acquire simultaneously the array of optical responses to gases and/or vapors in terms of the absorption curves variations in the UV–Vis spectral range (300–700 nm). All the measurements were carried out at room temperature and at normal incidence of the light beam. The effect of volatile organic compounds (VOC) vapors on the absorption properties of the active layer was measured in a dynamic pressure system implemented in our laboratory where dry air at ambient pressure was used as carrier and reference gas. The spectrum of each thin active layer was first measured in dry air flow and used as the standard reference for the absorption spectrum of the film in the presence of different vapors. The experimental optical set-up for SPR measurements is based on Kretschmann configuration [108], as reported in Figure 16.

Surface plasmon excitation was achieved by focusing a p-polarized light beam of a He–Ne monochromatic laser source ($\lambda = 632.8$ nm) onto the prism/sample interface and the intensity of the reflected light was measured as a function of the incident angle using a photodiode. The dynamic sensing measurements were performed by keeping the incident angle of the laser beam at a fixed value at a given exposure time. In Figure 17, we represented the optical absorption spectra of the sample implanted with a fluence of 5×10^{16} Au^+/cm^2 and in presence of methanol vapor. As can be observed, the presence of the vapor produces an increase of the optical absorption in the entire spectra region larger than the optical absorption edge of the nanocomposite. Similar effect is observed in presence of ethanol vapor, but the experiments performed with NO_2 and NH_3 gases do not produce change in the optical spectrum of the nanocomposite. Similar experiments realized onto samples implanted with smaller ion fluences show that there were no changes in their optical properties in presence of all the analytes. In conclusion, only implanted samples at a fluence of 5×10^{16} Au^+/cm^2 can be used for vapor sensing.

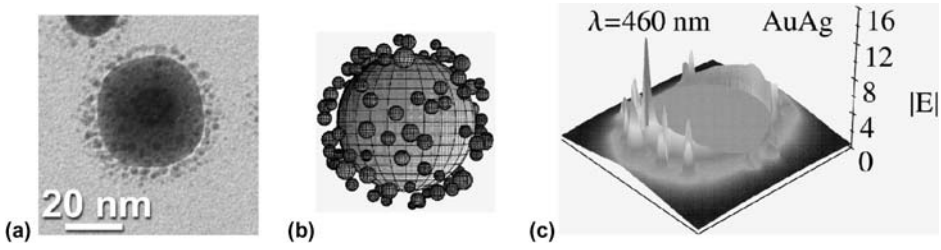

Figure 15. (a) The experimental core-satellite nanostructure obtained upon He irradiation on AuAg nanocluster, (b) its corresponding model, (c) the computed modulus of the local field on a section in the equatorial plane of the system shown in (b) and calculated at the SPR position of the system (460 nm).

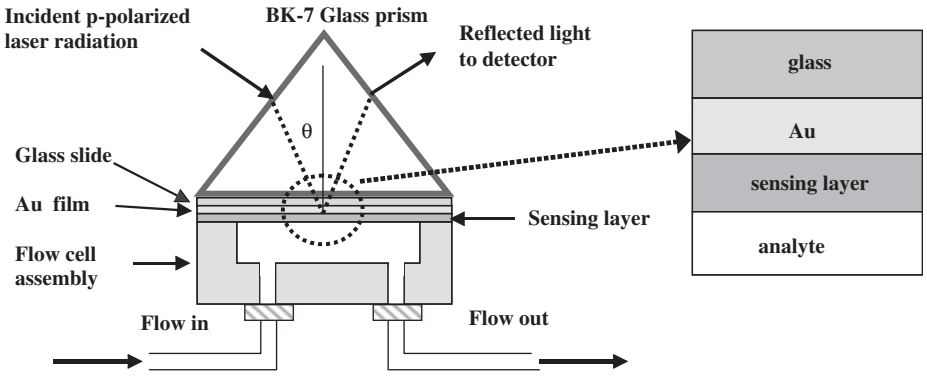

Figure 16. SPR measurement experimental set-up. The zoom on the right is a sketch of the sensing layered structure.

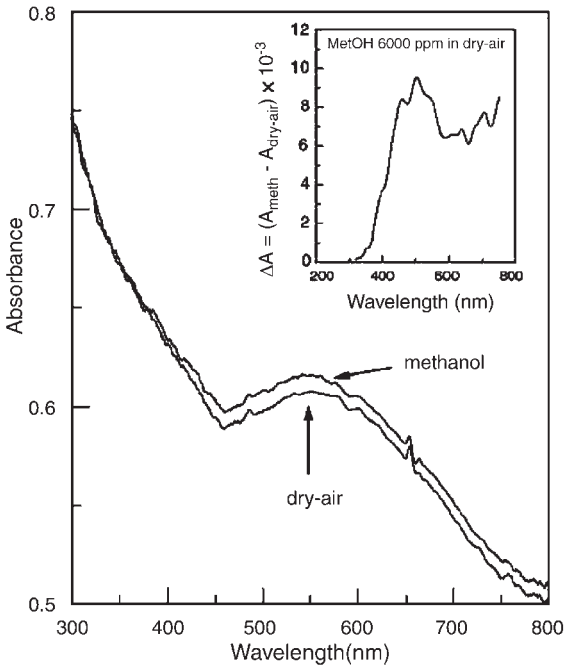

Figure 17. Optical absorption spectra of the polyimide implanted with $5 \times 10^{16}\,Au^{+}/cm^{2}$ in presence of dry air and of methanol vapor (6000 ppm). Inset: optical absorption difference calculated taking into account both spectra. (Reprinted from Ref. [68], © 2005, with permission from Elsevier.)

In the inset of Figure 17, the difference in the absorbance spectra of the implanted sample in presence of dry air and of methanol has been represented. As can be observed, there is an increase in the absorbance that begins in 350 nm and has a maximum around 500 nm in the same wavelength range characteristic of the gold nanoparticles SPR. The dynamic response obtained onto virgin polymer and onto the implanted polymer samples were measured by recording the absorbance intensity on two independent channels fixing in 5 min the time interval of the exposure to the vapors and the recovering. Figure 18 report the dynamic response curves relative to the virgin polyimide film (b,d) and $5 \times 10^{16}\,Au^{+}/cm^{2}$ implanted film (a,c) in the presence of a mixture of dry air containing methanol vapors (a,b) and ethanol vapors (c,d) at a concentration of about 6000 ppm, respectively. The response curves have been obtained by monitoring as a function of time the integral area calculated under the absorption curve in the 350–800 nm spectral range in the case of polyimide film and 450–650 nm spectral range in the case of implanted polyimide film. In the last case, we have analyzed the spectral region centered around the typical plasmon peak of the gold implanted nanoparticles. The virgin polyimide film does not present any variation in the absorption curves in the presence of alcohol vapors. A response appears in the case of gold implanted polyimide film with an increase of the integral area around the region of the plasmon peak that is not limited at this region but involves all the mixed structure gold nanoparticles/polymer as evidenced from the absorption spectra carried out in dry air and in alcohol vapors and reported in Figure 17. The above results show that the structure of the polyimide film undergoes a modification due to the gold implantation and the interaction between vapors and the sensing layer is imputable to this new mixed structure.

In Figure 19, the SPR reflectivity (measured by using the set-up described in Figure 16) of the film in presence of dry-air and methanol vapor (6000 ppm) is shown. It can be observed that the change consists of a shift in the SPR angle. No change of the reflectivity value is observed. Such modification only can be related to the change of refractive index and/or the film thickness but not to a change of absorption. However, by implanting Au, the absorption of the vapor produces the variation of absorption. Then we conclude that the interaction process between the vapors and the virgin polymer and the high fluence implanted sample are very different. As is well-known that gold nanoparticles and clusters show a strong catalytic activity [109,110], we think that in the implanted sample there will be a combined chemical interaction of the vapors with the nanoparticles and the polymeric matrix.

Comparing the two optical transduction techniques (absorption or SPR) used in this work, we can conclude that SPR technique appears to be more suitable for gas sensing even if it presents some limitation regarding the suitable film thickness for SPR excitation. Moreover, the response and recovery times during the analyte/sensing layer interaction appears shortest in the case of optical absorption measurements. Further investigations are in

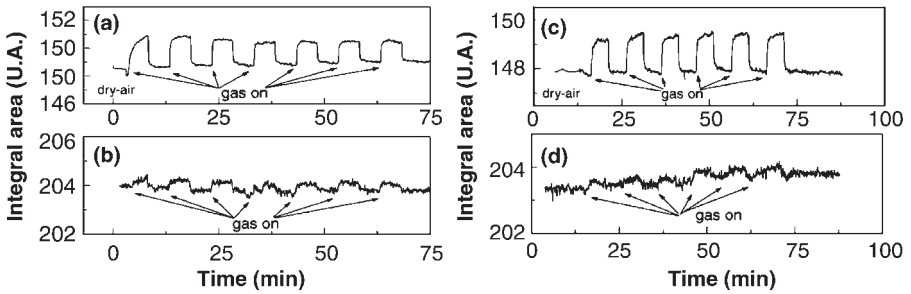

Figure 18. Dynamical optical absorption responses for (a,c) the polyimide film implanted with $5 \times 10^{16}\,Au^{+}/cm^{2}$ and for (b,d) the virgin film obtained upon different exposures to (a,b) methanol vapors (6000 ppm) or (c,d) to ethanol vapors (6000 ppm).

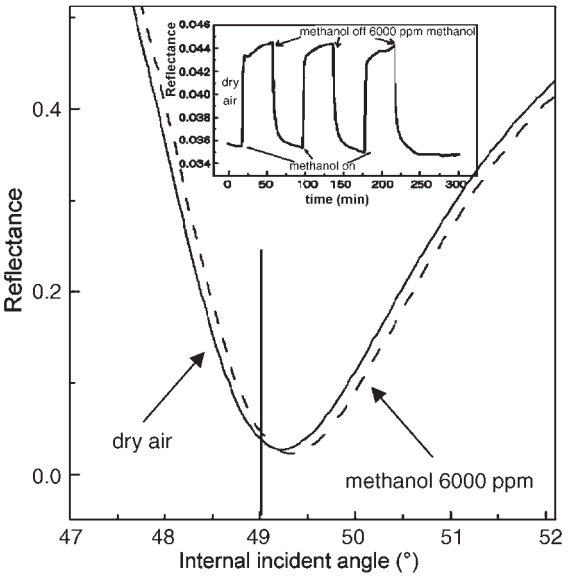

Figure 19. Film SPR spectra of the virgin polyimide in dry air (full line) and in presence of 6000 ppm methanol vapors (dashed line). Inset: dynamic response upon repeated exposure to saturated methanol vapors at a fixed angle of incidence. (Reprinted from Ref. [68], © 2005, with permission from Elsevier.)

progress in order to increase the performance of the sensing layer, formed by polymers containing nanoparticles, in terms of sensitivity, selectivity, and stability.

4.3. Energy Transfer Towards Rare Earths

In the past few years, erbium doped materials gained much attention in the field of optical communications, since the Er^{3+} ion shows a broad optical emission at 1540 nm [111], within the main wavelengths window in the telecommunication technology. For this reason Er can be suitable as an active element for the generation and amplification of light in optical devices [112,113], also if limitations for the realization of an efficient planar amplifier are related to the small cross section for Er excitation (typically 10^{-21}–$10^{-19}\,cm^{2}$ according to the matrix). In order to enhance Er ion pumping efficiency, a possible solution is represented by the interaction with sensitizing species such as other rare earths like Yb [114], semiconductor nanostructures like Si [115–119] and Ge [120] nanoaggregates, organic complexes [121], and more recently metals like Ag [7,122]. The possibility of Er sensitization by Ag has been suggested by previous observations of an optical activity in the visible and near ultraviolet in Ag-doped glasses [123,124]. Concerning metallic species, an enhancement of the Er luminescence has been evidenced in sol–gel silica samples triggered by the SPR of 20 nm Au nanoclusters and by the gettering of the OH groups at the Au clusters surface [125]. On the other hand, Ref. [126] on Ag clusters as Er sensitizers in silica pointed out that a photoluminescence enhancement can be attained without development of SPR, that is without large metallic clusters. We investigated the possibility of an energy transfer to Er ions triggered by ultra-small Au nanoclusters, by implanting Er and Au in silica matrix. A silica substrate was implanted with Er ions at three different energies in order to produce a constant Er concentration profile of about $10^{20}\,Er^{+}/cm^{3}$, extended over a 70 nm thick subsurface layer [127]. This Er concentration was chosen below the reported threshold for concentration quenching in silica glasses [123] to avoid cooperative non-radiative de-excitation effects. This sample labeled 'Er-reference' was thermally treated in a conventional furnace at 900 °C in N_2 for 1 h to anneal radiation-induced defects and to activate the Er^{3+} luminescence. Gold was subsequently introduced in the Er-reference sample by a further triple implantation process at different energies corresponding to a constant Au concentration profile of about $10^{21}\,Au^{+}/cm^{3}$ (over the Er-doped layer). Post Au-implantation thermal treatments were carried out in N_2 atmosphere for 1 h in the temperature range from 400 to 900 °C. The occurrence of an energy-transfer process after the introduction of gold ions in Er implanted silica has been evidenced by a photoluminescence (PL) study of the Er^{3+} emission around 1540 nm both in resonant (488 nm) and non-resonant (476.5 nm) pumping conditions. Figure 20(a) compares the PL spectra of the Au-implanted sample annealed at 600 °C (Er + Au 600 °C) and of the Er reference. Exciting both samples at the resonant wavelength of 488 nm the PL signal from the Er + Au 600 °C sample is higher than the one from the Er reference, with an enhancement factor of about 7. Moreover, the co-implanted (Er + Au) sample shows the Er emission when excited out of resonance, at 476.5 nm: this is the

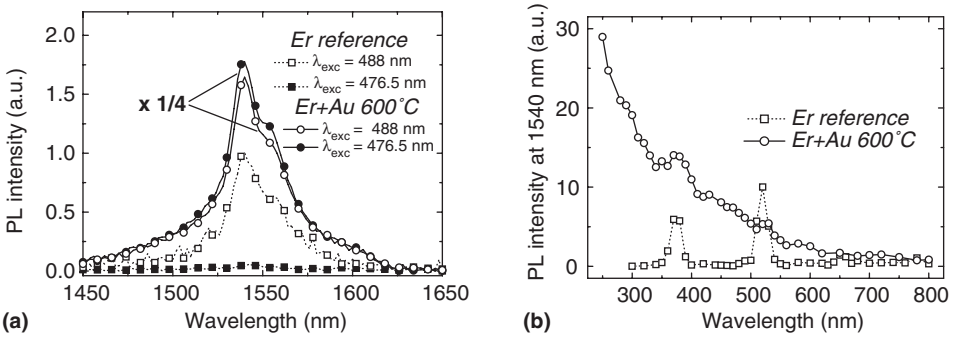

Figure 20. (a) In resonance (488 nm) and out of resonance (476.5 nm) Er PL emission around 1540 nm for the Er reference sample before and after Au implantation followed by a thermal treatment at 600 °C; PL intensity is normalized to 1 for the Er reference and consequently rescaled for the co-implanted sample. (b) PLE spectra for the reference and the co-doped sample annealed at 600 °C, measured using a tunable Xe lamp.

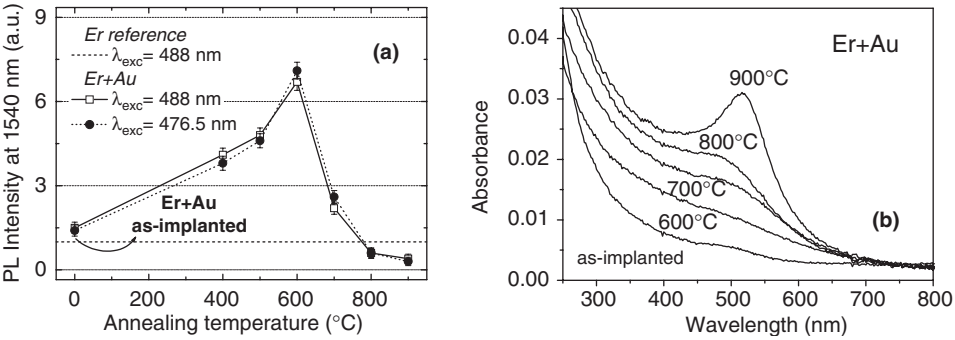

Figure 21. (a) Evolution of PL intensity at 1540 nm in both pumping conditions as a function of the annealing temperature for the Er and Au codoped samples; dashed line is referred to the emission signal at 1540 nm for the only Er-doped film (annealed at 900 °C) and it is normalized to 1, while the intensity for the coimplanted samples was consequently rescaled. (b) Optical absorption spectra of Er-doped silica after Au ion implantation followed by annealing at different temperatures. Measurements were performed using an undoped silica film as a reference.

fingerprint of an Er excitation mechanism through energy-transfer process from Au-related sensitizing centers. In this sample, the possibility of a broadband excitation of Er is evidenced by the excitation spectrum (PLE) for the luminescence signal at 1540 nm, as shown in Figure 20(b). While in absence of any interactions with sensitizing species a series of peaks corresponding to transitions towards the discrete energy levels of Er ions is commonly observed, [118,122] in the case of the Er + Au 600 °C sample, rare earth can be stimulated in a continuous range of excitation wavelengths with an increasing efficiency towards the UV spectrum. A similar behavior in the PLE spectrum has been obtained for Er and Ag co-doped glasses [7,122] and the energy-transfer mechanism was related to silver ions or atom pairs rather than to nanoclusters.

In order to clarify the mechanism responsible of the energy transfer, we investigated the aggregation state of Au atoms and the chemical environment of Er ions in our samples, by performing an EXAFS analysis on the Er + Au 600 °C sample. The experiment evidenced an Au–Au coordination proving the presence of Au metallic aggregates, with an estimated Au–Au distance $R = 2.78 \pm 0.01$ Å, consistent with the presence of small (about 1 nm in size) Au clusters, that are known to exhibit a contraction of the interatomic distances [128]. To analyze the influence of gold aggregation on the energy-transfer process, a set of isochronal (1 h) thermal annealings in N_2 in the temperature range 400–900 °C was performed after Au implantation.

It is interesting to note (Figure 21(a)) that already after Au implantation a 50% increase of Er emission at 1540 nm with respect to the Er reference takes place both in resonant and non-resonant pumping conditions. A further enhancement is obtained upon thermal treatment at higher temperature up to 600 °C. Above this temperature, the PL signal falls off progressively. The initial PL intensity increase could be related to the thermal recovery of Au-implantation induced defects and to the consequent activation of rare earth optical behavior. The decrease of the PL emission above 600 °C has been related to the onset of a competitive mechanism that we attribute to the further growth of the Au aggregates through an Ostwald ripening process, which induces Au clustering and consequently a change from molecular-like (i.e., discrete) to bulk-like (quasi continuous) energy levels of the aggregates and an increase of average distance between Au clusters and Er ions, promoting a progressive reduction of

the efficiency in the energy transfer from the Au-related sensitizing centers. This modification of gold nanostructure is clearly visible in Figure 21(b), which shows the OD of the Er + Au samples as a function of the annealing temperature. The Er + Au sample annealed at 900 °C exhibits a well-developed SPR absorption near 520 nm (typical of Au nanoclusters in SiO_2), which is very weak or absent at lower temperatures. Indeed, as obtained by the EXAFS analysis, up to 600 °C annealing temperature, a large fraction of gold are mainly in the form of sub-nm aggregates that are too small to have a continuous density of states necessary to support a well-developed SPR resonance characteristic of larger free-electron metal nanoparticles. All the Er + Au samples exhibit an absorbance intensity increasing from the red to the near UV range. This feature is consistent with absorption spectra of few-atom gold aggregates [129], showing an upward inflection at an energy of about 1.6 eV related to the onset of electron interband transitions from the top of the d-levels to the lowest unoccupied sp-conduction level. In summary, this work demonstrates that sub-nanometric Au metallic aggregates are efficient sensitizers for Er luminescence in silica, resulting in a broadband increase of rare earth ion emission at 1540 mm. From the evolution of the optical properties of the co-doped samples as a function of the annealing temperature, we concluded that Er sensitization process can be related to a photon absorption involving d-to sp-levels transitions in small Au nanoaggregates with metallic character. Such results support the observed energy transfer from Ag nanostructures to Er, as evidenced in Ref. [7].

5. Conclusions

The advantages and the perspectives of the ion-implantation technique in the formation of metal or metal alloys nanoclusters in dielectric matrix have been presented in detail. The most relevant technological parameters for ion implantation (fluence, energy) and for subsequent treatments (thermal annealing, ion irradiation with low-mass ions) were investigated to control cluster composition, size, and stability. Nanocluster growth mechanisms have been discussed and correlated to theoretical approaches. The formation of metal alloys nanoclusters can be obtained through sequential ion implantation. The temporal sequence of implants is important in the formation of core–shell structures. Particularly intriguing is the modification induced by ion irradiation on the topology and composition of Au–Ag and Au–Cu nanoclusters: around each original cluster a halo of small satellites develops with a preferential out-coming of Au, indicating an elemental selective de-alloying.

As far as the technological properties of the systems investigated are concerned, very interesting results have been obtained about the non-linear optical properties of MNCGes and energy transfer from metal nanostructures and rare earths for optical amplifiers. Metal nanoclusters doped glasses represent a new branch of optical materials and are potentially useful for many applications in digital optical processing, optoelectronics, integrated and nano-optics. Much experimental and theoretical effort is focused on the unique physical properties of these materials, which are quite different from those of the bulk matrix materials and depend on the cluster size, shape, and packing density. In the huge volume of work in the field of materials science for nano-scale applications, nanocluster-doped glasses have become one of the most promising materials. Interesting perspectives are present for dielectric materials containing magnetic nanoclusters and polymers containing gold nanoclusters for gas-sensing devices. Ion-implantation technique presents, in nanotecnology field, peculiar characteristic related to a control of the composition of nanostructured materials, cluster size and a technological approach, derived by the long activity in microelectronics.

Appendix A

List of the acronyms and symbols used in the text.

EDS	Energy dispersive X-ray spectrometry
EXAFS	Extended X-ray absorption fine structure
FEG-TEM	Field-emission gun – transmission electron microscope
GDVDP	Glow discharge vapor deposition polymerization
GIXRD	Grazing incidence X-ray diffraction
GMM	Generalized multiparticle Mie theory
MNCG	Metal nanocluster composite glass
NC	Nanocluster
OD	Optical density
PL	Photo-luminescence
RED	Radiation-enhanced diffusion
R_P	Ion projected range
ΔR_P	Ion straggling
SAED	Selected-area electron diffraction
S_e	Electronic component of the stopping power
S_n	Nuclear component of the stopping power
SPR	Surface plasma resonance
SRIM	Stopping and range of ions in matter (Monte Carlo code)
TEM	Transmission electron microscopy
VOC	Volatile organic compound
XPS	X-ray photoelectron spectroscopy

Appendix B: Experimental Set-Ups Used

Transmission Electron Microscopy (TEM): the microscope used is a FEI field-emission gun FEG-(S)TEM F20 S-Twin operating at 200 kV of accelerating voltage and equipped with: (i) EDAX energy dispersive X-ray microanalysis (EDS); (ii) GATAN parallel electron energy loss spectrometer (EELS); (iii) GATAN Digital Slow-scan CCD camera. Operational modes: conventional, atomic-resolution (point-to-point resolution 0.23 nm), scanning TEM (STEM), diffraction, nanoanalysis with EDS and EELS with a nanobeam of FWHM $\leq$ 1 nm. The microscope is at the CNR-IMM Section of Bologna (Italy).

X-ray Diffraction (XRD): Panalytical X'Pert Pro MRD High-resolution diffractometer working at CuKα with a parabolic mirror (high X-ray flux, low azimuthal divergence) working in parallel beam geometry. It is used in grazing incidence mode for thin film analysis or for reflectivity measurements. The diffractometer is at the Department of Physics, Padova (Italy).

Extended X-ray Absorption Fine Structure (EXAFS): the measurements were mostly made at the Gilda Italian Beamline (equipped with a bending magnet) at the European Synchrotron Radiation Facility in Grenoble (France).

X-ray photoelectron spectroscopy (XPS): XPS and X-ray-excited Auger electron spectroscopy (XE-AES) measurements were performed with a Perkin Elmer F 5600ci at a working pressure lower than 1027 Pa at the Department of Inorganic Organometallic and Analytical Chemistry in Padova (Italy).

Rutherford Backscattering Spectrometry (RBS): in-depth concentration profiles were determined by Rutherford backscattering spectrometry by using a 2.2 MeV $^4He^+$ beam at INFN-Legnaro National Laboratories, Legnaro-Padova (Italy).

Optical absorption (OA): absorption spectra for all the samples were collected with a CARY 5E UV–VIS–NIR or a Jasco V570 dual-beam spectrophotometers in the 200–800 nm wavelength range at the Department of Mechanical Engineering (Materials Division) in Padova (Italy).

References

1 P. Mazzoldi, G. Mattei, *Rivista del Nuovo Cimento* 28(7) (2005) 1.
2 P. Mazzoldi, G. Mattei, C. Maurizio, E. Cattaruzza, F. Gonella, in E. Knystautas (ed.) *Metal Alloy Nanoclusters by Ion Implantation in Silica, in Engineering Thin Films and Nanostructures with Ion Beams*, Chapter 7, CRC Press, New York, 2005, 82.
3 P. Mazzoldi, G. W. Arnold, G. Battaglin, F. Gonella, R. Haglund Jr., *J. Nonlin. Opt. Phys. Mat.* 5 (1996) 285.
4 F. Gonella, P. Mazzoldi, Metal nanocluster composite glasses, in H. S. Nalwa (ed.) *Handbook of Nanostructured Materials and Nanotechnology*, Vol. 4, Academic Press, San Diego, 2000, 82.
5 C. Flytzanis, F. Hache, M. C. Klein, D. Ricard, P. Roussignol, *Prog. Opt.* 29 (1991) 321.
6 F. Tihay, M. Richard-Plouet, J. M. Pourroy, A. C. Roger, A. Kienneman, *Appl. Catal. A: General* 206 (2001) 29.
7 A. Martucci, M. de Nuntis, A. Ribaudo, M. Guglielmi, S. Padovani, F. Enrichi, G. Mattei, P. Mazzoldi, C. Sada, E. Trave, G. Battaglin, F. Gonella, E. Borsella, M. Falconieri, M. Patrini, J. Fick, *Appl. Phys. A* 80 (2005) 557.
8 M. Respaud, J. M. Broto, H. Rakoto, A. R. Fert, L. Thomas, B. Barbatra, M. Verelst, E. Snoek, P. Lecante, A. Mosset, J. Osuna, T. O. Ely, C. Amiens, B. Chaudret, *Phys. Rev. B* 57 (1998) 2925.
9 P. Mazzoldi, G. Righini, in F. Agullo-Lopez (ed.) *Glasses for Optoelectronic Devices, in Insulating Materials for Optoelectronics*, World Scientific, Singapore, 1995, 367.
10 R. F. Haglund Jr., Quantum-dot composites for nonlinear optical applications, in R. E. Hummel, P. Wissmann (eds.) *Handbook of Optical Properties II: Optics of Small Particles, Interfaces, and Surfaces*, Vol. 2, CRC Press, New York, 1997, 191.
11 J. Perenboom, P. Wyder, *Phys. Rep.* 78 (1982) 173.
12 W. Halperin, *Rev. Mod. Phys.* 58 (1986) 533.
13 F. Hache, D. Ricard, C. Girard, *Phys. Rev. B* 38 (1988) 7990.
14 J. Haus, N. Kalyaniwalla, R. Inguva, M. Bloemer, C. Bowden, *J. Opt. Soc. Am. B* 6 (1988) 797.
15 U. Kreibig, M. Vollmer, *Optical Properties of Metal Clusters*, Springer-Verlag, Berlin Heidelberg, 1995.
16 R. H. Doremus, *Glass Science*, Wiley, New York, USA, 1973.
17 L. Yang, D. J. Osborne, R. F. Haglund Jr., R. H. Magruder III, C. W. White, R. A. Zuhr, H. Hosono, *Appl. Phys. A* 62 (1996) 403.
18 C. N. Ironside, *Contem. Phys.* 34 (1993) 1.
19 M. Faraday, *Philos. Trans .R. Soc.* 147 (1857) 145.
20 J. C. Maxwell-Garnett, *Philos. Trans. R. Soc. A* 203 (1904) 385.
21 J. C. Maxwell-Garnett, *Philos. Trans. R. Soc. A* 205 (1904) 237.
22 G. Mie, *Ann. Phys. (Leipzig)* 25 (1908) 377.
23 E. Cattaruzza, *Nucl. Instrum. Methods B* 169 (2000) 141.
24 F. Gonella, *Nucl. Instrum. Methods B* 166–167 (2000) 831.
25 G. Mattei, *Nucl. Instrum. Methods B* 191 (2002) 323.
26 R. F. Haglund Jr., L. Yang, R. H. Magruder III, C. W. White, R. A. Zuhr, L. Yang, R. Dorsinville, R. R. Alfano, *Nucl. Instrum. Methods B* 91 (1994) 493.
27 N. Skelland, P. Townsend, *Nucl. Instrum. Methods B* 93 (1994) 433.
28 A. L. Stepanov, D. E. Hole, *Recent Res. Devel. Appl. Phys.* 5 (2002) 1.
29 A. Meldrum, R. F. Haglund Jr., L. A. Boatner, C. W. White, *Adv. Mater.* 13 (2001) 1431.
30 G. Mattei, G. De Marchi, P. Mazzoldi, C. Sada, V. Bello, G. Battaglin, *Phys. Rev. Lett.* 90 (2003) 085502/1.
31 G. Battaglin, E. Cattaruzza, F. Gonella, G. Mattei, P. Mazzoldi, C. Sada, X. Zhang, *Nucl. Instrum. Methods B* 166–167 (2000) 857.
32 F. Gonella, G. Mattei, P. Mazzoldi, C. Sada, G. Battaglin, E. Cattaruzza, *Appl. Phys. Lett.* 75 (1999) 55.
33 R.B. Fair, *Proc. IEEE* 86 (1998) 111.
34 P. R. Rose, Nucl. Instrum. Methods B 6 (1985) 1.
35 P. Mazzoldi, G. W. Arnold, *Ion Beam Modification of Insulators*, Elsevier Science Publisher B. V., New York, 1987.
36 J.P. Biersack, L. Haggmark, *Nucl. Instrum. Methods B* 174 (1980) 257.
37 J. F. Ziegler, J. P. Biersack, U. Littmark, *The Stopping and Range of Ions in Matter*, Vol 2–6, Pergamon, New York, 1977, 1985.
38 W. Moller, W. Eckstein, *Nucl. Instrum. Methods Phys. Res. B* 2 (1984) 824.
39 V. Konoplev, *Radiat. Eff. Lett.* 87 (1986) 207.
40 A. Stepanov, V. Zhikharev, D. Hole, P. Townsend, I. Khaibullin, *Nucl. Instrum. Methods B*, 166–167 (2000) 26.
41 E. Valentin, H. Bernas, C. Ricolleau, F. Creuzet, *Phys. Rev. Lett.* 86 (2001) 99.
42 A. Perez, G. Marest, B. Sawicka, J. Sawicki, T. Tyliszczac, *Phys. Rev. B* 28 (1983) 1227.
43 A. Perez, *Nucl. Instrum. Methods B* 1 (1984) 621.
44 T. Futagami, Y. Aoki, O. Yoda, S. Nagai, *Nucl. Instrum. Methods B* 88 (1994) 261.
45 H. Hosono, *Jpn. J. Appl. Phys.* 32 (1993) 3892.
46 H. Hosono, N. Matsunami, *Phys. Rev. B* 48 (1993) 13469.
47 H. Hosono, H. Imagawa, *Nucl. Instrum. Methods Phys. Res. B* 91 (1994) 510.
48 R. Kelly, *Mater. Sci. Eng. A* 115 (1989) 11.
49 A. Miotello, G. De Marchi, G. Mattei, P. Mazzoldi, C. Sada, *Phys. Rev. B* 63 (2001) 075409.
50 G. De Marchi, G. Mattei, P. Mazzoldi, C. Sada, A. Miotello, *J. Appl. Phys.* 92 (2002) 4249.

51 D. R. Collins, D. K. Schroder, C. T. Sah, *Appl. Phys. Lett.* 8 (1966) 323.
52 G. W. Arnold, J. A. Borders, *J. Appl. Phys.* 48 (1977) 1488.
53 I. M. Lifshitz, V. V. Slezof, *Zh. Eksp. Teor. Fiz.* 35 (1958) 479.
54 H. Yukselici, P. D. Persans, T. M. Hayes, *Phys. Rev. B* 52 (1995) 11763.
55 S. A. Gurevich, A. I. Ekimov, I. A. Kudrayavtsev, O. G. Lyublinskaya, A. V. Osinnskii, A. S. Usikov, N. N. Faleev, *Semiconductor* 28 (1994) 486.
56 C. Wagner, *Z. Elektrochem.* 65 (1961) 582.
57 G. Battaglin, G. Della Mea, G. De Marchi, P. Mazzoldi, A. Miotello, *Nucl. Instrum. Methods B* 7/8 (1985) 517.
58 G. Arnold, G. Battaglin, G. Della Mea, G. De Marchi, P. Mazzoldi, A. Miotello, *Nucl. Instrum. Methods B* 32 (1988) 315.
59 M. A. Lamkin, F. L. Riley, R. J. Fordham, *J. Eur. Ceram. Soc.* 10 (1992) 347.
60 F. Norton, *Nature* 191 (1961) 701.
61 P. Buffat, J.-P. Borel, *Phys. Rev. A* 13 (1976) 2287.
62 G. Maggioni, G. Mattei, A. Quaranta, A. Vomiero, S. Carturan, M. Bazzan, C. Scian, C. de Julián Fernandez, G. Della Mea, P. Mazzoldi, *Appl. Phys. Lett.* 85 (2004) 5712.
63 G. Maggioni, S. Carturan, V. Rigato, G. Della Mea, *Surf. Coat. Technol.* 142–144 (2001) 156.
64 T. Kobayashi, A. Nakao, M. Iwaki, *Surf. Coat. Technol.* 158–159 (2002) 108.
65 V. N. Popok, R. I. Khaibullin, A. Toth, V. Beshliu, V. Hnatowicz, A. Mackova, *Surf. Sci.* 532–535 (2003) 1034.
66 M. Guenther, G. Gerlach, G. Suchaneck, K. Sahre, K. J. Eichhorn, B. Wolf, A. Deineka, L. Jastrabik, *Surf. Coat. Technol* 158–159 (2002) 108.
67 J. Hernandez, M. Lucia, I. Martil, G. Gonzalez-Diaz, J. Santamaria, F. Sanchez-Quesada, *Appl. Opt.* 31 (1992) 1606.
68 C. de Julián Fernández, M. G. Manera, J. Spadavecchia, G. Maggioni, A. Quaranta, G. Mattei, M. Bazzan, E. Cattaruzza, M. Bonafini, E. Negro, A. Vomiero, S. Carturan, C. Scian, G. Della Mea, R. Rella, L. Vasanelli, P. Mazzoldi, *Sens. Actuators B* 111 (2005) 225.
69 H. Yasuda, H. Mori, *Z. Phys. D* 31 (1994) 131.
70 T. Ito, O. Kitakami, Y. Shimada, Y. Kamo, S. Kikuchi, *J. Magn. Magn. Mater.* 235 (2000) 165.
71 G. Battaglin, M. Catalano, E. Cattaruzza, F. D'Acapito, C. de Julián Fernández, G. De Marchi, F. Gonella, G. Mattei, C. Maurizio, P. Mazzoldi, A. Miotello, C. Sada, *Nucl. Instrum. Methods B* 178 (2001) 176.
72 G. Mattei, C. de Julián Fernández, G. Battaglin, C. Maurizio, P. Mazzoldi, C. Scian, *Nucl. Instrum. Methods B* 250 (2006) 225.
73 C. de Julián Fernández, M. Tagliente, G. Mattei, C. Sada, V. Bello, C. Maurizio, G. Battaglin, C. Sangregorio, D. Gatteschi, L. Tapfer, P. Mazzoldi, *Nucl. Instrum. Methods B* 216 (2004) 245.
74 G. Mattei, G. Battaglin, V. Bello, E. Cattaruzza, C. de Julián Fernández, G. De Marchi, C. Maurizio, P. Mazzoldi, M. Parolin, C. Sada, *Nucl. Instrum. Methods B* 218 (2004) 433.
75 C. de Julián Fernández, G. Mattei, C. Sangregorio, M. Tagliente, V. Bello, G. Battaglin, C. Sada, L. Tapfer, D. Gatteschi, P. Mazzoldi, *J. Non-Cryst. Solids* 345–346 (2004) 682.
76 G. Mattei, C. Maurizio, P. Mazzoldi, F. D'Acapito, G. Battaglin, E. Cattaruzza, C. de Julián Fernández, C. Sada, *Phys. Rev. B* 71 (2005) 195418.
77 E. Cattaruzza, F. D'Acapito, F. Gonella, A. Longo, A. Martorana, G. Mattei, C. Maurizio, D. Thiaudiere, *J. Appl. Cryst.* 33 (2000) 740.
78 C. de Julián Fernández, C. Sangregorio, G. Mattei, C. Maurizio, G. Battaglin, F. Gonella, A. Lascialfari, S. Lo Russo, D. Gatteschi, P. Mazzoldi, J. Gonzalez, F. D'Acapito, *Nucl. Instrum. Methods B* 175–177 (2001) 479.
79 R. Bertoncello, S. Gross, F. Trivillin, F. Caccavale, E. Cattaruzza, P. Mazzoldi, G. Mattei, G. Battaglin, S. Daolio, *J. Mater. Res.* 14 (1999) 2449.
80 E. Borsella, S. Dal Toe', G. Mattei, C. Maurizio, P. Mazzoldi, A. Saber, G. Battaglin, E. Cattaruzza, F. Gonella, A. Quaranta, F. D'Acapito, *Mater. Sci. Eng. B* 82 (2001) 148.
81 G. Mattei, C. de Julián Fernández, P. Mazzoldi, C. Sada, G. De, G. Battaglin, C. Sangregorio, D. Gatteschi, *Chem. Mater.* 14 (2002) 3440.
82 T. R. McGuire, J. A. Aboaf, E. Klokholm, *J. Appl. Phys.* 52 (1982) 2205.
83 J. Q. Wang, G. Xiao, *Phys. Rev. B* 49 (1994) 3982.
84 K. Takanashi, S. Mitani, M. Sano, H. Fujimori, H. Nakajima, A. Osawa, *Appl. Phys. Lett.* 67 (1995) 1016.
85 P. Allia, M. Coisson, J. Moya, V. Selvaggini, P. Tiberto, F. Vinai, *Phys. Stat. Sol. (a)* 189 (2001) 321.
86 L. M. Socolovsky, F. H. Sanchéz, P. H. Shingu, *Physica B* 320 (2002) 149.
87 K. W. Kim, Y. H. Hyun, R. Gontarz, Y. V. Kudryavtsev , Y. L. Lee, *Phys. Stat. Sol. (a)* 196 (2003) 197.
88 Y. P. Lee, Y. V. Kudryavtsev, V. V. Nemoshkalenko, R. Gontarz, J. Y. Rhee, *Phys. Rev. B* 67 (2003) 104424.
89 E. E. Carpenter, C. Sangregorio, C. J. O'Connor, *IEEE Trans. Mag.* 35 (1999) 3496.
90 E. E. Carpenter , A. Kumbhar, J. A. Wiemann, H. Srikanth, J. Wiggins, W. Zhou, C. J. O'Connor, *Mater. Sci. Eng A* 286 (2000) 82.
91 T. Kinoshita, S. Seino, K. Okitsu, T. Nakayama, T. Nakagawa, T. A. Yamamoto, *J. Alloys Comp.* 359 (2003) 46.
92 K. Sato, B. Bian, Y. Hirotsu, *Jpn. J. Phys.* 41 (2002) L1.
93 L. T. Kong, B. X. Liu, *Appl. Phys. Lett.* 84 (2004) 3627.
94 A. Perez, M. Treilleux, T. Capra, D. L. Griscom, *J. Mater. Res.* 2 (1987) 910.
95 E. Cattaruzza, G. Battaglin, F. Gonella, G. Mattei, P. Mazzoldi, R. Polloni, B. Scremin, *Appl. Surf. Sci.* 247 (2005) 390.
96 R. H. Magruder III, D. H. Osborne Jr., R. A. Zuhr, *J. Non-Cryst. Solids* 176 (1994) 299.
97 K. Uchida, S. Kaneko, S. Omi, C. Hata, H. Tanji, Y. Asahara, A. Ikushima, T. Tokizaki, A. Nakamura, *J. Opt. Soc. Am. B* 11 (1994) 1236.
98 M. Sheik-Bahae, A. A. Said, T. H. Wei, D. Hagen, E. W. Van Stryland, *IEEE J. Quantum Electron.* 26 (1990) 760.
99 J. Wang, M. Sheik-Bahae, A. A. Said, D. J. Hagen, E. W. Van Stryland, *J. Opt. Soc. Am. B* 11 (1994) 1009.
100 E. W. Van Stryland, M. Sheik-Bahae, in R. A. Lessard, H. Franke (eds.) *Materials Characterization and Optical Probe Techniques*, Vol. CR96, SPIE, Bellingham 1997.
101 M. Falconieri, G. Salvetti, E. Cattaruzza, F. Gonella, G. Mattei, P. Mazzoldi, M. Piovesan, G. Battaglin, R. Polloni, *Appl. Phys. Lett.* 73 (1998) 288.
102 G. Mattei, G. Battaglin, E. Cattaruzza, C. Maurizio, P. Mazzoldi, C. Sada, B. F. Scremin, *J. Non-Cryst. Solids* 353 (2007) 697.
103 E. Cattaruzza, G. Battaglin, F. Gonella, R. Polloni, G. Mattei, C. Maurizio, P. Mazzoldi, C. Sada, C. Tosello, M. Montagna, M. Ferrari, *Philos. Mag. B* 82 (2002) 735.
104 N. Pincon-Roetzinger, D. Prot, B. Palpant, E. Charron, S. Debrus, *Mater. Sci. Eng. C* 19 (2002) 51.
105 J. C. Pivin, G. Rizza, *Thin Solid Films* 366 (2000) 284.
106 G. Rizza, M. Strobel, K. H. Heining, H. Bernas, *Nucl. Instrum. Methods B* 178 (2001) 78.
107 G. Pellegrini, V. Bello, G. Mattei, P. Mazzoldi, *Mater. Sci. Eng. C* 00 (2007) 00.

108 E. Kretschmann, *Z. Phys.* 241 (1971) 313.
109 M. Haruta, *Catal. Today* 36 (1997) 153.
110 G.C. Bond, *Catal. Today* 72 (2002) 5.
111 S. Hüfner, *Optical Spectra of Transparent Rare Earth Compounds*, Academic Press, New York, 1978.
112 W. J. Miniscalco, *J. Lightwave Technol.* 9 (1991) 234.
113 G. N. van den Hoven, R. J. I. M. Koper, A. Polman, C. van Dam, J. W. M. van Uffelen, M. K. Smit, *Appl. Phys. Lett.* 68 (1996) 1886.
114 M. P. Hehlen, N. J. Cockroft, T. R. Gosnell, A. J. Bruce, *Phys. Rev. B* 56 (1997) 9302.
115 M. Fujii, M. Yoshida, Y. Kanzawa, K. Yamamoto, *Appl. Phys. Lett.* 71 (1997) 1198.
116 C. E. Chryssou, A. J. Kenyon, T. S. Iwayama, C. W. Pitt, D. E. Hole, *Appl. Phys. Lett.* 75 (1999) 2011.
117 G. Franzò, V. Vinciguerra, F. Priolo, *Appl. Phys. A* 69 (1999) 3.
118 F. Enrichi, G. Mattei, C. Sada, E. Trave, D. Pacifici, G. Franzò, F. Priolo, F. Iacona, M. Prassas, M. Falconieri, E. Borsella, *J. Appl. Phys.* 96 (2000) 3925.
119 R. A. Senter, Y. Chen, J. L. Coffer, L. R. Tessler, *Nano Lett.* 1 (2001) 383.
120 C. L. Heng, T. G. Finstad, P. Storås, Y. J. Li, A. E. Gunnæs, O. Nilsen, *Appl. Phys. Lett.* 85 (2004) 4475.
121 H. L. Slooff, A. van Blaaderen, A. Polman, G. A. Hebbink, S. I. Klink, F. C. J. M. van Veggel, D. N. Reinhoudt, J. W. Hofstraat, *J. Appl. Phys.* 91 (2002) 3955.
122 C. Strohhöfer A. Polman, *Appl. Phys. Lett.* 82 (2002) 1414.
123 M. Mesnaoui, M. Maazaz, C. Parent, B. Tanguy, G. LeFleu, *Eur. J. Solid State Inorg. Chem.* 29 (1992) 1001.
124 E. Borsella, F. Gonella, P. Mazzoldi, A. Quaranta, G. Battaglin, R. Polloni, *Chem. Phys. Lett.* 284 (1998) 429.
125 M. Fukushima, N. Managaki, M. Fujii, H. Yanagi, S. Hayashi, *J. Appl. Phys.* 98 (2005) 024316.
126 A. Polman, *J. Appl. Phys.* 82 (1997) 1.
127 E. Trave, G. Mattei, C. Maurizio, P. Mazzoldi, G. Pellegrini, C. Scian, G. Battaglin, *Appl. Phys. Lett.* 89 (2006) 151121-1-3.
128 A. Balerna, E. Bernieri, P. Picozzi, A. Reale, S. Santucci, E. Burattini, S. Mobilio, *Phys. Rev. B* 31 (1985) 5058.
129 T. G. Schaaff, M. N. Shafigullin, J. T. Khoury, I. Vezmar, R. L. Whetten, W. G. Cullen, P. N. First, C. Gutierrez-Wing, J. Ascensio, M. J. Jose-Yacaman, *J. Phys. Chem. B* 101 (1997) 7885.

This page intentionally left blank

CHAPTER 15

Size Controlled Pd Nanoparticles Anchored to Carbon Fiber Fabrics: Novel Structured Catalyst Effective for Selective Hydrogenation

Lioubov Kiwi-Minsker, Natalia Semagina, and Albert Renken

Group of Catalytic Reaction Engineering, Swiss Federal Institute of Technology (GGRC-ISIC-EPFL), Lausanne, Switzerland

1. Introduction

Metal particles of nano-dimensions are known to be active catalytic materials due to their high surface-to-volume ratio and unique electronic properties. Among a variety of methods for the nanoparticles fabrication [1–5], a microemulsion (ME) technique is widely used to control the particle size [6–8]. Monometallic particles, bimetallic particles and mixed metal oxides have been successfully prepared by this method [9–11]. ME are thermodynamically stable and optically isotropic dispersions of oil-in-water, or vice versa, mainly in the form of droplets of nanometer dimensions stabilized by the interfacial film of surface active agent(s). Water-in-oil (w/o) MEs are also known as reverse micelles. They have been generally used for the synthesis of ultra fine metal particles with narrow size distribution by the precipitation/reduction of metal salts dissolved in water droplets [11–14]. The main advantage of w/o ME is their one-pot fabrication without sophisticated, time-consuming synthetic steps. The water droplets can be considered as spatially confined nanoreactors of 5–100 nm size for the formation of monodispersed particles with a standard deviation less than $\pm 10\%$. The observed monodispersity is thermodynamically controlled since the system has a minimum free energy at a defined fraction of the dispersed phase (water) governing its droplet size. The final metal nanoparticle size varies in accordance to the preparation conditions, like a nature of surfactant, metal precursor, reducing agent, their concentrations, pH, temperature and the presence of a co-surfactant. The most important factor influencing the size of the final nanoparticles is the water-to-surfactant ratio, ω_0: the higher is the ratio the bigger is the metal particle size.

ME technique is of special interest in the preparation of catalytically active materials, as the control of particle size and monodispersity are very important for structure-sensitive reactions, like hydrogenations [15]. Metal particle morphology and the size influence the turnover frequency (TOF) and selectivity due to electronic and geometric effects.

There are different ways in which the nanoparticles prepared by ME-technique can be used in catalysis. The use of ME *per se* [16,17] implies the addition of extra components to the catalytic reaction mixture (hydrocarbon, water, surfactant, excess of a metal reducing agent). This leads to a considerable increase of the reaction volume, and a catalytic reaction may be affected by the presence of ME via the "medium" and "solubilization" effects. The complex composition of ME does not allow performing solvent-free reactions.

Nanoparticles may be purified from the ME constituting components (surfactant and organic phase) via freeze-drying [18] or a cross-flow ultrafiltration [19]. However, the use of isolated nanoparticles as the catalysts requires their separation from the reaction mixture after reaction via ultrafiltration.

Supported catalysts are more suitable for industrial applications. Different methods for the preparation of the supported catalysts via a ME-mediated technique have been recently summarized [6]. Usually the preparation is based on the mixing of powdered supports/monolith or support precursors with the ME containing metal nanoparticles [20]. This step is followed by washing with a solvent to remove the excess of the surfactant. Sometimes tetrahydrofuran (THF) is added to the mixture in order to release nanoparticles from the water droplets. Then, the catalysts are calcined at 200–600 °C for 2–12 h in air or hydrogen flow. Non-calcined samples often do not show any catalytic activity because the surfactant is strongly adsorbed on its surface hindering the access of reacting molecules [16]. The support impregnation uses an amount of ME corresponding to the pore volume in order to minimize the lost of solvent [21]. This requires a high metal concentration in ME. To attain ~1 wt.% of the

Metal Nanoclusters in Catalysis and Materials Science: The Issue of Size Control
Edited by B. Corain, G. Schmid and N. Toshima

supported metal, its concentration in the water core should be at least ~0.5 M. This limits the use of the ME technique for the preparation of the supported catalyst. Moreover, an increase of the metal concentration in the water core results in bigger metal particles. Besides, the calcination step leads to the sintering of metal particles. A challenging task in preparation of the supported catalysts is a recovery of the organic phase and surfactant.

The proposed method for preparation of supported Pd-nanoparticles involving ME allows the recovery of organic phase and the surfactant preserving the uniform particle size and avoids the expensive energy/time-consuming calcination step. The catalytic material comprises structured support and monodispersed Pd-nanoparticles prepared via a modified ME technique. The fabrics of activated carbon fibers (ACF) are used as a support. The advantages of this structured catalyst are: easy reuse due to simple handling, low resistance to the passage of fluid and high permeability. These properties make them an attractive alternative to powdered catalytic materials [22].

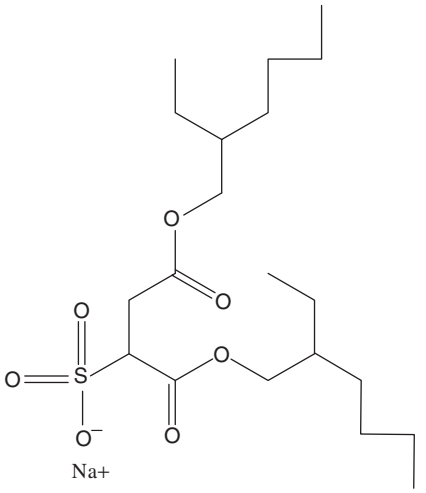

Figure 1. Anionic surfactant aerosol OT for a microemulsion preparation.

2. Synthesis Strategy

General route of the preparation of ME containing nanoparticles consists in the addition of an aqueous metal precursor to the surfactant-containing hydrocarbon forming ME. The size of the final metallic particle will depend on the size of the droplets in the ME. The droplet size will be influenced by the water-to-surfactant ratio, ω_0. The ME formation is followed by a reduction with hydrogen, hydrazine or borohydrates. If a reducing agent is liquid, it is often introduced as a ME with the same ω_0. This allows obtaining necessary ω_0 and corresponding particle size after mixing of two MEs. The ME is a dynamic system, which means that during the process of particle formation permanent collision of the aggregates takes place. Consequently the formation of particles proceeds in two steps, first the nucleation process inside the droplet and then the aggregation to form the final particle. Nanoparticles reach their final size in 15–60 min.

As an initial reverse ME, a wide range of hydrocarbons, surfactants, metal precursors and reducing agents may be used [6]. The hydrocarbon may be any aliphatic linear or branched chain, or cycloaliphatic hydrocarbon. The ME can be stabilized by a surfactant of any type (i.e., cationic, anionic, non-ionic). Examples of cationic surfactants are cetyltrimethylammonium bromide (CTAB) and cetyltrimethylammonium chloride (CTAC); an anionic surfactant is aerosol OT (AOT, sodium bis(2-ethylhexyl) sulphosuccinate, or docusate sodium salt); and non-ionic surfactants are Berol 02 (nonylphenolethoxylate); Berol 050 (pentaethyleneglycol dodecyl ether, PEGDE), NP-*X* (poly (oxyethylene)nonylphenol ether). CTAB and CTAC are used with a co-surfactant such as *n*-hexanol (10 vol.% to hydrocarbon). One of the most suitable surfactants is AOT (Figure 1). Water/AOT/hydrocarbon MEs are considered to be an ideal media to synthesize nanoparticles due to the well-established structural and dynamic properties of AOT reversed micelles, the surfactant's ability to solubilize relatively large amounts of water without a co-surfactant and the high stability of ME. Palladium monodispersed nanoparticles, for example, may be synthesized in the range from 3 to 18 nm [6,23].

Figure 2 schematically presents a synthetic strategy for the preparation of the structured catalyst with ME-derived palladium nanoparticles. After the particles formation in a reverse ME [23], the hydrocarbon is evaporated and methanol is added to dissolve a surfactant and flocculate nanoparticles, which are subsequently isolated by centrifugation. Flocculated nanoparticles are redispersed in water by ultrasound giving macroscopically homogeneous solution. This can be used for the incipient wetness impregnation of the support. By varying a water-to-surfactant ratio in the initial ME, catalysts with size-controlled monodispersed nanoparticles may be obtained.

Two other conventional techniques may be also used for a supported catalyst preparation [6]. One includes mixing of a ME and a support via ACF dipping into the formed ME. In the second one, THF is added during this mixing to release nanoparticles.

3. Results

The most important issue in the synthetic strategy applied is that it allows preserving the nanoparticles size and monodispersity obtained in the initial ME. This means that once the conditions for nanoparticle preparation of desired size using reverse ME have been chosen, the size control in the supported catalyst is insured. As an example, two MEs were prepared with a water-to-surfactant ratios of 3 and 7, which should give the Pd nanoparticle size of 6 and 12.5 nm, respectively [23]. Figure 3 shows microphotographs of the particles obtained after the isolation procedure, as well as the histograms of the particle size distribution. No coagulation takes place during evaporation and flocculation. The isolated particles obtained preserve their size and dispersion. These particles possess a face-centered cubic (fcc) crystalline lattice according to high-resolution transmission electron microscopy

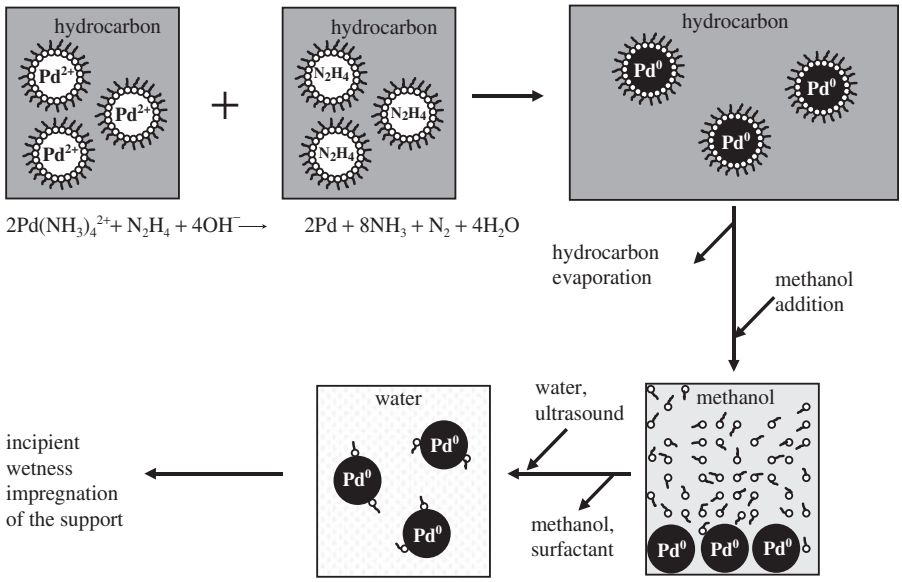

Figure 2. Scheme of the catalyst preparation via a modified microemulsion technique.

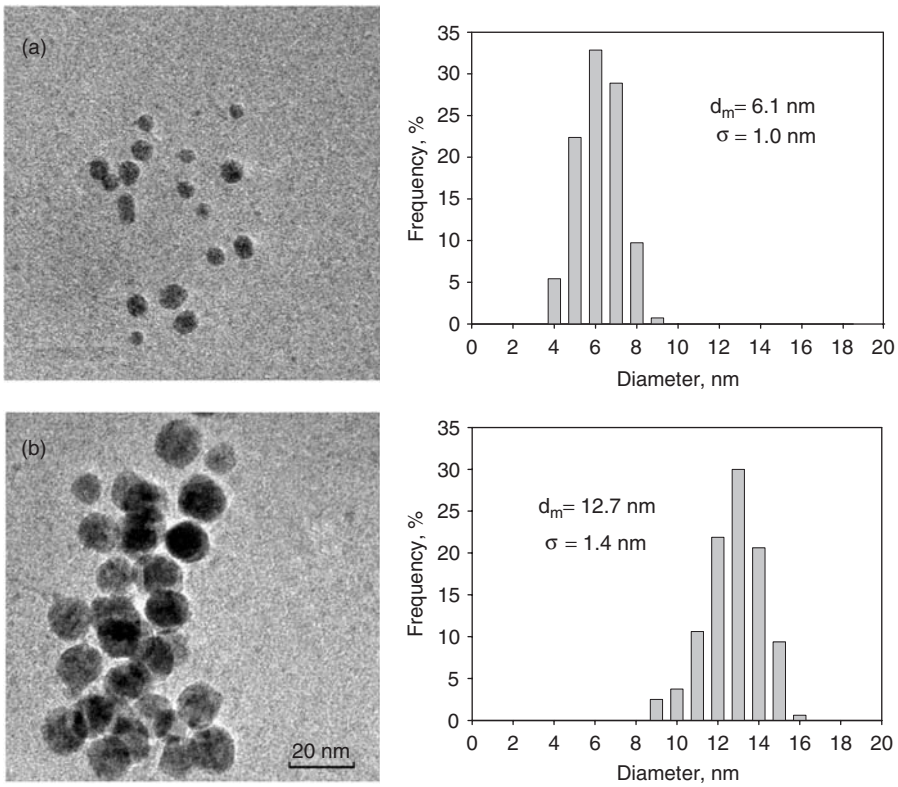

Figure 3. Transmission electron microphotographs and histograms of the particle size distribution for Pd nanoparticles synthesized at ω_0 3 (a) and 7 (b) [23] and isolated via the proposed method.

(HR-TEM, Figure 4). X-ray diffraction analysis revealed the presence of pure palladium with the characteristic peaks at 2θ of 40°, 46° and 68° corresponding to {1 1 1}, {2 0 0} and {2 2 0} planes of a fcc lattice.

Energy-dispersive X-ray analysis showed the absence of nitrogen, indicating that the Pd colloids are free from the metal precursor and reducing agent. Sulfur surface content is three orders of magnitude below the amount in the

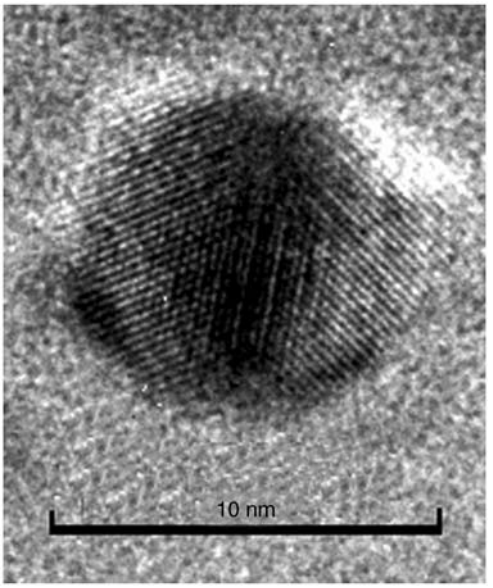

Figure 4. High-resolution transmission electron microphotograph of an isolated Pd nanoparticle.

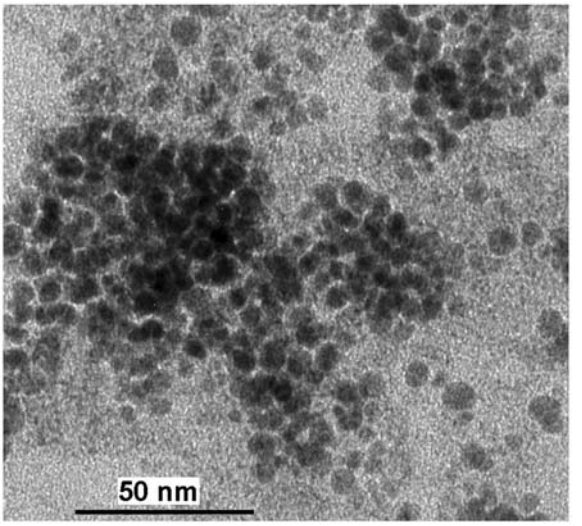

Figure 5. TEM image of the carbon-supported Pd nanoparticles prepared via a typical synthetic procedure.

initial ME confirming that the major part of the surfactant is removed by washing with methanol.

To produce supported catalyst, isolated Pd nanoparticles synthesized at a water-to-surfactant ratio of 3 were used for incipient wetness impregnation of the ACF support. After the Pd loading, the catalyst was washed in heptane. Different ACF samples with/without oxygen-containing groups [24] were used for Pd loading showing the ~0.5 wt.% Pd content. When the ACF fabrics were used for the Pd-particle deposition via the conventional techniques (dipping of ACF into nanoparticle-containing ME) [6], only 0.05 wt.% Pd could be loaded. This amount increased up to 0.1 wt.% upon addition of THF.

In conclusion, the method proposed herein allows high loading of Pd irrespectively of the support surface functionality.

4. A Case History

The synthesis of Pd/ACF (0.42 wt.% Pd) catalyst with monodispersed nanoparticles carried out at $\omega_0 = 3$ is illustrated, as well as its catalytic performance in a liquid-phase hydrogenation of 1-hexyne in comparison with a traditional powdered Lindlar catalyst.

4.1. Typical Synthesis

KoTHmex® activated carbon fiber fabrics AW-1101 (BET specific surface area of 880 m^2/g, average pore diameter of 2 nm) was provided by Taiwan Carbon Technology Co. Ltd. The support is pretreated in a boiling aqueous solution of 6.5 wt.% HNO_3 for 1 h. Then the support is rinsed with distilled water, air-dried for 12 h at room temperature and for 5 h at 393 K. BET specific surface area of the ACF is 950 m^2/g.

All chemicals are of reagent grade; bidistilled water is used throughout this work. Anionic surfactant AOT is vacuum-dried for 24 h at 333 K directly before use. Water-free hydrocarbon (e.g., extra dry isooctane, water < 30 ppm) is used for a ME preparation. All glassware is air-dried at 393 K.

An aqueous solution of $Pd(NH_3)_4Cl_2$ (0.05 M) with pH of 8.5 adjusted with ammonia is used as a metal precursor. The reducing agent, 1 M hydrazine hydrate solution is prepared before use. A 0.35 M solution of AOT is prepared in 200 mL of isooctane and divided in half. To obtain a final ME with $\omega_0 = 3$, 1.88 mL of the palladium precursor and reductant solutions are injected separately into an AOT/isooctane solution and stirred for several minutes until a transparent ME is obtained. Both MEs are mixed and stirred at room temperature for 1 h. Dark-brown color appears indicating Pd reduction to metal state. Nanoparticle-containing ME is then placed into a rotary evaporator at 323 K for 20 min under vacuum. To the resulting foam containing nanoparticles and a surfactant, 50 mL of methanol is added at room temperature to dissolve AOT and to flocculate the palladium nanoparticles. After centrifugation at 8000 rpm (20 min), the supernatant is decanted and washed with methanol. Centrifugation is repeated two more times. The precipitate is then redispersed in 12 mL of water by ultrasonic treatment for 10 min. This macroscopically homogeneous black colloidal dispersion is used to impregnate 0.5 g of dry ACF. Several incipient-wetness impregnations are necessary to load the whole suspension of nanoparticles onto the support. Between the impregnations, Pd/ACF material is air-dried at 393 K for 30 min, washed in heptane and dried for 10 min more. Finally, the catalyst is air-dried overnight at 393 K. The Pd loading attained was 0.5 ± 0.1 wt.%. TEM image of the Pd supported on ACF catalyst is presented in Figure 5.

Pd content was determined by atomic absorption spectroscopy at 247.6 nm with an air–acetylene flame.

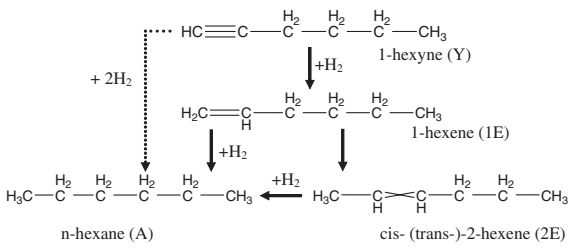

Figure 6. Reaction network of 1-hexyne hydrogenation.

Pd/ACF material is heated in air at 970 K for 3 h to burn out carbon, the residuals are dissolved in a hot mixture of concentrated acids ($HCl:HNO_3 = 3:1$ vol.) and several drops of aqueous HF.

4.2. Typical Catalytic Test

A liquid-phase 1-hexyne hydrogenation (Figure 6) is carried out using the synthesized Pd/ACF catalyst. The reaction is performed in a semi-batch stainless steel reactor of 150 mL volume equipped with a heating jacket and a hydrogen supply system. The structured Pd/ACF catalyst is placed between two metal gauzes (2×4 cm) fixed on the self-gassing hollow shaft stirrer [25]. At the working temperature, the reactor is filled with the reaction mixture and the catalyst, flushed with Ar (0.8 MPa) and kept for 5 min under stirring to equalize the temperature. Then the reactor is flushed with hydrogen and pressurized. During the course of the reaction, the pressure in the reactor is maintained constant. Typical experiment is carried out at 303 K and 1.3 MPa H_2 pressure, stirring of 1500 rpm to avoid external diffusion limitations. *n*-heptane is used as a reaction medium containing 0.5 $kmol/m^3$ of 1-hexyne in total volume of 100 mL. Substrate-to-palladium molar ratio is 20,000/30,000. In the reuse experiments, the catalyst is air-dried at room temperature between the reaction runs.

The samples of the reaction mixtures were periodically withdrawn from the reactor and analyzed by GC. The GC analysis was performed using a 100 m Petrocol DH 0.25 mm capillary column with a 0.5 μm coating at the oven temperature of 333 K and the carrier gas (He) ressure of 280 kPa. Injector and FID temperature is 493 K. *n*-Octane is used as the internal standard.

4.3. Typical Catalytic Behavior of the Pd/ACF Material

Typical concentration–time profiles during the 1-hexyne hydrogenation over 0.4 wt.% Pd/ACF catalyst are presented in Figure 7 showing the experimental and simulated curves (Langmuir-Hinshelwood mechanism). Pd/ACF materials with the same particle size but different Pd loading (0.4, 0.6, 1.2 wt.%) show identical initial activity of 0.140 ± 0.004 $kmol_{H_2}/kg_{Pd}/s$. This indicates the absence of diffusion limitations. Selectivity to 1-hexene is $97.1 \pm 0.4\%$ up to 80% conversion, and $95.9 \pm 0.4\%$ at 90% conversion.

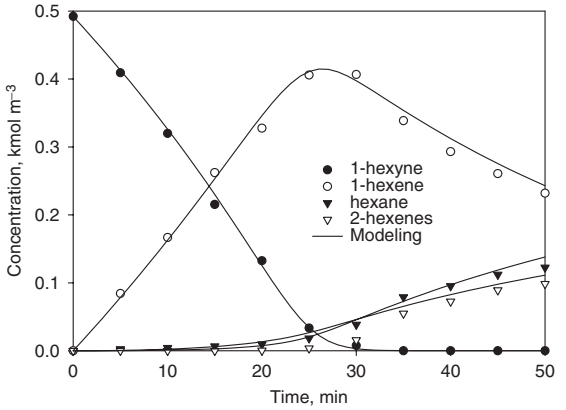

Figure 7. Concentration–time profiles during 1-hexyne hydrogenation over 0.4 wt.% Pd/ACF. Reaction conditions: 0.5 $kmol/m^3$ 1-hexyne in *n*-heptane (100 mL); substrate-to-Pd molar ratio of 23,000; 303 K; pressure of 1.3 MPa; 1500 rpm.

The catalyst reuse is carried out without treating Pd/ACF between the runs. Negligible leaching ($<10\%$ within the experimental error) was observed after catalyst reuse. Figure 8 shows the initial reaction rate and the selectivity for several runs. After activity drops in the first run, it stabilizes at $0.085 \pm 0.008 \cdot kmol_{H_2}/kg_{Pd}/s$, while selectivity to 1-hexene is $94 \pm 1\%$. Kinetic curves are identical from the second to the sixth runs.

Catalytic behavior of the synthesized material is superior in comparison with a traditional hydrogenation catalyst which is a powdered Lindlar catalyst ($5\%Pd–3.5\%Pb/CaCO_3$), as can be seen from Figure 9(a) and (b).

The used Pd/ACF catalyst shows a higher selectivity than the fresh Lindlar catalyst, for example, $94 \pm 1\%$ versus $89 \pm 2\%$, respectively, at 90% conversion. The higher yield of 1-hexene is $87 \pm 2\%$ with the used catalyst versus $82 \pm 3\%$ of the Lindlar in a 1.3-fold shorter reaction time. Higher catalyst activity and selectivity is attributed to Pd size and monodispersity. Alkynes hydrogenation is structure-sensitive. The highest catalytic activity and alkene selectivity are observed with Pd dispersions $<20\%$ [26]. This indicates the importance of the Pd size control during the catalyst preparation. This can be achieved via the modified ME technique.

5. Conclusions

The reverse ME technique provides an easy route to obtain monodispersed metal nanoparticles of the defined size. To prepare supported catalyst, metal nanoparticles are first purified from the ME components (liquid phase and excess of surfactant) while retaining their size and monodispersity and then deposited on a structured support. Due to the size control, the synthesized material exhibits high catalytic activity and selectivity in alkyne hydrogenation. Structured support allows suitable catalyst handling and reuse. The method of the catalyst preparation is not difficult and is recommended for the

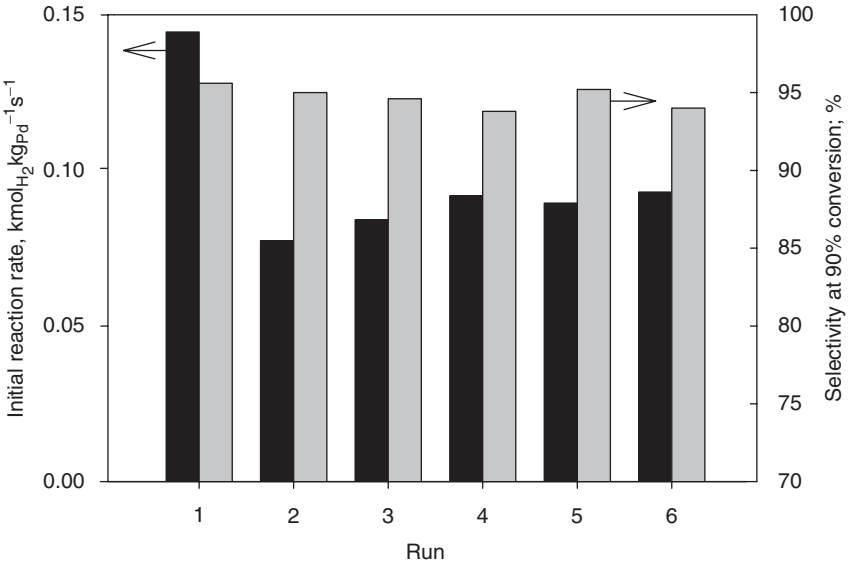

Figure 8. 0.4 wt.% Pd/ACF performance in the repeated runs. Reaction conditions: see Figure 7.

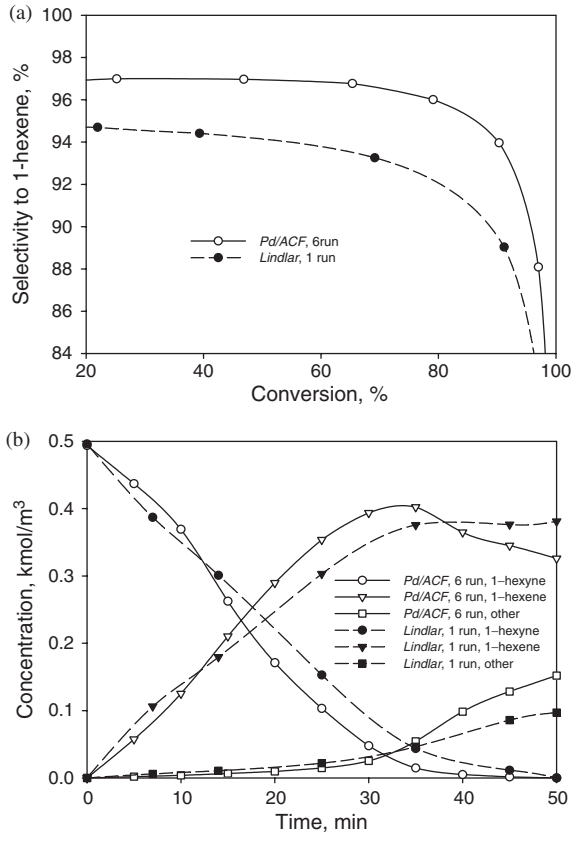

Figure 9. Catalytic performance of the used Pd/ACF catalyst in the sixth run and fresh Lindlar catalyst. Reaction conditions: see Figure 7.

preparation of both unsupported and supported ME-derived nanoparticles.

References

1 C. Burato, P. Centomo, M. Rizzoli, A. Biffis, S. Campestrini, B. Corain, *Adv. Synth. Catal.* 348 (2006) 255.
2 P. Centomo, M. Zecca, S. Lora, G. Vitulli, A. M. Caporusso, M. L. Tropeano, C. Milone, S. Galvagno, B. Corain, *J. Catal.* 229 (2005) 283.
3 B. Corain, C. Burato, P. Centomo, S. Lora, W. Meyer-Zaika, G. Schmid, *J. Mol. Catal. A* 225 (2005) 189.
4 B. Corain, K. Jerabek, P. Centomo, P. Canton, *Angew. Chem. Int. Ed.* 43 (2004) 959.
5 G. Schmid, B. Corain, *Eur. J. Inorg. Chem.* 17 (2003) 3081.
6 S. Eriksson, U. Nylen, S. Rojas, M. Boutonnet, *Appl. Catal. A* 265 (2004) 207.
7 D. G. Shchukin, G. B. Sukhorukov, *Adv. Mater.* 16 (2004) 671.
8 C. Burda, X. Chen, R. Narayanan, M. A. El-Sayed, *Chem. Rev.* 105 (2005) 1025.
9 V. Chhabra, V. Pillai, B. K. Mishra, A. Morrone, D. O. Shah, *Langmuir* 11 (1995) 3307.
10 J. Esquena, T. F. Tadros, K. Kostarelos, C. Solans, *Langmuir* 13 (1997) 6400.
11 J. Z. Jiang, C. Cai, *J. Coll. Int. Sci.* 299 (2006) 938.
12 M. Ojeda, S. Rojas, M. Boutonnet, F. J. Perez-Alonso, F. J. Garcia-Garcia, J. L. G. Fierro, *Appl. Catal. A* 274 (2004) 33.
13 S. Rojas, F. J. Garcia-Garcia, S. Jaras, M. V. Martinez-Huerta, J. L. G. Fierro, M. Boutonnet, *Appl. Catal. A* 285 (2005) 24.
14 X. Zhang, K. Y. Chan, *Chem. Mater.* 15 (2003) 451.
15 A. Molnar, A. Sarkany, M. Varga, *J. Mol. Catal. A* 173 (2001) 185.
16 H. Sato, T. Ohtsu, I. Komasawa, *J. Chem. Eng. Japan* 35 (2002) 255.

17 D. M. de Jesus, M. Spiro, *Langmuir* 16 (2000) 4896.
18 A. J. Zarur, J. Y. Ying, *Nature* 403 (2000) 65.
19 R. J. Higgins, R. L. Goldsmith, Patent WO 99/11243 (1999).
20 M. Kishida, T. Hanaoka, H. Nagata, K. Wakabayashi, *Catal. Today* 45 (1998) 203.
21 R. S. Tanke, Patent WO 97/33690 (1997).
22 L. Kiwi-Minsker, *Chimia* 56 (2002) 143.
23 D.-H. Chen, C.-C. Wang, T.-C. Huang, *J. Coll. Int. Sci.* 210 (1999) 123.
24 D. A. Bulushev, I. Yuranov, E. I. Suvorova, P. A. Buffat, L. Kiwi-Minsker, *J. Catal.* 224 (2004) 8.
25 E. Joannet, C. Horny, L. Kiwi-Minsker, A. Renken, *Chem. Eng. Sci.* 57 (2002) 3453.
26 J. P. Boitiaux, J. Cosyns, S. Vasudevan, *Appl. Catal.* 6 (1983) 41.

This page intentionally left blank

CHAPTER 16

Synthesis of Morphologically Controlled Pt Nanoparticles and Their Application in Catalytic Reactions

Akane Miyazaki[1] and Ioan Balint[2]

[1]*Japan Women's University, Mejirodai, Bunkyo-ku, Tokyo*
[2]*Institute of Physical Chemistry, Splaiul Independentei, Bucharest*

1. Introduction

The synthesis of metal particles with well-controlled shapes and sizes is critical for catalytic applications in structure-sensitive reactions because the rates depend significantly on the metal crystallite size as well as on the orientation of the crystalline planes [1]. In order to bridge the gap existing between the science of clean single crystals surface and the world of real catalysis, it is necessary to obtain morphologically controlled metal particles supported on suitable oxides. There are some preparation methods such as vapor [2] and metal cluster deposition [3], electron beam lithography [4], etc. By using these methods, it is possible to control, to some extent, the size, but not the crystallographic orientation, of the metal particles. Synthesis of metal particles via colloid formation is one of the most promising ways to obtain monodispersed metal particles with controlled shapes [5,6]. It is useful challenge to obtain metal nanoparticles having well-controlled morphology, to support them onto suitable support oxides without changing morphology, and then to analyze catalytic behavior of the obtained material.

2. Synthesis Strategy: Usage of Thermosensitive Polymers

The reduction of transition metal salts in solution is the most widely practiced method for synthesis of metal colloidal suspensions [7]. In the preparation process, polymer is often used in order to prevent the agglomeration of metal particles as well as to control their size. Ahmadi et al. [5] reported that the concentration of the capping polymer affects the shape of platinum particles obtained by salt reduction. This means that the addition of a polymer can control not only the size of particles but also their morphology. Among the polymers, we adopted thermosensitive polymers due to their unique feature, e.g., hydrophilic–hydrophobic transition as a function of temperature.

Thermosensitive polymer is a group of polymers, which change their hydration states by temperature. When the temperature is lower than the phase transition point, the polymer is hydrophilic and its aqueous solution is transparent. If the temperature increases above the critical point, the polymer chains become hydrophobic and start to shrink. The aqueous solution of the dehydrated polymer is opaque. This hydrophilic–hydrophobic change is reversible. The morphology of colloidal metal obtained by salt reduction can be affected by many factors, such as type of precursor, polymer, reducing agents, and concentration. However, by using thermosensitive polymers, it is possible to change the interaction between the polymer and metals (ions) by tuning the temperature without any change in the chemical composition of the solution. Among thermosensitive polymers, we selected a series of poly-acrylamides. Here the results obtained by using poly-(*N*-isopropylacrylamide) and poly-(*N*-ethylacrylamide) are presented. Both of these polymers, poly-(*N*-isopropylacrylamide) (poly-NIPA) and poly-(*N*-ethylacrylamide) (poly-NEA) were prepared by radical polymerization.

In order to obtain Pt nanoparticles, aqueous solution of 10^{-4} M K_2PtCl_4, which contained 10^{-2} M (as monomer unit) of poly-NIPA or poly-NEA, was bubbled with Ar gas and then H_2 gas. Then the reaction vessel was sealed tightly and kept in a water bath at a suitable temperature. At given reaction times, the vessels were opened and the samples for transmission electron microscopy (TEM) were prepared by soaking a grid (carbon substrate, Oken) in the colloidal solution and then drying it in the air. The TEM (Hitachi H-8100) was operated at 200 kV.

Metal Nanoclusters in Catalysis and Materials Science: The Issue of Size Control
Edited by B. Corain, G. Schmid and N. Toshima

3. Results

The phase transition temperatures (lower critical solution temperature, LCST) of the polymers were obtained from the change in the transmittance of their aqueous solutions (Figure 1). The aqueous solution of the obtained polymer was prepared and its transmittance at 500 nm was monitored with increase in the ambient temperature. Both of poly-NIPA and poly-NEA showed a sudden decrease in the transmittance at 37.5 and 69.2 °C, respectively. The result shown in Figure 1 clearly suggests the thermosensitivity of the polymers, and the obtained LCST values are close to those reported for poly-NIPA (34.8 °C) [8] and poly-NEA (72 °C) [9].

Figure 2 shows the TEM images of the obtained Pt nanoparticles. Pt nanoparticles prepared by using poly-NIPA (Figure 2A and B) show a clear morphological dependence on the reaction temperature. The particles obtained at 25 °C, temperature below LCST (Figure 2A), had unclear outlines and a variety of shapes: hexagonal, square, round, and so on. On the other hand, the particles obtained at 40 °C, a temperature above LCST (Figure 2B), had clear outlines and were mainly square. Same tendency was observed for the Pt nanoparticles obtained by using poly-NEA. Figure 2C and D show the image of Pt nanoparticles obtained at 40 and 80 °C, i.e., below and above LCST, respectively. Most of the Pt nanoparticles obtained at 40 °C had irregular shapes. The highly defected surfaces of the large Pt particles are suggesting a formation mechanism involving the agglomeration of the very small particles in the early stages of the growth. On the other hand, the amount of well-faceted particles increased significantly at 80 °C. As an interesting fact, a large fraction of triangular Pt particles was obtained at 80 °C.

In order to evaluate the morphological distribution, the shapes of Pt nanoparticles observed by TEM were classified into six categories: hexagonal, square, round, triangular, irregular, and too small to be distinguished. These two-dimensional shapes may correspond, e.g., to icosahedrons, cubes, tetrahedrons, polyhedrons, and small bodies, respectively [5,10]. Figure 3 shows the morphological distribution of the particles obtained at different temperatures, after 12 h of growth. The shapes of particle were classified according to the above classification, and more than 100 particles on the TEM images were counted. From Figure 3 it can be said that the morphological distribution changes remarkably between particles obtained at higher and lower temperatures than LCST of poly-NIPA (LCST = 34.8 °C) and poly-NEA (LCST = 72 °C). At temperatures below LCST, the majority of the particles have irregular shapes, while at temperatures above LCST, the majority of the particles have square or triangular shapes for poly-NIPA and poly-NEA, respectively. From the results shown in Figure 3A, it can be said that the best morphological distribution (68% of cubic particles) could be obtained at 40 °C, a bit higher than the LCST (37.5 °C). The Pt nanoparticles obtained by using poly-NEA did not show such dramatic difference between below and above LCST, but the same tendency can be seen in Figure 3B. The increase of the triangular particle fraction with temperature was

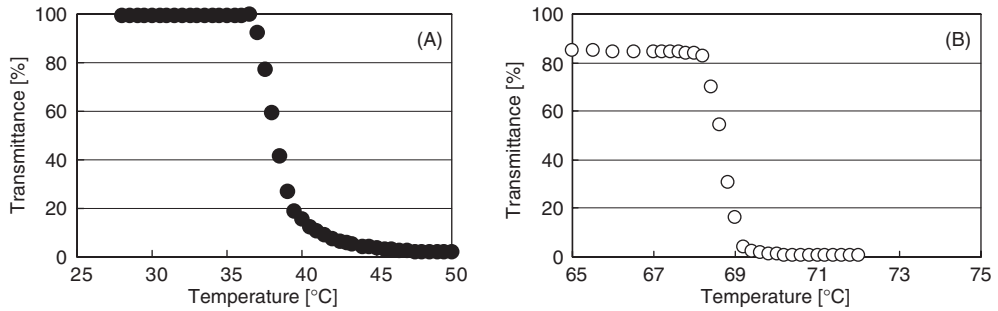

Figure 1. Transmittance of the polymer solutions at 500 nm with increase in the ambient temperature. (A) poly-NIPA and (B) poly-NEA.

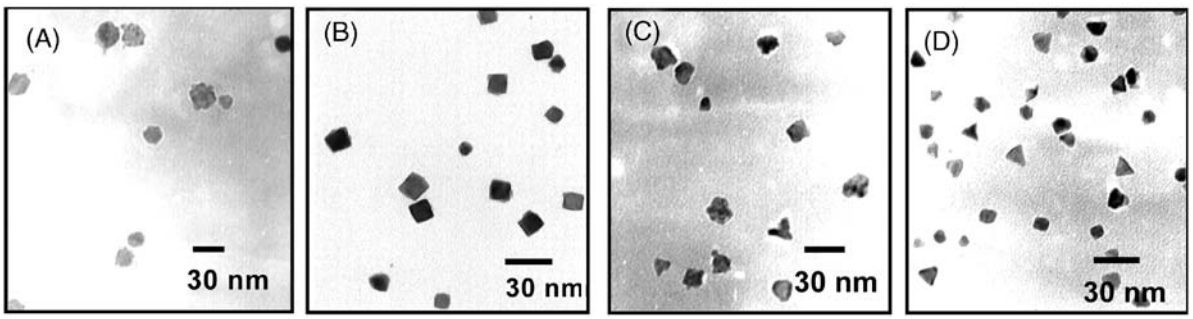

Figure 2. TEM images of Pt nanoparticles obtained by using poly-NIPA as capping material at (A) 25 °C and (B) 40 °C, together with the images of particles obtained by using poly-NEA at (C) 40 °C and (D) 80 °C.

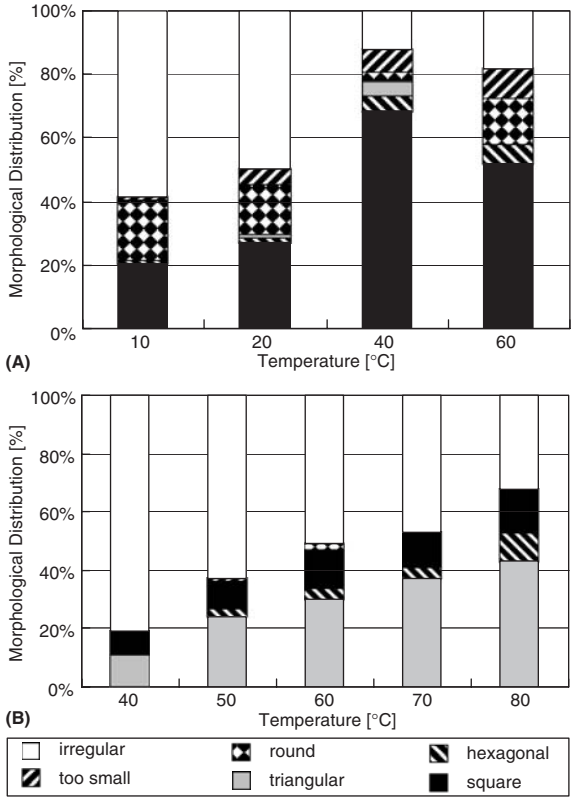

Figure 3. Morphological distribution of Pt nanoparticles obtained by using (A) poly-NIPA (LCST = 37.5 °C) and (B) poly-NEA (LCST = 69.2 °C), at different temperatures.

accompanied by a corresponding decrease in the amount of irregular particles. The formation of small amounts of round-, hexagonal-, square-shaped particles was relatively independent of the synthesis temperature.

The common feature of two thermosensitive capping polymers, poly-NIPA and poly-NEA, is that they give a better morphological control at temperatures higher than LCST. However, the contrast between the predominant morphologies obtained below and above LCST was much stronger in the case of poly-NIPA. The fraction of cubic particles increased dramatically from 30% (at 25 °C) to 68% (at 40 °C). In the case of poly-NEA, the fraction of the triangular particles is affected slightly by LCST (Figure 3B). The differences observed between the capping ability of the two polymers can be explained by their dehydration behavior with temperature. The decrease of the poly-NEA transmittance with temperature is less sharp than that of the poly-NIPA (Figure 1). This means that the poly-NEA chain is dehydrated to some extent even at temperatures lower than LCST (69.2 °C). Therefore, the structure-directing effect of the partially dehydrated poly-NEA made the effect of LCST less pronounced compared to poly-NIPA.

A square and triangular Pt nanoparticle obtained by using poly-NIPA and poly-NEA, respectively, was observed by high resolution TEM (HRTEM) (JEM-2010F). The images (Figure 4) show a crystalline structure with clearly resolved lattice fringes. The square Pt nanoparticle

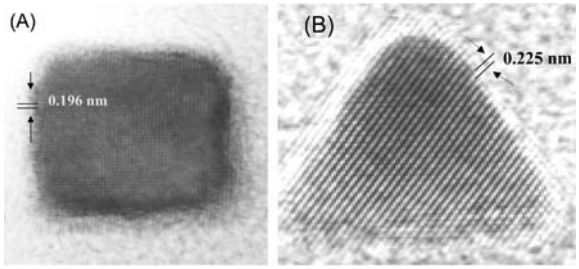

Figure 4. High resolution TEM images of (A) a square Pt particle and (B) a triangular Pt particle obtained by using poly-NIPA at 40 °C and poly-NEA at 80 °C, respectively.

shown in Figure 4A is bounded by (1 0 0) facets because the distance between the adjacent lattice fringes of 0.196 nm corresponds to the interplanar distance of Pt(2 0 0). On the other hand, in the image of triangular Pt nanoparticle shown in Figure 4B, the orientation as well as the lattice spacing of 0.225 nm corresponds to (1 1 1) plane of the face-centered cubic modification of Pt metal. The TEM results prove that the triangular particles are in fact Pt nanotetrahedrons bounded by Pt(1 1 1) crystalline facets, relatively free of structure defects. Since TEM image always displays the projection of the atoms onto the observation plane, the trigonal prismic shape cannot be completely excluded. Other crystallographic orientations as steps and edges are possible at the slightly rounded corners of tetrahedrons. However, the observation by HRTEM proved that the square and triangular Pt nanoparticles have (1 0 0) and (1 1 1) facet on their surface, respectively. This means that by using acrylamide thermosensitive polymer and also by tuning their hydration states by changing reacting temperature, it is possible to obtain Pt nanoparticles having (1 0 0) and (1 1 1) facets, i.e., two typical facets for face-centered cubic structure, on their surface.

The mean particle size of the Pt nanoparticles obtained by using poly-NIPA at 40 °C (68% of cubic particles) and poly-NEA at 80 °C (43% of tetrahedral particles) were 12 and 7.3 nm, respectively. The time course of particle growth was studied for the Pt nanoparticles prepared by using poly-NIPA at 40 °C, the temperature where the best morphological control could be obtained (see Figure 3A). Figure 5 shows the course over time in regard to the percentage of square particles and particle size. It can be seen clearly that the average size of the particles and the percentage of square particles are strongly related to each other. It can be concluded that the morphology of the Pt nanoparticles was determined during their growth process.

Comparing the structure-directing effect of poly-NIPA and poly-NEA, it can be said that there are at least two factors which are controlling the final morphology of Pt nanoparticles: (i) hydrophobicity and (ii) nature of the functional groups. Hydrophobicity of polymers gives better morphological control, while the nature of the functional groups decides the direction of growth. By selecting adequate polymers and optimal reduction conditions, it is possible to control not only the size but also the shape (i.e., the dominant facet orientation) of the colloidal Pt nanoparticles. Either cubic Pt nanocrystals (with

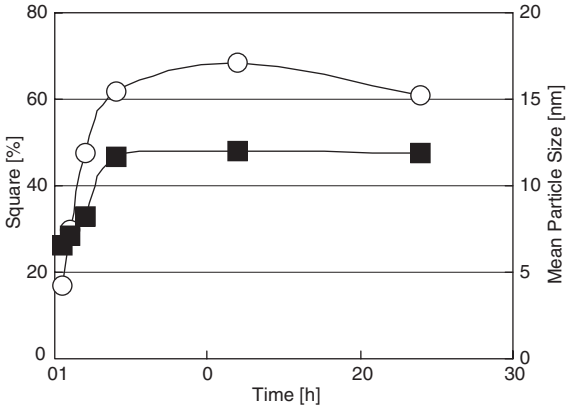

Figure 5. Percentage of square Pt nanoparticles (○) and mean particle size (■) over time obtained at 40 °C.

predominant (1 0 0) faces) or tetrahedral Pt nanocrystals (rich in (1 1 1) facets) can be obtained by using poly-NIPA or poly-NEA, respectively.

4. A Case History

The synthesis of Pt nanocrystals with controlled morphology must have interesting applications in practice, since the catalytic activity for structure-sensitive reactions depends on the orientation of the crystalline facets. Using the obtained morphologically controlled Pt nanoparticles, Pt/Al_2O_3 catalysts were prepared and applied for a structure-sensitive reaction, i.e., NO reduction by CH_4.

Support for the Pt nanoparticles in the colloidal solution was given as follows: 0.1 g of alumina was added to 50 ml of the colloidal Pt solution under stirring in order to obtain a final loading of 1 wt%. Water was removed from the suspension by freeze-drying, and the remaining solid was calcined in the air at 400 °C in order to remove the capping polymers. The calcined catalysts were pelettized, crushed, and sieved. The 335–1000 μm fraction was used for catalytic test.

The average size of the Pt nanoparticles on the Pt/Al_2O_3 obtained by TEM, XRD, CO chemisorption were $d_{TEM} = 13.4$ nm, $d_{XRD} = 11.7$ nm, and $d_{CO} = 23$ nm, respectively. Because the size of colloidal Pt nanoparticles obtained by TEM was 13.6 nm, it can be said that the Pt nanoparticles do not change after deposition on alumina. Figure 6A shows the TEM image of Pt nanoparticle on the 1 wt% Pt/Al_2O_3 obtained. It can be seen that neither the size nor the shape of the Pt nanoparticles were affected after the deposition of the Pt colloid on the support.

The Pt/Al_2O_3 prepared by supporting Pt colloid will be referred as $Pt(1\,0\,0)/Al_2O_3$, hereafter. The catalytic activity of 1 wt% $Pt(1\,0\,0)/Al_2O_3$ was tested for the reduction of NO with CH_4. The catalyst (0.05 g) was tested in flow system by using a quartz microreactor (i.d. = 5 mm) operating at atmospheric pressure. The reactor was mounted vertically in a furnace heated by Shimaden (model SR 25) temperature controller. The flow of each gas was controlled by Kofloc (model 3660) electronic flow controllers. The total flow rate of reactant mixture (NO, CH_4, and Ar)

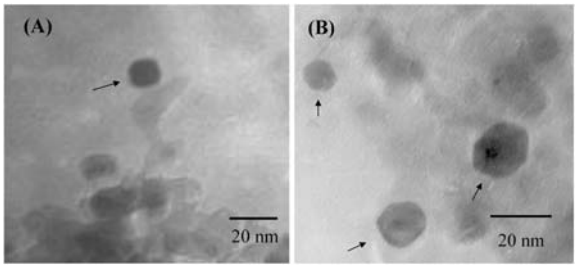

Figure 6. TEM images of cubic Pt nanoparticles supported on alumina: (A) before reaction and (B) aged in NO/CH_4 reaction mixture for 4 h at 950 °C.

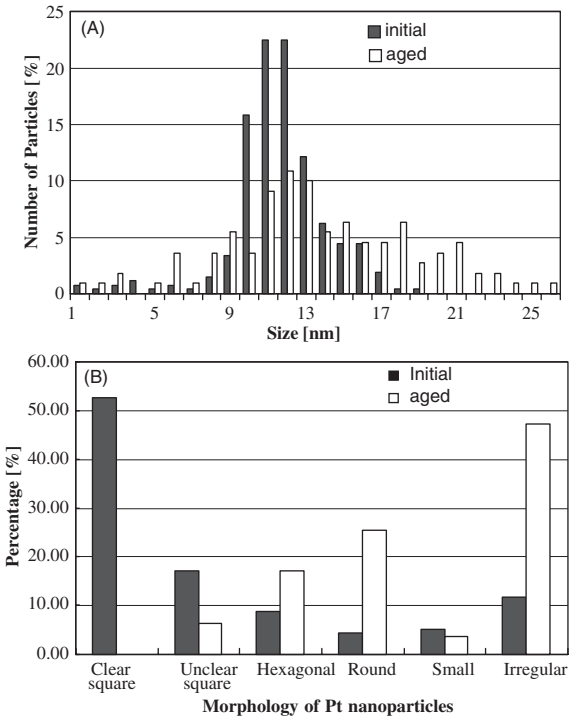

Figure 7. Comparison between initial and aged catalysts in terms of (A) size distribution and (B) morphological distribution.

was 50 $cm^3\,min^{-1}$ at standard temperature and pressure (STP). The corresponding gas hour space velocity (GHSV) was 60,000 h^{-1}. The typical composition of the reactant mixture was 0.6% NO and 1% CH_4, using Ar as balance gas.

In order to check the stability of the well-structured Pt nanoparticles in the reaction mixture, the $Pt(1\,0\,0)/Al_2O_3$ was aged at 950 °C for 4 h in the NO/CH_4 reaction mixture. Figure 7 shows the size and morphological distribution obtained for the same catalyst (1 wt% $Pt(1\,0\,0)/Al_2O_3$) before and after thermal aging. The size distribution of Pt nanoparticles (Figure 7A) became apparently broader after thermal aging at 950 °C for 4 h, but the average size increased only slightly, from 13.4 to 15.1 nm. Figure 6B shows the TEM image of Pt nanoparticle on the aged catalyst. It can be seen that the square Pt nanoparticles converted to other shapes (i.e., irregular,

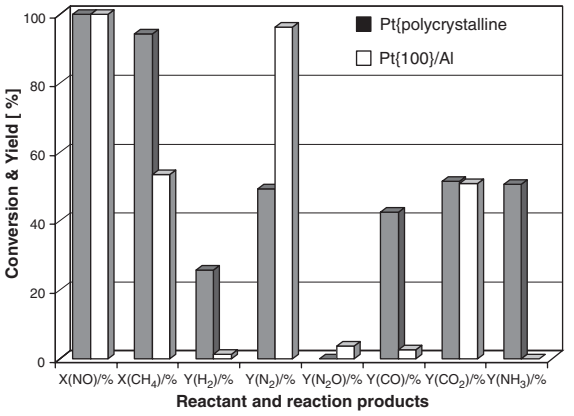

Figure 8. Comparison between catalytic properties of Pt(polycrystalline)/Al_2O_3 (Engelhard) and Pt(1 0 0)/Al_2O_3 (morphologically controlled Pt nanoparticles): the NO/CH_4 reaction conversion (X) and yield (Y), and the reaction products at 500 °C.

round, and hexagonal) after aging in NO/CH_4 mixture. The morphological change can be seen more clearly in Figure 7B, where the morphologies of the Pt nanoparticles in the original colloidal solution and on the 1 wt% Pt(1 0 0)/Al_2O_3 catalyst after thermal aging are compared.

The aging effect on the morphology of Pt nanoparitcles was not observed after catalytic reaction up to 600 °C in the NO/CH_4 reaction mixture. It can be said that morphological feature of the well-structured platinum nanoparticles on Pt(1 0 0)/Al_2O_3 catalysts can be maintained in the reaction mixture of NO/CH_4 reaction in the temperature range up to 600 °C. Therefore, morphological effect of the 1 wt% Pt(1 0 0)/Al_2O_3 will be discussed on the experimental data obtained below 600 °C.

The catalytic behavior of Pt(1 0 0)/Al_2O_3 for the NO/CH_4 reaction was compared with that of a standard catalyst supplied by Engelhard Corporation Japan (lot no. H-T 1150–01), Pt(polycrystalline)/Al_2O_3, at 500 °C (Figure 8). In this manner, the differences would be ascribed to the morphological effect of the Pt particles on the NO/CH_4 reaction. Both catalysts investigated exhibited comparable activity for NO conversion, increasing yield of N_2 (opposite trend for N_2O) and increasing CH_4 conversion with temperature. Interestingly, significantly lower yields of CO and NH_3 were observed for the Pt(1 0 0)/Al_2O_3 catalyst compared with the Pt(polycrystalline)/Al_2O_3 catalyst. On the other hand, the well-structured Pt nanoparticles showed higher yield to N_2O.

The catalytic tests show that, over the Pt(1 0 0)/Al_2O_3 catalyst, the formation of CO and NH_3 is largely prevented, whereas the yield of N_2O increases compared with the Pt(polycrystalline)/Al_2O_3 catalyst. These main differences observed should be ascribed to the morphological differences between two catalysts, i.e., the dominant orientation of the crystallographic facets and the average size of Pt crystallites. The large Pt nanoparticles (~13 nm) of the Pt(1 0 0)/Al_2O_3 catalyst were, in majority (~70%) cubic-shaped. In contrast, the conventional Pt(polycrystalline)/Al_2O_3 catalyst had small, round-shaped Pt particles of ~2.4 nm with random crystallographic orientations.

The practical achievement using the morphologically controlled Pt nanoparticle was to improve significantly the conversion and selectivity of structure-sensitive reactions. The experimental results suggested that the decrease in the average size (to increase the specific concentration of catalytically active sites) along with an accurate tuning of the shape of Pt nanocrystals (to increase the N_2/N_2O ratio) can bring improvements in terms of activity for NO_x conversion and selectivity to N_2.

5. Conclusions

By using thermosensitive poly-acrylamides, it is possible to prepare cubic Pt nanocrystals (with predominant (1 0 0) facets) and tetrahedral Pt nanocrystals (rich in (1 1 1) facets). These Pt nanocrystals can be supported on oxide (alumina) and used as a catalyst in structure-sensitive reaction, NO reduction by CH_4. The results proved that morphologically controlled metal nanoparticles supported on adequate support give us a novel tool to connect the worlds of surface science with that of real catalysis.

The potential of morphologically controlled metal nanoparticles should be expanded by further improvement of their preparation method. It is highly required to develop preparation methods to obtain a better morphological control, i.e., perfect facet control on the particles of optional size. Better morphological control of metal nanoparticles is expected to be achieved in near future and the obtained metal particles will find new exciting applications, not only in catalysis but also in other technically important fields.

References

1 B. C. Gates, *Chem. Rev*. 95 (1995) 511.
2 Y. Iwasawa, in G. Ertl, H. Knoezinger, J. Weitkamps (eds.) *Preparation of Solid Catalysts*, Wiley-VCH Verlag GmbH, Weinheim, 1999, 427.
3 B. C. Gates, *Top. Catal*. 14 (2001) 173.
4 G. A. Somorjai, *Appl. Surf. Sci*. 121–122 (1997) 1.
5 T. S. Ahmadi, Z. L. Wang, T. C. Green, A. Henglein, M. A. El-Sayed, *Science* 272 (1996) 1924.
6 A. Miyazaki, Y. Nakano, *Langmuir* 16 (2000) 7109.
7 J. S. Bradley, in G. Schmid (ed.) *Clusters and Colloids*, VCH Verlagsgesellschaft mbH, Weinheim, 1994, 459.
8 C. W. Chen, M. Akashi, *Langmuir* 13 (1997) 6465.
9 S. Itho, S. Fujishige, *Kenkyu Hokoku-Sen'I Kobunshi Zairyo Kenkyusho* 168 (1991) 5.
10 Z. L. Wang, *Adv. Mater*. 10 (1998) 13.

This page intentionally left blank

CHAPTER 17

Multipods and Dendritic Nanoparticles of Platinum: Colloidal Synthesis and Electrocatalytic Property

Hong Yang, Xiaowei Teng, and Sean Maksimuk

Department of Chemical Engineering, University of Rochester, 206 Gavett Hall, Rochester, NY 14627-0166, USA

1. Introduction

Metal nanoparticles have been used in a range of technological important areas for over a century [1–3]. With the recent rapid advances in our ability to process metal nanoparticles with well-controlled size, size distribution, and shape, one can expect new properties and applications for metal nanoparticles [4,5]. Besides their traditional use as catalysts, metal nanoclusters find new applications in sensing, detection, and manipulation of chemical and biological molecules based on surface plasmonic and other surface-enhanced photophysical effects of metal nanoparticles [6]. Even for those traditional applications such as catalysts, monoshape, and monodispersed metal nanoparticles can have potential advantages [7]. For example, electrocatalytic oxygen reduction reaction (ORR) kinetics depends strongly on the crystalline face of given Pt (*khl*) surfaces [8]. In many cases Pt nanoparticles with predominantly (1 1 1) surfaces can be more reactive than those with (1 0 0) surfaces.

One of the most widely used methods for making monodispersed nanoparticles is solution phase colloidal synthesis. In recent years significant advancement has been made in controlling the size and size distribution of metal nanoclusters, but with limited success in controlling their shapes. To achieve control over the shape of metal nanoparticles, the growth kinetics has to be sufficiently different along various low-index crystallographic directions. While surfactants can be used to stabilize the various surfaces of metal nanoparticles in solution, the inhibition of different facets is not trivial. Besides the use of surfactants, various other factors such as inorganic mediating species, defects, reduction rate, and temperature can all affect the morphology of metal nanoparticles. In this chapter, we will use Pt as an example to examine several strategies primarily for controlling the shape of metal nanoparticles. The focus is on our work on the application of a combination of surfactants, inorganic mediating species, and the role of defects in the shape control of Pt multipods and other higher-ordered nanostructures, such as nanodendrites.

2. Synthetic Strategy

2.1. Principle for Size Control

In general, homogeneous nucleation of nanoparticles occurs when a solute (C) diffuses to surface of a cluster from a bulk solution, and then incorporates into the cluster through surface reaction until a nucleus (C_n) is obtained:

$$\underbrace{C + C + \cdots + C}_{n} \leftrightarrow C_n \tag{1}$$

$$C_n + C \leftrightarrow C_{n+1} \tag{2}$$

Equation (1) describes the cluster growth from the saturated solution and Equation (2) represents the diffusion-controlled growth from C_n to C_{n+1}. To form monodispersed particles, the rapid nucleation and the ability to separate the nucleation and growth are typically required. This principle was first outlined by LaMer and Dinegar [9]. The kinetics of nucleation can be quite complicated, whereas the subsequent growth may be examined systematically based on the given reaction parameters. In a diffusion-controlled closed system, the growth of nanoparticles at a fixed solute concentration can be evaluated by the following equation [10,11]:

$$\frac{dr}{dt} = K\left(\frac{1}{r} + \frac{1}{\delta}\right)\left(\frac{1}{r^*} - \frac{1}{r}\right) \tag{3}$$

where r is the radius of a particle, t the reaction time, K a constant proportional to the diffusion constant of the solute, δ the thickness of the diffusion layer, and r^* the critical radius for which the solubility of the particles is equal to the concentration of the solute in solution (zero growth rate). Generally there exists a critical size r^*, corresponding to an equilibrium stage at any given solute concentration. Nanoparticles that are smaller than the critical size may dissolve, while large ones continue to grow. Narrowing size distribution occurs when all particles in solution are larger than the critical size. After the

Metal Nanoclusters in Catalysis and Materials Science: The Issue of Size Control
Edited by B. Corain, G. Schmid and N. Toshima

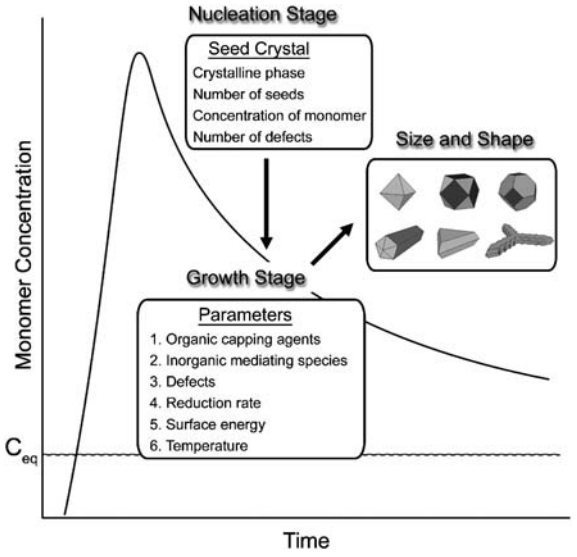

Figure 1. Change of concentration during the nucleation and growth of faceted nanoparticles.

solute is depleted, the stable size can further change because large particles can grow at the expense of dissolution of small ones via the ripening process.

As mentioned above, critical size (r^*) at a given equilibrium stage is an important factor for determining the size of resultant nanoparticles. This critical size can be further derived from Gibbs–Thomas equation [12]:

$$r^* = \frac{2\gamma V_m}{RT \ln S} \quad (4)$$

where γ is the specific surface energy of particle, V_m the molar volume of the particle, R the gas constant, T the reaction temperature, and S the supersaturation of the solute. Based on Equations (3) and (4), particle size increases with reaction time, while the critical particle size decreases with the increase of reaction temperature and supersaturation ratio of the solute, Figure 1.

The formation of particles is triggered by the reduction of metal salts using reducing agents or through the decomposition of organometallic compounds. Parameters that are important in controlling the size of particles include reaction time, temperature, and concentration of the reagents. Another important factor affecting the size of nanoparticles is surfactant, which is generally used to control the growth of particles, prevent particle from aggregation, and help particles dispersing in different solvents.

2.2. Shape Control Based on the Crystal Growth Habit

Nanoclusters tend to form facets in order to minimize surface energy. Since the surface energy of a face-centered cubic (fcc) metal follows the order of (1 1 1)<(1 0 0) <(1 1 0), most nanoclusters are bounded by (1 1 1) and (1 0 0) surfaces, Figure 2a and b. In many cases, the ratio of the growth rate along the (1 0 0) versus (1 1 1)

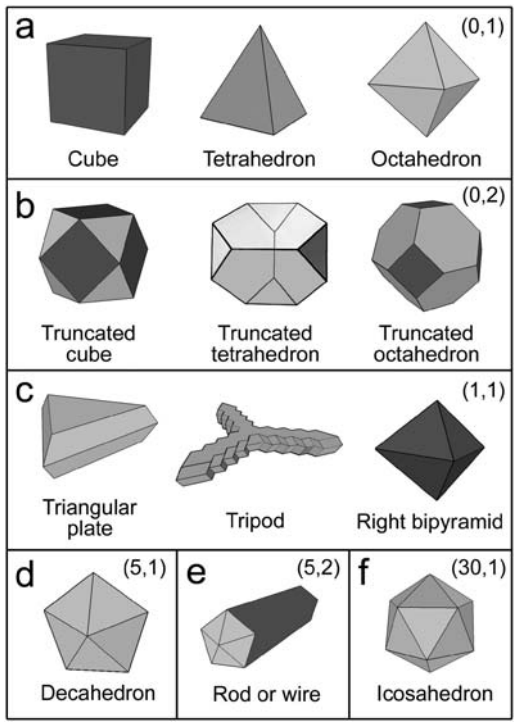

Figure 2. Selected common shapes of fcc metals based on crystal habits, where the notation (*d, f*) represents the number of defects, *d*, and different facets, *f*, displayed: (a) (0,1), (b) (0, 2), (c) (1, 1), (d) (5,1), (e) (5, 2), and (f) (30, 1) groups. The light and dark faces are (1 1 1) and (1 0 0) planes, respectively.

directions, or the so-called R value, can be used to describe the final shape of the nanocrystal. The cube, truncated cube, and octahedron have an R value of 0.58, 0.87, and 1.73, respectively [13,14].

Besides those simple morphologies that are defined by the single crystal habit, crystal defect in a seed crystal can lead to the formation of various other interesting shapes including multipods. Here we coin a term of *crystal shape parameter* (*d,f*), where *d* is the number of defects and *f* is the number of exposed facets in the final nanocrystals. This parameter (*d,f*) is used to classify the morphology of the final crystals. Figure 2 summarizes a range of common shapes classified according to our notation. Figure 2a and b show the defect-free shapes of nanocrystals with (0,1) and (0,2), respectively. These are the commonly encountered shapes for nanocrystals. One of the strategies for making other shapes with low-symmetry is to introduce twin planes in the seeds. Twin planes are observed on the (1 1 1) planes in fcc nanocrystals. Figure 2c shows several shapes that are observed experimentally when one twin plane is introduced into the nanoclusters [15,16]. These shapes include triangular plates, planar tripods, and right bipyramids, which are all bounded by a single type of crystal plane with (1,1). Another commonly observed shape is a decahedron (Figure 2d), which is composed of five tetrahedra bounded by (1 1 1) planes. Anisotropic shapes of fcc metals such as silver and gold based on the decahedron have been observed as shown in Figure 2e [15,17–19]. These nanorods and nanowires grow parallel

to the center axis of the decahedron along the (1 1 0) directions. Since the interplanar angle of a tetrahedron is 70.5°, the decahedron accommodates a gap of 7.5°. Another commonly observed nanocluster is the icosahedron, which is composed of 20 tetrahedrons and 30 twin planes, Figue 2f [20]. Thus, the number of defects can determine the morphology of anisotropic nanoclusters observed in many fcc metals.

2.3. Shape Control by Heterogeneous Species in Solutions

2.3.1. Organic Species Surfactant or Polymer-Capping Agents

Among the several strategies used to achieve size and shape control, by far the most common one is to employ organic capping agents that can bind to the surface of the growing nanoclusters, Figure 3a. These organic species are typically surfactants or polymers that can interact with the surface of nanoclusters to reduce the total surface energy, and thus inhibit the growth into bulk crystals. In general, high concentration of surfactant or polymer leads to the formation of small nanoparticles. Various capping agents have been identified for the synthesis of nanocrystals. For instance, oleic acid has been used for the synthesis of various metal and metal oxide nanoparticles [21–23]. Polyacrylate and sodium polyacrylate has been used to selectively synthesize Pt nanoparticles with various shapes such as cubes and tetrahedrons [24–26]. Polyvinylpyrrolidone (PVP) has been used to grow metal nanowires and nanorods [19,27]. Tetradecyltrimethylammonium bromide has also been used to obtain cubic, cuboctahedral, and porous Pt nanoparticles [28]. Amine-functionalized molecules have been commonly used for Pt-based nanostructures

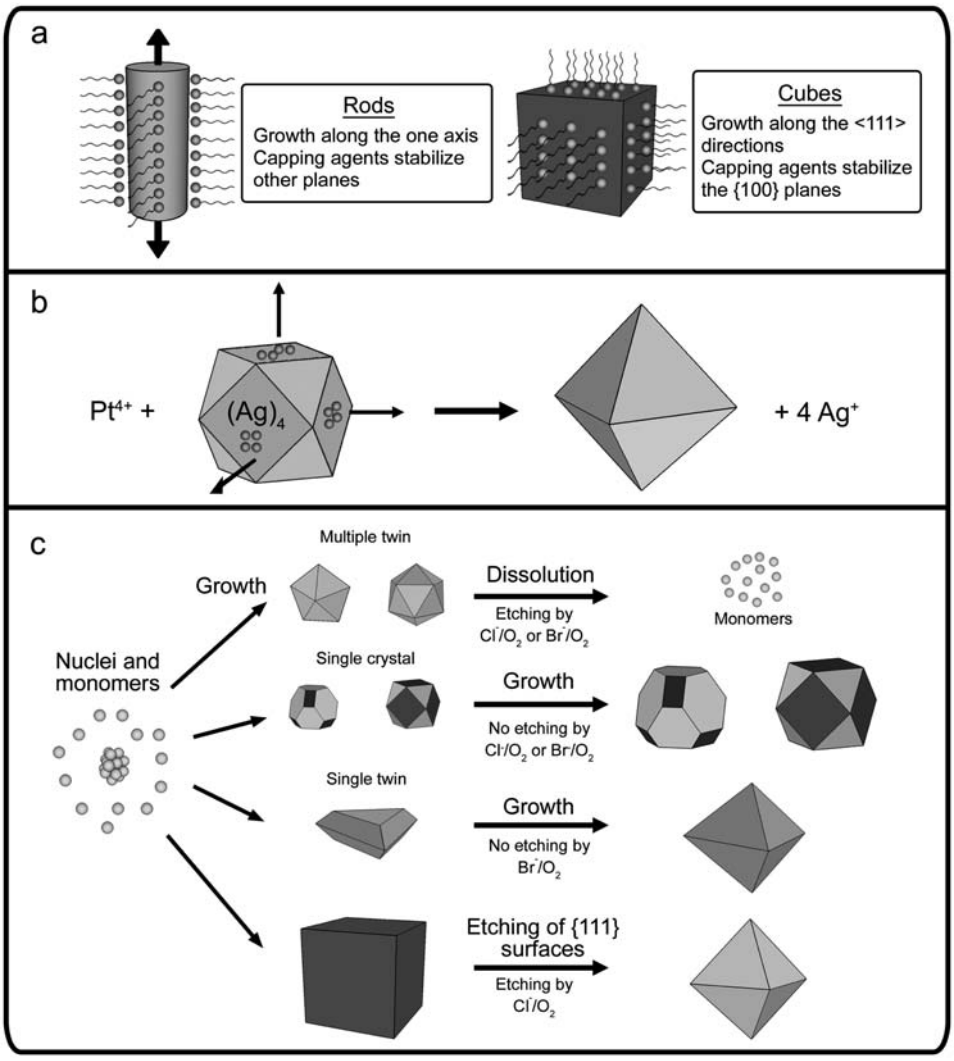

Figure 3. Several strategies on controlling the shape of nanoparticles: (a) organic molecules or polymers as capping agents, (b) inorganic molecules as face-selective catalysts, and (c) inorganic molecules as face-selective etchants.

[22,29]. In some cases, capping agents can bind selectively to different crystal facets and in turn alter the surface energy. The direct consequence is the visible change in the different growth rates along the various crystallographic directions. One such example is the use of ACA and hexadecanylamine to synthesize cubic nanocluster of Pt [30].

2.3.2. Inorganic Species to Catalyze the Growth of Selective Surfaces

Another strategy to achieve shape control is to use inorganic species to catalyze the growth of selective surfaces. This is a relatively underexplored area in terms of the shape control of nanoparticles. The principle idea is to promote the growth of a given set of facets by using species that catalyze the surface growth instead of inhibition. Shape control of Pt nanoclusters by using silver species is one such example [13]. By adding varying amount of Ag^+ in the reaction solution, Pt nanoclusters can grow into different shapes, ranging from cube to octahedron. The amount of silver cation used determined the final shape of the nanoparticles. Small amount of silver ions resulted in the nanocubes and a large amount led to the octahedrons. It has been proposed that silver species in the form of Ag_4^{2+} or Ag^0 can adsorb preferentially on the Pt (1 0 0) planes and Pt-based cations can replace the Ag species by a favorable electrochemical reaction, Figure 3b. Thus, the increase in Ag^+ resulted in a higher R value. Silver species have also been used to synthesize multipod nanoclusters of Pt, which we will discuss in details [31].

2.3.3. Inorganic Species to Etch Selective Surfaces

One other method developed recently to obtain shape control is to use inorganic species to etch selective surfaces. Oxygen and chloride anion have been used in the selective dissolution of multiply twinned particles and the growth of single crystal Ag or Pd nanoclusters, Figure 3c [32–34]. Judicious choice of etchant can sometimes lead to control of the final products with very subtle difference in crystal structure and morphology. For instance, the use of Br^-, a weaker etchant than Cl^-, led to the selective dissolution of only those nanocrystals with multiple twin planes but not the nanocrystals with a single twin plane [16]. This difference in etching results in silver nanoparticles with a single twin plane that are right bipyramids bounded by (1 0 0) planes, Figure 2c. The use of iron species in conjunction with O_2 and Cl^- has been used in the shape control of metal nanocrystals. A Fe^{2+}/Fe^{3+} pair has been introduced in the synthesis of Pt nanowires and multipods [35,36]. In this procedure, Fe^{3+} is able to oxidize Pt^0 to Pt^{2+} and reduce the supersaturation of Pt atoms, which leads to the subsequent change in reduction kinetics. In addition, oxygen can slow the growth by surface adsorption and etching mechanism. The Fe^{2+} species could be oxidized back to Fe^{3+} by aerial oxygen. Thus the shape control of metal nanoparticles in such reactions is sensitive to air.

2.4. Kinetic and Thermodynamic Regime for the Growth of Nanoparticles

Chemical reaction to synthesize nanoparticles is influenced by the stability (thermodynamic factor) and the rate of formation (kinetic factor). The kinetically controlled reaction is a non-equilibrium and irreversible process, which most likely happens at a low temperature or at the beginning of the reaction and is characterized by abundant solutes in the solution. Nanoparticles generated are dominated by the fastest reaction and the size can be highly dependent on reaction time. For a thermodynamically controlled reaction, it reaches equilibrium and is reversible. These reactions most likely happen when the solute is depleted. The thermodynamic products are typically generated from a stable system, while the shape anisotropy is usually achieved in the kinetically controlled regime of the reaction. Size focusing usually happens in the thermodynamic-controlled regime when the solute concentration is low and near saturation. At this stage, the nanoparticles undergo shape changes through the dissolution and redeposition processes [37].

2.5. Choice of Metal Precursors

Several aspects should be considered in the selection of appropriate Pt precursors. Solubility of precursor is important as this parameter determines how well a precursor can be dissolved in a given solvent so as to facilitate the nucleation and growth. Reduction potential is another parameter, which governs the ease with which the precursor can be reduced to Pt metal. Finally, the thermal stability of the precursor partly determines the reaction temperature for the formation of Pt nanoparticles.

Inorganic compounds such as chloroplatinic acids and various salts are the most frequently used Pt precursors for aqueous reactions. Ahmadi et al. reported the synthesis of Pt nanoparticles by using potassium tetrachloroplatinate (K_2PtCl_4). Pt tetrahedrons and cubes were observed at ambient room temperature using hydrogen gas as reducing agent [24]. Herricks et al. reported the synthesis of Pt nanoparticles using H_2PtCl_6 as precursor. In this reaction, ethylene glycol functioned as both solvent and reducing agent [38]. Similarly, Fu et al. reported the synthesis of cubic Pt nanoparticles by reducing potassium *bis*(oxalato) platinato(II) $K_2[Pt(C_2O_4)_2]$ and chloroplatinic acids in aqueous solutions with hydrogen [39].

Organometallic precursors are commonly used in non-aqueous reaction systems. Pt acetylacetonate ($Pt(acac)_2$) is often used as the precursor in organic phase synthesis mostly because of its solubility [22]. Yang and coworkers have reported an approach to monodispersed Pt nanoparticles using $Pt(acac)_2$ [31]. Ely et al. reported synthesis of Co–Pt bimetallic nanoparticles with organometallic precursors $Co(\eta^3\text{–}C_8H_{13})(\eta^4\text{–}C_8H_{12})$ and $Pt_2(dba)_3$ (dba = dibenzyl-ideneacetone) using hydrogen gas as reducing agent [40].

2.6. Choice of Solvents

Both hydrophobic and hydrophilic solvents can be used in the synthesis of Pt and its alloys. Octyl ether [22,41], diphenyl ether [29], benzyl ether [42], and toluene [43], have been reported as solvent when organometallic Pt precursors are used. Water and other hydrophilic reagents such as ethylene glycol are the choices of solvents when inorganic Pt precursors are used [24,38]. In some cases, inorganic salts are used as Pt precursors in organic solvent through a phase-transfer approach. In this case, tetrakisdecylammonium bromide (TDAB) served as the phase-transfer agent to transfer Pt ions from aqueous to non-aqueous phases [43].

3. Results

3.1. Synthesis and Characterization

3.1.1. Synthesis of Faceted Pt Nanoparticles

In a typical synthesis, a mixture of $Pt(acac)_2$ (Gelest Inc., 100 mg), 1-admantinecarboxylic acid (1-ACA, 99%, Aldrich, 100 mg), 1,2-hexadecanediol (90%, Aldrich, 400 mg), hexadecylamine (HDA, 90%, Aldrich, 4 g), and diphenyl ether (99%, Aldrich, 2 mL) was added into a 15 mL three-neck round-bottom flask under argon protection. The reaction mixture was heated to 180 °C via heating mantle. At this temperature, a small amount of silver acetylacetonate (Ag(acac), 99%, Aldrich, 3 mg) was added into the flask. This reaction solution was heated to refluxing temperature (260 °C) and kept at this temperature for 30 min. After separation from solvent using centrifuge and washing with chloroform and methanol, the nanoparticles were recovered and suspended in chloroform.

3.1.2. Synthesis of Pt Multipods in the Presence of Ag(acac)

A mixture of 1,2-hexadecanediol (HDD, Aldrich, 90%, 800 mg), $Pt(acac)_2$ (Gelest Inc., 200 mg), diphenyl ether (Aldrich, 99%, 2 mL), HDA (Aldrich, 90%, 4 g), and ACA (Aldrich, 99%, 180 mg) was added into a 25 mL three-neck round-bottom flask under argon protection. The reaction mixture was held at the designed temperature using an oil bath. Small amount of Ag(acac) (Aldrich, 99%, 3 mg) was then quickly added into the flask, which resulted in rapid formation of gray suspension, indicating the formation of nanoparticles or multipods. The color of suspension quickly turned into black. The reaction solution was maintained at 180 °C within ± 1 °C during the reaction period of up to 60 min. Small amount of samples (200 μL) were taken every minute, starting from the first half minute, to monitor the growth kinetics. After washing with chloroform and methanol alternatively, the nanoparticles and multipods were suspended in chloroform.

3.1.3. Synthesis of Pt Multipods Based on Crystal Defects

For the synthesis of Pt tripods, $Pt(acac)_2$ (100 mg or 0.25 mmol), ACA (135 or 180 mg, 0.75 or 1.0 mmol), HDD (1.6 g or 6.2 mmol), and HDA (2 g or 8.3 mmol) were mixed with diphenyl ether (DPE, 1 mL or 6.3 mmol) in a 15 mL three-neck round-bottom flask equipped with a magnetic stirrer. The flask was evacuated and flushed with argon several times. The reaction flask was then immersed into a heating bath at 130 °C and the reaction mixture dissolved and subsequently turned yellow. This flask was then transferred to another heating bath at 160 °C. The color of the mixture turned into gray in ~10 min, indicating the formation of Pt nanoclusters.

3.1.4. Synthesis of Pt-Porous Nanoparticles

In a typical synthesis, a mixture of $Pt(acac)_2$ (Gelest Inc., 200–400 mg), ACA (Aldrich, 99%, 180–360 mg), HDD (Aldrich, 90%, 0.8–1.6 g), HDA (Aldrich, 90%, 4 g), and diphenyl ether (Aldrich, 99%, 2 mL), was added into a 25 mL three-neck flask under argon protection. This mixture was heated to 150 °C using a heating mantle. The $Pt(acac)_2$ and surfactants were dissolved at this temperature and the color of solution turned into transparent light yellow. The reaction flask was then quickly immersed in an oil bath with 200 mL of glycerol, which was preheated to 210 °C. The temperature of the oil bath dropped by 2–3 °C after the flask immersed in oil, and recovered to the preset temperature (210 °C) within 2 min. The color of the reaction solution turned black in about 2 min, indicating the formation of Pt-porous nanoparticles. Aliquots of samples (~200 μL) were taken at 2, 3, 4, 5, 10, 15, 20, 40, and 60 min after the flask was immersed in the oil bath. The setup was covered with alumina foil to reduce the heat loss. After washing with chloroform and methanol alternatively, the nanoparticles were suspended in chloroform.

3.1.5. Fabrication of Porous Thin Film using the Langmuir–Blogdett (LB) Technique

Anodic aluminum oxide (AAO)-porous substrates were used as templates to make ultra-thin porous membranes of 9 nm Pt particles. In a standard process, an AAO template was attached on a piece of glass slide using a double-sided sticky tape. Before the deposition, the AAO-porous substrate was submerged in aqueous phase. The filling of AAO-porous channels could be accomplished when the substrate was dipped into the Langmuir trough that contained the nanoparticles. Langmuir films of particles were deposited as a monolayer on the surface of AAO template using a KSV 3000 trough. The typical surface pressure was set at 45 $mN\,m^{-1}$, which was optimized for making densely packed oleic acid-stabilized nanoparticles. The LB film of nanoparticles together with the AAO template was removed from the glass support. Vacuum was applied from the non-deposited side to remove water and the

excess nanoparticles at the porous entrance regions, if any. The AAO template was then placed in a tube furnace (Lindberg/Blue M) to carbonize the surfactant molecules on nanoparticle surfaces at 450 °C for 30 min under a flow of argon. After this thermal treatment, the AAO template was dissolved in a sodium hydroxide aqueous solution (0.5 M), leaving behind the free-standing membrane. This membrane was washed by continuously diluting the sodium hydroxide solution with copious amount of water and could be moved to the air/water interface using tweezers. This porous membrane could be deposited in a horizontal fashion onto a solid substrate, such as carbon electrode and films, similar to those procedures for the deposition of the films using Langmuir–Schaefer method. The membrane preserves its integrity over a large area at the air/water interface, and folded or cracked in the air upon removal from aqueous solution without a solid substrate. The AAO substrate obtained from the commercial source (Whatman, Anodisc 13) typically had an average porous entry of ~180 nm in diameter as evaluated by field-emission scanning electron microscopy (FE-SEM, LEO 982).

3.1.6. Characterization

Electron microscope specimens were prepared by dispersing the particles in chloroform (~1 mg mL^{-1}) and drop casting onto carbon-coated copper grids. The regular transmission electron microscopy (TEM) images were recorded on a JEOL JEM 2000EX microscope at an accelerating voltage of 200 kV. Energy dispersive X-ray (EDX) analysis was obtained with an FE–SEM (model: LEO 982) equipped with EDAX detector. EDX analysis on individual nanoparticles was recorded on a Hitachi HD-2000 scanning TEM (STEM) equipped with Oxford Instruments Inc EDX system which has a resolution of 0.18 nm. The high-resolution TEM (HR-TEM) images were recorded on a FEI Tecnai F20 microscope at an accelerating voltage of 200 kV or on an ultra-high vacuum STEM (UHV–STEM, Cornell VG HB501 STEM). Powder X-ray diffraction (PXRD) pattern were recorded using a Philips MPD diffractometer with a Cu K_α X-ray source ($\lambda = 1.5405$ Å) at a scan rate of 0.013° 2θ s^{-1}. Particles-size distribution was obtained by analyzing ~100 particles based on TEM images using the Image J software from NIH.

The electrochemical catalytic activities of Pt-containing nanostructures were characterized using a three-electrode system on a CHI 760 dual channel electrochemical workstation (CH Instrumentation, Inc). A Pt wire and an Ag/AgCl were used as the counter and reference electrodes, respectively. The glassy carbon working electrode was polished with Al_2O_3 powder (Aldrich, 1 μm) and rinsed with Millipore deionized water prior to the test. Cyclic voltammetry (CV) was conducted in the supporting electrolyte for multiple cycles until a stable curve was obtained. All the solutions were prepared using Millipore deionized water. Perchloric acid ($HClO_4$, Aldrich, 99.999%, 0.1 M) was used as the supporting electrolyte. Methanol (CH_3OH, anhydrous) was analytical reagent from Aldrich. All solutions were deaerated with argon for at least 15 min before the measurements were conducted at ~22 °C, unless indicated otherwise. A 10 μL dispersion of catalysts, which were prepared by sonicating nanoparticles in ethanol at a concentration of 0.5 mg Pt mL^{-1} for 10 s, was drop cast onto a carbon electrode (5 mm in diameter). Cyclovoltammetry was performed at 22 °C and the temperature variation was controlled within ±0.1 °C using a circulating bath (Polyscience, Model 1180A). The potential was swept between 0 and 1 V at a rate of 50 mV s^{-1}. The chronoamperometry of nanoparticles was recorded at certain bias voltage. The change in current density with time was recorded. The activation energy was obtained from the slope of the Arrhenius relationship, in which the log i (A cm^{-2}) was plotted against $1000/T$ (K^{-1}) (i is the current density).

3.2. Results and Discussion

3.2.1. Synthesis of Pt Nanoparticles

Figure 4 shows the representative TEM image of as-made Pt nanoparticles. In this reaction, Ag(acac) was used to facilitate the formation of nanoparticles at 180 °C. Various shapes were observed for Pt nanoparticles, including pseudo-sphere, truncated cubo-octahedron (six edges), truncated tetrahedron (six edges), icosahedron (five edges), cube (four edges), and tetrahedron (three edges). The control of nanocrystal morphology could be explained in terms of selective adsorption of capping groups on different planes during the crystal growth. The ratio of growth rate along (1 0 0) versus (1 1 1) directions determines the final morphology [14]. The coexistence of all these shapes indicates that the growth rates were comparable along the major low-index directions.

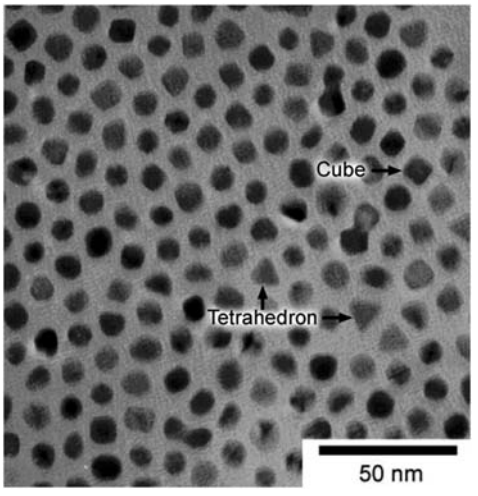

Figure 4. Representative TEM image showing different shapes of faceted Pt nanoparticles.

3.2.2. Formation of Multipods in the Presence of Ag(acac)

Various silver salts can be reduced to silver metal readily at temperatures well below 200 °C through different pathways [32]. We therefore used silver salt as nucleation inducing agent. Ag(acac) was used because of its good solubility in diphenyl ether. The morphology evolution of Pt multipods and nanoparticles was followed by TEM.

Figure 5 shows the typical TEM images of Pt nanoparticles obtained at 180 °C for a reaction time ranging from 4.5 to 60 min after a small amount of Ag(acac) was added into the flask. At the initial stage, largely faceted, rather than spherical, nanocrystals began to appear at 4.5 min after adding the silver precursor, Figure 5a. The concentration of multipods was rather low at this stage. These nanocrystals grew rapidly into multipods within the next minute, which was indicated by rapid change of reaction color from brown to black. A large population of multipods with various shapes, including embryo of triangular shapes, monopod, bipods, tripods, and tetrapods, was observed, Figure 5b. As the reaction continued, the growth along the branch directions became obvious, Figure 5c and d. The overall aspect ratio of multipods branches in Figure 5c and d was visibly higher than those in Figure 5b, while the diameter of branches were relatively constant. After reaction for ~10 min, no distinct growth along the branch direction was observed; while the diameter of each branch began to increase, Figure 5e, followed by a continuous disappearing of multipods. These multipods turned into bullet-shaped irregular particles with the progress of the dissolution and growth process, Figure 5f and g. Upon 40 min after adding silver precursor, multipods evolved into spherical nanoparticles, Figure 5h. The size distribution of nanoparticles became more monodispersed at the reaction time of 60 min and no further shape change was observed, Figure 5i.

Pt nanocrystals triggered by the trace amount of silver could play an important role in directing the preferential growth along particular crystallographic directions. Although no silver could be detected in the Pt multipods, we noted no multipod formation without using silver precursors. In addition, the Ag seeds have been used in the synthesis of different metal particles. Addition of Ag(acac) into hot organic solvent led to the formation of

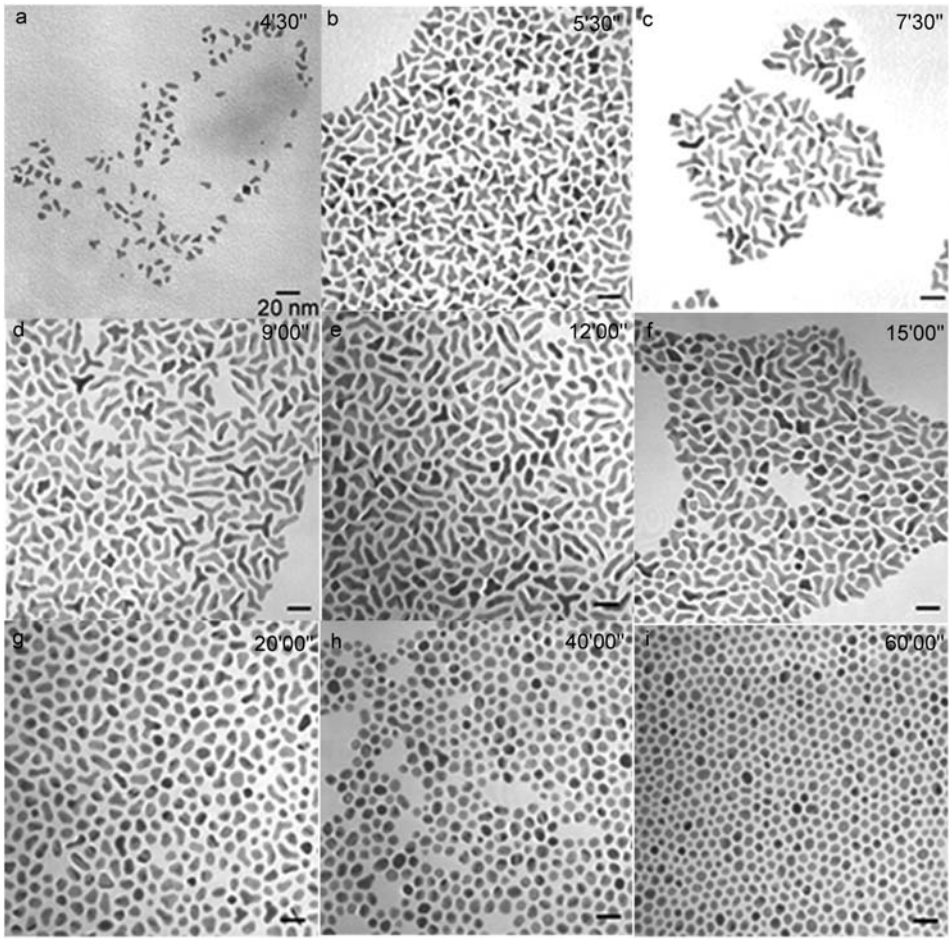

Figure 5. Time-dependent shape evolution of Pt multipods in the presence of Ag(acac). (Reprinted with permission from Ref. [41], © 2005, American Chemical Society.)

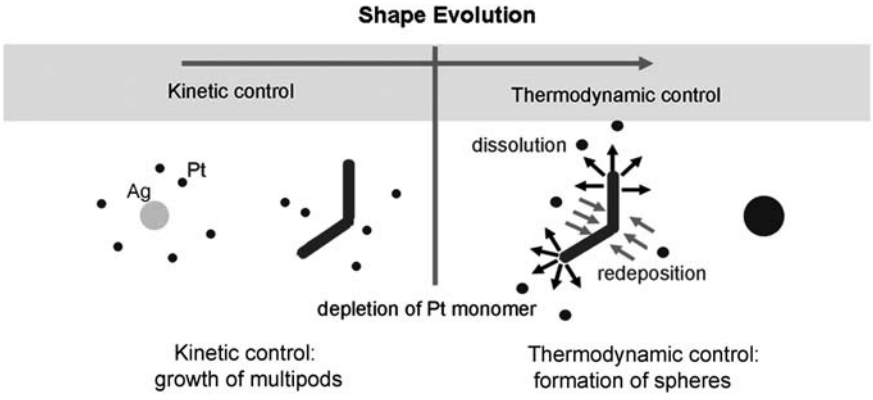

Figure 6. Proposed mode of formation for Pt multipods in the presence of silver species.

silver clusters that promoted the Pt precursors decomposition and growth of Pt on the low-index planes. These Ag clusters could contain as few as four atoms. This seeded growth process allowed the Pt nanocrystal to form below the nucleation and growth temperature in the absence of silver species, which was experimentally determined to be about 210 °C in our reaction system. At the early stages after the nucleation, the kinetic growth governed the branched shapes of Pt particles. In the presence of Ag cluster, growth rates of different Pt facets might be different as well, resulting in the preferential growth of multipods along low-index planes of Pt nanoparticles.

The shape evolution from multipods to spherical nanoparticles could be understood based on the competing growth mechanism, Figure 6. Growth of multipods happened in a kinetic-control regime at the early stage of the reaction. When the monomer of Pt was depleted, the thermodynamic control took place. There is a critical size corresponding to a given equilibrium state. Particles that were smaller than the critical size dissolved while the large ones continued to grow. In another word, the Oswald ripening process became dominant. The branches of multipods began to dissolve, resulting in the disappearance of multipods. Thermodynamically stable spherical particles with relatively large diameters were formed.

3.2.3. *Synthesis of Pt Tripods and Other Anisotropic Nanocrystals Based on Crystal Twinning*

Several types of crystal shapes are observed and can be classified according to the number of twin planes [44]. Synthesis of tripods and other anisotropic nanoclusters of Pt were made by using ACA as surfactant, Figure 7a. These tripods were planar and confirmed by tilting the specimen during TEM imaging, Figure 7b–d. A fourth arm in the axis of the electron beam could not be observed, indicating that the TEM images were planar tripod nanocrystals, not three-dimensional (3D) tetrapods. Figure 7e shows the electron diffraction (ED) pattern of a single tripod. The pattern is of the (1 1 1) zone axis of Pt. Furthermore the formally forbidden 1/3 (4 2 2) diffraction spots were observed. These spots indicate that the nanocluster contains a single twin-plane perpendicular to

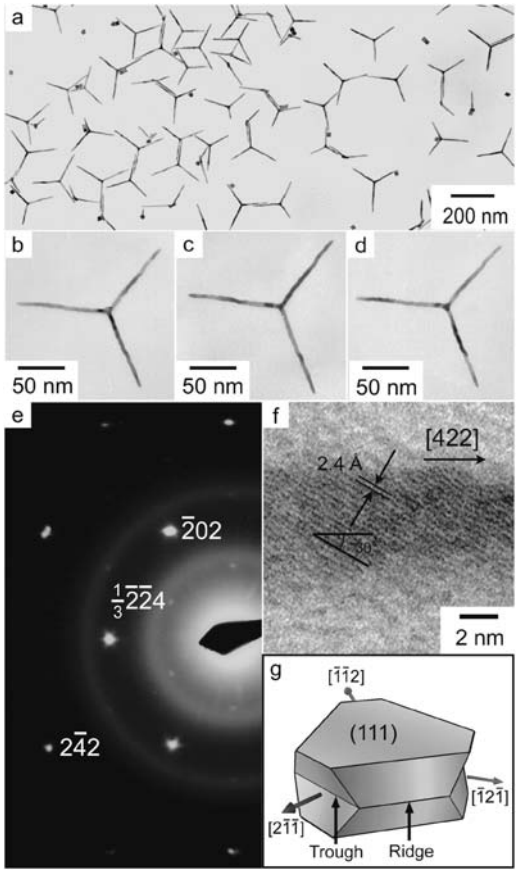

Figure 7. (a) TEM image of Pt planar tripods at low magnification; (b–d) TEM images of a single tripod taken at beam-to-image plane angles of −25°, 0°, and 25°, respectively; (e) ED of a single tripod; (f) HR-TEM image of a branch; and (g) schematic illustration of a possible seed and preferred growth directions. (Reprinted with permission from Ref. [44], © 2006, Royal Society of Chemistry.)

the electron beam. Hexagonal streaking of individual spots were also observed and were perpendicular to the (2,−1,−1), (−1,2,−1), and (−1,−1,2) directions, further indicating that the nanocrystal was tripod with branches

growing along these corresponding directions. The lattice fringe of the branches for a tripod obtained using a STEM agreed well with this ED analysis. Figure 7f shows that the lattice fringe of a branch was 2.4 Å. This value was three times of that for (2 2 4) planes of Pt. The 3 × (2 2 4) fringes were at either 30° or 90° angles with respect to the growth directions of these branches.

Based on the analysis above, the tripods had a single twin plane with branches growing along the (2,−1,−1), (−1,2,−1), and (−1,−1,2) directions. Triangular plates that are observed for various fcc metals also have a single twin plane with three ends pointed toward the same directions as the tripods. These triangular plates grow from a bicrystal bounded by (1 1 1) planes with two types of edges schematically represented in Figure 7g. One is a reentrant trough with the two (1 1 1) planes with an interplanar angle of 141°. The other is a ridge with an interplanar angle of 219°. The reentrant troughs are active sites for nucleation [45,46]. Calculations suggest that the energy barrier for nucleation on a trough is lower than layer advancement across a ridge [46]. It is also worth mentioning that hexagonal plates commonly observed in many fcc metals contain more than one coplanar (1 1 1) twin planes. The formation of hexagonal plates is thought to be the result of the twin planes, which create active sites for nucleation. In this case, however, no triangular or hexagonal plate was observed and the tripods formed a triangular crystal. Once the triangular crystal was formed and all three reentrant troughs were closed, the preferential nucleation occurred at the tips of the triangular crystal. This growth mode in turn generated the reentrant trough. The hypothesis on the preferential nucleation at the tips of the triangular crystal is still not fully understood. One possible reason is that the supersaturation of monomers might be low at the surface of particle but increased with distance. This situation occurred when the diffusion of an add-atom was slow in comparison to the adsorption of Pt atom onto the crystal surface [38]. Thus the ridge or bump in the nanocrystals led to high local-monomer concentration and the preferential growth along these directions. For the tripods, the region around a tip can have a higher monomer concentration than other places in the solution and leads to its subsequent growth while the center region has a slow growth rate. The formation of tripods most likely results from a combination of various factors, such as preferential binding of capping agents, regeneration of the reentrant trough and its preferential nucleation, and a supersaturation gradient.

Several types of morphologies other than tripods can be observed. Those most commonly observed ones in this system are bipods, monopods, and cubes, Figure 8. The nanoparticles can be classified by the number of twin planes and the shape of the core. If there was no twin plane, the nanoparticles adopted the cubic shape, Figure 8a. If one twin plane was introduced, the nanocrystal evolved into a tripod. When the core has an elongated shape, the nanocrystal grew into a *cis*-bipod with two arms typically at an angle of about 120°, Figure 8c. In some cases, the two arms (*trans*-bipod) could have an angle of close to 180°, as seen in Figure 8d. Unsymmetrical planar tripods or tetrapods could also exist, Figure 8e and f. The common feature of these types of nanocrystals was that they had an elongated core containing twin planes that could be clearly supported by the ED patterns. The observed ED was the same as the one observed for nanorods and nanowires based on the fivefold twinned crystal. The observed pattern for Figure 9a is a superposition of an ED pattern from the (1 1 1) and (1 1 0) zone axes. The ED pattern for a tetrapod with an elongated core is a superposition of a pattern from (2 1 1) and

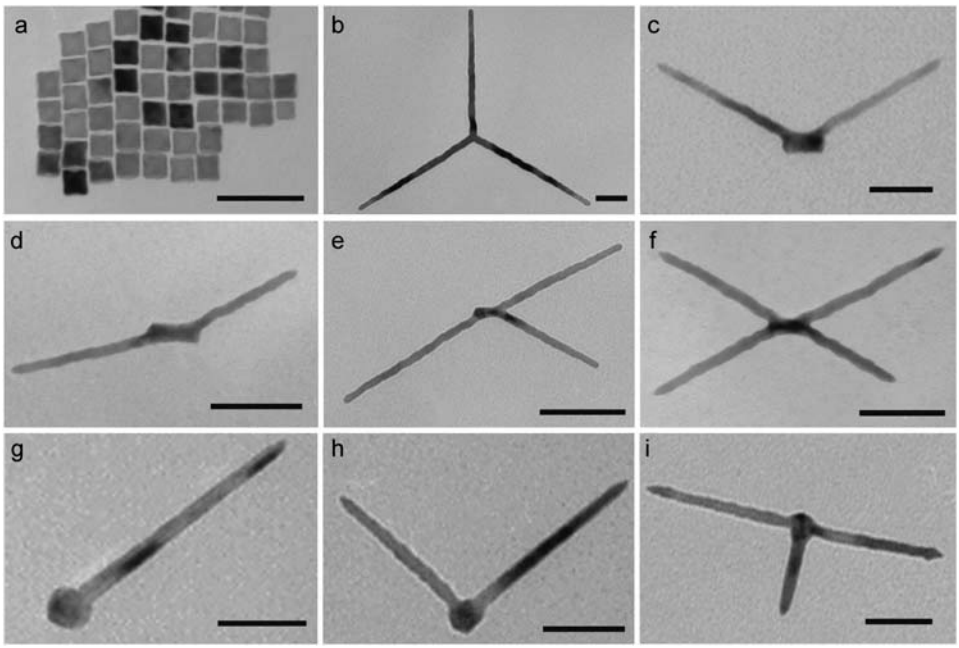

Figure 8. A collage of TEM images of Pt shapes: (a) cubes, (b) symmetrical planar tripod, (c) *cis*-bipod, (d) *trans*-bipod, (e) unsymmetrical tripod, (f) tetrapod, (g) monopod, (h) V-shaped bipod, and (i) tripod. Scale bar is 50 nm.

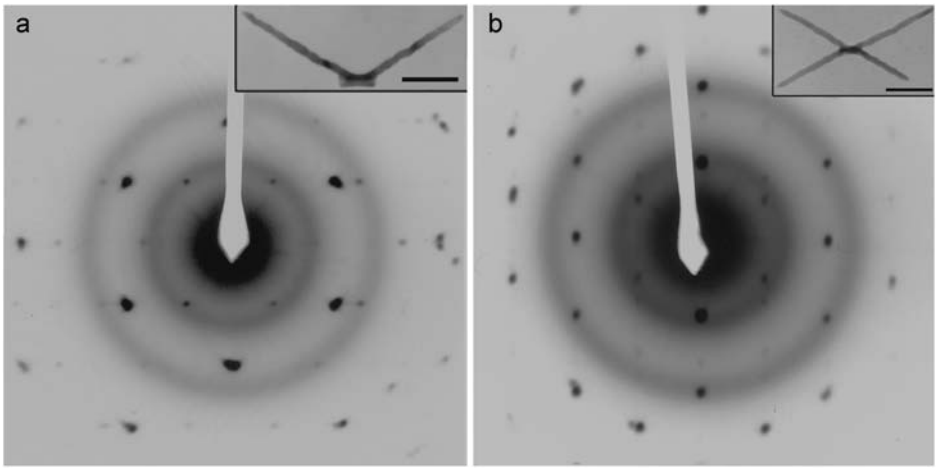

Figure 9. ED patterns of (a) *cis*-bipod and (b) planar tetrapod and their corresponding TEM images (inset). Scale bar is 50 nm.

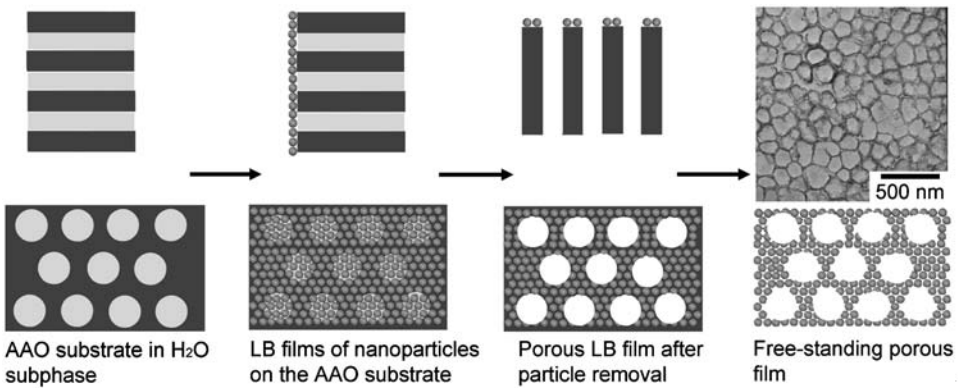

Figure 10. Fabrication of porous Pt nanoparticle membranes by the LB technique. (Reprinted with permission from Ref. [31], © 2005, Wiley-VCH.)

(1 0 0) zone axes, Figure 9b. These results suggest that the elongated core is composed of a five-fold twinned crystal while the arms grow in a similar fashion as the tripods.

The last class is one with arms extending from a spherical multiply twinned core. These structures generally have one arm, (monopod, Figure 8g), but can have a second (V-shaped bipod, Figure 8h) or third arm (tripod, Figure 8i). The shape of the core is most likely an icosahedron. Since the energy barrier between the different types of seed crystals, namely single crystal, one twin plane, decahedron, and icosahedron, is low, they could coexist at the early stage of the reaction and subsequently grew into different final shapes.

3.2.4. Secondary Structures of Pt Nanoparticles

3.2.4.1. Porous Membranes of Nanoparticles from Templating Against AAO Membranes Using LB Technique. AAO-porous substrate has broad applications in making metal and semiconductor nanowires, aligned mesostructured nanorods, inorganic nanotubes, and other 1D nanomaterials. The structured AAO surface, however, has seldom been used as templates in making 2D nanostructures. In this case, AAO template was used as a sacrificial support to generate free-standing membrane of nanoparticles. Porous membranes of Pt nanoparticles can be useful in the fabrication of fuel cell catalyst membranes because of their high surface area and nanoporous nature.

Figure 10 shows the procedure and representative TEM image of a porous membrane of ~9 nm Pt nanoparticles made on the AAO-porous templates (Whatman, Anodisc 13) that had an average pore diameter of 180 nm. The pores in the membrane had the similar shapes and dimensions as those of channel openings of the AAO substrates. No obvious sintering of nanoparticles was observed in the membrane, and the monodispersity of the nanoparticles maintained. From X-ray photoelectron spectroscopy (XPS) analysis on as-made porous membrane of nanoparticles, dominant peak observed at 284.3 eV could be assigned to the binding energy of C 1s orbital, suggesting the existence of sp^2-hybridized carbon. A recent study showed a similar dehydrogenation behavior of oleic acid on the surface of cobalt nanoparticles

at elevated temperatures (~400 °C) [21]. In that case, the carbonized products included graphitic carbon and various alkane fragments. The formation of carbon-rich layers on nanoparticle surfaces at the elevated temperatures could help porous membrane of nanoparticles hold together and prevent the nanoparticles from coalescing. The homogeneity in the monolayer of nanoparticles was critical for making large area of nanoporous membrane. In this context, the LB technique was critical as it was an effective method for the generation of uniform nanoparticle layer.

3.2.4.2. Porous Pt Through Oriented Attachment. Figure 11 shows the structural evolution of Pt-porous nanoparticles from a flower-like porous network to a largely non-porous structure made at $Pt(acac)_2$: HDD:HDA:ACA:DPE molar ratio of 6:36:118:12:100 [47]. These nanoparticles were formed for the reaction at 2, 3, 5, and 20 min, respectively. For the product formed with a reaction time at 2 min, individual particle was composed of dozens of building blocks that interconnected to form the porous structures. These building blocks were primary nanoparticles (PNPs) that had an average dimension of 4.2 ± 0.5 nm in width, Figure 11a. The average diameter of Pt-porous nanoparticles was 36 ± 4.3 nm. The BET (Brunauer–Emmett–Teller) specific surface area for the Pt-porous nanoparticles measured based on nitrogen gas absorption and desorption isotherm measurement was about $14\,m^2\,g^{-1}$. This value was close to those reported for mesoporous Pt ranging from 17 to $23\,m^2\,g^{-1}$ [48]. After the reaction for 3 min, the average width of the PNPs increased to 5.1 ± 0.4 nm, while overall morphology remained to be porous. The structure changed rapidly after the reaction for 5 min. The individual PNPs changed from rod-like to spherical shapes, while the overall diameter of Pt particles reduced to 31 ± 2.9 nm. Most of particles lost the porosity and the average diameter reduced to 22 ± 2.4 nm after the reaction for 20 min, Figure 11d.

A mechanism based on the continuous formation of seeds and rapid autocatalytic growth has been discussed for the formation of metal nanoparticles including Pt [49]. In this process, Pt ions were slowly reduced by 1,2-hexadecanediol and formed Pt clusters. Once the clusters reached the critical size, which was about 50 atoms, the reduction of Pt ions could be accelerated through an autocatalytic reduction process. Thus supersaturation could be achieved in a very short time because of the high precursor concentration and the autocatalytic process of Pt, which resulted in fast, kinetically controlled growth. Therefore, high concentration of PNPs was generated in a short period. An oriented attachment of primary nanocrystals occurred as shown in Figure 11e. ACA seemed to preferentially adsorb on the (1 0 0) facets of Pt nanoparticles and facilitate the growth along (1 1 1) directions. The secondary growth of PNPs proceeded through the attachment growth along (1 1 1) directions, leading to the formation of porous Pt nanostructures. With the depletion of Pt ions, thermodynamic growth took over, and the Ostwald ripening process became dominant, which led to the dissolution of small PNPs in favor of the growth of large ones.

3.2.5. Catalytic Property

The porous nanostructures of Pt possess good catalytic properties. Figure 12 shows CV curves of LB film of 9 nm as-made Pt nanoparticles and the porous membrane of the same type of Pt nanoparticles. The estimated loadings of Pt in the LB monolayer and the porous membrane deposited on a working electrode were about 0.28 and 0.062 μg, respectively. These values were equal to Pt loading densities of $3.9\,\mu g\,cm^{-2}$ for LB monolayer and $0.88\,\mu g\,cm^{-2}$ for porous membrane electrodes. The value for porous membrane was calculated based on the TEM images, which gave a packing density of ~800 Pt nanoparticles μm^{-2}. To calculate the total mass of Pt in the membrane, we assumed the Pt nanoparticles were spherical and obtained the volume of individual nanoparticles according to the equation, $\pi D^3/6$, where D is the diameter of the Pt nanoparticle measured from the TEM images. Pt density of $21.09\,g\,cm^{-3}$ was used. The same method and density were used for the electrode deposited with

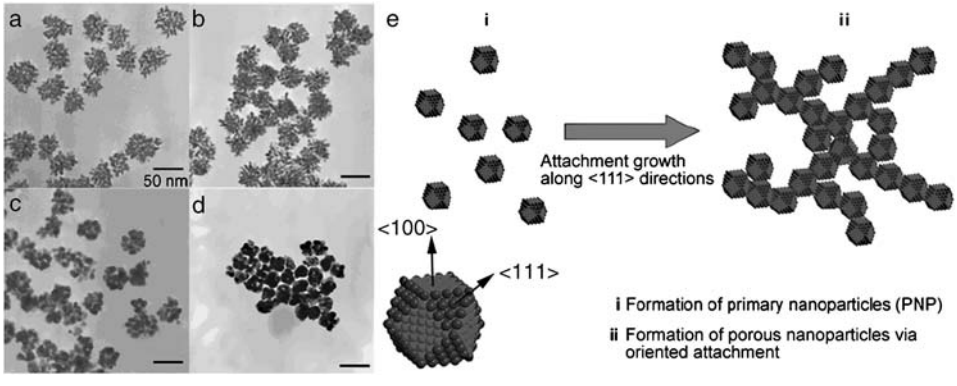

Figure 11. (a–d) Time-dependent shape evolution of Pt-porous nanoparticles at $Pt(acac)_2$: HDD: HDA: ACA: DPE molar ratio of 6:36:118:12:100. The reaction times were (a) 2, (b) 3, (c) 5, and (d) 20 min after the reaction flask was transferred to the oil bath at 210 °C. The scale bar is 50 nm, applicable to all the images. (Reprinted with permission from Ref. [47], © 2006, Wiley-VCH.) (e) A proposed growth model based on the oriented attachment principle.

monolayer LB film of as-made Pt nanoparticles. The peak current density in forward sweep corresponded to a current density of ~0.84 mA cm^{-2}. On the other hand, the as-made Pt nanoparticles deposited as a LB monolayer had no detectable current, even though the Pt loading was about five times higher than that in the porous membrane. These data indicates that the porous membrane possessed much better catalytic property in methanol oxidation than the as-made Pt nanoparticles based on the values of current density and Pt loading. One possible reason could be that the membrane contained high percentage of graphitic carbon than the as-made Pt nanoparticles, which had non-conducting surfactants on the surfaces.

The electrochemical catalytic activity of various Pt-porous nanoparticles for the oxidation of methanol was shown in Figure 13. The peak mass current densities recorded after 100 scan cycles were 80 mA mg^{-1} Pt for those porous Pt nanoparticles. The peak mass current densities were 72, 62, 58 and 51 mA mg^{-1} Pt for those products formed for reaction time of 3, 5, 10, and 20 min at the $Pt(acac)_2$: HDD: HDA: ACA: DPE molar ratio of 6:36:118:12:100, respectively. As a reference point, the catalytic activity of a commercial carbon-supported Pt catalyst (XC-72R, E-Tek, 60% Pt, diameter of Pt particle: ~6 nm) was measured, which had a mass current density of 51 mA mg^{-1} Pt. The porous nanoparticles could be ~60% more reactive than this commercial catalyst based on the unit mass of Pt, Figure 13a. The chronoamperometric characterization further indicated that the mass current density of Pt-porous nanoparticles were at least ~60% higher than that for the reference catalyst tested when the oxidation reaction reached the steady state (5×10^4 s), Figure 13b. The small size of PNPs, the interconnected morphology of the nanoparticles and the reactant diffusivity to catalyst surfaces could be important for the observed bulk catalytic activity.

The activation energy for the reaction, E_a, was determined for the above Pt-porous nanoparticles from the first cycle of CV measurement in the temperature range between 30 and 60 °C, Figure 13c. The activation energy was obtained from the slope, $-E_a/R$, of the Arrhenius relationship and equal to 30 kJ mol^{-1}. This value was similar to some of those obtained for the electro-oxidation of methanol on electrodes of Pt particles dispersed in Nafion® [50, 51].

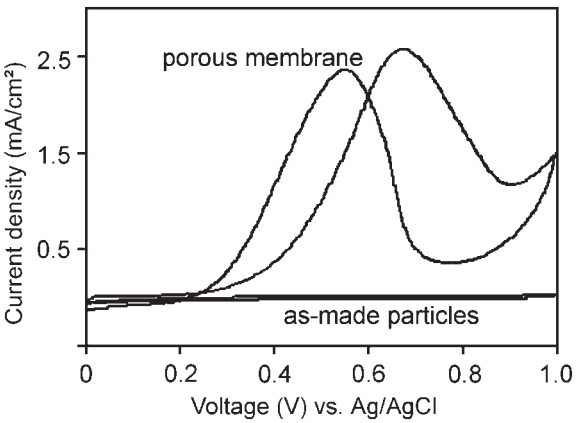

Figure 12. Cyclic voltammograms of direct methanol oxidation catalyzed by the porous Pt nanoparticle membrane and as-made Pt nanoparticles. The reaction solution was made of an aqueous mixture containing 0.1 M $HClO_4$ and 0.125 M methanol. (Reprinted with permission from Ref. [31], © 2005, Wiley-VCH.)

4. A Case History

In this section, we will discuss the formation and structural analysis of single crystal Pt octapods. Face-centered cubic crystal is highly symmetric without the introduction of twin plane. This phenomenon leads to the limited success in synthesizing anisotropic nanoparticles of fcc metals. By controlling the reaction condition and using appropriate capping agents that bind to certain crystallographic facets, however, anisotropic Pt nanoparticles, namely multipods with the arms growing in the (1 1 1) directions, can be obtained.

The synthesis of Pt octapods was achieved by mixing 100 mg of $Pt(acac)_2$, 180 mg of ACA, 1.6 g of HDD, 2 g of HDA, and 1 mL of DPE in a 15 mL three-neck round-bottom flask, which was evacuated and flushed with argon several times. The flask was immersed in an oil bath preset at 130 °C and the mixture turned to a transparent yellow color. The flask was then immersed into an oil bath preset at 180 °C. Within a couple of minutes the mixture turned black, indicating the formation of Pt nanoparticles. The

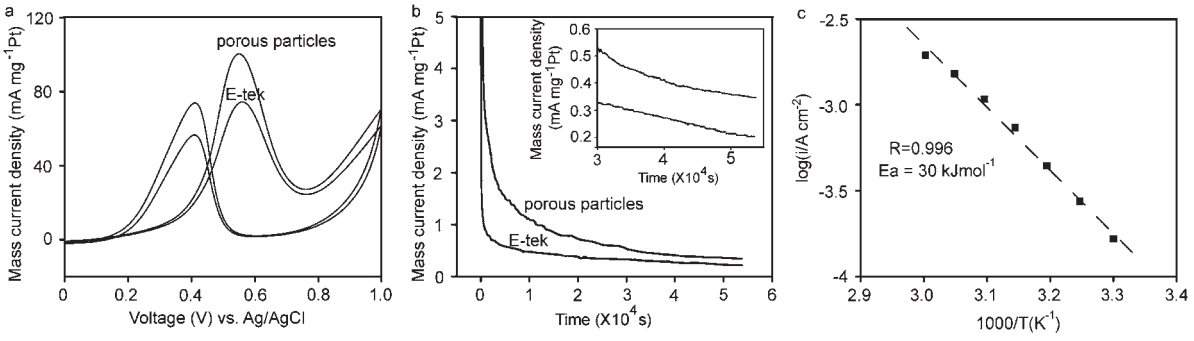

Figure 13. (a) Cyclic voltammograms, (b) chronoamperometric curves for oxidation of methanol catalyzed by the Pt-porous nanoparticles and a commercial catalyst, and (c) the Arrhenius plot for the reaction with the Pt-porous nanoparticles. (Reprinted with permission from Ref. [31], © 2005, Wiley-VCH.) (Reprinted with permission from Ref. [47], © 2006, Wiley-VCH.)

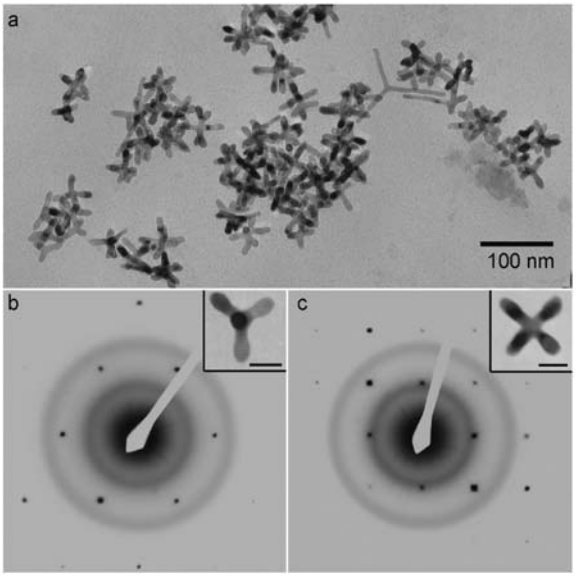

Figure 14. (a) TEM image of Pt multipods. ED of (b) a tetrapod and (c) an octapod. The corresponding TEM images are shown in the insets. The scale bar for the insets is 20 nm.

reaction was stopped after 20 or 40 min. The Pt nanoparticles were collected and washed by using chloroform as solvent and ethanol as antisolvent.

The TEM image of the Pt multipods obtained at 20 min is shown in Figure 14a. All of the multipods have at least four branches, although the exact number of branches and the precise morphology of the Pt nanoparticles have not been completely determined. ED was performed on two types of multipods, i.e., a tetrapod and an octapod. An ED pattern for a tetrapod from the sample obtained at 40 min, is shown in Figure 14b. The inset shows the TEM image of the tetrapod discernible by the contrast between the center and the arms. The pattern shows a hexagonal pattern typical of a single-crystal Pt with a (1 1 1) zone axis. This observation suggests that the center arm, which is parallel to the electron beam, grows along the (1 1 1) axis. The inset of Figure 14c is a TEM image of an octapod from the sample obtained at 40 min. The nature of octapod can be detected from the dark contrast in the arms and the bright contrast in the center. The ED pattern shows a cubic pattern, typical of a single crystal Pt with a (1 0 0) zone axis. This result suggests that the octapods are the result of extended growth along eight (1 1 1) directions from the corners of a cube.

The formation of multipods is thought to be a combination of two factors: selective growth along the (1 1 1) directions and preferential nucleation at the place furthest from the center of the nanocrystal. The selective growth along the (1 1 1) directions is thought to be a result of preferential binding of capping agents on (1 0 0) facets of Pt, leaving (1 1 1) facets relatively exposed for continuous growth. In some similar reaction systems, such as the one in synthesizing Pt tripods, Pt nanoparticles with cubic morphology was obtained, suggesting that the ACA has the ability to bind to Pt (1 0 0) surfaces, thus promoting the growth along the eight (1 1 1) directions. In the current

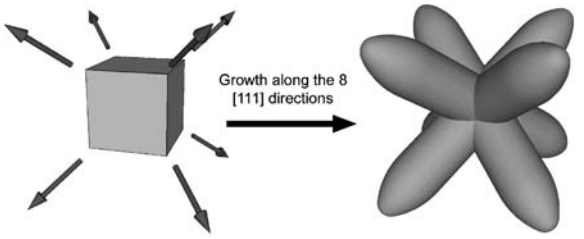

Figure 15. Schematic of preferential growth of octapods along eight (1 1 1) directions from a cube.

case, however, where the temperature is raised by 20 °C, the growth along (1 1 1) directions is enhanced significantly, yielding multipod structures with arms growing along (1 1 1) directions. The second factor, selective nucleation on the tips of the nanoparticle, could be a result of a concentration gradient of Pt monomers where the monomers were unsaturated near the center of nanoparticles [52]. This concentration gradient was the major cause for the selective nucleation at the places that were furthest from the center of nanoparticle. Thus both tetrapods and octapods can be observed in the same reaction system, as being shown in Figure 15.

5. Conclusions

We have presented several strategies for controlling the shape and nanostructure of Pt particles. Clearly, the principles discussed in this chapter can be readily applicable to other fcc metals or even alloys [53]. Identification of capping agents that bind a given facet specifically or selectively is critical for controlling the morphologies of both simple shape and complexed multipods that are defined by the underlining crystal habits. In this regard, crystal twinning can be critically important in the formation of various planar and 3D metal nanostructures. Adamantane-containing compounds and long-chain amines appear to be an effective mix of capping agents in making Pt nanocrystals with a range of interesting shapes.

References

1 A. Wieckowski, E. R. Savinova, C. G. Vayenas, *Catalysis and Electrocatalysis at Nanoparticle Surface*, Marcel Dekker, Inc., New York, 2003.
2 U. Kreibig, H. Bonnemann, J. Hormes, Nanostructured materials, micelles and colloids, in H. S. Nalwa (ed.) *Handbook of Surfaces and Interfaces of Materials*, Vol. 3, Academic Press, San Diego, 2001, 1.
3 Y. G. Sun, Y. N. Xia, *Science* 298 (2002) 2176.
4 C. Burda, X. B. Chen, R. Narayanan, M. A. El-Sayed, *Chem. Rev.* 105 (2005) 1025.
5 Y. N. Xia, N. J. Halas, *MRS Bull.* 30 (2005) 338.
6 D. A. Schultz, *Curr. Opin. Biotechnol.* 14 (2003) 13.
7 R. Narayanan, M. A. El-Sayed, *J. Phys. Chem. B* 109 (2005) 12663.
8 N. M. Markovic, V. Radmilovic, P. N. Ross Jr., in A. Wieckowski, E. R. Savinova, C. G. Vayenas (eds.) *Catalysis and Electrocatalysis at Nanoparticle Surface*, Marcel Dekker, Inc., New York, 2003, 311.

9 V. K. LaMer, R. H. Dinegar, *J. Am. Chem. Soc.* 72 (1950) 4847.
10 T. Sugimoto, *Adv. Colloid Interface Sci.* 28 (1987) 65.
11 X. G. Peng, J. Wickham, A. P. Alivisatos, *J. Am. Chem. Soc.* 120 (1998) 5343.
12 T. Sugimoto, F. Shiba, T. Sekiguchi, H. Itoh, *Colloids Surf. A* 164 (2000) 183.
13 H. Song, F. Kim, S. Connor, G. A. Somorjai, P. D. Yang, *J. Phys. Chem. B* 109 (2005) 188.
14 Z. L. Wang, *J. Phys. Chem. B* 104 (2000) 1153.
15 C. Lofton, W. Sigmund, *Adv. Funct. Mater.* 15 (2005) 1197.
16 B. J. Wiley, Y. J. Xiong, Z. Y. Li, Y. D. Yin, Y. A. Xia, *Nano Lett.* 6 (2006) 765.
17 N. R. Jana, L. Gearheart, C. J. Murphy, *Chem. Comm.* (2001) 617.
18 C. J. Johnson, E. Dujardin, S. A. Davis, C. J. Murphy, S. Mann, *J. Mater. Chem.* 12 (2002) 1765.
19 Y. G. Sun, B. Mayers, T. Herricks, Y. N. Xia, *Nano Lett.* 3 (2003) 955.
20 K. Koga, K. Sugawara, *Surf. Sci.* 529 (2003) 23.
21 V. Perez-Dieste, O. M. Castellini, J. N. Crain, M. A. Eriksson, A. Kirakosian, J. L. Lin, J. L. McChesney, F. J. Himpsel, C. T. Black, C. B. Murray, *Appl. Phys. Lett.* 83 (2003) 5053.
22 S. H. Sun, C. B. Murray, D. Weller, L. Folks, A. Moser, *Science* 287 (2000) 1989.
23 Y. Wang, H. Yang, *Chem. Commun.* (2006) 2545.
24 T. S. Ahmadi, Z. L. Wang, T. C. Green, A. Henglein, M. A. El-Sayed, *Science* 272 (1996) 924.
25 T. S. Ahmadi, Z. L. Wang, A. Henglein, M. A. El-Sayed, *Chem. Mater.* 8 (1996) 1161.
26 J. M. Petroski, Z. L. Wang, T. C. Green, M. A. El-Sayed, *J. Phys. Chem. B* 102 (1998) 3316.
27 B. Wiley, Y. G. Sun, B. Mayers, Y. N. Xia, *Chem. Eur. J.* 11 (2005) 454.
28 H. Lee, S. E. Habas, S. Kweskin, D. Butcher, G. A. Somorjai, P. D. Yang, *Angew. Chem. Int. Ed. Engl.* 45 (2006) 7824.
29 E. V. Shevchenko, D. V. Talapin, A. L. Rogach, A. Kornowski, M. Haase, H. Weller, *J. Am. Chem. Soc.* 124 (2002) 11480.
30 E. V. Shevchenko, D. V. Talapin, H. Schnablegger, A. Kornowski, O. Festin, P. Svedlindh, M. Haase, H. Weller, *J. Am. Chem. Soc.* 125 (2003) 9090.
31 X. W. Teng, X. Y. Liang, S. Rahman, H. Yang, *Adv. Mater.* 17 (2005) 2237.
32 B. Wiley, T. Herricks, Y. G. Sun, Y. N. Xia, *Nano Lett.* 4 (2004) 1733.
33 Y. J. Xiong, J. Y. Chen, B. Wiley, Y. N. Xia, *J. Am. Chem. Soc.* 127 (2005) 7332.
34 S. H. Im, Y. T. Lee, B. Wiley, Y. N. Xia, *Angew. Chem. Int. Ed. Engl.* 44 (2005) 2154.
35 J. Y. Chen, T. Herricks, M. Geissler, Y. N. Xia, *J. Am. Chem. Soc.* 126 (2004) 10854.
36 J. Y. Chen, T. Herricks, Y. N. Xia, *Angew. Chem. Int. Ed. Engl.* 44 (2005) 2589.
37 J. W. Mullin, *Crystallization*, Butterworth-Heinemann, Oxford, 1997.
38 T. Herricks, J. Y. Chen, Y. N. Xia, *Nano Lett.* 4 (2004) 2367.
39 X. Y. Fu, Y. A. Wang, N. Z. Wu, L. L. Gui, Y. Q. Tang, *Langmuir* 18 (2002) 4619.
40 T. O. Ely, C. Pan, C. Amiens, B. Chaudret, F. Dassenoy, P. Lecante, M. J. Casanove, A. Mosset, M. Respaud, J. M. Broto, *J. Phys. Chem. B* 104 (2000) 695.
41 X. W. Teng, H. Yang, *Nano Lett.* 5 (2005) 885.
42 M. Chen, J. Kim, J. P. Liu, H. Y. Fan, S. H. Sun, *J. Am. Chem. Soc.* 128 (2006) 7132.
43 K. Wikander, C. Petit, K. Holmberg, M. P. Pileni, *Langmuir* 22 (2006) 4863.
44 S. Maksimuk, X. W. Teng, H. Yang, *Phys. Chem. Chem. Phys.* 8 (2006) 4660.
45 D. R. Hamilton, R. G. Seidensticker, *J. Appl. Phys.* 31 (1960) 1165.
46 J. W. Lee, U. J. Chung, N. M. Hwang, D. Y. Kim, *Acta Crystallogr., Sect. A: Found. Crystallogr.*, 61 (2005) 405.
47 X. W. Teng, X. Liang, S. Maksimuk, H. Yang, *Small*, 2 (2006) 249.
48 G. S. Attard, P. N. Bartlett, N. R. B. Coleman, J. M. Elliott, J. R. Owen, J. H. Wang, *Science* 278 (1997) 838.
49 Y. J. Song, Y. Yang, C. J. Medforth, E. Pereira, A. K. Singh, H. F. Xu, Y. B. Jiang, C. J. Brinker, F. van Swol, J. A. Shelnutt, *J. Am. Chem. Soc.* 126 (2004) 635.
50 A. Aramata, T. Kodera, M. Masuda, *J. Appl. Electrochem.* 18 (1988) 577.
51 G. Meli, J. M. Leger, C. Lamy, R. Durand, *J. Appl. Electrochem.* 23 (1993) 197.
52 J. Aizenberg, A. J. Black, G. M. Whitesides, *Nature* 398 (1999) 495.
53 X. Teng, S. Maksimuk, S. Frommer, H. Yang, *Chem. Mater.* 19 (2007) 36.

CHAPTER 18

Spreader-Bar Structures as Molecular Templates for Electrochemical Synthesis of Nanoparticles

Vladimir M. Mirsky

Institute of Analytical Chemistry, Chemo- and Biosensors, University of Regensburg, Regensburg, Germany

1. Introduction

Immobilized nanoparticles are of great interest for many applications including electrocatalysis, data storage systems, new electronic devices, electrochemical chemo- and biosensors, refractometric and fluorescent sensors based on localized plasmon effects, and many other fields of science and high technology [1–4]. Most strategies of preparation of these systems are based on the deposition of pre-synthesized nanoparticles with [5] or without [6,7] further treatment. Such depositions were mostly performed by electrospray technique [8] or by adsorption [6,9]. Several techniques are based on in situ synthesis of the nanoparticles. In particular, such a synthesis can be performed by electroless deposition or by electroplating. An electroless synthesis of nanoparticles, being first described in M. Faraday works on preparation of gold sol, is used now for the deposition of gold, silver, nickel, palladium, copper and cobalt nanoparticles onto different surfaces [1,2,10]. Within this procedure, a reducing agent is added into the liquid or is deposited onto the surface, as it, e.g. has been done in the case of silver nanocluster formation, which was performed by reduction of silver on the monolayer of hydroquinone derivate [11]. Template-based techniques for synthesis of nanostructures are reviewed in Ref. [12]. This approach can be applied in both aqueous and organic solutions. An electroplating is used for formation of bulk phases of nanocrystalline metals by reduction of corresponding salts in ionic liquids [13,14]. A combination of electroplating and electroless deposition was developed [15,16]: metallic nanoparticles are formed by electrochemical reduction on the tip of scanning tunneling microscope and then transferred to planar metal electrodes by mechanical contact with them. This technology was reproduced in other groups and used for investigation of electrochemical reactivity [17].

Recently, another template-based technique for preparation of metallic nanoparticles on electrode surfaces was described [18]. This technique does not need any nanomanipulation by STM or AFM. It is based on reduction of metals on nanoelectrodes formed by the recently developed spreader-bar technique [19]. Variations of the reduction current provide a simple way to control size of the nanoparticles formed. In contrast to other template-based techniques reviewed in Refs. [12,20], the current method exploits ultrathin template based on self-assembled monomolecular layer.

2. Synthetic Strategy

Electrochemical template-controlled synthesis of metallic nanoparticles consists of two steps: (i) preparation of template and (ii) electrochemical reduction of metals. The template is prepared as a nanostructured insulating monolayer with homogeneously distributed planar molecules. This is a crucial step in the whole technology. The insulating monolayer has to possess perfect insulating properties while the template has to provide electron transfer between electrode and solution. Probably, the mixed nanostructured monolayer consisting of alkylthiol with cavities which are stabilized by the spreader-bar approach [19] is the only known system which meets these requirements.

2.1. Preparation of Template

In general, a preparation of mixed monolayer can be realized by either a kinetic control or a thermodynamic control (Figure 1, left). Kinetic control is based on a suggestion that for an initial deposition step the desorption rate is ignorable in comparison with the adsorption rate. In this case, the concentration ratio of the adsorbed species A and B on the surface corresponds to the ratio of products of their adsorption rate constant (k_A or k_B) and concentration (C_A or C_B): $k_A C_A / k_B C_B$. The validity of the initial assumption on low desorption rate means that the total surface coverage obtained under kinetic control is essentially lower than 100%. This non-complete coverage does not disturb most of optical applications of the

Metal Nanoclusters in Catalysis and Materials Science: The Issue of Size Control
Edited by B. Corain, G. Schmid and N. Toshima

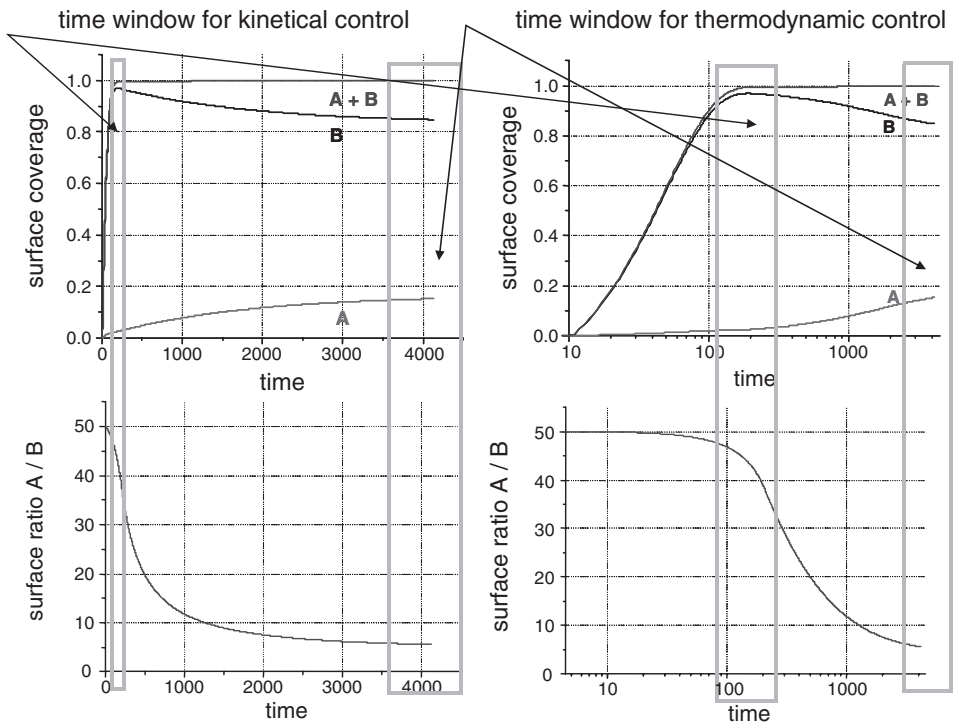

Figure 1. Theoretical curves for surface coverage (up) by substance A (curves A), by substance B (curve B), for total surface coverage (curves A + B) and ratio of substances A and B on the surface (down) for competitive adsorption of the substances A and B. The data are presented in linear (left) and in logarithmic (right) time scales.

formed mixed monolayers, but complicates essentially their electrochemical applications: the uncoated electrode surface has typically much higher electrical conductance than the coated one, thus shunting electrical current through coated electrode surface. Another difficulty in kinetic deposition of mixed monolayers is caused by the requirement to define the deposition time very precisely. Possible temperature fluctuations, data scattering between different samples and widely used blind deposition of self-assembled monolayers (without on-line monitoring) make this technique poorly reproducible.

Thermodynamic control (Figure 1, right) is based on adsorption of substances until quasi-equilibrium stage. In this case, the surface ratio of the adsorbed species is defined by the ratio of products of their concentration and binding constant. This deposition is much less influenced by poorly controllable fluctuations of external conditions and provides much better reproducibility. The total coverage can be almost 100%. Because of these reasons, the thermodynamic control is advantageous for preparation of mixed nanostructured monolayers for electrochemical applications including a formation of spreader-bar structures for their application as molecular templates for synthesis of nanoparticles.

However, an application of thermodynamic control may be complicated by too large difference in binding constant of adsorbed species. The highest concentration of an adsorbate in deposition solution cannot exceed its solubility. The lowest concentration should provide enough high amounts of molecules for formation of a monomolecular layer. For most of compounds and typical geometry of deposition cells, these requirements result in the range of possible variations of concentrations of $\sim 10^4$ times. A difference in binding constants of adsorbed species can be much higher. Therefore, it may be impossible to compensate strong difference in binding constants of adsorbed species by adjustment of their concentrations. Because of this reason it is impossible to prepare mixed monolayers on gold surface by co-adsorption of thiols and molecules without thiol moiety. For example, large planar molecules with large π-electron systems form perfect monolayer being adsorbed as an individual compound. However, a co-adsorption of this compound with linear alkylthiol lead to its fast replacement by alkylthiol [21]. It is observed even at high excess of the non-thiolated compounds.

Therefore, the spreader-bars should be also formed from thiolated compounds. The largest thiolated molecule used so far for this purpose was a thiolated derivative of tetraphenylporphyrine (TMPP) obtained from commercially available 5,10,15,20-tetrakis(sulfonatophenyl)porphyrin by partial reduction of its sulfonato groups [18]. TMPP was co-adsorbed on thoroughly cleaned gold surface from ethanol solution containing 15 mM TMPP and 1.5 μM 1-dodecanethiol (C12) for 72 h. This time exceeds a typical time for surface–solution exchange of thiolated compounds [22]; therefore, one can expect a quasi-equilibrium ratio of TMPP (template) and C12 (matrix) molecules in the film.

The deposition conditions should be optimized to obtain approximately equal amounts of matrix and spreader-bar molecules on the surface [18,21]. Analysis of monolayers by near-edge X-ray absorption fine-structure spectroscopy,

X-ray photoemission spectroscopy and X-ray absorption spectroscopy demonstrated that the mixed film can be precisely adjusted by the composition of the solution used for co-adsorption of C12 and TMPP. The monolayer formed from the C12/TMPP = 1/10,000 mol mol^{-1} solution contains only TMPP moieties, while that from the 1/1000 solution is mostly TMPP with a few percent of C12. The monolayer formed from the 1/100 solution contains a minor amount of TMPP, and that from the 1/10 solutions consists exceptionally of C12 moieties [18].

2.2. *Template-Controlled Electrochemical Synthesis of Nanoparticles*

Gold electrodes coated by nanostructured self-assembled monolayer of TMPP and C12 are used as template for in situ synthesis of metallic nanoparticles (Figure 2). Electrodeposition of metals can be performed under different electrochemical modes. In the work mentioned in Ref. [18], it was performed in potentiostatic mode. The potential value for formation of platinum nanoparticles is −25 mV vs. SCE; the deposition is performed from 2.5 mM solution of $H_2[PtCl_6]$ in 50 mM KCl. The size of nanoparticles formed depends on the reduction charge. Continuous monitoring of the charge in potentiostatic mode is provided by different potentiostats, for example, by Autolab-PG-stat (EcoChemie, The Netherlands). Conditions for deposition of other metals should be selected according to their electrochemical properties.

3. Results

The electrochemically formed nanoparticles can be visualized by scanning electron microscopy (Figure 3). At the

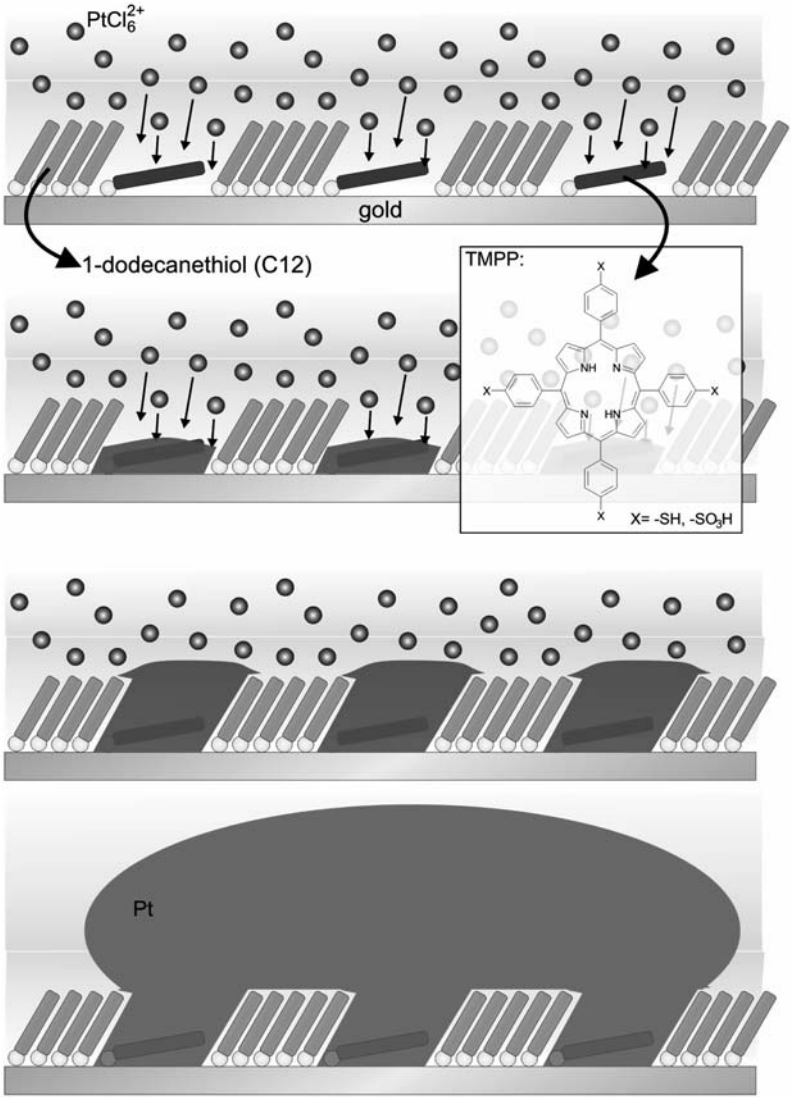

Figure 2. Electrochemical template-controlled synthesis of nanoparticles on nanostructured monolayer. The size of nanoparticles depends on the reduction charge and can be adjusted easily. (Reprinted from Ref. [18], © 2005, with permission from Wiley-VCH.)

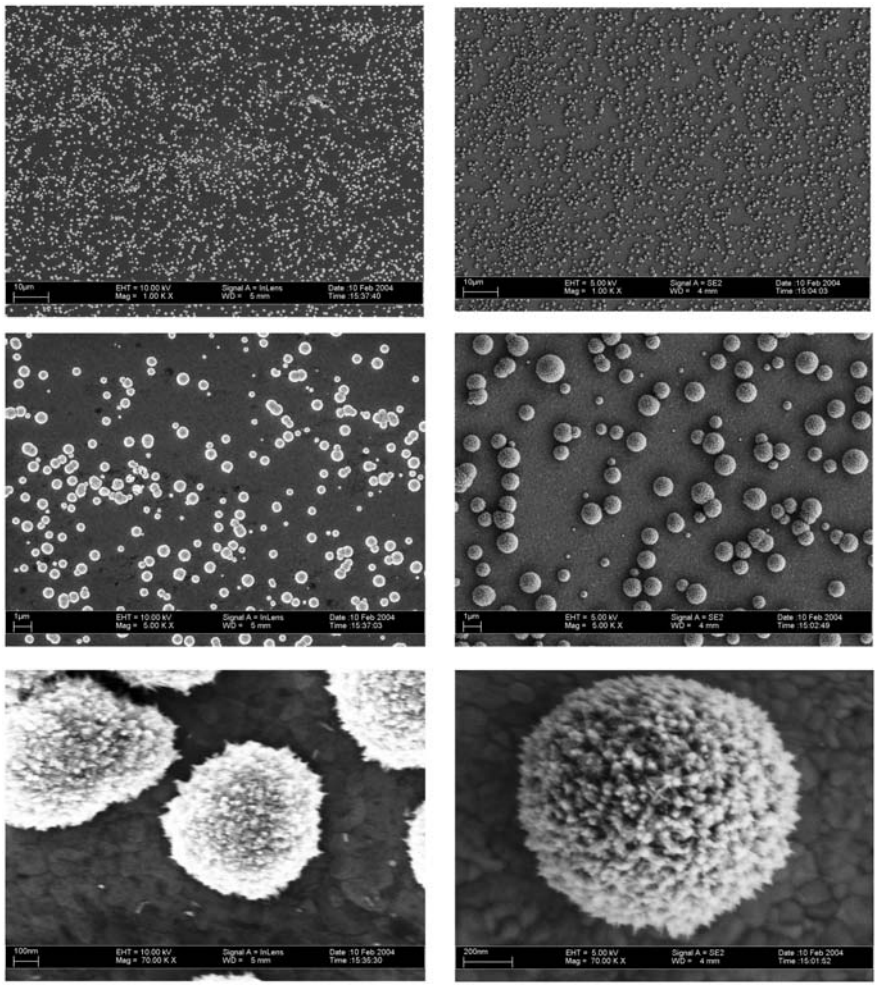

Figure 3. Scanning electron microscopy images of gold electrodes coated by the nanostructured TMPP/C12 monolayer after the electrochemical platinum deposition. The deposition charge was 41 and 160 C m^{-2} for the left and right images, respectively. (Reprinted from Ref. [18], © 2005, with permission from Wiley-VCH.)

conditions described above (from Ref. [18]), the size of nanoparticles was ~500 nm at deposition charge 40 C m^{-2} and increased up to ~1000 nm at deposition charge 160 C m^{-2}. This dependence provides a simple possibility to control the size of nanoparticles. By further decreasing of the deposition charge, 20 nm nanoparticles were obtained. Most probably, the approach can be applied for a template-controlled formation of much smaller metallic nanoclusters on the electrode surface.

A total area of the fabricated platinum nanoelectrodes was estimated by underpotential deposition of copper [18]; a total surface area of ~220% of the geometrical electrode area was obtained. From geometrical considerations, an increase of surface due to formation of a densely packed monolayer with a square lattice is less than π times for spherical structures or less than $\pi/2$ times for semispherical structures. Taking into account that a mean distance between nanoparticles is larger than their size, a 220% increase of the surface area cannot be reached without increase of surface roughness. Such a roughness was really detected by scanning electron microscopy (Figure 3). This roughness can be caused by a fusion of smaller nanoparticles during their growth (Figure 2).

4. A Case History

According to Ref. [12], template for synthesis of nanomaterials is defined as a central structure within which a network forms in such a way that removal of this template creates a filled cavity with morphological or stereochemical features related to those of the template. The template synthesis was applied for preparation of various nanostructures inside different three-dimensional nanoporous structures. Chemically, these materials are presented by polymers, metals, oxides, carbides and other substances. Synthetic methods include electrochemical deposition, electroless deposition, chemical polymerization, sol–gel deposition and chemical vapor deposition. These works were reviewed in Refs. [12,20]. An essential feature of this

approach is that the used templates were formed by relatively thick three-dimensional phase. Correspondingly, the formed nanostructures have typically a shape of filled or hollow nanotubes.

A number of electronic, optical and sensor applications demand arrays of nanoparticles deposited on solid surfaces [23,24]. Such structures can be prepared by reduction through nanopores in monomolecular template, as it is described in the present publication. A crucial step in this technology is preparation of stable nanoporous monolayer: because of lateral diffusion, nanoporous monolayers with defects are not temporarily stable. The solution was found in 1999: it is based on filling of defects by planar chemically adsorbed molecules ("spreader-bars") [19]. A preparation of the spreader-bar stabilized nanostructured monolayers is performed by co-adsorption of two types of organic moieties: chain-like molecules (matrix) and large rigid planar molecules (template or molecular spreader-bar) [18,19,21]. This system has been tested for many applications. It was applied to form stable artificial receptors for different purines and pyrimidines [25] and to fabricate a sensor array (artificial tongue) to analyze these compounds. Later, a preparation of enantioselective receptors was reported [26]. Nanostructured monolayers with spreader-bars were used as a model system for biophysical investigation of ionic pump [27]. Finally, the spreader-bar-nanostructured monolayers were used as arrays of "molecular" electrodes for template-controlled reduction of metals [18].

5. Conclusions

The described technology was tested for preparation of copper and platinum nanoparticles on coated gold electrodes by electrochemical reduction. But most probably it can be extended for many other systems. Instead of gold electrode, other metals which can be coated by thiolated compounds, for example, silver, nickel, copper and palladium [28,29], can be tested. There is no principal limitation for extension of this technology for fabrication of nanoparticles consisting of conductive or non-conductive electrochemically polymerized compounds; in this case the synthesis will be performed by electrochemical oxidation. Electrochemically controlled precipitation of polymers induced by local pH changes [30] presents another class of chemical compounds for this technology.

A large number of possible applications of arrays of nanoparticles on solid surfaces is reviewed in Refs. [23,24]. They include, for example, development of new (electro)catalytical systems for applications as chemical sensors, biosensors or (bio)fuel cells, preparation of optical biosensors exploiting localized plasmonic effect or surface enhanced Raman scattering, development of single electron devices and electroluminescent structures and many other applications.

Acknowledgments

Author is thankful to all co-workers participating in the development and establishment of the spreader-bar technique and its applications. The main part of experimental work was performed by Dr. T. Hirsch. Development of particular applications and characterization of structures was performed in collaboration with Drs. H. Kettenberger, A. Lenz, B. Liedberg, M. Östblom, S. Piletsky, V.I. Portnov, M. Prodramidis, A. Shaporenko, V.S. Sokolov, J. Stahl, D. Weiss, O.S. Wolfbeis and M. Zharnikov.

References

1 G. Schmid, B. Corain, *Eur. J. Inorg. Chem.* 2003 (2003) 3081.
2 U. Erb, K. T. Aust, G. Palumbo, in C. C. Koch (ed.) *Nanostructured Materials. Processing, Properties and Potential Applications*, Noyes Publication, New York, NY, 2002, 179.
3 W. A. Goddard III, D. W. Brenner, S. E. Lyshevski, G. J. Iafrate (eds.) *Handbook of Nanoscience, Engineering, and Technology*, CRC Press, Boca Raton, FL, 2002.
4 P. Mulvaney, in K. J. Klabunde (ed.) *Nanoscale Materials in Chemistry*, Wiley, New York, NY, 2001, 121.
5 D.-Q. Yang, M. Meunier, E. Sacher, *J. Appl. Phys.* 9 (2004) 5023.
6 J. J. Kakkassery, J.-P. Abid, M. Carrara, D. J. Fermín, *Faraday Discuss.* 125 (2004) 157.
7 Y. Jin, Y. Shen, S. Dong, *J. Phys. Chem. B* 108 (2004) 8142.
8 F. Schultz, S. Franzka, G. Schmid, *Adv. Funct. Mater.* 12 (2002) 532.
9 C.-J. Zhong, M. M. Maye, *Adv. Mater.* 13 (2001) 1507.
10 G. Martra, L. Prati, C. Manfredotti, S. Biella, M. Rossi, S. Coluccia, *J. Phys. Chem. B* 107 (2003) 5453.
11 U.-W. Grummt, M. Geissler, T. Drechsler, H. Fuchs, R. Staub, *Angew. Chem. Int. Ed.* 37 (1998) 3286.
12 A. Huczko, *Appl. Phys. A* 10 (2000) 365.
13 F. Endres, M. Bukowski, R. Hempelmann, H. Natter, *Angew. Chem. Int. Ed.* 42 (2003) 3428.
14 J. A. Switzer, in G. Hodes (ed.) *Electrochemistry of Nanomaterials*, Wiley-VCH, Weinheim, 2001, 67.
15 D. M. Kolb, R. Ullmann, T. Will, *Science* 275 (1997) 1097.
16 D. M. Kolb, R. Ullmann, J. Ziegler, *Electrochim. Acta* 43 (1998) 2751.
17 J. Meier, K. A. Friedrich, U. Stimming, *Faraday Discuss.* 121 (2002) 365.
18 T. Hirsch, M. Zharnikov, A. Shaporenko, J. Stahl, D. Weiss, O. S. Wolfbeis, V. M. Mirsky, *Angew. Chem. Int. Ed.* 44 (2005) 6775.
19 V. M. Mirsky, T. Hirsch, S. A. Piletsky, O. S. Wolfbeis, *Angew. Chem. Int. Ed.* 38 (1999) 1108.
20 J. C. Hulteen, C. R. Martin, *J. Mater. Chem.* 7 (1997) 1075.
21 T. Hirsch, A. Shaporenko, V. M. Mirsky, M. Zharnikov *Langmuir* 23 (2007) 4373.
22 J. B. Schlenoff, M. Li, H. Ly, *J. Am. Chem. Soc.* 117 (1995) 12528.
23 A. N. Shipway, E. Katz, I. Willner, *Chem. Phys. Chem* 1 (2000) 18.
24 E. Katz, I. Willner, *Angew. Chem. Int. Ed.* 43 (2004) 6042.
25 T. Hirsch, H. Kettenberger, O. Wolfbeis, V. M. Mirsky, *Chem. Commun.* 3 (2003) 432.
26 M. I. Prodromidis, Th. Hirsch, V. M. Mirsky, O. S. Wolfbeis, *Electroanalysis* 15 (2003) 1795.
27 A. Lenz, V. S. Sokolov, V. M. Mirsky, in preparation.
28 M. Riepl, V. M. Mirsky, M. Östblom, B. Liedberg, *Electrochemistry in Molecular and Microscopic Dimensions, 53rd Annual Meeting*, ISE, Dusseldorf, 2002.
29 J. C. Love, D. B. Wolfe, R. Haasch, M. L. Chabinus, K. E. Paul, G. M. Whitesides, R. G. Nuzzo, *J. Am. Chem. Soc.* 125 (2003) 2597.
30 S. Janiak, A. Vilkanauskyte, T. Erichsen, W. Schuhmann, *Macromol. Rapid Commun.* 25 (2004) 348.

This page intentionally left blank

CHAPTER 19

Solvent and Simple Ion-Stabilized Metal Nanoclusters: Chemical Synthesis and Application

Yuan Wang and Xiaodong Wang

Beijing National Laboratory for Molecular Sciences, State Key Laboratory for Structural Chemistry of Unstable and Stable Species, College of Chemistry and Molecular Engineering, Peking University, Beijing, China

1. Introduction

To prepare stable metal nanoclusters with small particle size and narrow size distribution in colloidal solutions, protective agents of polymers, such as poly(*N*-vinyl-2-pyrrolidone) (PVP) and polyvinylalcohol (PVA), coordination ligands such as PPh_3 and mercaptans, or surfactants are usually required. The protective agents can adjust the aggregation process of metal atoms to form metal nanoclusters with narrow size distribution, and provide potential barriers to prevent the metal nanoparticles from aggregating. However, the interaction between the metal colloidal particles and the protective agents may affect or alter the physical and chemical properties of the nanoscopic metal particles, thereby restricting the applications of protected metal nanoclusters in some aspects. For the purpose of studying the intrinsic properties of metal nanoparticles and employing the metal nanoclusters as nanosized building blocks for assembling some important functional systems conveniently, ''unprotected'' metal nanoclusters with sufficient stability are desirable.

The so-called ''unprotected'' metal nanoclusters are prepared in the absence of usual protective agents; however, they are not truly bare but stabilized by solvents and simple ions adsorbed on them, or by both. Successful examples for preparing such metal colloidal solutions are still limited. Klabunde and co-workers developed a solvated metal atom dispersion technique (SMAD), which involves vaporization of a metal under vacuum and co-deposition of the metal atoms with the vapors of a solvent on the walls of a reactor cooled to 77 K, followed by warming the frozen matrix to produce metal nanoclusters stabilized by solvent and negative charge [1,2]. Stable Pd colloids with average diameters of 6–8 nm in acetone or propanol could be prepared using the SMAD technique [3]. The syntheses of Au nanoparticles and their immobilization [4] or surface modification with mercaptan [5] were studied. Esumi et al. reported the preparation of stable Pd colloids with average particle sizes of 8–10 nm from the thermal decomposition of Pd complexes in methyl isobutyl ketone [6,7]. Organosols of Ti, Zr, V, Nb and Mn with small particle size, stabilized by intact THF molecules, were prepared in Bonnemann's group by reducing the corresponding metal halides in THF using $K[BEt_3H]$ as a reductant [8]. Curtis et al. prepared a Cu colloid with a mean metal particle size of 13.3 nm in methanol by reducing Cu^{2+} salts with hydrazine hydrate [9]. Stable colloidal solutions of cubic Pt nanoparticles stabilized by oxalate with an average particle size of 6.5 nm and a shape selectivity larger than 90% were successfully prepared via the reduction of $K_2Pt(C_2O_4)_2$ in water with hydrogen at room temperature. After exposure to air and treatment with hydrogen, the oxalate-stabilized Pt nanoparticles could self-assemble into Pt nanowires with almost the same diameters as the original Pt particles and lengths of several hundreds of nanometers [10].

The achievements described above made remarkable contributions to the preparation of unprotected metal nanoclusters. However, limiting the discussion to developing metal nanocluster-based catalytic systems, there are still great challenges in relation to the unprotected metal nanoclusters as pointed out behind: (1) effectively preparing unprotected metal and alloy nanoclusters with controllable particle size, shape and composition, which can be used as tractable building blocks for assembling various catalysts, in which the circumjacent environment of the metal nanoclusters can be modulated easily; (2) in virtue of the unique properties of unprotected metal nanoclusters, investigating the structure–property relationships of metal nanocluster-based catalysts, including the metal particle size effect, alloying effect, ligand effect and the support effect, as well as distinguishing these effects; (3) developing practical nanocomposite catalysts with excellent properties by immobilizing the unprotected metal nanoclusters on nanostructured supports, controlling the size and distribution of metal nanoparticles at demanding metal loading.

Metal Nanoclusters in Catalysis and Materials Science: The Issue of Size Control
Edited by B. Corain, G. Schmid and N. Toshima

A novel synthesis method (alkaline ethylene glycol (EG) method) has been proposed for the effective preparation of small noble metal and bimetallic nanoclusters (1–3 nm), such as Pt, Rh, Ru [11], Os, Pt/Rh [12] and Pt/Ru [13,14] nanoclusters, which are stabilized with EG and simple ions. These unprotected metal nanoclusters are very tractable as building blocks for fabricating novel catalytic materials due to the high efficiency of synthesis, the convenience of separation, the flexibility of modification and the controllability of particle size. Recently, Liu and co-workers [15] and Gedanken and co-workers [16], respectively, further improved greatly the synthesis rate of the alkaline EG method by microwave irradiation on the reaction system. The unprotected Pt, Rh and Ru nanoclusters could be produced within 20–30 s using this microwave-assisted alkaline EG synthesis technique. The unprotected metal nanoclusters have been successfully applied to the fabrication of highly selective hydrogen sensor [17] and highly selective catalysts for the hydrogenation of chloronitrobenzene (CNB) [18,19]. Xin and co-workers [20–24] and Mao and Mao [25] have succeeded in preparing promising electrocatalysts for fuel cells with metal loadings of 10–50 wt.% by some modifications in the alkaline EG synthesis method.

This chapter will mainly deal with the advantages of the alkaline EG synthesis method for the chemical preparation of noble metal nanoclusters stabilized by EG and simple ions, as well as the excellent performances of the functional materials assembled using these unprotected metal nanoclusters as building blocks.

2. Synthesis Strategy

2.1. Alkaline Ethylene Glycol Synthesis Method

The strategy usually adopted for the chemical preparation of metal nanoclusters is to lead metal atoms produced in situ to aggregate and generate metal cores, followed by depositing metal atoms on these cores. Due to the huge specific surface energy, small metal particles in colloidal solutions have a great tendency to aggregate and form precipitates in the absence of suitable stabilizers. The charge effect derived from the electrostatic repulsion of adsorbed ions on the small metal particles and the solvent effect, namely decreasing the particles' surface energy by adsorbing solvent molecules, have been known to be effective for stabilizing tiny metal nanoclusters in colloidal solutions [3]. A great handicap in the chemical preparation of unprotected metal nanoclusters with small particle size in colloidal solutions of high metal concentration is derived from the difficulty in controlling the processes of core formation and its further growth in the previous methods.

A strategy to solve this problem is to separate the core formation process from the reduction of metal ions in the cores as shown in Scheme 1, and use solvent (EG) and simple ions (OH^-, etc.) as the stabilizers [11]. In the first step of this process, metal salts hydrolyzed in the alkaline solution of EG to give rise to metal hydroxide or oxide colloids, which were then reduced by EG at elevated temperature to produce colloidal metal nanoclusters in the second step. TEM measurements showed the formation of the metal hydroxide or oxide colloidal particles before the reduction process in the preparation [11]. Liu and co-workers monitored the reaction course using UV–vis spectroscopy and investigated the evolution of metal species in the synthesis process by XPS [15]. Their results also support the two-step formation mechanism of the unprotected metal nanoclusters.

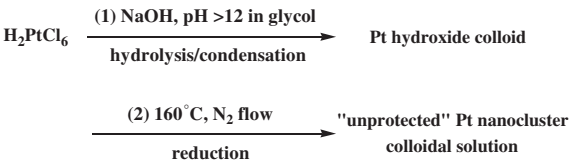

Scheme 1. Procedure of alkaline EG method for the chemical preparation of metal nanoclusters stabilized by EG and sample ions.

2.2. Preparation of Nanocomposite Catalysts

Metal nanoclusters are promising building blocks in the preparation of heterogeneous catalysts, providing new possibilities of universal significance for designing and constructing structure-controllable catalysts. The support-entrapment method provides a realistic strategy, which builds a framework of inorganic supports via stacking metal oxide nanoparticles around preformed metal nanoclusters protected with organic ligand or polymer. In this method, to obtain a close contact of the metal nanoparticles with inorganic supports, organic stabilizers originally adsorbed on the metal nanoclusters usually have to be removed by extraction [26,27] or pyrolysis [28–31] at the end of the catalyst preparation, which may cause the aggregation of metal nanoclusters in some cases, especially at high metal loading. However, these processes are not necessary in the preparation of heterogeneous catalysts using unprotected metal nanoclusters as building blocks. The solvent molecules and simple ions absorbed on the surface of metal nanoclusters can be easily removed during the immobilizing process.

Recently, a new strategy for synthesizing the nanocomposites of metal nanoclusters and inorganic semiconductor nanoparticles was proposed [18,19]. As illustrated in Scheme 2, this strategy includes capturing the unprotected metal nanoclusters on the colloidal particles of metal oxides via electrostatic interaction and gelating the complex sol by adjusting its pH value or heating. This assembling process, using two kinds of nanoparticles stabilized with solvent and simple ions as building blocks, is different from those based on an in situ hydration process of $M(OR)_n$ compounds in the presence of ligand-protected metal nanoclusters as reported previously [26,29]. The catalysts prepared by this strategy are more regulable in structure, i.e. it is convenient to control both the size and composition of the metal and support nanoparticles in the formed catalysts, and to modulate the catalytic properties by the interaction between the different nanoparticles as well as the external environment surrounding the catalytic sites.

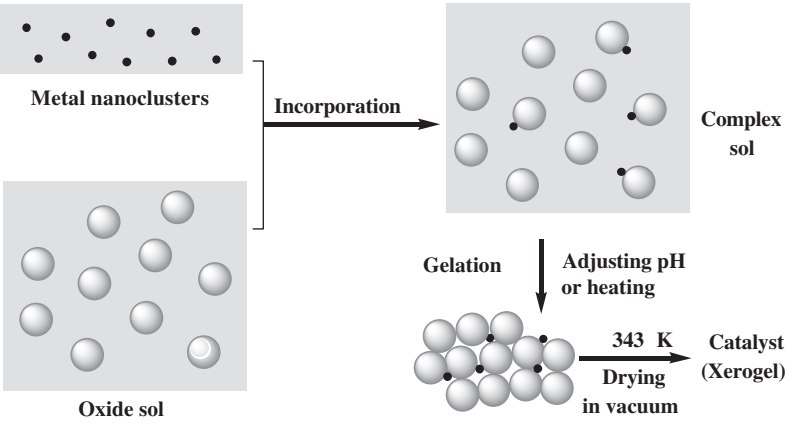

Scheme 2. General scheme showing the entrapment process of unprotected noble metal nanoclusters within the matrix of metal oxide nanoparticles. (Reprinted from Ref. [18], © 2004, with permission from Elsevier.)

3. Results

3.1. Synthesis of Metal Nanoclusters Stabilized by Ethylene Glycol and Simple Ions

The unprotected Pt, Rh and Ru nanoclusters prepared according to the alkaline EG synthesis method in EG with metal concentrations of 0.3–3.7 g/l have small average particle sizes of 1.1–1.3 nm and narrow size distributions from 0.7 to 2.2 nm, as measured by TEM (Figure 1 and Table 1) [11]. The Os nanoclusters (3.7 g/l) prepared by this method have an average diameter of 0.9 nm and a size distribution of 0.6–1.8 nm (Figure 2) [12].

The reduction of metal hydroxides or oxides powder by polyol was first reported by Figlarz and co-workers, which gave rise to fine powders of Cu, Ni, Co and some noble metals with micrometer sizes (polyol process) [32,33]. The polyol process was first modified for the preparation of PVP-protected bimetallic and monometallic nanoclusters such as Pt/Cu, Pd/Pd, Pt/Co, Pt, Pd, etc. [34–38]. The previous results definitely revealed that Pt, Pd, Cu and Co in these PVP-protected metal or alloy nanoclusters were in a zero-valent metallic state.

In the XRD patterns of the unprotected metal nanoclusters prepared by the alkaline EG synthesis method, no signals derived from their corresponding oxides could be detected. XPS measurements also revealed that the prepared metals nanoparticles had the binding energies close to those of their corresponding zero valence species, 70.9 eV for Pt $4f_{7/2}$, 280.0 eV for Ru $3d_{5/2}$, 307.1 eV for Rh $3d_{5/2}$ and 50.0 eV for Os $4f_{7/2}$, respectively, indicating that the metal species were in a metallic state.

The alkaline EG synthesis method has been successfully applied to the preparation of unprotected bimetallic nanocluster colloids with controllable composition. Figure 3 shows the TEM image of bimetallic Pt/Ru nanoclusters (Pt/Ru molar ratio = 1:1.9, total metal concentration: 1.85 g/l) with an average particle size of 1.9 nm and a size distribution from 1.4 to 2.4 nm. XRD pattern of the bimetallic nanoclusters is shown in Figure 4. In addition to the wide peak centered at ~40° containing the signals of (1 1 1) and (2 0 0) reflections, there is another weak peak at $2\theta = 67^\circ$ assignable to the (2 2 0) diffraction line of fcc Pt/Ru alloy [13].

Pt/Rh bimetallic nanoclusters were similarly prepared by this alkaline EG method [12]. The particle sizes of bimetallic Pt/Rh nanoclusters (0.37 g/l in total metal concentration) ranged from 0.9 to 2.1 nm with an average diameter of 1.3 nm. A combined EDX analysis, using an electron beam of 1.0 nm in diameter, revealed that both signals of Pt and Rh existed in each individual particle and the average ratio of Pt to Rh (1.4:1) was close to the charged ratio (1.33:1) in the preparation, proving the formation of bimetallic nanoclusters.

In the chemical preparation of unprotected metal colloids, the metal concentration usually has a significant influence on the particle size of obtained metal nanoclusters. For example, when increasing Pd concentration from 0.1 to 1.0 mM in the preparation of Pd metal colloids by the thermal decomposition of Pd acetate in methyl isobutyl ketone, the average Pd particle size increased from 8 to ~140 nm [6,7]. However, in the alkaline EG synthesis method, the size of metal nanoclusters was only slightly dependent on the metal concentration of the colloidal solution. The colloidal Pt particles prepared with a metal concentration of 3.7 g/l had an average diameter of 1.3 nm, which was only 0.2 nm larger than that of the Pt particles prepared with a metal concentration of 0.37 g/l. In the case of Os nanoclusters, when the metal concentration in a colloidal solution was elevated from 3.7 to 7.4 g/l, the average metal particle size had only a slight increase from 0.9 to 1.0 nm. These results suggest that the alkaline EG synthesis method is very effective for preparing unprotected metal nanoclusters having small particle size and narrow size distribution.

Different from the metal concentration, the content of water in the reaction system exhibits an obvious effect on the particle size of the resulted metal nanoclusters. In a mixture of EG and water (10:1 in volume ratio), Pt hydroxide colloidal particles formed in the first synthesis step were 4.0 nm in average diameter, and the finally obtained Pt nanoclusters had an average particle size of 2.4 nm, which was much larger than that of the Pt nanoclusters prepared in pure EG with the same metal concentration (0.37 g/l).

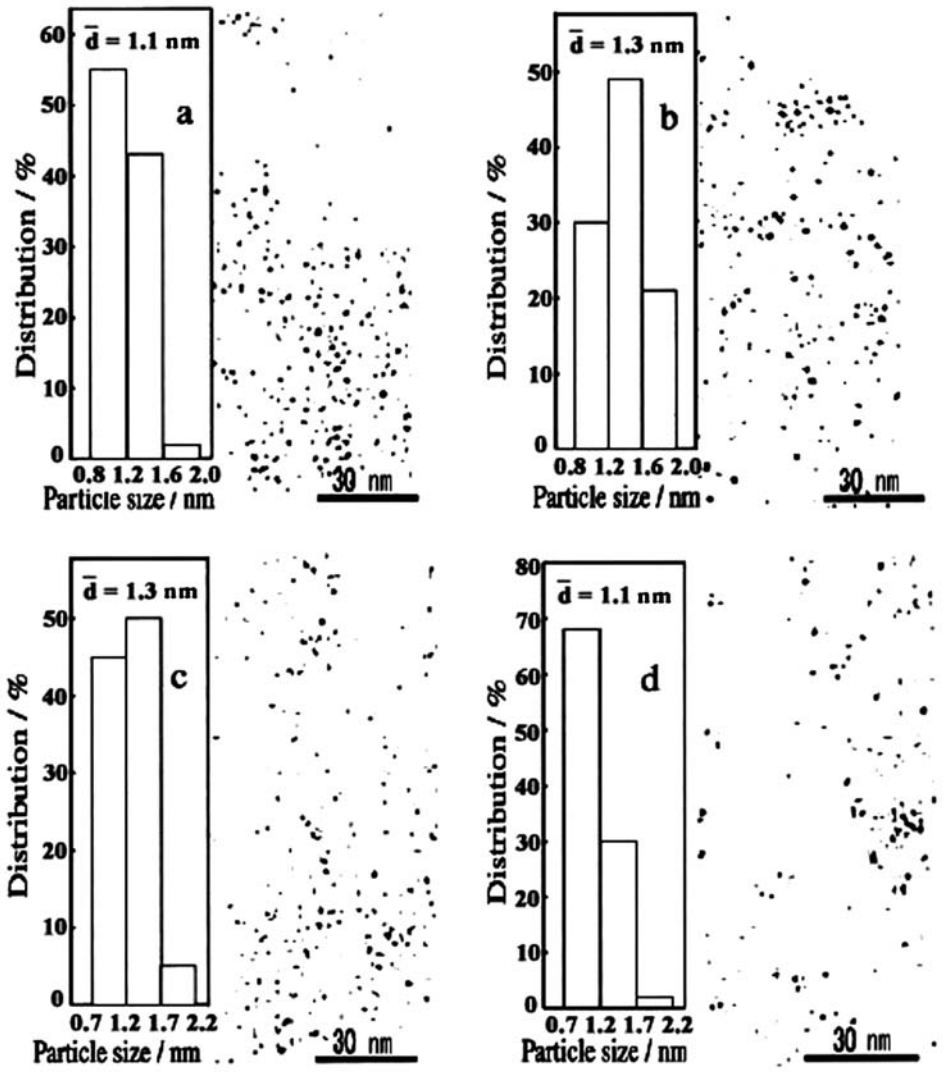

Figure 1. TEM images and size distributions of Pt, Rh and Ru nanoclusters stabilized by EG and simple ions [11]: (a) Pt nanoclusters (0.37 g/l); (b) Pt nanoclusters (3.7 g/l); (c) Rh nanoclusters (0.31 g/l); (d) Ru nanoclusters (0.32 g/l). (Reprinted from Ref. [11], © 2000, with permission from American Chemical Society.)

Table 1. Average diameters and size distributions of unprotected metal nanoclusters.

Metal nanoclusters	Metal concentration (g metal/l)	Average particle diameter (nm)	Particle size distribution (nm)
Pt	0.37	1.1	0.8–2.0
	3.7	1.3	0.8–2.0
Rh	0.31	1.3	0.7–2.2
Ru	0.32	1.1	0.7–2.2
Os	3.7	0.9	0.6–1.8
	7.4	1.0	0.6–1.8
Pt/Ru (1/1.90)	1.85	1.9	1.4–2.4
Pt/Rh (1.33/1)	0.37	1.3	0.9–2.1

Source: Refs. [11–13].

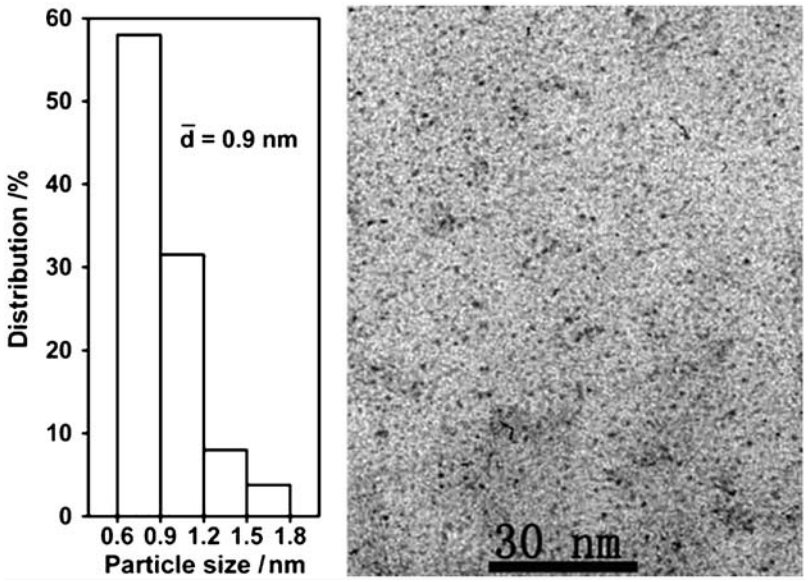

Figure 2. TEM image and size distribution of Os nanoclusters (3.7 g/l) stabilized by EG and simple ions. (Reprinted from Ref. [12], © 2005, with permission from Springer.)

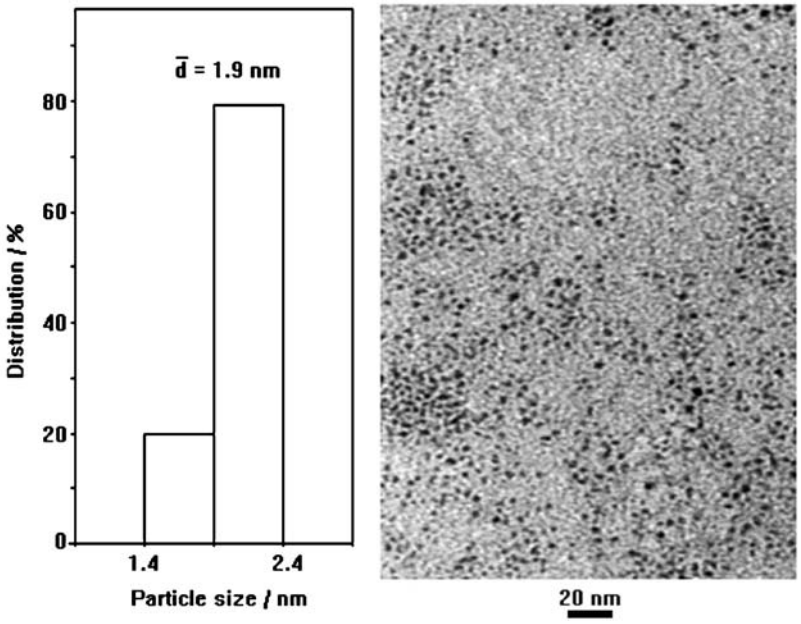

Figure 3. TEM image and size distribution of Pt/Ru bimetallic nanoclusters (1.85 g/l) stabilized by EG and simple ions [13].

Xin and co-workers modified the alkaline EG synthesis method by heating the metal hydroxides or oxides colloidal particles in EG or EG/water mixture in the presence of carbon supports, for preparing various metal and alloy nanoclusters supported on carbon [20–24]. It was found that the ratio of water to EG in the reaction media was a key factor influencing the average size and size distribution of metal nanoparticles supported on the carbon supports. As shown in Table 2, in the preparation of multiwalled carbon nanotube-supported Pt catalysts (Pt/MWNT) [20,21], fine and homogeneous Pt nanoparticles deposited on MWNTs were obtained when pure EG was used as the solvent or less water (<5 vol.%) was introduced. With the increase in water content, aggregation of the metal nanoparticles occurred, the average particle size increased and the particle size distribution became wider.

Generally, the absence of water favors the formation of stable metal nanocluster colloids, while its presence favors the formation of metal hydroxide or oxide colloids in the

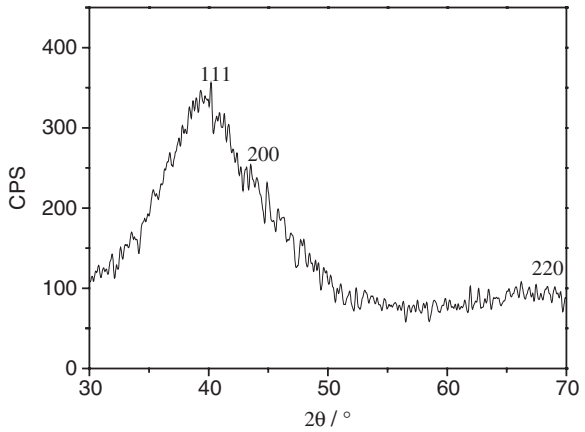

Figure 4. XRD diffraction pattern of bimetallic Pt/Ru nanoclusters [13].

Table 2. Effect of water content in EG on the particle size of Pt nanoparticles deposited on MWNTs.

Water content (%, volume ratio)	Average size of Pt particles (nm)	Size distribution of Pt particles (nm)
0	2.0	1–4
5	2.5	2–5
40	4.0	2–8
70	4.5	2–12

Source: Refs. [20,21].

first step of the synthesis process. Therefore, the particle size and the size distribution of the unprotected metal nanoclusters can be controlled to some extent by simply adjusting the content of water in the starting reaction mixture.

A great advantage of the solvent and simple ion-stabilized metal nanoclusters prepared according to the alkaline EG synthesis method is that they can be conveniently separated as precipitates from the original colloidal solution by adding a dilute aqueous solution of HCl, adjusting the colloidal solution to be acidic. Based on different requirements in application, the precipitated metal nanoclusters can be redispersed into many kinds of organic solvents, such as alcohol, ketone, THF, acetonitrile, DMF and DMSO, giving rise to different colloidal solutions of the unprotected metal nanoclusters. It was found that the Pt nanoclusters "dissolved" in some ketone solvents as well as DMF and DMSO were very stable. For example, the colloidal solution of Pt nanoclusters in cyclohexanone or cyclopentanone was transparent and homogeneous, no precipitate was observed after standing for at least several months. Besides, the metal concentration of Pt nanoclusters in colloidal solutions could be elevated to a level higher than 200 g/l by this separation–redispersion procedure. TEM characterizations showed that the Pt nanoclusters in these colloidal solutions had an average diameter of 1–2 nm, indicating that no obvious aggregation of the small Pt particles occurred during the transferring process.

Based on a series of experimental phenomena, it was suggested that EG adopted in the alkaline EG synthesis method acts not only as a solvent and a reductant, but also as a stabilizer [11]. When other glycols such as 1,2-propylene-glycol and 1,4-butylene-glycol were used in the similar reaction conditions, it was hard to prepare stable metal colloidal solutions of unprotected metal nanoclusters as reported by Liu and co-workers [15].

In the alkaline EG synthesis method, the pH value of the reaction mixture is very important for producing stable metal nanoparticles in EG. If the pH value is not high enough, instead of a metal colloidal solution, a metal precipitate will be obtained in the subsequent reduction process under heating [11]. During the reaction process, NaOH would react with metal chlorides and some organic acid resulted from the oxidation of EG; therefore, pH of the reaction mixture would decrease. To keep a basic reaction medium, an excess amount of base had to be added into the reaction system. Liu and co-workers systemically investigated the influence of the amount of NaOH on the stability of the unprotected metal nanoclusters [15]. In their experiments, the metal colloids were prepared at different OH^-/M^{n+} molar ratio, with constant metal concentration. The experimental results revealed that stable metal colloids can be obtained only in a definite concentration range of NaOH, the molar ratios of NaOH to metal ranging from 12 to 25 for Pt and 6 to 12 for Rh, which is the characteristic of electrostatic stabilization for metal colloids by the surface adsorbed anions [39,40].

A series of measurements, including GC–MS, HPLC, MS, UV–vis, FT-IR and element analysis, have been carried out to analyze the species formed in the alkaline EG synthesis process that may have a contribution to the stability of the nanoscopic Pt particles. These experimental results suggested that in the colloidal solutions of the unprotected metal nanoclusters, EG and the simple anions adsorbed on the surface of metal particles played important roles in stabilizing the nanosized metal clusters. It should be noticed that in the prepared metal colloidal solutions, there should be an adsorptive equilibrium on the metal nanoclusters between the existing simple anions such as OH^-, Cl^-, acetate, glycolate or oxalate ions, which depended not only on pH and solvents but also on the metal specificity. According to the DLVO theory for the colloid stability, all of the adsorbed anions would have their contribution to the stabilizing effect on the metal nanoclusters. Precipitating the Pt nanoclusters with a dilute aqueous solution of HCl, followed by "dissolving" the precipitated Pt nanoclusters in EG containing NaOH and repeating the precipitation–redispersion process for several times, could give rise to a very stable Pt colloidal solution [11]. A further intensive study is necessary for revealing the details in the stabilization mechanism.

3.2. Ligand Modification of the Unprotected Metal Nanoclusters

The species absorbed on the unprotected metal nanoclusters, i.e. EG and the simple anions, can be easily replaced by many kinds of coordination ligands or protective agents. This character makes it possible to prepare various metal nanoclusters with the same metal core and different modifying or protective shells. The metal

nanoclusters modified by different ligands with the same particle size of the metal core afford us an opportunity to distinguish the ligand effect from the size-dependent effect on some physical and chemical properties of nanoscopic metal particles. This section deals with the method for the preparation of surface-modified metal nanoclusters using the unprotected metal nanoclusters as precursors, and the effect of ligands on the core-level binding energies of metal nanoparticles based on the XPS measurements. Recently, the fabrication of high surface area heterogeneous catalysts [41,42] and excellent electrocatalysts [43] using the PVP-protected Pt and PPh_3-modified Pt metal nanoclusters prepared by the alkaline EG method and surface modification technique has also been reported.

PVP-protected noble metal nanoclusters have been intensively studied in many research groups and exhibited excellent stability and catalytic properties for many organic reactions. They are usually prepared by refluxing an alcohol solution of the corresponding metal compounds in the presence of PVP, a method set up by Hirai et al. [44]. In this preparation method, to obtain small metal nanoclusters with narrow size distribution, usually a molar ratio of PVP (as monomeric unit) to the metal higher than 40 has to be used. However, applying the unprotected metal nanoclusters as building blocks, it is convenient to prepare PVP-protected noble metal nanoclusters with a low PVP/metal ratio (0.35) [45]. In a typical procedure for the preparation of PVP-protected Pt nanoclusters, an EG solution of the unprotected Pt nanoclusters with an average particle size of 1.3 nm was mixed with an EG solution of PVP. After stirring for 2 h at room temperature, excessive acetone was added to the reaction system and the mixture was kept at $-20\,^{\circ}C$ for 2 h. A black precipitate of the PVP-protected Pt nanoclusters was obtained by centrifugation. The precipitate was very soluble in alcohol or water to form a stable, dark-brown, transparent colloidal solution. These results revealed that a small amount of PVP is enough to prevent the nanosized Pt clusters from aggregating in colloidal solutions. The large amount of PVP in the alcohol-refluxing preparation method may be the demand of adjusting the kinetic processes of the metal ions reduction and metal atom aggregation. By the similar method except the replacement of the EG solution of PVP by a water solution of PVA, the PVA-protected Pt nanoclusters were also prepared successfully with a PVA/metal ratio of 10.

Liu and Toshima have reported that adding a large amount of PPh_3 to a PVP-protected Pt nanocluster solution ($PPh_3/Pt = 15$) cannot directly transfer the Pt colloidal particles into toluene, but forms a flocculate of Pt colloids [46]. The flocculate can be "dissolved" in butanol or butanol–toluene (1/9, v/v) mixed solution but not in pure toluene, implying that PVP may still remain in the flocculate. On the contrary, the unprotected Pt nanoclusters prepared by the alkaline EG synthesis method can be easily transformed to PPh_3-modified Pt nanoclusters by adding a small amount of PPh_3 to the Pt nanocluster solution ($PPh_3/Pt = 0.5$) [11]. The obtained PPh_3-modified Pt nanoclusters can be extracted into toluene, giving rise to a toluene solution of PPh_3-modified Pt nanoclusters. The PPh_3-modified Pt nanoclusters in toluene have a tendency to deposit on many kinds of substrates, and a homogeneous film of the PPh_3–Pt nanoclusters could be obtained by marinating the substrates in the modified metal colloidal solution for a few days [17,47].

Dodecylamine ($C_{12}H_{25}NH_2$)- and dodecanethiol ($C_{12}H_{25}SH$)-modified Pt nanoclusters could also be prepared by a simple phase-transfer method [45]. Mixing a toluene solution (10 ml) of $C_{12}H_{25}NH_2$ (28.5 mM) or $C_{12}H_{25}SH$ (18.6 mM) with an EG solution (10 ml) of the unprotected Pt nanoclusters (19.3 mM), after stirring the mixture of two phases for 2 h, the toluene phase was isolated, washed and concentrated to 0.5 ml under flowing Ar. To this concentrated solution, 10 ml ethanol was added. When keeping the obtained mixture at $-20\,^{\circ}C$ for 12 h, the object product was precipitated effectively. The prepared Pt nanoclusters modified with $C_{12}H_{25}NH_2$ or $C_{12}H_{25}SH$ are very soluble in nonpolar solvents such as toluene, chloroform or cyclohexane, and the obtained colloidal solutions of $C_{12}H_{25}NH_2$–Pt or $C_{12}H_{25}SH$–Pt are very stable.

TEM measurements show that the $C_{12}H_{25}NH_2$–Pt, $C_{12}H_{25}SH$–Pt and PPh_3–Pt nanoclusters have an average particle size of $\sim$1.3 nm and a size distribution of 0.8–2.8 nm, which are in agreement with the values of the original unprotected Pt nanoclusters in EG solution. These results demonstrate that no aggregation of the nanoscopic metal clusters occurs during the coordination capturing–transforming process. The Pt nanoparticles in $C_{12}H_{25}NH_2$–Pt or $C_{12}H_{25}SH$–Pt separate from each other with an interparticle distance larger than 1 nm, indicating that amine or thiol molecules form a compact shell surrounding each metal core.

The effect of ligands on the properties of metal nanoclusters is a fundamental question. The interactions between different ligands and the same metal core are quite different. The obtained ligand-modified Pt-based nanoclusters with the same metal core and different ligand shells were used to systematically investigate the ligand modification effect on the core-level binding energies of nanosized metal clusters, which are also dependent on the metal particle size. For this purpose, XPS measurements were carried out on the Pt nanoclusters modified by PVP, PVA, PPh_3, $C_{12}H_{25}NH_2$ and $C_{12}H_{25}SH$, with the same average metal particle size of 1.3 nm [45]. The results are listed in Table 3. The binding energies of Pt ($4f_{7/2}$) in metal nanoclusters modified with different ligands are 0.5–0.8 eV higher than that of a bulk Pt sample (71.0 eV). In addition, it should be noted that the Pt 4f binding energy of a Pt powder prepared by precipitating and drying the unprotected Pt nanoclusters is the same as that of bulk Pt, suggesting that the original Pt nanoparticles are in the metallic state and the nanoparticles in the powder sample connect to each other owing to lack of protective agents.

The observed increase in Pt 4f binding energy may be derived from two factors. One is the size-dependent effect of the metal core. In general, higher binding energies of core levels in metal nanoparticles relative to the values of bulk metals can be observed when the metal particles are small enough [48], and the values increase with decreasing the metal particle size [49]. This phenomenon has been interpreted in terms of final state relaxation proposed by Wertheim et al. [50]. The other is the ligand effect, which is relatively seldom studied. In our experiments, since the ligand modification process does not alter the size of

Table 3. XPS data for the ligand-modified Pt nanoclusters and ligands.

Sample	Binding energy (eV)					
	Pt $4f_{7/2}$	N 1s	S 2p	O 1s	P 2p	C 1s
Pt–$C_{12}H_{25}NH_2$	71.5	399.5				285.0
$C_{12}H_{25}NH_2$		400.0				285.0
Pt–PVP	71.5			532.2		285.0
PVP				531.6		285.0
Pt–PVA	71.5					285.0
Pt–PPh_3	71.6				131.8	284.7
PPh_3					130.9	284.7
Pt–$C_{12}H_{25}SH$	71.8		163.3			285.0
$C_{12}H_{25}SH$			163.9			285.0

Reprinted from Ref. [45], © 2001, with permission from Elsevier.

the Pt core, it is reasonable to believe that the increment in the Pt 4f binding energy of the metal nanoclusters caused by the size-dependent effect is same for all of the modified Pt nanoclusters. Therefore, after deducting the small size effect, the ligand modification effect on the electronic properties of metal nanoparticles can be investigated.

PPh_3 is a strong coordination ligand for Pt(0); however, the coordination interaction between Pt(0) and $C_{12}H_{25}NH_2$ is not so strong. PVP coordinates weakly to the surface Pt atoms of the metal nanoclusters with carbonal groups, whereas the interaction between Pt(0) surface and hydroxyl groups in PVA is very weak. It is reasonable to believe that the weak interaction between PVA and Pt nanoclusters cannot affect the core-level binding energy of the Pt metal core to an observable extent. Therefore, the increase in the Pt 4f binding energy of the PVA–Pt nanoclusters is mainly derived from the small size effect. That is, the increment in Pt 4f binding energy of the Pt nanoclusters caused by the size-dependent effect is ~0.5 eV when the particle size decreases to ~1.3 nm. The Pt 4f binding energy in the $C_{12}H_{25}SH$–Pt nanoclusters increases by 0.8 eV relative to the value of bulk Pt. It can be deduced that an increment of 0.3 eV in the Pt 4f binding energy is derived from the thiol-bonded effect. The ligand effect may also have an impact on the conductive properties of the ligand-modified metal nanoclusters.

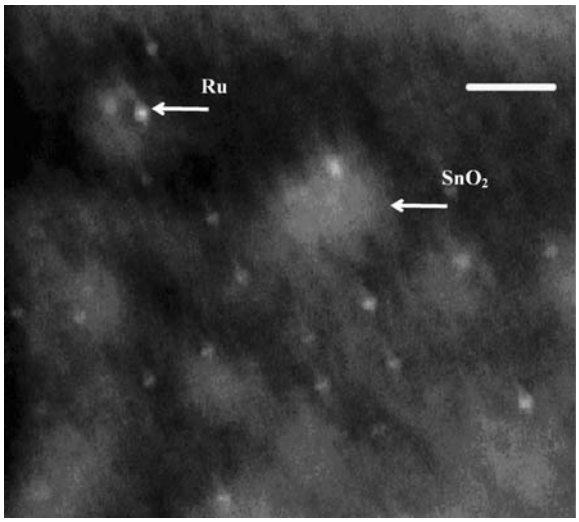

Figure 5. STEM image of Ru nanoparticles captured on the surface of SnO_2 particles; the bar expresses 20 nm. (Reprinted from Ref. [18], © 2004, with permission from Elsevier.)

3.3. Application in Assembling Nanocomposite Catalysts

In the traditional syntheses of heterogeneous catalysts, it is hard to prepare heterogeneous catalysts bearing the same metal particles on different supports; therefore, to clearly investigate the influence of supports on the catalytic properties of nanosized metal clusters is not convenient. The assembly process described in Section 2.2, characterized by the immobilization of unprotected metal nanoclusters on inorganic semiconductor nanoparticles, would provide promising opportunities for exploring the support effect and developing new catalytic systems.

Figure 5 shows the Z-contrast scanning transmission electron microscope (STEM) image of a Ru/SnO_2 nanocomposite catalyst prepared by the assembly process [18]. A combined EDX analysis, using an electron beam of 0.8 nm in diameter, revealed that the signal of Ru could be detected only at the small bright spots, while that of tin was widely present in the bright area. This result indicates that the brightest cores in the bright area are the images of Ru nanoclusters. The particle sizes of the Ru nanoclusters in the Ru/SnO_2 nanocomposite ranged from 1.0 to 2.5 nm with an average value of 1.3 nm, which agrees well with that of the original Ru nanoclusters in colloidal solution, suggesting that no obvious aggregation of the Ru nanoparticles occurred during the catalyst preparation. Pt/γ-Fe_2O_3 nanocomposite catalysts have been also prepared according to this strategy [19]. As shown in the STEM image of a Pt/γ-Fe_2O_3 nanocomposite catalyst (0.9 wt.%) (Figure 6), Pt metal nanoclusters, with an average size of 2.6 nm, were well dispersed in the matrix network of the γ-Fe_2O_3 support. This has also been confirmed by the combined EDX scanning analysis.

Aromatic chloroamines are important intermediates in the synthesis chemistry of herbicides, pesticides, dyes and medicines. Currently, these widely applied organic amines

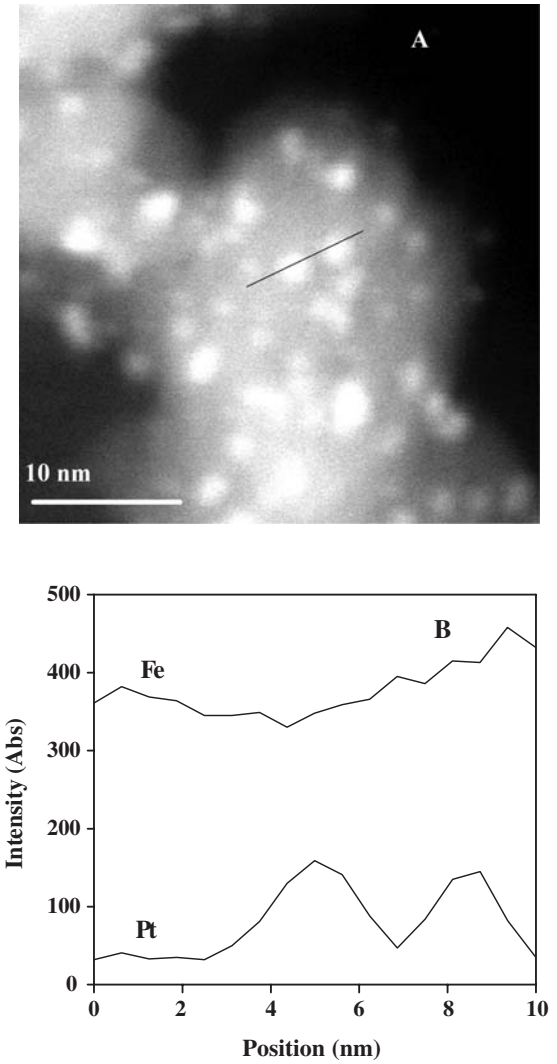

Figure 6. (A) STEM image of Pt nanoparticles captured on the surface of γ-Fe_2O_3 particles; (B) EDX patterns of the complex nanoparticles measured using an electron beam of 0.8 nm in diameter. (Reprinted from Ref. [19], © 2005, with permission from Elsevier.)

are produced by selective hydrogenation of their corresponding aromatic chloronitro compounds over transition-metal catalysts. However, hydrogenolysis of the Cl–C bond in aromatic chloroamines as a defect of the hydrogenation process is difficult to completely avoid over usual metal catalysts [51]. Many effective strategies have been developed in order to inhibit the hydrodechlorination in the selective hydrogenation of CNB to chloroaniline (CAN), such as modulating the interaction between metal particles and inorganic supports [52], alloying Pt with other metals [52,53] and adding metal cations or complexes as modifiers to polymer-protected metal colloid catalysts [54,55]. By these catalyst modifications, the selectivity to CAN can be greatly improved, whereas the intrinsic hydrogenolysis activity of the Cl–C bond cannot be effectively suppressed. It is still a challenge to produce CAN with high purity by highly efficient hydrogenation of CNB. Advanced modifications on metal catalysts for deeply or fully inhibiting the hydrogenolysis activity of the Cl–C bond in CAN combined with promoting the hydrogenation rate of the nitro group in CNB are desired. The Ru/SnO_2 [18] and Pt/γ-Fe_2O_3 [19] nanocomposite catalysts contributed examples for achieving this aim. They exhibited novel catalytic properties for the selective hydrogenation of *o*-CNB to *o*-CAN.

The catalytic activity of the Ru/SnO_2 nanocomposite was eight times higher than that of the most effective Ru metal catalyst reported previously [56]. An *o*-CAN selectivity over 99.9% at a substrate conversion of 100% was obtained over the Ru/SnO_2 catalyst. This selectivity was comparable to the result reported for a boride-modified PVP-Ru colloidal catalyst [56,57], and was better than that of the PVP-Ru catalyst with the same Ru nanoparticles. The SnO_2 nanoparticles remarkably promoted both the catalytic activity and selectivity of the Ru nanoclusters. An extremely low dechlorination rate of *o*-CAN in the absence of *o*-CNB was observed over this catalyst, which was 20-fold lower than that over the PVP-Ru colloidal catalyst, and was 73-fold lower when compared with a Ru/SiO_2 nanocomposite catalyst.

More excellent catalytic properties were observed over the Pt/γ-Fe_2O_3 catalyst. As shown in Table 4, no aniline (AN) derived from the dechlorination of CAN was detected in the hydrogenation of *o*-CNB over this nanocomposite catalyst even when the reaction time was extended after the substrate was completely exhausted. This is the first time to achieve the full inhibition of the hydrodechlorination of CAN in CNB hydrogenation. Furthermore, the hydrogenation rate of *o*-CNB over the Pt/γ-Fe_2O_3 catalyst could be elevated 34 times by increasing hydrogen pressure from 0.1 to 4.0 MPa, and no loss of the high catalytic selectivity was observed at the elevated hydrogen pressure. The Ru/SnO_2 and Pt/γ-Fe_2O_3 nanocomposite catalysts also exhibited perfect stability, suggesting that they are promising catalysts for industrial application.

The catalytic properties of metal nanoclusters in heterogeneous catalysts depend not only on the metal specificities of themselves but also on the environment surrounding them. The electronic interaction between metal nanoparticles and semiconductor supports as well as the surface species of the supports can have great influences on the catalytic behaviors of the catalysts for a specific reaction. With respect to the selective hydrogenation of *o*-CNB over the Ru/SnO_2 and Pt/γ-Fe_2O_3 nanocomposite catalysts, it has been suggested that the vacancies, i.e. the coordinatively unsaturated tin or iron cation species at the catalyst surface may play an important role in the excellent catalytic properties, which may activate the polar $-NO_2$ group in CNB and coordinate with the $-NH_2$ group in produced CAN molecules, thereby promoting the hydrogenation of CNB and depressing the dechlorination of CAN. On the other hand, the electronic interaction between the metal nanoparticles and the metal oxide supports may also have a significant contribution to the superior selectivity to *o*-CAN over these nanocomposite catalysts. Further investigations on the structure features of the activated catalysts and catalytic mechanism are under way [18,19].

Table 4. Catalytic properties of the Pt/γ-Fe_2O_3 catalyst for the hydrogenation of *o*-CNB.

Catalyst	Pt × 10^3 (mmol)	*o*-CNB (mmol)	P_H (MPa)	Conversion of *o*-CNB (%)	Reaction rate[a]	Selectivity (mol%)	
						o-CAN	AN
Pt-PVP	10.2	1.27	0.1	100	0.059	45.3	43.4
Pt/γ-Fe_2O_3	10.2	1.27	0.1	100	0.040	>99.9	0.0
Pt/γ-Fe_2O_3	10.2	13.0	0.1	100	0.22	>99.9	0.0
Pt/γ-Fe_2O_3	2.55	13.0	1.0	49.0	4.2	>99.9	0.0
Pt/γ-Fe_2O_3	2.55	13.0	2.0	76.0	6.5	>99.9	0.0
Pt/γ-Fe_2O_3	2.55	13.0	4.0	89.4	7.6	>99.9	0.0
Pt/γ-Fe_2O_3	2.55	13.0	4.0	100		>99.9	0.0
Pt/γ-Fe_2O_3	2.55	13.0	4.0	100		>99.9	0.0

Reaction conditions: solvent, 25 ml methanol; temperature, 60 °C. (Adapted from Ref. [19], © 2005, with permission from Elsevier.)
[a]Average rate of *o*-CNB hydrogenation [$mol_{o\text{-CNB}}/(mol_{Pt}\,s)$].

Table 5. Pt particle sizes in commercially available catalysts.

Catalyst	Degussa AG					E-tek				
Pt loading (wt.%)	20	30	40	50	60	10	20	30	40	60	80
Pt particle size (nm)	3.5	4.0	5.0	8.0	9.0	2.0	2.5	3.2	3.9	8.8	25
Pt surface area (m^2/g)[a]	80	70	56	35	31	140	112	88	72	32	11

Source: Ref. [25].
[a]Theoretical Pt surface area calculated from Pt particle sizes.

3.4. Application in Preparing Electrocatalysts for Fuel Cells

Pt-based electrocatalysts with high metal loading are widely employed as cathode catalysts for oxygen reduction reaction (ORR) or anode catalysts for gaseous or liquid fuel oxidation in polymer electrolyte fuel cells (PEFCs), which have been attracting increasing attention for their potential as clean and mobile power sources in the future. The usually applied methods for the preparation of Pt or Pt alloy electrocatalysts are mainly impregnation and colloid methods. As is well known, by the impregnation method it is very difficult to produce heterogeneous catalysts with high metal loadings without the concomitant increase in metal particle size. Table 5 demonstrates the relationship of Pt loading and particle size in commercially available catalysts [25]. Higher Pt loading appears to be linked to larger Pt particle size. The increased particle size reduces the available surface area of electrocatalysis and therefore limits the efficiency of the catalysts. The traditional colloid method is hindered by its complexity and the use of protecting agents, which can occupy the activated catalytic sites, leading to a decrease in catalytic activity. In addition, removal of the protecting agents at relatively high temperature may also result in the agglomeration of metal particles and the loss of available surface area. Though much effort has been paid to search for alternative routes, synthesis of electrocatalysts with high metal loading and well-dispersed small and uniform metal particles still remains a challenge.

The alkaline EG synthesis method described in this chapter is highly efficient for preparing colloidal solutions of small and narrowly distributed unprotected noble metal or alloy nanoclusters with high metal concentration. This character makes the synthesis technology very useful for the fabrication of electrocatalysts with well-controlled structures and excellent electrocatalytic properties. Xin and co-workers reported that Pt/MWNT nanocomposite could be successfully prepared by adding MWNTs to an EG colloidal solution (containing 5 vol.% of water) of Pt hydroxide or oxide nanoparticles, and heating the mixture to deposit Pt nanoclusters produced in situ on the support [20,21]. The well-dispersed spherical Pt metal nanoparticles in the synthesized Pt/MWNT electrocatalyst with a metal loading of 10 wt.% had a narrow particle size distribution of 2–5 nm and an average particle size of 2.6 nm. However, Pt nanoparticles in another Pt/MWNT catalyst with the same metal loading, prepared by immobilizing Pt nanoparticles formed in situ by a HCHO reduction method, had a wide particle size distribution ranging from 2 to 9 nm with a mean particle size of 3.4 nm, and an obvious tendency to agglomerate. When being employed as the cathode catalyst for direct methanol fuel cells (DMFCs), the Pt/MWNT catalyst prepared by the modified alkaline EG method exhibited higher ORR activity and superior cell performance in comparison with the catalyst prepared by the HCHO reduction method. Besides, carbon-supported Pt-Ru, Pt-Pd, Pt-W, Pt-Sn and Pt-Fe binary metallic electrocatalysts with sharp metal particle size distribution and constant Pt loading of 20 wt.% were also prepared successfully by the similar method [23,24].

Mao and Mao invented a method for synthesizing supported metal catalysts with small metal nanoparticles (1–3 nm) even at high metal loadings (30–50 wt.%) [25]. The obtained metal catalysts exhibited superior electrocatalytic performance in fuel cells. In this invention, the unprotected metal nanocluster colloids prepared according

to the alkaline EG synthesis method were used as building blocks. By adding carbon support particles to the colloidal solution of the unprotected metal nanoclusters, and then lowering pH of the mixture to deposit the metal nanoclusters on carbon support, a series of supported Pt or Pt-Ru alloy catalysts with high metal loading were prepared. The Pt nanoclusters supported on different types of carbon prepared by this technology had small metal particle sizes of ~2 nm and high electrochemical surface areas of 40–55 m^2/g, while a commercially available E-tek Pt/C catalyst (C3-30, 30 wt.% Pt) had an average Pt particle size of 3.2 nm and an electrochemical surface area of only 32 m^2/g. Figure 7 demonstrates a comparison of the dynamic performance of the Pt-Ru/C catalysts prepared by Mao et al. and that of a commercially available E-tek Pt-Ru/C catalyst (C14-30). In the test, a reformate fuel containing 35% hydrogen, 33% nitrogen, 22% CO_2 and 50 ppm CO, and a 2% air bleed were utilized. As illustrated in the figure, the polarization curves of the membrane electrode assemblies (MEA) made with the Pt-Ru/C catalyst prepared by Mao lay on that of MEA made of the commercial catalyst, indicating that the Pt-Ru/C catalysts prepared based on the modified alkaline EG process could provide higher cell efficiency. Moreover, these catalysts also exhibited better stability against CO poisoning.

It should be mentioned that the structure of carbon supports could have significant influence on the electrocatalytic properties of the nanocomposite catalysts. Recently, Pt/Ru nanoclusters prepared by the alkaline EG method were impregnated into a synthesized carbon support with highly ordered mesoporous. Although the Pt/Ru nanoclusters can be well dispersed in the pores of this carbon substrate, the long and narrow channels in this material seem not suitable for the application in electrocatalysts due to the higher ionic resistance and mass-transfer resistance [58].

The small metal particle size, large available surface area and homogeneous dispersion of the metal nanoclusters on the supports are key factors in improving the electrocatalytic activity and the anti-polarization ability of the Pt-based catalysts for fuel cells. The alkaline EG synthesis method proved to be of universal significance for preparing different electrocatalysts of supported metal and alloy nanoparticles with high metal loadings and excellent cell performances.

3.5. Application in Fabricating Hydrogen Sensor

As an important chemical for many industrial processes and an extremely clean energy source for fuel cells and internal combustion engines, hydrogen is widely applied in research and industry. For measuring the hydrogen concentration in flowing gas streams and monitoring leaked hydrogen in ambient air, reliable hydrogen sensors are needed. Great efforts have been made to develop hydrogen sensors and improve their selectivity. A new highly selective sensor for detecting hydrogen in air has been prepared successfully based on the unprotected Pt nanoclusters synthesized by the alkaline EG method [17]. The hydrogen sensor was composed of a continuous porous film of surface-oxidized Pt nanoparticles (PtO–Pt) on a glass substrate and a titania thin film covering the PtO–Pt film. The nanostructured dual-layer films were designed to utilize a process of partially reducing TiO_2 with H_2, catalyzed by the PtO–Pt porous film, to induce a change in the concentration of charge carriers in the TiO_2 film at relatively low temperature, which may increase the

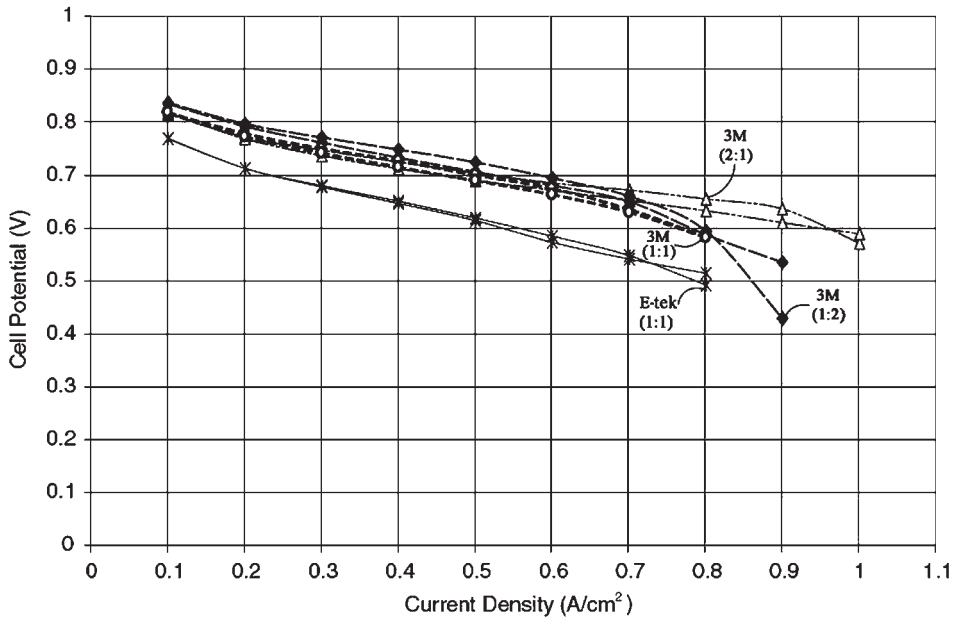

Figure 7. Cyclic voltammetry polarization curves for MEA made with different Pt-Ru/C catalysts [25]. 3 M (Pt/Ru = 1:1), 3 M (Pt/Ru = 1:2) and 3 M (Pt/Ru = 2:1) represent the catalysts prepared using the unprotected metal nanoclusters as building blocks; E-tek (Pt/Ru = 1:1) represents the commercially available catalyst (C14-30). All the catalysts have the same total metal loading of 30 wt.%.

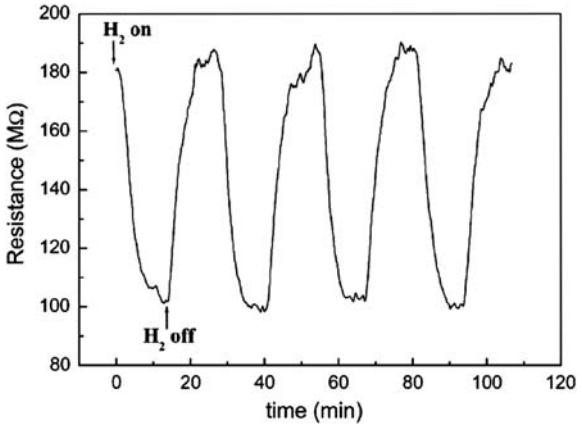

Figure 8. Sensing resistance of the TiO_2/PtO–Pt dual-layer sensor vs. time for exposures of air containing 2.0% H_2. (Reprinted from Ref. [17], © 2002, with permission from American Chemical Society.)

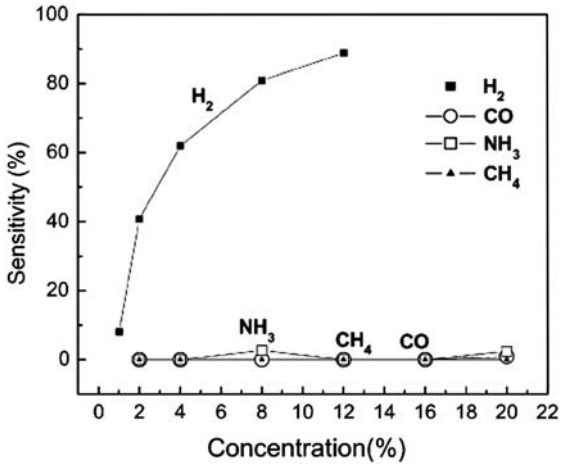

Figure 9. Gas sensitivities of the TiO_2/PtO–Pt dual-layer sensor to H_2, NH_3, CO and CH_4 in air. (Reprinted from Ref. [17], © 2002, with permission from American Chemical Society.)

sensing selectivity for H_2 due to the fact that H_2 as a reductant is more active than other usual reductive gases.

Figure 8 shows the hydrogen response ability of the prepared TiO_2/PtO–Pt dual-layer sensor. When an air flow containing 2.0% H_2 was introduced into the system at 200 °C, the measured resistance of the dual-layer sensor decreased from ~180 to 100 MΩ, whereas after the gas flow was turned off, the resistance reverted to its initial value. This response cycle could be repeated faithfully, suggesting that the sensing process of the sensor was reversible. Sensitivities of the dual-layer sensor to different reductive gases at 200 °C are shown in Figure 9. It can be seen that the sensitivities toward CO, NH_3 and CH_4 were quite low and independent of the gas concentrations. In contrast, the sensor was quite sensitive to H_2, and the selectivity to H_2 strongly depended on the concentration of H_2 in air. These phenomena indicated that the sensor had a satisfactory sensitivity and an extremely high selectivity to H_2, and was capable of semiquantitatively measuring the content of H_2 present in air with a concentration range from 1 to 10%. Besides, the nanostructured TiO_2/PtO–Pt dual-layer sensor also exhibited excellent stabilities to resist humidity and heat.

4. A Case History

In a typical experiment for preparing the unprotected Pt nanoclusters [11], an EG solution of NaOH (50 ml, 0.25 M) was added into an EG solution of $H_2PtCl_6 \cdot 6H_2O$ (50 ml, 38 mM) under stirring to obtain a transparent yellow mixture, which was then heated at 160 °C for 3 h, with an inert gas flow passing through the reaction system to take away water and organic byproducts. A transparent dark-brown colloidal solution of Pt metal nanoclusters (19 mM, 3.7 g Pt/l) with an average diameter of 1.3 nm and a size distribution from 0.8 to 2.0 nm was obtained without any precipitate. Using the similar synthesis method, transparent colloidal solutions of Rh, Ru [11] and Os [12] monometallic nanoclusters could also be prepared by replacing the starting compound of $H_2PtCl_6 \cdot 6H_2O$ with $RhCl_3 \cdot 3H_2O$, $RuCl_3 \cdot 3H_2O$ and $OsCl_3 \cdot 3H_2O$, respectively.

In the preparation of the unprotected Pt/Ru bimetallic nanoclusters, 50 ml EG solution of NaOH (0.5 M) was added dropwise into 50 ml EG solution containing 0.25 g of $H_2PtCl_6 \cdot 6H_2O$ and 0.25 g of $RuCl_3 \cdot 3.6H_2O$ under stirring. After heating the obtained mixture at 160 °C for 3 h, with an inert gas flow passing through the reaction system to take away water and organic byproducts, a transparent colloidal solution of Pt/Ru bimetallic nanoclusters with an average diameter of 1.9 nm and a size distribution from 1.4 to 2.4 nm was produced (Pt/Ru molar ratio = 1:1.9, total metal concentration: 1.85 g/l) [13,14]. Similarly, Pt/Rh bimetallic nanoclusters (Pt/Rh molar ratio = 1.33) with small particle sizes and narrow size distributions could be prepared by this alkaline EG method [12]. The obtained alloy colloidal solutions were very stable, no precipitation was observed after standing for several months.

In order to synthesize nanocomposite catalysts using the unprotected noble metal nanoclusters as building blocks, a new strategy has been proposed and validated to be quite effective as described in Section 2.2. Typically, for the preparation of a Ru/SnO_2 nanocomposite catalyst, a SnO_2 sol was prepared first as follows: 20 ml stannic chloride was dropped into 80 ml propanol and the solution was cooled to ambient temperature. A solution of 10 ml distilled water in 40 ml propanol was then added to the solution of stannic chloride. The obtained mixture was stirred for 1 h, and then a solution of 20 ml distilled water in 80 ml isopropanol was added. A SnO_2 sol was produced after further stirring the mixture for 1 h. The Ru/SnO_2 catalyst was synthesized by capturing unprotected Ru nanoclusters on SnO_2 colloidal particles via electrostatic interaction followed by gelating the obtained complex sol by adjusting its pH value. For example, 5.4 ml colloidal solution of Ru nanoclusters prepared according to the alkaline EG method was added to 99 ml of the prepared SnO_2 sol under stirring. After stirring for 20 min, the mixture was neutralized to pH 7 by adding an aqueous solution of sodium hydroxide (10 M), resulting in gelation

of the complex sol. The obtained precipitate was washed with water, separated by centrifugation and dried at 70 °C in vacuum to produce the Ru/SnO_2 catalyst [18]. The Ru content of the obtained catalyst was 0.9 wt.% as measured by means of ICP-AES. Ru nanoclusters in the Ru/SnO_2 nanocomposite had an average diameter of 1.3 nm with a size distribution from 1.0 to 2.5 nm as measured by TEM.

In the preparation of the magnetic $Pt/\gamma\text{-}Fe_2O_3$ nanocomposite catalyst, an aqueous solution of ammonia (10%) was added to 100 ml aqueous solution of $FeCl_3$ (4%) to adjust the pH to ~7.5, producing a precipitate that was separated by a filter, washed with water and peptized in 30 ml aqueous solution of $FeCl_3$ (1.2%), resulting in a transparent colloidal solution of ferric hydroxide. After mixing the unprotected Pt colloid prepared by the alkaline EG method and the ferric hydroxide colloid at the required ratio, the mixture was heated in a Teflon-lined autoclave at 80 °C for 3 days. A magnetic precipitate was produced, which was separated by centrifugation, washed with water and dried at 80 °C to give a brownish red solid of $Pt/\gamma\text{-}Fe_2O_3$ (1 wt.% Pt). The Pt nanoparticles distributed in the matrix of the $\gamma\text{-}Fe_2O_3$ nanoparticles had an average diameter of 2.6 nm as measured by STEM [19].

As an example of fabricating hydrogen sensor using the unprotected Pt nanoclusters as building blocks, a piece of glass or quartz substrate was immersed into a toluene colloidal solution of PPh_3-modified Pt nanoclusters (PPh_3–Pt) prepared by the method described in Section 3.2 and kept there for 2 days. During this period, a homogeneous self-assembly film of PPh_3–Pt nanoclusters formed on the surface of the glass or quartz substrate. The PPh_3–Pt film on the substrate was washed with toluene, dried at 100 °C and then annealed in air at 400 °C for 30 min to give a porous PtO–Pt film. Afterwards, 0.5 ml colloidal solution of TiO_2 nanoparticles with a mean diameter of 4.1 nm and a size distribution from 3.4 to 5.4 nm, prepared by hydrolyzing $Ti(OC_3H_7)_4$ in an aqueous solution of HNO_3 (0.1 M), was dropped onto the PtO–Pt film and spun at 1500 rpm for 20 s to form a TiO_2 film on the PtO–Pt film. After being dried in air at 100 °C, the films on the substrate were annealed at 400 °C for 30 min to finish the preparation of a dual-layer film sensor. The TiO_2 and PtO–Pt films in the hydrogen sensor are 110 and 100 nm in thickness, respectively, as measured by SEM [17].

5. Conclusions

The alkaline EG synthesis method is a very effective technology for the chemical preparation of "unprotected" metal and alloy nanoclusters stabilized by EG and simple ions. This method is characterized by two steps involving the formation of metal hydroxide or oxide colloidal particles and the reduction of them by EG in a basic condition. The strategy of separating the core formation from reduction processes provides a valid route to overcome the obstacle in producing stable unprotected metal nanoclusters in colloidal solutions with high metal concentrations. Noble metal and alloy nanoclusters such as Pt, Rh, Ru, Os, Pt/Rh and Pt/Ru nanoclusters with small particle sizes of 1–3 nm could be effectively prepared according to this method. Based on different requirements in application, the as-synthesized unprotected metal nanoclusters can be conveniently separated from the original colloidal solutions and redispersed into many kinds of organic solvents to form different stable metal colloids, or be flexibly modified by various organic ligands to produce protected metal nanoclusters with the same metal core and different ligand shells, which provide opportunities to systematically study the ligand effect on the electronic properties of the nanosized metal particles and distinguish it from the size-dependent effect.

As a unique kind of nanostructured building blocks, these unprotected metal nanoclusters could be used to fabricate many promising functional systems, such as heterogeneous catalysts for various chemical reactions, catalytic electrodes for fuel cells, sensors, etc. Assembling the unprotected metal or alloy nanoclusters on various supports provides a realistic protocol to prepare different heterogeneous catalysts with the same metal particles, which is of universal significance in better understanding of the catalysis principles and developing novel metal and alloy catalysts.

The emphases of future investigation on these unprotected metal nanoclusters should be mainly placed on: (1) further controlling the size, composition and shape of the unprotected metal or alloy nanoclusters; (2) better understanding the stabilizing mechanism of the unprotected metal nanoclusters in colloidal solutions prepared by the alkaline EG synthesis method; (3) developing novel catalytic and other functional systems for real applications.

References

1 S. Lin, M. T. Franklin, K. J. Klabunde, *Langmuir* 2 (1986) 259.
2 K. J. Klabunde, Method of Coating Substrates with Solvated Clusters of Metal Particles, U.S. Patent 4,877,647 (1989).
3 G. Cardenas-Trivino, K. Klabunde, D. E. Brock, *Langmuir* 3 (1987) 986.
4 F. Tian, K. J. Klabunde, *New J. Chem.* 22 (1998) 1275.
5 S. Stoeva, K. J. Klabunde, C. M. Sorensen, I. Dragieva, *J. Am. Chem. Soc.* 124 (2002) 2305.
6 K. Esumi, T. Tano, K. Meguro, *Langmuir* 5 (1989) 268.
7 T. Tano, K. Esumi, K. Meguro, *J. Colloid Interface Sci.* 133 (1989) 530.
8 H. Bonnemann, W. Brijoux, *Nanostruct. Mater.* 5 (1995) 135.
9 A. Curtis, D. Duff, P. Edwards, D. Jefferson, B. Johnson, A. Kirkland, A. Wallace, *J. Phys. Chem.* 92 (1988) 2270.
10 X. Fu, Y. Wang, N. Wu, L. Gui, Y. Tang, *Langmuir* 18 (2002) 4619.
11 Y. Wang, J. Ren, K. Deng, L. Gui, Y. Tang, *Chem. Mater.* 12 (2000) 1622.
12 Y. Wang, J. L. Zhang, X. D. Wang, J. W. Ren, B. J. Zuo, Y. Q. Tang, *Top. Catal.* 35 (2005) 35.
13 X. Fu, Dissertation for the Doctoral Degree, Peking University, China, 2002.
14 Y. Wang, K. Deng, L. Gui, Y. Tang, Chinese Patent No. ZL 99100052.8 (CN 1108858C, May 2003).
15 B. He, Y. Chen, H. Liu, Y. Liu, *J. Nanosci. Nanotechnol.* 5 (2005) 266.

16 R. Harpeness, Z. Peng, X. S. Liu, V. G. Pol, Y. Koltypin, A. Gedanken, *J. Colloid Interface Sci.* 287 (2005) 678.
17 X. Du, Y. Wang, Y. Mu, L. Gui, P. Wang, Y. Tang, *Chem. Mater.* 14 (2002) 3953.
18 B. Zuo, Y. Wang, Q. Wang, J. Zhang, N. Wu, L. Peng, L. Gui, X. Wang, R. Wang, D. Yu, *J. Catal.* 222 (2004) 493.
19 J. Zhang, Y. Wang, H. Ji, Y. Wei, N. Wu, B. Zuo, Q. Wang, *J. Catal.* 229 (2005) 114.
20 W. Li, C. Liang, W. Zhou, J. Qiu, Z. Zhou, G. Sun, Q. Xin, *J. Phys. Chem. B* 107 (2003) 6292.
21 W. Li, C. Liang, W. Zhou, J. Qiu, H. Li, G. Sun, Q. Xin, *Carbon* 42 (2004) 423.
22 Z. Zhou, S. Wang, W. Zhou, G. Wang, L. Jiang, W. Li, S. Song, J. Liu, G. Sun, Q. Xin, *Chem. Commun.* (2003) 394.
23 W. Zhou, Z. Zhou, S. Song, W. Li, G. Sun, P. Tsiakaras, Q. Xin, *Appl. Catal. B* 46 (2003) 273.
24 W. Li, W. Zhou, H. Li, Z. Zhou, B. Thou, G. Sun, Q. Xin, *Electrochim. Acta* 49 (2004) 1045.
25 S. Mao, G. Mao, Supported Nanoparticle Catalyst, US 6686308 B2 (2004).
26 M. T. Reetz, M. Dugal, *Catal. Lett.* 58 (1999) 207.
27 A. Martino, A. G. Sault, J. S. Kawola, E. Boespflug, M. L. F. Phillips, *J. Catal.* 187 (1999) 30.
28 H. Bonnemann, U. Endruschat, B. Tesche, A. Rufinska, C. W. Lehmann, F. E. Wagner, G. Filoti, V. Parvulescu, V. I. Parvulescu, *Eur. J. Inorg. Chem.* 5 (2000) 819.
29 J. P. M. Niederer, A. B. J. Arnold, W. F. Holderich, B. Spliethof, B. Tesche, M. T. Reetz, H. Bonnemann, *Top. Catal.* 18 (2002) 265.
30 Z. Konya, V. F. Puntes, I. Kiricsi, J. Zhu, J. W. Ager, M. K. Ko, H. Frei, A. P. Alivisatos, G. A. Somorjai, *Chem. Mater.* 15 (2003) 1242.
31 J. Zhu, Z. Konya, V. F. Puntes, I. Kiricsi, C. X. Miao, J. W. Ager, A. P. Alivisatos, G. A. Somorjai, *Langmuir* 19 (2003) 4396.
32 F. Fiever, J. P. Lagier, B. Blin, B. Beaudoin, M. Figlarz, *Solid State Ionics* 32–33 (1988) 198.
33 F. Fiever, J. P. Lagier, M. Figlarz, *MRS Bull.* 14 (1989) 29.
34 N. Toshima, Y. Wang, *Langmuir* 10 (1994) 4574.
35 N. Toshima, Y. Wang, *Chem. Lett.* 9 (1993) 1611.
36 N. Toshima, Y. Wang, *Adv. Mater.* 6 (1994) 245.
37 Y. Wang, N. Toshima, *J. Phys. Chem. B* 101 (1997) 5301.
38 W. Yu, Y. Wang, H. Liu, W. Zheng, *J. Mol. Catal. A* 112 (1996) 105.
39 A. Roucoux, J. Schulz, H. Patin, *Chem. Rev.* 102 (2002) 3557.
40 M. E. Labib, *Colloids Surf.* 29 (1988) 293.
41 H. Song, R. M. Rioux, J. D. Hoefelmeyer, R. Komor, K. Niesz, M. Grass, P. Yang, G. A. Somorjai, *J. Am. Chem. Soc.* 128 (2006) 3027.
42 R. M. Rioux, H. Song, J. D. Hoefelmeyer, P. Yang, G. A. Somorjai, *J. Phys. Chem. B* 109 (2005) 2192.
43 Y. Mu, H. Liang, J. Hu, L. Jiang, L. Wan, *J. Phys. Chem. B* 109 (2005) 22212.
44 H. Hirai, Y. Nakao, N. Toshima, *J. Macromol. Sci. Chem.* A13 (1979) 727.
45 X. Fu, Y. Wang, N. Wu, L. Gui, Y. Tang, *J. Colloid Interface Sci.* 243 (2001) 326.
46 H. Liu, N. Toshima, *J. Chem. Soc., Chem. Commun.* (1992) 1095.
47 T. Xie, Y. Wang, K. Jiang, J. Ren, K. Deng, J. Dong, L. Gui, Y. Tang, *Acta Chim. Sin.* 58 (2000) 781.
48 W. Ederhardt, P. Fayet, D. M. Cox, Z. Fu, A. Kaldor, R. Sherwood, D. Sondericker, *Phys. Rev. Lett.* 64 (1990) 780.
49 T. T. P. Cheung, *Surf. Sci.* 140 (1984) 151.
50 G. K. Wertheim, S. B. Dicenzo, S. E. Young, *Phys. Rev. Lett.* 51 (1983) 2310.
51 X. D. Wang, M. H. Liang, J. L. Zhang, Y. Wang, *Curr. Org. Chem.* 11 (2007) 299.
52 B. Coq, A. Tijani, R. Dutartre, F. Figueras, *J. Mol. Catal.* 71 (1992) 317.
53 X. X. Han, R. X. Zhou, G. H. Lai, B. H. Yue, X. M. Zheng, *Catal. Lett.* 89 (2003) 255.
54 X. L. Yang, Z. L. Deng, H. F. Liu, *J. Mol. Catal. A: Chem.* 141 (1999) 123.
55 X. L. Yang, H. F. Liu, *Appl. Catal. A* 164 (1997) 197.
56 M. H. Liu, W. Y. Yu, H. F. Liu, *J. Mol. Catal. A: Chem.* 138 (1999) 295.
57 X. Yan, M. H. Liu, H. F. Liu, K. Y. Liew, *J. Mol. Catal. A: Chem.* 16 (2001) 225.
58 J. Ding, K. Y. Chan, J. W. Ren, F. S. Xiao, *Electrochim. Acta* 50 (2005) 3131.

CHAPTER 20

Microgels as Exotemplates in the Synthesis of Size Controlled Metal Nanoclusters

Andrea Biffis

Department of Chemical Sciences, University of Padova, Padova, Italy

1. Introduction

In polymer chemistry, the term "microgel" [1] defines unimolecular, crosslinked polymer particles possessing a size comparable to the statistical dimensions of uncrosslinked macromolecules (10^1–10^2 nm), which give rise to stable, low-viscosity solutions in appropriate solvents. These materials, first described by Staudinger [2] in the 1930s, can be considered as an intermediate category of polymers, which combine the characteristics of both linear macromolecules and three-dimensional networks [3]. For a proper understanding of microgel structure, it may be helpful to remark that such macromolecules closely resemble, in their structure and behavior, soluble to crosslinked biological macromolecules such as proteins.

Microgels have found wide technological application as additives with binding or stabilizing properties in the industrial manufacture of coatings [4]. Furthermore, in recent years the recognition of their unique characteristics has stimulated considerable research on their use as drug-delivery systems [5], biomimetic receptors/catalysts [6], phase-transfer catalysts [7], and as soluble supports for low molecular weight reagents, scavenging agents, or (bio)catalysts [8]. Another advanced application of microgels, which forms the object of this chapter, is their use as stabilizers in the preparation of inorganic nanoparticles, most notably metal nanoparticles. Indeed, there is a large potential for the application of readily processable, size-controlled metal nanoparticles in catalysis as well as in the field of material science (photonics, electronics, optics, and biomedicine) [9,10], as outlined also elsewhere in this book. Research on this particular application of microgels has been actively pursued *inter alia* by the groups of Antonietti [11], Kumacheva [12], and Biffis [13]. The use of microgel stabilizers has been recently also extended to the preparation of technologically useful metal oxide or metal sulfide nanoparticles [12,14].

The first report on the preparation of microgel-stabilized metal nanoclusters was published in 1997 by Antonietti et al. [11a], who utilized polystyrene-based microgels prepared by microemulsion polymerization and fully sulfonated in a second step by treatment with concentrated sulfuric acid. The sulfonated microgels were soluble in water and could be loaded with metal ions, which were subsequently reduced thus forming microgel-stabilized metal nanoclusters.

Some years later, Biffis described the preparation of functional microgel stabilizers by an alternative route, namely by copolymerization of suitable functional monomers (Figure 1) [13a].

This methodology presents some fundamental advantages. First, it represents a much milder method for the introduction of the functional groups, which is not limited by the nature of the polymer backbone. Secondly, the method enables to easily control the amount of functional groups in the microgels, hence the hydrophilic/hydrophobic properties of the microgel stabilizer. Finally, alternative functionalities such as basic or metal coordinating groups can be incorporated into the microgel backbone simply upon utilization of suitable functional comonomers. This in turn makes it potentially possible to prepare microgel-stabilized metal nanoclusters from any metal-containing precursor suitable to be anchored to microgel-bound functional groups and subsequently to be reduced to the metal state.

In this contribution, recent results from the group of Biffis are summarized, which demonstrate that functional microgel stabilizers can act as true "exotemplates" for the preparation of metal nanoclusters with a high degree of control and with an average size depending on the nanomorphological features of the polymer framework. This peculiar feature of microgel stabilizers is of course related to the analogous effect exerted by insoluble polymer supports in the so-called "Template Controlled Synthesis" (TCS) approach (see the pertaining chapter in this book).

2. Synthesis Strategy

Radical polymerization in dilute solution has been used throughout this work for microgel synthesis [14,15]. This is

Metal Nanoclusters in Catalysis and Materials Science: The Issue of Size Control
Edited by B. Corain, G. Schmid and N. Toshima

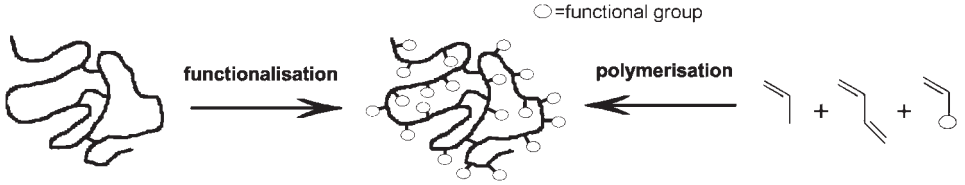

Figure 1. Possible strategies for the synthesis of functional microgel stabilizers: functionalization of preformed microgels (left) or copolymerization of suitable functional monomers (right, our approach). (Reprinted from Ref. [13b], © 2003, with permission from Wiley-VCH.)

probably the simplest available method for the preparation of microgels. It does not make use of surfactants or other additives in order to avoid gelation and maximize the microgel yield; it only requires a careful choice of the reaction parameters, most notably of the nature of the solvent. In fact, the stabilization of the growing microgels towards macrogelation is accomplished on the basis of the osmotic repulsion forces generated by the interaction of polymer chains and loops at the periphery of the microgel particles – namely through steric stabilization [16]. To achieve this, the monomer concentration must be reduced below a critical value (critical monomer concentration, C_m). This value is strongly dependent on many factors such as the nature and amount of initiator, the crosslinking degree, the polymerization temperature, and especially the nature of the solvent, which can be conveniently rationalized in terms of the solubility parameter δ [17].

In comparison to the more common preparation method by polymerization in miniemulsion, solution polymerization suffers from a less precise control of the size and size distribution of the resulting microgels. On the other hand, the polymerization in solution offers the considerable advantage of allowing the variation of parameters, such as the type and degree of microgel functionalization (by utilizing suitable comonomers), the nature of the nonfunctional comonomers, or the crosslinking degree, with less restrictions caused by the requirements of the polymerization procedure. As it will be apparent in the following, these parameters play an important role in determining the solubility of the microgels in different solvents as well as the size of the metal nanoclusters resulting from the coordination and reduction procedure.

Polymerization in dilute solution also allows a very straightforward isolation and purification of the microgels. After polymerization, the resulting microgels can be conveniently precipitated from the reaction solution by using suitable nonsolvents for the microgel molecules. The resulting powders can be filtered off, dried, and redispersed in suitable solvents when needed.

The generation of metal nanoclusters within microgels is performed in solution. First of all, the microgels are loaded with a predetermined amount of metal precursors upon reaction of the functional groups in the microgel with suitable metal ions or complexes through coordination or simple ion-exchange. Straightforward, high-yielding reactions that are already known to provide quantitative incorporation of the metal precursors into insoluble polymer supports are utilized in this step. Care must be taken that the resulting microgel-bound metal species remain stable until reduction takes place, since spontaneous decomposition to metal invariably results in the formation of large, polydisperse metal colloids [13a,d]. Metal reduction to nanoclusters is usually accomplished with a suitable reducing agent. The resulting microgel-stabilized nanoclusters can be purified by ultrafiltration, ultracentrifugation or precipitation. In the latter case, they can be obtained as powders and redispersed in suitable solvents for the microgel molecules, where they are stable for months without noticeable precipitation of metal and from which they can be also potentially casted as, for example films.

Table 1. Composition of the functionalized microgels employed in this work.

Microgel	DMAA (mol%)	MMA (mol%)	EDMA (mol%)	DMAEMA (mol%)
D5	85	–	5	10
D7.5	82.5	–	7.5	10
D10	80	–	10	10
D20	70	–	20	10
M5	–	85	5	10
M10	–	80	10	10
M20	–	70	20	10

Note: Polymerization conditions: 3% w/w AIBN, 10% w/w monomer mixture in cyclopentanone, 80 °C, 48 h.

3. Results

Microgels based on *N,N*-dimethylacrylamide (DMAA) or methyl methacrylate (MMA) with varying crosslinking degree have been prepared, following a well-established radical polymerization procedure in dilute solution (see the "Case History" section) [13]. Microgels were prepared from DMAA or MMA as the main comonomer, ethylene dimethacrylate (EDMA) as the crosslinker and *N,N*-dimethylamino-ethylmethacrylate (DMAEMA, 10 mol% in all cases) as the functional, metal binding comonomer. The composition of the monomer mixtures and the polymerization conditions are reported in Table 1.

The microgels could be conveniently isolated by precipitation as white powders, readily redispersable in many different organic solvents such as dialkylamides, nitriles, dichloromethane, acetone and THF. Further to this, the DMAA-based microgels exhibited a rather amphiphilic character and were also soluble in water and in alcohols such as methanol or ethanol; in contrast, their counterparts based on MMA turned out to be more lipophilic and therefore insoluble in water and alcohols but soluble in organic solvents of low polarity such as toluene.

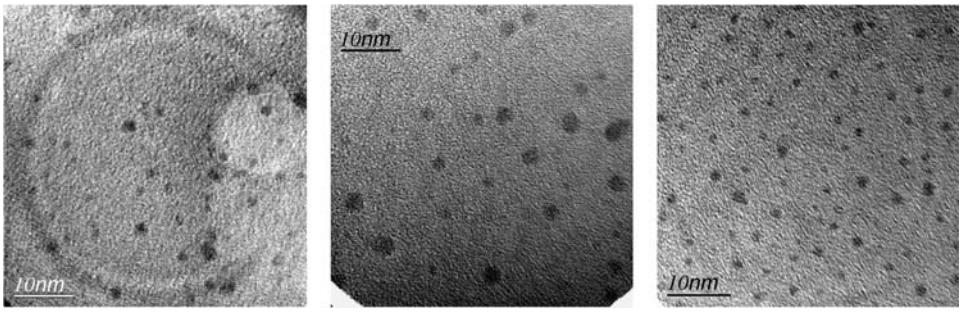

Figure 2. TEM micrographs of metal nanoclusters stabilized by microgel M5; from left to right: Pd (reduced with $NaHBEt_3$), Pd (reduced with EtOH), Pt (reduced with $NaHBEt_3$).

The microgels were loaded with palladium(II) or platinum(II) by letting them react with $Pd(OAc)_2$ or $PtCl_2(CH_3CN)_2$ (0.25 eq. with respect to the available amino groups, which implies a total metal content in the microgel of 2.4%, w/w, for Pd and of 4.2%, w/w, for Pt) in dichloromethane solution. Reduction of the resulting solution with $NaHBEt_3$ or with ethanol (in the case of Pd) yielded a solution of microgel-stabilized metal nanoclusters, which could be easily precipitated from the reaction mixture. The obtained dark-gray powders could be stored and readily redispersed in good solvents for the microgel stabilizer. The resulting solutions were clear and turned out to be stable for months without any observable precipitation of metal.

The average size and size distribution of the microgel-stabilized metal nanoclusters were investigated by TEM. Some representative TEM micrographs are reported in Figure 2. The numerical results are displayed in Figures 3–5 (the vertical bars show the standard deviations in the average metal nanocluster size).

Figure 3 reports the dependence of the Pd nanocluster size from the microgel crosslinking degree and from the nature of the main comonomer (DMAA or MMA). It can be appreciated that in the case of MMA-based microgels the average nanocluster size considerably decreases with increasing crosslinking degree of the microgel. It is important to remark that the observed change in nanocluster size depends solely on the nanomorphology of the employed microgel. The chemical nature of the microgel, its concentration with respect to the metal, and the reaction conditions for nanocluster formation are kept the same, so that the different "mesh size" of the polymer network building up the swollen microgel molecules remains the only factor that actually determines the average nanocluster size. This is confirmed by the observation that microgel stabilizers with the same crosslinking degree yield metal nanoclusters with very similar average size, irrespective both of the nature of the metal (e.g. 4.4 ± 0.6 nm obtained at 10 mol% crosslinking with Pt vs. 4.2 ± 0.7 nm with Pd) and of the functional groups present in the microgel (see below).

The average Pd nanocluster size obtained using DMAA-based microgel stabilizers is significantly smaller than that obtained with MMA-based microgels of the same crosslinking degree; this is also true for Pt nanoclusters (e.g. 1.7 ± 0.5 nm obtained at 10 mol% crosslinking with DMAA vs. 4.4 ± 0.6 nm with MMA). Thus, the change in main comonomer appears to have a marked

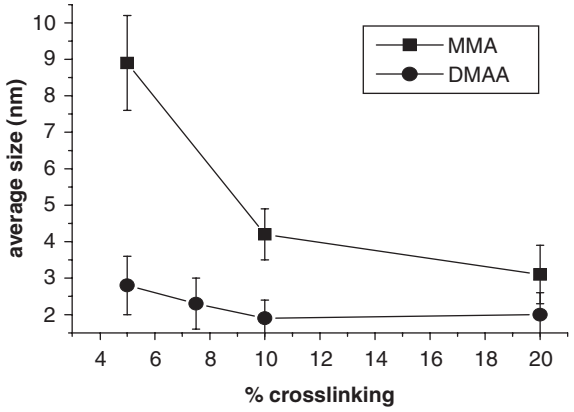

Figure 3. Dependence of the size of microgel-stabilized Pd nanoclusters from the crosslinking degree of the microgel and from the nature of the nonfunctional comonomer.

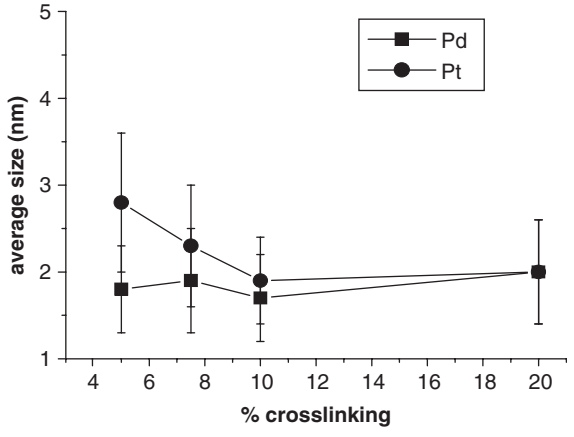

Figure 4. Dependence of the size of DMAA-based microgel-stabilized metal nanoclusters from the crosslinking degree of the microgel and from the nature of metal.

influence on the nanocluster size. Furthermore, a decreasing trend of the nanocluster size with increasing crosslinking degree is observed also for DMAA-based microgels, in line with the expectation that the increasing crosslinking degree reduces the mesh size of the polymer

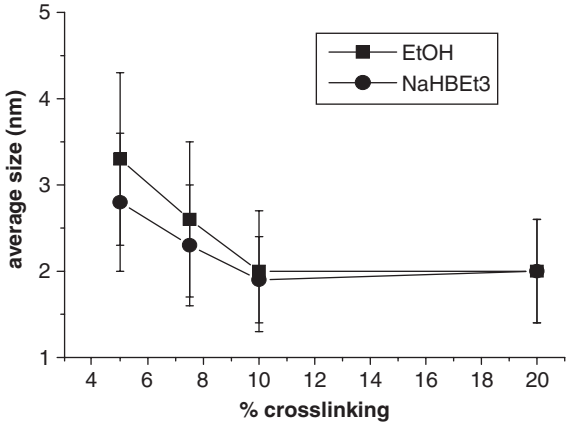

Figure 5. Dependence of the size of DMAA-based microgel-stabilized Pd nanoclusters from the crosslinking degree of the microgel and from the nature of the reducing agent.

network and consequently the nanocluster size. However, such a dependence is much less pronounced than for MMA-based microgels. Interestingly, a similarly weak dependence of the size of Ag nanoclusters on the crosslinking degree was very recently reported by Lu et al. for core–shell microgels based on *N*-isopropylacrylamide [18]. The dependence of the size from the crosslinking degree virtually disappears in the case of Pt nanoclusters (Figure 4). On the other hand, with DMAA-based microgels very similar Pd nanocluster sizes are obtained irrespective of the reducing agent used (EtOH or $NaHBEt_3$, Figure 5), which is not the case with MMA-based microgels (e.g., 3.4 ± 0.5 nm obtained at 10 mol% crosslinking with EtOH as reductant vs. 4.2 ± 0.7 nm with $NaHBEt_3$).

It can be speculated that the different behavior of DMAA- and MMA-based microgel stabilizers of equal crosslinking degree is related to the different interactions between DMAA- or MMA-based microgel stabilizers and the growing metal nanoparticles. On the basis of the state-of-the-art knowledge about the preparation of polymer-stabilized metal nanoparticles, it can be safely stated that the final size attained by the metal nanoparticle is the result of the combined influence of more than one parameter [19], the most important of which are (a) the kinetics of formation of the zerovalent metal precursors, (b) the kinetics of nucleation and growth of the metal nanoparticles, (c) the strength of the interaction of the polymer stabilizer with the growing nanoparticle surface, and finally (d) the steric effect (''cage'' effect) exerted by the polymer chains surrounding the growing nanoparticle.

N,N-dialkylamide groups are known to interact with the surface of the growing metal nanoparticles through the carbonyl oxygen [20], thereby controlling their growth and protecting them against sintering; incidentally, this is the main reason of the enduring success enjoyed by dialkylamide-functionalized linear polymers such as poly(vinylpyrrolidone) as stabilizers for metal nanoclusters, even if a very recent report casts some doubts about the true efficiency of such stabilizers [21]. In the presence of such groups, it has been proposed that interaction of the polymer with the growing metal surface takes place at a relatively early stage, thereby lowering the surface energy of the nanoparticles and creating a barrier towards further growth; consequently, under these conditions the physicochemical nature and amount relative to the metal of the polymer stabilizer gains importance in determining nanocluster growth [22]. In the case of our DMAA-based microgels, the chemical nature of the polymer stabilizer as well as the amount of metal relative to microgel are kept the same for all samples; this at least partially offsets the steric effect due to the increasing crosslinking degree, as well as the influence of the nature of the reducing agent. On the other hand, when polymers with a lower ability to interact with the growing metal nanoparticles are employed, such as MMA-based microgels, the stabilization by surface adsorption of the polymer chains occurs at a later stage and is less efficient in preventing further growth. In this case, control of metal nanocluster growth within microgels is exerted by steric effects and in part also by the kinetics of the formation of the zerovalent metal centers, namely, by the nature of the reducing agent. Other parameters such as the nature of the microgel-bound metal precursor appear to be less important. Substitution of the functional, metal binding comonomer DMAEMA with 4-vinylpyridine results in MMA-based microgels inducing almost exactly the same nanocluster size both with Pd (4.2 ± 0.8 vs. 4.2 ± 0.7 nm) and Pt (4.0 ± 0.6 nm vs. 4.4 ± 0.6 nm).

4. A Case History

In this section, a description of the experimental procedure used to prepare and characterize metal nanoclusters stabilized by DMAA-based microgels (M5, M10, M20) is provided. Details of the experimental procedure used to prepare nanoparticles stabilized by MMA-based microgels have been reported elsewhere [13b].

The monomers employed for microgel synthesis were freshly distilled to free them from inhibitors prior to use. Other chemicals and solvents were of reagent grade and were used as received.

4.1. Microgel Preparation

Monomers were mixed in the desired ratios (Table 1) in a round-bottomed flask. The resulting mixtures (5 g) were diluted with cyclopentanone (45 g). Azobis(isobutyronitrile) (AIBN) (0.18 g, 3% w/w with respect to the monomer mixture) was then added. The resulting solution was degassed, put under nitrogen, and placed for 48 h in a thermostated oven preheated at 80 °C. The polymerization solution was concentrated to about half of the original volume and subsequently poured in the fivefold volume of diethylether under efficient stirring. The precipitated solid was filtered off and dried under vacuum to constant weight. Isolated yields were about 80% in all cases.

4.2. Preparation of Metal Nanoclusters by Reduction with $NaHBEt_3$

General procedure: microgel (1 g) was dissolved in dichloromethane (80 mL) under an inert atmosphere.

$Pd(OAc)_2$ (50 mg, 0.25 eq. with respect to the available amino groups) or $PtCl_2(CH_3CN)_2$ (78 mg, 0.25 eq. with respect to the available amino groups) was then added, and the resulting solution was stirred at room temperature overnight. Subsequently, $NaHBEt_3$ (2.2 mL 1 M solution in THF, 10 eq. with respect to metal) was added and the resulting solution was stirred at room temperature for 1 day. The solution was concentrated to about half of the original volume and the nanocluster-containing microgel was subsequently precipitated by pouring the solution in the fivefold volume of diethylether under efficient stirring. Isolated yields were about 90% in all cases.

4.3. Preparation of Pd Nanoclusters by Reduction with EtOH

General procedure: microgel (1 g) was dissolved in dichloromethane (80 mL) under an inert atmosphere. $Pd(OAc)_2$ (50 mg, 0.25 eq. with respect to the available amino groups) was then added, and the resulting solution was stirred at room temperature overnight. Subsequently, the solution was brought to reflux and 6 mL ethanol were added. The solution was maintained at reflux with efficient stirring for 12 h. The solution was concentrated to about half of the original volume and the nanocluster-containing microgel was subsequently precipitated by pouring the solution in the fivefold volume of diethylether under efficient stirring. Isolated yields were about 90% in all cases.

4.4. TEM Measurements

Samples for TEM measurements were prepared by dissolving a drop of a solution of microgel-stabilized metal nanoclusters in dichloromethane on a carbon-coated copper grid followed by solvent evaporation at room temperature. TEM micrographs were taken at the University of Modena, Italy, with a JEOL 2010 microscope with GIF operated at an accelerating voltage of 200 keV. Average metal nanocluster sizes and size distributions were computed as the average of at least 100 particles taken from different fields.

5. Conclusions

In conclusion, it has been shown that the use of microgels as exotemplates and stabilisers for metal nanoclusters allows the easy preparation of nanoparticles with an average size depending on the crosslinking degree of the microgel molecule. The degree of nanocluster size control attainable through the "cage effect" exerted by the microgel can be modulated by changing the nature of the main comonomer building up the polymer chains. Size control is achieved irrespective of the nature of the employed metal (Pd or Pt), especially with crosslinking degrees of 10% or higher. Finally, in the case of DMAA-based microgels virtually the same degree of size control is obtained with widely different reducing agents like $NaBH_4$ and ethanol, the former being an ionic reductant potentially able to electrostatically stabilize the metal nanoparticles and interfere with their growth [21].

To the best of our knowledge, such a control of nanocluster size through the nanomorphology of the stabilizer cannot be achieved with any other system, not even with those in which the metal nanocluster precursors are physically confined within nanometer-sized cavities [23].

The resulting microgel-stabilized metal nanoclusters are easily isolated, stored and further manipulated. Their remarkable catalytic activity in technologically relevant reactions, such as C–C couplings [13a–c] and selective oxidations with molecular oxygen [13e] has been demonstrated. Extension of the applications of these nanoparticles to other areas of catalysis and materials science is currently underway.

References

1 W. O. Baker, *Ind. Eng. Chem.* 41 (1949) 511.
2 H. Staudinger, E. Husemann, *Chem. Ber.* 68 (1934) 1620.
3 For recent comprehensive reviews on microgels, see (a) W. Funke, O. Okay, B. Joos-Müller, *Adv. Polym. Sci.* 136 (1998) 139; (b) B. R. Saunders, B. Vincent, *Adv. Colloid Interface Sci.* 80 (1999) 1.
4 D. Saatweber, B. Vogt-Birnbrich, *Prog. Org. Coat.* 28 (1996) 33.
5 (a) Y. J. Kwon, E. James, N. Shastri, J. M. J. Frechet, *Proc. Natl. Acad. Sci. USA* 102 (2005) 18264; (b) M. Das, S. Mardyani, W. C. W. Chan, E. Kumacheva, *Adv. Mater.* 18 (2006) 80 and references therein.
6 (a) A. Biffis, G. Siedlaczek, S. Stalberg, G. Wulff, N. B. Graham, *Macromol. Chem. Phys.* 202 (2001) 163; (b) S. Maddock, P. Pasetto, M. Resmini, *Chem Commun.* (2004) 536; (c) C. E. Hunt, P. Pasetto, R. J. Ansell, K. Haupt, *Chem. Commun.* (2006) 1754; (d) G. Wulff, B.-O. Chong, U. Kolb, *Angew. Chem. Int. Ed.* 45 (2006) 2955.
7 W. T. Ford, J.-J. Lee, H. Yu, B. J. Ackerson, K. A. Davis, *Macromol. Symp.* 92 (1995) 333.
8 Selected examples: (a) A. K. Luthra, A. Williams, *J. Mol. Catal. A* 95 (1995) 83; (b) C. Otero, L. Robledo, A. R. Alcantara, *J. Mol. Catal. B: Enzymatic* 1 (1995) 23; (c) K. Ohkubo, Y. Funakoshi, T. Sagawa, *Polymer* 37 (1996) 3993; (d) N. Kihara, C. Kanno, T. Fukutomi, *J Polym. Sci. A* 35 (1997) 1443; (e) C. Schunicht, A. Biffis, G. Wulff, *Tetrahedron* 56 (2000) 1693; (f) C. Spanka, B. Clapham, K. D. Janda, *J. Org. Chem.* 67 (2002) 3045; (g) O. Shimomura, B. Clapham, C. Spanka, S. Mahajan, K. D. Janda, *J. Comb. Chem.* 4 (2002) 436.
9 (a) G. Schmid (ed.) *Nanoparticles*, Wiley-VCH, Weinheim, 2004; (b) D. L. Feldheim, C. A. Foss (eds.) *Metal Nanoparticles: Synthesis, Characterization and Applications*, Marcel Dekker, New York, 2002; (c) T. Sugimoto (ed.) *Fine Particles: Synthesis, Characterization and Mechanisms of Growth*, Marcel Dekker, New York, 2000.
10 Recent reviews: (a) D. Astruc, F. Lu, J. R. Aranzaes, *Angew. Chem. Int. Ed.* 44 (2005) 7852; (b) C. Burda, X. Chen, R. Naraynan, M. A. El-Sayed, *Chem. Rev.* 105 (2005) 1025; (c) M. Moreno-Mañas, R. Pleixats, *Acc. Chem. Res.* 36 (2003) 638; (d) A. Roucoux, J. Schulz, H. Patin, *Chem. Rev.* 102 (2002) 3757; (e) H. Bönnemann, R. M. Richards, *Eur. J. Inorg. Chem.* (2001) 2455; (f) N. Shipway, I. Willner, *Chem. Commun.* (2001) 2035; (g) J. D. Aiken III, R. G. Finke, *J. Mol. Catal. A: Chemical* 145 (1999) 1.
11 (a) M. Antonietti, F. Gröhn, J. Hartmann, L. Bronstein, *Angew. Chem. Int. Ed.* 36 (1997) 2080; (b) N. T. Whilton, B. Berton, L. Bronstein, H. Henze, M. Antonietti, *Adv. Mater.* 11 (1999) 12; (c) L. M. Bronstein, D. M.

Chernyshov, R. Karlinsey, J. M. Zwanziger, V. G. Matveeva, E. S. Sulman, G. N. Demidenko, H.-P. Hentze, M. Antonietti, *Chem. Mater.* 15 (2003) 2623.
12 (a) S. Xu, J. Zhang, C. Paquet, Y. Lin, E. Kumacheva, *Adv. Func. Mater.* 13 (2003) 468; (b) J. Zhang, S. Xu, E. Kumacheva, *J. Am. Chem. Soc.* 126 (2004) 7908; (c) I. Gorelikov, L. M. Field, E. Kumacheva, *J. Am. Chem. Soc.* 126 (2004) 15938; (d) J. Zhang, S. Xu, E. Kumacheva, *Adv. Mater.* 17 (2005) 2336.
13 (a) A. Biffis, *J. Mol. Catal. A: Chemical* 165 (2001) 303; (b) A. Biffis, N. Orlandi, B. Corain, *Adv. Mater.* 15 (2003) 1551; (c) A. Biffis, E. Sperotto, *Langmuir* 19 (2003) 9548; (d) L. Minati, A. Biffis, *Chem. Commun.* (2005) 1034; (e) A. Biffis, L. Minati, *J. Catal.* 236 (2005) 405.
14 (a) A. Pich, S. Bhattacharya, Y. Lu, V. Boyko, H.-J. P. Adler, *Langmuir* 20 (2004) 10706; (b) A. Pich, J. Hain, Y. Lu, V. Boyko, Y. Prots, H.-J. Adler, *Macromolecules* 38 (2005) 6610.
15 (a) N. B. Graham, UK Patent GB2090264b (1984); (b) N. B. Graham, J. Mao, A. Urquhart, *Angew. Makromol. Chem.* 240 (1996) 113; (c) N. B. Graham, A. Cameron, *Pure Appl. Chem.* 70 (1998) 1271.
16 K. E. J. Barrett, H. R. Thomas, in K. E. J. Barrett (ed.) *Dispersion Polymerization in Organic Media*, Wiley, London, 1975.
17 J. Brandrup, E. H. Immergut, E. A. Grulke (eds.) *Polymer Handbook*, 4th ed., Wiley, Hoboken, NJ, 1999.
18 Y. Lu, Y. Mei, M. Ballauff, M. Drechsler, *J. Phys. Chem. B* 110 (2006) 3930.
19 See for example: S. King, K. Hyunh, R. Tannenbaum, *J. Phys. Chem. B* 107 (2003) 12097 and references therein.
20 (a) Ch.-W. Chen, M.-Q. Chen, T. Serizawa, M. Akashi, *Chem. Commun.* (1998) 831; (b) M. Zecca, R. Fisera, G. Palma, S. Lora, M. Hronec, M. Kralik, *Chem. Eur. J.* 6 (2000) 1980.
21 L. Starkey Ott, B. J. Hornstein, R. G. Finke, *Langmuir* 22 (2006) 9357.
22 T. Teranishi, M. Miyake, *Chem. Mater.* 10 (1998) 594.
23 See for example: (a) M. Antonietti, S. Förster, S. Oestreich, *Macromol. Symp.* 121 (1997) 75 and references therein; (b) R. M. Crooks, M. Zhao, L. Sun, V. Chechik, L. K. Yeung, *Acc. Chem. Res.* 34 (2001) 181 and references therein.

CHAPTER 21

Magnetron Sputtering to Prepare Supported Metal Catalysts

Gabriel M. Veith, Andrew R. Lupini, and Nancy J. Dudney

Materials Science and Technology Division, Oak Ridge National Laboratory, Oak Ridge, TN 37831, United States of America

1. Introduction

Solution-based techniques are the dominant methodology for the preparation of catalytic nanoparticles [1]. The widespread use of solution synthetic methods is due to their simplicity, batch reproducibility (in well-developed systems like Pt), and low initial costs. In many instances these methods are less than ideal suffering from issues like: reproducibility (as in the case of supported gold catalysts) [2]; impurities affecting performance [3–5]; the expense of washing (potentially toxic) residual species off the catalyst and treating the waste stream; and the cost of precursors. In addition, classic solution-based methods, like impregnation, do not work for all catalysts systems, one of which is the supported gold catalyst. Since gold does not form a stable oxide, like for example platinum, it does not interact strongly with the oxide surface. When catalyst samples are annealed, residual chloride ions from the $HAuCl_4$ starting material act as mineralizers which, when coupled with elevated temperatures and the low melting point of gold (1064 °C) [6], promote the agglomeration of the gold nanoparticles [7]. This agglomeration is detrimental for the catalytic behavior since gold nanoparticles need to be smaller then ~5 nm for some reactions [5].

One solution-based approach that works for gold catalysts, in that it produces highly active catalysts, is the deposition–precipitation (DP) method [8]. The DP method entails adjusting the pH, temperature, and gold concentration of an $HAuCl_4$ solution to form a gold hydroxide species which is then deposited onto the support material [8]. This catalyst precursor is washed, dried, and annealed to form small (< 5 nm) catalyst particles [9]. The DP method has a number of limitations; for example, DP cannot produce Au particles with diameters less than 5 nm on support materials with low-isoelectric points (IEPs) like SiO_2 and WO_3 [5,10,11].

In order to investigate how the support material affects heterogenous gold catalysts, we sought a synthetic technique that could be easily applied to a variety of realistic bulk support materials, regardless of the surface properties. To accomplish this goal, we began developing the magnetron sputtering technique [12,13]. The magnetron sputtering technique entails the sputtering of a high purity metal target with an energetic argon ion. The sputtered metal species are then deposited onto the support surface where they form a nanoparticle. The sputtering method works well for the preparation of catalysts not easily obtainable from traditional solution methods.

Magnetron sputtering is one method, out of a group of methods, generally described as physical vapor deposition (PVD) techniques [14]. These techniques are widely used to prepare thin films and include evaporation, laser ablation, and sputtering. PVD processes involve the energetic removal of normally non-volatile species from a source material (target) by heating or energetic particle bombardment by ions, electrons, photons, or atoms [14]. The vaporized species are transported and deposited onto a support surface forming a film or island [14]. Synthetic processes based on PVD techniques should not be confused with chemical vapor deposition (CVD) methods. CVD techniques rely on the decomposition of an organometallic precursor to form a film or clusters. CVD techniques have been reported for the synthesis of supported catalyst and are reviewed by Serp et al. [15].

Magnetron sputtering offers a number of synthetic advantages, including: scalability, higher purity catalysts, accurate control of metal loadings, and solution-free synthesis, which could be useful when traditional chemical preparation methods fail for particular catalyst/support combinations. Since this technique relies on pure metal targets, there is no need for a reducing agent like sodium borohydride, wash treatments to remove residual reagents, or a high temperature reduction treatment. There are some drawbacks to this method, including the large initial costs associated with sputter equipment and high purity precious metal targets, as well as the cost of operating vacuum equipment, but for certain applications sputtering offers a distinct advantage over conventional preparation methods.

Metal Nanoclusters in Catalysis and Materials Science: The Issue of Size Control
Edited by B. Corain, G. Schmid and N. Toshima

There have been many reports in the literature where PVD techniques have been used to synthesize nanoparticles. These reports can be broken down into two categories: synthesis of bulk nanopowders and the synthesis of supported catalysts. The synthesis of bulk nanoparticles is accomplished from the gas phase condensation of the atomic vapor produced by a PVD technique [16,17]. The atomic vapor is cooled in a high-pressure gas mixture, up to about 0.2 torr, which promotes the nucleation and growth of nanoparticles [17,18]. The nanoparticles condense and can be collected off a cold trap or the reactor walls. This technique can produce a variety of complex oxides, such as TiO_2 and Cu_2O, from the sputtering of a metal target in an oxygen-containing atmosphere, with sizes between 5 and 50 nm [17,19]. There have been significantly fewer reports in the literature of a PVD technique being used to prepare supported nanoparticles. High energy (>50 keV) ion beam sputtering was first used to make supported nanoparticles [20,21]. Arrii et al. [22] reported the synthesis of catalytic nanoparticles by laser ablation. Diode-based sputtering has been reported for the synthesis of Pt and Cu nanoparticles [23–25]. One important difference between these previous studies is that we are using a magnetron-based source. Magnetron sources have a strong permanent magnet located behind the material being vaporized. This magnet confines the electrons produced in the plasma to a toroidal path close to the target surface increasing the probability of the electron interacting with the sputter gas to produce an ionized species and increasing the density of the plasma [14]. The introduction of the magnet also allows the source to operate at lower vacuum pressures, which when combined with the increased plasma density, significantly increases the deposition rates over other PVD techniques.

2. Synthesis Strategy

The goal of this work was to develop a support independent synthetic technique for the preparation of supported metal catalysts. There were three criteria that had to be simultaneously achieved:

(1) The technique had to be capable of quickly synthesizing catalytic nanoparticles – with diameters less than 5 nm – on a variety of support materials regardless of the material's IEP.
(2) The catalysts had to be free of residual impurities such as chloride ions, nitrates, solvent, or other precursor species.
(3) The technique had to be scaleable to synthesize large quantities with controllable weight loadings.

With these criteria in mind we modified an existing homemade vacuum deposition chamber (~0.07 m^3) in order to accommodate the powder support materials. A schematic of the components critical for the deposition is shown in Figure 1.

A 2-in diameter (5.1 cm) magnetron sputter source (Kurt J. Lesker – Torus type magnetron source) was fed into the top of the deposition chamber and positioned 12 cm above a custom made (~120 cm^3) stainless steel (SS) cup. This SS cup was attached to a vacuum compatible motor and tilted 45° from vertical. Two Teflon coated stir bars (<1.5 inches long) and the catalyst support were added to a second, smaller custom made SS cup (~60 cm^3). The Teflon stir bars were used to breakup agglomerates of the substrate material during the deposition. The SS cups were rotated between 43 and 48 RPM causing the powders to tumble constantly exposing a new region of the support material. The deposition chamber was evacuated, using a turbo pump, until an initial vacuum of 3.0×10^{-6} torr or better was obtained. A gate valve between the turbo pump and sample chamber was used to slow the rate of air egress from the deposition chamber during the initial pump down. Without a restricted pump down, the powder supports may be sucked out of the cup.

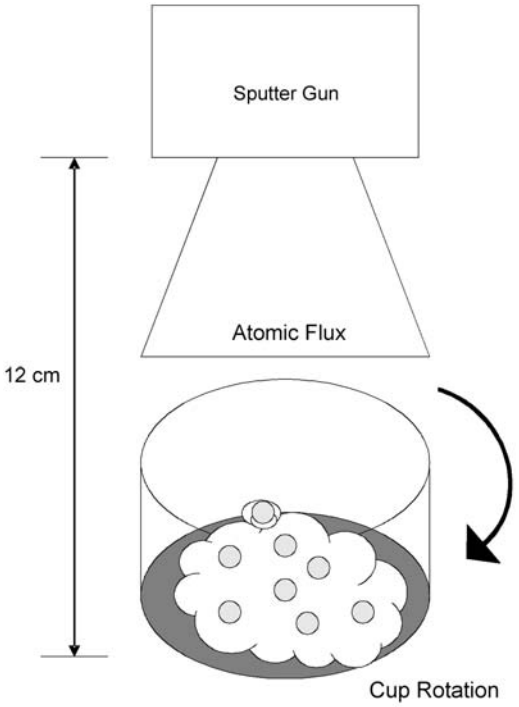

Figure 1. Schematic of the deposition apparatus.

Commercially produced high purity (>99.995%) precious metal sputtering targets were used for this work. High purity argon (Research Grade, 99.9995%) was used as the sputtering gas. The Ar was introduced into the chamber at a rate of 10.7 standard cubic centimeters per minute (sccm) and the total pressure of the system was fixed at 14.9 mtorr (0.02 mbar). The gold target was sputtered at an applied direct current (d.c.) power of 11 W, while the Pt target was sputtered at an applied d.c. power of 40 W. At the end of the deposition process some of the support material was stuck to the side of the SS cup, while most of the powder was freely tumbling. In order to collect the powder the SS cup was inverted onto a piece of weighing paper. The powder stuck to the side remained in the cup and was not used for the subsequent work.

Metal loading was controlled by varying the deposition time and the amount of support material loaded into the cup. Since the flux of sputtered atoms and the amount of

freely tumbling support material is generally consistent from deposition to deposition, a calibration plot can be constructed and the weight loading can be controlled by fixing the deposition time to the predicted value from the calibration plot. Actual weight loadings are usually within 1% of the predicted values. Between 1 and 4 g of catalysts can be made in a batch using this set up. The amount of catalyst prepared is a function of the density of the support material, how well it tumbles, and volume of the SS cup. Typical depositions require 1–4 h.

2.1. Characterization

Electron microscopy has been the most important analytical tool to study the particle sizes. Powder X-ray diffraction only works at very high weight loadings (>6 wt%) and chemisorption techniques do not work for gold nanoparticles. We imaged the gold clusters with a VG Microscopes HB603 UHV STEM operating at 300 kV equipped with a Nion Co. aberration corrector. The 603 system has been shown to have a resolution of better than 0.8 Å [26], although the main reason for using it was sensitivity. The relative brightness of a high angle annular dark field (HAADF) Z-contrast [27,28] image obtained on this instrument depends on the thickness and approximately the square of the atomic number. This mode is particularly suitable for investigating catalyst samples, especially those supported on carbon, because even the smallest nanoparticles, including single gold atoms, are visible on real supports that can be up to several nanometers thick. The Pt clusters were imaged with a Hitachi field emission gun transmission electron microscope (FEG-TEM) HF2000 operated at 200 kV and a Hitachi HD-2000 FEG scanning transmission electron microscope (FEG-STEM) operated in HAADF mode at 200 kV. Histograms of the catalyst cluster size were obtained by measuring the widest part of the nanoparticle in the microscopy data. Other characterization techniques are described in previous publications [13].

3. Results

The method described above has been used to prepare a variety of supported catalytic nanoparticles. In all the studies presented below the argon pressure and target –substrate distance was the same. One feature of the nanoparticles prepared in these studies is that they are preferentially formed on the outer surface of the support material, rather than within the pores of the supports or interior of the powder agglomerates. Whereas techniques such as impregnation tends to form catalysts particle within pores, vapor deposited particles are more likely formed on exterior surfaces unless the sticking coefficient is very low. Using the sputtering technique, we found that the noble metals were deposited in very homogeneous clusters ranging from single atoms to nanoparticles with average diameters less than 7 nm. We have also applied this technique to prepare a variety of non-noble metal catalyst such as tin and copper. All the samples presented below were found to be either catalytic towards the oxidation of carbon monoxide (Au/WO_3), the oxidation of glycerol (Au/C), or electrocatalytic in a proton exchange membrane fuel cell (Pt/C).

3.1. Deposition of Au onto Acidic WO_3

WO_3 is a reducible, narrow band gap oxide like TiO_2. The IEP of WO_3 is substantially less than 1, compared to 4.5–6 for TiO_2, making it impossible to apply DP to prepare Au catalysts on this support [10,11]. Investigating this support material may help provide insight into how the surface acidity of an easily reducible oxide support affects the catalytic oxidation of CO [29]. A 0.5 wt% Au–WO_3 sample was prepared by depositing Au onto tumbling WO_3 powder for 260 min. A STEM image of the Au–WO_3 sample is shown in Figure 2.

The average gold particle size was estimated to be about 2.1 nm. Gold particles were distinguished from the WO_3 support due to the concentration of heavy gold atoms, though a limited number of particles could be investigated due to the thickness of the WO_3. Analysis of the WO_3 supported gold particle sizes may underestimate the size of the gold nanoparticles, or miss some of the smallest particles because there is less contrast against the heavy support. The STEM image reveals that while there are a few larger gold particles (4–6 nm in diameter) magnetron sputtering successfully prepared a high concentration of small gold nanoparticles (<2.5 nm). This result demonstrates the utility of this technique. Without this method it would be very difficult to synthesize gold nanoparticles on WO_3.

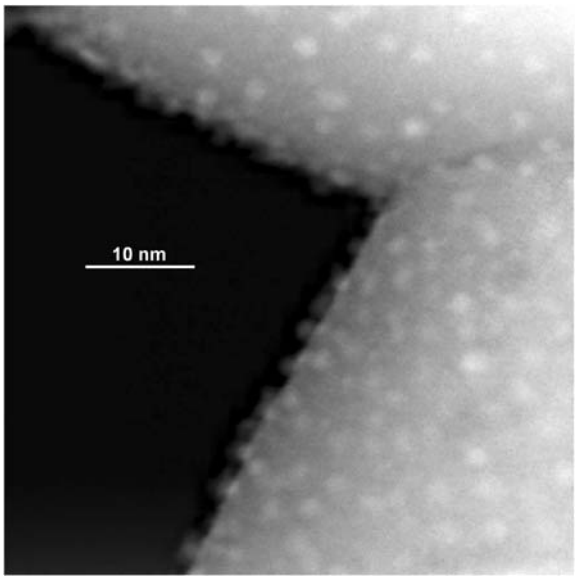

Figure 2. Z-contrast STEM image of the Au on WO_3 sample. The gold nanoparticles are the white spots on the WO_3 surface. The contrast of the small gold particles has been enhanced and the image smoothed, so that small particles are visible, despite the lack of contrast to the background. (Reprinted from Topics in Catalysis, 122(1) 2007, pg 248, with permission from Elsevier Science.)

4. A Case History

In this section we will discuss two studies that were performed to investigate factors which may effect particle size control: (1) the type of support material and (2) the weight loading.

4.1. Au Deposited onto Carbon

In order to gauge how the support affects the final particle sizes a set of experiments was performed where the same gold loadings (0.7 wt%) was deposited onto three different carbon supports. The three support materials were: (1) activated carbon from Camel (X40S; SA = 1100–1200 m^2/g; pH 8–9), (2) a decolorizing carbon from Aldrich (SA = 700 m^2/g), and (3) graphite from Alfa Aesar (Natural, Microcrystal grade, APS 2–15 μm, 99.9995%; SA = 2 m^2/g). The deposition times varied for each support material due to differences in the amount of material stuck to the side of the SS cups, but were generally about 1 h for each sample.

These experiments demonstrate the critical role the support material plays in determining the particle sizes for the sputtered catalyst. Figure 3(a) and (b) show representative images of gold deposited on the X40S activated carbon. Figure 3(c) and (d) present STEM data for gold deposited on the graphite and decolorizing carbon respectively.

Histograms of gold particle size distributions are shown in Figure 4.

Gold clusters deposited on the activated carbon had the smallest average diameter of 1.7 nm, while gold on graphite and decolorizing carbon had average particle sizes of 2.8 and 6.8 nm respectively.

The presence of both single gold atoms and gold clusters, evident in Figure 3(b), indicates that the deposition flux is largely atomic or very small clusters as expected from the process gas pressure.

The activated carbon apparently has enough nucleation sites or the correct functionalized surface sites to trap some of these single atoms before they can be incorporated into nanoparticles.

In contrast, using graphite, with its lower concentration of surface functional groups, compared to activated carbon [30], results in gold particles with a larger average diameter (d = 2.8 nm), Figure 3(c). One interesting aspect of the Au–graphite by sputtering is that there is a large concentration of gold nanoparticles along the step edges of the graphite sheets (Figure 3c), which would be the most probable place for the atoms to nucleate and grow [31].

It is unknown at this point why the gold particles on the decolorizing carbon had the largest average particle size. The decolorizing carbon had a surface area comparable to the X40S but the surface chemistry has not been studied. Previous studies have demonstrated the critical role carbon support properties have on the properties of

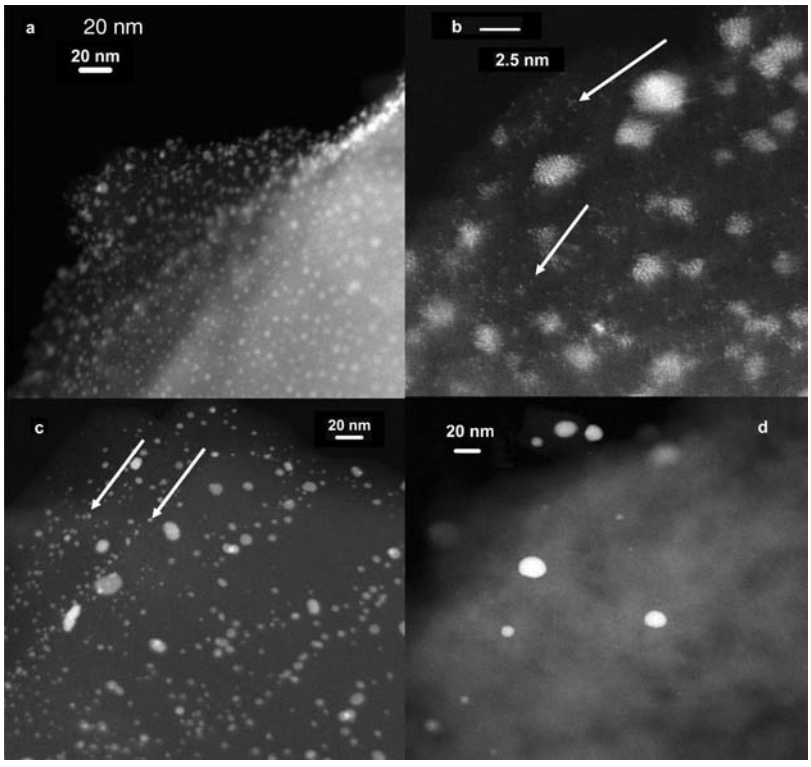

Figure 3. HAADF STEM images of Au deposited onto various carbon supports: X40S activated carbon (a, b); graphite powder (c); decolorizing carbon (d). Arrows highlight single gold atoms (b) and gold along the graphite step edges (c). (Partially reprinted from Topics in Catalysis, 122(1) 2007, pg 248, with permission from Elsevier Science).

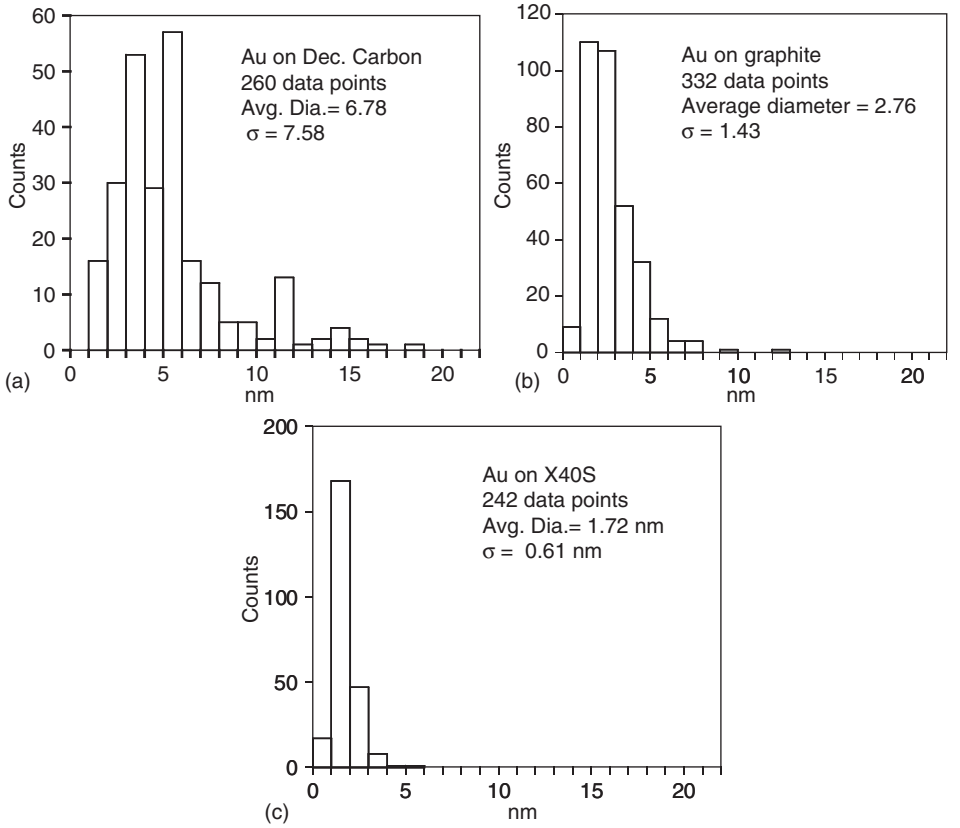

Figure 4. Particle size histograms for the gold deposited onto various carbon samples. (Partially reprinted from Topics in Catalysis, 122 (1) 2007, pg 248, with permission from Elsevier Science).

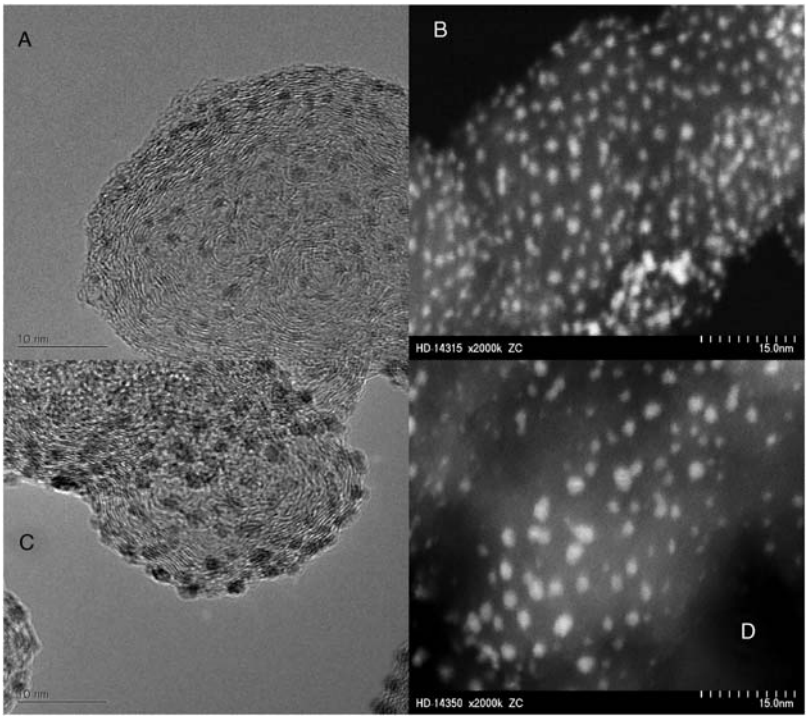

Figure 5. BF-TEM image of 1.1 wt% Pt (A); HAADF STEM image of 3.1 wt% Pt (B); BF-TEM image and HAADF STEM images of 11.1 wt% Pt (C and D respectively). Images were collected on the Hitachi microscopes.

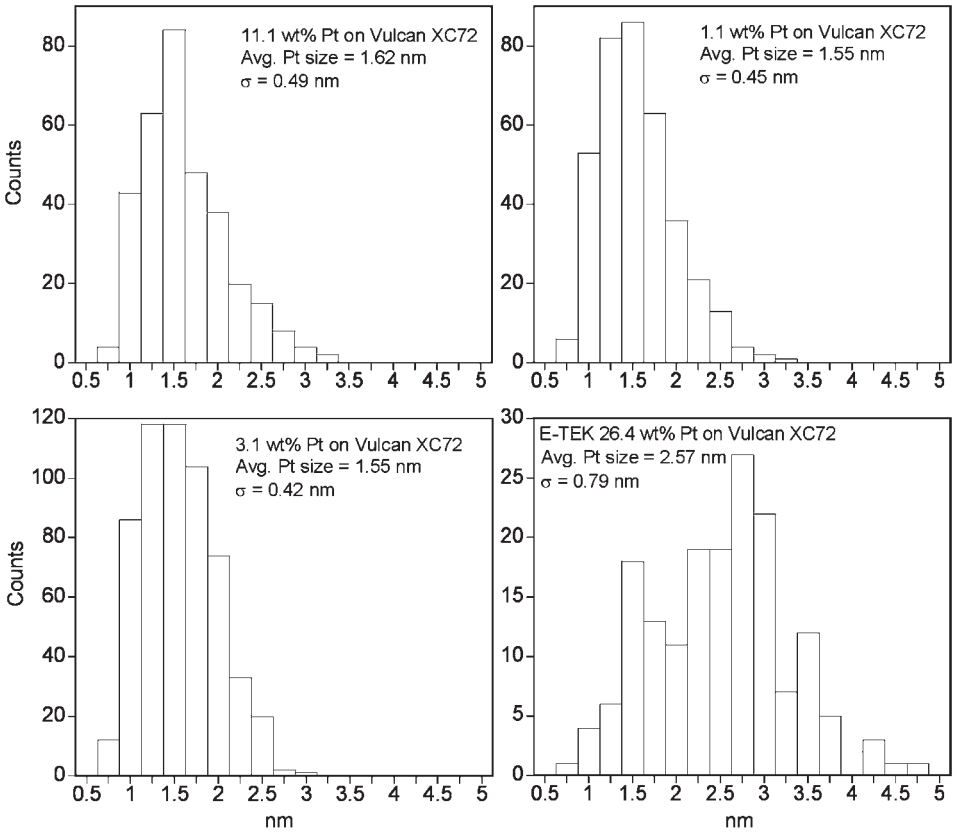

Figure 6. Pt particle size distributions measured from TEM images.

the catalyst [32], and presumably similar surface chemistry is critical for the growth of the nanoparticles.

4.2. *Pt on Carbon Black [33]*

In order to determine what effect increasing the weight loading has on the average particle size, we prepared a series of Pt/C electrocatalysts by varying the deposition time. Pt was deposited onto Vulcan XC-72 carbon black (Cabot, surface area 235 m^2/g). Samples were prepared with Pt weight loadings between 1.1 and 11.1 wt% Pt. Representative TEM and HAADF STEM images of these samples are shown in Figure 5.

Pt particle size distributions (histograms) measured directly from TEM images are shown in Figure 6.

These particle size distributions reveal that the average Pt particle size for all three samples prepared by sputtering was about 1.6 nm and independent of weight loading.

For comparison, a 20 wt% Pt/XC72 catalysts prepared commercially by E-TEK had an average diameter of 2.6 nm. The sputter deposited Pt had a standard deviation between 0.42 and 0.49 nm, whereas the commercial E-TEK catalyst has a standard deviation of 0.79 nm. Thus, the sputtering technique creates smaller and more uniformly dispersed Pt particles than those prepared chemically. It should be noted that the Pt/C samples having low loadings prepared via sputtering did not uniformly coat the entire carbon support, but the Pt coverage could be improved by modifying the method of tumbling the carbon powder.

5. Conclusions

From the results presented above we can derive the following:

1. The magnetron sputtering technique can prepare supported metal nanoparticles on a wide variety of support materials including WO_3 and carbon.
2. Changes in the substrate result in changes in particle size distributions, but almost always results in a narrow distribution of nanoparticle sizes.
3. Increasing the weight loading of the sample results in an increase in the number of particles, but up to 11 wt% has little effect on the particle size distribution.

It should be stressed that all of the depositions described above were performed at the same background pressure, substrate to target distance, tumbling speeds and powers. It is unknown at this point what affect changing these conditions will have on the produced nanoparticles. There are also additional parameters which could be adjusted which may have an affect on the particle size distribution. These parameters include the type of deposition

(d.c. vs. radio frequency), the concentration and type of active sites on the surface of the activated carbons, the method used to tumble the powders, as well as the use of unbalanced magnetron sputtering to promote the formation of defects on the support surfaces. Beyond simply controlling the particle size, active fields of research include the possibility of synthesizing alloy catalysts and complex oxides by sputtering.

References

1 B. Cushing, V. L. Kolesnichenko, C. J. O'Connor, *Chem. Rev.* 104 (2004) 3893.
2 A. Wolf, F. Schüth, *Appl. Catal. A: Gen.* 226 (2002) 1.
3 T. J. Schmidt, U. A. Paulus, H. A. Gasteiger, R. J. Behm, *J. Electroanal. Chem.* 508 (2001) 41.
4 H. H. Kung, M. C. Kung, C. K. Costello, *J. Catal.* 216 (2003) 425.
5 M. Haruta, *J. New Mater. Electrochem. Syst.* 7 (2004) 163.
6 D. R. Lide, (ed.) *CRC Handbook of Chemistry and Physics*, 78th ed., 1997.
7 M. B. Cortie, E. van der Lingen, *Mater. Forum* 26 (2002) 1.
8 M. Haruta, *CATTECH* 6 (2002) 102.
9 F. Moreau, G. C. Bond, A. O. Taylor, *J. Catal.* 231 (2005) 105.
10 S. E. S. El Wakkad, H. A. Rizk, *J. Phys. Chem.* 61 (1957) 494.
11 G. A. Parks, *Chem. Rev.* 65 (1965) 177.
12 G. M. Veith, A. R. Lupini, S. J. Pennycook, N. J. Dudney, in E. Gaigneaux (ed.) *Studies in Surface Science and Catalysis*, 2006, 71.
13 G. M. Veith, A. R. Lupini, S. J. Pennycook, G. W. Ownby, N. J. Dudney, *J. Catal.* 231 (2005) 151.
14 S. M. Rossnagel, *J. Vac. Sci. Technol. A* 21 (2003) S74.
15 P. Serp, P. Kalck, R. Feurer, *Chem. Rev.* 102 (2002) 3085.
16 M. T. Swihart, *Curr. Opin. Colloid Interface Sci.* 8 (2003) 127.
17 M. Ullmann, S. K. Friedlander, A. Schmidt-Ott, *J. Nanopart. Res.* 4 (2002) 499.
18 C. Xirouchaki, R. E. Palmer, *Phil. Trans. R. Soc. Lond. A* 362 (2004) 117.
19 P. Ayyub, R. Chandra, P. Taneja, A. K. Sharma, R. Pinto, *Appl. Phys. A* 73 (2001) 67.
20 W. Ensinger, H. R. Müller, *Surf. Coat. Technol.* 163–164 (2003) 281.
21 J. A. Cairns, R. S. Nelson, R. W. Barnfield, USA 4,046,712 (1977).
22 S. Arrii, F. Morfin, A. J. Renouprez, J. L. Rousset, *J. Am. Chem. Soc.* 126 (2004) 1199.
23 A. Takeuchi, H. Wise, *J. Catal.* 83 (1983) 477.
24 P. Albers, K. Seibold, A. J. McEvoy, J. Kiwi, *J. Phys. Chem.* 93 (1989) 1510.
25 B. Wang, Z. Ji, F. T. Zimone, G. M. Janowski, J. M. Rigsbee, *Surf. Coat. Technol.* 91 (1997) 64.
26 P. D. Nellist, M. F. Chisholm, N. Dellby, O. L. Krivanek, M. F. Murfitt, Z. S. Szilagyi, A. R. Lupini, A. Borisevich, W. H. Sides Jr., S. J. Pennycook, *Science* 305 (2004) 1741.
27 S. J. Pennycook, P. D. Nellist, in D. G. Rickerby, U. Valdré, G. Valdré (eds.) *Impact of Electron and Scanning Probe Microscopy on Materials Research*, Kluwer Academic Publishers, Dordrect, The Netherlands, 1999, 166.
28 P. D. Nellist, S. J. Pennycook, *Adv. Img. Elect. Phys.* 113 (2000) 147.
29 M. M. Schubert, S. Hackenberg, A. C. van Veen, M. Muhler, V. Plzak, R. J. Behm, *J. Catal.* 197 (2001) 113.
30 E. Auer, A. Freund, J. Pietsch, T. Tacke, *Appl. Catal. A: Gen.* 173 (1998) 259.
31 J. A. Venables, G. D. T. Spiller, M. Hanbücken, *Rep. Prog. Phys.* 47 (1984) 399.
32 C. L. Bianchi, S. Biella, A. Gervasini, L. Prati, M. Rossi, *Catal. Lett.* 85 (2002) 91.
33 G. M. Veith, J. Sayre, K. L. More, N. J. Dudney, *In-preparation*.

This page intentionally left blank

CHAPTER 22

Gold Colloidal Nanoparticles Sized to be Suitable Precursors for Heterogeneous Catalysts

F. Porta and L. Prati

Department CIMA, Centre of Excellence CIMAINA, INSTM Unit, University of Milano, Milano, Italy

1. Introduction

Gold has been recently demonstrated to be active in many catalytic reactions as reviewed by Bond and Thompson [1]. However, as highlighted by Haruta [2], many different parameters play a role in determining activity (i.e. particle size and shape, preparation methods, nature of support) sometimes making difficult the comparison of experimental results. For example, catalytic activity evaluated against different units showed different trends, showing convincingly that beside total surface area, some other size-dependent factor has to be involved.

The activity of gold catalyst is normally strongly size dependent and the control as well as the narrowest possible distribution of particle size represent the main goal for the production of an active gold catalyst. From a catalytic point of view, several preparation methods have been proposed for obtaining highly dispersed gold catalyst, most of them derived from deposition–precipitation method proposed by Haruta et al. [3].

Quite recently gold metallic sols have been used as precursors [4,5] for preparing heterogeneous catalysts. The advantage of using this technique principally lies in the applicability regardless of the type of support employed and the possible control on particle size/distribution, obtaining normally highly dispersed metal catalyst.

The techniques of metal colloid chemistry have been increasingly applied to the preparation of metals in highly dispersed form. The use of solutions of molecular precursors as starting materials and mild chemical treatment for the generation of metal particles in principle leads to a careful control of composition, size and morphology of the resulting particles [6,7]. Common procedures include: reduction of metal salts, photochemical or thermal decomposition and reduction of organometallic complexes [7,8]. Preparation of gold sols has been reviewed elsewhere [9]. For catalytic applications some constrains have to be taken into account; particularly, particle size has to be ranged from 2 to 25 nm, sols have to show a good stability under operative conditions, sols have to show an as long as possible catalyst life, i.e. sols have to be recycled.

In this paper, suitable gold sol preparations designed for catalytic purposes that fulfil the above-reported prerequisites have been reported.

2. Synthetic Strategy

Colloidal gold is a lypophobic sol. The gold particle is surrounded by a cloud of adsorbed ions/molecules whose presence is responsible for the stability of the colloid. Particles of colloidal gold carry a negative charge in water, due to surface adsorbed anions (mainly $AuCl_4^-$ and $AuCl_2^-$ in the case of $NaBH_4$ reduction) [10]. A considerable advance in the understanding of the behaviour of these systems was given by theory of Derjaguin, Verway, Landau and Overbeek (DVLO) [11,12]. In this assumption, the stability of the particle is considered to consist of two components: one arises from the overlap of the electrical double layer and leads to repulsion, the other from electromagnetic effects and leads to van der Waals attraction. The curve of potential energy of interaction against the distance of the particle surfaces is schematically represented in Figure 1.

At a finite distance, where the surface does not come into molecular contact, equilibrium is reached between electrodynamic attractive and electrostatic repulsive forces (secondary minimum). At smaller distance there is a net energy barrier. Once overcome, the combination of strong short-range electrostatic repulsive forces and van der Waals attractive forces leads to a deep primary minimum. Both the height of the barrier and secondary minimum depend on the ionic strength and electrostatic charges. The energy barrier is decreased in the presence of electrolytes (monovalent < divalent < trivalent) by compression of the double layer [8].

Thus the stability of a colloid is a function of the energy of interaction between the particles. The conventional strategies for the preparation of small precious metal

Metal Nanoclusters in Catalysis and Materials Science: The Issue of Size Control
Edited by B. Corain, G. Schmid and N. Toshima

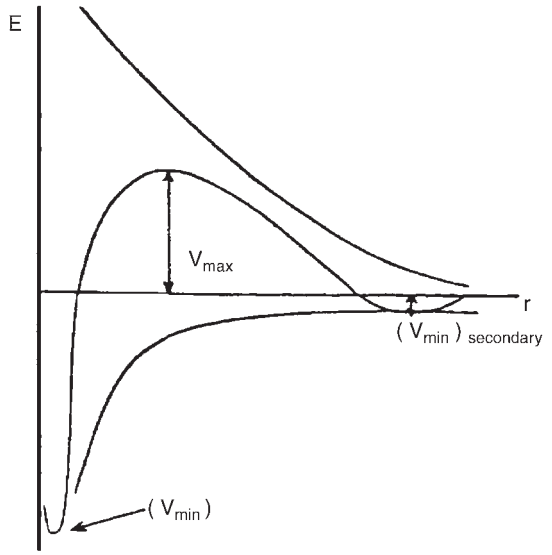

Figure 1. Attractive and repulsive forces.

nanoparticle in the presence of protective agent have been greatly developed in the last decade [9]. However stabilizer-free nanosized gold sols have been reported [13]. "Unprotected" metal colloids do not mean that the gold particles are truly bare: they are stabilized by solvents or simple anions adsorbed on them, or by both. "Naked" colloidal gold solutions have been prepared in toluene using a two-phase system. The phase-transfer reagent used, a quaternary ammonium bromide salt ($R_4N^+Br^-$), is specifically adsorbed on the clusters through the formation of surface ion pairs, probably with the Br^- ion attached to the Au surface [14]. Moreover, unsupported gold particles have been studied in aerobic oxidation of glucose and it has been found that they behave as an efficient catalyst, showing a similar activity to enzymatic systems. In particular, the catalytic activity has been found to be inversely proportional to the particle diameter [15].

For improving their resistance against coagulation, aqueous colloidal solution of metal particles have been stabilized by three methods: (a) surface potential and/or charge density are increased by the adsorption of surface active long-chain ions (i.e. surfactants); (b) van der Walls forces are reduced by adsorption of relatively rigid hydrophilic macromolecules (i.e. dextrin, starch); (c) besides these stabilizing effects depending on Coulomb or van der Waals forces, a third type of stabilization, "steric stabilization", has been considered [16]. The term is related to the absorption of flexible polymers of sufficiently high molecular weight, which leads to polymer chains protruding from the particle surfaces. The slight interpenetration of these chains, elongating from colliding particles, keeps them at a distance too large to give a van der Waals interaction sufficient for coherence [17]. This type of stabilization was confirmed using gold particles as test system and polyglycols as absorptive; the stabilization was found to increase with polymer concentration and particularly with the molecular weight of the polymer [16]. Macromolecules, such as proteins and polysaccharides and various synthetic polymers were also used [18]. The adsorbed layer of stabilizer prevents cohesion of one particle to another and the lypophobic gold colloid becomes lypophilic. In general, the lypophilic stabilizers give metal colloids stable in organic media, while hydrophilic agents yield water-stable colloids.

In general, the most used stabilizers are polymers [19], molecules coordinating through P and S atoms [20], long-chain alcohols [21], surfactants [22] and organometallics [23].

3. Results

3.1. Preparation of Gold Sols

Several stabilized hydrosols obtained from aqueous solutions of $HAuCl_4$ or $NaAuCl_4$ precursors (typically in the concentration range of $3–5\times10^{-4}$ M), in the presence of various stabilizers and reducing agents, have been reported contributing to the wide field of colloidal gold chemistry. In particular, the aim of some of these preparations was their use as precursors for heterogeneous catalyst. Thus, the immobilization of nanoparticle on support, the consecutive step after sol generation, was deeply investigated.

3.1.1. Stabilizers

Among the polymeric stabilizers, Brij35 (polyoxyethylene(23)-laurylether, MW_{av} 1200) [24], PVA (polyvinyl alcohol, MW 13,000–23,000, 98% hydrolyzed) [25], PEG (poly(ethylene glycol), reacted with bisphenol A diglycidyl ether, MW 15,000–20,000) [24] and PVP (polyvinylpyrrolidone, MW_{av} 55,000) [26], have been experienced to influence the stability of the gold sol by steric stabilization, taking into account the effect of the increasing average molecular weight. Moreover, long-chain alcohols of 15,000–20,000 Da, like PVA, are suitable stabilizers for nanoparticles of 3–8 nm mean diameter [7,25]. Typically, the amount of protector has been maintained at a weight stabilizer/Au ratio equal to one. The use of higher values of the ratio produces a high coverage of the particles that could further inhibit the catalytic behaviour. Dextrin has been experimented as a rigid hydroxyl protective agent, affecting the attractive van der Waals forces. Small sizes of nanoparticles have been obtained with water-stable sols (2–3 nm), but not greatly affecting the catalysis [24]. Better results have been achieved by increasing the surface potential and/or charge density by absorption of ionic surfactants such as polydiallyl dimethyl ammonium chloride, PDDA, [25b] and the polyion PEU (poly[bis(chloroethyl)ether-alt-1,3-bis-[3-(dimethylamino) propyl]urea) [24] and sulphobetaines, such as *N*-dodecil-*N*,*N*-dimethyl-3-amino-1-propanesulphonate [27]. This last represents a special case of stabilizer. In fact, it was demonstrated for Pt that colloidal nanoparticles (average size 2.8 nm) are surrounded by a double layer of the zwitterionic carboxybetaine (3–5 nm) [28]. The hydrophilic head group of betaine interacts with the charged metal surface and the lypophilic tail is associated with the tail of

a second surfactant molecule, resulting in the formation of a hydrophilic outer sphere.

The polycationic ammonium salt PEU can be chosen for increasing the ionic cloud in the electrical double layer, thus raising the electric repulsion between the gold particles in the sol. Small particles can be obtained (mean diameters between 3.1 and 4.2 nm) [24].

3.1.2. Reducing Agents

The main advantage of the salt reduction method in the liquid phase is that it is reproducible and allows colloidal nanoparticles with narrow size distribution to be prepared.

Schmid et al. introduced the diborane reducing agent for the synthesis of Au_{55} nanocluster stabilized by phosphine ligands [20,29]. The alcoholic reduction preparation, in the presence of PVP and PVA polymers, was developed mainly by Hirai and Toshima, exploiting the easy reduction of alcohol to aldehyde [19,30]. The H_2 reduction was applied mainly by Moiseev's for the "giant palladium cluster" [31] and Finke's for polyoxo and tetrabutylammonium iridium clusters [6,32,33]. The use of in situ hydrolysis of tetrakis(hydroxymethyl)phosphonium chloride (THPC) as a reducing agent was recently introduced [34] and allows the synthesis of small monodispersed gold nanoparticles (3 nm). The tetraalkyl ammonium hydrotriorganoborates route (combined with the use of surfactants) was intensely developed by Bönnemann [22,23,32,35]. Reetz et al. have reported the use of alkylammonium carboxylate ($NR_4^+RCO_2^-$) as both reducing agent and stabilizer [36]. Moreover the use of $NaBH_4$, a powerful reagent for the reduction of metal salts, has been developed in this last decade [7,25]. In the case of gold nanoparticles, the presence of the by-product metal borides was found not to affect the catalytic results. The Au/BH_4^- molar ratio was optimized and an excess corresponding to 1:3 was used with respect to the overall stoichiometry:

$$8\,AuCl_4^- + 3\,BH_4^- + 24\,OH^- \rightarrow 8\,Au + 32\,Cl^- + 3\,H_2BO_3^- + 15\,H_2O \quad (1)$$

Thus a typical preparation of PVA-protected gold sol is reported. $NaAuCl_4 \cdot 2H_2O$ (17.06 mg, 0.043 mmol) and PVA (410 μL of a 2% (wt/wt) stock aqueous solution) were added to 130 mL of MilliQ water. After 3 min, $NaBH_4$ (1.3 mL of a 0.1 M solution) was added to the yellow solution under vigorous magnetic stirring. The ruby red Au(0) sol was immediately formed. The UV–vis spectra of the precursor $NaAuCl_4$ and the final sol were recorded in H_2O, observing the $AuCl_4^-$ band at 222 nm and the Au(0) sol plasmon resonance peak at 510 nm.

3.2. Immobilization on Support

After few minutes of gold sol preparation, metal particles have to be immobilized on a suitable support for practical purpose. Normally this step is simply performed by dipping the support in the sol. The metal particles are spontaneously adsorbed from the solution. The kinetics of adsorption depends on sol stabilizer and on point of zero charge (PZC) and surface area of support. An inductively coupled plasma (ICP) measurement of residual metal in the solution gives the actual loading on the support. For example, in the case of PEU an incomplete absorption has been observed when a PEU/Au > 0.3 was used [37]. Also the maintenance of particle dimension during the immobilizing step depends on the same parameters. Table 1 reports the comparison of particle dimension in the sol and on the support as function of stabilizer (type and amount) and support.

Table 1. Characteristics of Au/support catalysts.

Stabilizer	Stabilizer/Au (wt/wt)	Particle dimension (sol)	Support	Particle dimension (supported)
THPC	0.8	4.0	Al_2O_3	3.9
			TiO_2	4.1
			C	8.6
	1	3.5	Al_2O_3	3.80
			TiO_2	3.71
			C	8.16
	2	2.71	Al_2O_3	4.3
			TiO_2	4.2
			C	4.2
PVA	0.62	5.2	Al_2O_3	4.8
			TiO_2	5.0
			C	5.6
		8.0	Al_2O_3	7.2
			TiO_2	6.8
			C	7.5
		26	Al_2O_3	24
			TiO_2	26
			C	23

As it is shown, different support differently influences the transferring of the metal particles. In the case of THPC, the particle dimension in the sol is maintained only when a high THPC/Au ratio is used, especially in the case of carbon as the support. A more bulky stabilizer as PVA provided in contrast a good stability of dimension during the immobilization step.

Carbon as the support has been deeply studied, and it has been noted that its coupling with PVA represents the best choice, assuring a quite large range of PVA/Au ratio and a good stability of gold particles. Table 2 shows the different behaviour of differently stabilized sols.

From a catalytic point of view, the particle dimension represents for sure an important factor but not the only one. In fact the nature of the support, the possible presence of residual stabilizing agent, metallic dispersion and accessibility of active phase by the reactant are also important.

4. A Case History

Glycerol has attracted attention as a usable starting material because of its easy availability (biosustainable sources) and its high functionalization. In addition,

growing programs for biodiesel fuels resulted in a production of large amounts of glycerol as a co-product. As a consequence, new applications for glycerol should be taken into account. Valuable products can be obtained by oxidation, thus selective oxidation of glycerol has been recently studied [38,39]. Given its high boiling point, the selective oxidation of glycerol with air/oxygen is usually carried out in liquid phase using water as the solvent and the compulsory presence of a base (NaOH).

Table 2. Immobilization step using carbon as the support.

Stabilizer	Stabilizer/Au (wt/wt)	Particle dimension (sol)	Particle dimension (supported)
THPC	0.8	4.0	8.6
	1	3.5	8.16
	2	2.71	4.2
PVA	0.62	5.2	5.6
	0.62	8.0	7.5
	0.62	26	23
PEG	0.3	5.3	14
	1	5.2	12
$C_{12}E_{23}$	0.3	5.3	8.2
	1	5.1	7.0
	1.8	4.3	7.0
Dextrin	0.3	3.5	12
	1	3.6	8.4
	1.8	2.8	9.5
PEU	0.3	3.1	4.7
PDDA	0.1	3.6	27
	0.3	2.8	22
	0.65	2.6	15

Au/C was established to be a good candidate for selective oxidation carried out in liquid phase showing a higher resistance to poisoning with respect to classical Pd- or Pt-based catalysts [40]. The reaction pathway for glycerol oxidation (Scheme 1) is complicated as consecutive or parallel reactions could take place. Moreover, in the presence of a base interconversion between different products through keto–enolic equilibria could be possible.

In the presence of Au/C catalyst, the reaction pathway was studied concluding that glycerate/tartronate amounts represents the probe of path 'a' and glycolate of path 'b' [41c] (Scheme 1). The overall selectivity of the reaction is dictated by the balance of path 'a' and 'b' and represents the most valuable parameter to be considered for evaluating the effectiveness of a catalyst.

Therefore, by using the sol technique different 1% Au/C catalysts have been prepared using the same supporting material (activated carbon) but varying the preparation method with the aim of changing the particle size. PVA/$NaBH_4$, THPC/NaOH and citrate methods were used (Table 3) obtaining sol of different mean size in the order citrate > PVA > THPC.

After supporting these sols on activated carbon, however, the obtained particle size depends on the capability of the protective agent to maintain the particle dimension. The obtained three catalysts, having different characteristics, are summarized in Table 3. As it is shown, mean size of gold nanoparticle obtained by TEM measurement did not always match with X-ray powder diffraction (XRPD) data. This result is not surprising as TEM measurements represent particle sizes, whereas from X-ray diffraction (XRD) it is possible to obtain crystallite dimensions that do not necessarily coincide with the size of

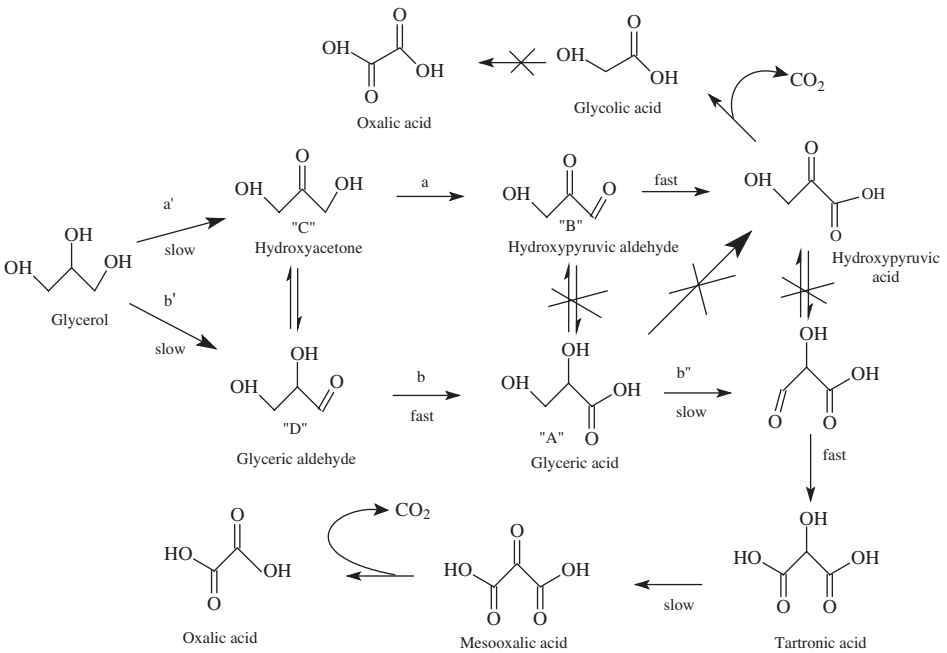

Scheme 1. Reaction pathways for glycerol oxidation with Au/C in the presence of a base. (Reprinted from Ref. [40], © 2004, with permission from Elsevier.)

Table 3. Selective oxidation of glycerol using 1%Au/C catalyst prepared via sol immobilisation.

Protective agent	*d* (nm)		Selectivity		Activity
	(XRPD)	(HRTEM)	S50[a]	S90[b]	TOF (h^{-1})
PVA	3	5	47	35	670
THPC	5.7	15	52	45	350
Citrate	7.4	21	75	75	300
Citrate-CALC[c]	10	30	90	89	198

Note: Reaction conditions: glycerol 10 wt%; glycerol/Au = 500; glycerol/NaOH = 1; T = 60 °C; pO_2 = 3 atm.
[a]Selectivity at 50% conversion.
[b]Selectivity at 90% conversion.
[c]Calcination was carried out in air at 150 °C for 6 h.

catalytically active particle. Thus, information can be obtained about metal particles through TEM and about their crystallinity from XRPD. The immobilization of PVA-protected sol as expected produced the most ordered particle, but evaluation of catalyst activities in the selective oxidation of glycerol follow the normal trend expected in heterogeneous catalysis (Table 3) (turnover frequency (TOF) increases by decreasing particle size) based on TEM results. However, the aim of the study was not finding a ''very'' active catalyst but a ''very'' selective one. By looking at selectivity data obtained at 50 and 90% conversion (S50 and S90 of Table 3), it can be observed there is an increase of selectivity to glycerate from 47 up to 75% by increasing particle size from 5 to ~20 nm. Conversely, as expected, catalyst activity decreased. For confirming this trend also a test using a calcined catalyst (150 °C, 6 h, air) has been carried out as it is worth noting that this method could increase particle size. In fact 30 nm-mean sized particles have been obtained that showed a low catalytic activity but selectivity to glycerate of 90%. Moreover, by adjusting reaction conditions, a 92% selectivity [41] has been reached.

From product distribution analysis it could be concluded that larger particles present higher selectivity to glycerate due to the reduction of consecutive reaction, i.e. oxidation of glycerate to tartronate, remaining glycolate amount being almost stable.

5. Conclusions

Immobilization of gold sols appears to be a useful method to prepare highly dispersed heterogeneous catalyst regardless of the type of support. However, beside a lot of methods available for generating sols, the one consisting in a chemical reduction in solution of salt is the simplest and widely applicable technology providing suitable sized particles with narrow distribution. In particular, we studied the preparation of heterogeneous catalyst designed for liquid phase applications. Parameters that have to be taken into account are not only particle size and diameter distribution in the sol, but also the capability of the sol for maintaining these properties during the immobilization step on a support. Principally important for this purpose is not only the nature and the amount of protective agent but also the nature of support. For active carbon (the most used support for liquid phase application) the best choice in terms of size control during not only the metal particles generation but also the immobilization step, has been found to be the PVA.

The importance of size control has been depicted for the selective oxidation of glycerol; it was shown that by increasing particle size a high selectivity to glycerate has been reached at the expense of the consecutive oxidation of glycerate to tartronate.

References

1 G. C. Bond, D. T. Thompson, *Catal. Rev. Sci. Eng.* 41 (1999) 319.
2 (a) M. Haruta, *Nature,* 437 (2005) 1098; (b) M. Haruta, *Gold Bull.* 37 (2004) 27; (c) G. J. Hutchings, M. Haruta, *Appl. Catal. A,* 291 (2005) 2; (d) M. Haruta, in H. S. Nalwa (ed.) *Encyclopedia of Nanoscience and Nanotechnology*, Vol. I, Elsevier Science, Amsterdam, 2004, 655.
3 M. Haruta, S. Tsubota, T. Kobayashi, A. Ueda, Y. Nakahara, in G. Poncelet, P. A. Jacobs, P. Grange, B. Delmon (eds.) *Preparation of Catalysts*, Vol. V, Elsevier Science, Amsterdam, 1991, 695.
4 D. G. Duff, A. Baiker, P. P. Edwards, *J. Chem. Soc. Chem. Commun.* (1993) 96.
5 L. Prati, G. Martra, *Gold Bull.* 32 (1999) 96.
6 J. D. Aiken III, Y. Lin, R. G. Finke, *J. Mol. Catal. A: Chem.* 114 (1996) 29.
7 F. Porta, L. Prati, in ''Transworld Research Network,'' *Recent Res. Devel. Vacuum Sci. & Tech.* (Kerala, India), 4 (2003) 99.
8 J. S. Bradley, G. Schmid (ed.) *Cluster and Colloids: From Theory to Applications*, Chapter 6, VCH Publishers, New York, 1994.
9 Y. Tan, Y. Li, D. Zhu, in H. S. Nalwa (ed.) *Encyclopedia of Nanoscience and Nanotechnology*, Vol. VIII, American Scientific Publishers, CA, 2004, 9.
10 (a) H. B. Wieser, *Inorganic Colloid Chemistry*, J. Wiley & Sons, New York, 1933; (b) A. Kumar, S. Mandal, P. R. Selvakanna, R. Parischa, L. E. Mandale, M. Sastry, *Langmuir* 19 (2003) 6277; (c) D. V. Leff, L. Brandt, J. R. Heath, *Langmuir* 12 (1966) 4724.
11 B. V. Derjaguin, L. Landau, *Acta Physicochem.URSS* 14 (1941) 633.
12 E. J. W. Verwey, J. T. G. Overbeeck, *Theory of the Stability of Lyophobic Colloids*, Chapter 1, Elsevier, New York, 1948.
13 D. Andrescu, T. K. Sau, D. V. Goia, *J. Colloid Interface Sci.* 298 (2006) 742.
14 J. Fink, C. J. Kiely, D. Bethell, D. J. Schiffrin, *Chem. Mater.* 10 (1998) 922.
15 M. Comotti, C. Della Pina, R. Matarrese, M. Rossi, *Angew. Chem. Int. Ed.* 43 (2004) 5812.
16 W. Heller, T. L. Pugh, *J. Polym. Sci.* 47 (1960) 203.
17 D. F. Evans, H. Wennerstrom, *The Colloidal Domain*, VCH Publishers, New York, 1994.
18 J. Boutoux, A. Dauplan, R. Marignan, *J. Chim. Phis. Physicochim. Biol.* 66 (1969) 1259.
19 (a) H. Hirai, Y. Nakao, N. Toshima, *Chem. Lett.* (1978) 545; (b) H. Hirai, Y. Nakao, N. Toshima, *J. Macromol. Sci. Chem.* A13 (1979) 727.
20 (a) G. Schmid, *Chem. Rev.* 92 (1992) 1709; (b) G. Schmid, A. Lehnert, *Angew. Chem. Int. Ed. Engl.* 28 (1989) 780.
21 (a) J. Tanori, M. P. Pileni, *Langmuir* 13 (1997) 639; (b) M. P. Pileni, *Langmuir* 13 (1997) 3266; (c) M. Antonietti, C. Göltner, *Angew. Chem. Int. Ed. Engl.* 36 (1997) 910; (d) M. P. Pileni, *Adv. Mater.* 10 (1998) 259; (e) J. P. Wilcoxon,

P. Provencio, *J. Phys. Chem. B* 103 (1999) 9809; (f) M. M. Maye, W. Theng, F. L. Leibowitz, N. K. Ly, C. J. Zhong, *Langmuir* 16 (2000) 490.
22 (a) H. Bonnemann, W. Brijoux, R. Brinkmann, R. Fretzen, Th. Joussen, R. Koppler; P. Neiteler. J. Richter, *J. Mol. Catal.* 86 (1994)129; (b) H. Bonnemann, W. Brijoux, in A. Fürstner (ed.) *Active Metals*, VCH Publishers, Weinheim, 1996, 339; (c) H. Bonnemann, W. Brijoux, in W. Moser (ed.) *Advanced Catalysts and Nanostructured Materials*, Chapter 7, Academic Press, San Diego, CA, 1996, 165.
23 (a) J. Singzig, L. J. De Jongh, H. Bonnemann, W. Brijoux, R. Koppler, *Appl. Organomet. Chem.* 12 (1998) 387; (b) H. Bonnemann, W. Brijoux, R. Brinkmann, U. Endruschat, W. Hofstadt, K. Angermund, *Rev. Roum. Chim.* 44 (1999) 1003.
24 F. Porta, M. Rossi, *J. Mol. Catal. A: Chem.* 204–205 (2003) 553.
25 (a) C. L. Bianchi, F. Porta, L. Prati, M. Rossi, *Top. Catal.* 13 (2000) 231; (b) F. Porta, L. Prati, M. Rossi, G. Scarì, *J. Catal*. 211 (2002) 464.
26 F. Porta, L. Prati, M. Rossi, *Catal. Today* 61 (2000) 165.
27 S. Biella, F. Porta, L. Prati, M. Rossi, *Catal. Lett*. 90 (2003) 23.
28 H. Bonnemann, R. M. Richards, *Eur. J. Inorg. Chem.* (2001) 2455.
29 (a) G. Schmid, *Polyhedron* 7 (1988) 2321; (b) G. Schmid, B. Morum, J. Malm, *Angew. Chem. Int. Ed. Engl*. 28 (1989) 778; (c) G. Schmid, V. Maihach, F. Lantermann, S. Peschel, *J. Chem. Soc., Dalton Trans.* (1996) 589; (d) G. Schmid, H. West, J.-O. Malm, J.-O. Bovin, C. Grenthe, *Chem. Eur. J.* 2 (1996) 1099; (e) U. Simon, R. Flesch, H. Wiggers, G. Schon, G. Schmid, *J. Mater. Chem.* 8 (1998) 517; (f) G. Schmid, R. Pugin, J.-O. Malm, J.-O. Bovin, C. Grenthe, *Eur. J .Inorg. Chem.* (1998) 813.
30 (a) N. Toshima, T. Yonezawa, *New J. Chem.* (1998) 1179; (b) H. Hirai, Y. Nakao, N. Toshima, *Chem. Lett.* (1976) 905; (c) P. Lu, T. Teranishi, K. Asakura, M. Miyake, N. Toshima, *J. Phys. Chem. B* 103 (1999) 9673.
31 (a) M. N. Vergaftik, V. P. Zargorodnikov, I. P. Stolarov, I. I. Moiseev, D. I. Kochubey, V. A. Likholobov, A. L. Chuvilin, K .I. Zarnaraev, *J. Mol. Catal.* 53 (1989) 315; (b) V.V. Vokov, G. van Tendeloo, A.Tsirkov, N. V. Cherkashina, M. N. Vergaftik, I. I. Moiseev, V. M. Novotortsev, A. V. Kvit, A. I. Chuvilin, *J. Cryst. Growth* 163 (1996) 377.
32 (a) J. D. Aiken III, R. G. Finke, *J. Mol. Catal. A: Chem.* 145 (1999) 1; (b) Y. Lin, R. G. Finke, *J. Am. Chem. Soc.* 116 (1994) 8335; (c) H. Bönnemann, G. A. Braun, *Angew. Chem. Int. Ed. Engl*. 35 (1996) 1992; (d) L. N. Lewis, N. Lewis, *J. Am. Chem. Soc.* 108 (1986) 7228; (e) J. P. Wilcoxon, T. Martino, E. Klavetter, A. P. Silwester, *Nanophase Mater*. (1994) 771; (f) T. J. Schmidt, M. Noeske, H. A.Gasteiger, R. J. Behm, P. Britz, W. Brijoux, H. Bönnemann, *Langmuir* 13 (1997) 2591; (g) M. T. Reetz, G. Lohmer, *J. Chem. Soc. Chem. Commun*. (1996) 1921; (h) M. T. Reetz, R. Breinbauer, P. Wedemann, P. Binger, *Tetrahedron* 54 (1998) 1233.
33 (a) M. A.Watzky, R. G. Finke, *J. Am. Chem. Soc*. 119 (1997) 10382; (b) J. D. Aiken III, R. G. Finke, *J. Am. Chem. Soc.* 120 (1998) 9545; (c) J. D. Aiken III, R. G. Finke, *Chem. Mater.* 11 (1999) 1035.
34 (a) D. G. Duff, A. C. Curtis, P. P. Edwards, D. A. Jefferson, B. F. G. Johnson, *J. Chem. Soc. Chem. Commun*. (1987) 1264; (b) D. G. Duff, A. C. Curtis, P. P. Edwards, D. A. Jefferson, B. F. G. Johnson, A. I. Kirkland, A. S. Wallace, *Angew. Chem. Int .Ed. Engl.* 27 (1988) 1530; (c) D. G. Duff, P. P. Edwards, J. Evans, J. T. Gauntlett, D. A. Jefferson, B. F .G. Johnson, A. I. Kirkland, D. J. Smith, *Angew. Chem. Int. Ed. Engl.* 28 (1989) 590; (d) W. Vogel, D. G. Duff, P. P. Edwards, A. Baiker, *Langmuir* 11 (1995) 401.
35 (a) H. Bonnemann, W. Brijoux, R. Brinkmann, E. Dinjus, T. Joussen, B. Korrall, *Angew. Chem. Int. Ed. Engl.* 30 (1991) 1344; (b) H. Bonnemann, W. Brijoux, R. Brinkmann, J. Richter (to Studiengesellschaft KohlembH) US Patent 849482 (August 29,1997).
36 (a) M. T. Reetz, M. Maase, *Adv. Mater*. 11 (1999) 773; (b) J. S. Bradley, B. Tesche, W. Busser, M. Maase, M. T. Reetz, *J. Am. Chem. Soc*. 122 (2000) 4631.
37 H. Liu, G. Mao, M. Meng, *J. Mol. Catal.* 74 (1992) 2775.
38 (a) H. Kimura, K. Tsuto, T. Wakisaka, Y. Kazumi, Y. Inaya, *Appl. Catal. A: Gen.* 96 (1993) 217; (b) H. Kimura, *Appl. Catal. A: Gen*. 105 (1993) 147; (c) R. Garcia, M. Besson, P. Gallezot, *Appl. Catal. A: Gen.* 127 (1995) 165; (d) M. Besson, P. Gallezot, *Catal. Today* 57 (2000) 127; (e) H. Kimura, *J. Polym. Sci.: Part A. Polym. Chem.* 34 (1996) 3595.
39 R. J. H. Grisel, P. J. Kooyman, B. E. Nieuwenhuys. *J. Catal.* 191 (2000) 430.
40 (a) M. Besson, P. Gallezot, *Catal. Today* 57 (2000) 127; (b) T. Mallat, A. Baiker, *Catal. Today* 19 (1994) 247.
41 (a) S. Carrettin, P. McMorn, P. Johnston, K. Griffin, G. J. Huthchings, D. E. Logan, *Chem.Commun*. (2002) 696; (b) S. Carrettin, P. McMorn, P. Johnston, K. Griffin, G. J. Huthchings, C. J. Kielly, *Phys. Chem. Chem. Phys.* 5 (2003) 1329; (c) L. Prati, F. Porta, *J. Catal*. 224 (2004) 397.

CHAPTER 23

Liquid Phase Structural Control of Mono- and Bimetallic Nanoparticles

Toshiharu Teranishi, Masafumi Nakaya, and Masayuki Kanehara

Department of Chemistry, Graduate School of Pure and Applied Sciences, University of Tsukuba, Ibaraki 305-8571, Japan

1. Introduction

There are two approaches to build up the metal nanoparticles from atoms. One is the physical approach, including the gas phase synthesis of metal nanoparticles on some substrates. These nanoparticles are naked without any protective agents on the nanoparticle surface to prevent the nanoparticles from further aggregation, and they are subjected to the physical investigations. This method possesses an advantage that one need not consider the interaction of the surface atoms with other molecules, resulting in providing information of metal nanoparticles themselves. However, there are two big disadvantages for these naked nanoparticles: One is that it is difficult to uniform their sizes and another is that they cannot be isolated and handled like chemical compounds. The wide size distributions of metal nanoparticles would give us only averaged information, and numerous physical methods could not be used without isolating metal nanoparticles as a solid. Consequently, these two disadvantages are fatal for investigating the detailed physical and chemical properties of metal nanoparticles.

Another approach is the chemical one, that is, the liquid phase synthesis. In general, to obtain the uniformly sized metal nanoparticles that can be isolated, they have to be protected by some protective agents, such as linear and branched polymers, organic molecules, surfactants, and so on [1]. Moreover, the protective agents make the metal nanoparticles soluble in solvent, which contributes the fabrication of secondary structures of metal nanoparticles [2]. They can be soluble not only in organic solvent but aqueous media by modifying the protective agents. In the formation process of metal nanoparticles, when metal ions are reduced to metal atoms, successive aggregation of metal atoms rapidly proceeds to form the polycrystalline metal precipitates. It is obvious that the concentration of the protective agents controls the growth rate of monocrystalline aggregates. Controlling both the reduction rate of metal ions to metal atoms and the growth rate of metal aggregates is important to precisely control the size of metal nanoparticles.

The recent liquid phase synthetic techniques provide us the metal nanoparticles with the standard deviation smaller than 10%. So a lot of scientists have been attracted by an investigation on the transition from molecular to bulk properties from both the fundamental and technological points of view. Here we present our recent liquid phase techniques to control the size and composition of Au and FePt nanoparticles.

2. Synthesis Strategy

When synthesizing the metal nanoparticles by the chemical method, the system contains metal salt, protective agent, reducing agent, and solvent (the reducing agent sometimes plays a role of the protective agent or solvent). These four chemical species and temperature can be the parameters to control the particle size. Controlling both the reduction rate of metal salts to metal atoms and the growth rate of metal atoms is indeed responsible for controlling the particle size (Figure 1). Many researches have been dedicated to the control of particle sizes so far.

The noteworthy synthetic method of ligand-protected metal nanoparticles was reported by Brust and coworkers [3]. The strategy of their method consists of growing the metal nanoparticles with the simultaneous attachment of self-assembled ligand monolayers on the growing nuclei. In order to allow the surface reaction to take place during metal nucleation and growth, the nanoparticles are grown in a two-phase system. In this method, for example, $AuCl_4^-$ is transferred from aqueous solution to toluene using tetraoctylammonium bromide (TOAB) as the phase-transfer reagent (Equation (1)) and reduced

Metal Nanoclusters in Catalysis and Materials Science: The Issue of Size Control
Edited by B. Corain, G. Schmid and N. Toshima

with aqueous sodium borohydride in the presence of a long-chain thiol as a protective agent (Equation (2)).

$$AuCl_4^-(aq) + N(C_8H_{17})_4^+(toluene) \rightarrow N(C_8H_{17})_4^+AuCl_4^-(toluene) \quad (1)$$

$$mAuCl_4^-(toluene) + nC_{12}H_{25}SH(toluene) + 3me^- \rightarrow 4mCl^-(aq) + (Au_m)(C_{12}H_{25}SH)_n(toluene) \quad (2)$$

At the molar ratio of ligand/Au = 1, the Au nanoparticles have diameters in the range 1–3 nm and a maximum in the particle-size distribution at 2.0–2.5 nm. The heat-treatment of these small metal nanoparticles enables us to easily obtain the larger-sized metal nanoparticles. Needless to say, one-phase system containing the metal precursor, protective agent, and reducing agent is also effective to control the particle size. It is important to choose the reaction system according to the kind of nanoparticles that one needs.

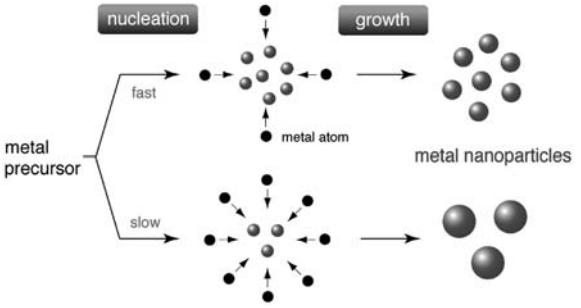

Figure 1. Schematic illustration for the size control of metal nanoparticles.

On the other hand, one of the mildest chemical procedures is an alcohol reduction of metal salts in the presence of the protective agents [4,5]. The reaction proceeds according to the Equation (3).

$$M^{n+} + \frac{n}{2}RCH_2OH \rightarrow M^0 + \frac{n}{2}RCHO + nH^+ \quad (3)$$

This technique is also applicable to the formation of bimetallic nanoparticles, according to the Equation (4), where two metal ions are reduced simultaneously or successively [6].

$$xM_1^{m+} + yM_2^{n+} + \frac{(mx+ny)}{2}RCH_2OH \rightarrow M_{1x} + M_{2y} + \frac{(mx+ny)}{2}RCHO + (mx+ny)H^+ \quad (4)$$

This alcohol reduction method is applied to the control of size and composition of not only the noble metal/noble metal [7] but the 3d-transition metal/noble metal nanoparticles [8] like magnetic FePt nanoparticles.

3. Results

In 2001, we developed a simple and quite useful method to manipulate the size of Au nanoparticles by using the heat-treatment of small Au nanoparticles [9,10], which is far from the conventional techniques. The 1-dodecanethiol-protected Au nanoparticles ($C_{12}S$–Au) of 1.5 ± 0.2 nm in size synthesized by the Brust's two-phase (toluene/water) reaction procedure [3] were heat treated at 150–250 °C at the heating rate of 2 °C min^{-1}, and held for 30 min. This heat treatment of as-synthesized $C_{12}S$–Au nanoparticles

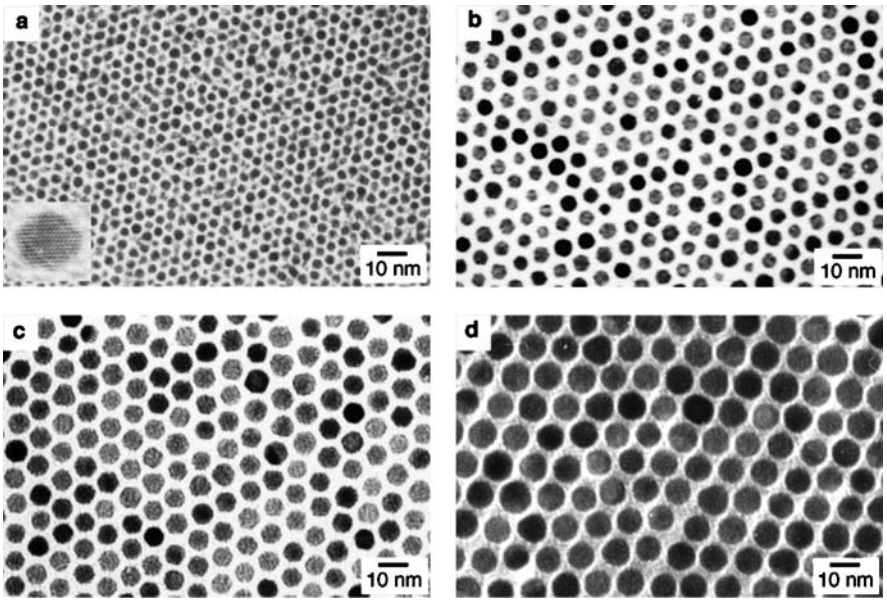

Figure 2. TEM images of $C_{12}S$–Au nanoparticles after the heat treatment of 1.5 nm $C_{12}S$–Au nanoparticles at (a) 150, (b) 190, and (c) 230 °C and (d) $C_{18}S$–Au nanoparticles heat treated at 250 °C. (Reprinted from Ref. [10], © 2003, American Chemical Society.)

at 150, 190, and 230 °C led to the thermodynamical particle growth, the particle sizes becoming 3.4 ± 0.3, 5.4 ± 0.7, and 6.8 ± 0.5 nm, respectively. Figure 2a–c present the TEM images of $C_{12}S$–Au nanoparticles heat treated at 150, 190, and 230 °C, respectively. The particle sizes are proportional to the heat treatment temperatures in this region.

For the heat-treatment process, TOAB, adopted as a phase-transfer agent during the preparation of $C_{12}S$–Au nanoparticles, plays a key role because the uniform growth of nanoparticles was not observed without TOAB molecules. Presumably, molten TOAB serves as a solvent in the particle growth process. When the $C_{12}S$–Au nanoparticles were heat treated at 250 °C, they were not redispersed in toluene because of the aggregation. This might result from the vaporization of $C_{12}SH$ ligands because the heat-treatment temperature of 250 °C is very close to the boiling point of $C_{12}SH$.

To obtain the larger particles, 1-octadecanethiol ($C_{18}SH$), having a higher boiling point (204–210 °C/11 mmHg) than $C_{12}SH$, was used as a protective ligand in place of $C_{12}SH$. At the heat-treatment temperature of 250 °C, $C_{18}S$–Au nanoparticles grew to 9.7 ± 0.9 nm, as observed from TEM image shown in Figure 2d. The relationship between the mean diameters of the heat-treated $C_{12}S$- and $C_{18}S$–Au nanoparticles and the heat-treatment temperatures is summarized in Figure 3.

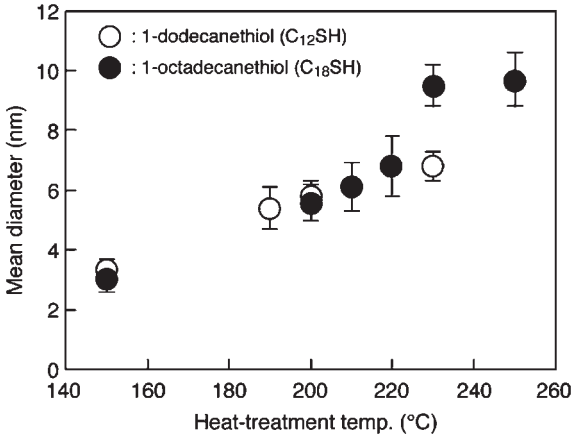

Figure 3. Temperature dependence of the sizes of $C_{12}S$–Au (○) and $C_{18}S$–Au nanoparticles (●). (Reprinted from Ref. [10], © 2003, American Chemical Society.)

Once the small nanoparticles were synthesized, we could easily obtain the monodispersed Au nanoparticles from 3.4 to 9.7 nm in size depending on the heat-treatment temperature from 150 to 250 °C. Thus the heat-treatment method is easily applicable to the metal nanoparticles with relatively low melting points like Ag as well.

Generally, to synthesize the small metal nanoparticles, a large amount of protective ligands and low-reaction temperature have been employed, because the growth rate of the metal core may decrease with the increasing amount of ligands and decreasing reaction temperature. However, monodentate ligand-protected small metal nanoparticles are unstable both in solutions and on substrates. Actually, 1.5 nm $C_{12}S$–Au nanoparticles easily aggregate to generate the precipitates. Recently, we have succeeded in synthesizing quite stable Au nanoparticles with the size of ca. 2 nm by using a 2,6-*bis*(1′-(*n*-thioalkyl)benzimidazol-2-yl) pyridine (TC_nBIP, $n = 3, 6, 8, 10, 12$; see Figure 4) as a protective ligand [11,12].

This bulky ligand has two thiols to produce small Au nanoparticles. Figure 5 presents the TEM images of self-assembled monolayers of 1.5 nm TC_8BIP- and 1.6 nm TC_6BIP-protected Au nanoparticles at the air–water interface.

Table 1 presents the mean diameters and standard deviations of Au nanoparticles synthesized at various TC_nBIP/Au molar ratios. Both the mean diameter and standard deviation decreased with an increase in the amount of the protective agent, TC_nBIP, which was also observed in the cases involving polymer-protected Pd [13], Pt [14,15], and Au nanoparticles [16]. For TC_nBIP ($n = 8, 10, 12$), Au nanoparticles smaller than 2 nm could be

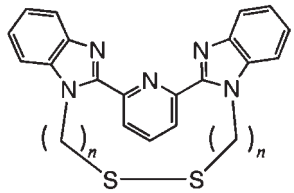

Figure 4. Chemical structure of TC_nBIP.

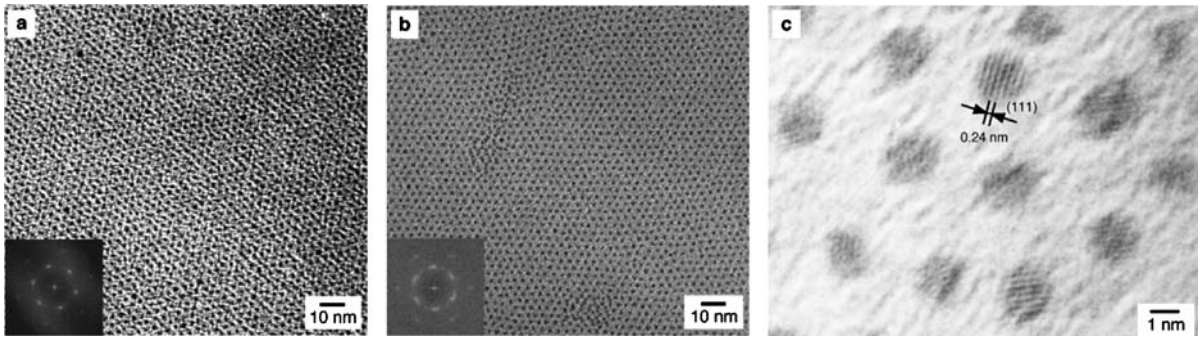

Figure 5. TEM images of nearly perfectly ordered hexagonal close-packed monolayers of (a) 1.5 nm TC_8BIP–Au and (b) 1.6 nm TC_6BIP–Au nanoparticles. Insets show FFT spots of each monolayer. (c) HRTEM image of 1.5 nm TC_8BIP–Au nanoparticles. (Reprinted from Ref. [12], © 2006, American Chemical Society.)

Table 1. Mean diameters and standard deviations of a series of TC_nBIP–Au nanoparticles synthesized at various TC_nBIP/Au molar ratios.

Ligand	TC_nBIP/Au (mol/mol)	Mean diameter (nm)	Standard deviation (nm)
TC_3BIP	1.0	2.7	1.0
	2.0	2.2	0.5
TC_6BIP	1.0	2.6	0.9
	2.0	1.6	0.5
TC_8BIP	0.05	3.2	0.8
	0.1	2.7	0.5
	0.5	2.3	0.4
	1.0	1.9	0.4
	2.0	1.5	0.2
$TC_{10}BIP$	1.0	1.6	0.3
	2.0	1.5	0.2
$TC_{12}BIP$	0.4	1.6	0.5
	0.5	1.6	0.4
	1.0	1.5	0.3
	2.0	1.5	0.3

Source: Reprinted with permission from Ref. [12], © 2006, American Chemical Society.

obtained for TC_nBIP/Au molar ratios larger than 1.0. For TC_6BIP–Au, 1.6 nm particles were obtained when the TC_6BIP/Au molar ratio was 2.0. On the other hand, when using TC_3BIP as a protective ligand, only Au nanoparticles larger than 2 nm were produced even at large TC_3BIP/Au molar ratios. Generally speaking, in order to synthesize the kinetically stabilized small Au nanoparticles, sterically bulky ligands have been employed, because the growth rate of the metal core may decrease with increasing ligand bulkiness. Our TC_nBIP–Au nanoparticles follow this tendency, that is, TC_nBIP ligands with longer alkyl chain tend to produce smaller Au nanoparticles at the similar TC_nBIP/Au ratio.

Fe/Pt alloys are an important class of materials in permanent magnetic applications because of their large uniaxial magnetocrystalline anisotropy [$Ku \approx 7 \times 10^6\,J\,m^3$] and good chemical stability. As the magnetic stability of individual particles scales with the anisotropy constant, K_u, and the particle volume, V, small Fe/Pt nanoparticles may be suitable for future ultra-high density magnetic recording media applications [17].

In 2000, Sun and co-workers succeeded in synthesis of monodispersed Fe/Pt nanoparticles by the reduction of platinum acetylacetonate and decomposition of $Fe(CO)_5$ in the presence of oleic acid and oleylamine stabilizers [18]. The Fe/Pt nanoparticle composition is readily controlled, and the size is tunable from 3 to 10 nm in diameter with a standard deviation of less than 5%. For practical use, we developed the novel synthetic method of FePt nanoparticles by the polyol reduction of platinum acetylacetonate ($Pt(acac)_2$) and iron acetylacetonate ($Fe(acac)_3$) in the presence of oleic acid and oleylamine stabilizers in di-*n*-octylether [19,20]. The Fe contents in FePt nanoparticles can be tuned from 23 to 67 atomic%, and the particle sizes are not significantly affected by the compositions, retaining to be 3.1 nm with a very narrow size distribution, as shown in Figure 6.

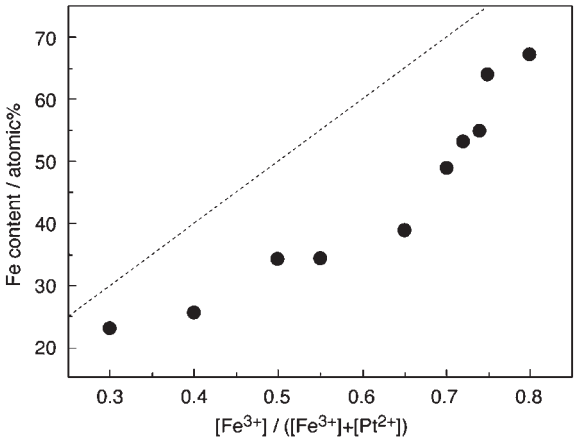

Figure 6. Influence of the molar ratio of precursors on the Fe content of FePt nanoparticles. The dashed line indicates the Fe content in feeing precursors. (Reprinted from Ref. [19], © 2004, The Chemical Society of Japan.)

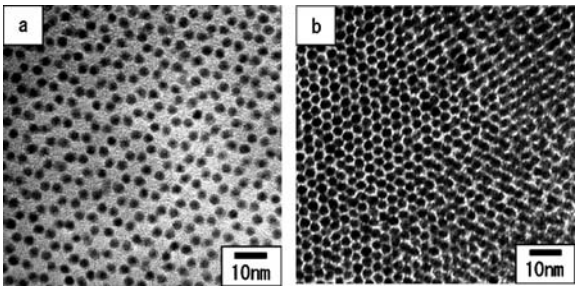

Figure 7. TEM images of (a) bilayer of 3.1 nm $Fe_{34}Pt_{66}$ nanoparticles and (b) trilayer of 3.1 nm $Fe_{53}Pt_{47}$ nanoparticles. (Reprinted from Ref. [19], © 2004, The Chemical Society of Japan.)

Figure 7a shows the bilayer of 3.1 nm $Fe_{34}Pt_{66}$ nanoparticles. This bilayer consists of AB stacking of hcp monolayer of $Fe_{34}Pt_{66}$ nanoparticles forming the quasi-honeycomb structure, where the nanoparticles at the second layer occupy the threefold hollow sites of the first layer. When more concentrated solution was dropped on a TEM grid, the particles assembled to give the trilayer with an ABC close-packed (fcc type) structure, as shown in Figure 7b. Annealing such small FePt nanoparticle assemblies at 600 °C to change the crystal structure from chemically disordered face-centered cubic phase to chemically ordered face-centered tetragonal phase always leads to the coalescence of nanoparticles except for several particular cases [21,22], meaning that the dramatic change in the magnetic properties resulting from the crystal structural change of nanoparticles is generally owing to the coalescence of the small nanoparticles. Therefore, the novel synthetic route of thermally stable larger FePt nanoparticles should be developed.

Very recently, we have developed one-pot synthesis of FePt nanoparticles larger than 5 nm with controlled composition by the polyol reduction of $Pt(acac)_2$ and $Fe(acac)_3$ in excess ligands without using the conventional solvents [23]. Figure 8 presents the TEM images

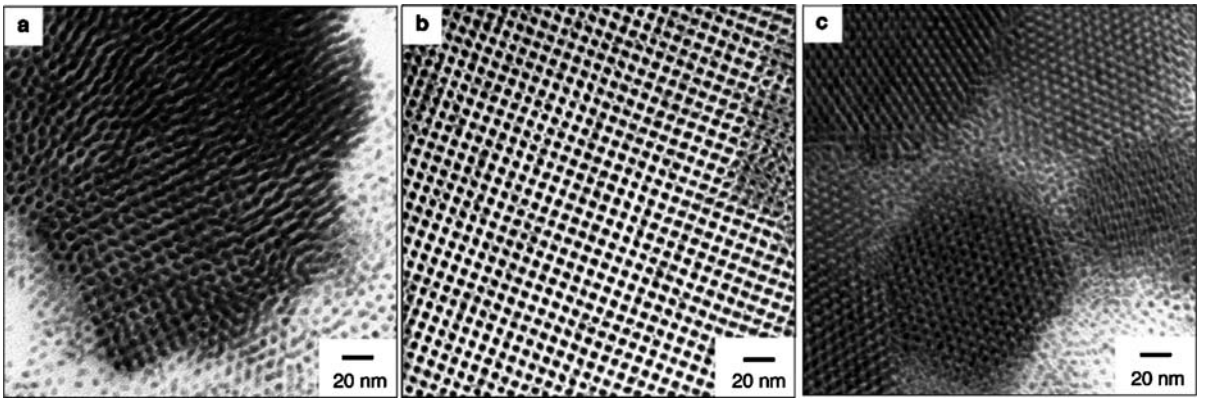

Figure 8. TEM images of (a) 6.1 ± 0.6 nm $Fe_{36}Pt_{64}$, (b) 5.8 ± 0.7 nm $Fe_{44}Pt_{56}$, and 5.1 ± 0.7 nm $Fe_{49}Pt_{51}$ nanoparticles formed by a self-assembly process of hexane solution on an amorphous carbon substrate. (Reprinted from Ref. [23], © 2006, American Chemical Society.)

of 6.1 ± 0.6 nm $Fe_{36}Pt_{64}$, 5.8 ± 0.7 nm $Fe_{44}Pt_{56}$, and 5.1 ± 0.7 nm $Fe_{49}Pt_{51}$ nanoparticles.

From the viewpoint of the synthesis of large FePt nanoparticles, our recipe works better than the previous reported ones. An excess amount of ligands (oleylamine and oleic acid) would proceed the complexation with metal ions, as proved from UV–vis spectra showing the change of coordination condition around metal ions. To be more specific, the coordination of ligands to easily reducible Pt^{2+} ions better proceeds without the conventional solvent than with the solvent, which would provide slower nucleation and larger nanoparticles [24]. In support of our results, when the concentration of ligands in di-*n*-octylether was increased from 74 mmol L^{-1} to 750 mmol L^{-1}, no significant change in the size of FePt nanoparticles (3.1 nm) was observed. Once the $Pt(acac)_2$ and $Fe(acac)_3$ dissolved in oleic acid and oleylamine at 115 °C were cooled down to room temperature, no precipitates were observed, and the solution was immiscible in di-*n*-octylether even at high temperature. Therefore, we concluded that extremely higher concentration of ligands can better coordinate the metal ions and hence provide slower nucleation and larger nanoparticles. The obtained large FePt nanoparticles were thermally more stable than the small ones, and hard to coalesce in the in-plane direction for their monolayer. The coercivity of these ferromagnetic assemblies is tunable by controlling annealing temperature and time, as well as the Fe:Pt ratio and particle size.

4. A Case History

The synthesis of $C_{12}S$–Au nanoparticles as a source for the heat treatment followed the Brust's two-phase (toluene/water) reaction procedure [3]. The organic (toluene) phase was then separated, evaporated completely in a rotary evaporator at 40 °C, and dried in vacuo at 30 °C for a day. The crude solid obtained was heat treated at 150–250 °C at the heating rate of 2 °C min^{-1}, and held for 30 min. The heat-treated product was dissolved in toluene and mixed with methanol to remove excess free $C_{12}SH$ and TOAB. The dark brown precipitate was filtered off, washed with methanol, and redispersed in toluene. Octadecanethiol ($C_{18}SH$) was also used as a protective agent in place of $C_{12}SH$.

In a typical synthesis of a series of the TC_nBIP-protected Au nanoparticles, 2.5 mL of 1 mM aqueous solution of $HAuCl_4 \cdot 4H_2O$ (2.5 mmol) was added to the mixture of 1 mL of 2.5 mM DMF solution of TC_nBIP (2.5 mmol) and 44 mL of DMF. After heating the solution at 60 °C or cooling in an ice-water bath, 2.5 mL of 10 mM aqueous solution of $NaBH_4$ (25 mmol) was swiftly added to the solution under vigorous stirring, and the solution was continuously stirred for 1 h to obtain TC_nBIP–Au nanoparticles. The solvent was evaporated to ca. 3 mL at 40 °C under reduced pressure. Distilled methanol was then added and the mixture was centrifuged to give a crude precipitate of Au nanoparticles. The precipitate was dissolved in 0.5 mL of distilled chloroform and reprecipitated with distilled methanol and centrifuged. The reprecipitation processes were repeated for three times to give pure TC_nBIP-Au nanoparticles.

The FePt nanoparticles were synthesized by the polyol reduction of $Pt(acac)_2$ and $Fe(acac)_3$ in the mixture of oleic acid and oleylamine under nitrogen. First, both metal precursors (total amount was 1.0 mmol), oleic acid (5.0 mmol), and oleylamine (5.0 mmol) were placed in a flask. The mixture was subjected to a degassing process including an evacuation at room temperature and a replacement of atmosphere with nitrogen three times, and was then heated up to 140–160 °C to completely dissolve the precursors with a vigorous stir under a nitrogen flow. When the solution temperature reached at 140–160 °C, 1,2-hexadecanediol (1.5 mmol) was added to the solution, and then quickly heated up to 240–250 °C. After stirring the solution for 30 min at the same temperature, the heat source was removed to allow the black solution to cool down to room temperature. The obtained black precipitate was dissolved in hexane (10 mL) and reprecipitated with ethanol for purification. The resulting black precipitate was redispersed in hexane (50 mL) containing oleic acid (50 μL) and oleylamine (50 μL) as stabilizers, followed by being bubbled with a nitrogen gas to remove oxygen.

5. Conclusions

Since nanoscale metal nanoparticles are applicable to a number of areas of technological importance, the nanostructured materials chemistry will occupy much attention of scientists. It is certain that controlling the primary structures of metal nanoparticles, that is, size, shape, crystal structure, composition, and phase-segregation manner is still most important, because these structures dominate the physical and chemical properties of metal nanoparticles. Now the liquid phase synthesis facilitates the precise control of the primary structures.

References

1 T. Teranishi, in A. Hubbard (ed.) *Encyclopedia of Surface and Colloid Science*, Marcel Dekker, New York, 2002, 3314.
2 T. Teranishi, M. Miyake, in H. S. Nalwa (ed.) *Encyclopedia of Nanoscience and Nanotechnology*, American Scientific Publishers, Stevenson Ranch/California, 2004, 421.
3 M. Brust, D. Walker, D. Bethell, D. J. Schiffrin, R. Whyman, *J. Chem. Soc., Chem. Commun.* (1994) 801.
4 H. Hirai, Y. Nakao, N. Toshima, *J. Macromol. Sci., Chem.* A12 (1978) 1117.
5 H. Hirai, *J. Macromol. Sci., Chem.* A13 (1979) 633.
6 N. Toshima, M. Harada, T. Yonezawa, K. Kushihashi, K. Asakura, *J. Phys. Chem.* 95 (1991) 7448.
7 N. Toshima, Y. Shiraishi, T. Teranishi, M. Miyake, T. Tominaga, H. Watanabe, W. Brijoux, H. Bönneman, G. Schmid, *Appl. Organometal. Chem.* 15 (2001) 178.
8 T. Teranishi, M. Miyake, *Chem. Mater.* 11 (1991) 3414.
9 T. Teraishi, S. Hasegawa, T. Shimizu, M. Miyake, *Adv. Mater.* 13 (2001) 1699.
10 T. Shimizu, T. Teranishi, S. Hasegawa, M. Miyake, *J. Phys. Chem. B* 107 (2003) 2719.
11 T. Teranishi, M. Haga, Y. Shiozawa, M. Miyake, *J. Am. Chem. Soc.* 122 (2000) 4237.
12 M. Kanehara, E. Kodzuka, T. Teranishi, *J. Am. Chem. Soc.*, 128 (2006) 13084
13 T. Teranishi, M. Miyake, *Chem. Mater.* 10 (1998) 594.
14 T. Teranishi, M. Hosoe, T. Tanaka, M. Miyake, *J. Phys. Chem. B* 103 (1999) 3818.
15 T. Teranishi, M. Hosoe, M. Miyake, *Adv. Mater.* 9 (1997) 65.
16 T. Teranishi, I. Kiyokawa, M. Miyake, *Adv. Mater.* 10 (1998) 596.
17 D. Weller, A. Moser, *IEEE Trans. Magn.* 35 (1999) 4423.
18 S. Sun, C. B. Murray, D. Weller, L. Folks, A. Moser, *Science* 287 (2000) 1989.
19 M. Nakaya, Y. Tsuchiya, K. Ito, Y. Oumi, T. Sano, T. Teranishi, *Chem. Lett.* 33 (2004) 130.
20 M. Nakaya, T. Teranishi, *Trans. Mater. Res. Soc. Jpn.* 30 (2005) 579.
21 K. Elkins, D. Li, N. Poudyal, V. Nandwana, Z. Jin, K. Chen, J. P. Liu, *J. Phys. D: Appl. Phys.* 38 (2005) 2306.
22 S. Yamamoto, Y. Morimoto, T. Ono, M. Takano, *Appl. Phys. Lett.* 87 (2005) 032503.
23 M. Nakaya, M. Kanehara, T. Teranishi, *Langmuir* 22 (2006) 3485.
24 W. W. Yu, X. Peng, *Angew. Chem. Int. Ed. Engl.* 41 (2002) 2368.

CHAPTER 24

Solvent-Free Controlled Thermolysis for Facile Size-Regulated Synthesis of Metal and Alloy Nanoparticles

Masami Nakamoto, Mari Yamamoto, and Yukiyasu Kashiwagi

Osaka Municipal Technical Research Institute, Morinomiya, Joto-ku, Osaka, Japan

1. Introduction

In the early work on the thermolysis of metal complexes for the synthesis of metal nanoparticles, the precursor carbonyl complex of transition metals, e.g., $Co_2(CO)_8$, in organic solvent functions as a metal source of nanoparticles and thermally decomposes in the presence of various polymers to afford polymer-protected metal nanoparticles under relatively mild conditions [1–3]. Particle sizes depend on the kind of polymers, ranging from 5 to >100 nm. The particle size distribution sometimes became wide. Other cobalt, iron [4], nickel [5], rhodium, iridium, rutheniuim, osmium, palladium, and platinum nanoparticles stabilized by polymers have been prepared by similar thermolysis procedures. Besides carbonyl complexes, palladium acetate, palladium acetylacetonate, and platinum acetylacetonate were also used as a precursor complex in organic solvents like methyl-*iso*-butylketone [6–9]. These results proposed facile preparative method of metal nanoparticles. However, it may be considered that the size-regulated preparation of metal nanoparticles by thermolysis procedure should be conducted under the limited condition.

On the other hand, the solvent-free controlled thermolysis proposed by our group means the thermolysis procedure of precursor noble metal complexes such as gold, silver, platinum, and palladium is conducted with no use of solvent. The controlled thermolysis initiates the melting of the powder of noble metal complex to afford the precursor liquid and then the liquid gradually decomposes. In spite of no use of solvent, stabilizer, and reducing agent, reduction reaction is thermochemically induced to afford noble metal nanoparticles stabilized by organic components derived from the organic ligands of precursor complexes.

2. Synthesis Strategy of the Solvent-Free Controlled Thermolysis

Solvent-free controlled thermolysis of metal complexes is conducted by heating the powder of metal complex with no use of solvent. Scheme 1 gives a good example of gold nanoparticles to show the synthesis strategy of the solvent-free controlled thermolysis of $[C_nH_{2n+1}NMe_3][Au(SR)_2]$ [10].

The thiolate ligand SR of the precursor gold(I) complex causes reductive elimination reaction by heating to reduce metal center Au(I) to Au(0) and to produce liquid disulfide RS–SR. Here, thiolate ligand and the produced disulfide function as a reducing agent and as a solvent, respectively. The counter-cation of the precursor containing a long alkyl chain and NMe_3 part is also decomposed by heating to evolve gaseous NMe_3 and long alkyl chains in a reaction mixture. The formed gold nuclei grow through thermolysis procedure, but the remaining long alkyl chains can attach on the surface of the gold nuclei to inhibit further agglomeration. Since the organic parts in the precursor complex play an important role in the action as a reducing agent, a solvent, and a stabilizer, the thermolysis procedure effectively produces metal nanoparticles. Furthermore, the decrease in the volume of the precursor after melting can easily make the thermolysis procedure to apply to large-scale synthesis of metal nanoparticles.

For the purpose of the size regulation of the gold nanoparticles, equimolar primary, secondary, or tertiary alkylamines are added as a stabilizer and a mild reductant to the controlled thermolysis of gold(I) complex [11]. The obtained gold nanoparticles by the controlled thermolysis in the presence of various amines are well regulated and almost monodispersed nanoparticles. Such size regulation effectively resulted from the inhibition of the growth of gold nuclei by transforming reaction from ammonium and thiolate moieties to neutral tertiary amine, thiol, and sulfide, which function as stabilizers for gold nanoparticles as shown in Scheme 2.

Based on the molecular design of precursor metal complexes, the solvent-free controlled thermolysis of metal complexes may cause the thermal reduction and simultaneous attachment of organic moiety on the growing metal nuclei and give us a solution of the defects of ordinary

Metal Nanoclusters in Catalysis and Materials Science: The Issue of Size Control
Edited by B. Corain, G. Schmid and N. Toshima

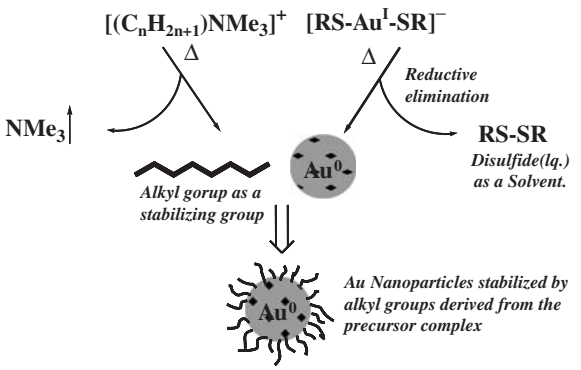

Scheme 1. The solvent-free controlled thermolysis of gold(I) thiolate complex producing gold nanoparticles stabilized by alkyl groups derived from the precursor.

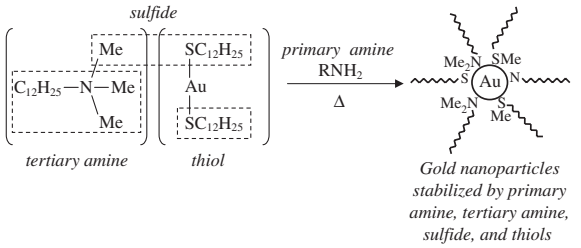

Scheme 2. Production of size-regulated gold nanoparticles stabilized by primary amines, tertiary amines, sulfides, and thiols formed by the controlled thermolysis of gold(I) thiolate complex in the presence of amine (reprinted from Ref. [11], © 2005, with permission from Elsevier).

chemical synthetic methods of metal nanoparticles: (1) low concentration preparation, (2) using large amount of stabilizer and reducing agent, and (3) difficulty of purifying the nanoparticles.

3. Results

3.1. Gold Nanoparticles

A series of gold(I) thiolate complexes, $[RN(CH_3)_3][Au(SC_{12}H_{25})_2]$ (C14Au: R = $C_{14}H_{29}$, C12Au: R = $C_{12}H_{25}$), are first used to prepare gold nanoparticles [10]. The controlled thermolysis of $[C_{14}H_{29}(CH_3)_3N][Au(SC_{12}H_{25})_2]$ was conducted at 180 °C for 5 h to afford novel gold nanoparticles (C14AuNP) stabilized by alkyl groups rather than by alkanethiolate ligands confirmed by ^{1}H NMR, XPS, and GC/MS analyses. The aggregation of gold nuclei is smoothly regulated and the growth of core gold is limited to be 22 nm in average diameter in spite of thermal procedure. However, the obtained spherical gold nanoparticles, C14AuNP, display the size distribution ranging from 11 to 76 nm as shown in Figure 1(a).

In order to regulate the size of gold nanoparticles, equimolar amount of primary, secondary, or tertiary alkylamines [$CnNH_2$, $(Cn)_2NH$, or $(Cn)_3N$] is added to the controlled thermolysis procedure of

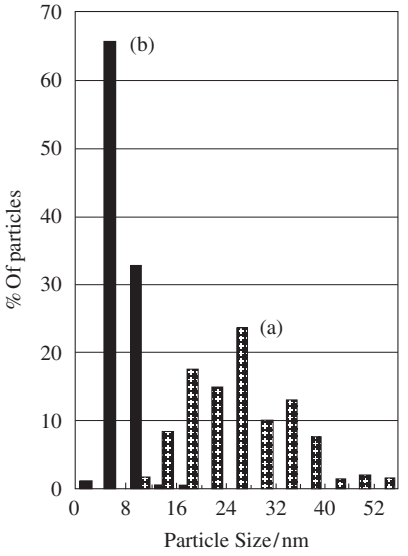

Figure 1. Particle size distribution of (a) C12AuNP and (b) C12AuNP/$C18NH_2$.

Table 1. Properties of gold nanoparticles CmAuNP and CmAu NP/amines.

Nanoparticles	Yield (%)	Metal content (%)	Average diameter (nm)	Range of diameter (nm)
C12AuNP	99	99	22	11–76
C14AuNP	93	93	26	5.0–50
$(C18)_2$AuNP	79	98	46	13–107
C12AuNP/$C8NH_2$	97	98	–	–
C12AuNP/$C12NH_2$	99	99	23	16–91
C12AuNP/$C18NH_2$	67	95	7.5	4.0–11
C12AuNP/$C8NH_2$	97	98	–	–
C12AuNP/$(C8)_2NH$	99	98	12	5.9–17
C12AuNP/$(C8)_3N$	75	97	15	6.9–30

Source: Reprinted from Ref. [11], © 2005, with permission from Elsevier.

$[RN(CH_3)_3][Au(SC_{12}H_{25})_2]$ (C14Au: R = $C_{14}H_{29}$, C12Au: R = $C_{12}H_{25}$), resulting in the production of well-regulated gold nanoparticles, CmAuNP/amine (Figure 1(b)) [11]. Table 1 shows the properties of gold nanoparticles CmAuNP together with the properties of CmAuNP/$CnNH_2$. Figure 2 shows a typical TEM photograph of the gold nanoparticles, C12AuNP/$C18NH_2$, with average diameter 7.5 nm, produced by the thermolysis of $[C_{12}H_{25}N(CH_3)_3][Au(SC_{12}H_{25})_2]$ in the presence of stearylamine $C_{18}H_{37}NH_2$. The controlled thermolysis in the presence of amines achieved to produce narrow size dispersed small nanoparticles under milder condition. The synthesized gold nanoparticles in the presence of amines were stabilized by the tertiary amines, thiols, and sulfide derived from gold(I) complex, confirmed by GC/MS. Therefore, such size regulation resulted from the inhibition of the growth of gold nuclei by transforming reaction from ammonium and thiolate moieties to neutral tertiary amine, thiol, and sulfide, which function as stabilizers for gold nanoparticles as shown in Scheme 2 (vide supra).

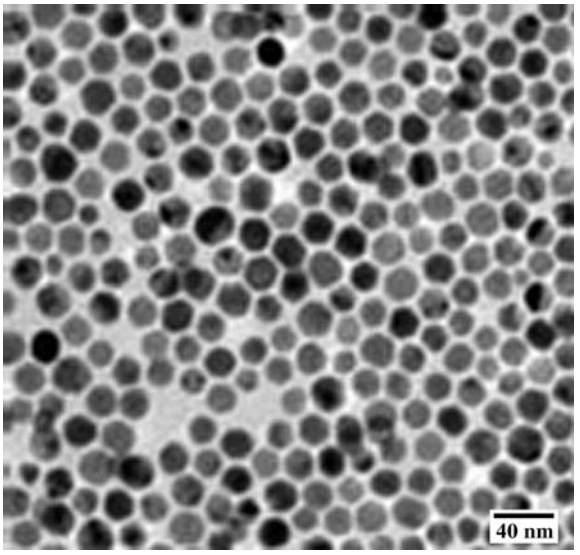

Figure 2. TEM photograph of gold nanoparticles C12AuNP/$C18NH_2$ (reprinted from Ref. [11], © 2005, with permission from Elsevier).

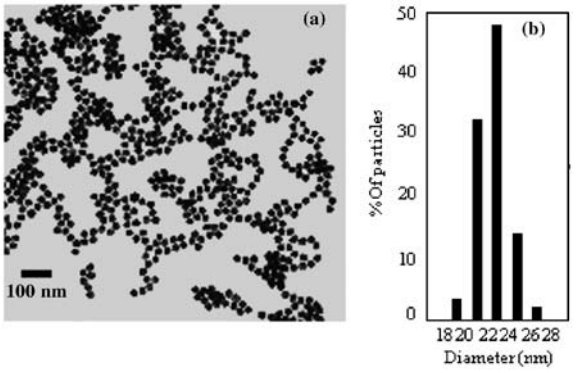

Figure 3. (a) TEM photograph of the monodispersed gold nanoparticles (average diameter 23 nm) and (b) the histogram showing particle size distribution (reprinted from Ref. [12], © 2006, with permission from The Chemical Society of Japan).

As the second candidate for the monodispersed gold nanoparticles by the solvent-free controlled thermolysis, $[Au(C_{13}H_{27}COO)(PPh_3)]$ was chosen as a precursor complex [12]. This precursor decomposes at low temperature and supplies carboxylate and PPh_3 ligands as organic protecting groups to prevent the agglomeration. The obtained gold nanoparticles are the monodispersed ones with diameter 23 nm capped by $C_{13}H_{27}COO$ and a small amount of PPh_3 ligands (the ratio of 80:1) as shown in Figure 3.

These types of complexes, $[Ag(C_{13}H_{27}COO)(PPh_3)]$ and $[Pt\ (C_{13}H_{27}COO)_2(PPh_3)_2]$, are also chosen as the precursors for the solvent-free controlled thermolysis to produce silver nanoparticles with average size 5.7 nm and platinum nanoparticles with average size 2.7 nm, respectively [13].

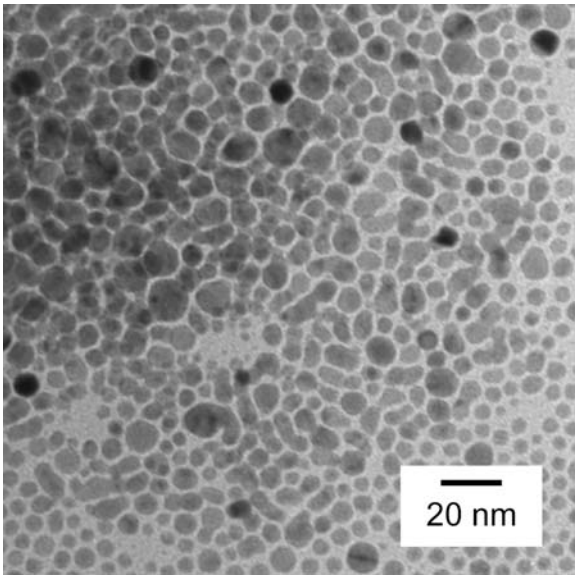

Figure 4. TEM photograph of silver nanoparticles prepared by the thermolysis of $C_{13}H_{27}CO_2Ag$ (reprinted from Ref. [18], © 2006, with permission from Elsevier).

3.2. Silver Nanoparticles

The solvent-free controlled thermolysis of a series of silver alkylcarboxylates $C_nH_{2n+1}CO_2Ag$ ($n = 6$–18) affords the alkylcarboxylate-stabilized silver nanoparticles, but the reaction requires high temperature heating [14,15]. For example, tetradecanoate-stabilized silver nanoparticles (C13AgNP) with particle size less than 10 nm were synthesized by heating of $C_{13}H_{27}CO_2Ag$ (abbreviated C13COOAg) at 250 °C for 5 h as shown in Figure 4 [11].

On the other hand, the controlled thermolysis of $C_{13}H_{27}CO_2Ag$ in the presence of triethylamine, NEt_3, can be conducted under the mild condition of 80 °C for 2 h to produce the monodispersed silver nanoparticles (average diameter 4.4 ± 0.2 nm) as shown in Figure 5 [16]. The silver nanoparticles are capped by tetradecanoate ligand, where NEt_3 does not function as the capping ligand. The silver nanoparticles are produced by the reaction mechanism via the intermediate 1:2 adduct, bis(amine)silver(I) carboxylate; the first step is the formation of the adduct and the second step is thermal decomposition of the adduct.

Table 2 shows the metal content and average diameter of silver nanoparticles synthesized by the controlled thermolysis of CnCOOAg with tertiary amines such as NEt_3 and tri-*n*-octylamine, $NOct_3$. A short alkylcarboxylate, RCOOAg (R = C7: C_7H_{15}), showed insufficient size control to produce the large and polydispersed nanoparticles, while long alkylcarboxylates, RCOOAgs (R = C13: $C_{13}H_{27}$, C17: $C_{17}H_{35}$), produced smaller nanoparticles with narrow size distributions.

To compare NEt_3 with $NOct_3$, there was no obvious effect to regulate the size distribution of nanoparticles, because they could not function as a capping ligand of nanoparticles due to their weak coordination to silver in the growth process of silver nucleus [17].

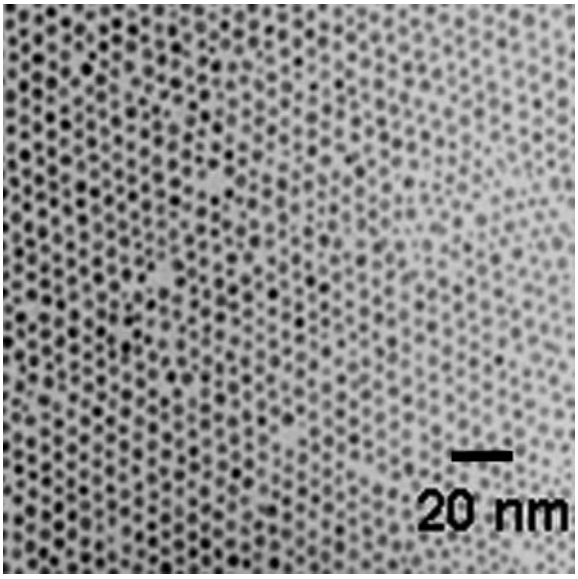

Figure 5. TEM photograph of C13AgNP prepared by the controlled thermolysis of $C_{13}H_{27}CO_2Ag$ in NEt_3 (reprinted from Ref. [16], © 2003, with permission from Royal Society of Chemistry).

Table 2. Metal content and average diameter of silver nanoparticles $CmAgNP/N(Cn)_3$s.

Nanoparticles	Yield (%)	Metal content (%)	Average diameter (nm)
$C7AgNP/NEt_3$	89	94	15.4 ± 5.1
$C13AgNP/NEt_3$	94	83	4.4 ± 0.2
$C17AgNP/NEt_3$	94	77	2.7 ± 0.3
$C7AgNP/N(Oct)_3$	92	77	5.1 ± 1.7
$C13AgNP/N(Oct)_3$	81	79	3.6 ± 0.3
$C17AgNP/N(Oct)_3$	68	75	4.4 ± 0.3

Source: Reprinted from Ref. [17], © 2006, with permission from American Chemical Society.

This procedure has been developed for thermolysis of silver alkylcarboxylates, $C_7H_{15}COOAg$, $C_{13}H_{27}COOAg$, and $C_{17}H_{35}COOAg$, in the presence of various alkylamines, $C_8H_{17}NH_2$, $C_{12}H_{25}NH_2$, and $C_{18}H_{37}NH_2$ (vide infra) [18].

3.3. Au–Ag Alloy Nanoparticles

Homogeneous Au–Ag alloy nanoparticles with narrow size distribution and nearly the same average diameter (3.0–3.7 nm) for various Au–Ag compositions were quantitatively prepared by the reduction of gold(I) complex, $[Au(C_{13}H_{27}CO_2)(PPh_3)]$, in the presence of silver tetradecanoate, $C_{13}H_{27}CO_2Ag$, in NEt_3 at 80 °C for 2 h [19]. This is a new approach for the Au–Ag alloy nanoparticle formation through the reduction of Ag(I) to Ag(0) by NEt_3 and intermetallic electron transfer from Ag(0) to gold(I) complex as shown in Scheme 3.

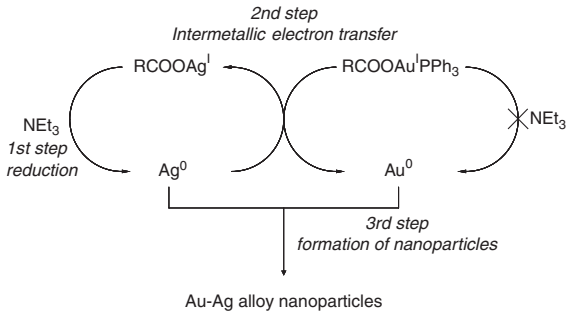

Scheme 3. Reaction mechanism of Au–Ag alloy nanoparticle formation.

Table 3 shows properties of Au–Ag alloy nanoparticles obtained by this preparative procedure.

Furthermore, this procedure can be applied to the gram-scale synthesis of alloy nanoparticles with various compositions. Amine acts as reducing agent and the organic ligands of the precursor metal complexes play an important role of stabilizer for the Au–Ag alloy nanoparticles to realize the nanometer size and narrow size distribution. The obtained nanoparticles contain 10–20% organic capping ligand such as $C_{13}H_{27}CO_2$ and PPh_3 ligands. The Au–Ag ratio is approximately compatible with that of the precursor complexes.

4. A Case History

The case of size-regulated synthesis of silver nanoparticles is illustrated here.

The solvent-free controlled thermolysis of silver alkylcarboxylates, C7COOAg, C13COOAg, and C17COOAg, in the presence of alkylamines, $C8NH_2$, $C12NH_2$, and $C18NH_2$, can regulate the growth of silver nuclei and afford silver nanoparticles stabilized by alkylcarboxylate and alkylamine (Scheme 4). Table 4 shows the metal content and average diameter of silver nanoparticles $CmAgNP/CnNH_2$. The sizes of silver nanoparticles are strongly affected by the alkyl chain length of alkylcarboxylates, but not affected by that of amines except for $C18NH_2$. It is noticeable that $C18NH_2$ acts as a strong stabilizer of silver nanoparticles specifically, as shown in Table 4. The controlled thermolysis in the presence of amines achieved to produce narrow size dispersed small silver nanoparticles under milder condition. The synthesized silver nanoparticles in the presence of amines were stabilized by the alkylcarboxylate and alkylamine. It is characteristic that these silver nanoparticles contain a high metal content, up to 97%. The synthetic method in this study may be highly promising as a facile new route to prepare size-regulated silver nanoparticles.

All solvents and chemicals were reagent grade quality, obtained commercially and used without further purification. A series of silver alkylcarboxylates, RCOOAg (C7COOAg: $R = n\text{-}C_7H_{15}$, C13COOAg: $R = n\text{-}C_{13}H_{27}$, C17COOAg: $R = n\text{-}C_{17}H_{35}$), were prepared by the modified literature method [14,16] as follows: aqueous solution of NaOH (0.150 mol) was added to the suspension of

Table 3. Properties of Au–Ag alloy nanoparticles.

Metal sources, Au:Ag[a]	Yield (%)	Metal content (%)[b]	Diameter (nm)[c]	λ_{max} (nm)[d]	Au:Ag ratio of nanoparticles[e]
1:5	89	81	3.7±0.49	441	15:85
1:2	87	83	3.1±0.48	459	33:67
1:1	84	83	3.0±0.39	484	50:50
2:1	82	86	3.2±0.34	506	66:34
5:1	56	89	3.2±0.66	514	70:30

Source: Reprinted from Ref. [19], © 2004, with permission from The Chemical Society of Japan.
[a]Mole ratio of precursors.
[b]Total amount of metals by TG analysis.
[c]TEM data.
[d]UV–vis spectral data in toluene.
[e]XPS data.

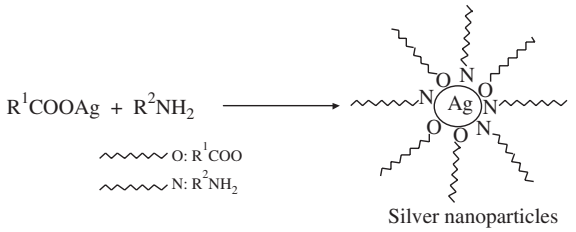

Scheme 4. Size-regulated synthesis of silver nanoparticles by controlled thermolysis (reprinted from Ref. [18], © 2006, with permission from Elsevier).

Table 4. Metal content and average diameter of silver nanoparticles CmAgNP/CnNH$_2$s.

Ag nanoparticles	Metal content (%)	Average diameter (nm)
C7AgNP/C8NH$_2$	96	30.0±11.0
C7AgNP/C12NH$_2$	97	33.0±8.60
C7AgNP/C18NH$_2$	95	4.3±0.86
C13AgNP/C8NH$_2$	85	3.8±0.60
C13AgNP/C12NH$_2$	84	4.0±0.40
C13AgNP/C18NH$_2$	74	3.8±0.45
C17AgNP/C8NH$_2$	26	Not determined
C17AgNP/C12NH$_2$	51	3.6±0.45
C17AgNP/C18NH$_2$	62	3.4±0.41

Source: Reprinted from Ref. [18], © 2006, with permission from Elsevier.

corresponding alkylcarboxylic acids (0.150 mol) in hot water (1.0 L). An aqueous solution of $AgNO_3$ (0.165 mol) was added to the resulting solution and then the white precipitate was afforded. The precipitate was collected and dried under reduced pressure at 60 °C to give silver alkylcarboxylates quantitatively.

4.1. Controlled Thermolysis of Silver Stearate

Stearate-stabilized silver nanoparticles, C17AgNP, were prepared by the simple one-pot thermolysis of silver stearate, C17COOAg. The powder of C17COOAg (1.0 mmol) was placed in the bottom of three necked flask, and then heated up to 250 °C to afford a liquid. Heating the liquid at that temperature for 5 h caused gradual decomposition to produce a brownish blue dispersion with metallic luster. The reaction mixture was cooled to 80 °C and then MeOH was added. The MeOH extraction of organic by-product was repeated several times until the extract became clear, and then the insoluble silver nanoparticles were collected by filtration, washed with MeOH, and dried under vacuum (90% yield based on silver). TEM photograph in Figure 6 indicates the spherical nanoparticles with the average diameter 5.0 nm and the properties of silver nanoparticles are shown in Table 5.

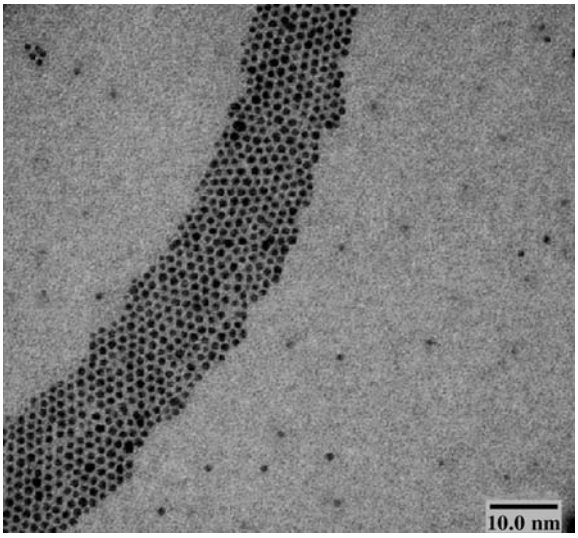

Figure 6. TEM photograph of C17AgNP prepared by the controlled thermolysis of silver stearate C17COOAg.

Table 5. Properties of silver nanoparticles C17AgNP prepared by the controlled thermolysis of C17COOAg.

Yield	90% (based on Ag)
Ag content	83% (TG/DTA analysis)
XRD	$2\theta = 38.8, 43.7, 64.6, 77.1°$ (fcc) (diameter 3 nm estimated by Scherrer equation)
Average diameter	5.0 nm (TEM)
UV–vis	$\lambda_{max} = 420$ nm (plasmon absorption)

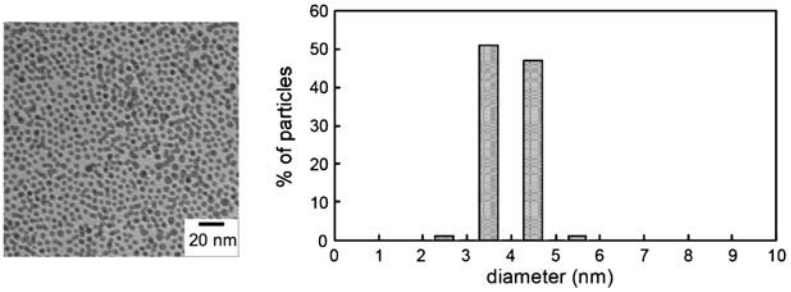

Figure 7. (a) TEM photograph of C13AgNP/C12NH$_2$ and (b) the particle size distribution (reprinted from Ref. [18], © 2006, with permission from Elsevier).

4.2. Controlled Thermolysis of Silver Alkylcarboxylate in the presence of Alkylamine

Silver nanoparticles, C13AgNP/$C_{12}NH_2$, were also prepared by simple one-pot thermolysis of silver tetradecanoate, C13COOAg, in the presence of dodecylamine, C12NH$_2$. The powder of C13COOAg (1.0 mmol) and equimolar amount of C12NH$_2$ (1.0 mmol) were placed in the bottom of three necked flask, and then heated up to 180 °C to afford a liquid of reaction mixture. Heating the liquid at that temperature for 5 h caused gradual decomposition to produce a brown dispersion with metallic luster. The reaction mixture was cooled to 80 °C and then MeOH was added. The MeOH extraction was repeated several times until the extract became clear, and then the precipitates were collected by filtration, washed with MeOH, and dried under vacuum (67% yield based on silver). Figure 7 displays the obtained silver nanoparticles, indicating the monodispersed spherical forms.

5. Conclusions

The solvent-free controlled thermolysis of metal complexes in the absence or presence of amines is the simple one-pot synthesis of the metal nanoparticles such as gold, silver, platinum, and palladium nanoparticles and Au–Ag, Au–Pt, and Ag–Pd alloy nanoparticles. In spite of no use of solvent, stabilizer, and reducing agent, the nanoparticles produced by this method can be well size regulated. The controlled thermolysis in the presence of amines achieved to produce narrow size dispersed small metal nanoparticles under milder condition. This synthetic method may be highly promising as a facile new route to prepare size-regulated metal nanoparticles. Finally, solvent-free controlled thermolysis is widely applicable to other metal nanoparticles such as copper and nickel besides noble metals, and metal oxide nanoparticles such as tin oxide, indium oxide, and zinc oxide [20].

References

1 J. S. Bradley, in G. Schmid (ed.) *Clusters and Colloids: From Theory to Applications*, VCH, Weinheim, 1994, 473.
2 P. H. Hess, P. H. Parker, *J. Appl. Polym. Sci.* 10 (1966) 1915.
3 J. R. Thomas, *J. Appl. Phys.* 37 (1966) 2914.
4 C. H. Griffiths, H. P. O'Horo, T. W. Smith, *J. Appl. Phys.* 50 (1979) 7108.
5 M. Kilner, G. J. Russell, S. R. Hoon, B. K. Tanner, *J. Magn. Magn. Mater.* 39 (1983) 107.
6 T. Tano, K. Esumi, K. Meguro, *J. Colloid Interface Sci.* 133 (1989) 530.
7 K. Esumi, M. Suzuki, T. Tano, K. Torigoe, *Colloids Surf.* 55 (1991) 9.
8 K. Esumi, O. Sadakane, K. Torigoe, K. Meguro, *Colloids Surf.* 62 (1992) 255.
9 T. Tano, K. Esumi, K. Meguro, *Langmuir* 5 (1989) 268.
10 M. Nakamoto, M. Yamamoto, M. Fukusumi, *J. Chem. Soc., Chem. Commun.* (2002) 1622.
11 M. Nakamoto, Y. Kashiwagi, M. Yamamoto, *Inorg. Chim. Acta* 358 (2005) 4229.
12 M. Yamamoto, M. Nakamoto, *Chem. Lett.* 32 (2003) 452.
13 M. Yamamoto, M. Nakamoto, *Kagaku To Kogyo (Sci. Ind.)* 80 (2006) 146.
14 K. Abe, T. Hanada, Y. Yoshida, N. Tanigaki, H. Takiguchi, H. Nagasawa, M. Nakamoto, T. Yamaguchi, K. Yase, *Thin Solid Films* 327–329 (1998) 524.
15 K. Abe, T. Hanada, T. Yamaguchi, H. Takiguchi, H. Nagasawa, M. Nakamoto, K. Yase, *Mol. Cryst. Liq. Cryst.* 322 (1998) 173.
16 M. Yamamoto, M. Nakamoto, *J. Mater. Chem.* 13 (2003) 2064.
17 M. Yamamoto, M. Nakamoto, *Langmuir* 22 (2006) 8581.
18 Y. Kashiwagi, M. Yamamoto, M. Nakamoto, *J. Colloid Interface Sci.* 300 (2006) 169.
19 M. Yamamoto, M. Nakamoto, *Chem. Lett.* 33 (2004) 1340.
20 M. Yamamoto, M. Nakamoto, *Kagaku To Kogyo (Sci. Ind.)* 78 (2004) 503.

CHAPTER 25

Systematic Synthesis of Monolayer-Protected Gold Clusters with Well-Defined Chemical Compositions

Tatsuya Tsukuda[1,2], Hironori Tsunoyama[1], and Yuich Negishi[1]

[1]*Research Center for Molecular-Scale Nanoscience, Institute for Molecular Science, 5-1 Higashiyama, Myodaiji, Okazaki, Aichi 444-8585, Japan*
[2]*CREST, Japan Science and Technology Agency, Kawaguchi, Saitama 332-0012, Japan*

1. Introduction

Gold clusters isolated in the gas phase have provided platforms for studying the basic principles governing the stability, structure, and properties of meso-scopic metallic systems [1]. It is well established that the stability and properties of gold clusters are mostly governed by the number of valence electrons [2,3]. For example, the high stability of Au_2, Au_8, Au_{18}, Au_{20} can be explained by the electronic-shell model, in which the delocalized conduction electrons occupy shells in an almost spherical potential. The stabilization of bare gold clusters against their agglomeration provides a chance to promote fundamental studies for the purpose of development for several applications, such as nanodevice, sensors, and catalysts. Among various stabilization methods, the protection by ligands allows for the isolation and manipulation of gold clusters as molecular entities. The most conventional systems include phosphine-stabilized gold clusters, such as $Au_{11}(PTMB)_7X_3$ [4], $[Au_{11}(TPP)_8X_2]^+$ [5,6], and $[Au_{20}(TPP)_8]^{2+}$ [7], where PTMB and TPP represent 4,4′,4″-phosphinidyne-tris(*N*-methylbenzamide) and triphenylphosphine, respectively. Since the interaction between Au and phosphine is weak, compared with that of Au–Au, the stability is explained in a similar fashion to that for free gold clusters [8,9].

The report by Schiffrin's group in 1994 [10] has given rise to a new class of gold cluster compound, in which a gold cluster is protected by monolayer of thiolates (RS). The Au:SR clusters are widely referred to as monolayer-protected clusters (MPCs) [11,12]. The facile synthesis and high stability of MPCs have resulted in interest from the viewpoint of fundamental research and applications [13]. The geometric and electronic structures of MPCs with a core larger than 1 nm have been extensively studied by Whetten and coworkers [14]. The alkanethiolate-protected gold clusters with core masses of 8, 14, 22, and 29 kDa have been isolated by fractional reprecipitation and explained in terms of a truncated octahedral motif. Thanks to these extensive studies, it is accepted that MPCs with cores larger than ca. 1 nm can be viewed as three-dimensional (3-D) version of self-assembled monolayer of thiolates formed upon Au nanocrystals. The major interest in these MPCs has been shifted to applicable usage. On the contrary, the structures and basic properties on MPCs with a smaller (sub-nanometer size) core have been little understood. They are expected to exhibit novel electronic and optical properties arising from quantized energy levels and strong interaction at the Au-S interface. There are a number of points regarding the small MPCs that are not clarified because of the difficulty of synthesis while controlling the numbers of core atoms and thiolate ligands at an atomic or molecular level. Such precision synthesis cannot be achieved by the approach typically used in the preparation of relatively large MPCs as described below.

1. Generally, MPCs are prepared by chemical reduction of gold ions in the presence of thiols. The average core size can be controlled in the range of 2–10 nm by controlling the preparation conditions, such as the molar ratios of gold ions and RSH. However, control of size at an atomic resolution is not feasible by this approach.
2. TEM is conventionally used as a tool to evaluate the size and shape of the cores by direct imaging. However, the core size cannot be determined with atomic resolution from low contrast and 2-D projection of the 3-D core. There are several subjective factors in the estimation of size; e.g., how to select the area from which the core size is derived and how to measure this precisely from the vague projections of cores in the TEM micrographs.

In order to overcome these difficulties, we developed a precision synthesis method on the basis of high-resolution size separation and mass spectrometric characterization.

Metal Nanoclusters in Catalysis and Materials Science: The Issue of Size Control
Edited by B. Corain, G. Schmid and N. Toshima

Our approach is similar to that employed in research of free cluster ions in the gas phase, where various measurements are conducted on the cluster which is mass selected out of the size-distributed clusters generated by laser sputtering. Based on the chemical compositions of the isolated MPCs, we discuss the determining factors of core size in connection with the formation processes. Some core-size dependent properties of the MPCs are also presented.

2. Synthesis Strategy

2.1. Chemical Preparation

The molecular structures of thiols (RSH) used in the present study are summarized in Scheme 1; glutathione (GSH), homo-glutathione (h-GSH), *N*-(2-mercaptopropionyl)glycine ((PG)SH), and mercaptosuccinic acid ((SA)SH), and alkanethiol (C_nSH). "Crude mixtures" of the Au:SR clusters were prepared using one of the following methods (Figure 1). Average core size was adjusted by optimizing the preparative conditions.

2.1.1. Chemical Reduction of Au(I):SR

The following chemical reaction has been used widely [13] since the first report by Schiffrin and cowokers [10].

$$\begin{aligned} \mathrm{Au(III)Cl_4^-(+RSH)} &\rightarrow \mathrm{Au(I):SR\,(+NaBH_4)} \\ &\rightarrow \mathrm{Au:SR\ clusters} \end{aligned} \quad (1)$$

We prepared water-soluble Au:SR (RSH = GSH, h-GSH, (PG)SH, (SA)SH, β-CD-SH) clusters using this method [15–18]. Firstly, RSH was added to a methanol solution of $HAuCl_4$ to form Au(I):SR polymeric species. The molar ratio [RSH]:[$HAuCl_4$] was typically in the range of 3–6 and the solvent temperature was reduced to 0 °C, in order to suppress the core growth. Then, an aqueous solution of a strong reducing agent, such as $NaBH_4$, was rapidly injected into the solution with vigorous stirring to form Au:SR clusters. Free excess thiols were removed by precipitating the clusters by the addition of methanol or by centrifugal ultrafilteration.

2.1.2. Ligand Exchange of Au:TPP with RSH

The ligand exchange approach was first developed by Hutchison and coworkers in the preparation of alkanethiolate-protected gold clusters [6].

$$\begin{aligned} \mathrm{Au(I):TPP\,(+NaBH_4)} &\rightarrow \mathrm{Au:TPP\ clusters\ (+RSH)} \\ &\rightarrow \mathrm{Au:SR\ clusters} \end{aligned} \quad (2)$$

Here, we have used this method for the synthesis of Au:SG clusters. Undecagold clusters (Au_{11}^{3+}) stabilized by triphenyl phosphine (TPP) were prepared according to the literature [6]. An aqueous solution of GSH was placed on top of a chloroform solution of Au_{11}^{3+}:TPP. The Au:SG clusters were transferred to the aqueous phase as a result of ligand exchange reactions [19].

2.1.3. Thiolation of Polymer-Stabilized Gold Cluster

This method is similar to the ligand exchange described in Section 2.1.2 except that the precursor clusters are stabilized by the polymer through much weaker interactions [20].

$$\begin{aligned} \mathrm{Au(III)Cl_4^-:PVP\,(+NaBH_4)} \\ \rightarrow \mathrm{Au:PVP\ clusters\ (+}C_n\mathrm{SH)} \rightarrow \mathrm{Au:SC}_n\ \mathrm{clusters} \end{aligned} \quad (3)$$

We first prepared gold clusters stabilized by conventional water-soluble polymer, PVP (PVP = poly(*N*-vinyl-2-pyrrolidone), M_w = 40 kDa) [21].

The Au:SC_n clusters were obtained by mixing a biphasic mixture of toluene solution of C_nSH and an aqueous dispersion of Au:PVP [22].

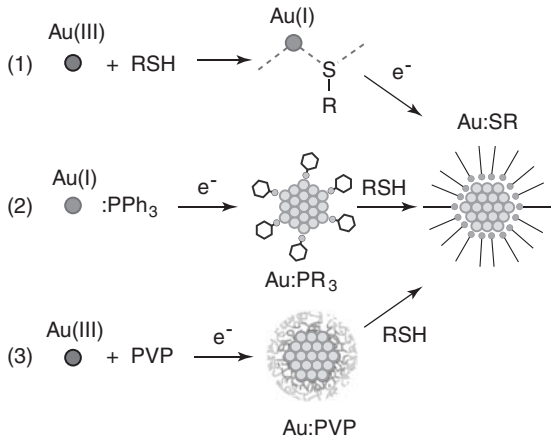

Figure 1. Preparation method of Au:SR clusters.

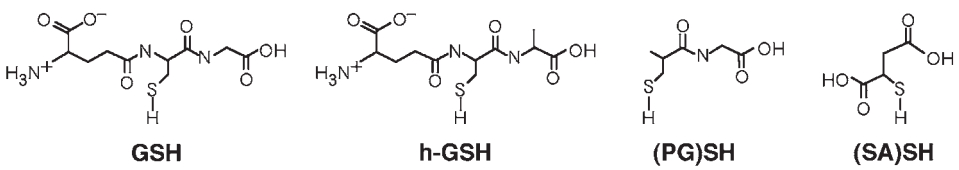

Scheme 1. Molecular structures of thiols.

2.2. Size Separation

A gold cluster covered by thiolates mimics polypeptides or polymers depending on the nature of the head groups. For example, the Au clusters protected by GSH and C_nSH appear to be a polypeptide and a spherical polymer, respectively. Such structural features enable us to fractionate the as-prepared Au:SR clusters by size using polyacrylamide gel electrophoresis (PAGE) [15–18,23–26] and size exclusion chromatography (SEC) [22,27–32], respectively (See Figure 2). Larger Au:SR clusters require more time for passage through polyacrylamide gels than smaller ones in PAGE, whereas larger clusters have a shorter residence time passing through porous hydrophobic microgels in SEC. However, further effort should be made in order to realize the separation of Au:SR clusters, where the core size differs by only 0.1 nm. The resolution of PAGE separation was greatly improved by using gels that were much more dense than conventional ones used in protein separation, whereas that of SEC was enhanced by employing a recycling SEC system where the clusters are allowed to pass through the column several times. The details of the separation are described below.

2.2.1. PAGE

Hydrophilic Au:SR (RSH = GSH, h-GSH, (PG)SH, (SA)SH, β-CD-SH) clusters were size selected using a slab gel electrophoresis unit, which employs a single gel (NA1120, Nihon Eido) or six gels (NA1116P, Nihon Eido) with a size of $3t \times 160 \times 160$ mm [15–18]. The sample solution of the as-prepared Au:SR clusters was loaded onto a stacking gel and eluted for typically 9 h under a constant voltage mode (150 V) to achieve sufficient separation. In order to minimize the possibility of thermal decomposition of the clusters, the elution was performed in a refrigerator. Parts of the separating gel containing the fractions were cut out, crushed, and placed in distilled water. The gel lumps suspended in the solution were removed using a filter with 0.2 μm pores. The Au:SR clusters were then precipitated by the addition of 2% acetic acid and methanol, and further purified by centrifugal ultrafiltration.

2.2.2. Recyling SEC

Hydrophobic $Au:SC_n$ clusters were size selected using a recycling preparative high-performance liquid chromatography (HPLC) system (LC-908, Japan Analytical Industry Co. Ltd.) equipped with two columns (JAIGEL-W253, Japan Analytical Industry Co. Ltd.) in series [22,32]. The upper limit of the size fractionation, *the total exclusion limit*, for the W253 column is 5×10^4. Toluene was used as an eluant and the flow rate was typically 3.5 mL/min. The UV-Vis absorbance detector was operated at 290 nm. The elution times for molecules are governed solely by the hydrodynamic sizes when the affinity between the molecules and the porous microgels in the column is negligibly small. A calibration curve was prepared using monodisperse polystyrene standards, to obtain the hydrodynamic diameter (d). A least-squares fit of the data gave the following conversion equation for our system

$$d(\text{nm}) = 265.2 \times \exp(-0.1064 \times t(\text{min})) \qquad (4)$$

where t represents the retention time. Equation (4) was used to estimate the hydrodynamic diameters of the $Au:SC_n$ clusters. The clusters with concentrations less than ca. 52 mM were injected into the columns in a typical operation. The recycling SEC allows size separation of the $Au:SC_n$ clusters with high reproducibility, resolution, and throughput [22]. The quantity obtained by the preparative SEC system was typically ca.10 mg, which is sufficient for most measurements and applications.

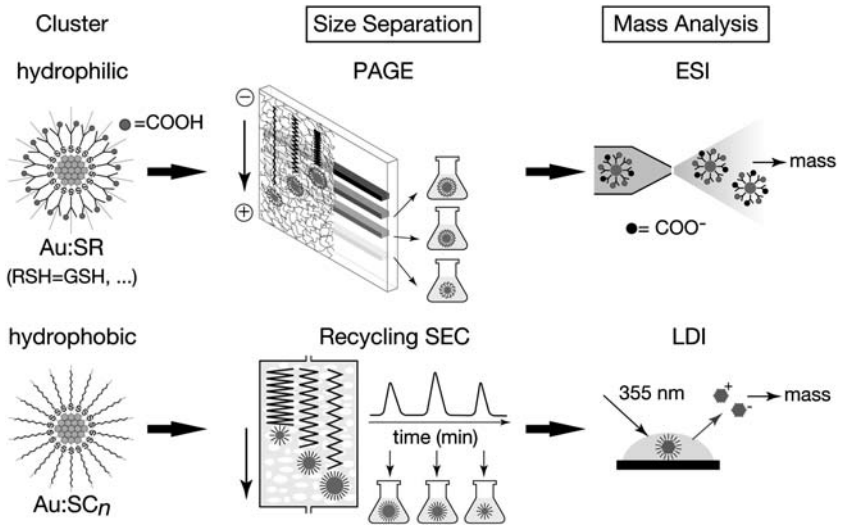

Figure 2. Experimental flow chart showing fractionation of as-prepared Au:SR clusters by size and mass spectrometric characterization.

2.3. Mass Spectrometric Determination of Chemical Compositions

The chemical compositions of the isolated Au:SR clusters were investigated by mass spectrometry [15,16,18, 22,32–35]. TEM was used to confirm that the species detected by the mass spectrometer represents the clusters in the sample. Figure 3a is a schematic representation of the top view of the mass spectrometer, which consists of five stages of differentially pumped vacuum chambers. The apparatus accommodates two types of ion sources, electrospray ionization (ESI) and laser-desorption ionization (LDI), and a time-of-flight (TOF) mass spectrometer with a reflectron. Details of the apparatus and the measurement protocols are described below.

2.3.1. LDI

The hydrophobic Au:SC_n clusters were ionized by the LDI method [11,22,32–37] (Figures 2 and 3b).

Specimens were prepared by depositing aliquots (ca. 1–5 μL) of toluene solutions containing the samples onto the surface of a stainless steel target. After the solvent was evaporated at ambient atmosphere, the target was fed into the mass spectrometer through a load-lock chamber and attached to one of the acceleration grids. The film samples were irradiated with the third harmonic (355 nm) of a Nd:YAG laser (INDI-HG, Spectra Physics) operated at 10 Hz; the laser fluence was adjusted in the range of 10–40 $\mu J/mm^2$/pulse. The desorbed ions were accelerated by application of a pulsed high voltage (15–20 kV) to the electrode plates after a delay of 4–8 μs with respect to the laser irradiation and then introduced into the mass spectrometer of Wiley–McLaren type configuration.

2.3.2. ESI

The hydrophilic Au:SR (RSH = GSH, h-GSH, (PG)SH, (SA)SH) clusters were ionized by the ESI method [15,16,18,23,24] (Figures 2 and 3c). The details of the ESI source are depicted in Figure 3c, together with typical pressures of the chambers under operation. A 50%(v/v) water–methanol solution of the fractionated Au:SR cluster with a typical concentration of 0.5 mg/mL was electrosprayed into the ambient atmosphere through the stainless steel needle of a syringe biased at ca. −3 kV. The solution was delivered by a syringe pump (SP310I, World Precision

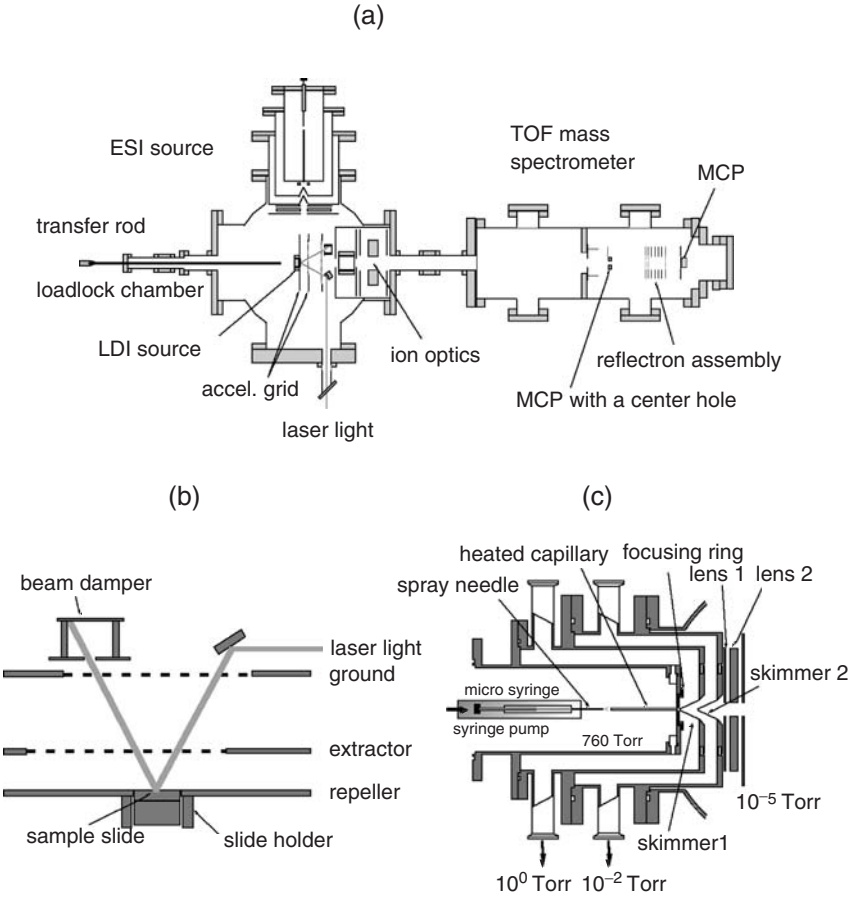

Figure 3. Mass spectrometer: (a) whole apparatus, (b) LDI source, and (c) ESI source. (Adapted with permission from Ref. [16], © 2005, American Chemical Society.)

Instruments) at a typical flow rate of 2 μL/min; the syringe pump was mounted on an *xyz* stage to optimize the needle position. The central part of the sprayed cone containing large droplets was fed into a resistively heated capillary to promote desolvation. Under an optimized capillary temperature (ca. 180 °C), evaporation of the solvents from the droplets proceeds efficiently so that only the desolvated intact cluster ions were formed at maximum yield. Dissociation of the intact clusters into small fragments was observed at higher capillary temperatures. Only small Au thiolate fragment ions were observed using commercially available ESI mass spectrometers employing a nebulizer gas and an orthogonal extraction scheme. Thus, it is crucial to introduce large droplets containing the water-soluble Au:SR clusters directly into a heated capillary in order to vaporize them non-destructively. The cluster ions exiting the capillary were focused by a ring electrode, skimmed by two sets of skimmers, and guided by an Einzel lens toward the acceleration region of the TOF mass spectrometer. The ions were extracted perpendicular to the initial beam by application of a pulsed high voltage (ca. −14 kV with ca. 30 ns rise time and 100 μs duration) to the acceleration grids.

2.3.3. TOF Mass Spectrometer

The cluster ions were counted either by a microchannel plate detector located at the end of the flight path (F4655-10, Hamamatsu) or by that with a center hole (LPD-25, Burle) after reflection by the retarding field of the reflectron. Pulsed signals from the detector were accumulated by a multichannel scaler/averager (SR430, Stanford Research Systems). The data were transferred and stored in a Windows computer using a LABVIEW program. The repetition rate was 130 and 10 Hz for collecting the ESI and LDI mass spectra, respectively. The resolution of the mass spectrometer (M/ΔM), with and without the reflectron, was typically 1000 and 400, respectively. Mass spectra of the ions of either polarity were recorded by changing the polarities of the power supplies. The LDI and ESI mass spectra obtained were calibrated by referencing with those of C_{60} and NaI cluster ions recorded under the same conditions, respectively.

3. Results

3.1. Size-Selective Synthesis of Au:SR Clusters

This section summarizes the results of size-selective synthesis of the Au:SR clusters formed in reactions (1)–(3) of Figure 1.

3.1.1. Core Sizes of Au:SR Clusters Formed by Reductive Decomposition of Au(I):SR Polymer

The clusters of Au:SG, Au:S(h-G), Au:S(PG), and Au:S(SA) were prepared by employing reaction (1) [16,17]. Using PAGE, the as-prepared clusters were separated into nine (**1**–**9**), five (**10**–**14**), six (**15**–**20**) and two (**21**, **22**) bands, respectively, as shown in Figure 4.

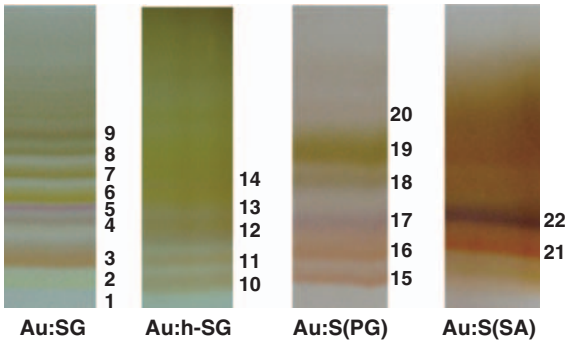

Figure 4. PAGE results of Au:SR (**1**–**22**). (Adapted with permission from Ref. [18], © 2006, American Chemical Society.)

Note that fraction **1** having the highest mobility is visible to the eye only under irradiation with a UV lamp. The chemical compositions of fractions **1**–**22** were studied by ESI mass spectrometry by taking advantage of the fact that clusters **1**–**22** are negatively charged in the sprayed solution, because some of the carboxyl groups of the thiolate ligands are dissociated. As expected, the negative-ion ESI mass spectra of **1**–**22** shown in Figure 5 comprise a series of peaks associated with multiple-charged anions originating from deprotonation of the carboxyl moieties of the corresponding thiolates, $[Au_n(SG)_m - pH^+]^{p-}$, $[Au_n(S(h\text{-}G))_m - pH^+]^{p-}$, $[Au_n(S(PG))_m - pH^+]^{p-}$, and $[Au_n(S(SA))_m - pH^+]^{p-}$. The major peaks are assigned by the $(n, m)^p$ index.

The mass spectral assignments for Au:SG (**1**–**9**) were confirmed by comparing the spectra with that calculated using the isotopic abundance and those of Au:S(h-G) clusters with the same mobility (**10**–**14**). Clusters **1**–**9** can be assigned to $Au_{10}(SG)_{10}$, $Au_{15}(SG)_{13}$, $Au_{18}(SG)_{14}$, $Au_{22}(SG)_{16}$, $Au_{22}(SG)_{17}$, $Au_{25}(SG)_{18}$, $Au_{29}(SG)_{20}$, $Au_{33}(SG)_{22}$, and $Au_{39}(SG)_{24}$, respectively. The mass assignment for **15**–**22** was not as straightforward as that for the Au:SG clusters, mainly due to the coincidence of the mass numbers. By combining the results of thermogravimetric analysis reported previously [38], we concluded that clusters **15**–**22** can be assigned to $Au_{18}(S(PG))_{14}$, $Au_{21\pm1}(S(PG))_{15\pm1}$, $Au_{23}(S(PG))_{16}$, $Au_{25}(S(PG))_{18}$, $Au_{27}(S(PG))_{19}$, $Au_{31}(S(PG))_{22}$, $Au_{20}(S(SA))_{14}$, and $Au_{23}(S(SA))_{16}$, respectively. We ascribed the poor separation by PAGE and the relatively broad-mass peaks for the Au:S(h-G), Au:S(PG), and Au:S(SA) clusters to impurities contained in the thiols used in the synthesis.

The numbers of gold atoms and thiolate ligands for **1**–**22** are plotted in Figure 6.

The plot shows that the gold-to-thiolate ratios are nearly the same regardless of the thiolate structure. It is apparent that the core sizes do not always have common values expected from the electronic shell model [2,3] or geometrically close-packed structures. This indicates that the core sizes of small Au:SR clusters formed in reaction (1) are not governed solely by the intrinsic stability of the gold cores, but are affected by thiolate ligation. This is in sharp contrast to the Au:SR clusters with relatively large cores (>1.5 nm [14]). In the chemical reduction of the Au(I):SR polymer, the growth of gold clusters proceeds irreversibly, and strongly competes with surface

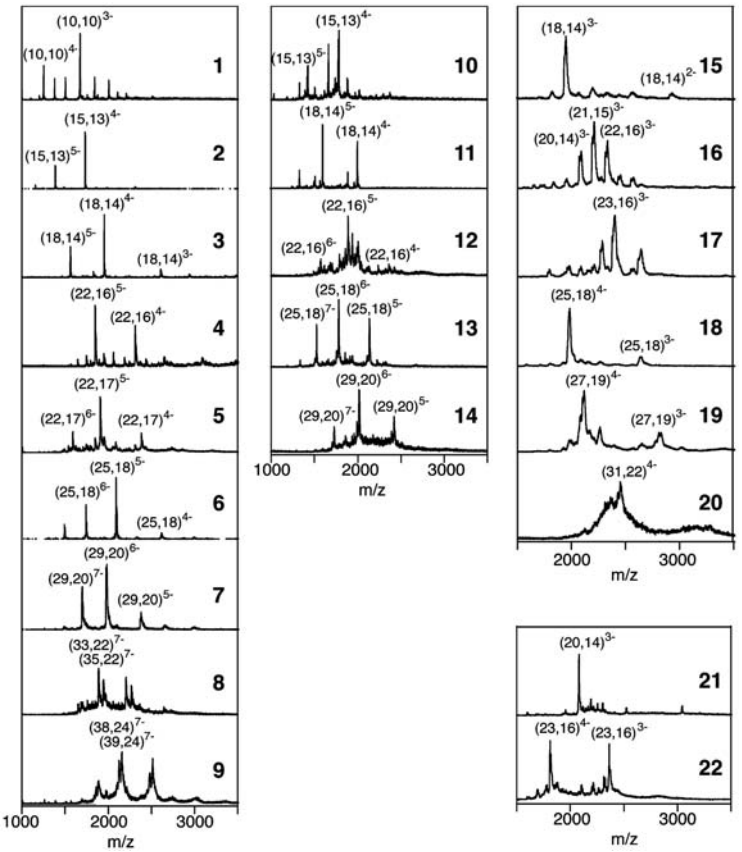

Figure 5. ESI mass spectra of Au:SR (**1**–**22**). (Adapted with permission from Ref. [18], © 2006, American Chemical Society.)

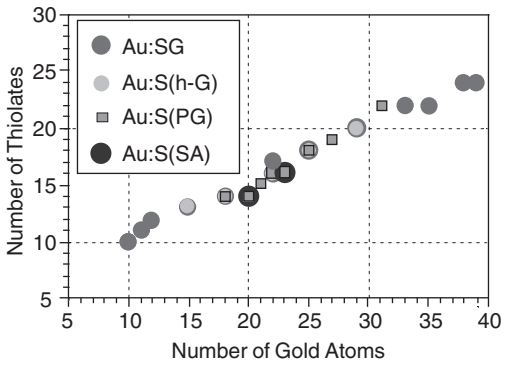

Figure 6. Chemical composition of **1**–**22**. (Adapted with permission from Ref. [18], © 2006, American Chemical Society.)

protection by thiolates. Under such circumstances, the consecutive core growth is kinetically hindered at every stage where the core is completely surrounded by the thiolate ligand shell. Thus, we interpret the variety of chemical compositions of the isolated Au:SR clusters as indicating correspondence to trapped intermediates of growing clusters whose surfaces are fully passivated. The stage at which growth is terminated may be determined by the monolayer structures of the thiolates with different molecular frameworks and/or ligation probability of the thiolates with different pK_a values to the gold cores.

3.1.2. Size Focusing via Core Etching: Selective Formation of $Au_{25}(SR)_{18}$

As demonstrated in Section 3.1.1, the Au:SR clusters formed in reaction (1) correspond to trapped intermediates of the growing clusters and are thus not always thermodynamically stable. The stabilities of the Au:SG clusters (**1**–**9**) are acutely dependent on the core sizes. The $Au_{18}(SG)_{14}$, $Au_{25}(SG)_{18}$, and $Au_{39}(SG)_{24}$ clusters were found to be stable when allowed to stand in aqueous solution while other Au:SG clusters were degraded into smaller clusters (Figure 7a) [16].

More remarkably, $Au_{25}(SG)_{18}$ is [39] found to be extremely stable against etching with free thiols. Figure 7b shows the color changes of the aqueous solutions of **1**–**9** before and after the addition of GSH at 328 K. The colors of the Au_n:SG ($n<25$) aqueous solutions faded, becoming cloudy after 3 h, while the Au_n:SG ($n\geq25$) solutions did not exhibit drastic change in color (Figure 7b). Investigation using optical spectroscopy revealed that the Au_n:SG ($n<25$) and Au_n:SG ($n>25$) clusters are etched into Au(I)-thiolate complexes and $Au_{25}(SG)_{18}$, respectively and that

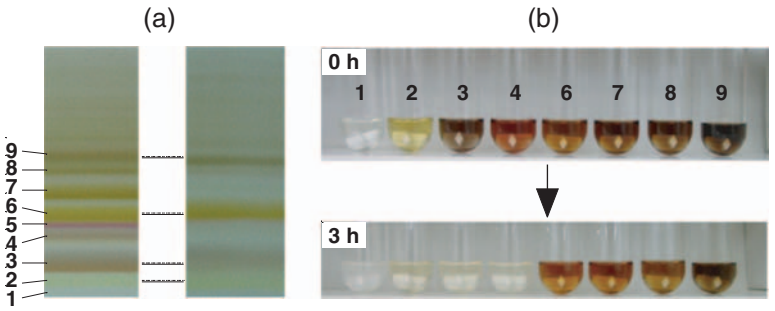

Figure 7. (a) PAGE images of the as-prepared Au:SG clusters (left) and those stored in water for two weeks (right), (b) color changes of aqueous solutions of **1**–**4** and **6**–**9** before (0 h) and after (3 h) etching reactions with GSH. (Adapted with permission from Reference [16], © 2005, American Chemical Society.)

$Au_{25}(SG)_{18}$ is stable against etching by GSH. By using this size-specific stability, we succeeded in selective formation of $Au_{25}(SG)_{18}$ by reaction (2), as described in Section 2.1.2 [19]. The reaction of Au_{11}:TPP clusters with an excess (200 mol%) amount of GSH yielded $Au_{25}(SG)_{18}$ with ca. 90% purity. We propose the following two processes as the selective formation mechanism of $Au_{25}(SG)_{18}$. First, the core agglomeration of Au_{11}:TPP takes place rapidly during the ligand exchange, to form polydisperse Au_n:SG clusters including $Au_{25}(SG)_{18}$ in the aqueous phase. The Au_n:SG ($n > 25$) clusters are then etched into $Au_{25}(SG)_{18}$, together with the formation of Au(I):SG complexes as by-products, while the Au_n:SG ($n < 25$) clusters are etched into smaller clusters to finally form Au(I):SG complexes. Once the $Au_{25}(SG)_{18}$ clusters are produced, they remain almost unchanged due to the high stability and resistance against etching by GSH. We conclude at this moment that $Au_{25}(SR)_{18}$ is the smallest magic cluster within a family of Au:SR on the basis of its high stability and preferential formation from various thiols. These results show that the stability of the clusters against size-reduction processes such as chemical etching should be monitored to determine a series of "magic core sizes" out of the Au:SR clusters formed by reaction (1).

3.1.3. Formation of Missing Au_{55}:SC_n via Thiolation of Polymer-Stabilized Gold Clusters

According to the observation described in the previous section, there is a possibility that the formation of some stable cores is skipped in reaction (1). Probably one of the mysteries of the conventional Au:SC_n system is that the Au_{55}:SC_n, a counterpart of the well known $Au_{55}(TPP)_{12}Cl_6$ cluster [40], has not been synthesized so far. Recently, Murray's group has reported that the Au_{55}:SC_6 clusters are formed as a minor species in the reaction of $Au_{55}(TPP)_{12}Cl_6$ with hexanethiol [41]. This finding suggests that the thiolate ligation of gold cluster samples containing preformed Au_{55} yields novel Au_{55}:SC_n compounds, which are not obtained by the chemical reduction of Au(I):SC_n polymers. In this section, the first isolation of "missing" Au_{55}:SR clusters is described by decoupling the core formation and thiolate protection processes, that is, via reaction (3) [22].

The Au:SC_n clusters ($n = 12$, 18) were prepared by reaction of PVP-stabilized gold clusters ($\varphi = 1.3 \pm 0.3$ nm [21]) with C_nSH. The Au:SC_n clusters obtained were incubated at 80 °C for 24 h in neat C_nSH liquid under air.

Figure 8a shows a typical recycling chromatogram of the Au:SC_{18} clusters (60 mg in 2.5 mL of toluene).

The efficiency of the elution estimated from the optical absorbance was 90–100%. After repeated passage through the column, the peak separates into two. Although the relative intensities of the two peaks varied with batches of the cluster samples, their retention times were highly reproducible. In contrast, the chromatogram of clusters prepared without incubation in neat $C_{18}SH$ exhibits a broad and featureless peak (the dotted line in Figure 8a). This remarkable difference indicates that the etching treatment is essential to enhance the population of certain stable clusters. Namely, two Au:SC_{18} having distinct hydrodynamic diameters are formed by the preparation method employed here. In order to isolate these two dominant clusters, the eluent at the 5th recycle was separated into two fractions (I and II). These crude fractions were then reinjected into the column individually and fractionated in two (**23** and **24**). Typical LDI mass spectra of fractions **23** and **24** are displayed in Figure 8b. The peaks are assigned to $Au_nS_m^+$ [11,34–37]. Fraction **23** contains only 11 kDa clusters, while fraction **24** is dominated by the 8 kDa clusters. Fraction **24** corresponds to the well-known Au_{38}:SC_n clusters, with a purity much higher than that obtained previously by fractional recrystallization. Since the 11 kDa clusters in fraction **23** are formed more abundantly as compared with their neighbors, we conclude that they correspond to highly stable Au_{55} clusters with a closed-shell structure. The Au_{55}:SC_{12} clusters could be isolated in a similar manner. TEM analysis confirms that the Au_{55}:SC_{18} clusters that were isolated are highly monodispersed in size and are of reasonable sizes, namely in the 1.2–1.4 nm range (Figure 8c). Thermogravimetric analysis suggests that the chemical composition can be represented as $Au_{55}(SC_{18})_{32}$.

3.2. Size-Dependent Optical Properties

The Au:SR clusters isolated above are treated as conventional chemical compounds. We have been studying the basic properties (e.g., optical [15–18,22,34], photophysical [16,35], chiroptical, magnetic [42]) and geometric structures [43] of Au:SG clusters (**1**–**9**) as a prototypical system. As an

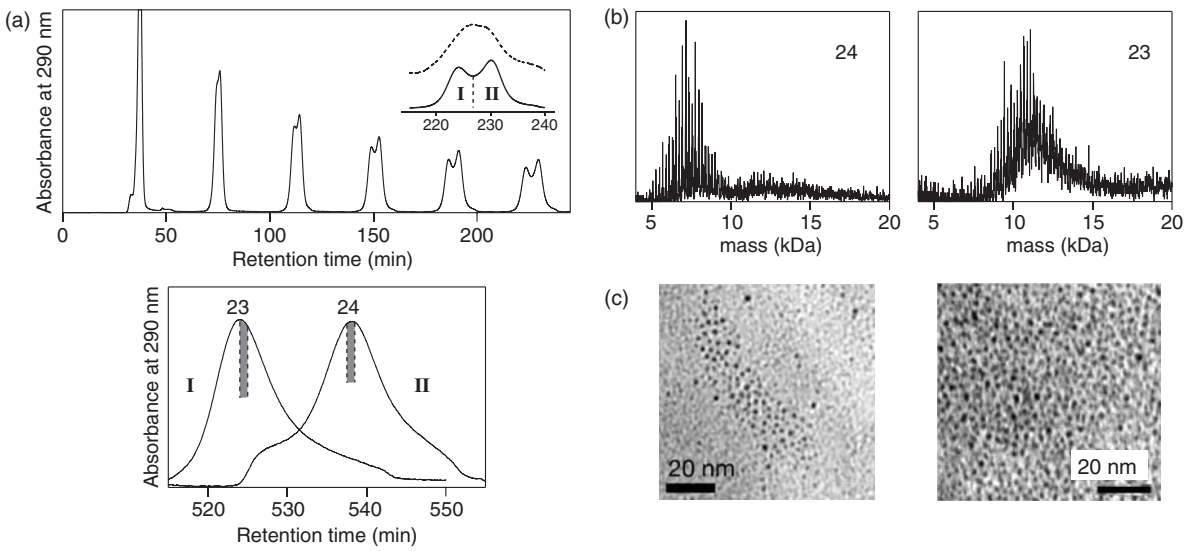

Figure 8. (a) Chromatograms, (b) LDI mass spectra, (c) TEM images of Au:SC_n (**23** and **24**). (Adapted with permission from Ref. [22], © 2006, American Chemical Society.)

example of these investigations, the optical properties of the Au:SG clusters are presented here.

3.2.1. Optical Absorption

Figure 9 summarizes the optical absorption spectra of the aqueous solutions or solid film of **1**–**9** and sodium gold(I) thiomalate (SGT) at ambient temperature.

The spectral profiles of **1**–**9** are in sharp contrast with those of thiolate-protected Au nanocrystals (>2 nm), which exhibit the surface plasmon band at ca. 2.4 eV on otherwise smooth profile. Clear absorption onsets appear for **1**–**9** in the range of 0.8–3.0 eV, which are indicated by downward arrows in Figure 9. The onsets are followed by humps, which tend to be blue shifted with decrease in the core size as indicated by upward arrows. These features demonstrate that the electronic structures of **1**–**9** are well quantized and are better viewed as non-metallic molecular assemblies rather than metallic particles protected by thiolates. The spectra can be qualitatively interpreted with the help of recent density functional studies on the photoabsorption spectra of $[Au_{13}(SCH_3)_8]^{3+}$, in which eight (1 1 1) facets of the cuboctahedral Au_{13} cluster are passivated by eight CH_3S ligands [44]. The calculated absorption spectrum of $[Au_{13}(SCH_3)_8]^{3+}$ exhibits two sharp peaks at 532 and 395 nm and shoulder structures at 224–268 nm. The former two peaks have been assigned to the transitions from the high-lying occupied Au 6s orbitals to the low-lying unoccupied Au 6s/6p orbitals. The latter bands in the higher energy region have been assigned to the transitions from Au–S bonding or Au 5d orbitals to the unoccupied Au 6s/6p orbitals. These optical transitions correspond to the "intraband" and "interband" transitions of bulk gold, respectively. By applying these terminologies, we assign the peaks denoted by the upward arrows and broad bands in the UV region of **1**–**9** to the transitions corresponding to the Au 6sp intraband and interband transitions of the bulk gold, respectively. The blue shift of the absorption onset

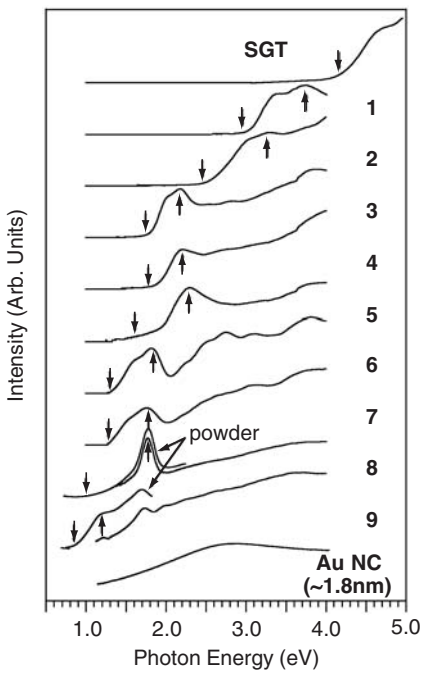

Figure 9. Optical spectra of **1**–**9**. SGT represents sodium gold(I) thiomalate. (Adapted with permission from Ref. [16], © 2005, American Chemical Society.)

with decrease in cluster size indicates the evolution of the HOMO-LUMO gap in this size regime.

A close comparison of the optical spectra of $Au_{22}(SG)_{16}$ and $Au_{22}(SG)_{17}$ indicates that the degree of thiolate ligation also affects the electronic structures of gold clusters. We found a more surprising effect of thiolate ligation on the electronic structures of the Au:SR clusters. Figure 10 compares the optical spectra of three

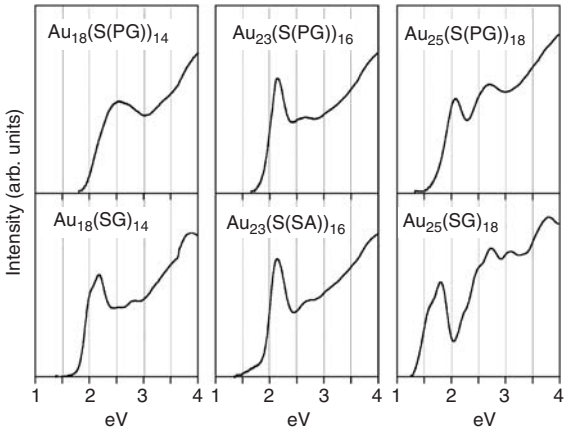

Figure 10. Optical spectra of isomers. (Adapted with permission from Ref. [18], © 2006, American Chemical Society.)

sets of the Au:SR clusters with identical chemical compositions: $Au_{18}(S(PG))_{14}$(**15**)/$Au_{18}(SG)_{14}$(**3**), $Au_{23}(S(PG))_{16}$(**17**)/$Au_{23}(S(SA))_{16}$(**22**), and $Au_{25}(S(PG))_{18}$(**18**)/$Au_{25}(SG)_{18}$(**6**). Figure 10 clearly shows that the optical spectra in the region of metal-centered optical transitions exhibit different profiles for the clusters with the above identical chemical compositions.

This implies that the electronic structures of the Au_{18}, Au_{23}, and Au_{25} cores are different, reflecting the molecular structures of the thiolates. Two possible mechanisms may contribute to the modification of the electronic structures of the gold cores. One is that the sub-nanometer size gold cores with large surface-to-volume ratios are deformed as a result of non-covalent interaction (e.g., hydrogen bonding) between adjacent thiolates. The other is that the degree of electron transfer from the gold core to the thiolate layer varies with the pK_a values of the corresponding thiols. At any rate, Figure 10 affords an example wherein the electronic structures of the small gold clusters can be manipulated externally by proper design or precise control of the thiolate headgroups.

3.2.2. Circular Dichroism

Circular dichroism (CD) is another interesting example of an optical property of the small Au:SR clusters. Since the first observation of Schaaff et al. [23,24], several reports have appeared regarding the CD activities of gold clusters protected by chiral thiols such as penicillamine [25] and *N*-isobutyryl-cysteine [26]. Figure 11 shows the CD spectra of **1**–**9**, which is a good reproduction of the original report by Whetten's group [23,24].

The Au:SG clusters were optically active in the visible and UV spectral range, with the anisotropy factors in the order of several tens to hundred parts per million. The origin of the observed optical activity in core-based electronic transitions has been previously discussed [24]. The key question is whether the gold cluster is intrinsically chiral or whether the optical activity is induced by the chiral ligation environment. The first possibility has been supported by theoretical studies performed by Garzón and

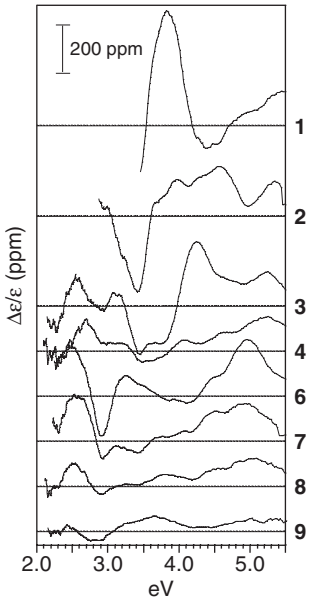

Figure 11. Circular dichroism of **1**–**9**.

coworkers, which indicate that small gold clusters such as Au_{28} prefer low symmetry chiral structures over high-symmetry, non-chiral ones [45]. Several mechanisms for the optical activity were proposed for non-chiral metal particles in a chiral environment. These include the chiral arrangement of ligands and the influence of the asymmetric centers of the chiral ligands (through space or through bonds) on the electronic structure of the metal [25,46]. Recently, the vibrational CD investigation by Gautier and Bürgi indicates that the carboxyl group also interacts with the gold cluster, which may induce a chiral "footprint" on the surface of the particle and lead to the observed optical activity [26]. However, the origin of optical activity in metal-based electronic transitions is still unclear due to the very few examples of CD-active clusters with well-defined compositions and the lack of structural information.

4. A Case History

Here we describe a large-scale synthesis of $Au_{25}(SG)_{18}$ using the ligand exchange reaction of $[Au_{11}(PPh_3)_8Cl_2]^+$ with GSH [19]. The aqueous solution (100 mL) of GSH (1.88 g) and the chloroform solution (100 mL) of $[Au_{11}(PPh_3)_8Cl_2]^+$ (67 mg) were put into a three-necked flask and the mixture was stirred vigorously in an oil bath kept at 328 K. After the reaction for 15 h under an air atmosphere, the profile of the optical spectrum of the aqueous phase becomes quite similar to that of $Au_{25}(SG)_{18}$. Evaporation of the solvent from the aqueous phase left a residue, which was purified three times by dispersing into methanol (ca. 200 mL). Then the product was redissolved in the buffer solution (30 mL) containing 19.2 mM glycine and 2.5 mM *tris*(hydroxymethyl) aminomethane. Small impurities were removed by repeated centrifugal ultrafiltration (4000 g); a filter with a cutoff molecular weight of 5 kDa was used. The residue was

dried in vacuo, leaving 72 mg of $Au_{25}(SG)_{18}$ in a powder form. The yield is about 50 times larger than that typically obtained by PAGE fractionation of the as-prepared Au:SG clusters using a single gel (Section 2.2.1).

5. Conclusions

The Au:SR clusters with sub-nanometer size cores were prepared by reductive decompositions of Au(I):SR polymer or reactions of RSH with gold clusters stabilized by phosphines or polymers. The resulting Au:SR clusters were further separated by size using PAGE/SEC and characterized by mass spectrometry. The analysis showed that several metastable Au:SR clusters are formed in the reductive decomposition process. By studying the stability against spontaneous decomposition and etching by free thiols, we discovered that $Au_{25}(SR)_{18}$ clusters exhibit magic stability. Selective synthesis of $Au_{25}(SR)_{18}$ on a large scale has been established. The thiolation of preformed gold clusters (1.3 nm) gave Au_{55}:SR clusters, which have not been accessed by the reductive decomposition method. The precise and systematic synthesis of Au:SR clusters reported here is versatile and highly reproducible so that it will contribute to the development of cluster-based nanomaterials.

References

1 W. A. deHeer, *Rev. Mod. Phys*. 65 (1993) 611.
2 K. J. Taylor, C. L. Pettiette-Hall, O. Cheshnovsky, R. E. Smalley, *J. Chem. Phys.* 96 (1992) 3319.
3 J. Li, H. J. Zhai, L. S. Wang, *Science* 299 (2003) 864.
4 D. Safer, B. Lizann, J. S. Leigh, *J. Inorg. Biochem.* 26 (1986) 77.
5 F. A. Vollenbroek, J. J. Bour, J. W. A. Van der Velden, *Rec. Trav. Chim. Pays-Bas.* 99 (1980) 137.
6 G. H. Woehrle, M. G. Warner, J. E. Hutchison, *J. Phys. Chem. B* 106 (2002) 9979.
7 H. F. Zhang, M. Stender, R. Zhang, C. Wang, J. Li, L. S. Wang, *J. Phys. Chem. B* 108 (2004) 12259.
8 D. M. P. Mingos, *Chem. Soc. Rev.* 15 (1986) 31.
9 P. Pyykkö, *Angew. Chem. Int. Ed. Engl.* 43 (2004) 4412.
10 M. Brust, M. Walker, D. Bethell, D. J. Schiffrin, R. Whyman, *J. Chem. Soc., Chem. Commun.* (1991) 801.
11 R. L. Whetten, J. T. Khoury, M. M. Alvarez, S. Murthy, I. Vezmar, Z. L. Wang, P. W. Stephens, C. L. Cleveland, W. D. Luedtke, U. Landman, *Adv. Mater*. 8 (1996) 428.
12 A. C. Templeton, W. P. Wuelfing, R. W. Murray, *Acc. Chem. Res*. 33 (2000) 27.
13 M. Daniel, D. Astruc, *Chem. Rev*. 104 (2000) 293.
14 T. G. Schaaff, M. N. Shafigullin, J. T. Khoury, I. Vezmar, R. L. Whetten, W. G. Cullen, P. N. First, C. Gutiérrez-Wing, J. Ascensio, M. Jose-Yacamán, *J. Phys. Chem. B* 101 (1997) 7885.
15 Y. Negishi, Y. Takasugi, S. Sato, H. Yao, K. Kimura, T. Tsukuda, *J. Am. Chem. Soc*. 126 (2004) 6518.
16 Y. Negishi, K. Nobusada, T. Tsukuda, *J. Am. Chem. Soc*. 127 (2005) 5261.
17 Y. Negishi, H. Tsunoyama, Y. Yanagimoto, T. Tsukuda, *Chem. Lett*. 34 (2005) 1638.
18 Y. Negishi, Y. Takasugi, S. Sato, H. Yao, K. Kimura, T. Tsukuda, *J. Phys. Chem. B* 110 (2006) 12218.
19 Y. Shichibu, Y. Negishi, T. Tsukuda, T. Teranishi, *J. Am. Chem. Soc*. 127 (2005) 13464.
20 T. Yonezawa, N. Toshima, in H. S. Nalwa (ed.) *Advanced Functional Molecules and Polymers*, Gordon and Breach, London, 2001, 65.
21 H. Tsunoyama, H. Sakurai, N. Ichikuni, Y. Negishi, T. Tsukuda, *Langmuir* 20 (2004) 11293.
22 H. Tsunoyama, Y. Negishi, T. Tsukuda, *J. Am. Chem. Soc.* 128 (2006) 6036.
23 T. G. Schaaff, G. Knight, M. N. Shafigullin, R. F. Borkman, R. L. Whetten, *J. Phys. Chem. B* 102 (1998) 10643.
24 T. G. Schaaff, R. L. Whetten, *J. Phys. Chem. B* 104 (2000) 2630.
25 H. Yao, K. Miki, N. Nishida, A. Sasaki, K. Kimura, *J. Am. Chem. Soc.* 127 (2005) 15536.
26 C. Gautier, T. Bürgi, *J. Am. Chem. Soc.* 128 (2006) 11079.
27 J. P. Wilcoxon, J. E. Martin, P. Provencio, *Langmuir* 16 (2000) 9912.
28 V. L. Jimenez, M. C. Leopold, C. Mazzitelli, J. W. Jorgenson, R. W. Murray, *Anal. Chem.* 75 (2003) 199.
29 H. Wellsted, E. Sitsen, A. Caragheorgheopol, V. Chechik, *Anal. Chem.* 76 (2004) 2010.
30 A. M. Al-Somali, K. M. Krueger, J. C. Falkner, V. L. Colvin, *Anal. Chem.* 76 (2004) 5903.
31 H. Murayama, T. Narushima, Y. Negishi, T. Tsukuda, *J. Phys. Chem. B* 108 (2004) 3496.
32 H. Tsunoyama, P. Nickut, Y. Negishi, K. Al-Shamery, Y. Matsumoto, T. Tsukuda, *J. Phys. Chem. C* 111 (2007) 4153.
33 Y. Negishi, H. Murayama, T. Tsukuda, *Chem. Phys. Lett.* 366 (2002) 561.
34 Y. Negishi, T. Tsukuda, *J. Am. Chem. Soc.* 125 (2003) 4046.
35 Y. Negishi, T. Tsukuda, *Chem. Phys. Lett.* 383 (2004) 161.
36 R. J. Arnold, J. P. Reilly, *J. Am. Chem. Soc.* 120 (1998) 1528.
37 T. G. Schaaff, *Anal. Chem.* 76 (2004) 6187.
38 S. Chen, H. Yao, K. Kimura, *Langmuir* 17 (2001) 733.
39 Y. Shichibu, Y. Negishi, H. Tsunoyama, M. Kanehara, T. Teranishi, T. Tsukuda, Small 3 (2007) 835.
40 (a) G. Schmid, R. Pfeil, R. Boese, F. Bandermann, S. Meyer, G. H. M. Calis, J. W. A. van der Velden, *Chem. Ber.* 114 (1981) 3634; (b) G. Schmid, *Inorg. Synth.* 7 (1990) 214.
41 R. Balasubramanian, R. Guo, A. J. Mills, R. W. Murray, *J. Am. Chem. Soc.* 127 (2005) 8126.
42 Y. Negishi, H. Tsunoyama, M. Suzuki, N. Kawamura, M. M. Matsushita, K. Maruyama, T. Sugawara, T. Yokoyama, T. Tsukuda, *J. Am. Chem. Soc.* 128 (2006) 12034.
43 K. Ikeda, Y. Kobayashi, Y. Negishi, M. Seto, T. Iwasa, K. Nobusada, T. Tsukuda, N. Kojima, *J. Am. Chem. Soc.* 129 (2007) 7230.
44 K. Nobusada, *J. Phys. Chem. B* 108 (2004) 11904.
45 (a) I. L. Garzón, J. A. Reyes-Nava, J. I. Rodríguez-Hernández, I. Sigal, M. R. Beltrán, K. Michaelian, *Phys. Rev. B* 66 (2002) 073403; (b) C. E. Román-Velázquez, C. Noguez, I. L. Garzón, *J. Phys. Chem. B* 107 (2003) 12035.
46 M. R. Goldsmith, C. B. George, G. Zuber, R. Naaman, D. H. Waldeck, P. Wipf, D. N. Beratan, *Phys. Chem. Chem. Phys.* 8 (2006) 63.

CHAPTER 26

Template Synthesis and Catalysis of Metal Nanoclusters in Ordered Mesoporous Silicas

Paresh L. Dhepe[1,2] and Atsushi Fukuoka[1]

[1]*Catalysis Research Center, Hokkaido University, Sapporo, Japan*
[2]*Japan Science and Technology Agency, Kawaguchi, Japan*

1. Introduction

Zeolites have ordered micropores smaller than 2 nm in diameter and are widely used as catalysts and supports in many practical reactions. Some zeolites have solid acidity and show shape-selectivity, which gives crucial effects in the processes of oil refining and petrochemistry. Metal nanoclusters and complexes can be synthesized in zeolites by the ship-in-a-bottle technique (Figure 1) [1,2], and the composite materials have also been applied to catalytic reactions. However, the decline of catalytic activity was often observed due to the diffusion-limitation of substrates or products in the micropores of zeolites. To overcome this drawback, newly developed mesoporous silicas such as FSM-16 [3,4], MCM-41 [5], and SBA-15 [6] have been used as catalyst supports, because they have large pores (2–10 nm) and high surface area (500–1000 $m^2 g^{-1}$) [7,8]. The internal surface of the channels accounts for more than 90% of the surface area of mesoporous silicas. With the help of the new incredible materials, template synthesis of metal nanoclusters inside mesoporous channels is achieved and the nanoclusters give stupendous performances in various applications [9]. In this chapter, nanoclusters include nanoparticles and nanowires, and we focus on the synthesis and catalytic application of noble-metal nanoclusters in mesoporous silicas.

Mesoporous silicas have larger pores than zeolites and serve as a suitable template for the synthesis of nanoclusters with a diameter of 2–10 nm (Figure 2). It is known that metal nanoclusters in this size range often show high catalytic performances [10–12]. This template synthesis is the extension of the ship-in-a-bottle synthesis in zeolites, where the growth of particles is restricted by the micropore. If the mesoporous material has one-dimensional (1D) channels as seen in typical MCM-41 and FSM-16 (Figure 2b), metal is able to grow along that particular direction to give nanowires.

Schüth et al. reported that Pt particles on MCM-41 show high catalytic activity in CO oxidation [13]. The Pt particles have bimodal size distribution of 2 and 20 nm, and the latter particles are not located in the pores. However, this work suggested a promotional effect of ordered mesoporous silica which is different from the effect of conventional silica. As the first trial for the synthesis of Pt nanoclusters located only in the pores, Pt carbonyl clusters $[Pt_{15}(CO)_{30}]^{2-}$ were prepared in mesoporous silicas, and the Pt nanoparticles were obtained by the decomposition of the molecular clusters [14].

The direct synthesis of Pt nanoclusters in the mesoporous silicas was studied by several groups. Ryoo first reported the synthesis of Pt nanowires inside the channels of MCM-41 [15,16]. For the nanowire formation, hydrogen reduction of $[Pt(NH_3)_4]^{2+}$ with metal loading of 0.1 wt.% was accomplished, and then the impregnation of 5 wt.% Pt ions and the subsequent hydrogen reduction were performed. This illustrates the mechanism of seeding tiny Pt particles for the afterward impregnated Pt ions to reduce over. This group also showed the formation of Pt nanowires inside the 3D channel structure of MCM-48 [17]. Similarly, nanowires of Pt, Au, and Ag (5–7 nm in diameter) were prepared in SBA-15 by hydrogen reduction of metal ions at high temperature [18,19]. It was also found that SBA-15 has the interconnection between adjacent mesoporous channels by micropores [20]. The 3D network of the pore interconnection was applied to the synthesis of mesoporous carbon as a replica of SBA-15 [21].

The above syntheses of metal nanowires are based on the thermal hydrogen reduction. However, we found that the reproducible synthesis is difficult by this method, because the hydrogen reduction needs careful control of the reaction conditions. For the reproducible and selective synthesis of wires and particles, we need to clarify the factors controlling the sintering of metals. The key factors are the concentration of residual solvent and the relative rate of reduction and migration of metal ions. The details are shown in the next section.

Recently, Somorjai reported the hydrothermal synthesis of SBA-15 in the presence of PVP-stabilized Pt nanoparticles [22]. This is a one-step synthesis of composites of metal nanoparticles and mesoporous silica.

Metal Nanoclusters in Catalysis and Materials Science: The Issue of Size Control
Edited by B. Corain, G. Schmid and N. Toshima

2. Synthesis Strategy: The Sintering-Controlled Synthesis (SCS) Approach

Our basic strategy for the template synthesis of noble-metal nanoclusters is the SCS approach as illustrated in Figure 3. In this approach, the selective synthesis of nanowires and nanoparticles is possible by controlling the sintering mechanism of metals. First of all, mesoporous silicas (a) are impregnated with metal precursors by a typical impregnation method. For the synthesis of nanowires, vapors of water and methanol are added to the impregnated sample (b), where water is a promoter of the migration of metal ions and methanol is a precursor to reductant. Then the sample (c) is irradiated with UV light to give metal nanowires in the mesoporous silica (d). Under these reaction conditions, organic radicals generated from methanol reduce the metal ions to give tiny metal nanoparticles. The metal ions migrate to the particles in the quasi solution phase, and the ions are catalytically reduced to grow into nanowires (photoreduction). Since it is known that metal colloids are formed by thermal or radiochemical reactions in water/alcohol solutions [23,24], we applied this solution chemistry to the solid-phase system with modifications using water/alcohol vapors and UV irradiation. The similar situation can be obtained when H_2 flow saturated with water vapor is used for the reduction at high temperature (wet H_2-reduction). This method is very effective for the synthesis of metal nanowires in organosilica HMM-1 [25]. On the other hand, the migration of metal ions is not promoted in dry H_2 flow (e), thus forming metal nanoparticles (f) in the mesoporous silica (dry H_2-reduction).

In order to synthesize highly dispersed metal nanoparticles, the treatment with supercritical carbon dioxide ($scCO_2$) is used before dry H_2-reduction (Figure 4). High dispersion of metal ions is achieved due to high diffusivity and low viscosity of $scCO_2$. Subsequent dry H_2-reduction forms highly dispersed metal nanoparticles. This method ($scCO_2$ treatment & dry H_2-reduction) is markedly effective for the synthesis of alloy nanoparticles.

The above methods are applicable to many kinds of mesoporous silicas, and we used siliceous FSM-16 and HMM-1 in our work.

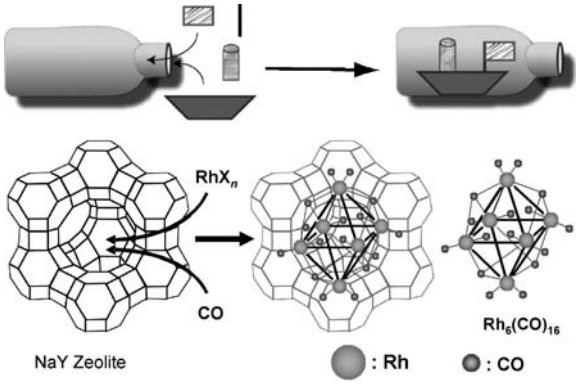

Figure 1. Ship-in-a-bottle synthesis of metal carbonyl clusters in NaY zeolite.

3. Results

After initial works on the synthesis of Pt nanowires [26–28], we found out the conditions for the selective synthesis of Pt wires and particles in FSM-16 [29] and HMM-1 [30]. In a typical procedure, H_2PtCl_6 was impregnated on FSM-16 (Pt, 5 wt.%) from aqueous solution and the impregnated sample was dried under vacuum (ca. 0.1 Pa) for 24 h. Although water vapor was again added to the dry sample in the next procedure, this vacuum-drying process was a key to the reproducible synthesis of Pt wires and particles only inside the mesopores. Without the vacuum drying, a mixture of wires and particles was formed inside and outside the mesopores. It was observed that the vacuum drying had H_2PtCl_6 dispersed uniformly on mesoporous silicas [31,32]. Then water (3 kPa) and methanol (13 kPa) vapors were again adsorbed on the sample as described above, and the sample was irradiated with a UV lamp (100 W, 250–600 nm) at room temperature for 24–48 h. In the course of this photoreduction, the sample color slowly changed from pale yellow to gray, and after the UV irradiation the sample was dried under vacuum. On the other hand, dry H_2-reduction of H_2PtCl_6/FSM-16 was performed at 673 K for 2 h for the synthesis of Pt nanoparticles.

In the TEM observation, Pt nanowires are clearly seen for the photo-reduced sample (Figure 5a). The Pt wires

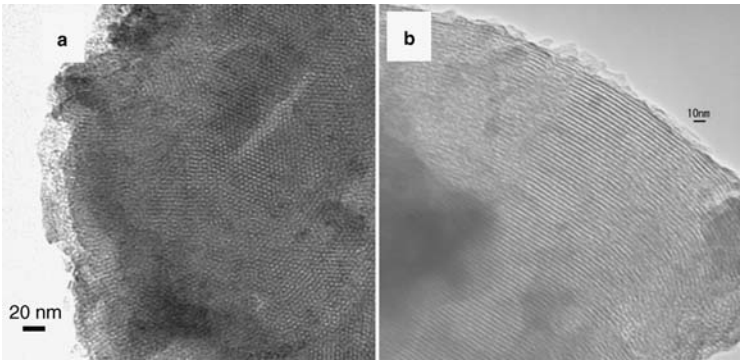

Figure 2. TEM images of FSM-16 (pore diameter 2.7 nm). (a) Front view of 2D hexagonal windows. (b) Side view of 1D channels.

are 2.5 nm in diameter corresponding to the pore diameter (2.7 nm), and the length ranges up to several hundreds of nanometers reflecting the 1D channel structure. These results show that the wires are formed inside the channels. In contrast to the photoreduction, Pt wires are not observed but well-dispersed Pt particles (2.5 nm in diameter) are seen for the sample after dry H_2-reduction (Figure 5b). Although some other groups reported the formation of metal nanowires by dry H_2-reduction, we speculate that their samples were not well dried containing a small amount of solvent, because in our experiments the wire formation was difficult by using well-dried samples.

In the XRD patterns, no significant change was observed at low 2θ angles before and after incorporating Pt in FSM-16 (Figure 6a). This confirms the 2D-hexagonal channel structure remains intact during the synthetic procedures. The XRD patterns at high 2θ angles were similar to that of bulk Pt, but lattice fringes were observed in the HRTEM images of the Pt wires. Hence, we concluded that the Pt wires have high crystallinity.

Similarly, monometallic Rh, Pd, and Au and bimetallic Pt–Rh and Pt–Pd nanowires were prepared in FSM-16 or HMM-1 by the photoreduction method [30,33,34]. The bimetallic wires gave lattice fringes in the HRTEM images, and the EDX analysis indicated the homogeneous composition of the two metals. These results show that the wires are alloys of Pt–Rh and Pt–Pd. Mesoporous silica films were also used as a template for the synthesis of uniform metal particles and wires in the channels [35,36]. Recently, highly ordered Pt nanodot arrays were synthesized in a mesoporous silica thin film with cubic symmetry by the photoreduction method [37]. The

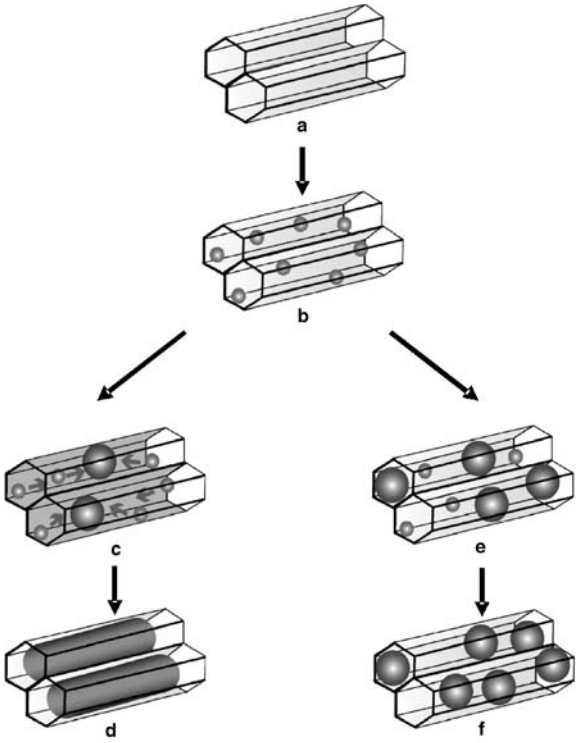

Figure 3. Schematic representation of the selective synthesis of metal nanowires and nanoparticles by the Sintering Controlled Synthesis approach. (a) Mesoporous silica, (b) impregnation of mesoporous silica with metal ions, (c) addition of water/alcohol vapors and UV-irradiation, or wet H_2-reduction, (d) formation of metal nanowires, (e) dry H_2-reduction, (f) formation of metal nanoparticles.

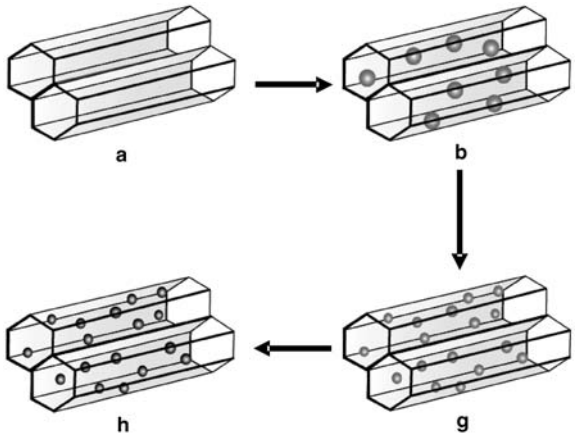

Figure 4. Synthesis of metal nanoparticles by $scCO_2$ treatment and subsequent dry H_2-reduction. (a) Mesoporous silica, (b) impregnation of mesoporous silica with metal ions, (g) $scCO_2$ treatment for high dispersion, (h) formation of small metal nanoparticles.

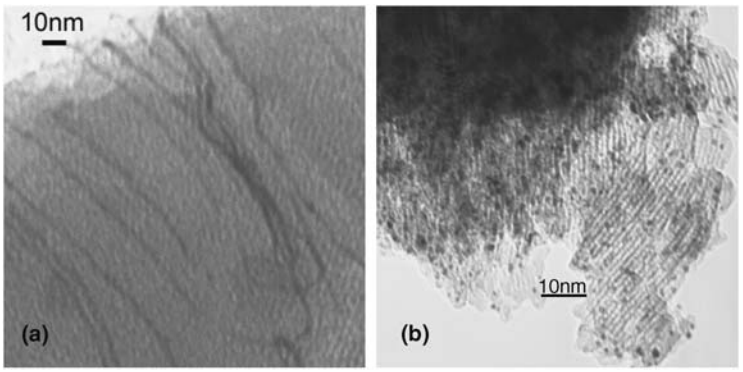

Figure 5. TEM images of (a) Pt nanowires and (b) Pt nanoparticles in FSM-16.

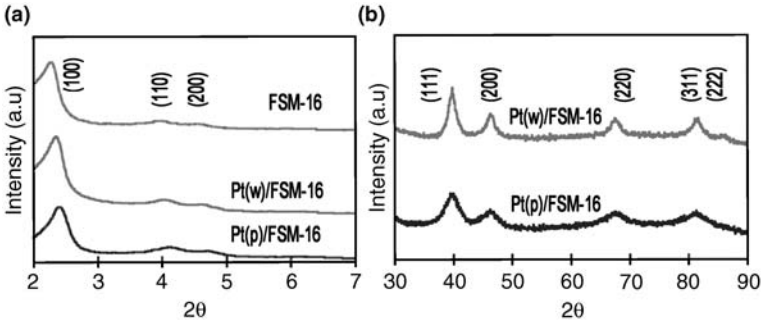

Figure 6. XRD pattern of FSM-16, Pt wire/FSM-16, and Pt particle/FSM-16.

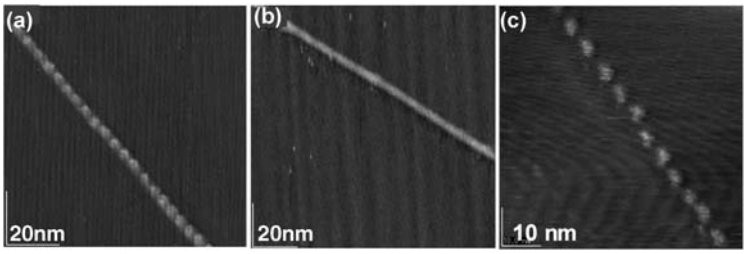

Figure 7. STM images of Pt wires extracted from Et-HMM-1 (a), FSM-16 (b), and Ph-HMM-1 (c). Pt wires were extracted with HF and deposited on HOPG. (Adapted from Ref. [32], © 2006, with permission from American Chemical Society.)

nanodot arrays thus obtained may find use as a device in nanotechnology.

In the mechanistic study of nanowire formation in the photoreduction, the formation of wire and particles greatly depends on the relative rate of migration and reduction of Pt ions [38]. Based on this mechanism, we came up with the idea that the migration of Pt ions may be enhanced in the water-saturated H_2-reduction. The powder sample of H_2PtCl_6/HMM-1 was subjected to H_2 flow with water vapor (3 kPa) at 473 K for 2 h. In fact, this wet H_2-reduction is simple but very effective in the large-scale synthesis of Pt wires in HMM-1 for short reaction time [32]. Up to 36 wt.% loading, the synthesis of Pt wire is possible using this method. The Pt wires were extracted by dissolving HMM-1 with HF, and the obtained Pt wires gave aspect ratios over 8000. In the STM image of the Pt wire extracted from HMM-1 (Figure 7a), the surface is uneven with a necklace-like structure. The Pt nanonecklace is 3 nm in diameter, and the antinode distance is 4 nm. This is in contrast with the nanorod structure of the Pt wire extracted from siliceous FSM-16 (Figure 7b). It is noticeable that the Pt wire extracted from phenylene-bridged HMM-1 (Ph-HMM-1) [39] has a slightly longer antinode distance (5–6 nm) (Figure 7c) than those from ethylene-bridged HMM-1 (Et-HMM-1). We suggest that the nanonecklace structures result from the hydrophobicity induced by the presence of aliphatic CH_2CH_2 in Et-HMM-1 and aromatic C_6H_4 in Ph-HMM-1.

It is known that Au nanoparticles efficiently catalyze various reactions, but its activity greatly depends on the degree of dispersion, support, and preparation method. We tried to synthesize Au wires and particles by our photo- and H_2-reduction. For the synthesis of Au nanowires, several groups use $HAuCl_4$ as a precursor. However, we found that $HAuCl_4$ was easily decomposed during the handling, and that a mixture of Au wires and particles were formed inside and outside the mesopores. To control the decomposition of $HAuCl_4$, $HAuCl_4$ was treated with aqueous NaOH to adjust pH at 12, and this *in situ* generated $[Au(OH)_4]^-$ species was stable and easy to handle during the impregnation procedures. $[Au(OH)_4]^-$ was impregnated on HMM-1, and Au wires and particles were selectively synthesized by the wet and dry H_2-reduction (Figure 8) [32]. Extracted Au wires also have a necklace structure, confirming that the necklace structure is formed in organosilica HMM-1.

For application to heterogeneous catalysis, highly dispersed metal nanoparticles are in great demand as active and selective catalysts. Supercritical fluids have unique properties such as high diffusivity and low viscosity, and they are regarded as a hybrid of gas and liquid. We utilized $scCO_2$ (critical temperature: 304 K, pressure: 7.3 MPa) for high dispersion of nanoparticles inside the mesoporous channels. The $scCO_2$ conditions can be obtained using a typical stainless steel autoclave for high pressure. For bimetallic catalysts, formation of homogeneous alloy particles is also expected using the $scCO_2$ treatment by dissolving two metal precursors. In our work, Rh and RhPt nanocluster catalysts were treated with $scCO_2$ (348 K, 16 MPa) after the impregnation of $[Rh(OAc)]_2$ (Ac = acetyl) and $Pt(acac)_2$ (acac = acetylacetonate) on FSM-16 or HMM-1. Since acetone is miscible in $scCO_2$, we assumed that these compounds with acetyl moieties are miscible in $scCO_2$. Although methanol is often used as a solvent in the impregnation, we observed that a small amount of remaining methanol generated a reductant during the $scCO_2$ treatment to give ill-dispersed metal particles. Hence we chose an inert solvent THF for

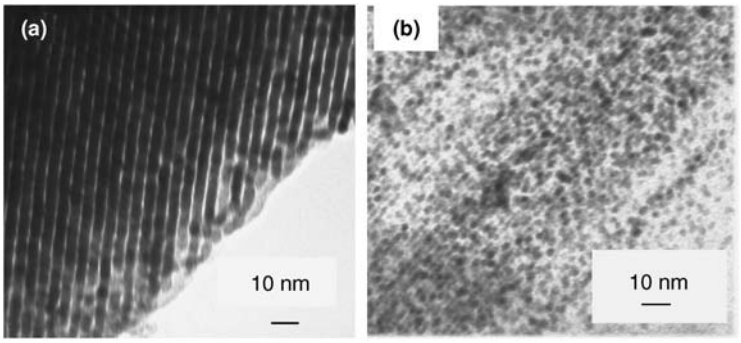

Figure 8. TEM images of Au wires (a) and particles (b) in HMM-1. (Adapted from Ref. [32], © 2006, with permission from American Chemical Society.)

Table 1. Hydrogenolysis of butane by supported Rh and RhPt catalysts.

Catalyst	Treatment	CO/M	Temperature (K)	Butane conversion (%)	Product distribution (mol%)		
					CH_4	C_2H_6	C_3H_8
Rh/SiO_2	Non-treat	0.16	463	5	27	49	24
	$scCO_2$	0.23	463	15	34	35	29
Rh/FSM-16	Non-treat	0.15	463	22	28	57	14
	$scCO_2$	0.71	463	81	20	72	8
Rh/HMM-1	Non-treat	0.53	463	84	11	81	9
	$scCO_2$	0.71	463	86	10	81	9
$RhPt/SiO_2$	Non-treat	0.36	463	15	10	81	9
			473	54	11	80	9
	$scCO_2$	0.36	463	16	15	72	13
			473	55	15	72	13
RhPt/FSM-16	Non-treat	0.67	453	46	11	79	10
			473	100	15	79	6
	$scCO_2$	0.91	453	71	7	86	6
			473	100	14	82	4
RhPt/HMM-1	Non-treat	0.38	463	38	19	62	18
			473	50	20	61	18
	$scCO_2$	0.79	463	78	8	85	7
			473	100	13	82	5

Conditions: Catalyst 0.15 g, Rh/support (2.5 wt.%), RhPt/support (Rh 2.0 wt.%, Pt 0.75 wt.%, Pt/Rh = 0.2), $C_4H_{10}/H_2 = 1/9$, GHSV = 3800 h^{-1}, 101 kPa. Results are obtained after 4 h reaction time under steady-state conditions.

the impregnation. The resulting materials were subjected to typical calcination and dry H_2-reduction. The catalysts thus prepared gave highly dispersed Rh and RhPt alloy nanoparticles in the mesoporous channels. Catalytic performances of these materials were studied using hydrogenolysis of butane as a test reaction. The $scCO_2$-treated Rh and RhPt catalysts showed higher activity and selectivity for ethane production than the non-treated catalysts [40–42]. The details of the synthesis and catalysis of the $scCO_2$-treated catalysts are illustrated in the next section.

4. A Case History

4.1. Synthesis and Characterization of RhPt Nanoparticles in Mesoporous Silica

Silicas used in this study were FSM-16 (BET surface area 950 $m^2 g^{-1}$, pore diameter 2.7 nm), ethylene bridged HMM-1 (812 $m^2 g^{-1}$, 3.1 nm), and conventional SiO_2 (Cariact Q-10, 300 $m^2 g^{-1}$). In a typical procedure, HMM-1 was dried under vacuum at 473 K for 16 h. Then HMM-1 (2.0 g) was added to a THF solution (15 ml) of $[Rh(OAc)_2]_2$ (0.086 g, 0.37 mmol) and $Pt(acac)_2$ (0.030 g, 0.075 mmol), and the mixture was stirred for 16 h. After evaporation and vacuum drying, the sample was treated with $scCO_2$ in an autoclave at 348 K and 16 MPa for 24 h. Then the sample was calcined in O_2 flow at 473 K for 2 h and reduced in H_2 flow at 473 K for 2 h (Rh 2.0 wt.%, Pt 0.75 wt.%, molar ratio Pt/Rh = 0.2).

As summarized in Table 1, the formation of small metal particles was shown in the CO chemisorption at 323 K over the Rh and RhPt on FSM-16 and HMM-1. For Rh/SiO_2 and $RhPt/SiO_2$, the dispersion slightly increased, which was due to the low surface area of SiO_2 support (300 $m^2 g^{-1}$) compared to FSM-16 (950 $m^2 g^{-1}$) and HMM-1 (812 $m^2 g^{-1}$). In line with the dispersion results, the XRD patterns for the $scCO_2$-treated samples showed broadening of the peaks (Figure 9b). In the low 2θ

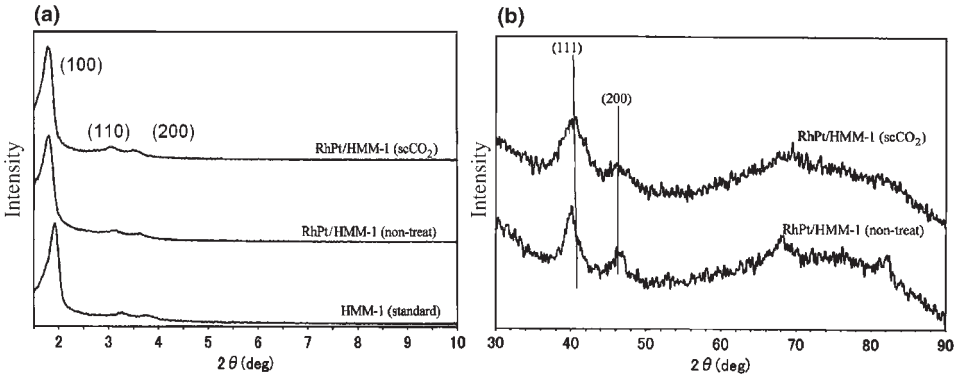

Figure 9. XRD patters for HMM-1, RhPt/HMM-1 (non-treated), and RhPt/HMM-1 ($scCO_2$-treated). (a) Low 2θ angle region and (b) high 2θ angle region.

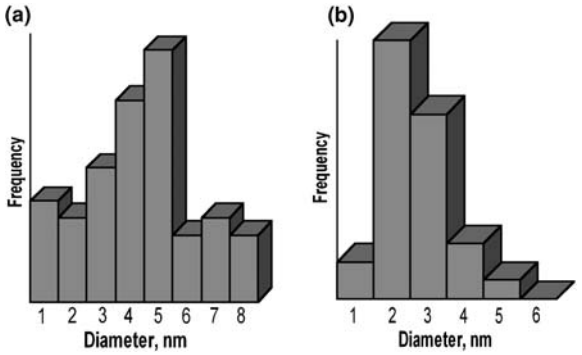

Figure 10. Distribution of particle size for RhPt/HMM-1 (non-treated) (a) and RhPt/HMM-1 ($scCO_2$-treated) (b).

angle region, the diffraction patterns indicated that mesoporous structure remained unchanged after the procedures of catalyst preparation (Figure 9a). Size distribution of RhPt particles on HMM-1 was analyzed in TEM (Figure 10). For the $scCO_2$-treated RhPt/HMM-1, the mean particle size was 2.6 nm which was smaller than that for non-treated one (4.5 nm). These results suggest that the RhPt particles are located inside the channels (diameter 3.1 nm) of HMM-1 for the $scCO_2$-treated catalyst. Similar results were obtained for RhPt/FSM-16 catalysts.

In order to study the electronic states of the RhPt surface, CO was used as a probe molecule and the IR study of CO chemisorption was performed as shown in Figure 11, where the deconvolution of the IR spectra were done using a wave-analysis program. RhPt/FSM-16 (non-treated) gave a pair of bands at 2108–2038 and 2094–2027 cm^{-1} that are assigned to $Rh(CO)_2$ species. The band at 2068 cm^{-1} is ascribed to CO coordinated to Rh^0 metal. On the other hand, RhPt/FSM-16 ($scCO_2$-treated) showed weak bands at 2109 and 2094 cm^{-1} due to $Rh(CO)_2$ species, and their contribution is low and their counterparts are masked by a broad 2045 cm^{-1} band. Since the Pt/Rh ratio is 0.2 in the RhPt catalysts, the contribution of Pt–CO (ca. 2090 cm^{-1}) is minor and overlapped with Rh–CO in the region of 2100–2080 cm^{-1}. It is noticeable that RhPt/FSM-16 ($scCO_2$-treated) gave strong bands at 2067 and 2045 cm^{-1} due to Rh^0–CO species. We propose that Rh and Pt form alloy particles in the RhPt/FSM-16 ($scCO_2$-treated) catalyst, and that the formation of electron-deficient $Rh(CO)_2$ species is suppressed by adjacent electron-rich Pt. Therefore, Pt not only divides Rh ensemble but also works as a ligand (ensemble and ligand effects). The major peaks of $Rh(CO)_2$ over RhPt/FSM-16 (non-treated) suggest the formation of separate Rh and Pt particles.

4.2. Catalysis of RhPt Particles in Mesoporous Silica

Hydrogenolysis of butane was used to study the catalysis of the RhPt particles in mesoporous silica. This is a test reaction of reforming of alkanes in oil refinery, and methane, ethane, and propane are formed by the cleavage of terminal or central C–C bond (Scheme 1).

The reaction was performed in a plug flow reactor (inner diameter 8 mm) made of Pyrex. Mass flows of butane (99.8%) and H_2 (99.999%) were controlled by mass flow controllers. The RhPt catalyst (0.15 g, 20–42 mesh) was charged in the reactor and was reduced in H_2 flow at 473 K for 0.5 h to clean the catalyst surface. Then the catalyst was cooled to a desired temperature under H_2 flow and a reaction gas was flowed into the reactor ($C_4H_{10}/H_2 = 1/9$, GHSV = 3800 h^{-1}, 101 kPa). After reaching the steady state in 4 h, products were analyzed by on-line gas chromatography (FID, column KCl/Al_2O_3).

Table 1 summarizes the results over Rh and RhPt catalysts supported on SiO_2, FSM-16, and HMM-1 after 4 h reaction time under the steady-state conditions. The $scCO_2$-treated Rh catalysts gave higher conversions of butane than the corresponding non-treated catalysts. By comparing the support effect of SiO_2, FSM-16, and HMM-1 for monometallic Rh catalysts, higher conversions were obtained over FSM-16 and HMM-1. Therefore, the use of mesoporous silica and the $scCO_2$-treatment benefit for the promotion of catalytic activity due to the formation of highly dispersed metal particles. Bimetallic RhPt/support ($scCO_2$-treated) catalysts gave enhanced butane conversions. Since

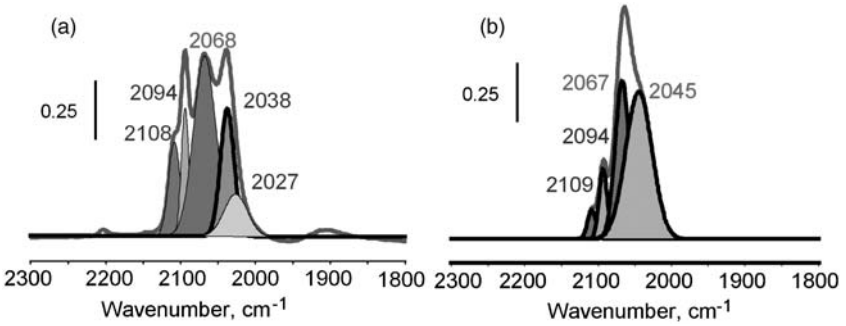

Figure 11. IR spectra of CO chemisorption over RhPt/HMM-1 (non-treated) (a) and RhPt/HMM-1 ($scCO_2$-treated) (b).

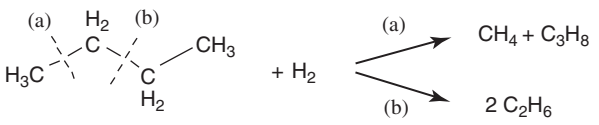

Scheme 1. Hydrogenolysis of butane.

Table 2. Hydrogenolysis of butane by supported Rh and RhPt catalysts under constant conversion levels (ca. 20%).

Catalyst	Treatment	Product distribution (mol%)		
		CH_4	C_2H_6	C_3H_8
Rh/SiO_2	Non-treat	33	38	28
	$scCO_2$	34	35	29
Rh/FSM-16	Non-treat	28	57	14
	$scCO_2$	15	77	8
$RhPt/SiO_2$	Non-treat	10	81	9
	$scCO_2$	15	72	13
RhPt/FSM-16	Non-treat	9	82	9
	$scCO_2$	6	87	6

Conditions: Catalyst 0.15 g, Rh/support (2.5 wt.%), RhPt/support (Rh 2.0 wt.%, Pt 0.75 wt.%, Pt/Rh = 0.2), $C_4H_{10}/H_2 = 1/9$, GHSV = 3800 h^{-1}, 101 kPa, Results after 4 h reaction time (under steady-state conditions).

monometallic Pt/FSM-16 gave no activity even at 473 K, Rh works as an active center for hydrogenolysis, and Pt is a co-catalyst of Rh. In addition to the high conversion of butane, we also found that the $scCO_2$-treated RhPt over FSM-16 and HMM-1 yielded high selectivity for ethane over 80%. The selectivity exceeds 50% simply derived from Scheme 1, which was observed over the non-treated Rh/SiO_2. Hence, it is concluded that the central C–C bond cleavage (path b) is more favorable than the terminal one (path a) over the highly dispersed RhPt/FSM-16 or HMM-1 catalysts. The cleavage of inner C–C bonds has an advantage to produce useful chemical feedstocks such as alkenes without the formation of less-important methane. Under similar conversion levels of ca. 20%, bimetallic RhPt catalysts are more ethane selective compared to monometallic Rh catalysts (Table 2). In our work, the results suggested that reaction is not influenced by mass transport phenomena.

5. Conclusions

Noble-metal nanoparticles and nanowires can be selectively synthesized in mesoporous silicas by controlling the sintering mechanism based on the relative rates of reduction and migration of metal ions. Photoreduction and wet H_2-reduction are useful to synthesize nanowires, and dry H_2-reduction is a good method for nanoparticles. In these methods, tuning of the concentration of water (or solvent) is needed for the reproducible synthesis of wire and particle. The treatment with $scCO_2$ and subsequent dry H_2-reduciton gives high dispersion of metal nanoparticles, and small alloy particles are obtained for bimetallic system. The alloy nanoparticles give high activity and selectivity in heterogeneous catalysis. Mesoporous silicas MCM-41, FSM-16, and SBA-15 have been widely used as catalyst supports so far. However, we believe that the other types of mesoporous silica, alumina, titania, and carbon will be more used as catalyst supports.

References

1 M. Ichikawa, *Adv. Catal.* 38 (1992) 283.
2 S. Kawi, B. C. Gates, in G. Schmid (ed.) *Clusters and Colloids*, VCH, Weinheim, 1994, 299.
3 T. Yanagisawa, T. Shimizu, K. Kuroda, C. Kato, *Bull. Chem. Soc. Jpn.* 63 (1990) 988.
4 S. Inagaki, Y. Fukushima, K. Kuroda, *J. Chem. Soc. Chem. Commun.* (1993) 680.
5 C. T. Kresge, M. E. Leonowicz, W. J. Roth, J. C. Vartuli, J. S. Beck, *Nature* 359 (1992) 710.
6 D. Zhao, J. Feng, Q. Hua, N. Melosh, G. H. Fredrickson, B. F. Chmelka, G. D. Stucky, *Science* 279 (1998) 548.
7 A. Corma, *Chem. Rev.* 2372 (1997) 97.
8 J. M. Thomas, R. Raja, *Stud. Surf. Sci. Catal.* 148 (2004) 163.
9 A. Fukuoka, M. Ichikawa, in Y. Waseda, A. Muramatsu (eds.) *Morphology Control of Materials and Nanoparticles*, Springer, Berlin, 2003, 201.
10 C.-J. Zong, M. M. Maye, J. Luo, N. Kariuki, in V. Rotello (ed.) *Nanoparticles*, Kluwer, New York, 2004, 113.
11 M. Haruta, *Catal. Today* 36 (1997) 153.
12 M. Valden, X. Lai, D. W. Goodman, *Science* 281 (1998) 1647.
13 U. Junges, W. Jacobs, I. Voigt-Martin, B. Krutzsch, F. Schüth, *Chem. Commun.* (1995) 2283.
14 T. Yamamoto, T. Shido, S. Inagaki, Y. Fukushima, M. Ichikawa, *J. Am. Chem. Soc.* 118 (1996) 5810.

15 C. H. Ko, R. Ryoo, *Chem. Commun.* (1996) 2467.
16 Z. Liu, Y. Sakamoto, T. Ohsuna, K. Hiraga, O. Terasaki, C. H. Ko, H. J. Shin, R. Ryoo, *Angew. Chem. Int. Ed.* 39 (2000) 3107.
17 H. J. Shin, R. Ryoo, Z. Liu, O. Terasaki, *J. Am. Chem. Soc.* 123 (2001) 1246.
18 Y.-J. Han, J. M. Kim, G. D. Stucky, *Chem. Mater.* 12 (2000) 2068.
19 M. H. Huang, A. Choudrey, P. Yang, *Chem. Commun.* (2001) 1063.
20 Z. Liu, O. Terasaki, T. Ohsuma, K. Hiraga, H. J. Shin, R. Ryoo, *Chem. Phys. Chem.* 4 (2001) 229.
21 S. H. Joo, S. J. Choi, I. Oh, J. Kwak, Z. Liu, O. Terasaki, R. Ryoo, *Nature* 412 (2001) 1062.
22 H. Song, R. M. Rioux, J. D. Hoefelmeyer, R. Komor, K. Niesz, M. Grass, P. Yang, G. A. Somorjai, *J. Am. Chem. Soc.* 128 (2006) 3027.
23 H. Hirai, Y. Nakao, N. Toshima, *J. Macromol. Sci.-Chem.* A12 (1978) 1117.
24 M. Michaelis, A. Henglein, *J. Phys. Chem.* 96 (1992) 4719.
25 S. Inagaki, S. Guan, Y. Fukushima, T. Ohsuna, O. Terasaki, *J. Am. Chem. Soc.* 121 (1999) 9611.
26 M. Sasaki, M. Osada, N. Sugimoto, S. Inagaki, Y. Fukushima, A. Fukuoka, M. Ichikawa, *Micro. Meso. Mater.* 21 (1998) 597.
27 M. Sasaki, M. Osada, N. Higashimoto, T. Yamamoto, A. Fukuoka, M. Ichikawa, *J. Mol. Catal. A: Chemical* 141 (1999) 223.
28 A. Fukuoka, N. Higashimoto, Y. Sakamoto, M. Sasaki, N. Sugimoto, S. Inagaki, Y. Fukushima, M. Ichikawa, *Catal. Today* 66 (2001) 23.
29 A. Fukuoka, N. Higashimoto, Y. Sakamoto, S. Inagaki, Y. Fukushima, M. Ichikawa, *Micro. Meso. Mater.* 48 (2001) 171.
30 A. Fukuoka, Y. Sakamoto, S. Guan, S. Inagaki, N. Sugimoto, Y. Fukushima, K. Hirahara, S. Iijima, M. Ichikawa, *J. Am. Chem. Soc.* 123 (2001) 3373.
31 M. T. Bore, T. L. Ward, A. Fukuoka, A. K. Datye, *Catal. Lett.* 167 (2004) 167.
32 A. Fukuoka, T. Higuchi, T. Ohtake, T. Oshio, J. Kimura, Y. Sakamoto, N. Shimomura, S. Inagaki, M. Ichikawa, *Chem. Mater.* 18 (2006) 337.
33 H. Araki, A. Fukuoka, Y. Sakamoto, S. Inagaki, N. Sugimoto, Y. Fukushima, M. Ichikawa, *J. Mol. Catal. A: Chemical* 199 (2003) 95.
34 A. Fukuoka, H, Araki, Y. Sakamoto, S. Inagaki, Y. Fukushima, M. Ichikawa, *Inorg. Chim. Acta.* 350 (2003) 371.
35 A. Fukuoka, H. Araki, Y. Sakamoto, N. Sugimoto, H. Tsukada, Y. Kumai, Y. Akimoto, M. Ichikawa, *Nano Lett.* 2 (2002) 793.
36 A. Fukuoka, H. Araki, J. Kimura, Y. Sakamoto, T. Higuchi, N. Sugimoto, S. Inagaki, M. Ichikawa, *J. Mater. Chem.* 14 (2004) 752.
37 Y. Kumai, H. Tsukada, Y. Akimoto, N. Sugimoto, Y. Seno, A. Fukuoka, M. Ichikawa, S. Inagaki, *Adv. Mater.* 18 (2006) 760.
38 Y. Sakamoto, A. Fukuoka, T. Higuchi, N. Shimomura, S. Inagaki, M. Ichikawa, *J. Phys. Chem. B* 108 (2004) 853.
39 S. Inagaki, S. Guan, T. Ohsuna, O. Terasaki, *Nature* 416 (2002) 304.
40 P. L. Dhepe, A. Fukuoka, M. Ichikawa, *Catal. Lett.* 81 (2002) 69.
41 P. L. Dhepe, A. Fukuoka, M. Ichikawa, *Chem. Commun.* (2003) 590.
42 P. L. Dhepe, A. Fukuoka, M. Ichikawa, *Phys. Chem. Chem. Phys.* 5 (2003) 5565.

CHAPTER 27

Liquid-Phase Reductive Deposition of Metal Nanoclusters Selective onto Oxide Surfaces

Atsushi Muramatsu, Hideyuki Takahashi, and Katsutoshi Yamamoto

Institute for Multidisciplinary Research of Advanced Materials, Tohoku University, Sendai, Japan

1. Introduction

Among various methods to synthesize nanometer-sized particles [1–3], the liquid-phase reduction method as the novel synthesis method of metallic nanoparticles is one of the easiest procedures, since nanoparticles can be directly obtained from various precursor compounds soluble in a solvent [4]. It has been reported that the synthesis of Ni nanoparticles with a diameter from 5 to 10 nm and an amorphous-like structure by using this method and the promotion effect of Zn addition to Ni nanoparticles on the catalytic activity for 1-octene hydrogenation [4]. However, unsupported particles were found rather unstable because of its high surface activity to cause tremendous aggregation [5]. In order to solve this problem, their selective deposition onto support particles, such as metal oxides, has been investigated, and also their catalytic activities have been studied.

In this article, the novel technique on selective deposition of noble metal particles will be introduced. Then, the novel synthesis method of single-nanosized metal particles, nanoclusters, will be described, in which metallic Ni nanoclusters with an amorphous-like structure were selectively deposited on TiO_2 fine particles through the reduction from the liquid phase. The addition of Zn proved to decrease the nanoparticles size, leading to the increase in the total area of catalytically active Ni surface. In addition, nanoclusters were highly stabilized by the deposition on TiO_2, so that the catalytic activity of Zn-added TiO_2-supported Ni nanoclusters (Ni–Zn/TiO_2) in the olefin hydrogenation was ca. 10 times higher than that of unsupported Ni nanoparticles.

The selective deposition technique seems a surface modification of oxides. In this regard, the modification of material surface is generally carried out in the field of the catalyst preparation. Catalysts are divided into heterogeneous and homogeneous catalysts. The former is well known to be used in the petroleum industry and almost all catalysts are solid, in particular, the supported catalysts. The supported catalysts are composed of the main catalysts and the supporting materials, which well support the catalyst metal so as not to be aggregated and then to suppress the decrease in catalytic activity during the use. The preparation methods for the supported catalysts are generally classified as impregnation, coprecipitation, precipitation, kneading, ion exchange, and melting methods [6]. Based on the information acquired in the catalyst search stage, these are established as preparation techniques of catalysts so that the catalyst performance can be demonstrated to be the most excellent in a certain reaction. In the case of industrial use, the generalization of these techniques is required so as not to show the difference between batches for the preparation of catalysts. Therefore, the impregnation method, in which the procedure is simple and the difference for every batch is easily suppressed, is adopted in many cases.

Titania, alumina, zirconia, silica, active carbon, zeolite, and silica–alumina are often used as a supporting material. The ion exchange method is the technique of exchanging metal cation for the proton on the surface of a supporting material and the impregnation method is to prepare the supported catalyst by impregnating a support in metal salt solution and then drying, followed by calcining it. For both the methods, as-prepared catalysts are reduced by H_2 or CO before use in necessity. pH of the starting metal salt solution is remarkably effective to the catalytic performance, because a size of catalyst metal particle is changed by pH due to the dependency of the adsorptivity of the support on pH [7]. However, by the conventional catalyst-preparation method, a metal loading (the amount of metal put on the support) could not be increased, while the size of metal particles is kept in several nanometers. For example, in the preparation of Pt catalyst supported on alumina, the Pt loading cannot exceed 3–5 wt% in order to reduce the size to be about 1–2 nm [8]. The attempt to increase the metal loading much more was failed owing to the agglomeration of the metal particles [8] and/or the poor selectivity in their deposition onto the supports [9]. On the other hand, the catalytic activity of noble metals strongly dependent on the

Metal Nanoclusters in Catalysis and Materials Science: The Issue of Size Control
Edited by B. Corain, G. Schmid and N. Toshima

particle size [10] is maintained by inhibiting aggregation and sintering [11]. In addition to the increase in the specific surface area, a significant increase in surface density of unsaturated kink sites is expected of nanoclusters, leading to the remarkable promotion of the catalytic activity [12] and/or selectivity [13].

2. Synthetic Strategy

The goal of the present study is to establish the general method of metallic nanoclusters deposition onto any support. For this purpose, the synthesis procedure has been designed due to the following manners, which are four quite important keys.

The first one is the direct synthesis of metallic nanoclusters, not via formation of (hydro)oxides and their reduction in gas-phase, because the successive reduction for formed (hydro)oxides sometimes results in the size growth of metal particles due to the aggregation and/or sintering. The second one is the use of precisely designed metal complexes, which are well adsorbed on the support surfaces, as shown in Figure 1.

Unless complexes are adsorbed on surfaces, the successive reduction will not occur so that nanoclusters might not be grown on the surface. The third one is the direct deposition of metal from solution by the reduction of the reducing agent, as shown in Figure 2.

If only adsorbed complexes take part in the formation of nanoclusters, metal loading, the quantity of nanoclusters formed on the surface, is only proportional to the amount of the adsorption. Hence, the loading is quite small, even if so large amount of complexes is located in solution phase. So, the solute species should be deposited directly onto sites for nanoparticle formation, in order to establish high loading of nanoclusters on the surface. In addition, the resultant nanoclusters are expected smaller and higher dispersed, compared with the particles formed only via surface reaction between adsorbed species, as shown in Figure 3.

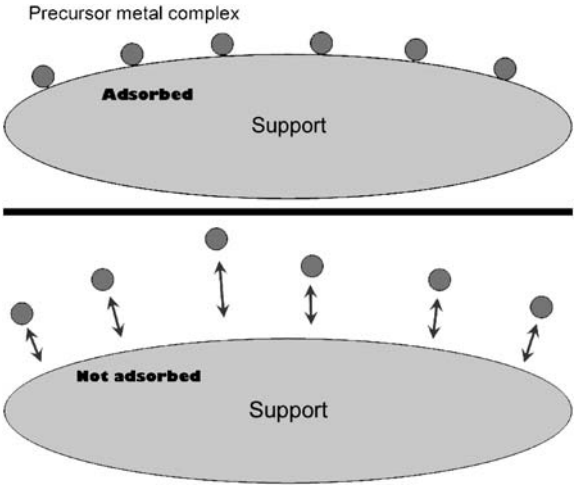

Figure 1. Design of suitable complexes easily approaching to surfaces of the support.

The final one is to nucleate particles heterogeneously only on the support surfaces, not homogeneously independently from the surfaces, as shown in Figure 4.

Generally speaking, homogeneous nucleation needs the supersaturation level higher than heterogeneous one. In the system consisting of support solid and metal salt solution, the nucleation occurs on the surfaces of the solid. The selective reductive deposition is performed by the adsorption of metal ion or complexes on the surfaces and hereby the reduction. Namely, the initial adsorption of metal ions or complexes is the key point of this technique. Hence, key points of this method are

(1) precise control of the metal complex by adjusting solute conditions, such as composition and structure of metal complex,
(2) storing of the suspension until the equilibrium composition, and
(3) aging suspension at controlled temperature.

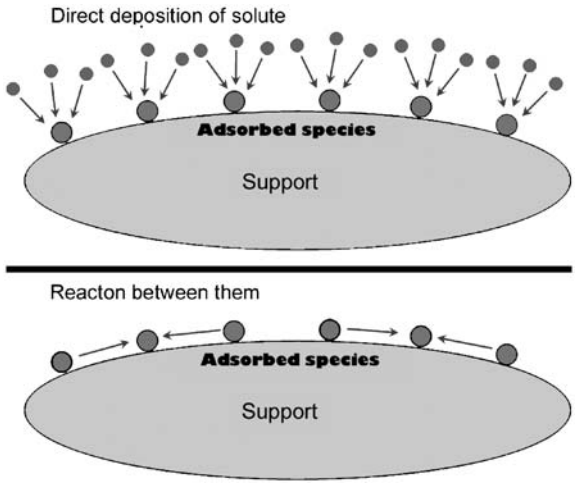

Figure 2. Direct deposition mechanism for particle growth compared with aggregation of adsorbed species.

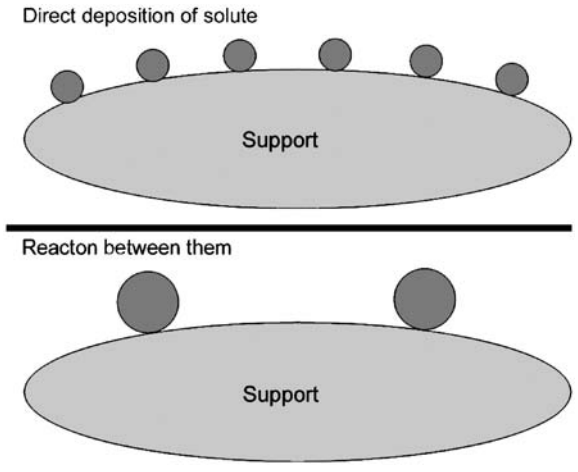

Figure 3. Direct deposition mechanism leading to highly dispersed and nanosized particle formation, compared with reaction between adsorbed species.

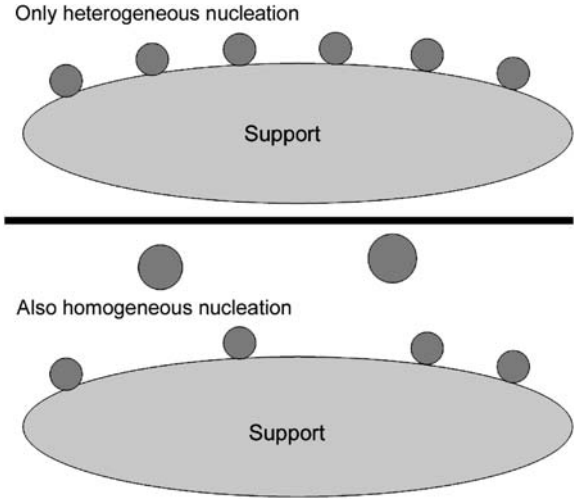

Figure 4. Homogeneous nucleation to be inhibited completely for highly dispersed nanocluster formation.

First, the selective deposition method was developed. It is the novel preparation technique, where the maximum loading around 20 wt% with keeping the particle size below 2 nm [14]. Figure 6 shows Pt metal particles supported on monodispersed spindle titania particles.

This selective deposition method is a general technique for the preparation of solid catalysts, in particular, nanoclusters of noble metal such as Au, Pt, Ir, Pd, Rh, and Ru supported on carrier materials, such as monodispersed particles and conventional metal oxides. Selective reductive deposition is based on the liquid phase reduction method. First, precursor metal salts were dissolved in aqueous or organic media. By adding the solution of reducing agent, the reduction occurs and then metal particles are selectively deposited on supports. If it is completely homogeneous solution, nanoclusters are formed through homogeneous nucleation and the growth. However, in the presence of the supports, nanoclusters are nucleated and grown on the surfaces of carrier materials.

3. Results

3.1. Selective Deposition of Gold Nanoclusters on Well-Defined Materials

Gold has long been recognized inactive as a catalyst till the advent of the report by Haruta et al. [15,16], who have demonstrated that gold functions as a highly active catalyst for oxidation of CO to CO_2 when it is deposited as ultrafine particles with high dispersion on metal oxide supports, such as hematite and titania. Since the turnover frequency of the CO conversion per unit number of exposed surface Au atoms markedly increased with size reduction, their efforts have been directed towards minimizing the particle size of Au with narrow size distribution [17–21]. Besides, Sugimoto et al. [22–25] have reported the development of a new method for the synthesis of nanosized Au particles of around 1 nm or less in mean diameter with narrow size distribution selectively formed on supports in the absence of a specific reducing agent. Established procedure will be described below. Namely, 5 cm^3 of 1.0×10^{-2} mol/dm^3 $HAuCl_4$ was mixed with 10 cm^3 of 2.0×10^{-2} mol/dm^3 NaOH at room temperature with stirring and distilled water was added to the mixture to make the total volume 25 cm^3. This solution containing 2.0×10^{-3} mol/dm^3 $HAuCl_4$ and 8.0×10^{-3} mol/dm^3 NaOH ($[OH^-]_0/[Au^{3+}]_0 = 4.0$) was aged quiescently for 24 h at room temperature to complete the hydroxylation of Au^{3+} ions. The color of the solution changed from yellow to transparent, while pH shifted from 10.81 to 6.02, by this aging. Then, 40 mg of a support powder was added to the solution and, after ultrasonic dispersion for 30 min, the suspension was aged in a laboratory oven preheated at 100 °C for 48 h. The pH was slightly changed by addition of support powder (e.g., from 6.02 to 5.90 with addition of 40 mg of α-Fe_2O_3) and finally became ca. 5.5 (e.g., 5.42 with addition of 40 mg of α-Fe_2O_3) after the aging at 100 °C for 48 h. Aging operation was done in the darkness.

As a result, nanometer-sized metallic Au particles were selectively deposited onto monodispersed polycrystalline ellipsoidal hematite particles without addition of any specific reducing agent, as shown in Figure 5.

It seems that Au^{3+} ions of $Au(OH)_nCl^-_{4-n}$ complex, formed by the first aging at room temperature, are reduced to Au particles by electron transfer from the coordinated OH^- ions on the surface of hematite as a catalyst of the electron transfer. As a consequence, the essential reducing agent is water. The optimum pH to yield the maximum quantity of Au particles was ca. pH 5.9, as measured at room temperature, corresponding to the pH of the above standard system. Au^{3+} ions are reduced to metallic Au^0 by electron transfer from coordinated OH^- ions on the surfaces of hematite particles through their catalytic action.

Figure 6 shows transmission electron micrographs of Au particles supported by (a) monocrystalline ellipsoidal (B), (b) monocrystalline pseudocubic, and (c) monocrystalline platelet-type hematite particles (see also Figure 5 for Au particles on polycrystalline ellipsoidal (A) particles). Figure 7 shows Au particles deposited on: (a) α-FeOOH, (b) β-FeOOH, (c) ZrO_2 (A), (d) ZrO_2 (B), and (e) TiO_2 (anatase).

The yield of AuO(OH) and Au^0 on each support and approximate particle size of the Au^0 are listed in Table 1.

As a rule, the specific surface area is the most important determinant of the yield and size of Au particles for a given kind of support. The larger the specific surface area is, the higher yield and the smaller particle size are obtained, because of the increase in probabilities of reduction and thus of nucleation. The extremely small yield and the large size of Au^0 particles with the platelet hematite are given for this reason. The exceedingly high yields and small sizes with zirconia (A) and (B) may be explained in a similar manner. The size difference of Au^0 with hematite supports different in specific surface area may also be elucidated based on the same reason. In this case, the yield difference is rather small, because all these systems were close to the saturation of the reaction. However, one may find a significant effect of the species of the support on the yield and final particle size of Au^0. Namely, the yield of

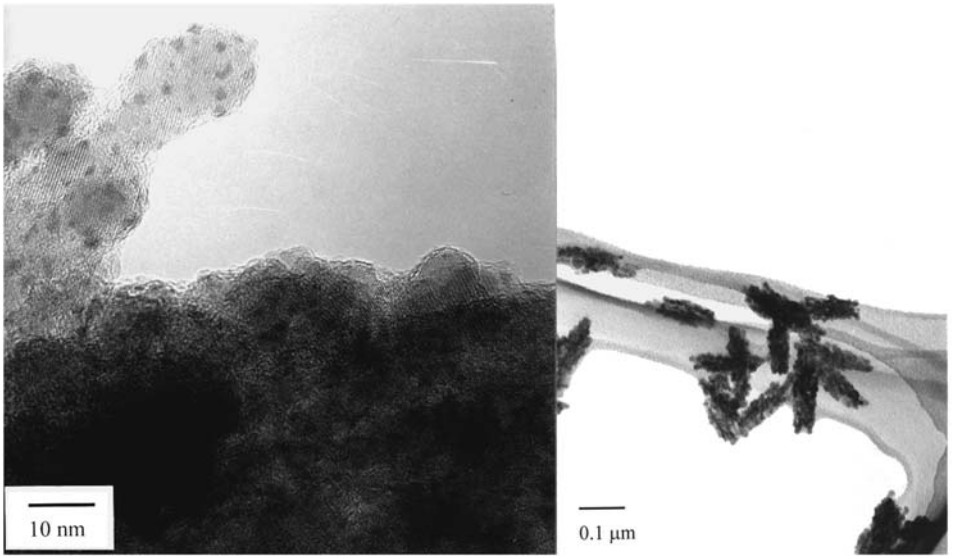

Figure 5. Transmission electron micrographs of Au nanoclusters deposited on the surfaces of the polycrystalline ellipsoidal hematite particles. The left photograph is a close-up view of the right one.

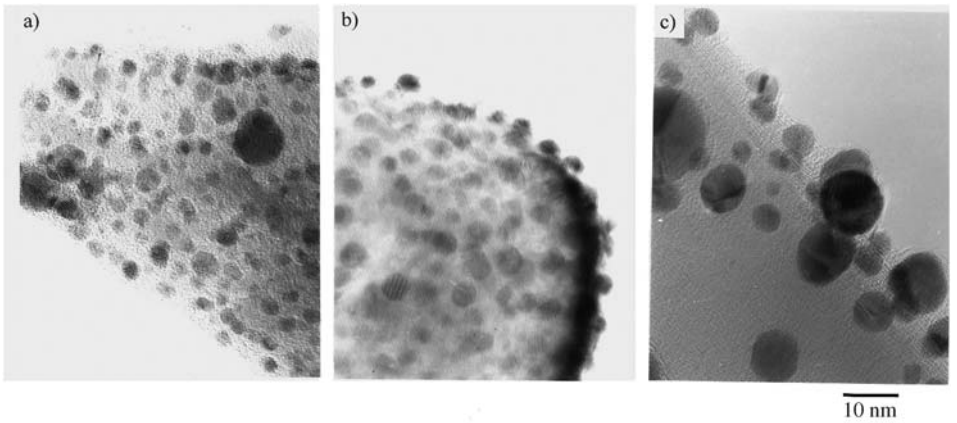

Figure 6. Au particles deposited on monodispersed hematite particles different in size and structure: (a) monocrystalline ellipsoid, (b) monocrystalline pseudocube, and (c) monocrystalline platelet. Hematite particles were also prepared by the authors.

Au^0 per unit surface area is particularly high with the ZrO_2 supports and decreases in the order of α-Fe_2O_3, α-FeOOH $\simeq$ TiO_2, β-FeOOH (the specific surface area of the TiO_2 is estimated to ca. 1.6 times as much as that of monocrystalline ellipsoidal α-Fe_2O_3). Also, the final size of Au^0 per unit surface area is especially small with the ZrO_2 supports and increases in the order of α-Fe_2O_3, TiO_2, α-FeOOH, and β-FeOOH. These effects of support species on the yield and size of Au^0 particles are deemed to be elucidated in terms of the catalytic activity of each particle. Nevertheless, in view of the significant difference in the particle size of Au^0 between TiO_2 and α-FeOOH despite the comparable yields of Au^0, it is likely that the surface roughness also contributes to size reduction of Au^0 by inhibiting the aggregative growth on the support.

Interestingly, it was found that gold particles were not produced with monodisperse amorphous SiO_2 particles prepared by the method of Stöber et al. [26]. Hence, silica has no catalytic activity for the reduction of Au (III) in the present system.

3.2. *Selective Deposition of Pt Nanoclusters on Well-Defined Materials*

Sugimoto et al. extended this novel technique to the selective deposition of noble metal nanoclusters of the platinum group (Ru, Rh, Pd, Ir, and Pt) onto well−defined metal oxide particles, since these noble are widely used as active catalysts for numerous purposes [14,25]. The established standard procedure will be described as follows. Five cubic centimeter of 1.0×10^{-2} mol/dm^3 noble metal salt ($RuCl_3$, $RhCl_3$, $PdCl_2$, H_2IrCl_6, or H_2PtCl_6) was mixed with 10 cm^3 of given concentration of NaOH at room temperature with stirring and distilled water was

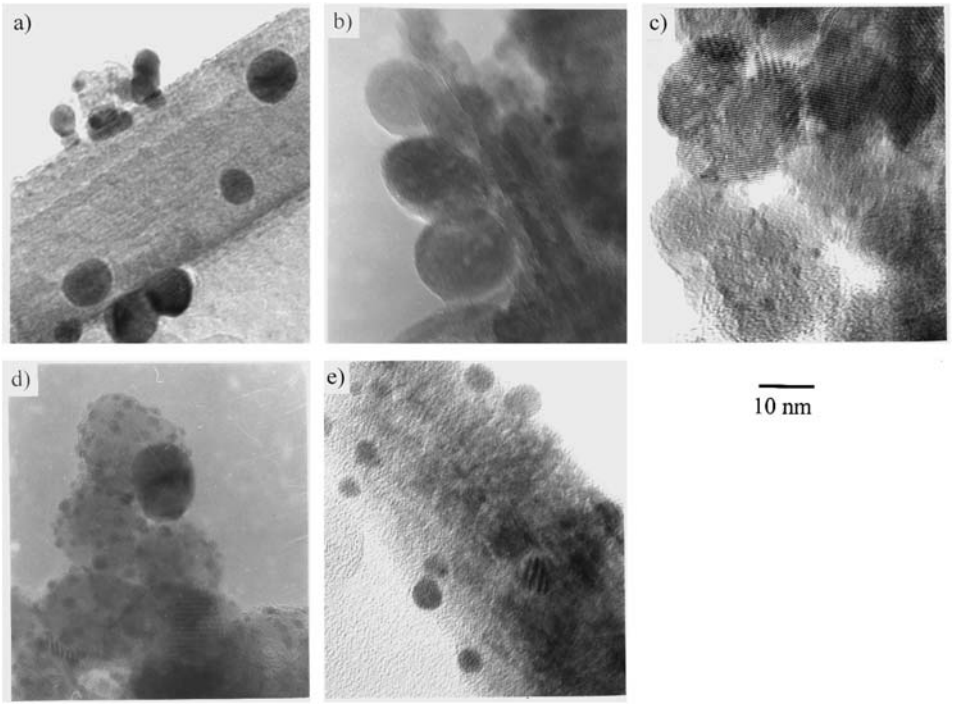

Figure 7. Au particles deposited on different supports: (a) α-FeOOH, (b) β-FeOOH, (c) ZrO_2 (A) (rough surface), (d) ZrO_2 (B) (smooth surface), and (e) TiO_2 particles. Support particles were also prepared by the authors.

Table 1. Characteristics of the supports used for deposition of metallic Au particles, yields of the metallic Au and Au hydroxide, and the size of metallic Au particles on the different supports.

Supporting particles	Size (μm)	Structure	Specific surface area (m^2/g)	Yield (mol%)		Size of Au^0 (nm)
				Au hydroxide	Au^0	
α = -Fe_2O_3, ellipsoids (A)	0.20 × 0.038	Polycrystal	136	19.9	75.1	1–2
α-Fe_2O_3, ellipsoids (B)	0.46 × 0.10	Single crystal	21.8	13.8	60.6	2–5
α-Fe_2O_3, pseudocubes	0.09	Single crystal	15.9	10.5	74.7	3–5
α-Fe_2O_3, platelets	13.3 × 1.5	Single crystal	0.70	74.3	8.5	5–15
α-FeOOH, needles	0.50 × 0.020	Single crystal	41.0	18.8	67.6	5–15
β-FeOOH, needles	0.25 × 0.012	Polycrystal[a]	112	10.3	62.7	5–20
ZrO_2 (A), spheres (rough surfaces)	0.015	Single crystal	153	0.6	99.0	0.2–1
ZrO_2 (B), spheres (smooth surfaces)	0.015	Single crystal	118	2.8	95.1	1–3
TiO_2, ellipsoids	0.35 × 0.045	Single crystal		15.8	54.8	2–5

[a]Each needle-like crystal of β-FeOOH is known to consist of a bundle of much thinner subcrystals.

added to the mixture to make the total volume 25 cm^3. This solution containing 2.0×10^{-3} mol/dm^3 noble metal salt was aged quiescently for 24 h at room temperature to stabilize the metal complexes. After 24 h, pH was stabilized to be ca. 7.0. Then, 40 mg of a support powder was added to the solution and, after ultrasonic dispersion for 30 min, the suspension was aged in a laboratory oven preheated at 100 °C for 48 h.

Effects of the initial pH on the selective deposition of the precursor particles were investigated. For the Ru, Rh, and Pd precipitates, their yields reached 100% at maximum, while the maximum yield of the Ir precipitate was somewhat lower than 100% and that of the Pt precipitate was still lower around 90%. The difference in the maximum yield is due to the difference in solubility of each precipitate, based on the complexation of the metal ions with hydroxide ions. Except for the Ru precipitate, the yield was found to be more or less lowered with decreasing pH in the acidic media, suggesting the precipitates being metal hydroxides or oxides, which are dissolved with decreasing OH^- ions. From the detailed observation by high-resolution transmission micrographs of the as-precipitated nanosized precursor particles on α-Fe_2O_3 ellipsoid support, little pH dependence of the final particle size of each metal compound was found, as compared to the significant metal-species dependence; i.e., ~0.4 nm for Ru compound, ~0.7 nm for Rh compound, ~3 nm for Pd compound, ~0.6 nm for Ir compound, and

~1.5 nm for Pt compound. In addition, there was no precipitate apart from the support particles for all samples, suggesting that the metal precipitates selectively deposited only on the support particles. This fact implies that the support particles provide specifically stable sites for the deposition of the metal compounds.

As a result of X-ray photoelectron spectroscopy, the as-precipitated metal compounds are mostly characterized by a binding energy higher than that of each bulk metal, suggesting that the precipitates are hydroxides or oxides, in contrast to the case of gold systems in which Au^{3+} ions are mostly reduced to metallic gold on the metal oxide supports. As a consequence, some reduction process is needed for these metal compounds in the platinum group to be reduced to the metallic nanoclusters. Figure 8 illustrates the yield of the precursor particles changing with aging time, in the presence or absence of the α-Fe_2O_3 ellipsoid support (1.6 g/dm^3), showing the precipitation of the precursor kinetically enhanced by the support.

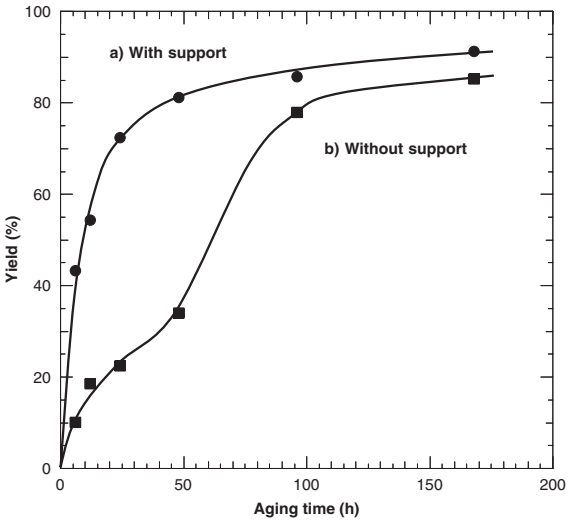

Figure 8. Changes in the yield of the precursor particles of Pt in the presence (a) and absence (b) of the α-Fe_2O_3 ellipsoid (A) support.

These results suggest that the surfaces of the α-Fe_2O_3 ellipsoid support play the role of nucleation centers of the precursor particles. The large precursor particles of 20−50 nm were formed by aging for 72 h in the absence of any support. The size distribution was relatively narrow and each particle consisted of much smaller particles of 2−3 nm. As a consequence, the support plays an important role in the formation of the well-dispersed precursor nanoclusters.

The precursor particles of Pt, $PtO_2 \cdot nH_2O$, were tried to be deposited on hematite (α-Fe_2O_3) supports: (a) polycrystalline ellipsoid (A), (b) monocrystalline ellipsoid (B), (c) monocrystalline pseudocube, and (d) monocrystalline platelet. Also, the precursor particles of Pt were tried to be formed on other supports other than α-Fe_2O_3: (a) α-FeOOH, (b) β-FeOOH, (c) ZrO_2 (A) with rough surfaces, (d) ZrO_2 (B) with smooth surfaces, and (e) TiO_2 (anatase). The mean sizes and yield of the precursor particles are summarized in Table 2 with the specific surface area of the supports.

For the platelet-type α-Fe_2O_3 and α-FeOOH supports, the large precursor particles independently precipitated apart from the supports, but not for the other supports. As a rule, the specific surface area is the most important determinant of the yield of the precursor particles for a given material of the supports. The larger the specific surface area is, the higher yield is obtained, because of the increase in probability of nucleation. The small yield and some independent precipitation of the precursor particles with the platelet-type hematite support is for this reason. However, the independent precipitation of the precursor particles with the α-FeOOH support may not be explained by the effect of the surface area, since the independent precipitation is not observed with the monocrystalline ellipsoidal α-Fe_2O_3 (B) and TiO_2 supports of rather smaller specific surface areas. This fact may suggest the relatively small affinity of α-FeOOH to the precursor particles. As different from Au particles deposited on various supports, where not only the yield but also the size of Au depended on the surface area, the sizes of the precursor particles of Pt on the different supports were almost the same around 1~2 nm, probably because the mobility of the precursor on the support surfaces necessary for the aggregative growth is extremely small as compared to the metal particles. Incidentally, it seems

Table 2. Effect of support particle on the size of precursor and metal particles of Pt.

Support particles	Specific surface area (m^2/g)	Yield (%)	Size of $PtO_2 \cdot nH_2O$ (nm)	Size of Pt (nm)
α-Fe_2O_3, ellipsoid (A)	136	88.8	1.3±0.5	2.0±0.5
α-Fe_2O_3, ellipsoid (B)	12.92	68.5	1.3±0.5	2.5±1.0
α-Fe_2O_3, pseudocube	15.9	50.0	1.5±0.5	2.0±0.5
α-Fe_2O_3, platelet	0.70	46.1	1.5±0.5, 20–30[a]	5.5±2.0[b]
α-FeOOH, needle	41.0	64.0	1.7±0.8, 10–20[a]	−[c]
β-FeOOH, needle	112	75.1	1.3±0.5	−[c]
ZrO_2(A), sphere (rough surface)	153	84.1	1.5±0.5	2.2±0.5
ZrO_2(B), sphere (smooth surface)	118	72.4	1.6±0.7	2.4±0.6
TiO_2, ellipsoid (anatase)	37.5	76.2	1.5±0.5	1.3±0.5
None		36.6	20–50	

[a]Size of the particles deposited apart from the support.
[b]Aggregated.
[c]Pt particles could not be observed, since they were occluded into the support drastically deformed by the reduction with H_2 gas.

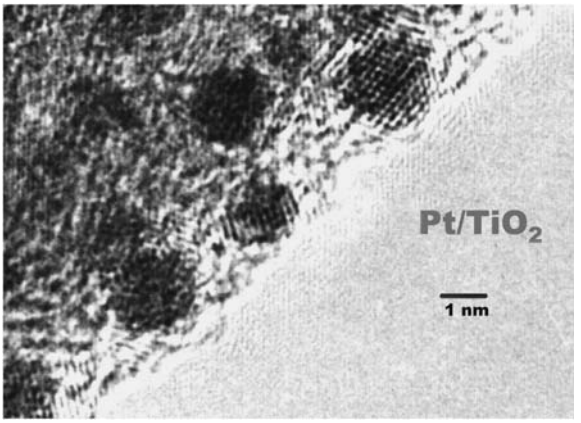

Figure 9. High-resolution transmission electron micrograph of Pt deposited on spindle type monocrystalline anatase TiO_2 prepared by the selective deposition method.

noteworthy that the internal surfaces of a porous support such as α-Fe_2O_3 ellipsoid (A), measured by the BET method, may not be used for the precipitation of the precursor, since the independent precipitation of the precursor is already observed with 1.2 g/dm^3 of α-Fe_2O_3 ellipsoid (A) despite its very high specific surface area of 136 m^2/g. Hence the distribution of the final Pt particles seems to be limited to the external surfaces of supports. The precursor particles were reduced to Pt particles with H_2 gas at 250 °C for 2 h. For α-FeOOH and β-FeOOH, the original shapes were drastically deformed by the reduction to magnetite and thus the Pt particles occluded into the deformed supports could not be identified. In the case of hematite supports, though it was confirmed by XRD that they were completely converted into magnetite, the original shapes were retained, except for the platelet-type particles partly deformed. The mean size of the Pt particles on the supports but α-FeOOH and β-FeOOH are listed in the last column of Table 2. As a rule, the Pt particles are more or less grown from the precursor particles by coagulation or Ostwald ripening through two-dimensional diffusion of atomic or ionic species of Pt, but one may find a significant effect of the species of the support on the final particle size of metallic Pt. The finest Pt particles were obtained with ellipsoidal TiO_2 (anatase) support, in which the Pt particles appeared rather smaller than the precursor particles, as shown in Figure 9.

4. A Case History

The liquid-phase reduction method was applied to the preparation of the supported catalyst [27]. Virtually, Muramatsu et al. reported the controlled formation of ultrafine Ni particles on hematite particles with different shapes. The Ni particles were selectively deposited on these hematite particles by the liquid-phase reduction with $NaBH_4$. For the concrete manner, see the following process. Nickel acetylacetonate ($Ni(AA)_2$) and zinc acetylacetonate ($Zn(AA)_2$) were codissolved in 40 ml of 2-propanol with a Zn/Ni ratio of 0–1.0, where the concentration of Ni was 5.0×10^{-3} mol/dm^3. 0.125 g of TiO_2 fine particles (Ishihara Ind., ST01) were dispersed in the Ni–Zn solution in a 4-neck flask under refluxing conditions with a continuous N_2 flow for 30 min. Ni and Zn complexes were promptly reduced by the addition of 10 ml of 1.0×10^{-1} mol/dm^3 $NaBH_4$ 2-propanol solution.

The residual concentrations of Ni in filtrates are estimated at 0–1.0% and those of Zn at 0.5–2.5% from the ICP measurements. The color of the particles was black in the case of Zn/Ni < 0.5, while it was dark gray in the case of Zn/Ni $= 1.0$. It seems that larger amount of reducing agent is needed for the reduction in the case of Zn/Ni $= 1.0$, although the $NaBH_4$/ (Ni or Zn) molar ratio was two, larger than stoichiometric value according to the following equation [27].

$$2Ni^{2+}(\text{or}Zn^{2+}) + BH_4^- \rightarrow 2Ni\ (\text{or}\ 2Zn) + 2H_2 + B^{III}$$

Even when the amount of reducing agent was increased by two or three times, the color of the Zn/Ni $= 1.0$ particles was basically not changed. These results imply that metallic Ni was formed through the adsorption of Ni on TiO_2 by their successive reduction on the surface, whereas a part of zinc was hydrolyzed to form ZnO and/or $Zn(OH)_2$ on the surface, because of its less reductive nature.

Figure 10 shows the TEM micrographs of (a) TiO_2 and as-prepared Ni–Zn particles on TiO_2 with Zn/Ni ratios of (b) 0.0, (c) 0.2, and (d) 1.0.

It is to be noted that Ni or Ni–Zn nanoclusters were selectively deposited on TiO_2 surfaces and that they were not found apart from TiO_2 particles. Taking the ICP results into consideration, more than 96% of Ni and Zn were formed predominantly on TiO_2 surfaces. Therefore, it can be considered that the formation of Ni–Zn nanoclusters in this experiment might proceed from the adsorption of Ni and/or Zn species on the surface and the successive reduction by adsorbed $NaBH_4$, and that Ni–Zn nanoclusters formed apart from TiO_2 must not be deposited via their heterocoagulation with TiO_2 since there was no evidence of any aggregation. The sizes of Ni–Zn nanoclusters were estimated at (b) 5–6 nm, (c) 3–5 nm, and (d) 1–2 nm. The particle size seems to decrease with increasing amount of Zn added.

Figure 11 shows the ESCA spectra for (I) Ni $2p_{3/2}$ region and (II) Zn $2p_{3/2}$ region of Zn/Ni $= 1.0$ particles on TiO_2.

For the spectra of Ni, peaks corresponding to Ni oxide and Ni metal are observed in the as-prepared sample [28–30]. After the etching with Ar^+, however, the peak of Ni metal is predominant. This implies that the state of Ni in the Ni–Zn nanoclusters is metallic, although their surface was oxidized under the atmospheric conditions. On the other hand, the identification of Zn state is difficult because the peak positions of Zn and ZnO in ESCA spectra are very close to each other. Furthermore, the B/Ni ratio determined by ESCA was increased with increasing Zn added; e.g., Ni: B = 73.3:26.7 and 60.6:39.4 for Zn/Ni $= 0.0$ and 1.0, respectively. Because no crystalline structure was found except for TiO_2 from both electron and X-ray diffraction patterns of the respective samples, it can be concluded that formed nanoclusters were amorphous. Ni–Zn nanoclusters would be composed of amorphous intermetallic compounds through the

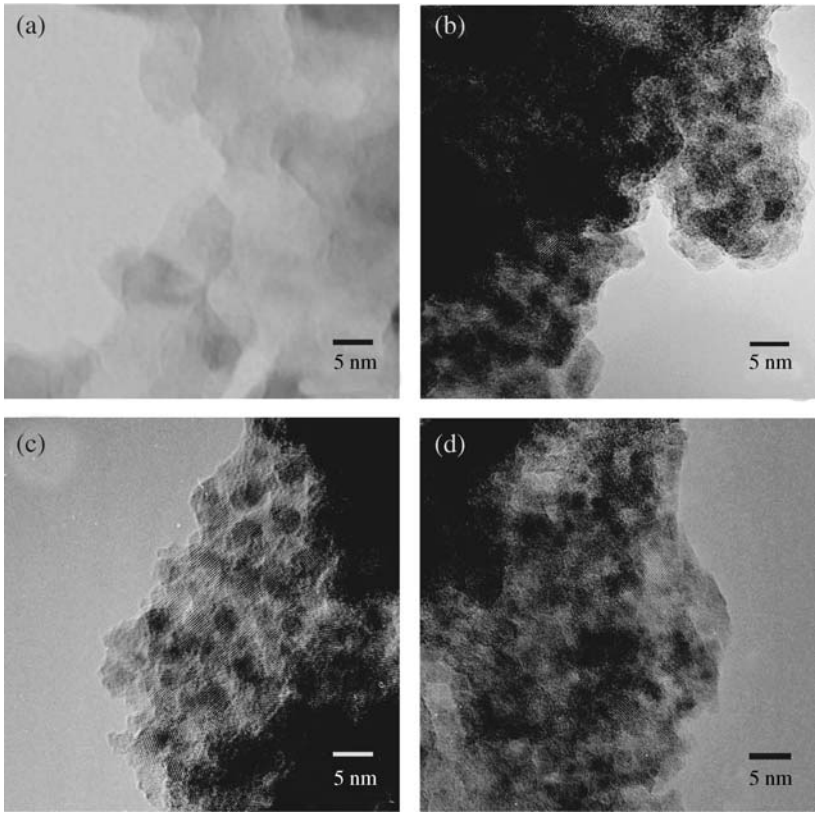

Figure 10. High-resolution transmission electron micrographs of (a) TiO_2 support and Ni–Zn nanoclusters with (b) Ni only, (c) Zn/Ni = 0.2, and (d) Zn/Ni = 1.0.

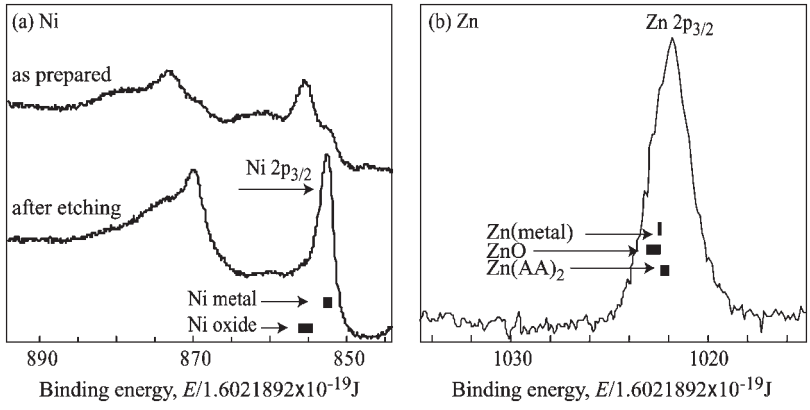

Figure 11. ESCA spectra for (I) the Ni $2p_{3/2}$ region of (a) before and (b) after etching and (II) the Zn $2p_{3/2}$ region of the Ni–Zn (Zn/Ni = 1.0) nanoclusters.

coordination of B, formed by the decomposition of $NaBH_4$ as a side reaction, with Ni and/or Zn atoms [31,32]. Virtually, Ni nanoclusters synthesized by this method was crystallized by the heat treatment at 400 °C in N_2 stream, where B could be removed from the bulk.

The catalytic activities of Ni and Ni–Zn nanoclusters with and without TiO_2 supports were evaluated through 1-octene hydrogenation. The GC analyses confirmed that only *n*-octane was obtained as a product in this hydrogenation reaction. Figure 12 shows the change in the yield of *n*-octane with time on stream. The good linearity between the yield and the reaction time indicates that the surface properties of the catalysts did not change during the hydrogenation. The hydrogenation activity increased in the following order: $Ni < Ni/TiO_2 < Ni–Zn < Ni–Zn/TiO_2$. The catalytic activity of $Ni–Zn/TiO_2$ was ca. 10 times higher

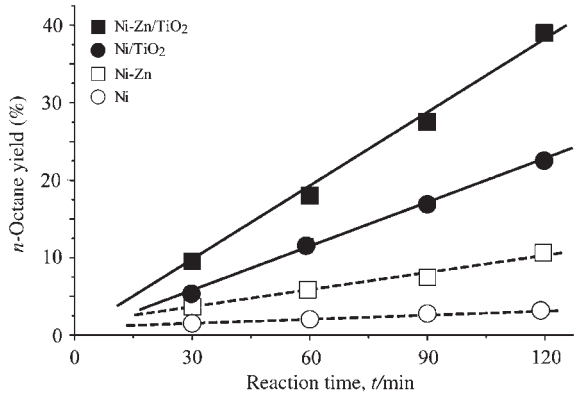

Figure 12. Catalytic activities of the Ni and Ni–Zn nanoclusters with and without TiO_2 for the hydrogenation of 1-octene.

than that of the unsupported Ni nanoclusters. TiO_2 seems to play an important role to disperse Ni nanoclusters by supporting them. Also, the addition of Zn clearly promoted the hydrogenation activity of Ni. Since the Zn addition resulted in the decrease in the particle size, this promotion effect of the catalytic activity would be mainly due to the increase in the catalytically active surface. In addition, Ni–Zn/TiO_2 gave the excellent activity in spite of its gray color, so that Ni species of the catalyst may be metallic since 1-octene can be hydrogenated only on the metallic Ni and not on oxides. Consequently, the role of Zn is to decrease the size of Ni nanoclusters and to inhibit the growth of the size, but Zn addition did not substantially affect Ni nature itself, taking the ESCA analysis into consideration.

5. Conclusion

In addition to Au and noble metals, Ni–Zn nanoclusters with an amorphous structure were successfully deposited on TiO_2 nanoclusters. The state of Ni was metallic. The catalytic activity of Ni–Zn/TiO_2 in olefin hydrogenation was ca. 10 times higher than unsupported Ni nanoclusters. Selective deposition onto TiO_2 and the addition of Zn seemed to play an important role to stabilize Ni nanoclusters and to decrease the size of Ni nanoclusters, respectively. Also, clearly Zn promoted the hydrogenation activity of Ni and inhibit the growth of the size, but did not substantially affect Ni nature itself.

References

1 P. N. Barnes, P. T. Murray, T. Haugan, R. Rogow, G. P. Perram, *Physica C* 377 (2002) 578.
2 K. Wegner, B. Walker, S. Tsantilis, S. E. Pratsinis, *Chem. Eng. Sci.* 57 (2002) 1753.
3 B. Xia, K. Okuyama, I. W. Lenggoro, *Adv. Mater.* 13 (2001) 1744.
4 A. Muramatsu, S. Shitara, H. Sasaki, S. Usui, *Shigen-to-Sozai* 106 (1990) 805–810.
5 H. Takahashi, A. Muramatsu, E. Matsubara, Y. Waseda, *Shigen-to-Sozai* 118 (2002) 211.
6 F. Fievet, J. P. Lagier, B. Blin, B. Beaudouin, M. Figlarz, *Solid State Ionics* 32 (1989) 198.
7 H. Arai, *Shokubai (Catalyst)* 19 (1977) 365.
8 H. C. Yao, M. Sieg, H. K. Plummer Jr., *J. Catal.* 59 (1979) 365.
9 J. C. Summers, S. A. Ausen, *J. Catal.* 52 (1978) 447.
10 B. C. Gates, J. R. Katzer, G. C. A. Schuit, *Chemistry of Catalytic Processes*, McGraw-Hill, New York, 1979, 184.
11 P. Wynblatt, N. A. Gjostein, *Progr. Solid State Chem.* 9 (1975) 21.
12 M. Boudart, *Adv. Catal.* 26 (1969) 153.
13 G. A. Somorjai, *Adv. Catal.* 26 (1977) 1.
14 A. Muramatsu, H. Kawasaki, T. Sugimoto, *Proceedings of 86th Catalysis Meeting, Catalysis Society of Japan, Tottori* (2000) 308.
15 M. Haruta, T. Yamada, T. Kobayashi, S. Iijima, *J. Catal.* 115 (1989) 301.
16 M. Haruta, S. Tsubota, H. Kobayashi, M. Genet, B. Delmon, *J. Catal.* 144 (1993) 175.
17 S. D. Gardner, G. B. Hoflind, B. T. Upchurch, D. R. Schryer, E. J. Kielin, J. Schryer, *J. Catal.* 129 (1991) 114.
18 S. D. Lin, M. Bollinger, M. A. Vannice, *Catal. Lett.* 17 (1993) 245.
19 A. Baiker, M. Kilo, M. Maciiejewski, S. Menzi, A. Wokaun, in L. Guczi, F. Solymosi, P. Tetenyi (eds.) *Proceedings of 10th International Congress on Catalysis, Budapest, 1992*, Elsevier, Amsterdam, 1993, 1257.
20 S. Tsubota, M. Haruta, T. Kobayashi, A. Ueda, Y. Nakahara, in G. Poncelet, P. A. Jacobs, P. Grange, B. Delmon (eds.) *Studies in Surface Science and Catalysis,* Vol. 63, Elsevier, Amsterdam, 1991, 695.
21 M. Okamura, K. Tanaka, A. Ueda, M. Haruta, *Solid State Ionics* 95 (1997) 143.
22 (a) T. Sugimoto, *Monodispersed Particles*, Elsevier, Amsterdam, 2001, 323; (b) T. Sugimoto, Y. Shintoku, A. Muramatsu, *Proceedings of 72nd Annual Meeting, Chemical Society of Japan* 1 (1997) 90.
23 (a) T. Sugimoto, *Monodispersed Particles*, Elsevier, Amsterdam, 2001, 326; (b) T. Sugimoto, Y. Shintoku, A. Muramatsu, *Proceedings of 50th Symposium on Colloid Interface Chemistry, Chemical Society of Japan, Saga* (1997) 320.
24 (a) T. Sugimoto, *Monodispersed Particles*, Elsevier, Amsterdam, 2001, 329; (b) T. Sugimoto, H. Kawasaki, A. Muramatsu, *Proceedings of 52nd Symposium on Colloid Interface Chemistry, Chemical Society of Japan, Morioka* (1999) 136.
25 T. Sugimoto, *Monodispersed Particles*, Elsevier, Amsterdam, 2001, 322.
26 W. Stöber, A. Fink, E. Bohn, *J. Colloid Interface Sci.* 26 (1968) 62.
27 A. Muramatsu, S. Ichikawa, T. Sugimoto, *Colloids Surf. A* 82 (1994) 29.
28 A. Lebugle, U. Axelsson, R. Nyholm, N. Martensson, *Phys. Scr.* 23 (1981) 825.
29 T. Dickinson, A. F. Povey, P. M. A. Sherwood, *J. Chem. Soc. Faraday Trans.* 173 (1977) 332.
30 K. Ng, D. M. Hercules, *J. Phys. Chem.* 80 (1976) 2094.
31 R. Paul, P. Buisson, N. Joseph, *Ind. Eng. Chem.* 44 (1952) 1006.
32 H. C. Brown, C. A. Brown, *J. Am. Chem. Soc.* 85 (1963) 1003.

This page intentionally left blank

CHAPTER 28

Production of Metal Nanoparticles by Plants and Plant-Derived Materials

Jorge L. Gardea-Torresdey[1,2], Jose R. Peralta-Videa[1], Jason G. Parsons[1], Ntebogeng S. Mokgalaka[1], and Guadalupe de la Rosa[3]

[1]*Chemistry Department, University of Texas at El Paso, USA*
[2]*Environmental Science and Engineering, University of Texas at El Paso, USA*
[3]*Facultad de Quimica, Universidad de Guanajuato, Mexico*

1. Introduction

Nanotechnology is a term used to describe the creation and utilization of materials with structural features between those of atoms and bulk materials, with at least one dimension in the nanometer range. The field of nanotechnology is still in its infancy and is expected to grow enormously in the years to come. Several methods have been reported for the synthesis of nanomaterials, which include various inorganic, organic, living, and nonliving biological systems that control size, shape, and structure of nanostructures. Gold nanoparticles were among the first nanoparticles to be synthesized and used in the staining of glass and enamels. Traditional methods for the production of gold colloids included the chemical reduction of gold salts [1]. Other methods that have been successful in producing pure and well-defined nanoparticles still remain expensive and pose possible health hazards [2–9]. Therefore, to fulfill the growing need to develop environmentally friendly nanoparticle synthesis methods, researchers are now taking advantage of plants, plant materials, and other biological systems.

Microorganisms have been widely used for the biosynthesis of metal nanoparticles. A study in the late 1980s by Dameron et al. [10] reported the biosynthesis of CdS quantum semiconductor crystallites using two yeast cultures. They attributed the intracellular nucleation and growth of CdS crystallites to short chelating peptides and were able to produce particles of 20 Å in diameter. Several years later, additional CdS biosynthesis methods were developed using bacteria [11] and fungi [12]. Recently, Gerieke and Pinches [13,14] used a variety of bacterial, fungal and yeast cultures for the synthesis of gold nanoparticles of various shapes and sizes. Other studies have shown that algae are able to bind gold ions from aqueous solutions and form colloidal particles on their surfaces [15–19].

More recently, plant extracts have been used as reducing agents for nanoparticle production. Leaf extracts of tamarind (*Tamarindus indica*) [20], *Aloe vera* [21], and geranium [22] have been used for the synthesis of gold and silver nanotriangles. Another novel approach is the synthesis of nanoparticles using plant biomass. Several manuscripts have been published using this technique [23–27].

Pioneering studies by Gardea-Torresdey et al. [28,29] reported for the first time the formation of gold and silver nanoparticles by living plants. Their study demonstrated that alfalfa plants can form gold and silver nanoparticles. Furthermore, these researchers reported that nucleation/growth of the metallic nanoparticles took place inside the plants. This study opened new and exciting ways to synthesize metallic nanoparticles [30,31].

Currently, nanotechnology research is propelled by the need to develop strategies for the synthesis of nanoparticles with controlled shape and size distributions. The aim of this chapter is to provide some insight into the recent advances in nanoparticle synthesis using plants and plant derived materials.

2. Synthesis Strategy

2.1. Inorganic Synthesis

Classical methods used for the production of colloidal metals date back to the 16th century, when colloidal gold and silver were used as coloring agents for glass and enamels. Gold colloids display colors such as red, violet, or blue, depending upon the particle size and shape [1,32]. The chemical reduction of gold salts was the most frequently used method for the production of colloid gold. However, the method by which particles are prepared dictates both the shape and size of the colloids, as

Metal Nanoclusters in Catalysis and Materials Science: The Issue of Size Control
Edited by B. Corain, G. Schmid and N. Toshima

demonstrated by the work of Turkevich and Stevenson [1]. Pyramidal particles result from the reduction of auric chloride in boiling citric acid, whereas spherical particles are formed through the reduction of auric chloride in hot sodium nitrate. One of the classical methods to form gold nanoparticles involves the reduction of tetrachloraurate in hot sodium citrate or sodium borohydride [1,9,33]. However, the reduction of auric chloride with carbon monoxide has shown to produce elongated cylinders [1,9,32,34]. The production of size specific gold nanorods has been performed by seeding a solution with specific size nanoparticles to promote growth followed by the addition of cetyltrimethylammonium bromide (CETAB) [5]. Thus, differences in the chemical methods used to form particles affect their final shape and size, as well as their chemical and physical properties.

Although the chemical formation of nanoparticles has been well known for a long time, significant advances in this area have recently occurred. Several different solvent extraction/chemical reduction methods have been studied as well as photoreduction and thermal decomposition processes to obtain small particle sizes with narrow distributions [2–4,6–8,35,36]. Although high redox potentials associated with the auric salts and relatively poor stability and large particle size distribution have been a problem, the use of polymers and surfactants as colloid protective agents has shown some promise [37–40]. High concentrations of solvent stabilized metallic nanoparticles can be achieved through the combination of metals and organic molecules such as acetone, toluene, methylcyclohexane, formamide, as well as phosphine-stabilization methods. However, many of these methods have proven to be burdensome and give rise to toxic end products that may endanger public health. Therefore, scientists have tried to develop better methods that allow for a high degree of colloidal stability and small particle size distribution while reducing the potentially toxic end products.

2.2. Biological Synthesis

2.2.1. Microorganisms

The use of biomaterials to form nanoparticles is a more attractive and novel alternative to chemical synthesis. The paucity of information regarding biologically derived compounds for colloidal stabilization is one of the main hindrances to progress in the field of biological synthesis of nanoparticles. Several researchers have established that living biological systems such as algae have the ability to adsorb metal ions from solutions through their cell walls and bind them through their various cellular constituents [41–43]. Several studies have shown that algae are able to bind gold ions from aqueous solutions and form colloidal particles on their surfaces, yet the mechanisms are still not understood well [15–19]. Researchers from Uppsala University found that the bacterial strain *Pseudomonas stutzeri* AG259 is able to fabricate silver nanoparticles as well as silver-carbon composite materials [44,45]. Whereas researchers at the Madras Institute found that *Lactobacillus* strains formed submicron crystallites of gold, silver, and a gold–silver alloy [46]. In addition, it has been shown that living fungi have the capacity to uptake and bioreduce Ag(I) ions from solution to form silver nanoparticles with no effects on mycelia growth [47,48]. Furthermore, researchers found that the fungus *Fusarium oxysporum* synthesize gold nanoparticles on its surface while the fungus *Verticillium* spp. has the ability to bioreduce $AuCl_4^-$ ions and trap the resulting gold nanoparticles formed on the mycelium surface [48,49]. To further complicate matters, many difficulties are associated with the isolation of living microbial systems from their nutrient growth media, thus making them generally less applicable for the mechanistic study of nanoparticle synthesis, especially in small nanoparticle size ranges.

2.2.2. Plant Extracts

Plants and plant extracts on the other hand, may provide a better alternative to nanoparticle production. Several plants have been studied for their ability to accumulate metal compounds over an extended period of time. In fact, plant species such as Douglas fir and rye grass are utilized as biological indicators of geologic gold deposits [50,51]. Many other plants including Indian mustard have been utilized for phytomining, which is the accumulation of valuable metals by plants from low concentrations in soils [52,53]. Furthermore, by using plant tissues alone, researchers have found significant adsorption and recovery of gold from aqueous solutions [54]. In addition, Lujan et al. [55] reported that a purple color, similar to that of the ''Purple of Cassius'' resulted when they reacted aqueous Au(III) with the biomaterials, indicating the formation of gold colloids. Plants may contain an exceptional natural chemical stabilization mechanism that allows for the formation of nanoparticles. Therefore, by taking advantage of the naturally occurring compounds found within the plant systems, a novel method to generate stable metal colloids was developed. For example, geranium leaves (*Pelargonium graveolens*) exposed to an aqueous chloroaurate solution quickly reduced gold ions and formed stable gold nanoparticles. It appears that terpenoid compounds present in the leaves of this plant are the reducing agent [56]. Ankamwar et al. [20] reported the synthesis of gold nanotriangles ranging from 20 to 40 nm by reducing a chloroauric acid solution with tamarind leaf extract. Other researchers also reported the production of gold nanotriangles and spherical silver nanoparticles using *Aloe vera*, *P. graveolens* [21,56], and lemon grass (*Cymbopogon citratus*) plant extracts [57]. Gold and silver nanoparticles have also been obtained using polysaccharides and heparin [58]. While consistency in nanoparticle size and shape is important to many materials, differences in nanoparticle synthesis may also lead to changes in particle conformation and spatial arrangement, which may provide for the development of better nano-sized building blocks to form new materials with distinctly different properties.

2.2.3. Non-Living Plants

The synthesis of nanoparticles using plant biomass has been investigated by many [24,26]. Using high resolution transmission electron microscopy (HRTEM), it has been

observed that alfalfa (*Medicago sativa*) biomass was able to passively bind and reduce gold(III) to form five different types of gold nanoparticles with the following shapes: cubic octahedral, tetrahedral, hexagonal platelets, icosahedral multiple twinned, decahedral multiple twinned, and irregular shaped particles [24]. The bioformed multiple twinned colloidal gold particles are similar in structure and size to previously described particles for gold samples prepared by evaporation of bulk metals under vacuum and other appropriate chemical methods for ultra fine particle synthesis [59,60]. In addition, research groups led by Dr. Jose-Yacaman at the University of Texas at Austin [61] and Dr. Gardea-Torresdey at the University of Texas at El Paso [24] were able to produce a truncated icosahedral gold particle. This is a low energy configuration for gold particles. Most likely, the bio-based production of this new particle has resulted from the passive nucleation and growth mechanisms occurring in the biomass which may allow for the production of stable new nanoparticles, contrasting those previously seen with rapid vapor growth or fast chemical reduction methods. Armendariz et al. [25,26] have extensively studied the production of gold nanoparticles using oat and wheat biomass. These researchers assayed the reaction of Au(III) solution with oat and wheat biomass at different pH values and reaction times. They found that the pH is an important factor to control the size and shape of bioproduced gold nanoparticles. This new technology offers the advantages of low cost and no byproducts generation.

2.2.4. Living Plants

The formation of gold and silver nanoparticles by living plants was reported for the first time by Gardea-Torresdey et al. [28,29]. These researchers demonstrated, using transmission electron microscopy (TEM) coupled to an energy dispersive spectroscopic (EDS) device, that alfalfa plants can form ultra fine metal clusters, when grown in agar containing gold(III). The TEM images also showed that the nucleation of the particles inside the plants occurs in preferential zones. After that, researchers at Western Kentucky University found that seedlings of *Sesbania drummondii*, a leguminous plant, accumulate lead ions and produce similar types of ultrafine lead crystals [30]. Lead crystals were observed to be aggregates of much finer crystals in the order of 10 nm in diameter. Recently, syntheses of gold nanoparticles were also observed by TEM in the cell wall of *S. drummondii* (unpublished data). Other researchers found metal nano-sized materials in plant tissues after hydroponically exposing morning glory (*Ipomoea lacunosa*) and alfalfa to aqueous solutions of Ag, Au, Tu, Cr, and Zn [31]. To our knowledge, the separation of the nanoparticles from biological systems has not been reported and needs to be investigated in order to make this a usable system.

3. Results

A number of different studies have been performed on the production of metal nanoparticles using plant-based biological systems [21–26,28,29,56,57,62–67]. These studies into biological synthesis of metallic nanoparticles can be broken down further into three broad categories, which consist of inactivated tissues, aqueous plant extracts, and living biological systems. More specifically, the synthesis of gold and silver nanoparticles has been shown to occur through the use of algae, plants, bacteria, and fungi in both living and nonliving systems [13,14,20–26,28,29,56,57,62–71]. These studies have shown that the biological systems enforce both size and shape constraints on the metallic nanoparticles formed. Gerieke and Pinches [13], found that variations in pH affected not only the size and shape of Au nanoparticles, but also the number of particles produced per cell in two microbial cultures. In the same study [13], the authors reported faster particle growth rate at elevated temperatures, however at lower temperatures, spherical particles with an average diameter less than 10 nm could be collected in just 1 h of exposure to Au solution. Klaus et al. [44] produced Ag nanoparticles in bacteria grown in 50 mM $AgNO_3$, at 30 °C for 48 h in the dark. In these conditions, well-defined Ag nanoparticles with composition and shapes, such as equilateral triangles and hexagons were formed. The crystals were up to 200 nm in size and were often located at the cell poles.

3.1. Inactivated Tissues

Specific studies have been performed to investigate the formation of gold nanoparticles with inactivated tissues of oat, wheat, hops, and alfalfa biomasses [23–26,28,62,64]. Investigations into the effects of different chemical modification to the biomass, pH, time, and temperature of the reactions have shown to affect both the size and shape of gold nanoparticles synthesized using different biological materials [23–26,28,62,64,72]. In the case of alfalfa biomass reacted with a gold solution at pH 2.0, gold nanoparticles with different shapes and sizes varying from 10 to 300 nm were produced. The shape distribution of the nanoparticles included five predominate shapes (from the highest to the lowest occurrence) irregular, icosahedral, dodecahedral, tetrahedral, and hexagonal [24]. It should be noted that irregular shaped nanoparticles are formed from the coalescence of the regular shaped nanoparticles as a function of the reaction time. Thus the longer the reaction time the higher the number of irregular nanoparticles that are formed. The gold nanoparticles formed by reactions of gold chloride with biological materials are shown in Figure 1.

This figure gives a reference to the reader of the variety of shapes of nanoparticles produced by reactions of gold chloride with inactivated tissues, plant extracts, and live plants.

Results also show that the nanoparticles formed from these types of reactions are stabilized and can continually grow until the reaction is physically stopped. In an investigation into the mechanism of the bioprecipitation of gold using alfalfa biomass, it was shown that a quick reduction of gold(III) to gold(I) occurs through the release of chloride ions, followed by a slower reduction of the gold(I) to gold(0). The Au(0) atoms coalesce forming Au

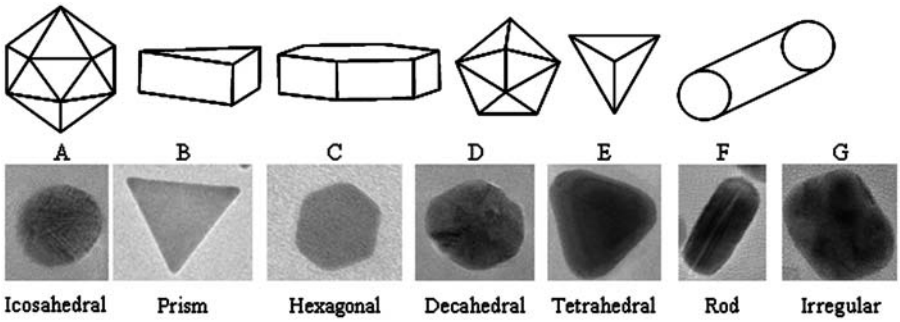

Figure 1. Representative geometrical drawings and TEM micrographs of different nanoparticles formed by the reaction of tetrachloroaurate with inactive plant tissues, aqueous plant extracts, and live plants.

nanoparticles [65]. Through the uses of X-ray absorption near edge structure (XANES) and extended X-ray absorption fine structure (EXAFS), both analytical techniques of X-ray absorption spectroscopy (XAS), it was possible to determine that the initial gold(III) concentration affected the reduction process. The higher the initial gold(III) concentration in the reaction solution, the larger the gold features observed, and also indicated that the nanoparticle sizes increased at higher initial gold(III) concentration. On the other hand, the EXAFS showed that the samples had chlorine, oxygen, and gold as the nearest neighboring atoms, indicating multiple oxidation states and gold compounds in the samples. The XAS results also showed that alfalfa biomass required approximately 12 h for a complete Au(III) reduction. In the period from 5 min to 3 h, N or O atoms (as the nearest neighbor) were bound to the Au atoms in the samples. However, in the 12 h samples the EXAFS showed that almost only Au atoms were present, giving further indication of a complete reduction of Au(III) to Au(0). The oxidized gold shown by the XAS spectra could probably be the one deposited on the surface of the particles as has been observed after chemical reduction of Au(III) ions [65]. Another conclusion derived from the XANES spectra is that the native or unmodified biomass has a higher reduction power compared to the esterified biomass. This was assumed by the higher concentration of gold(I) observed in the XANES spectra. The effect of pH on the size of gold nanoparticles was shown by Gardea-Torresdey et al. [64] through the use of XAS studies and the Borowski equation [73]. From this study, it was found that at pH 2.0 the average size of the gold nanoparticles synthesized using alfalfa biomass was 9.0 Å, while at pH 5.0 the nanoparticles had an average size of 6.2 Å. The results suggest that a "shrinking" in the size of the nanoparticles occurred by an increase in the pH of the reaction mixture. This change in nanoparticle size has also been observed in other biomasses [25,26,62]. Similar studies have been performed using hops biomass. In this investigation the reduction of gold was examined using chemical modification and pH changes in the range from 2 to 6. According to the results, the maximum binding occurred at pH 3. The results also showed that the binding and bioreduction of gold by hops biomass was independent of time at pH 2, while at pH 5 the binding/bioreduction was time dependent [62]. The chemical modifications of the biomass included hydrolysis (increasing the number of carboxyl groups) and esterification (reducing the number of carboxyl groups). The XANES investigations into the gold bioreduction by the chemically modified hops biomass showed that after a 4.0 h reaction time at pH 4, the amount of oxidized gold remaining on the biomass was 20%, 20%, and 30%, on the native (unmodified), hydrolyzed, and esterified biomass, respectively. This was determined by obtaining the atomic percent of gold in the samples. However, the EXAFS spectra of the gold biomass samples showed that the predominate nearest neighbor in the samples was gold at approximately 2.85 Å, indicative of gold(0). As mentioned earlier, the presence of a small percent of oxidized gold in a sample containing gold nanoparticles is normal, due to surface effects and induced surface charges in the samples. From the EXAFS spectra it was determined that the average size of the gold nanoparticles for the native and hydrolyzed hops biomass were approximately 17 and 9 Å, respectively. TEM images of hops biomass reacted with tetrachloroaurate at pH 2 and pH 6 have shown that the gold nanoparticles produced by the native biomass were predominately icosahedral multi-twinned, the hydrolyzed biomass produced more nanorods, and the esterified biomass produced spherical shaped nanoparticles [63].

The effect of the reaction time on nanoparticle formation was studied on a range of 15 min to 48 h using oat biomass [72]. The results demonstrated that the longer the reaction time, the higher the reduction, reaching almost a complete Au(III) to Au(0) reduction after 48 h. The reduction of gold(III) on oat biomass takes at least 2 h to have a significant amount of gold(0) in the sample. After 2 h of reaction, the diameter of the nanoparticles was 8.2 nm, which started to increase slowly as time increases until they reached a diameter of about 40 Å after 48 h. These data also suggest that after 19 h, the size of the nanoparticles was kept constant, indicating that the reaction reached equilibrium [72].

Figure 2 shows a representative XANES spectrum from a bulk gold sample (a 1 μm gold film) and a representative spectrum of gold reacted with oat biomass.

The vertical lines within the figure show the similarities between the bulk gold and the gold nanoparticle. The gold white line, which is an electronic feature originated by the transition of the d shell electrons in oxidized gold due to the partially filled d orbitals, is shown in the spectrum of the Au(0) nanoparticle. The small edge feature is probably due to the presence of oxidized gold on the surface of the gold nanoparticles.

The results indicated that the reaction time of 1 h was insufficient for the total reduction of gold. Figure 3 shows the Fourier transformed EXAFS of both a bulk gold(0) sample and nanoparticles produced by the reduction of tetrachloroaurate by oat biomass.

As seen in Figure 3A, the nearest neighboring atoms in both the bulk gold and colloidal gold have the same interatomic distance. However, in the colloidal gold sample the amplitude of the Fourier transformed EXAFS is dampened drastically. In addition, the higher shell interaction observed in the bulk gold samples is missing from the nanoparticulate sample, indicating that the gold neighbors only exist in the first and second shells at 2.85 Å and 4.10 Å. Furthermore, Figure 3B shows the raw EXAFS of the same samples and again the amplitude in the raw EXAFS for the nanoparticulate gold sample are dampened. However, they are in the same phase indicating that the samples contain the same material, in this case gold(0).

In this study, the size of the nanoparticles produced from the hydrolyzed biomass could not be determined as they were too large for this technique to be applied. This result shows that the chemical modification of the biomass has a large effect on the size of the nanoparticles produced. The average size of nanoparticles produced by esterified biomass was almost reduced by half, while the average size of the nanoparticles increased when the biomass was hydrolyzed as compared to the unmodified biomass.

Studies performed by Armendariz et al. [25,26] using oat and wheat biomasses have shown that by varying the pH it is possible to have more control on the size and shape of the gold nanoparticles formed by the biomasses. When wheat biomass was reacted with Au(III) in a pH range from 2 through 6, seven different nanoparticle shapes were produced. These include tetrahedral, decahedral, hexagonal, icosahedral, multi-twinned, irregular, and rod shaped. The sizes of these nanoparticles ranged from 10 to 30 nm. Binding studies showed that gold binding to oat biomass occurred in an inversely pH dependent manner. Inverse binding trend is indicative of anions (in this case the binding of the gold/chlorine/hydroxide anion) binding to biomass materials, which was higher at lower pH and lower at higher pH. In addition, at pH values of 2 and 3, the majority of the nanoparticles found on oat biomass were particles of approximately 20 nm with some of them larger than 100 nm. On the other hand, at pH 2 and pH 5 the nanoparticles had a distribution between 10 and 50 nm [26]. It should be noted that at low pH values (around 2 and 3), the nanoparticles have a tendency to aggregate so they form larger nanoparticles. This fact could explain the presence of nanoparticles larger than 100 nm at these pH values.

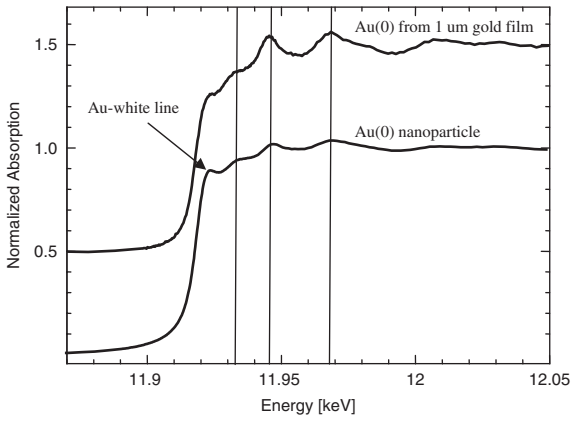

Figure 2. Representative XANES of gold nanoparticles from an oat sample reacted with tetrachloroaurate for 24 h and a bulk gold sample recorded from a 1 μm gold film.

3.2. *Aqueous Plant Extracts*

In addition to performing reactions with inactivated tissues of plants, recent research has been performed using plant extracts to produce gold nanoparticles [22,56,57,67]. In these studies only the aqueous extractable organic/biochemical compounds are used. The results have shown that the type of plant used in the extraction process influences the shape of nanoparticles produced. Chandran

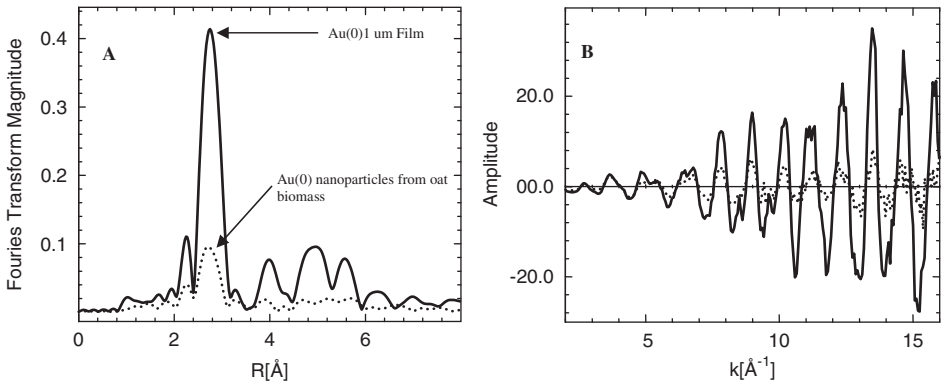

Figure 3. (A) Fourier transformed EXAFS of gold nanoparticles from an oat sample reacted with tetrachloroaurate for 24 h (dotted line) and a bulk gold sample recorded from a 1 μm gold film (solid line). (B) Raw EXAFS of gold nanoparticles from an oat sample reacted with tetrachloroaurate for 24 h (dotted line) and a bulk gold sample recorded from a 1 μm gold film (solid line).

et al. [21] found that aqueous extracts from *Aloe vera* produced triangular gold nanoparticles with side lengths ranging between 2.6 and 7.9 nm. In addition, the reaction of the *Aloe vera* extract with silver ions produces silver nanoparticles that had a spherical shape and sizes ranging from 11 to 19 nm [21]. In a similar study Shankar et al. [22] reported the synthesis of gold nanoprisms using both the aqueous extracts of geranium leaves and its endophytic fungus. The nanoparticles produced by the geranium extract had various sizes and shapes with capping agents from the leaves consisting of terpenoids. However, through IR and TEM analyses, these investigators found that the nanoparticles produced by the endophytic fungi had spherical shapes capped with polypeptides and enzymes. From the UV data collected by the authors, it was concluded that the reduction of the gold in solution started within the first 2 min of reaction between the chloroaurate ions and the extracts. The results of this study indicated that the reduction process is quick and efficient. Furthermore, the TEM analyses of the gold nanoparticles obtained by this route resulted in the majority of the nanoparticles being decahedral and icosahedral with sizes ranging from 20 to 40 nm [22]. Shankar et al. [57], using an aqueous extract from lemon grass obtained gold nanoprisms. However, in this case, the gold nanoparticles were rather large in size; some of the prisms had side lengths of 2000 nm (or 2 μm). Furthermore, the size diameter of the nanoprisms was bimodal with very high diameter frequencies at approximately 100 and 1000 nm. Further studies on the mechanisms of formation of the gold nanoparticles showed that at very short reaction times, the resulting particles were spherical in shape. These small particles then coalesce to produce larger nanoparticles over time. Shankar et al. [22] have also used geranium leaves to synthesize silver nanoparticles. From UV measurements performed in this study, it was found that silver reduction was initiated approximately 30 min after the reaction mixture was prepared, indicating that the kinetics for this process was much slower than that for gold reduction in similar systems. In general, the reduction of silver is usually slower as compared to the reduction of gold even when using traditional methods with the exception of borohydride reactions. After approximately 1 h of reaction time, the silver nanoparticle UV signal (at approximately 450 nm) became predominate and very intense up to 24 h of reaction time. TEM measurements performed on these nanoparticles showed spherical aggregates with sizes ranging from 16 to 40 nm, averaging approximately 27 nm. In addition, a small fraction of the nanoparticles was found to have an ellipsoidal shape. Finally, Shankar et al. [67] have reported the production of both monometallic and bimetallic gold–silver nanoparticles from the individual and successive reduction of gold and silver by extracts of Neem (*Azadirachta indica*) leaf broth. The reduction of gold produced predominately spheres and platelets, which were polydispersed and the reduction of silver ions resulted in spherical nanoparticles ranging from 5 to 30 nm. In the production of bimetallic nanoparticles, the reduction of gold required only 2 min if silver ions were present. The reduction of the silver(I) in the presence of the gold(III) was also accelerated and started within the first 5 min. The FTIR analysis of the nanoparticles showed that the stabilizing agents over both monometallic and bimetallic nanoparticles were aromatic compounds, methyl groups, and ester linkages. The bimetallic nanoparticles formed from this reaction were gold core with a silver shell, more likely due to the difference in the reduction kinetics of the individual ions in the Neem leaf broth.

3.3. Living Plants

In conjunction with the formation of gold and silver nanoparticles with inactivated tissues and aqueous plant extracts, it has also been shown within the literature that precious metal nanoparticles can be formed and grow within living plants [28,29,66]. Initially, the formation of gold nanoparticles was shown within living alfalfa plants [28]. The formation of gold nanoparticles within live alfalfa plants will be discussed later in detail within the case study part of this book chapter. However, it was also shown that silver nanoparticles could be formed within or uptaken by living alfalfa plants [29]. Through a combination of uptake, XAS, and TEM studies, it was shown that alfalfa plant could uptake silver from agar-based growth media. Further investigation of these plants using XANES analysis showed that the plants contained silver as Ag(0). The EXAFS spectra of silver laden alfalfa plants showed small elongated particles, probably silver nanowires, within the roots. The EXAFS spectra also showed that silver atoms in the root were at an interatomic distance of 2.88 Å and a coordination number of 4.3. The interatomic distance confirmed the results of the XANES analysis demonstrating that silver was present as silver(0) and the coordination number indicated that the average particle size was 9 Å or less. Further dark field TEM analysis showed that the silver nanoparticles were present throughout the roots and distributed in groups in segmented regions of the plants, possibly correlated to the position of the xylem and phloem of alfalfa.

More recently, Gardea-Torresdey et al. [66] reported the uptake and formation of gold nanoparticles by desert willow (*Chilopsis linearis*) exposed to gold-thiocyanate in hydroponics. The XAS spectra of the plant samples showed gold(0) in both the roots and stems; however, the Au concentration in leaves was too low to determine the gold oxidation state. EXAFS spectra of root samples showed that the gold absorber atoms were coordinated to approximately 7 gold backscattering atoms with an interatomic distance of 2.86 Å. The EXAFS results indicated that the average size of the gold nanoparticles was approximately 1.1 nm. The findings of this study are very important because they show that this plant maintains nanoparticles even in the presence of thiocyanate, a commonly used gold chelating/extraction agent. These results also indicate that the gold nanoparticles formed within living plants are very stable. This may provide a means to extract gold nanoparticles from living plants for future use. This is a new and emerging filed of nanotechnology and the studies performed within this field are few and limited. However, research is beginning to accelerate within this subdivision of nanobiotechnology.

4. A Case History

4.1. Gold Nanoparticles Formation by Living Alfalfa Plants

The production of gold nanoparticles by alfalfa plants is described. Seeds of alfalfa (*M. sativa* L.) were treated and germinated as previously published [28,74]. After harvesting, triplicate samples of 10 plants were submerged in 0.01 M HCl for 10 s and rinsed three times with deionized water. Roots were separated from shoots, oven dried for two days at 60 °C, weighed, and microwave digested (CEM MarsX, Mathews, NC, USA). The digestion was accomplished using trace pure HNO_3 and HCl in a 1:1 ratio. The volume of the digested samples was adjusted to 10 ml with deionized water and subsequent analysis was carried out using a Perkin-Elmer Optima 4300 DV inductively coupled plasma optical emission spectrometer (ICP-OES) (Perkin-Elmer, Shelton, CT, USA) [75].

4.2. Sample Preparation for X-Ray Spectroscopy Analysis

For XAS analyses, alfalfa samples were prepared as described in the literature [28,76]. The samples were taken to Stanford Synchrotron Radiation Laboratory (SSRL, Palo Alto, CA, USA) and analyzed by XAS using the Au L_{III} edge. The beam line 7-3 had a current of 3 GeV and 60–100 mA as operating conditions and silicon(2 2 0) monochromator crystal detuned 50% to reject harmonics. All samples were run at 15 K using a helium cryostat. The fluorescence spectra were collected with a Canberra 13-element germanium detector (Canberra Industries, Meriden, CT, USA). Intensity transmitted by the sample was monitored by a N_2-purged ion chamber beyond the sample, and the spectrum of a gold foil was measured for calibration in another N_2-purged ion chamber. The model compound tetrachloroaurate was diluted with boron nitride before the analysis. The XANES and EXAFS spectra were analyzed using the WinXAS software [77].

4.3. Sample Preparation for Transmission Electron Microscopy Analysis

Synthetic resin-embedded alfalfa samples were oven dried at 65 °C for 24 h and cut at 40–90 nm. The slides were analyzed using a JEOL 2010-F TEM prepared with field emission gun, EDS, and a high angle annular dark field detector for the analysis of solitary nanoparticles.

4.4. Results

4.4.1. Plant Growth

The growth of alfalfa plants exposed to gold treatments varying from 0 to 320 mg l^{-1} is shown in Table 1. As shown in this table, gold treatments between 10 and 160 mg l^{-1} increased the shoot growth of alfalfa plants and none of the concentrations reduced the root growth. In addition, none of the treatments produced sign of toxicity such as a yellowish color or floppiness in plants.

Table 1. Average size of alfalfa plants exposed to gold treatments.

	Gold concentration (mg l^{-1})						
Size (mm)	0 (control)	10	20	40	80	160	320
Root	35	50	54	48	45	37	23
Shoot	28	35	29	38	29	35	27

Note: The data are average of 20 plants grown for two weeks in the Hoagland medium spiked with Au concentrations (from $KAuCl_4$) varying from 0 to 320 mg l^{-1}.

Table 2. Gold concentration in roots and shoots of alfalfa plants exposed for two weeks to gold treatments varying from 10 to 320 mg l^{-1}.

	Au concentration in tissues mg Au kg^{-1} DWM[a]		
mg Au l^{-1} in the medium	Root	Shoot	Shoot/root
10	356 ± 54	56 ± 6	0.2
20	317 ± 26	16 ± 1	0.05
40	357 ± 17	33 ± 2	0.09
80	998 ± 63	34 ± 3	0.03
160	1779 ± 161	88 ± 3	0.04
320	5704 ± 109	264 ± 22	0.04

Note: Plants were grown in agar-based modified Hoagland nutrient medium. The data are average of three replicates ± SE.
[a]Dry weight mass.

4.4.2. Gold Uptake

The uptake data showed that alfalfa plants concentrated Au mainly in roots (Table 2).

No differences were observed in the Au concentration found in roots of plants treated with 10–40 mg Au l^{-1} (317–350 mg kg^{-1} dry mass). However, the roots of plants exposed to 80, 160, and 320 mg Au l^{-1}, concentrated (average ± SE) 998 ± 63, 1779 ± 161, and 5704 ± 109, respectively [75]. On the other hand, it was observed that the translocation of Au from roots to shoots was higher in plants exposed to 10 mg Au l^{-1} (ratio shoot/root of 0.2) and lower in plants exposed to 320 mg Au l^{-1} (ratio of 0.04).

4.4.3. XANES and EXAFS Results

For the energy calibration the spectrum from the Au(0) foil measured at the same time as the alfalfa spectra was used. The value of 11.918 keV was assigned to the first inflexion point of the Au(0) foil. The XANES energy

spectra of Au laden alfalfa root and shoot samples matched the position of the Au(0) foil and the agar sample, not the one of the tetrachloroaurate, the compound supplied to plants (Figure 4).

These results corroborated that alfalfa absorbed the Au(0) from the medium and translocated it through the vascular system. The EXAFS results (Figure 5, Table 3) showed that the Au atoms in plant samples had longer distances that the Au atoms in the tetrachloroaurate, but had equivalent distance to the Au atoms in the gold foil, which confirmed that the Au in plant samples was Au(0).

4.4.4. Transmission Electron Microscopy Results

The TEM images of alfalfa shoots (Figure 6a) and the EDS analysis (Figure 6b) show that Au atoms were dispersed through the longitudinal axis of alfalfa seedlings. EDS was performed on many particles to corroborate that all of them were pure gold.

The data from the XAS and TEM analysis showed for the first time that higher plants (alfalfa) grown in a gold enriched medium can form gold nanoparticles [28]. The data from the TEM images also showed that the Au particles produced by alfalfa had structural defects similar to

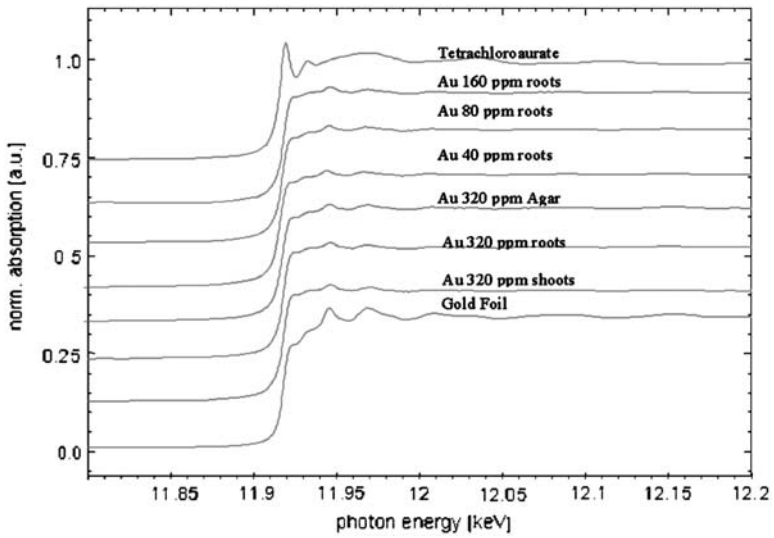

Figure 4. XANES spectra of the tetrachloroaurate compound, the Au foil [Au(0)], and the Au in the agar and plant samples. (Reprinted from Ref. [28], © 2002, with permission from American Chemical Society.)

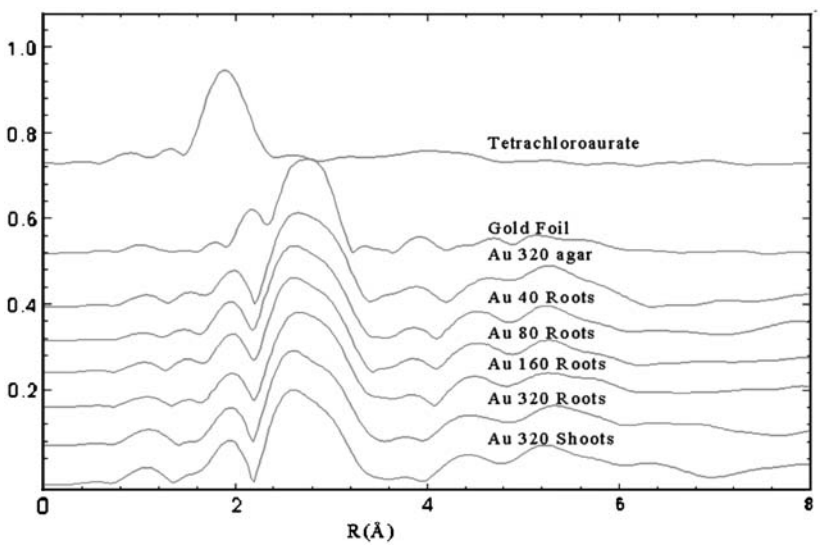

Figure 5. EXAFS spectra of the tetrachloroaurate compound, the Au foil [Au(0)], and the Au in the agar and plant samples. (Reprinted from Ref. [28], © 2002, with permission from American Chemical Society.)

those observed in Au nanoparticles obtained by inorganic methods (evaporation) [78].

The fast Fourier transform showed the splitting of the particles (Figure 7, inset).

According to Gardea-Torresdey et al. [28], the angle of splitting indicated that the nanoparticles of 4 nm formed by alfalfa plants are ''icosahedrons at an angle about 18° out of the threefold orientation''. These data suggest that Au atoms inside the plants assemble into the lowest energy configuration. However, when the size of the Au aggregate in ranges between 6 and 10 nm, they exhibited a face-centered cubic twinned structure. This structure was also observed in larger gold nanoparticles found within alfalfa seedlings.

Figure 8 shows some of the Au aggregate within the stem of alfalfa seedlings.

The measurement of the particles showed sizes varying from 4 to 40 nm. This suggests that the particles had continuous grow that could be regulated by time and changes in the size of the plant transport system. Gardea-Torresdey and coworkers [28] concluded that the results (a) ''provide a new method for the synthesis of Au nanoparticles, (b) will generate new studies concerning the interaction between plants, metals and metal ions, and (c) may constitute a new method for the mining of gold from solution and soils as an inexpensive method for the purification of economically important elements''.

Table 3. Results from the EXAFS data of alfalfa plants.

Sample	Bond	N	R(Å)	σ^2
Tetrachloroaurate	Au–Cl	4.0	2.28	0.0141
Gold foil (Au(0))	Au–Au	12	2.86	0.0081
Au 320 roots	Au–Au	5.47	2.85	0.0044
Au 320 shoots	Au–Au	4.43	2.86	0.0046
Au 160 roots	Au–Au	6.16	2.86	0.0056
Au 80 roots	Au–Au	6.37	2.86	0.0069
Au 40 roots	Au–Au	6.42	2.86	0.0070

Note: Gold neighbor, coordination number (N), interatomic distance [R(Å)], and mean square relative displacement (σ^2).

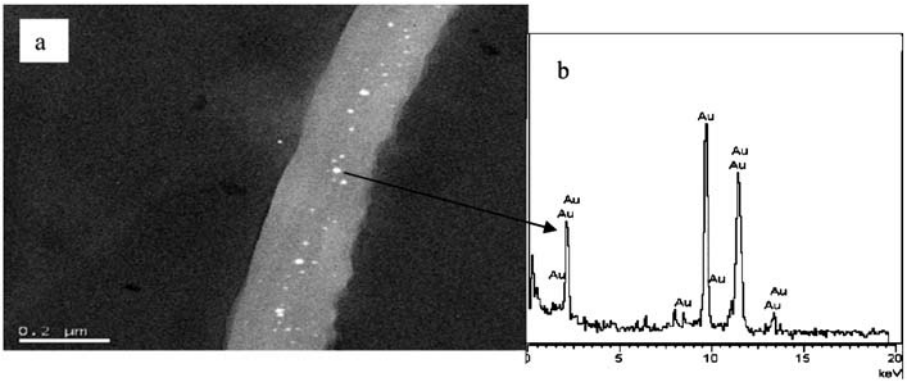

Figure 6. (a) TEM image of an alfalfa shoot howing Au particles, and (b) X-ray EDS spectrum of a single particle showing that it is pure gold. (Reprinted from Ref. [28], © 2002, with permission from American Chemical Society.)

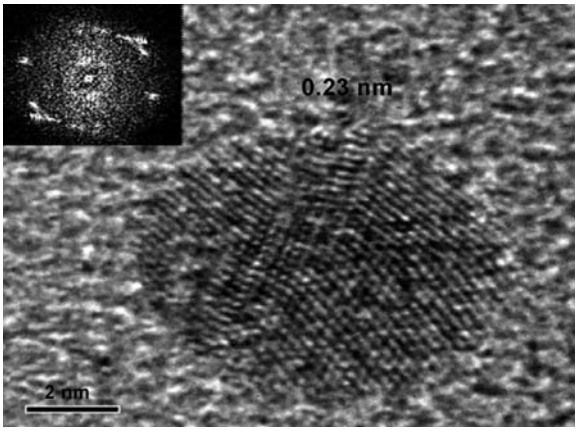

Figure 7. High resolution TEM image of a single Au nanoparticle observed inside a stem of alfalfa seedlings grown in gold enriched medium. The inset corresponds to the fast Fourier transform of the crystalline particle. (Reprinted from Ref. [28], © 2002, with permission from American Chemical Society)

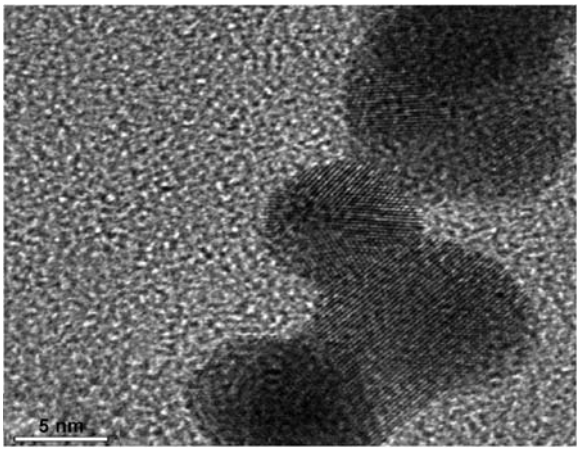

Figure 8. Coalescence of Au nanopartilces within the stem of alfalfa plants. (Reprinted from Ref. [28], © 2002, with permission from American Chemical Society.)

5. Conclusions

This chapter provides insight to a new emerging field of nanobiotechnology using plants and plant derived materials to produce nanoparticles. The increasing success of microorganisms, plants, plant extracts and plant derived materials in the formation of nanomaterials provides a significant potential of nanobiotechnology in science. Even though successful procedures have been reported for the biofabrication of nanoparticles, a number of issues still need to be addressed. Time studies to characterize the nanoparticle formation by living plants are still pending. Also, the elucidation of the mechanisms leading to metal ion reduction and subsequent nanoparticle formation at cellular and molecular levels still requires further research. Furthermore, extracellular formation of nanoparticles would be advantageous since it will eliminate the problem of harvesting the nanoparticles formed within cells and cell walls. The applications of nanotechnology encompass physics, chemistry, biology, material science, and engineering. Nanoparticles will find great use in photocatalysis, for the treatment of wastewaters and removal of organics. In addition photocatalysis has gained popularity in purification, decontamination and deodorization of air.

Nanotechnology will be extremely useful to biology. Drug and gene delivery will be more effective with the use of nanoparticles and nanocapsules. Similarly, cancer cells, bacteria, and viruses can be destructed using nanomaterials. Further applications include the use of nanosensors for monitoring the environment and sensing for potentially dangerous gases and chemicals.

The results have shown that in general, a gold(III) solution starts to be reduced to gold(0) by different biomasses after 2 h; however, the time required for a complete reduction varies with the biomass. For example, alfalfa biomass required approximately 12 h, while oat required 48 h for a complete Au(III) reduction; yet the effects of a longer reaction time on the size and form of the biogenic metal nanoparticles are still unknown. The results have also shown that just varying the pH solution it is possible to control the size and shape of the biogenic nanoparticles. These results suggest that the biosynthesis of metal nanoparticles can reach production rates comparable to those achieved by classical chemical methods.

References

1 J. H. Turkevich, P. C. Stevenson, *Discuss. Faraday Soc.* 11 (1951) 55.
2 L. O. Brown, J. E. Huthison, *J. Am. Chem. Soc.* 119 (1997) 12384.
3 K. Esumi, A. Suzuki, N. Aihara, K. Usui, K. Torigoe, *Langmuir* 14 (1998) 3157.
4 L. Bronstein, D. Chernyshov, P. Valetsky, N. Tkachenko, H. Lemmetyinen, J. Hartmann, S. Forster, *Langmuir* 15 (1998) 83.
5 M. Y. Han, C. H. Quek, W. Huang, C. H. Chew, L. M. Gan, *Chem. Mater.* 11 (1999) 1144.
6 S. M. Marinakos, D. A. Shultz, D. L. Feldheim, *Adv. Mater.* 11 (1999) 34.
7 T. Zhu, X. Fu, T. Mu, J. Wang, Z. Liu, *Langmuir* 15 (1999) 5197.
8 M. Y. Han, C. H. Quek, *Langmuir* 16 (2000) 362.
9 N. R. Jana, L. Gearheart, C. J. Murphy, *J. Phys. Chem. B* 105 (2001) 4065.
10 C. T. Dameron, R. N. Reese, R. K. Mehra, A. R. Kortan, P. J. Carroll, M. L. Steigerwald, L. E. Brus, D. R. Winge, *Nature* 338 (1989) 596.
11 J. Holmes, P. R. Smith, R. Evans-Gowing, D. J. Richardson, D. A. Russel, J. R. Sodeau, *Arch. Microbiol.* 163 (1995) 143.
12 A. Ahmad, P. Mukherjee, D. Mandal, S. Senapati, M. I. Khan, R. Kumar, M. Sastry, *J. Am. Chem. Soc.* 124 (2002) 12108.
13 M. Gerieke, A. Pinches, *Gold Bull.* 39 (2006) 22.
14 M. Gerieke, A. Pinches, *Hydrometallurgy* 83 (2006) 132.
15 M. Hosea, B. Greene, R. A. McPherson, M. T. Henzl, M. D. Alexander, D. W. Darnall, *Inorg. Chim. Acta* 123 (1986) 161.
16 D. W. Darnall, B. Greene, J. Gardea-Torresdey, *Biohydrometall. Proceedings of International Symposium.* (1988) 487.
17 A. V. Pethkar, K. M. Paknikar, *J. Biotechnol.* 63 (1998) 121.
18 N. Kuyucak, B. Volesky, *Proceedings of 10th International Precious Metals Conference.* (1986) 211.
19 N. Kuyucak, B. Volesky, *Biorecovery* 1 (1989) 189–204.
20 B. Ankamwar, M. Chaudhary, M. Sastry, *Synth. React. Inorg. Met.-Org. Chem.* 35 (2005) 19.
21 S. P. Chandran, M. Chaudhary, R. Pasricha, A. Ahmad, M. Sastry, *Biotechnol. Prog.* 22 (2006) 577.
22 S. S. Shankar, A. Ahmad, M. Sastry, *Biotechnol. Prog.* 19 (2003) 1627.
23 J. L. Gardea-Torresday, K. J. Tiemann, G. Gamez, K. Dokken, S. Tehuacanero, M. J. Yacaman, *J. Nanopart. Res.* 1 (1999) 397.
24 J. L. Gardea-Torresdey, K. J. Tiemann, G. Gamez, K. Dokken, N. E. Pingitore, *Adv. Environ. Res.* 3 (1999) 83.
25 V. Armendariz, I. Herrera, J. R. Peralta-Videa, M. Jose-Yacaman, H. Troiani, P. Santiago, J. L. Gardea-Torresdey, *J. Nanopart. Res.* 6 (2004) 337.
26 V. Armendariz, M. Jose-Yacaman, A. Duarte-Moller, J. R. Peralta-Videa, H. Trioani, I. Herrera, J. L. Gardea-Torresdey, *Revista Mexicana de Fisica* 50(Suplemento 1) (2004) 7.
27 R. N. Das, P. Pramanik, *J. Nanosci. Nanotechnol.* 4 (2004) 97.
28 J. L. Gardea-Torresdey, J. G. Parsons, E. Gomez, J. R. Peralta-Videa, H. E. Troiani, P. Santiago, M. Jose-Yacaman, *Nano Lett.* 2 (2002) 397.
29 J. L. Gardea-Torresdey, E. Gomez, J. R. Peralta-Videa, J. G. Parsons, H. Troiani, M. Jose-Yacaman, *Langmuir* 19 (2003) 1357.
30 S. V. Sahi, N. L. Bryant, N. C. Sharma, S. R. Singh, *Environ. Sci. Technol.* 36 (2002) 4676.
31 B. J. Yates, E. Myre, D. Breetz, D. D. Dionysiou, *Am. Chem. Soc. Div. Environ. Chem.* 45 (2005) 740.
32 J. Turkevich, *Gold Bull.* 18 (1985) 125.
33 V. K. Iya, G. S. Gopal, S. Y. Chaudhary, *Indian J. Chem.* 3 (1995) 317.
34 N. R. Jana, L. Gearheart, C. J. Murphy, *Langmuir* 17 (2001) 6782.
35 A. G. Dhere, R. J. De Angelis, P. J. Reucroft, J. Bentley, *Ultramicroscopy* 18 (1985) 415.
36 S. Ravaine, G. E. Fanucci, C. T. Seip, J. H. Adair, D. R. Talham, *Langmuir* 14 (1998) 708.
37 T. Yonezawa, T. Kunitake, *Colloids Surf.* 149 (1999) 193.
38 S. T. Selvan, Y. Ono, M. Nogami, *Mater. Lett.* 37 (1998) 156.
39 A. B. Mayer, J. E. Mark, *Eur. Polym. J.* 34 (1997) 103.
40 K. Esumi, A. Suzuki, A. Yamahira, K. Torigoe, *Langmuir* 16 (2000) 2604.

41 D. W. Darnall, B. Greene, M. T. Henzl, M. J. Hosea, R. A. McPherson, J. Sneddon, *J. Environ. Sci. Technol.* 20 (1986) 260.
42 A. C. Augusto da Costa, S. G. F. Leite, *Biotechnol. Lett.* 13 (1992) 559.
43 J. Chang, J. Huang, *Biotechnol. Prog.* 14 (1998) 735.
44 T. Klaus, R. Joerger, E. Olsson, C.-G. Granqvist, *Proc. Natl. Acad. Sci. USA* 96 (1999) 13611.
45 R. Joerger, T. Klaus, C.-G. Granqvist, *Adv. Mater.* 12 (2000) 407.
46 B. Nair, T. Pradeep, *Cryst. Growth Des.* 2 (2002) 93.
47 P. Mukherjee, A. Ahmad, D. Mandal, S. Senapati, S. T. Sainkar, M. I. Khan, R. Parishcha, P. V. Ajaykumar, M. Alam, R. Kumar, M. Sastry, *Nano Lett.* 1 (2001) 515.
48 P. Mukherjee, A. Absar, D. Mandal, S. Senapati, R. Sudhakar, M. I. Khan, R. Ramani, R. Parischa, P. V. Alayakumar, M. Alam, M. Sastry, R. Kumar, *Angew. Chem. Int. Ed.* 40 (2001) 3585.
49 P. Mukherjee, S. Senapati, D. Mandal, A. Ahmad, M. I. Khan, R. Kumar, M. Sastry, *Chem. Biochem.* 3 (2002) 461.
50 J. A. Erdman, B. F. Leonard, D. M. Mckown, *A Case for Plants in Exploration: Gold in Douglas-Fir at the Red Mountain Stockwell, Yellow Pine District, Idaho*. United States Department of the Interior Geological Survey, Open-File Report, (1985) 85.
51 K. C. Jones, P. J. Peterson, *Biogeochemistry* 7 (1989) 3.
52 C. W. N. Anderson, R. R. Brooks, A. Chiarucci, C. J. LaCoste, M. Leblanc, B. H. Brobinson, R. Simcock, R. B. Stewart, *J. Geochem. Explor.* 67 (1999) 407.
53 A. L. Kovalevskii, O. M. Kovalevskaya, *Appl. Geochem.* 4 (1989) 369.
54 A. Nakajima, T. Sakaguchi, *J. Chem. Technol. Biotechnol.* 57 (1993) 321.
55 J. R. Lujan, D. W. Darnall, P. C. Stark, G. D. Rayson, J. L. Gardea-Torresdey, *Solvent Extr. Ion Exch.* 12 (1994) 803.
56 S. S. Shankar, A. Ahmad, R. Pasricha, M. Sastry, *J. Mater. Chem.* 13 (2003) 1822.
57 S. S. Shankar, A. Rai, B. Ankamwar, A. Singh, A. Ahmad, M. Sastry, *Nature Mater.* 3 (2004) 482.
58 H. Huang, X. Yang, *Carbohydr. Res.* 339 (2004) 2627.
59 D. G. Duff, A. C. Curtis, P. Edwards, *Angew Chem. Int. Eng.* 26 (1987) 676.
60 S. Mobilio, C. Meneghini, *J. Non-Cryst. Solids* 232 (1998) 25.
61 J. A. Ascencio, M. Perez, M. Jose-Yacaman, *Surf. Sci.* 447 (2000) 73.
62 M. L. Lopez, J. L. Gardea-Torresdey, J. R. Peralta-Videa, G. de la Rosa, V. Armendariz, I. Herrera, H. Troiani, J. Henning, *Bioinorg. Chem. Appl.* 3 (2005) 29.
63 M. L. Lopez, J. G. Parsons, J. R. Peralta-Videa, J. L. Gardea-Torresdey, *Microchem. J.* 81 (2005) 50.
64 J. L. Gardea-Torresdey, K. J. Tiemann, G. Gamez, K. Dokken, I. Cano-Aguilera, L. R. Furenlid, M. W. Renner, *Environ. Sci. Technol.* 34 (2000) 4392.
65 J. L. Gardea-Torresdey, K. J. Tiemann, J. G. Parsons, G. Gamez, I. Herrera, M. Jose-Yacaman, *Microchem. J.* 71 (2002) 193.
66 J. L. Gardea-Torresdey, E. Rodriguez, J. G. Parsons, J. R. Peralta-Videa, G. Meitzner, G. Cruz-Jimenez, *Anal. Bioanal. Chem.* 382 (2005) 347.
67 S. S. Shankar, A. Rai, A. Ahmad, M. Sastry, *J. Colloid Interface Sci.* 275 (2004) 496.
68 K. C. Bhainsa, S. F. D'Souza, *Colloids Surf. B* 47 (2006) 60.
69 M. F. Lengke, M. E. Fleet, G. Southam, *Langmuir* 22 (2006) 7318.
70 R. R. Naik, J. Stringer, G. Agarwal, S. E. Jones, *Nat. Mater.* 1 (2002) 169.
71 Y. Konishi, T. Tsukiyama, K. Ohno, N. Saitoh, T. Nomura, S. Nagamine, *Hydrometallurgy* 81 (2006) 24.
72 V. Armendariz, Bioreduction of Gold(III) to Gold(0) and Nanoparticle Formation by Oat and Wheat Biomasses: The Use of Plants in Nanobiotechnology. Master Thesis, the University of Texas at El Paso, Chemistry Department, El Paso, TX, 2005, p. 107.
73 M. Borowski, *J. Phys. IV* 7 (C2, X-ray Absorption Fine Structure, Vol. 1) (1997) 259.
74 J. R. Peralta, J. L. Gardea-Torresdey, K. J. Tiemann, G. Gomez, S. Arteaga, E. Rascon, J. G. Parsons, *Bull. Environ. Contam. Toxicol.* 66 (2001) 727.
75 E. Gomez, The Nanoparticle Formation and uptake of Precious Metals by Living alfalfa Plants. Master Thesis, the University of Texas at El Paso, Chemistry Department, El Paso, TX, 2002, p. 81.
76 C. M. Lytle, F. W. Lytle, N. Yang, J. Quian, A. Zayed, *Environ. Sci. Technol.* 32 (1998) 3087.
77 T. J. Ressler, *J. Synchrotron Radiat.* 5 (1998) 118.
78 M. J. Yacaman, J. Ascencio, H. Liu, J. Gardea-Torresdey, *J. Vac. Sci. Technol. B* 19 (2001) 1091.

This page intentionally left blank

CHAPTER 29

Gel-Type Cross-Linked Functional Polymers as Template in the Synthesis of Size Controlled Metal Nanoclusters

B. Corain[1,2], P. Centomo[1], C. Burato[1], and P. Canton[3]

[1]*Department of Chemical Sciences, University of Padova, Padova, Italy*
[2]*Institute of Molecular Sciences and Technologies, CNR, Section of Padova c/o Department of Chemical Sciences, University of Padova, Padova, Italy*
[3]*Department of Physical Chemistry, University of Venezia, Venezia-Mestre, Italy*

1. Introduction

Cross-linked gel-type functional polymers (CFPs) are organic materials built up with interconnected polymer chains [1]. Pendants hanging from the polymer chains may render CFPs reactive materials particularly suitable for anchoring metal centres removed from a liquid phase, by means of covalent or ionic bonds [2]:

$$Ⓟ - L'(s) + ML''_n(\text{solution}) \rightarrow -ⓅL' - ML''_n(s) \qquad (1)$$

The macromolecular metal complexes or ion-pair $Ⓟ - L^{I} - ML^{II}_n$ might be hybrid phase catalysts, e.g. $R425 \cdot Me^{+}Rh(CO)_2I_2^{-}$ (R425 = Reillex cross-linked poly-4-vinylpyridyne-divinylbenzene [3]; $R425 \cdot Me^{+}$ = methyl form) or precursors of M^0 nanoclusters produced by the chemical reduction of M^n, i.e.:

$$Ⓟ - L' - M^nL''_m(s) + \text{red (solution)} \rightarrow M^0/Ⓟ - L'(s) + \text{ox (solution)} + \text{m}\,L''(\text{solution}) \qquad (2)$$

Reactions (1) and (2) have been quite actively pursued from the early nineties [4] and a possible connection between the M^0 nanoclusters size produced inside the swollen resin and the nanoporosity of the macromolecular support was discovered in 2000. This amazing observation led us to develop an operational hypothesis for what was appearing as an unprecedented means for the synthesis of size-controlled metal nanoclusters.

2. Synthesis Strategy: The TCS Approach

The rationale at the basis of what was later called Template Controlled Synthesis (TCS) [5] approach, is illustrated in Figure 1.

A gel-type CFP is designed (Figure 1b) to posses a polymer chain concentration [6] (or a "nanoporosity") [7] that is featured by meshes with lumina ranging from 2 to 5 nm. It is worthwhile to stress the circumstances that the TCS-related rule dictates that *metal nanoclusters should not be larger than the largest nanopores available in the polymer framework*, after swelling in a given solvent: they might be only smaller. Another point to raise in evidence is the circumstance that the mass percentage of the metal component in the final M^0/CFP nanocomposite should be large enough so that the individual metal atoms turn out to be able to properly fill the available largest (vide infra) nanopores.

A related and very attractive approach is going to be developed in these Laboratories, to be named Template Controlled Synthesis Deposition, TCS-D, the rationale of which is illustrated in Figure 2.

In view of the expected generality of application, the prospects of TCS-D are amazing. A tricky point that has to be solved is the final thermal decomposition of the M^0/Ⓟ/S nanocomposite that should be carried out at relatively low temperature for preserving the geometric features of metal nanoclusters. CFPs currently employed in this strategy do decompose at 290–330 °C and CFPs able to decompose at 250 °C are being looked for [8].

3. Results

The first project [9] dealt with the evaluation of the effect of cross-linking degree (c.l.d.) in a series of five gel-type resins, on the diameter of Pd^0 nanoclusters obtained upon reducing resin-bound Pd^{II} centres. In this project c.l.d. was let to range from 1 to 9% mol (Figure 3).

In fact, the idea was rather naïve at that time and started from the expectation that more dense polymer

Metal Nanoclusters in Catalysis and Materials Science: The Issue of Size Control
Edited by B. Corain, G. Schmid and N. Toshima

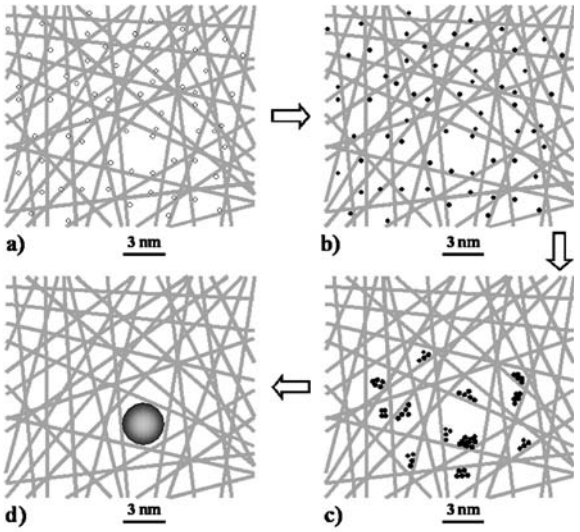

Figure 1. Graphical model for the generation of size-controlled metal nanoparticles inside metallated resins. (a) Pd^{II} is homogeneously dispersed inside the polymer framework; (b) Pd^{II} is reduced to Pd^0; (c) Pd^0 atoms start to aggregate in subnanoclusters; (d) a single 3 nm nanocluster is formed and ''blocked'' inside the largest mesh present in that ''slice'' of polymer framework (Reprinted from Ref. [5], © 2004, with permission from Wiley-VCH.)

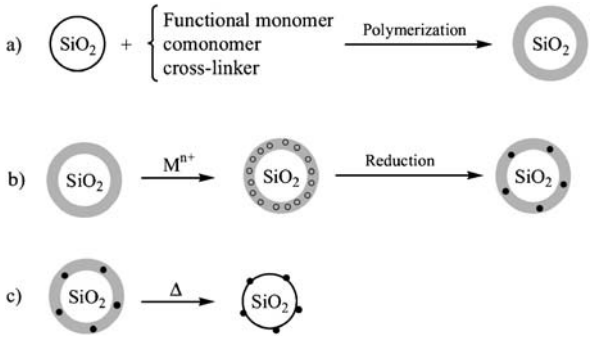

Figure 2. TCS-D strategy. A resin layer is produced outside each support particle. Metallation-reduction of the polymer shell will lead to size-controlled metal nanoclusters. Gentle thermal degradation of the organic shell will lead to size-controlled metal nanoclusters, expected to be evenly dispersed on the support particles surface.

frameworks (higher c.l.d.) should promote the formation of smaller Pd^0 nanoclusters.

The surprising result was the substantial independence of the observed nanoclusters diameters of the c.l.d. More precisely the 2–4 nm range turned to be altogether the dominating size, as the consequence of the circumstance that in all resins nanopores from 2 to 4 nm in diameter turned out to be present in the various polymer frameworks.

A second project [10] was based on the production of Pd^0 nanocluster inside poly-methacrylic acid (8% mol)–*N,N*-dimethylacrylamide (88% mol)–*N,N*-methylenebisacrylamide (4% mol). ISEC (Inverse Size Exclusion Chromatography) analysis of the resin in water in terms of cylindrical pores [7]

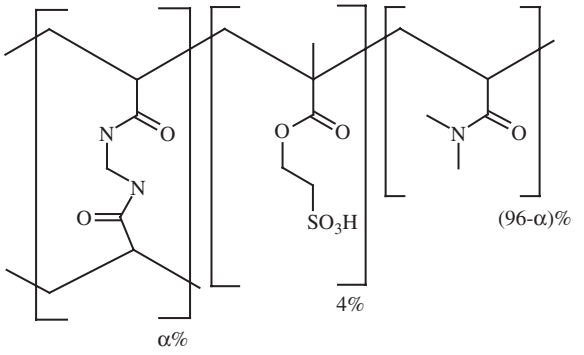

Figure 3. Primary structure of resins Aα (α = 1–9) [9].

Table 1. ISEC characterization of the cross-linked functional polymer $MPIF^- Na^+$.

Pore diameter (nm)	Volume fraction (cm^3/g)
0.6	0.47
1.1	0.00
1.6	0.00
2.7	0.00
3.2	1.54
4.3	0.84
8.1	0.00
13.2	0.00

distribution, did show that resin coded as MPIF in Na^+ form had prevalent pores in the 3.2–4.3 nm range and that in Pd^0/MPIF(Na^+) the most prevalent largest (see Table 1) pores were 3.2 nm in diameter.

TEM analysis informed that the most-abundant Pd^0 nanocluster diameters were in the 1.8–2.4 nm range. This observation, although the agreement was mediocre, provided a first-level confirmation of what would have become the TCS strategy.

A turning point in favour of the intuitions, was a third project [5].

In this case we took care of a very major question concerning the reliability of the metal nanocluster diameters determination to be compared with the ISEC-based nanostructural outcomes of the macromolecular mold. In fact TEM analysis is based on the ''counting'' of some hundreds of metal nanoclusters and the pretence to propose such universal criterion as TCS had to cope with a far more reliable verification.

We choose resin DOMA-VP (4-vinylpyridine (4% mol)–dodecylmethacrylate (92% mol)–ethyleneglycoledimethacrylate (4% mol)), Figure 4, support for testing the intuition. A Pd^0/DOMA-VP nanocomposite was produced in THF and ISEC analysis in THF (Table 2) gave the pattern illustrated in Figure 5.

The histogram reveals that only pores from 2.5 to 4.0 nm in diameter do characterize the resin framework in THF (see also Table 1).

TEM analysis provides results extremely compatible with ISEC analysis (Figure 6).

XRD analysis perfected by the application of Rietveld method [11,12] provided an average metal nanocluster diameter equal to 3.3 nm (Table 3).

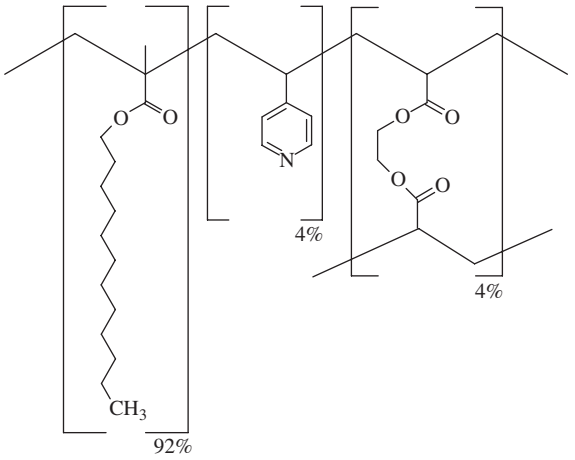

Figure 4. Sketch of the primary structure of DOMA-VP.

Table 2. ISEC characterization of resin DOMA-VP in THF.

Pore diameter (nm)	Volume fraction (cm^3/g)
2.5	0.158
3.0	0.791
3.5	1.038
4.0	0.544
Average diameter (nm)	3.4[a]
Cumulative pore volume (cm^3/g)	2.531
Cumulative surface (m^2/g)	3037.9
Sum of squared errors	0.340
Number of iteration	15.212

Note: Pores smaller than 2.5 nm and larger than 5 nm are not detected.
[a]Ref. [5].

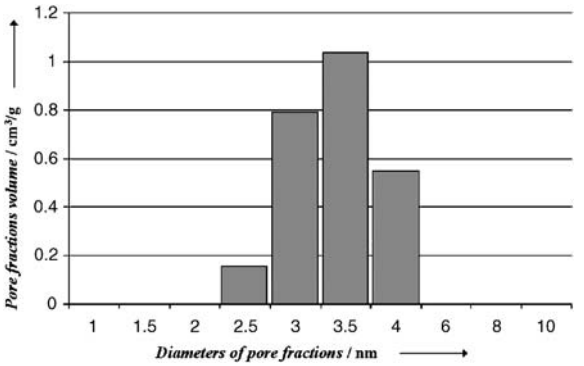

Figure 5. Nanoporosity of DOMA-VP as determined with ISEC. (Reprinted from Ref. [5], © 2004, with permission from Wiley-VCH.)

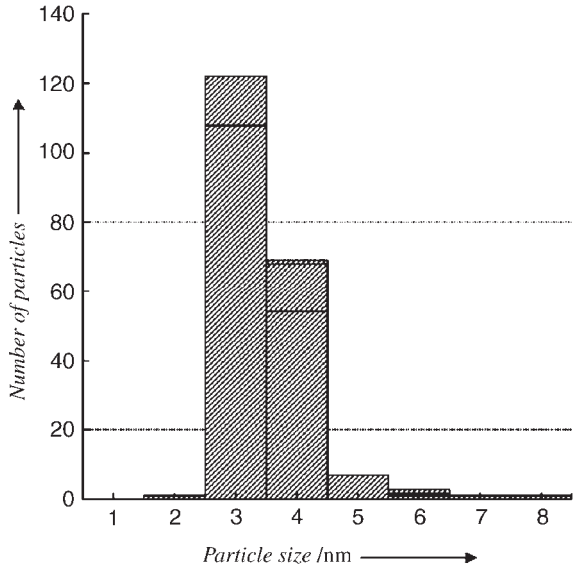

Figure 6. Size dispersion of Pd^0 nanoclusters in Pd^0/DOMA-VP. (Reprinted from Ref. [5], © 2004, with permission from Wiley-VCH.)

It is essential to stress the circumstance that this peculiar structural analysis of a Pd^0/resin nanocomposite provide a dimensional information that is based on some 10^{16} metal nanoclusters.

There is no doubt that this Pd^0/DOMA-VP nanocomposite should be considered the paradigm of TCS approach.

Another project was based on resins MTEMA–DMAA 4-4 (Figure 7) and MTEMA–DMAA 4-8 (Figure 8) [13,14] that were employed for preparing M^0/MTEMA DMAA 4-4 (M = Pd, Au) and M^0/MTEMA–DMAA 4-8 nanocomposites. In these materials the agreement between the largest predominant pore diameter, 2.5 nm and the average determined (TEM) metal nanoclusters diameters, 2.3 nm for Pd and 2.2 nm for Au is very good for MTEMA–DMAA 4-8. For M^0/MTEMA–DMAA 4-4 the agreement is good for Pd^0 but somewhat poorer for Au^0 (Table 4).

Rather significant is the Pd^0 nanoclusters size trend upon increasing the cross-linking degree. In this case both the expectations based on the simple argument of the cross-linking degree effect and the full compliance of the TCS approach, are fulfilled.

Very recent relevant observations reveal that the TCS approach albeit certainly significant as conceptual and operational tool in the issue of metal nanoclusters size control, requires a substantial further perfection. Resin sulfonated Bayer K1221 is a co styrene-divinylbenzene commercially available gel-type resin, in beaded form. Its cross-linking degree is ca. 4% mol and therefore K1221 is expectedly quite similar to DOMA-VP and MTEMA–DMAA 4-4 for example. In fact ISEC analysis reveals a nanoporosity featured by 4.0 and 2.0 nm nanopores only. The expectation is that a Pd^0/K1221 nanocomposite obtained with a classic procedure [5,9,10] will exhibit diameters strictly ranging from 2 to 4 nm.

Data are presented in Figure 9. TEM analysis, based on counting 259 Pd^0 nanoclusters, reveals a really remarkable size-control exerted by the macromolecular mold on the

Table 3. Consistency among nanostructural features of Pd^0/DOMA-VP.

Feature	Technique	Datum	Remarks
Cavities size (nm)	ISEC	3.4	–
Nanocluster diameter (nm)	TEM	3.6	–
Nanocluster diameter (nm)	XRD	3.3	Rietveld
Nanocluster diameter (nm)	XRD	2.6	From number distribution function[a]

[a]Ref. [12].

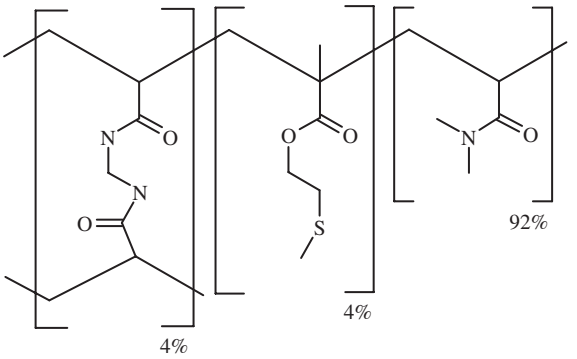

Figure 7. Primary structure of resin MTEMA–DMAA 4-4. (Adapted from Ref. [15] © 2006, with permission from Wiley-VCH.)

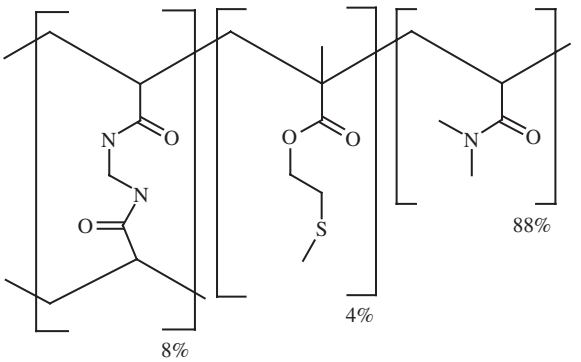

Figure 8. Sketch of the primary structure (vide infra) of MTEMA–DMAA 4-8. (Adapted from Ref. [15] ® 2006, with permission from Wiley-VCH.)

produced Pd^0 nanoclusters. However the intriguing observation is that Pd^0 nanoparticles, while expected to be 2–4 nm in diameter turn to be ca. 6 nm large in Pd^0/K1221.

In the light of the findings illustrated so far, the disagreement between expected and observed nanopores diameter, cannot be defined but significant and this datum reveals that the TCS model needs further testing.

4. A Case History

The case of M^0/Ⓟ (M = Pd, Au) nanocomposites is illustrated. Ⓟ is a gel-type cross-linked functional polymer coded as MTEMA–DMAA 4-8 [14] (Figure 8).

The resin was synthesized upon γ-irradiating at room temperature a homogeneous mixture of MTEMA (2-(methylthio)ethyl methacrylate, 8% mol), DMAA (*N,N*-dimethylacrylamide, 88% mol), and MBAA (*N,N′*-methylenebisacrylamide, 4% mol). It is believed that a similar material should be obtainable also upon conventional radical polymerization.

Tables 5 and 6 illustrate the mixture composition, the expected molar composition, and relevant elemental analysis.

Solvents and chemicals are of reagent grade.

(a) In a typical experiment DMAA 11.12 g, MTEMA 0.81 g, and MBAA 1.57 g, are mixed in a cylindrical glass vessel to give a clear colourless solution. After oxygen removal with nitrogen bubbling, the solution is γ-irradiated (^{60}C) for 18 h, at a distance of 17.1 cm from the source (total dose is ca. 10 kGy) at room temperature. The solution becomes a transparent, pale yellow cylindrical block, which is ground with an impact grinder, sieved to

Table 4. Pd^0 and Au^0 nanoclusters size vs. determined nanoporosity in water.

	MTEMA–DMAA 4-4	MTEMA–DMAA 4–8
Largest available pores (Ref. [2], Figure 1) (nm)	3.5	2.5
Metal nanoclusters average diameter (nm)		
Au^0	4.9	2.2 3.3[b]
Pd^0	3.8	2.3 2.6[b]

[a]Not determined.
[b]After 12 months since the preparation of the M^0/Ⓟ catalysts.

Table 5. Details of the synthesis and experimental elemental composition of resin MTEMA–DMAA 4–8.

Code	Monomers (g)	C%	H%	N%	S%
MTEMA–DMAA 4–8	MTEMA (0.81) DMAA (11.12) MBAA (1.57)	56.65	8.87	13.16	1.39 (0.38)[a]

Abbreviations: DMAA, *N,N*-dimethylacrylamide; MTEMA, 2-(methylthio)ethyl methacrylate; MBAA, *N,N′*-methylenebisacrylamide.
[a]mmol/g of MTEMA.

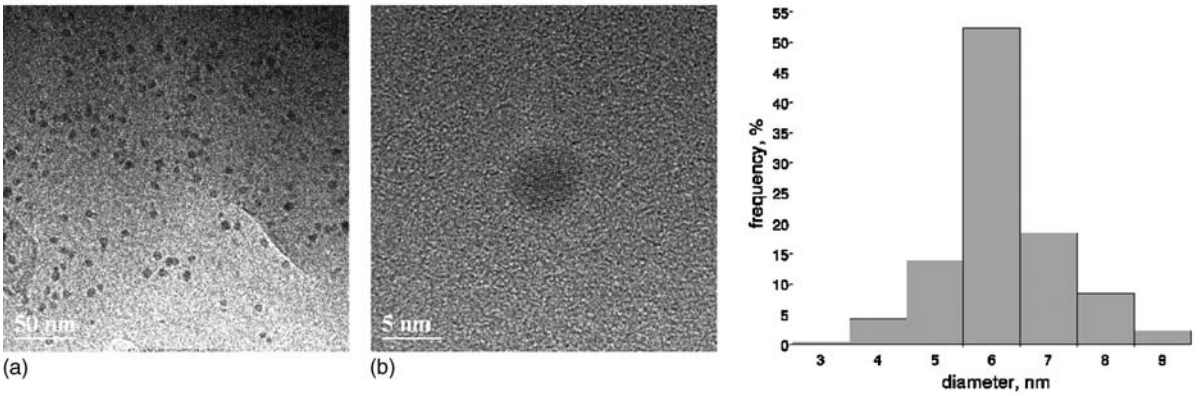

Figure 9. TEM micrographs of Pd^0/K1221 in low (a) and high (b) resolution; Pd^0 nanoclusters diameter distribution (c).

Table 6. Designed composition and observed polymerization yield of resin MTEMA–DMAA 4–8.

Code	Monomer composition	mol (%)	Polymerization yield %
MTEMA–DMAA 4–8	DMAA	88	
	MTEMA	4	99
	MBAA	8	

Table 7. Data for Au^0, Pd^0/Ⓟ composites.

Code	Au (%)	Pd (%)	Colour
Pd^0/Ⓟ	0.75		Burgundy red (Au)
Pd^0/Ⓟ		0.70	Black (Pd)

Table 8. ISEC characterization of the macromolecular template MTEMA–DMAA 4–8.

	MTEMA–DMAA 4–8
Sample wt. (g)	1.54
Dead volume (mL)	1.22
Pore diameter (nm)	mL/g
0.5	2.17
1	0
2.2	0.19
2.5	0.79
2.7	0.01
3.2	0.04
3.5	0.06
4	0
Average pore diameter, nm	2.5

Table 9. Predominant largest pores diameter in MTEMA–DMAA 4–8 vs. observed average nanoclusters diameter in M^0/MTEMA–DMAA 4–8 catalysts (M = Au, Pd).

Nanocomposite	Average nanoclusters diameter	Predominant largest pores
Pd^0/Ⓟ	2.2[a]	2.5
Au^0/Ⓟ	2.2[b]	2.5

[a]2.6 nm after 12 months storage under air.
[b]3.3 nm after 6 months storage.

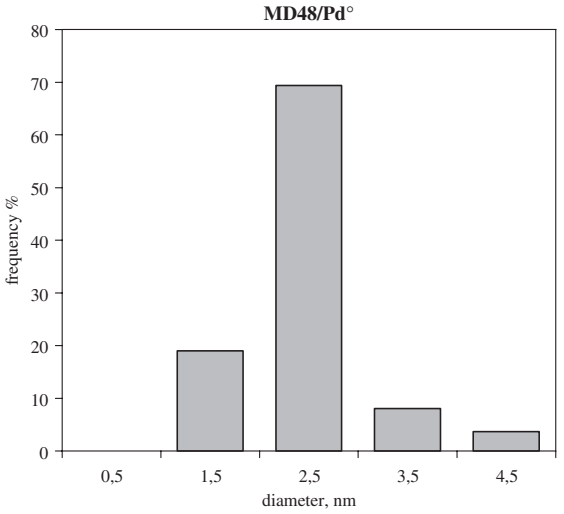

Figure 10. TEM characterization of Pd^0/MTEMA–DMAA 4-8 composite. (Reprinted from Ref. [13], © 2004, with permission from Wiley-VCH.)

180–400 nm, washed with methanol in a Soxhlet apparatus for 4 days, and dried at 5 Torr and 60 °C for 24 h. (b) MTEMA–DMAA 4-8 (1 g, ca. 0.4 mmol-SMe) is suspended in the required medium (see below) and left under moderate stirring for 2 h. Approximately 20 mg (0.06 mmol) of $AuCl_3$ or ca. 25 mg (0.11 mmol) of Na_2PdCl_4 dissolved in 40 ml MeCN (Au) and water (Pd) are added under manual stirring and then left under moderate mechanical stirring for ca. 4 days. The colourless supernatant phase is separated from the metalled resins (colourless for Au^{III} and pale brown in the case of Pd^{II}) upon filtration and the relevant Ⓟ/Au^{III} and Ⓟ/Pd^{II}

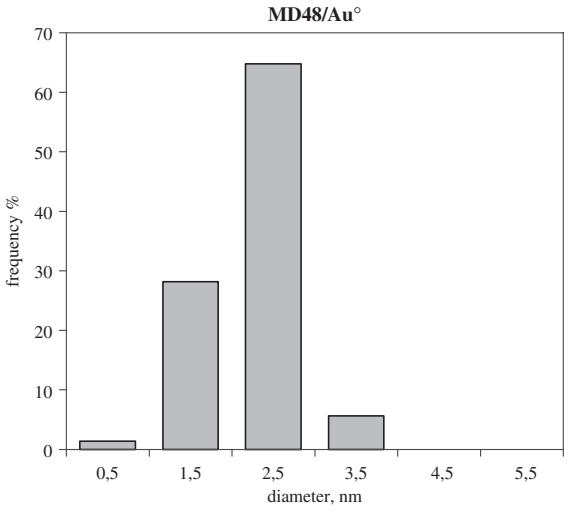

Figure 11. TEM characterization of Au^0/MTEMA–DMAA 4–8 composite. (Reprinted from Ref. [13], © 2004, with permission from Wiley-VCH.)

macromolecular complexes are dried at 5 Torr and 60 °C to constant weight. (c) Each metallated resin, Ⓟ/M^n (ca. 1.2 g) is suspended in ca. 200 ml water under moderate stirring for 2 h. Approximately 250 mg $NaBH_4$ (6.6 mmol) dissolved in 50 ml water are added to the suspension under vigorous stirring for 90 min. The supernatant appears now colourless and the M^0/Ⓟ nanocomposites appear burgundy red (Au) and black (Pd). Reduced materials are recovered with filtration, washed with water, and dried *in vacuo* to constant weight. From this point, for sake of simplicity products Au^0/MTEMA–DMAA 4-8 and Pd^0/MTEMA–DMAA 4-8 are recoded as Pd^0/Ⓟ and Au^0/Ⓟ (Table 7). (d) ISEC analysis of MTEMA–DMAA 4-8 is shown in Table 8. The resin appears to be built up with domains that are predominantly featured by 2.5 and 0.5 nm "cylindrical [7] pores". Consequently, the prevalent formation of 2.5 nm Pd^0 and Au^0 nanoclusters (see legend of Figure 1) is expected. (e) TEM analysis of Pd^0/Ⓟ and Au^0/Ⓟ reveals that Pd^0 and Au^0 nanoclusters are well spaced, narrowly size-dispersed, spheroidal particles (Figures 10 and 11).

The extremely good agreement between M^0 nanoclusters size production and the ISEC-based prediction is illustrated in Table 9.

5. Conclusions

Gel-type cross-linked functional polymers, with moderate cross-linking degree (4–8% mol) are effective templates for the production of size-controlled metal nanoclusters. Metal centers are first anchored to the polymer framework with ionic or covalent bonds and subsequently reduced to the zero-valent state. The consequent aggregation of the metal atoms occur under conditions that drive the event to the formation of size-controlled metal nanoclusters, the size of which is conditioned by the size of the larger nanopores present in each volume element.

References

1 (a) A. Guyot, D. C. Sherrington, in P. Hodge (ed.) *Synthesis and Separations Using Functional Polymers*, Wiley, New York, 1988, 1; (b) B. Corain, M. Zecca, K. Jerabek, *J. Mol. Catal. A: Chem.* 177 (2001) 3.
2 A. Warshawsky, in A. Guyot, D. C. Sherrington, P. Hodge (eds.) *Synthesis and Separations Using Functional Polymers*, Wiley, New York, 1988, 1; (b) for a recent review paper see B. Corain, P. Centomo, M. Zecca, *Chim. Ind. (Milan)* 86 (2004) 114 and the many selected references therein.
3 N. Yoneda, S. Kusano, M. Yasui, P. Pujado, S. Wilcher, *Appl. Catal. A: General* 221 (2001) 253.
4 (a) B. Corain, M. Kralik, *J. Mol. Catal. A: Chem.* 159 (2000) 153; (b) B. Corain, M. Kralik, *J. Mol. Catal. A: Chem.* 173 (2001) 99 and its corrigendum *J. Mol. Catal. A: Chem.* 200 (2003) 333.
5 B. Corain, K. Jerabek, P. Centomo, P. Canton, *Angew. Chem. Int. Ed.* 43 (2004) 959.
6 (a) K. Jerabek, *Anal. Chem.* 57 (1985) 1595; (b) K. Jerábek, *Anal. Chem.* 57 (1985) 1598.
7 K. Jerabek, in M. Potschka, P. L. Dubin (eds.) *Cross Evaluation of Strategies in Size-Exclusion Chromatography, ACS Symposium Series 635*, American Chemical Society, Washington, DC, USA, 1996, 211.
8 (a) P. Centomo, PhD Thesis, 2006, University of Padova, Italy; (b) P. Centomo, M. Zecca, B. Corain, *J. Cluster Sci.* 00 (2007) 00.
9 A. Biffis, A. A. D'Archivio, K. Jeràbek, G. Schmid, B. Corain, *Adv. Mater.* 12 (2000) 1909.
10 F. Artuso, A. A. D'Archivio, S. Lora, K. Jeràbek, M. Kralik, B. Corain, *Chem. Eur. J.* 9 (2003) 5292.
11 (a) P. Riello, G. Fagherazzi, D. Clemente, P. Canton, *J. Appl. Cryst.* 28 (1995) 115; (b) G. Fagherazzi, P. Canton, P. Riello, N. Pernicone, F. Pinna, M. Battagliarin, *Langmuir* 16 (2000) 4539.
12 P. Canton, C. Meneghini, P. Riello, A. Benedetti, in B. M. Weckhuysen (ed.) *In-Situ Spectroscopy of Catalysts in X-ray Diffraction and Scattering*, American Scientific Publishers, 2004, 281.
13 B. Corain, C. Burato, P. Centomo, S. Lora, W. Meyer-Zaika, G. Schmid, *J. Mol. Catal. A: Chem.* 2245 (2004) 189.
14 C. Burato, P. Centomo, G. Pace, M. Favaro, L. Prati, B. Corain, *J. Mol. Catal. A: Chemical* 238 (2005) 26.
15 C. Burato, P. Centomo, M. Rizzoli, A. Biffis, S. Campestrini, B. Corain, *Adv. Synth. Catal,* 348 (2006) 255.

CHAPTER 30

Size and Shape Selective Synthesis of Metal Nanoparticles by Seed-Mediated Method and the Catalytic Activity of Growing Microelectrodes (GME) and Fully Grown Microelectrodes (FGME)

Tarasankar Pal and Snigdhamayee Praharaj

Department of Chemistry, Indian Institute of Technology, Kharagpur, India

1. Introduction

During the last few decades the emerging field of nano-sized transition metal particles has stimulated much research interest due to their unique physical and chemical properties, which are quite different from those of the corresponding bulk materials [1–4]. In 1857 Faraday first scientifically elucidated the preparative method for aqueous dispersions of gold nanoparticles [5]. To cater the need-based advancement, metal nanoparticles have been produced by chemical reduction of metal salts with suitable reducing agents (bottom up method) such as sodium citrates, borohydride, aldehydes, alcohols, di-ketones, sugars, etc. [6–10]. Gold nanoparticles (AuNPs), because of their noble character and rich plasmon absorption in the visible region, have been studied in great detail [11]. Among the conventional methods of synthesis of AuNPs citrate reduction of $HAuCl_4$ in water was introduced by Turkevitch et al. in 1951 [12]. In an early effort, reported in 1973 by Frens, to obtain AuNPs of prechosen size (between 16 and 147 nm) a method was proposed where the ratio between the reducing/stabilizing agents (the trisodium citrate-to-gold ratio) was varied [13]. Toshima and coworkers invented the alcohol reduction method to prepare metal colloids in presence of protective polymers [14,15]. These nanomaterials are of special interest in catalysis as they provide access to more number of catalytically active sites due to large surface-to-volume ratio than the corresponding bulk components. Since the catalytic activity and selectivity is strongly affected by particle size and shape, precise control of the particle size is essentially required [16]. There are various methods in literature for the size and shape controlled evolution of the particles. These methods are based on surfactant-based seed-mediated growth [17,18], thermal growth [19,20], photoreduction of metal salts in solution [21] and template synthesis technique [22]. Among all these procedures for controlled fabrication of particles the seed-mediated synthesis is easily achieved and hence deserves special mention for various applications especially in catalysis.

2. Synthetic Strategy

The seeding-growth procedure is a popular technique that has been used for a century to synthesize metal particles in solution. Recent studies have successfully led to control the dimensionality of the particles where the sizes can be manipulated by varying the ratio of seed to metal salt [23–25]. The step-by-step particle enlargement is more effective than a one-step seeding method to avoid secondary nucleation [26,27]. This mechanism involves a two-step process, i.e. nucleation and then successive growth of the particles as illustrated in Scheme 1.

In the first step precursor ions are reduced to form seed particles. In the second step, appropriate amounts of precursor ions are reduced onto the preformed 'seed' or 'germ', i.e. small particles by suitable reducing agents. The reducing agent used in the second stage of 'seed'-mediated growth is generally a weaker one, viz., H_2NOH, ascorbate ion, etc. They reduce only the adsorbed precursor ions without creating any nucleation center. Kinetics of this step can be followed easily and the result authenticates autocatalytic growth of the nucleation centers. The reduction potentials of $metal_{ion}/metal_{atom}$ and $metal_{ion}/metal_{particle}$ systems become more negative compared to those of the corresponding bulk metal [28–31]. For example, the reduction potential of the Au^{III}/Au_{metal}(aqueous) system is +1.5 V versus NHE. But for the Au^{III}/Au_{atom}(aqueous) system it is −1.5 V and for

Metal Nanoclusters in Catalysis and Materials Science: The Issue of Size Control
Edited by B. Corain, G. Schmid and N. Toshima

Au^{III}(aqueous)/$Au_{cluster}$ system the reduction potential has an intermediate value depending on the agglomeration number of the Au cluster. The thermodynamics of the reduction suggests that the formation of the metal atoms from its ions is very difficult. This result has a great significance in understanding the mechanism of particle synthesis. The formation of metal atoms from its ions is very difficult because of the large negative potential of the $metal_{ion}$(aqueous)/$metal_{atom}$ system. Conventional strong reducing agents like free radicals ($E^0 = -1.0$ to 1.5 V vs. NHE) and borohydride ($E^0 = -1.33$ V vs. NHE) and reducing agents like hydrazine and alcohol may not be able to reduce the metal ions. Often a trace impurity acts as nucleation center as it generally increases the reduction potential of $metal_{ion}$/$metal_{atom}$ system causing a favorable metal ion reduction. Once the nucleation center is created, it acts as a catalyst for the reduction of remaining metals. Recently radiolytic method and chemical size control with improved monodispersity via seed-mediated growth of colloidal gold particles have been reported by Henglein, Meisel and Natan's group [32–34]. They followed the iterative growth method, i.e. particles grown in the immediately previous step were used as seeds in the next growth step. We have also proposed a combination of photochemical/wet chemical approach with an iterative growth method to develop a simple way for size control [24,35,36]. We have successfully employed the seed-mediated growth process first to control the size and then shape and finally extend the procedure for the synthesis of bimetallic nanoparticles.

Gold nanoparticles having prechosen size ranging from 5 to 110 nm have been prepared in two steps. First, small spherical particles (seed) of average diameters between 5 and 20 nm were prepared by varying the ratio of gold ion concentration to reductant, TX-100 concentration and using UV-irradiation. Second, 20–110 nm particles were formed by seed-mediated growth in such a way that the total amount of gold remains constant, whereas gradually [Au(III)]/[seed] ratio was varied from 2 to 100 (Table 1). Successive size development/growth has been done taking the particles from the previous step as seeds. For the set A 5 ± 2 nm particles act as seeds and the seeds grow to form 31 ± 3 nm particles. For set B the set A particles (~31 nm) act as seeds and the growth occurs to form 51 ± 7 nm particles. In this way sets C and D particles are formed from sets B and C, respectively. The fresh Au(III) ions were reduced onto the surface of the seed particles by ascorbic acid. Ascorbate ion could not produce gold nanoparticles from Au(III) ions in TX-100 medium. But when a small amount of seed particles were added to Au(III) ion, it immediately started forming gold particles by particle catalyzed reduction of Au(III) ions. The size of the particle was calculated using the following equation [37]:

$$d_{\text{final}} = d_{\text{seed}} \left\{ \frac{[\text{Au(0)}] + [\text{Au(III)}]}{[\text{Au(0)}]} \right\}^{1/3} \quad (1)$$

where d stands for diameter of the particle. The calculated sizes for sets A, B, C and D are 33, 50, 72 and 107 nm, respectively, which agree well with the obtained sizes 31 ± 3, 51 ± 7, 82 ± 9 and 112 ± 17 nm. Set D contained not only spherical particles but also a significant amount (10%) of rods and triangles. The result suggests ascorbic acid reduces only the surface adsorbed Au(III) ions creating hardly any nucleation centers by autocatalytic growth [38].

The growth kinetics of the reaction followed an autocatalytic behavior for the 51 ± 7, 82 ± 9 and 112 ± 17 nm particles. Figure 1(a) shows there is a fall in rate constant which is determined from the particle size A to D (Table 1) and slope of the $\ln A_t/(A_\alpha - A_t)$ versus time plot (here A_t stands for absorbance at any time t and A_α that for time $t \to \alpha$). A first-order kinetics was observed for the particle evolution. The kinetics of particle development was followed at $\lambda = 532$ nm at 28 ± 1 °C. UV–vis spectroscopy was performed using 1 cm quartz cuvette with Shimadzu UV-160 (Kyoto, Japan) spectrophotometer. The increase in particle size was revealed by gradual shifts of UV–vis spectra toward the red region shown in Figure 1(b). The red shift of the plasmon absorbance with particle size can be explained according to Mie theory. For large particles ($2R > 25$ nm) the plasmon bandwidth increases with increasing size as the wavelength of the interacting light becomes comparable to the dimension of the nanoparticle. This leads to an inhomogeneous polarization of the nanoparticle by the electromagnetic field. In this extrinsic size region the peak position shifts to longer wavelengths

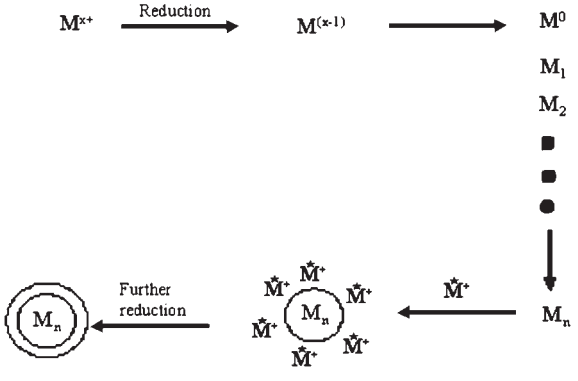

Scheme 1. Schematic representation of seed-mediated growth of the particles. (Reprinted from Ref. [35], © 2001, with permission from American Chemical Society.)

Table 1. Conditions for the growth of gold nanoparticles via seed (S)-mediated method.

Sample set	$[M^0]/[M^+]$	$[M^0]+[M^+]$	Ascorbic acid (M)	Particle size (nm) and standard deviation
A (from S)	1:2	5×10^{-4}	6×10^{-4}	31 ± 3
B (from A)	1:9	5×10^{-4}	6×10^{-4}	51 ± 7
C (from B)	1:29	5×10^{-4}	6×10^{-4}	82 ± 9
D (from C)	1:100	5×10^{-4}	6×10^{-4}	112 ± 17

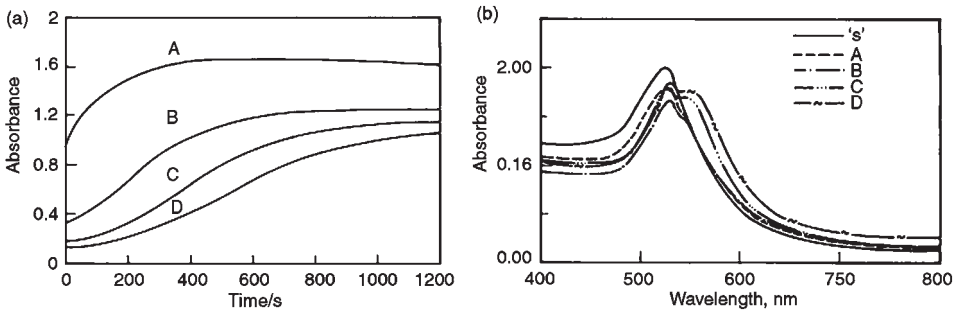

Figure 1. (a) Kinetics of Au nanoparticle development by seed mediation. (b) UV–vis spectra of Au nanoparticles grown via non-iterative seed mediation. Conditions: $S = 5 \times 10^{-4}$ M Au(III) ions; and [Au(III)]/[Au(0)] = 2 (for A), 9 (for B), 29 (for C) and 100 (for D). Total gold concentration was 5×10^{-4} M in all cases. [TX-100] = 1×10^{-2} M and [ascorbic acid] = 6×10^{-4} M. (Reprinted from Ref. [24], © 2001, with permission from Springer.)

Table 2. Conditions for preparation of cubic copper nanoparticles via seed (S)-mediated method.

Sample set	$[M^0]/[M^+]$	$[M^0]+[M^+]$	Ascorbic acid (M)	Particle size (nm) and standard deviation
A (from S)	1:99	2×10^{-4}	4×10^{-4}	100 ± 5 and 125 ± 5
B (from A)	1:8935	2×10^{-4}	4×10^{-4}	130 ± 5 and 155 ± 5
C (from B)	1:806360	2×10^{-4}	4×10^{-4}	~75–250

or correspondingly to lower energies [39]. In Figure 1(b) all the particles are above 25 nm and for them the peak becomes broader and red shift occurs with increase in particle size which follows Mie theory. The red shift is due to increase in particle size rather than aggregation.

Among all the three coinage metals it is very difficult to control size and shape of copper nanoparticles because of their highest reactivity. Exploiting the seed-mediated method we have successfully obtained cubic copper nanoparticles in the size range 75–250 nm [36], whereas under identical condition silver, gold and palladium systems form mostly spherical and hexagonal particles. At first copper sulfate ($CuSO_4$) solution (2×10^{-4} M) was reduced by sodium borohydride (0.1 M) to produce the seed particles. TEM figure showed that half of the population of the particles is of 4–6 nm and the rest are 9–12 nm. Then required amount of seed particles was mixed with the $CuSO_4$ solution and finally ascorbic acid was added drop by drop to reduce the adsorbed Cu(II) on the Cu seed particles. The whole experiment was carried out in N_2 atmosphere. The plasmon peak shifts to longer wavelength with the increase in particle size. Table 2 shows the copper particles having size range ~75–250 nm were produced by varying the ratio of copper particle to the added copper(II) ion concentration. The larger size regular shaped particle formation is an indication of slow reduction of copper ions onto the particle surfaces (Figure 2). The seed particles grow to give two different batches of particles in the sizes 100 ± 25 nm (25%) and 125 ± 5 nm (75%) particles for set A. For set B two different batches of particles in the sizes 130 ± 5 nm (22%) and 155 ± 5 nm (78%) are formed. In set C where the ratio of copper ion to copper particle concentration is reasonably high, wide range of particles are formed. The small metal particles generally act as electron relay system for electron transfer

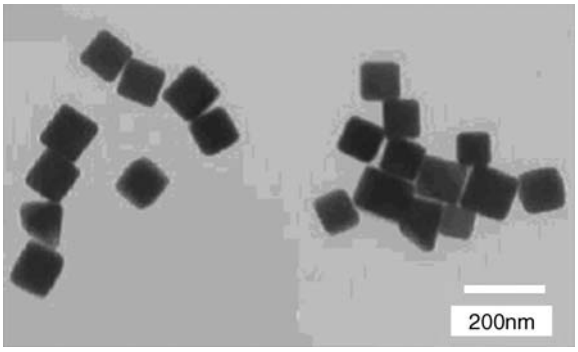

Figure 2. Transmission electron micrographs of the copper nanocube from the spherical seed particles. Conditions: total copper concentration 2×10^{-4} M and $[M^0]/[M^+] = 1{:}99$. (Reprinted from Ref. [30], © 1998, with permission from Current Science Association.)

from donor to acceptor. As a result, reduction of copper ion occurs at the surface of the seed particles. The chance of formation of new nucleation center is very rare because of weak reducing character of the ascorbate ion.

We have extended the seed-mediated technique for the synthesis of bimetallic nanoparticles, having 'core–shell' type structure appending photoreduction of metal ions. It has been proved that the deposition of a less noble metal (M) as 'shell' on a preformed nobler nanoparticle 'core' (M*) seems to be very effective by UV activation. Using this seed-mediated method we were able to synthesize Au_{core}–Ag_{shell} particles. First for the preparation of gold seeds (S), TX-100 (10^{-2} M) and $HAuCl_4$ (5.0×10^{-3} M) were taken in a quartz cuvette so that the final concentration of Au(III) ion remained 5.0×10^{-4} M. Then the

cuvette was placed directly under the UV light source of wavelength ~365 nm. After 20 min irradiation, the solution turned pink and showed a plasmon absorption band with a peak position at ~523 nm indicating the formation of gold particles. TEM image shows the particle diameter lies within ~20 nm. Final concentrations of metal sol and silver ion were adjusted to 1.67×10^{-4} and 3.33×10^{-4} M, respectively, in TX-100 medium. The overall metal concentration in this mixture, i.e. $[Au(0)] + [AgNO_3]$, was 5.0×10^{-4} M. Next the solution was taken in a quartz cuvette and placed directly under UV light source. After prolonged irradiation, the plasmon absorption band fixed and showed a peak at ~435 nm. TEM images reflect the enlargement of the particles (~50 nm) than the size of the seeds indicating the formation of silver layer on gold seeds, i.e. Au_{core}–Ag_{shell} structure formation. For another layer of silver on Au_{core}–Ag_{shell}, the final concentrations of metal sol and silver ion were adjusted to 5×10^{-5} and 4.5×10^{-4} M, respectively, in the TX-100 medium. Overall metal concentration in this mixture was 5.0×10^{-4} M. The TEM images after UV-irradiation reflect further increase of size by another layer of photoproduced silver on Au_{core}–Ag_{shell} and the particle size increases from ~50 to ~100 nm. This was also revealed from the successive red shifted (peaks changing from 438 to 450 nm) UV–vis spectra.

Both gold and silver have rich plasmon absorption band and thus the growth process of shell over the core was easily monitored from the UV–vis spectra. In case of Au_{core}–Ag_{shell} irradiation of a mixture of gold seed and Ag(I) after 10 min, the pink colored solution turned brown and the plasmon absorption peak shifted from 523 to 450 nm (Figure 3, A1). After irradiation for another 15 min, the absorption peak position shifted to 440 nm (Figure 3, A2) and after prolonged irradiation resulted in an absorption band with λ_{max} fixed at 435 nm (Figure 3, A3) and a golden brown appearance of the solution was

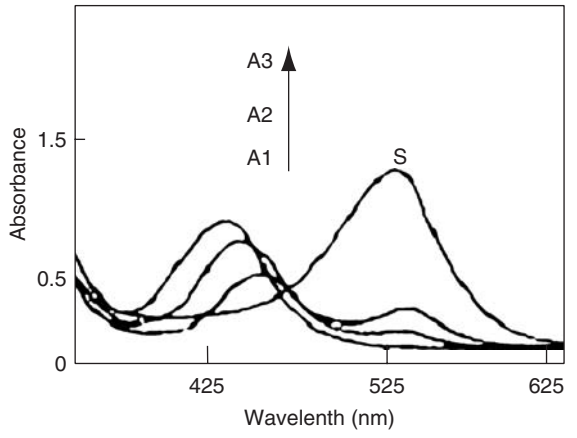

Figure 3. Absorption spectra of Au seed particles (S), UV-irradiation of the mixture of $[Au(0)] + [AgNO_3]$: (A1) after 10 min, (A2) after 15 min and (A3) after prolonged time. Condition: for gold seed TX-100 (10^{-2} M) and $HAuCl_4$ (5.0×10^{-3} M), of which the final concentration of Au(III) ion remains 5.0×10^{-4} M. For A1 and A2, $[Au] = 1.67 \times 10^{-4}$ and $[AgNO_3] = 3.33 \times 10^{-4}$ M. (Reprinted from Ref. [35], © 2001, with permission from American Chemical Society.)

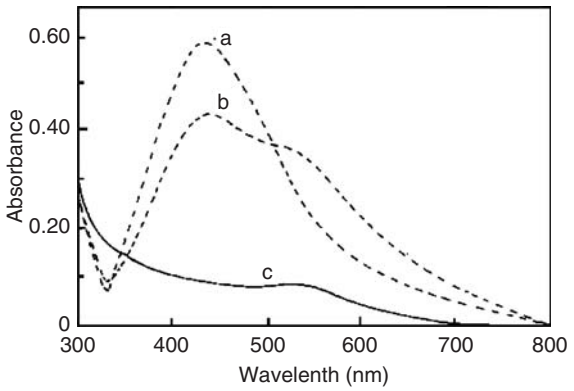

Figure 4. UV–vis spectra of (a) gold seed (S), (b) partially covered gold seed and (c) core–shell structure in TX-100 (10^{-2} M) medium. Conditions: (a) [gold seed] = 1.25×10^{-5} M; (b) [gold seed] = 1.25×10^{-5} M and $[AgNO_3] = 2.5 \times 10^{-4}$ M, irradiation time 2 min; (c) [gold seed] = 1.25×10^{-5} M and $[AgNO_3] = 2.5 \times 10^{-4}$ M, irradiation time 10 min. (Reprinted from Ref. [35], © 2001, with permission from American Chemical Society.)

an indication of the formation of silver particles on the gold seeds, i.e. Au_{core}–Ag_{shell}. On UV-irradiation of a mixture of gold seed and Ag(I) for longer time or increasing the UV light flux, the plasmon peak shifted toward the blue region. The blue shift has been attributed to the progressive covering of Au particle by silver layers. Due to the Ag covered Au, the plasmon band was Ag dominated.

With the higher amounts of Ag(I) ion (10–100 times excess), gold seed particles were covered with Ag layers after 10 min of photoactivation (Figure 4(c)). The peak position remained at ~435 nm region. But after 2 min of irradiation the gold seeds are partially covered and showed a double-hump absorption band (Figure 4(b)). Further confirmation of the core–shell (Au_{core}–Ag_{shell}) structure was authenticated from the well-known cyanide dissolution of the Ag layers under ambient condition [40]. For core–shell structure cyanide dissolves successive silver layers only in the first stage of dissolution. However, both the plasmon peaks due to the mixture of gold and silver in solution are diminished simultaneously for a mixture containing both the metals.

3. Results

The metal clusters are formed as transient intermediates during the formation of metal colloids by the reduction of metal ions in solutions. This growth process is similar to the autocatalytic seed-mediated process of particle enlargement. At the initial stage of colloid formation, the metal atoms are formed, which subsequently agglomerate [8,31,38,41,42]. Henglein et al. considered these particles as growing microelectrodes (GME). The progressive decrease in size of metal particles having a diameter in the nanometer regime is accompanied by an increase in Fermi potential. Thus, a stepwise lowering in the redox potential value takes place. The redox potential of the particle for a particular metal depends on the value of agglomeration

number, n, and the nature of associated ligand [31,41]. Exploitation of the growing metal nanoparticles in catalysis has already brought a revolution in chemistry. Spiro and coworkers suggested catalysis proceeds through an electrochemical mechanism where electron transfer occurs via the metal nanoparticles [43,44]. The catalytic efficiency of such particles for electron transfer processes is generally explained by their size-dependent redox properties which control their role as an electron relay. The required potential of the particle is intermediate between that of the electron donor and the acceptor. Keeping this idea in mind, the activities of GME and fully grown microelectrodes (FGME) in catalysis have been studied [28–30,45,46].

Growing small particles of silver have been observed to be more efficient catalysts than stable and larger colloidal particles. It has been observed that the growing particles catalyze the borohydride assisted reduction of several organic dyes like methylene blue (MB), phenosafranin (PS), fluorescein (F), 2,7-dichlorofluorescein (DCF), eosin (E) and Rose Bengal (RB) [28]. The rate of the reduction, catalyzed by growing particles, is distinctly faster compared to that of stable and larger silver particles, which are the final products of growing particles. To study the growing silver particle (GME) catalyzed dye reduction, dye was added to aqueous surfactant solution of metal salt before the addition of reducing agent. In case of FGME, the particles were produced in the first step and then were used for dye reduction. The dye was added to aqueous solution of preformed particles. Figure 5 shows a representative but successive dye reduction in the presence of $AgNO_3$ and $NaBH_4$ in aqueous CTAB media. The color of the dye gradually vanishes, which is indicated by the gradual decrease in absorbance value at the dye λ_{max}. But in the 350–500 nm region, absorbance gradually increases which ultimately gives a peak at ~400 nm due to the evolution of silver. The catalytic amount of metallic nanoparticles becomes effective to bring out the changes, i.e. the reduction. However, we have exploited large excess of catalyst particles only to take note of the dye degradation and successive evolution of plasmon absorption peak. Under this condition UV–vis spectrophotometry becomes routinely very useful to monitor the progress of the catalytic reduction involving different dye reductions in aqueous medium.

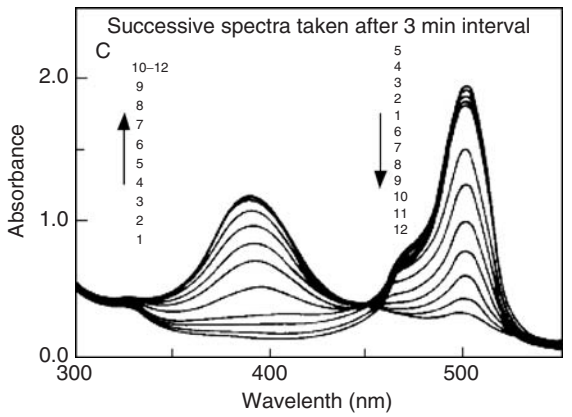

Figure 5. Successive UV–vis spectra of silver particle evolution and fluorescein (F) reduction in aqueous CTAB solutions containing $[AgNO_3] = 10^{-4}$ M, $[CTAB] = 0.01$ M, $[NaBH_4] = 5 \times 10^{-3}$ M and $[F] = 5 \times 10^{-5}$ M. (Reprinted from Ref. [28], © 1999, with permission from American Chemical Society.)

The growing silver particle plays the role of a true redox catalyst. To explain the rate of catalysis, we propose the electron transfer process via the growing particles, similar to (stable) colloid particle catalyzed redox reactions [47,48]. Earlier work shows that the reduction potential of a silver wire decreases with the increase in BH_4^- concentration in water due to the adsorption of BH_4^- ion onto the electrode surface [49]. A similar effect is also expected in silver particles. However, the potential of growing particles containing BH_4^- adsorbed on their surface will gradually increase with the increasing size of the particle unlike that for stable particles. The resultant potential of the particles with adsorbed BH_4^- will obviously be anodic to the reductant (BH_4^- ion) and cathodic to the oxidant (dye). Thus, an electron relay via particle to dye is possible. Scheme 2 shows the schematic representation of this electron transfer, where the growing particle in its intermediate stage accepts electrons from BH_4^- ions and transfers them to the dye.

In most cases growing silver particles are found to be superior catalysts as compared to the stable particles. This behavior of growing particles may be attributed to the following two properties: first, its continuously renewable surface and second, its large negative electrochemical potential which arises owing to the very small size. As usual, the rate of catalytic reduction should be determined by the difference in potential of the BH_4^- adsorbed particle and the potential of the oxidant system. The smaller the size of the particle, the more is the potential difference leading to a higher rate of reduction [3].

Similar observation was recorded for the GME and FGME catalyzed reduction of 4-nitrophenol (4NP) [46]. The GME and FGME nanoparticles are prepared in the

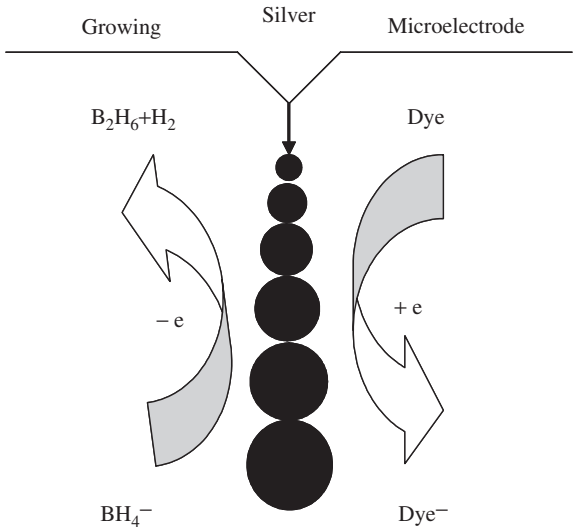

Scheme 2. Scheme for growing silver catalyzed redox reaction. (Reprinted from Ref. [28], © 1999, with permission from American Chemical Society.)

same way as has been described previously in case of dye reduction.

4. A Case History

As a specific case history nitrophenol reduction in aqueous solution by both GME and FGME has been demonstrated here. The FGMEs (0.1 mL, $\sim 10^{-4}$ M) were added into aqueous solution of 4NP ($\sim 10^{-5}$ M, 1.6 mL) taken in a quartz cuvette of 1 cm path length. Finally, aqueous $NaBH_4$ ($\sim$0.3 mL, 1.0×10^{-1} M) was introduced and time-dependent spectra were recorded. The rate of the reaction decreases slowly and followed a first-order kinetics without any induction time, IT (Figure 6(a)). In $NaBH_4$ medium (pH > 12.0) 4NP (λ_{max}~377 nm) is converted to 4-nitrophenolate ion which shows absorption peak at $\lambda_{max} \sim 400$ nm [46,50,51]. On the other hand, in GME catalyzed reaction, the reaction mixture was prepared from 4NP and $NaBH_4$. With the introduction of $AgNO_3$ (5×10^{-6} M), the reduction starts with an IT and then the rate increases slowly to a maximum value which then follows zero-order kinetics shown in Figure 6(b). As the reaction was over involving GME, the peak at 400 nm vanished and a new peak in the blue region appeared due to the corresponding amino compound ($\lambda_{max} \sim 290$ nm) shown in Figure 6(a).

The reaction was studied for all coinage metal nanoparticles. In the case of GMEs the rate follows zero-order kinetics with IT for all the coinage metal cases. The observed IT for the Cu catalyzed reaction was maximum but its rate of reduction was found to be minimum. Just the reverse was the case for Au and an intermediate value was obtained for the Ag catalyzed reaction (Figure 7). The adsorption of substrates is driven by chemical interaction between the particle surface and the substrates. Here phenolate ions get adsorbed onto the particle surface when present in the aqueous medium. This caused a blue shift of the plasmon band. A strong nucleophile such as $NaBH_4$, because of its diffusive nature and high electron injection capability, transfers electrons to the substrate via metal particles. This helps to overcome the kinetic barrier of the reaction.

5. Conclusions

In conclusion, we can say that the synthesis of metal nanoparticles and tuning of their sizes is achievable through 'seed-mediated' synthetic route. Again, this method helped us to obtain shape selective evolution of

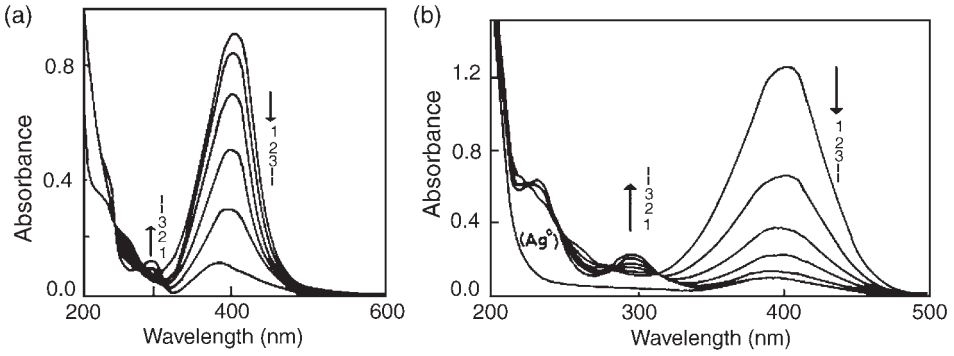

Figure 6. Successive UV–vis spectra (1 min time interval) of 4-nitrophenol using (a) GME and (b) FGME of silver colloids. (Reprinted from Ref. [46], © 2001, with permission from American Chemical Society.)

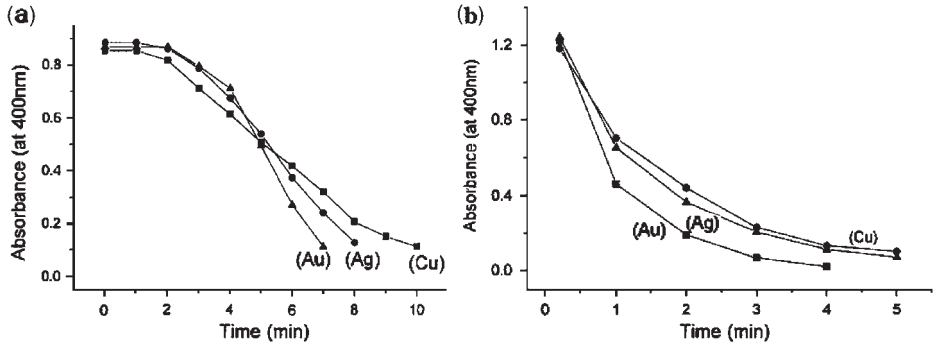

Figure 7. Absorbance versus time plot of reduction of 4-nitrophenol (4NP) using Cu, Ag and Au colloids: (a) GMEs and (b) FGMEs. Conditions: (a) [Cu] = [Ag] = [Au] = 1.0×10^{-6} mol dm^{-3}, [4NP] = 4.0×10^{-5} M, [$NaBH_4$] = 1.0×10^{-2} M; (b) [Cu] = [Ag] = [Au] = 5.0×10^{-6} M, [4NP] = 6.0×10^{-5} M, [$NaBH_4$] = 3.0×10^{-2} M. The time of addition of 4NP to the reaction mixture is 15 min. (Reprinted from Ref. [46], © 2001, with permission from American Chemical Society.)

particles. As a fundamental aspect we have underlined the Fermi potential shift for metal nanoparticles with size and nucleophile induced cases. Thus, exploitation of metal nanoparticles in catalysis for many important reactions has been possible using GME and FGME metal particles. However, real size-dependent properties are still to be accounted for. This particular field is presently expanding dramatically, and it is anticipated that these key challenges will be met in the near future in the confluence of laboratory and industry. It might so happen one day that only one metal would be thought of to perform innumerable redox reactions because of the size- and shape-dependent redox potential values of that particular metal.

References

1 R. G. Freeman, K. C. Grabar, K. J. Allison, R. M. Bright, J. A. Davis, A. P. Guthrie, M. B. Hommer, M. A. Jackson, P. C. Smith, D. J. Walter, M. J. Natan, *Science* 267 (1995) 1629.
2 S. Praharaj, S. K. Ghosh, S. Nath, S. Kundu, S. Panigrahi, S. Basu, T. Pal, *J. Phys. Chem. B* 109 (2005) 13166.
3 R. Elghanian, J. J. Storhoff, R. C. Mucic, R. L. Letsinger, C. A. Mirkin, *Science* 277 (1997) 1078.
4 T. K. Sau, A. Pal, T. Pal, *J. Phys. Chem. B* 105 (2001) 9266.
5 M. Faraday, *Philos. Trans. R. Soc. Lond.* 147 (1857) 145.
6 K. K. Caswell, C. M. Bender, C. J. Murphy, *Nano Lett.* 3 (2003) 667.
7 S. Nath, S. K. Ghosh, S. Panigrahi, T. Pal, *Ind. J. Chem. A* 43A (2004) 1147.
8 A. Henglein, *J. Phys. Chem.* 97 (1993) 5457.
9 S. Kundu, A. Pal, S. K. Ghosh, S. Nath, S. Panigrahi, S. Praharaj, T. Pal, *Inorg. Chem.* 43 (2004) 5489.
10 S. Panigrahi, S. Kundu, S. K. Ghosh, S. Nath, T. Pal, *J. Nanopart. Res.* 6 (2004) 411.
11 U. Kreibig, M. Vollmer, *Optical Properties of Metal Clusters*, Springer, Berlin, 1995, 15.
12 J. Turkevitch, P. C. Stevenson, J. Hillier, *Discuss. Faraday Soc.* 11 (1951) 55.
13 G. Frens, *Nat.: Phys. Sci.* 241 (1973) 20.
14 H. Hirachi, Y. Nakao, N. Toshima, K. Adachi, *Chem. Lett.* (1976) 905.
15 H. Hirachi, Y. Nakao, N. Toshima, *Chem. Lett.* (1978) 545.
16 R. Narayanan, M. A. El-Sayed, *J. Phys. Chem. B* 108 (2004) 8572.
17 N. R. Jana, L. Gearheart, C. J. Murphy, *Chem. Commun.* (2001) 617.
18 S. H. Chen, Z. Y. Fan, D. L. Carroll, *J. Phys. Chem. B* 106 (2002) 10777.
19 R. Jin, C. Cao, E. Hao, G. S. Metraux, G. C. Schatz, C. A. Mirkin, *Nature* 42 (2003) 487.
20 M. Maillard, P. Huang, L. Brus, *Nano Lett.* 3 (2003) 1611.
21 L. Francois, M. Mostafavi, J. Belloni, *J. Phys. Chem. B* 104 (2000) 6133.
22 M. Mandal, S. K. Ghosh, K. Esumi, T. Pal, *Langmuir* 18 (2002) 7792.
23 N. R. Jana, L. Gearheart, C. J. Murphy, *Chem. Mater.* 13 (2001) 2313.
24 T. K. Sau, A. Pal, N. R. Jana, Z. L. Wang, T. Pal, *J. Nanopart. Res.* 3 (2001) 257.
25 S. Meltzer, R. Resch, B. E. Koel, M. E. Thompson, A. Madhukar, A. A. G Requicha, P. Will, *Langmuir* 17 (2001) 1713.
26 G. Carrot, J. C. Valmalette, C. J. G. Plummer, S. M. Scholz, J. Dutta, H. Hofmann, J. G. Hilborn, *Colloid Polym. Sci.* 276 (1998) 853.
27 B. D. Busbee, S. O. Obare, C. J. Murphy, *Adv. Mater.* 15 (2003) 414.
28 N. R. Jana, T. K. Sau, T. Pal, *J. Phys. Chem. B* 103 (1999) 115.
29 N. R. Jana, Z. L. Wang, T. Pal, *Langmuir* 16 (2000) 2457.
30 N. R. Jana, T. Pal, *Curr. Sci.* 75 (1998) 145.
31 A. Henglein, *Chem. Rev.* 89 (1989) 1861.
32 A. Henglein, *Langmuir* 15 (1999) 6738.
33 A. Henglein, D. Meisel, *Langmuir* 14 (1998) 7392.
34 K. R. Brown, M. J. Natan, *Langmuir* 14 (1998) 726.
35 K. Mallick, M. Mandal, N. Pradhan, T. Pal, *Nano Lett.* 1 (2001) 319.
36 N. Jana, Z. L. Wang, T. K. Sau, T. Pal, *Curr. Sci.* 79 (2000) 1367.
37 G. Schmid, *Chem. Rev.* 92 (1992) 1709.
38 J. D. Aiken III, R. G. Finke, *J. Am. Chem. Soc.* 120 (1998) 9545.
39 S. Link, M. A. El-Sayed, *J. Phys. Chem. B* 103 (1999) 4212.
40 T. Pal, A. Ganguly, D. Maity, *Anal. Chem.* 58 (1986) 564.
41 M. Mostafavi, J. L. Marignier, J. Amblard, J. Belloni, *Radiat. Phys. Chem.* 34 (1989) 605.
42 J. Belloni, *Curr. Opin. Colloid Interface Sci.* 1 (1996) 184.
43 (a) M. Spiro, *J. Chem. Soc., Faraday Trans. 1* 75 (1979) 1507; (b) M. Spiro, P. L. Freund, *J. Chem. Soc., Faraday Trans. 1* 79 (1983) 1649; (c) P. L. Freund, M. Spiro, *J. Phys. Chem.* 89 (1985) 1074; (d) P. L. Freund, M. Spiro, *J. Chem. Soc., Faraday Trans. 1* 82 (1986) 2277.
44 D. S. Miller, A. J. Bard, G. McLendon, J. Ferguson, *J. Am. Chem. Soc.* 103 (1981) 5336.
45 N. R. Jana, T. Pal, *Langmuir* 15 (1999) 3458.
46 N. Pradhan, A. Pal, T. Pal, *Langmuir* 17 (2001) 1800.
47 K. George Thomas, J. Zajicek, P. V. Kamat, *Langmuir* 18 (2002) 3722.
48 J. Z. Zhang, *Acc. Chem. Res.* 30 (1997) 423.
49 P. J. Tarcha, J. Desaja-Gonzalez, S. Rodriguez-Llorente, R. Aroca, *Appl. Spectrosc.* 53 (1993) 43.
50 S. Praharaj, S. Nath, S. K. Ghosh, S. Kundu, T. Pal, *Langmuir* 20 (2004) 9889.
51 S. K. Ghosh, M. Mandal, S. Kundu, S. Nath, T. Pal, *Appl. Catal. A: Gen.* 268 (2004) 61.

This page intentionally left blank

CHAPTER 31

Metal Nanoparticles Dispersed in Solution: Tests to Identify the Catalyst Nature

Montserrat Gómez and Isabelle Favier

Laboratoire Hétérochimie Fondamentale et Appliquée, UMR CNRS 5069, Université Paul Sabatier, 118 route de Narbonne, 31062 Toulouse cedex 9, France

1. Introduction

Conventionally, the solubility condition has been used to classify "homogeneous" and "heterogeneous" catalysts. Then, in this context, the word "homogeneous" refers to the presence of catalyst and substrate in one or more phases, without taking into account the kind of the active catalytic sites. But from the point of view of the substrate, this can meet only one type of active site (homogeneous catalyst) or many (heterogeneous catalyst), as defined by Schwartz [1]. Hence, homogeneous catalytic species could be insoluble in the reaction medium or soluble nanoclusters can act as heterogeneous catalysts. The catalyst size has been also considered to distinguish both types of catalysts. In this way, Collman et al. proposed that metal particles greater than 80 Å behave as heterogeneous catalysts for the hydrogenation of polymeric substrates [2]. When metal nanoparticles (NPs) are involved, it is even more difficult to conclude about the catalyst nature, due to their state placed at the frontier between classical homogeneous and heterogeneous catalysts. As a result, terminologies like "hybrid homogeneous–heterogeneous catalyst" (proposed by Finke [3]) or "semi-heterogeneous catalyst" (proposed by Astruc [4]) are used. For NPs catalysts, it is important to differentiate between metal colloid and nanocluster. Schmid defines colloids as metal aggregates larger than 100 Å, while metal nanoclusters are considered as aggregates smaller than 100 Å [5].

In the present chapter, we focus on the catalyst nature in solution using well-defined metal NPs as catalytic precursors; it means, soluble (or dispersible) heterogeneous pre-catalysts, as stated by Finke [6]. Some experiments described in the literature concerning the distinction between homogeneous and heterogeneous catalysts are discussed (see Section 3), followed by a particular case studied by us with regard to the catalyst nature in the allylic alkylation reaction, using preformed palladium NPs as catalytic precursors (see Section 4).

2. Synthesis Strategy

In order to know the true nature of active catalytic species, several control experiments must be carried out to get coherent data. In this way, some authors have proposed strategies, each of them involving various tests.

In 1982, Laine reviewed simple chemical tests and application of some techniques to distinguish between homogeneous and heterogeneous catalysis. He proposed five criteria for detecting homogeneous cluster catalysts: (i) TOF increases when catalyst concentration increases; (ii) the reaction selectivity or the mechanism is different for cluster and mononuclear catalytic precursors; (iii) hetero-metallic clusters give different reactivity and/or selectivity than monometallic systems; (iv) conditions favouring metal-metal bond increase the catalytic activity; and (v) chiral metal clusters induce different asymmetric induction with respect to monometallic complexes [7].

At the same time, Crabtree suggested three experiments to prove the homogeneous nature of the catalyst and to exclude the colloidal character of the catalyst. First, a catalyst is homogeneous if the selectivity resembles to that of authentic homogeneous catalysts but differs from known heterogeneous catalysts; for example $[Ir(cod)(PCy_3)(py)]PF_6$ used as catalyst for the reduction of steroidal dienones reduces selectively the less hindered C=C bond of $\Delta^{1,4}$-androstanedione, like observed using Wilkinson catalyst, $[RhCl(PPh_3)_3]$, but not with any heterogeneous catalyst. Second, choosing a reaction only catalysed by metal colloids but not by homogeneous catalyst, like nitrobenzene hydrogenation catalysed by heterogeneous systems. Third, application of light-scattering technique to check the formation of NPs when a molecular complex is used as pre-catalyst [8].

In 2003, Finke [6a] and Dyson [9] have reviewed tests commonly used to evaluate the nature of the catalyst starting with metallic molecular pre-catalysts, in order to estimate the *in situ* formation of heterogeneous active catalysts, in particular for hydrogenation processes.

Metal Nanoclusters in Catalysis and Materials Science: The Issue of Size Control
Edited by B. Corain, G. Schmid and N. Toshima

Finke and co-workers have analysed different chemical tests to differentiate metal–complex homogeneous catalysis from metal–particle heterogeneous catalysis under reducing conditions, discussing their limitations. In view of that, they propose a general methodology to distinguish homogeneous from heterogeneous catalysts which comprises four aspects: (i) catalyst isolation and characterisation; (ii) kinetic studies (including catalytic reproducibility, reactivity of the different isolated metallic compounds and observation of induction periods); (iii) poison experiments, in particular mercury test and quantitative Lewis bases addition; and (iv) consistence of all the data previously indicated to can conclude about the homogeneity or heterogeneity of the catalyst [6a].

3. Results

This section deals with the most important control experiments to be considered when molecular complexes or NPs want to be proved as true catalysts. But in some cases both types of catalysts can be present in the same reaction. For example, in the ring opening polymerisation of 1,1,3,3-tetramethyl-1,3-disilacyclobutane catalysed photochemically by $Pt(acac)_2$, the co-existence of both homogeneous and colloidal catalytic species has been proved, giving each of them different type of polymers [10].

3.1. Characterisation Techniques

3.1.1. Transmission Electron Microscopy (TEM)

TEM is a direct analysis tool for knowing if metal clusters are present in catalytic solutions. This technique permits to define the size, structure, morphology and state of aggregation of the metal particles [11]. Hence, this technique can be in particular useful to identify nanoclusters in metal-catalysed reactions, using molecular complexes as catalytic precursors. But the catalytic activity of these observed nanoclusters must be further checked.

Accordingly, TEM investigations confirmed the NPs formation in Pt-catalysed hydrosilylation from a solution of $[PtCl_2(cod)]$. The particles formed *in situ* showed a mean size of 2.3 nm. Moreover, XPS (X-ray Photoemission Spectrometry) analysis confirmed that the colloid characteristics are distinct from bulk metal and monometallic complex (binding energy for Pt bulk metal is 71.0 eV; for $[PtCl_2(cod)]$, 72.45 eV; and for Pt colloid, 72.24 eV) [12].

TEM analysis has also confirmed the formation of Pd NPs (mean size: 1.6 nm) during the Heck coupling between styrene and bromobenzene using $[PdCl_2(PhCN)_2]$ as pre-catalyst. Before the induction period of the reaction, no colloids were detected, but after this induction time colloids were identified, related to the catalytic activity observed. The mechanism proposed is a rapid exchange between $[PdCl_2(PhCN)_2]$ and NaOAc to form $Pd(OAc)_2$, which under the catalytic conditions used, formation of Pd(0) colloids is favoured. When $Pd(OAc)_2$ was used as pre-catalyst for the Suzuki coupling between phenylboronic acid and 4-bromoacetophenone, TEM micrographs from the catalytic solution also showed the presence of small Pd NPs (mean size: 1.3 nm). Control experiments using preformed Pd NPs corroborated the catalytic activity associated to colloids [13].

Rh colloids were isolated during the hydrosilylation of trimethy(vinyl)silane with triethoxysilane using $RhCl_3$ in EtOH as pre-catalyst. The colour changes observed during the catalytic reaction (from yellow, to red and black) are due to the formation of colloids as demonstrated by TEM; this fact was in agreement with the catalytic activity behaviour observed [14].

But structural changes, metal atom rearrangements, cluster growth and even aggregation can happen under the influence of the electron beam during the TEM analysis [5a]. Thus, Manners and co-workers have observed the formation of Rh NPs under 75 kV electron beam from a sample containing a solution of $[Rh(1,5\text{-cod})(\mu\text{-Cl})]_2$ complex. This degradation can be prevented if samples are analysed by a lower energy electron beam (30 kV) [15]. More recently, Finke and co-workers have reported similar observations when $[Ru(\eta 5\text{-}C_5Me_5)Cl_2]_2$ or $[Ru_3(\mu_2\text{-}H)_3(\eta^6\text{-}C_6H_6)(\eta^6\text{-}C_6Me_6)(\mu_3\text{-}O)]BF_4$ were analysed by TEM. But in this case, TEM micrographs from grids prepared containing these complexes, even working under very mild conditions (40 kV and $-168\,^{\circ}C$), show the formation of Ru nanoclusters [16,17]. Consequently, just TEM results are not enough to conclude about the catalyst nature.

3.1.2. Dynamic Light Scattering

Dynamic light scattering experiment can be also used to detect the presence of colloidal particles in solution. Both scattered light and fluctuations in the amplitude of signals are analysed. An autocorrelation function characterises the particles with respect to their diffusion constant and therefore their size. The NPs size limit using this technique is higher than 1 nm [18]. Crabtree and co-workers reported for the first time in this context, the use of light scattering together with other control experiments, to exclude the formation of Ir colloids in alkane dehydrogenation processes homogeneously catalysed by $[Ir(H)_2(MeCO)(PPh_3)_2]BF_4$ [19].

3.1.3. NMR Spectroscopy

Parahydrogen induced polarisation (PHIP) is an effective tool extensively used for the investigation of homogeneous catalysed hydrogenation. The spin polarisation due to the break down of the high symmetry of the *p*-H_2 molecule, leads to a ^1H NMR signal enhancement of hydrogenated molecules, if the two transferred H atoms takes place simultaneously. In addition, heterogeneous catalysts are not expected to show this PHIP effect because the spin correlation is lost when the dihydrogen molecules interact with the metallic surface. It has been described that the colloidal Pd catalyst, $[Pd_x((N(octyl)Cl)_y]$, which catalyses the ethynylbenzene hydrogenation as well as the subsequent styrene hydrogenation, exhibits this PHIP

phenomenon, inferring that the hydrogenation process is homogeneously catalysed [20].

3.2. Kinetics Study

For a long time, one decisive factor to distinguish homogeneous from heterogeneous catalysis was the kinetics reproducibility, where homogeneous catalysis was thought to be kinetically reproducible and heterogeneous were not [7]. But reproducible kinetics does not exclude heterogeneous NPs catalysts, because $\pm 15\%$ kinetic reproducibility has been reported for soluble heterogeneous catalyst [3].

The formation of heterogeneous species (NPs or bulk metal) from homogeneous catalysts (molecular complexes) is not instantaneous, and then an induction period can be observed, if the heterogeneous catalyst formation is slow enough with respect to the catalysed organic process. In this case, the graph of substrate conversion versus time results in a sigmoidal-shaped kinetics curve: first, nucleation ($A \rightarrow B$) and second, autocatalytic surface growth ($A + B \rightarrow 2B$) [6]. Moreover, if the pre-catalyst decomposition and the catalytic process show the same induction period, this fact represents strong evidence for stating the presence of heterogeneous catalysts.

For example, when cyclohexene reduction using $(NBu_4)_5Na_3[Ir(1,5\text{-cod}) \cdot P_2W_{15}Nb_3O_{62}]$ as catalytic precursor was monitored, an induction period was detected corresponding to the formation of active species. Ir nanoclusters formed *in situ* were isolated from the reaction solution, characterised and reused as catalyst for the same organic process; in the latter case, no induction period was observed [3].

Benzene hydrogenation using $[NMe(C_8H_{17})_3][RhCl_4]$ as pre-catalyst under mono- or bi-phasic conditions was studied. Both colour changes of the solution and incubation period point to the formation of Rh nanoclusters stabilised by ammonium and chloride ions. These nanoclusters were isolated from the catalytic reaction, characterised and next used as catalysts; when recovered metallic species were used as catalyst, hydrogenation proceeded immediately. In this case, a black precipitate was formed during the reaction which was also catalytically active. The kinetic irreproducibility of the unfiltered component from the catalytic solution was superior at 100–200%, while for the soluble Rh(0) nanoclusters was less than 15%. Consequently, the authors suggest that this kinetic behaviour allow the distinction of soluble nanoclusters from agglomerated and bulk metal catalysts [21].

Laine and co-workers have studied the mechanism involved in rhodium-catalysed benzaldehyde hydrogenation, using $[Rh_6(CO)_{16}]$ as catalyst precursor. Following kinetic arguments, the authors proposed cluster catalysis with a limiting step corresponding to the break of metal–metal bond and/or isomerisation of the cluster formation [22].

For the amino–borane dehydrocoupling using $[Rh(1,5\text{-cod})(\mu\text{-Cl})]_2$ as starting catalyst, an induction period and a sigmoid-shaped kinetic curve (plot of substrate conversion versus time) were also observed, consistent with metal–particle formation. But, for $Ph_2PH \cdot BH_3$ dehydrocoupling, a nearly linear curve was obtained in agreement, together other control experiments, with a homogeneous catalytic behaviour [15].

3.3. Poison Experiments

3.3.1. Mercury Test

Mercury is a classical test to identify heterogeneous catalysts (bulk metal or colloids) due to its ability to poison metal(0) heterogeneous catalysts by formation of amalgam or adsorption on the metal surface [23]. If the catalytic activity remains unaffected when mercury is present, this fact represents an evidence for a homogeneous catalyst. But mercury can induce side reactions [23c] and also react with some molecular complexes [23c,24]. Consequently, the results obtained with mercury are not enough to conclude about the catalyst nature. From a practical point of view, it is important to use a large excess of Hg(0) with respect to the catalyst to favour the contact with it.

This test was successfully applied for the hydrosilylation of trimethyl(vinyl)silane by triethoxysilane catalysed by Rh or Pt colloids. The addition of mercury to catalytic mixture led to catalytic activity loss, consistent with a heterogeneous catalyst [12,14].

In cyclohexene hydrogenation, the Hg(0) test pointed to that the true catalyst involved in the catalytic process was heterogeneous, using either $(Bu_4N)_5Na_3[1,5\text{-cod})Ir \cdot P_2W_{15}Nb_3O_{62}]$ or Ir colloids (isolated from the solution) as catalytic precursors; in both cases Hg(0) stops the reaction [3]. For Pt-catalysed cyclohexene hydrogenation using $[PtCl_2(1,5\text{-cod})]$ as pre-catalyst, the production of cyclohexane is also halted by addition of Hg(0). Together with other control experiments, the authors prove that bulk metal and platinum NPs are the true catalysts [25]. Other Hg(0) tests for arene hydrogenations have been described, concluding that the catalyst nature is heterogeneous [6b,21,26].

For the Rh-catalysed amino–borane dehydrocoupling using $[Rh(1,5\text{-cod})(\mu\text{-Cl})]_2$ as catalytic precursor, the catalytic activity was completely suppressed by the addition of an excess of mercury. But for phosphino–borane, Hg(0) addition had no effect. Consequently, the authors proved that the catalyst nature depends on the substrate using the same catalytic precursor [15].

3.3.2. Lewis Bases Test

Quantitative tests using ligands (CS_2, PPh_3, thiols) as poisons represent an important tool to identify homogeneous catalysts. This kind of poisons can inhibit the catalytic activity of homogeneous molecular catalysts and also heterogeneous catalysts, mainly metal NPs, depending on the relative ratio ligand to metal. If less than 1 equivalent of ligand stops the catalysis, this result evidences the presence of a heterogeneous catalyst. Logically, for a heterogeneous catalyst, only a fraction of the total metal atoms are on the surface depending on the particle

size; therefore ligand/metal ratios smaller than 1 can completely poison the catalyst [6a].

Finke and co-workers carried out a quantitative catalyst poisoning experiment using CS_2 for hydrogenation of cyclohexene catalysed by both polyoxoanion- and tetrabutylammonium-stabilised Rh(0) nanoclusters and 5% Rh/Al_2O_3 heterogeneous catalysts. These studies led to determine the percentage of catalytically active metal atoms on the metallic surface [27]. 1,5-Phenanthroline and *N*-heterocyclic carbene have been also applied by Finke to identify the catalyst nature for benzene hydrogenation using $[Ru_3(\mu_2\text{-}H)_3(\eta^6\text{-}C_6H_6)(\eta^6\text{-}C_6Me_6)(\mu_3\text{-}O)]$ as catalytic precursor. These studies, together with other experiments mainly kinetics, evidenced that Ru nanoclusters and not molecular clusters are the true catalysts [17].

Manners and co-workers have studied the catalyst nature for the dehydrocoupling of amine–borane and phosphine–borane using $[Rh(1,5\text{-cod})(\mu\text{-Cl})]_2$ as pre-catalyst. Concerning the poison tests, when 0.5 equivalent of PPh_3 were added to $Me_2NH.BH_3$, a partial activity diminution was observed due to an incomplete surface coverage of the catalyst by PPh_3. In contrast, when $Ph_2PH \cdot BH_3$ was used as substrate, PPh_3 effect on activity was undetectable (neither using Hg as poison, see above), showing that the catalyst is heterogeneous for Me_2NH-BH_3 and homogeneous for Ph_2PH–BH_3 [15,28].

3.3.3. Diene Test

An elegant complementary test to mercury poison is the use of dienes as selective poisons for homogeneous catalysts, due to their strong coordination to metal centres yielding inert catalytic complexes. In addition, their interaction with metal surfaces is weak. If the presence of diene (diene:metal = 1:1) inhibits the catalytic process and Hg test does not, homogeneity can be strongly supported.

Crabtree found that dibenzo[a,e]cyclooctatretaene (dct) binds strongly with platinum group transition metals and it is stable under hydrogenation conditions, probably due to its sterically demanding structure. But dct binds weak with first-row transition metals. This poison was first tested for the hydrogenation of 1-hexene with various catalytic systems like $[RhCl_3(py)_3]/NaBH_4/DMF$, Pd colloid, Pd/C/hexane, $[Ir(cod)(PMePh_2)_2]PF_6$, and $[RhCl(PPh_3)_3]$ [29].

1,7-octadiene has been also used as poison for the homogeneous platinum ring-opening polymerisation catalysis of 1,1,3,3-tetramethyl-1,3-disilylcyclobutane [10]. In this case, the diene shows an inhibitory effect but not Hg(0).

3.4. Other Experiments

3.4.1. Polymer Test

According to Collman et al.'s work [2], the utilisation of polymer-bound substrates in hydrogenation processes can be used to distinguish homogeneous from heterogeneous metal NPs (particles bigger than 8 nm), because of the lack of mobility of the heterogeneous catalysts in and around the polymer matrix in contrast to the homogeneous ones; only truly soluble molecular catalysts are expected to diffuse readily into the polymer network and react easily with the attached functional groups. It is an elegant method to distinguish both types of catalysts because the reactivity observed is due to the active catalytic compounds without influence of the inactive species present in the catalytic mixture. Additional poisoning experiments were carried out by thiol functionalisation of polymers. Therefore, the incorporation of benzenethiol moieties in cross-linked polystyrene inhibited the polymer hydrogenation catalysed by $[RhCl(PPh)_3]$, pointing to a homogeneous catalyst.

In this way, Davies and co-workers proved that for monomeric organohalide carbonylation, the catalyst was homogeneous, although Pd/C was used as pre-catalyst. This fact was in addition supported by the catalytic activity observed with related polymeric halides [30].

3.4.2. Physical Separation of the Catalyst: Filtration and Centrifugation

When colloids are involved in catalysis, the separation of catalyst by means of solvent evaporation becomes inappropriate because the agglomeration of particles is then favoured [3]. "Soft" methods like filtration or centrifugation turn out to be more convenient.

Filtration of the catalytic mixture using pore membrane filters or filter aids allows the distinction between soluble and insoluble catalysts. Further catalytic activity analysis from the solution and insoluble residue can give information about the state of the real catalyst. In turn, centrifugation can be appropriated to separate metal NPs from the catalytic solutions, due to their high molecular weight and density, and thus to be separated from molecular species.

A first filtration test described in the literature corresponds to the use of pore membrane filter in the water gas shift reaction catalysed by $[Ru_3(CO)_{12}]$ complex. The catalytic reaction was filtered using a fluoropore filter of 0.5 μm pore size and the same rate of hydrogen production before and after filtration was observed [31]. For Rh-catalysed olefin hydrogenations and boranes dehydrocouplings, filtration tests have also been used to separate the catalysts [15,21]. These observations about filtration tests exclude bulk metal as heterogeneous catalyst, but not metallic NPs smaller than the pore size employed. Recently, recycling of gold colloids used as catalysts for 1,2-diols oxidation has been successfully achieved by means of membrane filtration (cellulose acetate for aqueous filtration or poly(dimethyl)siloxane membranes for organic solvents) [32].

Another filtration approach concerns the addition of a filter aid after reaction, like powered cellulose, celite or powdered graphite [6a]. The solution is filtered and the catalytic behaviour of both components, solution and filter aid, is then tested and compared with the catalytic behaviour before the filter aid addition. This methodology was first described by Maitlis and co-workers for distinguishing a heterogeneous component in a starting

homogeneously catalysed cyclohexene hydrogenation, using $[Rh_2(C_5Me_5)(OH)_3]Cl \cdot 4H_2O$ as a pre-catalyst [33].

TEM and XPS analysis of the solid recovered by centrifugation from the catalytic solution corresponding to Heck coupling reaction using $[RuCl_2(p\text{-cymene})]_2$ as pre-catalyst, showed the formation of Ru(0) NPs (2–3 nm). This fact, together with other control experiments, proved that the catalytic behaviour observed is due to the colloids formed *in situ* from the molecular starting material [34]. Centrifugation has also been applied to recycle TiN NPs used as catalyst for diphenylethyne reduction, allowing the solid separation, which was reused up to four times without alteration of its catalytic activity [35].

3.4.3. Model Catalytic Reactions

Hydrogenation of aromatic nitro compounds [8,18,29] and hydrogenation of benzene derivatives [2,9,21] have been generally accepted as model reactions to check the heterogeneous nature of catalyst, because homogeneous species are not believed to be active. But at least two well-studied examples show that molecular catalysts can hydrogenate benzene [36,37].

Hydrogenolysis of the C–O bond can represent another reaction model for verifying the heterogeneous identity of the catalysts, because this reaction has been only observed when metal surfaces are involved [38]. Therefore, Dupont and co-workers have proved that preformed iridium NPs catalyse acetophenone and anisole hydrogenation giving, in variable extension, the corresponding hydrogenated product together with that corresponding to C–O bond breaking, showing their heterogeneous nature [39].

Recently, Manners and co-workers have found another type of reaction, the inorganic process corresponding to Rh-catalysed dehydrocoupling of borane adducts, which is homogeneous or heterogeneous catalysed depending on the substrate, in particular the nature of the Lewis base, phosphine or amine respectively [15].

But not only the (in)activity can suggest the identity of the catalyst. Examples reported recently point to a distinction taking into account the selectivity behaviour.

Thus, $[W(CO)_3(CH_3CN)(TPPMS)_2]$ (TPPMS = PPh_2 (m-$C_6H_4SO_3Na$)) can behave as homogeneous (yellow colour solution) or heterogeneous (blue colour solution) catalyst depending on proton concentration, for bi-phasic alkenes hydrogenations. It is known that the relative hydrogenation rates for homogeneous systems follow the trend: mono-substituted alkenes > di-substituted alkenes > tri-substituted alkenes > tetra-substituted alkenes > aromatics and the inverse order is followed for heterogeneous catalysts [40]. The authors observed that the reaction was homogeneously catalysed at pH > 6 and heterogeneously catalysed at acidic pH [41].

Concerning enantioselective processes, Fujihara and Tamura have proved that palladium NPs containing (S)-BINAP (2,2′-bis(diphenylphosphino)-1,1′-binaphthyl) as chiral stabiliser, catalyse the hydrosilylation of styrene with trichlorosilane, obtaining (S)-1-phenylethanol as the major isomer (ee = 75%) [42]. In contrast, the palladium complex $[Pd(BINAP)(C_3H_5)]Cl$ is inactive for the same reaction [43].

Another more specific characteristic can allowed the differentiation between homogeneous and colloidal catalysts. In Pd-catalysed allylic alkylation *rac*-3-acetoxy-1,3-diphenyl-1-propene with dimethyl malonate, homogeneous and colloid species reacts at different rates with both substrate enantiomers, obtaining in the case of Pd colloids an excellent kinetic resolution (see Section 4) [44].

4. A Case History: Enantioselective Allylic Alkylation Catalysed by Pd Nanoparticles

As described above, the formation of heterogeneous catalysts from molecular precursors has been largely studied. But the reactivity of heterogeneous catalysts to give homogeneous catalysts has been less considered. In this line, it is known that bulk metals, under hydroformylation conditions, can form active complexes [45], and rhodium colloids employed in the Monsanto reaction lead to the formation of molecular ionic species, $[RhI_2(CO)_2]^-$ [46]. The studies concerning aromatic aminations and Kumada couplings, using nickel on charcoal as starting heterogeneous catalyst, have recently demonstrated that the true catalyst are soluble nickel species [47]. Additionally, in Pd-catalysed C–C coupling reactions [48], palladium NPs can act as a reservoir of molecular palladium species, as proposed by Dupont [49] and in agreement with the results obtained by de Vries using ligand-free palladium catalysts [50]. Concerning enantioselective processes, few examples are described in the literature involving NPs. Platinum and also palladium colloidal systems containing cinchonidine, have been found to display an interesting activity for the hydrogenation of ethyl pyruvate [51]. Also, palladium particles stabilised with the chiral diphosphine BINAP have proved to be the responsible of the asymmetric induction observed in styrene hydrosilylation [42].

Since Pd complexes are well-known catalysts for enantioselective allylic substitution reactions, here the catalytic behaviour of palladium NPs for this reaction is examined (Scheme 1). One example involving a chiral phosphite with a carbohydrate backbone, able to coordinate firmly at the surface of NPs together with oxygen atoms capable to interact weakly with this surface, is presented. In particular,

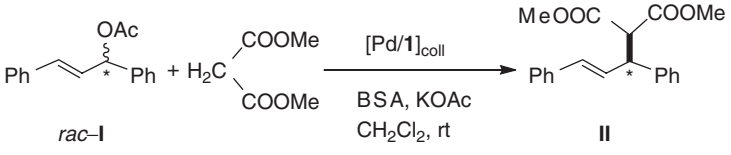

Scheme 1. Asymmetric allylic alkylation of *rac*-3-acetoxy-1,3-diphenyl-1-propene (*rac*-**I**) with dimethyl malonate catalysed by Pd/**1** colloidal system. (Reprinted from Reference [44], © 2004, with permission from American Chemical Society.)

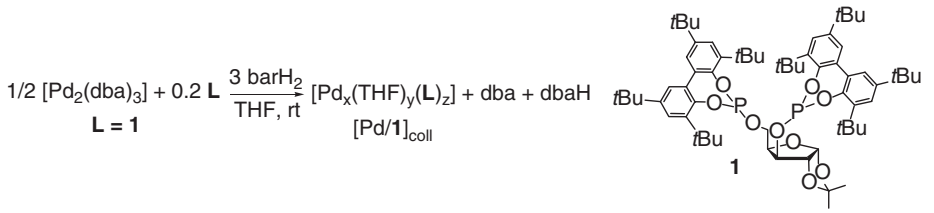

Scheme 2. Synthesis and TEM micrograph of Pd NPs containing ligand **1**, $[Pd/\mathbf{1}]_{coll}$. (Reprinted from Ref. [44], © 2004, with permission from American Chemical Society.)

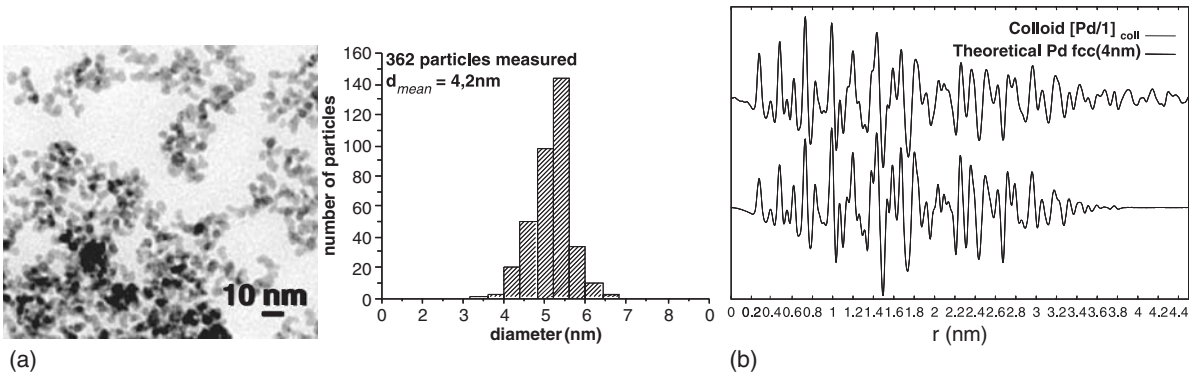

Figure 1. (a) TEM micrograph of $[Pd/\mathbf{1}]_{coll}$ with the size distribution diagram; (b) WAXS analysis, comparing the rdf of colloid $[Pd/\mathbf{1}]_{coll}$ with a theoretical rdf calculated for 4 nm fcc Pd NPs. (Reprinted from Ref. [44], © 2004, with permission from American Chemical Society.)

the catalytic behaviour corresponding to colloidal palladium/ligand **1** system (Scheme 2) [52], which has been successfully used for the formation of molecular Pd complexes involved in catalytic C–C coupling [53], is described.

Pd NPs were isolated as a black powder from $[Pd_2(dba)_3]$ under hydrogen pressure at room temperature in THF in the presence of **1** ($Pd/\mathbf{1} = 1/0.2$); by-products, dba and its hydrogenated products, were eliminated by pentane washings (Scheme 2). This methodology leads to reproducible synthesis and nearly monodisperse particles of small size [54].

Transmission electron microscopy for $[Pd/\mathbf{1}]_{coll}$ reveals the presence of small spherical but in some cases agglomerated particles of ca. 4 nm mean size, and wide angle X-ray scattering analyses evidence the fcc structure of bulk palladium [44] (Figure 1).

The reaction of *rac*-3-acetoxy-1,3-diphenyl-1-propene (*rac*-**I**) with dimethyl malonate under basic conditions [55] was studied using as catalyst either $[Pd/\mathbf{1}]_{coll}$ ($Pd/\mathbf{1}/\mathbf{I} = 1/1.05/100$) or a molecular complex, $[Pd/\mathbf{1}]_{mol}$ ($Pd/\mathbf{1}/\mathbf{I} = 1/1.25/100$), generated *in situ* by reaction of $[Pd(C_3H_5)Cl]_2$ and **1**, according to literature [56]. Both systems lead to the expected alkylated product. The enantiomeric excess found using the molecular catalyst is in agreement with the published data, while using the colloid catalyst the ee in (*S*)-**II** was slightly higher (90% for $[Pd/\mathbf{1}]_{mol}$ versus 97% for $[Pd/\mathbf{1}]_{coll}$). The reactions observed using the two catalytic systems however display some clear differences, the most striking ones being the absence of completion of the reaction associated to a high kinetic resolution (89% ee in the remaining substrate) when $[Pd/\mathbf{1}]_{coll}$ was used as catalyst [57]. Thus, only ca. 55% of product (**II**) was obtained after 24 h and this value did not change after 168 h. In contrast, quasi total conversion but no kinetic resolution of the substrate was observed after 1.5 h using $[Pd/\mathbf{1}]_{mol}$ as catalyst.

Since the reaction rates were found very different in the two catalytic systems, a direct comparison is not possible because the formation of small amounts of active molecular catalyst from the particles could not be excluded. In order to be able to rule out this possibility and more generally to characterise better the colloidal system, control experiments were carried out, founding all of them reproducible.

4.1. Monitoring Pd-Catalysed Allylic Alkylation

In order to achieve a true comparison between both catalytic systems, colloidal and molecular, which display very different reaction rates, a series of experiments were carried out with the homogeneous molecular system, decreasing the catalyst concentration in the studied allylic alkylation reaction. The reaction evolution is monitored taking samples at different reaction times and analysing each of them by ^1H NMR spectroscopy (to determine the conversion) and HPLC chromatography with chiral column (to determine the enantioselectivity of **I** and **II**). For molecular catalyst systems, the Pd/substrate ratio was varied between 1/100 and 1/10,000. For the latter ratio, the initial reaction rate was found comparable to that of the colloidal system (Figure 2a), but interestingly the conversion of the substrate is quasi complete after ca. 100 h in

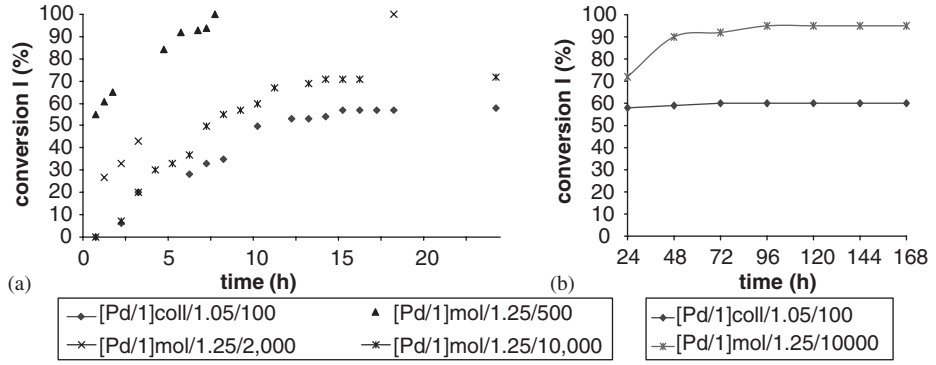

Figure 2. Plot of *rac*-**I** conversion versus time for colloidal and molecular catalytic systems. (a) Reactions monitored during 24 h for colloidal and molecular (Pd/**I** = 1/500, 1/2,000 and 1/10,000) catalysts. (b) Reactions monitored during one week for colloidal and molecular (Pd/**I** = 1/10,000) catalysts. (Reprinted from Ref. [44], © 2004, with permission from American Chemical Society.)

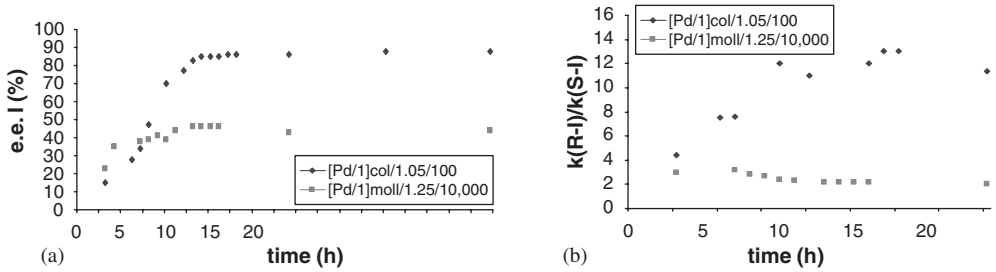

Figure 3. (a) Plot of enantiomeric excess corresponding to **I** versus time for colloidal and molecular (Pd/**I** = 1/10,000 catalysts). (b) Plot of $k((R)\text{–}\mathbf{I})/k((S)\text{–}\mathbf{I})$ versus time for colloidal and molecular (Pd/**I** = 1/10,000 catalysts). $k((R)\text{–}\mathbf{I})/k((S)\text{–}\mathbf{I}) = \ln[(1\text{–}C/100)(1\text{–}ee/100)]/\ln[(1\text{–}C/100)(1+ee/100)]$, C = conversion of *rac*-**I**; ee = enantiomeric excess of recovered **I**. (Reprinted from Ref. [44], © 2004, with permission from American Chemical Society.)

contrast to colloidal catalyst which remains at less than 60% conversion (Figure 2b).

For molecular catalytic systems, it is remarkable to note that the conversion at short times (< 5 h), increases with increasing Pd/substrate ratio. Actually, the nanoclusters formation seems to be less probable, in contrast to analogous experiments carried out for other Pd-catalysed reactions like C–C Heck couplings [58].

Concerning the enantioselectivity, the enantiomeric excess of the substrate remained limited and constant at ca. 40% for molecular catalyst when Pd/**I** ratio was 1/10,000; for less dilute systems, the ee was found lower (for Pd/**I** = 1/2,000, 27%; for Pd/**I** = 1/500, 0%). But the colloidal catalyst leads to ee of ca. 90% for **I** (Figure 3a). Plots of k((*R*)-**I**)/k((*S*)-**I**) [59] versus time calculated for both colloidal and molecular 1/10,000 catalysts (Figure 3b), revealed two different stable values, namely ca. 12 for the colloidal and 2 for the dilute molecular system (a similar value was obtained for molecular catalyst using a Pd/**I** ratio of 1/100,000).

4.2. Hg(0) and CS_2 Poison Tests [6a]

Both poisons were separately added to two catalysts, colloidal ($[Pd/\mathbf{1}]_{coll}/\mathbf{1}/rac\text{-}\mathbf{I}$ = 1/1.05/100) and molecular ($[Pd/\mathbf{1}]_{mol}/\mathbf{1}/rac\text{-}\mathbf{I}$ = 1/1.25/50) systems. Addition of mercury or CS_2 at the beginning of the reaction totally inhibits the allylic alkylation catalysed by colloids (entries 5 and 6 versus 4, Table 1), whereas it has little or no effect on the molecular ones (CS_2 slows down the reaction but no kinetic resolution was observed: entries 2 and 3 versus 1, Table 1). Addition of CS_2 after ca. 4 h of reaction stops the colloidal catalytic system (entry 9 versus 7, Table 1). However addition of mercury after the same reaction time has only a slowing effect (entry 8 versus 4, Table 1).

4.3. TEM Analysis

TEM analyses of the colloids do not evidence any significant change in the size and shape of the particles after seven days' catalytic reactions (Figure 4). No NPs were observed at long times of reaction (up to one week) starting with molecular catalysts.

4.4. Reuse of Colloidal Catalytic System

In order to verify if the colloidal catalytic system is still active after 24 h of reaction, several additions of the substrate *rac*-**I**, were done on the reaction catalytic mixture. The data are collected in Table 2. Up to the third run, further conversion of (*R*)-**I** enantiomer of the substrate towards (*S*)-**II** alkylated product and accumulation of

Table 1. Poison effects in activity and selectivity for the allylic alkylation reaction (Scheme 1), using $[Pd/\mathbf{1}]_{coll}$ and $[Pd/\mathbf{1}]_{mol}$ as catalysts.

Entry	Catalyst	Poison	Pd/**1**/poison	Time (h)	Conversion(%)[a]	ee **II**(%)[b]	ee **I** (%)[b]
1	$[Pd/\mathbf{1}]_{mol}$	–	1/1.25/0	1.5	95	87 (*S*)	nd
2[c]	$[Pd/\mathbf{1}]_{mol}$	Hg	1/1.25/100	1.5	97	97 (*S*)	nd
3[c]	$[Pd/\mathbf{1}]_{mol}$	CS_2	1/1.25/4	5	79	98 (*S*)	0
4	$[Pd/\mathbf{1}]_{coll}$	–	1/1.05/0	24	45	97 (*S*)	84 (*S*)
5[d]	$[Pd/\mathbf{1}]_{coll}$	Hg	1/1.05/100	24	0	–	0
6[d]	$[Pd/\mathbf{1}]_{coll}$	CS_2	1/1.05/0.3	20	0	–	0
7[d]	$[Pd/\mathbf{1}]_{coll}$	–	1/1.05/0	3.75	6	Nd	4 (*S*)
8[e]	$[Pd/\mathbf{1}]_{coll}$	Hg	1/1.05/100	24	33	98 (*S*)	84 (*S*)
9[e]	$[Pd/\mathbf{1}]_{coll}$	CS_2	1/1.05/0.3	24	11	98 (*S*)	10 (*S*)

[a]Determined by ^{1}H NMR.
[b]Determined by HPLC on a Chiralcel-OD column. Absolute configurations of **I** (S. R. Gilberston, P. Lan, *Org. Lett.* 3 (2001) 2237) and **II** (U. Leutenegger, G. Umbricht, C. Fahrni, P. V. Matt, A. Pfaltz, *Tetrahedron* 48 (1992) 2143) in parentheses.
[c]Catalytic reaction conditions: Molecular catalyst was generated from $[Pd(C_3H_5)Cl]_2$ (0.02 mmols) and **1** (0.05 mmols) in 2 cm^3 of CH_2Cl_2, stirring for 30 min at rt. *rac*-1,3-diphenyl-2-propenyl acetate (252 mg, 1 mmol), dissolved in 2 cm^3 of CH_2Cl_2, was added, followed by dimethyl malonate (396 mg, 3 mmols), BSA (610 mg, 3 mmols), and a catalytic amount of KOAc. The poison (Hg or CS_2) was then added.
[d]Catalytic reaction conditions: $[Pd/\mathbf{1}]_{coll}$ (ca. 2.35×10^{-2} mmols) and **1** (5.8×10^{-3} mmols) were dissolved in 2 cm^3 of CH_2Cl_2. *rac*-1,3-diphenyl-2-propenyl acetate (252 mg, 1 mmol), dissolved in 7 cm^3 of CH_2Cl_2, was added, followed by dimethyl malonate (396 mg, 3 mmols), BSA (610 mg, 3 mmols), and a catalytic amount of KOAc. The poison (Hg or CS_2) was then added.
[e]Catalytic conditions described in footnote d, but the poison (Hg or CS_2) was added after 3.75 h of reaction.

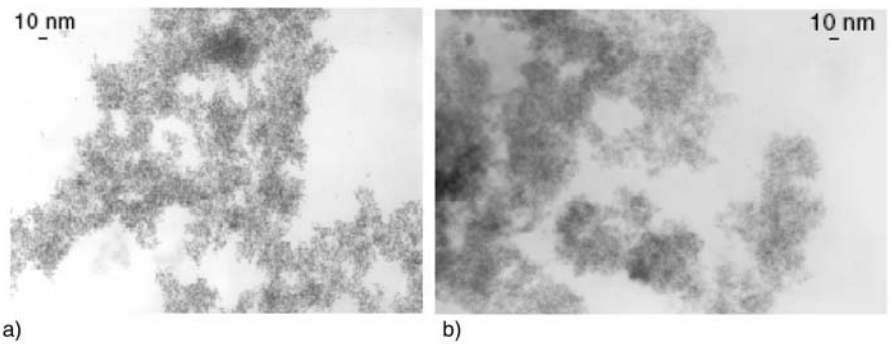

Figure 4. TEM micrographs of: (a) before catalysis; (b) after catalysis (seven days). (Reprinted from Ref. [44], © 2004, with permission from American Chemical Society.)

Table 2. Effect of substrate additions in activity and selectivity for the allylic alkylation reaction (Scheme 1), using $[Pd/\mathbf{1}]_{coll}$ as catalyst[a].

Run	Time (h)	Conversion (%)[b]	ee **II**(%)[c]	ee **I** (%)[c]
1	24	53	98 (*S*)	83 (*S*)
2	24 (total time: 48 h)	46	97 (*S*)	87 (*S*)
3	24 (total time: 72 h)	53	97 (*S*)	93 (*S*)

[a]Catalytic reaction conditions: $[Pd/\mathbf{1}]_{coll}$ (ca. 2.35×10^{-2} mmols) and **1** (5.8×10^{-3} mmols) was dissolved in 2 cm^3 of CH_2Cl_2. *rac*-1,3-diphenyl-2-propenyl acetate (252 mg, 1 mmol), dissolved in 7 cm^3 of CH_2Cl_2, was added, followed by dimethyl malonate (396 mg, 3 mmols), BSA (610 mg, 3 mmols), and a catalytic amount of KOAc. After each 24 h, 1 mmol of *rac*-**I** was added.
[b]Determined by ^{1}H NMR.
[c]Determined by HPLC on a Chiralcel-OD column. Absolute configurations of **I** (S. R. Gilberston, P. Lan, *Org. Lett.* 3 (2001) 2237) and **II** (U. Leutenegger, G. Umbricht, C. Fahrni, P. V. Matt, A. Pfaltz, *Tetrahedron* 48 (1992) 2143) in parentheses.

(*S*)-**I** was observed after each *rac*-**I** addition, without noticeable changes in activity and selectivity. After the fourth run, the catalyst loses its activity.

4.5. Enriched Substrate

Enriched **I** (more than 75% (*S*)-**I**) was used as substrate for Pd-catalysed allylic alkylation, using both colloidal $[Pd/\mathbf{1}]_{coll}$ and molecular $[Pd/\mathbf{1}]_{mol}$ catalysts. As observed in Scheme 3, the colloidal system reacts more slowly with (*S*)-**I** enantiomer: only 8% of (*R*)-**I** is present in the starting substrate, leading to a substrate conversion of ca. 10% with an ee of the remained substrate higher than 99% (*S*), in agreement with the relative rate calculated previously, $k((R)\text{-}\mathbf{I})/k((S)\text{-}\mathbf{I}) \approx 12$ (see above). This relative rate is actually smaller for the molecular catalyst (see above) and consequently a higher conversion was obtained in this case: 67% conversion is achieved after 30 h of reaction from a starting substrate constituted by 88.5(*R*)-**I** and 11.5(*S*)-**I**.

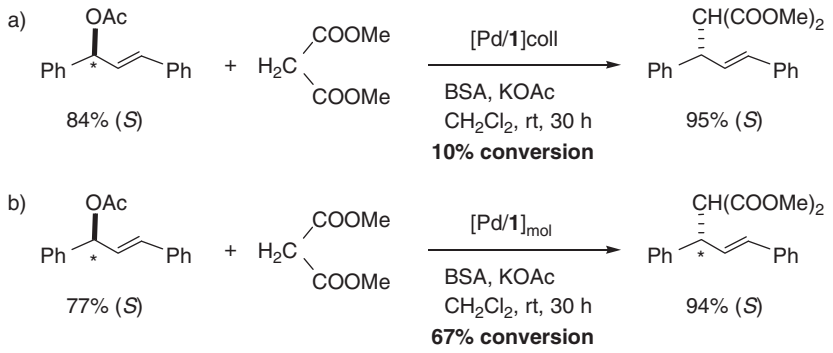

Scheme 3. Pd-catalysed allylic alkykation using an enriched substrate: (a) colloidal catalyst (Pd/**1**/**I** = 1/1.05/100); (b) molecular catalyst (Pd/**1**/**I** = 1/1.25/10,000).

4.6. Conclusion

The main difference between the colloidal and molecular systems described here lies in their relative rates of alkylation of the two enantiomers of the substrate. The kinetic preference for the (*R*)-substrate is only a factor 2 in the molecular system whereas it is clearly higher in the colloidal catalyst (12–20). This induces an apparent absence of reaction with the substrate enriched in the (*S*)-isomer for the colloidal catalyst. The apparent lack of reactivity observed at 58–60% conversion starting with the racemic substrate, is not due to the colloidal catalyst deactivation as demonstrated by further addition of substrate, which leads to its alkylation at the same rate and with the same selectivity. This distinctive colloidal behaviour leads to a very high kinetic resolution giving at the end of the reaction both nearly enantiomerically pure substrate and product. In addition, TEM analyses (up to one week of reaction) did not evidence significant changes when NPs were used as catalytic precursor or NPs formation from the molecular precursor. Furthermore, experiments with poisons, although questionable, distinguish the catalytic behaviour between colloidal and molecular species. In summary, the experiments described here shows the colloidal character of the catalyst when the catalytic precursor used is formed by palladium NPs, previously prepared and isolated.

5. Conclusions

In order to answer the key question: "is homogeneous or heterogeneous the true catalyst?", a set of control experiments should be carried out, taking into account their limitations.

In particular when NPs are involved, either formed *in situ* from molecular complexes or preformed to be used as catalytic precursors, the catalyst identity remains difficult to prove.

Starting from molecular pre-catalysts some signs can pointed to the formation of metallic NPs: colour changes during the reaction or precipitate formation are observed, or induction time is determined, or "hard" reaction conditions (high temperature and/or high pressure) are used, or potential stabilisers for metal nanoclusters are present in solution … But starting from preformed metal NPs, the control tests to exclude the presence of molecular complexes are more subtle.

References

1 J. Schwartz, *Acc. Chem. Res.* 18 (1985) 302. (See also Ref. 6).
2 J. P. Collman, K. M. Kosydar, M. Bressan, W. Lamanna, T. Garrett, *J. Am. Chem. Soc.* 106 (1984) 2569.
3 Y. Lin, R. G. Finke, *Inorg. Chem.* 33 (1994) 4891.
4 D. Astruc, F. Lu, J. Ruiz Aranzaes, *Angew. Chem. Int. Ed.* 44 (2005) 7852.
5 (a) G. Schmid, *Chem. Rev.* 92 (1992) 1709; (b) G. Schmid (ed.) *Nanoparticles: From Theory to Application*, Wiley-VCH, Weinheim, 2003.
6 (a) J. A. Widegren, R. G. Finke, *J. Mol. Catal. A: Chem.* 198 (2003) 317; (b) J. A. Widegren, M. A. Bennett, R. G. Finke, *J. Am. Chem. Soc.* 125 (2003) 10301.
7 R. M. Laine, *J. Mol. Catal.* 14 (1982) 137.
8 R. H. Crabtree, P. C. Demou, D. Eden, J. M. Mihelcic, C. A. Parnell, J. M. Quirk, G. E. Morris, *J. Am. Chem. Soc.* 104 (1982) 6994.
9 P. J. Dyson, *Dalton Trans.* (2003) 2964.
10 (a) X. Wu, D. C. Neckers, *Macromolecules* 32 (1999) 6003; (b) K. Temple, F. Jäkle, J. B. Sheridan, I. Manners, *J. Am. Chem. Soc.* 123 (2001) 1355.
11 J. S. Bradley, in G. Schmid (ed.) *Clusters and Colloids: From Theory to Applications*, Chapter 6, VCH, Weinheim, 1994, 459.
12 L. N. Lewis, N. Lewis, *J. Am. Chem. Soc.* 108 (1986) 7228.
13 M. T. Reetz, E. Westermann, *Angew. Chem. Int. Ed.* 39 (2000) 165.
14 L. N. Lewis, R. J. Uriarte, N. Lewis, *J. Mol. Catal.* 66 (1991) 105.
15 (a) C. A. Jaska, I. Manners, *J. Am. Chem. Soc.* 126 (2004) 9776; (b) C. A. Jaska, I. Manners, *J. Am. Chem. Soc.* 126 (2004) 1334.
16 C. M. Hagen, J. A. Widegren, P. M. Maitlis, R. G. Finke, *J. Am. Chem. Soc.* 127 (2005) 4423.
17 C. M. Hagen, L. Vieille-Petit, G. Laurenczy, G. Süss-Fink, R. G. Finke, *Organometallics* 24 (2005) 1819.
18 L. N. Lewis, *J. Am. Chem. Soc.* 108 (1986) 743.
19 R. H. Crabtree, M. F. Mellea, J. M. Mihelcic, J. M. Quirk, *J. Am. Chem. Soc.* 104 (1982) 107.
20 A. Eichhorn, A. Koch, J. Bargon, *J. Mol. Catal. A: Chem.* 174 (2001) 293.

21 K. S. Weddle, J. D. Aiken III, R. G. Finke, *J. Am. Chem. Soc.* 120 (1998) 5653.
22 B. R. Cho, R. M. Laine, *J. Mol. Catal.* 15 (1982) 383.
23 For the first work described in the literature, see: (a) C. Paal, W. Hartmann, *Ber. Dtsch. Chem. Ges.* 51 (1918) 711. Later, Whitesides and co-workers have largely exploited this kind of test: (b) P. Foley, R. DiCosimo, G. M. Whitesides, *J. Am. Chem. Soc.* 102 (1980) 6713; (c) G. M. Whitesides, M. Hackett, R. L. Brainard, J.-P. P. M. Lavalleye, A. F. Sowinski, A. N. Izumi, S. S. Moore, D. W. Brown, E. M. Staudt, *Organometallics* 4 (1985) 1819.
24 (a) R. van Asselt, C. J. Elsevier, *J. Mol. Catal.* 65 (1991) L13; (b) J. Stein, L. N. Lewis, Y. Gao, R. A. Scott, *J. Am. Chem. Soc.* 121 (1999) 3693.
25 E. E. Finney, R. G. Finke, *Inorg. Chim. Acta* 359 (2006) 2879.
26 A. F. Borowski, S. Sabo-Etienne, B. Chaudret, *J. Mol. Catal. A: Chem.* 174 (2001) 69.
27 B. J. Hornstein, J. D. Aiken III, R. G. Finke, *Inorg. Chem.* 41 (2002) 1625.
28 For other related poisoning tests concerning borane dehydrocouplings, see: C. A. Jaska, T. J. Clark, S. B. Clendenning, D. Grozea, A. Turak, Z.-H. Lu, I. Manners, *J. Am. Chem. Soc.* 127 (2005) 5116.
29 D. R. Anton, R. H. Crabtree, *Organometallics* 2 (1983) 855.
30 I. W. Davies, L. Matty, D. L. Hughes, P. J. Reider, *J. Am. Chem. Soc.* 123 (2001) 10139.
31 R. M. Laine, R. G. Rinker, P. C. Ford, *J. Am. Chem. Soc.* 99 (1977) 252.
32 P. G. N. Mertens, M. Bulut, L. E. M. Gevers, I. F. J. Vankelecom, P. A. Jacobs, D. E. De Vos, *Catal. Lett.* 102 (2005) 57.
33 J. E. Hamlin, K. Hirai, A. Millan, P. M. Maitlis, *J. Mol. Catal.* 7 (1980) 543.
34 Y. Na, S. Park, S. B. Han, H. Han, S. Ko, S. Chang, *J. Am. Chem. Soc.* 126 (2004) 250.
35 S. Kaskel, K. Schlichte, T. Kratzke, *J. Mol. Catal. A: Chem.* 208 (2004) 291.
36 I. P. Rothwell, *Chem. Commun.* (1997) 1331.
37 J. A. Widegren, R. G. Finke, *J. Mol. Catal. A: Chem.* 191 (2003) 187.
38 J. A. Moulijn, P. W. N. M. van Leeuwen, R. A. van Santen (eds.) *An integrated Approach to Homogeneous, Heterogeneous and Industrial Catalysis*, Elsevier, Amsterdam, 1995.
39 G. S. Fonseca, A. P. Umpierre, P. F. P. Fichtner, S. R. Teixeira, J. Dupont, *Chem. Eur. J.* 9 (2003) 3263.
40 R. H. Crabtree, *The Organometallic Chemistry of the Transition Metals*. 2nd ed., Wiley, New York, 1994, 212.
41 P. Baricelli, G. Morfes, D. E. Páez, *J. Mol. Catal. A: Chemical* 176 (2001) 1.
42 M. Tamura, H. Fujihara, *J. Am. Chem. Soc.* 125 (2003) 15742.
43 Y. Uozumi, H. Tsuji, T. Hayashi, *J. Org. Chem.* 63 (1998) 6137.
44 S. Jansat, M. Gómez, K. Philippot, G. Muller, E. Guiu, C. Claver, S. Castillón, B. Chaudret, *J. Am. Chem. Soc.* 126 (2004) 1592.
45 R. Whyman, *Applied Organometallic Chemistry*, Oxford University Press, Oxford, 2001.
46 H. Lui, Q. Wang, D. Jiang, X. Li, M. Han, *J. Mol. Catal. A: Chemical* 118 (1997) 145.
47 B. H. Lipshutz, S. Tasler, W. Chrisman, B. Spliethoff, B. Tesche, *J. Org. Chem.* 68 (2003) 1177.
48 For a general review concerning the Pd catalyst nature in Heck and Suzuki couplings, see: N. T. S. Phan, M. van der Sluys, C. W. Jones, *Adv. Synth. Catal.* 348 (2006) 609.
49 C. C. Cassol, A. P. Umpierre, G. Machado, S. I. Wolke, J. Dupont, *J. Am. Chem. Soc.* 127 (2005) 3298.
50 (a) M. T. Reetz, J. G. de Vries, *Chem. Commun.* (2003) 1787; (b) A. H. M. de Vries, J. M. C. A. Mulders, J. H. M. Mommers, H. J. W. Henderickx, J. G. de Vries, *Org. Lett.* 5 (2003) 3285.
51 (a) M. Studer, H.-U. Blaser, C. Exner, *Adv. Synth. Catal.* 345 (2003) 45; (b) H. Bönnemann, G. A. Braun, *Chem. Eur. J.* 3 (1997) 1200; (c) X. Zuo, H. Liu, D. Guo, X. Yang, *Tetrahedron* 55 (1999) 7787; (d) J. U. Köhler, J. S. Bradley, *Catal. Lett.* 45 (1997) 203; (e) J. U. Köhler, J. S. Bradley, *Langmuir* 14 (1998) 2730.
52 For the synthesis of ligand **1**, see: G. J. H. Buisman, P. C. J. Kamer, P. W. N. M. van Leeuwen, *Tetrahedron: Asymmetry* 4 (1993) 1625.
53 O. Pàmies, G. P. F. van Strijdonck, M. Dieguez, S. Deerenberg, G. Net, A. Ruiz, C. Claver, P. C. J. Kamer, P. W. N. M. van Leeuwen, *J. Org. Chem.* 66 (2001) 8867.
54 K. Philippot, B. Chaudret, *C. R. Chimie* 6 (2003) 1019.
55 B. M. Trost, D. J. Murphy, *Organometallics* 4 (1985) 1143.
56 For experimental details, see: M. Diéguez, S. Jansat, M. Gómez, A. Ruiz, G. Muller, C. Claver, *Chem. Commun.* (2001) 1132.
57 For references related to the kinetic resultion in Pd-catalysed allylic alkylation, see: (a) S. Ramdeehul, P. Dierkes, R. Aguado, P. C. J. Kamer, P. W. N. M. van Leeuwen, J. A. Osborn, *Angew. Chem. Int. Ed.* 37 (1998) 3118; (b) B. Dominguez, N. S. Hodnett, G. C. Lloyd-Jones, *Angew. Chem. Int. Ed.* 40 (2001) 4289; (c) S. R. Gilberston, P. Lan, *Org. Lett.* 3 (2001) 2237; (d) J. W. Faller, J. C. Wilt, J. Parr, Jonathan, *Org. Lett.* 6 (2004) 1301.
58 J. G. de Vries, *Dalton Trans.* (2006) 421.
59 C.-H. Chen, Y. Fujimoto, G. Girdaukas, C. J. Sih, *J. Am. Chem. Soc.* 105 (1982) 7294.

CHAPTER 32

Metal Vapor-Derived Nanostructured Catalysts in Fine Chemistry: The Role Played by Particle Size in the Catalytic Activity and Selectivity

Giovanni Vitulli, Claudio Evangelisti, Anna Maria Caporusso, Paolo Pertici, Nicoletta Panziera, Sergio Bertozzi, and Piero Salvadori

Institute of Chemistry of Organometallic Compounds, ICCOM-CNR, Section of Pisa, and Department of Chemistry and Industrial Chemistry, University of Pisa, Pisa, Italy

1. Introduction

Increasing attention is being paid to nanometer-scale metal particles; they are of great interest in several fields, ranging from material science and catalysis to biology [1]. Their behaviour is strongly related to the particle size distribution, and nanostructured metals are expected to have unusual electronic, optical, magnetic, and chemical properties that differ from those of atomic or molecular species and bulk metals [2]. The chemical reactivity of metal nanoparticles is strongly dependent on the size, not only because of the large surface area but also as a result of the significantly different electronic structure of small nanoparticles. Relevant examples of their size-dependent chemistry have been reported, thus widening the scope of this subject [3].

2. Synthesis Strategy

Among the various preparative routes [1] metal vaporization chemistry provides a valuable synthetic route to weakly stabilized nanostructured metal particles [4].

The co-condensation at low temperature of a metal vapor (commonly produced by resistance or electron-beam heating of metals) with a vapor of weakly stabilizing organic ligands (such as *n*-pentane, toluene, tetrahydrofuran, acetone, or acetonitrile), using commercially available reactors, affords solid matrices, where reactions between the ligand molecules and metal atoms can take place (Scheme 1(A); Figure 1) [5].

After co-deposition the frozen matrix is allowed to melt (Scheme 1(B)). This generates solvent-stabilized metal microclusters (Solvated Metal Atoms, SMA), which are soluble in the excess of ligand and can be recovered and handled at low temperature (−50 to –30 °C) under an inert atmosphere [5]. The warming up of SMA solutions from the isolation temperature (−50 to –30 °C) to room temperature results in a further clustering process which affords nanostructured metal particles as nanopowders or, in the presence of supports, as supported metal nanoaggregates.

These metal vapor-derived nanostructured systems are valuable catalytic precursors for a wide range of reactions of great interest in fine chemistry.

3. Results

3.1. Solvated Metal Atoms as Homogeneous Catalytic Precursors

SMA are solvent-stabilized metal microclusters in which the interaction of the organic ligand (solvent) with the metal is so weak that they can be regarded as naked metal clusters [6]. They are valuable homogeneous catalytic precursors for a wide range of reactions such as the cocyclization of α,ω-diynes and nitriles, the hydroformylation of conjugated dienes to β,γ-unsaturated aldehydes, the hydrosilylation of acetylenes and nitriles, and the intramolecular hydrosilylation of propargyl alcohols (Table 1) [7−12].

To give some new examples of the remarkable catalytic activity of SMA, we report here some recent results obtained on the silyl-carbocyclization of alkynes, promoted by arene-solvated Rh atoms, and on the hydrosilylation of functionalized alkenes, catalyzed by arene-solvated Pt atoms.

3.1.1. Silylformylation of 1-Alkynes

Mesitylene-solvated Rh atoms are valuable catalytic precursors for the selective silylformylation of a wide

Metal Nanoclusters in Catalysis and Materials Science: The Issue of Size Control
Edited by B. Corain, G. Schmid and N. Toshima

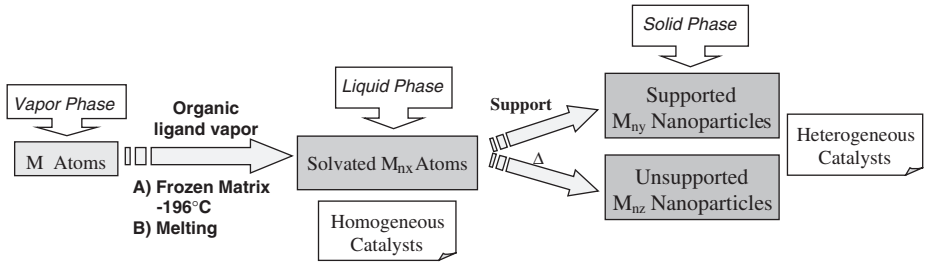

Metal: Fe, Co, Ni, Rh, Pd, Pt, Cu, Ag, Au
Solvent: Arenes, nitriles, olefins, acetone

Solvent / Metal molar ratio = 100 ÷ 1000

Scheme 1.

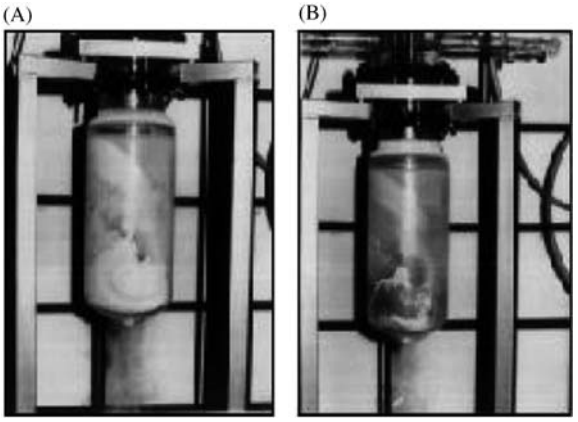

Figure 1. Condensation of solvent vapor (A) and co-condensation of metal vapor with solvent vapor (B).

range of 1-alkynes to the corresponding β-silylalkenals (Scheme 2) [11].

Their catalytic activity is significantly higher than that of more common species such as $Rh_4(CO)_{12}$ [11]. (*Z*)-Silylalkenals are exclusively formed in high yields (60–95%) indicating *syn* addition both of CO and of silane (Me_2PhSiH) to the triple bond.

Using propargyl alcohols and propargylamine derivatives as acetylenic compounds, the silylformylation reaction affords, in the presence of a base, α-silylmethylene-β-lactones, I, and β-lactams, II, respectively (Scheme 3) [13].

The reactions were carried out at 100 °C under 30 atm of CO, using 1,8-diazabicyclo[5.4.0]undec-7-ene (DBU) as base. A comparison with the catalytic activity of $Rh_4(CO)_{12}$ catalyst, reported in Table 2, shows that the Rh/mesitylene catalyst is the more active system.

3.1.2. Hydrosilylation of Functionalized Alkenes

There is much interest in the hydrosilylation of functionalized alkenes as a powerful synthetic tool [14]. Mesitylene-stabilized Pt nanoaggregates, obtained by reaction of Pt vapor and mesitylene, which have already been reported to be very active homogeneous catalysts in the hydrosilylation of acetylenic compounds, including propargyl alcohols [8], also show specific properties in the hydrosilylation of functionalized alkenes, such as allyl amines (Scheme 4).

Under the same reaction conditions traditional catalysts, such as H_2PtCl_6 in ^{i}PrOH (Speier catalyst) and Pt_2(divinyltetramethyldisiloxane)$_3$ (Karstedt Catalyst) are completely inactive.

3.2. Unsupported Metal Nanoparticles

3.2.1. Platinum Nanopowders

The co-deposition of platinum vapors with mesitylene at liquid nitrogen temperature (−196 °C) affords red-brown matrices which give, on melting, brown solutions, that are stable at low temperature (−40 °C) and contain very small Pt_n clusters ($n \leq 5$) stabilized by mesitylene, as indicated by MALDI-TOF analysis [15]. The warming up to room temperature causes further clustering and the precipitation of Pt as a powder. As indicated by SEM and HRTEM analysis, the Pt powder consists of small aggregates ($\leq 1\,\mu m$) formed by Pt nanoparticles of average diameter 3.8 nm. Such particle sizes are smaller than these observed for traditionally prepared Pt black powder ($d_{av} = 6.5$ nm) and for samples of commercial Pt powder ($d_{av} = 20$ nm) [16]. Their catalytic behavior in the hydrogenation of *p*-chloronitrobenzene, a reference substrate, offers a valuable example of size-dependent chemistry (Scheme 5) [17].

The formation of dicyclohexylamine as the main product using MVS-derived Pt powders presumably involves dehydrogenation of cyclohexylamine to the corresponding imine with further addition of cyclohexylamine and elimination of NH_3 (Scheme 6) [18].

3.2.2. Copper Nanopowder

The reaction of Cu vapor with acetone and the further clustering at room temperature affords Cu nanostructured powders containing metal particles averaging 3–4 nm in diameter (Figure 2).

The Cu vapor-derived nanopowders are efficient catalytic precursors for the oxidation of a wide range of organic substrates with molecular oxygen or air and are

Table 1. Catalytic reactions promoted by solvated metal atom solutions.

Reagents	Catalyst	Main product	Reagents	Catalyst	Main product
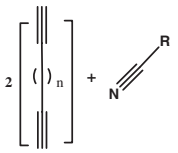	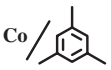	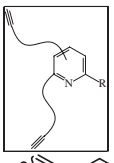	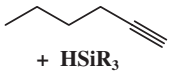	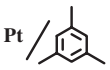	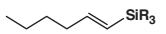
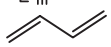	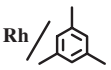	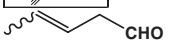	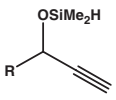	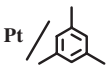	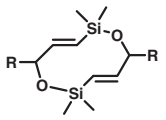
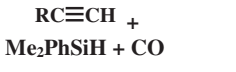	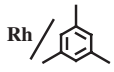	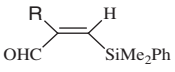	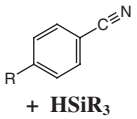	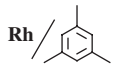	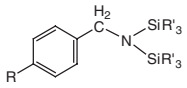

Scheme 2.

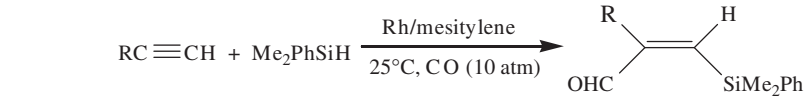

Scheme 3.

DBU: 1,8-diazabicyclo[5.4.0]undec-7-ene
pTs: *p*-toluensulfonamide

considerably more efficient than commercial samples [19,20] (Scheme 7).

3.3. Supported Metal Nanoparticles

Supported metal nanoparticles are of great interest in catalysis, because they offer the opportunity to combine the high reactivity and selectivity of the nanosized metals with the easy separation of the catalysts from the reaction mixture and recycling.

SMA, obtained by reaction of metal nanoparticles with weakly stabilizing organic ligands, are excellent starting materials for the gentle deposition of ligand-free metal nanoparticles on a wide range of organic and inorganic supports (Scheme 8) [21].

This method ensures the deposition of very reactive metal nanoparticles that require no activation steps before use. We shall review here the following examples of catalytic reactions that are of interest in fine chemical synthesis: (a) the hydrogenation of substituted arenes, (b) the selective hydrogenation of α,β-unsaturated carbonyl compounds, (c) the arylation of alkenes with aryl halides (Heck reaction). The efficiency and selectivity of commercial catalysts and of differently prepared nanosized metal systems will be compared.

Table 2. Silylcarbocyclization of propargyl alcohols and propargyl amines with Rh catalysts[a].

Reagents	Catalyst	Product	Yield (%)[b]	Catalytic activity (/h)
 CO / Me_2PhSiH	Rh/mesitylene $Rh_4(CO)_{12}$	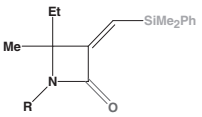	74 58	120 23
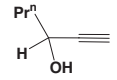 CO / Me_2PhSiH	Rh/mesitylene $Rh_4(CO)_{12}$	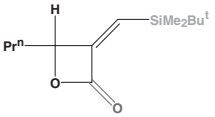	87 66	134 21

[a]Reaction conditions: alkyne (2 mmols), R_3SiH (2 mmols), DBU (0.2 mmols), solvent = CH_2Cl_2 (3 ml), molar ratio alkyne/silane = 1, $T = 100\,^{\circ}C$, $P(CO) = 30$ atm, time = 4 h; molar ratio substrate/Rh = 650 using Rh/mesitylene, molar ratio substrate/Rh = 160 using $Rh_4(CO)_{12}$.
[b]Calculated by v.p.c.

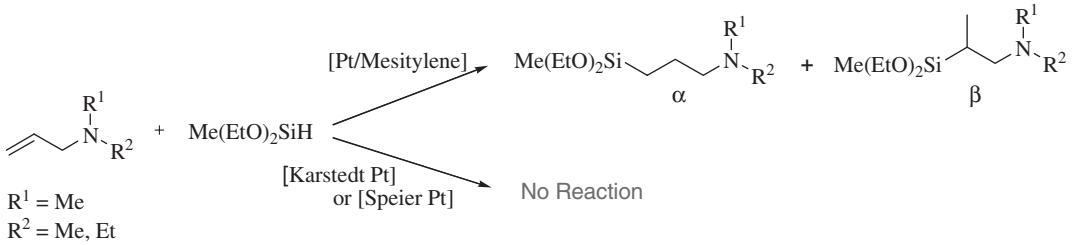

Reaction conditions: silane/substrate = 1, silane / Pt = 10^4 (mmol/mg.atoms), T = 25°C, t = 24 h,
yields = 80-90 %, R^2 = Me α/β= 85/15; R^2 = Et α/β = 100.

Scheme 4.

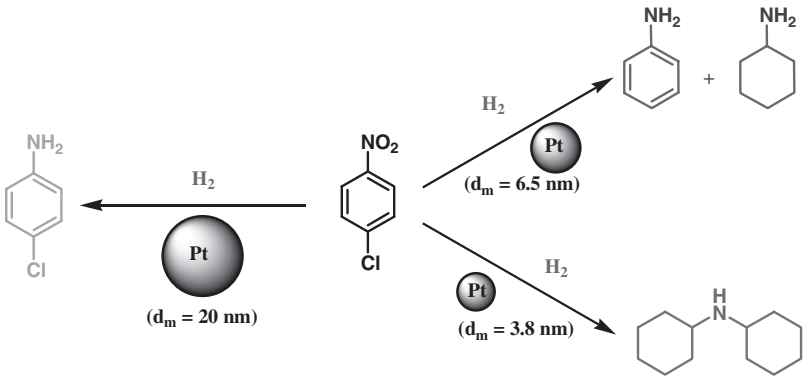

Reaction conditions: substrate/Pt =100; P(H2)=1 atm; T=25°C
Conv. 100%, Pt commercial (d_m = 20 nm) time 20 h, Conv. = 100%, Pt MVS (d_m = 3.8 nm), time 1 h.

Scheme 5.

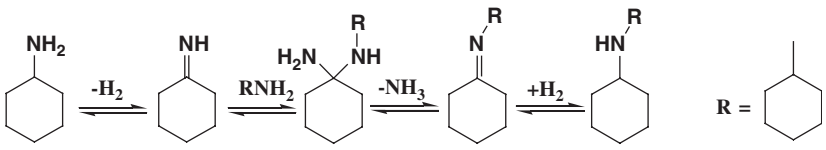

Scheme 6.

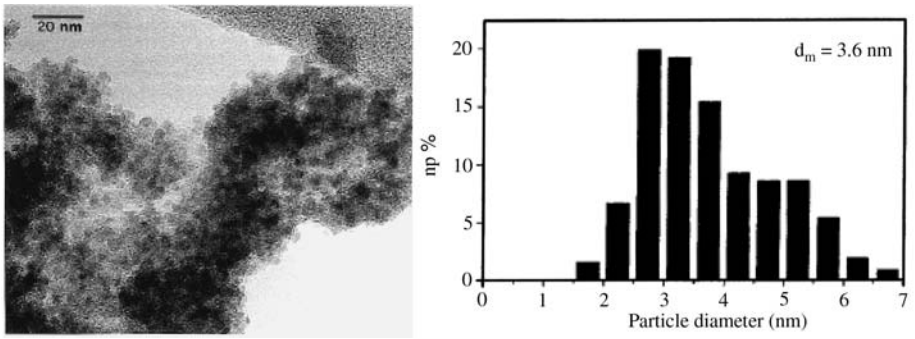

Figure 2. Particle size distribution of the CuMVS powder.

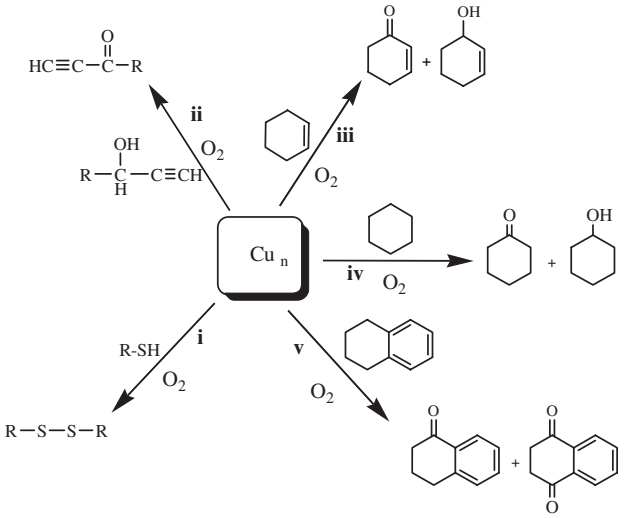

i) Substrate 5 mmols, Substrate / catalyst = 100 mol/g.atom, T=25°C, $P(O_2)$=1 atm.

ii) Substrate / catalyst = 50 mol/g.atom, T=80°C, $P(O_2)$=12 atm, solvent=acetone (5 ml) in the presence of *p*-toluensulfonic acid (acid/cat = 5.5 mol/g.atom)

iii) Substrate = 10 mmols, substrate/catalyst = 5 mol/g.atom, T=80°C, $P(O_2)$=12 atm, solvent=acetone (10 ml).

iv) and v) Substrate = 10 mmols, substrate/catalyst = 50 mol/g.atom, T=120°C, $P(O_2)$=20 atm, solvent=acetone (10 ml).

Scheme 7.

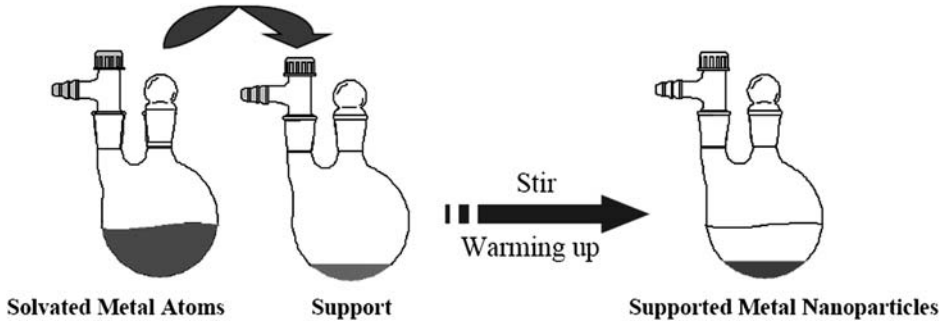

Scheme 8.

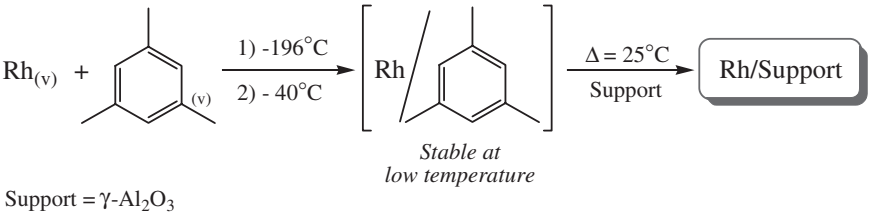

Scheme 9.

3.3.1. Hydrogenation of Aromatic Compounds

The preparation of substituted cyclohexanes from the corresponding substituted arenes is a common reaction step in fine chemical synthesis [22,23]. Nanostructured metal systems are valuable catalysts for the hydrogenation of arenes to the corresponding cyclohexanes, which enable very high yields to be achieved under quite mild reaction conditions. It has been reported recently that in the hydrogenation of methylbenzoate to cyclohexanoate, used as reference reaction, $Rh/\gamma\text{-}Al_2O_3$ nanostructured systems, prepared by gentle deposition of rhodium particles from mesitylene-solvated rhodium atoms (Scheme 9), are significantly more active than the corresponding commercial catalysts [24] (Figure 3).

HRTEM analysis indicates that the two systems have quite different distributions of particle size, the average values being 2.1 nm in the MVS system and 7.1 nm in the commercial sample (Figure 4), thus accounting for their different behavior.

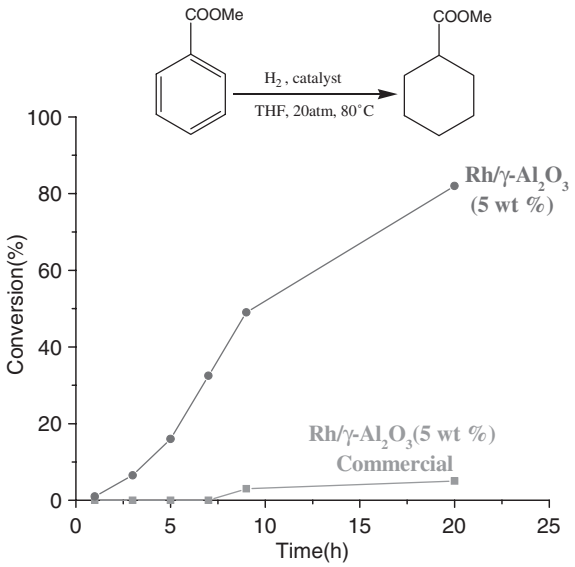

Figure 3. Hydrogenation of methyl benzoate to methyl cyclohexanoate with rhodium on γ-alumina catalysts. (Reprinted from Ref. [24], © 2003, with permission from Elsevier.)

3.3.2. Chemoselective Hydrogenation of α,β-Unsaturated Carbonyl Compounds

Nanostructured Pt(0) catalysts supported on cross-linked macromolecular matrices (Figure 5) have recently been evaluated in the hydrogenation of the α,β-unsaturated aldehyde, (*E,Z*)-3,7-dimethyl-2,6-octadienal (citral) (Scheme 10) [25].

The selective hydrogenation of α,β-unsaturated aldehydes to α,β-unsaturated alcohols is a frequent requirement in the industrial synthesis of specialty chemicals, typically in the liquid phase [26]. Currently, (*E,Z*)-citral is one of the most intensively investigated substrates because of its complex regiochemistry: it has two different olefinic double bonds, one of which is conjugated with a carbonyl group, which is the most difficult to hydrogenate [27]. Geraniol (*trans*-3,7-dimethyl-2,6-octadienol) and nerol (*cis*-3,7-dimethyl-2,6-octadienol) are the products formed by hydrogenation of the C=O group of the (*E*) and (*Z*) isomers of citral, respectively (Scheme 10).

The dispersion of Pt(0) inside the functionalized resins was carried out by two main routes. The first is based on impregnation of the resin with a mesitylene solution of Pt nanoclusters (Solvated Pt Atoms) obtained via MVS. The second procedure, called Chemical Incorporation and Reduction (CIR), implies the immobilization of convenient molecular Pt precursors (i.e. $[Pt(NH_3)_4]Cl_2$) in the pre-swollen resins, followed by chemical reduction of the metal center. Among the Pt catalysts obtained by the CIR procedure only Pt/CF3 exhibits a high conversion of the substrate but a very poor selectivity to geraniol and nerol (about 5%). In the case of the MVS-derived Pt catalysts, the Pt/CF2, Pt/CF3, and Pt/CF4 systems show a high selectivity to geraniol and nerol (about 50%), while the first two are also fairly active. HRTEM analysis indicates that the metal particles are monodispersed on the supports and are regularly shaped and spherical, their diameter being 2–3 nm. The selectivity enhancement in these catalysts can be attributed to the interaction of the very small metal nanoparticles with the functional groups of the support. The metal particles obtained by the CIR procedure are much larger and more irregularly shaped than the MVS catalysts, and we argue that the interaction, if any, of the CIR-derived metal nanoparticles with the functional groups of the polymeric supports is not effective. Interestingly the immobilization in the polymer framework of ions of a second metal ion, such as Fe(II), Co(II), or Zn(II), enhances the selectivity of the Pt catalysts by up to more than 90% [25].

3.3.3. Mizoroki–Heck Reaction

Studies on heterogeneous Pd metal catalysts for the arylation of alkenes with aryl halides (the Mirozoki–Heck reaction often reported as Heck reaction) [28] continue to

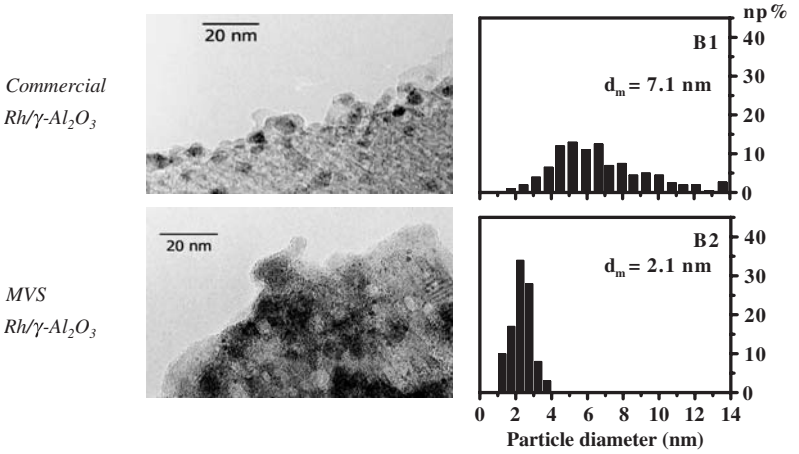

Figure 4. Electron micrographs and relative histograms of the particle size distribution of commercial Rh/γ-Al_2O_3 (B1) and Rh/γ-Al_2O_3 (MVS) (B2). (Reprinted from Ref. [24], © 2003, with permission from Elsevier.)

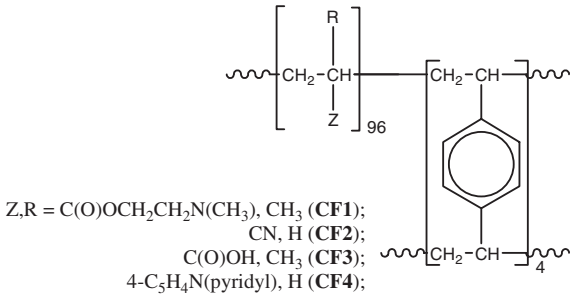

Figure 5. Cross-linked macromolecular matrices used as support. (Reprinted from Ref. [25], © 2005, with permission from Elsevier.)

attract considerable interest, mainly because heterogeneous catalysis is generally recognized to be a valuable tool in the synthesis of fine chemicals [29].

The catalytic activity, however, is generally associated with leaching of the metal into solution, the reaction being most likely catalyzed by soluble active Pd species. Palladium leaching is generally caused by oxidative attack of the aryl halide on the metal nanoparticles, giving catalytically active aryl halide Pd(II) species in solution [30].

Palladium metal catalysts supported on organic resins containing tertiary amino, cyano, carboxyl, and pyridyl groups have been recently investigated in some Heck reactions, such as the coupling of iodobenzene with methyl acrylate and methyl vinyl ether (Scheme 11) [31].

The catalysts were prepared by deposition of Pd nanoparticles on the CF1, CF2, CF3, and CF4 resins respectively, shown in Figure 5, by chemical reduction of Pd(II) precursors such as $Pd(OAc)_2$ and $PdCl_2(NCR)_2$ (R = Ph, Me), following the CIR procedure, or by deposition from Pd-solvated atoms obtained via MVS.

Particular attention was given to the question of whether the catalysis with these systems is homogeneous or heterogeneous. It was found that the nature of the functional groups bound to the polymer backbone affects the rate and the extent of metal leaching, which also

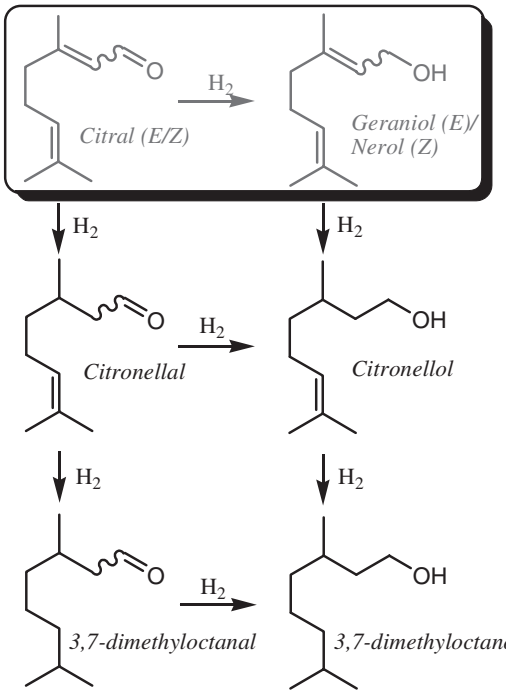

Scheme 10. (Reprinted from Ref. [25], © 2005, with permission from Elsevier).

depends on the size of the nanoclusters. In fact, a MVS 1% (w/w) palladium catalyst supported on a commercial cross-linked polyvinylpyridine resin CF_4, prepared as shown in Scheme 12, exhibited appreciable catalytic activity with no apparent contribution from active palladium species in the bulk liquid phase.

A strong interaction of the very small palladium particles (diameter 3.5 nm, as shown by HRTEM analysis) with the nitrogen atoms of the pyridyl groups in the polymeric support may account for this interesting result.

Similar behavior has been observed in the formation of methyl cinnamate from iodobenzene and methyl acrylate

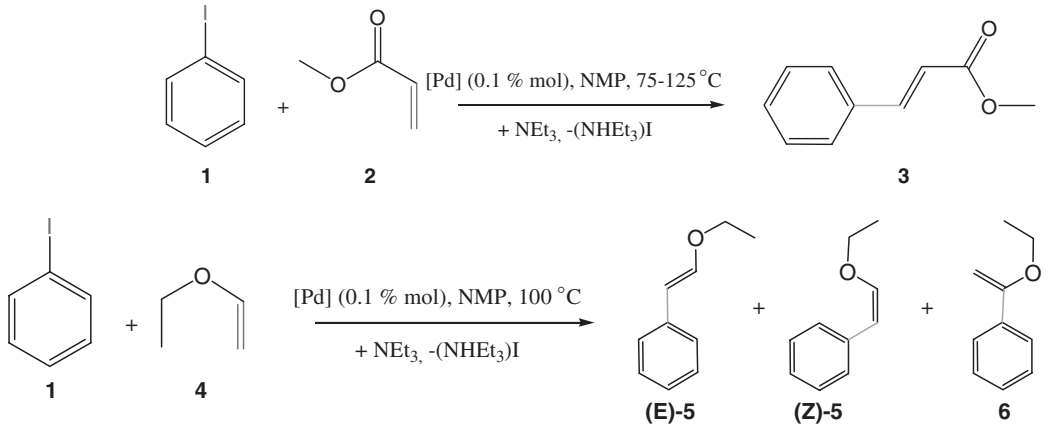

Scheme 11.

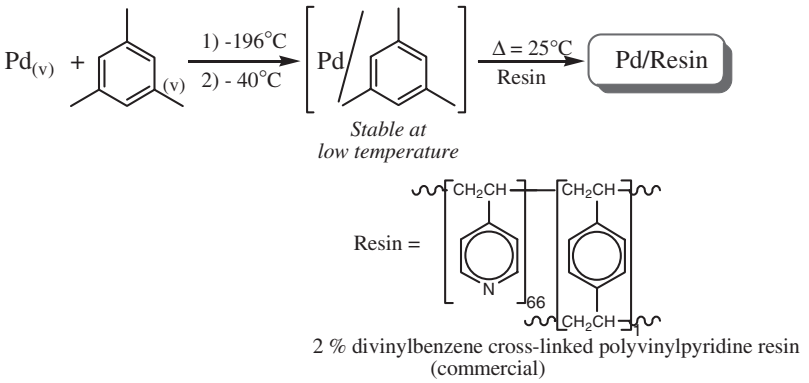

Scheme 12.

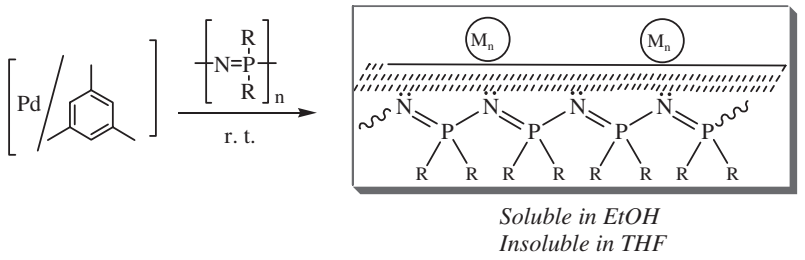

R = Me: polydimethylphosphazene, PDMP

Scheme 13.

in the presence of a Pd-based catalyst, which was prepared by deposition of Pd particles from Pd-solvated atoms obtained via MVS on polydimethylphosphazene (Pd/PDMP) (Scheme 13) [32].

PDMP is the first member of the polyalkylphosphazene series. These polymers are very attractive supports for metals because of their high thermal stability and the presence of the basic nitrogen in the main chain, which is able to bind metal atoms.

The catalyst is soluble in *N*-methylpyrrolidone and can be conveniently used in this solvent. At the end of the reaction the catalyst can be completely recovered by addition of THF or toluene. No leaching of palladium was observed as proved by analytical and chemical tests.

HRTEM analysis of the Pd/PDMP system indicates a narrow particle size distribution with an average diameter of 3.7 nm (Figure 6).

Interestingly, the Pd/PDMP catalyst is more active than commercially available homogeneous and heterogeneous palladium catalysts, such as palladium acetate and palladium on charcoal, respectively, as shown in Table 3.

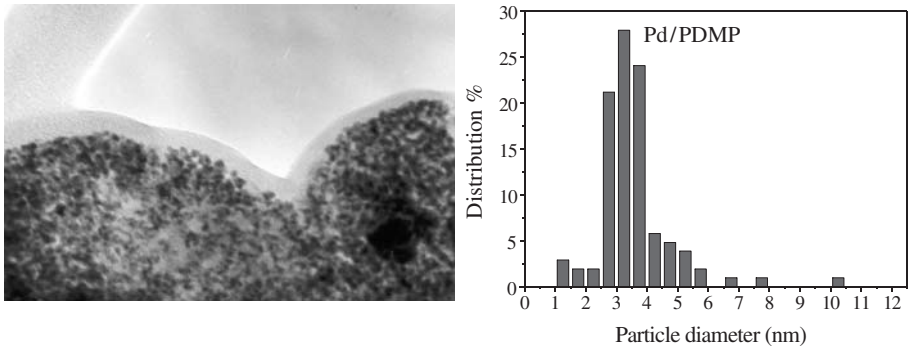

Figure 6. Electron micrographs and relative histograms of the particle size distribution of Pd/PDMP (MVS).

Table 3. Reaction between iodobenzene and methyl acrylate to methyl cinnamate in the presence of palladium catalysts

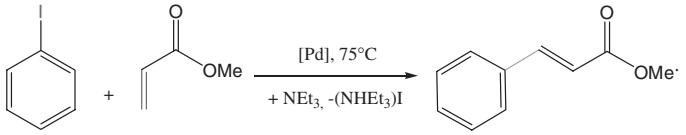

Catalyst	Time (h)	Conversion[a] (%)	Specific activity[b] (/h)
Pd/PDMP	1	80	780
Pd/C	1	20	235
$Pd(OAc)_2$	1	50	500

Note: Reaction conditions: iodobenzene (5 mmol); methyl acrylate (10 mmol); triethylamine (5 mmol); palladium catalyst (5×10^{-3} mg atoms); solvent = *N*-methylpyrrolidone (9 ml); $T = 75\,^{\circ}C$.

[a]Determined by GC analysis.

[b]Moles of methyl cinnamate/g atom of Pd × h.

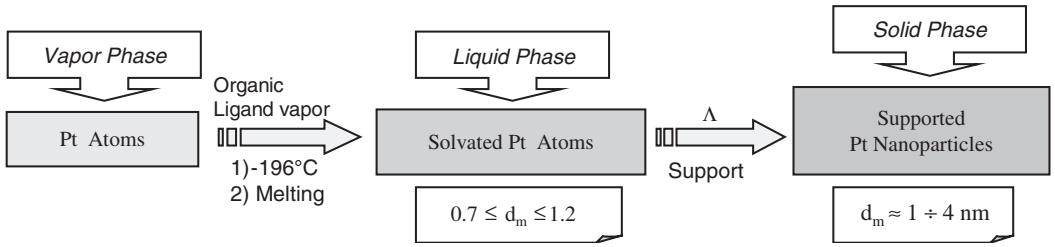

Scheme 14.

3.4. Recent Advances in the Preparation of Supported Catalysts Containing Metal Particles of Tailored Sizes

The size of the metal particles deposited from SMA is strongly dependent on the stabilization of the metal microclusters present in the starting SMA solutions. Their stability can be conveniently modulated by addition of suitable ligands. Examples related to γ-Al_2O_3-supported Platinum and Rhodium nanoparticles are reported here.

Arene and olefin compounds, pure or in admixture, are efficient ligands in promoting the aggregation of platinum atoms from mononuclear species to ligand-stabilized soluble clusters and solid-supported nanoparticles (Scheme 14).

The control of the clustering process in the liquid phase can be monitored by ^{1}H NMR-DOSY (Diffusion Ordered Spectroscopy) [33]. The basic 2D DOSY spectrum displays conventional chemical shifts in one dimension and diffusion coefficients in the other dimension. Because of the relationship between diffusion rates and molecular radii, the diffusion dimension reveals the distribution of molecular sizes of different species in solution. By using as starting material for the deposition of platinum particles a solvated Pt solution containing Pt particles of different hydrodynamic diameter, it is possible to prepare supported particles of different size. As an example, 5% (w/w) Pt/γ-Al_2O_3 samples with particle sizes of mean diameter $d_m = 1.7$ nm and 2.9 nm have been prepared from solutions containing Pt particles with hydrodynamic diameters of 0.9 and 1.5 nm respectively, as shown in Figure 7.

The clustering process in rhodium–mesitylene solutions can be conveniently controlled by use of trioctylamine (TOA), as additional ligand (Scheme 15).

Thus, it becomes possible to obtain supported Rh catalysts containing very small Rh particles. In samples of Rh(TOA)/γ-Al_2O_3 (1% (w/w)) the Rh particle sizes are around 1.1 nm, as indicated by HRTEM analysis (Figure 8). EXAFS (Extended X-ray Absorption Fine Spectroscopy) studies performed on the same samples give 0.7–1.0 nm as a better estimate of the d_m value [24]. It is noteworthy that the similar system Rh/γ-Al_2O_3 (1% (w/w)) obtained from mesitylene-solvated Rh atoms, without TOA (Section 3.1) contain a larger Rh particles ($d_m = 2.1$ nm), as shown in Figure 4.

Catalytic systems at very low metal loading 0.1% (w/w) obtained in this way can be conveniently used in the hydrogenation of α,β-unsaturated ketones to the corresponding saturated carbonyl compounds with very high efficiencies and selectivities. In Table 4 we report the results obtained in the selective hydrogenation of 4-(6-methoxy-2-naphthyl)-3-buten-2-one, **1**, and 2-acetyl-5,8-dimethoxy-3,4-dihydronaphthalene, **2**, to the corresponding saturated carbonyl products (**I**), which are important intermediates

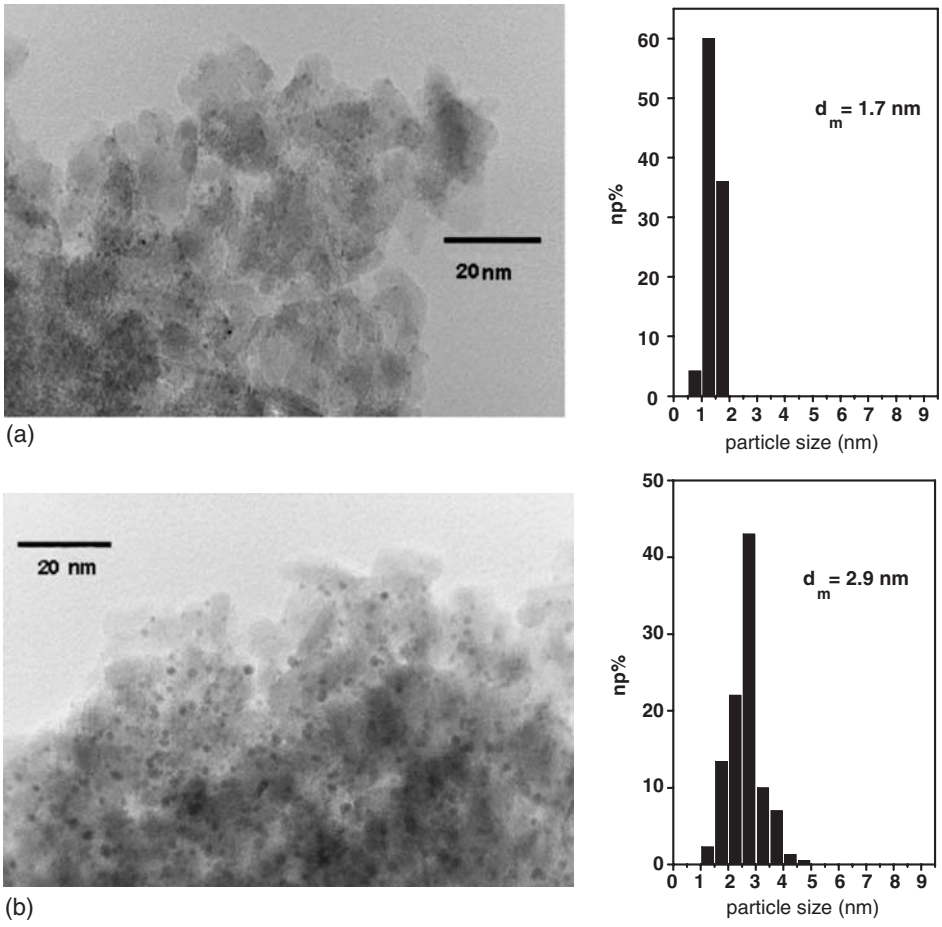

Figure 7. Electron micrographs and relative histograms of the particle size distribution of 5% (w/w) of Pt/γ-Al_2O_3 systems obtained: (a) from the solution containing Pt particles with hydrodynamic diameter of 0.9 nm; (b) from the solution containing Pt particles with hydrodynamic diameter of 1.5 nm.

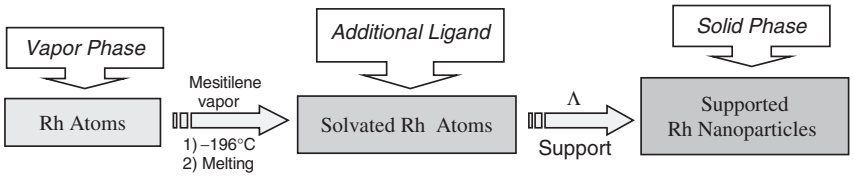

Scheme 15.

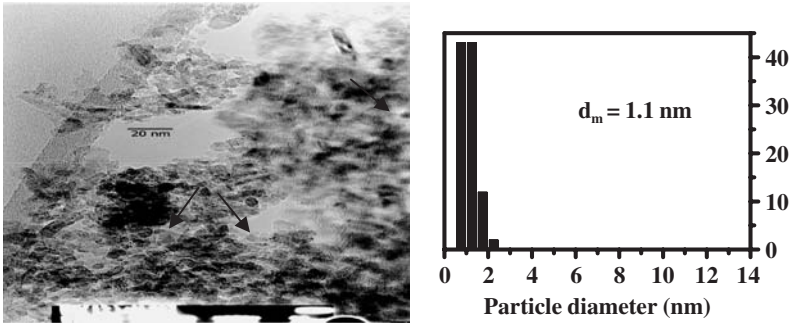

Figure 8. Electron micrographs and relative histograms of the particle size distribution of Rh(TOA)/γ-Al_2O_3. (Reprinted from Ref. [24], © 2003, with permission from Elsevier).

Table 4. Hydrogenation of α,β-unsaturated ketones 1 and 2 with Rh(TOA)/γ-Al_2O_3 0.1% (w/w)

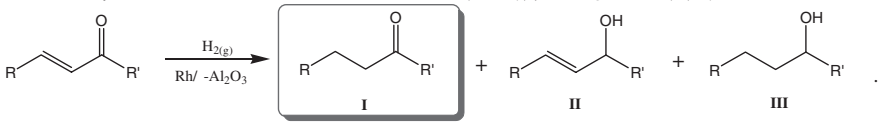

Catalyst	Substrate	Time (h)	Conversion (%)	Product distribution		
				I	II	III
Rh(TOA)/γ-Al_2O_3 0.1% (w/w)	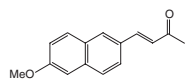	1	100	100	–	–
	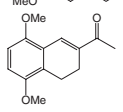	2	100	90	2	8

Note: Reaction conditions: solvent = toluene, $T = 25\,^{\circ}C$, [sub]/[M] = 1000 (mmol/mg atom), $P(H_2) = 1$ Atm.

in the synthesis of compounds of pharmaceutical importance [34].

Compound **1** is completely hydrogenated to the saturated ketone, 4-(6-methoxy-2-naphthyl)-3-butan-2-one. Compound **2** is hydrogenated in high yield (90%) to the saturated ketone, 2-acetyl-5,8-dimethoxy-tetrahydronaphthalene, which can be obtained in the pure form by fractional crystallization from chloroform.

The high activity of the Rh/γ-Al_2O_3 system even at such a low Rh loading (0.1% w/w) can be rationalized on the basis that, as indicated by IR studies of adsorbed CO and EXAFS analysis, all the Rh atoms are zerovalent; coordination by the NR_3 molecules protects them from oxidation by the solid support [24,35].

4. A Case History

4.1. Rhodium Atom-Derived Catalysts in the Hydroformylation of 1,3-Dienes and in the Hydrosilylation of Aromatic Nitriles

The reaction of rhodium vapor with arene affords arene-stabilized Rh microclusters, soluble in the excess of the ligand and stable at low temperature (solvated rhodium atoms). They have been directly used as efficient catalytic precursors or as source of unsupported activated rhodium nanoparticles (Scheme 16).

We describe here: (i) the selective hydroformylation of 1,3-dienes to β,γ-unsaturated aldehydes promoted by catalyst A and (ii) the efficient hydrosilylation of aromatic nitriles to *N*,*N*-disilylamines using catalysts B and C.

4.2. Hydrofromylation of 1,3-Dienes with Rhodium-Solvated Metal Atoms: Catalyst A

The chemo- and regioselectivities of hydroformylation reactions of open chain, conjugated dienes using the usual catalyst are, in most cases, rather low [36]. The rhodium/mesitylene co-condensate (catalyst A), in the presence of bis(diphenylphosphino)ethane, DPPE, catalyses the hydroformylation of 1,3-butadiene, isoprene, and (*E*,*Z*)-1,3-pentadiene to the corresponding β,γ-unsaturated monoaldehydes, with unusually high chemo- and regioselectivities (Scheme 17).

The results obtained are reported in Table 5. Under the hydroformylation conditions, 1,3-butadiene is converted

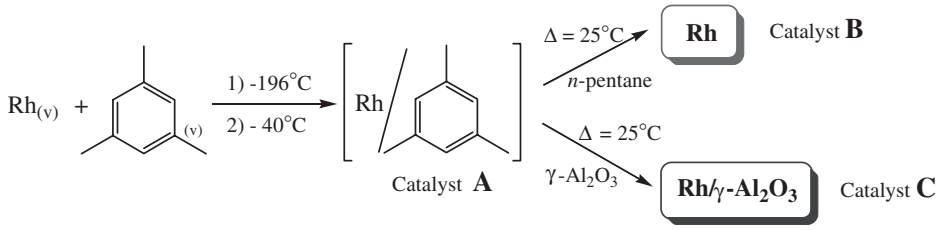

Scheme 16.

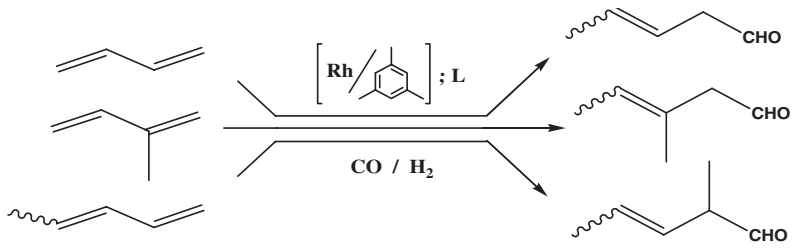

Scheme 17. (Reprinted from Ref. [9], © 1995, with permission from Elsevier).

Table 5. Hydroformylation of open-chain conjugated dienes by rhodium/mesitylene co-condensate, catalyst A[a].

Substrate	Time (h)[b]	Aldehyde yield (%)[c]	Aldehyde distribution (%)		
	6	95	96[d]	4	traces
	11	90	90[e]	10	
	6	95	90[f]	6	4

[a]Reaction conditions: 1,3-diene:Rh:DPPE = 650:1:1, $T = 80\,^{\circ}C$; $P = 120$ atm ($CO:H_2 = 1:1$).
[b]Conversion = 100%.
[c]Obtained by GLC analysis using *p*-xylene as internal standard; the other products are oligomers.
[d]$E/Z = 75/25$.
[e]$E/Z = 38/62$.
[f]$E/Z = 18/82$.

completely after 6 h to a mixture of aldehydes (95%) and oligomers (5%). The main product is (*E*,*Z*)-pentenal (96% yield), the other aldehydes being 4-pentenal (4% yield) and pentanal (traces). Isoprene furnished after 11 h a mixture of aldehydes (90%) of composition (*E*,*Z*)-3-methyl-3-pentenal (90% yield) and of 4-methyl-4-pentenal (10% yield). (*E*,*Z*)-1,3-pentadiene gives after 6 h a mixture (95%) of (*E*,*Z*)-2-methyl-3-pentenal (90% yield), (*E*,*Z*)-2-methyl-2-pentenal (6% yield), and 2-methylpentanal (4% yield).

4.3. Hydrosilylation of Aromatic Nitriles with Rhodium Powder and Rh/γ-Al_2O_3

The hydrosilylation of nitriles is unusual, since the cyano group is quite inert under the usual reaction conditions [37]. Rhodium metal particles, isolated as unsupported (catalyst B) or supported (catalyst C) samples are able to catalyze the hydrosilylation of aromatic nitriles to *N*,

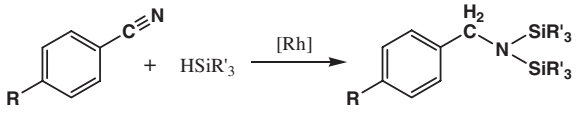

R = H, CH_3, OCH_3, CF_3, $COOCH_3$
R' = CH_3, OC_2H_5

Scheme 18. (Reprinted from Ref. [12], © 1999, with permission from Elsevier).

N-disilylamines, precursors of benzylamine derivatives, in high conversion and chemoselectivity (Scheme 18 and Table 6).

As shown in Table 6 all the reactions proceed with complete chemoselectivity to the corresponding *N*,*N*-disilylamine. The reactions have been performed without solvent facilitating the collection of the products. With catalyst B, using $HSiMe_3$, as hydrosilane reagent, quantitative yields of products have been obtained with benzonitrile, as well as with other nitriles, containing

Table 6. Catalytic hydrosilylation of aromatic nitriles promoted by catalyst B and catalyst C[a].

Run	Nitrile	Hydrosilane	Catalyst	Conversion[b] (%)	Yield of product[c] (%)
1	C_6H_5CN	$HSiMe_3$	Rh powder B	100	95
2	*p*-MeC_6H_4CN	$HSiMe_3$	Rh powder B	100	95
3	*p*-$MeOC_6H_4CN$	$HSiMe_3$	Rh powder B	100	95
4	*p*-$CF_3C_6H_4CN$	$HSiMe_3$	Rh powder B	100	95
5	*p*-$MeCO_2C_6H_4CN$	$HSiMe_3$	Rh powder B	100	95
6	C_6H_5CN	$HSi(OEt)_3$	Rh powder B	80	75
7	*p*-MeC_6H_4CN	$HSi(OEt)_3$	Rh powder B	75	70
8	*p*-$MeOC_6H_4CN$	$HSi(OEt)_3$	Rh powder B	75	70
9	*p*-$CF_3C_6H_4CN$	$HSi(OEt)_3$	Rh powder B	75	70
10	*p*-$MeCO_2C_6H_4CN$	$HSi(OEt)_3$	Rh powder B	70	65
11	C_6H_5CN	$HsiMe_3$	Rh/γ-Al_2O_3 C	80	75
12	*p*-MeC_6H_4CN	$HsiMe_3$	Rh/γ-Al_2O_3 C	75	70
13	*p*-$MeOC_6H_4CN$	$HsiMe_3$	Rh/γ-Al_2O_3 C	75	70
14	*p*-$CF_3C_6H_4CN$	$HsiMe_3$	Rh/γ-Al_2O_3 C	50	45
15	C_6H_5CN	$HSi(OEt)_3$	Rh/γ-Al_2O_3 C	65	60

[a]Reaction conditions: nitrile (9.8 mmol), hydrosilane (49 mmol), rhodium (0.1 mmol); $T = 100\,^{\circ}C$, time = 15 h.
[b]GLC conversion of nitrile.
[c]Isolated product yield.

electron-donating or electron-withdrawing groups in *para* position of the aromatic ring (run 1–5). High conversion (70–80%) has been obtained also with $HSi(OEt)_3$ (runs 6–10). A similar behavior has been found also with catalyst C (runs 11–15).

4.4. Preparation of the Catalysts

4.4.1. Rhodium-Solvated Metal Atoms: Catalyst A

All the operation concerning the MVS technique were performed under dry argon atmosphere. The co-condensation of rhodium and mesitylene was carried out in a static reactor previously described (Figure 1). The amount of rhodium present in the MVS solution was determined by atomic absorption spectroscopy. In a typical experiment, rhodium vapor, generated by resistive heating of a tungsten wire surface coated with electrodeposited rhodium (300 mg) was co-condensed at liquid nitrogen temperature with mesitylene (40 ml) in the glass reactor chamber of the MVS apparatus in about 30 min. The reactor chamber was warmed at the melting point of the solid matrix and the resulting brown solution was siphoned at low temperature ($-30\,^{\circ}C$) into a Schlenk tube. The content of metal in solution examined by Atomic Absorption Spectroscopy was 4.5 mg of rhodium/ml of solution (the total amount of Rh recovered was 160 mg with about 60% of yield). This solution is stable for about a week in a refrigerator at $-20\,^{\circ}C$.

Rhodium and platinum metals can be more conveniently vaporized with electron-beam vaporization source, in a stainless steel reactor, starting from metal powders deposited into a graphite crucible.

4.4.2. Rhodium Powder: Catalyst B

The rhodium powder was prepared directly in the Carius tube employed for the hydrosilylation experiment. *n*-Pentane (20 ml) was added to the brown Rh/mesitylene solution (2 ml, containing 6 mg of rhodium/ml) and the solution was slowly warmed at room temperature under stirring. After 4 h, when the solution became colorless, the liquid was removed and the powder obtained was washed with *n*-pentane and dried under reduced pressure.

4.4.3. Rhodium on γ-Al_2O_3: Catalyst C

The above brown Rh/mesitylene solution (2 ml, containing 6 mg of rhodium/ml) was added to a suspension of γ-Al_2O_3 (1.2 g, AKZO 000-1.5 E product, dried in an oven before the use) in toluene (10 ml). The mixture was stirred for 24 h at room temperature. The colorless solution was removed and the light-brown solid was washed with *n*-pentane and dried under reduced pressure whereupon the Rh/γ-Al_2O_3 catalyst, containing 1 wt.% Rh, was obtained.

4.4.4. General Procedure for the Hydroformylation Reaction

In a typical run, bis(l,2-diphenylphosphino)ethane (DPPE) (0.022 g, 0.05 mmol) and 1,3 diene (32.5 mmol) are added to a portion of the co-condensate, containing 5.2 mg of rhodium (0.05 mg. atom) in 10 ml of mesitylene. The solution is introduced by suction into an evacuated, 80 ml stainless steel autoclave. Carbon monoxide is introduced to the desired pressure and the autoclave is rocked and heated at $80\,^{\circ}C$. Hydrogen is rapidly charged to give 1:1 gas composition. When the pressure reaches the theoretical value corresponding to the desired conversion, the autoclave is cooled, depressurised, and the reaction mixture analyzed by GLC. The crude product is distilled. The aldehydes are obtained as pure samples by preparative GLC and characterized by ^1H NMR spectroscopy and GC–MS analysis.

4.4.5. General Procedure for the Catalytic Hydrosilylation of Aromatic Nitriles in the Presence of Rhodium Catalysts

The compounds benzonitrile, *p*-methylbenzonitrile, *p*-methoxybenzonitrile, *p*-trifluoromethyl-benzonitrile, *p*-methoxycarbonylbenzonitrile, and triethoxysilane are commercial products and are degassed and stored under argon before use. Trimethylsilane was prepared according to a literature report [38]. The nitrile (9.8 mmol) and the hydrosilane (49 mmol) are added to the rhodium catalyst (0.1 mmol) contained in a Carius tube. When using trimethylsilane, the operation is performed at −20 °C. The tube is closed and the mixture stirred at 100 °C for 15 h. The liquid is separated by filtration and the excess of hydrosilane removed under vacuum to leave the *N*, *N*-disilylamine derivative. If necessary, a bulb to bulb distillation is performed to obtain a completely colorless liquid. The yields obtained in the different runs are reported in Table 6. The product have been characterized by elemental analysis, ^{1}H NMR spectroscopy, and GC–MS analysis.

5. Conclusions

In this chapter the potential of nanostructured metal systems in catalysis and the production of fine chemicals has been underlined. The crucial role of particle size in determining the activity and selectivity of the catalytic systems has been pointed out; several examples of important reactions have been presented and the reaction conditions also described. Metal Vapor Synthesis has proved to be a powerful tool for the generation of catalytically active microclusters SMA and nanoparticles. SMA are unique homogeneous catalytic precursors and they can be very convenient starting materials for the gentle deposition of catalytically active metal nanoparticles of controlled size.

References

1 (a) B. Ziou, S. Hermans, G. A. Somorjai (eds.) *Nanotechnology in Catalysis*, Springer, New York, 2004; (b) D. L. Feldheim, C. A. Foss, Jr. (eds.) M*etal Nanoparticles: Synthesis, Characterization and Applications*, Marcel Dekker, New York, 2002; (c) B. A. Roucoux, J. Schultz, H. Patin, *Chem. Rev.* 102 (2002) 3757; (d) J. D. Aiken III, R. G. Finke, *J. Mol. Catal. A: Chemical* 145 (1999) 1; (e) G. Schmid, L. F. Chi, *Adv. Mater.* 10 (1998) 515; (f) J. S. Bradley, in Schmid (ed.), *Cluster and Colloids: From Theory to Applications*, VCH, Weinheim, 1994; (g) L. N. Lewis, *Chem. Rev.* 93 (1993) 2693; (h) C. Amiens, D. De Caro, B. Chaudret, J. S. Bradley, R. Mazel, C. Roncan, *J. Am. Chem. Soc.* 115 (1993) 11638 and references therein; (i) G. Schmid, *Chem. Rev.* 92 (1992) 1709; (j) T. Hayashi, *Physics Today* 40 (1987) 44; (k) G. Schmid, H. Harms, J.-O. Bovin, J. van Ruitenbeck, H. W. Zandbergen, W. T. Fu, *J. Am. Chem. Soc.* 115 (1993) 2046 and references therein.

2 W. A. de Heer, *Rev. Mod. Phys.* 65 (1993) 611.

3 (a) C. N. R. Rao, G. U. Kulkarni, P. J. Thomas, P. P. Edwards, *Chem. Eur. J.* 8 (2002) 29; (b) C. N. R. Rao, G. U. Kulkarni, P. J. Thomas, P. P. Edwards, *Chem. Soc. Rev.* 29 (2000) 27.

4 (a) G. Vitulli, P. Pertici, S. Bertozzi, A. M. Caporusso, R. Lazzaroni, P. Salvadori, in W. A. Herrmann (ed.) *Synthetic Methods of Organometallics and Inorganics Chemistry: Catalysis*, Brauer/Herrmann, Munich, 2002, 10; (b) G. Vitulli, P. Pertici, S. Bertozzi, A. M. Caporusso, E. Pitzalis, C. Evangelisti, L. Aronica, P. Salvadori, *Chim. Ind. (Milan)* 83(9) (2001) 60; (c) G. Vitulli, A. Verrazzani, A. M. Caporusso, E. Pitzalis, P. Pertici, P. Salvadori, in S. Daolio, E. Tondello, P. F. Vigato (eds.) *Syntheses and Methodologies in Inorganic Chemistry, New Compounds and Materials*, Vol. 7, La Photograph, Padova, 1997, 52; (d) K. J. Klabunde, *Free Atoms, Clusters and Nanoscale Particles*, Academic Press, San Diego, 1994; (e) K. J. Klabunde, *Chemistry of Free Atoms and Particles*, Academic Press, New York, 1980; (f) K. J. Klabunde, H. F. Efner, T. O. Murdock, R. Roppel, *J. Am. Chem. Soc.* 98 (1976) 1021.

5 (a) J. S. Bradley, in Schmid (ed.) *Cluster and Colloids: From Theory to Applications*, VCH, Weinheim, 1994; (b) J. R. Blackborow, D. Young, *Metal Vapour Synthesis in Organometallic Chemistry*, Springer-Verlag Ed., Berlin, 1979.

6 G. A Ozin, S. A. Mitchell, *Angew. Chem. Int. Ed. Engl.* 22 (1983) 674.

7 (a) A. Colligiani, G. Vitulli, J. Kraus, S. Biagi, P. Salvadori, R. Settambolo, M. Pasero, *J. Mol. Cat.* 53 (1989) 133; (b) G. Vitulli, S. Bertozzi, M. Vignali, R. Lazzaroni, P. Salvadori, *J. Organomet. Chem.* 326 (1987) C33.

8 C. Polizzi, A. M. Caporusso, G. Vitulli, P. Salvadori, *J. Organomet. Chem.* 451 (1993) C4.

9 S. Bertozzi, N. Campigli, G. Vitulli, R. Lazzaroni, P. Salvadori, *J. Organomet. Chem.* 487 (1995) 41.

10 M. Caporusso, S. Barontini, P. Pertici, G. Vitulli, P. Salvadori, *J. Organomet. Chem.* 564 (1998) 57.

11 L. A. Aronica, S. Terreni, A. M. Caporusso, P. Salvadori, *Eur. J. Org. Chem.* (2001) 4321.

12 A. M. Caporusso, N. Panziera, P. Pertici, E. Pitzalis, P. Salvadori, G. Vitulli, G. Martra, *J. Mol. Catal.* 150 (1999) 275.

13 (a) I. Matsuda, J. Sakakibara, H. Nagashima, *Tetrahedron Lett.* 32 (1991) 7431; (b) I. Matsuda, A. Ogiso, S. Sato, *J. Am. Chem. Soc.* 112 (1990) 6120.

14 (a) B. P. S. Chauhan, J. S. Rathore, *J. Am. Chem. Soc.* 127 (2005) 5790; (b) N. Sabourault, G. Mignani, A. Wagner, C. Mioskowski, *Org. Lett.* 4 (2002) 2117.

15 E. Pitzalis, PhD Thesis, University of Pisa, Pisa, Italy, 1993.

16 G. Vitulli, E. Pitzalis, A. Verrazzani, P. Pertici, P. Salvadori, G. Martra, *Mat. Sci. Forum* 235–238 (1997) 929.

17 G. Vitulli, E. Pitzalis, L. A. Aronica, P. Pertici, S. Bertozzi, A. M. Caporusso, P. Salvadori, S. Coluccia, G. Martra, *Synthesis and Methodologies in Inorganic Chemistry*, Vol. 7, La Photograph, Padova, 1997, 52G.

18 P. N. Rylander, *Hydrogenation Methods*, Accademic Press, New York, 1985, 125.

19 G. Vitulli, M. Bernini, S. Bertozzi, E. Pitzalis, P. Salvadori, S. Coluccia, G. Martra, *Chem. Mater.* 14 (2002) 1183.

20 C. Evangelisti, G. Vitulli, E. Schiavi, M. Vitulli, S. Bertozzi, P. Salvadori, L. Bertinetti, G. Martra, *Catalysis Letters* 116 (1–2) (2007) 57.

21 K. J. Klabunde, Y. X. Li, B. J. Tan, *Chem. Mater.* 3 (1991) 30.

22 J. A. Widegren, R. G. Finke, *J. Mol. Cat. A: Chem.* 191 (2003) 18.

23 P. N. Rylander, *Catalytic Hydrogenation in Organic Synthesis*, Accademic Press, New York, 1979, 168.

24 G. Vitulli, C. Evangelisti, P. Pertici, A. M. Caporusso, N. Panziera, P. Salvadori, M. G. Faga, C. Manfredotti, G. Martra, S. Coluccia, A. Balerna, S. Colonna, S. Mobilio, *J. Organomet. Chem.* 681 (2003) 37.

25 P. Centomo, M. Zecca, S. Lora, G. Vitulli, A. M. Caporusso, M. L. Tropeano, C. Milone, S. Galvagno, B. Corain, *J. Catal.* 229 (2005) 283.
26 P. Gallezot, D. Richard, *Catal. Rev.-Sci. Eng*. 40 (1998) 81.
27 See, as example, P. Reyes, H. Rojas, J. L. G. Fierro, *Appl. Catal. A: Gen.* 248 (2003) 59.
28 (a) T. Mizoroki, K. Mori, A. Ozaki, *Bull. Chem. Soc. Jpn.* 44 (1971) 581; (b) R. F. Heck, J. P. Nolley Jr., *J. Org. Chem.* 37 (1972) 2320.
29 (a) F. Alonso, I. P. Beletskaya, M. Yus, *Tetrahedron* 61 (2005) 11771; (b) A. Biffis, M. Zecca, M. Basato, *J. Mol. Cat. A: Chemical* 173 (2001) 249; (c) R. A. Sheldon, H. van Bekkum (eds.) *Fine Chemical through Heterogeneous Catalysis*, Wiley-VCH, Weinheim, 2001.
30 B. M. Choudary, S. Madhi, N. S. Chowdari, M. L. Kantam, B. Sreehdar, *J. Am. Chem. Soc.* 124 (2002) 14127.
31 A. M. Caporusso, P. Innocenti, L. A. Aronica, G. Vitulli, R. Gallina, A. Biffis, M. Zecca, B. Corain, *J. Catal.* 234 (2005) 1.
32 P. Pertici, G. Vitulli, P. Salvadori, E. Pitzalis, M. Gleria, in M. Gleria, R. De Jaeger, (eds.) *Applicative Aspects of Poly(organophosphazenes)*, NOVA Ed., New York, 2004, 255.
33 (a) R. H. Terrill, T. A. Postlethwaite, C. Chen, C. Poon, A. Terzis, A. Chen, J. E. Hutchison, M. R. Clark, G. Wignall, J. D. Londono, R. Superfine, M. Falvo, C. S. Johnson Jr., E. T. Samulski, R. W. Murray, *J. Am. Chem. Soc.* 117 (1995) 12537; (b) K. F. Morris, C. S. Johnson, *J. Am. Chem. Soc.* 115 (1993) 4291.
34 S. Del Nero, C. Gandolfi, P. Lombardi, F. Arcamone, *Chem. and Ind.* 22 (1981) 810.
35 (a) M. G. Faga, L. Bertinetti, C. Manfredotti, G. Martra, C. Evangelisti, P. Pertici, G. Vitulli, *Stud. Surf. Sci. Catal.* 155 (2005) 227; (b) M. Frolov, *Plat. Met. Rev.* 40 (1996) 143.
36 P. W. N. M. van Leeuven, C. F. Roobek, *J. Mol. Catal.* 31 (1985) 345.
37 E. Keinan, D. Perez, *J. Org. Chem.* 52 (1987) 2576.
38 O. W. Steward, O. R. Pierce, *J. Am. Chem. Soc.* 83 (1961) 1916.

This page intentionally left blank

CHAPTER 33

Wet Preparation of Metal Nanoparticles and their Immobilization on Silicon Substrates

Tetsu Yonezawa, Yoshinori Yamanoi, and Hiroshi Nishihara

Department of Chemistry, Graduate School of Science, The University of Tokyo
7-3-1, Hongo, Bunkyo-ku, Tokyo 113-0033, Japan

1. Introduction

The rapid development of nanotechnology has revolutionized scientific developments in recent decades [1]. The synthesis, characterization, and application of functionalized nanoparticles are currently a very active field of research [2]. Due to the size limitation of metal nanoparticles, they show very unique properties, which are called "nano-size effect" or "quantum-size effect", which is different from those of both bulk metals and metal atoms. Such specific properties are usually dominated by the atoms located on the surface. In nanoparticles systems, the number of atoms located on the surface of the particles increases tremendously with decreasing of the particle diameter [3].

Wet preparation procedure is the most widely used preparative system for nanoparticle synthesis. Various stabilizers and reducing reagents have been proposed in order to prepare small and uniform-sized metal nanoparticles from the era of Michael Faraday. Faraday firstly reported hydrosol of gold nanoparticles, which are highly stably dispersed for many years [4]. He showed the formation of wine-colored dispersions by using phosphorus as the reducing reagent. Until now, various preparative procedures for gold nanoparticles have been proposed. They have been used as a good stain reagent for TEM observation of organic compounds especially biomolecules [5].

For transition and precious metals, thiols have been successfully employed as the stabilizing reagent (capping reagent) of metal nanoparticles [6]. In such cases, various functionalities can be added to the particles and the obtained nanoparticles may be very unique. It is well known that thiols provide good self-assembled monolayers (SAM) on various metal surfaces. When this SAM technique is applied to the nanoparticle preparation, nanoparticles can be covered constantly by functionalized moieties, which are connected to the terminal of thiol compounds.

On the other hand, modification of substrate surfaces, especially semiconductor surfaces, has been an intensively investigated topic in the field of applied surface sciences and technologies [7]. The mostly used semiconductor material is silicon [8]. On silicon, one can readily prepare organic monolayers via covalent bonds. These monolayers were usually prepared from organosilicon materials (such as alkylchlorosilanes, alkylalkoxysilanes, alkylaminosilanes) on a silica layer or silicon surface. This modified surface was connected via Si–O–Si bonds on silicon substrates. Therefore, the surface of the substrates is always covered by a silica layer. Another approach to the covalent immobilization of organic molecules is the hydrosilylation reaction of 1-alkenes with a hydrogen-terminated (H–Si) silicon surface [8]. Si(1 1 1) and Si(1 0 0) surfaces can be candidates for this monolayer-formation process, so that as porous silicons [9]. As a porous silicon is readily oxidized under ambient condition, such organic monolayer system is very important to prevent the oxidization of the surface.

Si–C formation technique with hydrogen-terminated silicon substrates can also be used as the covalent attachment of nanomaterials onto silicon surface. The possibility of assembling nanomaterials in order is strongly desired in order to enable efficient utilization of their unique "nano-sized" properties. Ordered arranging and position controlling of nanomaterials on solid substrates especially on silicon surface have been intensively studied [10]. In this manuscript, the nanoparticle immobilization by thermal Si–C formation will be discussed [11].

2. Wet Preparation of Metal Nanoparticles

Preparation of metal nanoparticles can be divided largely into two categories, that is, physical process and chemical process (Figure 1).

The physical process is usually a dry process, that is, crush of bulk metals and cooling drops of metals generated at high temperature. It also includes arc discharge between metal electrodes [12]. The chemical process is

Metal Nanoclusters in Catalysis and Materials Science: The Issue of Size Control
Edited by B. Corain, G. Schmid and N. Toshima

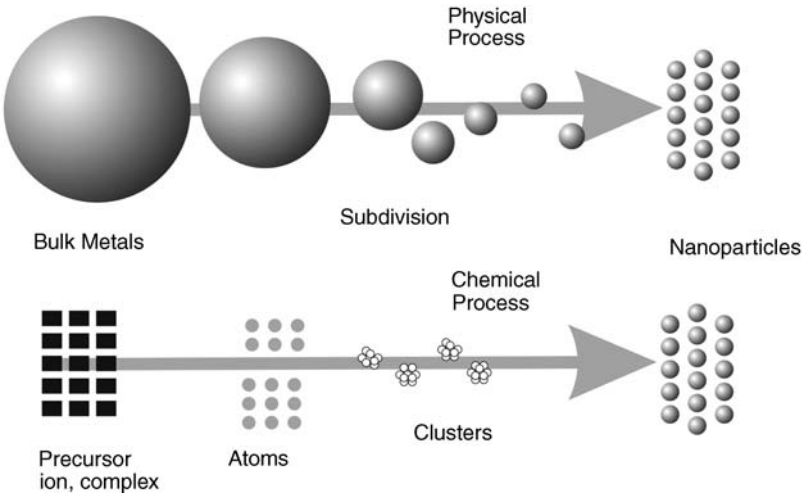

Figure 1. Schematic illustration of the preparation procedures of metal nanoparticles.

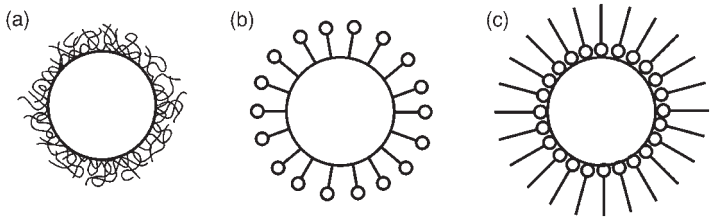

Figure 2. Schematic illustrations of (a) polymer-stabilized, (b) surfactant-stabilized, (c) ligand-stabilized metal nanoparticles.

growth of zero-valent metal atoms to form nanoparticles. This process has been studied intensively in the last decade including chemical reduction of metal ions or complexes in solutions, photochemical reduction, electrochemical process, and thermal decomposition of metal complexes [13]. Evaporation of metals under vacuum can also be classified into chemical process. In these cases, zero-valent metal atoms are generated and they aggregate themselves to form nanoparticles. This aggregation is usually controlled by an organic stabilizing reagent. Natural or synthesized polymers, such as gelatin and poly(vinylpyrrolidone) [2e], have been used as a good stabilizing reagent. Surfactants forming micelles can also be good protecting materials. Metal-coordinative ligand molecules are important candidates (Figure 2). Such wet preparative processes are usually included into the chemical process.

Chemical reduction of metal salts in solution is the most widely used method of preparation of metal nanoparticles, especially in laboratories. In general, the reducing reagents are added into the solution of the precursor ions, but in some cases, a solvent works as a reductant. Various reducing reagents have been proposed to prepare metal nanoparticles. Ethanol or small alcohols can reduce precious metal ions such as Au^{3+}, Pt^{4+}, Pd^{2+}, Ag^{+}, and so on [3]. Polymer-stabilized precious metal nanoparticles and their alloy particles can be used as good catalysts for various reactions. Polyols, such as ethylene glycol, were used to prepare transition metal nanoparticles such as copper and cobalt [14].

Lithium or sodium tetrahydroborate (MBH_4), and diborane (B_2H_4) have been frequently used as the reducing reagent for various metal ions. PVP-stabilized copper nanoparticles from copper(II) sulfate were proposed by Komiyama et al. [15]. Small gold nanoparticles stabilized by PVP, which are a good candidate of catalyst, were reported by Tsukuda [16]. A very famous Au_{55} using diborane as the reductant was proposed by Schmid [17].

In 1994, thiols were firstly used as stabilizers of gold nanoparticles [6a]. Thiols form monolayer on gold surface [18] and highly stable nanoparticles could be obtained. Purification of nanoparticles can be carried out, which makes chemical method of metal nanoparticles a real process for nanomaterial preparation. Various thiol derivatives have been used to functionalize metal nanoparticles [6b, 19]. Cationic and anionic thiol compounds were used to obtain hydrosols of metal nanoparticles. Quaternary ammonium-thiol compounds make the nanoparticle surface highly positively charged [20]. In such cases, cationic nanoparticles were densely adsorbed onto oppositely charged surfaces. DNA or other biomolecule-attached gold nanoparticles have been proposed for biosensors [21].

In this study, three α,ω-alkenethiols (ω-alkene-1-thiol compounds) were used as the stabilizing reagent of gold nanoparticles (Figure 3).

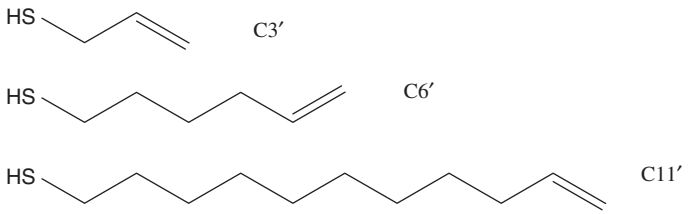

Figure 3. Structures of α,ω-alkenethiols used for immobilization of gold nanoparticles.

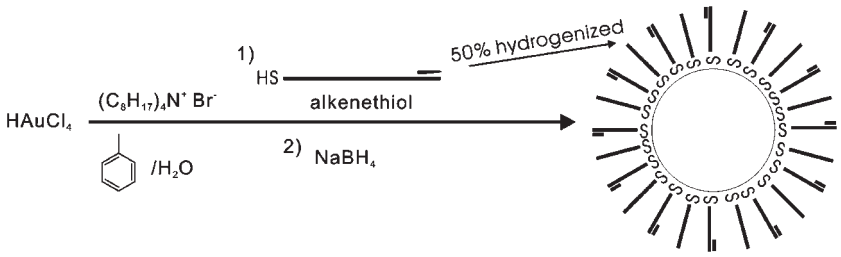

Figure 4. Preparative procedure of alkene thiol-stabilized gold nanoparticles. 50% of hexenethiol bounded to the particle surface is hydrogenated to hexanethiol [11b].

5-Hexene-1-thiol (C6′) and 10-undecene-1-thiol (C11′) were synthesized from the corresponding alkenyl bromide substrates according to the well-known thiourea route with relatively good yield (34 and 83%, respectively). Allylthiol (C3′) was used as received. The preparative process was the two-phase $NaBH_4$-reduction of $AuCl_4^-$ ions in the presence of stabilizing thiols. Allylthiol-stabilized gold nanoparticles were prepared by the ligand-change process following the $NaBH_4$ reduction in the presence of propane thiol. The yields of the C6′ and C11′-stabilized nanoparticles in dry form were relatively high, 78% and 80%, respectively [11].

3. Characterization of Metal Nanoparticles

Sizes or structures of metal nanoparticles are usually carried out by TEM measurements. The gold nanoparticles obtained in this study are relatively unique. Unfortunately, allylthiol-stabilized gold nanoparticles were slightly larger than other nanoparticles. It can be attributed to the low-stabilization ability of allylthiol molecules according to the very short molecular lengths. TEM observation provides direct evidence of the size and morphology of the particles, and is indispensable for nanoparticle study. Other systems, such as XRD spectrum with Sherrer's equation, dynamic light scattering, can also be used in order to determine nanoparticle sizes. However, TEM images are quite useful because it is a clear evidence of the size and crystallinity. Seeing is believing.

NMR measurements are very useful to understand the properties of the stabilizing reagents of metal nanoparticles. Author's group reported the structure of stabilization of non-ionic and cationic surfactants on platinum nanoparticles [22] and that of ternary amines on rhodium nanoparticles [23]. Such information is considerably important for applications of nanoparticles such as nanoparticle catalysis or nanoparticle assembling. For example, the stabilizing structures of non-ionic surfactant and cationic surfactants are considerably different. In the case of non-ionic surfactant, hydrophobic parts are strongly adsorbed onto nanoparticle surface.

In this study, ^1H NMR measurement has been carried out with the obtained samples in order to assess their purity as well as the saturation ratio of the terminal C=C double bonds of the stabilizing reagents: α,ω-alkenethiols. The obtained nanoparticles after purification were redispersed into deuterized solvents. The ^1H NMR spectra of the nanoparticles obtained in this study showed broad peaks and no sharp NMR peaks of unbound (free) α,ω-alkenethiol molecules can be observed. The broadening of NMR peaks can be attributed to the longer relaxation times of protons of the bounded α,ω-alkenethiol molecules on nanoparticle surface, which show slow rotation of molecular bonds. Furthermore, the ^1H NMR of these nanoparticles can suggest the hydrogenation ratio of C=C unsaturated bonds which could be determined by comparing the integrated areas of the protons for the vinyl protons and the terminal methyl groups of alkanethiols. The obtained surface ratios of α,ω-alkenethiol/alkylthiol on C3′, C5′, and C11′-stabilized gold nanoparticles are 49/51, 50/50, and 83/17, respectively [11].

C5′- and C11′-stabilized gold nanoparticles were prepared by the same procedure, that is, reducing $AuCl_4^-$ in the presence of the corresponding α,ω-alkenethiols by $NaBH_4$ (Figure 4).

During this reduction process, C=C unsaturated bonds may be hydrogenised probably by H_2 generated during the decomposition of $NaBH_4$. A high C=C ratio was observed in the case of C11′-stabilized gold nanoparticles. Thiol-SAMs with a long alkyl chain may form a better-ordered structure on gold surface according to the strong intermolecular interaction. This may be the reason for this high C=C ratio.

4. Hydrogen-Terminated Silicon Surface

It is very clear that silicon is one of the most important materials in modern technologies, especially in electronics. Silicon is also one of most common element on the earth. Silicon surface is readily oxidized under ambient condition. A silicon substrate is covered by a silica (SiO_x) layer. This silica layer can be controlled easily by chemical reagents, heating, electrochemical treatment, and so on.

Hydrogen-terminated silicon surfaces are relatively active, but they can be handled even under ambient condition. Of course, it is much better if they are treated in an inert atmosphere in order to avoid any oxidation of the surface. The hydrogen-terminated silicon surface can be modified with organic monolayers with addition of some energy. Hydrogen-terminated silicon surface can be obtained readily by immersing as-received silicon wafer into a diluted HF solution. By this process, the oxide layer (SiO_x) is removed by F^- then the surface silicon atoms bond to hydrogen atoms. In order to obtain atomically flat surface, a more complicated process is applied. First, SiO_x layer is artificially generated in an oxygen atmosphere at high temperature. Then, HF treatment is carried out. After that, atomically flat surface is achieved by a treatment with a degassed NH_4F_{aq} (40%) for several minutes [24]. The formation of hydrogen-terminated Si surface can be confirmed by IR analysis.

5. Si–C Link Formation

In 1993, Linford firstly reported a quite useful method to prepare monolayers of alkyl chains by thermal hydrosilylation of hydrogen-terminated silicon surfaces [25]. Alkyl chains are covalently bound to Si surface by Si–C bonds. This thermal hydrosilylation could be attributed to a free-radical process with 1-alkene. First, a diacyl peroxide initiator was used to produce free radicals. However, at higher temperature, only hydrogen-terminated silicon and a neat solution of 1-alkene or 1-alkyne can form Si–C linkages [26]. Furthermore, lately it is found that such Si–C covalent links can be observed even in dilute solutions of 1-alkenes [27]. In that case, the density of monolayer packing strongly depends on the reaction temperature.

Also, photochemical approach can be used for hydrosilylation on hydrogen-terminated silicon. Light sources with a wavelength at ca. 350 nm can be employed for radical formation under degassed condition [28]. The monolayer packing density can be controlled by the wavelength of the irradiation. The shorter wavelength makes shorter irradiation time and forms more densely packed monolayers.

Hydrogen-terminated silicon has an effective functional surface for various applications. Si–C linked monolayers are highly stable because of its high bonding energy (Si–C 347 kJ/mol) [11b, 29]. The monolayer cannot be destroyed below 350 °C. Si–C monolayer covered surface has about 20 times static friction coefficient than that of an oxidized surface. Furthermore, Si–C linked monolayers show high stability against environmental humidity. Therefore, Si–C linked monolayers received much attention in various fields of Si applications, especially for MEMS (Micro Electro Mechanical Systems), stabilizers for silicon materials, electronic devices, etc.

Thermal hydrosilylation with dilute solutions of 1-alkenes can make Si–C based monolayers of organic molecules, which are in a powder form or nanomaterials, whose surface is covered by alkenes. Author's group proposed biomaterial arrays formed on hydrogen-terminated silicon surface. A hydrogen-terminated silicon surface has many advantages for biodevices or biosensors [30]. For example, such surface has an Angstrom-order flatness and a surface homogeneity. And it is easily prepared under ambient atmosphere, highly reproducible, and stable. Sugar derivatives have been selected to immobilize on Si wafers for biosensors. Sugars are very useful materials for sensing various biomolecules, however, one sugar molecule cannot show a high selectivity, but a cluster of sugar molecules play a good role to carbohydrate–protein-specific interactions. Such sugar-based biosensing tips are usually fabricated by a printing system (e.g., ink-jet). However, interactions for self-assembly are strongly affected by concentration and orientation of the sensor molecules. Such printing systems cannot control such molecular positioning. On the contrary, the Si–C covalent bonding monolayer system on hydrogen-terminated silicon substrate with an atomically flat surface is highly suitable for controlling molecular orientation and packing density. The molecular density on hydrogen-terminated silicon surface can be controlled by reaction temperature of hydrosilylation. Moreover, as Si–C bonds are covalent bonds, the molecules on the surface do not move, that is different from the thiols (S)–gold system.

The possibility of lithography on silicon surface is also very important. Patterning of Si–C-based monolayers can be readily carried out by using UV light irradiation (photolithography), electron beam, and cathodic electrografting by a scanning probe as well as anodic oxidation [31]. In the case of photolithography, the decomposition rate of the Si–C-based monolayer strongly depends on the wavelengths of the light source. After removing monolayers by such lithographic systems, the substrate surface is then covered by a SiO_x layer. This oxidation is highly important for fabrication of biosensors. SiO_x surface is highly hydrophilic and the static water-contact angle is of $< 5^\circ$. When patterned sugar-attached silicon wafer was immersed into lectin (RCA_{120}) solution, RCA_{120} molecules were clearly and specifically observed on sugar surface but on the SiO_x area, lectins were not observed [30]. When comparing the resistant ability against non-specific adsorption of lectins of SiO_x surface with a very well-known surface, PEG-SH-SAM on Au by using QCM (quartz crystal microbalance) measurement, SiO_x surface showed high-resistant ability as PEG-SAM [30b].

6. Immobilization of Gold Nanoparticles onto Hydrogen-Terminated Silicon Surface by Si–C Covalent Bonds

On such very useful hydrogen-terminated surfaces, immobilization of α,ω-alkenethiol-stabilized gold nanoparticles was carried out. The thermal hydrosilylation was selected for this immobilization. Under dry nitrogen

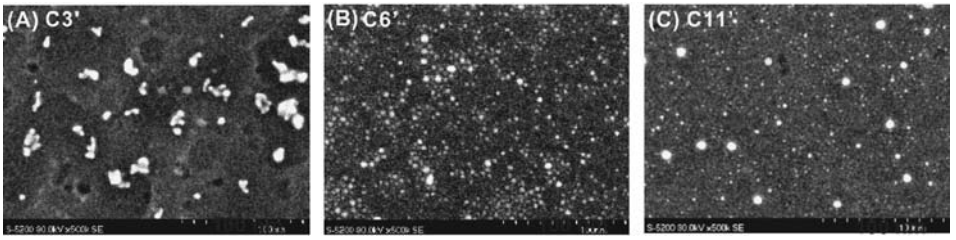

Figure 5. High-resolution SEM images of the Si surface covalently linked to the nanoparticles stabilized by (A) C3′, (B) C6′, and (C) C11′. (Reprinted with permission from Ref. [11a], © 2004, American Chemical Society.)

atmosphere, into a degassed toluene dispersion of the obtained gold nanoparticles at a relatively high concentration (30 mg/10 cm^3), hydrogen-terminated silicon wafers were introduced. The dispersion was kept stirred and heated at 50 °C for 24 h. The functionalized substrate was then rinsed with toluene under sonication and dried with a nitrogen flow.

Before testing this procedure, the dispersion was kept heating at higher temperature. Then, the particles were fused on the surface. Therefore, this low-reaction temperature (50 °C) was selected for hydrosilylation but longer reaction time was applied. The surface was analyzed by HR-SEM as well as XPS.

Gold nanoparticles can be clearly observed as white dots and silicon wafers are black in HR-SEM images of the gold nanoparticles-immobilized silicon surface. When immobilizing the allylthiol (C3′, $HS–CH_2–CH=CH_2$)-stabilized gold nanoparticles, even the reaction temperature was as low as 50 °C, the white dots with diameters about 10–40 nm are observed (Figure 5A).

This can be probably due to the short chain thiols used for stabilization. However, in dispersion, allylthiol-stabilized gold nanoparticles did not show any fusion. Similar situation was already reported. Thiocholine bromide ($HS–CH_2–CH_2–N(CH_3)_3^+$ Br^-)-stabilized gold nanoparticles were also fused immediately when they were densely adsorbed on bundles of DNA molecules even when they were stably dispersed in water for months [20a]. Traditional Ostwald ripening may be a possible explanation of this fusion of the gold nanoparticles on the surface. Also, the melting temperature of gold nanoparticles depends on the particle size and it becomes much lower when the particle size is very small [32]. However, fusion of nanoparticles on DNA was not observed in the case of palladium. On the other hand, C6′-SH or C11′-SH-stabilized gold nanoparticles could be immobilized independently on hydrogen-terminated silicon surfaces by thermal hydrosilylation at 50 °C (Figure 5B, C). All three types of gold nanoparticles do not show clear size growth at 50 °C in the dispersed media.

Formation of Si–C covalent bonds between gold nanoparticles and hydrogen-terminated silicon surface was revealed by XPS observation. However, the surfaces of the gold nanoparticles are fully covered by α,ω-alkenethiol molecules, XPS signals from Si–C covalent bonds were too small to be detected. Therefore, the gold nanoparticles should have been removed from the surface without detaching α,ω-alkenethiol molecules covalently attached to the silicon surface. For that purpose, ligand-exchange method was applied. After removing the particles completely, the XPS peak at C(1 s) can be fitted with two peaks corresponding to C–Si and C–C. This ligand-exchange technique may be useful to determine the surface condition by XPS [11b].

7. Conclusion

Wet preparation of metal nanoparticles and their covalent immobilization onto silicon surface has been surveyed in this manuscript. Thiol–metal interaction can be widely used in order to functionalize the surface of metal nanoparticles by SAM formation. Various thiol molecules have been used for this purpose. The obtained functionalized particles can be purified to avoid the effect of unbounded molecules. On the other hand, hydrogen-terminated silicon surface is a good substrate to be covered by Si–C covalently bonded monolayer and can be functionalized readily by this link formation. Nanomaterials, such as biomolecules or nanoparticles, can be immobilized onto silicon surface by applying this monolayer formation system.

References

1 (a) K. J. Klabunde, *Nanoscale Materials in Chemistry*, Wiley-Interscience, NY, 2001; (b) M. Köhler, W. Fritzsche, *Nanotechnology*, Wiley-VCH, Weinheim, 2004.
2 (a) G. Schmid (ed.) *Nanoparticles*, Wiley-VCH, Weinheim, 2004; (b) G. Schmid (ed.) *Colloids and Clusters*, Wiley-VCH, Weinheim, 1994; (c) F. Caruso (ed.) *Colloids and Colloid Assemblies*, Wiley-VCH, Weinheim, 2003; (d) T. Yonezawa, in Y. Waseda, A. Muramatsu (eds.) Well-dispersed bimetallic nanoparticles, *Morphology Control of Materials and Nanoparticles*, Springer-Verlag, New York, 2003, 85; (e) T. Yonezawa, N. Toshima, in H. S. Nalwa (ed.) Polymer-stabilized metal nanoparticles, *Advanced Functional Molecules and Polymers*, Gordon and Breach, London, 2001, 65; (f) G. Schmid, *Chem. Rev.* 92 (1992) 1709; (g) G. Schmid, M. Bäumle, M. Greekens, I. Heim, C. Osemann, T. Sawitowski, *Chem. Soc. Rev.* 28 (1999) 179.
3 H. Hirai, N. Toshima, in Y. Iwasawa (ed.) *Tailored Metal Catalysts*, D. Reidel Publishing Co., Dordrecht, 1986, 121.
4 M. Faraday, *Philos. Trans. R. Soc. London* 7 (1857) 145.
5 M. A. Hayat (ed.) *Colloidal Gold*, Vol. I–III, Academic Press, New York, 1989.
6 (a) M. Brust, M. Walker, D. Bethell, D. J. Schiffrin, R. Whyman, *J. Chem. Soc., Chem. Commun.* (1994) 804; (b) M. Brust, J. Fink, D. Bethell, D. J. Schiffrin, C. Kiely, *J. Chem. Soc., Chem. Commun.* (1995) 1655.

7 a) D. Y. Petrovykh, F. J. Himpsel, in H. S. Nalwa (ed.) Self-assembled nanostructures on silicon surface, *Encyclopedia of Nanoscience and Nanotechnology*, Vol. 9, American Scientific Publishers, California, 2004, 497.

8 (a) J. M. Buriak, *Chem. Rev.* 102 (2002) 1271; (b) N. Shirahata, A. Hozumi, T. Yonezawa, *Chem. Rec.* 5 (2005) 145.

9 M. P. Stewart, J. M. Buriak, *Angew. Chem. Int. Ed. Engl.* 23 (1998) 3257.

10 (a) Z. M. Fresco, J. M. Fréchet, *J. Am. Chem. Soc.* 127 (2005) 8302; (b) C. F. Chen, S. D. Tzeng, M. H. Lin, S. Gwo, *Langmuir* 22 (2006) 7819; (c)T. Zhu, X. Fu, T. Mu, J. Wang, Z. Liu, *Langmuir* 15 (1999) 5197; (d) R. H. Tian, T. N. Rao, Y. Einaga, J. F. Zhi, *Chem. Mater.* 18 (2006) 939; (e) S. Nakao, K. Torigoe, K. Kon-no, T. Yonezawa, *J. Phys. Chem. B* 106 (2002) 12097; (f) J. Zheng, Z. Zhu, H. Chen, Z. Liu, *Langmuir* 16 (2000) 4409.

11 (a) Y. Yamanoi, T. Yonezawa, N. Shirahata, H. Nishihara, *Langmuir* 20 (2004) 1054; (b) Y. Yamanoi, N. Shirahata, T. Yonezawa, N. Terasaki, N. Yamamoto, Y. Matsui, K. Nishio, H. Masuda, Y. Ikuhara, H. Nishihara, *Chem. Eur. J.* 12 (2006) 314.

12 (a) C. Qin, S. Coulombe, *Mater. Lett.* 60 (2006) 1973; (b) R. Fernandez-Pacheco, M. Arruebo, C. Marquina, R. Ibarra, J. Arbiol, J. Santamaria, *Nanotechnology* 17 (2006) 1188; (c) Z. Q. Wei, T. D. Xia, L. F. Bai, J. Wang, Z. G. Wu, P. X. Yan, *Mater. Lett.* 60 (2006) 770.

13 (a) K. Esumi, M. Suzuki, T. Tano, K. Torigoe, K. Meguro, *Colloids Surf.* 55 (1991) 9; (b) K. Esumi, O. Sadakane, K. Torigoe, K. Meguro, *Colloids Surf.* 62 (1992) 255; (c) K. Esumi, T. Tano, K. Meguro, *Langmuir* 5 (1989) 268.

14 (a) N. Toshima, Y. Wang, *Chem. Lett.* (1993) 1611; (b) Y. Wang, H. Liu, N. Toshima, *J. Phys. Chem.* 100 (1996) 19533; (c) P. Lu, N. Toshima, *Bull. Chem. Soc. Jpn.* 73 (2000) 751; (d) P. Lu, T. Teranishi, K. Asakura, M. Miyake, N. Toshima, *J. Phys. Chem. B* 103 (1999) 9673; (e) Y. Gao, P. Jiang, D. F. Liu, H. J. Yuan, X. Q. Yan, Z. P. Zhou, J. X. Wang, L. Song, L. F. Liu, W. Y. Zhou, G. Wang, C. Y. Wang, S. S. Xie, *Chem. Phys. Lett.* 380 (2003) 146.

15 H. Hirai, H. Wakabayashi, M. Komiyama, *Bull. Chem. Soc. Jpn.* 59 (1986) 367.

16 H. Tsunoyama, Y. Negishi, T. Tsukuda, *J. Am. Chem. Soc.* 128 (2006) 6036.

17 G. Schmid, R. Pfeil, R. Böse, F. Bandermann, S. Meyer, G. H. M. Calis, J. W. A. van der Valden, *Chem. Ber.* 114 (1981) 3634.

18 A. Ulman, *Chem. Rev.* 96 (1996) 1533.

19 (a) T. Yonezawa, S. Onoue, N. Kimizuka, *Stud. Surf. Sci. Catal.* 132 (2001) 623; (b) T. Yonezawa, K. Yasui, N. Kimizuka, *Langmuir* 17 (2001) 271; (c) T. Yonezawa, H. Matsune, N. Kimizuka, *Adv. Mater.* 15 (2003) 499; (d) S. Chen, K. Kimura, *Langmuir* 15 (1999) 1075; (e) T. Teranishi, A. Sugawara, T. Shimizu, M. Miyake, *J. Am. Chem. Soc.* 124 (2003) 4210; (f) I. Quiros, M. Yamada, K. Kubo, J. Mizutani, M. Kurihara, H. Nishihara, *Langmuir* 18 (2002) 1413.

20 (a) T. Yonezawa, S. Onoue, N. Kimizka, *Chem. Lett.* (2002) 1172; (b) T. Yonezawa, S. Onoue, T. Kunitake, *Kobunshi Ronbunshu* 56 (1999) 855; (c) T. Yonezawa, S. Onoue, N. Kimizuka, *Langmuir* 16 (2000) 5218; (d) M. G. Warner, J. E. Hutchison, *Nature Mater.* 2 (2003) 232; (e) A. Y. Koyfman, G. Braun, S. Magonov, A. Chworos, N. O. Reich, L. Jaeger, *J. Am. Chem. Soc.* 127 (2005) 11886.

21 (a) A. Y. Soohyoun, T. R. Decory, A. J. Baemner, R. A. Durst, *Anal. Chem.* 75 (2003) 2256; (b) H. Ohtsuka, Y. Akiyama, Y. Nagasaki, K. Kataoka, *J. Am. Chem. Soc.* 123 (2001) 8226; (c) D. C. Hone, A. H. Haines, D. A. Russell, *Langmuir* 19 (2003) 7141; (d) C. A. Mirkin, R. L. Letsinger, R. C. Mucic, J. J. Storhoff, *Nature* 382 (1996) 607; (e) A. P. Alivisatos, K. P. Johnsson, X. Peng, T. E. Wilson, C. J. Loweth, M. P. Brochez, P. G. Schultz, *Nature* 382 (1996) 609; (f) Y. C. Cao, R. Jin, C. A. Mirkin, *Science* 297 (2002) 1536.

22 (a) T. Yonezawa, Y. Gotoh, N. Toshima, *Chem. Express* 8 (1993) 545; (b) T. Yonezawa, Y. Gotoh, N. Toshima, *React. Polym.* 23 (1994) 43; (c) T. Yonezawa, T. Tominaga, N. Toshima, *Langmuir* 11 (1995) 4601.

23 T. Yonezawa, T. Tominaga, D. Richard, *J. Chem. Soc., Dalton Trans.* (1996) 783.

24 (a) G. S. Higashi, Y. J. Chabal, G. W. Trucks, K. Raghavachari, *Appl. Phys. Lett.* 56 (1990) 656; (b) C. P. Wade, C. E. D. Chidsey, *Appl. Phys. Lett.* 71 (1997) 1679.

25 M. R. Linford, C. E. D. Chidsey, *J. Am. Chem. Soc.* 115 (1993) 12631.

26 M. R. Linford, C. E. D. Chidsey, P. Fenter, P. M. Eisenberger, *J. Am. Chem. Soc.* 117 (1995) 3145.

27 N. Shirahata, T. Yonezawa, W. S. Seo, K. Koumoto, *Langmuir* 20 (2004) 1517.

28 R. L. Cicero, M. R. Linford, C. E. D. Chidsey, *Langmuir* 16 (2000) 5688.

29 R. T. Sanderson, *Chemical Bonds and Bond Energy*, Academic Press, New York, 1976.

30 (a) N. Shirahata, T. Yonezawa, Y. Miura, K. Kobayashi, K. Koumoto, *Langmuir* 19 (2003) 9107; (b) N. Shirahata, A. Hozumi, Y. Miura, K. Kobayashi, Y. Sakka, T. Yonezawa, *Thin Solid Films* 499 (2006) 213.

31 (a) F. Effenberger, G. Götz, B. Bidlingmaier, M. Wezstein, *Angew. Chem. Int. Ed. Engl.* 37 (1998) 2462; (b) N. Saito, K. Hayashi, H. Sugimura, O. Takai, *Jpn. J. Appl. Phys.* 42 (2003) 2534; (c) M. Ara, H. Graaf, H. Tada, *Appl. Phys. Lett.* 80 (2002) 2565; (d) M. Ara, H. Tada, *Appl. Phys. Lett.* 83 (2003) 578.

32 (a) P. A. Buffat, J. P. Borel, *Phys. Rev., A* 13 (1976) 2287; (b) T. Castro, R. Reifenberger, E. Choi, R. P. Andres, *Phys. Rev. B* 42 (1990) 8548.